UTS UNIVERSITY OF TECHNOLOGY SYDNEY

Evaluating High-Resolution Site Characterisation Tools and Multiphase Modelling to Predict LNAPL Distribution and Mobility

by Jonás García Rincón

Thesis submitted in fulfilment of the requirements for the degree of

Doctor of Philosophy

under the supervision of Dr. Robert G. McLaughlan (UTS) and Mr. John L. Rayner (CSIRO)

University of Technology Sydney
Faculty of Engineering and Information Technology

August 2020

Certificate of original authorship

I, Jonás García Rincón declare that this thesis, is submitted in fulfilment of the requirements for the award of Doctor of Philosophy, in the Faculty of Engineering and Information Technology at the University of Technology Sydney.

This thesis is wholly my own work unless otherwise referenced or acknowledged. In addition, I certify that all information sources and literature used are indicated in the thesis.

This document has not been submitted for qualifications at any other academic institution.

This research is supported by the Australian Government Research Training Program.

Production Note:
Signature: Signature removed prior to publication.

Date: 10th of August of 2020.

Acknowledgements

CRC CARE (Cooperative Research Centre for Contamination Assessment and Remediation of the Environment), whose activities are funded by the Australian Government's Cooperative Research Centres Programme, has supported this research as part of the project 'Endpoints for Petroleum LNAPL Remediation—Technology Performance and Risk Reduction' in collaboration with University of Technology Sydney and the Commonwealth Scientific and Industrial Research Organisation (CSIRO) Land and Water Flagship. The continued assistance and cooperation of the site owners are greatly appreciated as well as the participation of eDrill for the installation of monitoring points and Numac for the high-resolution site characterisation (HRSC) campaign.

My supervisors Robert G. McLaughlan (University of Technology Sydney) and John L. Rayner (CSIRO Land and Water) have provided constant help and valuable feedback throughout the development of the thesis. Both have participated in the collection and analysis of field data, with John leading most of the field campaigns. Additionally, they have co-authored most of the publications associated to the thesis. Colin D. Johnston gave me the opportunity of joining the Pollutant Fate and Remediation Team in January 2015 and supervised my work during the first year at CSIRO.

Robert J. Lenhard has also provided constant support, advice, and direction since he joined CSIRO. Furthermore, Bob developed one of the multiphase models evaluated in the thesis (LNAPLTRANS). To date, we have co-authored one journal paper (Lenhard et al., 2019) and one conference poster (García-Rincón et al., 2018).

Greg B. Davis (CSIRO Land and Water) has been equally indispensable for the completion of this dissertation and the Endpoints for Petroleum LNAPL Remediation project as the leader of the Contaminants & Biotechnology Program until July 2020. We have co-authored two journal papers (Gatsios et al., 2018b; García-Rincón et al., 2020).

Evangelos Gatsios participated in practically all the field campaigns in the petrol station site since 2014 and we have extensively collaborated in the analysis of field data. In particular, the interpretation of baildown tests was a central part of his doctoral

dissertation (Gatsios, 2018) and we worked together in the assessment of LNAPL confinement conditions (with my analyses being presented in section 5.2). We have co-authored most of publications associated to our theses.

Elise B. Bekele (CSIRO Land and Water) contributed to the analysis and management of field data in several ways. In particular, she improved the format of databases containing field data and updated them after every field campaign. Furthermore, she chose samples from the petrol station site for a second round of particle-size analyses and was involved in the interpretation of methods to quantify water-saturated hydraulic conductivity k_{sw}. More specifically, she conducted analyses of aquifer test data with the software AQTESOLV presented in section 5.2.3, updating and improving some of my initial calculations. We have co-authored one report (Bekele et al., 2019).

Robert Woodbury set up a new soil physics laboratory and assisted in the measurement of LNAPL physical properties. Furthermore, he regularly assisted in the instrumentation, characterisation, and monitoring of the field sites along with other CSIRO Land and Water staff such as Gabriel Paiva Lago, Andrew Furness, Mike Donn, and Geoffrey Puzon. Trevor Bastow and Yasuko Geste assisted in the preparation and chemical analysis of the samples. Other current and former CSIRO staff (Rodrigo Rojas, Mike Trefry, Kaveh Sookhak Lari, Greg Lekmine, John Knight, Jungho Park) have provided valuable input and fruitful discussions.

Michael Rivett (University of Strathclyde and GroundH2O Plus), Andrew Kirkman (BP), Randy St. Germain (Dakota Technologies), and several anonymous reviewers provided excellent comments that contributed to enhance the quality of the doctoral dissertation and/or journal papers.

Finally, I would like to thank my family and friends for their patience, support, and encouragement all these years.

List of publications

Peer-reviewed journal papers

García-Rincón, J., Gatsios, E., Rayner, J.L., McLaughlan, R.G., Davis, G.B. (2020). Laser-induced fluorescence logging as a high-resolution characterisation tool to assess LNAPL mobility. Science of the Total Environment, 725, Article 138480. Impact factor (2019): 6.551.

Lenhard, R.J., Rayner, J.L., García-Rincón, J. (2019). Testing an analytical model for predicting subsurface LNAPL distributions from current and historic fluid levels in monitoring wells: A preliminary test considering hysteresis. Water, 11, Article 2404. Impact factor (2018): 2.524.

Gatsios, E., García-Rincón, J., Rayner, J.L., McLaughlan, R.G., Davis, G.B. (2018). LNAPL transmissivity as a remediation metric in complex sites under water table fluctuations. Journal of Environmental Management, 215, 40–48. Impact factor (2017): 4.005.

Martínez-Santos, P., Martín-Loeches, M., García-Castro, N., Solera, D., Díaz-Alcaide, S., Montero, E., García-Rincón, J. (2017). A survey of domestic wells and pit latrines in rural settlements of Mali: implications of on-site sanitation on the quality of water supplies. International Journal of Hygiene and Environmental Health, 220(7), 1179–1189. Impact factor (2017): 4.848.

Technical reports

Bekele, E.B., García-Rincón, J., Rayner, J.L., McLaughlan, R.G., Gatsios, E., Paiva Lago, G. (2019). Groundwater pumping test analyses for a gasoline contaminated site at Donnybrook, Western Australia. Commonwealth Scientific and Industrial Research Organisation.

Conference presentations, papers, and posters

García-Rincón, J., Gatsios, E., Rayner, J.L., McLaughlan, R.G. (2020, March). High-resolution vertical profiling in challenging subsurface settings [Conference session]. High Resolution Characterisation Conference, Sydney, NSW, Australia.

Gatsios, E., García-Rincón, J., Rayner, J.L. (2018, September). LNAPL transmissivity: comparison of theoretical, field and modelling estimations in a multi-layered aquifer in Western Australia [Paper presentation]. 6th International Conference on Industrial and Hazardous Waste Management, Chania, Greece.

García-Rincón, J., Gatsios, E., Rayner, J.L., Lenhard, R.J. (2018, May). Comparison of analytical models to estimate LNAPL distribution and transmissivity in a heterogeneous site [Poster presentation]. New Zealand 5th Contaminated Land Conference, Christchurch, New Zealand.

García-Rincón, J., Johnston, C.D., McLaughlan, R.G. (2015, September). Multiphase modelling of LNAPL remediation options in aquifers with complex geologies [Poster presentation]. CleanUp 2015: 6th International Contaminated Site Remediation Conference, Melbourne, VIC, Australia.

Table of contents

Certificate of original authorship i

Acknowledgements ii

List of publications iv

Peer-reviewed journal papers iv

Technical reports iv

Conference presentations, papers, and posters iv

Table of contents vi

List of illustrations xiii

List of tables xxix

Nomenclature and acronyms xxxiv

Abstract xl

1 Introduction 1

1.1 Significance of the problem 1

1.2 Research objectives 2

1.3 Contribution to knowledge 3

1.4 Thesis outline 4

2 Literature review 8

2.1 LNAPL contamination in the subsurface 8

2.1.1 Subsurface environments 8

2.1.2 LNAPL contamination 8

2.1.3 Chemical composition 9

2.1.4 Density 10

2.1.5 Interfacial tensions and wettability 11

2.1.6 Capillary pressure and hysteretic effects 12

2.1.7 Retention models 15

2.1.8 Mobile and near-immobile NAPL 17
2.1.9 Relative permeability 21
2.2 LNAPL source zone characterisation 22
2.2.1 Field-scale LNAPL distribution 22
2.2.2 Field-scale LNAPL mobility 29
2.2.3 Field delineation of LNAPL distribution 33
2.2.4 High-resolution site characterisation 38
2.3 Partitioning and degradation of petroleum hydrocarbons 45
2.3.1 Overview of natural source zone depletion phenomena 45
2.3.2 Souce zone longevity 48
2.3.3 Partitioning 48
2.3.4 Biological processes and degradation 53
2.3.5 Diagnostic ratios and forensic investigations 55
2.4 Transport in heterogeneous media 55
2.4.1 Main transport mechanisms 55
2.4.2 Scaling issues in subsurface systems 56
2.4.3 Heterogeneous permeability fields 57
2.4.4 Preferential migration pathways 58
2.4.5 Low-permeability zones and diffusion 59
2.5 Modelling approaches 60
2.5.1 Numerical modelling 60
2.5.2 Stochastic frameworks 61
2.5.3 Analytical solutions 62
2.5.4 Model evaluation approaches and types of uncertainty 63
2.5.5 Parametric uncertainty and sensitivity analysis methods 64
2.5.6 Structural and conceptual site model uncertainty 65
2.6 Summary of the literature review and research gaps 65
3 Characteristics of the field sites 68
3.1 Characteristics of the petrol station site 68
3.1.1 Location and climate 68
3.1.2 Land use and potential receptors 68
3.1.3 Topographic and hydraulic gradients 69
3.1.4 Hydrogeological setting 70

3.1.5 Contaminant release, distribution and mobility 71
3.1.6 Justification of the site selection 72
3.2 Characteristics of the industrial site 75
3.2.1 Location and climate 75
3.2.2 Land use and potential receptors 75
3.2.3 Hydrogeological setting 75
3.2.4 Contaminant releases and distribution 75
3.2.5 Justification of the site selection 76
4 Materials and methods 77
4.1 Rationale for the research design 77
4.2 Well installation, sampling and analysis 81
4.2.1 Drilling and installation of monitoring points 81
4.2.2 Coring locations 84
4.2.3 Coring process 86
4.2.4 Soil gas screening and sample preparation 88
4.2.5 Chemical analysis 92
4.2.6 Estimation of bulk density, porosity, and LNAPL saturation 94
4.2.7 LNAPL, groundwater, and vapour samples 96
4.3 Monitoring campaigns 97
4.3.1 Main characteristics of the monitoring campaigns 97
4.3.2 Fluid level monitoring 98
4.3.3 Quality and variability of fluid level measurements 99
4.3.4 Single-well LNAPL diagnostic gauge plots 101
4.3.5 Multi-well LNAPL diagnostic gauge plots 105
4.4 Ultra-Violet Optical Screening Tool (UVOST®) 105
4.4.1 UVOST® technology 105
4.4.2 LIF logging campaigns 111
4.4.3 LIF metrics 113
4.4.4 Subtraction of natural fluorescence of the geological medium 114
4.4.5 LIF data interpolation 117
4.5 Hydraulic Profiling Tool (HPT) 118
4.5.1 HPT technology 118
4.5.2 HPT data collection 123

4.5.3 Dissipation tests 125
4.5.4 Interpolation of HPT logs 127
4.5.5 Determination of aquifer heterogeneity 128
4.6 Hydraulic testing 129
4.6.1 Overview of hydraulic tests conducted in the petrol station site 129
4.6.2 Aquifer testing 130
4.6.3 Baildown testing 134
4.7 Particle-size data correlations 139
4.7.1 Correlations of hydraulic conductivity with particle-size data 139
4.7.2 Prediction of retention parameters 144
4.7.3 Neural network predictions 148
4.8 Multiphase analytical models 150
4.8.1 LNAPLTRANS 150
4.8.2 LDRM 152
4.8.3 Design of modelling scenarios 153
4.8.4 Model testing and comparison 153
4.8.5 Sensitivity analysis of multiphase analytical models 154
4.9 Statistical data analysis procedures 156
5 Identification of hydrostratigraphic layers and confinement conditions 160
5.1 Chapter structure 160
5.2 Petrol station site 161
5.2.1 Particle-size analysis 161
5.2.2 Hydrographs 168
5.2.3 Aquifer testing 172
5.2.4 Baildown testing 180
5.2.5 Analysis of LNAPL diagnostic gauge plots 182
5.2.6 HPT logging 192
5.2.7 Summary of results and conclusions 201
5.3 Industrial site. Areas T3/T4 205
5.3.1 Particle-size analysis 205
5.3.2 Hydrographs 207
5.3.3 Analysis of LNAPL diagnostic gauge plots 209

5.3.4 HPT logging 211
5.3.5 Summary of results and conclusions 217
6 Laser-induced fluorescence (LIF) logging of LNAPL distribution and mobility 218
6.1 Chapter structure 218
6.2 Overview of LIF profiles and their relationship with LNAPL mobility 218
6.2.1 Section structure 218
6.2.2 Overview of logs with weak LIF response 219
6.2.3 Relationship between LIF response and LNAPL distribution and mobility 221
6.3 Multi-wavelength waveforms and identification of near-immobile LNAPL 229
6.3.1 LNAPL signatures and correlation between excitation channels 229
6.3.2 Identification of long-term near-immobile LNAPL in the petrol station site 233
6.4 Comparison of LIF and coring in the areas of study 237
6.4.1 Section structure 237
6.4.2 LNAPL distribution in adjacent coring and LIF locations 237
6.4.3 Petrol station site. Area A 240
6.4.4 Petrol station site. Area B 253
6.4.5 Petrol station site. Area C 262
6.4.6 Industrial site. Area T3/T4 274
6.5 Summary of results and conclusions 283
7 Quantification of subsurface parameters 287
7.1 Chapter structure 287
7.2 Literature values 287
7.2.1 Porosity 287
7.2.2 Hydraulic conductivity 290
7.2.3 Retention parameters 292
7.3 Petrol station site 294
7.3.1 Porosity 294
7.3.2 Hydraulic conductivity 298
7.3.3 Retention parameters 328
7.3.4 LNAPL properties 336
7.3.5 LNAPL transmissivity 337
7.4 Industrial site 348

7.4.1 Porosity 348
7.4.2 Hydraulic conductivity 357
7.4.3 Retention parameters 375
7.4.4 LNAPL properties 393
7.4.5 LNAPL transmissivity 398
7.5 Summary of results and conclusions 398
8 Evaluation of multiphase analytical models 400
8.1 Chapter structure 400
8.2 Base-case scenarios 400
8.2.1 Summary of base-case scenarios 400
8.2.2 Calibration issues 401
8.2.3 Relative permeability models and residual LNAPL saturation options 403
8.2.4 Comparison between LNAPLTRANS and LDRM 406
8.3 Layering implications on LNAPL distribution and recoverability 411
8.3.1 Comparison with preliminary tests in area T4 411
8.3.2 LNAPL distribution predictions in fining-upward sequences 413
8.4 Sensitivity analysis 415
8.4.1 Summary of parameter ranges 415
8.4.2 Computation of sensitivity indices 417
8.4.3 Analysis of best- and worst-case scenarios 421
8.5 Summary of modelling results and conclusions 422
9 Conclusions and future lines of research 423
9.1 Conclusions 423
9.2 Limitations and future lines of research 426
10 References 428
Appendix A: Publications A-1
Appendix B: Maps B-1
Appendix C: UVOST® profiles C-1
Appendix D: HPT profiles D-1
Appendix E: Particle-size data and correlations with hydraulic conductivity E-1

Appendix F: Retention curves F-1

Appendix G: Computation of sensitivity indices G-1

List of illustrations

Fig. 2.1. Simplified representation of some key features influencing NAPL fate and transport in porous systems (after Mackay and Cherry, 1989; Rivett et al., 2011). EPS stands for extracellular polymeric substances. 11

Fig. 2.2. Retention curves, showing main and intermediate NAPL drainage and imbibition paths (Johnston and Adamski, 2005). 13

Fig. 2.3. Typical effects of median particle size and breadth of the particle-size distribution on P_c–S curves and vG retention parameters (modified after Benson et al., 2014). 16

Fig. 2.4. Visualisation of LNAPL distribution in the unsaturated and saturated zones with fluorescence (after Skinner, 2013; Tracy, 2015; M. Tracy, personal communication, April 2019). 20

Fig. 2.5. VEQ model predictions of LNAPL vertical distribution in a hypothetical soil according to vG and B–C relationships (adapted from Lenhard and Parker, 1990a). 25

Fig. 2.6. Field measured S_n values versus predictions from the VEQ model for one and multiple layers in a fine-grained sandstone (adapted from Beckett and Huntley, 2015). 26

Fig. 2.7. Field redistribution of LNAPL under changes in z_{aw} (modified after Tomlinson et al., 2012).....27

Fig. 2.8. Sources of variability of T_n (Gatsios et al., 2018b).....30

Fig. 2.9. Comparison of trichloroethylene concentration profiles as analysed through cryogenic HSA in 2014 and conventional HSA in 2010 (modified after Sale et al., 2016). 38

Fig. 2.10. Variability of k_{sw} estimations from methods with different support (Vienken, 2011). 39

Fig. 2.11. Main processes and factors affecting NSZD (Sookhak Lari et al., 2019). 46

Fig. 2.12. Permeability connected and disconnected fields with identical probability distribution functions and near identical variograms (adapted from Renard and Allard, 2013, after Zinn and Harvey, 2003). 59

Fig. 2.13. Simulations of b_n after periods of LNAPL redistribution and recovery operations in (a) homogeneous, and (b) heterogeneous uniform scenarios. Selected subsurface properties exhibited a correlation scale of 3.66 m (adapted from Waddill and Parker, 1997b). 62
Fig. 3.1. Climate data collected from the SILO database corresponding to the town where the field site was located. All the values were averaged between 1970 and 2015. *Tmax* stands for maximum temperature, while *Tmin* is minimum temperature. 68
Fig. 3.2. Topographic and groundwater hydraulic gradients (averages of 20–21 records from 2014 to 2018) between perimeter wells. Gradients from the first well of the pair to the second well. 69
Fig. 3.3. Groundwater hydraulic gradients considering multiple well pairs in the petrol station site. 70
Fig. 3.4. Simplified CSM of the petrol station site including (a) low z_{aw} at an initial time t_0 and (b) high z_{aw} at time t_1. It depicts the stratigraphy (aquitard–aquifer–aquitard), UST location (in red), mobile LNAPL body (in purple), areas A, B and C, and illustrative in-well fluid columns of water (W), LNAPL (N) and air (A). 74
Fig. 4.1. Coring locations in area T4 (adapted from Johnston et al., 2010). Well IDs NS7A and NS7B refer to long-screened installations. 85
Fig. 4.2. Labelled tins and cores recovered at MP10 in the petrol station site. 87
Fig. 4.3. Drill cuttings and tins obtained every 0.5 m at PB29-A 88
Fig. 4.4. Soil gas measurements of tins containing core samples 89
Fig. 4.5. Collecting potential subsamples for TPH analysis with a small tubular sampler (a) and samples for screening delineation of LNAPL contamination (soil gas) with disposable syringes (b). 90
Fig. 4.6. Bags containing samples for soil gas analysis. 91
Fig. 4.7. Setting for the preparation of subsamples including a solvent dispenser, a precision scale and labelled glass tubes. 92
Fig. 4.8. S_n values derived from air-dried and oven-dried samples at C66-T3 95
Fig. 4.9. Measurement of in-well fluid levels with an interface probe at MP30. 98
Fig. 4.10. Potential errors in the computation of z_{aw} derived from assuming a ρ_{rn} of 0.7378 instead of 0.8053 (extreme value measured at PB12-C). 100

Fig. 4.11. Emulsion of LNAPL and water after a hydraulic test using an electric pump. 101
Fig. 4.12. Behaviour of fluid interfaces under unconfined, confined, and perched LNAPL conditions (modified after Sale et al., 2018).....102
Fig. 4.13. Correspondence between the concepts of wavelength-time matrix (top) and multi-wavelength waveform (bottom) for a LNAPL mixture (adapted from St. Germain, 2014). 108
Fig. 4.14. Emission spectra of BTEX and PAHs and multi-wavelength waveform of naphthalene (adapted from St. Germain, 2014). 109
Fig. 4.15. Impact of heterogeneity on LIF response (St. Germain, 2014). 111
Fig. 4.16. Direct-push rig for the HRSC campaign at the petrol station site (the drilling campaign was conducted by Numac and eDrill under supervision of the CSIRO team). 113
Fig. 4.17. Integral LIF response before and after filtering at (a) LIF59-5D and (b) LIF43-A. 117
Fig. 4.18. LIF signal interpolation every 0.01 m at LIF51-B (negative values excluded). 118
Fig. 4.19. Negative values resulting from cubic spline interpolation at LIF51-B. 118
Fig. 4.20. Effects of heterogeneities on discontinuous DPIL pressure readings. Numerical simulations considered: (a) the base-case scenario, (b) the presence of a low-permeability layer near the screen, and (c) the presence of a high-permeability layer near the screen (adapted from Liu et al., 2019). 120
Fig. 4.21. Examples of dissipation tests where (a) full dissipation was reached, (b) excess pressure was still dissipating and completing the test could require more than 30 min, and (c) excess pressure was still rising after the water flow was turned off, completing such a test could take several hours (modified after McCall, 2010, 2011). 121
Fig. 4.22. Model to quantify k_{sw} proposed by Geoprobe® after calibration with slug test data in multiple field sites (McCall, 2010). 123
Fig. 4.23. Example of effects of flow injection rate on the Q/P ratio and calibration with DPP measurements (modified after Dietrich et al., 2008). 123
Fig. 4.24. Real-time monitoring of HPT measurements.....124

Fig. 4.25. HPT reference tube.....125
Fig. 4.26. Comparison of Q/P (only corrected for atmospheric pressure) and EC logs adjacent to PB40-C interpolated through IDW using constant power factors of 1 (I1DW), 2 (I2DW), and 4 (I4DW).....128
Fig. 4.27. Initial z_{aw} values of aquifer tests. The orange rectangle represents the transition range between unconfined and confined LNAPL conditions according to Gatsios et al. (2018b).....131
Fig. 4.28. Typical log-log (top) and log-linear plots (bottom) of (a) confined, (b) unconfined, and (c) leaky confined aquifers (modified after Kruseman and de Ridder, 2000).....132
Fig. 4.29. Typical log-log and log-linear plots showing the effects of (a) partial-penetration wells, (b) wellbore storage, and (c) recharge and (d) barrier boundaries in a confined aquifer (modified after Kruseman and de Ridder, 2000).....133
Fig. 4.30. Example of identification of filter pack discharge in DvD plots (ASTM International, 2013).....137
Fig. 4.31. DvD plots of baildown tests as interpreted in Gatsios (2018) at (a) PB27-B on 20/05/2016, and (b) PB40-C on 06/04/2016.....138
Fig. 4.32. Example of confined or perched LNAPL conditions as indicated by DvD plots (after ASTM International, 2013).....139
Fig. 4.33. Splines and linear interpolation on data from the industrial site (040610/1-T4 sample at 1.025 m AHD). Note the wrong values predicted with splines between the widest sieve openings.....144
Fig. 4.34. Empirical correlation between vG parameters, d_{60}, and C_u (modified after Benson et al., 2014).....146
Fig. 4.35. Neural network design (Schaap and Leij, 1998b).....149
Fig. 4.36. Measures of location in (a) lognormal, and (b) multimodal distributions. *MEAN* and *G* refer to the arithmetic and geometric means, respectively (adapted from Reimann et al., 2008).....157
Fig. 5.1. Particle-size analysis aggregating data from the petrol station site. *d25*, *d50*, and *d90* stand for the 25th, 50th, and 90th percentiles of particle diameters, respectively. 162

Fig. 5.2. Stratigraphic column in the petrol station site according to aggregated particle-size data. 163
Fig. 5.3. USDA soil texture triangle showing samples from the aquitard (red dots; samples between 57.051 and 58.980 m AHD), transition between the aquitard and the coarser-grained aquifer (yellow dots; samples between 55.917 and 56.760 m AHD), the upper aquifer (blue dots; samples between 55.030 and 55.760 m AHD), and the lower aquifer (green dots; samples between 53.160 and 54.710 m AHD) in the petrol station site. 164
Fig. 5.4. Φ estimates from cores in areas A, B and C in the petrol station site. 167
Fig. 5.5. Hydrograph of the petrol station site between 24/06/2014 and 29/05/2018, including (a) raw data, (b) observations from CSIRO wells after excluding perimeter wells and periods of active operations, and (c) same as above but also excluding observations of in-well LNAPL. 170
Fig. 5.6. Hydrograph of wells PB29-A, PB27-B, and PB40-C during fluctuation periods 2-4.....172
Fig. 5.7. Log-log and log-linear plots from PB13-C during WT1 (modified after Bekele et al., 2019).....172
Fig. 5.8. Log-log and log-linear plots from PB13-C during WT2 (modified after Bekele et al., 2019).....173
Fig. 5.9. Fit of data observed at PB13-C during WT1 with (a) Cooper-Jacob, (b) Butler, and (c) Hantush solutions (modified after Bekele et al., 2019). 173
Fig. 5.10. Log-log and log-linear plots at PB29-A during WT28 (modified after Bekele et al., 2019).....174
Fig. 5.11. Fit of observed data at PB29-A during WT28 with (a) Tartakovsky–Neuman and (b) Moench–Prickett solutions (modified after Bekele et al., 2019). 175
Fig. 5.12. Log-log and log-linear plots at (a) PB40-C during WT27, (b) observation wells during WT27, and (c) PB40-C during WT30 (adapted from Bekele et al., 2019).....176
Fig. 5.13. Fit of observed data at PB40-C during WT27 with (a) Tartakovsky–Neuman and (b) Hantush solutions (adapted from Bekele et al., 2019).....177
Fig. 5.14. Log-log and log-linear plots from PB39-C during WT15 (modified after Bekele et al., 2019). 177

Fig. 5.15. Log-log and log-linear plots from observation wells presumably exhibiting unconfined (top panels) and confined (bottom panels) behaviour at WT15 (modified after Bekele et al., 2019). 178
Fig. 5.16. (a) Tartakovsky–Neuman fit of PB39-C (unconfined) and (b) Theis–Hantush fit of PB40-C (confined) at WT15 (modified after Bekele et al., 2019). 179
Fig. 5.17. Distance to the pumping well versus drawdown of the observation wells. Different slopes in aligned wells (red and green lines) suggested anisotropic conditions. 179
Fig. 5.18. Discharge vs. drawdown (left panels) and discharge vs. fluid interface elevations (right panels) during baildown tests at (a) PB29-A on 15/06/2016, (b) PB27-A on 14/06/2016, and (c) PB40-C on 14/06/2016. Q/P logs correspond to (a) HPT73-A, (b) HPT74-B, and (c) PB40-C through IDW of values from HPT59-C, HPT60-C, and HPT62-C corrected for atmospheric pressure. 181
Fig. 5.19. DGPs of PB29-A including data until (a) 2018 and (b) the end of the fourth fluctuation period (20/05/2016). 182
Fig. 5.20. DGPs of PB29-A for fluctuation periods (a) 2, (b) 3, and (c) 4 as well as (d) data from other wells (PB33-A, MP34-A, MP50-A) in area A until 20/05/2016. 183
Fig. 5.21. DGPs of PB27-B with data (a) until 20/05/2016 (discontinuous lines correspond to linear regression models of z_{an}, z_{aw}, and z_{nw} under relatively constant z_{nw}) and from fluctuation periods (b) 2 (discontinuous lines correspond to linear regression models of z_{an} under potentially leaky confined and unconfined LNAPL periods; the arrow indicates the direction followed with time), (c) 3, and (d) 4 (the discontinuous line corresponds to the linear regression model of z_{an} under potentially unconfined LNAPL conditions; the arrow indicates the direction followed with time). 185
Fig. 5.22. DGP of PB40-C with data (a) until 20/05/2016 (the discontinuous line corresponds to the linear regression model of z_{nw} under likely confined LNAPL conditions) and (b) from fluctuation period 4 (discontinuous lines correspond to linear regression models of z_{an} under likely confined and unconfined LNAPL periods; the arrow indicates the direction followed with time). 188
Fig. 5.23. (a) DGP and (b) hydrograph of MP02 for fluctuation periods 2–4, showing measurements with z_{nw} values below 57.0 m AHD only. One anomalous measurement

from 08/10/2015 (with a b_n value of 0.734 m and z_{an} at 57.286 m AHD) was collected with a different interface probe and excluded from the DGP. 189
Fig. 5.24. b_n-based multi-well DGPs from (a) Hawthorne (2014) and (b) the petrol station site showing transmissive zones and hydrogeologic conditions (black and purple lines indicate unconfined and confined LNAPL conditions, respectively). Hawthorne (2014) presented elevations as ft above mean sea level (AMSL). 191
Fig. 5.25. Multi-well DGP at the petrol station site (fluctuation periods 1-4) after filtering data. 192
Fig. 5.26. Cross-section of HPT average pressure before correcting for atmospheric and hydrostatic pressure (green) and EC (black) logs between the UST and areas A and B. HPT64 was in the UST location, HPT75 between the UST and area A, HPT73-A next to PB29-A, HPT72 between areas A and B, and HPT74 adjacent to PB27-B. The dashed orange lines connect points of 500 kPa. 193
Fig. 5.27. Cross-section of HPT average pressure before correcting for atmospheric and hydrostatic pressure (green) and EC (black) logs between the UST and area C. HPT64 was in the UST location, HPT63-C adjacent to PB13-C, HPT59-C near PB11-C and PB40-C, HPT62-C Southwest of PB40-C, HPT60-C Northeast of PB40-C, and HPT61-C adjacent to PB39-C. 195
Fig. 5.28. Q/P (after correcting for atmospheric and hydrostatic pressure) and EC logs at HPT73-A (adjacent to PB29-A). The three layers depicted ('aquitard', 'transition', and 'aquifer' with occasional presence of clay lenses) represent a plausible interpretation of the hydrostratigraphy. 196
Fig. 5.29. Q/P (after correcting for atmospheric and hydrostatic pressure) and EC logs at HPT74-B (adjacent to PB27-B). Dashed red and purple lines refer to the confining contact according to the analysis of DGPs with data from fluctuation period 2 and aggregate data, respectively. 198
Fig. 5.30. Q/P (corrected for atmospheric pressure) and EC logs adjacent to PB40-C: (a) HPT59-C, (b) HPT60-C, and (c) HPT62-C. The x-axis was exaggerated compared to area A and B. 199
Fig. 5.31. Interpolated Q/P and EC logs at PB40-C including a simplified three-layer geological model. 201

Fig. 5.32. Four scenarios with different LNAPL hydrogeologic conditions: (a) unconfined LNAPL at low z_{aw}, (b) unconfined LNAPL at high z_{aw}, (c) fully confined LNAPL at high z_{aw}, and (d) semi-confined LNAPL at high z_{aw}. 202
Fig. 5.33. Vertical profiles of particle size and Φ at 040610/1-T4, 040610/6-T4, 040610/3-T4, and 050210/1-T4. *d25*, *d50*, *d75*, and *d90* stand for the 25th, 50th, 75th, and 90th percentiles of particle diameters, respectively. 206
Fig. 5.34. Hydrograph of 040610/3-T4. Two periods of decreasing (highlighted in yellow) and increasing z_{aw} (highlighted in blue) are depicted throughout two years of monitoring data. 208
Fig. 5.35. Hydrograph of 040610/3-T4 compared to maximum and minimum z_{aw} values recorded in other five wells monitored weekly in area T4 located less than 50 m away from 040610/3-T4. Anomalous z_{aw} values over 0.9 m AHD were surely due to measurement errors. 209
Fig. 5.36. DGP at NS7A-T4 between 27/07/2004 and 26/04/2006 showing coefficients of determination (a) for the entire set of data and (b) for each period of increasing or decreasing z_{aw}. 210
Fig. 5.37. HPT20-T3 pressure, flow and EC logs. 211
Fig. 5.38. Cross-section of HPT average pressure logs (before correcting for hydrostatic pressure) in the industrial site. 212
Fig. 5.39. EC logs revealing a transition towards high EC values at low elevations across the entire industrial site. 214
Fig. 5.40. Correlation between HPT P and EC at HPT20-T3. 215
Fig. 5.41. Groundwater specific conductance [mS/cm] (red colour) and ratio between EC and corrected HPT P (blue colour) in (a) the industrial site and (b) the petrol station site. 216
Fig. 6.1. Hydrograph and b_n at MP36-B. 220
Fig. 6.2. (a) Peak and (b) integral LIF signals across the petrol station site. 222
Fig. 6.3. Scatterplot of LIF response versus S_n in areas A, B, and C. The red and black dotted lines represent site-specific linear and exponential models, respectively. 225
Fig. 6.4. Scatterplot of filtered LIF response at LIF18-T3 versus S_n in coring area T3. 226
Fig. 6.5. Total LIF signal at LIF57-C versus EC at HPT60-C. 227

Fig. 6.6. LIF57-C log and HPT60-C EC log. 228
Fig. 6.7. Fluorescence signatures of several LNAPLs in the petrol station site and the industrial site. The presumed type of LNAPL is indicated between parenthesis. LIF51-B* and LIF51-B** depict the signature of LNAPL at LIF51-B above and below 55.854 m AHD, respectively. 230
Fig. 6.8. Mass percentage of the analysed chemical compounds in samples of different LNAPL types. LIF51-B* only considers samples above 55.854 m AHD. 231
Fig. 6.9. Correlation between the 500-nm channel and total LIF response at LIF57-C. 232
Fig. 6.10. Correlation between the four channels (blue, green, orange, and red represent the 350-nm, 400-nm, 450-nm, and 500-nm channels) and total LIF response at LIF69-C. The numbers in the upper panels correspond to the coefficients of determination... 233
Fig. 6.11. Relation between historical fluid levels and distinct LIF signatures at LIF51-B along HPT data. Fluid level elevations correspond to PB27-B (1.378 m away). *HPT data correspond to HPT74-B (0.985 m away) where Q/P is given in units of mL/(kPa·min). 234
Fig. 6.12. Long-term residual LNAPL at LIF69-C. Fluid level elevations correspond to MP08-C (3.475 m away). *HPT data correspond to HPT61-C (0.863 m away) where Q/P is given in units of mL/(kPa·min). 236
Fig. 6.13. S_n profiles measured through coring in areas A, B, and C. Cores MP50-A, MP58-B, and MP44-C were collected during the HRSC campaign in May 2016. Cores MP77-A, MP76-B, and MP78-C were collected in August 2016 after a rise in z_{aw} and the application of LNAPL mass recovery operations. 238
Fig. 6.14. Integrated LIF and S_n data from adjacent locations in areas A, B, and C. 240
Fig. 6.15. Butterfly plot of LIF47-A and LIF43-A (interpolated values). 241
Fig. 6.16. Comparison of core analysis (S_n and TPH concentration) at PB33-A, MP50-A, and MP77-A, including soil gas measurements at PB33-A and MP50-A. 243
Fig. 6.17. Linear correlation between PAH concentration and BTEX or TPH concentrations. 244
Fig. 6.18. LIF signal versus S_n profile in area A. 245
Fig. 6.19. Comparison of LNAPL distribution profiles (MP50-A, LIF43-A, MP70-A) with HPT73-A. 247

Fig. 6.20. Closer look at the HPT73-A EC log (the columns at the right side represent the fluid columns at PB29-A: ***W*** stands for water and ***N*** for LNAPL). 248
Fig. 6.21. Relative LIF signals for every wavelength channel at (a) LIF43-A and (b) LIF47-A. 251
Fig. 6.22. Average LIF lifetime profiles at (a) LIF43-A and (b) LIF47-A. 251
Fig. 6.23. Total LIF signals from area A in a logarithmic scale.....252
Fig. 6.24. Butterfly plot of LIF51-B and LIF71-B (interpolated values).....254
Fig. 6.25. LNAPL distribution profile (LIF and S_n) in area B in wells surrounding PB27-B (the columns at the right side represent the fluid columns at PB27-B: ***W*** stands for water and ***N*** for LNAPL). 256
Fig. 6.26. Comparison of core analysis (S_n and TPH concentration) at PB33-A, MP50-A, and MP77-A, including soil gas measurements at PB33-A and MP50-A. 257
Fig. 6.27. LNAPL distribution before and after the LNAPL mass recovery trial (the columns at the right side represent the fluid columns at PB27-B: ***W*** stands for water and ***N*** for LNAPL). 258
Fig. 6.28. Closer look at the EC log at HPT74-B. 258
Fig. 6.29. Relative LIF signals at every wavelength channel at (a) LIF51-B, (b) LIF52-B, and (c) LIF71-B. 259
Fig. 6.30. Average LIF lifetime profiles at (a) LIF51-B, (b) LIF52-B, and (c) LIF71-B. Note the different scale in the x-axis. 260
Fig. 6.31. Total LIF signals from area B in a logarithmic scale. 261
Fig. 6.32. Butterfly plot of LIF56-C and LIF68-C (interpolated values). 263
Fig. 6.33. Butterfly plot of LIF57-C and LIF68-C (interpolated values). 264
Fig. 6.34. Comparison of LIF57-C with MP44-C and in-well fluid levels (the columns at the right side represent the fluid columns at PB40-C: ***W*** stands for water and ***N*** for LNAPL). 265
Fig. 6.35. Core analyses (S_n, TPH, and soil gas) in area C. 267
Fig. 6.36. S_n profile before and after the LNAPL mass recovery trial (the columns at the right side represent the fluid columns at PB40-C: ***W*** stands for water and ***N*** for LNAPL). 269
Fig. 6.37. LNAPL distribution at PB13-C and hydrostratigraphic barriers. 269

Fig. 6.38. Comparison of EC and HPT Q logs at HPT60-C and HPT61-C. 270
Fig. 6.39. Relative LIF signals at (a) LIF56-C, (b) LIF57-C, and (c) LIF68-C. 271
Fig. 6.40. Lifetime data from LIF68-C. 272
Fig. 6.41. Relative LIF signals at every wavelength channel at (a) LIF69-C, (b) LIF66-C, and (c) LIF65. 273
Fig. 6.42. Total LIF signals from area C in a logarithmic scale. 273
Fig. 6.43. Correlation between TPH concentrations and individual PAH compounds at C66-T3. 275
Fig. 6.44. Comparison between TPH and S_n profiles at C66-T3. The TPH value at -0.134 m AHD (presented as raw data) was doubled up and therefore removed. 275
Fig. 6.45. Linearly interpolated z_{aw} and b_n values at 182-T3 (monthly monitored) in June and September during the period 2010–2012 (most recent data available). 276
Fig. 6.46. S_n profile at C66-T3 versus LIF18-T3. 277
Fig. 6.47. S_n profile at C66-T3 versus LIF19-T3. 277
Fig. 6.48. Comparison of LIF and S_n profiles in area T3. 278
Fig. 6.49. HPT20-T3 and S_n profiles in area T3. 280
Fig. 6.50. Vertical profile of S_n and particle size at 050210/1-T4. *d25*, *d50*, *d75*, and *d90* stand for the 25th, 50th, 75th, and 90th percentiles of particle diameters, respectively. The value of z_{aw} corresponds to the date of coring (10/02/2005). 281
Fig. 6.51. Vertical profiles of S_n and particle size at 040610/3-T4 and 040610/6-T4. *d25*, *d50*, *d75*, and *d90* stand for the 25th, 50th, 75th, and 90th percentiles of particle diameters, respectively. The values of z_{aw} corresponds to the date of coring (10/06/2004). 282
Fig. 6.52. Graphical representation of how peak LIF signal was correlated with T_n, unlike S_n. Relative LIF signals (the right panel depicts the case of area A) and lifetime data could be used to enhance the identification of the interval impacted with LNAPL through LIF logging. 286
Fig. 7.1. Density trace of 183 Φ measurements from MP50-A, MP77-A, PB27-B, MP58-B, MP76-B, MP44-C, and MP78-C. 296
Fig. 7.2. Density trace of RETC predictions of θ_{ws} versus core measurements of Φ. 297
Fig. 7.3. Boxplots of k_{sw} predictions through multiple empirical correlations in the petrol station site. 300

Fig. 7.4. Boxplots of k_{sw} predictions considering all the empirical methods applied in four main subsurface materials of the petrol station site. 301
Fig. 7.5. Range and geometric mean of empirical k_{sw} predictions discriminating by material. 305
Fig. 7.6. Predicted values of k_{sw} derived from particle-size data in the petrol station site considering (a) linear, and (b) logarithmic scales. Values correspond to Slichter and Barr using d_{VS} and d_{UU}, Sauerbrei, Alyamani and Sen, Krumbein and Monk, and the geometric mean of all the methods implemented in HydrogeoSieveXL. 307
Fig. 7.7. Neural network predictions of k_{sw} compared to the geometric mean of multiple empirical correlations in the petrol station site. 309
Fig. 7.8. Distance–drawdown plots at (a) WT29, (b) WT27, (c) WT30, and (d) WT15 (adapted after Bekele et al., 2019). 311
Fig. 7.9. Estimations of T_w in m^2/day through Tartakovsky–Neuman (T–N) and Moench–Prickett (M–P) during (a) WT28 and (b) WT29. Observation wells with only two measurements are not included. 312
Fig. 7.10. Averages of k_{sw} estimated through HPT and geometric means of k_{sw} from empirical correlations implemented in HydrogeoSieveXL (PSA in the graph) in areas A, B, and surroundings (A, B), areas C and UST (C, UST), and other locations (ML15 and ML32). Aquifer zones considered in the analysis of empirical correlations (transition, upper aquifer, and lower aquifer) are separated with dashed lines. 315
Fig. 7.11. HPT predictions of k_{sw} in (a) areas A, B, and surroundings, and (b) area C and UST. PSA refers to the geometric mean of k_{sw} estimated through empirical correlations implemented in HydrogeoSieveXL. Aquifer zones considered in the analysis of empirical correlations (transition, upper aquifer, lower aquifer) are separated with dashed lines. 318
Fig. 7.12. Histogram, density trace, and one-dimensional scatterplot (left panels), as well as cumulative probability plots (right panels) of (a) cumulative HPT k_{sw} data from the petrol station site, (b) same data excluding non-detects, and (c) log-transformed data excluding non-detects. 323

Fig. 7.13. Histogram, density trace, and one-dimensional scatterplot untransformed (left panels) and transformed (right panels) k_{sw} data in (a) areas A, B and surroundings, and (b) areas C and UST. 325
Fig. 7.14. Boxplots of $vG\text{-}\alpha$, $vG\text{-}N$, and S_{wr} predictions in the petrol station site. 330
Fig. 7.15. Profiles of $vG\text{-}\alpha$ estimations according to multiple methods. 331
Fig. 7.16. Values of $vG\text{-}\alpha$ aggregating data from all the methods and discriminating by type of material. 331
Fig. 7.17. Profiles of $vG\text{-}N$ and S_{wr} in the petrol station site. 333
Fig. 7.18. Fluid interfaces during baildown test at PB29-A. 338
Fig. 7.19. DvD plot at PB29-A (Gatsios, 2018). 339
Fig. 7.20. Estimation of J-ratio at PB29-A (Gatsios, 2018). 340
Fig. 7.21. Bouwer and Rice curves fitted to measured data considering drawdown adjustments of -0.0012 m (blue squares) and -0.00012 m (green circles). 341
Fig. 7.22. Fluid interfaces during baildown test at PB27-B. 342
Fig. 7.23. DvD plot at PB27-B (after Gatsios, 2018). 342
Fig. 7.24. Estimation of J-ratio at PB27-B (Gatsios, 2018). 343
Fig. 7.25. Fluid interfaces during baildown test at PB40-C on 06/04/2016. 344
Fig. 7.26. DvD plot at PB40-C on 06/04/2016 (after Gatsios, 2018). 345
Fig. 7.27. Estimation of J-ratio at PB40-C on 06/04/2016 (Gatsios, 2018). 345
Fig. 7.28. Fluid interfaces during baildown test at PB40-C on 14/06/2016. 346
Fig. 7.29. DvD plot at PB40-C on 14/06/2016 (after Gatsios, 2018). 347
Fig. 7.30. Estimation of J-ratio at PB40-C on 14/06/2016 (Gatsios, 2018). 347
Fig. 7.31. (a) Density traces of Φ data from areas T3 and T4; (b) comparison between cores in T4. 352
Fig. 7.32. Density traces discriminating layers using (a) cumulative data and (b) data from individual cores. NS7A-T4 density trace groups data from 040610/3-T4 and 050210/1-T4. 354
Fig. 7.33. Measured Φ values and RETC predictions of θ_{ws} used as proxies of Φ in area T4. 356

Fig. 7.34. Boxplots of k_{sw} predictions through multiple empirical correlations. Terzaghi, Kozeny–Carman and Zamarin boxplots correspond to only four data points, USBR to nine and Chapuis to 22.....358
Fig. 7.35. Comparison of predictions with the approach of Wang et al. (2017) versus the geometric mean of multiple empirical methods in (a) the petrol station site and (b) the industrial site.....361
Fig. 7.36. Absolute differences between the use of d_{VS} and d_{UU} in Slichter and Barr compared to the geometric mean of other methods in the petrol station site (site 1) and the industrial site (site 2). Samples corresponding to C_u values over 5 (found at the petrol station site) did not follow any clear trend (not shown). 362
Fig. 7.37. Boxplots of k_{sw} predictions discriminating by location (well and layer). NS7A-T4 refers to the sum of data from 040610/3-T4 and 050210/1-T4.....365
Fig. 7.38. Boxplots of k_{sw} predictions obtained with RETC. 367
Fig. 7.39. Influence of ρ_b on k_{SW} (core 040610/3-T4).....368
Fig. 7.40. Density traces of k_{sw} and corrected HPT pressure below the presumed water table and in the vadose zone at HPT20-T3. 'k_{sw} (all HPT logs)' corresponds to all the available HPT data from the industrial site in the saturated zone. 371
Fig. 7.41. Comparison of k_{sw} estimates from HPT logging at HPT20-T3 versus empirical correlations and neural network predictions in four cores from area T4. Samples from 040610/6-T4 were combined with samples from the other cores collected 0.1 m deeper. 374
Fig. 7.42. Effects of the method used to predict vG-α in Ghanbarian et al. (2010) at 040610/3-T4 (1.025 m AHD). *Ellithy* refers to Ellithy (2017), *Lenhard* to Lenhard et al. (1989b), *MS* to Morel-Seytoux et al. (1996) and *Tinjum* to Tinjum et al. (1999). Initial values of h_{min} were taken as geometric means of sands from *Rawls* (Rawls et al., 1982) and SP samples from the *API* database (API, 2006).....376
Fig. 7.43. Box-plots of retention parameters. *Lenhard* and *MS* refer to the methods of Lenhard et al. (1989b) and Morel-Seytoux et al. (1996) to estimate vG-α. *Rawls* and *API* refer to Rawls et al. (1982) and API (2006) as sources of h_{min}. *Ghanbarian*, *Benson,* and *RETC* refer to the methods of Ghanbarian et al. (2010), Benson et al. (2014), and Schaap

et al. (2001), respectively. Benson et al. (2014) produced *Drainage* and *Imbibition* parameters. 377
Fig. 7.44. Retention parameters as estimated through RETC versus elevation in area T4. 380
Fig. 7.45. Density traces of retention parameters discriminating between two layers in area T4. 381
Fig. 7.46. Experimental measurements of P_c–S relationships at 040610/2-T4 (1.036 m AHD) and retention curves derived from hydrogeological data at 040610/1-T4 (1.025 m AHD). 384
Fig. 7.47. Retention curves obtained in the laboratory and following the method of Ghanbarian et al. (2010) with different determinations of vG-α, including the default of Ellithy (2017). 386
Fig. 7.48. Experimental retention curves at 040610/2-T4 (1.036 m AHD) versus Ghanbarian at 040610/1-T4 (1.025 m AHD), forcing vG-N to be 3.2 instead of 1.6468. 387
Fig. 7.49. Experimental measurements of P_c–S relationships at 040610/2-T4 (0.586 m AHD) and retention curves derived from hydrogeological data at 040610/1-T4 (0.575 m AHD). 388
Fig. 7.50. Fitted vG curve considering entrapment of the non-wetting fluid along the imbibition path at 040610/2-T4 (0.586 m AHD). 389
Fig. 7.51. Experimental measurements of P_c–S relationships at 040610/2-T4 (0.086 m AHD) and retention curves derived from particle-size data at 040610/1-T4 (0.075 m AHD). 390
Fig. 7.52. ρ_n measurements from 27 wells in areas T3/T4 (minimum of 846 mg/cm^3 and maximum of 885 mg/cm^3). 395
Fig. 7.53. Density traces of η_n, σ_{an}, and σ_{nw} as measured in area T4. 396
Fig. 8.1. Comparison of T_n values from baildown testing and LDRM simulations in area B according to the input parameter set used in Gatsios et al. (2018a). Dot labels correspond to the initial value of b_n [m] when baildown tests were conducted. 403
Fig. 8.2. Effects of S_{nr} and relative permeability models on S_n profiles in (a) area C and (b) area T4. 405

Fig. 8.3. Effects of S_{nr} and relative permeability models on S_{nr} profiles in (a) area C and (b) area T4. 406
Fig. 8.4. Comparison between field S_n measurements and predictions of S_n, S_{nr}, and S_{ne} through LNAPLTRANS and LDRM in area C. Blue (*W*) and orange (*N*) columns represent in-well water and LNAPL fluid columns, respectively. 407
Fig. 8.5. LNAPLTRANS prediction of LNAPL distribution considering a lower b_n value. Blue (*W*) and orange (*N*) columns represent in-well water and LNAPL fluid columns, respectively (b_n = 0.756 m). 408
Fig. 8.6. Comparison of field S_n measurements with LNAPLTRANS and LDRM predictions in (a) area A and (b) area B. Blue (*W*) and orange (*N*) columns represent in-well water and LNAPL fluid columns, respectively. 409
Fig. 8.7. Comparison of field S_n measurements with LNAPLTRANS and LDRM predictions of S_n, S_{nr}, and S_{ne} in area T4. The blue (*W*) and orange (*N*) columns represent in-well water and LNAPL fluid columns, respectively. 410
Fig. 8.8. LNAPLTRANS predictions of LNAPL distribution considering a higher vG-α value. Blue (W) and orange (N) columns represent in-well water and LNAPL fluid columns, respectively. 412
Fig. 8.9. Single-layer versus multi-layered scenarios in area T4. The prediction of S_n from Lenhard et al. (2019) correspond to the use of imbibition retention parameters in LNAPLTRANS.....413
Fig. 8.10. LDRM prediction of LNAPL distribution in multi-layered scenarios of area A. 414
Fig. 8.11. Tornado diagram of sensitivity indices corresponding to calculations of (a) V_n and (b) T_n through LNAPLTRANS and LDRM. For illustrative purposes, *SI* values for LNAPLTRANS are given as negative quantities. 419

List of tables

Table 2.1. Adopted definitions of NAPL mobility states. 18
Table 4.1. Details of the areas of research in the petrol station site and the industrial site. 79
Table 4.2. Construction details of monitoring and production wells as well as the creek monitoring points. 83
Table 4.3. Core sampling and analysis details in the areas of study. z_{aw} values presented for the petrol station site were measured at PB11-C close to the coring events, while interpolated z_{aw} values from 182-T3 were used for the industrial site. PSA and LOD refer to 'particle-size analysis' and 'limit of detection', respectively. 85
Table 4.4. Details of HPT dissipation tests. 126
Table 4.5. Main characteristics of representative aquifer tests conducted in the petrol station site. 131
Table 4.6. Main assumptions of presented aquifer test solutions (modified after Bekele et al., 2019). 134
Table 4.7. Main details of the baildown tests representative of the modelling scenarios. 135
Table 4.8. Empirical models implemented in HydrogeoSieveXL v2.3 including ID numbers and the year when they were published. Details can be found in Devlin (2015). 141
Table 4.9. Geometric mean value of h_{min} for different USDA and USCS texture classes according to samples from Rawls et al. (1982) and API (2006), respectively. 147
Table 4.10. Methods employed to estimate retention parameters from particle-size data. 147
Table 4.11. LNAPLTRANS inputs and parameters. 151
Table 5.1. Classification of samples according to the USDA and USCS systems. 165
Table 5.2. Periods of quasi-monotonic raising or falling z_{aw} with higher measurement frequency in the petrol station site. 171
Table 6.1. Ranks of T_n as well as peak and integral LIF signals. 223

Table 6.2. Summary of key parameters measured in the three coring areas during the HRSC campaign. Data from areas A, B and C correspond to cores MP50-A, MP58-B and MP44-C, LIF logs LIF43-A, LIF51-B and LIF57-C, and wells PB29-A, PB27-B and PB40-C, respectively. The T_n value for PB40-C was linearly interpolated using measurements of 0.577 m^2/day on 06/04/2016 and 0.304 m^2/day on 14/06/2016. 224
Table 7.1. Representative ranges of Φ (in percentage) for silt and different types of sand according to multiple references. Average values are shown between parentheses. Carsel and Parrish (1988) reported θ_{ws} values. *One asterisk indicates that the value corresponds to sandy loam. **Two asterisks indicate that the value correspond to the sum of sands and loamy sands. 288
Table 7.2. Representative ranges of k_{sw} (in m/day) for different types of sand according to multiple references. Average values are shown between parentheses. The conversion of s^{-1} into day^{-1} was done with a factor of 10^5 instead of $8.64 \cdot 10^4$ for simplicity purposes. *Values marked with one asterisk corresponded to different types of fine sediments, for instance fine sand, silt or loess. **Two asterisks indicated coarse sands, sands mixed with gravels or from glacial outwash. Materials from Carsel and Parrish (1988), and Nemes et al. (2001) are consistent with those used for Φ values. 290
Table 7.3. Typical retention parameters of sands according to literature sources. Estimations of S_{wr} from Carsel and Parrish (1988) were assumed to be the ratio between average residual and saturated water contents. Arithmetic means are given between parentheses. 292
Table 7.4. Statistics of Φ measurements from the petrol station site. 295
Table 7.5. Statistics of θ_{ws} values predicted with RETC in the petrol station site. 297
Table 7.6. Reference Φ values and ranges [%] for the petrol station site. 298
Table 7.7. Statistics of empirical k_{sw} estimations [m/day] for the four main subsurface materials from the petrol station site and the aggregated data. 302
Table 7.8. Estimations of T_w, k_{sw}, and specific storage by the distance–drawdown method in the petrol station site. 310
Table 7.9. Estimations of T_w, k_{sw}, and S through aquifer testing in the petrol station site. 313

Table 7.10. Summary statistics of HPT k_{sw} estimates in the petrol station site. HPT72 and HPT75 were included in the analysis of areas A and B due to their proximity. The data set used for the analysis of PB40-C included data from HPT59-C, HPT60-C, and HPT62-C. 320
Table 7.11. Summary statistics of HPT k_{sw} estimates in the petrol station site excluding non-detects. The columns refer to the same HPT logs as the unfiltered data. 322
Table 7.12. Logconductivity variance in different hydrostratigraphic intervals at HPT73-A. 326
Table 7.13. Reference values and ranges of k_{sw} [m/day] for the analytical models in the petrol station site. 327
Table 7.14. Statistics of $vG\text{-}\alpha$ estimates [m^{-1}] in the petrol station site. 329
Table 7.15. Statistics of $vG\text{-}\alpha$ [m^{-1}] of aggregated data and discriminating by type of material. 332
Table 7.16. Central values and ranges of $vG\text{-}N$ [-] (cumulative and by type of material aggregating estimations through RETC and averages of Benson drainage and imbibition paths) and S_{wr} [%] (aggregation of estimations through RETC and Ghanbarian) in the petrol station site. 333
Table 7.17. Reference values and ranges of retention parameters for the analytical models. 334
Table 7.18. Ranges and geometric means (between parenthesis) of LNAPL physical properties in gasoline samples from API (2006) and representative values of gasoline reported by Mercer and Cohen (1990) and Johnston (2010). 336
Table 7.19. Reference values and ranges of LNAPL properties for model testing. 337
Table 7.20. Lower and upper bound Tn values according to alternative interpretations. 338
Table 7.21. Summary of statistics of Φ measurements from samples with particle-size data in areas T3 and T4. Limits for the identification of outliers were computed according to Iglewicz and Hoaglin (1993). 349
Table 7.22. Statistics of Φ measurements in area T4 including samples without particle-size data. NS7A-T4 refers to the combination of data from 040610/3-T4 and 050210/1-T4. 350

Table 7.23. Summary of Φ measurements in area T4 discriminating between layers. 353
Table 7.24. Statistics of Φ discriminating by hydrofacies including samples without particle-size data. NS7A-T4 refers to the combination of data from 040610/3-T4 and 050210/1-T4. 355
Table 7.25. Reference values and ranges of Φ [%] for the analytical models. 357
Table 7.26. Statistics from HydrogeoSieveXL estimations. ID indicates the empirical method. *G* and *A* refer to geometric and arithmetic means including averages of results with d_{VS} and d_{UU}. 359
Table 7.27. Summary statistics of k_{sw} predictions in area T4 discriminating by location (well and/or layer). *Layer 1* refers to the top layer and *Layer 2* to the bottom layer. . 364
Table 7.28. Summary statistics of k_{sw} predictions obtained with RETC. *Layer 1* refers to the top layer (above 0.4 m AHD), while *Layer 2* refers to the bottom layer (below 0.4 m AHD). 366
Table 7.29. Summary statistics of HPT logs at HPT20-T3 discriminating between saturated (excluding the capillary fringe) and vadose zones. 370
Table 7.30. Reference values and ranges of k_{sw} [m/day] for the analytical models. ... 374
Table 7.31. Summary statistics of retention parameters in area T4. 378
Table 7.32. Summary statistics of retention parameters discriminating between two layers and different locations in area T4. G refers to the geometric mean. 382
Table 7.33. Drainage retention parameters estimated at 040610/2-T4. 383
Table 7.34. Imbibition retention parameters estimated at 040610/2-T4. 383
Table 7.35. Reference values and ranges of retention parameters for the analytical models. 391
Table 7.36. Literature values of diesel physical properties and statistical summary of field measurements from areas T3/T4. Values between parentheses represent averages. 393
Table 7.37. Reference values and ranges of LNAPL properties for model testing. 397
Table 8.1. Details of base-case scenarios in areas A, B, C, and T4. 401
Table 8.2. T_n values at PB27-B measured through baildown testing (Gatsios, 2018) and predicted with LDRM using input parameters from Gatsios et al. (2018a). Baildown tests on 20/05/2016 and 14/06/2016 were conducted twice obtaining almost identical results (Gatsios, 2018). 402

Table 8.3. LDRM predictions of V_n [m] and free T_n [m^2/day] with different models of k_{rn} and S_{nr}.....404
Table 8.4. LNAPLTRANS predictions of V_n [m] and free T_n [m^2/day] in areas A, B, C, and T4.....411
Table 8.5. Summary of input values corresponding to most likely ('-1', '+1'), extended ('-2', '+2'), and conservative ranges ('-3', '+3') for the computation of sensitivity indices in area C. 416
Table 8.6. Sensitivity indices of V_n with LDRM.....417
Table 8.7. Sensitivity indices of V_n with LNAPLTRANS. 417
Table 8.8. Sensitivity indices of T_n with LDRM. 418
Table 8.9. Sensitivity indices of T_n with LNAPLTRANS.....418
Table 8.10. LDRM and LNAPLTRANS predictions of V_n [m] and free T_n [m^2/day] in best- and worst-case scenarios as defined in area C. 421

Nomenclature and acronyms

Symbol	Definition	Units
AHD	Australian Height Datum	n/a
AIC	Akaike information criterion	-
API	American Petroleum Institute	n/a
b_n	In-well NAPL thickness	m
bgl	Below ground level	n/a
B–C	Brooks and Corey	n/a
BTEX	Benzene, toluene, ethylbenzene, xylene	n/a
CP	Cumulative probability	-
CRC CARE	Cooperative Research Centre for Contamination Assessment and Remediation of the Environment	n/a
CSIRO	Commonwealth Scientific and Industrial Research Organisation	n/a
CSM	Conceptual site model	n/a
CV	Coefficient of variation	%
CVR	Robust coefficient of variation	%
d	Diameter	mm
d_E	Effective grain size	mm
d_{UU}	d_E from Urumović and Urumović Sr (2017)	mm
d_{VS}	d_E from Vuković and Soro (1992)	mm
D^{max}	Output value when input is set at the maximum	output's
D^{min}	Output value when input is set at the minimum	output's
DGP	Diagnostic gauge plot	n/a
DNAPL	Dense non-aqueous phase liquid	n/a
DPIL	Direct-push injection logging	n/a

DTN	Depth to NAPL	m
DTW	Depth to water	m
DvD	Discharge versus drawdown	n/a
e	Residual error	variable's
EC	Electrical conductivity	mS/m
ECDF	Empirical cumulative distribution function	n/a
EEM	Excitation–Emission Matrix	n/a
EPS	Extracellular polymeric substances	n/a
ETBE	Ethyl tert-butyl ether	n/a
f_{oc}	Fraction of organic carbon	-
FID	Flame ionisation detector	n/a
GC	Gas chromatography	n/a
h_{min}	Threshold pressure in the B–C model	cm
∇H_n	Lateral gradient in the LNAPL head	-
∇H_w	Groundwater hydraulic gradient	-
HPT	Hydraulic Profiling Tool®	n/a
HPT P	HPT average pressure	kPa
HPT Q	HPT flow injection rate	mL/min
HRSC	High-resolution site characterisation	n/a
HSA	Hollow stem augering	n/a
IDW	Inverse distance weighting	n/a
IQR	Interquartile range	variable's
ITRC	Interstate Technology and Regulatory Council	n/a
k_{rn}	NAPL relative permeability	-
k_{rw}	Water relative permeability	-
k_{sw}	Water-saturated hydraulic conductivity	m/day

k_n	NAPL hydraulic conductivity	m/day
K	Intrinsic permeability	m^2
LDRM	LNAPL Distribution and Recovery Model®	n/a
LIF	Laser-induced fluorescence	n/a
LNAPL	Light non-aqueous phase liquid	n/a
LNAPLTRANS	Updated version of LNAPLVOL	n/a
LNAPLVOL	Lenhard et al. (2017) model	n/a
LOD	Limit of detection	mg/kg
m_{od}	Mass of oven-dried sample	kg
m_{water}	Mass of water	kg
m_{wet}	Wet mass of sample	kg
M	Median	variable's
M_n	Inherent LNAPL mobility	m/day
MAD	Median absolute deviation	variable's
MAE	Mean absolute error	variable's
MIP	Membrane Interface Probe®	n/a
ML	Silt material or ID code for mult-level wells	n/a
MN	Methylnaphthalene	n/a
MS	Mass spectrometry	n/a
MTBE	Methyl tert-butyl ether	n/a
n	Number of samples	-
NAPL	Non-aqueous phase liquid	n/a
NIQ	Normalised interquartile range	variable's
NSZD	Natural source zone depletion	n/a
OIP	Optical Image Profiler	n/a
pxx	xx^{th} percentile	variable's

P_c-S	Capillary pressure-saturation	n/a
PAH	Polycyclic aromatic hydrocarbon	n/a
PARAFAC	Parallel factor analysis	n/a
PID	Photo-ionisation detector	n/a
PPE	Personal protective equipment	n/a
Q/P	Ratio between HPT P and HPT Q	mL/(kPa·min)
Qx	*x* quartile (first quartile or third quartile)	variable's
R^2	Coefficient of determination	-
RAIS	Risk Assessment Information System	n/a
RE	Reference emitter	n/a
RETC	RETention Curve computer program	n/a
RMSE	Root mean square error	variable's
S_n	NAPL saturation	-
S_{ne}	Entrapped NAPL saturation	-
S_{ne}^{max}	Maximum entrapped NAPL saturation	-
S_{nr}	Residual NAPL saturation	-
S_{nr}^{max}	Maximum residual NAPL saturation	-
S_w	Water saturation	-
S_{wr}	Residual water saturation	-
SD	Standard deviation	variable's
SI	Sensitivity index	-
SM	Silty sand	n/a
SP	Poorly sorted sand	n/a
SW	Well-sorted sand	n/a
t	Time	day
T_n	NAPL transmissivity	m^2/day

T_w	Aquifer transmissivity	m^2/day
TMB	Trimethylbenzene	n/a
TPH	Total petroleum hydrocarbon	n/a
UNSODA	Unsaturated Soil hydraulic Database	n/a
USCS	Unified Soil Classification System	n/a
USDA	United States Department of Agriculture	n/a
UVOST®	Ultra-Violet Optical Screening Tool®	n/a
v_n	NAPL velocity	m/day
V_n	NAPL specific volume	m
V_{sample}	Volume of sample	m^3
VEQ	Vertical hydrostatic equilibrium	n/a
vG	van Genuchten	n/a
$vG\text{-}\alpha$	van Genuchten *α* parameter	m^{-1}
$vG\text{-}m$	van Genuchten *m* parameter	-
$vG\text{-}N$	van Genuchten *N* parameter	-
VOC	Volatile organic compound	n/a
z_{an}	Air-NAPL interface elevation	m AHD
z_{an}^{max}	Historical maximum air-NAPL interface elevation	m AHD
z_{an}^{min}	Historical minimum air-NAPL interface elevation	m AHD
z_{aw}	Potentiometric surface elevation	m AHD
z_{nw}	NAPL–water interface elevation	m AHD
z_{nw}^{max}	Historical maximum NAPL–water interface elevation	m AHD
z_{nw}^{min}	Historical minimum NAPL–water interface elevation	m AHD
η_n	NAPL viscosity	kg m^{-1} s^{-1}
η_{rn}	Relative NAPL viscosity, NAPL viscosity ratio	-
Φ	Porosity	-

ρ_b	Bulk density	mg/kg
ρ_n	NAPL density	mg/kg
ρ_{rn}	Relative NAPL density, NAPL specific gravity	-
ρ_s	Particle density	mg/kg
θ_g	Gravimetric water content	-
θ_n	Volumetric NAPL content	-
θ_{wr}	Irreducible water content	-
θ_{ws}	Saturated water content	-
σ_{an}	NAPL surface tension	mN/m
σ_{aw}	Water surface tension	mN/m
σ_{nw}	NAPL–water interfacial tension	mN/m

Abstract

Petroleum hydrocarbons in the form of light non-aqueous phase liquids (LNAPLs) are some of the most common subsurface contaminants in urban and industrial environments. LNAPLs may persist in soil and groundwater systems for decades because of their challenging characterisation and remediation. In this research, high-resolution site characterisation (HRSC) tools such as direct-push injection logging (DPIL) and laser-induced fluorescence (LIF) as well as a recently developed multiphase analytical model (LNAPLTRANS) were evaluated in the assessment of LNAPL distribution and mobility.

Two field sites from Western Australia (a petrol station site showing seasonal LNAPL confinement in a heterogeneous aquifer–aquitard system and an industrial site with multiple types of LNAPL in a sandy aquifer) were investigated. The variability and most likely values of subsurface parameters required by the models were quantified through field methods, laboratory measurements, and the analysis of previous reports. DPIL, LIF, and LNAPLTRANS were compared to other tools such as LNAPL diagnostic gauge plots, hydraulic testing, coring, and the LDRM model.

DPIL allowed rapid collection of comprehensive data sets revealing hydrostratigraphic features overlooked by conventional methods. Predictions of water-saturated hydraulic conductivity were typical of sandy aquifers and not strongly influenced by the presence of LNAPL. The DPIL quantification model could have underestimated the variability of water-saturated hydraulic conductivity according to other field measurements.

LIF logging was used to assess LNAPL mobility. LIF response was correlated with LNAPL transmissivity, unlike LNAPL saturation values from coring. Furthermore, LIF logging facilitated the identification of intervals with long-term entrapped and residual LNAPL because of the multi-wavelength waveforms associated with distinct subsurface characteristics. LIF lifetime data and other LIF metrics could improve the delineation of LNAPL-impacted intervals, although non-unique interpretations of HRSC logs may exist. Therefore, investigators should always consider multiple lines of evidence.

The application of multiphase analytical models represented a practical way to investigate subsurface scenarios partly accounting for the strong variability of

subsurface parameters. LNAPL transmissivity exhibited the largest sensitivity to retention parameters and water-saturated hydraulic conductivity, being also influenced by the relative permeability model. Changes in residual LNAPL saturation affected LNAPLTRANS and LDRM predictions of LNAPL transmissivity in opposite ways. Thus, further research should be conducted on characterisation and modelling of near-immobile LNAPL fractions and retention parameters. Future HRSC approaches should exhibit a more quantitative nature and better integrate scale-appropriate measurements in time and space, eventually resulting in more effective and sustainable management of LNAPL contaminated sites.

1 Introduction

1.1 Significance of the problem

Environmental pollution may be 'the most underrated, under-investigated and poorly understood of all the essential risks facing humans in the 21st Century' (CRC CARE, 2018). Air, water, soil, chemical, and occupational pollution causes more diseases and deaths than any other environmental risk factor (around nine million deaths in 2015; most of them linked to air pollution), resulting in welfare losses as high as 6.2 % of gross world product (Landrigan et al., 2018).

Soil and groundwater pollution affects the quality of land and water and thus may have a negative impact on vital aspects such as food, soil, and water security as well as the health, wellbeing, and development of exposed humans and ecosystems in general. It is expected that climate change, population growth, and human activity will keep intensifying these issues in the near future (e.g. Rodell et al., 2018).

Environmental pollution related to industrial activities is globally increasing (especially in low- and middle-income countries) despite numerous advances in pollution control (Landrigan et al., 2018). Five million potentially contaminated sites may exist worldwide (CRC CARE, 2018) with annual management (and mismanagement) costs representing billions of dollars (Payá Pérez and Rodríguez Eugenio, 2018). Thus, there is a need for better pollution control and site management strategies.

Petroleum hydrocarbons such as petrol, diesel, and crude oil are some of the most common subsurface contaminants in urban and industrial environments. These complex chemical mixtures are sparingly soluble in water and are typically found in the form of light non-aqueous phase liquids (LNAPLs) which may persist in the subsurface for decades (Essaid et al., 2015). Thousands of new releases occur every year, although this number is generally decreasing—at least in high-income countries (Sale et al., 2018)—and the associated risks may be limited by natural attenuation phenomena. Nevertheless, the characterisation and remediation of new and existing LNAPL contaminated sites is challenging and requires substantial investments.

Many of these challenges are derived from the complex and heterogeneous nature of the hydrogeological system and the LNAPL body even at fine scales (Essaid et al., 2015; Sale et al., 2018; Rivett and Wealthall, 2019). Consequently, high-resolution site characterisation (HRSC) approaches providing scale-appropriate measurements of subsurface properties represent a step forward in the management of contaminated sites and a promising area of research as further discussed in chapter 2. In particular, better delineation and assessment of LNAPL distribution and mobility is crucial for the definition of effective remediation strategies and LNAPL remediation endpoints (Lenhard et al., 2017). However, adoption of these new tools has been limited due to a lack of guidance and misperceptions about their availability and applications (Interstate Technology and Regulatory Council [ITRC], 2019), even if their implementation can result in cost savings (Dyment and Kady, 2019) and better protection of human health and the environment.

1.2 Research objectives

This thesis aims to evaluate the application of HRSC tools and a recently developed multiphase analytical model to predict LNAPL distribution and mobility in unconsolidated aquifers at field scale. Outcomes from this thesis may be beneficial for the definition of improved characterisation and remediation strategies as well as the determination of remediation endpoints in heterogeneous sites contaminated with non-aqueous phase liquids (NAPLs).

Main objectives include:

1. evaluate if laser-induced fluorescence (LIF) and direct-push injection logging (DPIL) may accurately identify hydrostratigraphic features, especially those causing confined LNAPL conditions;
2. evaluate if LIF response may be related to LNAPL mobility in common unconsolidated subsurface settings, working as an indicator of NAPL transmissivity T_n and helping to identify long-term near-immobile LNAPL intervals;
3. assess if DPIL may adequately quantify water-saturated hydraulic conductivity k_{sw} without site-specific calibrations, in particular evaluating if LNAPL presence

may negatively affect DPIL readings and if the obtained logconductivity variance may be adopted as a measure of aquifer heterogeneity in stratified aquifer systems;

4. evaluate the capabilities of a recently developed multiphase analytical model (LNAPLTRANS) and the effects of the field measurements variability on predictions of LNAPL distribution and T_n. Accordingly, characterisation works also aimed to design modelling scenarios and determine reference values and plausible ranges of subsurface parameters.

In addition, many secondary objectives rise from the comparison of HRSC methods to conventional approaches and the application of multiphase analytical models. These secondary objectives are summarised at the beginning of the corresponding results chapters.

1.3 Contribution to knowledge

This thesis contributes to a better understanding of HRSC applications, presenting novel approaches to characterising LNAPL contaminated sites through LIF and DPIL systems. Some examples are:

- it is proposed the use of LIF response as a potential indicator of LNAPL mobility even when good correlation with LNAPL saturation S_n does not exist in heterogeneous systems. This approach may be better suited for the characterisation of early-stage releases. Mulry and Lundy (2013) have encouraged further investigation on the nexus between LIF and T_n after a study in a saprolite aquifer, while Teramoto et al. (2019) and ITRC (2019) have reported the existence of different quantitative relationships between LIF response and S_n in laboratory experiments;
- methods are presented to identify intervals with presumably less-mobile LNAPL through the analysis of LIF data;
- DPIL readings were not found to be greatly impacted by LNAPL contamination despite the expected decrease in the relative permeability of water k_{rw}.

These outcomes were obtained in a relatively fine-grained system with light fuels that could be defined as a challenging environment for the application of some HRSC tools

(ITRC, 2019). However, LIF and DPIL greatly contributed to a better site characterisation and provided essential information about the subsurface conditions.

Furthermore, field studies in multi-layered systems exhibiting a mix of unconfined and confined LNAPL periods are scarce, although confined LNAPL conditions may have strong consequences on the analysis and interpretation of subsurface measurements (Kirkman et al., 2013). It was possible to investigate the capabilities of HRSC tools to identify boundaries between aquifers and overlying aquitards due to the hydrostratigraphy of the petrol station site. Some authors have recently encouraged the assessment of aquitard integrity through HRSC approaches (Filippini et al., 2020).

Furthermore, the study of a multi-layered site made possible to evaluate the applicability of aquifer heterogeneity metrics such as DPIL logconductivity variance in stratified systems as questioned by Gómez-Hernández et al. (2017).

In addition, the comparison and testing of two multiphase analytical models exposed limitations and discrepancies between both models that could lead to better model designs and code modifications as well as further research in the characterisation of residual LNAPL saturation S_{nr}, entrapped LNAPL saturation S_{ne}, and relative permeability functions in laboratory, field, and modelling studies. Further testing of these models has been encouraged by Lenhard et al. (2019).

1.4 Thesis outline

Field data collected in two sites from Western Australia (a petrol station site with seasonal LNAPL confinement and an industrial site with multiple types of LNAPL on a sandy aquifer) were used for the scope of this work.

In addition to conventional methods, subsurface characteristics were investigated through DPIL, while LNAPL distribution was assessed through LIF logging. Measured values and ranges of subsurface parameters were employed to test the recently developed multiphase analytical model LNAPLTRANS, which is an updated version of LNAPLVOL (Lenhard et al., 2017, 2018). LNAPLTRANS was compared to the LNAPL Distribution and Recovery Model LDRM (Charbeneau, 2007a, 2007b; Jeong and

Charbeneau, 2014) which is available through the website of the American Petroleum Institute and has been employed by numerous researchers in the past.

Chapter 1 is an introduction to the rest of the doctoral thesis. It presents the significance of the problem, research objectives, contribution to knowledge, and this thesis outline.

Chapter 2 comprises a comprehensive literature review on LNAPL fundamentals from pore scale to field scale, characterisation of source zones (the subsurface region containing LNAPL), partitioning and degradation mechanisms influencing the source zone evolution, transport issues in heterogeneous media, and modelling approaches. Other important topics such as risk assessment and remediation technologies were not included for the sake of conciseness. The literature review ends with a summary of research gaps.

Chapter 3 briefly introduces the conceptual site model (CSM) of the two field sites, including details of the hydrostratigraphic setting and the contaminant release. CSMs are further developed throughout the results chapters.

Chapter 4 describes the materials and methods employed for the characterisation and analysis of field data. Extensive fieldwork was conducted in the petrol station site between 2014 and 2018, while data from the industrial site have been collected by other CSIRO Land and Water staff in different periods of time. The chapter is divided in nine sections:

- section 4.1 contains the rationale of the adopted materials and methods;
- section 4.2 describes the installation of monitoring points, and the collection and analysis of samples;
- section 4.3 presents the main features of the periodic monitoring campaigns;
- section 4.4 focuses on the collection and analysis of LIF data with the Ultra-Violet Optical Screening Tool (UVOST®);
- section 4.5 presents the collection and analysis of DPIL data. The DPIL system employed was the Hydraulic Profiling Tool® (HPT);
- section 4.6 defines the aquifer testing and baildown testing procedures to estimate T_n, aquifer transmissivity T_w, and hydrogeologic conditions;

- section 4.7 summarises methods the derive k_{sw} and retention parameters from particle-size data;
- section 4.8 presents the multiphase analytical models employed and the testing procedure;
- finally, section 4.9 introduces the rationale for the statistical data analysis procedures.

Chapter 5 is the first results chapter. It defines the geological setting in both sites and determines the existence of confining layers through particle-size data, hydrographs, diagnostic gauge plots (DGPs), HPT logs, and hydraulic testing. The chapter has three sections:

- as in every results chapter, the first section (5.1 in this case) introduces the chapter structure to the reader;
- sections 5.2 and 5.3 determine the geological layers of each area of study in the petrol station site and the industrial site, respectively (further developed in section 6.4) while critically evaluating the applicability of the employed methods.

Chapter 6 explores the application of LIF logs to assess LNAPL distribution and mobility. The paper 'Laser-induced fluorescence logging as a high-resolution characterisation tool to assess LNAPL mobility' published in Science of the Total Environment is based on this chapter. It is divided in six sections:

- section 6.1 introduces the chapter structure;
- section 6.2 investigates the correlation between LIF signal and T_n at field scale, in particular in the petrol station site. To best of the authors' knowledge, this potential correlation has been explored only once in the literature;
- section 6.3 further elucidates the relationship between LIF signal and LNAPL distribution and mobility in the petrol station site, specifically by identifying long-term entrapped and residual LNAPL due to changes in the multi-wavelength waveforms;
- section 6.4 compares results from LIF logging and more conventional methods such as soil gas measurements, LNAPL saturation (S_n) obtained through coring, and in-well fluid levels. These comparisons were separately made for each area

of study and contributed to design single- and multi-layered model scenarios used in chapter 8;

- section 6.5 is a summary of results and conclusions from chapter 6.

Chapter 7 quantifies ranges and most likely values of the parameters used in the modelling scenarios proposed for every area of study and simulated in chapter 8. These parameters included porosity Φ, k_{sw}, retention parameters, LNAPL properties, and T_n, giving more depth to the analysis of the most sensitive parameters for the model.

Chapter 8 evaluates and compares two multiphase analytical models (LDRM and LNAPLTRANS) used to predict LNAPL distribution and T_n from in-well fluid levels and subsurface parameters. The manuscript titled 'Testing an analytical model for predicting subsurface LNAPL distributions from current and historic fluid levels in monitoring wells: a preliminary test considering hysteresis' published in Water is associated to the content of the chapter. The chapter has five sections:

- section 8.1 introduces the chapter structure;
- section 8.2 tests capabilities and predictive power of LDRM and LNAPLTRANS in the base-case scenarios considering estimations of LNAPL distribution profiles, NAPL specific volume (V_n), and T_n using Burdine and Mualem relative permeability models;
- Section 8.3 investigates the effects of layering in LNAPL distribution and mobility;
- In section 8.4, a sensitivity analysis of the two analytical models is performed considering the effects on V_n and T_n. Thus, the underlying assumptions of both models were compared. Implications of the uncertainty associated to the determination of hydrogeological settings and input parameters were explored;
- Section 8.5 presents a summary of results and conclusions from the chapter.

Lastly, **chapter 9** summarises the main conclusions and limitations of the thesis and suggests future lines of research. **Chapter 10** contains all the references cited throughout the thesis. Multiple **appendices** include field data and supporting information.

2 Literature review

2.1 LNAPL contamination in the subsurface

2.1.1 Subsurface environments

Subsurface geological environments are multiphase systems comprising solid (inorganic minerals and organic matter), liquid (groundwater and NAPLs), and gaseous (soil gas and trapped gases) phases as well as living organisms and anthropogenic elements. They frequently exhibit a strong complexity and are interrelated with surface waters, ecosystems, and human activity (e.g. Vereecken et al., 2016; Tomlinson et al., 2017).

Fluid behaviour in geological media is largely controlled by the geometry of the pore space (Corey, 1994) and other medium properties. Therefore, subsurface systems are commonly classified as porous or fractured depending on their type of porosity. These systems can be further classified depending on their hydrogeologic properties (Meyer et al., 2016), degree of consolidation, type of geologic material (e.g. Gee and Or, 2002), and depositional environment (Payne et al., 2008). Strong correlation frequently exists between stratigraphic and hydrogeologic units in unconsolidated media (Meyer et al., 2016). Fundamentals of soil and groundwater systems can be found in many classic textbooks (e.g. Bear, 1972; Freeze and Cherry, 1979; Custodio and Llamas, 1983; Hillel, 1998; Todd and Mays, 2005).

2.1.2 LNAPL contamination

One of the most common and widespread cases of soil and groundwater contamination in urban and industrial environments is the release of organic substances such as petroleum and chlorinated hydrocarbons into the subsurface, where they can be found as NAPLs because they are sparingly soluble in water. The management of NAPL contaminated sites is particularly challenging due to the complex and heterogeneous nature of the hydrogeological system and the NAPL body even at fine scales (Essaid et al., 2015; Sale et al., 2018; Rivett and Wealthall, 2019). The characterisation and remediation of new and existing LNAPL contaminated sites is challenging and requires substantial investments (Dyment and Kady, 2019). Consequently, there is a need for improved pollution control and site management strategies.

Details about NAPL fundamentals and mechanics of immiscible fluids in the subsurface can be found in the literature (e.g. Corey, 1994; Pankow and Cherry, 1996; Helmig, 1997; Mayer and Hassanizadeh, 2005; Pinder and Gray, 2008; Johnston, 2010; Contaminated Land: Applications in Real Environments [CL:AIRE], 2014; Essaid et al., 2015; Blunt, 2017).

2.1.3 Chemical composition

NAPLs may be found in the form of pure chemical compounds and frequently as complex mixtures comprising thousands of compounds with different physical and chemical properties (Sookhak Lari et al., 2020) and toxicity (ITRC, 2018b).

In particular, petrol is primarily composed of monoaromatic hydrocarbons such as BTEX (benzene, toluene, ethylbenzene, and xylenes), some polycyclic aromatic compounds such as naphthalene and other PAHs (polycyclic aromatic hydrocarbons), aliphatics (in the case of petrol, mainly short chains of carbon atoms in the range C_4-C_{12}), and potentially additives such as MTBE (methyl tert-butyl ether), ETBE (ethyl tert-butyl ether), and ethanol (Johnston, 2010).

Aliphatics can be saturated (alkanes) or unsaturated (alkenes and alkynes). They can also be classified as cyclic (naphtenes) or acyclic (paraffins). Acyclic alkanes can be linear (normal alkanes; *n*-alkanes) or branched (*iso*-alkanes). In addition, a high number of isomers may exist. The term TPH (Total Petroleum Hydrocarbon) is typically employed to refer to the total amount of hydrocarbons in the carbon range (fraction) considered without identification of individual constituents (ITRC, 2018b).

The composition of petroleum hydrocarbons released into the subsurface varies with time (Peters et al., 1999; Logeshwaran et al., 2018; Sookhak Lari et al., 2020) due to natural and active depletion mechanisms, including natural source zone depletion (NSZD) processes. The chemical composition determines the toxicity of the mixture (Peters et al., 1999) and influences its longevity, depletion, and mass transfer processes. Furthermore, the NAPL chemical composition determines its physical properties (including density ρ_n, viscosity η_n, and surface tension σ_{an}). Combined with the groundwater composition, it also determines the interfacial tension σ_{nw}. All these

properties are key aspects to understand NAPL distribution and mobility (Johnston, 2010). Physical properties may vary according to other factors such as temperature.

2.1.4 Density

The role of ρ_n is fundamental to understand NAPL behaviour. NAPLs are usually divided in two groups depending on ρ_n: LNAPLs when they are lighter than water and dense non-aqueous phase liquids (DNAPLs) in the opposite case. The most common LNAPLs are petroleum hydrocarbons, while the most common DNAPLs are industrial chlorinated solvents. Mercury is an inorganic substance that behaves as a DNAPL in the subsurface (D'Aniello, 2017).

After being released into the subsurface in sufficient quantity, both LNAPLs and DNAPLs migrate downwards through the unsaturated zone due to gravity forces. However, as illustrated in Fig. 2.1, DNAPLs penetrate into the saturated zone and percolate down to the bedrock due to their high ρ_n, while LNAPLs get initially accumulated at the top of the saturated zone due to the action of buoyancy forces. This is followed by a redistribution period greatly influenced by fluctuations of the potentiometric surface elevation z_{aw} (Steffy et al., 1995, 1998; Chompusri et al., 2002; Oostrom et al., 2006b; Gatsios et al., 2018b; Atteia et al., 2019) under existence of capillary, viscous, and adsorptive forces. Biological processes and partitioning mechanisms are also indispensable to understand LNAPL fate and transport (presented in section 2.3). The rest of features depicted in Fig. 2.1 are discussed in the following sections.

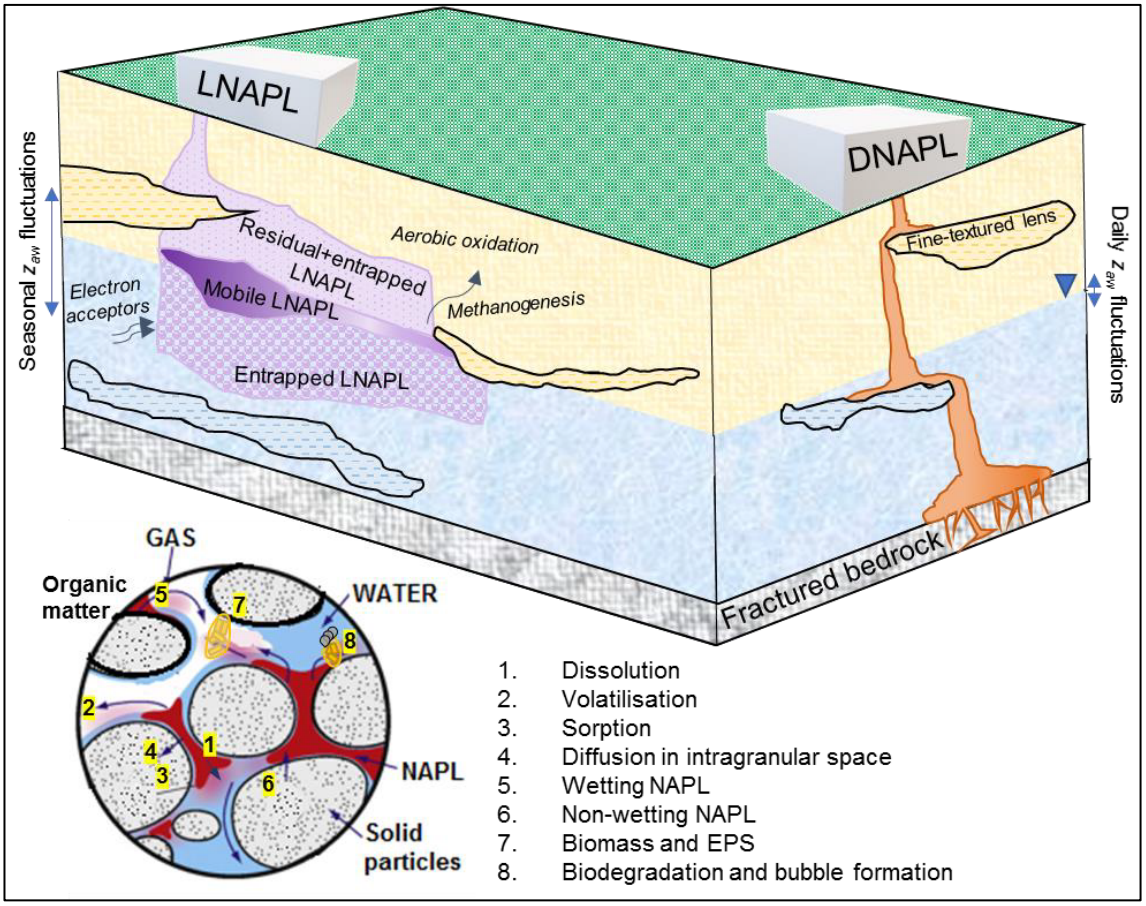


Fig. 2.1. Simplified representation of some key features influencing NAPL fate and transport in porous systems (after Mackay and Cherry, 1989; Rivett et al., 2011). EPS stands for extracellular polymeric substances.

2.1.5 Interfacial tensions and wettability

NAPL coexists with water and gas in the pore space. The configuration of all the phases at pore-scale depends on the wettability hierarchy. Water is generally assumed to be the wetting fluid, NAPL the intermediate-wetting fluid, and air the non-wetting fluid. Nevertheless, the properties of the medium and the fluids involved determine the resulting contact angles (Francisca and Montoro, 2014) and wettability hierarchy in the system, thus influencing multiphase flow characteristics (Molnar et al., 2020).

Consequently, aquifers may exhibit variable wetting conditions (Anderson, 1987; Newell et al., 1995; Bradford et al., 1997; O'Carroll et al., 2005) due to the heterogeneity of subsurface features such as mineralogy, grain roughness, and presence of organic matter. Therefore, hydrophilic and hydrophobic media may coexist in the subsurface.

The addition of NAPL into the system, in particular creosote and petrol, may further alter the wettability characteristics (Powers et al., 1996).

The spreading coefficient (calculated as the difference between the water surface tension σ_{aw} and the sum of σ_{an} and σ_{nw}) defines if the NAPL spreads over the medium surface (positive spreading coefficients) or form globules and lenses that do not totally wet the medium (negative spreading coefficients). The spreading coefficient may strongly influence NAPL distribution and the formation of near-immobile NAPL (Zhou and Blunt, 1997). The dissolution of NAPL constituents into water may alter the sign of the spreading coefficient over time (Keller and Chen, 2003) as in the case of benzene in water.

2.1.6 Capillary pressure and hysteretic effects

Capillary pressure has been traditionally defined as the difference between the non-wetting fluid pressure and the wetting fluid pressure (Mercer and Cohen, 1990; Hassanizadeh and Gray, 1993; Miller et al., 2019) and is a distinctive feature of multifluid systems in porous media. Capillary effects are even more relevant in cases of NAPL contamination than in other environments such as oil reservoirs due to the relatively small S_n values and spatial scales (Bear et al., 1996).

In porous media, entry pressure is defined as the non-wetting fluid head required to displace wetting fluid from the pore space (Farr et al., 1990; Corey, 1994). According to the Young-Laplace equation, the smaller the pore, the greater the entry pressure. Thus, non-wetting fluids preferentially occupy larger pores first. Total liquid saturation and S_n in the pore space may be assumed to depend on the air–NAPL and NAPL–water capillary heads, respectively (Parker et al., 1987).

Many of the processes controlling fluid distribution in porous media are lumped into an empirical relationship between capillary pressure and fluid saturation (Hassanizadeh and Gray, 1993) commonly called retention curve or P_c–S curve. Thus, this relationship depends on the properties of the geological medium and both fluids, including pore-size distributions, interfacial tensions, wettability (Anderson, 1987; Drake et al., 2013), and the history of fluid saturation changes because of the hysteretic nature of the retention curve as traditionally defined at macroscopic scale (Mualem, 1974; Johnston, 2010). The

retention curve characteristic of a pair of fluids may be scaled to a different pair of fluids in the same medium according to their interfacial tensions (Parker et al., 1987).

As depicted in Fig. 2.2, the shape of retention curves reflects many characteristic features of multifluid systems such as S_{ne}, S_{nr}, residual water saturation S_{wr}, and the non-wetting fluid entry pressure head. Since these features are incorporated in macroscopic retention models as fitting parameters, differences may exist with the physical entry pressure and near-immobile fluid saturations found in the subsurface (Farr et al., 1990; Corey, 1994).

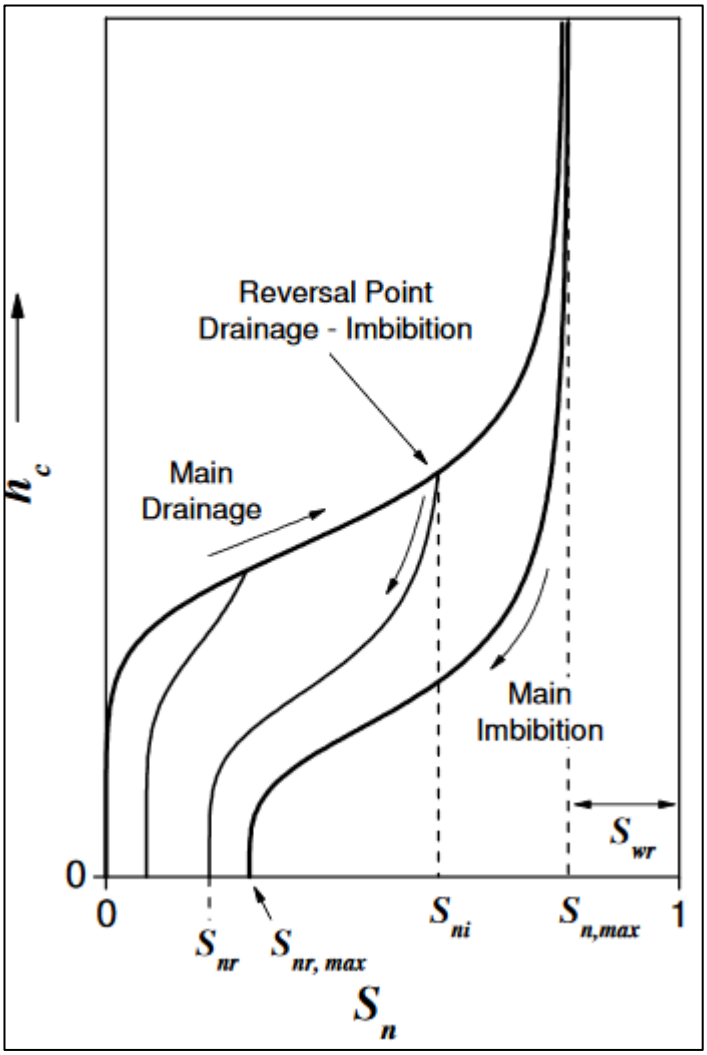


Fig. 2.2. Retention curves, showing main and intermediate NAPL drainage and imbibition paths (Johnston and Adamski, 2005).

As illustrated in Fig. 2.2, the hysteretic behaviour of the retention curve leads to infinite scanning paths potentially occurring between the main drainage and imbibition paths

('drainage' or 'imbibition' frequently refer to the path followed by the wetting fluid). Furthermore, the study of three-phase systems requires the additional analysis of total fluid paths.

Multiple studies have shown the relevance of considering hysteresis in the prediction of LNAPL distribution and mobility (Essaid et al., 1993; Sookhak Lari et al., 2016a; Lenhard et al., 2019). Nevertheless, hysteresis effects may be greatly influenced by subsurface heterogeneity. Therefore, a better subsurface characterisation may contribute to obtain improved predictions of LNAPL distribution without explicitly accounting for hysteresis, for instance through the application of a multimodal permeability model (Dillard et al., 1997).

In fact, it has been defended that capillary pressure is also function of the interfacial area (Hassanizadeh and Gray, 1990; Joekar-Niasar et al., 2010; Miller et al., 2019) and that the relationship between capillary pressure, fluid saturations, and interfacial area may be non-hysteretic, being hysteresis caused by an incomplete parametrisation (Niessner and Hassanizadeh, 2008; Miller et al., 2019). It has been shown that the traditional definition of capillary pressure does not adequately represent dynamic or non-equilibrium conditions (Das and Hassanizadeh, 2005; Joekar-Niasar et al., 2010; Diamantopolous and Durner, 2012; Essaid et al., 2015), being dynamic effects more relevant in finer-grained materials (Camps-Roach et al., 2010).

Some authors have indicated that hysteresis may still exist after accounting for interfacial area changes. Thus, additional factors such as fluid connectivity (Armstrong et al., 2016; Meisenheimer et al., 2020), complex pore geometries, mixed wettability, and contact angle hysteresis (Essaid et al., 2015) should be considered. Improved understanding of pore-scale phenomena is being achieved thanks to developments in areas such as X-ray tomography (Wildenschild and Sheppard, 2012), lattice Boltzmann simulations, and pore-network modelling (Blunt, 2017).

In this doctoral dissertation, the traditional definition of capillary pressure as the difference between the non-wetting and wetting pressures under equilibrium conditions is used. Accordingly, the concept of hysteresis is employed, although it is

acknowledged that many observations could be explained by changes in interfacial area or other factors.

2.1.7 Retention models

Many retention parametrical models exist (Brooks and Corey, 1964; van Genuchten, 1980; Fredlund and Xing, 1994; Leong and Rahardjo, 1997), including models accounting for mixed-wetting conditions (O'Carroll et al., 2005) and multimodal pore-size distributions (Durner, 1994; Alfaro Soto et al., 2019). The Brooks and Corey (1964) and van Genuchten (1980) equations (hereafter B–C and vG, respectively) have been the most applied in cases of LNAPL contamination.

The vG model considers that any non-wetting fluid pressure is able to produce a displacement, while the B–C model includes a pressure threshold h_{min} (Lenhard et al., 1989b) that may better represent NAPL physics and experimental data (Oostrom and Lenhard, 1998).

Leong and Rahardjo (1997) found that models with four parameters such as vG were generally more accurate than others with three parameters such as B–C. However, some authors have found that conventional constitutive models may not yield adequate predictions of NAPL behaviour (Gerhard and Kueper, 2003).

The vG model is frequently preferred over B–C due to complexities in the implementation of B–C equations in numerical models. Furthermore, vG functions may provide a better representation of field conditions in some cases, always depending on the parameterisation employed.

The model of vG includes four fitting parameters, θ_{wr}, $vG\text{-}\alpha$, $vG\text{-}m$, and $vG\text{-}N$, where θ_{wr} represents the irreducible water content, $vG\text{-}m$ and $vG\text{-}N$ are commonly assumed to be interrelated, and $vG\text{-}\alpha$ has been seen by many authors as the inverse of the air-entry pressure. There may be a link between $vG\text{-}\alpha$ and the air-entry pressure under certain circumstances, but $vG\text{-}\alpha$ does not necessarily have a clearly determined physical meaning and is actually larger than the maximal slope of the retention curve (Ippisch et al., 2006). In general, the relationships depicted in Fig. 2.3 may be seen in sandy materials for vG retention parameters (Benson et al., 2014).

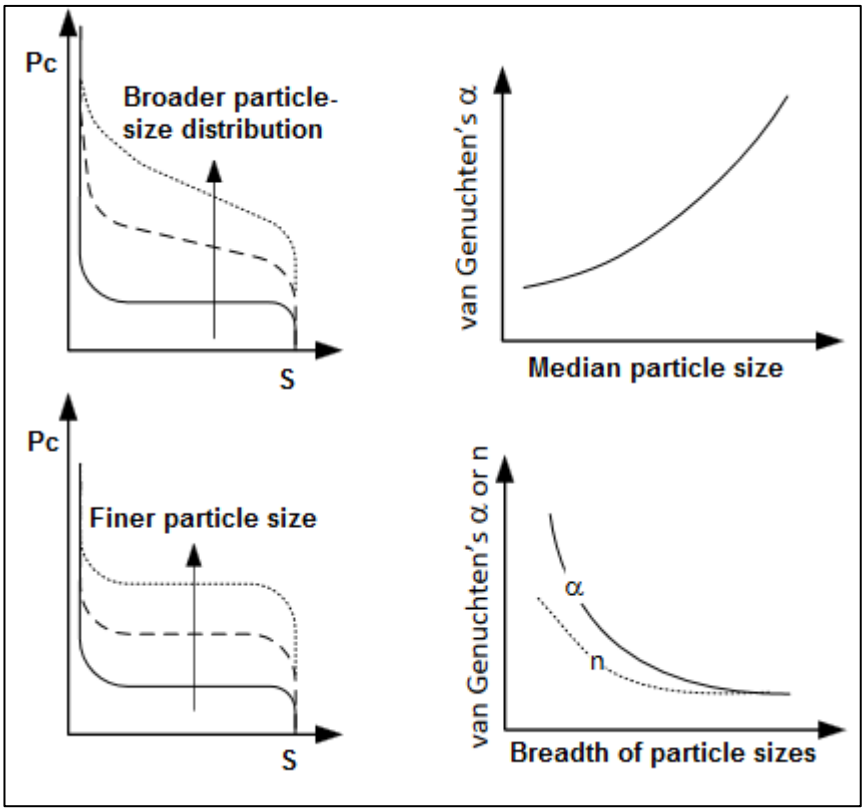


Fig. 2.3. Typical effects of median particle size and breadth of the particle-size distribution on P_c–S curves and vG retention parameters (modified after Benson et al., 2014).

Retention parameters can be estimated by experimental methods (Klute, 1986), but such approach is relatively time-consuming. Consequently, many efforts have been done in the field of vadose zone hydrology to estimate retention parameters through empirical or physical relationships such as point and parametric pedotransfer functions (Saxton et al., 1986; Vereecken et al., 2010), including neural network analysis (Schaap et al., 1998) and fractal approaches (Ghanbarian et al., 2010), or other derivations from particle-size data (Arya et al., 1999).

Pedotransfer functions make use of inputs that are easier to collect than retention parameters and that can be found in multiple sources like the Carsel and Parrish tables (Carsel and Parrish, 1988), the UNSODA database (Nemes, 2001) or the LNAPL parameters database from the American Petroleum Institute (API, 2006). These pedotransfer functions have been implemented in software tools such as RETC (van Genuchten et al., 1991), Hydrus (Šimůnek et al., 2012) and more comprehensively in Rosetta (Schaap et al., 2001).

A potential issue regarding the measurement of retention properties is that microorganisms and associated products such as EPS (Laspidou and Rittmann, 2002; Or et al., 2007; Flemming and Wingender, 2010) may modify retention characteristics and other subsurface properties, including wettability, k_{sw}, and near-immobile fluid saturations (Herman et al., 1997; Rockhold et al., 2002; Or et al., 2007; Atekwana and Atekwana, 2010; Rosenzweig et al., 2012; Brangarí et al., 2017). Methanogenic outgassing may also result in entrapped gases reducing k_{sw} (Amos and Mayer, 2006). Nevertheless, few retention models have incorporated microbial behaviour in their formulation (e.g. Mostafa and Van Geel, 2012; Brangarí et al., 2017).

Rosenzweig et al. (2012) recorded non-monotonic variations in $vG\text{-}\alpha$ between 1.96 and 3.24 m^{-1} in sands and between 2.17 and 4.24 m^{-1} in soil after changing the saturation of xanthan (a common EPS analogue with a large water retention capacity) in a water–air system. Other authors have reported a decrease in $vG\text{-}\alpha$ from 8.7 to 2.9 m^{-1} in a natural unsaturated soil affected by an engineered bioclogging process (see Brangarí et al., 2017). These numbers may greatly differ in NAPL–water systems and therefore further research should be conducted on this topic. Herman et al. (1997) observed similar formation of residual hexadecane in sand columns with and without bacteria (*Pseudomonas aeruginosa*). They acknowledged the attributes of biosurfactants to enhance the recovery of residual NAPL. Further discussion about the effects of biological processes in porous media are provided in section 2.3.4.

2.1.8 Mobile and near-immobile NAPL

NAPL may be classified as mobile or near-immobile NAPL depending on the fluid saturations and retention properties of the system. NAPL mobility has implications on the interpretation of field observations and the design of remediation strategies. Table 2.1 summarises the classification and definitions of LNAPL mobility states adopted hereafter, with details being presented in the following paragraphs. These definitions are consistent with those given by Lenhard et al. (2017). The terms ‘migrating NAPL’ and ‘stationary NAPL’ have been presented by Johnston (2010). It should be noted that different definitions have been adopted in other works (e.g. ITRC, 2018a). Further discussion about commonly adopted terminologies can be found in the literature (Lenhard et al., 2004; Johnston, 2010).

Table 2.1. Adopted definitions of NAPL mobility states.

NAPL mobility state and definition
• **Total NAPL**: sum of mobile and near-immobile NAPL.   ○ **Mobile (or free) NAPL**: NAPL able to move if a pressure gradient exists.   ▪ **Migrating NAPL**: NAPL moving within the NAPL body or beyond its edge.   ▪ **Stationary NAPL**: mobile NAPL not migrating due to absence of a pressure gradient or existence of barriers.   ▪ **Recoverable NAPL**: any mobile NAPL at a fluid pressure above atmospheric pressure.   ○ **Near-immobile NAPL**: NAPL not able to substantially move even if a pressure gradient exists.   ▪ **Residual NAPL**: near-immobile NAPL not occluded by water.   ▪ **Entrapped NAPL**: near-immobile NAPL occluded by water.

Mobile NAPL has the potential to migrate throughout the subsurface if a pressure gradient exists. Therefore, it can be recovered through LNAPL mass recovery systems such as skimming recovery, vacuum-enhanced recovery, and water-enhanced recovery if desired (Huntley and Beckett, 2002; Johnston, 2010; Beckett and Huntley, 2015; Gatsios et al., 2018b; Sookhak Lari et al., 2018; van Hullebusch et al., 2020).

This mobile NAPL may be stationary, that is, at greater saturation than entrapped and residual NAPL fractions but not migrating due to the absence of a pressure gradient or the existence of barriers impeding its movement (Johnston, 2010).

NAPL may enter screened wells and therefore be recoverable only if it exists at a fluid pressure greater than atmospheric pressure. Mobile NAPL is not recoverable when it exists at sub-atmospheric pressure (Johnston, 2010; Lenhard et al., 2017). Therefore, these are physical terms not fully accounting for the practicality of LNAPL mass recovery operations.

Near-immobile NAPL cannot substantially migrate throughout the subsurface even if a pressure gradient exists. Thus, the existence of near-immobile NAPL mass in the subsurface limits the effectiveness of NAPL mass recovery operations and represents one of the main challenges for the remediation of petroleum hydrocarbons (Sale et al., 2018). Furthermore, near-immobile NAPL may persist in the subsurface for decades as a source of groundwater pollution and vapour intrusion problems. Approaches such as engineered bioremediation (Gallego et al., 2001; Alvarez and Illman, 2006), NSZD (Garg et al., 2017), and surfactant-enhanced recovery (Robert et al., 2017; Huo et al., 2020; Sharma et al., 2020) may be required to successfully manage sites contaminated with near-immobile NAPL.

Despite the importance of entrapped and residual NAPL, there has not been a unified approach to characterise and define these near-immobile NAPL fractions in the literature (Lenhard et al., 2004; Oostrom et al., 2005). In petroleum engineering, the term 'residual saturation' has been commonly employed to refer to oil entrapped due to bypassing and snap-off mechanisms (Chatzis et al., 1983). Many authors have assumed entrapped and residual NAPL to be identical (e.g. Jeong and Charbeneau, 2014) and completely immobile at any flow rate, although experimental observations have suggested the existence of ganglia dynamics (Joekar-Niasar and Hassanizadeh, 2012).

Lenhard et al. (2004, 2017) have defended that entrapped and residual NAPL correspond to near-immobile, water-occluded NAPL and non-occluded NAPL, respectively, and therefore formed according to different physical mechanisms. It has been shown the importance of considering not just S_{ne} but also S_{nr} in predictions of LNAPL distribution (Van Geel and Sykes, 1997; Oostrom et al., 2005) and how values of near-immobile S_n in the saturated and unsaturated zones differ (Mercer and Cohen, 1990). S_{ne} values are generally greater than S_{nr} values (Johnston, 2010).

Accordingly, residual NAPL can be found in the unsaturated zone in films (or lenses in the case of non-spreading NAPLs), pore wedges, and bypassed pores (Lenhard et al., 2017). Entrapped NAPL in the form of blobs or ganglia is mostly located in the saturated zone (Johnston, 2010), although water can also occlude minor amounts of NAPL mass in the unsaturated zone, especially during the imbibition path. Entrapped NAPL is

discontinuous, while residual NAPL may be either continuous or discontinuous. Fig. 2.4 shows a sand column with connected and disconnected LNAPL in the unsaturated and saturated zones.

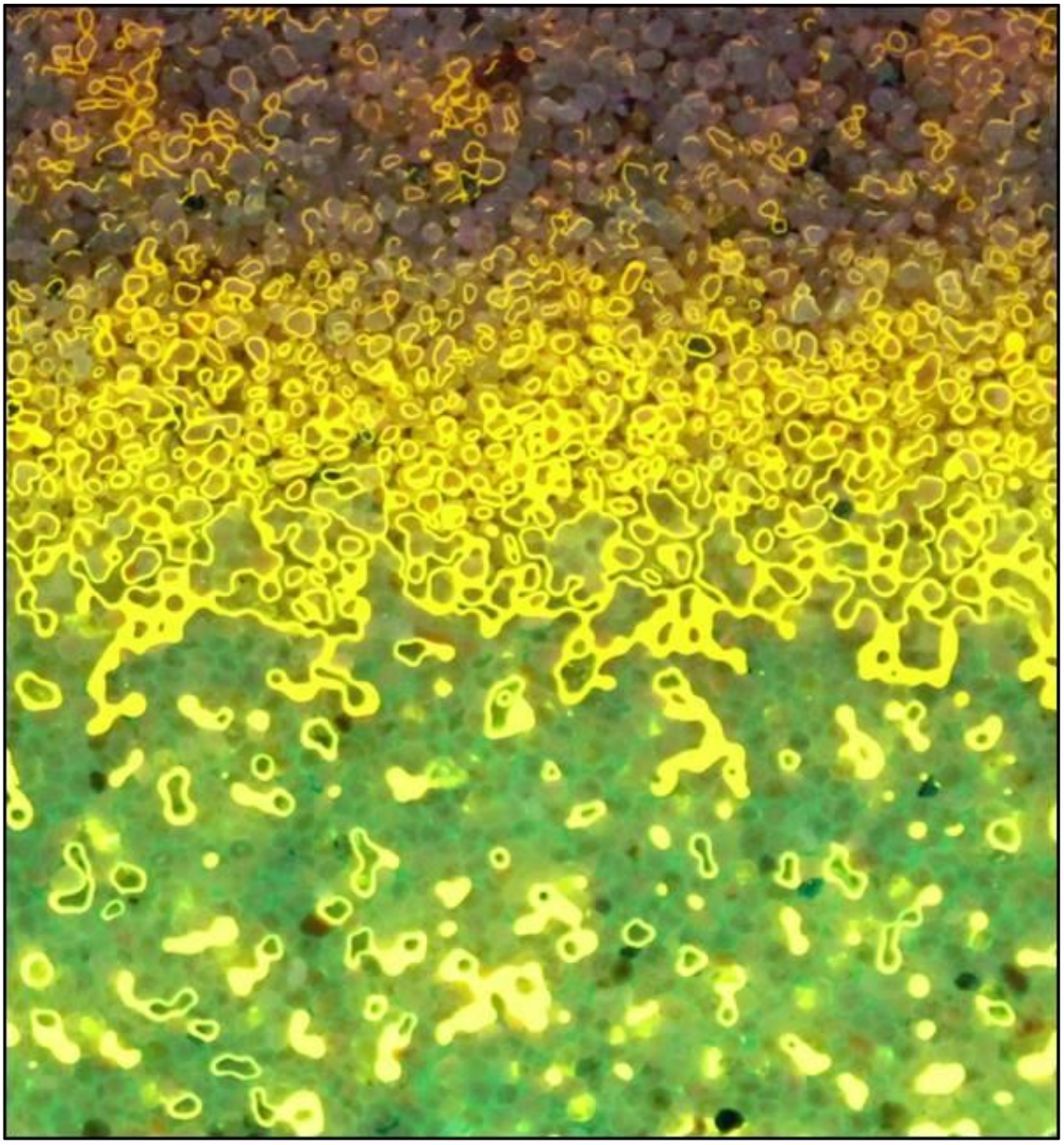


Fig. 2.4. Visualisation of LNAPL distribution in the unsaturated and saturated zones with fluorescence (after Skinner, 2013; Tracy, 2015; M. Tracy, personal communication, April 2019).

Methods have been developed to predict S_{nr} (Van Geel and Roy, 2002; Lenhard et al., 2004; Oostrom et al., 2005) and S_{ne} (Land, 1968; Kueper et al., 1993; Johnston and Adamski, 2005). The history of fluid saturation (as illustrated in Fig. 2.2) and imbibition rate have been found to control the formation of near-immobile NAPL (Land, 1968; Kueper et al., 1993; Johnston and Adamski, 2005; Nguyen et al., 2006; Patterson, 2011;

ITRC, 2018a) along other factors such as fine-scale subsurface heterogeneities (Wilson et al., 1990), moisture content (Steffy, 1997b; Van Geel and Roy, 2002), and the spreading coefficient (Zhou and Blunt, 1997). The influence of multiple factors on the formation of entrapped and residual NAPL leads to non-uniform distributions of near-immobile NAPL fractions at field scale (ITRC, 2018a).

Laboratory studies have been reported to measure gasoline residual saturations as high as a 60 % in fine sands (Hoag and Marley, 1986; Mercer and Cohen, 1990). However, it has been suggested that laboratory experiments may have overestimated the presence of near-immobile NAPL (ITRC, 2018a) because of the pressures and flow conditions typically considered in these experiments (Kueper et al., 1993).

2.1.9 Relative permeability

The constitutive relationships for multiphase systems link the fluid relative permeability with the characteristic retention curves. If NAPL is the intermediate-wetting fluid, its saturation and relative permeability depend not only on its own saturation but on the saturation of the aqueous and gaseous phases (Leverett and Lewis, 1941; Parker et al., 1987). Many relative permeability models exist (Childs and Collis-George, 1950; Burdine, 1953; Mualem, 1976; Delshad and Pope, 1989; Blunt, 2000), many of them derived from the same principles applying different assumptions (Mualem and Dagan, 1978). Relative permeability is also affected by the medium and fluid properties, including interfacial tension, viscosity, and the saturation history (Alizadeh and Piri, 2014).

The vG function is usually linked with Mualem's pore-size distribution model, while the B–C function is associated to Burdine's pore-size distribution model (Oostrom and Lenhard, 1998). These linkages may constrain the retention parameters and limit the validity of the models (Ippisch et al., 2006; Likos and Yao, 2014). Brooks and Corey (1964) modified Burdine's equations since they may underestimate non-wetting relative permeabilities when the saturation of the wetting phase if large (Corey and Brooks, 1999).

Parker and Lenhard developed non-hysteretic (Parker et al., 1987) and hysteretic constitutive relationships (Parker and Lenhard, 1987) based on the vG–Mualem model. A good definition of the constitutive relationships is imperative to properly represent

the source zone and its evolution. Some authors have advocated that non-wetting fluid near-immobile saturation is the key parameter to adequately model relative permeabilities in three-phase systems (Kianinejad et al., 2015).

2.2 LNAPL source zone characterisation

2.2.1 Field-scale LNAPL distribution

The spatial and temporal distribution of NAPL released into the subsurface depends on the dynamic interaction between the NAPL mass, the hydrogeological medium and their properties. The resulting complex distribution of NAPL saturations is known as the source zone architecture (Sale and McWhorter, 2001).

NAPL distribution may reflect phenomena such as fingering (Kueper and Frind, 1988; Held and Illangasekare 1995; Zhang et al., 2011), formation of near-immobile and mobile NAPL, penetration of LNAPL below the initial water table mainly as a function of buoyancy and capillary forces (CL:AIRE, 2014) or development of confined and perched LNAPL conditions due to the presence of fine-grained materials acting as capillary barriers (Illangasekare et al., 1995; Johnston, 2010; Kirkman et al., 2013). In detrital sedimentary deposits, NAPL may preferentially occur at higher S_n in coarser-grained intervals (Essaid et al., 2011).

Nevertheless, even small-scale physical, chemical, and biological heterogeneities may contribute to create complex NAPL distributions and affect the remediation performance (Kueper and Frind, 1991; Essaid et al., 1993; Bradford et al., 1998; Lemke and Abriola, 2006; Johnston and Trefry, 2009). The source zone architecture also influences aspects such as the associated risks to human health and the environment, source zone longevity, mobility, and depletion (Christ et al., 2006; Zhang et al., 2008).

Hence, deficiencies in the management of LNAPL contaminated sites have been frequently related to inadequate CSMs as concerns the characterisation of the LNAPL source zone (Tomlinson et al., 2017). Before the paradigm shift fostered by the works of Lenhard and Parker (1990a) and Farr et al. (1990), it was assumed that the spilled LNAPL mass would float over the water table within an interval in the formation corresponding to a 'true thickness' of LNAPL. Field observations of LNAPL below z_{ow} would be typically explained by a depression in the water capillary fringe. Within this true LNAPL thickness,

it was generally assumed that the pores (at least all the pore space without irreducible water content) were fully saturated with LNAPL. This conceptualisation has been usually referred to as the 'pancake model' (Frollini and Petitta, 2018) and ignored much of the multiphase flow theory developed in other fields, notably in the petroleum engineering industry.

Theoretical developments and observations at laboratory and field scales suggested that the in-well NAPL thickness b_n was an apparent thickness distinct to the true LNAPL thickness in the formation. This contrast was considered to be due to the water capillary fringe and therefore influenced by grain size (Testa and Paczkowski, 1989; Mercer and Cohen, 1990; Newell et al., 1995), potentially generating apparent LNAPL thicknesses greater than the true LNAPL thickness by a factor between 2 and 10 (Mercer and Cohen, 1990). The importance of estimating LNAPL volumes in the subsurface from gauged b_n values led to the development of simple equations trying to relate apparent and true LNAPL thickness (Pastrovich et al., 1979; Testa and Paczkowski, 1989; Ballestero et al., 1994; Saleem, 2005) or to estimate true LNAPL thickness from baildown testing (Testa and Paczkowski, 1989).

However, the limitations of these simplistic approaches were noted by other researchers (Hampton, 1989; Kemblowski and Chiang, 1990). Schiegg (1985) developed relationships already taking into consideration capillarity effects affecting three-phase systems (Schiegg and Schwille, 1991). Hampton (1989) concluded that there was not a simple approach to predict LNAPL distributions, being the use of constitutive theory from Parker et al. (1987) the best choice. Assuming vertical hydrostatic equilibrium (VEQ) conditions, Parker and Lenhard (1990) developed vertically integrated constitutive relationships of three-phase systems that could be used to predict V_n (NAPL volume within the vertical interval impacted by NAPL per unit area) and T_n, a measure of NAPL mobility. This model did not incorporate immobile NAPL nor could predict elevation-dependent S_n values. VEQ conditions can be seen as analogous to the Dupuit–Forchheimer assumption in groundwater systems (Bear and Ryzhik, 1998).

The role of water table fluctuations smearing LNAPL and entrapping it below the current z_{aw} was also emphasised (Schwille, 1984; Hunt et al., 1988; Kemblowski and Chiang,

1990; Durnford et al., 1991). In particular, it was noted that differences between magnitudes of entrapped and residual LNAPL and the predominance of such dynamic conditions complicate the prediction of LNAPL volumes in the subsurface (Kemblowski and Chiang, 1990; Atteia et al., 2019).

Two physically based analytical models refuting the existence of LNAPL 'pancakes' were then developed making use of B–C and vG P_c–S relationships and published at the same time (Lenhard and Parker, 1990a; Farr et al., 1990). Both models assumed VEQ conditions and were identical when proper integration limits were chosen (Lenhard and Parker, 1990b). This conceptualisation has been labelled as the 'vertical equilibrium model' (Frollini and Petitta, 2018). Input requirements included LNAPL and medium properties as well as in-well fluid levels that should be representative of the fluid pressures in the formation.

LNAPL was demonstrated not to distribute itself as a distinct layer of constant S_n floating over the capillary fringe. The VEQ model did not predict the outdated concept of true LNAPL thickness but elevation-dependent S_n values and V_n. As illustrated in Fig. 2.5, S_n profiles were predicted to resemble a shark fin in homogeneous porous media under VEQ conditions. The formation interval containing free LNAPL was coincident with b_n when it was predicted according to the vG relationship. On the contrary, b_n differed from the B–C prediction due to the positive value of entry pressure.

It could also be demonstrated that V_n is generally greater in coarse-grained materials than in fine-grained materials for the same b_n (Lenhard et al., 2017). Analogously, a fine-grained material would result in a higher b_n than a coarse-grained material for the same V_n (Huntley et al., 1994a, 1994b). In addition, the dependence of S_n would allow the inverse calculation of retention parameters from field saturation data (Lundegard and Mudford, 1998).

Nevertheless, this VEQ model did not implement hysteretic effects nor estimations of entrapped and residual LNAPL. In addition, the effects of heterogeneous geological scenarios were not assessed at first. Lenhard and Parker (1990a) identified and discussed these complicating factors (non-equilibrium conditions, layered media, P_c–S hysteresis and the generation of near-immobile LNAPL) and suggested to conduct

further research in the future. Subsequently, the VEQ model was evaluated and adapted in several occasions. VEQ conditions have been assumed to develop other sets of analytical equations, for instance to predict LNAPL migration on a horizontal or sloping plane (Bear et al., 1996; Bear and Ryzhik, 1998).

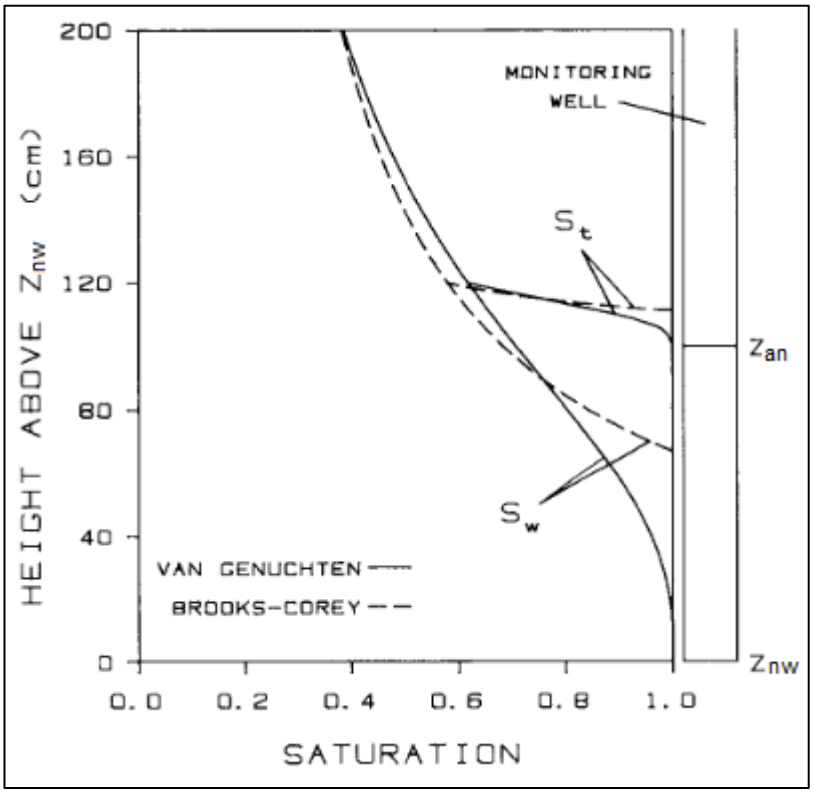


Fig. 2.5. VEQ model predictions of LNAPL vertical distribution in a hypothetical soil according to vG and B–C relationships (adapted from Lenhard and Parker, 1990a).

As regards geological heterogeneity, vertical variability in the medium properties was found to greatly impact the S_n profiles creating abrupt discontinuities in S_n as depicted in Fig. 2.6. Therefore, predictions of S_n distribution and V_n were improved through the incorporation of multiple layers on the VEQ model, although still showing clear discrepancies with field measured data (Huntley et al., 1994a, 1994b).

Horizontal variability in the medium properties was equally found to strongly influence the VEQ predictions, even at small scales in relatively homogeneous sites. For instance, a fivefold variation in V_n was predicted according to samples taken at the same depth and at a distance of just 7.5 m (Huntley et al., 1994b). Consequently, the collection of few field samples considered to represent site averages and the extrapolation of results from one monitoring well to another may lead to misleading conclusions. Using particle-

size data to estimate P_c–S relationships was also found to induce significant errors in the VEQ model predictions (Huntley et al., 1994b).

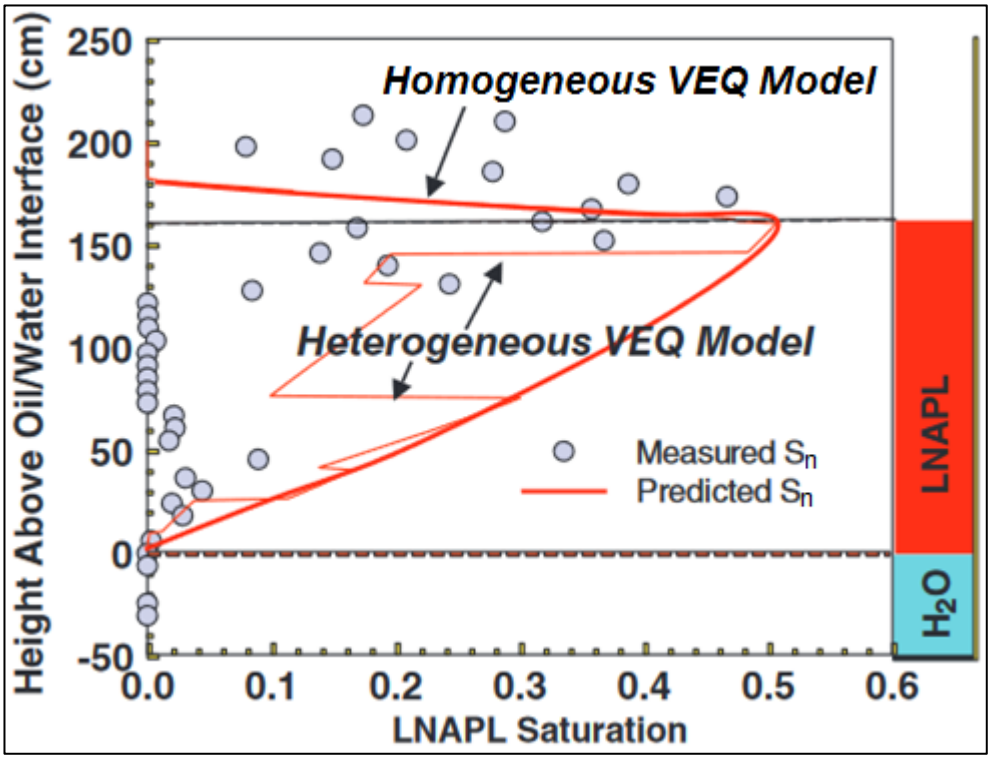


Fig. 2.6. Field measured S_n values versus predictions from the VEQ model for one and multiple layers in a fine-grained sandstone (adapted from Beckett and Huntley, 2015).

In addition, vG relationships have been developed for cases of LNAPL contamination in porous media with multimodal pore-size distributions (Alfaro Soto and Chang, 2015; Alfaro Soto et al., 2019) following analogous work in air–water systems (Durner, 1994).

As concerns P_c–S hysteresis and the presence of near-immobile LNAPL, several laboratory, field, and modelling studies have demonstrated the influence of water table fluctuations on LNAPL redistribution (Lenhard et al., 1993; Steffy et al., 1995, 1998; Chompusri et al., 2002; Kechavarzi et al., 2005; Oostrom et al., 2006b; Sun, 2016).

Fig. 2.7 depicts field observations of LNAPL redistribution made over decades. It is shown that the LNAPL profile changed with z_{aw}. The contrast between Fig. 2.7(a) and Fig. 2.7(b) indicates that an induced drawdown of z_{aw} was followed by a migration of LNAPL mass downwards, although some LNAPL remained at higher elevations in residual form or under non-equilibrium conditions.

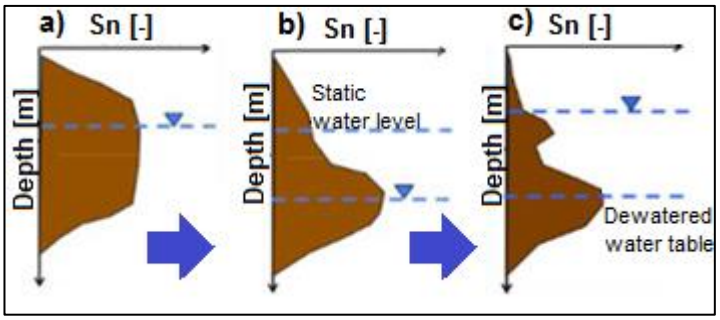


Fig. 2.7. Field redistribution of LNAPL under changes in z_{aw} (modified after Tomlinson et al., 2012).

Furthermore, other aspects such as non-equilibrium conditions, borehole effects, and the existence of confining materials may alter the relationship between the impacted interval in the formation and in-well fluid levels (Aral and Liao, 2002; Oostrom et al., 2006b; Kirkman et al., 2013; Atteia et al., 2019).

In particular, the existence of confined LNAPL conditions imply an increase of b_n with z_{aw}, while unconfined LNAPL conditions are represented by opposite trends in b_n and z_{aw}. On the other hand, perched LNAPL conditions correspond to an increase of b_n with constant z_{an} and decreasing z_{aw}. (Kirkman et al., 2013). Therefore, monitoring of in-well fluid levels may allow identification of LNAPL hydrogeologic conditions (unconfined, confined, leaky confined, perched) and provide information about the subsurface setting. Further discussion on this topic is presented in section 4.3.4. Hawthorne et al. (2015) analysed 489 wells in multiple sites and found 57.5 % of wells with unconfined LNAPL, 34.4 % with confined LNAPL, only 1.6 % with perched LNAPL, and 6.5 % with conditions categorised as 'complex'.

A hysteretic model including LNAPL and air entrapment (Lenhard, 1992) was adapted to estimate V_n (Marinelli and Durnford, 1996). The hysteretic model was a refinement of a previous model (Parker and Lenhard, 1987) that followed a similar approach as hysteretic models of air–water systems (Kool and Parker, 1987) and made use of empirical LNAPL entrapment relationships from the field of petroleum engineering (Land, 1968). This model was already refined by Lenhard et al. (1989a) who concluded that models considering hysteresis due to entrapment only and models also implementing contact angle hysteresis and 'ink bottle' effects yield similar results, being the former less computationally expensive.

In addition, models were developed to predict V_n accounting for transient effects and not only VEQ conditions. However, several existing approaches have not explicitly implemented hysteretic behaviour nor elevation-dependent S_n values (Aral and Liao, 2002; Atteia et al., 2019) and may require numerical methods for their resolution or not differentiate between residual and entrapped LNAPL saturations (Aral and Liao, 2002).

Recently, a transient fully analytical model discriminating between residual and entrapped LNAPL saturations was developed focusing on highly viscous LNAPLs (Atteia et al., 2019). The results were compared to the VEQ model for the case of a highly viscous LNAPL in absence of VEQ conditions. Alternatively, a numerical approach was followed to account for elevation-dependent S_n values, hysteresis, geological layering and non-equilibrium conditions (Sleep et al., 2000) under the assumption that residual and entrapped LNAPL saturations were identical. The results were compared to the VEQ model but using a homogeneous version, so it did not allow discrimination of the influence of VEQ assumption.

Other two VEQ models have included the formation of near-immobile LNAPL, although without implementing hysteretic effects: LDRM (Charbeneau, 2007a, 2007b; Jeong and Charbeneau, 2014) and LNAPLVOL (Lenhard et al., 2017, 2018). Lenhard et al. (2017) accounted for water table fluctuations by using current and historic fluid levels as input parameters, while LDRM could be used to simulate changes in b_n. The two models predict LNAPL distributions, V_n and T_n. LDRM has been modified by other authors to include up to 14 layers incorporating linear variability of any property within each layer (Al Awar, 2008) or up to 10 layers in multiple locations interpolating the results by kriging (de Blanc and Farhat, 2018). On the other hand, LNAPLTRANS is a modified version of LNAPLVOL incorporating up to five layers and different input formats (R. Lenhard, personal communication, June 2018). A more detailed description of LNAPLTRANS and LDRM is included in sections 4.8.1 and 4.8.2, respectively.

Despite the advantages of the VEQ model over the pancake model, many environmental regulations worldwide still rely on b_n as a remedial endpoint. Fortunately, the use of b_n as a remedial endpoint has been reported to decrease in the last years (Kimball et al., 2017) and many other metrics have been proposed and are being used for the

management of LNAPL contaminated sites. For instance, measures of NSZD to estimate the longevity of the source zone (see section 2.3), NAPL mass fluxes in the vapour and water phases to assess risks to human health and the environment (see section 2.3), and T_n to evaluate NAPL mobility and recoverability. Alternatively, Ebrahimi el al. (2019) have suggested to conduct LNAPL mass recovery operations in locations with the highest LNAPL specific yield, that is the highest ratio between recoverable and total V_n, aiming to minimise the generation of near-immobile LNAPL.

2.2.2 Field-scale LNAPL mobility

2.2.2.1 LNAPL transmissivity

T_n is a measure of LNAPL mobility defined in an analogous way to T_w (Kirkman, 2013), relating LNAPL drawdown to LNAPL flow (ITRC, 2018a). Lenhard et al. (2017) classified T_n as free T_n and recoverable T_n. The concept of recoverable T_n only considers the LNAPL fraction above atmospheric pressure (therefore able to flow into a well), while free T_n also considers mobile LNAPL at a pressure below atmospheric pressure (LNAPL not able to flow into a well) and near-immobile LNAPL (although its contribution may be negligible).

T_n is being increasingly adopted instead of b_n as an improved metric for quantifying LNAPL recoverability (Kimball et al., 2017) and in some cases DNAPL recoverability (Reyenga and Hawthorne, 2017). T_n has been proposed as a remediation metric for many purposes (ITRC, 2018a) but with some limitations on its applicability due to many sources of variability (Kirkman and Hawthorne, 2014; Beckett and Huntley, 2015; Gatsios et al., 2018b) as illustrated in Fig. 2.8. For instance, water table fluctuations have been found to greatly affect T_n and LNAPL recovery in LNAPL contaminated sites (Pede, 2009; Kirkman and Hawthorne, 2014; Beckett and Huntley, 2015; Kuo et al., 2016; Gatsios et al., 2018b).

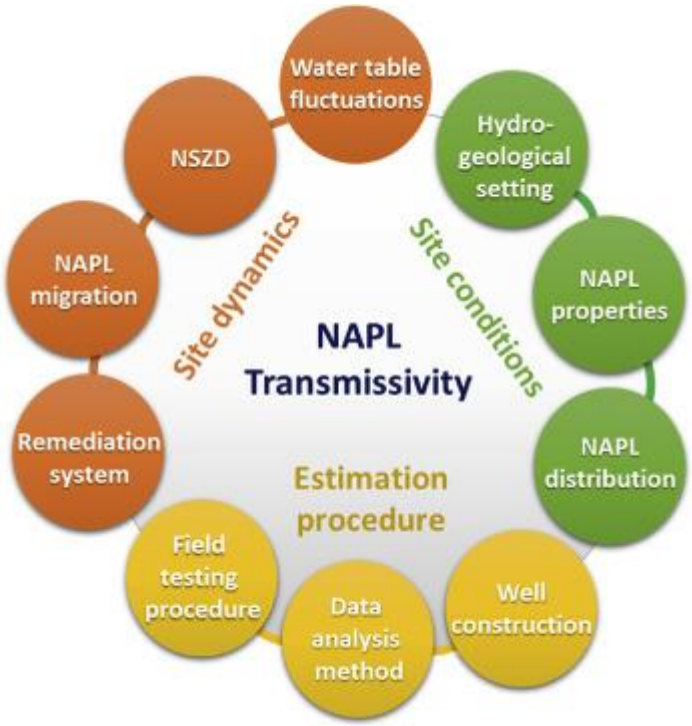


Fig. 2.8. Sources of variability of T_n (Gatsios et al., 2018b).

2.2.2.2 Methods to assess LNAPL recoverability

Methods to assess LNAPL recovery include baildown testing (ASTM International, 2013; API, 2016; Butler, 2019), manual LNAPL skimming tests (ASTM International, 2013), LNAPL recovery system evaluation (Charbeneau et al., 2000; Sale, 2001), LNAPL tracer testing (Mahler et al., 2012a; Pennington et al., 2016), as well as simplified approaches such as qualitative assessments of LNAPL recoverability, Darcy's Law calculations along integration of k_n values supported by petrophysical studies, and type-curve matching. LNAPL baildown tests are analogous to groundwater slug and baildown tests, while LNAPL recovery system evaluations are based on Thiem equation analogously to its application for aquifer testing. Qualitative assessments have also been employed to predict the productivity of wells for water supply purposes (MacDonald et al., 2008). An overview of existing methods to estimate T_n can be found in ITRC (2018a).

Aral and Liao (2000) showed that the baildown test method referenced by Testa and Paczkowski (1989) could not generally be used to determine a value of LNAPL thickness in the formation. Nevertheless, baildown testing has become the most commonly applied T_n estimation technique because it requires less resources than other methods. Therefore, improved field protocols, as well as analytical, semianalytical, and numerical

solutions have been developed to measure T_n through baildown testing (Zhu et al., 1993; Huntley, 1994a; Lundy and Zimmerman 1996; Huntley, 2000; Beckett and Lyverse, 2002; Hampton, 2003; ASTM International, 2013; Kirkman, 2013; API, 2016; Holmes, 2019).

Huntley et al. (1994a) analysed a baildown test with the Jacob and Lohman solution (Jacob and Lohman, 1952) and compared the results to k_n values calculated with the vertically integrated constitutive relationships developed by Parker and Lenhard (1990) in three sandstone samples following the Mualem model. The obtained values were compared to a baildown test, finding a relatively good agreement between both methods (20–50 % difference). The constitutive model of Parker et al. (1987) also predicted k_n values consistent with baildown testing at laboratory scale (Palmier et al., 2017).

This similarity between T_n estimation methods contrasted to more recent analyses of multi-site T_n data where petrophysical analysis did not provide repeatable results (Hawthorne, 2015), although it could have been due to the limited number of analyses. As regards other field-based methods, differences in the estimation of T_n within a factor of 2 have been considered reasonable (ASTM International, 2013).

2.2.2.3 Analytical solutions to predict LNAPL transmissivity

In addition to the Jacob and Lohman approach for constant drawdown (an approximation of the Cooper and Jacob and therefore Theis equations), the Bouwer and Rice solution (Bouwer and Rice, 1976) for slug testing was also adapted to the analysis of baildown tests in multiphase systems under unconfined conditions (Lundy and Zimmerman 1996; Huntley, 2000). The Bouwer and Rice method is based on Thiem equation.

The Bouwer and Rice approach was derived in two distinct ways by Lundy and Zimmerman (1996) and Huntley (2000) with different boundary conditions (constant LNAPL drawdown or constant z_{aw}) and resulting T_n values. Both derivations were unified by incorporating the slope of the presumably linear relationship between LNAPL drawdown and b_n as an additional parameter, the J-ratio (Kirkman, 2013). High variability associated to this ratio indicates an increasing error in the application of the Bouwer and Rice solution, thus favouring the application of the Jacob and Lohman

method, better suited for transient conditions according to ASTM International (2013). In addition, expressions for confined and perched LNAPL conditions, as well as the Cooper–Bredehoeft–Papadopulos method for unconfined LNAPL conditions, have also been adopted (API, 2016). Similar approaches based on Thiem equation have been developed for LNAPL recovery system evaluation (Charbeneau et al., 2000; Sale, 2001).

Nonetheless, the Bouwer and Rice solution has been demonstrated to underestimate T_w and possibly T_n (Butler, 2019), while other methods (Jacob–Lohman and Cooper–Jacob) are based on pumping test solutions and therefore their application to the analysis of baildown tests has been discouraged (Butler, 2019). Similarly, the applicability in multifluid systems of many of the assumptions behind the Bouwer and Rice expression has been disputed by some authors (Batu, 2012). However, field and laboratory observations have suggested that the current analytical solutions may be robust enough for practical purposes (Charbeneau et al., 2013; Palmier et al., 2017). For instance, good agreement between the Jacob and Lohman solution, the generalised version of the Bouwer and Rice approach and a modified Cooper solution (Beckett and Lyverse, 2002) has been reported under unconfined LNAPL conditions in a field site contaminated with highly viscous LNAPL (Palmier et al., 2016).

Additional studies on baildown testing have included laboratory experiments (Palmier et al., 2017) and modelling works (Ahmed et al., 2018) exploring the accuracy of the methods. Zhu et al. (1993) and Lundy (2006) adopted inverse approaches to estimate van Genuchten retention parameters from baildown test data. Current predictive tools such as LDRM and LNAPLTRANS include the calculation of T_n values.

2.2.2.4 LNAPL stability

Besides of a positive T_n value, migration of mobile LNAPL within the LNAPL body requires the existence of a gradient in the LNAPL head. In an analogous way to Darcy's law (Darcy, 1856; Hubbert, 1940), the LNAPL velocity within the LNAPL body v_n has been defined as in equation 2.1 (Johnston, 2010).

$$v_n = M_n \nabla H_n = \frac{T_n}{V_n} \nabla H_n \qquad (2.1)$$

where:

- M_n is the inherent LNAPL mobility;
- ∇H_n is the lateral gradient in the LNAPL head.

Gradients in the LNAPL head have been estimated considering z_{an} values at multiple well locations and the distance between them (Smith, 2008), although using z_{aw} values within the LNAPL body has also been proposed (Mahler et al., 2012a). Many assumptions are commonly adopted when calculating gradients in the LNAPL head, for instance linear hydraulic head gradients, homogeneous LNAPL properties, isotropic medium and equilibrium conditions (Smith, 2008). Nevertheless, some of these assumptions are frequently violated and there are errors associated to the measurement of in-well fluid levels as in the case of water-saturated (not multifluid) systems (Devlin and McElwee, 2007; Rau et al., 2019), besides of additional errors due to the presence of emulsions, highly viscous LNAPL or strong biological activity (Smith, 2008).

Under natural conditions, gradients in the LNAPL head generally tend to diminish with time after the initial spill (Beckett and Huntley, 2015; ITRC, 2018a). The occurrence of LNAPL natural losses may lead to a stable (eventually shrinking) LNAPL body (Lundy, 2014) in a relatively short timeframe (Mahler et al., 2012b; Tomlinson et al., 2017) as it has also been observed in the case of dissolved plumes due to natural attenuation processes (Wiedemeier et al., 1999). LNAPLs with low viscosity such as petrol and diesel may become stable in weeks or months (ITRC, 2018a). Fluctuations in z_{aw} may also contribute to this stabilisation (Hawkins, 2013). In such scenarios, the velocity of the LNAPL body edge is negligible despite temporal redistributions of mass within the LNAPL body due to water table fluctuations and other factors. Further details about NSZD phenomena are given in section 2.3.1.

2.2.3 Field delineation of LNAPL distribution

2.2.3.1 Non-invasive characterisation

Building a CSM requires careful interpretation of multiple sources of information (CL:AIRE, 2014). In particular, field-scale delineation of complex LNAPL distributions is challenging and demanding in terms of resources. Tiered judgemental sampling approaches are commonly followed, with initial efforts directed to confirm the existence of contamination and sources of release, choosing subsequent sampling locations and

techniques according to data already collected with the goal of effectively manage the site contamination risks. The first steps of a contaminated site sampling strategy may involve the use of non-invasive screening methods, although the design of a field campaign is always site-specific (French et al., 2014; Algreen et al., 2015) and depend on cost–benefit analyses.

Screening methods are usually qualitative or semi-quantitative in nature and include soil gas measurements, radon emanometry, phytoscreening, and geophysics. Soil gas measurements (Rivett, 1995; Cohen et al., 2016) of CH_4, CO_2, O_2, or multiple gases using a photo-ionisation detector (PID) or a flame ionisation detector (FID) have likely been the most common screening method. Measurements are usually taken at shallow depths after doing a small perforation in the soil, but they may also be taken on extracted cores to better select sampling intervals (Einarson et al., 2016). Radon has been used as a natural tracer indicating the presence of LNAPL and emanometry techniques have been developed and successfully applied in the field (De Miguel et al., 2018). Phytoscreening involves taking samples of plants, frequently tree cores, and analysing them to detect chemicals of concern (Algreen et al., 2015).

Increasing awareness of the spatiotemporal variability of groundwater pollution problems has contributed to the growth of the field of hydrogeophysics (Rubin and Hubbard, 2005; Binley et al., 2015). Some of the most common near-surface geophysical techniques used in hydrogeological studies are electrical conductivity EC methods (Loke, 1999; Halihan et al., 2017; ITRC, 2019)—including vertical electrical soundings and electrical resistivity tomography—, electromagnetic methods (Telford et al., 1990), induced polarisation (Flores Orozco et al., 2014), and ground-penetrating radar (Gueting et al., 2017). Borehole geophysical techniques such as cross-borehole radar, neutron logs, gamma ray logs, temperature logs, and calliper logs offer greater vertical resolution than surface-based and airborne methods (Rubin and Hubbard, 2005).

Geophysical methods generally provide better information about geological features than the contaminant distribution itself. However, they may also be employed to investigate contamination processes. For instance, despite fresh LNAPL contamination being commonly associated to low EC due to Archie's Law (Archie, 1942) and the

resistive nature of LNAPLs (Halihan et al., 2017), factors related to LNAPL weathering such as microbial activity and chemical alteration of the pore solution cause high EC values (Atekwana et al., 2000; Atekwana and Atekwana, 2010). These findings have given birth to a discipline referred to as biogeophysics (Atekwana and Slater, 2009). In addition, nuclear magnetic resonance is the only geophysical method with enough specifity to respond to specific fluids (water) and pore structure instead of giving a bulk response (Behroozmand et al., 2015). It has been adopted in hydrogeological studies (Knight et al., 2016) and cases of NAPL contamination (Kiaalhosseini et al., 2019; Tsai et al., 2020).

2.2.3.2 Invasive characterisation

Quantitative sampling methods generally involve drilling boreholes, potentially recovering the core to collect solid samples and describe the geology, and the installation of monitoring wells where samples of LNAPL, water and gas can be collected, fluid levels can be gauged, and hydraulic and remediation tests can be conducted. The well construction design and the sampling protocols should be adequately designed to obtain results as representative as possible of the subsurface conditions. Errors derived from the field sampling procedure commonly far exceed those derived from chemical analysis in environmental investigations (J.L. Zhou et al., 2014).

Multiple drilling techniques exist, including hollow stem augering (HSA), direct-push drilling, sonic drilling, and cryogenic drilling. HSA and direct-push drilling are widely adopted approaches for environmental purposes (Sale et al., 2013; Kiaalhosseini et al., 2016; McGenity et al., 2017). They enable collection of near-continuous cores without employing drilling fluids that could compromise the integrity of the samples. Nevertheless, collection of samples through HSA and direct-push systems is not free of errors and uncertainties (Hess et al., 1992a; Kiaalhosseini et al., 2016) that may have implications on the design and success of remediation projects:

- the percentage of core recovery may be far below 100 %, especially in the case of unconsolidated materials in the saturated zone (Murphy and Herkelrath, 1996). For instance, Kiaalhosseini et al. (2016) obtained poor recovery rates below 15 % using conventional HSA equipment in alluvium

sediments, mainly due to the presence of cobbles. This rate increased to 16–100 % with a median of 80 % using an improved cryogenic method. Einarson et al. (2018) employed a direct-push platform in layers of fine sand and silt with few clay layers and reported recovery rates between 50 % and 85 % with an average of 65 %. Zapico et al. (1987) reported frequent recovery rates over 90 % using a wireline piston system. These methods may not be able to penetrate certain materials, thus narrowing their applicability range;

- drilling operations along core handling and storage may also induce loss and redistribution of pore fluids (Hess et al., 1992a; Murphy and Herkelrath, 1996; Sale et al., 2013; McCall et al., 2014; Kiaalhosseini et al., 2016), which may critically affect the estimation of S_n values;

- volatile losses during the sampling process may limit the representativeness of the results. Heating generated through drilling may increase volatile losses (Artiola et al., 2004), which is a particularly important concern for sonic methods (Kiaalhosseini et al., 2016). Cores should be cooled—Artiola et al., 2004; National Environment Protection (Assessment of Site Contamination) Measure 1999—or frozen in the field (CL:AIRE, 2014) and samples should be placed in solvent (Kram et al., 2001a) as soon as practicable. Use of internal and surrogate standards may help to determine subsequent losses. Prediction of evaporation processes may be challenging for many NAPLs due to their multicomponent nature (Fingas, 2015) and other complexities related to porous media (Ma et al., 2014);

- S_n values are commonly derived from TPH concentrations (Parker et al., 1996). However, partitioning phenomena imply that concentrations of NAPL constituents are in the sorbed, aqueous, and gas phases (Feenstra et al., 1991; CL:AIRE, 2014; Rivett et al., 2014). Further errors are linked to the analytical quantification of TPH concentrations (ITRC, 2018b);

- collection of discrete samples in limited numbers and volumes may not suffice to capture the heterogeneity of subsurface environments contaminated by petroleum hydrocarbons (Sale et al., 2013; Hyde et al., 2019), thus alternative

approaches such as the incremental sampling methodology and HRSC have been proposed. McCall et al. (2014) and García-Rincón et al. (2020) have shown dissimilarities found in discrete samples collected in neighbouring locations. Conventional sampling methods are typically associated to low resolution of measurements due to cost and operational constraints.

Cryogenic methods have been developed to overcome many of these limitations, although they have not yet fully replaced conventional techniques. Cryogenic methods consists of freezing samples down-hole aiming to minimise fluid redistribution and volatile losses, improve core recovery, and preserve chemical and biological properties as they are found in-situ, including DNA/mRNA attributes and redox conditions (Durnford et al., 1991; Murphy and Herkelrath, 1996; Johnson et al., 2013; Kiaalhosseini et al., 2016; Trost et al., 2018). These methods generally assume that low temperatures and freeze-thaw cycles do not cause undesired changes in LNAPL and core properties (Sale, 2001) as it has been in part supported by measurements of biomolecules at laboratory scale (Johnson et al., 2013). However, changes may occur according to other authors (Artiola et al., 2004).

Murphy and Herkelrath (1996) attached a sample-freezing drive shoe to an HSA tool and used carbon dioxide to freeze the bottom 7.5 cm of cores at -78 ºC (when both evaporation and deposition of carbon dioxide occur). Trost et al. (2018) adapted this drive shoe to incorporate it to direct-push systems, freezing the lowest 8–15 cm of the core. Kiaalhosseini (2016) modified an HSA drilling rig to freeze entire cores with liquid nitrogen at -20 ºC, although many NAPLs exhibit lower freezing points (Kiaalhosseini et al., 2016). As shown in Fig. 2.9, this last method resulted in contaminant distribution profiles different to cores collected with conventional HSA in neighbouring locations. Both methods still presented certain consistency with each other, but the analysis of frozen cores commonly resulted in higher contaminant concentrations. Nevertheless, direct comparison between contaminant profiles was limited due to the subsurface heterogeneity and potential NAPL redistribution occurring between the conventional coring campaign in 2010 and the cryogenic coring campaign in 2014.

There are also multiple well configurations and groundwater sampling systems and techniques recognising the spatiotemporal variability of contamination plumes, including low-flow sampling (Sundaram et al., 2009), passive fluxmeters (Hatfield et al., 2004; Annable et al., 2005), well nests, and multilevel wells (Pickens et al., 1978; Cherry et al., 1983; Einarson and Cherry, 2002; McMillan et al., 2018).

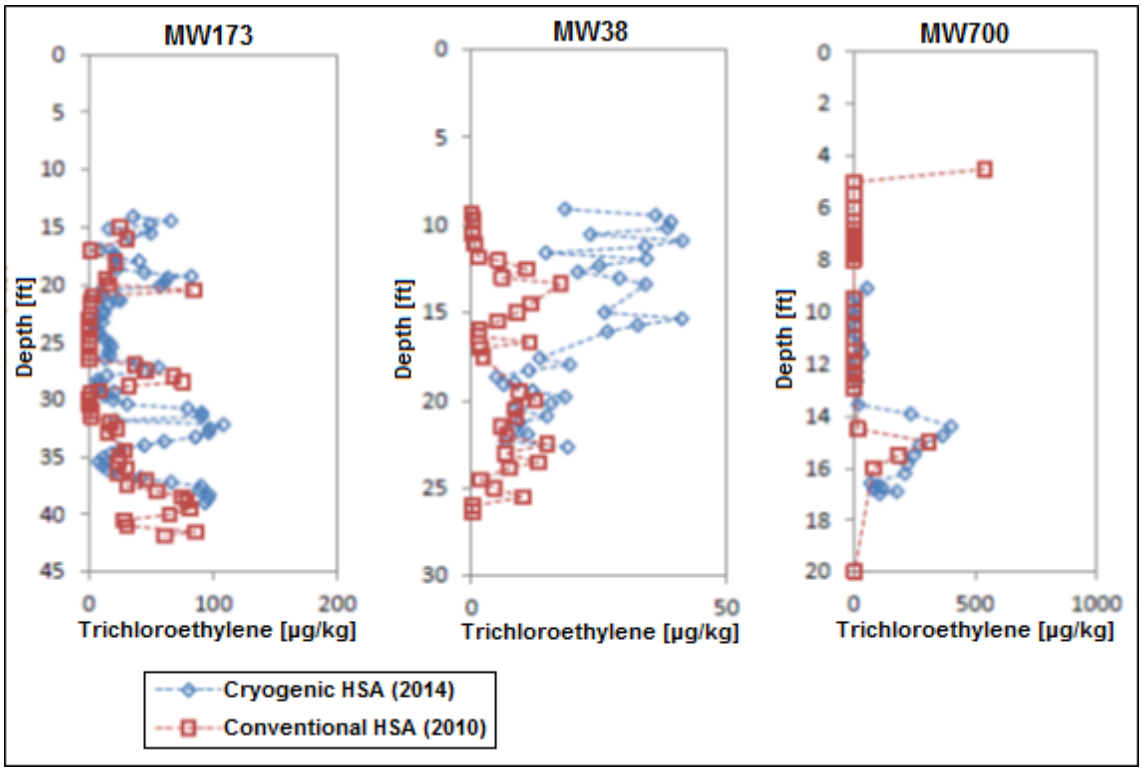


Fig. 2.9. Comparison of trichloroethylene concentration profiles as analysed through cryogenic HSA in 2014 and conventional HSA in 2010 (modified after Sale et al., 2016).

2.2.4 High-resolution site characterisation

2.2.4.1 HRSC approaches

Effective environmental investigation and remediation of soil and groundwater systems generally requires an understanding of hydrologic processes occurring at small scales, although low sampling resolutions are typically achieved with conventional methods. HRSC tools are applied to delineate contaminant distributions and geological medium properties at an adequate scale, resulting in faster and more effective remediation strategies (U.S. Environmental Protection Agency, 2016). Similarly, simplistic layer-cake descriptions of the site geology should be avoided while the use of sequence stratigraphy principles has been encouraged (de Marsily et al., 2005; Payne et al., 2008). Hydrogeologic units should be defined according to their hydraulic properties, although

close agreement with sedimentary strata is expected in the case of unconsolidated systems (Meyer et al., 2016). Thus, further development and evaluation of HRSC approaches are required by the remediation industry, although their adoption may be limited due to a lack of guidance and misperceptions about their availability and applications (ITRC, 2019).

HRSC methods may include distributed temperature sensing, high-resolution slug and packer testing, hydraulic tomography, installation of liners, distributed temperature sensing, high-resolution sampling and analysis, conventional geophysics, and direct-push logging. These methods are described in the following paragraphs. Tables giving further details of every technique may be found in the literature (Kueper et al., 2014; ITRC, 2019).

Field estimations of k_{sw} generally differ between techniques because of differences in the estimation procedure itself (Butler and Healey, 1998) and the support scale (Neuman, 1994; Koltermann and Gorelick, 1996; Neuman and di Federico, 2003)—also named intrinsic area of influence or intrinsic volume by other authors (Vienken, 2011). This may result in different ranges of applicable conditions for each method (Devlin, 2015). Values of k_{sw} may exhibit greater variability when the support scale is small as depicted in Fig. 2.10. Further details about scale issues in hydrogeological systems are presented in section 2.4.2.

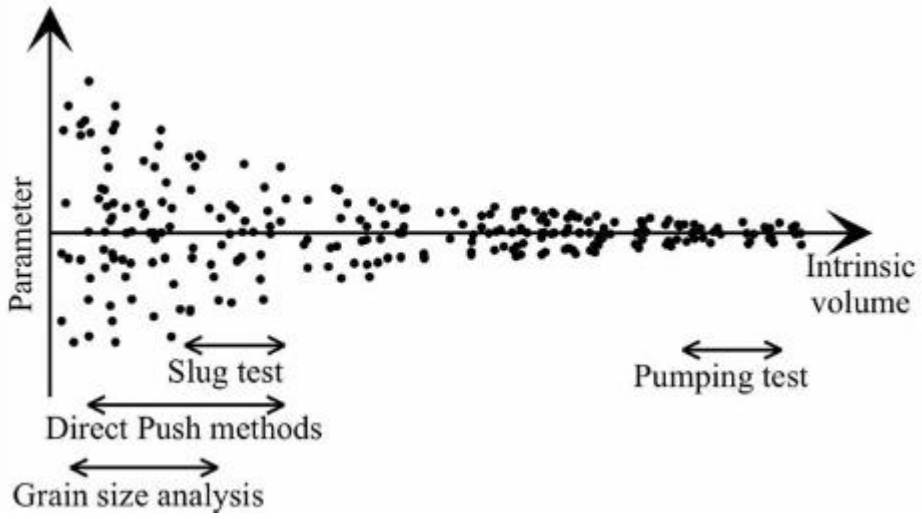


Fig. 2.10. Variability of k_{sw} estimations from methods with different support (Vienken, 2011).

Pumping tests have traditionally been conducted at constant and variable pumping rates (Villanueva Martínez and Iglesias López, 1984; Kruseman and de Ridder, 2000) and their interpretation may be enhanced using diagnostic plots (Gringarten, 2008; Renard et al., 2009). Nevertheless, pumping tests produce effective parameters at larger scales than other methods and therefore may not be adequate for problems related to cases of groundwater contamination (Butler, 2005) and the estimation of subsurface parameters in heterogeneous environments (Wu et al., 2005). Metrics of aquifer heterogeneity (such as variance and correlation scale of k_{sw}) may be inferred from the analysis of pumping test data as suggested by some authors (Zech et al., 2015).

Other hydraulic testing methods such as packer testing isolate depth intervals in the well to analyse these specific intervals, while slug testing induces a near instantaneous change in in-well fluid levels and requires less resources than pumping tests (Bouwer and Rice, 1976; Butler, 2019). However, slug tests have been found to generally produce lower values of k_{sw} than pumping tests (Rovey and Cherkauer, 1995)—especially in the presence of low-permeability skins (Butler and Healey, 1998)—and potentially inaccurate estimates that may be improved after enhancing the data collection and analysis procedure (Butler et al., 1996). Packer and slug testing have been combined as multilevel slug testing to increase the resolution of the measurements (Butler et al., 1994; McElwee et al., 2011). The use of borehole flowmeters is also based on well hydraulics and results in vertical profiles of k_{sw} with elevation (Hess et al., 1992b).

An alternative to the aforementioned hydraulic tests is the inversion of hydraulic tomography data (Gottlieb and Dietrich, 1995; Yeh and Liu, 2000; Zhu and Yeh, 2005; Illman et al., 2008; Bohling and Butler, 2010; Berg and Illman, 2015) as well as inter-well tracer testing data (Ptak et al., 2004). These methods may affect the LNAPL distribution in the subsurface and require the management of extracted groundwater.

In fractured media, Flute® liners have been successfully installed and used to predict k_{sw} and connectivity between fractures (Cherry et al., 2007; Parker et al., 2012; Keller et al., 2014). Other liners such as Flute MLS™, FACTS™, CORE-DFN™, NAPL ribbon™, and NAPL Flute™ have been developed to be installed inside boreholes with the purpose of sealing them or collect information about the medium properties and the contaminant

distribution (Riha et al., 2000; Griffin and Watson, 2002; Broholm et al., 2016; Pierce et al., 2018). In unconsolidated aquifers, the lack of borehole stability may impede their installation. The application of distributed temperature sensing systems (Selker et al., 2006) to investigate temperature gradients, aquifer heterogeneity, and groundwater flow has also been explored in fractured and porous media (Bense et al., 2016).

In unconsolidated sediments, HRSC may be carried out by increasing the sampling frequency on extracted cores. The samples could be directly analysed in the laboratory or previously screened with soil gas measurements or dyes (Horst et al., 2018). Alternatively, novel tools such as portable infrared spectrometers have presented promising results when compared to laboratory analyses (Soriano-Disla et al., 2017; Douglas et al., 2017; Khudur and Ball, 2018). Nuclear magnetic resonance may also be applied to cores (Kiaalhosseini et al., 2019).

Sample collection and analysis (through permeameter measurements or correlations with particle-size analysis data) also have the potential of being applied as an HRSC approach for the estimation of k_{sw} (Bianchi et al., 2011). Permeameter measurements can be conducted with a constant or falling head, being the former preferred for analysis of coarse-grained materials (Klute and Dirksen, 1986). Methods based on particle-size data include empirical and semi-empirical models (Vienken, 2011; Chapuis, 2012; Devlin, 2015) as well as neural network predictions (Schaap et al., 2001). These empirical correlations may present a large variability and require and modifications of constants according to site-specific conditions (Rosas et al., 2014). Further information about methods based on particle-size data is included in section 4.7.

Direct-push platforms have also been used for high-resolution vertical profiling with sensors such as the Membrane Interface Probe (MIP) developed by Geoprobe® (Adamson et al., 2014, 2015; Rivett et al., 2014), although LNAPL contamination may exceed its upper limit of detection and saturate the system (ITRC, 2019). In addition, an EC probe has been developed to delineate hydrostratigraphic features through direct-push logging (Schulmeister et al., 2003; ITRC, 2019). EC methods may be applied to derive quantitative values of k_{sw} (Slater and Lesmes, 2002; Butler, 2005; Slater, 2007; ITRC, 2019), although with considerable uncertainties (Liu et al., 2019). The EC probe has

also been applied to assess groundwater quality and the presence of brine (McCall et al., 2017). Measurements from the EC probe correspond to the bulk conductivity of the geological medium and the pore fluids within a radius between approximately 5 cm and 10 cm (ITRC, 2019). Other methods discussed in the following sections include direct-push injection logging and laser-induced fluorescence. Many of these methods may be combined to obtain multiple logs in the same location at the same time. In addition, direct-push profiling produces less waste than conventional drilling techniques and consequently investigators are less exposed to hazardous substances.

2.2.4.2 Direct-push injection logging

Direct-push logging tools for hydrostratigraphic characterisation and k_{sw} estimation (Butler, 2005; Dietrich and Leven, 2009) include systems such as direct-push slug test (DPST), direct-push permeameter (DPP), and direct-push injection logging (DPIL) as well as cone penetrometer testing (Dietrich and Leven, 2009; Vienken et al., 2012). These direct-push methods may be combined with others such as ground-penetrating radar to enhance the delineation of facies (Dogan et al., 2011; Schmelzbach et al., 2011; Meerschaert et al., 2013; Gueting et al., 2017) and contribute to obtain better predictions of flow and solute transport (Dogan et al., 2014).

Furthermore, DPST estimations (Butler et al., 2002, Sellwood et al., 2005) have been used to evaluate methods based on particle-size analysis, finding relatively good agreement with many of the models after discarding intervals with high amounts of fines (Vienken and Dietrich, 2011; Vienken et al., 2012).

DPP logging has also been used to quantify k_{sw} (Butler et al., 2007; Zschornack et al., 2013), although the operation of DPIL is faster and more robust, since the probe can be hammered into the subsurface. This is because pressure transducers may be installed in the connection tube or even up-hole instead of in the probe (Dietrich et al., 2008). However, DPIL is a qualitative/semi-quantitative technique that requires calibration with other methods to quantify k_{sw}. Consequently, both DPIL and DPP have been combined to build a High-Resolution K tool (Liu et al., 2009).

In addition, DPIL measurements have been transformed into k_{sw} estimations according to their statistical moments (Lessoff et al., 2010) and site-specific calibrations with

particle-size analyses (Dietze and Dietrich, 2012) or DPST measurements (Köber et al., 2009). They have also been compared to flowmeter measurements, slug test data, DPP logs (Dietrich et al., 2008; Liu et al., 2009; McCall, 2010; Bohling et al., 2012, 2016; Xiao et al., 2019), and numerical simulations (Liu et al., 2019).

Two DPIL variants—discontinuous (Dietrich et al., 2008; Lessoff et al., 2010) and continuous DPIL (McCall et al., 2005; Liu et al., 2009)—have been developed (Liu et al., 2019). In the discontinuous mode, the probe is stopped in the intervals of interest and the induced pressure is recorded at multiple injection rates (Dietrich et al., 2008). Therefore, the continuous mode is faster but may result in lower accuracy than discontinuous DPIL due to the application of only one injection rate as well as the additional pressure term caused by the continuous probe advancement. Consequently, dissipation tests must be applied right before advancing the probe into the aquifer to improve the predictions of k_{sw}. In particular, the combination of a continuous DPIL system and an EC Wenner array have been commercialised as the Hydraulic Profiling Tool (HPT) by Geoprobe® (McCall and Christy, 2020). Further details about HPT logging are presented in section 4.5.

The error induced by inherent differences between methods may be more important in the evaluation of the permeability field than the variability associated to different realisations of a heterogeneous permeability field (Barth et al., 2001).

2.2.4.3 Laser-induced fluorescence vertical profiling

Many optical screening tools have been developed to be coupled with direct-push rigs. These optical screening tools frequently make use of LIF technology, taking advantage of the fluorescence properties of aromatic hydrocarbons when they are excited with a source of ultraviolet light. Most popular LIF tools have included ROST®, UVOST®, and SCAPS—all of them incorporating an ultraviolet laser source and fiber optics (Bujewski and Rutherford, 1997; Kram et al., 2001b; ITRC, 2019)—, TarGOST®—incorporating a visible-wavelength laser source to detect heavy fuels such as coal tars and creosotes (ITRC, 2019)—, and DyeLIF™—with a dye system to detect non-fluorescing NAPLs (Einarson et al., 2018). Alternatively, the Optical Image Profiler (OIP) combines an ultraviolet source, a visible light LED, and a camera to capture images that are analysed

by the system (McCall et al., 2018; ITRC, 2019; Reischer et al., 2020). Details of the UVOST® system are given in section 4.4.

Fluorophores are molecules (PAHs for instance) that fluoresce when exposed to an ultraviolet light source (Lakowicz, 2006; Lu et al., 2014). The ability of fluorescence spectroscopy sensors to identify the presence of hydrocarbons because of their content in fluorophores has found applications in many fields, including environmental monitoring of natural and engineered water systems (Carstea et al., 2020) and as a screening method to select core samples (Riyis, 2019).

LIF systems have to date identified the presence of LNAPL under laboratory (Teramoto et al., 2019) and field conditions (Mulry and Lundy, 2013; Baedecker et al., 2018; Sharma et al., 2020). The geological material and LNAPL type influence the LIF response (Kram and Keller, 2004; Alostaz et al., 2008; Lu et al., 2014), in particular light fuels and fine-grained materials may have a negative impact on LIF system performance (Lu et al., 2014; ITRC, 2019). The comparison between LIF response and measurements of S_n through coring has frequently exhibited many discrepancies under heterogeneous conditions at field scale (ITRC, 2019), while different quantitative relationships (linear, exponential) between LIF response and S_n values have been found by different authors at laboratory scale (ITRC, 2019; Teramoto et al., 2019). Additional phenomena affecting LIF response include energy transfer to large PAHs, weathering processes, and oxygen quenching. Fluorescence lifetimes are typically longer in solvent-rich environments and shorter under the effects of quenching (Lu et al., 2014).

Fluorophores have characteristic absorption and emission spectra. However, the analysis of complex mixtures such as gasoline and diesel may require the use of Excitation–Emission Matrices (EEMs) or wavelength–time matrices. EEMs represent fluorescence emission spectra over a range of excitation wavelengths. Parallel factor analysis (PARAFAC) has been widely applied in the analysis of EEMs to quantify the concentration of specific compounds in mixtures (Alostaz et al., 2008; Murphy et al., 2013). Nevertheless, there are complexities associated with PARAFAC and the analysis of EEMs in heterogeneous media with significant concentrations of organic compounds (Alostaz et al., 2008; Murphy et al., 2013).

Wavelength–time matrices incorporate fluorescence lifetimes, which may be used to identify the type of LNAPL and subsurface conditions (ITRC, 2019). However, the associated data processing may require long periods of time. An alternative approach implemented in UVOST® and other LIF systems consists of computing two-dimension diagrams representing multi-wavelength waveforms considering values of fluorescence intensity and lifetime at specific wavelengths (Aldstadt et al., 2002; Grundl et al., 2003) as further explained in section 4.4.1. The analysis and interpretation of LIF data in cases of LNAPL contamination have typically relied on qualitative interpretations of LIF profiles and quantitative calibrations with S_n measurements (Mulry and Lundy, 2013; Teramoto et al., 2019).

An exponential relationship between S_n and LIF signal has been recently reported at laboratory scale (Teramoto et al., 2019), measuring diesel response in a sandstone matrix. Furthermore, cumulative LIF response (sum of all the LIF signal throughout the log) could be an indicator not just of S_n but also LNAPL mobility as reported in a saprolite aquifer (Mulry and Lundy, 2013), since LNAPL mobility also increases with higher S_n values and coarser-grained materials. This study inferred that some of the observations were due to fractures and other secondary porosity features in the saprolite aquifer system.

2.3 Partitioning and degradation of petroleum hydrocarbons

2.3.1 Overview of natural source zone depletion phenomena

NSZD includes partitioning and degradation mechanisms and has been defined as the 'biggest new idea that will affect LNAPL management in the future' (Sale et al., 2018). NSZD is influenced by multiple factors (Essaid et al., 2011, 2015; Garg et al., 2017; ITRC, 2018a; Sookhak Lari et al., 2019; Rivett and Sweeney, 2019) as illustrated in Fig. 2.11. Some partitioning processes may transfer LNAPL constituents into more mobile phases such as groundwater and soil vapour, thus increasing the risk of exposure. However, degradation processes typically limit the extension and longevity of dissolved and vapour plumes (and the LNAPL body) as discussed in the following paragraphs.

Current understanding of LNAPL depletion has evolved from the concept of Monitored Natual Attenuation (MNA), which commonly focused on the attenuation of

contaminants dissolved in the aqueous phase only and ignored the effects of methanogenesis (Garg et al., 2017; Sookhak Lari et al., 2019). MNA phenomena contributed to explain the frequent stability and limited extension of dissolved plumes observed at field scale (Naidu et al., 2012), with more than 70 % of plumes being shorter than 60 m and around 85 % of plumes under 90 m in a study considering 604 contaminated sites (Wiedemeier et al., 1999).

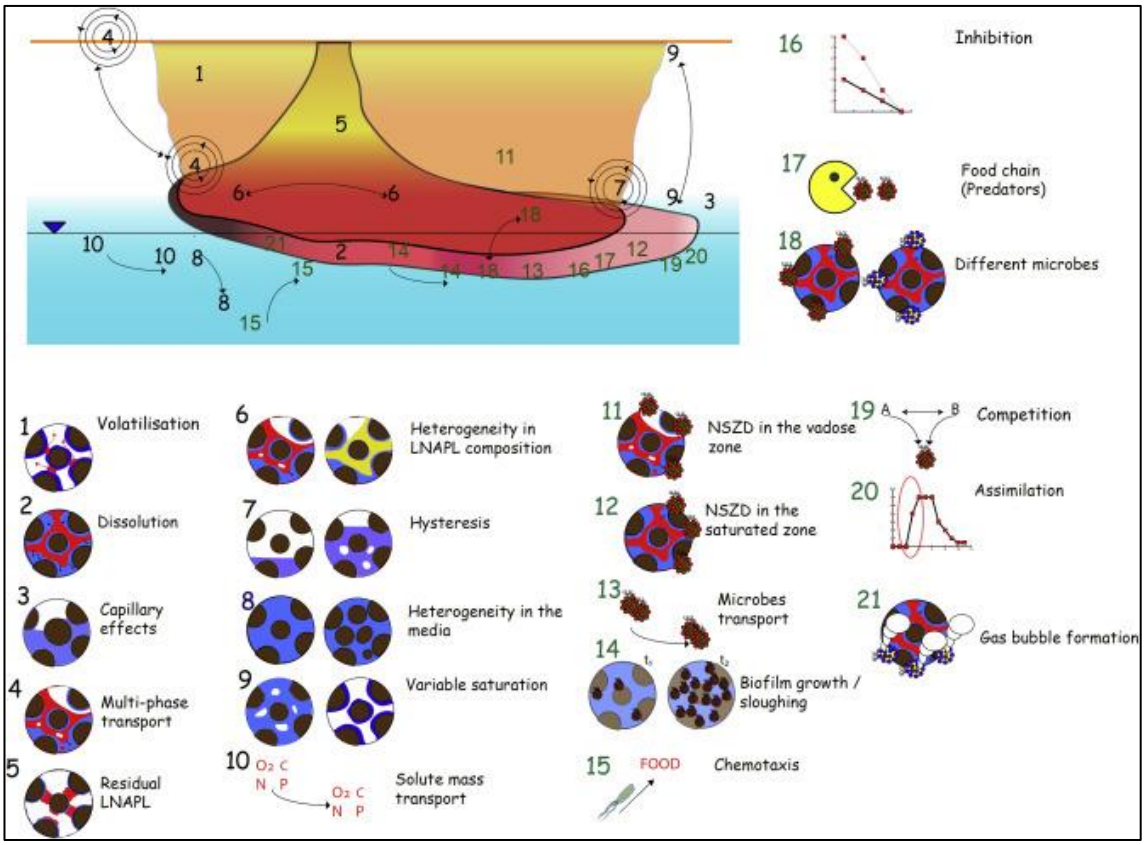


Fig. 2.11. Main processes and factors affecting NSZD (Sookhak Lari et al., 2019).

Nevertheless, methanogenesis is being increasingly accepted as a dominant mechanism in LNAPL depletion (Baedecker et al., 1993; Essaid et al., 2011, 2015; Garg et al., 2017) and significant direct biodegradation of LNAPL (not just of contaminated groundwater and vapours) has been inferred from field observations (Ng et al., 2014). Therefore, NSZD phenomena may play a key role in the behaviour and stability of LNAPL bodies (Lundy, 2014) as well as in their toxicity and longevity. Field studies have reported that depletion in the vadose zone may be one or two orders of magnitude greater than in the saturated zone (Lundegard and Johnson, 2006; Mackay et al., 2018) and NSZD rates may exceed active LNAPL mass recovery rates (Rayner et al., 2020).

Methanogenesis has been typically assumed to only occur after complete removal of all electron acceptors (Wiedemeier et al., 1999) since it generates less energy than other reactions such as oxygen reduction and denitrification (ITRC, 2018a). It is understood now that different communities of microorganisms may degrade petroleum hydrocarbons cooperatively, with fermenting microorganisms producing dissolved hydrogen and acetate while methanogenic microorganisms convert these byproducts (metabolites) into methane and carbon dioxide. These processes occur in both the saturated zone and the unsaturated zone under anaerobic conditions (Garg et al., 2017), although some compounds such as VOCs may pose an inhibitory effect on methanogenesis (Sherry et al., 2014). Subsequently, the generated methane flows upwards due to buoyancy forces, being oxidised into carbon dioxide which may be measured near the surface.

Accordingly, NSZD rates in contaminated sites have been commonly estimated through carbon dioxide efflux methods such as dynamic closed chambers and passive flux traps (Tracy, 2015). Other approaches have included the measurement of gradients in the vertical distribution of soil gases and the installation of thermistors at multiple depths to monitor LNAPL biodegradation since it has been recognised as an exothermic process (ITRC, 2018a; Rivett and Sweeney, 2019). Nevertheless, these measurements may be affected by background noise and their correction may be challenging (Askarani, 2019).

Another recognised issue has been the great variability of NSZD processes and NSZD rates in space and time (Cozzarelli et al., 1999; Bekins et al., 2005; Baedecker et al., 2011, 2018; Eichert et al., 2017; Garg et al., 2017; Teramoto et al., 2020). For instance, Baedecker et al. (2018) observed minor losses 10 years after a release of crude oil into the subsurface, while 25–85 % of the crude oil mass got depleted in the following two decades. Volatilisation and aerobic biodegradation may control LNAPL losses in the early stages of a spill (Chaplin et al., 2002), but the importance of anaerobic biodegradation generally increases with time (Garg et al., 2017). Aerobic biodegradation may still prevail in certain regions of the source zone depending on the subsurface conditions (Teramoto et al., 2020).

2.3.2 Souce zone longevity

Source zone longevity is an important issue because mass depletion of complex NAPL architectures is a relatively slow process and NAPL contamination may persist in the subsurface for decades or centuries (Chapman and Parker, 2005; Seyedabbasi et al., 2012; Rodríguez and Kueper, 2013; Schaefer et al., 2016), affecting also the longevity of the contaminated groundwater and vapour plumes (Rivett et al., 2011; Sookhak Lari et al., 2016b; Dafny, 2017). Diffusion of NAPL constituents into low-permeability zones may contribute to increase the longevity of the source zone as further discussed in section 2.4.

2.3.3 Partitioning

2.3.3.1 Mass transfer mechanisms

Partitioning (dissolution, volatilisation, absorption) refers to mass transfer phenomena between phases (NAPL, groundwater, soil gas, solid particles, biota), which is controlled by intermolecular forces (Agaoglu et al., 2015). It may occur under ideal near-equilibrium conditions (commonly quantified through a partition coefficient) or non-equilibrium, rate-limited conditions (frequently represented by first-order kinetic models including some parameters that may be challenging to estimate at field scale).

Partitioning phenomena affect the chemistry and mobility of organic contaminants. Therefore, they may have a great impact on remediation performance, the creation of complete risk exposure pathways, NSZD rates, and NAPL longevity. Mechanisms such as dissolution and volatilisation transfer NAPL constituents to other transport media (groundwater and soil gas) increasing their mobility and potentially the risks for human health and the environment (Soga et al., 2004). Risks may also be influenced by plant uptake and other biota–water partitioning processes. Furthermore, sorption phenomena may limit remediation performance and increase NAPL longevity. Consequently, remediation design must account for all the environmental compartments (Falta, 2008) to effectively manage NAPL contaminated sites.

2.3.3.2 Dissolution

In this doctoral dissertation, dissolution refers to the mass transfer process between NAPL and the aqueous phase. During dissolution, water molecules surround and

establish electrostatic bonds with polar (such as organic contaminants) and ionic substances incorporating them to the water phase. The dissolution rate mostly depends on the NAPL effective solubility and diffusivity in water, its architecture, interfacial area, and flow conditions (Pankow and Cherry, 1996; Heyse et al., 2002). The activity of subsurface microorganisms may increase NAPL solubility in water (Rockhold et al., 2002).

Non-equilibrium effects may be notable if there are non-uniform flow fields caused by heterogeneities and contrasts in relative permeabilities (Powers et al., 1991) and several rate-limited models have been proposed (Miller et al., 1990, 1998; Powers et al., 1992; Imhoff et al., 1994; Zhu and Sykes, 2000a; Kokkinaki et al., 2013), commonly based on a Sherwood dimensionless number relating convective mass transfer to diffusive mass transport.

However, near-equilibrium conditions have been frequently assumed. According to their octanol-water partition coefficients, aromatic hydrocarbons are generally more soluble in water than aliphatic hydrocarbons and the longer the alkylate chain and the higher the molecular weight, the lower the solubility (Stout et al., 2006). Considering similar carbon number, alkynes are typically more soluble in water than alkenes and alkanes, while cyclic aliphatics are more soluble than acyclic aliphatics.

Many experiments have been carried out to investigate the NAPL dissolution phenomenon (Oostrom et al., 2006a), some of them considering the influence of water table fluctuations (Dobson et al., 2007; Teramoto and Chang, 2017) or multicomponent NAPLs defining the effective solubilities according to Raoult's Law (Lekmine et al., 2014; Teramoto and Chang, 2017). Preferential dissolution pathways due to channelling (Farthing et al., 2012) and higher depletion rates for ganglia than for pools (Parker and Park, 2004) have been found, leading to direct implications on downstream solute fluxes (Maji and Sudicky, 2008) and remedial system design.

Downstream solute fluxes (Stauffer, 2006) are directly related to the dissolution processes occurring in the source zone and have been increasingly recognised as one of the main indicators of remediation performance (Rao et al., 2001; Sale and McWhorter, 2001; Rao and Jawitz, 2003; Soga et al., 2004) since they are intimately linked to human

health risks. The study of these fluxes also allows to assess attenuation processes and prioritise sites (Newell et al., 2011).

Simplified analytical and experimental relationships have been employed to relate source depletion and mass flux (Sale and McWhorter, 2001; Rao and Jawitz, 2003; Zhu and Sykes, 2004a; Basu et al., 2008a), typically predicting a decrease in flux after NAPL mass recovery operations (Jawitz et al., 2005). Nonetheless, numerical simulations have suggested that NAPL mass recovery in heterogeneous media may increase dissolution and downstream solute fluxes in some cases (Alexandra et al., 2012). The main reason behind this behaviour would be the increase in groundwater flow and surface area available for mass transfer after the reduction of S_n in the pores (Alexandra et al., 2012).

Passive flux meters have been successfully deployed in contaminated sites to quantify fluxes at field scale (Hatfield et al., 2004; Annable et al., 2005). Multilevel monitoring wells (Rivett et al., 2014; McMillan et al., 2018) and hydraulic testing (Béland-Pelletier et al., 2011) have also contributed to a better understanding of mass fluxes at field scale. These methods are not free of certain uncertainties (Kübert and Finkel, 2006; Béland-Pelletier et al., 2011; Klammler et al., 2012) but are more adequate for measuring fluxes than conventional long-screened wells.

Heterogeneity (Zhu and Sykes, 2000a, 2000b; Lemke et al., 2004; Troldborg et al., 2010; Koch and Nowak, 2015), especially regarding the existence of low-permeability zones (Brusseau et al., 2008), and the source zone architecture (Fure et al., 2006) has a decisive role on mass flux. As concerns heterogeneity, 80 % of mass discharge has been found to occur within a 10 % or less of the cross-sectional area impacted by DNAPL and 60 % of mass discharge within less than 5 % of the area. This strong variability occurred under conditions defined by the authors as near homogeneous, with k_{sw} estimations contained within less than half an order of magnitude (Guilbeault et al., 2005).

One central aspect of the source zone architecture governing downstream fluxes is the ganglia to pool ratio (Lemke et al., 2004), since ganglia tends to get depleted faster than pool due to the greater interfacial area exposed to groundwater flow. Simulations whose input data was solely based on the initial ganglia to pool ratio differed from

experimental observations for later stages of mass removal (DiFilippo and Brusseau, 2011) since NAPL architecture changes with time (Basu et al., 2008b).

2.3.3.3 Volatilisation

Volatilisation is an essential mechanism for understanding NSZD phenomena, vapour losses affecting sample representativeness, risks to human health, and remediation design. Volatilisation may control LNAPL behaviour to a greater extent than dissolution in some cases (Kim and Corapcioglu, 2003) and may represent a primary depletion mechanism in early stages of LNAPL spills (Chaplin et al., 2002). The medium and source zone characteristics influence the volatilisation rate (Petri et al., 2015).

The equilibrium partition coefficient related to volatilisation between water contaminated with volatile organic compounds (VOCs) and air is the Henry's Law constant. Regarding common petroleum hydrocarbons, ethylbenzene shows the highest affinity for air according to the RAIS database, followed by toluene and xylenes, then benzene, and finally MTBE. In general, volatilisation rates and vapour pressures decrease with molecular weight (Stout et al., 2006). As in the case of NAPL dissolution studies, Raoult's Law is used for NAPL mixtures (CL:AIRE, 2014).

Nevertheless, further research is needed to improve the parameterisation of expressions predicting volatilisation from the NAPL and water phases (Rivett et al., 2011). Prediction of long-term evaporation of many NAPLs is challenging due to their multicomponent nature (Fingas, 2015) and other complexities found in porous media (Ma et al., 2014). Evaporation rates of NAPL petroleum hydrocarbons (including crude oils, diesel, and petrol) have been reported to be primarily governed by molecular diffusion processes and therefore not strongly controlled by wind speed or the area exposed to the gaseous phase (Fingas, 2015). However, other authors have found diesel evaporation rate to be boundary-layer regulated after conducting experiments in porous media (Ma et al., 2014).

Problems of vapour intrusion into buildings and indoor environments are directly related to the volatilisation phenomenon and represent a central issue for risk assessment and decision-making (Mumford et al., 2016; Ma et al., 2020). Nevertheless,

biodegradation processes in the unsaturated zone may limit their occurrence in the case of sites contaminated with petroleum hydrocarbons (Lahvis et al., 2013).

Vapour transport from the source zone to the surface typically responds to diffusion mechanisms. Advective transport may be enhanced by density gradients (Falta et al., 1989; Sleep and Sykes, 1989), fluctuations in barometric pressure, methanogenesis, and pressure contrasts with buildings, especially if preferential pathways exist. Wind, temperature, and mechanical ventilation may cause these pressure contrasts (Ma et al., 2020). Sampling protocols must account for the potential variability of vapour intrusion in time and space.

Multiple screening models of vapour intrusion have been proposed (Davis et al., 2009; Bekele et al., 2013; Yao et al., 2013). The Johnson and Ettinger model (Johnson and Ettinger, 1991) has been one of the most applied by practitioners. However, this model has been found to frequently overpredict vapour intrusion from petroleum hydrocarbons (Lahvis et al., 2013; Verginelli and Baciocchi, 2014). Jury's model (Jury et al., 1983) has been commonly applied in the risk assessment of outdoor environments.

2.3.3.4 Sorption

The term sorption (Brusseau et al., 1989; Delle Site, 2001) comprises surface precipitates, absorption/co-precipitation, and adsorption processes. Organic contaminants may be adsorbed by inorganic mineral matter (staying held on the surface of the mineral grains and being susceptible to be replaced by other ions through ionic exchange in the case of ionic contaminants) or absorbed by organic matter (an actual mass transfer process with the contaminant being transferred into the organic matter matrix). In some cases, hydrocarbons sorbed into colloids may be misinterpreted as present in the dissolved phase (King et al., 2007).

In general, absorption effects may be more relevant for remediation purposes than those derived from adsorption processes. Nevertheless, site-specific conditions such as the fraction of organic carbon f_{oc} may be assessed in every project. Partition coefficients to organic matter are commonly defined for organic substances only. Ethylbenzene is the common petrol constituent with the highest affinity for organic matter followed by xylenes, toluene, benzene, and MTBE. On the other hand, adsorption is frequently

determined by linear (a distribution coefficient) or non-linear isotherms (for instance, Freundlich and Langmuir models).

Sorption effects have been traditionally lumped into a retardation factor to solve the classical advection-dispersion transport equation, sometimes lumping diffusion effects as well (Roberts et al., 1986). Non-equilibrium approaches have been also followed in the study of sorption processes (Brusseau et al., 1989). Thus, sorption also affects transport, although it transfers mass to an immobile medium instead of a more mobile medium like in the cases of dissolution and volatilisation. Furthermore, a change in physico-chemical properties such as pH and redox conditions may release contaminants from the solid matrix, potentially producing a rebound effect in contaminant concentrations downstream. This has direct consequences for remediation performance.

2.3.4 Biological processes and degradation

Petroleum hydrocarbons can be metabolised and eventually mineralised by subsurface microorganisms (bacteria and fungi). Uptake of hydrocarbons is influenced by subsurface properties and the type of hydrocarbons and microorganisms involved (Rojo, 2009; Das and Chandran, 2010). It may occur through several mechanisms: direct uptake from LNAPL droplets, direct uptake from water when the hydrocarbons are dissolved, and uptake after emulsification of LNAPL with biosurfactants secreted by microorganisms (Semple et al., 2007; Wentzel et al., 2007; Rojo, 2009; Das and Chandran, 2010; Abbasian et al., 2015).

Thus, biodegradation phenomena depend on multiple parameters, including pH, redox, aerobic or anaerobic conditions, electron acceptors and donors, pore space, local communities of microorganisms, chemotactic behaviour, presence of nutrients, aquifer recharge, topography, water table fluctuations, and temperature (Yadav and Hassanizadeh, 2011; Garg et al., 2017; Adadevoh et al., 2018; Baedecker et al., 2018; ITRC, 2018a). Biodegradation processes have typically been modelled according to Monod kinetics (Monod, 1949; Yadav and Hassanizadeh, 2011), which predict unbound microbial growth despite the existence of inhibiting factors such as nutrient depletion (Kindred and Celia, 1989) or the toxicity of subsurface contaminants (Gupta et al., 2019).

Cyclic alkanes are generally the least susceptible petroleum hydrocarbons to biodegradation (Das and Chandran, 2010), while short linear alkanes are typically more susceptible to aerobic biodegradation than long linear chains, branched alkanes, and small aromatics. Nevertheless, biodegradation rates may differ depending on the subsurface conditions (Garg et al., 2017). For instance, long linear alkanes have been observed to get degraded first under anaerobic conditions (Bekins et al., 2005).

Releases of LNAPL substances into the subsurface commonly lead to the eventual creation of anaerobic conditions in certain regions of the aquifer and excess of electron donors (organic matter, organic pollutants) compared to electron acceptors (oxygen, Fe^{3+}, Mn^{4+}, sulfate, nitrate, carbon dioxide). As a consequence, methanogenesis (outgassing of methane and carbon dioxide) may become an important process in the source zone, with bubbles migrating from the saturated zone to the unsaturated zone through ebullition due to buoyancy forces (Garg et al., 2017). Further discussion about methanogenesis can be found in section 2.3.1. Oxic areas may still persist in the source zone depending on the subsurface conditions (Teramoto et al., 2020).

The influx of electron acceptors results in degradation of petroleum hydrocarbons and downgradient observations of sulfate, iron, nitrate (to NH_4) and manganese reduction, denitrification (to N_2), and aerobic respiration (Cozzarelli et al., 1994; Chapelle, 2000; ITRC, 2018a). These processes may cause secondary groundwater quality impacts. For instance, iron reduction may lead to the release of naturally occurring arsenic (Cozzarelli et al., 2015). Oxidation and reduction reactions may be caused by both biotic and geochemical (abiotic) processes (Lovley et al., 1989; Alvarez and Illman, 2006).

Depending on the specific characteristics found in the subsurface, these processes may also produce secondary porosity features or contribute to clog the existing pores (Chapelle, 2000). Bioclogging induced by microbial biomass and associated products such as EPS (Laspidou and Rittmann, 2002; Or et al., 2007; Flemming and Wingender, 2010) may lead to reductions of k_{sw} by several orders of magnitude (Vandevivere and Baveye, 1992), although this is not always observed, since multiple inhibiting factors exist (Essaid et al., 2015). Bioclogging may occur because of the accumulation of biomass, secretion of EPS, and release of insoluble gases (Baveye, 2020). In particular,

the formation of bubbles through methanogenic outgassing in LNAPL contaminated sites may decrease k_{sw} more than a 75 % (Amos and Mayer, 2006). Biological processes may also increase the NAPL solubility in water (Rockhold et al., 2002) and alter the retention characteristics of the system as described in section 2.1.7.

2.3.5 Diagnostic ratios and forensic investigations

Due to the different effects of all these NSZD and partitioning processes on specific compounds, multiple diagnostic ratios may be used as forensic tools to characterise sources and weathering conditions. Examples of weathering indices can be found in the literature (Morrison and Murphy, 2006), for instance *n*-pentane/*n*-heptane or *n*-heptane/*n*-decane as indicators of volatilisation, (benzene + toluene)/(ethylbenzene + xylenes), aromatics/naphthenes or naphtalene/*n*-dodecane as signs of dissolution as well as (cyclic alkanes + aromatics)/(acyclic alkanes), nC_{17}/pristane and nC_{18}/phytane to diagnose biodegradation processes. In addition, the octane rating of a gasoline (*iso*-octane/*n*-heptane) is a measure of its resistance to self-ignition and may be used to identify the pollution source. Diagnostic ratios used in environmental forensics must be interpreted with caution because of the potential influence of multiple simultaneous subsurface processes and LNAPL characteristics (Alvarez et al., 1998).

Forensic investigations may require the analysis of isotopes, biomarkers, and other compounds not typically considered for risk assessment purposes (Stout et al., 2015; Andersson and Achten, 2015) as well as techniques such as compound-specific isotope analysis and the study of DNA and mRNA (Hunkeler and Aravena, 2000; Sherwood Lollar et al., 2001; Bouchard et al., 2018; Teramoto et al., 2020).

2.4 Transport in heterogeneous media

2.4.1 Main transport mechanisms

Transport phenomena mainly involves processes of advection, mechanical dispersion, and diffusion, being the former two processes frequently lumped as a hydrodynamic dispersion term dependent of the medium tortuosity (Whitaker, 1967). These phenomena have been traditionally represented by partial differential equations corresponding to the classical advection-dispersion equation in saturated porous media.

Advective flow is usually determined by Darcy's law in saturated porous media (Darcy, 1856; Hubbert, 1940, 1956; Hassanizadeh, 1986; Haitjema and Anderson, 2015) and Richards' equation in unsaturated porous media (Richards, 1931), while longitudinal and transversal dispersivities and Fick's law of diffusion (Hassanizadeh, 1986) account for hydrodynamic dispersion. The application of Darcy's and Fick's laws (analogous to Ohm and Fourier laws in other fields) has limitations that have been explored in the literature (Hassanizadeh, 1986; Gray and Miller, 2004).

In the case of multifluid systems, macro-scale NAPL advective transport depends on its relative permeability, as derived from the established constitutive relationships. As mentioned in section 2.1.9, these relationships between fluid saturation, capillary pressure, and relative permeability have a great impact on NAPL behaviour (Kaluarachchi, 1996; Waddill and Parker, 1997c; Bennett et al., 1998; Lemke et al., 2004). Since relative permeability and the constitutive relationships depend on the fluid properties (Alizadeh and Piri, 2014), NAPLs with different compositions exhibit different behaviours in the subsurface.

Therefore, the presence of NAPL implies the necessity of a multifluid version of Darcy's law (Abriola and Pinder, 1985; Blunt, 2017), resulting in a set of coupled non-linear partial differential equations requiring constitutive relationships to close the system. These equations can be derived through volume averaging techniques (Hassanizadeh and Gray, 1979; Abriola and Pinder, 1985), although also presenting limitations (Whitaker, 1986; Armstrong et al., 2016). For instance, periodic disconnection and reconnection of fluid phases during steady-state multiphase flow has been observed using pore-scale X-ray imaging (Reynolds et al., 2017), behaviour not captured by macro-scale Darcy's law and relative permeability models.

2.4.2 Scaling issues in subsurface systems

It is a common practice to make use of representative elementary volumes to model subsurface transport phenomena (Bear, 1972). This volume depends on the property considered (Al-Raoush and Willson, 2005; Jackson et al., 2020) and may be difficult to define in the field because geological systems are naturally heterogeneous and exhibit discontinuities and scale-dependent properties (Neuman and Di Federico, 2003). Thus,

alternative approaches not relying on this concept have been developed (Neuman, 2020).

Some of the identified scales are the support (Neuman, 1994), the extent of the observed phenomenon (observation scale), the domain size (or window; affecting parameter identification processes), and the spatial and temporal resolution used to describe the processes in modelling and field studies. Furthermore, field measurements typically exhibit different spatial resolution in the horizontal and vertical planes. These scale issues introduce uncertainties in the system (Carrera, 1993) and illustrate the importance of adopting HRSC approaches to build sound CSMs.

Changes in these scales reveal changes in properties such as permeability (Gómez-Hernández and Gorelick, 1989; Rovey and Cherkauer, 1995; Wen and Gómez-Hernández, 1996; Renard and de Marsily, 1997; Sánchez-Vila et al., 2006; Dagan et al., 2013), T_w (Sánchez-Vila et al., 1996), diffusion (Liu et al., 2007), dispersivity (Wheatcraft and Tyler, 1988), and solute concentration (Mackay et al., 1986; Sudicky, 1986; Neuman, 1990; Gelhar et al., 1992; Fernàndez-Garcia and Gómez-Hernández, 2007). The scale-dependent nature of geological phenomena has led to the application of fractal theories on soil, groundwater, and contamination studies (Wheatcraft and Tyler, 1988; Bonnet et al., 2001; Molz et al., 2004; Liu et al., 2007; Ghanbarian et al., 2010; Dogan et al., 2014).

2.4.3 Heterogeneous permeability fields

Geological media is naturally heterogeneous and k_{sw} may exhibit great variability in the subsurface. Anisotropy may also exist due to multiple reasons, including the preferential orientation of particles during the deposition process. Consequently, vertical k_{sw} is generally lower than horizontal k_{sw} in sedimentary depositional environments (Freeze and Cherry, 1979; Todd and Mays, 2005).

Heterogeneity in the permeability field has been commonly acknowledged as a main factor governing NAPL and solute transport (Rehfeldt et al., 1992; Carrera, 1993; Bennett et al., 1998). Nonetheless, aquifers are typically characterised with few measurements of k_{sw} (Alexander et al., 2011) and other parameters.

The permeability field may be defined by upscaled effective parameters, continuous geostatistical models (Rehfeldt et al., 1992) such as variogram-based ordinary Kriging (Isaaks and Srivastava, 1989), discontinuous Boolean or geostatistical facies models defined through multiple-point geostatistics (Huysmans and Dassargues, 2009; Mariethoz and Caers, 2014), and Markov chain Monte Carlo methods (Arshadi et al., 2020). Genetic models have also been applied as an alternative consisting of simulating all the depositional history by imitation of sedimentary processes (Koltermann and Gorelick, 1996). This approach has been shown to carry large uncertainties but may reveal features that are not possible to obtain through other methods (Koltermann and Gorelick, 1996).

Furthermore, many additional factors besides k_{sw} also influence subsurface transport phenomena, especially in multifluid systems (de Marsily, 2005; Cirpka and Valocchi, 2016). However, models explicitly accounting for the heterogeneity of some of these properties in cases of LNAPL contamination are scarce (Essaid et al., 1993; Dillard et al., 1997; Waddill and Parker, 1997b; Johnston and Trefry, 2009).

2.4.4 Preferential migration pathways

The importance of the permeability field is in part related to the definition of low-permeability barriers and preferential migration pathways. The existence of high-permeability pathways of interconnected pores and channels may be appreciated in breakthrough curves from tracer tests (Siirila-Woodburn et al., 2015). It is probably easier to understand the role of structural connectivity in the case of fractured rocks (Berkowitz, 1995, 2002; Le Borgne et al., 2007), although an adequate characterisation of these features should be conducted in porous media too (Trinchero et al., 2008; Fernàndez-Garcia et al., 2010; Zheng et al., 2011; Dell'Arciprete et al., 2014; Dogan et al., 2014) and several connectivity metrics have been proposed (Knudby and Carrera, 2005; Renard and Allard, 2013). Preferential pathways may also include low-permeability intervals (Bianchi et al., 2011).

Thus, structural connectivity may greatly affect transport of solutes and NAPL as it may be inferred from Fig. 2.12, where the characteristics (more specifically, its probability distribution function and variogram) of the two depicted permeability fields remain the

same, but the degree of connectivity differs. Other authors have indicated that a k_{sw} variability of two orders of magnitude may cause more than 90 % of groundwater flow to be constrained to a 20 % of the aquifer (Payne et al., 2008). Thus, most groundwater flow is restricted to a fraction of the effective porosity, called 'mobile porosity' by Payne et al. (2008) and suggested to be typically lower than 0.10 in unconsolidated sediments. The analysis of 141 borings in 43 sites found 90 % of groundwater flow occurring in 30 % of the aquifer cross-section, yielding an average mobile porosity of 0.11 (Kulkarni et al., 2020). The role of connectivity may be more relevant on NAPL migration than on groundwater flow and solute transport (Neuweiler et al., 2011), although this issue has not been broadly explored in the literature.

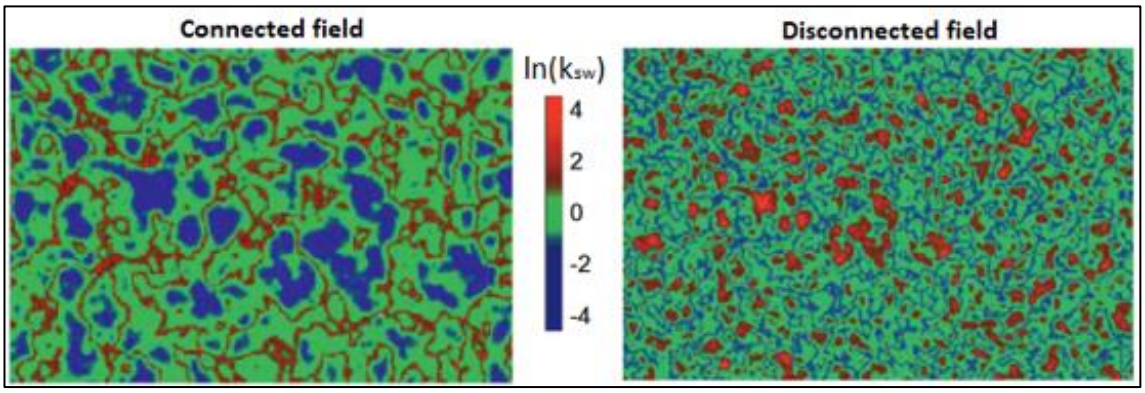


Fig. 2.12. Permeability connected and disconnected fields with identical probability distribution functions and near identical variograms (adapted from Renard and Allard, 2013, after Zinn and Harvey, 2003).

2.4.5 Low-permeability zones and diffusion

Low-permeability zones may act as capillary barriers, creating complex NAPL distributions and potentially confined or perched NAPL conditions (Illangasekare et al., 1995; Johnston, 2010; Kirkman et al., 2013). Even thin low-permeability zones may negatively influence remediation performance, decreasing NAPL mass recovery rates (Johnston and Trefry, 2009) and impeding effective reagent delivery into the subsurface (Sale et al., 2013). Shallow aquitards may not be able to protect underlying aquifers from pollution releases due to the presence of preferential migration pathways (Parker et al., 2004) that can be overlooked by conventional characterisation techniques (Filippini et al., 2020).

Diffusion processes are linked to low-permeability zones (Carrera et al., 1998) and may explain rebound effects following remediation operations due to back-diffusion phenomena and contamination persistence over decades (Parker et al., 1994; Chapman and Parker, 2005; Mundle et al., 2007; Yang et al., 2017). Diffusion may be more relevant increasing NAPL longevity than dissolution decreasing it (Seyedabbasi et al., 2012). Furthermore, it may be possible to reconstruct the NAPL source history after analysing diffused concentration profiles (Adamson et al., 2015).

Low-permeability zones may present distinct biogeochemical conditions (McMahon, 2001). Biodegradation may occur despite the small pore sizes, thus decreasing the longevity of diffuse sources (Wanner et al., 2018). Nevertheless, most of these studies focused on DNAPLs. Further research is needed to gain insight into the nexus between LNAPL contamination and low-permeability zones, elucidating to what extent natural depletion mechanisms counterbalance diffusion phenomena.

The concept of diffusion has also gained attention in the last years over other concepts such as dispersion and sorption to explain anomalous observations of contaminant transport. Thus, some authors have suggested the use of advection-diffusion equations and mobile-immobile (dual-porosity) models (Gillham et al., 1984; Payne et al., 2008; Hadley and Newell, 2014) as well as other non-local formulations. Methods to account for mobile-immobile interactions, heterogeneities at multiple scales, non-Fickian anomalous transport (Neuman and Tartakovsky, 2009), and absence of local equilibrium have been developed (Haggerty and Gorelick, 1995; Harvey and Gorelick, 2000; Berkowitz et al., 2006; Silva et al., 2009; Benson et al., 2013; Cvetkovic et al., 2014).

2.5 Modelling approaches

2.5.1 Numerical modelling

The evolution of quantitative hydrogeology has been strongly associated with advances in numerical modelling (de Marsily et al., 2005)—including the improved access to computational resources and the development of methods that require less computational costs—as well as the necessity to solve transport problems and the possibility of getting better experimental data (Kitanidis, 2015), including high-resolution measurements. Numerical methods offer approximate solutions instead of

exact ones and are better suited to represent complex scenarios than analytical solutions. Numerical simulators such as NAPL Simulator, STOMP, TMVOC, and UTCHEM have been employed in the study of NAPL contamination problems (e.g. Sookhak Lari et al., 2016a, 2018, 2020). Further discussion about numerical modelling schemes applied to multifluid systems can be found in the literature (Helmig, 1997; Pinder and Gray, 2008).

Nevertheless, deterministic simulations may not adequately match field observations of the modelled system under certain circumstances, especially when dealing with transport phenomena and highly heterogeneous media (de Marsily et al., 2005; Neuman, 2005; de Dreuzy, 2008). Therefore, the application of calibration procedures and inverse modelling techniques is commonly required (Yeh, 1986; Zimmerman et al., 1998; Carrera et al., 2005; H. Zhou et al., 2014; Doherty, 2015; Linde et al., 2015; Koch and Nowak, 2016; Arshadi et al., 2020) to properly represent complex subsurface systems, although certain procedures may result in overfitted models (Hill, 2006). There is a necessity for improved data collection and modelling approaches (both forward and inverse) to better identify and characterise NAPL source zones (Arshadi et al., 2020).

2.5.2 Stochastic frameworks

Stochastic frameworks (Matheron, 1967; Dagan, 1986; Renard, 2007; Fiori et al., 2015a; Cirpka and Valocchi, 2016) may be more adequate to address the subsurface heterogeneity and associated uncertainties than deterministic approaches (Essaid et al., 1993), especially those occurring at small scales (Wheatcraft and Tyler, 1988). Fig. 2.13 illustrates the great impact that heterogeneous conditions may have on model predictions of LNAPL distribution.

However, adoption of stochastic approaches in cases of NAPL contamination has been limited due to the following reasons: (i) computational requirements (Johnston and Trefry, 2009; Koch and Nowak, 2016; Arshadi et al., 2020), (ii) absence of enough field data to adequately define the probability distribution of not only k_{sw} but many other relevant parameters (de Marsily, 2005; Cirpka and Valocchi, 2016), and (iii) the complexity in the development, application, interpretation, and communication of stochastic models and the obtained results. Models seldom represent the variability of

not just k_{sw} but also other subsurface parameters influencing LNAPL fate and transport such as the retention characteristics (Essaid et al., 1993; Dillard et al., 1997; Waddill and Parker, 1997b; Johnston and Trefry, 2009).

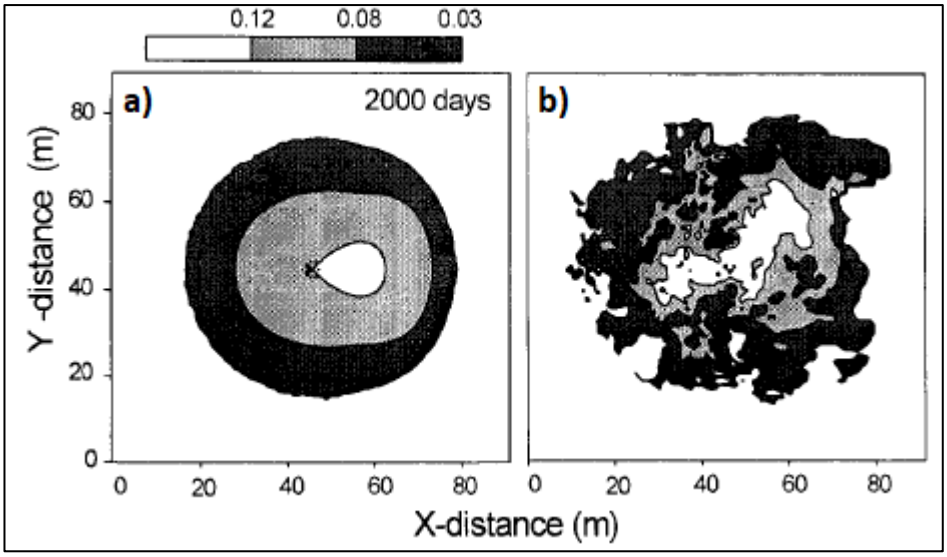


Fig. 2.13. Simulations of b_n after periods of LNAPL redistribution and recovery operations in (a) homogeneous, and (b) heterogeneous uniform scenarios. Selected subsurface properties exhibited a correlation scale of 3.66 m (adapted from Waddill and Parker, 1997b).

2.5.3 Analytical solutions

Simple models may be more easily adopted by practitioners and in some cases provide greater insight on the study of subsurface phenomena than highly parameterised, calibrated, and complex models (Hill, 2006; Voss, 2011a, 2011b; Schöniger et al., 2015; Neuman, 2020). In addition, complex models may lead to an illusory perception of accuracy when the great uncertainty associated to the characterisation of subsurface properties is ignored (Al Awar, 2008).

Analytical solutions typically assume homogeneous conditions, but they have been proven useful to solve many practical problems. Some analytical or semianalytical solutions of interest have been developed to describe LNAPL mass recovery methods (Corapcioglu et al., 1994; Waddill and Parker, 1997a; Charbeneau et al., 2000), deal with vapour intrusion problems (Yao et al., 2013), estimate mass discharge from source zones (Sale and McWhorter, 2001; Rao and Jawitz, 2003; Jawitz et al., 2005; Christ et al., 2006; Basu et al., 2008a), investigate the transport of contaminants in fractures (Sudicky and Frind, 1982), back diffusion processes from aquitards or clayey fillings (Rodríguez and

Kueper, 2013), and represent the system behaviour during hydraulic testing (Huntley, 2000, Kirkman, 2013).

Many simple-to-use tools based on analytical solutions are available and contribute to analyse and gain a better understanding of subsurface phenomena. Some of these software tools are LDRM (Jeong and Charbeneau, 2014) and its version for heterogeneous environments HELRM (Al Awar, 2008), REMFuel, REMChlor (developed for US EPA), NDM (NAPL Depletion Model, developed by Porewater Solutions), Bioscreen, the Mass Flux Toolkit, the Matrix Diffusion Toolkit and the Source History Tool (all from GSI), and more recently a model to predict LNAPL distribution and transmissivity accounting for current and historic fluid levels, S_{nr}, and S_{ne} (Lenhard et al., 2017, 2018).

These tools appear in response to a lack of simple models that can be used by practitioners. The evolution of our understanding of LNAPL distribution and mobility in the subsurface and the development of the corresponding analytical solutions is reviewed in section 2.2.

2.5.4 Model evaluation approaches and types of uncertainty

Both analytical and numerical models can be studied through different model evaluation families of methods (Matott et al., 2009):

- data analysis to evaluate input and output data (see Reimann et al., 2008);
- identifiability analysis to evidence inadequacies in the data or the model;
- uncertainty analysis to quantify parametric and structural uncertainties;
- sensitivity analysis of the relationship between input and output parameters;
- parameter estimation to calibrate the model through inverse modelling;
- multimodel analysis to assess structural uncertainty;
- Bayesian networks to update probabilistic distributions from prior information.

Uncertainties found during the modelling effort always comprise an irreducible aleatory term since the model deals with a complex open system (Konikow and Bredehoeft, 1992; Oreskes et al., 1994; Linde et al., 2017). Thus, model predictions are always uncertain, although this issue does not invalidate the usefulness of environmental

modelling in the analysis of subsurface phenomena (Konikow and Bredehoeft, 1992; de Marsily et al., 1992; Voss, 2011b). In addition to the irreducible uncertainty, there is also an epistemic uncertainty that can be reduced through the collection of more and better data and improving its interpretation (Tartakovsky, 2013). This epistemic uncertainty mainly comprises parametric and structural uncertainty.

2.5.5 Parametric uncertainty and sensitivity analysis methods

The effects of parametric uncertainty can be investigated through a sensitivity analysis. k_{sw} is typically acknowledged as one of the most important factors in cases of groundwater contamination, while retention parameters have a great impact on multiphase systems (Kaluarachchi, 1996; Waddill and Parker, 1997b, 1997c; Bennett et al., 1998; Lemke et al., 2004; Cirpka and Valocchi, 2016).

A sensitivity analysis studies how the uncertainty in the output of a model can be apportioned to different sources of uncertainty in the input parameters (Saltelli et al., 2004, 2008), being the sensitivity of the model outputs to input parameters due to two factors: uncertainty propagation and physical correlation between input and output parameters (Hamby, 1994). These analyses have been proven useful in several ways, for instance supporting decision making, improving the communication of results, increasing the understanding of the system and helping to further develop the applied model (Pannell, 1997). Similarly, the analysis of best-case and worst-case scenarios has been used as an alternative to full stochastic frameworks to account for modelling uncertainties, although in a simpler and less comprehensive way (Renard, 2007).

Different sensitivity analysis methods do not necessarily provide the same results. They can be classified according to several aspects (Song et al., 2015): local or global; deterministic, statistical or graphical; qualitative or quantitative; and as screening or refined techniques.

Local sensitivity analysis evaluates the effects of input parameters one at a time, while probabilistic global methods allow to account for the joint effects of multiple input parameters in the whole parameter range (Song et al., 2015). Consequently, global sensitivity analysis methods are preferred in most situations (Saltelli and Annoni, 2010), although they are usually linked to a good understanding of the probability distributions

of model parameters that may not be easily achievable in problems of NAPL contamination (Cirpka and Valocchi, 2016).

Nevertheless, certain simpler methods have shown a good performance in previous studies (Hamby, 1995). However, application of one-at-a-time fixed perturbations should be avoided and measures of spread of the probability distribution or other approaches should be considered (Pannell, 1997).

2.5.6 Structural and conceptual site model uncertainty

Structural uncertainty can be investigated through the comparison of different models (Zimmerman et al., 1998; Berg and Illman, 2015; Ciriello et al., 2015). Besides of the represented setting and physical phenomena, other sources of model uncertainty are those related to numerical errors and the parameterization of subgrid-scale related processes (Kitanidis, 2015). This reveals the uncertainties associated to the scale issue (Dagan, 1986; Neuman and di Federico, 2003; Dagan et al., 2013). The effects of subgrid-scale properties and upscaling have been investigated with pore-network models (Das and Hassanizadeh, 2005; Joekar-Niasar and Hassanizadeh, 2012; Agaoglu et al., 2015; Blunt, 2017) and Monte Carlo solute transport simulations (Fernàndez-Garcia and Gómez-Hernández, 2007).

Additionally, it is possible to account for the conceptual site model uncertainty (Beven, 1993; Enemark et al., 2019) through Bayesian averaging techniques such as MLBMA (Neuman, 2003) or GLUE-BMA (Rojas et al., 2008, 2010) for instance. Conceptual site model uncertainty may have a greater impact on model predictions than parametric uncertainty (Neuman, 2020). However, this uncertainty has not been addressed many times for cases of NAPL contamination (James and Oldenburg, 1997; Troldborg et al., 2010; He et al., 2012; Koch and Nowak, 2015).

2.6 Summary of the literature review and research gaps

Subsurface environments are naturally complex, heterogeneous, and exhibit scale-dependent properties (Neuman and Di Federico, 2003), with many challenges related to the management of LNAPL contaminated sites being related to an inappropriate understanding of the source zone characteristics (Tomlinson et al., 2017). Furthermore, aquifers have been commonly characterised based on few data and field estimations of

subsurface properties generally differ depending on the characterisation method employed (Alexander et al., 2010). Uncertainties exist in the CSM, the estimated parameters, and the proposed models.

Thus, development and evaluation of improved theories (e.g. Lenhard et al., 2004; Miller et al., 2019), field characterisation approaches (e.g. Kiaalhosseini, 2016; Bouchard et al., 2018; ITRC, 2019), and practical modelling techniques (e.g. Lenhard et al., 2017; Arshadi et al., 2020) are required to enhance the design of effective management solutions under physical, chemical, biological, and hydrogeological heterogeneous conditions (Essaid et al., 2015; Rivett and Wealthall, 2019).

HRSC methods have gained popularity to overcome the typically low sampling resolution achieved with conventional site characterisation methods. However, direct sensing tools such as LIF and DPIL produce qualitative or semi-quantitative data and their implementation in the industry has been less than expected due to a lack of guidance and misperceptions about their availability and applications (ITRC, 2019). Further research and development of HRSC approaches on heterogeneous systems should be conducted, including the characterisation of preferential pathways and low-permeability zones (e.g. Filippini et al., 2020). Conventional methods should also be improved, for instance to ensure the representativeness of samples collected through coring and other techniques (Kiaalhosseini et al., 2016).

Many of the uncertainties associated to field characterisation methods and modelling tools are caused by the complexity of processes occurring at pore scale in the subsurface, which may for instance result in mixed-wetting conditions, bioclogging, and formation of near-immobile LNAPL. Non-equilibrium conditions are another important issue found in the field that may affect VEQ assumptions (Atteia et al., 2019).

Consequently, macro-scale constitutive relationships may need improvements in order to better capture and represent these processes (Essaid et al., 2015). Lenhard et al. (2017) have developed a model incorporating an improved definition of near-immobile S_n fractions, while Miller et al. (2019) among others have proposed state equations describing capillary pressure without hysteresis. In addition, recent progress made in the study of other subsurface multifluid systems in fields such as carbon sequestration

and petroleum engineering (e.g. Blunt, 2017) as well as in hydrogeological research could positively influence future LNAPL developments.

Despite the complexity of LNAPL contamination problems, adoption of stochastic modelling and uncertainty analysis approaches has been limited due to requirements in terms of computational resources, field data, and expertise. There is a need for practical tools (e.g. Lenhard et al., 2017) that can be used by practitioners to gain insight into the mechanisms occurring in the subsurface. The study of site investigation approaches, LNAPL mobility, and modelling tools are all within the scope of this doctoral dissertation and have been active fields of LNAPL research in the last decade (Rivett, 2019).

Another active area of research is NSZD phenomena and biological processes (Essaid et al., 2015), especially after acknowledging the primary role that methanogenesis may play in LNAPL fate and transport (Garg et al., 2017). NSZD is fundamental to understand the evolution of LNAPL source zones and may reduce LNAPL mass at greater rates than active recovery systems (Rayner et al., 2020). Thus, remediation approaches enhancing NSZD (ensuring efficient reagent delivery if needed) may represent an efficient and sustainable management strategy.

Nevertheless, NSZD rates may be variable in time and space and their measurement may be challenging. Geophysical tools may contribute to monitor some of the related biological processes (Atekwana and Atekwana, 2010) along methods specifically designed for this purpose (ITRC, 2018a). Additional issues such as predicting the chemical evolution of multicomponent LNAPL bodies in the subsurface, the effects of biological processes on subsurface properties, and the nexus between NSZD, source zone architecture, source zone longevity, and risks to human health and the environment have not been fully resolved yet.

3 Characteristics of the field sites

3.1 Characteristics of the petrol station site

3.1.1 Location and climate

Information about the characteristics of the petrol station site has been previously presented by Gatsios (2018) and Gatsios et al. (2018a, 2018b). The petrol station site was located in a rural town of the South West region of Western Australia. The area experiences a dry Summer climate (classified as *Csa* by the Köppen–Geiger system) and receives an average of 910 mm of precipitation every year considering the period 1970–2015. More than three quarters of this precipitation are generally concentrated between the months of May and September when the precipitation amount is greater than the evaporation losses as shown in Fig. 3.1.

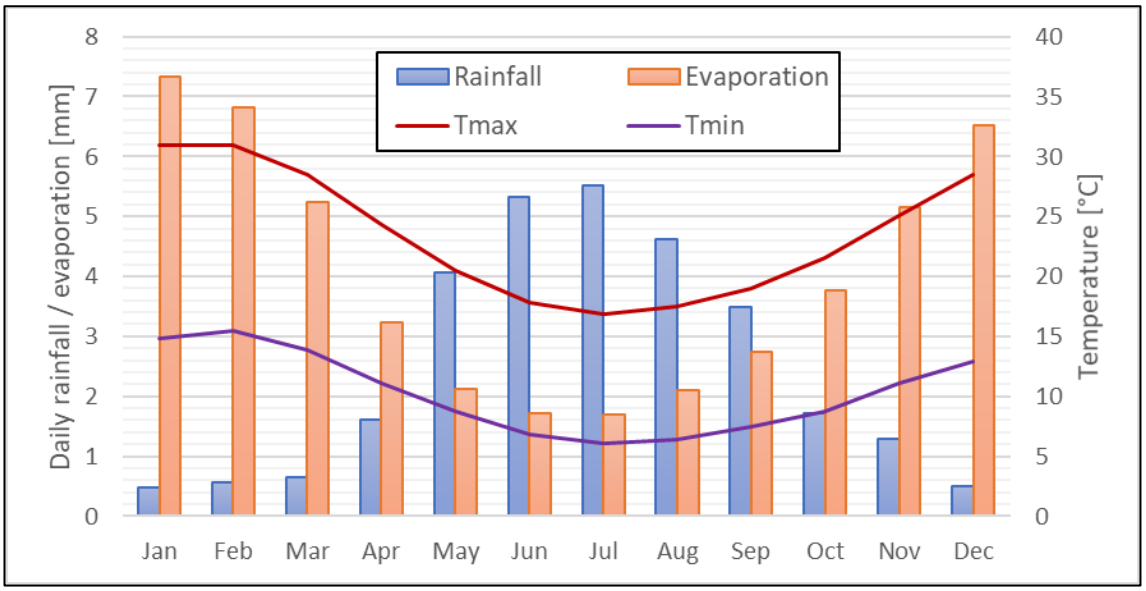


Fig. 3.1. Climate data collected from the SILO database corresponding to the town where the field site was located. All the values were averaged between 1970 and 2015. *Tmax* stands for maximum temperature, while *Tmin* is minimum temperature.

3.1.2 Land use and potential receptors

The petrol station site covered an area of approximately 2,750 m^2. According to reports from other stakeholders, the site was previously used as a truck depot and thus fuels containing petroleum hydrocarbons have been delivered to the site since 1975 with no evidence of spills until the rupture of an underground storage tank (UST) in 2013 as

described in section 3.1.5. The activity of the petrol station site started in 1985. Part of the site surface is covered with concrete, thus limiting potential risks from vapour intrusion. The site has been planned to keep operating as a petrol station site in the future. Therefore, changes in the land use were not considered.

Regarding the potential receptors, there were two commercial buildings on the site with adult workers as well as adult and children customers. The site was surrounded by residential properties with adult and children residents who did not have any domestic wells in their backyards. There was also a creek more than 100 m away towards the West and a river more than 150 m Northeast.

3.1.3 Topographic and hydraulic gradients

The topography was relatively flat and groundwater flow mainly went towards the creek (West) with a low ∇H_w (generally below 0.002). Some of the greatest hydraulic and topographic gradients were linked to the creek (well MP30) as shown in Fig. 3.2, although the water table was not clearly controlled by the topography.

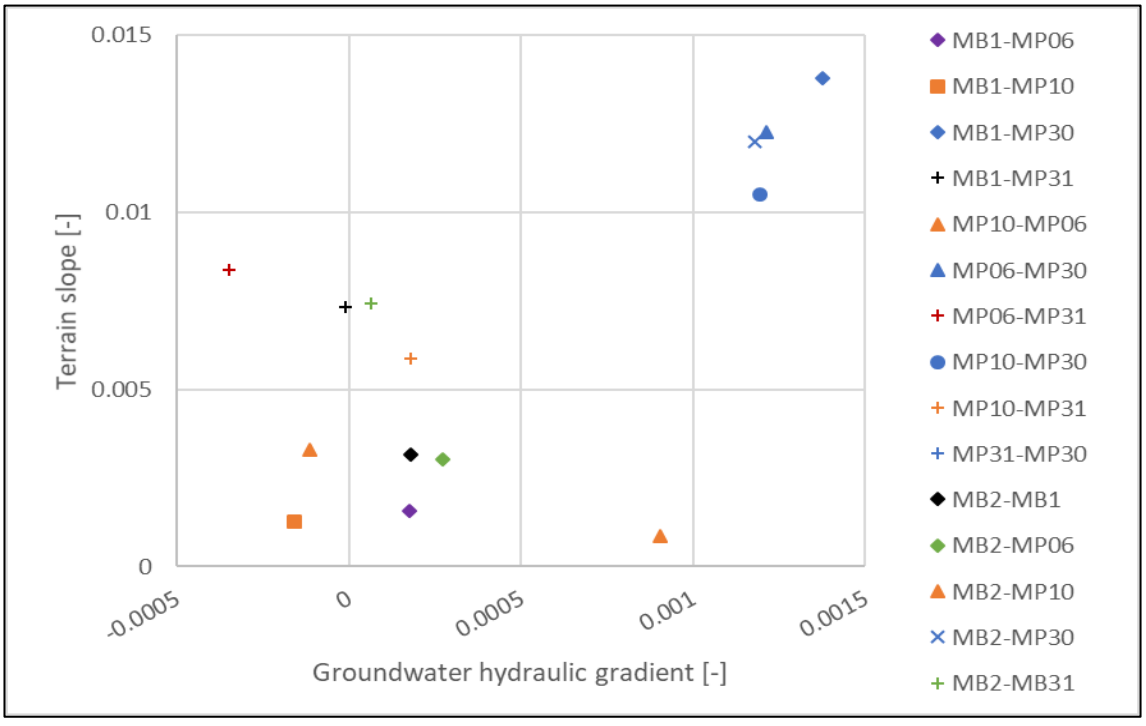


Fig. 3.2. Topographic and groundwater hydraulic gradients (averages of 20–21 records from 2014 to 2018) between perimeter wells. Gradients from the first well of the pair to the second well.

The strongest variations in ∇H_w were usually associated to wet months, with frequent local changes in flow direction as depicted in Fig. 3.3.

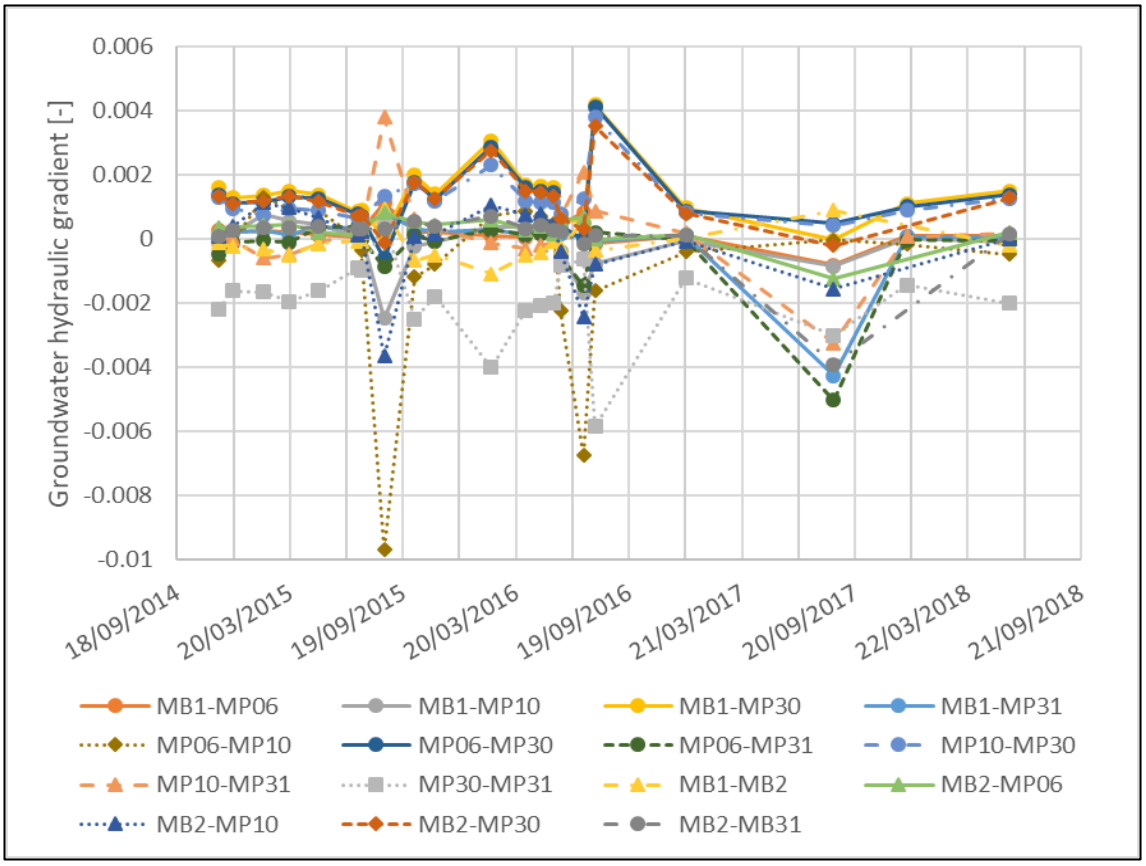


Fig. 3.3. Groundwater hydraulic gradients considering multiple well pairs in the petrol station site.

3.1.4 Hydrogeological setting

The subsurface geology consisted of an unconsolidated aquifer system, most likely formed in a fluvial depositional environment. The hydrostratigraphic profile essentially comprised a heterogeneous sandy aquifer with variable amounts of clays, silts and gravels, overlain by a confining layer and underlain by clays. The overlying aquitard had a thickness of 4–5 m, while the sandy aquifer reached a depth of 7–8 m. z_{aw} was found to fluctuate between the aquifer and the overlying aquitard, recording annual fluctuations of 1–3 m.

Chapter 5 further investigates the subsurface characteristics in the petrol station site, while Chapter 7 quantifies and assesses the variability of hydrogeological parameters. Some parameters were relatively constant and are not discussed elsewhere. For instance, ρ_s presented an average of 2.661 g/cm^3 within the range 2.524–2.693 g/cm^3

(according to 14 samples also used for sieve analysis) and therefore was consistent with the value of 2.65 g/cm^3 characteristic of quartz density and frequently employed in the literature. f_{oc} exhibited an average of 0.113 % in the range 0.045–0.190 % (according to 17 samples also used for particle-size analysis).

3.1.5 Contaminant release, distribution and mobility

The site has been contaminated with fresh gasoline at least since the rupture of a 15,000 L UST in April 2013, which was subsequently removed from the subsurface. It has been suspected that the tank was leaking before the accident and that a total volume between 67,000 and 83,000 L was released. Despite the UST being located in the overlying aquitard, the LNAPL release could reach the aquifer, therefore suggesting the existence of migration pathways within the aquitard.

Petrol remained relatively fresh between the LNAPL release and the last sampling campaigns, when it still contained C_5 hydrocarbons. The average mass percentage of the C_4–C_9 TPH fraction measured in core samples was 86 % in September 2014 and 80 % in May 2016. TPHs in the carbon range C_{16}–C_{28} were not reported. Compositional data from LNAPL samples can be found in Gatsios (2018). Physical and chemical properties of the LNAPL body are further explored in chapters 6 and 7.

The LNAPL body has been practically stable (low spreading rates) since 2015 as inferred by the continued absence of LNAPL in monitoring wells in the perimeter of the petrol station site. Further investigation of multiple lines of evidence should be conducted to corroborate these observations.

Due to the fluctuations in z_{aw}, LNAPL confinement varied seasonally and it became practically immobile during the wet months (Gatsios et al., 2018b). T_n reached a maximum of 2.1 m^2/day, while b_n records exceeded 3 m under confined LNAPL conditions, although being generally below 1 m. Measurements of S_n were generally below 20 %.

The conversion from unconfined to confined LNAPL conditions implied that LNAPL was mainly part of a fully saturated system during most of the wet season and its redistribution was constrained by confining unit. Thus, NSZD phenomena such as

volatilisation were likely limited, contributing to the relatively low weathering degree of the LNAPL chemical composition.

A simplified graphical representation of the CSM is depicted in Fig. 3.4. The CSM shows three areas of study (A, B, and C) where most of the work occurred. These areas of study are presented in section 4.1. The hydrostratigraphic column was simplified as three layers (an aquifer over- and underlain by aquitards, being the top aquitard a potentially confining layer) where the LNAPL body would loss mobility and/or become confined after a z_{aw} increase.

During unconfined LNAPL conditions, a z_{aw} increase implied a reduction in b_n according to field observations, potentially leading to absence of in-well LNAPL as shown for area A in Fig. 3.4(b). In contrast, the well depicted in area C represented an exaggeration of b_n compared to the mobile LNAPL interval in the formation caused by LNAPL confinement. The different evolution of LNAPL distribution and mobility in different locations was due to the heterogeneity within the stratigraphic layers (Gatsios et al., 2018b).

The scale of some elements in the CSM shown in Fig. 3.4 (for instance the two wells and the interval impacted by mobile LNAPL) was exaggerated for illustrative purposes. Similarly, other features were not represented (including intra-layer heterogeneity, variations in the boundary between layers, different material around the UST, presence of residual and entrapped LNAPL or details from the surface). Many of these aspects are further investigated elsewhere in the thesis or detailed in previous works (Gatsios, 2018; Gatsios et al., 2018b).

3.1.6 Justification of the site selection

As described in the following paragraphs, several characteristics of the petrol station site were typical of cases of LNAPL contamination, for instance occurring in an unconsolidated porous aquifer after a spill of petrol. It is also archetypal that LNAPL bodies become stable shortly after the release (Mahler et al., 2012b; Beckett and Huntley, 2015; ITRC, 2018a) and z_{aw} fluctuations may contribute to this stabilisation (Hawkins, 2013).

Measurements of S_n (up to 20 %, not higher than 10 % in some areas) were consistent with observations made in other sites (e.g. Adamski et al., 2003). Middle-stage sites

frequently present S_n values up to 10 % (Sale et al., 2018). Furthermore, b_n values were also within typical ranges (Hawthorne et al., 2015), although some measurements of T_n were very high (reaching a maximum of 2.1 m^2/day). A study found 90 % of 987 T_n values below 0.46 m^2/day and 95 % below 0.93 m^2/day in a 12-year interval (Hawthorne et al., 2015). This could be expected since the petrol station site represented a relatively early-stage release, which are generally less common than middle-stage sites and present higher T_n values (Sale et al., 2018).

Another characteristic frequently observed in LNAPL contaminated sites is the existence of unconfined and confined LNAPL. Hawthorne et al. (2015) found 34.4 % of 489 wells from multiple sites exhibiting confined LNAPL conditions, while 57.5 % of wells corresponded to unconfined LNAPL. The petrol station site allowed investigation of the effects of the overlying aquitard on LNAPL behaviour, modelling predictions, and measurements from conventional and HRSC methods. In addition, some authors have recently encouraged the assessment of the integrity of aquitards with HRSC tools in contaminated sites (Filippini et al., 2020). The relatively fine-grained materials and light LNAPL product could be defined as a challenging environment (ITRC, 2019) for the application of LIF and DPIL systems.

Therefore, many results could be generalised to other sites because of some common characteristics. Other features such as the presence of an overlying aquitard allowed investigation of problems that are less often reported but still significant under field conditions since they may influence the interpretation of field observations and the design of remediation strategies.

The petrol station site was selected for this study because it met the following research requirements: (i) existence of fine-grained unconsolidated materials and heterogeneous conditions to investigate the use of HRSC tools in these common and challenging environments; (ii) presence of a common LNAPL type—petrol; (iii) presence of recoverable LNAPL to evaluate the applicability of LIF logging for the assessment of LNAPL mobility; and (iv) easy access to gather all the data needed for characterisation purposes, including direct-push logs.

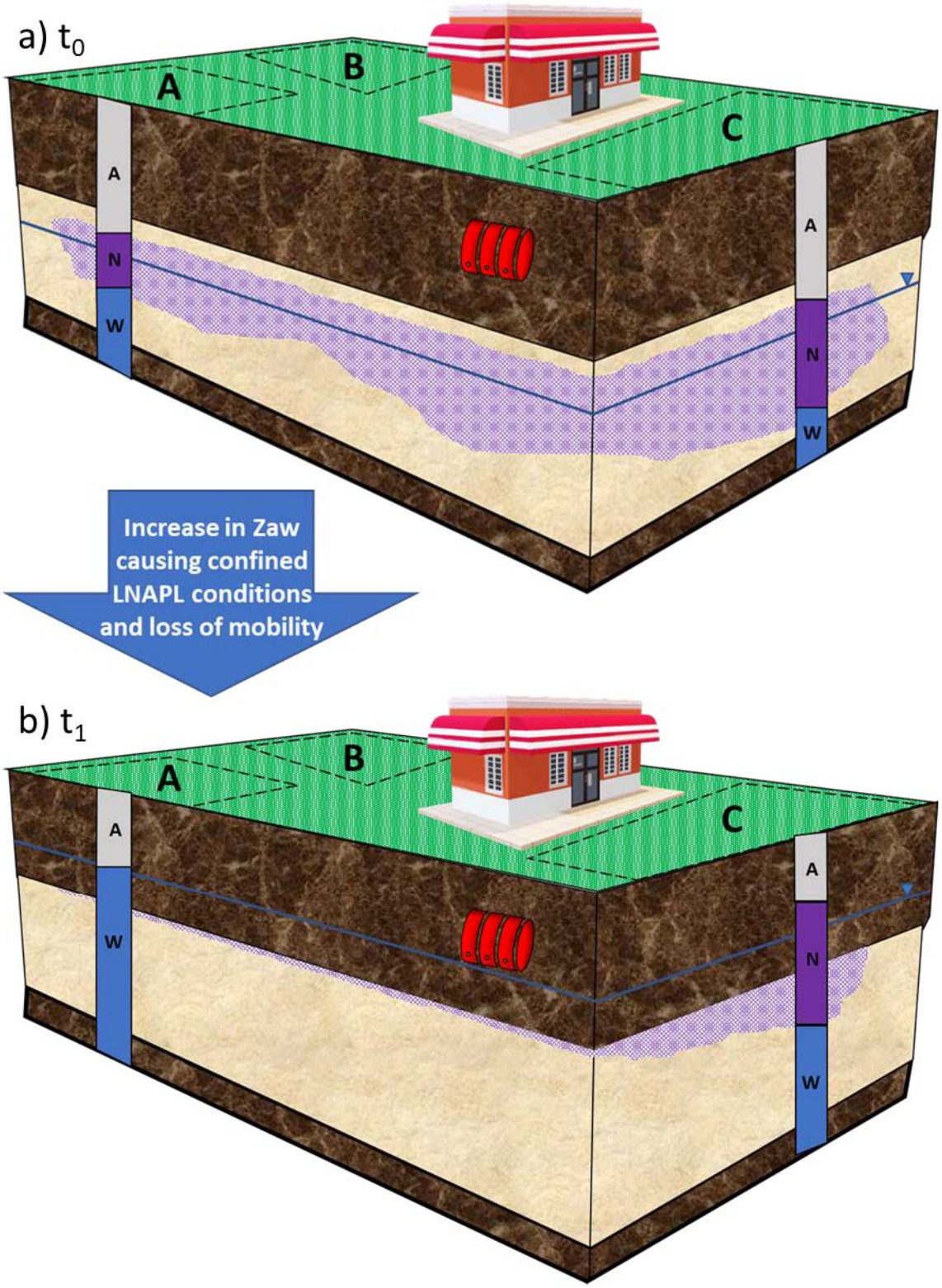


Fig. 3.4. Simplified CSM of the petrol station site including (a) low z_{aw} at an initial time t_0 and (b) high z_{aw} at time t_1. It depicts the stratigraphy (aquitard–aquifer–aquitard), UST location (in red), mobile LNAPL body (in purple), areas A, B and C, and illustrative in-well fluid columns of water (W), LNAPL (N) and air (A).

3.2 Characteristics of the industrial site

3.2.1 Location and climate

The industrial site was located in Western Australia. The proximity to the ocean influences the Mediterranean climate existing in the region, causing cool and wet Winters and hot and dry Summers. The site receives an average of 759 mm of precipitation every year. Most of this precipitation is generally concentrated between the months of May and September, causing significant recharge to the aquifer (Johnston et al., 2010).

3.2.2 Land use and potential receptors

The industrial site was located within an industrial zone occupying an area more than 10 times larger than the petrol station site. Different industrial activities have taken place during the last decades, including storage of organic liquids. Potential receptors included workers from the industrial zone and the ocean.

3.2.3 Hydrogeological setting

The hydrogeological setting mainly consisted of an unconfined aquifer largely formed by fine-to-medium calcareous sands. The calcareous nature of the sands reflected their deposition under a marine environment (Lenhard et al., 2019). Two facies and fine layers of coarser- and finer-grained materials have been reported to exist in the shallow subsurface of the industrial site and other sites from the same geographic region (Johnston and Trefry, 2009; Johnston et al., 2010; Lenhard et al., 2019). The upper facies consisted of sands with potential presence of shells (mollusc and foraminifera) and coral fragments, while the lower facies consisted of generally finer-grained sands than the upper facies. Some cementation could exist, especially below the water table (Johnston et al., 2010).

3.2.4 Contaminant releases and distribution

Releases of multiple LNAPL types (from light fuels such as kerosene-type jet fuel, petrol, and diesel to crude oil) have occurred over decades. Therefore, mixtures of different LNAPL types could exist in some areas of the industrial site. LNAPL mass recovery operations and other remediation approaches have been conducted over the years to ensure the control and depletion of the LNAPL bodies.

3.2.5 Justification of the site selection

Two of the most attractive characteristics of the industrial site were the presence of (i) multiple types of LNAPL under similar subsurface conditions and (ii) calcareous sands instead of silica sands. Thus, it was possible to investigate if the LNAPL type and sand type influenced the measurements of some characterisation methods. For instance, calcareous sands have been reported to produce false positives in LIF investigations (Lu et al., 2014).

Furthermore, the industrial site represented a more homogeneous geological setting than the petrol station site, mainly consisting of sands, and therefore the extrapolation of findings to similar sites could be more feasible and straightforward than in the petrol station site. Sandy settings have been more commonly investigated in the literature and several characterisation and modelling approaches have been developed considering only these environments. Moreover, the industrial site could be classified as a middle-stage site, which is generally more common than early-stage sites (Sale et al., 2018).

These differences between the petrol station site and the industrial site in terms of aquifer heterogeneity, types of LNAPL, and other characteristics could provide insight into the design of investigation strategies depending on the site complexity. Testing if findings from the petrol station site could be extrapolated to sites such as the industrial site or if there were some limiting conditions was also possible.

Therefore, using data from the industrial site was beneficial for this research, although characterising in detail all the LNAPL releases that have occurred in the industrial site over decades was out of scope of this thesis due to resource limitations. Consequently, most of the research focused on the petrol station site, including the comparison between LIF response and T_n and all the experiments related to the existence of an aquitard and confined LNAPL conditions. Data from the industrial site were sufficient to evaluate the application of high-resolution vertical profiling tools compared to conventional methods and test LNAPLTRANS.

4 Materials and methods

4.1 Rationale for the research design

This thesis aims to evaluate the application of HRSC tools and a recently developed multiphase analytical model to predict LNAPL distribution and mobility in unconsolidated aquifers at field scale. Many current challenges associated to the management of LNAPL contaminated sites are due to the complex and heterogeneous nature of the hydrogeological setting and the LNAPL body (Essaid et al., 2015; Sale et al., 2018; Rivett and Wealthall, 2019), and therefore HRSC tools and approaches providing scale-appropriate measurements of subsurface parameters represent a step forward in the effective investigation and remediation of LNAPL contaminated sites.

Field-scale research has not been as frequent as desirable due to the required resources and engagement of external stakeholders. Nevertheless, laboratory and simulation works cannot capture all the complexity of subsurface systems and therefore field studies have been and will be essential to further develop our knowledge and understanding of LNAPL contamination problems.

Two field sites were investigated to widen the range of conditions considered for the evaluation of HRSC tools and analytical models and compare their performance in different subsurface settings. Field characterisation works were conducted in one field site between 2014 and 2018 (the petrol station site), while data from a second field site (the industrial site) collected by other CSIRO staff and the site owners over decades were also gathered and analysed.

The sites were chosen to be representative of commonly found subsurface settings. Thus, both sites corresponded to unconsolidated porous media systems impacted by typical types of LNAPL (relatively fresh petrol in the petrol station site and weathered petrol, diesel, kerosene-type jet fuel, and crude oil in the industrial site). Subsurface materials were mostly sandy (silica sands in the petrol station site and calcareous sands in the industrial site), although with a much greater presence of fines in the petrol station site (representing a fluvial depositional environment) than in the industrial site (representing a marine depositional environment). Further site selection requirements

included the presence of recoverable LNAPL in the subsurface and easy access to gather all the data required for this research.

In the petrol station site, field characterisation works initially covered the entire site to develop the CSM and define the areas of research, while subsequent fieldwork focused on these specific areas (areas A, B, and C; see Appendix B: Maps) due to their contrast in LNAPL distribution, T_n, and hydrostratigraphic profile. Pairs of cores and HRSC logs were collected in adjacent locations to assess the effects of fine-scale heterogeneity.

Similarly, nine additional areas exhibiting differences in LNAPL architecture, LNAPL type, and stratigraphic profile were investigated in the industrial site. Areas A, B, and C from the petrol station site and areas T3 and T4 from the industrial site were selected to evaluate in detail the application of HRSC tools and design modelling scenarios for the analytical models because these areas had the best and more complete datasets. Some relevant results from other areas are also presented for the assessment of HRSC logs.

Table 4.1 summarises details of the twelve areas initially considered. In the petrol station site, Area A exhibited smaller b_n, coarser-grained materials, and higher T_n than the other areas, while area C exhibited greater b_n, finer-grained materials, and lower T_n. Area B was an intermediate case, although it was much closer and similar to area A than area C. In the industrial site, areas T3 and T4 presented similar subsurface material and LNAPL type (presumably diesel), thus analysis of data from both areas was sometimes discussed together, although there was a distance of 150 m between both locations.

The selected HRSC methods included DPIL and LIF logging, in particular the HPT and UVOST® systems because of their suitability for LNAPL contaminated sites, availability, and frequent application by remediation professionals. Thus, research outcomes could have a greater impact and benefits for the remediation industry and other stakeholders.

As discussed in section 2.2.4, the application of other HRSC methods such as MIP logging or hydraulic tomography may be more convenient in sites without LNAPL contamination because of waste management reasons and the upper limit of detection of MIP sensors. The installation of FLUTE® liners is better suited for consolidated and fractured aquifers. More accurate predictions of k_{sw} could likely be achieved with the High-Resolution K tool

developed by Liu et al. (2009) combining DPIL and DPP, although this system is not as available nor commonly employed by remediation practitioners as HPT.

Table 4.1. Details of the areas of research in the petrol station site and the industrial site.

Site	Area	Presumed LNAPL type	Particle-size data	LIF logs	DPIL logs	Modelled
Petrol station site	A	Petrol	Yes	Yes	Yes	Yes
	B	Petrol	Yes	Yes	Yes	Yes
	C	Petrol	Yes	Yes	Yes	Yes
Industrial site	T3	Diesel	No	Yes	Yes	Yes
	T4	Diesel	Yes	No	No	Yes
	B6	None (background)	No	Yes	Yes	No
	D5	Petrol	No	Yes	No	No
	D6	Diesel	No	Yes	Yes	No
	T5D9	Kerosene-type jet fuel	No	Yes	Yes	No
	T6	Crude oil	No	Yes	Yes	No
	T7	Crude oil	No	Yes	Yes	No
	T7D1	Crude oil	No	Yes	Yes	No

The capability of DPIL and LIF logging for the delineation of the subsurface hydrostratigraphy (including the assessment of aquifer heterogeneity) and LNAPL distribution (including mobile and near-immobile fractions), the identification of confining boundaries, and the assessment of LNAPL mobility was evaluated.

HRSC tools were compared to conventional methods such as coring, monitoring of in-well fluid levels, soil gas measurements, aquifer testing, baildown testing, and empirical correlations of k_{sw} with particle-size data. Discrepancies between predictions with different methods are common and reflect some of the many uncertainties associated to remediation projects and the difficulty to identify true values of subsurface parameters.

The main features of the site characterisation plan between 2014 and 2018 included:

- installation of dozens of monitoring points (long-screened wells, multilevel wells, vapour points, and thermistors arrays) as well as collection and in-house chemical and physical analysis of samples (LNAPL, water, soil gas, cores) as presented in section 4.2;

- periodic measurement of fluid levels and subsurface temperature profiles as presented in section 4.3;
- one campaign with HRSC vertical profiling tools (LIF and DPIL) in May 2016 as presented in sections 4.4 and 4.5;
- execution of dozens of hydraulic tests (baildown tests, manual skimming tests, and aquifer tests) as presented in section 4.6;
- a two-week LNAPL mass recovery (LNAPL skimming) trial in July–August 2015 and a one-month LNAPL mass recovery (LNAPL skimming, water-enhanced skimming, vacuum-enhanced skimming, water- and vacuum-enhanced skimming) trial including tracer testing in June–July 2016. Details of the LNAPL mass recovery trials can be found in Gatsios (2018) and Gatsios et al. (2018b).

Section 4.7 describes methods to derive k_{sw} and retention parameters from particle-size data, while section 4.9 presents the rationale for the statistical analysis of field data.

In addition, field measurements of subsurface parameters were compared to literature values and ranges reported in classic references and popular databases. A discussion about the differences between the Carsel and Parrish (1988), UNSODA (Nemes et al., 2001), and API (2006) databases can be found in Charbeneau (2007b). The API (2006) database presumably addresses limitations of the other alternatives for the investigation of LNAPL contaminated sites according to Charbeneau (2007b).

Thus, measurements and estimations from the HRSC tools and other conventional methods (as well as literature values) were employed as input data to test a recently developed analytical model (LNAPLTRANS) as described in section 4.8. The most popular alternative (LDRM) was also tested and the capabilities and underlying assumptions of both models were compared in the designed model scenarios. The effects of the field data variability in the model predictions and potentially in LNAPL remediation projects was investigated through a sensitivity analysis and the study of best- and worst-case scenarios.

4.2 Well installation, sampling and analysis

4.2.1 Drilling and installation of monitoring points

Details about the installation of monitoring points in the industrial site are included in section 4.2.2. As regards the field characterisation works in the petrol station site, external environmental consultants assessed the site conditions and installed the first monitoring wells (MB1, MB2, MB3, and MB4) after the LNAPL release occurred in April 2013.

The CSIRO team started characterising and monitoring the site in 2014 (first monitored fluid levels from June 2014) and kept doing it until 2018, with most of the field campaigns being conducted between 2015 and 2016. All the data was incorporated into a database to facilitate its management.

The drilling and installation of characterisation and monitoring points were conducted by eDrill under supervision of the CSIRO team. The location of these points initially aimed to cover the entire site extension to develop the CSM and define the areas of research. Later, drilling operations focused on areas A, B, and C. The location of the characterisation and monitoring points can be found in Appendix B: Maps.

Boreholes were drilled with 4" or 6" hollow stem augers, generally reaching the underlying aquitard. Six types of characterisation and monitoring points were employed:

i) 100-mm fully penetrating long-screened production wells (name code: PB);
ii) 50-mm fully penetrating long-screened monitoring wells (name codes: MB and MP);
iii) multilevel wells (name code: ML);
iv) vapour points (name code: VP);
v) HPT logs (name code: HPT);
vi) LIF logs (name code: LIF).

In addition, two points (CRK1 and CUL1) were used as reference marks to monitor the level of the nearby creek. The naming convention consisted of a name code (indicating the installation type) followed by a number (indicating when it was installed), and an area code (for instance, A, B, or C). The terms 'production' and 'monitoring wells' were

just working definitions. The only difference between them was that the 100 mm diameter of the production wells allowed using a pump, a logger, and the dipper at the same time. The study of dissolved and vapour fluxes was out of scope of the thesis and therefore results from sampling events in multilevel wells and vapour points are not presented.

A total of 13 production and 26 monitoring wells were installed in the petrol station site. Additionally, the monitoring network included five multilevel wells (slotted intervals every meter) with thermistors arrays, 16 vapour points (usually in pairs, one deep point at 1 m and one shallow point at 0.5 m), 10 HPT logs, and 20 LIF logs.

Regarding the installation dates, PB09-B had a larger diameter than other wells and was installed by the site owners for different purposes before the contamination event happened. There was no information available about its construction design or exact installation date.

Wells MB1–4 were installed in June 2013 (before CSIRO involvement in the fieldwork). Subsequently, there were six main drilling campaigns in April 2014 (MP/PB 01–08), August 2014 (10–13), November 2014 (26–31), August 2015 (33–42), May 2016 (MP44–58; completed in parallel with the HRSC campaign), and August 2016 (MP76–78). Details are summarised in Table 4.2.

For the installation of production and monitoring wells, a PVC casing with a bottom plug was introduced into the borehole after removing the auger. The PVC well commonly included a 6-m long screen with 0.5 mm slots. The top of the screen commonly started at the overlying aquitard to ensure that free LNAPL in the formation could flow into the well. The annulus was backfilled with gravel generally up to 0.5 m above the top of screen with bentonite sealing the top of the borehole.

To further enhance the connection between the well and the formation, wells were developed until the pumped water did not exhibit significant amounts of fines and ensuring that at least five well volumes were pumped out. LNAPL was also purged weeks before the performance of some hydraulic tests to contribute to the existence of equilibrium conditions at the time of the tests.

Table 4.2. Construction details of monitoring and production wells as well as the creek monitoring points.

Installation ID	Date installed	Datum [m AHD]	Stick-down correction [m]	Top of screen [m AHD]	Bottom of screen [m AHD]
CRK1	n/a	54.465	n/a	n/a	n/a
CUL1	n/a	57.185	n/a	n/a	n/a
MB1	10/06/2013	61.326	0.059	57.326	55.826
MB2	10/06/2013	61.424	0.072	57.924	56.424
MB3	10/06/2013	60.973	0.072	57.473	55.973
MB4	11/06/2013	61.452	0.053	57.502	56.002
MP01	01/04/2014	61.196	0.186	57.696	51.696
MP02	04/04/2014	61.226	0.186	58.026	52.026
MP03-C	04/04/2014	61.303	0.097	56.803	53.803
MP04	04/04/2014	61.196	0.166	57.696	51.696
MP06-C	04/04/2014	61.111	0.074	58.111	52.111
MP07-C	04/04/2014	61.219	0.139	58.969	52.969
MP08-C	04/04/2014	61.291	0.151	60.541	54.541
MP10	05/08/2014	61.182	0.114	59.182	53.182
MP30	06/11/2014	59.366	0.138	56.366	50.366
MP31	06/11/2014	60.643	0.221	57.443	51.443
MP34-A	03/08/2015	61.049	0.194	58.049	52.049
MP36-B	04/08/2015	61.088	0.105	57.888	51.888
MP37	04/08/2015	60.864	0.157	57.664	51.664
MP38	04/08/2015	60.894	0.166	57.694	51.694
MP41-C	05/08/2015	61.288	0.126	58.188	52.188
MP42	06/08/2015	61.272	0.119	58.072	52.072
MP44-C	17/05/2016	61.269	0.096	58.069	52.069
MP50-A	18/05/2016	61.134	0.102	58.034	52.034
MP58-B	19/05/2016	60.978	0.123	57.978	51.978
MP76-B	16/08/2016	61.002	0.120	58.002	52.002
MP77-A	16/08/2016	61.144	0.078	58.144	52.144
MP78-C	17/08/2016	61.227	0.113	58.227	52.227
PB05	04/04/2014	61.322	0.216	57.822	51.822
PB09-B	unknown	61.470	0.095	unknown	unknown
PB11-C	05/08/2014	61.233	0.154	58.233	52.733
PB12-C	06/08/2014	61.253	0.153	57.503	51.503
PB13-C	07/08/2014	61.239	0.191	57.989	51.989
PB26	04/11/2014	61.334	0.121	59.334	53.334
PB27-B	05/11/2014	60.997	0.163	58.997	53.397
PB28	05/11/2014	61.293	0.143	59.093	53.093
PB29-A	05/11/2014	61.084	0.145	58.934	52.934
PB33-A	03/08/2015	61.210	0.112	58.560	52.560
PB35-B	04/08/2015	61.103	0.120	58.103	52.103
PB39-C	05/08/2015	61.310	0.091	58.210	52.210
PB40-C	05/08/2015	61.256	0.101	58.156	52.156

Once the wells were installed, a mark was put at the top of casing to be used as the well datum. Elevations according to the Australian Height Datum (AHD; where 0.000 m AHD is the mean sea level throughout Australia in 1966–1968) were determined through navigation satellite positioning. Measurements were repeated in several occasions and compared to dumpy level estimations to enhance the quality of the data. Additionally, stick-down corrections were measured as the distance between the top of casing and the ground level. They were important since data from coring and HRSC campaigns referred to depths below ground level (bgl), while in-well fluid levels referred to depths below top of casing. Further discussion about geopositioning errors can be found in Rau et al. (2019).

Appropriate Personal Protective Equipment (PPE) was worn during the drilling investigations. PPE included resistant high visibility clothing, long-sleeved shirt and long trousers, safety boots, helmet, gloves (nitrile or leather depending on the task), safety googles, and earplugs.

4.2.2 Coring locations

Multiple installations in the industrial site (including one in area T3 and five in area T4), as well as 17 installations in the petrol station site were continuously cored and generally cut up for chemical and particle-size analysis. Coring locations in the industrial site and the petrol station site are shown in Appendix B: Maps. Further details of the cores collected in the areas of research are summarised in Table 4.3.

In the industrial site, there were three main coring campaigns of interest for the purpose of this thesis. The campaigns took place in June 2004, February 2005, and September 2016. Cores 040610/1-T4, 040610/2-T4, 040610/3-T4, and 040610/6-T4 were collected on 10/06/2004, while 050210/1-T4 was cored six months later on 10/02/2005 and C66-T3 was obtained 12 years later on 08/09/2016, two months after a HRSC campaign. All these cores were cut up for chemical analysis, except 040610/2-T4 which was only sampled to estimate retention parameters in the laboratory. Monitoring well NS7A-T4 was installed at 040610/3-T4 location and the ID NS7A-T4 was used for sets of aggregated data from cores 040610/3-T4 and 050210/1-T4. Fig. 4.1 depicts the core locations in area T4.

Table 4.3. Core sampling and analysis details in the areas of study. z_{aw} values presented for the petrol station site were measured at PB11-C close to the coring events, while interpolated z_{aw} values from 182-T3 were used for the industrial site. PSA and LOD refer to 'particle-size analysis' and 'limit of detection', respectively.

Site	Area	Core ID	Date	z_{aw}	TPH	PSA	vG	Comment
Petrol station site	A	PB33-A	03/08/2015	56.34	X	-	-	
		MP50-A	18/05/2016	56.15	X	X	-	
		MP77-A	16/08/2016	58.86	X	-	-	
	B	PB27-B	04/11/2014	57.65	X	X	-	
		PB35-B	04/08/2015	56.34	X	-	-	TPH < LOD
		MP58-B	19/05/2016	56.17	X	-	-	
		MP76-B	16/08/2016	58.86	X	-	-	
	C	PB11-C	05/08/2014	58.38	-	-	-	Only 0.5 m recovered
		PB12-C	06/08/2014	58.37	X	X	-	
		PB13-C	07/08/2014	58.37	X	X	-	
		PB39-C	05/08/2015	56.36	X	X	-	
		MP44-C	17/05/2016	56.15	X	X	-	
		MP78-C	17/08/2016	58.86	X	-	-	
Industrial site	T3	C66-T3	08/09/2016	-	X	-	-	
	T4	040610/1-T4	10/06/2004	0.45	X	X	-	TPH < LOD
		040610/2-T4	10/06/2004	0.45	-	-	X	
		040610/3-T4	10/06/2004	0.45	X	X	-	
		040610/6-T4	10/06/2004	0.45	X	X	-	
		050210/1-T4	10/02/2005	0.23	X	-	-	

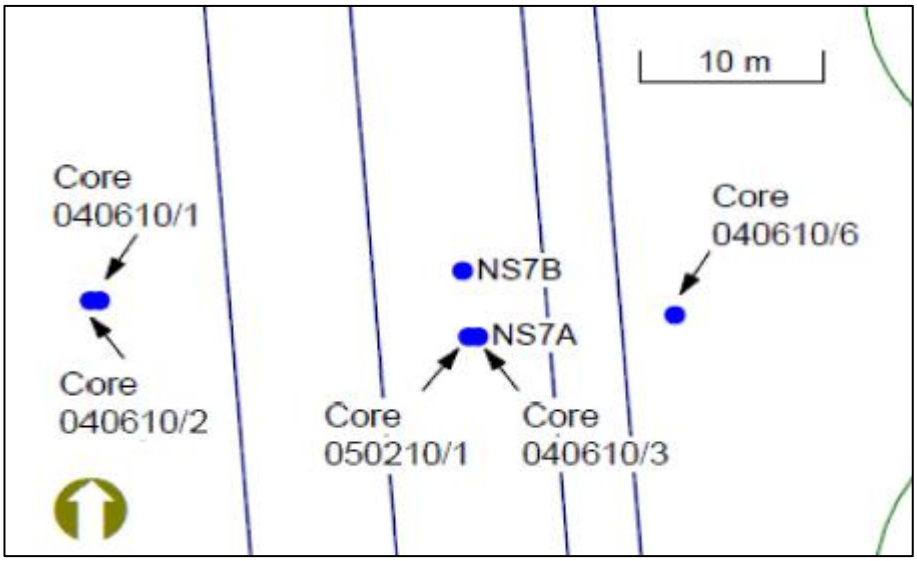


Fig. 4.1. Coring locations in area T4 (adapted from Johnston et al., 2010). Well IDs NS7A and NS7B refer to long-screened installations.

4.2.3 Coring process

A 4” or 6” hollow stem auger with a wireline retrieval system for withdrawing the core barrel from the lead auger was employed for coring purposes. HSA enabled collection of near-continuous cores in the locations of interest without circulation fluids, thus minimising the disturbance of the potential samples. Continuous coring leads to less sampling gaps than other methods such as split spoons.

The percentage of core recovery in the petrol station site was typically high compared to other works (e.g. Kiaalhosseini et al., 2016; Einarson et al., 2018), indicating little compaction or loss of material. The recovery rate was over 90 % in May 2016 (HRSC campaign) and August 2016. Similarly, core recovery was over 80–85 % in August 2015, with losses occurring in the saturated zone at PB33-A and MP42. Material losses were a greater concern in 2014, only achieving 45–65 % recovery at several locations (including PB13-C and PB27-B).

Core shoes were immediately placed into tins labelled according to the sample identification details (job number, sample number, well ID, core number, acquisition date, depth) and sealed with the corresponding lid. The cores were also sealed as they were encircled by a sleeve (a polycarbonate tube with an external diameter of 0.05 m) augered into the profile and capped after the extraction. Subsequently, the cores were labelled and put into an insulated box with ice or ice cooler bricks straightaway, subsampled, and transported to the laboratory as soon as possible, reducing losses by volatilisation, photodegradation, and biodegradation. Fig. 4.2 depicts tins and cores obtained at MP10.

Additional samples were taken for in-house measurement of particle density ρ_s, inorganic and organic carbon as well as particle-size analysis to evaluate and enhance the visual stratigraphic descriptions besides of deriving soil properties such as Φ, k_{sw}, and retention parameters. However, values derived from particle-size data are commonly considered preliminary estimates since there is not a unique relationship between these parameters and particle-size distributions due to the influence of multiple factors including differences between the particle-size distribution and the pore-size distribution (Chapuis, 2012).



Fig. 4.2. Labelled tins and cores recovered at MP10 in the petrol station site.

The particle-size distribution is a cumulative distribution function representing particle diameters in a decimal logarithmic scale versus the percentage of smaller particles contained in the sample. Particle-size analysis was done through laser diffraction with a Malvern particle-size analyser (size fractions between 0.02 and 500 µm) and wet sieving (size fractions between 500 and 10,000 µm). Water was employed as a dispersant after adding 10 mL of sodium hexametaphosphate. Samples were put in an ultrasonic bath for 20 min and a total of 90 size fractions were reported to build particle-size distributions of each sample. Using the correct protocols in laser diffraction analysis has been found to lead to adequate estimations of hydraulic properties (Segal et al., 2009).

Notes about the stratigraphy were taken during the extraction of the cores and core shoes, which were further inspected in the field or laboratory once the sampling process was completed.

Parameters such as the content in fines (clay and silt), coefficient of uniformity C_u and coefficient of curvature C_c were employed to describe the samples and classify them as

uniform (if C_u was lower than 2), well sorted (C_u between 2 and 5) or poorly sorted (if C_u was higher than 5) as it is also done through HydrogeoSieveXL (Devlin, 2015) and presented in Appendix E: Particle-size data and correlations with hydraulic conductivity. These coefficients are given by equation 4.1 and equation 4.2, where d_i was the linearly interpolated value of the sieve diameter letting pass an *i*-% of the sample:

$$C_u = \frac{d_{60}}{d_{10}}; \tag{4.1}$$

$$C_c = \frac{{d_{30}}^2}{d_{10} \times d_{60}} \tag{4.2}$$

As shown in Fig. 4.3, even when cores were not recovered, the resulting drill cuttings were still visually inspected.



Fig. 4.3. Drill cuttings and tins obtained every 0.5 m at PB29-A.

4.2.4 Soil gas screening and sample preparation

An Eagle 2® gas monitoring device by RKI Instruments was available and therefore used as part of a screening method to delineate the presence of LNAPL in cores and select the best sampling intervals in cores taking into consideration resource and budget constraints. The device was equipped with a catalytic sensor to detect combustible gases, a galvanic sensor to measure oxygen, and electrochemical sensors for carbon monoxide and hydrogen sulphide.

The catalytic sensor employed methane as a calibration gas and therefore estimated the amount of combustible gases using methane as a reference. Since the detector was not specific for the measurement of methane, it was employed to screen potential core intervals with VOCs. Results were reported as volume of methane in air in percentage, being 5 % the upper limit of quantification.

Initially, soil gas measurements were restricted to tins storing core shoes, contributing to discriminate between LNAPL contaminated and likely uncontaminated cores. In 2015, the field procedure experimented some modifications as it was refined to provide data with a greater resolution. Modifications were justified because the primary goal was to improve the selection and representativeness of samples for TPH analysis, not to replicate soil gas measurements from different campaigns. One variant of the screening method followed in the 2016 campaigns included sectioning the core and placing 5-cm sections into sealed tins to measure soil gas concentrations and collect subsamples accordingly. As it can be appreciated in Fig. 4.4, a tin lid was adapted and joined to the suctioning tube of the Eagle 2® detector to minimise vapour losses.



Fig. 4.4. Soil gas measurements of tins containing core samples.

A second variant employed in 2015 involved collecting a high number of potential subsamples for TPH analysis directly from the core while measuring soil gas concentrations from intermediate elevations to select the intervals where contamination could be found. More specifically, the core sleeve was cut up and substituted by a cover with entry points every 0.1 m as shown in Fig. 4.5(a) where potential subsamples for TPH analysis were collected with a small tubular soil sampler and stored. Using a cover and collecting the subsamples straightaway was done to reduce losses by volatilisation and obtain representative samples for TPH analysis. Similar sampling methods have been followed by other researchers (Einarson et al., 2016), although using aluminium foil to cover the cores and not complementing the method with soil gas measurements as described below.

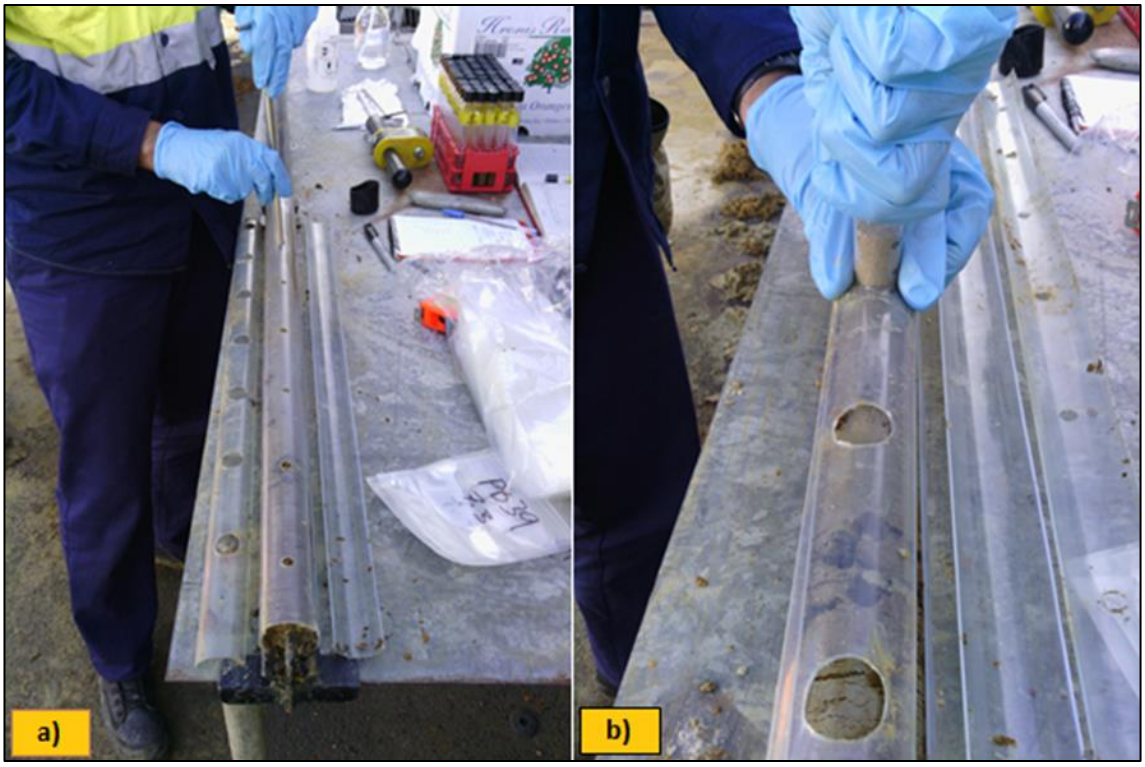


Fig. 4.5. Collecting potential subsamples for TPH analysis with a small tubular sampler (a) and samples for screening delineation of LNAPL contamination (soil gas) with disposable syringes (b).

Then, a cover with entry points every 0.1 m but at alternate elevations as shown in Fig. 4.5(b), was placed over the core to take samples for soil gas analysis. These samples were taken with disposable (sectioned) syringes to avoid cross-contamination. Next, as depicted in Fig. 4.6, they were put into labelled bags under direct sunlight for a reasonable period of time before using Eagle 2® to analyse the vapours. Once these soil

gas results were obtained, subsamples were confirmed or discarded for chemical analysis in the laboratory.



Fig. 4.6. Bags containing samples for soil gas analysis.

Therefore, in both variants as well as in campaigns before 2015, subsamples of around 2-5 g for TPH analysis were collected with a tubular sampler and placed into labelled glass tubes with PTFE liners. Then, the weight of the sealed glass tubes and the subsamples was recorded using a precision scale before adding 4–5 mL of solvent (DCM/methanol) including deuterated internal and surrogate standards (*d6*-benzene, *d8*-toluene, *d10*-*p*-xylene, and *d8*-naphthalene) with a pump action dispenser as shown in Fig. 4.7. Sampling tins with the corresponding lids were also weighed before and after collecting any sample as well as before and after extracting any subsample for chemical or biological analyses.



Fig. 4.7. Setting for the preparation of subsamples including a solvent dispenser, a precision scale and labelled glass tubes.

All the sampling utensils were cleaned with paper and ethanol between samples or directly disposed. Two tubular samplers were alternated between samples allowing them to air dry. The addition of solvent with surrogate standards was aimed to reduce losses by volatilisation and allow for quality control in the laboratory. The subsamples were stored at low temperature and sent for in-house chemical analysis as soon as possible.

4.2.5 Chemical analysis

Solvent from the core samples was extracted with a pipette after tumbling and sonication. Subsequently sub-samples were collected to analyse the concentration of TPH fractions and compounds through gas chromatography–flame ionisation detector (GC–FID) and gas chromatography–mass spectrometry (GC–MS), as well as a gravimetric method when LNAPL was diesel or a heavier product. Detailed discussion about the application of methods for TPH analysis can be found in the literature (Total Petroleum Hydrocarbon Criteria Working Group, 1998; ITRC, 2018b).

GC–MS was used to quantify individual TPH compounds such as BTEX and PAHs due to the high sensitivity and selectivity of the method after a proper integration and interpretation of the chromatogram. An Agilent 7890 gas chromatograph was fitted with a vaporising injector (operating in split mode) to introduce the organic compounds using helium as carrier gas. The compounds got separated in a capillary column (Phenomenex, ZB-1ms, 30 m length, 0.25 mm internal diameter, and 0.25 µm thick film of dimethyl polysiloxane or equivalent column) and analysed with an Agilent 7000B mass spectrometer, which was operated with an ionisation energy of 70 eV at 230 °C in scan and SIM modes. The resulting chromatogram allowed quantitation of selected compounds after calibration.

Nevertheless, the determination of short alkane chains ($<C_6$) through GC–MS may present significant uncertainties, since highly volatile compound may elute before the solvent peak and produce interferences (Total Petroleum Hydrocarbon Criteria Working Group, 1998). Consequently, GC–FID was used to analyse TPH fractions in the carbon range C_4–C_{40}. For this purpose, the procedure was similar as with GC–MS, but an Agilent 6890 gas chromatograph was used and fitted to a FID instrument.

Quantitation for both GC–FID (for TPHs) and GC–MS (for BTEX and selected aromatic components) was performed using external standards (unleaded petrol, benzene, toluene, ethylbenzene, *p*-xylene, *o*-xylene, 1,3,5-trimethylbenzene, 1,2,4-trimethylbenzene, naphthalene, 2-methylnaphthalene, 1-methylnaphthalene, 1,2-dimethylnaphthalene, phenanthrene, and 1,2,4,5-tetramethylbenzene) and internal/surrogate standards (*d6*-benzene, *d8*-toluene, *d10*-*p*-xylene and *d8*-naphthalene with *d10*-*p*-xylene used as the surrogate standard for TPH analysis by GC–FID). The distribution and abundance of internal/surrogate standards were also used to validate whether each analysis was within limits of the method calibration as well as identification of injection or chromatography issues (analyses outside the limits of the method calibration were reanalysed). Laboratory control samples, mid-point standards, and blank samples were analysed every 20 samples as well as method blanks and field blanks at the start and end of cores.

Additionally, a gravimetric method was also applied in the industrial site to measure the TPH concentration above C_{10}. The gravimetric method did not allow identification of individual compounds, but the estimation of total TPH concentration was faster and simpler than with GC–MS or GC–FID.

4.2.6 Estimation of bulk density, porosity, and LNAPL saturation

After transporting the cores and sample tins back to the laboratory (with few exceptions when all the work was carried out in the field), the sleeves were removed and their weight, height and inner diameter were determined. Meanwhile, the samples were air-dried and oven-dried (at 105 °C) with their weight being measured after both processes. Sample weights and sleeve dimensions have been reported in Gatsios (2018). It should be noted that sleeve dimensions were not measured for a sample collected at MP44-C at 55.81 m AHD. This sample contained a significant TPH concentration and a S_n value of 4.44 % could be derived assuming average sleeve dimensions from other samples.

In the case of C66-T3, samples with high LNAPL contents were air-dried only, so air-dried weights instead of oven-dried weights were used for the rest of calculations at C66-T3. According to the S_n profiles depicted in Fig. 4.8, this assumption was not expected to affect any conclusions of qualitative nature, although S_n values derived from air-dried measurements were likely overestimated by 14–19 %. Similar differences (generally within a 10–30 % range) were measured in cores from the petrol station site when comparing S_n values derived from air-dried and oven-dried samples.

Subsequently, the wet mass of sample m_{wet} was obtained as the difference between the weight of the tin with the wet sample and the weights of the empty tin and the sleeve. In addition, the mass of water m_{water} was derived from the differences before and after oven-drying the sample (accounting for the removed sleeve) and the mass of oven-dried sample m_{od} (air-dried in the case of C66-T3) was calculated by removing the weight of the empty tin to the mass of the tin plus the sample after drying it.

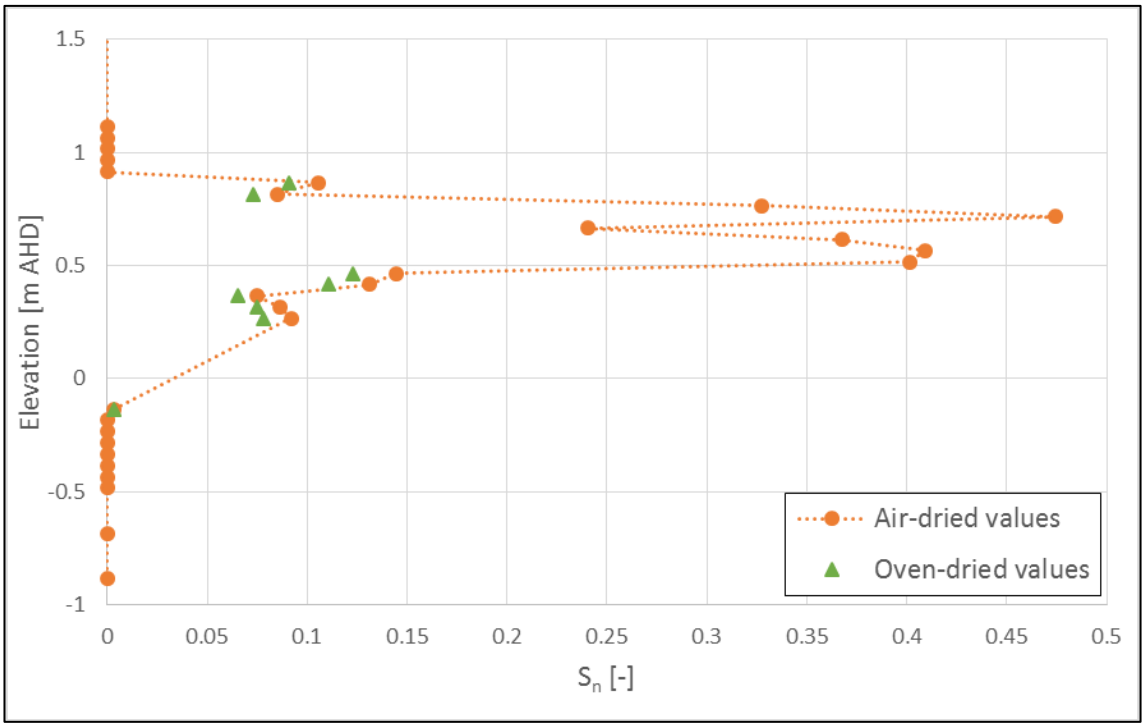


Fig. 4.8. S_n values derived from air-dried and oven-dried samples at C66-T3.

Furthermore, m_{water}/m_{od} gave the gravimetric water content θ_g and $m_{wet}/(1+\theta_g)$ provided the total mass of the bulk sample. This value was used for the estimation of ρ_b accounting for the volume of the sample V_{sample} as given by the sleeve dimensions. Therefore, ρ_b was calculated according to equation 4.3:

$$\rho_b = \frac{m_{wet}/(1+\theta_g)}{V_{sample}} \qquad (4.3)$$

Moreover, ρ_s was generally assumed to be 2.65 mg/kg since quartz is typically the predominant mineral in unconsolidated sediments (Todd and Mays, 2005; Fetter, 2018). This assumption applies to silica sands, but it may induce errors in other materials. Then, Φ was derived from ρ_b as in equation 4.4 (the variability of Φ was assessed by also considering values from the literature presented in section 7.2.1 and neural networks predictions as explained in section 4.7.3):

$$\Phi = 1 - \frac{\rho_b}{\rho_s} \qquad (4.4)$$

Finally, the TPH concentration analysed in the laboratory as milligram per kilogram of wet sample was converted to milligram per kilogram of dry sample by dividing by $1+\theta_g$.

Thus, S_n was estimated by using equation 4.5 (Parker et al., 1996), where θ_n was the volumetric NAPL content:

$$S_n = \frac{\theta_n}{\Phi} = \frac{[TPH]}{10^{-6}} \times \frac{\rho_b}{\rho_n} \times \frac{1}{\Phi} \quad (4.5)$$

Water saturation and total liquid saturation were estimated in an analogous way. During all the weighting process, several measurements were repeated and some values were obtained through different procedures to ensure and control the quality of the data.

Wiedemeier et al. (1999) supported that ignoring equilibrium mass transfer phenomena in equation 4.5 does not introduce considerable errors if f_{oc} is low. Errors associated to the calculation of S_n of some of the samples from the petrol station site were below 2 % compared to the consideration of equilibrium partitioning phenomena to the dissolved and sorbed phases (Gatsios, 2018). Nevertheless, these analyses focused on samples with high S_n values. Errors were presumably higher in samples with low S_n as also shown by Feenstra et al. (1991) and Rivett et al. (2014). Furthermore, aspects such as non-equilibrium partitioning, the influence of colloids, and the analytical procedure to determine TPH concentration (ITRC, 2018b), could have had an additional impact on the estimation of S_n. Section 6.4.2 provides further insight regarding errors derived from the coring process.

4.2.7 LNAPL, groundwater, and vapour samples

In addition to samples from coring, LNAPL samples were collected to measure ρ_n, η_n, molecular weights, chemical compositions, and equilibrium coefficients in water-LNAPL systems. LNAPL was bailed or skimmed from wells and stored in glass vials. Measurement of ρ_n was done with an oscillating piston viscometer (Cambridge Viscosity VISCOlab 4000). The temperature was set at approximately 20 °C, which resembled subsurface conditions at the petrol station site.

The study of dissolved and vapour fluxes was out of the scope of this thesis. However, a few groundwater and vapour samples were collected to gain insight on the extension of the contamination plumes.

More specifically, there was a campaign to collect groundwater samples on May 2015. Low-flow (100–500 mL/min) sampling procedures were followed to minimise the disturbance of the subsurface. Therefore, instead of purging, groundwater properties displayed were monitored in a flow-through cell with calibrated devices until three consecutive measurements fell within acceptable stability limits.

Groundwater samples were stored at low temperature and promptly sent for in-house chemical analysis. Analyses of inorganic cations and TPH concentrations were carried out using internal standards. GC–MS results showed positive BTEX concentrations at MB3, MP06, MP31, and ML32, while values at MB1, MP04, MP10, and MP30 remained low or below the detection limit.

Vapour samples were collected with glass syringes on November 2014 (concentrations over the GC–MS detection limit only at VP20D and VP20S) and on November 2015 (concentrations over the GC–MS detection limit only at both VP24, both VP25 and ML32 at 3.00 m bgl).

4.3 Monitoring campaigns

4.3.1 Main characteristics of the monitoring campaigns

In the petrol station site, monitoring campaigns started on June 2014 and were generally conducted every 1–2 months until October 2016 and then every 4–5 months until mid-2018. The objective was to monitor some dynamic subsurface conditions on a regular basis, including fluid levels, temperature profiles, and LNAPL, groundwater and soil gas properties. This information feeds. The following methods were periodically applied:

- manual dipping of fluid levels (z_{aw}, elevation of the air–NAPL interface z_{an}, and elevation of the NAPL–water interface z_{nw}) in wells and the creek;
- automatic recording of z_{aw} with four pressure transducers and data loggers;
- measurement of temperature profiles with five thermistor arrays placed into multilevel wells;
- occasional collection of LNAPL, groundwater, and vapour samples.

PPE (including resistant high visibility clothing, long-sleeved shirt and long trousers, safety boots, nitrile gloves, and safety googles when manipulating fluids or soils) was

always worn during the monitoring campaigns. Dipping of in-well fluid levels in areas with potential traffic was done in groups of two people within perimeters delimited by safety cones. The ground lead of the interface probes was always clipped to the frame.

4.3.2 Fluid level monitoring

In-well fluid levels (depth to water DTW and depth to LNAPL DTN when present—both measured from the well datum) were monitored using intrinsically safe interface probes from Heron Instruments (H.OIL® and Sm.OIL® models) like the one shown in Fig. 4.9. The creek water level was also measured in almost every campaign.



Fig. 4.9. Measurement of in-well fluid levels with an interface probe at MP30.

Interface probes have two sensors (Dalton et al., 2006): (i) a circuit with an infrared beam to discriminate between air and liquids because of their different refractive index; (ii) a conductivity sensor to differentiate between LNAPL (non-conductive) and water (conductive). As the probe was carefully lowered down, the interface probe communicated the presence of LNAPL with a steady tone, while it emitted an intermittent tone when water was detected. The probe was lowered below any in-well LNAPL and slowly withdrawn to check both recorded fluid levels were accurate.

Recorded DTN values were converted into z_{an} after accounting for the elevation datum as indicated by equation 4.6. Analogously, DTW was converted to z_{nw} if LNAPL was present or z_{aw} if LNAPL was absent.

$$z_{an}[m\ AHD] = Datum\ [m\ AHD] - DTN\ [m] \tag{4.6}$$

In the presence of LNAPL, z_{aw} was computed accounting for the density ratio between LNAPL and water (ρ_{rn}) as shown in equation 4.7.

$$z_{aw} = z_{nw} + \rho_{rn} \times (z_{an} - z_{nw}) \tag{4.7}$$

4.3.3 Quality and variability of fluid level measurements

Measurements of in-well fluid levels were frequently repeated by multiple investigators to control the quality of the readings, generally obtaining values within a 2-mm difference (and typically not more than 1 mm). This high level of precision was most likely due to the type of LNAPL found in the subsurface: a relatively fresh gasoline with low viscosity. Other actions to increase the quality of the measurements included keeping details about the investigators reading and recording the measurements, the time of the measurement, the serial number of the interface probe (always using the same one for the same tasks if possible), and any other relevant observations. Using different interface probes may greatly decrease the precision of measurements of in-well fluid levels (Rau et al., 2019).

Errors associated to fluid level measurements included additional sources of uncertainty such as fluid density variability, absence of VEQ conditions, poor hydraulic connection between the well and the formation, and natural fluctuations of z_{aw} during the monitoring campaigns.

Water density ρ_w was assumed to be 1000 g/cm^3, which typically introduces errors of 0.20 % at 20 °C. A total of 22 LNAPL samples were collected in 10 wells on 05/12/2014 to measure ρ_n in triplicate. The average of the 22 samples was 0.739 g/cm^3 with a range of 0.725–0.805 g/cm^3. The maximum value corresponded to PB12-C (standard deviation—SD—of 0.002 g/cm^3) followed by ρ_n values of 0.760 g/cm^3 at PB09-B, 0.747 g/cm^3 at MP03-C, and 0.739 g/cm^3 at MP07-C. When a well did not have a ρ_n measurement, the average of nine wells (0.7378 g/cm^3 after excluding the extreme

value of PB12-C and considering only one average ρ_n value for each location) was employed to compute z_{aw}. Fig. 4.10 illustrates errors in the estimation of z_{aw} that could have resulted from assuming this average value instead of a possible ρ_n of 0.805 g/cm^3 (which could become higher with time due to NSZD phenomena).

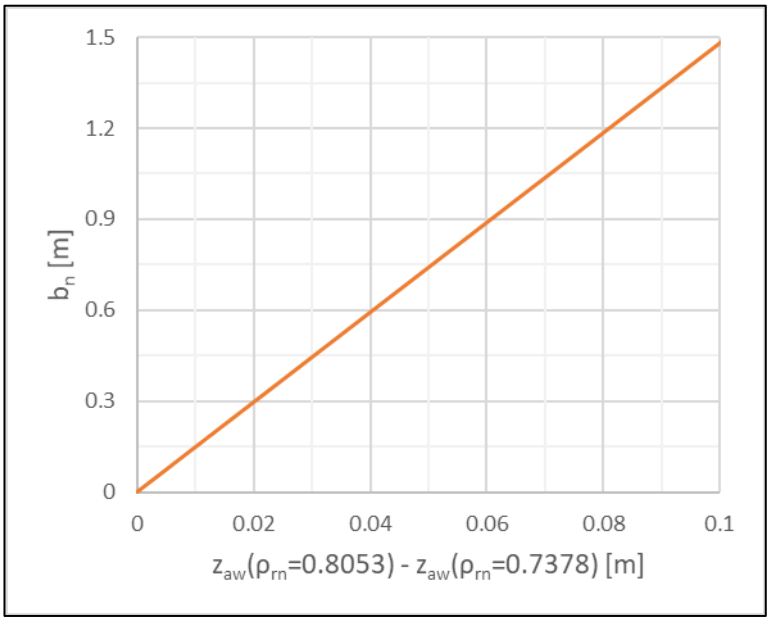


Fig. 4.10. Potential errors in the computation of z_{aw} derived from assuming a ρ_{rn} of 0.7378 instead of 0.8053 (extreme value measured at PB12-C).

Regarding the lack of equilibrium conditions, a clear example was derived from the extraction of LNAPL and/or water with electric pumps for some tests. It was complicated (and in some cases not possible) to accurately dip the LNAPL–water interface in such situations since both fluids could get emulsified as shown in Fig. 4.11. LNAPL extraction with skimmers, bailers or some specific pumps did not generally produce emulsions in the well and were more adequate for hydraulic testing.



Fig. 4.11. Emulsion of LNAPL and water after a hydraulic test using an electric pump.

4.3.4 Single-well LNAPL diagnostic gauge plots

In-well fluid levels represented in the form of DGPs were used for the assessment of LNAPL hydrogeologic conditions (unconfined, confined, or perched). This assessment was essential because it is directly related to the identification of subsurface strata and it may also affect T_n data analysis methods and the comparisons between LIF and b_n data.

As described in the literature, groundwater and LNAPL confinement are not caused by the same phenomena (Hawthorne et al., 2011). Groundwater confinement is due to changes in the medium intrinsic permeability that impede the flow of water through the confining layer. In multifluid systems, LNAPL may become confined depending on the corresponding entry pressure of the medium (Illangasekare et al., 1995; Mayer and Hassanizadeh, 2005; Hawthorne et al., 2011). A similar argumentation could be followed for the case of perched groundwater and LNAPL conditions. It was possible to compare if both groundwater and LNAPL were confined when aquifer tests were performed (as described in section 4.6).

Single- and multi-well DGPs are b_n-based (monitored elevation of fluid interfaces versus b_n) or z_{aw}-based scatter plots (z_{an}, z_{nw}, and b_n versus z_{aw}) that mainly allow identification of LNAPL hydrogeologic conditions and the contact (hereafter 'confining contact') between two layers inducing a transition between different hydrogeologic conditions (Kirkman et al., 2013; Hawthorne, 2014). Ideal behaviour patterns exhibited under perched, confined, and unconfined LNAPL conditions are illustrated in Fig. 4.12.

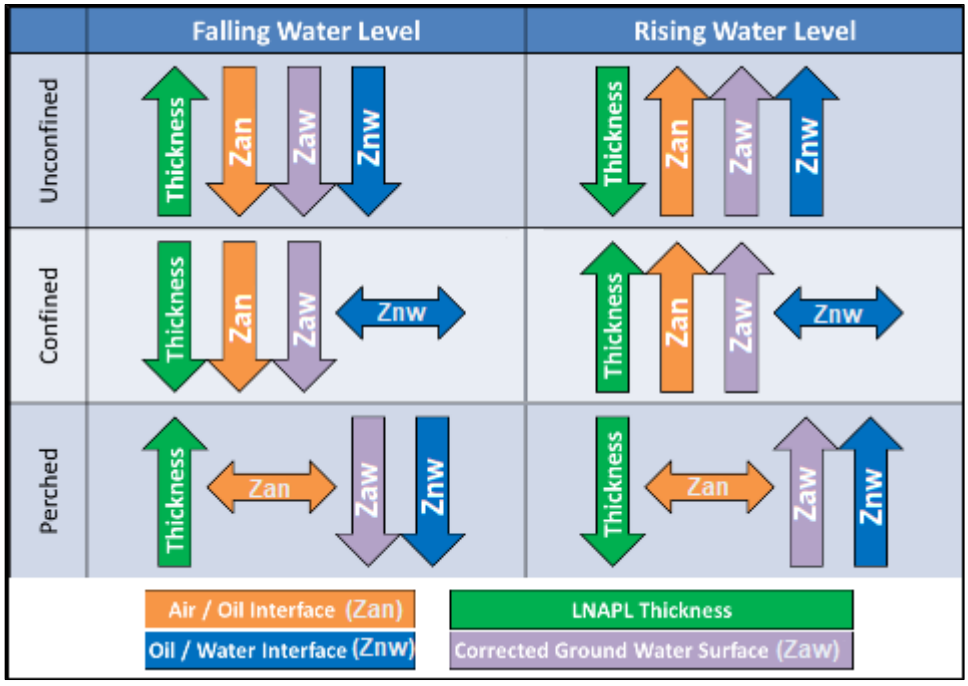


Fig. 4.12. Behaviour of fluid interfaces under unconfined, confined, and perched LNAPL conditions (modified after Sale et al., 2018).

In summary:

- unconfined LNAPL conditions imply that changes in b_n are inversely related to changes in all the fluid interfaces;
- confined LNAPL conditions imply a constant z_{nw} over time, while b_n and z_{an} are functions of z_{aw} and ρ_n;
- on the contrary, perched LNAPL conditions imply a constant z_{an}, while b_n and z_{nw} are functions of z_{aw} and ρ_n.

If z_{nw} is not constant under presumed confined LNAPL conditions, it may partly indicate the existence of a leaky confined unit. Artefacts may be caused by measurement errors, poor hydraulic connection between the well and the formation, and non-equilibrium

phenomena (Atteia et al., 2019). Thus, some data was filtered before generating DGPs (including observations with z_{nw} above the top of the well screen, some measurements collected just after the well installation or after an abrupt change in z_{aw} producing large residual errors, and periods when LNAPL mass recovery trials were being conducted). Well construction design has been reported to influence the subsurface flow fields and therefore the representativeness of in-well observations (Houben, 2015).

Furthermore, interpretation of DGPs with multi-year field data may be complicated by factors such as NSZD phenomena, LNAPL migration and redistribution, non-equilibrium and hysteretic effects, changes in LNAPL physical properties, and measurement errors (including borehole effects). It was hypothesised that the interpretation of DGPs could be improved by analysing seasonal periods (hereafter 'fluctuation periods') exhibiting quasi-monotonic rising (or falling) z_{aw} conditions. DGPs of individual fluctuation periods were compared to the original DGP to test this hypothesis. This approach has not been previously presented in the literature beyond the work of Gatsios (2018). Trends in z_{an} from single-well DGPs where commonly employed to infer the confining contact elevation at PB29-A, PB27-B, and PB40-C, generally resulting in a range between 56.7 and 56.8 m AHD (Gatsios, 2018; Gatsios et al., 2018b).

In chapter 5, the applied methodology was further refined by implementing the least squares method to the linear regression analysis of trends followed by the monitored elevation of fluid interfaces. The reason for this modification was to standardise the methodology and reduce the potential bias of the analyses. Moreover, by applying least squares, the precision of estimations of the confining contact elevation in different fluctuation periods could be evaluated in a standardised way. Thus, equations of linear models for presumed unconfined and confined LNAPL periods were used to calculate the intersection of both equations and therefore the confining contact elevation.

If data representing one of the hydrogeologic periods (perched, confined, unconfined) were insufficient for the analysis, the intercept of the other linear model with the y-axis ($b_n = 0$) could be adopted as an indication of the maximum (when using unconfined data) or the minimum (in case of analysing confined data only) possible elevation of the

confining contact. This approach may result in strong uncertainties mainly due to non-linear effects as discussed below.

Previous works (Kahraman, 2013; Hartsock, 2014) have also applied least squares regression to the analysis of DGPs. They did not consider individual fluctuation periods and frequently obtained low coefficients of determination. Measurement errors and variability of field conditions (including redistribution of LNAPL in heterogeneous media and poor hydraulic connection between wells and the formation) were presumably more relevant than errors of the linear regression model in the petrol station site and the industrial site.

Nevertheless, analysing the elevation of fluid interfaces as if they followed linear trends may imply an assumption of ideal conditions not truly representative of the subsurface environment. Loss of linearity may occur not just because of measurement errors but also because of changes in time of subsurface characteristics. For instance, vertical redistribution of LNAPL throughout a heterogeneous hydrostratigraphic profile imply changes in the relationship between in-well fluid levels and fluid pressures in the formation due to the variable characteristics of the medium. This effect may be stronger near the confining contact, which may not be abrupt but gradual or diffuse for example.

Furthermore, the estimation of the confining contact through DGPs commonly assumes that b_n practically coincides with the mobile LNAPL interval in the formation under unconfined LNAPL conditions (Gatsios, 2018). However, this may not be the case if a positive entry pressure exists (Farr et al., 1990). Thus, the confining contact could be shallower than suggested by DGPs. Moreover, in-well fluid levels may represent the fluid pressures of multiple mobile LNAPL intervals disconnected from each other in the formation, for instance in fractured rock settings (Kirkman and Koons, 2020).

In addition, the confining contact itself could be dynamic to some extent, since the retention curve and entry pressure responsible of creating LNAPL confinement depend not only on the LNAPL and medium properties but on the fluid saturation history as well. This phenomenon is likely of limited importance when the contact between layers is abrupt, but further research should be conducted in other scenarios.

4.3.5 Multi-well LNAPL diagnostic gauge plots

Multi-well DGPs illustrating z_{aw} versus b_n have been suggested as a tool to identify LNAPL transmissive zones across entire sites as well as their hydrogeologic conditions and b_n ranges (Hawthorne, 2014). The objective of section 5.2.5.4 is precisely to test this hypothesis and assess whether phenomena such as water table fluctuations may favour misleading interpretations of multi-well DGPs.

Data aggregation issues could also affect the interpretation of multi-well DGPs, for instance because of the combination of locations with different V_n values and therefore variable z_{nw} even with a constant confining contact. Additional factors such as higher ∇H_w values or variable ρ_n may further complicate the analysis and interpretation of multi-well DGPs.

The elevation of fluid interfaces in z_{aw}-based multi-well DGPs was normalised in an attempt to improve the interpretation of the data, gaining insight into the range of elevations where the confining contact was found across the entire site according to this line of evidence compared to the range of 56.7–56.8 m AHD previously reported after the analysis of single-well DGPs (Gatsios et al., 2018b).

4.4 Ultra-Violet Optical Screening Tool (UVOST®)

4.4.1 UVOST® technology

4.4.1.1 UVOST® fundamentals

UVOST® is a geophysical logging tool commonly delivered using cone penetrometer systems or percussion-based direct-push rigs. It is a spectroscopic indirect method based on LIF technology with high vertical, centimetre-scale resolution. UVOST® systems mainly consist of a laser source (with a narrow spectral width by definition) placed up-hole, fiber optics within the rod string, a down-hole probe with a sapphire window, and finally a digital storage oscilloscope with processing software to record the spectral data.

As the UVOST® probe is advanced into the subsurface, the laser source emits light pulses of 1-2 nanoseconds (Einarson et al., 2016) at wavelengths of 308 nm. These light pulses are transmitted via fiber optics to the geological medium through the probe sapphire window. Then, any excitable molecules absorb this energy and may release part of it in

form of photons. Lastly, the emitted photons are counted and captured by a second fiber and transmitted to the processing unit.

The phenomenon described in the previous paragraph is called luminescence. After some compounds absorb energy, their electrons become temporary excited. Then, energy is released in form of photons when all these electrons go back to their ground state as commonly represented in Jablonski diagrams (Lakowicz, 2006). This process is called fluorescence if it lasts less than a microsecond and phosphorescence otherwise. Consequently, UVOST® systems can record the fluorescent response of the medium even with a high rate of push of the rig (1 cm/s for instance).

4.4.1.2 Fluorophore response

Compounds with the ability to fluoresce are called fluorophores. Aromatic compounds usually belong to the group of fluorophores, being those with higher number of aromatic rings the ones with higher absorption and emission wavelengths and lower emitted energy. Therefore, LIF methods may be used to detect important chemicals of concern in LNAPL contaminated sites such as BTEX and PAHs.

Nevertheless, UVOST® cannot detect BTEX due to intrinsic limitations of using fiber optics, since BTEX absorption spectra is below the fiber optics absorption spectrum and the 308 nm wavelength employed by the laser source. Thus, 308 nm represents a longer wavelength and a lower energy than that needed to excite BTEX molecules. Laser sources with shorter wavelengths exist, but they would require systems not based on fiber optics to detect BTEX.

As a consequence, petrol and kerosene-type jet fuel are responsive to UVOST® excitation primarily because of their naphthalene concentration, since heavier molecules are less abundant. In contrast, diesel response to UVOST® may be 10 times higher than petrol or kerosene-type jet fuel under the same conditions (St. Germain, 2014). Thus, detection of light fuels may be challenging. Furthermore, more than one order of magnitude of difference in LIF response can be found depending on the soil type and other factors such as moisture content (Apitz et al., 1992).

Every fluorophore has characteristic absorption and emission spectra and as a consequence compounds can be identified according to their emission spectra (intensity

versus wavelength). In addition, the emission spectrum of a pure substance is constant and not a function of the laser source (Aldstadt et al., 2002). Nonetheless, petroleum hydrocarbons such as petrol or diesel are not pure substances but complex mixtures of chemicals. Hence, it is not generally possible to discriminate between individual compounds by simply inspecting the complex emission spectrum obtained under field conditions (Aldstadt et al., 2002).

4.4.1.3 Multi-wavelength waveforms

UVOST® separates the measured fluorescence in four wavelength channels of the spectrum (350 nm, 400 nm, 450 nm, and 500 nm). Then, the response from every channel is delayed in time and represented in two-dimensional multi-wavelength waveforms displaying fluorescence intensity and lifetime (Aldstadt et al., 2002; Grundl et al., 2003). Fig. 4.13 illustrates the correspondence between wavelength–time matrices and multi-wavelength waveforms. As it can be seen in Fig. 4.14, every UVOST® channel is represented by one colour (blue for 350 nm, green for 400 nm, orange for 450 nm, and red for 500 nm). Then, the results are plotted as a log of the total UVOST® signal (sum up of the four channels) versus depth along several callouts showing multi-wavelength waveforms at specified depths. The total UVOST® signal is calibrated with a reference emitter (RE) to normalise it as %RE and be able to compare logs taken under different operational conditions. A colour is assigned to the total UVOST® signal at every point by combining the colours representing each channel (Lu et al., 2014). This approach may contribute to identify different types of LNAPL and its degree of weathering by inspecting the colourisation of a UVOST® log.

In general, every compound will simultaneously fluoresce in multiple channels as depicted in Fig. 4.14. However, some may fluoresce mostly in one channel, for instance naphthalene as easily appreciated in the multi-wavelength waveform shown in Fig. 4.14 (top right corner). Regarding chemical mixtures, fresh petrol and kerosene-type jet fuel exhibit a greater response at 350 nm than in other channels—although weathering may alter the LIF signature (ITRC, 2019). This is accompanied by positive LIF lifetime values. Diesel is usually more responsive at 400 nm and exhibits a short-long-long-long lifetime pattern in the four channels, while heavier hydrocarbons present a signal shifted towards the 450 and 500 nm channels.

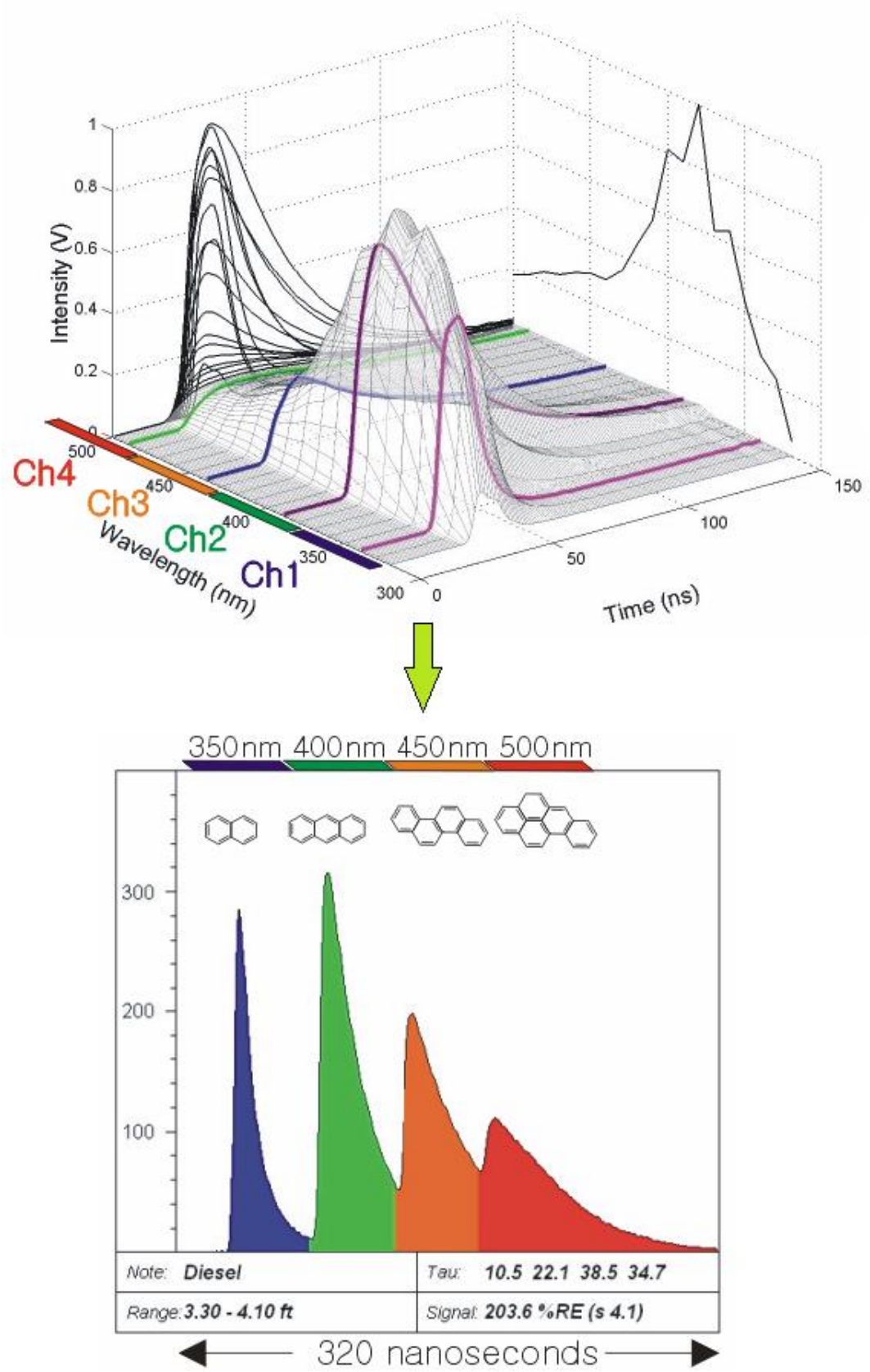


Fig. 4.13. Correspondence between the concepts of wavelength-time matrix (top) and multi-wavelength waveform (bottom) for a LNAPL mixture (adapted from St. Germain, 2014).

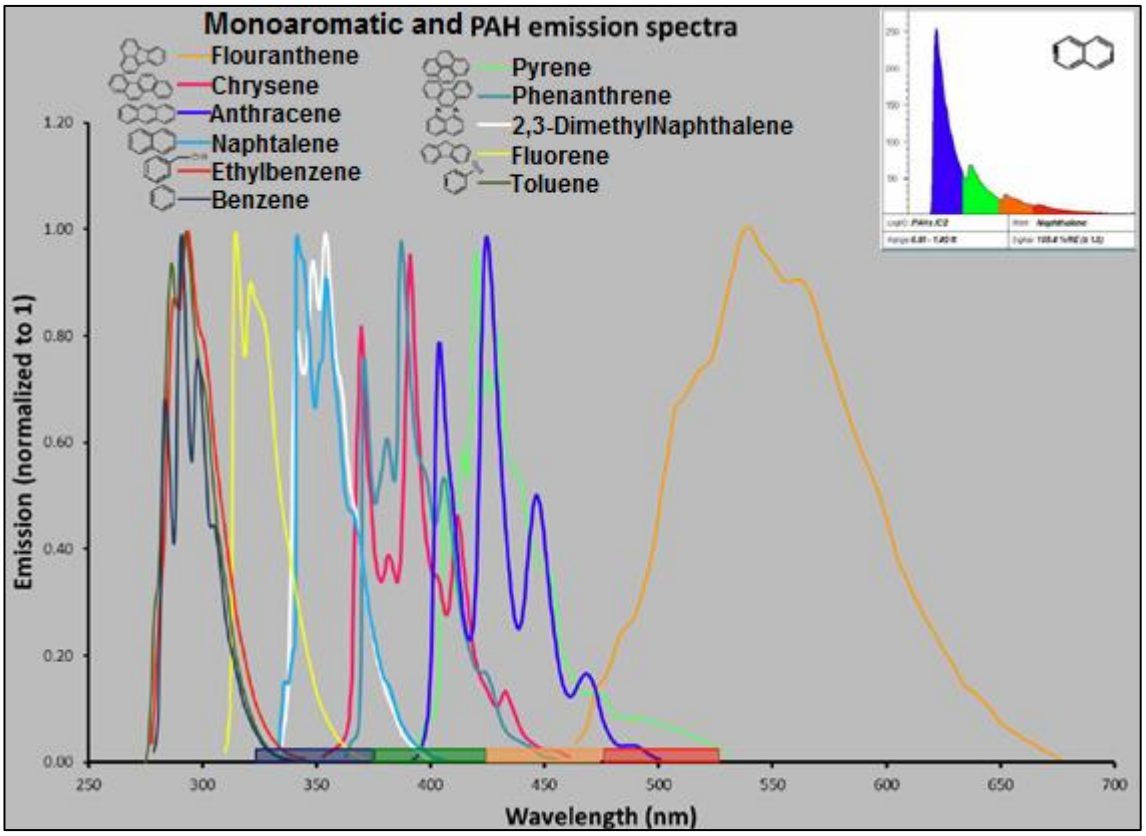


Fig. 4.14. Emission spectra of BTEX and PAHs and multi-wavelength waveform of naphthalene (adapted from St. Germain, 2014).

However, Fig. 4.13 shows that consecutive channels will overlap if the fluorescence decay time at a given channel is longer than the delay applied to the following channel. For this purpose, the processing software isolates the response from each channel by assuming exponential decays (St. Germain, 2014). Thus, values of wavelength and lifetime at every channel may be predicted by fitting exponential functions to LIF data. Long decay times may indicate a solvent-rich environment or lack of oxygen (Lu et al., 2014). On the other hand, short decay times are frequently related to energy transfer phenomena. In particular, environments rich in oxygen cause fluorescence quenching because oxygen molecules transform the absorbed energy into heat.

Similarly, fluorescence quenching and shifting towards longer wavelengths may occur if heavy PAHs are present and energy is transferred from lighter PAH molecules to them. As a consequence of this phenomenon, UVOST® is not recommended for sites contaminated with heavy hydrocarbons such as coal tar or creosotes (Lu et al., 2014; St. Germain, 2014; ITRC, 2019).

4.4.1.4 Factors influencing LIF response

There are some additional uncertainties and limitations associated to the use of UVOST® systems. First, it is important to note that light cannot travel more than very short distances in the subsurface. Consequently, the sapphire window needs to be practically in contact with the LNAPL product to be able to detect it (Lu et al., 2014). More specifically, fine-grained materials may represent a challenging environment, since LNAPL may not be visible to the sensor (ITRC, 2019). Furthermore, the advancement of the probe may compress the LNAPL mass and the formation, resulting in local increases of S_n (ITRC, 2019). In addition, UVOST® cannot typically detect dissolved PAH in groundwater because of the low maximum concentrations of PAHs in water and the high quantity of dissolved solids (St. Germain, 2011).

The geological medium is an important factor influencing the LIF response because of the varying particle size, pore geometry, grain colour, soil gas composition, moisture content, the medium effects on LNAPL distribution, and the presence of materials potentially producing false positives and negatives (Lu et al., 2014; ITRC, 2019). It has been stated that the same TPH concentration in gravels or sands may exhibit a signal 10 times stronger than in silts or clays (St. Germain, 2011). Additionally, heterogeneous conditions may affect the LIF response in non-linear ways as illustrated in Fig. 4.15.

False positives caused by subsurface conditions have been classified as weak (1–3 %RE), medium (3–10 %RE), and strong (>10 %RE) in the literature (Lu et al., 2014). For instance, sewer lines (medium–strong), sea shells (weak–strong), calcareous sands (weak–strong), tree roots (weak–medium), and organic matter are potential sources of false positives (Lu et al., 2014; ITRC, 2019) that could affect the logs from the field sites investigated in this doctoral dissertation, in particular the industrial site.

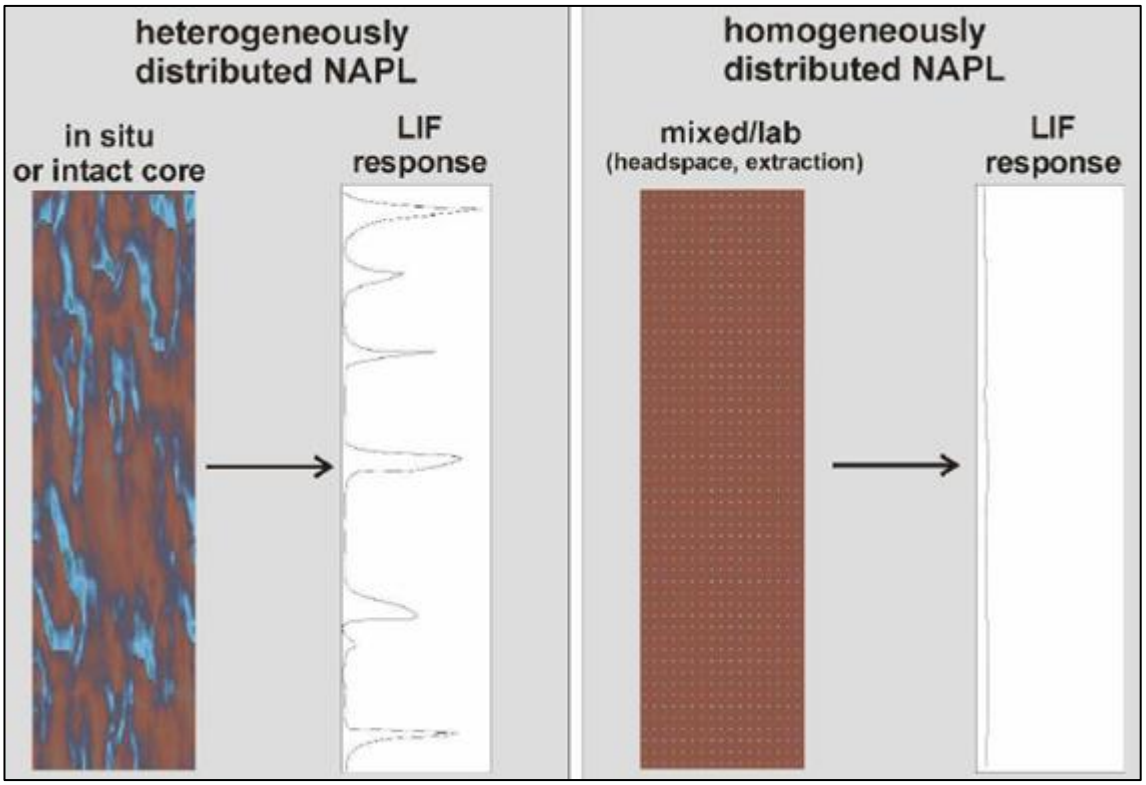


Fig. 4.15. Impact of heterogeneity on LIF response (St. Germain, 2014).

4.4.2 LIF logging campaigns

The UVOST® probe was used as a HRSC tool to delineate LNAPL distribution at the petrol station site and the industrial site. The field assessment of LNAPL distribution was justified to:

i) further develop the CSMs of the investigated field sites;

ii) study a potential link between LIF response and LNAPL mobility;

iii) design the modelling scenarios as well as evaluate the resulting predictions.

Every field method (LIF, coring, soil gas measurements, and in-well fluid levels) suggested different LNAPL distributions. Therefore, the performance of LIF was assessed against a conventional and widely used method such as coring. One main hypothesis arose from preliminary analyses: the LIF signal may be related to LNAPL mobility and may work as an indicator of T_n. These aspects have only been previously suggested in one conference paper for the case of a saprolite aquifer (Mulry and Lundy, 2013) and are theoretically supported by the presumably exaggerated effects of the geological medium on the LIF signal compared to the effects on other methods. The hypothesis

was mainly investigated at the petrol station site, since there were better data (LIF and T_n data) than in the industrial site in terms of spatial and temporal resolution.

The HRSC campaign was conducted in the petrol station site between 17/05/2016 and 20/05/2016. A total of 20 logging locations were selected to further develop the detailed CSM, in particular placing them near the original location of the UST, in areas A, B, and C as well as in potential migration pathways between these zones. The LIF sites are shown in map 7 (see Appendix B: Maps). LIF profiles were obtained at less than 2 m from wells PB29-A, PB27-B, and PB40-C. More than one LIF log was collected in each area. Thus, the effects of fine-scale heterogeneity could be investigated.

As concerns the industrial site, the purpose of the campaign was to get a better understanding of the subsurface in six specific areas and not to develop the whole CSM exploring new areas or pathways between the existing ones. A total of 51 LIF profiles were collected in these six areas between 31/05/2016 and 17/06/2016. In particular, one of the modelling scenarios was based in area T3 and four LIF profiles were obtained on 13/06/2016 to gain insight on the subsurface conditions. The LIF sites from area T3 are shown in map 12 (see Appendix B: Maps).

In both field sites, the LIF probe was attached to the percussion direct-push rig (Geoprobe® 6620DT) shown in Fig. 4.16. The planned drilling locations were marked beforehand (pink and yellow spots in Fig. 4.16). When the terrain was covered by concrete (approximately 0.1 m thick), it was perforated with a diamond drill bit before using the direct-push rig. The depth of the direct-push profiles was less than 10 m and the rate of push was around 1 cm/s, frequently shifting between 0.5 and 2 cm/s with few exceptions. Therefore, completion of a LIF profile usually took less than 1 h.

A single-point calibration was done with a reference emitter (RE) before recording every LIF log. The LIF signal was recorded and monitored in real time, facilitating the adoption of an adaptive sampling strategy according to professional judgement. Multi-wavelength waveforms were printed at multiple depths. In addition, one sample of in-well LNAPL was measured above ground at each site. The elevation of the ground level was measured and used as datum.



Fig. 4.16. Direct-push rig for the HRSC campaign at the petrol station site (the drilling campaign was conducted by Numac and eDrill under supervision of the CSIRO team).

4.4.3 LIF metrics

Several metrics were employed to enhance the analysis of LIF logs, the comparison of LIF response with T_n, the evaluation of the confining contact elevation, and the assessment of aquitard integrity through LIF logging.

Total LIF signal was presented in LIF logs as the sum of LIF response at every channel at specific depths. Total LIF signal does not fully capture the information included in multi-wavelength waveforms and therefore should be applied with caution.

LIF lifetime data was also employed as an indicator of LNAPL presence even when total LIF signal was low. In the case of petrol, even minimal LIF response may reflect LNAPL presence if the signal is blue-shifted (stronger in the 350-nm channel) and accompanied by significant lifetimes (ITRC, 2019). Profiles of LIF lifetime from the petrol station site are included in García-Rincón et al. (2020).

Peak LIF signal (or maximum LIF signal) was simply the maximum total LIF signal found in the log. Logs in the petrol station site exhibited great differences in terms of LIF signal maxima.

Cumulative LIF signal has been defined by Mulry and Lundy (2013) as the sum of all the total LIF signal records within one log. They used this metric to reduce the influence of spikes and peak LIF signals in the comparison with T_n.

Integral LIF signal was computed as the integration through Riemann sums of total LIF signals across the log. Thus, every log was divided in rectangles considering the midpoints between LIF measurements and the value of total LIF signal in each interval. This metric had units of %RE·m and was used in the comparison between LIF response and T_n as an alternative to the cumulative LIF signal proposed by Mulry and Lundy (2013).

Integral LIF signals y_C were calculated as indicated in equation 4.8.

$$y_C = \sum_{i=1}^{n_L} \frac{z_{i+1} - z_{i-1}}{2} y_i \qquad (4.8)$$

n_L is the number of records in the interval presumably impacted by LNAPL, y is the total LIF signal, z is the elevation and i is a subindex indicating the record number.

Finally, relative LIF signal was defined as the ratio of LIF response at each wavelength channel to the total LIF signal at specific depths. Relative LIF signals were employed along LIF lifetime data for the identification of intervals with less-mobile LNAPL and to evaluate the location and integrity of the overlain aquitard. The presentation of total LIF signals adopting a logarithmic scale in the x-axis (total LIF signal) was also a valid tool for these purposes.

4.4.4 Subtraction of natural fluorescence of the geological medium

Improper characterisation of the natural fluorescence of the geological medium may cause misleading interpretations of LIF results. This natural fluorescence was one of the

most contrasting characteristics between the LIF logs in the petrol station site and the industrial site.

LIF profiles at the petrol station site commonly reflected weak natural fluorescence of the geological medium (less than 3 %RE), while the industrial site showed a medium-strong response (from 3 to more than 10 %RE) with maxima around 18 %RE. The presence of calcareous sands in the later was likely the main reason behind this disparity. The medium-strong signal magnitude was consistent with ranges presented in the literature for calcareous sands (Lu et al., 2014). Natural fluorescence in intervals presumably not impacted by LNAPL in both sites was generally characterised by a predominance of response in the 450 nm channel, followed by the 400 nm, 500 nm, and 350 nm channels.

Filtering procedures were evaluated and applied to each LIF profile when the natural fluorescence of the geological medium was strong. Dakota Technologies employs a non-negative least squares fitting process to discriminate between different sources of fluorescence (St. Germain, 2014).

A simplified method was adopted in this research. First, any negative values provided by the LIF probe were replaced by zeros, although this issue was uncommon. Duplicates were also removed when needed. Then, intervals presumably not impacted by LNAPL were identified according to professional judgement, LIF lifetime data, relative LIF signals at every wavelength channel (ratio of LIF signal at a specific wavelength channel to total LIF signal), and inspection of LIF logs using a logarithmic scale to represent the total LIF signal in the x-axis.

Intervals presumably not impacted by LNAPL were used to estimate the natural fluorescence of the geological medium in the four LIF channels in every location of interest, since the background %RE value is expected to be variable in space like other properties in geochemical surveys (Reimann and Garrett, 2005). The top of the profile (0.5 m at the petrol station site and 1.2 m at the industrial site) was also discarded for the estimation of this natural fluorescence because of frequent anomalous signals, most likely due to anthropogenic influence not representative of subsurface conditions in the interval presumably impacted by LNAPL (hereafter the ‘LNAPL filtering interval’).

In general, %RE values corresponding to natural fluorescence of the medium were calculated by linearly interpolating the averages of values overlying and underlying the LNAPL filtering interval (hereafter the 'shallow' and 'deep filtering intervals', respectively) according to equation 4.9.

$$y_B = \frac{\bar{y}_S(z_D - z) + \bar{y}_D(z - z_S)}{z_D - z_S} \tag{4.9}$$

where y_B is the estimated %RE value corresponding to natural fluorescence in each wavelength channel at elevation z, $\bar{y}_S$ and $\bar{y}_D$ are the average %RE of the shallow and deep filtering intervals, and z_S and z_D are the elevations just above and below the LNAPL filtering interval. The contribution of $\bar{y}_S$ and $\bar{y}_D$ to the resulting y_B value was weighted according to their distance to z. Instead of averages, upper tolerance limits (Singh and Maichle, 2015) or other threshold values (Matschullat et al., 2000; Reimann et al., 2005, 2008) could be used to determine the natural fluorescence of the geological medium.

The resulting y_B values were subtracted from each LIF channel to quantitatively determine the response in the four wavelength channels as well as total and integral LIF signals. Any negative values were replaced with zeros.

Results from the filtering procedure are illustrated in Fig. 4.17 with examples from the petrol station site (LIF43-A) and the industrial site (LIF59-D5). LIF43-A was a profile with a high peak LIF signal and weak natural fluorescence. On the contrary, LIF59-D5 exhibited relatively stable total LIF signal across the profile, although the multi-wavelength waveforms revealed the existence of LNAPL. In general, the subtraction of natural fluorescence was negligible in logs from the petrol station site. In the case of LIF43-A, the filtering process resulted in subtraction of 0.28–0.45 %RE across the LNAPL filtering interval. Accordingly, these logs were not filtered. Only intervals impacted with LNAPL were selected to compute integral LIF signals.

These formulas were simple to use but did not consider aspects like the spatial variability of the natural fluorescence (by assuming linearity), the potentially different number of records in the shallow and deep filtering intervals, nor lifetime data. The use of non-negative least squares or other improved methods accounting for lifetime data is therefore encouraged. An example of the application of non-negative least squares can

be found in García-Rincón et al. (2020), where this method was applied to the log exhibiting stronger background fluorescence in the petrol station site (LIF65).

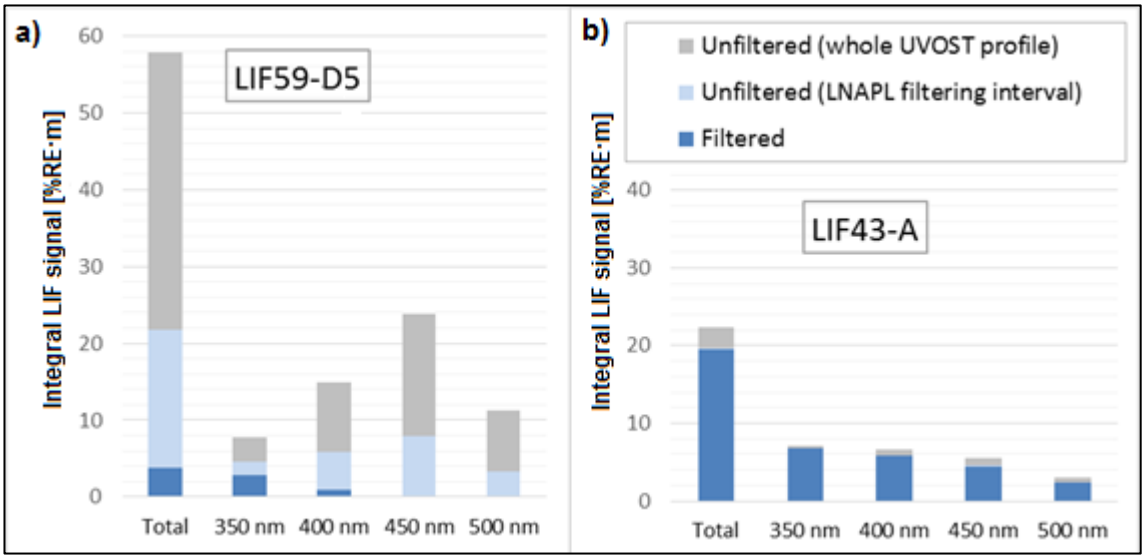


Fig. 4.17. Integral LIF response before and after filtering at (a) LIF59-5D and (b) LIF43-A.

4.4.5 LIF data interpolation

Comparison between LIF logs through butterfly plots was done considering the same elevation intervals. The LIF signal records were interpolated following a regular spacing of 0.01 m to combine multiple LIF profiles in section 6.4. Fig. 4.18 depicts a comparison of original LIF measurements with three interpolation methods: linear interpolation, exact cubic/Hermite spline interpolation (Forsythe et al., 1977), and monotone (if data were also monotonic) Hermite spline interpolation (Fritsch and Carlson, 1980). All the methods exhibited good agreement in intervals corresponding to natural fluorescence of the geological medium or less-mobile LNAPL. Linear interpolation attenuated the maximum peaks, while interpolating with splines generally introduced higher values than the original ones, particularly in the case of exact cubic splines.

Linear interpolation was preferred over spline interpolation to avoid negative values that would not make physical sense in this context. For instance, spline interpolation yielded some negative values at LIF51-B because of an anomalously low value of 0.584 %RE at 5.263 m bgl as shown in Fig. 4.19.

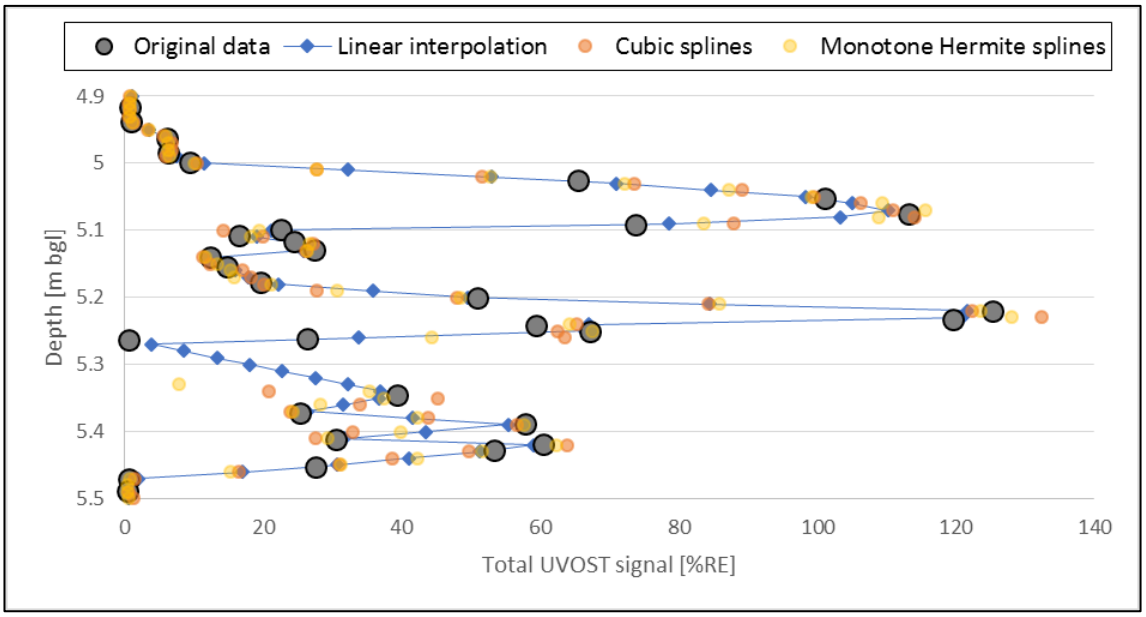


Fig. 4.18. LIF signal interpolation every 0.01 m at LIF51-B (negative values excluded).

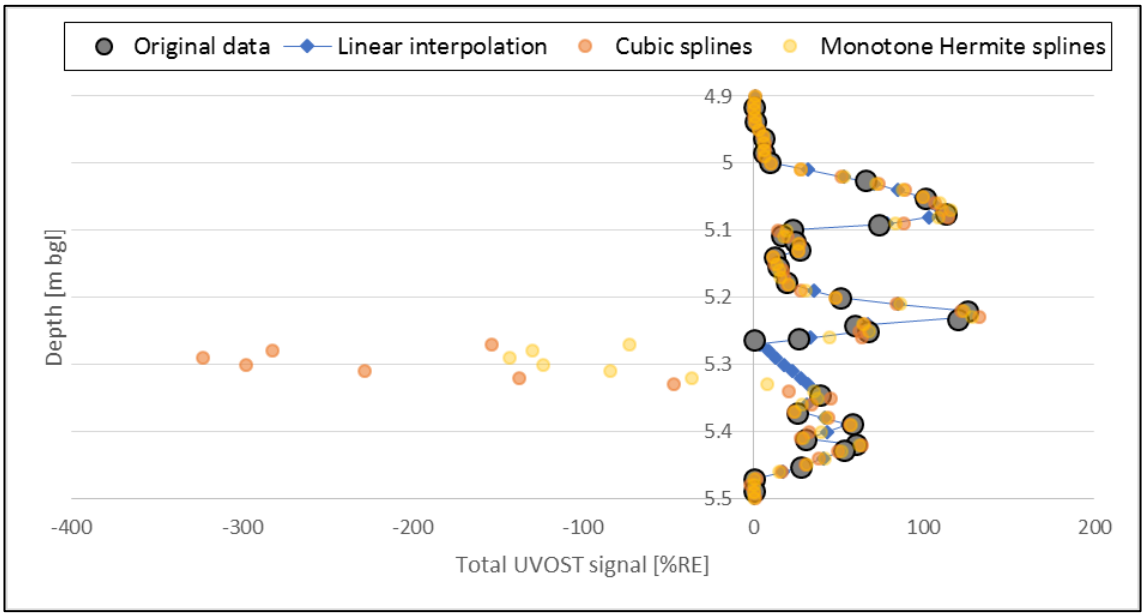


Fig. 4.19. Negative values resulting from cubic spline interpolation at LIF51-B.

4.5 Hydraulic Profiling Tool (HPT)

4.5.1 HPT technology

4.5.1.1 Overview of HPT systems

HPT by Geoprobe® is a high-resolution vertical profiling tool used for hydrostratigraphic characterisation and commonly deployed into the subsurface through direct-push platforms. HPT is the commercially available combination of a continuous DPIL system with an EC Wenner array. As the HPT probe advances into the subsurface, water is

injected at a monitored and ideally constant flow rate (HPT Q) through a screen port in the probe (Geoprobe, 2015). Then, the pressure resulting from injecting water at this rate into the medium (HPT P) is logged with an in-line sensor.

HPT contributes to the development of the CSM in two fundamental ways:

1. it permits a rapid and high-resolution vertical delineation of hydrostratigraphic features;
2. the ratio between HPT Q and HPT P (Q/P) can be used as a proxy of k_{sw} under certain conditions (Liu et al., 2019).

The continuous logging operation of HPT make it more rapid than discontinuous DPIL (Dietrich et al., 2008). A positive displacement pump is used to inject water into the subsurface, while an up-hole flow controller is employed to adjust HPT Q between 50 to 500 mL/min (Geoprobe, 2015). The system includes a reservoir where water can return if the formation resistance to water injection is too large.

4.5.1.2 Interpretation of HPT logs

High values of Q/P (or low HPT P if HPT Q is stable) suggest the presence of coarse-grained materials, while low values are assigned to fine-grained materials. Similarly, high EC values are generally a sign of fine-grained materials, in particular clay-rich sediments (Schulmeister et al., 2003) which commonly exhibit EC responses over 50 mS/m (McCall, 2011). Therefore, Q/P and EC profiles usually exhibit opposite trends.

Nevertheless, there are exceptions to this rule. For instance, clays such as kaolinite have a lower cation-exchange capacity than smectite and montmorillonite and may be more difficult to detect through EC logging (ITRC, 2019). Similarly, fine sands, silts, and cemented materials may significantly increase Q/P but not alter EC (McCall, 2011), while salt intrusion would affect EC but practically not Q/P. The transition between the saturated and unsaturated zones may also induce a step increase in EC, especially in coarse-grained materials as consequence of the abrupt change in S_w (Schulmeister et al., 2003).

LNAPL presence could also affect Q/P and EC profiles because of the impacts on the relative permeability of water as well as on the EC response of the pore fluid and the

medium. The EC sensor installed in the HPT system may be relatively insensitive to the particle-size fractions controlling k_{sw} (Schulmeister et al., 2003) and therefore k_{sw} quantification is commonly done according to Q/P measurements only.

4.5.1.3 HPT pressure and required corrections

HPT P is the sum of injection-induced pressure (at current and previous depths), atmospheric pressure, hydrostatic pressure and advancement pressure (Liu et al., 2019), including linear and non-linear losses associated to the formation and the HPT system (Liu et al., 2012). As depicted in Fig. 4.20, low- and high-permeability layers not intersecting the screen may still work as barriers or preferential flow pathways for the injected water, but numerical simulations have not found them to significantly alter Q/P readings in the interval of interest (Liu et al., 2019).

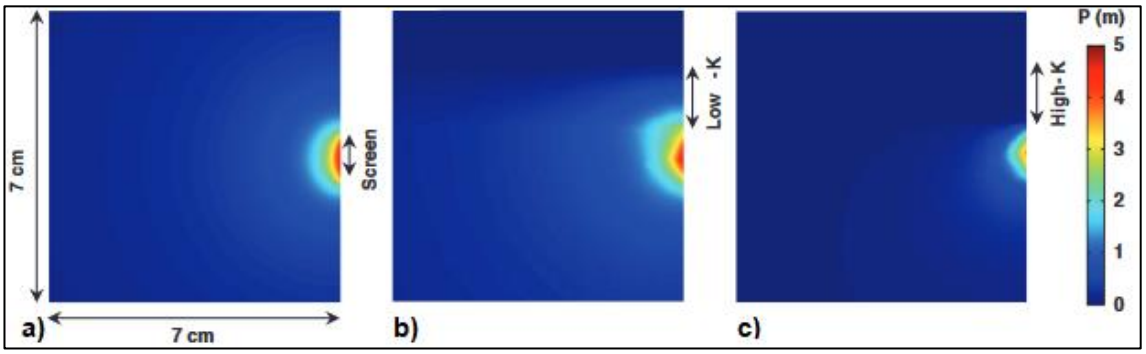


Fig. 4.20. Effects of heterogeneities on discontinuous DPIL pressure readings. Numerical simulations considered: (a) the base-case scenario, (b) the presence of a low-permeability layer near the screen, and (c) the presence of a high-permeability layer near the screen (adapted from Liu et al., 2019).

Corrections for hydrostatic pressure (variable below z_{aw}) and atmospheric pressure (relatively constant) are commonly applied in the prediction of k_{sw}. An HPT reference test and an EC load test must be performed in the surface prior logging to calibrate the instruments and quantify the atmospheric pressure (Geoprobe, 2015).

Due to the continuous operation of HPT, it is necessary to stop the probe advancement right before logging the interval of interest and perform a dissipation test. As depicted in Fig. 4.21, these tests simply consist in ceasing the water injection and wait for the pressure dissipation. Thus, it is possible to subtract the hydrostatic pressure existing below z_{aw} and also reduce the pressure induced by injection at higher elevations and the

system advancement. Dissipation takes more time in fine-grained materials and an incomplete dissipation test may invalidate the estimation of hydrostatic pressures and the correction procedure. The slope of the estimated absolute static pressures should approach a value of 9.81 kPa per meter of column of water in unconfined aquifers assuming ρ_w as 1 g/cm^3 and gravity acceleration equal to 9.81 m/s^2. Non-linear effects may be due to vertical flow gradients (McCall, 2011).

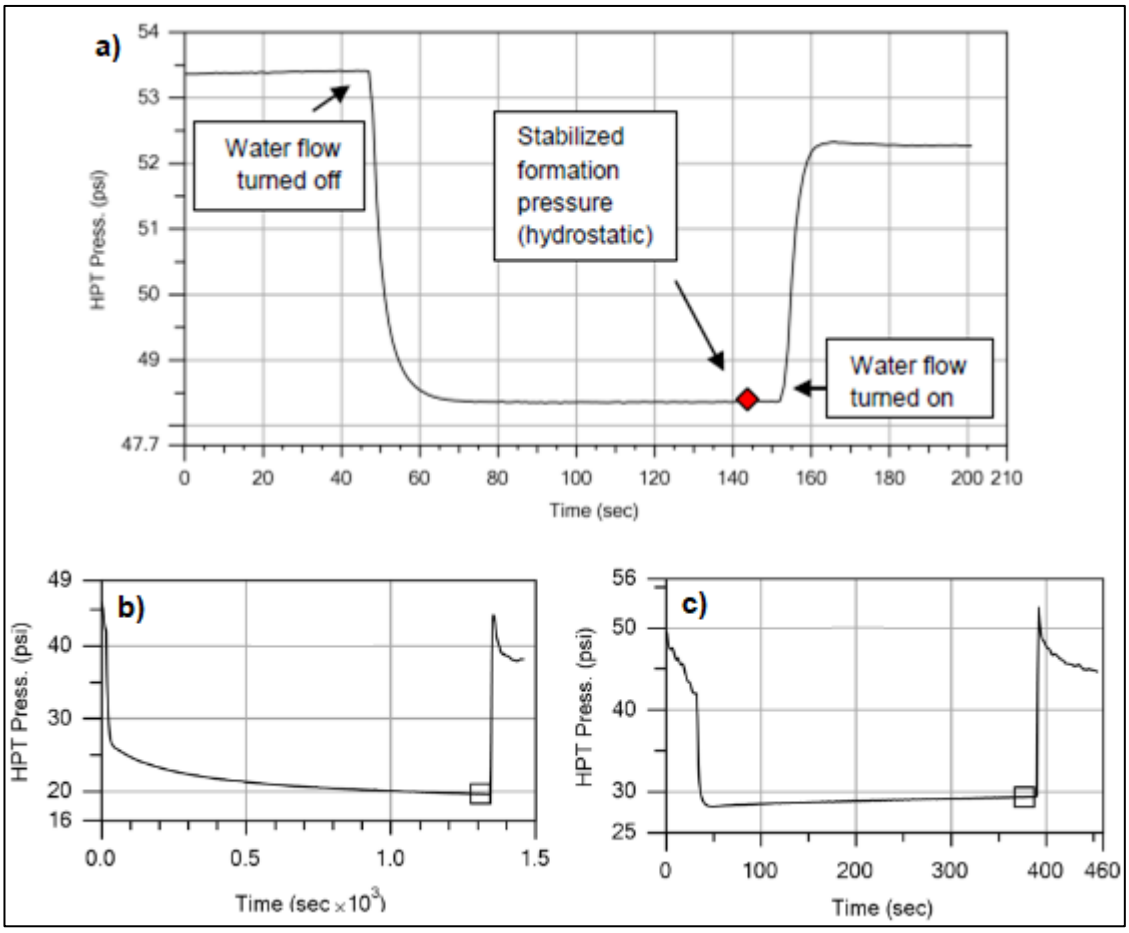


Fig. 4.21. Examples of dissipation tests where (a) full dissipation was reached, (b) excess pressure was still dissipating and completing the test could require more than 30 min, and (c) excess pressure was still rising after the water flow was turned off, completing such a test could take several hours (modified after McCall, 2010, 2011).

In addition, it is possible to neglect HPT line and screen losses in the analysis if they are relatively constant, which can be achieved through the application of a stable HPT Q (Liu et al., 2019). HPT pressure transducers are commonly installed in the probe itself, so frictional head losses within the rod may be ignored (Maliva, 2016). In sandy materials, HPT advancement speeds around 2 cm/s are acceptable, not greatly increasing the

advancement pressure term. In fine-grained materials, HPT speed should be as low as possible (Liu et al., 2019).

Furthermore, direct-push methods reliability may be adversely affected by screen clogging and compaction generated by the system (Dietrich et al., 2008; Paradis et al., 2011; Liu et al., 2012, 2019). Using small diameters in the HPT tubing reduces the compaction but causes frictional losses and impose an upper limit of quantification of k_{sw}, while larger diameters may generate significant non-linear flow losses (Bohling et al., 2011). The upper limit of k_{sw} quantification has been suggested to be around 25 m/day.

4.5.1.4 HPT quantification of hydraulic conductivity

Moreover, there is also a lower limit of k_{sw} quantification produced by the maximum pressure that can be recorded with the sensor (being the maximum reported 689.48 kPa) as well as the maximum pressure that does not alter the formation condition. This lower limit of k_{sw} quantification has been suggested to be around 0.03 m/day but could be decreased through the installation of low-flow pumps or other modifications to the method (Liu et al., 2017). Numerical simulation has suggested that k_{sw} may be quantified when its value is higher than 0.09 m/day, while lower k_{sw} values may require additional information on the specific storage of the formation (Liu et al., 2019).

Geoprobe® has proposed a formula to derive k_{sw} values from Q/P readings (McCall, 2010). This formula corresponds to a model fitting Q/P records to measurements from slug tests in five sites from the United States. It can be seen in Fig. 4.22. that very subtle changes in Q/P may correspond to a wide k_{sw} range, while k_{sw} values within a narrow range correspond to more than one order-of-magnitude differences in measurements of Q/P. One objective of chapter 6 is to evaluate the applicability of this quantification model.

Applying site-specific calibrations is recommended to improve the confidence on k_{sw} estimations (Geoprobe, 2015). It is important to note that Q/P measurements depend on the HPT Q applied (Dietrich et al., 2008). Therefore, Q/P values need to get calibrated

with other methods as exemplified in Fig. 4.23. Nevertheless, evaluation of calibration procedures was out of scope of this research.

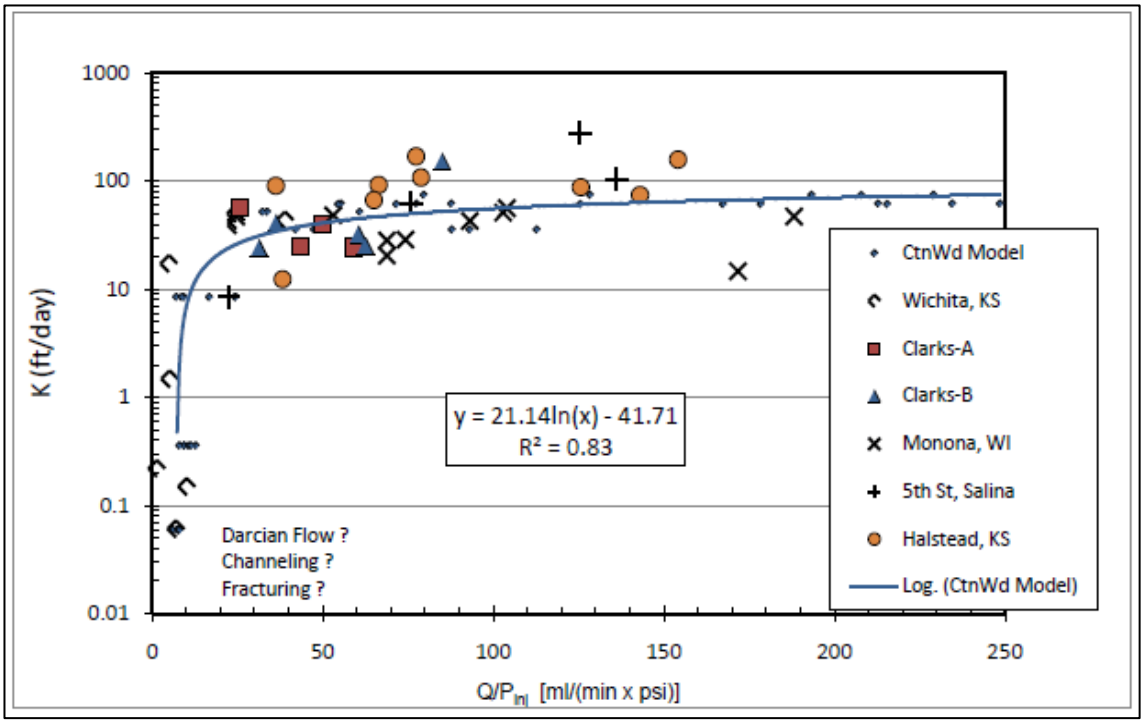


Fig. 4.22. Model to quantify k_{sw} proposed by Geoprobe® after calibration with slug test data in multiple field sites (McCall, 2010).

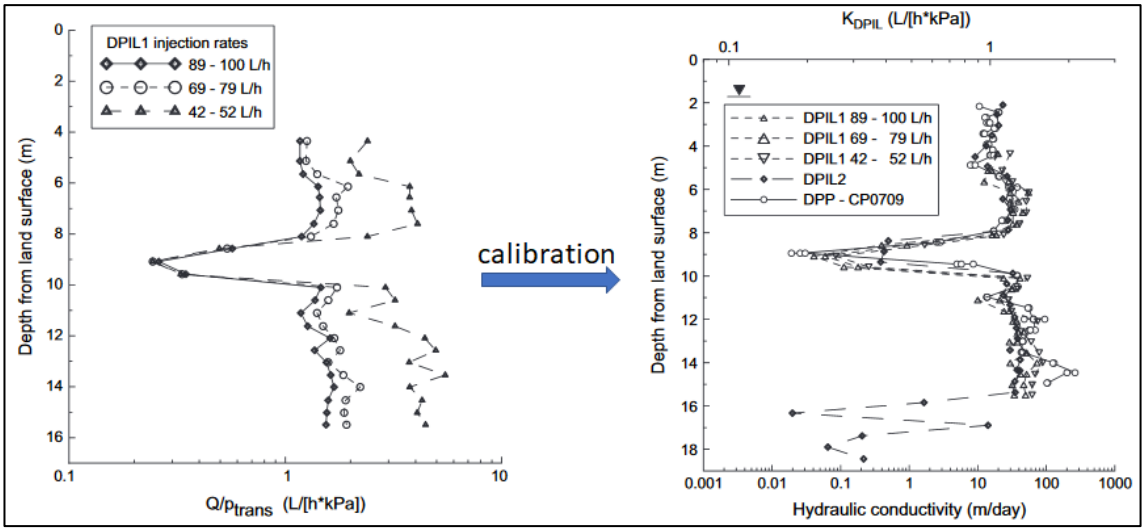


Fig. 4.23. Example of effects of flow injection rate on the Q/P ratio and calibration with DPP measurements (modified after Dietrich et al., 2008).

4.5.2 HPT data collection

Details about the HRSC profiling campaign in the petrol station site have already been presented in section 4.4.2. The collected HPT logs are included in Appendix D: HPT

profiles. As in the case of LIF logging, it was possible to monitor HPT measurements in real time as depicted in Fig. 4.24.



Fig. 4.24. Real-time monitoring of HPT measurements.

A total of 10 HPT profiles were collected at the petrol station site with a k6050 HPT system (diameter of 1.5”): one in area A, one in area B, five in area C (three adjacent to PB40-C), one in the UST area and the other two between these areas (one between areas A and B and one between the UST and area A). HPT Q was generally stable around 450 mL/min and HPT locations were logged in less than two hours each at velocities around 2 cm/s.

EC load tests and HPT reference tests were conducted before and after logging each location, positively passing all the tests. The HPT reference test consisted of comparing the obtained stabilised values of pressure during and after the injection of water (at the desired HPT Q) in the HPT reference tube shown in Fig. 4.25 (the valve should remain closed during the test). The test is successful if the difference between both values is close to 1.50 kPa as inferred from the reference tube dimensions. Atmospheric pressure

was estimated subtracting 2.985 kPa from the average of measurements obtained in pre- and post-logging reference tests.

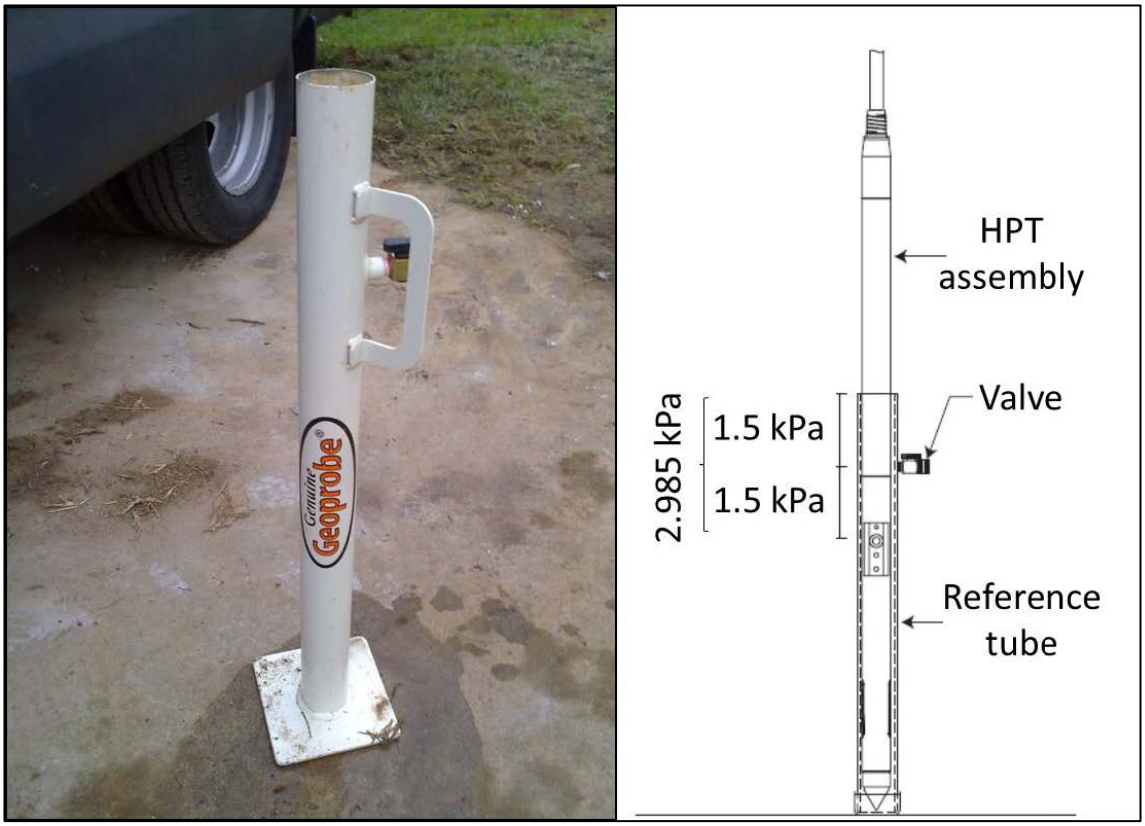


Fig. 4.25. HPT reference tube.

4.5.3 Dissipation tests

Table 4.4 summarises details of dissipation tests performed in logs HPT59-C, HPT64 (adjacent to the UST location), HPT72, HPT73-A, HPT74-B, and HPT75. In some occasions, dissipation tests were conducted at multiple depths to improve the application of the method. It was corroborated that hydrostatic pressure values followed a straight line and yielded reasonable z_{aw} values except for two tests. The subsequent correction for atmospheric and hydrostatic pressure as well as the graphical representation of some logs was done with the Direct Image® Viewer software (version 3.3, build 19067) by Geoprobe®.

In HPT73-A and HPT75, the first dissipation tests (conducted at 5.7 m bgl) were discarded due to an incomplete pressure dissipation which was inconsistent with z_{aw} values measured in nearby wells and yielded negative pressures in the aquifer in the case of HPT75.

Table 4.4. Details of HPT dissipation tests.

HPT ID	Depth [m]	Time [s]	Pressure [kPa]
HPT59-C	6.233	129	115.53
HPT64	7.026	134	122.68
HPT72	6.736	115	120.69
HPT72	6.965	95	122.93
HPT72	7.254	70	125.48
HPT73-A	6.949	132	122.52
HPT74-B	5.822	74	112.50
HPT74-B	6.218	100	116.25
HPT75	6.142	100	113.97
HPT75	6.782	75	118.53

For qualitative comparison of Q/P logs without dissipation tests, the atmospheric pressure was still subtracted using information from the reference tests. For estimation of k_{sw} in HPT sites without dissipation tests, z_{aw} values from adjacent wells were used to calculate and correct the hydrostatic pressure term. This methodology induced some errors derived from the assumption of a z_{aw} value (generally 56.15–56.16 m AHD) and a constant vertical hydrostatic gradient of 9.81 kPa per meter of column of water.

Therefore, this approach was also applied to the HPT logs with dissipation tests to investigate the magnitude of these errors. An average error of -0.075 % (median of 0.008 %) was found comparing the corrected pressure calculated using z_{aw} with the corrected pressure calculated using results from dissipation tests. The 99th percentile and maximum errors were 2.1 % and 6.8 %, respectively. These values were considered reasonable and therefore k_{sw} was estimated for all the HPT logs.

Regarding the industrial site, eight HPT profiles were collected, in general one per area. The field procedures were analogous as those applied in the petrol station site. The first dissipation test at HPT20-T3 was ignored. The test log followed an anomalous pattern and demonstrated that the dissipation test was not adequately completed. In addition, it produced an estimation of static water levels that was not consistent with field measurements. Furthermore, incorporating the second dissipation test resulted in an unrealistic slope of the absolute static pressures, clearly distinct from the value of 9.81 kPa per meter of column of water as expected for unconfined aquifers. Moreover, using both dissipation tests introduced inflections that would have reflected

hydraulically disconnected aquifer units and therefore only the second dissipation test was employed. This second dissipation test, even if not totally stable, facilitated the estimation of a static water level coherent with field measurements. The first dissipation test at HPT32 from the industrial site with a steady increase in pressure was also ignored.

4.5.4 Interpolation of HPT logs

In some cases, multiple HPT profiles could be considered representative of subsurface conditions at the same location (for instance, three HPT profiles were collected within a 3.1 m radius from PB40-C). The analysis and discussion of results considered the variability and distinct features of every log. For clarity purposes, part of the discussion referred to interpolated values at the location of interest (for instance, PB40-C).

Spatial interpolation of HPT profiles was done through inverse distance weighting IDW (Shepard, 1968), which is one of the most commonly applied techniques for spatial interpolation because of its robustness and simplicity despite not providing as much information as other approaches such as kriging variants (Babak and Deutsch, 2009). Counting on only a few HPT profiles (three in the case of PB40-C) discouraged the use of stochastic approaches.

The distance weighting parameter (commonly a constant power function) is one of the key elements in the IDW method and its choice may strongly influence the results (Lu and Wong, 2008). Thus, constant power values of 1, 2, and 4 were applied to investigate its effects in the interpolation of neighbouring HPT logs. As depicted in Fig. 4.26, the power value (especially when comparing values of 1 and 2) did not greatly affect most of the intervals of concern (above 55.5 m AHD) considering HPT profiles in the vicinity of PB40-C. Considering the location and characteristics of the HPT logs, a power value of 1 was chosen trying to impede that the nearest values would have an overwhelming influence on the estimated values (Lu and Wong, 2008). Further information about spatial interpolation techniques can be found in the literature (Li and Heap, 2014).

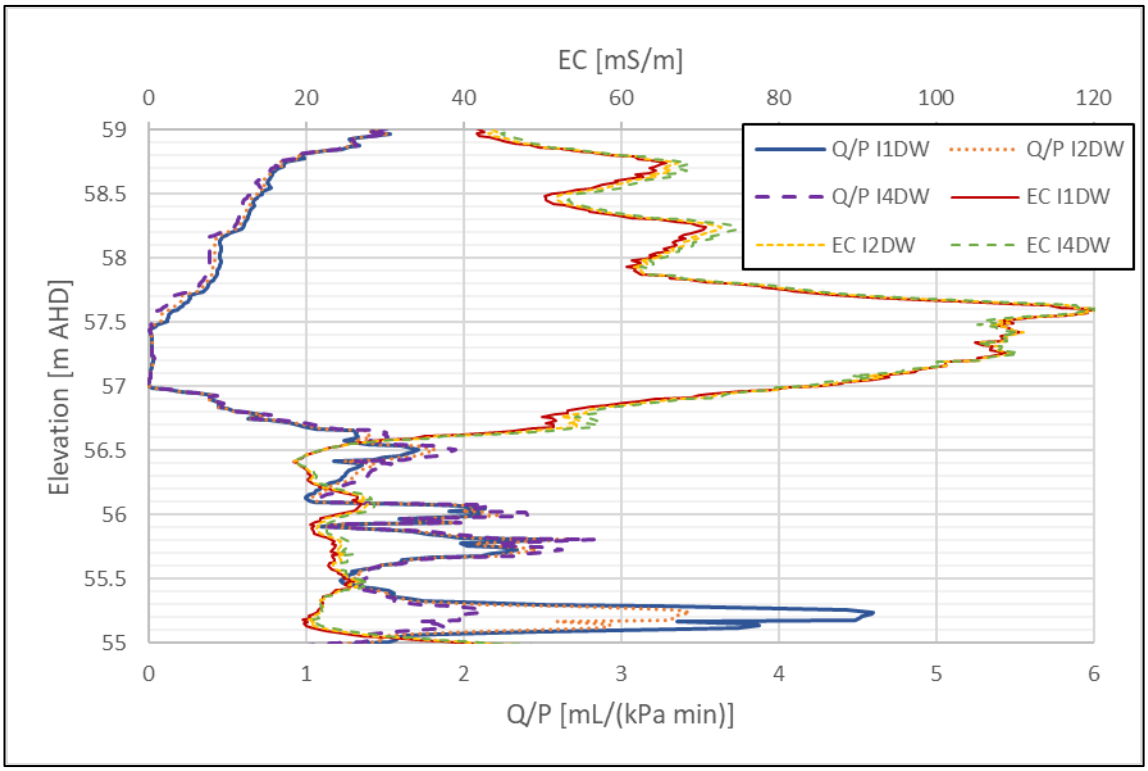


Fig. 4.26. Comparison of Q/P (only corrected for atmospheric pressure) and EC logs adjacent to PB40-C interpolated through IDW using constant power factors of 1 (I1DW), 2 (I2DW), and 4 (I4DW).

4.5.5 Determination of aquifer heterogeneity

Another issue related to the variability of subsurface conditions is to determine how heterogeneous a heterogeneous aquifer is. For this purpose, some authors have used the variability of k_{sw} estimates from direct-push methods, in particular the variance of the natural logarithm of k_{sw}—the logconductivity variance—as a measure of aquifer heterogeneity (Bianchi et al., 2011; Bohling et al., 2012; Dogan et al., 2014).

Following this criterium, sites with logconductivity variance below one has been considered at most mildly heterogeneous (Gómez-Hernández et al., 2017), including research sites such as Borden and Cape Cod with variances of 0.29 and 0.26, respectively (Bohling et al., 2012). On the contrary, the logconductivity variance of highly heterogeneous sites has been generally reported to be higher than one or two, being the MADE site a well-documented case of highly heterogeneous aquifer (Zheng et al., 2011; Gómez-Hernández et al., 2017) with a variance of 5.9±1.5 (Bohling et al., 2016).

It has also been questioned if aquifer heterogeneity should be defined according to the heterogeneity within a hydrofacies or the heterogeneity across multiple hydrofacies (Gómez-Hernández et al., 2017), since the variance of different units may vary reflecting heteroscedasticity. Consequently, chapter 7 explored the intra- and inter-variability of k_{sw} within layers found in LNAPL contaminated aquifers. The following k_{sw} strata were considered: LNAPL-impacted interval, aquifer materials excluding and including fine-grained lenses, and the entire aquifer-aquitard system.

4.6 Hydraulic testing

4.6.1 Overview of hydraulic tests conducted in the petrol station site

Both groundwater and LNAPL can be found under different hydrogeologic conditions (confined, unconfined, leaky confined, perched) in several geological settings. Aquifers may be confined by overlying less-permeable units such as aquitards, resulting in a groundwater pressure greater than atmospheric pressure (Custodio and Llamas, 1983). Leaky confined (semiconfined) aquifers are more common than idealised fully confined aquifers (Todd and Mays, 2005; Parker et al., 2004; Hawthorne et al., 2011). In multifluid systems, the non-wetting liquid becomes confined because of large entry pressures in the overlying unit (Illangasekare et al., 1995; Mayer and Hassanizadeh, 2005; Hawthorne et al., 2011). Although the definition of confinement in the two systems differ, both k_{sw} and entry pressure are related to the pore-size distribution of the subsurface materials.

Numerous hydraulic tests were conducted in the petrol station site to study the aquifer and/or LNAPL hydrogeologic conditions. Baildown tests, manual skimming tests, and LNAPL mass recovery trials aimed to evaluate LNAPL hydrogeologic conditions and/or T_n. LNAPL recovery techniques included skimming recovery, vacuum-enhanced recovery, water-enhanced recovery (dual pump inducing Z_{aw} drawdown), and water- and vacuum-enhanced recovery. Further details about the LNAPL mass recovery trials can be found in Gatsios (2018) and Gatsios et al. (2018b). In this particular site, baildown testing was considered more reliable than manual skimming even in wells exhibiting low b_n values, likely due to the equipment used and the subsurface characteristics (Gatsios, 2018).

On the other hand, monitoring data from water-enhanced recovery were also used for the analysis of aquifer characteristics, as well as in-well fluid levels during constant-rate pumping testing, which simply consists of pumping water at a relatively constant rate while drawdown measurements are recorded in the tested well and any observation wells during the drawdown (pumping) phase and the recovery phase (after pumping).

As described in section 2.2.4.1, aquifer testing analysis generates effective parameters representing relatively large aquifer volumes, while other methods to estimate k_{sw} were local and corresponded to different support scales (intrinsic volumes of measurement). Therefore, discrepancies between the results of various methods were expected (Neuman, 1994; Neuman and di Federico, 2003; Butler, 2005).

In addition, methods deriving k_{sw} from particle-size data are not affected by bioclogging nor LNAPL contamination. On the contrary, aquifer testing (as well as HPT) predictions could have been negatively influenced by the presence of LNAPL in the subsurface due to the associated decrease in k_{rw}. Potential effects derived from the presence of LNAPL in the subsurface were assessed by comparing estimates from aquifer testing and HPT logging to k_{sw} estimates obtained through the analysis of particle-size data.

4.6.2 Aquifer testing

4.6.2.1 Details of the field procedure

A total of 12 aquifer tests using a drawdown pump (five tests) or a total fluids pump (seven tests) took place in the petrol station site as detailed in Bekele et al. (2019). For clarity purposes, relevant aspects of seven tests conducted under high, intermediate, and low z_{aw} conditions were employed. In general, these seven tests were associated to a relatively high frequency of measurements, number of observation wells, and maximum water drawdown reached. Therefore, they represented some of the most reliable tests.

Details from the presented aquifer tests is summarised in Table 4.5. Fig. 4.27 illustrates z_{aw} values corresponding to the beginning of the aquifer tests relative to the transition range (56.7–56.8 m AHD) between unconfined and confined LNAPL conditions according to Gatsios et al. (2018b).

Table 4.5. Main characteristics of representative aquifer tests conducted in the petrol station site.

ID	Pumping well	Start date	Initial z_{aw} [m AHD]	Maximum drawdown [m]	Initial b_n [m]	Test duration [h]
WT1	PB13-C	04/09/2014	59.58	2.03	2.420	2.5
WT2	PB13-C	07/10/2014	58.75	2.35	0.339	3.4
WT15	PB39-C	11/11/2015	56.72	1.55	0.590	5.7
WT27	PB40-C	23/06/2016	56.50	0.21	0.077	25.1
WT28	PB29-A	23/06/2016	56.50	0.28	0.091	20.0
WT29	PB29-A	28/06/2016	56.53	0.42	0.085	22.1
WT30	PB40-C	28/06/2016	56.52	1.21	0.025	54.0

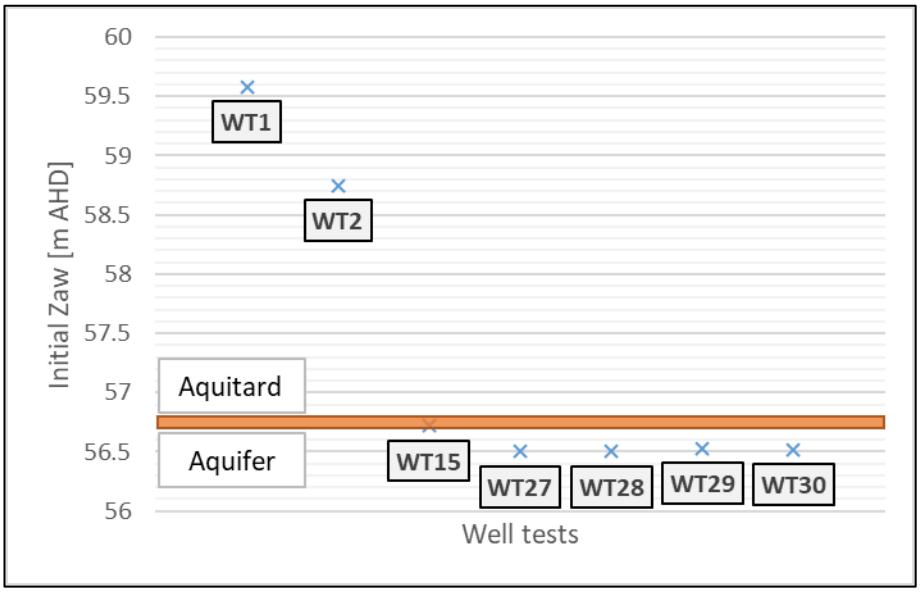


Fig. 4.27. Initial z_{aw} values of aquifer tests. The orange rectangle represents the transition range between unconfined and confined LNAPL conditions according to Gatsios et al. (2018b).

More specifically:

- WT28 and WT29 were conducted at PB29-A and tested conditions surrounding areas A and B. The other tests corresponded to area C;
- WT1, WT2, and WT15 were constant-rate pumping tests, while the others corresponded to periods of water-enhanced recovery;
- WT1 and WT15 were performed with a total fluids pump (extracting water and LNAPL simultaneously), while the others employed a drawdown pump (extracting groundwater only).

Despite the different definitions of aquifer and LNAPL confinement, it was expected that WT1 and WT2 suggested a confined aquifer while WT27, WT28, WT29, and WT30 likely represented an unconfined aquifer. WT15 was an intermediate case.

4.6.2.2 Interpretation of aquifer test data

Aquifer testing is conducted to evaluate T_w and values of storage and leakage parameters as well as other aspects such as confinement conditions, borehole effects, subsurface heterogeneity, and existence of flow boundaries. These characteristics were analysed through type-curve matching of log-log and log-linear plots of time versus drawdown and the application of the specialised software AQTESOLV (Bekele et al., 2019). Fig. 4.28 depicts typical log-log and log-linear of confined, unconfined, and leaky confined aquifers.

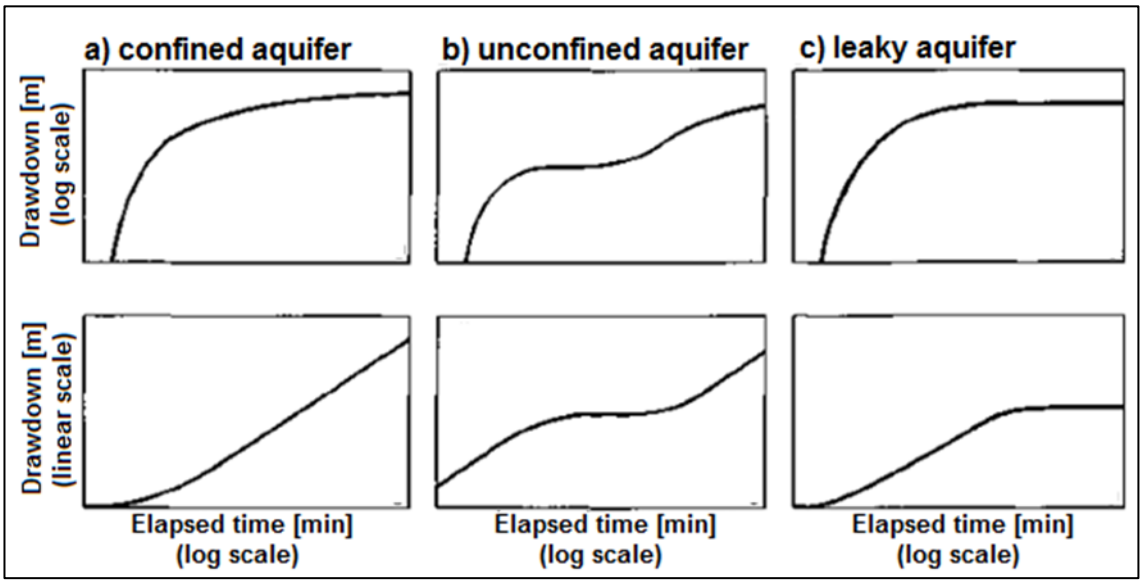


Fig. 4.28. Typical log-log (top) and log-linear plots (bottom) of (a) confined, (b) unconfined, and (c) leaky confined aquifers (modified after Kruseman and de Ridder, 2000).

Furthermore, Fig. 4.29 shows how log-log and log-linear plots may reflect multiple boundary conditions and borehole effects in a confined aquifer. In the petrol station site, the screened interval typically started at the overlying aquitard and did not fully penetrate the aquifer in some cases. This design was justified because the primary goal of the wells was to monitor LNAPL occurrence in the subsurface and enable LNAPL mass recovery operations.

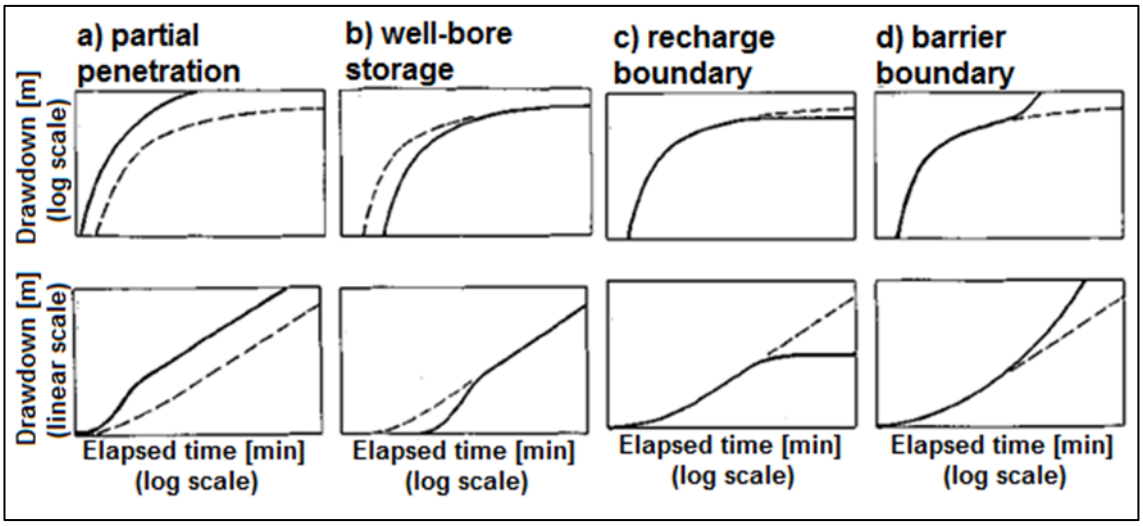


Fig. 4.29. Typical log-log and log-linear plots showing the effects of (a) partial-penetration wells, (b) wellbore storage, and (c) recharge and (d) barrier boundaries in a confined aquifer (modified after Kruseman and de Ridder, 2000).

More recent developments from the petroleum industry such as pressure derivative diagnostic plots and deconvolution techniques may also provide valuable information overlooked by conventional type-curve matching (Gringarten, 2008). Pressure derivative diagnostic plots depict drawdown and its logarithmic derivative versus time (Renard et al., 2009) and are being adopted as an informative tool in hydrogeological studies. However, they may be demanding in terms of the quality of monitoring data (Willmann et al., 2007), being drawdown derivatives frequently noisy (Ramos et al., 2017) as it was found in the case of the petrol station site. Thus, this methodology was not suitable for the analysis of aquifer tests.

The application of AQTESOLV allowed evaluation of the fit to observed data of multiple analytical and semianalytical solutions representing:

- unconfined aquifers (Moench; Tartakovsky–Neuman),
- leaky confined aquifers (Hantush),
- confined conditions in uniform (Cooper–Jacob; Theis–Hantush; Moench–Prickett) and non-uniform (Butler, 1998) aquifers.

The main assumptions of these solutions are presented in Table 4.6. Further details of the software application can be found in Bekele et al. (2019).

Table 4.6. Main assumptions of presented aquifer test solutions (modified after Bekele et al., 2019).

Aquifer test solution	Main assumptions	Reference
Moench	Unconfined aquifer with delayed gravity response; accounts for wellbore storage	Moench (1997)
Tartakovsky–Neuman	Unconfined aquifer allowing for non-instantaneous drainage; neglects wellbore storage	Tartakovsky and Neuman (2007)
Cooper-Jacob	Confined aquifer; neglects wellbore storage	Cooper and Jacob (1946)
Theis–Hantush	Confined aquifer; applicable to unconfined aquifers with a drawdown correction	Theis (1935); Hantush (1964)
Hantush	Leaky confined aquifer with aquitard storage; neglects wellbore storage	Hantush (1960)
Butler	Heterogeneous confined aquifer with a disk of distinct properties embedded in a matrix	Butler (1988)
Moench–Prickett	Confined aquifer undergoing conversion to water table conditions; neglects wellbore storage	Moench and Prickett (1972)

4.6.3 Baildown testing

4.6.3.1 Data collection and analytical solution

Baildown tests were conducted in a periodic basis for the characterisation of LNAPL mobility in terms of T_n. The tests were also used for the identification of LNAPL hydrogeologic conditions and hydrostratigraphic features as described in chapter 5. T_n values from a campaign in April 2016 were used to evaluate if LIF response could be linked to LNAPL mobility, which is a hypothesis tested in chapter 6. In addition, T_n was an output of the analytical models presented in chapter 8 and therefore its variability and alternative interpretations of baildown tests conducted during the HRSC campaign or closer dates were investigated in chapter 7. Additional details of the data collection and analysis procedures can be found in related works (Gatsios, 2018; Gatsios et al., 2018b), including a detailed study of the influence of water table fluctuations on T_n (Gatsios et al., 2018b). In this section, some of the most relevant aspects for the scope of the thesis are summarised and the application of new analyses is described.

Details of four baildown tests conducted during the HRSC campaign or close dates (considered to be representative of the modelling scenarios) are summarised in Table 4.7, including b_n values at the start of the tests and the estimations of T_n presented in

Gatsios (2018) and Gatsios et al. (2018b). Baildown tests were not conducted at PB40-C during the HRSC campaign and therefore measurements collected before and after the campaign (April and June 2016) were used for the assessment of T_n.

Table 4.7. Main details of the baildown tests representative of the modelling scenarios.

Bailed well	Date	Near-equilibrium b_n [m]	T_n value [m²/day] (Gatsios, 2018)
PB29-A	19/05/2016	0.324	1.510 (±0.093)
PB27-B	20/05/2016	0.320	0.572 (±0.011)
PB40-C	06/04/2016	0.740	0.577 (±0.025)
PB40-C	14/06/2016	0.528	0.304 (±0.008)

Baildown testing involved quick removal of in-well LNAPL using either bailers or a pump. The volume of recovered fluids (LNAPL and water) was measured and the recovery of fluid levels was monitored. When unconfined LNAPL conditions were found, baildown test data were analysed according to a modified Bouwer and Rice equation (Kirkman, 2013) as implemented in the API LNAPL Transmissivity Workbook (API, 2016) and presented in equation 4.10.

$$T_n = \frac{{r_e}^2 \, ln(R_{oi}/r_e) \, ln(s_{(0)}/s_{(t)})}{2(-J)t} \qquad (4.10)$$

where:

- R_{oi} = radius of influence for the LNAPL phase [L];
- r_e = effective well radius [L];
- $s_{(t)}$ = LNAPL drawdown at time t [L];
- J = ratio of change in LNAPL drawdown to change in b_n [-].

Therefore, the modified Bouwer and Rice equation implements a ratio (the 'J-ratio') relating b_n to LNAPL drawdown during the test instead of assuming a constant interface (theoretically z_{nw} when $T_n >> T_w$ or z_{aw} when $T_w >> T_n$). The J-ratio becomes lower than -1 if z_{nw} increases during the test and greater if it decreases (API, 2016). The J-ratio was calculated through linear regression and compared to visual estimates from Gatsios (2018).

In addition, r_e is the radius relating the change in LNAPL volume flux into the well dV_n and the increase in b_n. Thus, it depends on well design parameters (top of screen, casing radius, and borehole radius), the relative vertical position of LNAPL compared to the top of screen, and LNAPL specific yield of the filter pack (Lundy, 2005; API, 2016). Gatsios (2018) and Gatsios et al. (2018b) assumed a LNAPL specific yield of 0.175 as recommended in API (2016). However, due to the low η_n of approximately 0.48 cP characteristic of LNAPL from the petrol station site, the LNAPL specific yield could be as high as 0.231 according to the ASTM International (2013) equation 4. Consequently, the effects of modifying the LNAPL specific yield value were also explored.

Estimation errors within a factor of 2 have been considered reasonable (ASTM International, 2013), although errors exceeding one order of magnitude have been predicted for the prediction of T_w in water-saturated (not multifluid) systems, particularly in the presence of low-permeability skins (Hyder and Butler, 1995). Thus, the data collection and analysis procedures aimed to exclude discharge periods not representative of the formation T_n (API, 2016), maximise the induced LNAPL drawdown, and keep the removal time as short as possible as also recommended in the case of slug testing in water-saturated systems (McElwee et al., 1995).

In addition to these errors, variations in the system response have been reported in some groundwater (not multifluid) and LNAPL studies after applying different initial drawdowns (Hyder et al., 1993; Butler et al., 1996; Gatsios, 2018), most likely due to the mobilisation of fines or the presence of low-permeability skins and other heterogeneities (which could also be the cause of discrepancies between estimations of T_n through baildown testing and LNAPL recovery system evaluation observed by Gatsios et al., 2018b). Successive field experiments inducing different initial drawdowns were conducted in the petrol station site as described in Gatsios (2018).

4.6.3.2 Interpretation of discharge versus drawdown plots

The Bouwer and Rice solution is based on the Thiem equation and therefore assumes a linear relationship between LNAPL discharge and drawdown (due to continuity of LNAPL volume within the well). Discharge versus drawdown (DvD) plots were always inspected

to determine (i) cut-off times, (ii) drawdown adjustments, and (iii) hydrogeologic conditions and the potential existence of other hydrostratigraphic features.

Cut-off times were employed to exclude discharge data corresponding to period of discharge from highly permeable elements around the well such as the filter pack or the developed zone (Bouwer, 1989). Thus, borehole effects could be detected in DvD plots due to the distinct slope potentially associated to the initial test measurements corresponding to large discharge values as illustrated in Fig. 4.30.

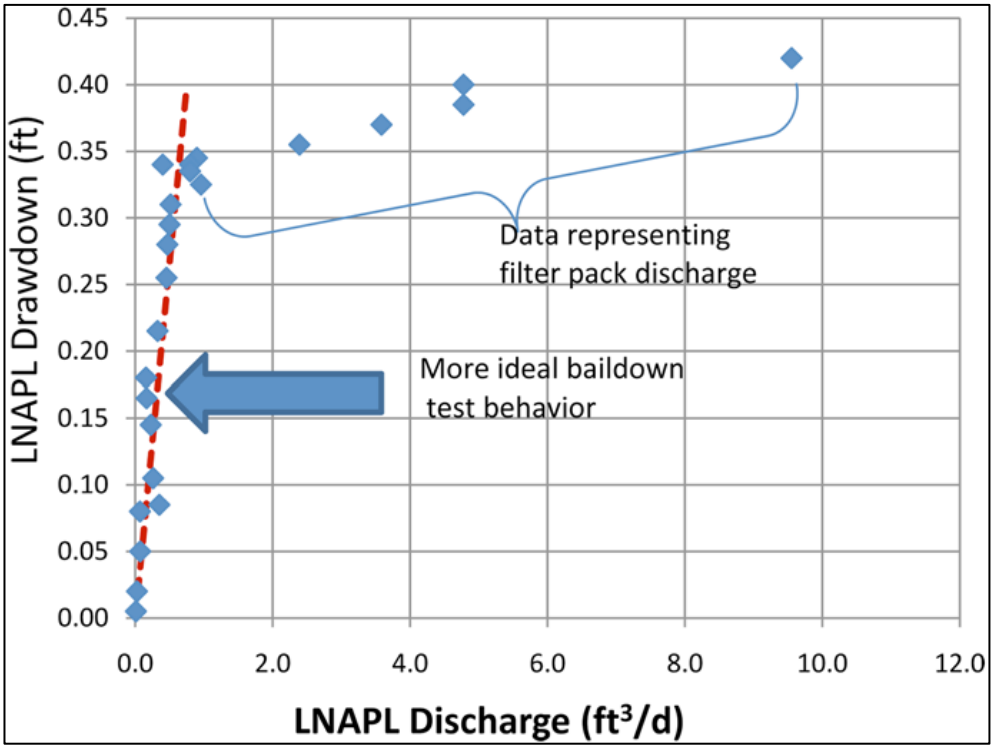


Fig. 4.30. Example of identification of filter pack discharge in DvD plots (ASTM International, 2013).

Nevertheless, the interpretation of baildown tests may not always be unique and depend on the understanding of the CSM. Therefore, it was justified to evaluate the effects of selecting different cut-off times in the estimation of T_n. For instance, Fig. 4.31 depicts the choices assumed in Gatsios (2018) for two baildown tests relevant for the modelling scenarios. In the case of PB27-B shown in Fig. 4.31(a), a cut-off time of 11 min was chosen. This value discarded the first six measurements of LNAPL discharge, thus only considering data with LNAPL drawdown values below 0.015 m. This approach could be justified since data from the first 11 min could be interpreted as affected by borehole effects, although late-time data could be affected by z_{aw} fluctuations. On the contrary,

in the case of PB40-C shown in Fig. 4.31(b), a cut-off time of just 4.2 min was chosen. This value excluded the first three measurement of LNAPL discharge (first value of 1.29 m^3/day with a drawdown of 0.18 m not shown). Thus, not only late-time data (corresponding to similar values of LNAPL discharge—below 0.08 m^3/day—and drawdown as in PB27-B) were considered for the analysis despite the distinct slope. Both choices could be acceptable, and the slope differences were smaller in the case of PB40-C. Nonetheless, they led to investigate the uncertainties associated to alternative interpretations of baildown tests.

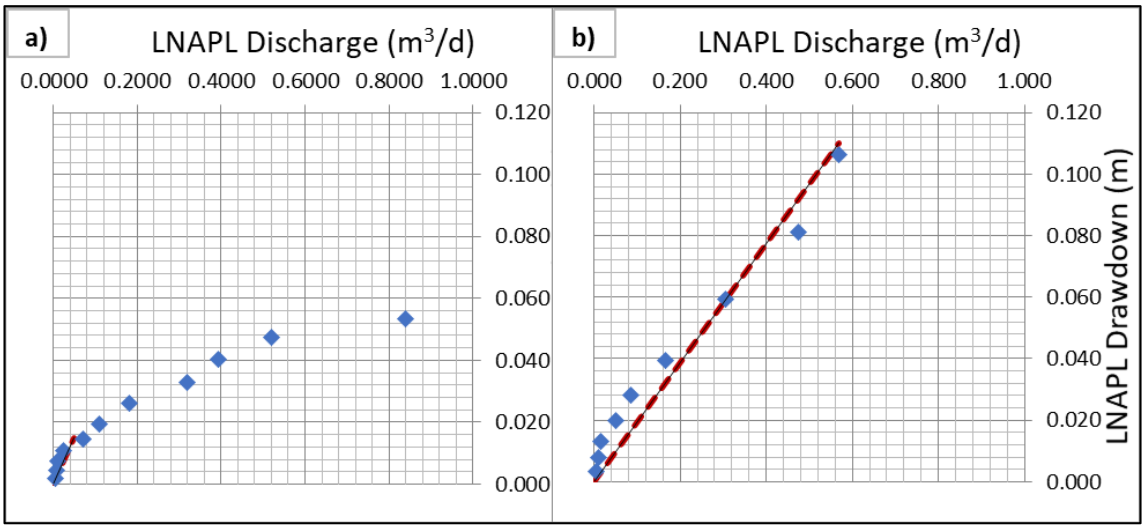


Fig. 4.31. DvD plots of baildown tests as interpreted in Gatsios (2018) at (a) PB27-B on 20/05/2016, and (b) PB40-C on 06/04/2016.

Furthermore, if late LNAPL discharge and drawdown data (represented by a dashed red line in Fig. 4.30) do not tend towards zero (one of both magnitudes intersects the corresponding axis, while the other is still positive), a drawdown adjustment may be required due to inaccuracies in the estimation of equilibrium in-well fluid levels. More specifically, T_n analyses presented in Gatsios (2018) employed linear regression to quantify this correction in a consistent way. Additional errors in the estimation of equilibrium in-well fluid levels could be derived from z_{aw} fluctuations during the tests and thus late data may be more affected by these errors (ITRC, 2018a). Consequently, chapter 7 explores the effects of different drawdown adjustment values in the tests of concern.

Moreover, periods of constant discharge as illustrated in Fig. 4.32 are representative of confined or perched LNAPL conditions, while unconfined LNAPL conditions are given by monotonic decreases of both LNAPL discharge and drawdown and therefore DvD plots were a valuable tool to inspect the underlying CSM and LNAPL hydrogeologic conditions.

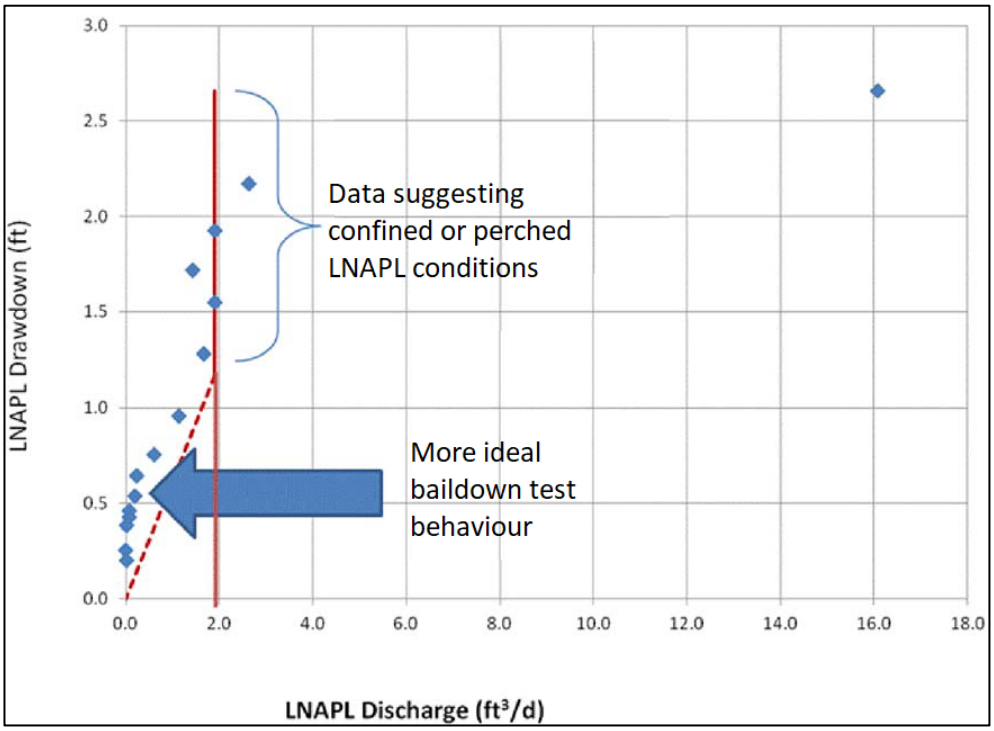


Fig. 4.32. Example of confined or perched LNAPL conditions as indicated by DvD plots (after ASTM International, 2013).

Moreover, non-linear trends in DvD plots may be caused by variable z_{aw} (especially at the beginning of the test) or measurement errors. Non-linear trends may also be influenced by the presence of layers of different geological materials in the subsurface. Thus, DTP and DTW versus LNAPL discharge plots were used as diagnostic tools to identify effects potentially caused by hydrostratigraphic contrasts (API, 2016).

4.7 Particle-size data correlations

4.7.1 Correlations of hydraulic conductivity with particle-size data

4.7.1.1 Empirical models

Use of particle-size data to predict k_{sw} is a relatively inexpensive approach requiring an adequate determination of particle-size fractions (Rogiers et al., 2012). Furthermore, the derived k_{sw} estimations are not potentially affected by the presence of LNAPL unlike other methods such as pumping tests and HPT logging. However, k_{sw} values obtained

through correlations with particle-size data are commonly associated to strong uncertainties (Rosas et al., 2014; Ren and Santamarina, 2018) since the samples get disturbed and many aspects affecting k_{sw} such as tortuosity and pore-size distribution are hard to estimate (Vienken and Dietrich, 2011). Therefore, these methods can be considered preliminary, encouraging the analysis of multiple lines of evidence to address the potential range of variability of k_{sw} (Devlin, 2015, 2017b, 2018).

A total of 15 theoretical and (semi-)empirical models correlating k_{sw} and particle-size data are implemented in HydrogeoSieveXL v2.3 (Devlin, 2015, 2017a), including the original Hazen's method and a simplified version presented in Freeze and Cherry (1979). Equations developed after Hazen included Slichter, Terzaghi (incorporating the influence of Φ) and Beyer (accounting for C_u).

Kozeny–Carman represented a step forward in the prediction of k_{sw} due to aspects such as the inclusion of a representative or referential grain size d_E commonly denominated effective grain size (Devlin, 2015), which is linked to the specific surface and frequently defined as a harmonic or geometric mean. This parameter, d_E, is more representative of the entire particle-size distribution than d_{10}. Alternative methods (not part of HydrogeoSieveXL v2.3) have characterised the entire particle-size distribution through fractal parameters or artificial neural networks (Boadu, 2000; Costa, 2006; Rogiers et al., 2012).

Other (semi-)empirical correlations implemented in HydrogeoSiveXL v2.3 (Krüger, Zunker, Kozeny–Carman, Sauerbrey, Zamarin, and Barr) also account for specific surface area effects. Additional methods include Krumbein and Monk, USBR (United Stated Bureau of Reclamation), Alyamani and Sen, and Chapuis. HydrogeoSieveXL is being actively updated by its developer to incorporate more models and options (Devlin, 2017a, 2017b; Cormican et al., 2020).

All these methods (simply referred as 'empirical correlations' or 'empirical models' from here on for readability purposes) are summarised in Table 4.8. Separate references and applicable conditions for every method can be found in Devlin (2015). Additionally, the method recently developed by Wang et al. (2017) was also tested against the sample sets from the petrol station site and the industrial site.

Table 4.8. Empirical models implemented in HydrogeoSieveXL v2.3 including ID numbers and the year when they were published. Details can be found in Devlin (2015).

ID	Method
1	Hazen (1892)
2	Hazen simplified (1979)
3	Slichter (1898)
4	Terzaghi (1925)
5	Beyer (1964)
6	Sauerbrei (1932)
7	Krüger (1919)
8	Kozeny–Carman (1953)
9	Zunker (1930)
10	Zamarin (1928)
11	USBR (1966)
12	Barr (2001)
13	Alyamani and Sen (1993)
14	Chapuis (2004)
15	Krumbein and Monk (1942)

In general, these empirical correlations are based on equation 4.11, which can be derived from the Darcy-Weisbach equation and where C and $f(\phi)$ are functions of the geological medium and ϕ, respectively. C and $f(\phi)$ are usually lumped as only one parameter (Bear, 1972; Vienken, 2011; Vienken and Dietrich, 2011). A recent dimensional analysis found that the most important parameters controlling the relationship between pore-size distribution and k_{sw} were C_u and a dimensionless term including d_{60} (Wang et al., 2017).

$$k_{sw} = \frac{\rho_w \times g}{\eta_w} \times C \times f(\phi) \times d_E^2 \qquad (4.11)$$

Empirical models were only employed when the sample characteristics did not fall out of their range of applicability assuming the criteria presented by Devlin (2015) as reasonable. Nevertheless, the applicability range of some methods may be stretched through further modifications and adequate data collection and analysis procedures, for instance to facilitate the application of Kozeny–Carman in fine-grained materials (Chapuis and Aubertin, 2003; Chapuis, 2012). Nevertheless, fine-grained materials commonly behave as capillary barriers impeding LNAPL migration and therefore the precise estimation of permeability in such materials is more relevant to phenomena such as mass transfer processes than the prediction of LNAPL distribution and mobility.

In previous research, Cheng and Chen (2007) evaluated results from Slichter, USBR, Hazen, Terzaghi, and Beyer to conclude that all of them presumably underestimated horizontal k_{sw} according to the analysis of pumping test data. In particular, Slichter and USBR have been found to likely underestimate k_{sw} compared to other empirical correlations (Vuković and Soro, 1992; Cheng and Chen, 2007; Odong, 2007). Song et al. (2009) indicated that Slichter and USBR exhibited the closest match with permeameter estimations of vertical k_{sw} in streambed sediments. This could be explained by the anisotropy typically observed in sedimentary depositional environments, with vertical k_{sw} being generally lower than horizontal k_{sw} (Freeze and Cherry, 1979; Todd and Mays, 2005). Cormican et al. (2020) concluded that, among all the models incorporated in HydrogeoSieveXL, Slichter and USBR resulted in the best estimations of k_{sw} compared to permeameter measurements in engineered porous media (mixtures of sand and granular iron).

Similar predictions of k_{sw} through Hazen and HPT logging have been presented in the literature (Butler, 2007), although estimations of k_{sw} though Hazen could not reproduce observations from tracer tests in previous studies (Taylor et al., 1987; Gierczak et al., 2006). Hazen has been reported to overestimate k_{sw} and underestimate its variability compared to permeameter measurements, reinforcing that d_{10} may not necessarily be the main factor controlling k_{sw} (Eggleston and Rojstaczer, 2001; Song et al., 2009; Cormican et al., 2020). Similarly, Kozeny–Carman has been found to overestimate k_{sw} compared to permeameter measurements and other empirical correlations (Song et al., 2009; Cormican et al., 2020). Alyamani and Sen has been found to be very sensitive to the shape of the particle-size distribution, being better suited for well-graded materials (Odong, 2007).

4.7.1.2 Determination of the effective grain size

Definition of the most adequate d_E for several empirical methods can be troublesome (Urumović and Urumović Sr, 2016, 2017, 2018; Devlin, 2017b, 2018). Consequently, HydrogeoSieveXL was modified to incorporate two possible options for d_E (Devlin, 2017a), defined in this thesis as d_{VS} and d_{UU}. The value of d_{VS} corresponded to d_{10} or an equivalent diameter as proposed by Vuković and Soro (1992), while d_{UU} corresponded to the geometric mean as proposed by Urumović and Urumović Sr (2017).

This discrepancy affected four models: Slichter, Terzaghi, Barr and Kozeny–Carman. Kozeny–Carman and Terzaghi have been found to present a better correlation with direct measurements of k_{sw} when d_{UU} was employed (Urumović and Urumović Sr, 2016, 2017).

Nevertheless, the most adequate choice of d_E may depend on site-specific conditions as defended by Devlin (2017b, 2018). For instance, Koltermann and Gorelick (1995) indicated that using a geometric mean in Kozeny–Carman may overestimate k_{sw} in materials with significant amounts of fines, while the harmonic mean may underestimate it in coarser-grained materials.

Consequently, both values of d_E were applied in chapter 7 and compared to other field methods as an attempt to elucidate the most adequate definition of d_E for the materials found in the subsurface as well as to obtain conservative ranges. Estimations with both d_E options were averaged before computing arithmetic and geometric means comprising all the methods implemented in Devlin (2015).

4.7.1.3 Interpolation of particle-size data

Linear interpolation was applied instead of splines to determine effective grain sizes as well as clay, silt, and sand contents according to the USDA (Hillel, 1998) and USCS (ASTM International, 2009) classification schemes.

Using linear interpolation was consistent with the other methods employed to predict k_{sw} and avoided wrong interpolations under strong gradient changes, as illustrated in Fig. 4.33. Nevertheless, both linear interpolation and interpolation with splines yielded similar results as depicted in Fig. 4.33 and extreme values did not generally represent effective grain sizes. The small error between the two methods was due to an adequate number of sieves used in the analysis.

Accuracy of the methods was expected to be generally higher in samples with low content of fines and higher in the industrial site than in the petrol station site due to the different depositional environments. It has been shown that the type of depositional environment may affect the accuracy of these empirical correlations (Rosas et al., 2014). Additional adjustments of the empirical formulas may improve their accuracy (Rosas et al., 2014), although modifications implemented according to specific sample sets may

not be extrapolated to other sites (Vienken and Dietrich, 2014) and collecting site-specific data for this purpose was out of scope of this research.

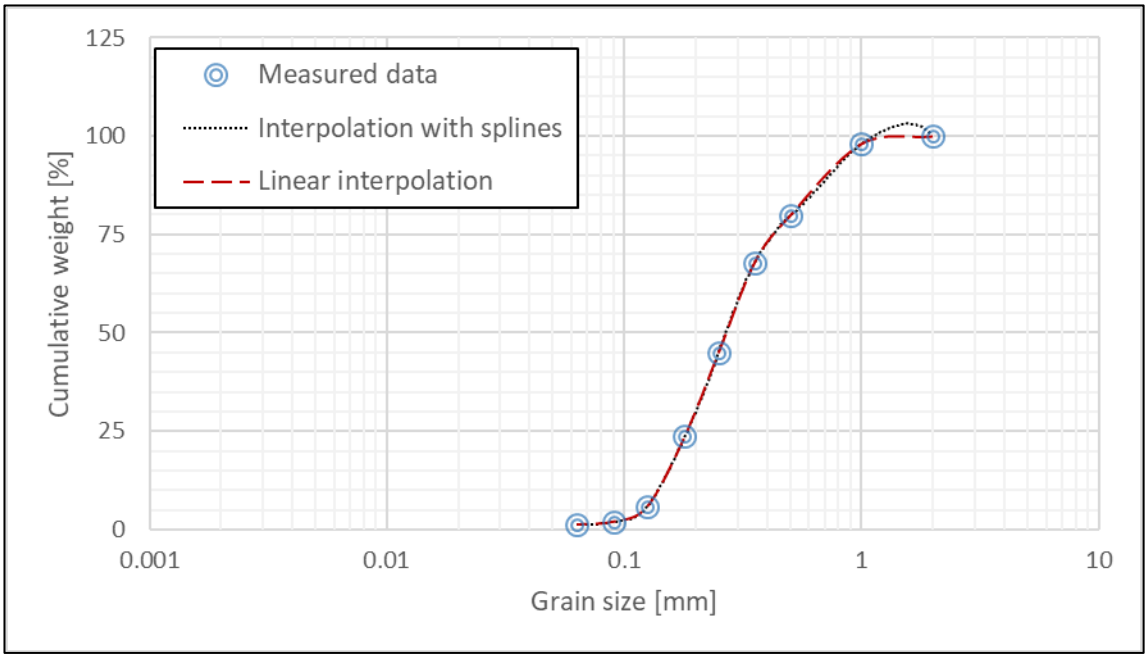


Fig. 4.33. Splines and linear interpolation on data from the industrial site (040610/1-T4 sample at 1.025 m AHD). Note the wrong values predicted with splines between the widest sieve openings.

4.7.2 Prediction of retention parameters

The methods proposed by Ghanbarian et al. (2010) and Benson et al. (2014) to predict retention parameters (vG-α and vG-N) from particle-size data were employed. The modification of a spreadsheet implementing multiple methods to estimate retention parameters from particle-size data (Ellithy, 2017) facilitated the presentation and comparison of part of the results.

Two errors affecting the way the method of Benson et al. (2014) was implemented in the spreadsheet (version 14) of Ellithy (2017) were identified, corrected and communicated to the author. These errors were associated to the calculation of C_u and the use of a wrong empirical constant instead of the value given by Benson et al. (2014). In addition, the particle-size upper limit of silts was modified to be 0.05 mm and not 0.075 mm as stated in the spreadsheet, since the method of Ghanbarian et al. (2010) and others (Saxton et al., 1986) were based on the USDA classification and not the USCS system. The method of Saxton et al. (1986) to obtain a B–C function from textural data

has been reported to be more appropriate for clay contents over 10 % (Saxton et al., 1986) and therefore was not applied in the cases of the petrol station site and the industrial site.

The method of Benson et al. (2014) is based on the empirical correlation of drainage and imbibition vG parameters with the C_u values of relatively clean and uniform sands depicted in Fig. 4.34. Thus, this method was particularly interested because of the estimation of both drainage and imbibition parameters and therefore could be used to consider hysteresis effects. However, its application could be questionable in the petrol station site due to the significant presence of fines. Therefore, the applicability of the method was evaluated comparing it to other approaches. Regarding S_{wr}, a constant θ_{wr} value of 0.04 or zero (without introducing significant error) was recommended for practical purposes (Benson et al., 2014).

Regarding the method of Ghanbarian et al. (2010), it consisted of a fractal approach where the fractal dimension *D* of the retention curve could be related to $vG\text{-}N$ through different assumptions on the correspondence between vG and B–C models. In particular, the method as implemented by Ellithy (2017) assumed large *h* values and the vG restriction $vG\text{-}m=1-1/vG\text{-}N$, leading to $vG\text{-}m=(3-D)/(4-D)$. The value of *D* was estimated through an empirical correlation with clay content (Huang and Zhang, 2005). This empirical model exhibited a relatively weak correlation with sand samples (Huang and Zhang, 2005). Consequently, the applicability of the Ghanbarian et al. (2010) approach in the petrol station site and the industrial site was evaluated. For the calculation of S_{wr}, the Φ and k_{sw} values were required. Thus, they were predicted with RETC, calculating Φ values through a linear model correlating Q1, M, and Q3 of θ_{ws} from RETC and Φ from laboratory measurements in the petrol station site.

Ghanbarian et al. (2010) did not present any novel approach to estimate $vG\text{-}\alpha$ but adopted the methods of Lenhard et al. (1989b) and Tinjum et al. (1997), being the later an empirical correlation based on clay samples and therefore probably not adequate for the materials found in the petrol station site and the industrial site.

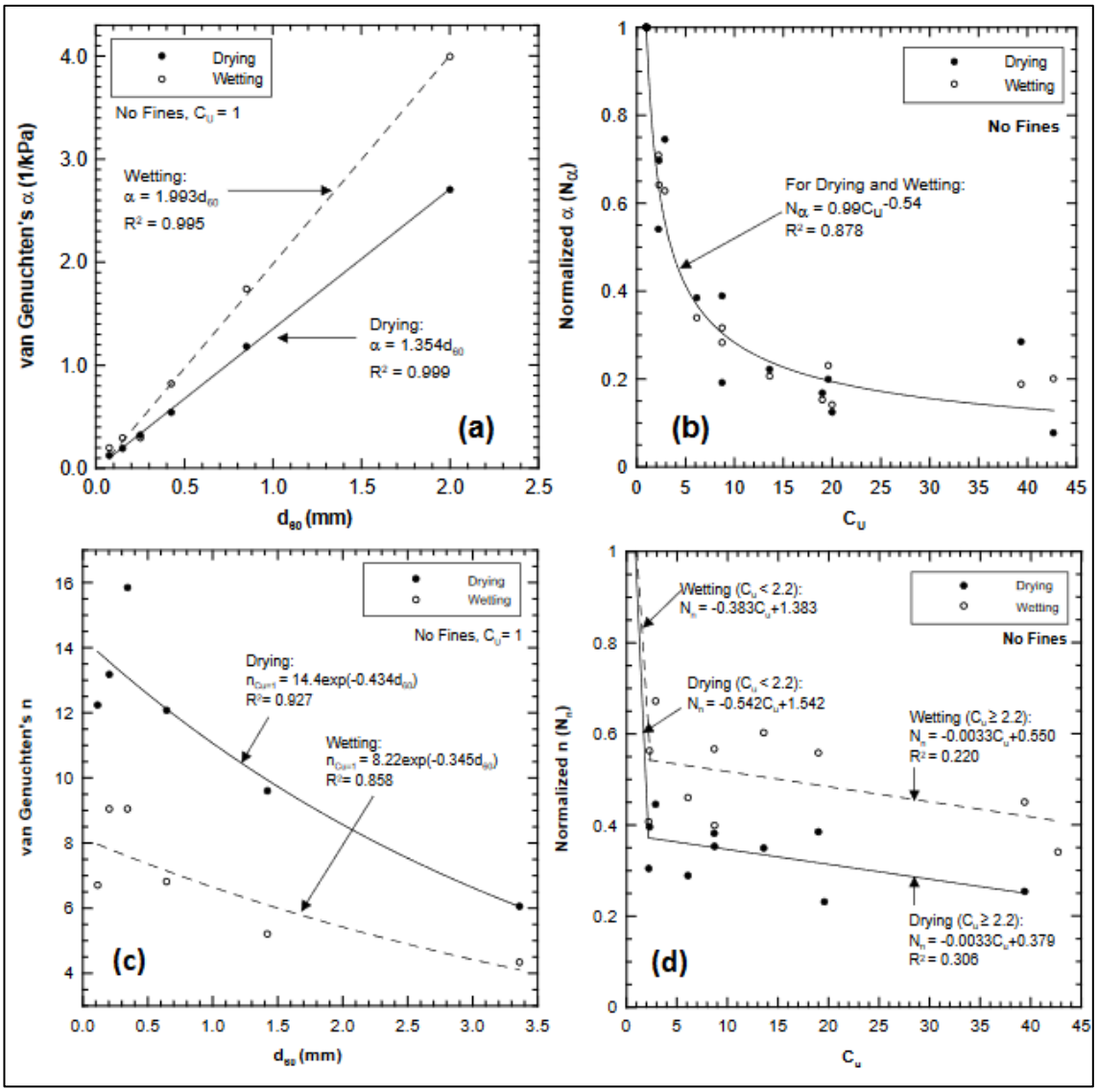


Fig. 4.34. Empirical correlation between vG parameters, d_{60}, and C_u (modified after Benson et al., 2014).

Lenhard et al. (1989b) proposed equation 4.12 where h_{min} is the entry pressure head for the non-wetting fluid as defined in the B–C model and S_x is a match-point empirically defined by equation 4.13.

$$vG\text{-}\alpha = \frac{S_x^{1/\lambda}}{h_{\min}}\left(S_x^{-1/\text{vG-M}} - 1\right)^{1-\text{vG-M}} \tag{4.12}$$

$$S_x = 0.72 - 0.35\exp(-vG\text{-}N^4) \tag{4.13}$$

Due to the influence of h_{min}, two distinct h_{min} options were tested for the analysis of field data: the geometric means for samples reported by (i) Rawls et al. (1982) and (ii) the API

database (API, 2006) according to USDA and USCS classifications as summarised in Table 4.9.

Table 4.9. Geometric mean value of h_{min} for different USDA and USCS texture classes according to samples from Rawls et al. (1982) and API (2006), respectively.

Textural class	USDA classification				USCS classification				
	Loam	Sandy loam	Loamy sand	Sand	ML	SM	SW–SM	SP–SM	SP
h_{min} [cm]	11.15	14.66	8.69	7.26	125.21	56.25	32.79	38.01	39.92

In addition, other two alternative approaches were employed to predict vG-α: (i) combining the method developed by Morel-Seytoux et al. (1996), which is based on a equivalence between the models of B–C and vG minimising the effective capillary drive (Morel-Seytoux et al., 1996), with the vG-m value obtained through Ghanbarian et al. (2010), and (ii) assuming a constant vG-α as done by Ellithy (2017) considering the average vG-α values reported by Carsel and Parrish (1988). Table 4.10 summarises the methods employed to derive retention parameters from particle-size data, including the shortened names (method IDs) used in chapter 7.

Table 4.10. Methods employed to estimate retention parameters from particle-size data.

Method ID	Reference	Source for h_{min} or vG-α	Outputs
Ellithy	Ellithy (2017)	Carsel and Parrish (1988)	vG-α
Lenhard–Rawls	Lenhard et al. (1989b)	Rawls et al. (1982)	vG-α
Lenhard–API	Lenhard et al. (1989b)	API (2006)	vG-α
MS–Rawls	Morel-Seytoux et al. (1996)	Rawls et al. (1982)	vG-α
MS–API	Morel-Seytoux et al. (1996)	API (2006)	vG-α
Ghanbarian	Ghanbarian et al. (2010)	-	vG-N, S_{wr}
Benson	Benson et al. (2014)	-	vG-α, vG-N, S_{wr}
Drainage	Benson et al. (2014)	-	vG-α, vG-N, S_{wr}
Imbibition	Benson et al. (2014)	-	vG-α, vG-N, S_{wr}
RETC	Van Genuchten et al. (1991), Schaaps et al. (2001)	-	vG-α, vG-N, S_{wr}

Finally, section 7.4.3.2 reports laboratory measurements of retention parameters from samples collected in the industrial site. These laboratory measurements were not new nor conducted for this thesis. SWRC fit (Seki, 2007) was employed to fit the data to

several retention models, more specifically vG, B–C, Fredlund and Xing (1994), Kosugi (1996), and the multimodal models of Durner (1994), and Seki (2007). Model evaluation was done through calculation of the Pearson's coefficient of determination R^2 and Akaike information criterion AIC values. The definition of these two metrics is presented in section 4.9.

4.7.3 Neural network predictions

Another common and inexpensive approach to derive values of k_{sw} as well as retention parameters ($vG\text{-}\alpha$, $vG\text{-}N$, and S_{wr}) from particle-size data consists of using neural networks as implemented in popular software options such as Rosetta (Schaap et al., 2001), Hydrus (Radcliffe and Šimůnek, 2010), and RETC (van Genuchten et al., 1991). Neural network predictions in Hydrus and RETC mainly follow the approach of Rosetta since they are performed through the implementation of the Rosetta Lite module (Radcliffe and Šimůnek, 2010).

RETC v6.02 with Rosetta Lite v1.1 was used to predict k_{sw} and vG retention parameters with particle-size data from the petrol station site and the industrial site. Texture percentages and ρ_b values (available in the industrial site) were used as input data. Textural classes in RETC correspond to the USDA classification. Therefore, particle-size fractions over 2 mm were removed and passing percentages corresponding to clay (0.002 mm) and silt contents (0.05 mm) were calculated through linear interpolation.

Rossetta Lite incorporates five pedotransfer functions to derive values of k_{sw} and retention parameters from surrogate data. They are organised in a hierarchical structure to facilitate the use of different types of input data (from soil textural class to texture percentages, ρ_b, and one or two retention points). These pedotransfer functions comprise one lookup table and four back-propagation neural network models (Schaap et al., 1998).

As the design illustrated in Fig. 4.35, the artificial neural networks consisted of three layers (thus, only one hidden layer). The first layer is used to introduce input values and therefore the number of nodes depends on the number of input parameters X_j considered. The input nodes are connected to the hidden nodes, where all input values are weighted (according to weight functions w_{jk}) and summed to derive an output value

at each hidden node. Analogously, these output values are used as input data for the output nodes, where they are weighted (according to weighting functions w_{kl}) and summed to produce the neural network predictions $\widehat{Y_L}$ (Schaap and Leij, 1998b).

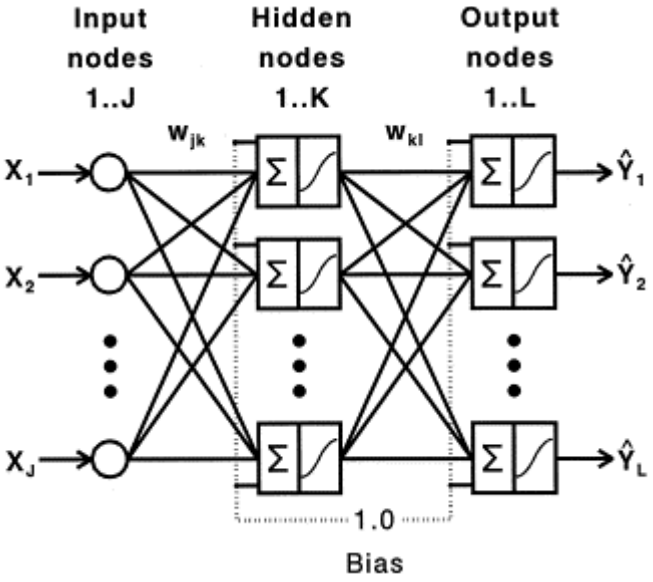


Fig. 4.35. Neural network design (Schaap and Leij, 1998b).

The best values of w_{jk} and w_{kl} were obtained after a calibration procedure that used samples from three databases (Schaap and Leij, 1998a). It consisted of minimising the objective function $O_{nn}(c_{nn})$ shown in equation 4.14 through the iterative Levenberg-Marquardt algorithm (Schaap et al., 1998).

$$O_{nn}(c_{nn}) = \sum_{i=1}^{N_s} \sum_{j=1}^{N_p} \left(\eta_{i,j} - \eta'_{i,j}\right)^2 \qquad (4.14)$$

The parameter c_{nn} represents the coefficient matrices of the neural networks, N_s and N_p are the number of calibration samples and output parameters, and finally η and η' are the fitted and estimated parameters, respectively (Schaap et al., 2001).

In addition, Rosetta includes bootstrapping for uncertainty analysis (Schaap et al., 2001). It has been found that the use of more predictors as input parameters generally increases the accuracy of the method (Schaap et al., 1998, 2001; Alvarez-Acosta et al., 2012). Predictions of θ_{ws} have been found to be significantly enhanced by ρ_b data, while θ_{wr} estimations may not present a high accuracy degree due to its asymptotic nature

(Schaap et al., 1998). Rosetta has been found to underestimate water contents and overestimate *vG-N* (Ghanbarian et al., 2010).

The original developers implemented B–C retention functions programmed for gravimetric water contents instead of volumetric contents in this and previous versions of RETC. The estimation of k_{sw} and vG retention parameters was not affected by this issue. New versions of Rosetta are being developed to update and improve the predictions of soil hydraulic data (Zhang and Schaap, 2017). Further details about the use of pedotransfer functions in soil science can be found in the literature (Minasny et al., 1999; McBratney et al., 2002; Vereecken et al., 2010; Van Looy et al., 2017).

4.8 Multiphase analytical models

4.8.1 LNAPLTRANS

LNAPLTRANS is a recently developed multi-layered version of LNAPLVOL (Lenhard et al., 2017) which allows definition of up to five layers with different medium properties. Thus, LNAPLTRANS predict vertical distribution profiles of residual, entrapped, free, and total S_n and V_n, as well as recoverable and free T_n. LNAPLVOL has been presented in Lenhard et al. (2017) and Lenhard et al. (2018), while LNAPLTRANS has been tested in García-Rincón et al. (2018), and Lenhard et al. (2019).

The model is based on the equations of Lenhard and Parker (1990a, 1990b) and Farr et al. (1990). Thus, fluid saturations are predicted from capillary heads, which are scaled according to ratios of interfacial tensions as proposed by Parker et al. (1987) and Lenhard and Parker (1988). The vG retention model is employed and the free V_n is integrated between z_{nw} and z_{an} plus the LNAPL capillary rise, which is only dependent on fluid properties and not in the medium (contrary to the case of the height of the capillary fringe in water-saturated systems). Lenhard and Parker (1990a) equations were modified to also predict variable, elevation-dependent S_{ne} and S_{nr}. The calculation of S_{nr} followed the approach of Lenhard et al. (2004), which considers current and historic apparent fluid saturations, as well as a calibration factor (maximum S_{nr}, S_{nr}^{max}). The relationship presents empirical exponents (Lenhard et al., 2004), which optimal value may depend on site-specific properties. S_{ne} was predicted following a similar procedure, therefore defining a maximum S_{ne}, S_{ne}^{max} (Lenhard et al., 2017). Entrapped air, which was

considered in the model of Parker et al. (1987), was not considered in LNAPLTRANS, although it may be relevant in methanogenic source zones (Amos and Mayer, 2006). Residual and entrapped V_n are integrated accounting for historic fluid levels.

Additionally, k_{rn} is calculated according to a modified Mualem model (modified so k_{rn} is below 1 at maximum S_n due to the presence of residual and entrapped fluid saturations) and free (above and below atmospheric pressure) and recoverable (above atmospheric pressure) T_n values are integrated across the profile.

Although P_c–S hysteresis is not implemented in LNAPLTRANS, the model accounts for saturation path history in the prediction of fluid saturations as well as relative permeabilities by considering current and historical fluid levels used to estimate current and historical fluid saturations. An assumption was made in the model that the predictions are not dependent on whether the historical highest or the historical lowest fluid level elevation in a well occur first. Numerical simulations suggested that this assumption is reasonable (Lenhard et al., 2018). Accordingly, LNAPLTRANS uses the input parameters summarised in Table 4.11, including historical highest z_{an}, z_{an}^{max}, and the historical lowest z_{nw}, z_{nw}^{min}.

Table 4.11. LNAPLTRANS inputs and parameters.

Hydraulic parameters	
$vG\text{-}\alpha$	van Genuchten alpha
$vG\text{-}N$	van Genuchten n
S_{wr}	residual water saturation
Φ	porosity
k_{sw}	saturated water hydraulic conductivity
S_{ne}^{max}	maximum entrapped LNAPL saturation
S_{nr}^{max}	maximum residual LNAPL saturation
Fluid parameters	
σ_{nw}	LNAPL/water interfacial tension
σ_{an}	air/LNAPL interfacial tension
ρ_{rn}	LNAPL specific gravity
η_{rn}	LNAPL/water specific viscosity
Model inputs	
z	elevation of ground surface
z_{an}	elevation of air/LNAPL interface in well
z_{nw}	elevation of LNAPL/water interface in well
z_{an}^{max}	historical highest z_{an}
z_{nw}^{min}	historical lowest z_{nw}

4.8.2 LDRM

LDRM has been a popular multiphase analytical model used in the remediation industry and many publications (Hernández-Espriú et al., 2012; Kahraman, 2013; Hartsock, 2014; McAlexander and Tuggle, 2015; García-Rincón et al., 2018; Gatsios et al., 2018a; Alfaro Soto et al., 2019; Ebrahimi et al., 2019). Some authors have modified it to add certain capabilities (Al Awar, 2008; de Blanc and Farhat, 2018).

Details of the model can be found in the literature (Charbeneau, 2007a, 2007b; Jeong and Charbeneau, 2014). LDRM is also partially based on equations from Parker et al. (1987), Lenhard and Parker (1990a, 1990b) and Farr et al. (1990), although differences with LNAPLTRANS exist, including:

1. up to three layers may be defined in LDRM (instead of five as in LNAPLTRANS);
2. it is possible to choose between Burdine (adopted by default) and Mualem relative permeability models, modified to account for the presence of S_{wr} and S_{nr} (Patterson, 2011). Charbeneau (2007a) has suggested to apply Burdine in coarse-grained materials and Mualem in relatively fine-grained materials due to the lower estimations of Burdine;
3. current version 2.0 of LDRM assumes that S_{ne} and S_{nr} are identical despite being formed according to distinct physical processes. The value can be set as (i) a constant set by the user, (ii) a constant derived from a f-factor, or (iii) an elevation-dependent function derived from a f-factor. This f-factor was introduced by Johnston and Adamski (2005) for the calculation of S_{ne};
4. recoverable V_n is calculated as the difference between total V_n and V_{nr}, therefore not accounting for free LNAPL below atmospheric pressure (thus non-recoverable). Similarly, the estimated T_n through LDRM was more comparable to the free T_n predicted with LNAPLTRANS than the recoverable T_n value;
5. historical fluid levels are not explicitly considered in LDRM, although the model allows to test the effects of changing b_n on conducted simulations;
6. additional features and capabilities of LDRM include a graphical interface, specify a water vertical gradient, and simulate some LNAPL mass recovery processes with input parameters to define the recovery system.

4.8.3 Design of modelling scenarios

LDRM and LNAPLTRANS were used to estimate S_n distributions, V_n, and T_n in areas A, B, C, and T4 to compare the capabilities of both models. These scenarios differed in geological and LNAPL properties (from loam to calcareous sands and from fresh petrol to weathered diesel) as well as in b_n and T_n values.

Reference input parameters for the base-case scenarios were chosen from the quantitative analysis of field and literature data presented in chapter 7. Reference values representing subsurface conditions were assumed to correspond to:

- measured values in the location of concern or adjacent monitoring points;
- central values of the distribution of values obtained in the area of interest or field site (if there was not a direct measurement in the location of concern or the value was not considered representative of the subsurface properties);
- literature values in a few cases if field data were not available or reliable.

In-well fluid levels corresponded to field measurements from 01/12/2005 (well 050210/1-T4), 19/05/2016 (well PB29-A) and 20/05/2016 (wells PB27-B and PB40-C, respectively). Historical fluid levels were defined according to field measurements and vertical profiles of S_n and LIF response. Elevations in the model scenarios were scaled to locate z_{aw} at 2 m due to model limitations representing negative elevations and regarding the number of accepted digits. Field and model estimations of z_{aw} could slightly differ due to the choice of ρ_n values, although not significantly affecting the discussion of results.

The predicted S_n profiles were compared to estimations derived from chemical analyses performed on extracted cores (MP50-A on 18/05/2016, MP58-B on 19/05/2016, and MP44-C 17/05/2016). Model predictions of T_n were compared to measurements from baildown tests conducted at PB29-A on 19/05/2016, PB27-B on 20/05/2016, PB40-C on 06/04/2016 and 14/06/2016, and in area T4 on 01/12/2005.

4.8.4 Model testing and comparison

The same number of layers (one, two or three) was used in both models to facilitate the comparison between LNAPLTRANS and LDRM. Similarly, vertical gradients were not

considered since they could only be explicitly modelled with LDRM, and total V_n and free T_n from LNAPLTRANS were used for comparison purposes instead of recoverable values. Nevertheless, discrepancies between LNAPLTRANS and LDRM were expected due to key aspects such as (i) the representation of S_{nr} and S_{ne}, (ii) the relative permeability model, and (iii) the treatment of water table fluctuations. Thus, the different options of LDRM regarding the definition of near-immobile S_n (constant values, constant value derived with a f-factor, and variable values derived with a f-factor) and relative permeability (Burdine and Mualem models) were tested in single-layer scenarios. The f-factor was assumed to be 0.23 as estimated by Johnston and Adamski (2005) for Safety Bay sands in Western Australia. Historical and current in-well fluid levels were used in LNAPLTRANS without affecting the estimation of T_n.

Due to the large number of simulations, specific IDs formed according to the following code were assigned to each simulation: 'area-layers-model'. In the case of using LDRM, the code was extended as follows: 'area-layers-model-relative permeability model-S_{nr} model'. For the sensitivity analysis, a final term was added. Every element was defined as follows:

- area: A, B, C, T4;
- layers: 1L (one layer), 2L (two layers), 3L (three layers);
- model: 2007 (LDRM), 2017 (LNAPLTRANS);
- relative permeability model: Bu (Burdine), Mu (Mualem);
- S_{nr} model: 1*Snr* (constant set by the user), 2*Snr* (constant with f-factor), 3*Snr* (variable with f-factor).

4.8.5 Sensitivity analysis of multiphase analytical models

The robustness of the solutions provided by the models (in terms of total V_n and free T_n) was evaluated through a sensitivity analysis. The analyses were done for selected areas according to the results from the single-layer base-case scenarios. It is common to use local sensitivity analysis methods to assess how the model performance changes when varying an optimal or reference parameter set (Pianosi et al., 2016) despite some possible inconveniences derived from this approach (Saltelli and Annoni, 2010).

Most sensitivity analysis methodologies require a good understanding of the probabilistic distributions associated to the input parameters. This is usually not the case in problems of LNAPL contamination because of the complexity of the system, the different measurement errors linked to each characterisation tool, and the relatively low number of collected samples compared to other disciplines. An analysis of the variability of the API database parameters can be found in the literature (Al Awar, 2008). The low number of samples (below 30 for the same type of LNAPL) did not facilitate an adequate determination of probability distributions.

Consequently, the deterministic sensitivity index SI defined in equation 4.15 (Hoffman and Gardner, 1983) was computed for each parameter and scenario as suggested in the literature (Hamby, 1995; Pannel, 1997).

$$SI = \frac{D^{max} - D^{min}}{D^{max}} \qquad (4.15)$$

where D^{max} is the value of the target output corresponding to the maximum value of an input parameter, while D^{min} corresponds to the minimum input value. Maxima and minima were selected considering the different tools and data analysis procedures employed in the field and the laboratory as well as ranges found in the literature. If an inverse relationship existed between the input and the output perturbations, SI was calculated as (D^{min}-D^{max})/ D^{min} to obtain a positive value that could be directly compared to the rest of indices in terms of identifying the most influential parameters.

Due to the strong uncertainty associated to problems of multiphase contamination in the subsurface, the sensitivity analysis methodology was evaluated by considering the following three data ranges:

1. the 'most likely range', generally comprising direct measurements from the location of concern or the IQR ($p25$–$p75$) of field data collected in the area or site (the IQR was extended to incorporate direct measurements from the location of concern if necessary);
2. an 'extended range', commonly representing the 5 %-trimmed range ($p5$–$p95$) of field data or the entire field range if anomalous values were not identified
3. a 'conservative range' including extreme values from the field and the literature.

In some cases, other criteria could be followed to ensure that the three ranges were different and comprised the reference values employed in the base-case scenarios. Due to the consideration of three parameter ranges, three SI values (SI_1, SI_2, SI_3) were computed for every parameter.

4.9 Statistical data analysis procedures

This section briefly summarises the statistical data analysis tools employed in the thesis and clarifies some aspects about their application. The reader is referred to the literature (Isaaks and Srivastava, 1989; Reimann et al., 2008; Helsel et al., 2020) for further details about the methods.

As it could be inferred from section 1.2, the analysis of data from subsurface environments presents many challenges. Typical issues include:

- several populations of the same variable may coexist due to the influence of multiple processes at different scales;
- data may not meet many common assumptions of parametric tests and classical confirmatory data analysis (Gaussianity, spatial independence, stationarity, ergodicity, homoscedasticity);
- extreme values, not necessarily representing outliers, are commonly measured;
- sample size is not large enough to ensure the accuracy of statistical estimators of population parameters, since sampling activities are demanding in terms of time and resources;
- sampling and analytical errors limit the representativeness of measurements;
- non-detect data are frequently reported.

Consequently, exploratory data analysis tools (scatterplots, histograms, density traces, boxplots, cumulative probability—CP—plots, and empirical cumulative distribution function—ECDF—plots) were employed to investigate the distribution of subsurface variables. Log-transformation of the variables of interest was frequently performed for the further inspection of right-skewed data.

Furthermore, descriptive statistics were used to quantitatively summarise characteristics of entire data sets and define representative values and ranges of the

variables of concern. Descriptive statistics for sets of data with low number of samples may be informative and therefore they were reported in some cases but should be interpreted with caution.

Descriptive statistics included measures of location (arithmetic mean—sometimes simply referred as 'average' or 'mean'—, geometric mean, median M, mode) and spread (SD, median absolute deviation MAD, variance, coefficient of variation CV, robust coefficient of variation CVR, range, interquartile range IQR, normalised interquartile range NIQ, trimmed ranges) as well as third- and fourth-order statistical moments (skewness and kurtosis). Waddill and Parker (1997b) supported that geometric mean values of subsurface parameters were adequate as inputs to predict LNAPL recoverability.

As illustrated in Fig. 4.36, the shape of the probability distribution may strongly influence several measures of location and spread. Consequently, it was particularly important the application of robust estimators (for instance, the median, MAD, CVR, and IQR) less affected by extreme values and strongly skewed distributions or other non-Gaussian effects. Thus, robust estimators could produce more representative central values and measures of spread of the main body of data. Along ECDF and CP plots, robust estimators also facilitated identification and further inspection of potential outliers.

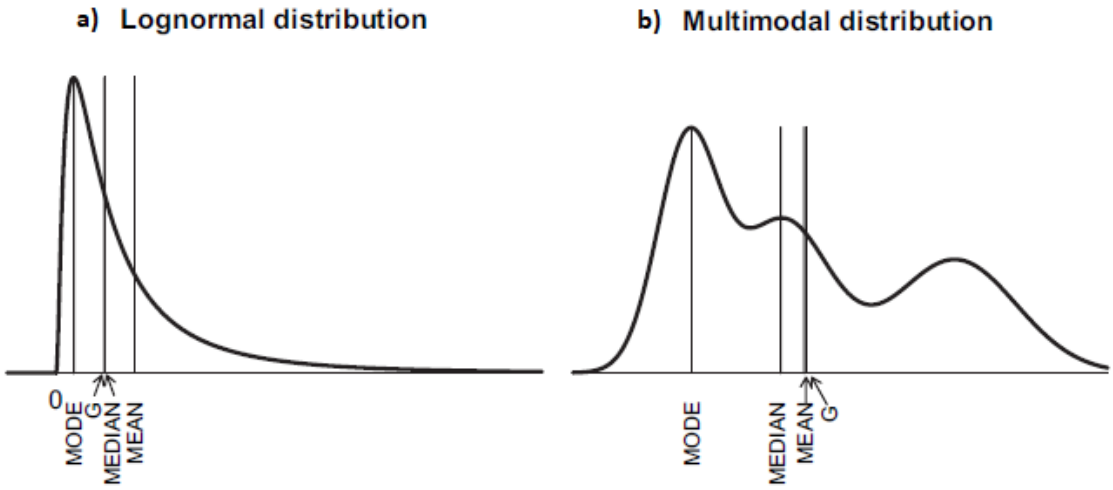


Fig. 4.36. Measures of location in (a) lognormal, and (b) multimodal distributions. *MEAN* and *G* refer to the arithmetic and geometric means, respectively (adapted from Reimann et al., 2008).

Additionally, the robust Z-score of Iglewicz and Hoaglin (1993) presented in equation 4.16 was also used to screen potential outliers from a set of data x_i for further inspection, labelling values as potential outliers when the Z-score was higher than 3.5 (Iglewicz and Hoaglin, 1993). Extreme data points could reveal information about extreme field conditions, valuable for the development of the CSM, and therefore the objective should never be to exclude them without further evidence exposing measurement errors.

$$Z\ score = \frac{0.6745(x_i - M)}{MAD} \tag{4.16}$$

Exploratory data analysis and determination of descriptive statistics were commonly performed with the programming language and statistical software R v3.5.1 implemented in the integrated development environment RStudio v1.1.453. Library package *StatDA* was installed to support exploratory data analysis. Geometric means were calculated with the library package *EnvStats*, while *fBasics* was used for the determination of skewness and kurtosis values.

The implemented methods provided an unbiased excess kurtosis estimator since Bessel's correction (dividing by *n-1* instead of *n*, where *n* is the number of samples) was applied. Negative excess kurtosis values represent thin-tailed (platykurtic) distributions, while positive values are characteristic of fat-tailed (leptokurtic) distributions (therefore presenting a greater spread and suggesting the study of ranges instead of central values only). Further discussion about kurtosis estimation methods can be found in the literature (Joanes and Gill, 1998). The mode value was computed from density kernels. NIQ was calculated as IQR divided by 1.349 (IQR value of a normal distribution) and is an estimator of SD in normal distributions. CVR was calculated as the ratio of MAD and median in percentage.

In some cases, R^2 was used as a metric to preliminary evaluate the linear correlation between two variables. The data was always plotted and examined, since R^2 values may produce misleading interpretations. For instance, R^2 is influenced by the slope of the linear regression model.

Thus, the Mean Absolute Error (MAE) and Root Mean Square Error (RMSE) were computed to evaluate models, for instance for the prediction of S_n from LIF data. Both metrics express average residual errors *e* in units of the variable of study, although RMSE assigns a greater weight to larger errors. Additionally, AIC was computed to evaluate the accuracy of retention models. R^2, MAE, RMSE, and AIC of a set of data y_i were defined as equations 4.17, 4.18, 4.19, and 4.20, where *k* was the number of estimated parameters.

$$R^2 = 1 - \frac{\sum(e^2)}{\sum(y_i - \bar{y})} \tag{4.17}$$

$$MAE = \frac{1}{n}\sum|e| \tag{4.18}$$

$$RMSE = \sqrt{\frac{1}{n}\sum(e^2)} \tag{4.19}$$

$$AIC = n \ln\left(\frac{\sum(e^2)}{n}\right) + 2\,k \tag{4.20}$$

Finally, Spearman's rank correlation coefficient, which is analogous to R^2 applied to ranked data and therefore less sensitive to extreme values, was used to assess the monotonic correlation between LIF response (peak LIF signal and integral LIF signal) and T_n values measured in wells not more than 3 m away on 05–06/04/2016. Absence of in-well LNAPL was assumed to represent zero T_n. Value ties were assigned average ranks as suggested in the literature (Helsel et al., 2020).

5 Identification of hydrostratigraphic layers and confinement conditions

5.1 Chapter structure

Chapter 5 analyses field characterisation data from conventional methods and HPT logs to define the subsurface hydrostratigraphy in the areas of study. In areas A, B, and C, the existence of confined LNAPL and aquifer conditions was assessed by comparing single- and multi-well DGPs with hydraulic tests as well as HPT logs and particle-size data.

Investigators should always evaluate multiple lines of evidence to take well-informed decisions while reducing and better acknowledging CSM uncertainty. However, the ability of investigators to embrace this approach may be limited due to project constraints. The inter-comparison between techniques presented in this chapter may provide insight into the applications, limitations, potential improvements, and different outcomes related to each technique, thus contributing to elucidate the value added by conventional and HRSC methods and how to better integrate all of them.

A report has been prepared focusing on the analysis of aquifer testing data (Bekele et al., 2019). Single-well DGPs and HPT P logs from three wells in the petrol station site have already been used to determine LNAPL confinement conditions as well as hydrostratigraphic layers for modelling purposes (Gatsios, 2018; Gatsios et al., 2018a). The importance and novelty of the materials presented in chapter 5 include the following aspects:

- analysis of site-wide data from two field sites with contrasting characteristics;
- application of a refined methodology for the interpretation of single-well DGPs;
- critical discussion on the interpretation of multi-well DGPs;
- inclusion of EC, HPT P, HPT Q, and Q/P logs as well as cross-sections, corrections for atmospheric and hydrostatic pressure, and IDW interpolations in the analysis of HPT profiles;
- comparison of LNAPL and aquifer confinement conditions.

The quantification of subsurface parameters obtained with some of these tools is presented in chapter 7.

5.2 Petrol station site

5.2.1 Particle-size analysis

5.2.1.1 Overview of the particle-size data in the petrol station site

Hydrogeologic units such as aquifers and aquitards are defined according to their hydraulic properties, although strong agreement with sedimentary strata frequently exists in the case of unconsolidated media (Meyer et al., 2016). Thus, particle-size data and stratigraphic descriptions of cores were used as lines of evidence to investigate the site hydrostratigraphy.

Particle-size analysis data from 25 samples collected across the petrol station site (included in Appendix E: Particle-size data and correlations with hydraulic conductivity) supported the existence of a sandy aquifer (containing variable amounts of clay, silt, and gravel) overlain by finer-grained materials as illustrated in Fig. 5.1. Area C was represented by 14 samples, while four samples were collected in area B and only three corresponded to area A. The finer-grained material from the overlying aquitard was indicated by considerably lower values of the 25-percentile diameter, which generally increased with depth representing a fining-upward sequence (Gatsios et al., 2018b). Similarly, values of the 50-percentile diameter corresponded to coarser-grained materials with depth, from fine sands in the overlying aquitard (even silts in one sample) to coarse sands towards the bottom of the aquifer.

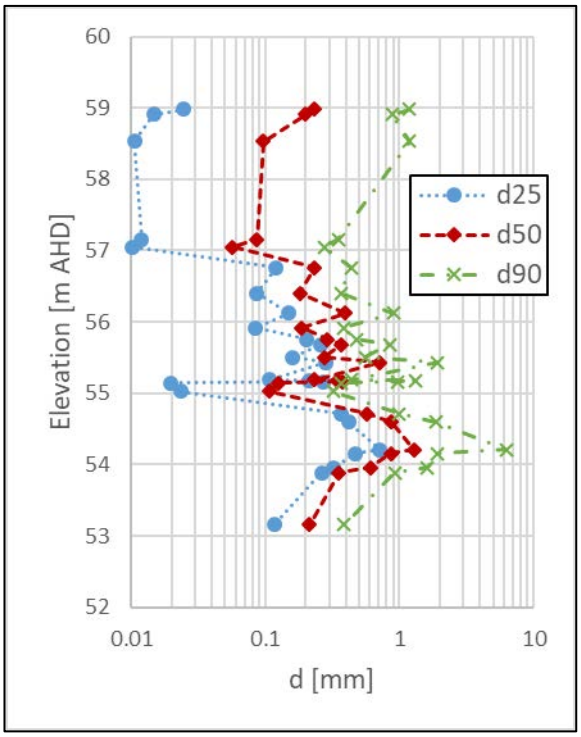


Fig. 5.1. Particle-size analysis aggregating data from the petrol station site. *d25*, *d50*, and *d90* stand for the 25th, 50th, and 90th percentiles of particle diameters, respectively.

According to particle-size data as presented in Fig. 5.2, a classification based on four materials could contribute to explain hydrostratigraphic conditions in the petrol station site:

1. 'aquitard materials': generally fine sand with fines (some silt and few clay particles; corresponding to the aquitard and low-permeability lenses);
2. 'transition materials': generally fine sand low in fines (little silt and clay traces; corresponding to the transition between the finer-grained materials in the aquitard and coarser-grained materials found below. They represent the top of the aquifer as explained below. The deepest sample at PB27-B was similar to this interval);
3. 'upper aquifer materials': generally medium sand low in fines (few silt and clay traces; characteristic of the upper half of the aquifer but coarser-grained than the 'transition materials');
4. 'lower aquifer materials': generally coarse sand low in fines (little gravel and silt traces; coarsest fractions found at the lower half of the aquifer).

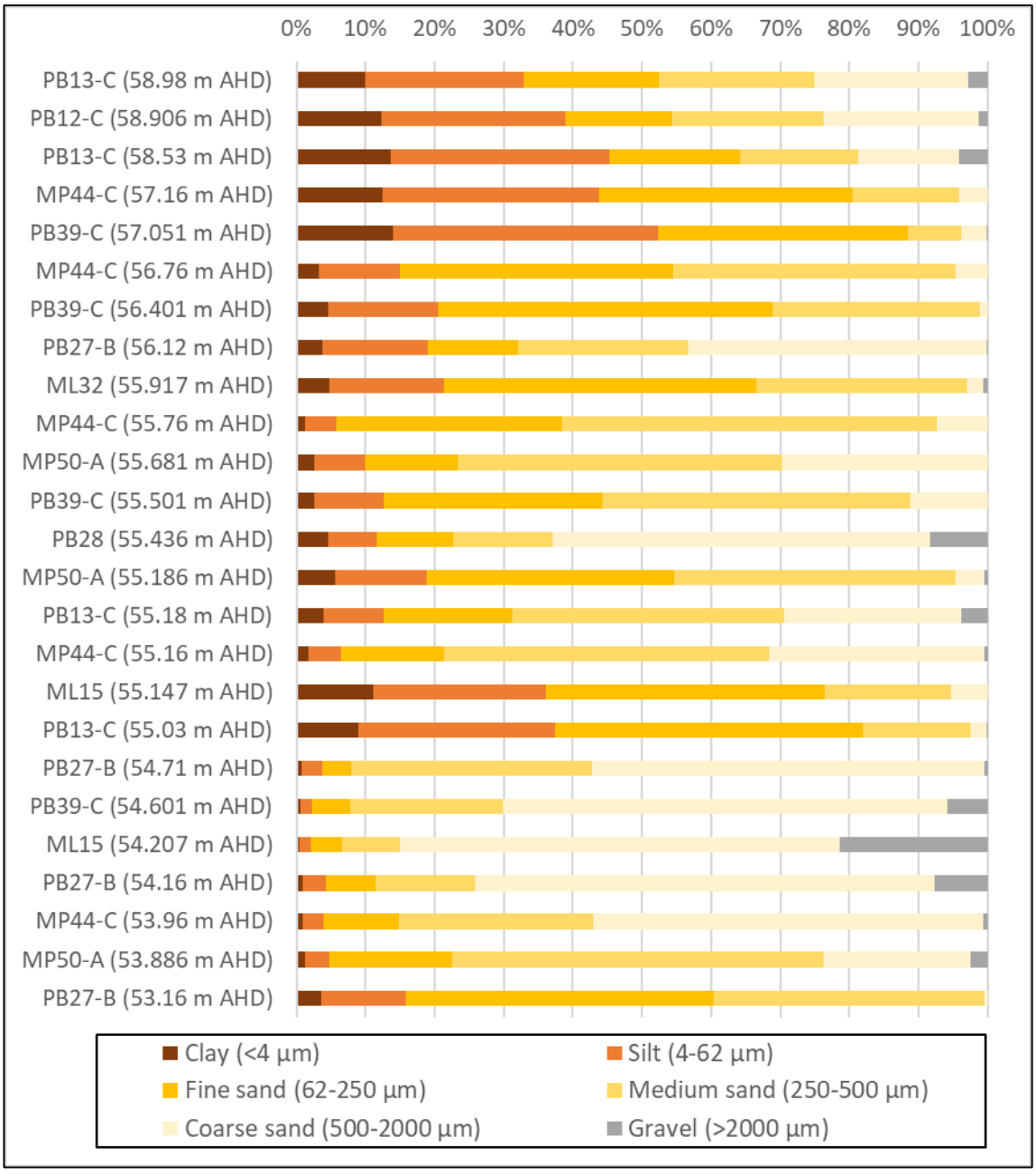


Fig. 5.2. Stratigraphic column in the petrol station site according to aggregated particle-size data.

Further details about the stratigraphic sequence are given in the following section. This discussion is mainly based in the classification shown in Fig. 5.2, although some values referring to the USDA and USCS schemes (Gee and Or, 2002; ASTM International, 2009) are also presented.

5.2.1.2 Details of the stratigraphic profile

Particle-size analysis agreed reasonably well with stratigraphic descriptions after visual inspection of extracted cores, although the aquitard contained less fines than what was

originally considered. In particular, the aquitard did not primarily consist of clay, but it could be better defined as clayey and silty sands with a content in fines ranging between 33 and 45 % according to the four shallowest samples shown in Fig. 5.2. Only one sample collected in PB39-C at 57.501 m AHD corresponded to material classified as sandy fine-grained soil according to ASTM International (2009) following the USCS classification (more than 50 % of fines). Clay content in the aquitard was between 10–15 % according to Fig. 5.2. Alternatively, the USDA classification suggested the presence of loam and sandy loam in the aquitard as illustrated in Fig. 5.3. According to the USDA classification, clay content in the aquitard was between 5 and 8 %. Table 5.1 summarises the soil textures percentages according to the USCS and USDA classifications.

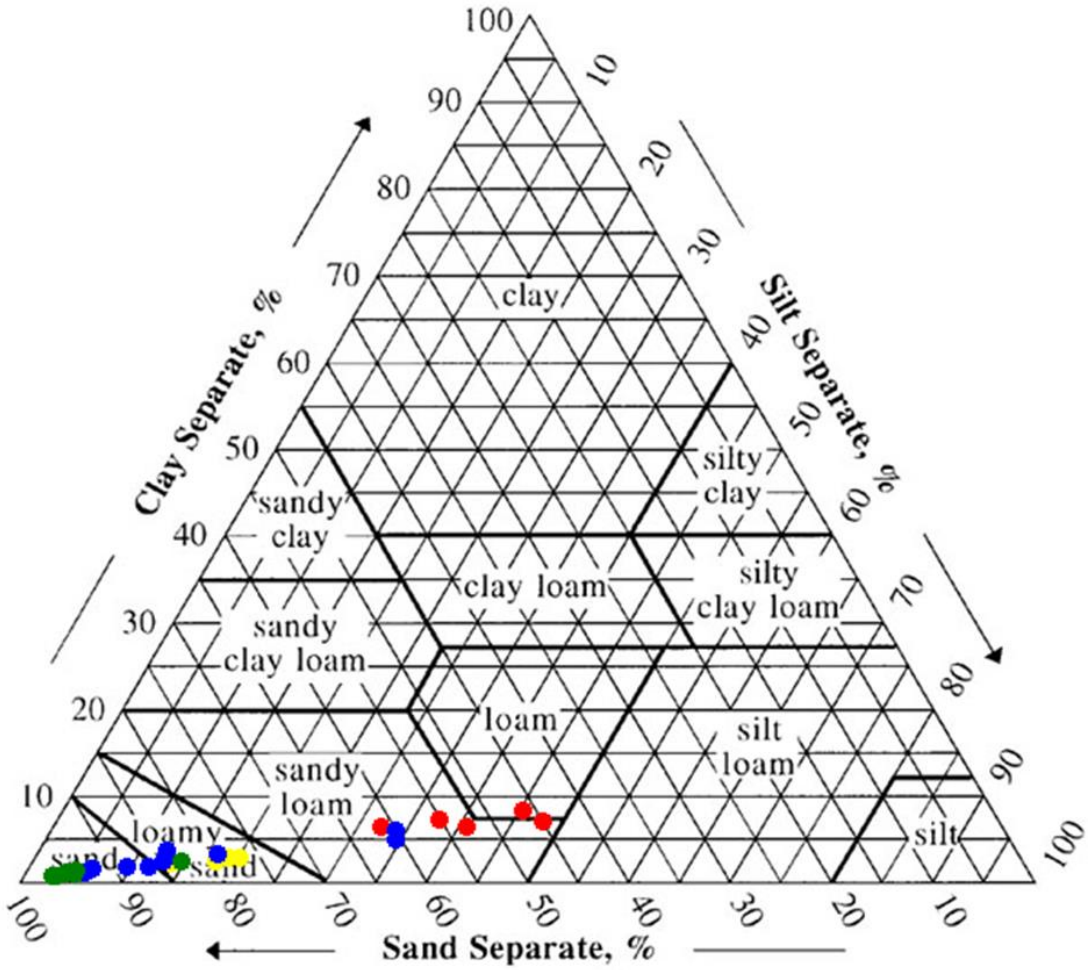


Fig. 5.3. USDA soil texture triangle showing samples from the aquitard (red dots; samples between 57.051 and 58.980 m AHD), transition between the aquitard and the coarser-grained aquifer (yellow dots; samples between 55.917 and 56.760 m AHD), the upper aquifer (blue dots; samples between 55.030 and 55.760 m AHD), and the lower aquifer (green dots; samples between 53.160 and 54.710 m AHD) in the petrol station site.

Table 5.1. Classification of samples according to the USDA and USCS systems.

Sample ID	USDA classification					USCS classification			
	Clay	Silt	Fines	Sand	Code	Fines	Sand	Gravel	Code
PB13-C 58.980 m AHD	5.77	31.75	37.52	62.48	Sandy loam	34.27	63.89	1.84	SM
PB12-C 58.906 m AHD	6.75	37.09	43.84	56.16	Sandy loam	40.67	58.47	0.85	SM
PB13-C 58.530 m AHD	7.85	44.74	52.60	47.40	Loam	47.13	50.12	2.76	SM/ML
MP44-C 57.160 m AHD	5.77	40.21	45.98	54.02	Sandy loam	46.93	53.07	0.00	SM/ML
PB39-C 57.051 m AHD	6.49	47.40	53.89	46.11	Sandy loam	56.45	43.42	0.13	ML
MP44-C 56.760 m AHD	1.59	13.01	14.60	85.40	Loamy sand	16.82	83.18	0.00	SM
PB39-C 56.401 m AHD	2.35	18.36	20.71	79.29	Loamy sand	22.73	77.27	0.00	SM
PB27-B 56.120 m AHD	1.89	17.37	19.26	80.74	Loamy sand	20.30	79.64	0.07	SM
ML32 55.917 m AHD	2.40	19.39	21.79	78.21	Loamy sand	23.28	76.33	0.39	SM
MP44-C 55.760 m AHD	0.67	4.99	5.66	94.34	Sand	6.54	93.46	0.00	SP–SM
MP50-A 55.681 m AHD	1.34	8.83	10.17	89.83	Sand	11.01	88.99	0.00	SW–SM
PB39-C 55.501 m AHD	1.26	11.10	12.36	87.64	Sand	13.94	86.06	0.00	SW–SM
PB28 55.436 m AHD	3.18	11.87	15.05	84.95	Loamy sand	12.30	82.18	5.51	SW–SM
MP50-A 55.186 m AHD	2.82	17.12	19.94	80.06	Loamy sand	20.42	79.32	0.26	SM
PB13-C 55.180 m AHD	1.92	12.12	14.04	85.96	Loamy sand	13.53	83.97	2.49	SW–SM
MP44-C 55.160 m AHD	1.05	5.58	6.64	93.36	Sand	7.03	92.70	0.26	SP–SM
ML15 55.147 m AHD	5.47	33.33	38.80	61.20	Sandy loam	38.49	61.51	0.00	SM
PB13-C 55.030 m AHD	4.46	33.76	38.22	61.78	Sandy loam	40.64	59.29	0.07	SM
PB27-B 54.710 m AHD	0.36	3.06	3.42	96.58	Sand	4.34	95.40	0.26	SP
PB39-C 54.601 m AHD	0.28	2.05	2.33	97.67	Sand	2.62	93.51	3.87	SP
ML15 54.207 m AHD	0.25	2.34	2.59	97.41	Sand	2.34	83.61	14.04	SP
PB27-B 54.160 m AHD	0.47	4.12	4.59	95.41	Sand	4.73	90.29	4.99	SP
MP44-C 53.960 m AHD	0.59	3.33	3.92	96.08	Sand	4.35	95.20	0.46	SP
MP50-A 53.886 m AHD	0.80	4.16	4.96	95.04	Sand	5.41	92.95	1.64	SP–SM
PB27-B 53.160 m AHD	1.81	14.04	15.86	84.14	Loamy sand	17.40	82.60	0.00	SM

In general, clay content decreased with depth. Right below the aquitard, a transition interval (four samples in the range 55.917–56.76 m AHD) with not more than 5 % of clay and a total of 15–21 % of fines was found as depicted in Fig. 5.2. The presence of these materials with still notable amounts of silt was frequently identified through visual inspection of cores.

LNAPL was frequently found in this interval and in coarser-grained materials under the lowest z_{aw} values. The fact that LNAPL at the interval with 15–21 % of fines was typically found under unconfined conditions (Gatsios, 2018; Gatsios et al., 2018b) indicated that this percentage of fines did not constitute a confining layer and could be considered as the upper zone of the aquifer unit. Further details about the subsurface LNAPL distribution can be found in other sections, including section 5.2.2 and section 6.4.2.

The sample from area B (56.12 m AHD) showed a smaller proportion of fine sand than in area C (13 % versus 40–48 %) and a greater percentage of coarse sand (43 % versus 1–5 %), in consonance with the observations of coarser-grained materials in areas A and B than in area C.

The rest of the aquifer exhibited low amounts of fines (2–13 % except one sample at MP50-A almost reaching 19 % and a deep sample at PB27-B with almost 15 %), becoming minimal in the interval between 53.886 and 54.71 m AHD).

Nevertheless, some low-permeability lenses with almost 40 % of fines and large amounts of fine sands were identified, for instance in samples from ML15 (55.147 m AHD) and PB13-C (55.03 m AHD). The low-permeability lenses in the aquifer and the deep sample at PB27-B could be clearly identified in Fig. 5.3 because of the distinct texture compared to other samples from the same intervals. On the contrary, a few short high-energy periods with presence of gravel fractions up to 21.4 % (generally below 10 %) were found, although they were uncommon and generally at the lower part of the aquifer. Gravel content was variable across the profile and almost 5 % of gravel could be observed in the shallowest samples.

5.2.1.3 Coefficients of uniformity and curvature

The variable amounts of multiple size fractions resulted in a wide range of C_u values between 2.18 and 98.34 with an arithmetic average of 23.77. In particular, the three

shallowest samples from the overlying aquitard exhibited the highest C_u values (over 75), while only eight samples corresponding to the coarser-grained materials had C_u values below 6. More specifically, the aquitard exhibited C_u values between 30.09 and 98.34, while C_u ranged between 9.61 and 34.33 in the fine sands at the top of the aquifer, between 2.68 and 26.61 in the generally medium sands found at the upper half of the aquifer, and within the range 2.18–4.64 in the generally coarse sands found at the lower half of the aquifer. Values of C_c were within the range 0.45–6.68 with an average of 2.38.

5.2.1.4 *Porosity profiles*

As illustrated in Fig. 5.4, estimates of Φ from samples collected to measure S_n were within a wide range and exhibited a great spatial variability in the vertical and horizontal scales. Even samples collected less than 2 m away from each other presented strong differences as shown in Fig. 5.4 and therefore did not give clear information for the definition of stratigraphic layers. This issue could influence the accuracy of k_{sw} estimates.

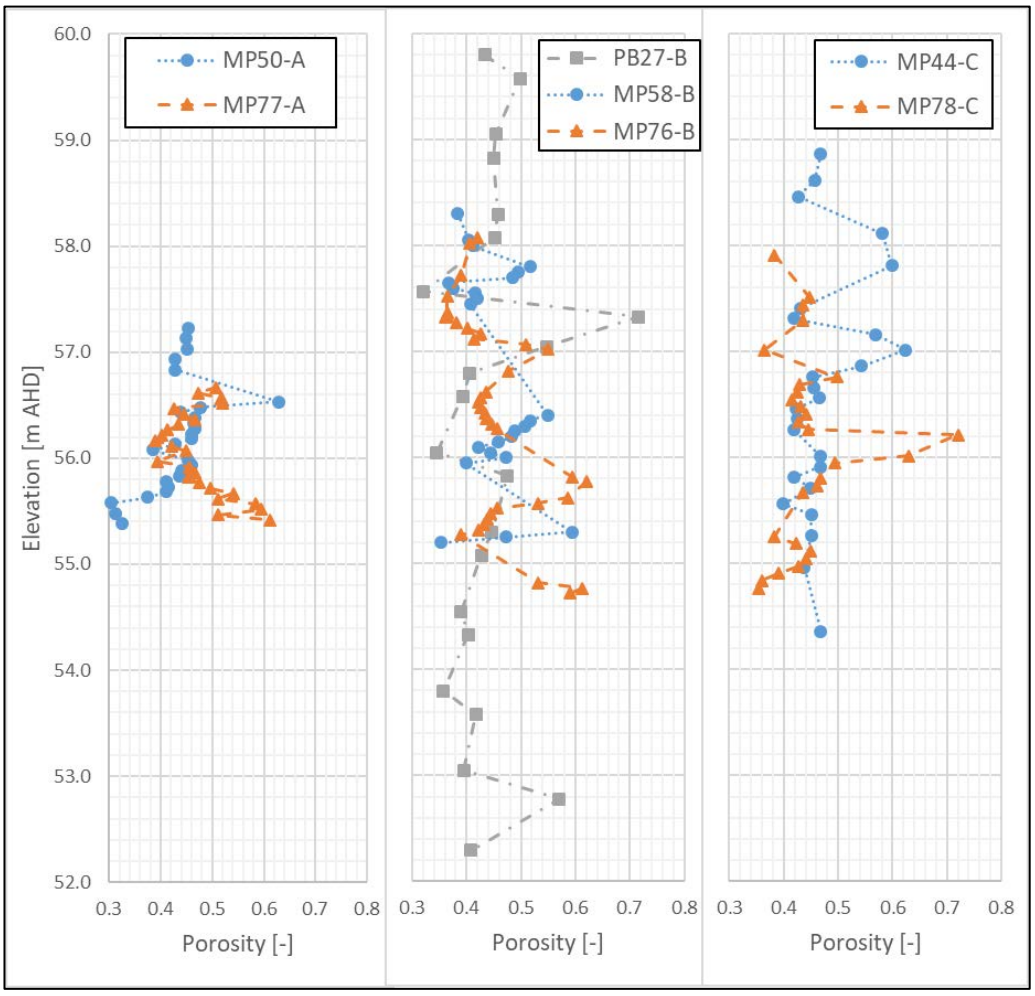


Fig. 5.4. Φ estimates from cores in areas A, B and C in the petrol station site.

5.2.1.5 *Determination of subsurface layers according to particle-size data*

According to this initial analysis of particle-size data, a three-layer model could presumably represent the main features of the LNAPL impacted area. These three layers were: (i) an overlying aquitard with a confining contact likely found between 56.76 and 57.051 m AHD according to particle-size data; (ii) a transition layer with fine-grained sand and little silt, whose contact with the rest of the aquifer could be presumed to be around 55.76–55.917 m AHD, and (iii) a coarser-grained layer with less than 13 % of fines. The aquifer materials included SP, SP–SM, SW–SM, and SM materials according to the USCS classification and sand, loamy sand, and sandy loam according to the USDA classification. A single-layer scenario considering only the properties of the transition layer or the coarser-grained layer could be also applicable for certain scenarios and time periods.

Nevertheless, the determination of hydrostratigraphic units through analysis of cores and particle-size data had limitations: (i) the number of samples for particle-size analysis was small to define location-specific stratigraphic columns; (ii) the stratigraphic information may not be enough to determine hydrogeologic units, for instance an investigator could assume that the 'transition materials' (samples between 55.8 m AHD and 56.8 m AHD) belong to the aquitard if other lines of evidence are ignored; (iii) visual descriptions of cores may be misleading (Sale et al., 2013), especially if the core recovery rate is low. Improved coring methods (e.g. Kiaalhosseini et al., 2016) and high-resolution sampling approaches (e.g. Bianchi et al., 2011) may contribute to better characterisation results from core analysis.

5.2.2 Hydrographs

Fig. 5.5 represents the hydrograph of the petrol station site between 24/06/2014 and 29/05/2018 considering (a) raw field data (1187 measurements of z_{aw}), (b) observations from CSIRO wells after excluding periods of active operations (hydraulic testing or LNAPL mass recovery) and perimeter wells (MP04, MP06, MP10, MP30, and MP31; MP37 and MP38 were still included due to their greater proximity to the source zone), and (c) same as before but also excluding observations of in-well LNAPL.

Fig. 5.5(a) shows the variability of field measurements of z_{aw} even in the same day due to ∇H_w, daily z_{aw} fluctuations, measurement errors, and the application of hydraulic testing and LNAPL mass recovery systems. Values of z_{aw} below 55.1 m AHD corresponded to observations of the creek water level.

Fig. 5.5(b) depicts a hydrograph combining 642 z_{aw} measurements from 29 wells. It revealed much better agreement between measurements at different wells after excluding observations from non-CSIRO wells (such as PB09-B whose construction details were unknown), perimeter wells, and LNAPL mass recovery trials of 2015 and 2016. This reflected the precision of measurements of in-well fluid levels, particularly between 2014 and 2016.

Most of the anomalous records in 2014–2016 (including z_{aw} values below 56 m AHD between May 2015 and June 2016) corresponded to MP07-C. Potential reasons behind these anomalous observations could have been an increase in ρ_n (which should have reached 0.9 g/cm^3), existence of a sink of anthropogenic nature (which was already a problem at MP04), or errors in the determination of the datum (although elevation surveys in 2014 and 2016 found a discrepancy of 0.008 m only). DGPs were generated with data from this hydrograph except any observations from MP07-C or when z_{nw} was above the top of the well screen.

Fig. 5.5(b) also illustrates the range of b_n values measured in the petrol station site. Maxima over 3 m corresponded to PB13-C. Correlation between b_n and z_{aw} revealed the influence of confined LNAPL conditions.

Fig. 5.5(c) depicts a site hydrograph combining 109 z_{aw} values from 17 wells (five wells with 1–2 measurements, six wells with 3–7 measurements, and six wells with 9–18 measurements). The low variability between measurements collected on the same day was indicative of the measurement precision and the low ∇H_w typically found within the source zone. Uncertainties were higher after mid-2016 due to the lower monitoring frequency and errors could still be observed on 28/04/2017 for instance.

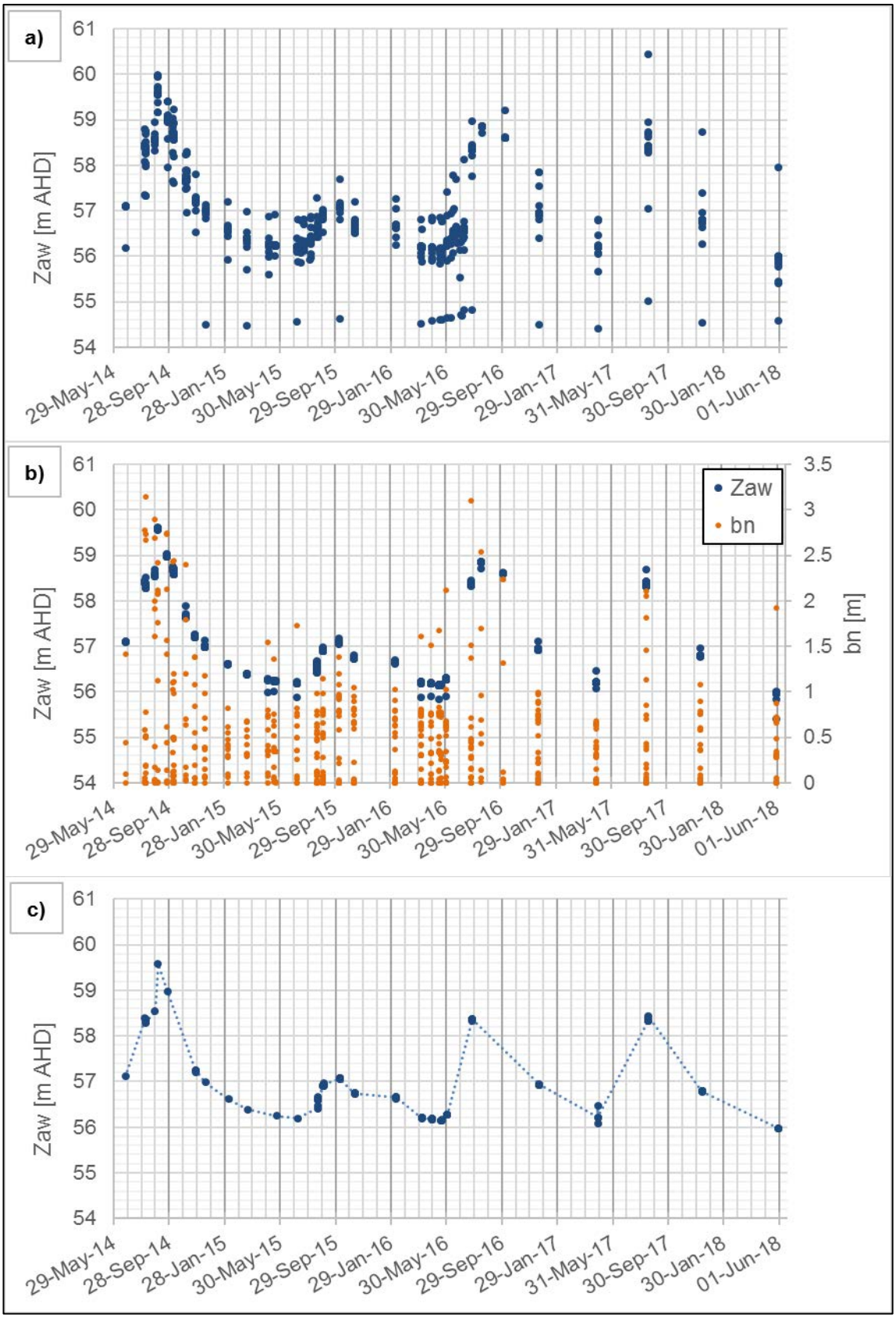


Fig. 5.5. Hydrograph of the petrol station site between 24/06/2014 and 29/05/2018, including (a) raw data, (b) observations from CSIRO wells after excluding perimeter wells and periods of active operations, and (c) same as above but also excluding observations of in-well LNAPL.

Eight periods of quasi-monotonic raising and falling z_{aw} conditions were monitored. Annual fluctuations of more than 3 m were recorded. One exception was the dry year of 2015 when the maximum z_{aw} (reached on 08/10/2015) was 2 m lower than in other years. The measurement frequency was higher in the first four periods (between 2014 and mid-2016), whose start and end dates are summarised in Table 5.2.

Table 5.2. Periods of quasi-monotonic raising or falling z_{aw} with higher measurement frequency in the petrol station site.

ID	z_{aw} conditions	Start date	End date
1	Raising	24/06/2014	03/09/2014
2	Falling	03/09/2014	14/07/2015
3	Raising	14/07/2015	08/10/2015
4	Falling	08/10/2015	20/05/2016

The HRSC campaign was conducted between 17/05/2016 and 20/05/2016, when z_{aw} was approximately between 56.14 and 56.17 m AHD in the LNAPL-impacted area. A LNAPL mass recovery trial took place between 15/06/2016 and 08/07/2016. Therefore, observations during fluctuation period 5 could have been influenced by these operations.

Fig. 5.6 shows the hydrograph of wells PB29-A, PB27-B, and PB40-C (which were more frequently monitored and tested than others) for fluctuation periods 2–4 after they were installed. There was good agreement between measurements of z_{aw} at different locations. PB40-C exhibited higher values of b_n than the others. PB29-A and PB27-B followed a similar behaviour, especially between February and September 2015 and after April 2016. The first measurements after installing the wells could have been the ones with more errors due to non-equilibrium conditions or lack of development.

Regarding the LNAPL body, b_n records sporadically exceeded 3 m under high z_{aw} values (confined LNAPL conditions), although were generally below 1 m. In average, z_{an} and z_{nw} were found at 56.9 and 56.4 m AHD, respectively (considering observations of LNAPL in wells installed by CSIRO excluding MP07-C and measurements with z_{nw} above the top of the screen). The 5th and 25th percentiles of z_{nw} were 55.6 and 55.9 m AHD, respectively, while the 75th and 95th percentiles of z_{an} were 57.1 and 59.0 m AHD. Further details

about the subsurface LNAPL distribution can be found in chapter 6, in particular section 6.4.2.

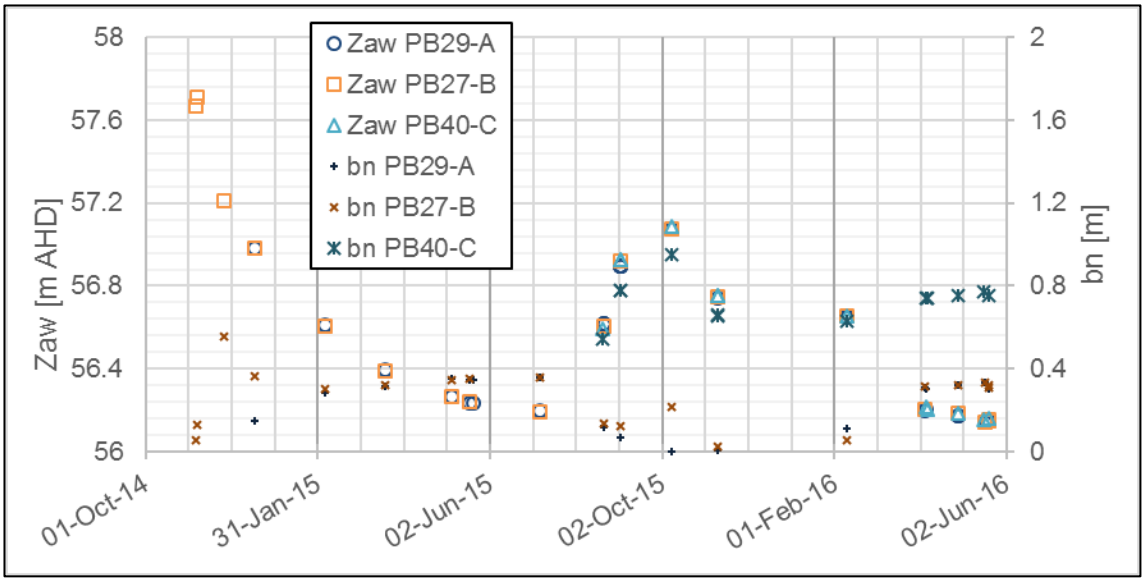


Fig. 5.6. Hydrograph of wells PB29-A, PB27-B, and PB40-C during fluctuation periods 2-4.

5.2.3 Aquifer testing

5.2.3.1 Aquifer tests under high z_{aw} conditions

WT1 was conducted at PB13-C and used MP02 and PB12-C as observation wells. As depicted in Fig. 5.7, PB13-C exhibited confined behaviour, which could be interpreted as leaky according to the last measurements of the test. A longer testing period could have provided valuable information, since this test only lasted 2.5 h. One inflection point observed after 8 min was near the top of the screen and therefore could have represented a measurement artefact.

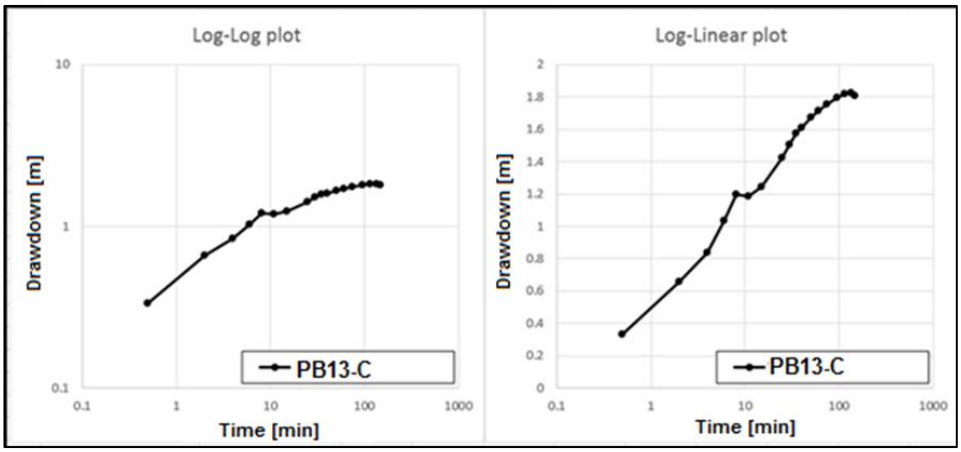


Fig. 5.7. Log-log and log-linear plots from PB13-C during WT1 (modified after Bekele et al., 2019).

As depicted in Fig. 5.8, log-log and log-linear plots of WT2 (3.4 h long) also supported the existence of a leaky confined aquifer. Constant drawdown was reached at an approximate elevation of 56.4 m AHD, which could indicate the location of the top of the aquifer at PB13-C. Thus, the confining contact elevation in this area could be deeper than in other parts of the petrol station site.

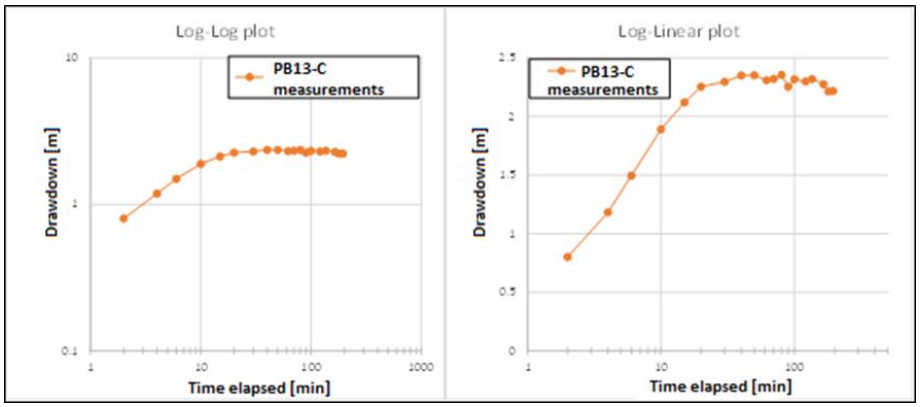


Fig. 5.8. Log-log and log-linear plots from PB13-C during WT2 (modified after Bekele et al., 2019).

Furthermore, Fig. 5.9 revealed that the Cooper-Jacob solution for confined aquifers exhibited worse fit with measurements from PB13-C during the drawdown phase of WT1 than Butler (for confined aquifers with non-uniform properties) and Hantush (for leaky confined aquifers with aquitard storage) solutions using drawdown and recovery data. The great fit with the Butler model suggested that lateral heterogeneity could have been an important factor in area C. Observation wells exhibited a similar behaviour. Solutions for leaky confined aquifers also presented a great fit with WT2 data and estimated specific storage values suggested the presence of plastic clays (see Bekele et al., 2019).

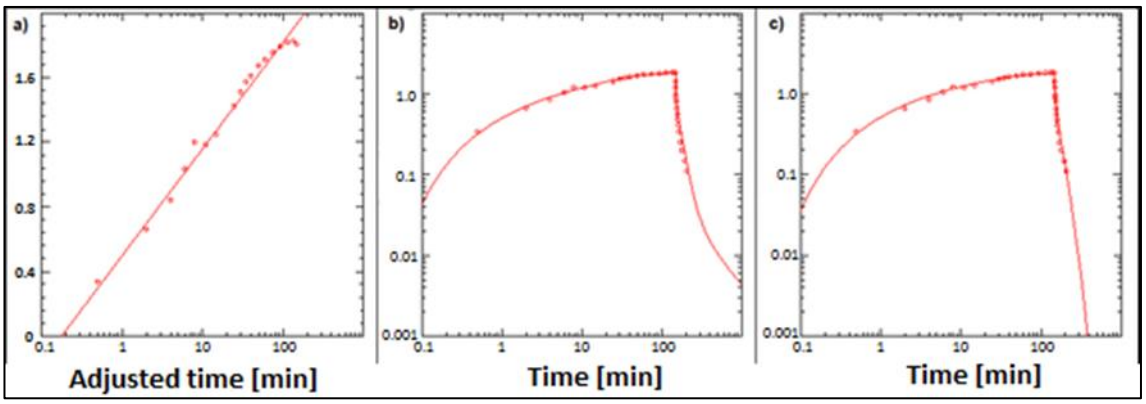


Fig. 5.9. Fit of data observed at PB13-C during WT1 with (a) Cooper-Jacob, (b) Butler, and (c) Hantush solutions (modified after Bekele et al., 2019).

5.2.3.2 *Aquifer tests under low z_{aw} conditions*

WT28 and WT29 were performed at PB29-A using multiple observation wells (between five and seven) from areas A and B and surroundings. As shown in Fig. 5.10, log-log and log-linear plots did not clearly reflect the confinement conditions during WT28 (similar in the case of WT29). The quality of the measurements could have been affected by the complexity of the multiphase recovery process (water-enhanced recovery extracting water and LNAPL through a dual pump system). According to stratigraphic descriptions and particle-size analyses, z_{aw} was located near the top of the aquifer fining-upward sequence, which could have also influenced the observations.

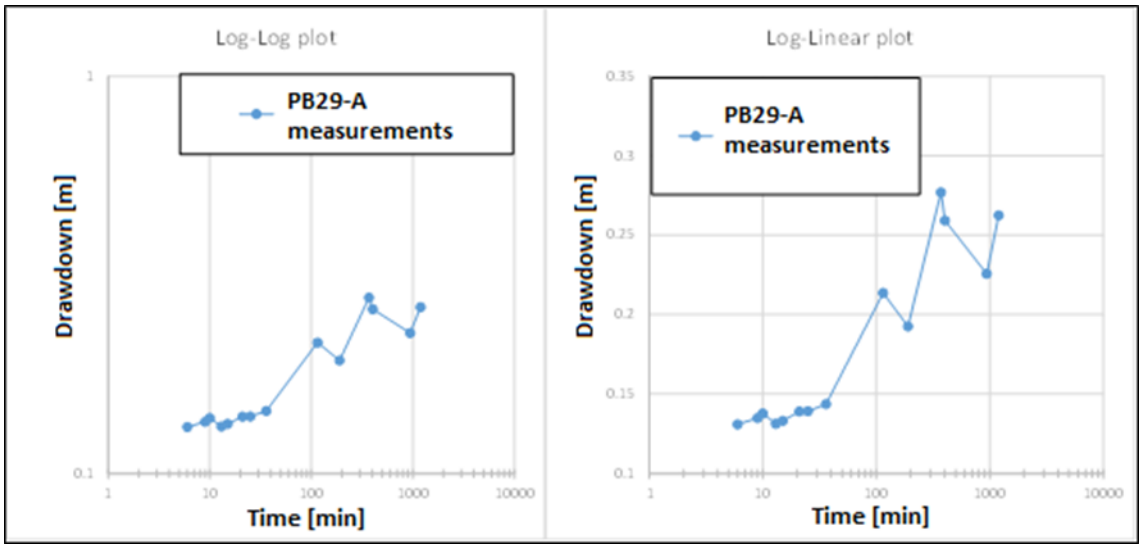


Fig. 5.10. Log-log and log-linear plots at PB29-A during WT28 (modified after Bekele et al., 2019).

As depicted in Fig. 5.11, the application of Tartakovsky–Neuman and Moench–Prickett solutions resulted in similar model fits, likely indicating unconfined conditions since Moench–Prickett presents negligible conversion effects and imperceptible shift from Theis solution when z_{aw} is close to the confining contact (Moench and Prickett, 1972). However, a transition from confined towards unconfined conditions could not be discarded (Bekele et al., 2019) and additional lines of evidence should be assessed.

Similarly, WT27 and WT30 corresponded to water-enhanced recovery operations at PB40-C and counted with manual and pressure transducer recordings (with a few anomalous values near the end of the test) as well as nine observation wells (MP07-C, MP08-C, MP41-C, PB05, PB11-C, PB12-C, PB13-C, PB26, and PB39-C) where manual measurements were collected. As illustrated in Fig. 5.12, log-log and log-linear plots

from both tests were dissimilar, with observations at PB40-C not clearly depicting unconfined conditions during WT27. Nevertheless, monitoring data from observation wells during WT27 and especially plots from WT30 supported the existence of unconfined conditions.

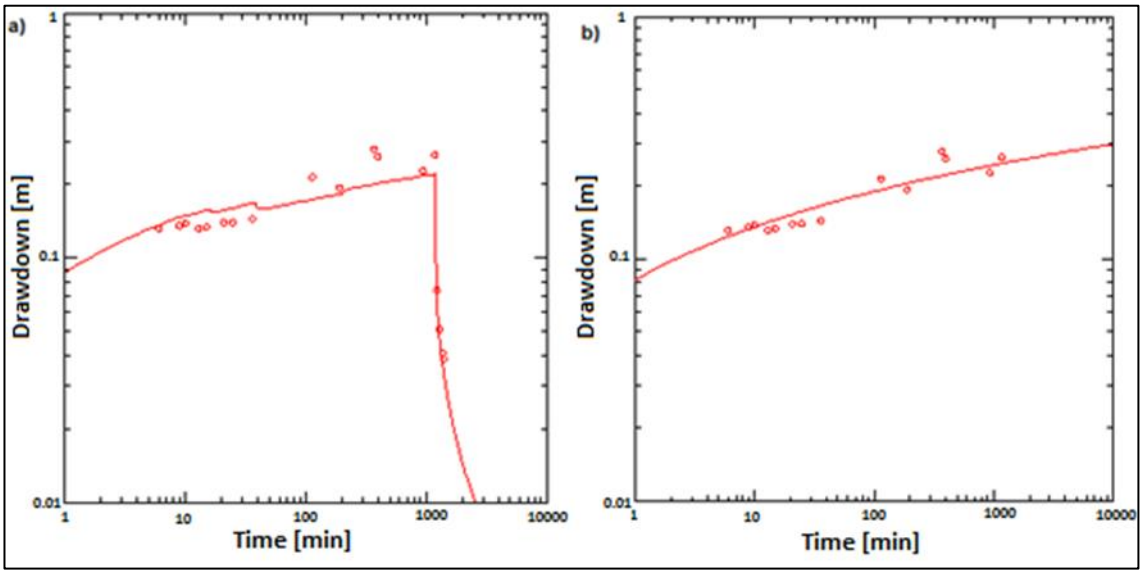


Fig. 5.11. Fit of observed data at PB29-A during WT28 with (a) Tartakovsky–Neuman and (b) Moench–Prickett solutions (modified after Bekele et al., 2019).

This was most likely due to the different pumping rates employed in the tests and the duration of the experiments. WT27 presented an average pumping rate of 0.04 L/s during 25.1 h, while the pumping rate in WT30 was 0.1 L/s during a period of 54 h. The maximum drawdowns were 0.21 and 1.21 m during WT27 and WT30, respectively.

Fig. 5.13 shows that there was good agreement between WT27 measurements and both Tartakovsky–Neuman (for unconfined aquifers) and Hantush (for leaky confined aquifers) solutions. This case again exemplified the necessity of using multiple lines of evidence. The Moench model for unconfined aquifers provided a satisfactory match to data from WT30, although some anomalies were observed (Bekele et al., 2019).

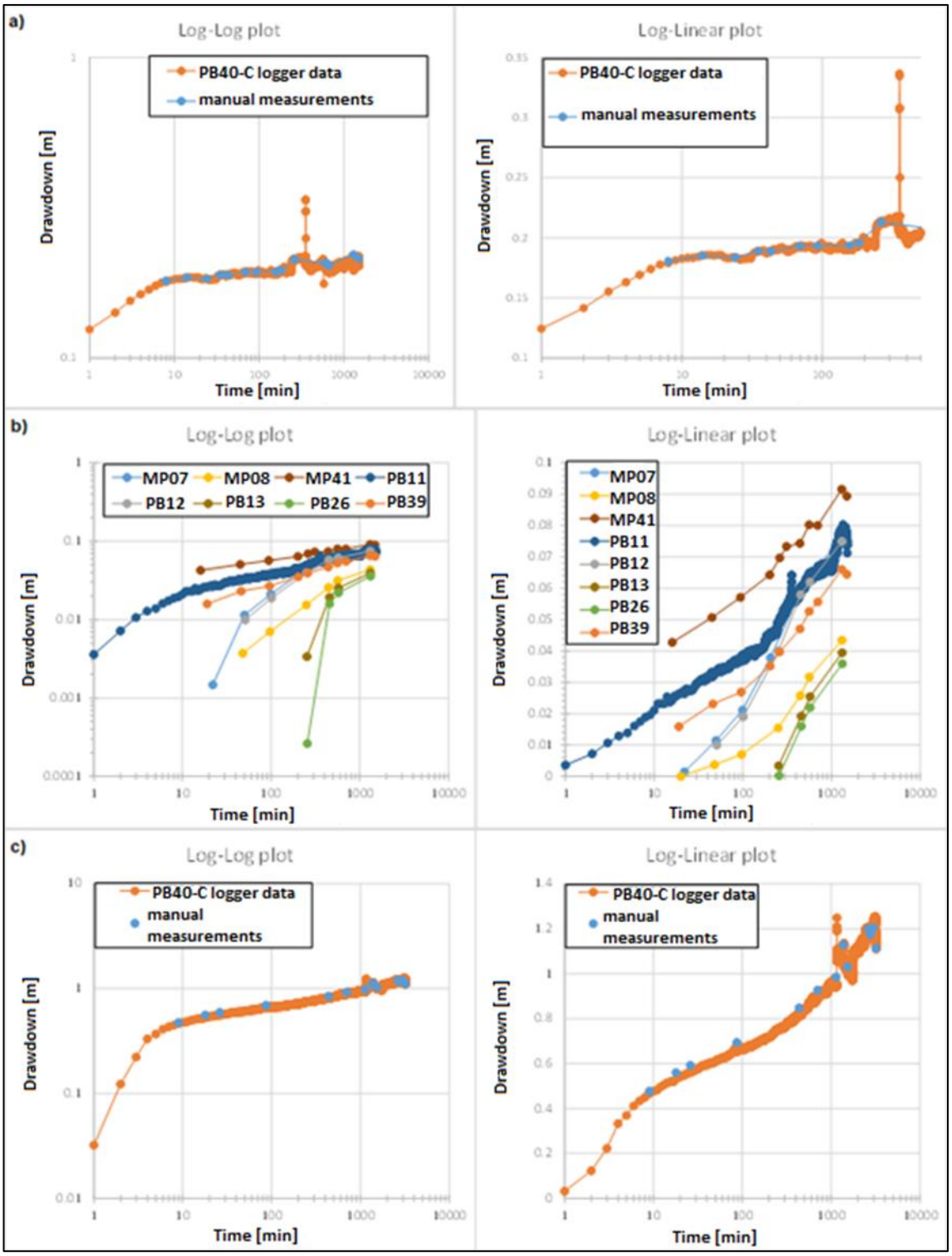


Fig. 5.12. Log-log and log-linear plots at (a) PB40-C during WT27, (b) observation wells during WT27, and (c) PB40-C during WT30 (adapted from Bekele et al., 2019).

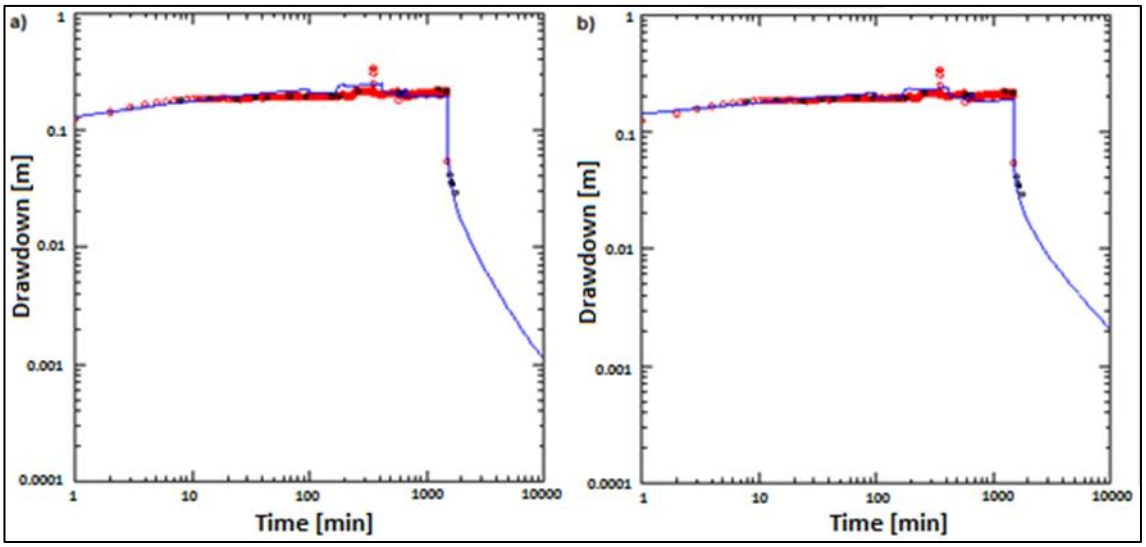


Fig. 5.13. Fit of observed data at PB40-C during WT27 with (a) Tartakovsky–Neuman and (b) Hantush solutions (adapted from Bekele et al., 2019).

5.2.3.3 Aquifer tests under intermediate z_{aw} conditions

WT15 was a constant-rate pumping test conducted at PB39-C using eight observation wells (MP03-C, MP07-C, MP08-C, MP41-C, PB11-C, PB12-C, PB13-C, PB40-C). Initial z_{aw} before the start of the test was 56.72 m AHD and thus it was within the predicted range where the confining contact for LNAPL was generally found (Gatsios et al., 2018b) and therefore the test represented 'intermediate' z_{aw} conditions. As depicted in Fig. 5.14, the behaviour observed at PB39-C indicated the presence of an unconfined aquifer. A maximum drawdown of 1.55 m was reached.

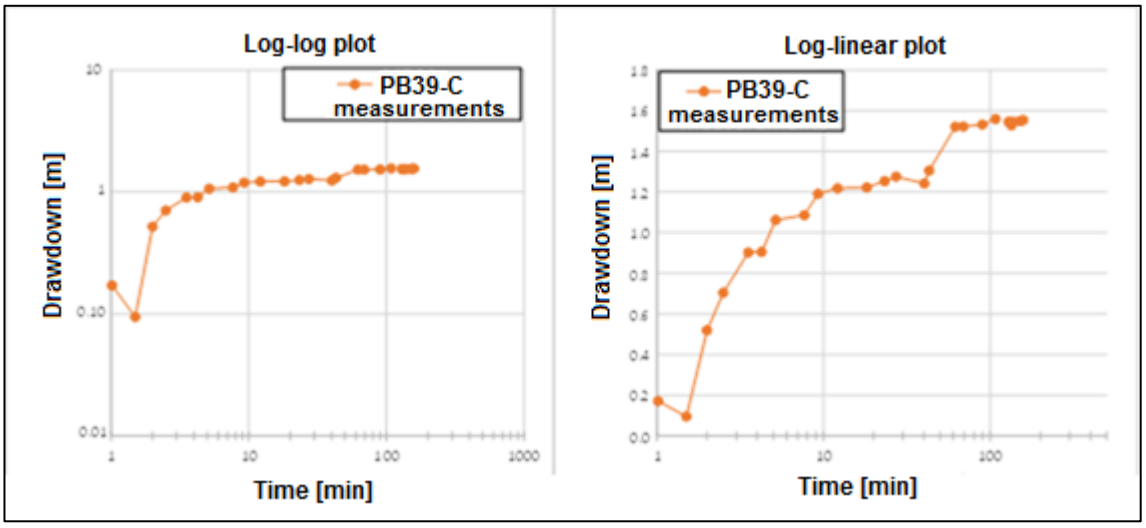


Fig. 5.14. Log-log and log-linear plots from PB39-C during WT15 (modified after Bekele et al., 2019).

Observation wells revealed different behaviours. MP03-C, MP07-C, PB11-C, and PB12-C were closer to unconfined conditions as shown in Fig. 5.15, while MP08-C, PB40-C, and MP41-C were presumably confined, supporting the existence of a variable confining contact elevation across the site. (Bekele et al., 2019). PB13-C experienced the lowest drawdown (roughly 0.03 m) and thus it was more influenced by measurement errors. None of the considered models matched well PB13-C data.

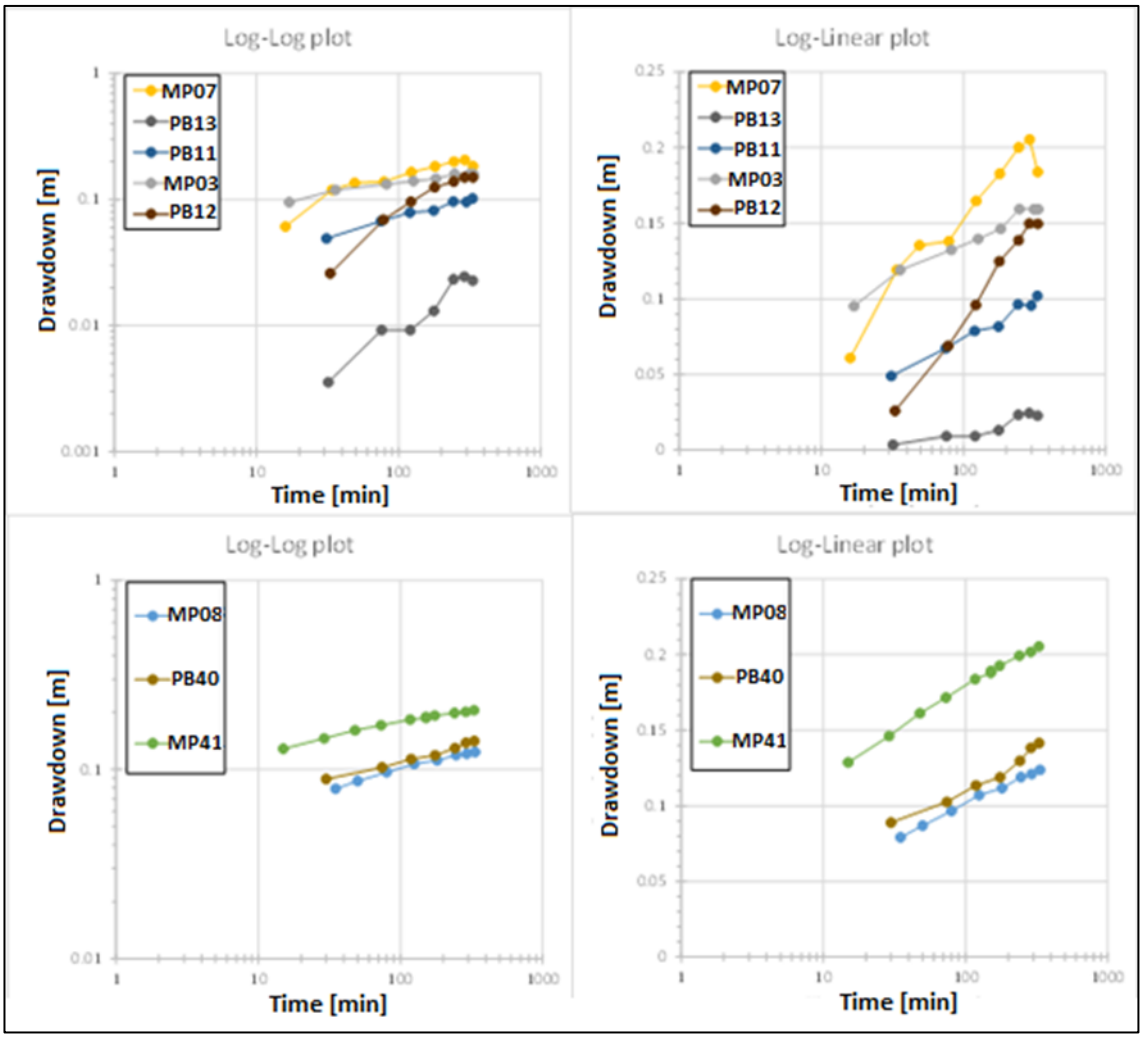


Fig. 5.15. Log-log and log-linear plots from observation wells presumably exhibiting unconfined (top panels) and confined (bottom panels) behaviour at WT15 (modified after Bekele et al., 2019).

Both sets of wells generally presented good fit with unconfined (such as Tartakovsky–Neuman) or confined solutions (such as Theis–Hantush) as illustrated in Fig. 5.16. Data from the first 3 min were not considered in the analysis because of the variability observed due to measurement errors.

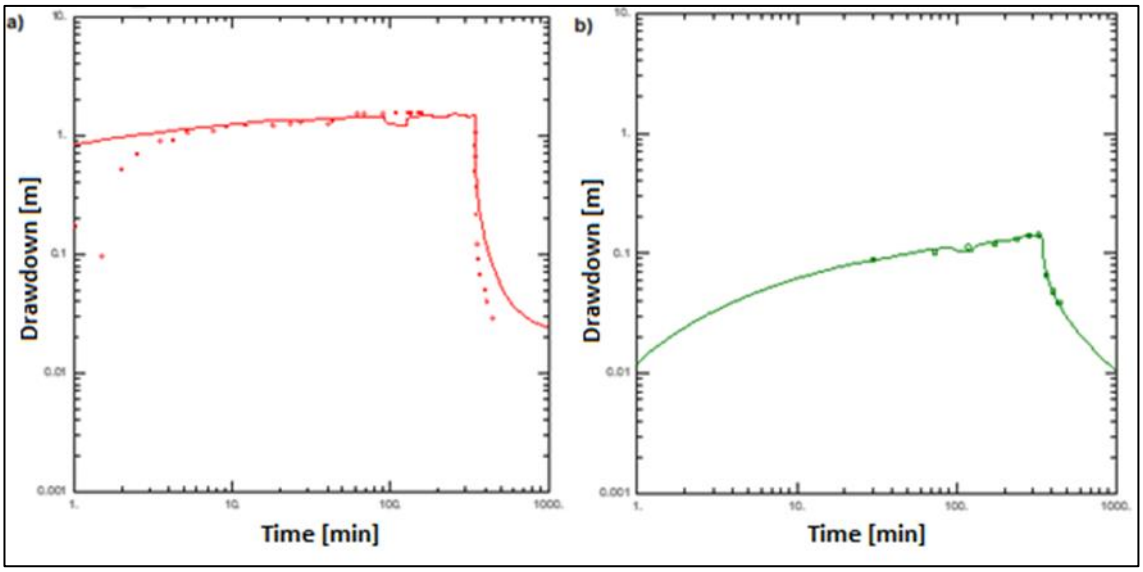


Fig. 5.16. (a) Tartakovsky–Neuman fit of PB39-C (unconfined) and (b) Theis–Hantush fit of PB40-C (confined) at WT15 (modified after Bekele et al., 2019).

Aquifer heterogeneity in area C was also reflected by multi-well plots of distance (to the pumping well) versus drawdown (of the observation wells) as illustrated in Fig. 5.17. PB39-C was aligned with MP08-C, PB11-C, PB40-C, and MP41-C in the North direction, while it was aligned with MP03-C and MP07-C in the North-West direction. PB13-C was also relatively aligned with the first group of wells.

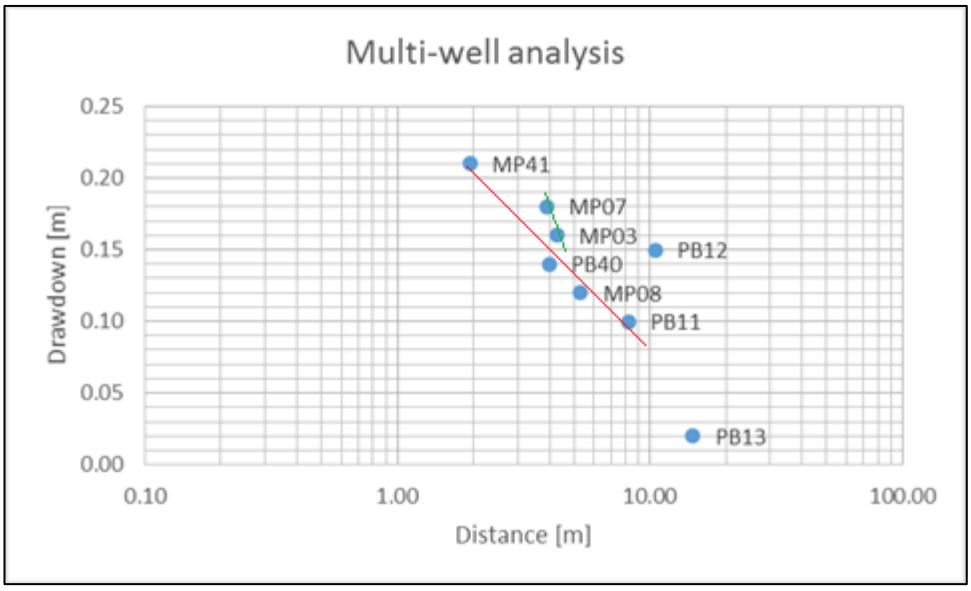


Fig. 5.17. Distance to the pumping well versus drawdown of the observation wells. Different slopes in aligned wells (red and green lines) suggested anisotropic conditions.

PB12-C maximum drawdown value was anomalous. A dissimilar behaviour at PB12-C could be suspected because it was the only well in area C that never exhibited large b_n

values, which could have been influenced by hydrogeological factors. PB12-C also presented extremely high ρ_n which could have been related to NSZD phenomena near the edge of the LNAPL body.

5.2.4 Baildown testing

Baildown testing could also give information about the subsurface stratigraphy and the confining contact elevation comparing discharge rates to LNAPL drawdown and to the elevation of fluid interfaces during the test (API, 2016). The Bouwer and Rice solution is based on the Thiem equation and therefore it assumes a linear relationship between discharge and drawdown (due to continuity of LNAPL volume within the well). If both magnitudes do not tend towards zero, it may indicate inaccuracies in the estimation of equilibrium in-well fluid levels, confining or perched conditions (when constant drawdown is observed), and borehole effects (ASTM International, 2013).

Fig. 5.18 depicts data from three baildown tests conducted at z_{aw} values corresponding to the upper zone of the aquifer unit in areas A, B, and C between 14/06/2016 and 15/06/2016. In particular, z_{aw} was found between 56.40 and 56.42 m AHD. As it could be expected, the three baildown tests indicated the existence of unconfined LNAPL conditions according to decreasing trends in both drawdown and discharge during the tests duration. Thus, baildown testing corroborated that LNAPL could be under unconfined conditions at the upper zone of the aquifer unit, where LNAPL was also located during the HRSC campaign.

The tests lasted 37, 78, and 159 min in areas A, B, and C, respectively. Similar durations were typically observed to recover the initial in-well fluid levels under low z_{aw} conditions at the three locations (less than one hour at PB29-A, around 2 hours at PB27-C, and sometimes incomplete recovery after several days in area C). Borehole effects could be clearly appreciated at PB29-A and PB40-C (discharge values over 0.2 m^3/day). Further changes in the relationship between discharge and drawdown could have been influenced by measurement errors or hydrostratigraphic features. The inclusion of Q/P logs clearly supported that LNAPL was found within a more transmissive interval at PB29-A than at PB27-B and PB40-C. Complimentary use of automatic logging systems could improve the collection and analysis of baildown testing data.

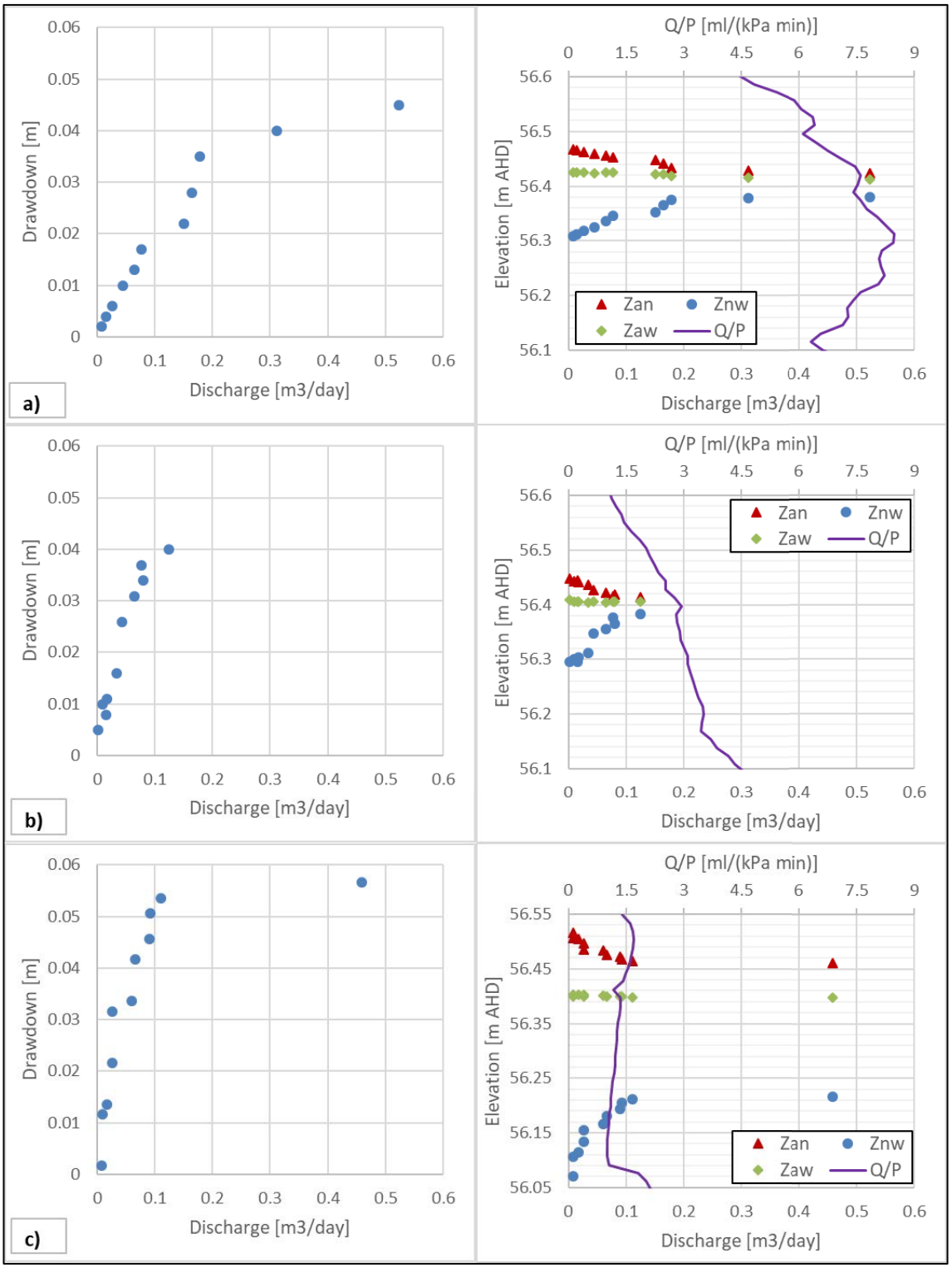


Fig. 5.18. Discharge vs. drawdown (left panels) and discharge vs. fluid interface elevations (right panels) during baildown tests at (a) PB29-A on 15/06/2016, (b) PB27-A on 14/06/2016, and (c) PB40-C on 14/06/2016. Q/P logs correspond to (a) HPT73-A, (b) HPT74-B, and (c) PB40-C through IDW of values from HPT59-C, HPT60-C, and HPT62-C corrected for atmospheric pressure.

In general, the fall in LNAPL recovery as LNAPL migrated upwards throughout the fining-upward sequence impeded the effective analysis and interpretation of baildown tests near the confining contact and therefore could not contribute to the evaluation of the confining contact elevation. Further details about the analysis of baildown tests in the petrol station site can be found in Gatsios (2018) and Gatsios et al. (2018b).

5.2.5 Analysis of LNAPL diagnostic gauge plots

5.2.5.1 Unconfined LNAPL conditions in area A

Section 5.2.5 presents single- and multi-well DGPs in the petrol station site with three goals: (i) perform a critical analysis on the applicability of these tools, (ii) test if considering individual fluctuation periods may facilitate the interpretation of DGPs, and (iii) use DGPs as a line of evidence to determine the confining contact elevation (which could be compared to outcomes from other techniques such as HPT in the following section). Details about the fluctuation periods considered are in section 5.2.2.

DGPs from PB29-A are shown in Fig. 5.19 and Fig. 5.20. In previous works, DGPs were not found to indicate confined LNAPL conditions at PB29-A in years 2014–2016. Data from monitoring campaigns conducted in 2016–2018 did not reveal unambiguously confined LNAPL conditions at PB29-A either as illustrated in Fig. 5.19(a).

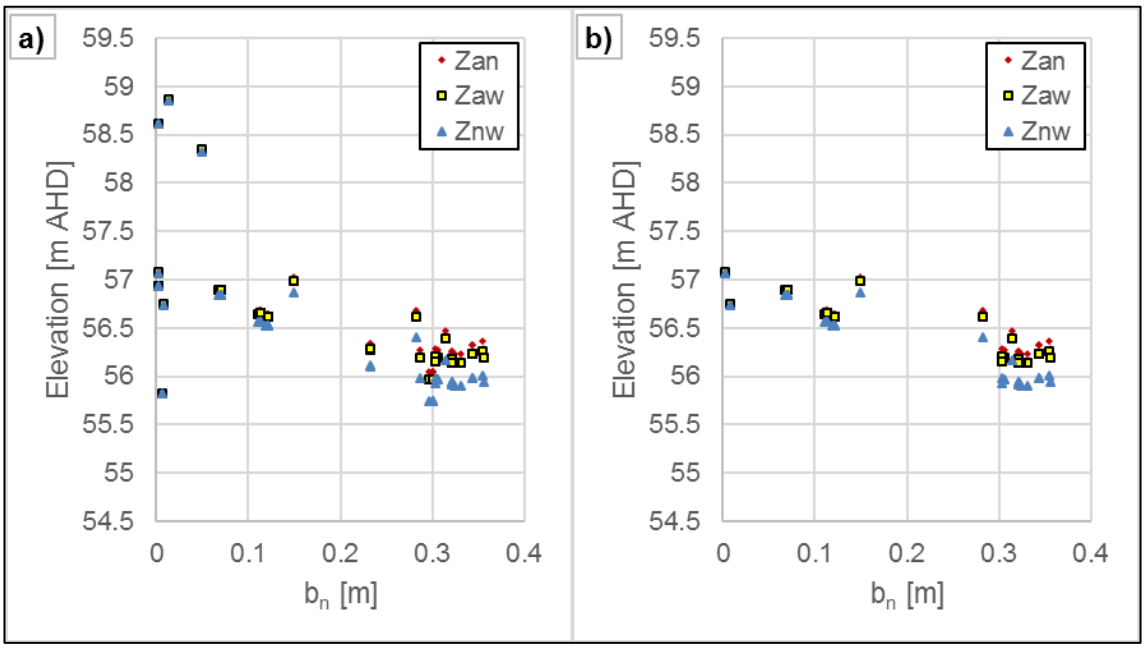


Fig. 5.19. DGPs of PB29-A including data until (a) 2018 and (b) the end of the fourth fluctuation period (20/05/2016).

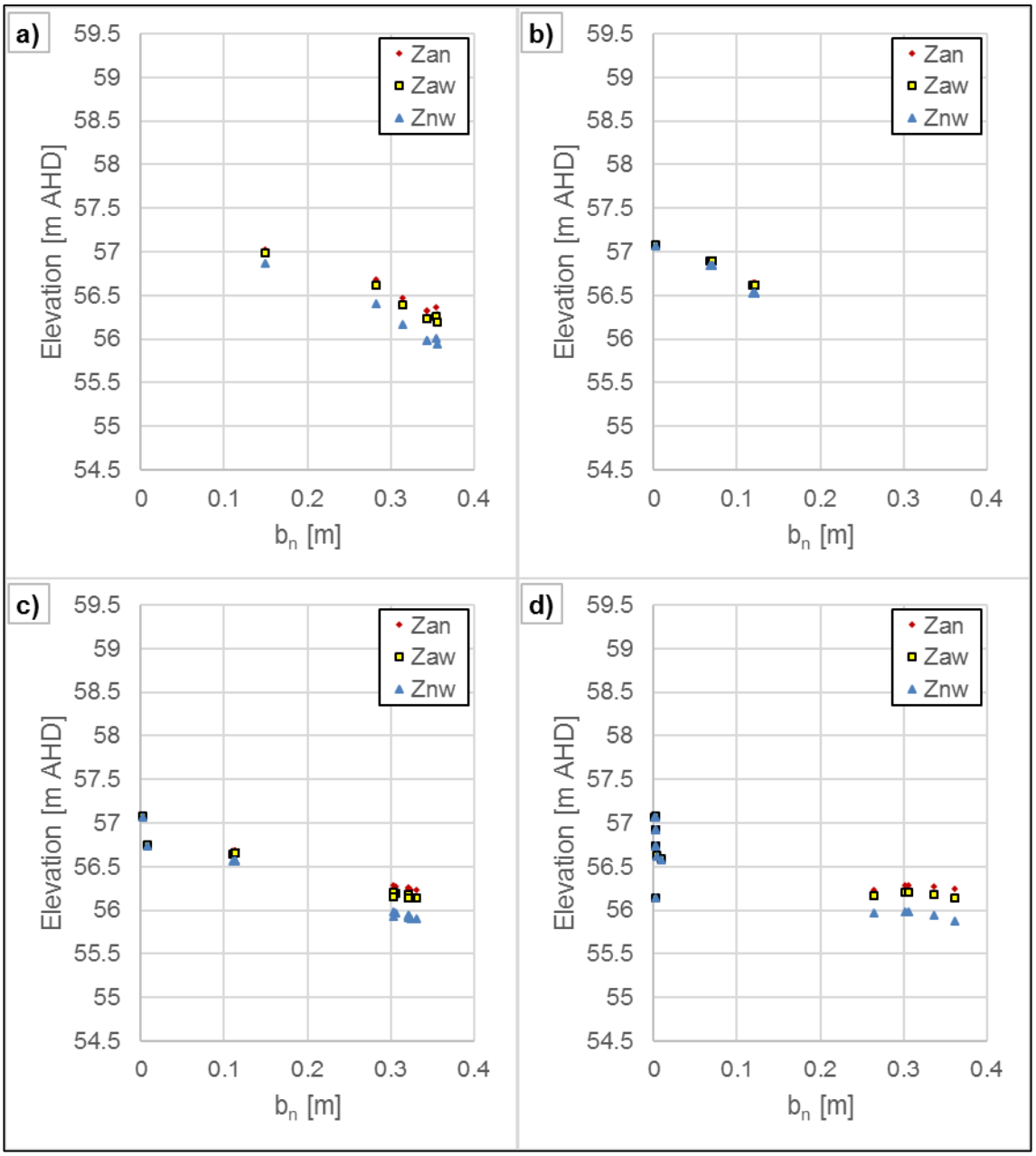


Fig. 5.20. DGPs of PB29-A for fluctuation periods (a) 2, (b) 3, and (c) 4 as well as (d) data from other wells (PB33-A, MP34-A, MP50-A) in area A until 20/05/2016.

Fig. 5.19(a) depicts a few anomalous records (for instance, positive b_n values above 58 m AHD), likely reflecting measurement errors or non-equilibrium conditions. These observations commonly corresponded to measurements from fluctuation periods 5 to 8 (from 20/05/2016 to 2018) when sampling frequency was low and fluctuations in z_{aw} were strong. As shown in Fig. 5.19(b), data collected prior to fluctuation period 5 did not reveal so many anomalies. Unconfined LNAPL conditions were dominant according to

the pattern followed by z_{an}, although it was not strongly linear due to aggregation of data from multiple fluctuation periods.

As depicted in Fig. 5.20(a–c), linearity in trends of z_{an} during monotonic fluctuation periods was higher than considering the entire monitoring period. Inverse relationship between b_n and z_{aw} (characteristic of unconfined LNAPL behaviour) could be observed up to 56.9 m AHD during fluctuation period 3 (increasing water table conditions). The measurement at 57.0 m AHD was the first collected after installing PB29-A and could not be used to unambiguously determine LNAPL hydrogeologic conditions. As shown in Fig. 5.20(d), neighbouring wells from area A did not suggest the existence of confined LNAPL either. Absence of recoverable LNAPL under confined conditions could have been caused by the low b_n values found at PB29-A (and area A in general) or the coarser-grained materials presumably found in this area.

5.2.5.2 LNAPL confinement at PB27-B in area B

Fig. 5.21 depicts DGPs generated with data collected at PB27-B. As illustrated in Fig. 5.21(a), linear regression of z_{nw} values between 56.714 m AHD and 56.914 m AHD (five records) exhibited a negligible slope (-0.01). For the same set of observations, z_{an} followed a slope of 1 and z_{aw} followed a slope of 0.73. These values were consistent with confined LNAPL behaviour given the existing measurements of ρ_{rn} and equation 4.7. The intersection between linear models of z_{an} values associated to this potentially confined period and deeper measurements of z_{an} was calculated at 56.79 m AHD.

However, there were uncertainties associated to this interpretation as reflected by two aspects. First, aggregation of data from multiple fluctuation periods (from the well installation date until 20/05/2016) hampered unambiguous identification of observations representing potentially unconfined or confined LNAPL. Some of the five records analysed could have corresponded to unconfined LNAPL periods. If the point exhibiting the lowest b_n value (0.025 m) was assumed to represent unconfined LNAPL, the intersection between linear models would have been computed at 56.84 m AHD.

Second, z_{nw} was not constant but varied within a 0.2-m interval and MAE was relatively high (0.06 m) in the three linear regression models (the low R^2 value of the z_{nw} model was explained by its negligible slope). These two issues could have been due to multiple

reasons including measurement errors, non-equilibrium conditions, and data aggregation artefacts. Similar high variations in z_{nw} can be seen in examples of confined LNAPL reported in the literature (Kirkman et al., 2013).

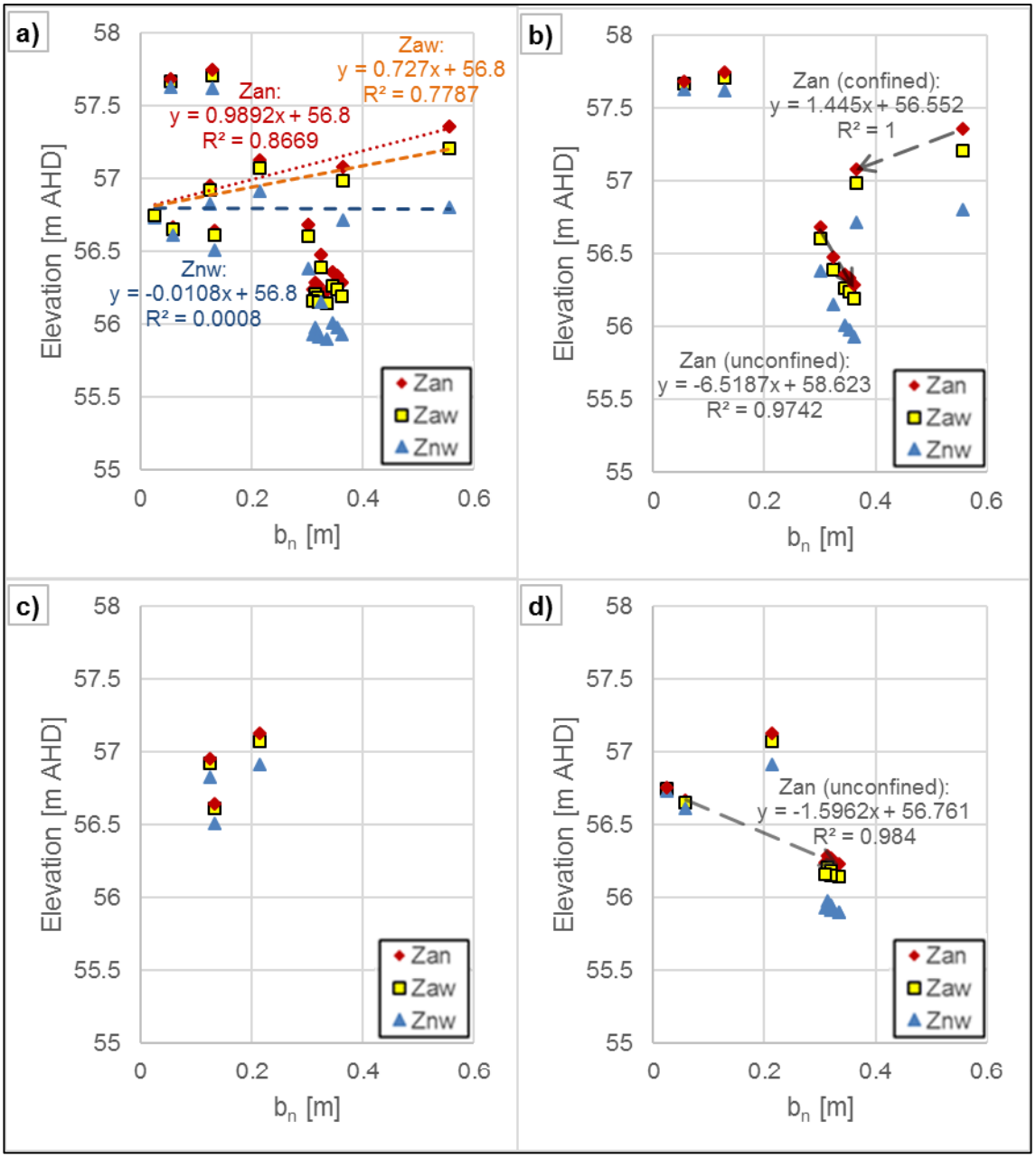


Fig. 5.21. DGPs of PB27-B with data (a) until 20/05/2016 (discontinuous lines correspond to linear regression models of z_{an}, z_{aw}, and z_{nw} under relatively constant z_{nw}) and from fluctuation periods (b) 2 (discontinuous lines correspond to linear regression models of z_{an} under potentially leaky confined and unconfined LNAPL periods; the arrow indicates the direction followed with time), (c) 3, and (d) 4 (the discontinuous line corresponds to the linear regression model of z_{an} under potentially unconfined LNAPL conditions; the arrow indicates the direction followed with time).

Fig. 5.21(b) shows that at least two points did not follow the same trend as the rest of observations in fluctuation period 2 (under decreasing z_{aw}). The first two measurements were collected at high z_{aw} values (over 57.5 m AHD) short after the well installation date and could have denoted non-equilibrium states. Therefore, they were not incorporated in regression models. DGPs from other wells from the petrol station site also revealed anomalous z_{nw} values over 57 m AHD, particularly when z_{aw} rose up to 57.5–59.5 m AHD during episodes of strong z_{aw} fluctuations.

The other two measurements when z_{aw} was over 56.9 m AHD displayed a decrease in b_n after a decrease in z_{aw}, which is a characteristic pattern of confined LNAPL. Ideal LNAPL confinement implies a constant z_{nw} value. However, linear regression of z_{nw} data resulted in a slope of 0.45. Analysis of DGPs may not fully elucidate the reason behind this type of LNAPL behaviour, since non-zero z_{nw} slopes could be caused by confounding factors such as measurement errors, non-equilibrium conditions, variation in retention properties with elevation, and existence of a leaky confining unit allowing partial movement of LNAPL. Therefore, investigators should always consider multiple lines of evidence.

In the petrol station site, the existence of a leaky confined aquifer was supported by other tools such as pumping test analysis. Thus, non-zero z_{nw} slopes could have been an indicator of leaky confined LNAPL conditions. The slope of the z_{nw} linear model at PB27-B was lower than the slopes of z_{an} (1.45) and z_{aw} (1.18) data.

The rest of points from fluctuation period 2 exhibited a typical trend of unconfined LNAPL behaviour, showing an increase in b_n with decreasing z_{aw}. The intersection of linear models of z_{an} data assumed to represent leaky confined and unconfined LNAPL behaviour was at 56.93 m AHD with b_n equal to 0.26 m. This was around 0.15 m higher than the confined contact elevation predicted with aggregate data.

Observations from fluctuation periods 3 and 4 were consistent with this potential confining contact elevation. However, the low number of measurements impeded accurate estimation of the confining contact elevation. The three measurements collected in fluctuation period 3 suggested the existence of unconfined and confined LNAPL patterns, although it was not possible to elucidate if the measurement at

56.92 m AHD belonged to unconfined or leaky confined LNAPL conditions. As depicted in Fig. 5.21(d), analysis of unconfined z_{an} data in fluctuation period 4 suggested that the confining contact elevation was over 56.75 m AHD. The measurement of z_{an} at 56.754 m AHD (b_n value of 0.025 m) most likely reflected unconfined LNAPL, which could not be easily determined analysing aggregate data.

Therefore, estimations of the confining contact elevation through single-well DGPs were consistent with the interpretation of stratigraphic data and supported that core samples collected between 55.917 and 56.760 m AHD did not represent a confining unit despite the increase in fines.

Analysis of monotonic fluctuation periods facilitated the identification of measurements likely representing unconfined and confined LNAPL behaviour and revealed potentially leaky confined LNAPL conditions suggested by a positive z_{nw} slope, although additional lines of evidence were needed to fully elucidate the behaviour of LNAPL in the subsurface. Patterns followed by in-well fluid levels during individual fluctuation periods exhibited a greater linearity than considering aggregate data. Values of b_n at specific elevations generally decreased between fluctuation periods, demonstrating that effects of dynamic phenomena such as LNAPL depletion, migration, redistribution, and hysteretic behaviour could occur between consecutive seasons.

There were not enough measurements in other wells from area B to properly assess LNAPL confinement by individual fluctuation periods. Wells PB35-B, MP36-B, MP58-B, and MP76-B did not exhibit two consecutive measurements with a direct relationship between b_n and z_{aw} in any fluctuation period, although the analysis of aggregate data at MP36-B suggested a confining contact around 56.75–56.80 m AHD. The use of automatic logging systems is encouraged to increase the temporal resolution of measurements and improve the interpretation of DGPs.

5.2.5.3 LNAPL confinement at PB40-C in area C

DGPs of PB40-C did not reveal unconfined LNAPL behaviour at high z_{an} values either. As depicted in Fig. 5.22(a), aggregate data showed distinct LNAPL behaviours depending on the in-well fluid levels elevation. Inverse relationship between z_{an} and b_n could be observed when z_{an} was lower than 56.5 m AHD, while direct relationship between z_{an}

and b_n could be observed when z_{an} was 56.734 m AHD (b_n equal to 0.545 m) or higher. A monotonic increase of z_{nw} with b_n existed during this later period, with z_{nw} varying between 56.189 m AHD and 56.384 m AHD (linear regression slope equal to 0.54) in a similar fashion to observations from PB27-B. Therefore, this pattern could have represented leaky confined LNAPL conditions combined with other factors.

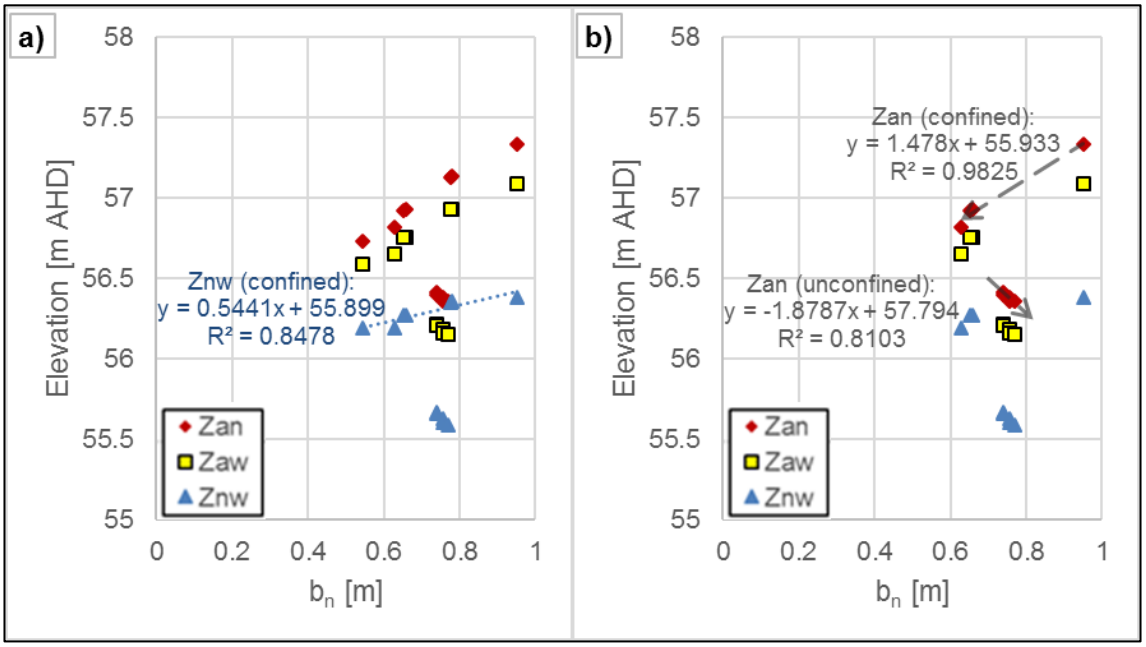


Fig. 5.22. DGP of PB40-C with data (a) until 20/05/2016 (the discontinuous line corresponds to the linear regression model of z_{nw} under likely confined LNAPL conditions) and (b) from fluctuation period 4 (discontinuous lines correspond to linear regression models of z_{an} under likely confined and unconfined LNAPL periods; the arrow indicates the direction followed with time).

As illustrated in Fig. 5.22(b), the intersection of linear models of z_{an} potentially representing the two LNAPL behaviours was determined at 56.75 m AHD (b_n equal to 0.55 m) in fluctuation period 4 (z_{nw} slope of 0.48). Alternatively, the measurement of z_{an} at 56.819 m AHD (b_n equal to 0.627 m) could have been assumed to reflect unconfined LNAPL conditions. This exemplified the uncertainty associated to the analysis procedure due to the limited temporal resolution of the measurements and the existence of non-ideal subsurface conditions. Analysis of fluctuation period 3 also suggested the existence of (semi-)confined LNAPL conditions, although this period did not include enough data to adequately evaluate the confining contact elevation.

Other wells from area C also suggested the presence of unconfined and confined LNAPL conditions with a transition point over 56.5 m AHD. However, a few wells located closer to the UST (MP02, PB05, PB13-C, and PB26) frequently exhibited direct relationship between b_n and in-well fluid levels (characteristic of confined LNAPL behaviour) at low elevations, supporting the existence of a deeper confining contact and the hypothesis of a variable confining contact elevation across the site. Fig. 5.23 depicts the DGP and hydrograph of MP02 (measurements with z_{nw} values below 57.0 m AHD) where patterns likely representing (semi-)confined LNAPL behaviour were observed for z_{an} values as low as 56.35 m AHD. This was consistent with the interpretation of aquifer test WT2 and further investigated in the analysis of HPT logs.

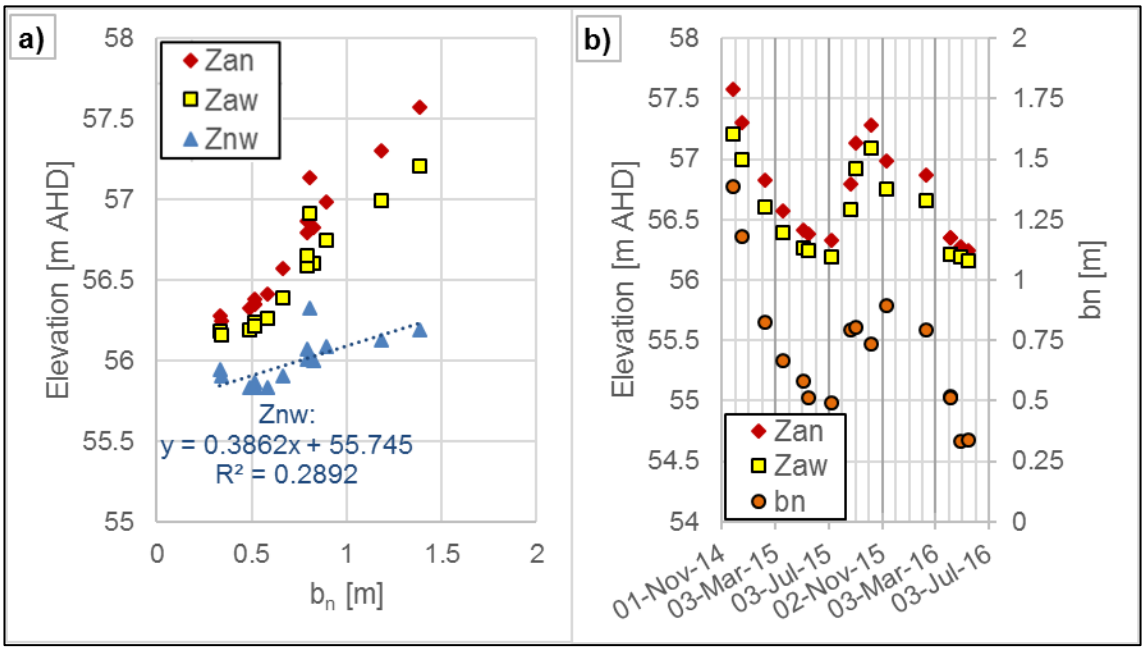


Fig. 5.23. (a) DGP and (b) hydrograph of MP02 for fluctuation periods 2–4, showing measurements with z_{nw} values below 57.0 m AHD only. One anomalous measurement from 08/10/2015 (with a b_n value of 0.734 m and z_{an} at 57.286 m AHD) was collected with a different interface probe and excluded from the DGP.

5.2.5.4 Critical analysis of multi-well DGPs as a tool to identify LNAPL transmissive zones

Multi-well DGPs depicting in-well fluid levels versus b_n have been proposed as a tool to identify LNAPL transmissive zones across an entire site as well as their hydrogeologic conditions and b_n range (Hawthorne, 2014). The objective of this section is to investigate the applicability and limitations of this tool in the petrol station site. Fig. 5.24 shows multi-well DGPs from (a) Hawthorne (2014) and (b) the petrol station site.

For illustrative purposes, Fig. 5.24(b) includes mostly unfiltered fluid level data collected in the source zone between 2014 and 2018 (the only exceptions were periods of active recovery operations and observations from MP07-C and wells not installed by CSIRO). Both multi-well DGPs exhibited multiple similarities, although also some unfiltered anomalous records.

Analogous trends with constant z_{an} and dropping z_{nw} representing the largest b_n values from both sites could be observed at the top of the multi-well DGPs. The largest b_n values in the petrol station site reached more than 3.1 m when z_{aw} was high. In periods of low z_{aw}, the maximum b_n value was 2.25 m with most of the measurements being less than 1 m.

Hawthorne (2014) was able to identify two distinct transmissive zones in the subsurface by analysing a multi-well DGP (z_{an} and z_{nw} versus b_n) with two clusters of data. Thus, he defined a deep zone and a shallow zone (including separable sub-zones). A similar interpretation of the multi-well DGP from the petrol station site could have led to discriminate between deep (approximately between 56.0 and 57.1 m AHD), intermediate (around 57.6–57.7 m AHD), and shallow zones (58.3–59.0 m AHD). However, absence of z_{aw} records between the clusters of in-well fluid level data (z_{nw} referred to z_{aw} when LNAPL was not observed in wells) indicated that these clusters were not more than an artefact derived from the frequency of monitoring campaigns and the periodically abrupt z_{aw} fluctuations.

Furthermore, measurements collected after abrupt increments in z_{aw} with z_{nw} over 57 m AHD were typically anomalous and possibly reflected non-equilibrium phenomena. Fig. 5.25 depicts an updated multi-well DGP where only gauge data of better quality were employed (connected LNAPL and z_{nw} values below 57 m AHD from fluctuation periods 1–4).

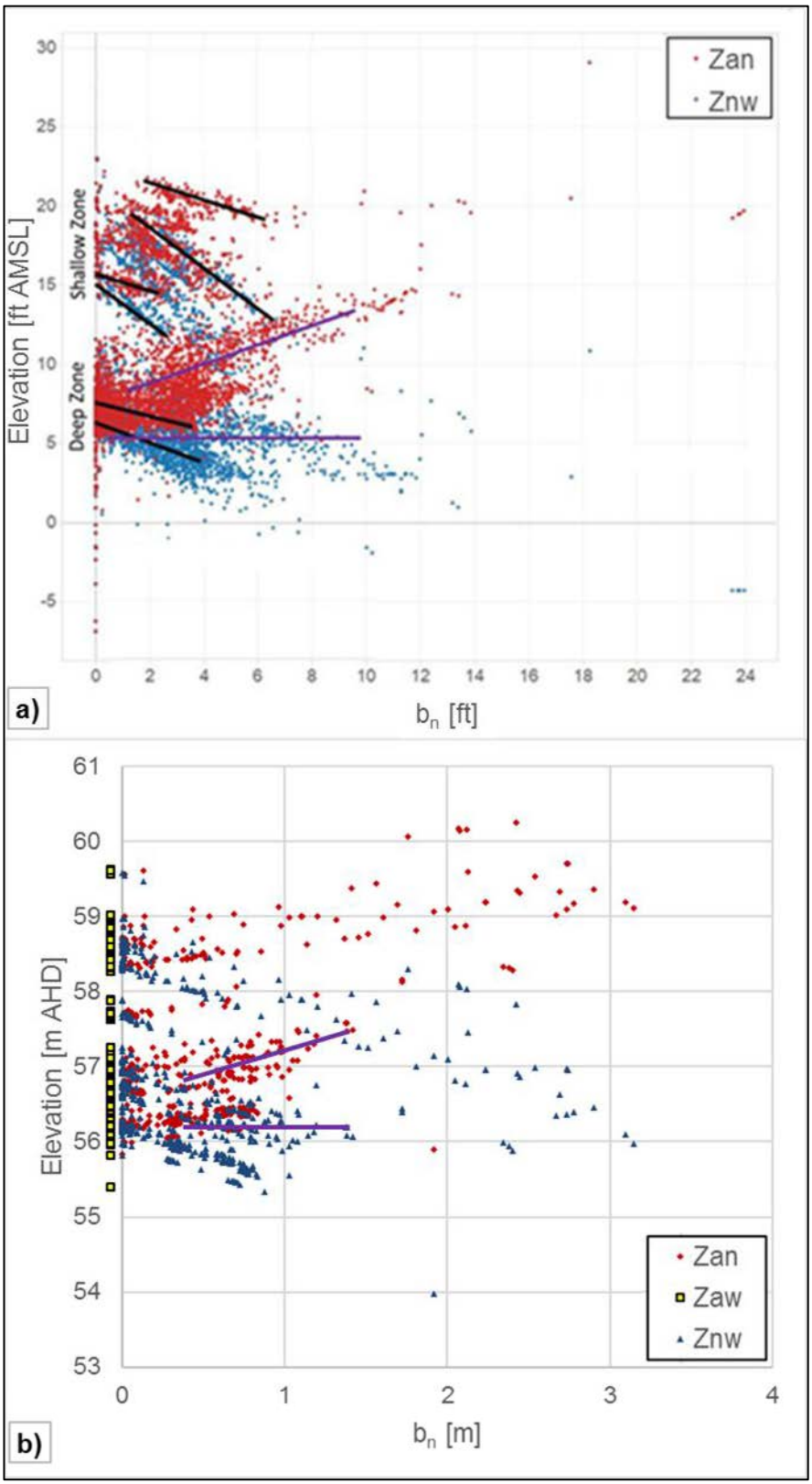


Fig. 5.24. b_n-based multi-well DGPs from (a) Hawthorne (2014) and (b) the petrol station site showing transmissive zones and hydrogeologic conditions (black and purple lines indicate unconfined and confined LNAPL conditions, respectively). Hawthorne (2014) presented elevations as ft above mean sea level (AMSL).

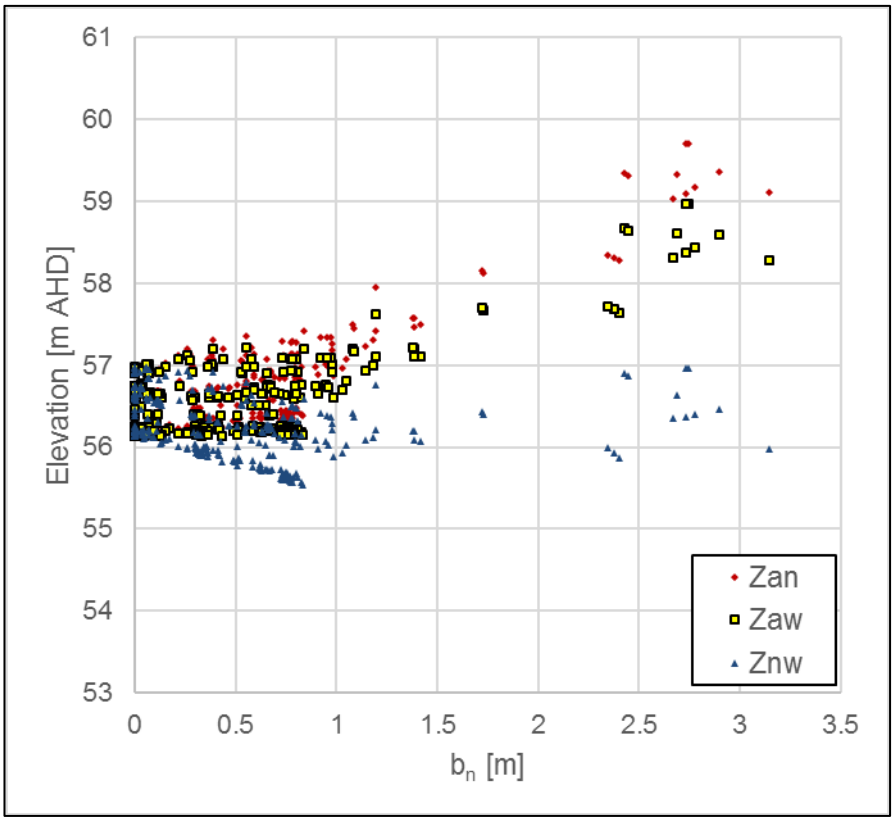


Fig. 5.25. Multi-well DGP at the petrol station site (fluctuation periods 1–4) after filtering data.

In conclusion, multi-well DGPs were a useful tool to rapidly detect ranges of b_n and in-well fluid level elevations as well as extreme data points. However, they did not allow accurate identification of separate transmissive zones with LNAPL due to methodological aspects such as the temporal and spatial resolution of field measurements in a site affected by z_{aw} fluctuations. Thus, management approaches designed according to these transmissive zones would have been ineffective. Incorporating z_{aw} data from wells with and without LNAPL in multi-well DGPs may help to identify periods without field observations, especially in small sites with low ∇H_w values such as the petrol station site. Use of automatic logging systems may also contribute to a better understanding of the subsurface.

5.2.6 HPT logging

5.2.6.1 Overview of HPT logs from the petrol station site

The 10 HPT logs collected in the petrol station site are included in Appendix D: HPT profiles. They provided a more detailed image of the heterogeneous site hydrostratigraphy than other lines of evidence. Fig. 5.26 collates five logs of HPT average

pressure and EC between the location of the UST, area A, and area B. HPT Q was generally stable around 450 mL/min and therefore HPT P could be adopted as a proxy of the Q/P ratio in many intervals. Nevertheless, HPT Q was highly variable in presumably finer-grained materials where HPT P records reached the upper limit of quantification. Thus, in these intervals, inspection of EC and HPT Q logs enhanced the interpretation of HPT logs.

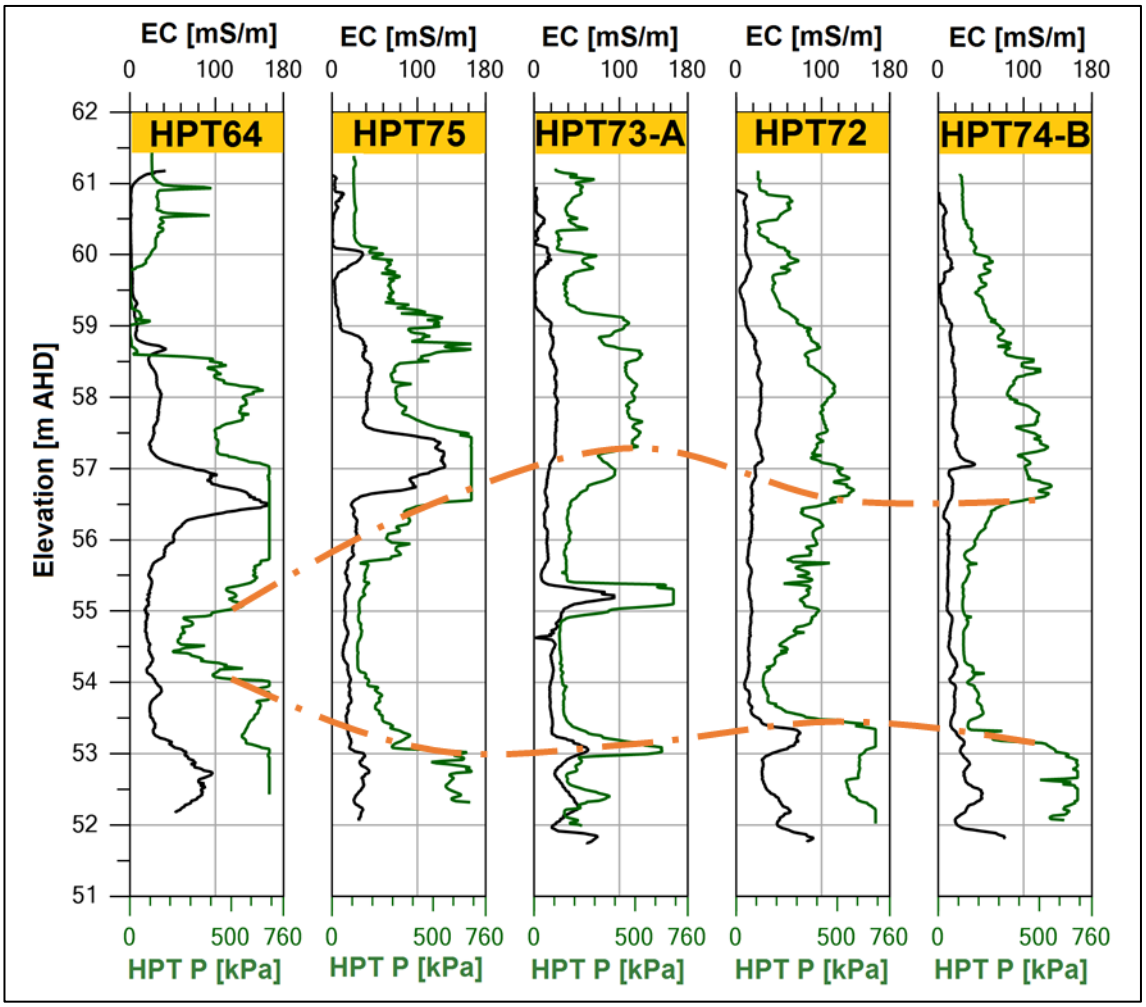


Fig. 5.26. Cross-section of HPT average pressure before correcting for atmospheric and hydrostatic pressure (green) and EC (black) logs between the UST and areas A and B. HPT64 was in the UST location, HPT75 between the UST and area A, HPT73-A next to PB29-A, HPT72 between areas A and B, and HPT74 adjacent to PB27-B. The dashed orange lines connect points of 500 kPa.

The cross-section between the UST location, area A, and area B provided evidence of the relatively coarse-grained materials in areas A and B according to relatively low HPT P and EC values. In particular, the aquitard in area A was represented by only a subtle

increase in EC with HPT P values roughly exceeding 500 kPa above 57.3 m AHD. The lack of responsiveness in EC compared to HPT P was likely due to a greater increase in the content of silts than the content of clay. Similarly, HPT P across the aquitard in area B (HPT74-B) was below 600 kPa, although the increase to 500 kPa occurred at a lower elevation (right below 56.6 m AHD), while the increase in EC was more pronounced with a peak around 40 mS/m at 57.0 m AHD.

These observations were consistent with the absence of records of confined LNAPL conditions in area A and the confining contact elevation inferred through DGPs in area B. HPT74-B also showed a minimum of EC of approximately 6 mS/m between 56.3 and 56.4 m AHD that could have been suitable as a preferential pathway of water and LNAPL flow.

On the other hand, HPT75 (located between the UST and area A) and HPT72 (located between areas A and B) showed finer-grained materials around 55.7–56.5 m AHD (where LNAPL was frequently found in the site) than logs from areas A and B. HPT logs also revealed a low-permeability lens at 55.0–55.4 m AHD in area A which could have influenced the flow field in the shallower region of the aquifer. In general, the cross-section was in accordance with the conceptualisation of the subsurface consisting of a heterogeneous sandy aquifer overlain by an aquitard (with variable amounts of fines and sands) and underlain by fine-grained materials. In addition, it supported the hypothesis of a variable confining contact elevation across the site.

As illustrated in Fig. 5.27, the cross-section between the UST location and area C corroborated the existence of finer-grained materials in area C than in areas A and B. For instance, the EC log at HPT63-C (adjacent to PB13-C) indicated the presence of low-permeability lenses between 54.5 and 56.0 m AHD as also inferred through particle-size analysis. An increase in clay was measured at 55.03 m AHD (although clay was still below 10 %, but fines and fine sands comprised more than 80 % of the sample) which could be assigned to an EC value near 100 mS/m. Furthermore, HPT P along this log was anomalously high, always over 400 kPa in the intervals of concern. These factors could have contributed to the confinement of LNAPL at relatively low elevations as inferred through the analysis of DGPs at MP02 and PB13-C.

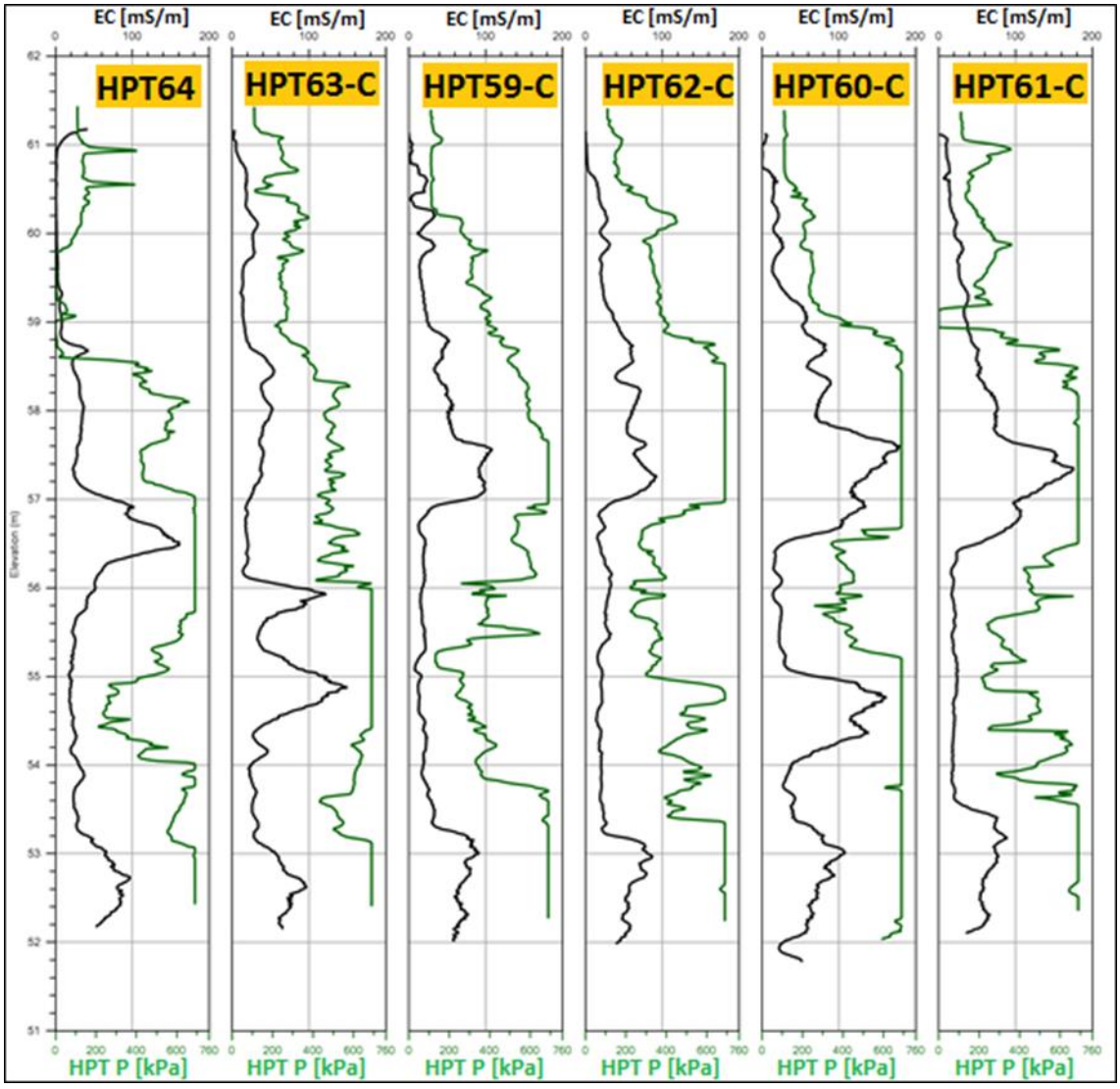


Fig. 5.27. Cross-section of HPT average pressure before correcting for atmospheric and hydrostatic pressure (green) and EC (black) logs between the UST and area C. HPT64 was in the UST location, HPT63-C adjacent to PB13-C, HPT59-C near PB11-C and PB40-C, HPT62-C Southwest of PB40-C, HPT60-C Northeast of PB40-C, and HPT61-C adjacent to PB39-C.

Moreover, HPT59-C (between PB11-C and PB40-C) and HPT62-C (adjacent to PB40-C) exhibited similar EC logs, with weaker responses than neighbouring logs and increases up to approximately 100 mS/m around 57.0 m AHD, which could also be assigned to a sample from MP44-C with more than 10 % of clay at 57.16 m AHD. Another MP44-C sample belonging to the top of the aquifer was collected at 56.76 m AHD, corresponding to increasing intervals in HPT P and EC but without reaching the limit of quantification. A difference between both profiles was that HPT P was lower between 56.0 and 57.0 m AHD at HPT62-C, consistent with PB40-C being the well with the highest T_n

estimations in area C. The heterogeneity of area C was also reflected by the comparison of HPT62-C with HPT60-C, being both logs located at practically the same distance from PB40-C. However, HPT60-C exhibited some of the strongest EC signals with HPT61-C (near 180 mS/m), suggesting high clay contents, probably over 15 % according to particle-size analyses from PB39-C.

5.2.6.2 Area A

Fig. 5.28 depicts the EC and Q/P (after correcting for atmospheric and hydrostatic pressure) logs from HPT73-A, which was adjacent to PB29-A. These recordings were consistent with the proposed CSM comprising a heterogeneous aquifer with more fines at the top (defined as a 'transition' layer in Fig. 5.28) and overlain by an aquitard. The EC log supported the relatively low measurements of clay content in the aquitard. EC records were below 30 mS/m, while clay-rich sediments frequently display more than 50 mS/m (McCall, 2011). One example of a less-permeable lens could be observed at HPT73-A below 55.4 m AHD, where EC reached almost 100 mS/m and Q/P became zero.

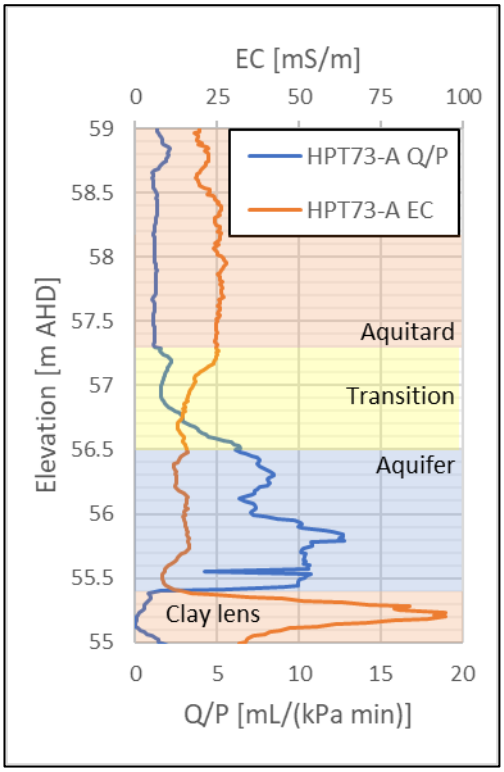


Fig. 5.28. Q/P (after correcting for atmospheric and hydrostatic pressure) and EC logs at HPT73-A (adjacent to PB29-A). The three layers depicted ('aquitard', 'transition', and 'aquifer' with occasional presence of clay lenses) represent a plausible interpretation of the hydrostratigraphy.

The identification of the confining contact elevation was not unambiguous, although it was likely above 56.5 m AHD as also supported by other lines of evidence (the analysis of DGPs suggested that it was above 56.9 m AHD). An interpretation of the HPT log without considering other areas could lead to infer a hydrostratigraphic boundary somewhere within the 'transition' layer. However, relatively high Q/P values compared to areas B and C—approximately 1.6 mL/(kPa·min) at 57.0 m AHD—could explain the absence of confined LNAPL conditions in adjacent wells. It was therefore essential to consider multiple logs and other lines of evidence in the interpretation of HPT profiles. The bottom of the aquitard was assumed to be around 57.3 m AHD because of the, respectively low Q/P, high HPT P, and high EC above this elevation. It was not clear if the aquitard materials in this area were fine-grained enough to induce confined conditions at high z_{aw} and z_{an} values.

Furthermore, the Q/P log suggested higher heterogeneity in the aquifer layer than the HPT P log. Multiple features not considered in the simplified three-layer CSM could have controlled LNAPL redistribution and migration phenomena. Thus, measurements of LNAPL presence should be added to the analysis before defining layers for modelling scenarios. For instance, the transition zone could be divided in two at 56.7 m AHD where there was a higher rate of change in EC above this elevation and a higher rate of change in Q/P below. In addition, the positive anomaly in Q/P at 55.8–58.9 m AHD or the increase in Q/P with decreasing EC at 56.2–56.4 m AHD could have reflected highly transmissive layers. High S_n values could have also influenced EC and Q/P values.

5.2.6.3 Area B

Fig. 5.29 depicts the EC and Q/P (after correcting for atmospheric and hydrostatic pressure) logs from HPT74-B, which was adjacent to PB27-B. These recordings were consistent with the proposed CSM as in the case of area A. However, Q/P and EC logs from both areas were visibly different. The decrease in Q/P associated to higher content in fines at the top of the profile occurred around 55.8 m AHD (with a deeper drop in Q/P around 55.4 m AHD) in area B instead of 56.5 m AHD as in area A. Particle-size analysis of a sample from PB27-B at 56.14 m AHD corroborated the increase in fines. This could explain the high LNAPL recoverability at PB29-A despite higher Q/P values found across

HPT74-B. Thus, this case illustrated the importance of characterising the LNAPL-impacted interval at an appropriate resolution.

HPT logging suggested that the bottom of the aquitard was likely above 56.6 m AHD where low Q/P and high EC values were found. Q/P was stable in this region, reaching a relative minimum value of 0.965 mL/(kPa·min) at 56.748 m AHD. The confining contact elevation could be as high as 57 m AHD where a less-permeable lens was detected. These observations were consistent with the interpretation of DGPs. The analysis of aggregate data suggested a confining contact elevation around 56.79 m AHD, while the analysis of data from fluctuation period 2 resulted in a confining contact around 56.93 m AHD. The three-layer model represented in Fig. 5.29 assumed that the bottom of the aquitard was around 57.0 m AHD, although considering a lower elevation would have been reasonable too.

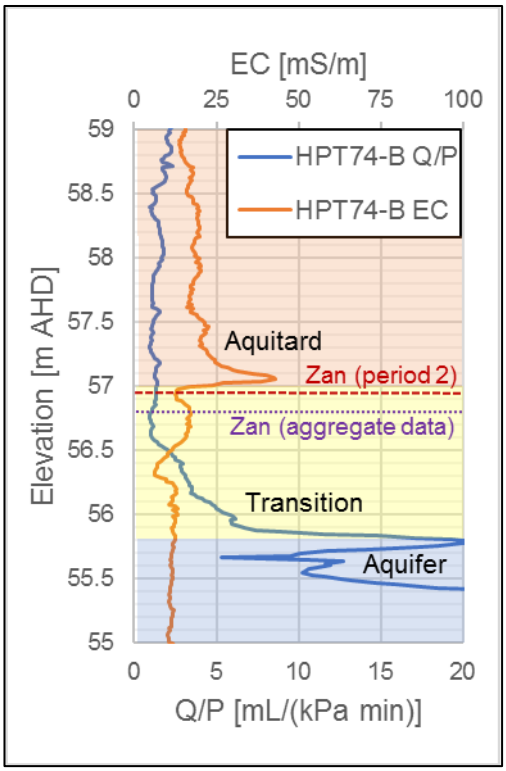


Fig. 5.29. Q/P (after correcting for atmospheric and hydrostatic pressure) and EC logs at HPT74-B (adjacent to PB27-B). Dashed red and purple lines refer to the confining contact according to the analysis of DGPs with data from fluctuation period 2 and aggregate data, respectively.

Additional features could have controlled LNAPL redistribution and migration phenomena. Thus, measurements of LNAPL presence should be added to the analysis

before defining layers for modelling scenarios. Some of these hydrostratigraphic features were a less transmissive coarse-grained lens between 55.4 and 55.7 m AHD and an interval with lower EC at 56.2–56.5 m AHD.

5.2.6.4 Area C

Fig. 5.30 collates three HPT profiles adjacent to PB40-C to further investigate the site hydrostratigraphy and the confining contact elevation through Q/P logs. Q/P values were considerably lower than in areas A and B, reflecting the low k_{sw} expected in area C. Dissimilarities between HPT profiles collected at short distances from each other exposed the uncertainties related to developing the CSM, estimation of LNAPL hydrogeologic conditions, design modelling scenarios, and eventually implement effective remediation approaches. Such observations supported the supplementary application of techniques such as baildown testing and DGPs to specifically evaluate the subsurface conditions in the well of concern, since the measurements in one point may not be representative of other locations (Huntley et al., 1994b; Gatsios et al., 2018b; Lenhard et al., 2019).

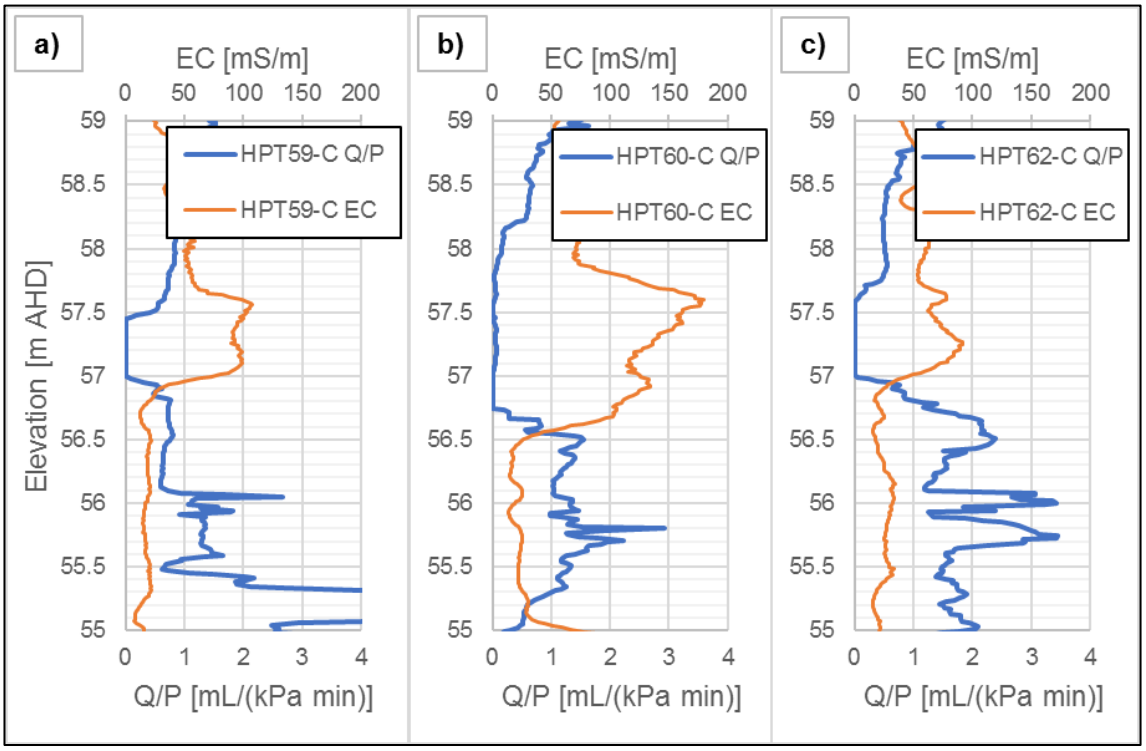


Fig. 5.30. Q/P (corrected for atmospheric pressure) and EC logs adjacent to PB40-C: (a) HPT59-C, (b) HPT60-C, and (c) HPT62-C. The x-axis was exaggerated compared to area A and B.

In terms of evaluating the confining contact elevation, HPT logs on its own could have led to multiple valid interpretations due to the variability of the logs. The distance between PB40-C and HPT59-C was greater than to HPT60-C and HPT62-C and therefore worse agreement with predictions from DGPs could be expected.

Regarding the hydrostratigraphic delineation, Q/P diminished above 56.5 m AHD at HPT60-C and HPT62-C, while it remained relatively stable up to 56.8 m AHD at HPT59-C and then dropped to 0 at 57.0 m AHD. Similarly, Q/P became 0 at 57.0 m AHD in HPT62-C, while this presumably finer-grained interval started at a lower elevation (around 56.75 m AHD) at HPT60-C. Distinct Q/P records were obtained at each profile below 56.5, likely indicating presence of fine layering in the subsurface. Fine layering may influence the performance of LNAPL mass recovery systems (Johnston and Trefry, 2009).

A simplified geological model of the subsurface was inferred through the analysis of spatial interpolated Q/P and EC values from HPT59-C, HPT60-C, and HPT62-C in PB40-C as depicted in Fig. 5.31. Both Q/P (corrected for atmospheric pressure) and EC logs were interpolated through IDW. The leaky confining aquitard was assumed to go from approximately 56.75 m AHD up to ground level. This confining contact as determined through DGPs corresponded to Q/P and EC values being, respectively lower and higher than those observed in the aquifer. Additional analyses supporting this interpretation are presented in section 6.4.5.3.

The aquifer exhibited lower Q/P values in area C than in areas A and B. The aquifer could be divided in multiple thin layers. The contrast in Q/P with subtle changes in EC around 56.1 m AHD was likely an indication of the increasing contribution of silts at the top of the aquifer (defined as a ‘transition’ zone in Fig. 5.31). Nevertheless, multiple features could have controlled LNAPL redistribution and migration phenomena. Thus, measurements of LNAPL presence should be added to the analysis before defining layers for modelling scenarios. Some of these hydrostratigraphic features were a more transmissive (higher Q/P) layer at 56.4–56.6 m AHD, an interval richer in clay (subtle increase in EC) around 56.1 m AHD or drops in Q/P at 55.9 m AHD and around 55.5 m AHD.

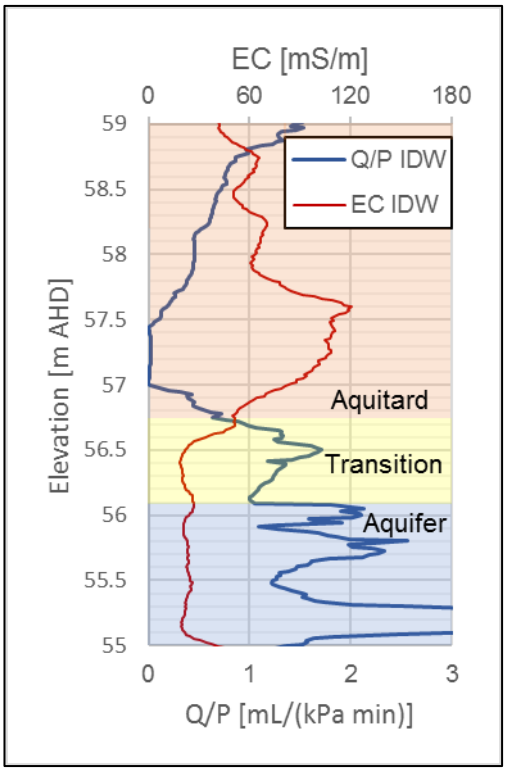


Fig. 5.31. Interpolated Q/P and EC logs at PB40-C including a simplified three-layer geological model.

5.2.7 Summary of results and conclusions

Integration of multiple lines of evidence suggested the existence of leaky confined (aquifer and LNAPL) conditions at high z_{aw} values with a variable confining contact elevation around 56.6–57.0 m AHD. Some LNAPL mass could have been (semi-)confined below 56.4 m AHD near the UST and area C, while the confining contact in area A could be as high as 57.3 m AHD according to HPT data. The existence of a confining unit led to b_n values up to 3.1 m near the UST, although b_n records under unconfined LNAPL conditions were generally below 1 m.

Fig. 5.32 depicts four different LNAPL hydrogeologic conditions possibly found in the petrol station site. For illustrative purposes, it assumes identical b_n and mobile LNAPL interval in the formation during unconfined LNAPL conditions and perfect hydraulic connection between the well and the formation, while it does not account for aspects such as non-equilibrium phenomena.

As depicted in Fig. 5.32(a), LNAPL was typically unconfined under low water table conditions. Fig. 5.32(b) shows that LNAPL could have been unconfined at high z_{aw} values

too in the case of an overlying unit not able to pose confined conditions. This was likely the scenario observed in area A and particularly PB29-A, although the overlying unit may have still limited LNAPL migration within the formation and the representativeness of in-well fluid levels to some extent.

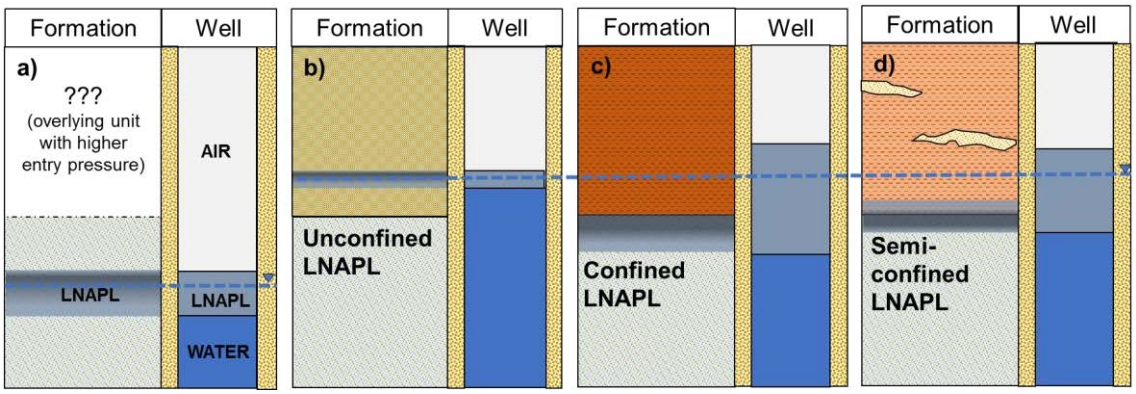


Fig. 5.32. Four scenarios with different LNAPL hydrogeologic conditions: (a) unconfined LNAPL at low z_{aw}, (b) unconfined LNAPL at high z_{aw}, (c) fully confined LNAPL at high z_{aw}, and (d) semi-confined LNAPL at high z_{aw}.

Fig. 5.32(c–d) depicts scenarios with confined and semi-confined LNAPL conditions. Thus, the aquitard represented in Fig. 5.32(c) is finer-textured and exhibits greater integrity than the aquitard depicted in Fig. 5.32(d) which may have coarse-textured lenses and other naturally occurring preferential pathways. In the later case, some LNAPL mass keeps migrating into the overlying unit under increasing z_{aw} values, while other LNAPL mass becomes essentially immobile. Therefore, z_{nw} would be likely higher than under ideal confined LNAPL conditions (depending on the retention properties of the system), which could have been an explanation for the non-zero z_{nw} slopes observed in DGPs from the petrol station site. This was likely interrelated with non-equilibrium effects.

Other lines of evidence suggesting the existence of leaky confined conditions included:

- the high content in sands and even some gravel within the aquitard according to visual inspection of cores and particle-size analysis of core samples;
- the good fit of models assuming a leaky confined aquifer in the analysis of pumping tests;
- the variable HPT P, HPT Q, and EC measured in the aquitard;

- LNAPL presence within the aquitard according to some cores and LIF profiles;
- the ability of LNAPL to infiltrate throughout the aquitard after the initial release into the subsurface.

Regarding the application of individual lines of evidence, stratigraphic descriptions and particle-size analyses contributed to develop a CSM comprising a heterogeneous sandy aquifer with variable amounts of clay, silt, and gravel, which was overlain by an aquitard with large proportions of sand. A fining-upward sequence was identified in many cores, with the content in fines increasing at the top of the aquifer where LNAPL was frequently found.

Four materials could be considered representative of the subsurface conditions: (i) 'aquitard materials' comprising poorly sorted fine sand with fines (some silt and few clay; corresponding to the aquitard and low-permeability lenses); (ii) 'transition materials' comprising poorly sorted fine sand low in fines (little silt and traces of clay particles; corresponding to the top of the aquifer fining-upward sequence); (iii) 'upper aquifer materials' comprising poorly sorted medium sands low in fines (few silt and traces of clay particles; corresponding to the upper half of the aquifer but coarser-grained than the 'transition materials'); and (iv) 'lower aquifer materials' comprising moderately well-sorted coarse sand low in fines (little gravel and silt traces; representing the coarsest-grained fractions found at the lower half of the aquifer).

The interpretation of single-well DGPs was enhanced through the analysis of monotonic fluctuation periods and the use of linear regression techniques. In some cases, the low number of observations may complicate the analysis of specific fluctuation periods and increase the uncertainty of the results. Future research could make use of automatic logging systems to increase the resolution of measurements (Rau et al., 2019) and also adopt non-linear methods to better estimate the confining contact elevation. Hydrographs should always be carefully inspected to identify non-equilibrium or non-representative records since more robust methods are needed to deal with non-equilibrium phenomena. Studying the variability of retention characteristics throughout the hydrostratigraphic profile would contribute to better interpret DGPs. Due to the

existence of confounding factors controlling LNAPL behaviour, multiple lines of evidence must be applied in any site to improve the understanding of the subsurface conditions.

Multi-well DGPs were affected by the frequency of field monitoring campaigns and thus the discrimination of transmissive and non-transmissive intervals could be misleading under certain conditions. Nevertheless, they are a valuable diagnostic tool for several purposes, including the identification of extreme values and a preliminary evaluation of the confining contact elevation across the site. Multi-well DGPs must include data from periods without mobile LNAPL to avoid erroneous interpretations.

HPT logging allowed rapid collection of high-resolution data generally consistent with other methods such as particle-size analyses and DGPs, facilitating the interpretation of subsurface conditions across the entire site. The use of EC and Q/P logs was valuable and provided information even when HPT P was over the limit of quantification. Furthermore, HPT logging also allowed identification of less apparent hydrostratigraphic features that could be considered for modelling scenarios at specific locations. Nevertheless, attempts to identify the confining contact elevation could lead to non-unique interpretations and therefore HPT logging should be accompanied by other lines of evidence. In particular, it was shown that adjacent HPT profiles logged in the proximity of the same well may suggest different hydrostratigraphic columns. Interpolation methods such as IDW and application of in-well techniques such as DGPs and baildown testing may contribute to elucidate the subsurface conditions at the well of concern in these cases. Furthermore, DGPs and baildown testing specifically assess if LNAPL is confined, while aquifer testing and HPT logging are better suited to study the hydrogeologic conditions of the aquifer itself.

Records of stable water drawdown (around the maximum drawdown induced during pumping tests) under confined aquifer conditions were used as an indication of the bottom of the aquitard, which resulted to be consistent with DGP interpretations. However, the number and duration of aquifer tests was limited because it is a demanding approach in terms of resources and may impact the subsurface conditions. Data from aquifer tests conducted when z_{aw} was near the confining contact could be frequently well fitted by unconfined and leaky confined models. Finally, baildown testing

results were also consistent with the CSM, although they could not be used to determine the confining contact elevation due to the negligible LNAPL recoverability at high z_{an} values (Gatsios et al. 2018a).

5.3 Industrial site. Areas T3/T4

5.3.1 Particle-size analysis

Particle-size analysis data from 66 samples collected in area T4 (150 m South–Southwest from area T3) demonstrated that the subsurface material was mostly fine to medium sand with only traces of clay and silt. No evidences of shell fragments were found by visual inspection of core C66-T3.

The materials were much more homogeneous than in the petrol station site. Out of 66 samples, 63 could be classified as uniform or moderately well sorted sand (41 sand samples with a C_u below 2 as well as 22 sand samples with a C_u between 2 and 5 as shown in Appendix E: Particle-size data and correlations with hydraulic conductivity). Exceptions included one sample classified as uniform gravelly sand (040610/6-T4 at -0.095 m AHD), another sample of moderately well sorted gravelly sand (050210/1-T4 at 0.475 m AHD) and one sample of poorly sorted sand (040610/1-T4 at 0.575 m AHD). All the samples were low in fines.

More specifically, sands were generally poorly graded as indicated by C_u ranging from 1.50 to 5.25, being the median, geometric mean, and $\mathrm{p95}$ equal to 1.84, 2.00, and 3.81, respectively. Coefficients of curvature ranged from 0.50 to 2.01 with 0.93, 0.92, and 1.07 corresponding to the median, geometric mean, and $\mathrm{p95}$ values.

Fines passing a 63-µm sieve remained practically constant throughout the profiles, representing contents within a range between 0.5 % and 4.9 % with median, geometric mean, and $\mathrm{p95}$ values of 1.2 %, 1.3 %, and 2.9 %, respectively, as well as a standard deviation of 0.83 % and MAD of 0.55 %. Similarly, the 25th percentile diameter remained relatively stable as shown in Fig. 5.33, with few exceptions for instance at 040610/1-T4 (0.975 m AHD) and 050210/1-T4 (0.825 m AHD).

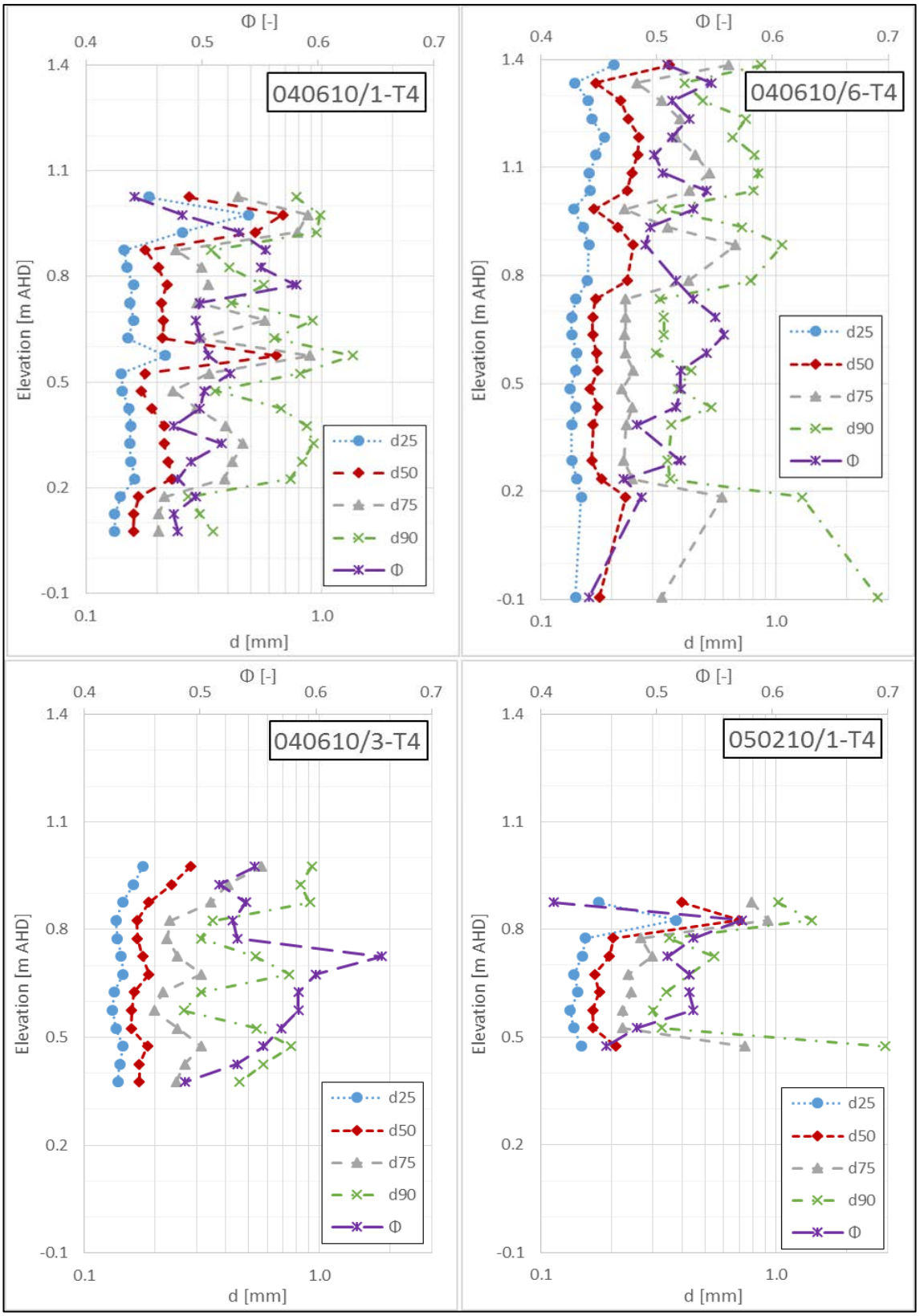


Fig. 5.33. Vertical profiles of particle size and Φ at 040610/1-T4, 040610/6-T4, 040610/3-T4, and 050210/1-T4. *d25*, *d50*, *d75*, and *d90* stand for the 25th, 50th, 75th, and 90th percentiles of particle diameters, respectively.

Particle size distributions and the vertical profiles illustrated in Fig. 5.33 revealed the presence of lenses with coarser material at multiple depths in each core. For instance, there was an increase in particle size at approximately 0.8–1.0 m AHD in the four profiles.

However, the underlying and overlying sequences were visibly dissimilar between profiles and not all of them showed a decrease in fines. Consequently, no layers of coarser material could be clearly identified comparing multiple profiles. In addition, Φ values derived from ρ_b measurements did not reflect a consistent decrease at 0.85–0.95 m AHD throughout the four wells.

Nonetheless, the presence of these lenses suggested that even a single-layer model should still explore scenarios with hydrogeological properties corresponding not just to fine to medium sands but also coarse sands that could work as preferential flow paths. Samples presenting high values of the 25-percentile diameter from 040610/1-T4 (0.975 m AHD) and 050210/1-T4 (0.825 m AHD) could be taken as conservative examples of the coarse sands' characteristics.

Stratigraphic descriptions mentioned cementation in the saturated zone on cores collected in June 2004 (z_{aw} between 0.56 m AHD on 040610/3-T4 and 0.60 m AHD on 040610/6-T4), mainly linked to a change in facies towards generally finer-grained sands presenting less internal layering. According to the Φ estimates, the facies contact could correspond to approximately 0.4 m AHD, although Φ slightly decreased downwards instead of increasing as it could be expected in a fining-downwards sequence. This could be due to cementation effects or different grain arrangements.

5.3.2 Hydrographs

Area T4 typically experienced annual water table fluctuations of 0.4–0.5 m according to fluid level data from monitoring wells, including the hydrograph of NS7A-T4 represented in Fig. 5.34 (see Lenhard et al., 2019 for logger records of a shorter period of time). In the period 2004–2006, the highest z_{aw} values were measured in the month of July (coincident with the beginning of the Australian water year), while the lowest records corresponded to February in both years. During periods of rising water table, the rate of

change of z_{aw} was 2.4–2.5 cm/week in average, while it decreased at a rate of 1.2–1.5 cm/week in average throughout the dry season.

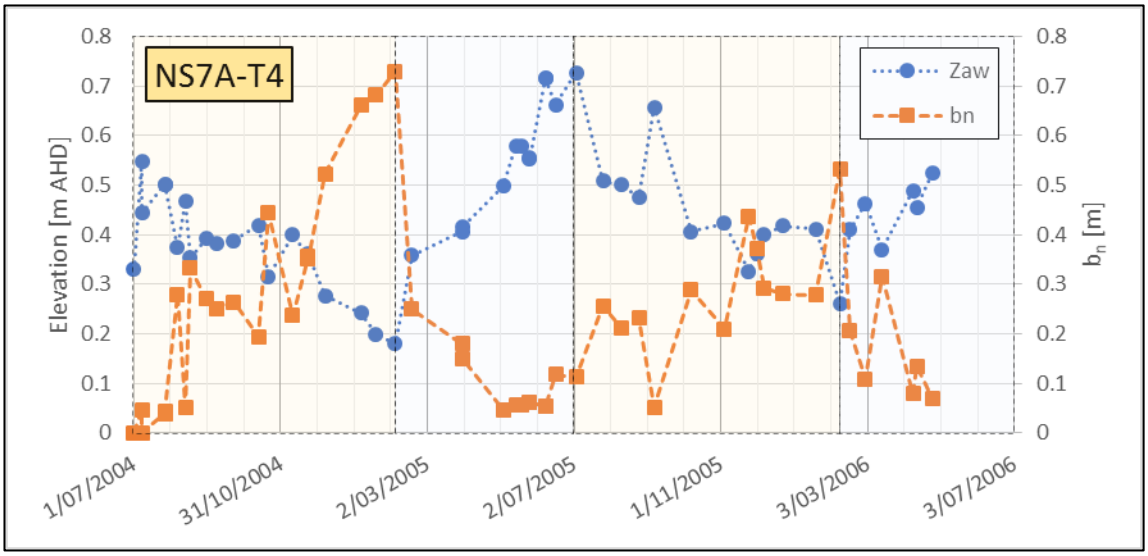


Fig. 5.34. Hydrograph of 040610/3-T4. Two periods of decreasing (highlighted in yellow) and increasing z_{aw} (highlighted in blue) are depicted throughout two years of monitoring data.

After April 2006, the monitoring frequency of manual measurements at 040610/3-T4 decreased and some anomalous high z_{aw} and b_n values were measured (z_{aw} = 1.105 m AHD and b_n = 0.287 m on 8/06/2006; z_{aw} = 0.929 m AHD and b_n = 0.738 m on 16/08/2006). However, these values were not consistently observed in the surrounding wells as illustrated in Fig. 5.35 and could not be explained under equilibrium conditions: an increase of b_n at higher z_{aw} would indicate confined LNAPL conditions, but both parameters followed opposite trends after a brief drop in z_{aw}, indicating unconfinement and suggesting non-equilibrium conditions, a sudden increment in LNAPL mass or measurement errors. Therefore, the use of these points was discarded for subsequent analyses.

The absence of accurate in-well fluid levels for 040610/1-T4, 040610/3-T4, and 040610/6-T4 when the cores were extracted discouraged their use for modelling scenarios. On the contrary, in-well fluid levels were monitored when 050210/1-T4 was extracted, being b_n equal to 0.672 m (z_{an} = 0.317 m AHD; z_{nw} = -0.355 m AHD) in the adjacent location of 040610/3-T4 (Lenhard et al., 2019). Consequently, 050210/1-T4 was selected for the modelling scenarios.

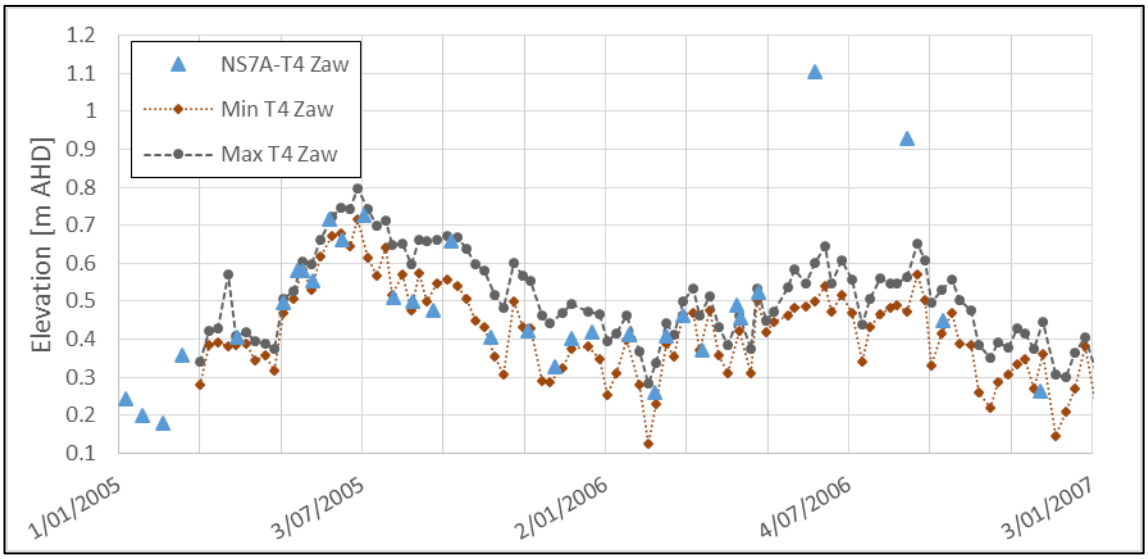


Fig. 5.35. Hydrograph of 040610/3-T4 compared to maximum and minimum z_{aw} values recorded in other five wells monitored weekly in area T4 located less than 50 m away from 040610/3-T4. Anomalous z_{aw} values over 0.9 m AHD were surely due to measurement errors.

5.3.3 Analysis of LNAPL diagnostic gauge plots

Fig. 5.36 depicts the DGP of NS7A-T4 between 27/07/2004 and 26/04/2006. In this period, the historical lowest z_{an} and z_{nw} were 0.27 m AHD and -0.459 m AHD, respectively, while the historical highest z_{an} and z_{nw} were 0.741 m AHD and 0.669 m AHD, respectively.

The negative relationship between z_{aw} and b_n suggested unconfined LNAPL conditions in 2004–2006. Fig. 5.36(b) shows that the low R^2 was mainly due to a few extreme values corresponding to high z_{aw}. Fig. 5.36 also shows that a prediction of b_n at a given z_{aw} with a linear model could be better achieved by considering data from that specific period of increasing or decreasing z_{aw} instead of the whole hydrograph.

The period between February 2005 and July 2005 (rising z_{aw}) was the only one presenting a lower R^2 than using the entire data set, since it included the highest z_{aw} values. When the four points with a higher z_{aw} were removed, R^2 for the complete data set increased from 0.735 to 0.871 with the slope of the regression line decreasing to -0.501. Analogously, increments in R^2 were obtained for the periods between February and July 2005 (from 0.656 to 0.886) and between July 2005 and February 2006 (from 0.829 to 0.833) with the slope of the regression lines decreasing to -0.560

and -0.668, respectively. The reason behind the lack of linearity at extreme values was likely due to a quick rate of change in z_{aw} at very low b_n.

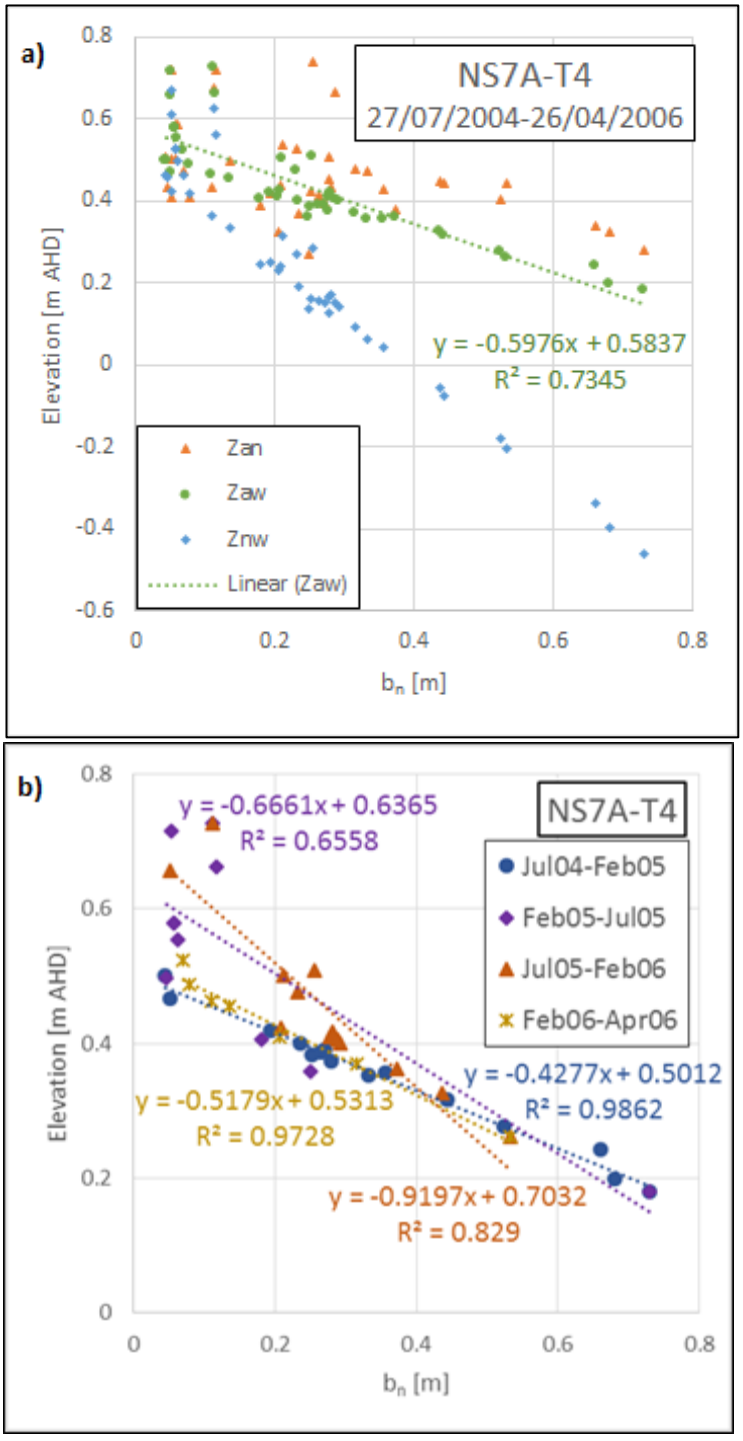


Fig. 5.36. DGP at NS7A-T4 between 27/07/2004 and 26/04/2006 showing coefficients of determination (a) for the entire set of data and (b) for each period of increasing or decreasing z_{aw}.

5.3.4 HPT logging

The nearest HPT log was HPT20-T3, located 150 m North–Northeast of area T4 and depicted in Fig. 5.37. It corroborated the absence of materials as fine-grained as at the petrol station site, presenting a maximum of HPT P slightly over 300 kPa. As in the case of the particle-size analysis data, it also showed a certain degree of variability in terms of intervals of finer and coarser material, although it was not possible to clearly identify stratigraphic layers comparing HPT20-T3 with cores from area T4. The HPT P log presented a standard deviation of 32.66 kPa, dropping to 22.28 kPa when analysing only data below 0.90 m AHD.

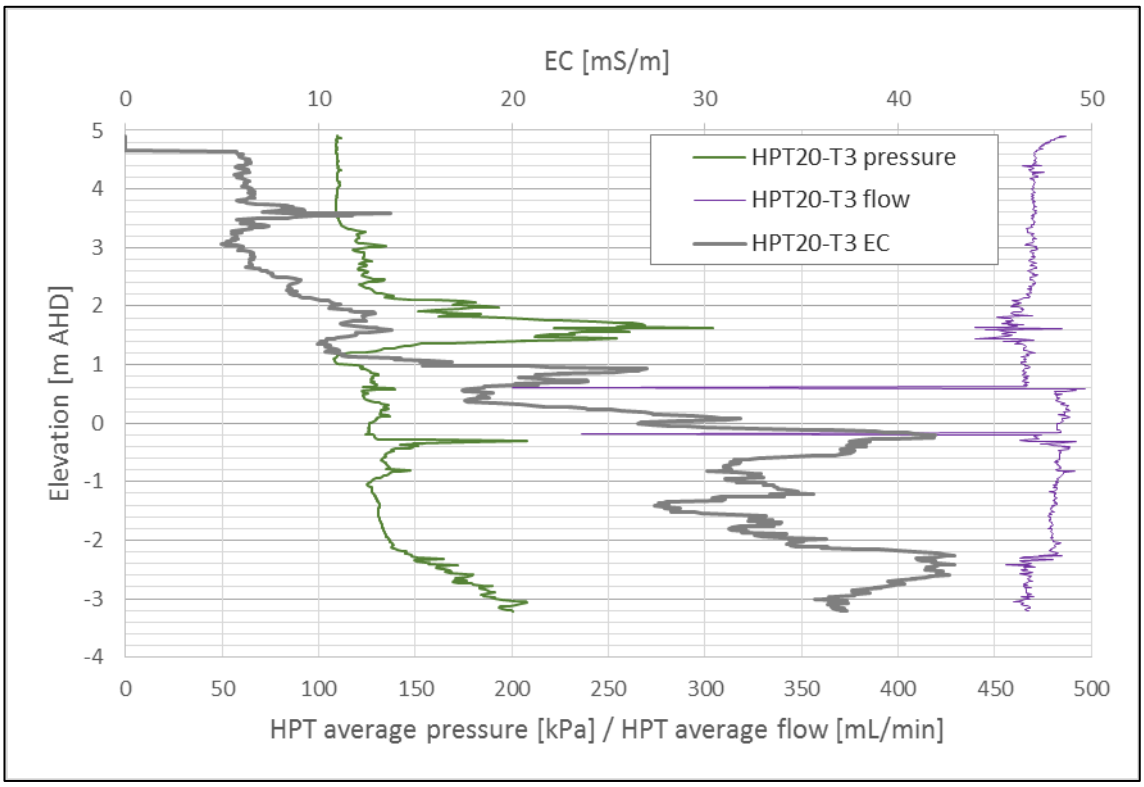


Fig. 5.37. HPT20-T3 pressure, flow and EC logs.

As depicted in Fig. 5.38, a cross-section of HPT P logs (before correcting for hydrostatic pressure) from other areas of the industrial site exposed some common features. The most prominent was a finer-grained layer with pressures over 200 kPa generally above an elevation of 0.8–1.2 m AHD. The highest values were usually above 1.2 m AHD, where maximum HPT P values over 300–400 kPa were recorded in some logs. The similarity between logs located hundreds of meters away from each other revealed that geological heterogeneity was much lower than in the petrol station site.

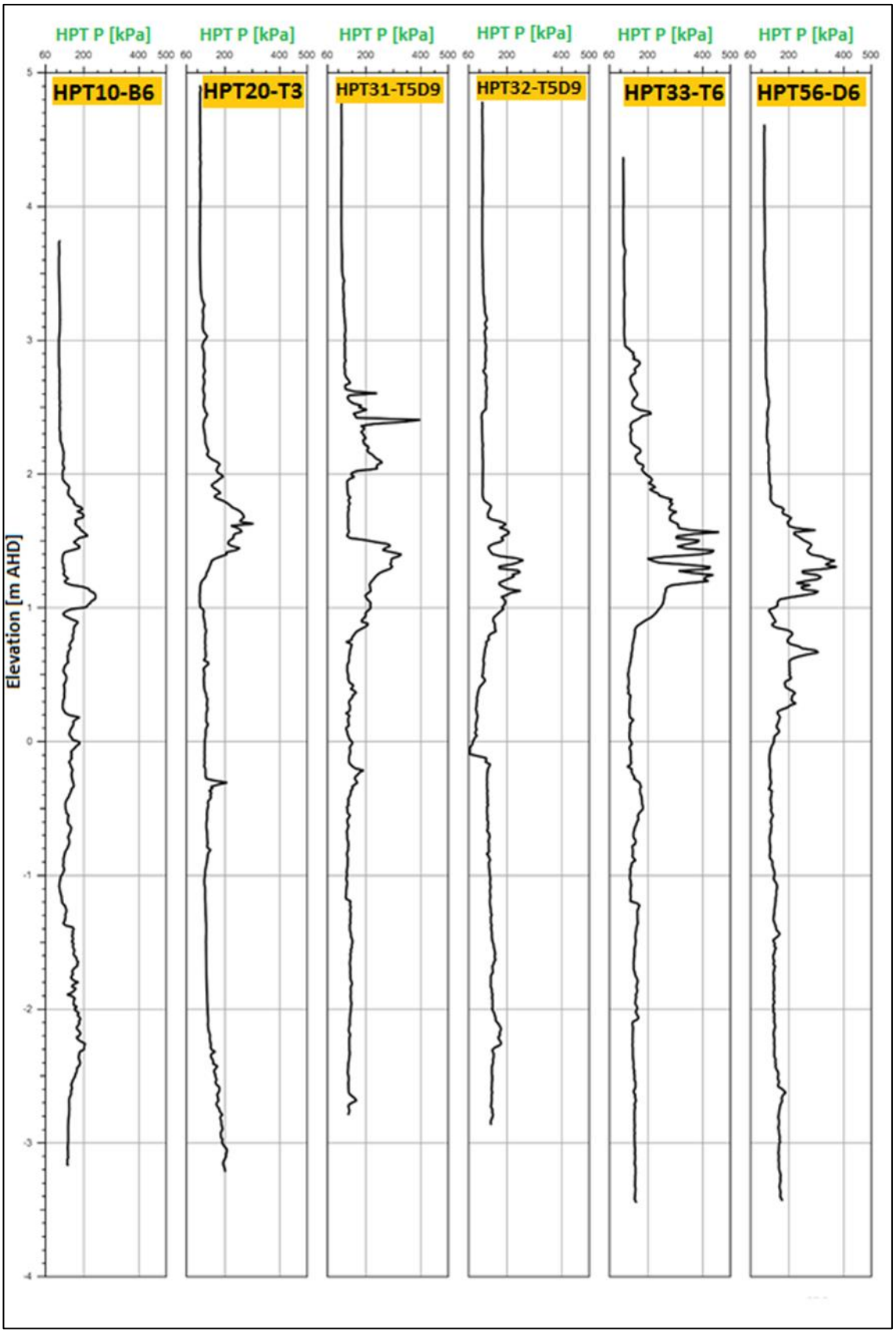


Fig. 5.38. Cross-section of HPT average pressure logs (before correcting for hydrostatic pressure) in the industrial site.

In the case of HPT20-T3 (second log from the left in Fig. 5.38), this finer-grained layer was shallower than in other logs, approximately located between 1.20 and 2.15 m AHD. Because of this reason, the finer-grained layer was not adequately represented by the particle-size data from area T4, where it could not be identified even at 040610/6-T4 with samples up to 1.4 m AHD.

Some anomalous observations regarding the finer-grained layer were at HPT50-T7D1 (not shown in Fig. 5.38), where this layer was not identified and at HPT10-B6, where the HPT pressure pattern was noticeably different to other logs. This made sense taking into consideration that area B6 was the most isolated area of study (approximately 700 m away from the others).

The EC log started shifting towards higher values at 2.60 m AHD with strong increments from 10 mS/m to 27 mS/m between 1.20 and 0.90 m AHD, from 18 mS/m to 31 mS/m between 0.35 and 0.05 m AHD, reaching almost a maximum of EC of 42 mS/m at -0.2 m AHD. Therefore, no coarse layer was identified around 0.8–1.0 m AHD and the increase of porosity at 0.4 m AHD did not clearly correspond to the EC response, although it could be linked to a wide interval of increasing EC that was observed across the entire industrial site.

Fig. 5.39 demonstrates that the increase in EC was not a local phenomenon but present across all the HPT profiles in the industrial site. The strongest EC increments with depth started between approximately 1.30 m AHD (HPT50-T7D1 for instance) and 0.75 or 0.80 m AHD (HPT09-T7D1 and HPT56-D6, respectively), reaching relative maxima between 1.00 m AHD (HPT50-T7D1) and -0.20 m AHD (HPT56-D6). Most EC values above this transition interval were within a range between 5 and 15 mS/m (with a peak of 30 mS/m at HPT32-T5D9), while they rose up to 30–55 mS/m after the transition (with a peak of almost 70 mS/m at HPT33-T6 and anomalous low values around 20–25 mS/m at HPT10-B6). The EC response was spatially correlated, as it can be seen comparing profiles from the same area or knowing that area T3 was near D6 (less than 200 m away). T6 was close to T5D9 and B6 was the most isolated area of study (approximately 700 m away from the others) as previously mentioned.

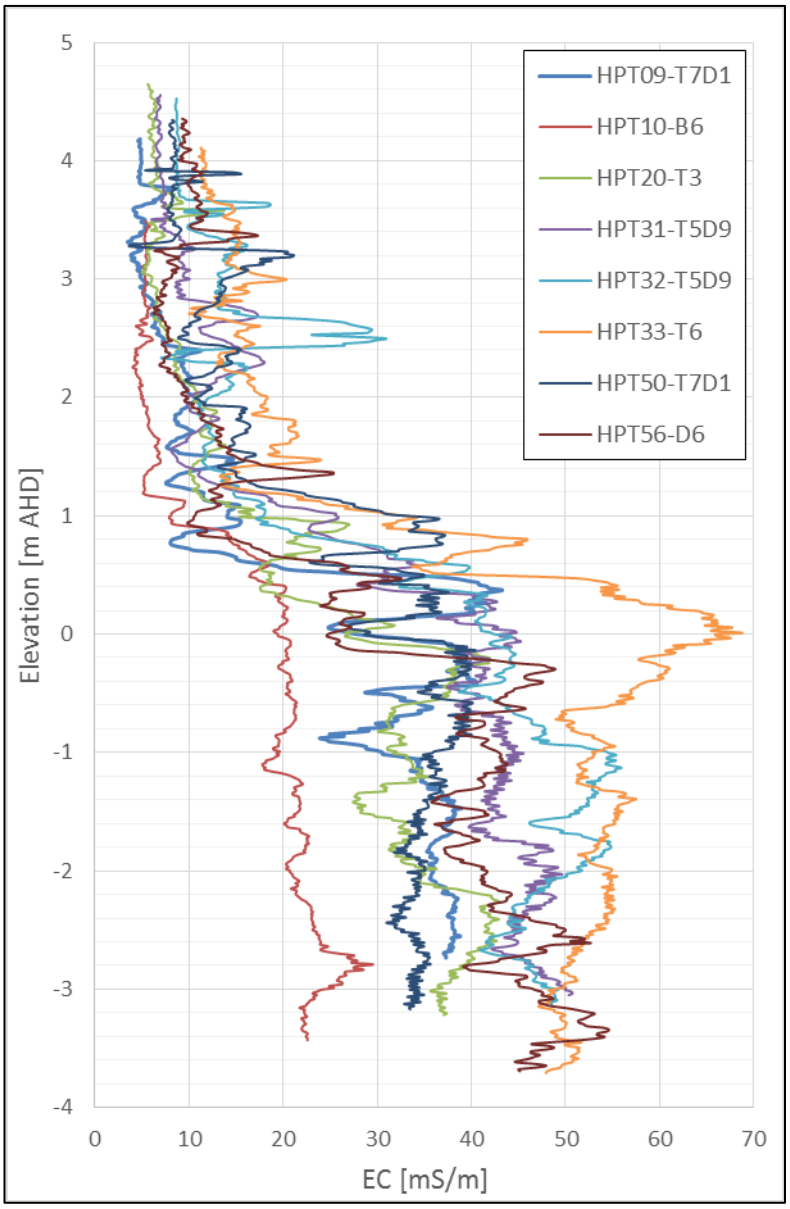


Fig. 5.39. EC logs revealing a transition towards high EC values at low elevations across the entire industrial site.

However, this shift in EC was not physically related to the shift in HPT pressure, since the later disappeared after correcting the absolute piezometric pressure (see Appendix D: HPT profiles). In addition, the correlation between both was clearly distinct at different elevations as shown in Fig. 5.40 for the case of area T3. Positive anomalies in HPT P reflected hydrostratigraphic changes.

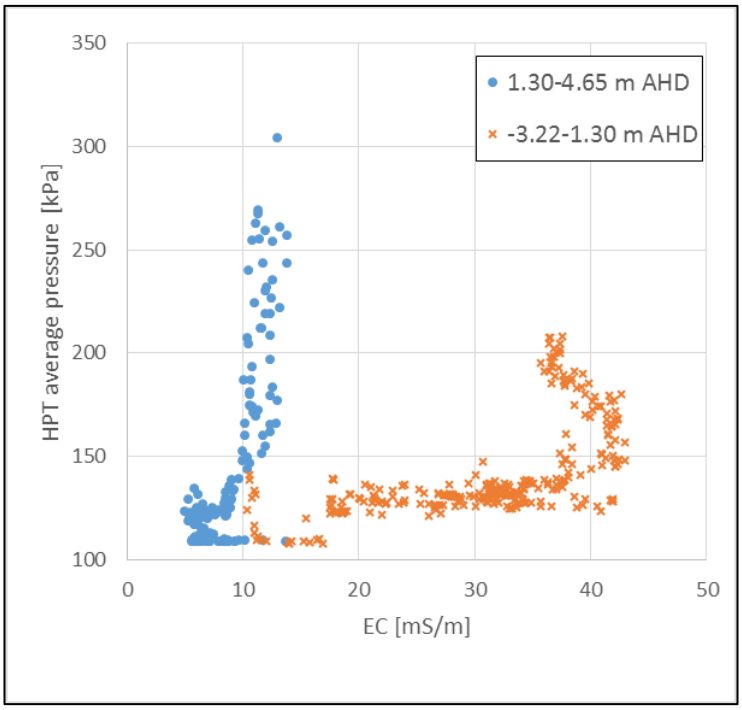


Fig. 5.40. Correlation between HPT P and EC at HPT20-T3.

According to the HPT dissipation test at 5.090 m bgl, the static water level was likely around 0.53 m AHD at HPT20-T3 the day of logging (showing close agreement with field measurements of 4.305 m bgl most likely corresponding to an elevation of 0.56–0.66 m AHD in area T3 during the HRSC campaign) and could be linked to the greatest increments in EC. Therefore, the main cause behind the EC behaviour was likely the strong contrast in S_w between the vadose and saturated zones. Increments greater than 10 mS/m have been reported in the literature (Schulmeister et al., 2003). Some reasons to clearly observe this phenomenon in the industrial site (with increments of more than 20 mS/m), but not in the petrol station site were:

- the contrast in S_w between the vadose and saturated zones is more subtle in finer-grained materials;
- EC response may be controlled to a greater extent by the presence of clays than by the contrast in moisture content;
- groundwater specific conductance was higher in the industrial site (generally 150–300 mS/m) than in the petrol station site (around 50–150 mS/m) and could have been affected by saline intrusion phenomena (although the values were far

from those of pure saltwater) as well as by the geological medium. A pair or logs from both field sites is presented in Fig. 5.41;

- LNAPL was more weathered in the industrial site, potentially contributing to create anomalies of high EC.

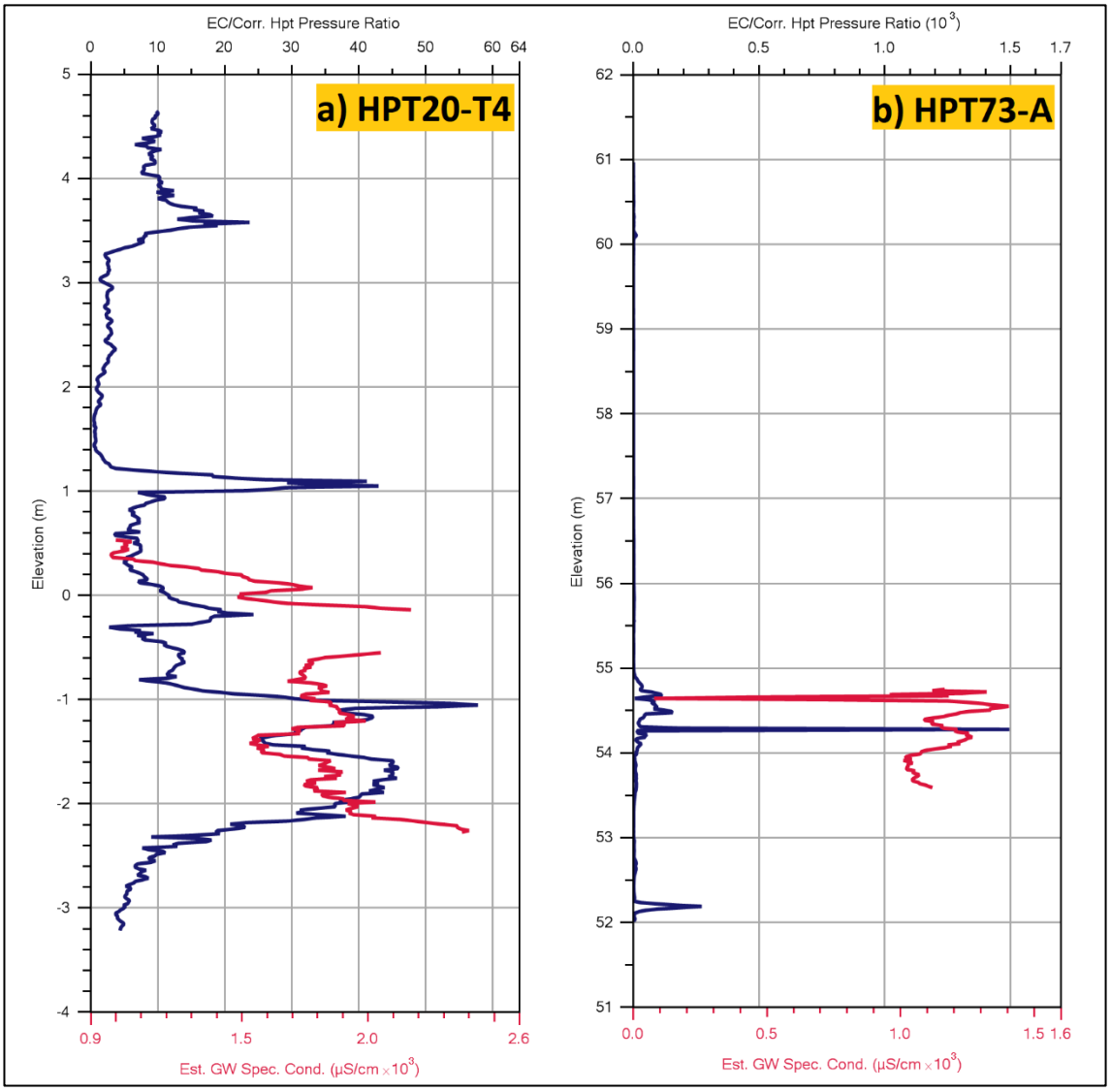


Fig. 5.41. Groundwater specific conductance [mS/cm] (red colour) and ratio between EC and corrected HPT P (blue colour) in (a) the industrial site and (b) the petrol station site.

Soil cementation would be generally accompanied by a relatively low ratio of EC and HPT P (McCall, 2013) and therefore was not considered a cause of the observed increase in EC with depth. Finally, a change of facies at similar elevations could not be discarded, although it was not likely the main cause behind the rise in EC.

5.3.5 Summary of results and conclusions

Conclusions related to the analysis of the hydrostratigraphic profile and confinement conditions in the petrol station site were presented in section 5.2.7.

The analysis of characterisation data in the industrial site suggested that a one-layer model representing fine to medium sands could be enough to replicate the subsurface conditions. Nonetheless, the presence of lenses of coarser sand indicated that it could be necessary to introduce thin layers (around 0.1 m wide) of coarse sands to match the LNAPL distribution profile as evaluated in section 6.4.6. However, there was not enough information to determine the elevation of these layers at this stage, although the most consistently observed was at approximately 0.8–1.0 m AHD. Instead of adding thin layers of coarser material, a second approach consequent with the field observations was to define only one layer with coarse sands giving more importance to the lenses that could work as preferential flow paths.

Measurements of ρ_b and stratigraphic descriptions also suggested that could be a facies boundary around 0.4 m AHD, where the top layer would be formed of fine to medium sands and the bottom layer of finer sands with more cementation and lower variability in particle sizes. An increase in EC from 1.2 m AHD downwards and higher HPT average P above that elevation suggested that the boundary between both facies was not necessarily clear, although the EC shift was probably due to the variation in moisture content.

To sum up, the following model scenarios were determined to potentially replicate area T3/T4 in an adequate way:

- a single layer consisting of fine to medium sand;
- a single layer consisting of coarse sand;
- two layers where the deeper one consists of finer sand, being the facies boundary around 0.4 m AHD;
- three layers with the middle one representing a diffuse facies boundary between 1.2 and 0.4 m AHD;
- any of the previous scenarios adding thin layers (around 0.1 m) of coarse sands if needed to match the LNAPL distribution profiles presented in section 6.4.6.

6 Laser-induced fluorescence (LIF) logging of LNAPL distribution and mobility

6.1 Chapter structure

Chapter 6 consists of an assessment of the LIF probe as a HRSC tool to delineate LNAPL distribution profiles, potentially investigate LNAPL mobility in unconsolidated aquifers, and evaluate LNAPL hydrogeologic conditions and aquitard integrity. Accordingly, section 6.2 compares measurements of LIF response and T_n in the petrol station site. Subsequently, section 6.3 incorporates the analysis of multi-wavelength waveforms to effectively identify intervals with less-mobile LNAPL. Section 6.4 provides a detailed examination of specific LIF profiles comparing them to other characterisation tools in areas considered for modelling purposes. Finally, section 6.5 summarises results and conclusions from this chapter.

A paper titled 'Laser-induced fluorescence logging as a high-resolution characterisation tool to assess LNAPL mobility' (García-Rincón et al., 2020) has been published in Science of the Total Environment. It succinctly discusses much of the data and outcomes from chapter 6. LIF logs are included in Appendix C: LIF profiles.

6.2 Overview of LIF profiles and their relationship with LNAPL mobility

6.2.1 Section structure

Section 6.2 investigates the relationship between LIF response and LNAPL mobility, in particular T_n values. This analysis was mainly done at the petrol station site, since there were better data (LIF and T_n data) than in the industrial site in terms of spatial and temporal resolution.

Section 6.2.2 focuses on LIF profiles exhibiting weak fluorescence, eventually linking them to areas with low T_n values or absence of LNAPL. Additionally, data from the industrial site was used to discuss the potential existence of false negatives caused by the natural fluorescence of the geological medium.

Section 6.2.3 analyses LIF logs with medium or strong LIF response, linking peak LIF signals and integral LIF signals to T_n values measured through baildown testing. Data

from the industrial site is just briefly summarised in the last paragraph and contrasted to some conclusions extracted from the petrol station site. This section also explores the shape of LNAPL distribution profiles found at the petrol station site and its relationship with the subsurface hydrostratigraphy and in-well fluid levels. A more detailed analysis was conducted for specific areas in section 6.4.

6.2.2 Overview of logs with weak LIF response

6.2.2.1 Observations from the petrol station site

Among the 20 LIF profiles obtained at the petrol station site (see map 7 in Appendix B: Maps), five (LIF46, LIF48, LIF53-B, LIF54, LIF67) did not reveal any presence of LNAPL and presented signals below 2.3 %RE that could be mainly associated to natural fluorescence of the geological medium according to their multi-wavelength waveforms and the CSM. LIF67 did not help to identify any migration pathway between the UST and the highly transmissive area A. LIF48 and LIF67 were probably located out of the LNAPL body edge. Similarly, the other logs were in areas exhibiting low T_n values. The only exception was LIF53-B as discussed in the following paragraph.

LIF53-B was less than 2 m away from PB27-B, practically in the same direction as MP36-B (2 m away from PB27-B) and PB35-B (4 m away from PB27-B). PB35-B only showed sheens of LNAPL sporadically (2 mm in May 2016 and 1 mm in April 2017; no more positive records between August 2015 and May 2018), while MP36-B started showing in-well LNAPL in June 2016. Initially, b_n was around 0.04–0.05 m at MP36-B, reaching a maximum of 0.346 m in May 2018 as depicted in Fig. 6.1. Accordingly, it is possible that there was no LNAPL around LIF53-B when this profile was logged, and LNAPL mass migration could have occurred afterwards.

LIF signals with a magnitude as low as the natural fluorescence of the geological medium could still indicate the presence of LNAPL in the subsurface. Three LIF profiles (LIF45, LIF52-B, and LIF55) showed very low signals with peaks of 0.9 %RE, 5.2 %RE, and 1.8 %RE, respectively. However, their multi-wavelength waveforms were similar to those from LNAPL-contaminated areas, suggesting the existence of less-mobile LNAPL.

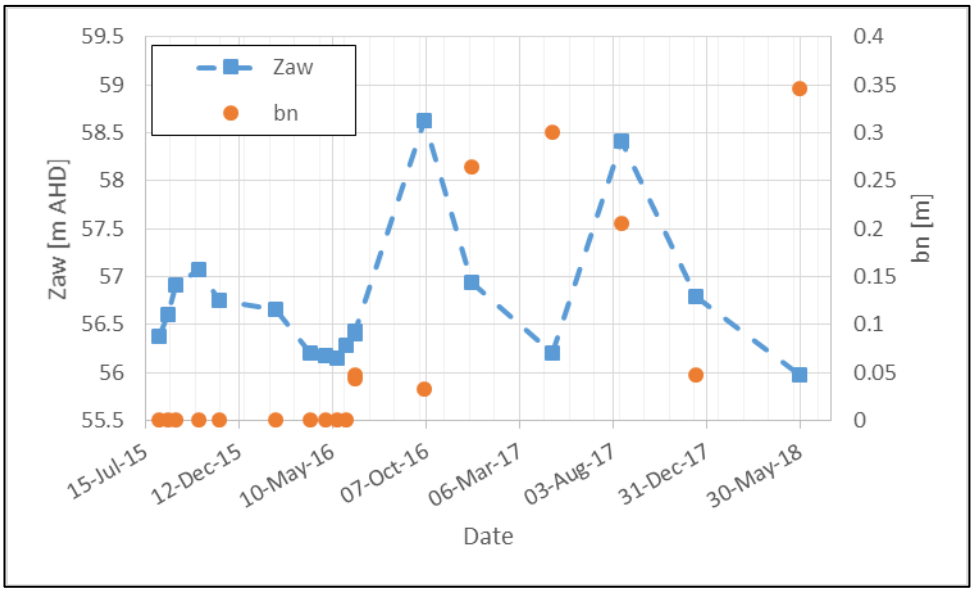


Fig. 6.1. Hydrograph and b_n at MP36-B.

LIF52-B was located near PB27-B (less than 1 m away) as in the case of LIF53-B, but in the South direction (LIF53-B was in the Northeast direction). Thus, it was closer to monitoring points showing LNAPL contamination (LIF51-B, LIF71-B, MP58-B). LIF55 was quite isolated from areas A and B (the nearest monitoring point was more than 5 m away). It exhibited extremely short lifetimes that could have been due to strong presence of oxygen or chemical differences. This could have been the case because the signal was recorded at an elevation almost 1 m shallower than in other logs and 0.3 m higher than the shallowest responses for S_n and soil gas measurements at PB33-A (7 m away; where similar hydrostratigraphy was expected). The weak signal supported the hypothesis of being in a low T_n area.

6.2.2.2 Observations from the industrial site

There were also a few LIF profiles with low responses in the industrial site, but mainly in designated background areas or relatively far away from other monitoring points. Evidences of LNAPL contamination could also be found in LIF profiles from the industrial site presenting low LIF response. In particular, profiles in area D5 (LIF57-D5, LIF58-D5, LIF59-D5) suggested the presence of weathered petrol, even if the magnitude of total LIF signal corresponding to LNAPL contamination and natural fluorescence were almost identical. The LNAPL product exhibited a fluorescence signature well differentiated from the natural fluorescence of the geological medium, making easier the identification of the impacted interval.

6.2.3 Relationship between LIF response and LNAPL distribution and mobility

6.2.3.1 Overview of logs with strong LIF response

LIF profiles displayed a stronger spatial variability in the petrol station site than in the industrial site. This phenomenon was due to different degrees of subsurface heterogeneity, considerably greater in the petrol station site as discussed in chapters 3 and 5. Maps 13, 14, and 15 (see Appendix B: Maps) include transects of LIF profiles between some areas of interest (UST–area A, area A–area B, and UST–area C, respectively).

Regarding the 12 LIF profiles showing medium or strong positive responses in the petrol station site, signal maxima ranged between 7.5 %RE and 289.2 %RE with a mean of 69.4 %RE and a median of 32.6 %RE. These peak values and the corresponding integral LIF signals (excluding LNAPL intervals found at high elevations potentially representing non-recoverable or stationary LNAPL; see section 6.3.2) are depicted in Fig. 6.2. The highest six peak LIF signals corresponded to areas A, B, and C (LIF43-A, LIF47-A, LIF51-B, LIF57-C, LIF71-B) or near the original location of the UST (LIF65). The highest peak (LIF43-A) was in the highly transmissive area A. All the other profiles were in area C or other low-transmissive areas.

In addition, LIF profiles from many areas at the industrial site exhibited strong signals: up to 650 %RE in D6 (presumably diesel), 380 %RE in T3 (diesel), 340 %RE in T6 (crude oil), 280 %RE in T7 (crude oil), and 250 %RE in T5-D9 (kerosene-type jet fuel). The strong signals were in part related to the coarser-grained material and the presence of LNAPL products with more PAH molecules than the petrol from the petrol station site, two factors that commonly increase the magnitude of LIF response (Lu et al., 2014). However, these peaks could not be easily linked to T_n because of the different types of LNAPL product, the vast domain scale, and the relatively low resolution of T_n measurements. Thus, the following section focuses on data from the petrol station site.

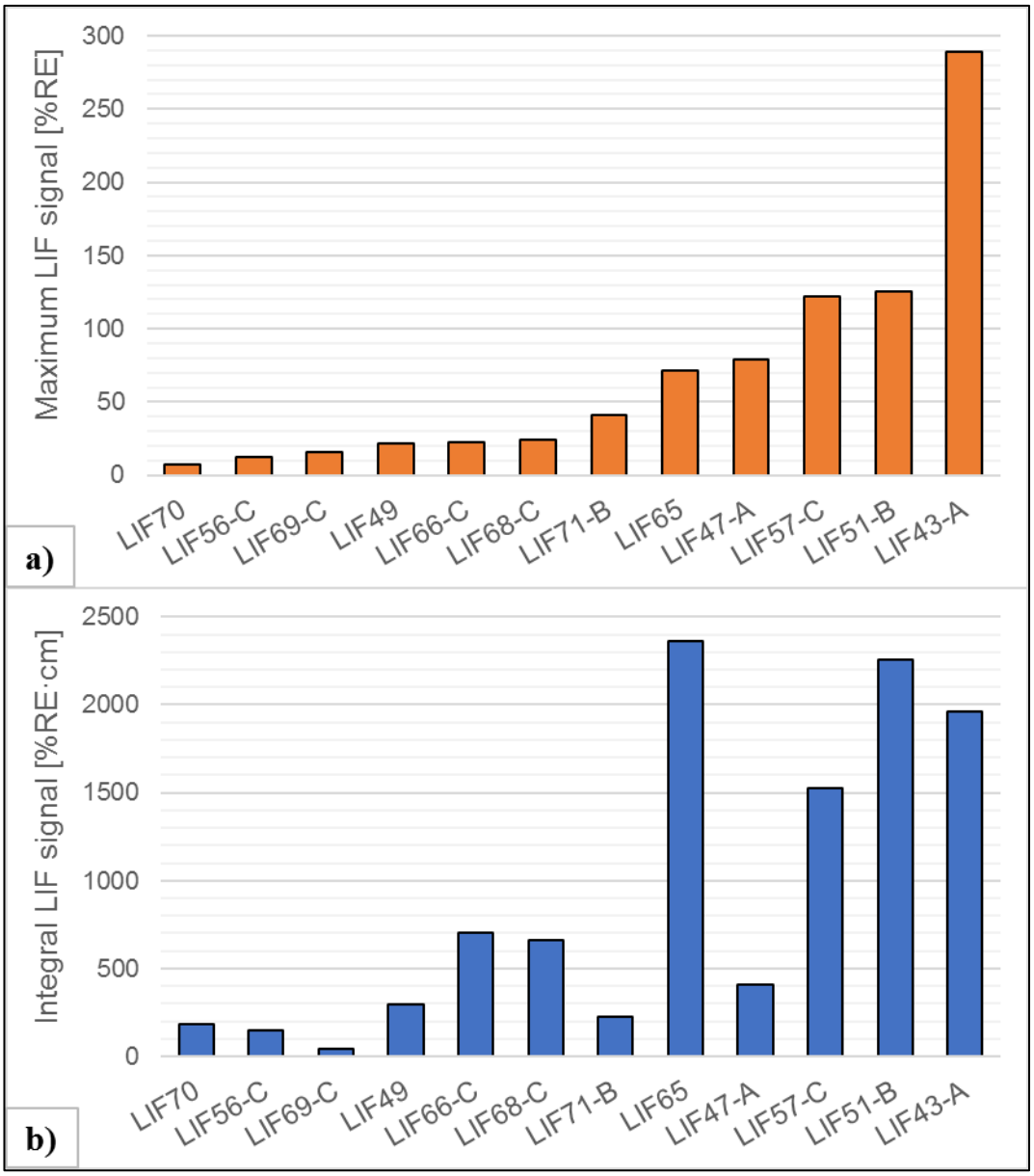


Fig. 6.2. (a) Peak and (b) integral LIF signals across the petrol station site.

6.2.3.2 Rank correlation between LIF response and T_n

Peak LIF signals were more meaningful for the evaluation of T_n than integral LIF signals. More specifically, T_n values and peak LIF signals within a distance of less than 3 m, as summarised in Table 6.1, exhibited a Spearman's rank correlation coefficient of 0.84, which decreased to 0.67 when considering integral LIF signals.

Some field observations may illustrate this correlation. For instance, the UST area presented the highest integral LIF signal, although LNAPL mobility was negligible in this area and period according to baildown testing (Gatsios, 2018). Similarly, two profiles

from low-transmissive (and finer-grained) areas exhibited relatively large integral LIF signals (LIF66-C and LIF68-C).

Table 6.1. Ranks of T_n as well as peak and integral LIF signals.

LIF location	Nearest T_n value	Distance (m)	Peak LIF signal (%RE)	Integral LIF signal (%RE x m)	T_n	Peak LIF signal rank	Integral LIF signal rank	T_n rank
LIF53	MP36	0.3298	0	0	0	13.5	13.5	13.5
LIF52	PB27	0.7438	5.2	0.343436	0.41	11	11	6
LIF45	PB28	0.8748	0	0	0	13.5	13.5	13.5
LIF43	PB29	1.1525	289.2	19.64315	1.97	1	3	1.5
LIF66	PB13	1.3058	22.5	7.035331	0.03	8	5	10.5
LIF47	PB29	1.3229	79.3	4.105246	1.97	4	7	1.5
LIF51	PB27	1.3775	125.4	22.5676	0.41	2	2	6
LIF54	PB35	1.4421	0	0	0	13.5	13.5	13.5
LIF68	PB40	1.7354	24.5	6.61586	0.58	7	6	3.5
LIF56	PB11	1.7553	12	1.483675	0.14	10	9	8
LIF57	PB40	1.8488	122.3	15.28796	0.58	3	4	3.5
LIF65	PB05	2.202	71.8	23.60217	0.04	5	1	9
LIF69	PB39	2.2686	15.4	0.433913	0.03	9	10	10.5
LIF71	PB27	2.3038	40.7	2.263107	0.41	6	8	6
LIF46	MP34	2.4564	0	0	0	13.5	13.5	13.5

On the contrary, the highest LIF peak (289.2 %RE at LIF43-A) was next to the well with highest T_n (1.51 m^2/day at PB29-A on 19/05/2016) and the next five highest LIF peaks were also found in the vicinity of highly transmissive wells (LIF47-A, LIF51-B, LIF57-C, LIF71-B) or near the original location of the UST (LIF65). With only one exception (LIF52-B), all the other profiles were in low-transmissive areas. This finding may be explained by the influence that geological heterogeneities may have on LIF response. Finally, the log near the UST (LIF65) represented a typical point-of-release profile because of the red-shifted LIF signature above 4.5 m deep, suggesting the existence of weathered gasoline in the vadose zone. This observation along the anomalously high fluorescence of the medium could have helped to identify the source of release if unknown.

Thus, LIF profiling did not detect new highly transmissive areas at the petrol station site besides of those already identified through the extensive monitoring network but still presented good agreement with the existing CSM and contributed to further develop it.

6.2.3.3 Quantitative relationship between LIF response and S_n

The good agreement between LIF and T_n contrasted with the poor correlation between LIF response and values of S_n measured in adjacent cores. Table 6.2 summarises the key elements of all three coring areas (A, B, and C), where area C exhibited the highest b_n and S_n values (0.70 m and 20 %, respectively) and area A the lowest ones (0.30 m of b_n and S_n equal to 6 %) among areas A, B, and C. Map 16 (see Appendix B: Maps) shows the spatial correlation between peak LIF signal, integral LIF signal, T_n, and b_n at the petrol station site.

Table 6.2. Summary of key parameters measured in the three coring areas during the HRSC campaign. Data from areas A, B and C correspond to cores MP50-A, MP58-B and MP44-C, LIF logs LIF43-A, LIF51-B and LIF57-C, and wells PB29-A, PB27-B and PB40-C, respectively. The T_n value for PB40-C was linearly interpolated using measurements of 0.577 m^2/day on 06/04/2016 and 0.304 m^2/day on 14/06/2016.

Coring area	T_n [m^2/day]	Maximum S_n [%]	b_n [m]	Peak LIF signal [%RE]	Integral LIF signal [%RE·cm]
A	1.51	6	0.324	289.2	1964.3
B	0.57	8	0.320	125.4	2256.8
C	0.45	20	0.750	122.3	1528.8

Thus, a potential inverse rank correlation between T_n and both b_n and S_n could have been inferred from the core values due to the site heterogeneity, while LIF signal (both integral and maximum) was positively correlated. Therefore, unlike the core S_n values, LIF response was a good indicator of T_n considering one site with one type of LNAPL product. The main outcome from Table 6.2 is that the type of geological material (finer-grained in area C than in areas A and B) where mobile LNAPLs exist may play a dominant role on LNAPL mobility and LIF response.

Fig. 6.3 illustrates the weak correlation between S_n and the natural logarithm of LIF response. The included data represent values of S_n and total LIF signal from areas A, B, and C excluding two logs in areas B and C with LIF signals below 10 %RE. LIF values were linearly interpolated at the same elevations where S_n was measured through coring. The

red and black dotted lines represent site-specific linear and exponential relationships between the tested parameters in the petrol station site.

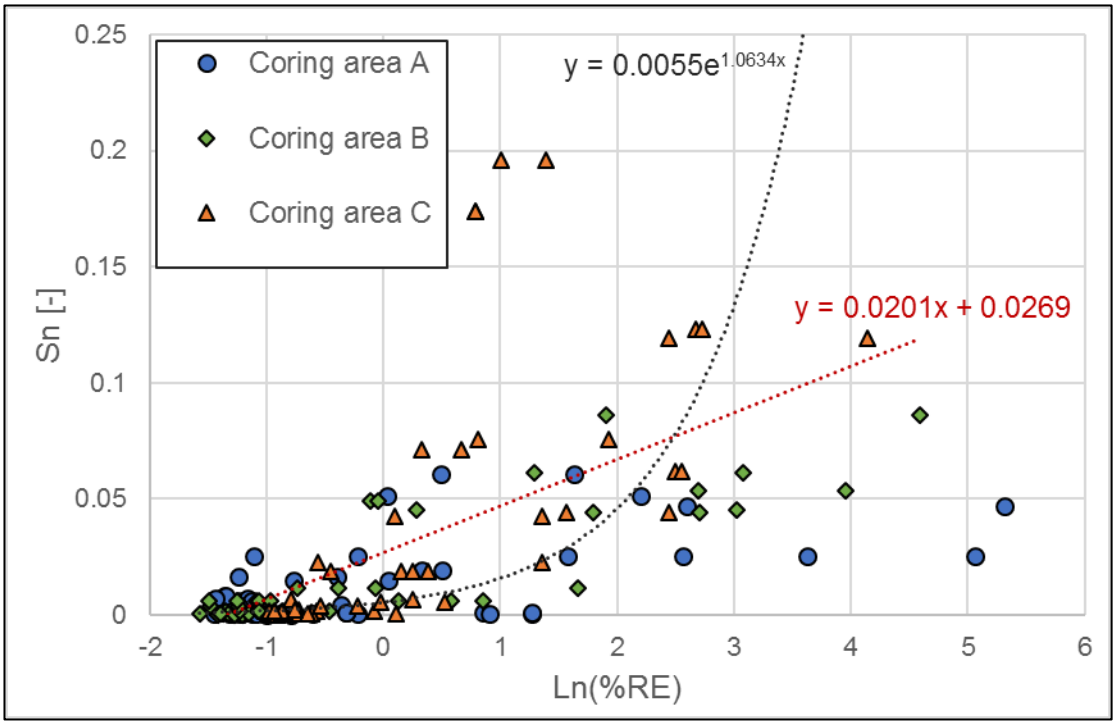


Fig. 6.3. Scatterplot of LIF response versus S_n in areas A, B, and C. The red and black dotted lines represent site-specific linear and exponential models, respectively.

Site-specific models exhibited high MAE and RMSE values: 4.4 % and 0.174, respectively, using an exponential relationship, and 1.9 % and 0.032 for a linear relationship. These errors were large considering that the arithmetic mean of S_n in the field was only 3.6 %, although they may be acceptable for some applications. Moreover, the lack of correlation was more apparent when only data points with S_n values over 1 % and LIF responses over 3 %RE were considered. It should be noted that this analysis already excluded two LIF logs in areas B and C with signals below 10 %. Consequently, designing a representative LIF network according to the site heterogeneity is essential to achieve an effective field site characterisation and also obtain scale-appropriate measurements in the horizontal plane.

The correlation between LIF response and S_n was also investigated in area T3. This scenario was closer to the one explored by Teramoto et al. (2019) at laboratory scale, who found a logarithmic correlation between LIF response and diesel in a sandstone matrix. As depicted in Fig. 6.4, LIF response from LIF18-T3 and S_n measurements from

core C66-T3 exhibited an even weaker relationship in area T3 than in the petrol station site. This lack of correlation occurred even if subsurface materials were relatively homogeneous sands. LIF logging produced a relatively constant response across the vertical profile at elevations where S_n was measured. One reason for the discrepancy between both methods could have been the considerable distance between LIF18-T3 and core C66-T3, although other LIF logs located at similar distances presented similar profiles (as shown in section 6.4.6).

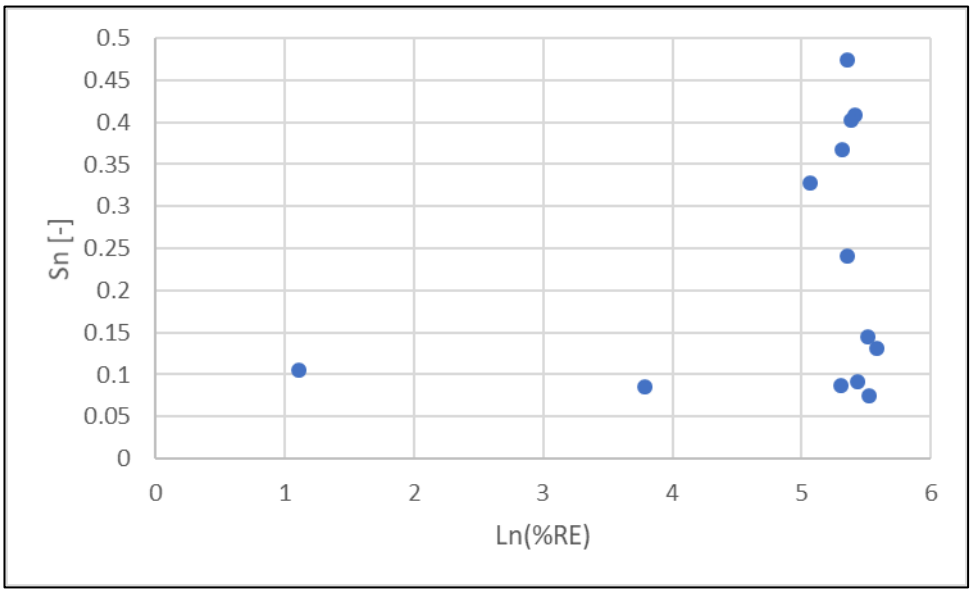


Fig. 6.4. Scatterplot of filtered LIF response at LIF18-T3 versus S_n in coring area T3.

6.2.3.4 Vertical LNAPL distribution according to LIF logs

There was clear disparity between the shape of the vertical profiles at the petrol station site and the industrial site, and the smooth shark-fin shapes theoretically predicted for homogeneous geological scenarios under VEQ conceptual models. The LIF profiles from the industrial site consisted of relatively wide bands, in particular those in diesel-impacted areas. The contours of these bands were smoother in the case of high-viscosity crude oils, while kerosene-type jet fuel profiles presented more spikes.

Such spikes were even more prominent at the petrol station site, where most of the profiles mainly consisted of narrow peaks. There was a certain degree of correlation between %RE and the stratigraphic profile represented by core descriptions, HPT logs and EC logs, but these tools could not quantitatively explain all the variability exhibited by the LIF profiles. Fig. 6.5 depicts the lack of linear correlation between LIF57-C and EC

from HPT60-C, being both logs obtained less than 1 m away from each other. The highest LIF responses were obtained at low EC values representing coarser-grained intervals as supported by HPT logs.

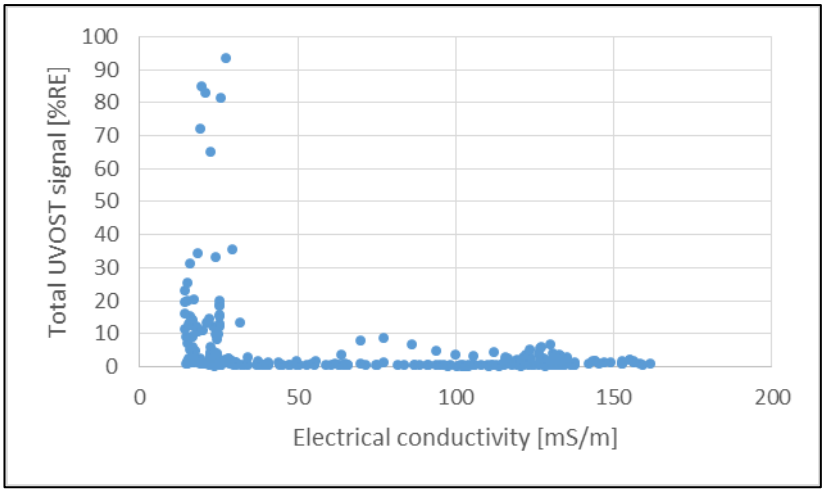


Fig. 6.5. Total LIF signal at LIF57-C versus EC at HPT60-C.

Fig. 6.6 shows good qualitative agreement between logs from LIF57-C and HPT60-C (EC). Multiple spikes were associated to reductions in EC, although higher degree of variability was shown by the LIF profile. For instance, two fluorescence peaks recorded at 55.90–56.00 m AHD could be linked to the same drop in EC. Similar observations could be made for other LIF spikes, for instance between 55.40 and 55.70 m AHD, suggesting that these spikes could have been partially caused by geological heterogeneity or that LNAPL presence decreased EC as expected in early-stage releases. Smoother profiles like those obtained by core sampling could not capture this degree of detail because of the lower sampling resolution and the different influence posed by the medium.

Therefore, LNAPL distribution profiles with more spikes and layering were linked to subsurface heterogeneity, whose effects could be magnified by the nature of the LIF sensor and potentially less viscous LNAPLs. Nevertheless, similar profile shapes with viscous LNAPLs can be found in the literature. In the past, spikes have been attributed to the presence of remaining fractures and other secondary porosity features, LNAPL weathering in water-washed features, and interference from fine-grained particles in the rock matrix (Mulry and Lundy, 2013). Results from the petrol station site corroborated that these profiles can be obtained in common sedimentary environments.

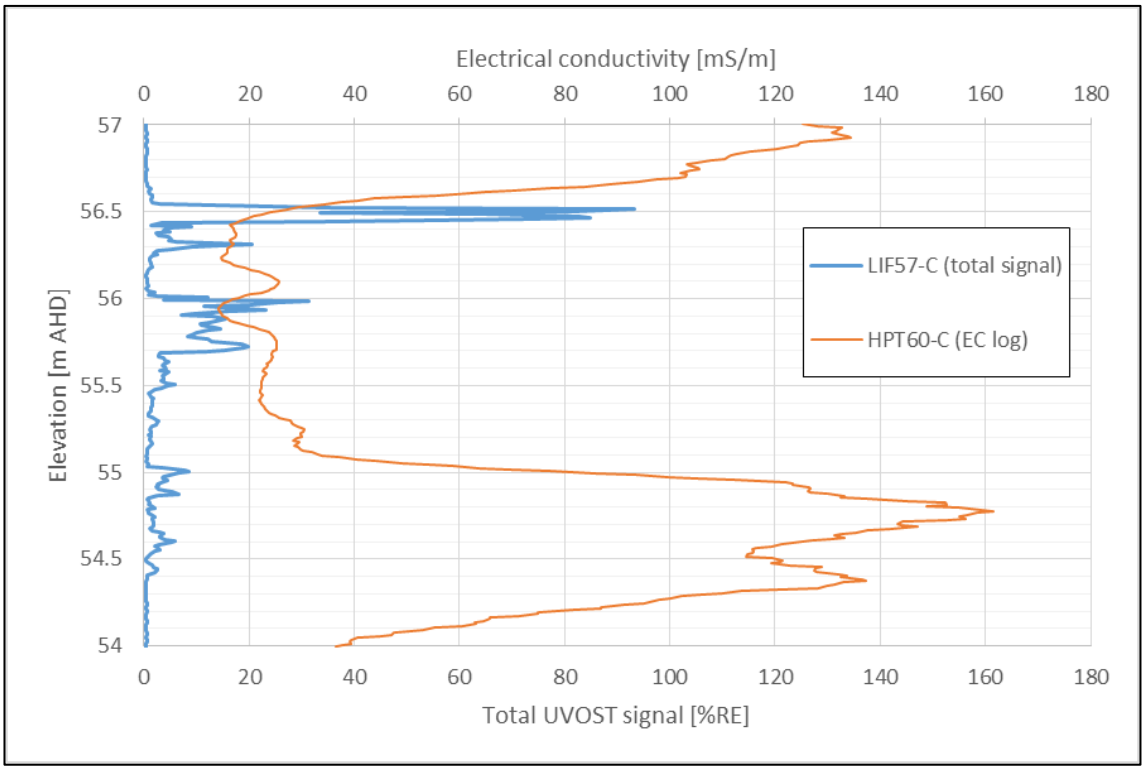


Fig. 6.6. LIF57-C log and HPT60-C EC log.

6.2.3.5 Impacted interval according to LIF logs

LIF profiles did not show much more than 1 m of fluorescence at any location in areas A and B. However, areas C and profiles close to the UST frequently presented more than 2 m of fluorescence. This was qualitatively consistent with measured values of b_n and the core LNAPL saturation profiles, typically higher in area C (average b_n was around 2.5 times higher in area C than in areas A and B). A quantitative comparison is not straightforward since each parameter (LIF response, b_n, S_n) is affected in different ways by the geological medium, the LNAPL properties, and the methodological procedure.

LIF profiles generally suggested a larger interval impacted by LNAPL than b_n, although the main LIF peaks were narrower than b_n. Accordingly, assuming near-equilibrium conditions, it could be inferred that LIF was able to detect not only mobile LNAPL but also near-immobile LNAPL (entrapped or residual).

The main LIF peaks were usually found at similar elevations in the petrol station site (approximately 56.1–56.5 m AHD, around 5 m bgl), roughly consistent with values of z_{aw} during the HRSC campaign (approximately 56.15 m AHD). Current multiphase theory

also predicts the highest S_n values just above z_{aw} under VEQ conditions with low entry pressures.

On the contrary, a few profiles (for instance LIF51-B) and other studies reported some maximum LIF signals below z_{aw} (Bujewski and Rutherford, 1997), which may be due to different reasons such as confined LNAPL conditions, entrapment of all the LNAPL, non-equilibrium conditions (a possible reason in the case of LIF51-B), subsurface heterogeneity (for instance, a fining-upward sequence, which was another possible reason for such kind of observations in the petrol station site), changes in the entry pressure, false positives and negatives, or inaccuracies in the elevation survey and the measurement of z_{aw}. Under confined or semi-confined LNAPL conditions, maximum LIF signals are expected to be typically found below z_{aw} as shown in the literature (McCall et al., 2018).

6.3 Multi-wavelength waveforms and identification of near-immobile LNAPL

6.3.1 LNAPL signatures and correlation between excitation channels

Section 6.3 investigates the spectral information given in the form of multi-wavelength waveforms by the LIF system. Section 6.3.1 examines the correlation between the four LIF channels (350 nm, 400 nm, 450 nm, and 500 nm) for different types of LNAPL product. This relationship between the multiple channels and the total signal may have implications on any analysis with LIF data. In addition to a few characteristic profiles from the petrol station site, data from the industrial site were also considered to explore the effects of several types of LNAPL product on LIF response. Section 6.3.2 makes use of these multi-wavelength waveforms to effectively identify intervals with long-term, near-immobile LNAPL at the petrol station site.

Different types of LNAPL, degrees of weathering, false positives, and other anomalies were inferred from the analysis of multi-wavelength waveforms. Dissimilar multi-wavelength waveforms were found at the industrial site due to the presence of several types of LNAPL (diesel, petrol, kerosene-type jet fuel, crude oil). Multi-wavelength waveforms corresponding to the main peak LIF responses at the petrol station site resembled those that would be expected for relatively fresh petrol (Lu et al., 2014).

However, a few logs like LIF69-C suggested the existence of anomalous weathering conditions.

Fig. 6.7 collates fluorescence signatures (without applying any filter) obtained at representative depths in different areas of the petrol station site and the industrial site. The multi-wavelength waveforms were in good agreement with the type of LNAPL product presumed according to the sites history and the chemical analyses performed. The highest response at 350 nm was from kerosene-type jet fuel followed by petrol and far weaker in the cases of diesel and crude oil. Weathering reduced the response of petrol at 350 nm increasing in different proportions the other three channels. The inspection of multi-wavelength waveforms at LIF69-C suggested that the LNAPL product at this location was weathered petrol. Diesel was characterised by a stronger increment of the 450 nm and 500 nm wavelength channels, more evident in the case of crude oil. Diesel also exhibited greater lifetimes than petrol and a characteristic short–long–long–long lifetime pattern in the four channels.

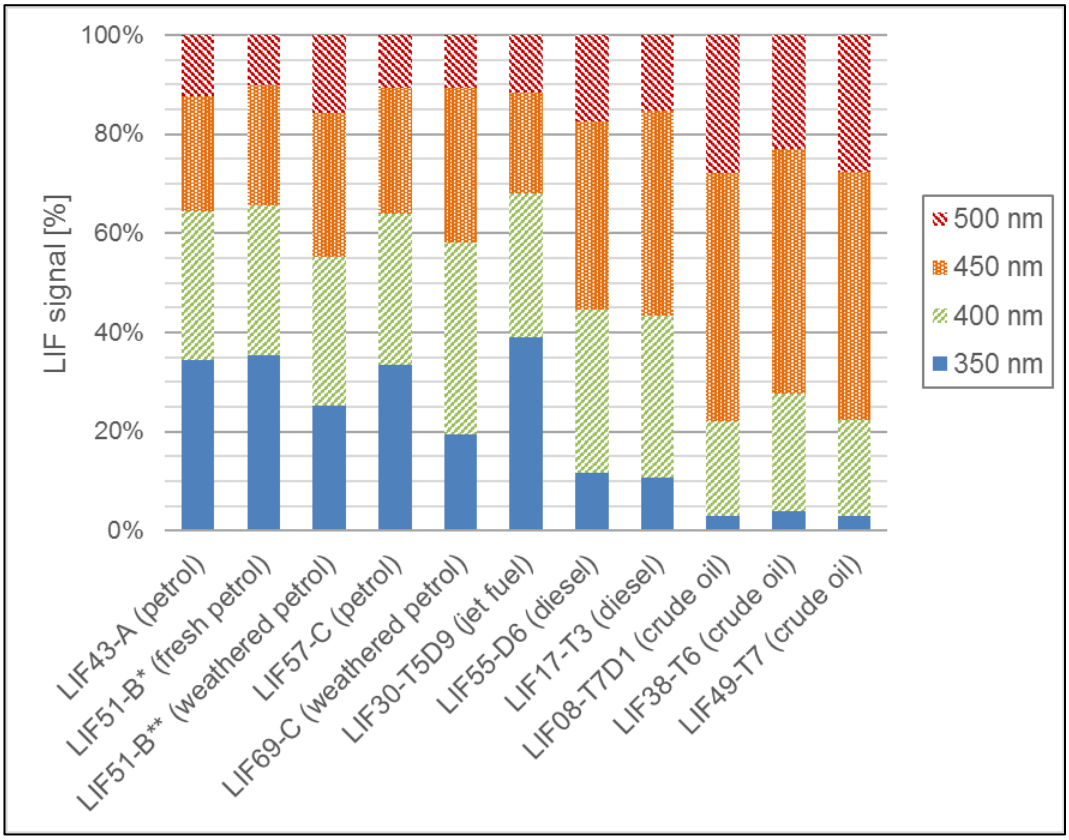


Fig. 6.7. Fluorescence signatures of several LNAPLs in the petrol station site and the industrial site. The presumed type of LNAPL is indicated between parenthesis. LIF51-B* and LIF51-B** depict the signature of LNAPL at LIF51-B above and below 55.854 m AHD, respectively.

As seen in Fig. 6.8, the contrast between different LNAPL types was more pronounced regarding the chemical composition (comparing concentrations in ppm) than in terms of LIF signature, being diesel and crude oil dominated by PAHs, while BTEX and TMBs were more important in the case of petrol and kerosene-type jet fuel. A clear quantitative correlation between chemical analysis results and fluorescence signatures was not found. Similarly, diagnostic forensic ratios were calculated aiming to identify distinct weathering conditions but not clear correlations were derived besides of a stronger depletion of C_5 hydrocarbons in the shallowest samples due to volatilisation phenomena.

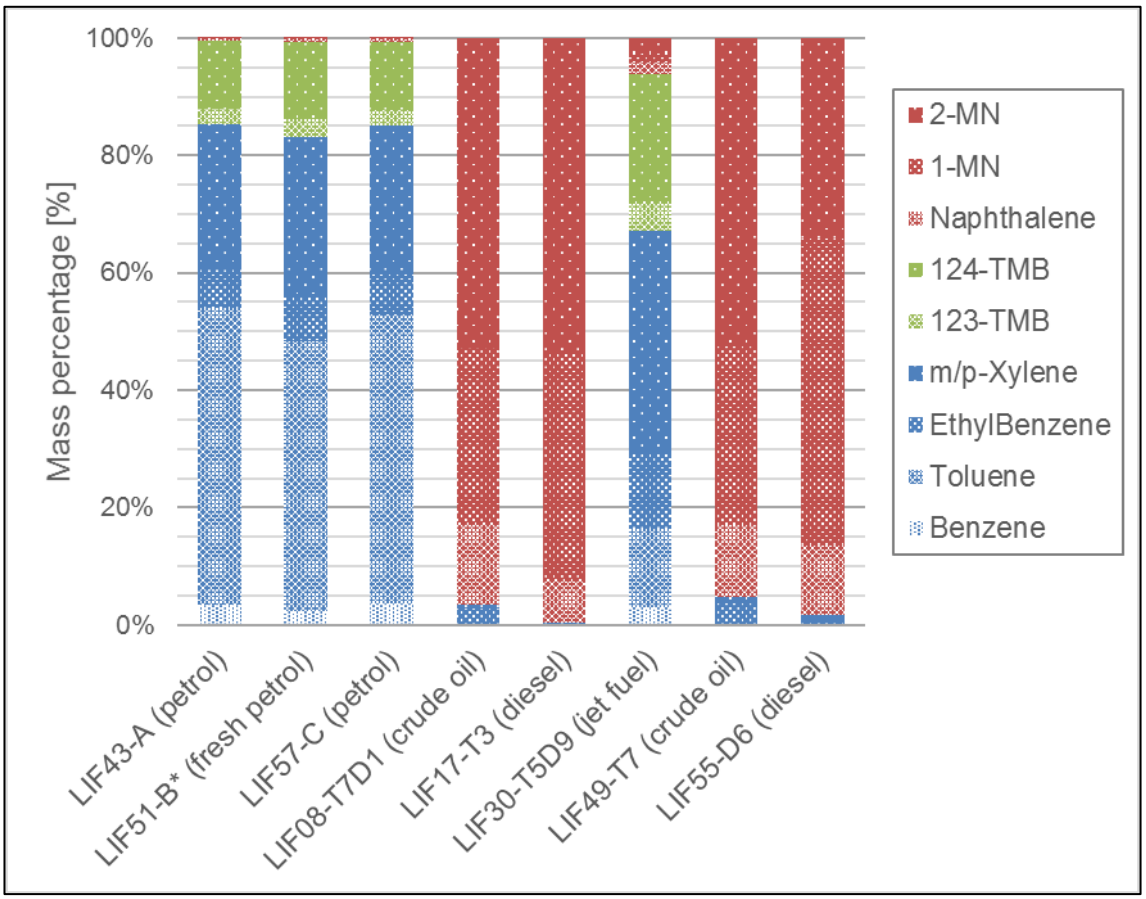


Fig. 6.8. Mass percentage of the analysed chemical compounds in samples of different LNAPL types. LIF51-B* only considers samples above 55.854 m AHD.

In addition to the subsurface heterogeneity, one reason impeding effective quantitative calibrations of LIF response was likely the limited number of PAHs analysed. Many polycyclic aromatic compounds are not commonly analysed for the assessment of contaminated sites, although they may be essential in forensic investigations

(Andersson and Achten, 2015; Stout et al., 2015). Thus, further research on assessing the potential impact of some of these compounds on LIF response is encouraged.

There was generally good correlation between the different channels at the petrol station site, although slightly worse with the 500-nm channel at high values. Fig. 6.9 shows the correlation with the 500-nm channel.

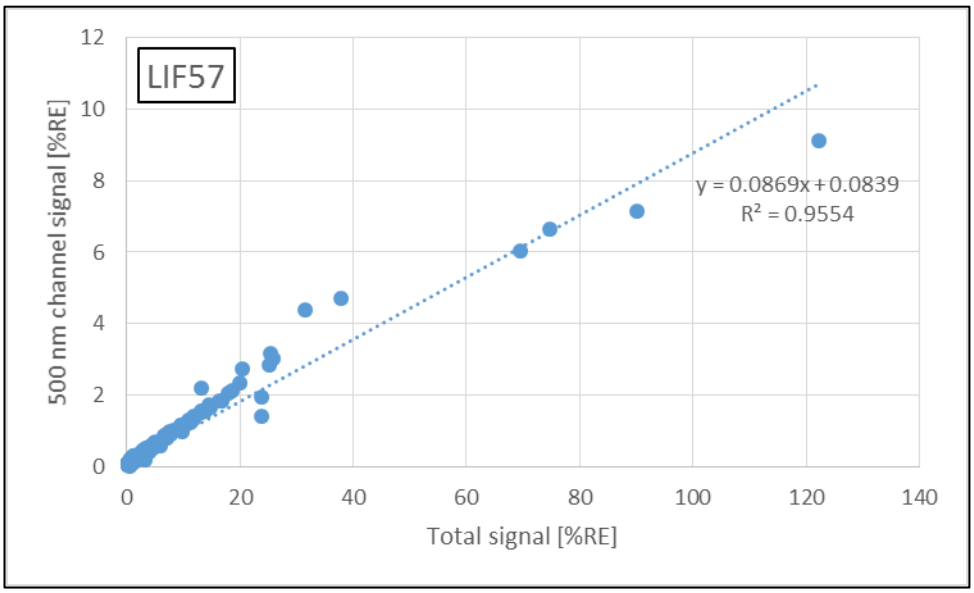


Fig. 6.9. Correlation between the 500-nm channel and total LIF response at LIF57-C.

For instance, Fig. 6.10 illustrates the case of LIF69-C that showed differentiated multi-wavelength waveforms as discussed in section 6.3.2. Even if the product at this location was also petrol (weathered), the correlation of the total LIF signal was noticeably better with the 400-nm and 450-nm channels than with the 350-nm band. In general, the type of LNAPL product determined which LIF channel exhibited the greatest correlation with the total signal in LNAPL-impacted intervals.

Total LIF signal was generally a good predictor of the channels affected by LNAPL contamination, but it could over- or underestimate values at certain ranges. This was especially relevant for the identification of presumably less-mobile LNAPL because of the lower total LIF response. Therefore, relative LIF signals and LIF lifetime data were considered in the analysis of specific areas presented in section 6.4.

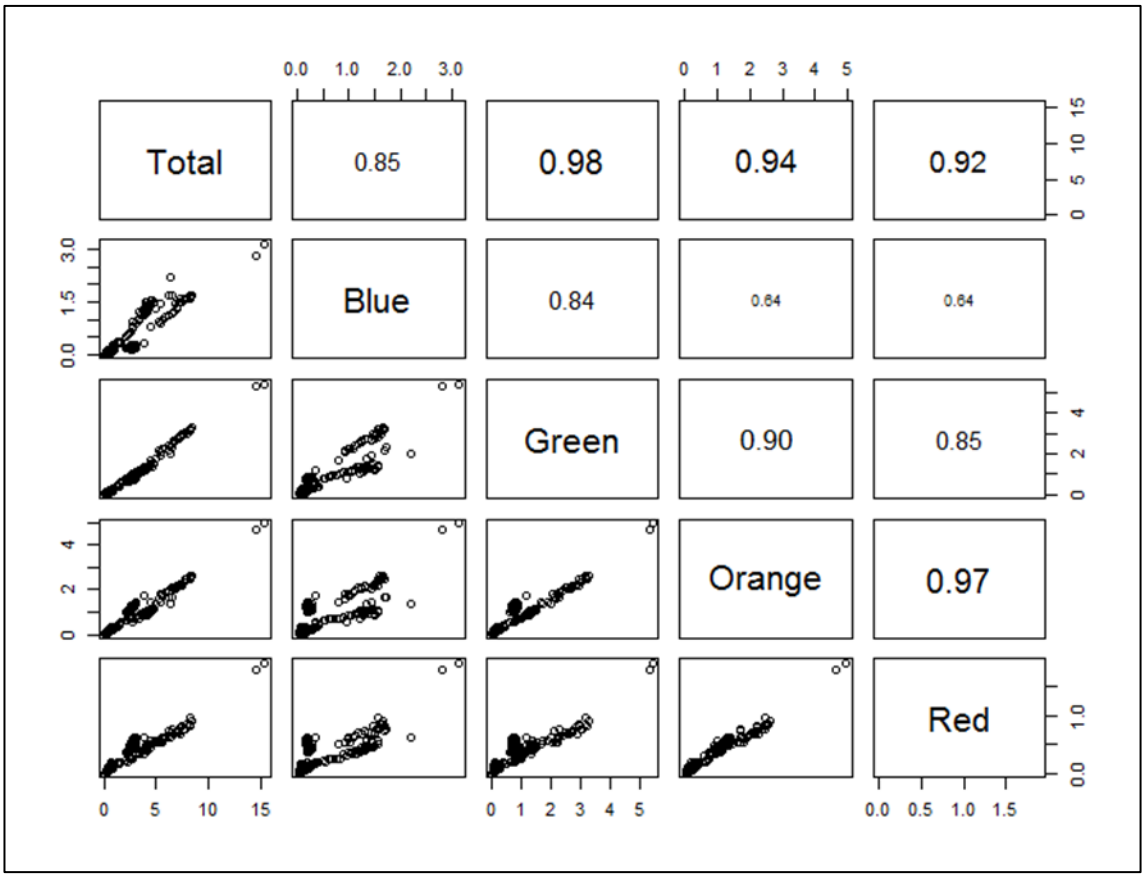


Fig. 6.10. Correlation between the four channels (blue, green, orange, and red represent the 350-nm, 400-nm, 450-nm, and 500-nm channels) and total LIF response at LIF69-C. The numbers in the upper panels correspond to the coefficients of determination.

6.3.2 Identification of long-term near-immobile LNAPL in the petrol station site

6.3.2.1 Identification of long-term entrapped LNAPL

Subtle changes in colourisation with depth and longer waveform lifetimes were frequently observed in the LIF logs and could be interpreted as a sign of distinct weathering conditions (lower response from the 350 nm channel compared to the other channels) at lower elevations. A comparison with z_{aw} indicated that distinct LIF signatures could be linked to historical fluid levels. More specifically, some LNAPL could have been entrapped at least since the start of the monitoring campaigns in 2014.

Fig. 6.11 illustrates the case of LIF51-B along fluid levels from PB27-B as well as vertical profiles of Q/P (after correcting for hydrostatic pressure) and electrical conductivity (EC) at HPT74-B. The LIF log showed entrapped LNAPL that could not be explained by the monitoring campaigns alone when it was registered (May 2016). Historical minimum

fluid elevations were obtained in May 2018 when z_{nw} reached the LNAPL interval below 55.854 m AHD after at least four years of entrapment conditions.

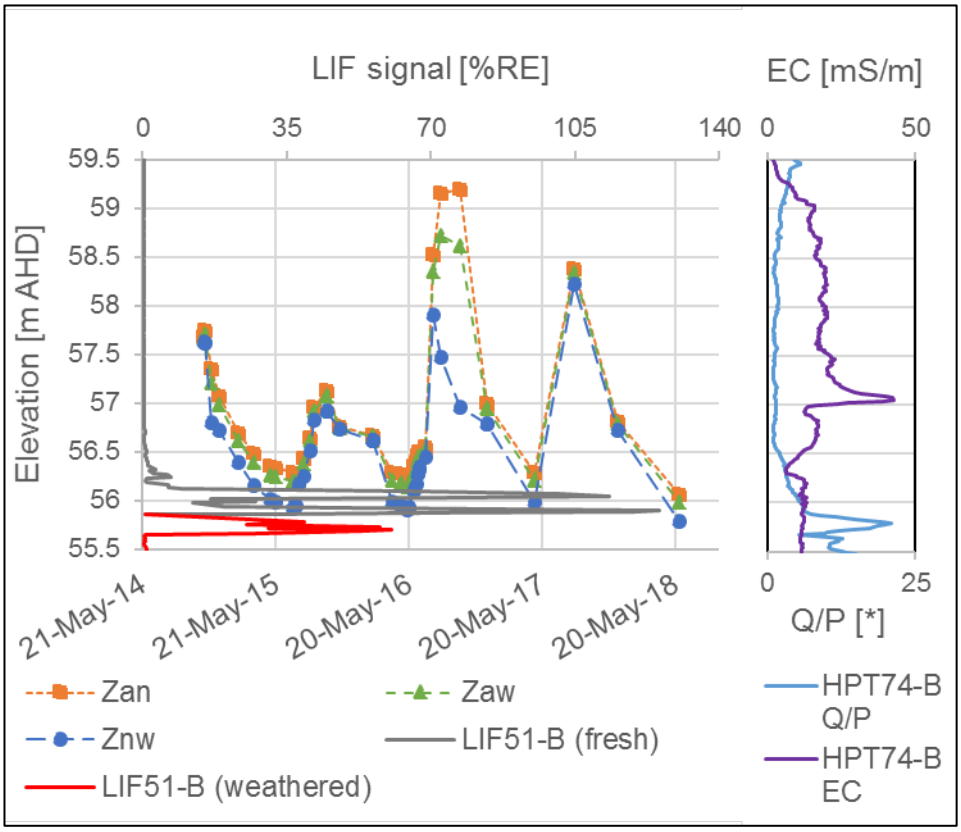


Fig. 6.11. Relation between historical fluid levels and distinct LIF signatures at LIF51-B along HPT data. Fluid level elevations correspond to PB27-B (1.378 m away). *HPT data correspond to HPT74-B (0.985 m away) where Q/P is given in units of mL/(kPa·min).

Fig. 6.11 also reveals that the distinct LIF signature was linked to a peak of 21 mL/(kPa·min) in the Q/P log. Shifts in relative LIF signals with depth indicated that the different medium characteristics also affected its fluorescence and presumably the LIF signature in the LNAPL-impacted interval. Thus, multi-wavelength waveforms were not only affected by the LNAPL type and the existing weathering conditions, but also the medium properties as it has been previously reported in the literature (Kram and Keller, 2004; Alostaz et al., 2008; Lu et al., 2014). Microbiological activity could have been another reason behind this change in the LIF signature that requires further investigation.

Furthermore, LNAPL presence was not clearly associated with high EC signatures as it has been frequently found in cases of weathered LNAPL because of factors such as

microbial activity and chemical alteration of the pore solution (Atekwana et al., 2000; Atekwana and Atekwana, 2010). Low EC values could be explained because of the coarser-grained materials where the entrapped LNAPL was found and the relatively short-term nature of the contamination event, since a few years is not necessarily enough time to appreciate an increase in the geophysical signature as measured with the EC method (Atekwana and Atekwana, 2010). On the contrary, the combination of coarser-grained materials and distinct weathering conditions could have contributed to the high LIF response even at low S_n values (low enough to represent entrapped LNAPL in these materials), explaining why entrapment conditions were not so easily identifiable in other logs.

6.3.2.2 Identification of long-term residual LNAPL

LIF profiling also provided signs of LNAPL contamination at shallow depths (see profiles LIF56-C, LIF66-C, LIF68-C, and LIF69-C in area C as well as LIF55). In-well fluid levels from adjacent locations did not suggest presence of LNAPL at this elevation. Therefore, these LIF measurements likely represented some form of non-recoverable or stationary LNAPL, which was assumed to be residual in the following paragraphs.

In addition, S_n profiles obtained from core analysis at ML15, PB13-C, and PB39-C showed positive S_n values at shallow depths, but it was not possible to discriminate between residual and mobile LNAPL intervals, partly due to the low frequency of sampling compared to the LIF system and potentially some redistribution of LNAPL mass throughout the core during the sampling procedure. Soil gas measurements from ML15, PB13-C, and PB39-C were not able to discriminate between different intervals either, although positive readings at shallow depths were also obtained in the case of MP44-C.

LNAPL could have reached this shallow zone after an increase in z_{aw} as suggested by Fig. 6.12 for LIF69-C, the clearest profile indicating the presence of LNAPL in this interval. The interval between 57.1 and 57.5 m AHD represented the most unique multi-wavelength waveform, with a stronger response in the 400-nm channel than in the 350-nm one. Thus, there was a stronger shift in the LIF signature corresponding to residual LNAPL at LIF69-C than in the case of entrapped LNAPL at LIF51-B due to the different weathering processes and medium characteristics.

An analysis of a neaby HPT log (HPT61-C) as presented in Fig. 6.12 provided some insight into the stratigraphic setting at LIF69-C. In general, there was an inverse relationship between Q/P and EC logs, which is likely due to their opposite response to fine-grained and coarse-grained materials. More specifically, a drop in Q/P between 56.6 and 57.1 m AHD was accompanied by an increase in EC, suggesting the presence of a clay lens just below most of the LNAPL mass. These clay lenses may become sources of back-diffusion contamination. Similarly, a decrease in Q/P above 59 m AHD constrained the upper limit of the LNAPL mass. In this case some overlapping occurred between the clay lens (high EC values) and the vertical LNAPL distribution despite the maximum LIF signal being found just above the maximum EC response. Nevertheless, high EC values could not be used as a clear indicator of LNAPL weathering due to the influence of the geological medium.

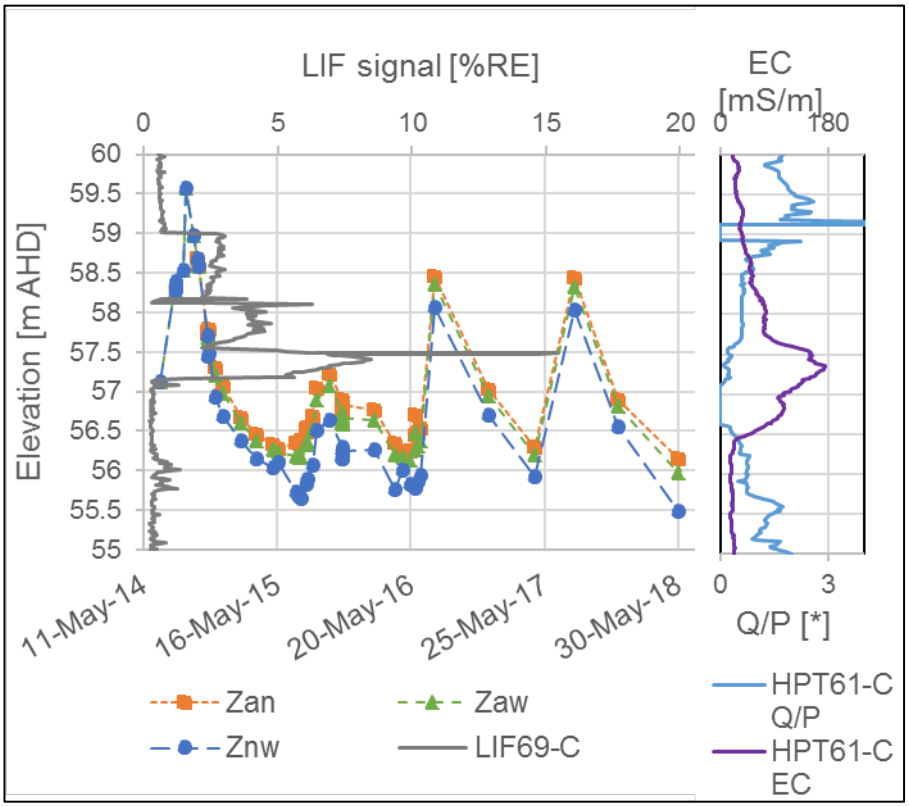


Fig. 6.12. Long-term residual LNAPL at LIF69-C. Fluid level elevations correspond to MP08-C (3.475 m away). *HPT data correspond to HPT61-C (0.863 m away) where Q/P is given in units of mL/(kPa·min).

6.4 Comparison of LIF and coring in the areas of study

6.4.1 Section structure

Section 6.4 includes further analysis of specific LIF profiles located in areas A, B, C, and T3. The analyses varied according to the area specificities, but generally involved:

- a comparison of twin LIF profiles logged less than 2 m away from the production well, usually illustrated with a butterfly plot;
- an evaluation of other LIF, S_n, and soil gas profiles in the area or next to the area;
- a comparison between in-well fluid levels and LIF profiles as well as S_n profiles obtained through coring at less than 2 m distance during the same drilling campaign;
- a discussion of the effects of the subsurface hydrostratigraphy on the LNAPL distribution through inspection of HPT logs (HPT P, HPT Q, and EC), comparing them to LIF and S_n profiles;
- an inspection of logs with relative LIF signals, total LIF signals represented in logarithmic scale, and lifetime data to further investigate the intervals impacted by LNAPL as well as the confining contact elevation and the integrity of the overlying aquitard;
- final recommendations to build model scenarios resembling the area of study considering multiple layers if needed.

6.4.2 LNAPL distribution in adjacent coring and LIF locations

Before analysing specific areas, cores collected in adjacent locations were compared to investigate if discrepancies between the obtained S_n profiles could indicate loss and redistribution of LNAPL mass during the core extraction process, which could have also contributed to the poor correlation between LIF response and field measurements of S_n presented in section 6.2.3.3. Cores were collected before and after the LNAPL mass recovery trial from 2016 (MP50-A, MP58-B, and MP44-C in May 2016; MP77-A, MP76-B, and MP78-C in August 2016).

As depicted in Fig. 6.13, multiple similarities existed between S_n profiles measured in the two sets of cores, including similar S_n ranges, maximum S_n values, impacted intervals, and shape of the vertical S_n distribution. Measurements of S_n in the petrol station site

and the industrial site were within ranges typically found in LNAPL contaminated sites (e.g. Adamski et al., 2003). Furthermore, many of the differences between both sets of cores (caused by the migration of the LNAPL body upwards, as well as the deep entrapment of some LNAPL mass) could be explained by the rise in z_{aw} between the two coring campaigns and the application of LNAPL mass recovery operations, including water-enhanced recovery.

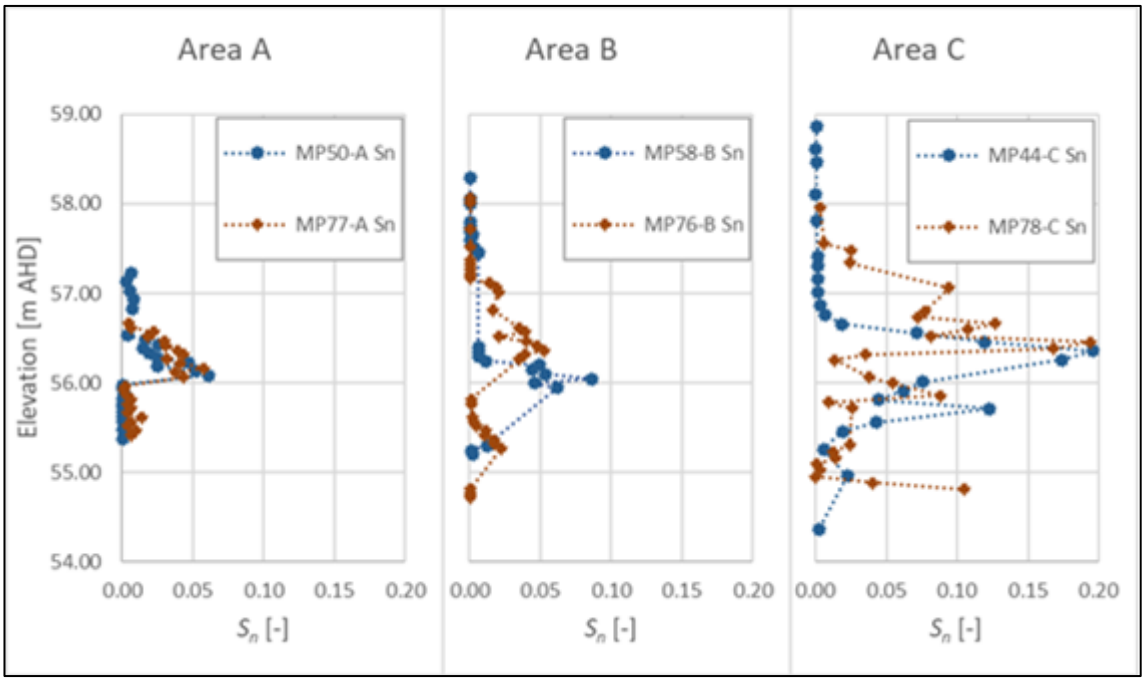


Fig. 6.13. S_n profiles measured through coring in areas A, B, and C. Cores MP50-A, MP58-B, and MP44-C were collected during the HRSC campaign in May 2016. Cores MP77-A, MP76-B, and MP78-C were collected in August 2016 after a rise in z_{aw} and the application of LNAPL mass recovery operations.

Nevertheless, cores collected after the LNAPL mass recovery trial did not corroborate the existence of LNAPL above 56.6 m AHD at MP50-A nor above 57.1 m AHD at MP58-B. Therefore, these low S_n values measured at MP50-A and MP58-B could have been due to fluid redistribution occurring during the extraction and handling of cores. Sharp changes in S_n could be interpreted as a sign of limited fluid redistribution (Hess et al., 1992a).

The measurement of total liquid saturation also provided insight into errors arising from coring operations. Total liquid saturation may be below 100 % in the saturated zone due to the presence of entrapped gases. Saturated water content θ_{ws} is frequently 5–10 %

lower than Φ in groundwater systems due to entrapped air (van Genuchten et al., 1991). Methanogenic outgassing associated to LNAPL bodies could further decrease the total liquid saturation in the saturated zone. Amos and Mayer (2006) predicted gas saturation values over 30 %. Removal of biomass and EPS during the estimation of liquid saturations may also affect the representativeness of the measurements.

Considering values below z_{aw} in the petrol station site, the average total liquid saturation was 85 % at MP50-A, 59 % at MP58-B, and 76 % at MP44-C, revealing loss of water and presumably LNAPL during the sampling process. Consequently, there were uncertainties associated to the S_n profiles, especially at MP58-B (measurements of total liquid saturation below 60 % were obtained at 55.296 m AHD and above 55.95 m AHD). Average total liquid saturations measured in August 2016 were 74 % at MP77-A, 73 % at MP76-B, and 87 % at MP78-C. The average total liquid saturation measured below z_{aw} in area T4 was over 85 %.

Despite multiple sources of error associated to coring, there was closer agreement between S_n profiles obtained in adjacent locations than between twin LIF logs. The S_n profiles were integrated by middle Riemann sums (calculating the area between the y-axis and measurements of S_n) and compared to those obtained in adjacent locations after an increase in z_{aw}. There was a change of 22 % between MP50-A and MP77-A, -11 % between MP58-B and MP76-B, and 8 % between MP44-C and MP78-C. As depicted in Fig. 6.14, integral LIF signals exhibited greater differences even if they were obtained in the same field campaign. The effects of fine-scale heterogeneity on LIF response (along uncertainties related to the monitoring network design and the complex LNAPL distribution in the subsurface) could represent an explanation for these differences. According to these observations, dissimilarities between twin LIF profiles likely contributed more to the poor correlation between LIF response and S_n values than coring errors.

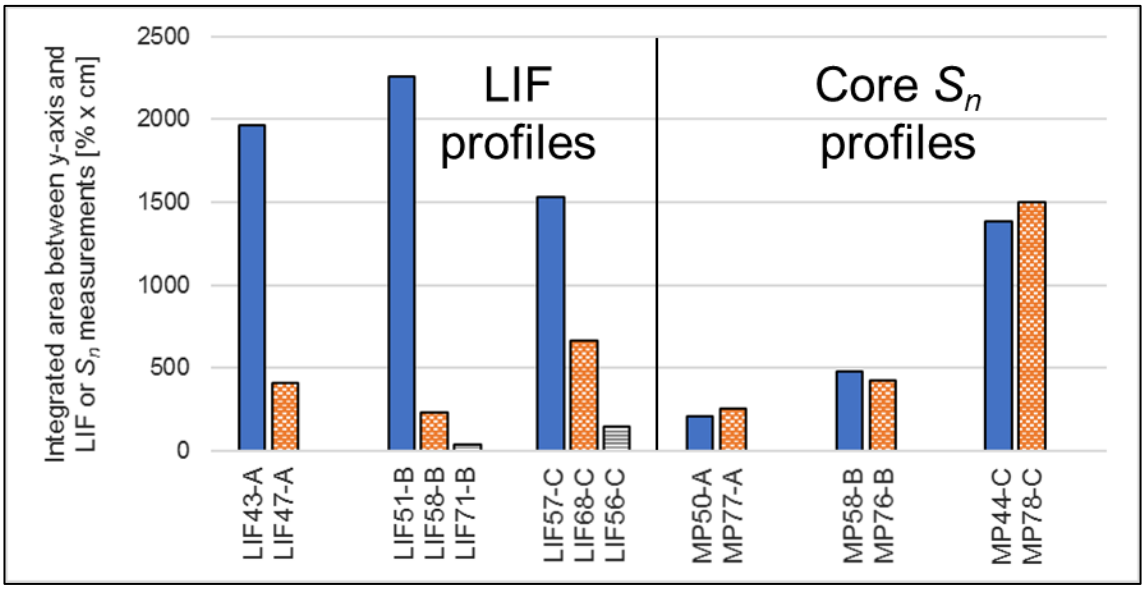


Fig. 6.14. Integrated LIF and S_n data from adjacent locations in areas A, B, and C.

Further analysis of the S_n distributions is presented in the following sections. Chapter 8 compares these field measurements of S_n with model predictions. In general, LNAPLTRANS predictions were in reasonably good agreement with field S_n data.

6.4.3 Petrol station site. Area A

6.4.3.1 Analysis of twin LIF logs

In area A, LIF43-A and LIF47-A (separated by a distance of 2.5 m) presented some similarities as illustrated in Fig. 6.15. The main peaks were located at the same elevation (56.27 m AHD), although the response at LIF43-A was almost four times stronger. LIF47-A still presented one of the highest peaks at the petrol station site as shown in Fig. 6.2. PB29-A was located just between both LIF profiles and was the well exhibiting the highest T_n at the petrol station site between 2015 and 2018.

Both LIF profiles recorded very low signals at lower elevations (around 55.9 m AHD in the case of LIF47-A and around 55.8 m AHD at LIF43-A), which were still indicative of LNAPL contamination according to their multi-wavelength waveforms.

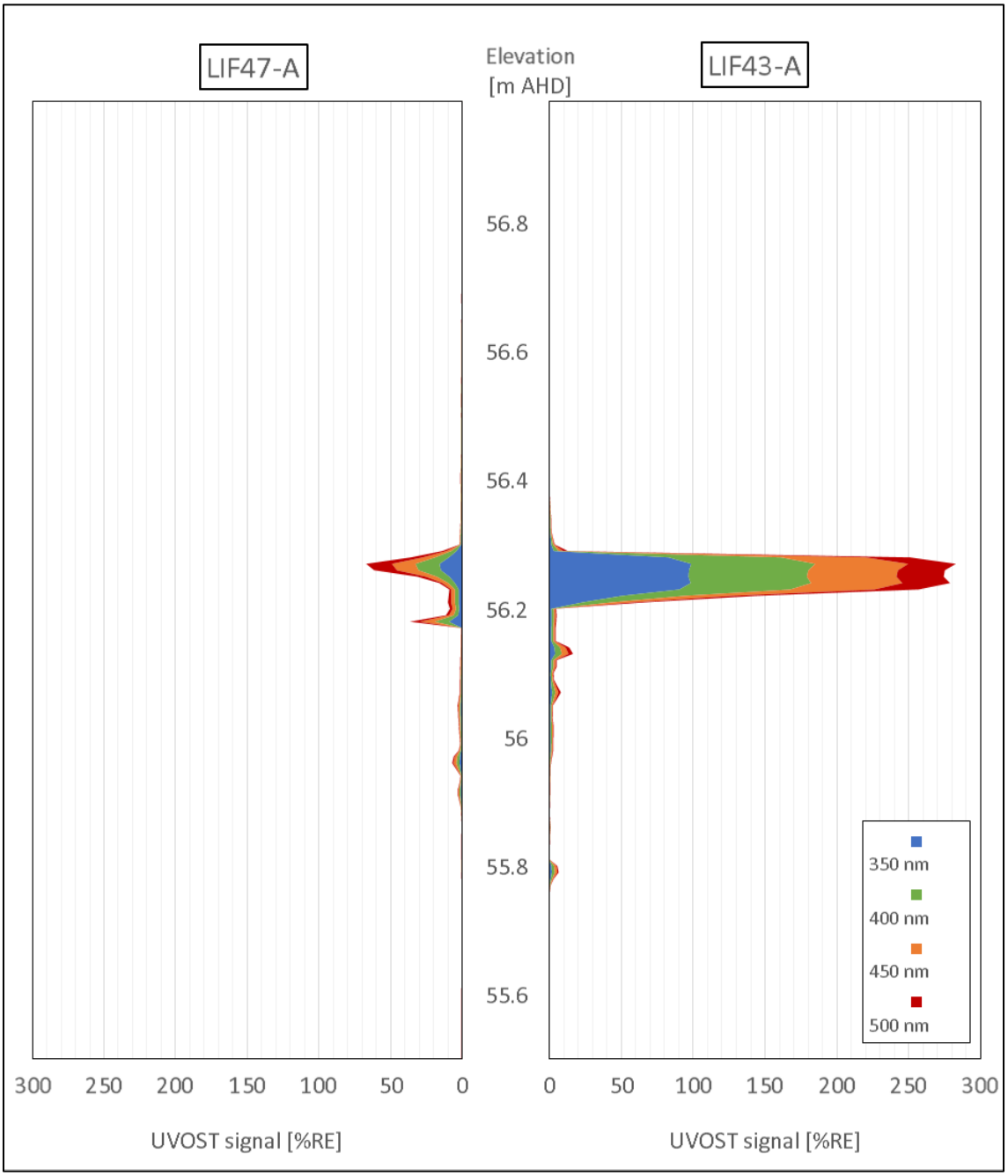


Fig. 6.15. Butterfly plot of LIF47-A and LIF43-A (interpolated values).

6.4.3.2 *Correspondence between conventional methods and adjacent LIF logs*

As measured at PB29-A, b_n was 0.331 m and z_{aw} was 56.142 m AHD on 17/05/2016, the day when the LIF profiles were logged. This value was likely measured under quasi-equilibrium conditions, since similar records were obtained before and after the drilling campaign (0.322 m on 28/04/2016; 0.303 m on 20/05/2016 after several baildown tests were performed). b_n decreased to 0.233 m on 01/06/2016. However, the main peaks obtained with LIF were roughly 0.1 m wide. z_{an} was dipped at 56.229 m AHD on

17/05/2016, which was within the LIF peak interval. z_{nw} was dipped at 55.898 m AHD, 0.2 m below the LIF peak. Accordingly, these low LIF values could have represented mobile LNAPL.

LIF profiles near area A (LIF46, LIF48, LIF70) showed weak or no response. This variation contrasted with the chemical analysis of soil cores, where a similar impacted area was found at PB33-A (more than 4 m away from MP50-A), even with this core being taken on 03/08/2015 (almost one year before MP50-A) when z_{aw} was 0.194 m higher (56.336 m AHD with b_n of 0.199 m at PB29-A on 03/08/2015 versus 56.142 m AHD with b_n of 0.331 m on 17/05/2016).

As depicted in Fig. 6.16(d), PB33-A and MP50-A showed low or no TPH concentration below 56 m AHD, maximum peaks around 56.25 m AHD and low TPH concentrations at shallower depths, reaching higher elevations in the case of MP50-A. TPH concentrations at MP50-A were more than twice as high as at PB33-A, although b_n values of PB33-A were similar to PB29-A (0.361 m at PB33-A on 17/05/2016 versus 0.331 m at PB29-A). This disparity can be explained by a finer material at PB33-A, which agreed with the fact of PB33-A being in a lower T_n region than PB29-A. LIF46 exhibited no response and was located less than 2 m away from PB33-A.

This comparison was done according to TPH concentrations and not S_n values (not calculated for PB33-A). Fig. 6.16(b) shows that qualitative differences between both parameters existed but were relatively small under typical subsurface conditions found in the petrol station site. Fig. 6.17 also indicates that the linear correlation between concentrations of PAH (as a sum of naphthalene, 1-MN, 2-MN, and phenanthrene) and BTEX, TPH, and S_n was considered good enough to assume that errors derived from chemical changes along the MP50-A profile were acceptable.

Fig. 6.16(a–b) show the MP50-A S_n profile. The shape did not resemble a shark fin and it looked inverted from what could be expected, with a deep peak and a gradual reduction in S_n upwards. The S_n peak was found at 56.081 m AHD, slightly below z_{aw} (56.142 m AHD) and the peaks of TPH concentration recorded at 56.231 m AHD. This could have been due to the geological setting and the corresponding entry pressure, non-equilibrium conditions, or errors associated to the sampling technique (for

instance, because of LNAPL redistribution across the core), the elevation survey, and the procedure to derive S_n values from TPH concentrations.

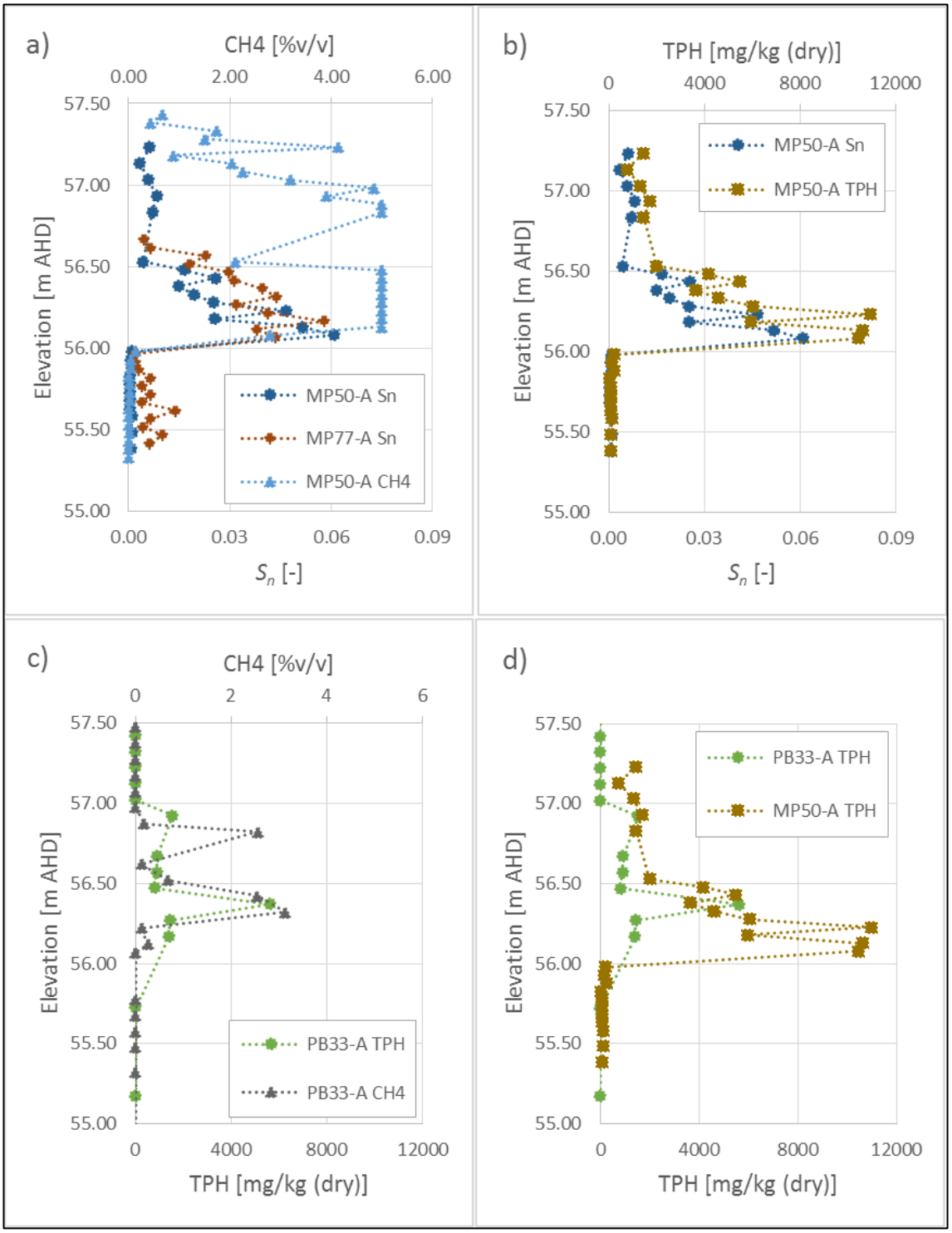


Fig. 6.16. Comparison of core analysis (S_n and TPH concentration) at PB33-A, MP50-A, and MP77-A, including soil gas measurements at PB33-A and MP50-A.

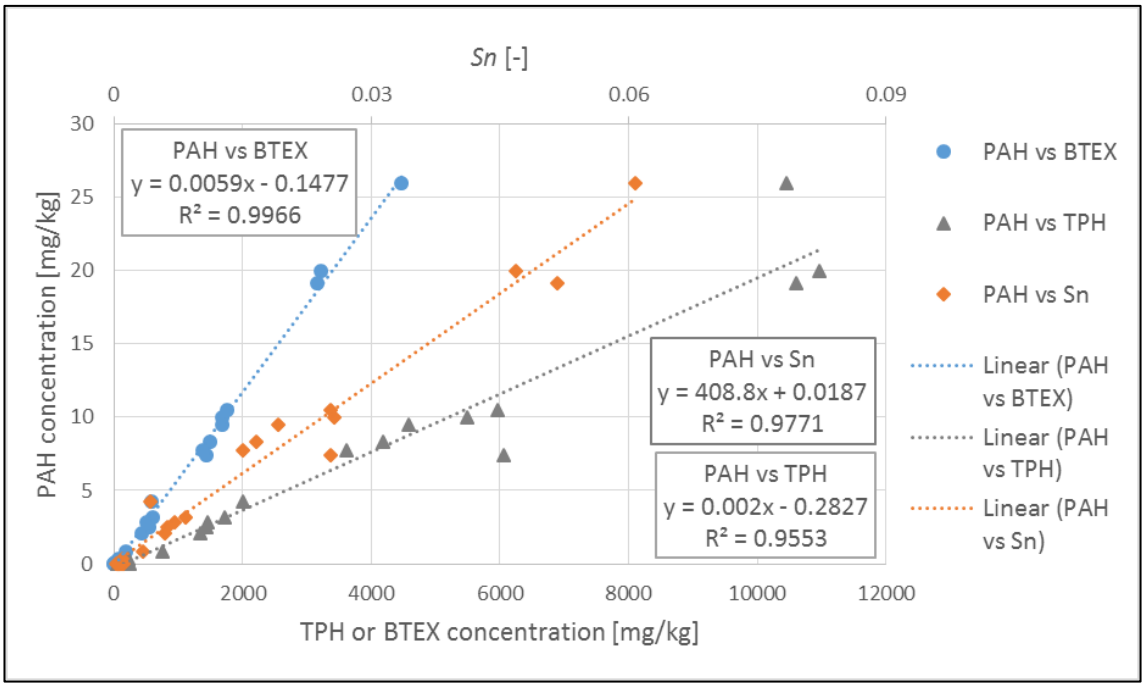


Fig. 6.17. Linear correlation between PAH concentration and BTEX or TPH concentrations.

A low S_n peak of 6 % at MP50-A contrasted with the high T_n of PB29-A and the high LIF signals registered in the surrounding monitoring points (LIF43-A, LIF47-A). Low mobile S_n values have also been reported in the literature as partially related to the differences in the range of pressures experienced in the laboratory and under field conditions (Adamski et al., 2003, 2005; Charbeneau, 2007a), which affect the resulting near-immobile LNAPL saturations (Land, 1968; Kueper et al., 1993; Lenhard et al., 2004; Johnston and Adamski, 2005). As illustrated in Fig. 6.18, the peak at LIF43-A did correspond to a relative maximum of MP50-A, but not exactly to the absolute maximum of S_n.

Values of S_n below this main peak were extremely low with maxima around 0.01 % and potentially represented entrapped LNAPL. Two of these maximum values were identified at 55.881 and 55.981 m AHD and could be linked to low LIF signals recorded at similar elevations. TPH concentrations were detected in the core even below 55.50 m AHD, but they could have represented dissolved hydrocarbons.

Regarding the presence of residual LNAPL, saturations higher than 0.3 % were found up to 57.23 m AHD, with a relative maximum of 0.8 % at 56.931 m AHD. Potential S_{nr} values higher than the presumed S_{ne} values could have been in part related to the low z_{aw}. However, LIF43-A did not show any response that could be discriminated from the

natural fluorescence of the geological medium above 56.37 m AHD. S_n values as high as 2.6 % at 56.431 m AHD or 1.7 % at 56.481 m AHD were not detected by LIF or linked to weak signals at best.

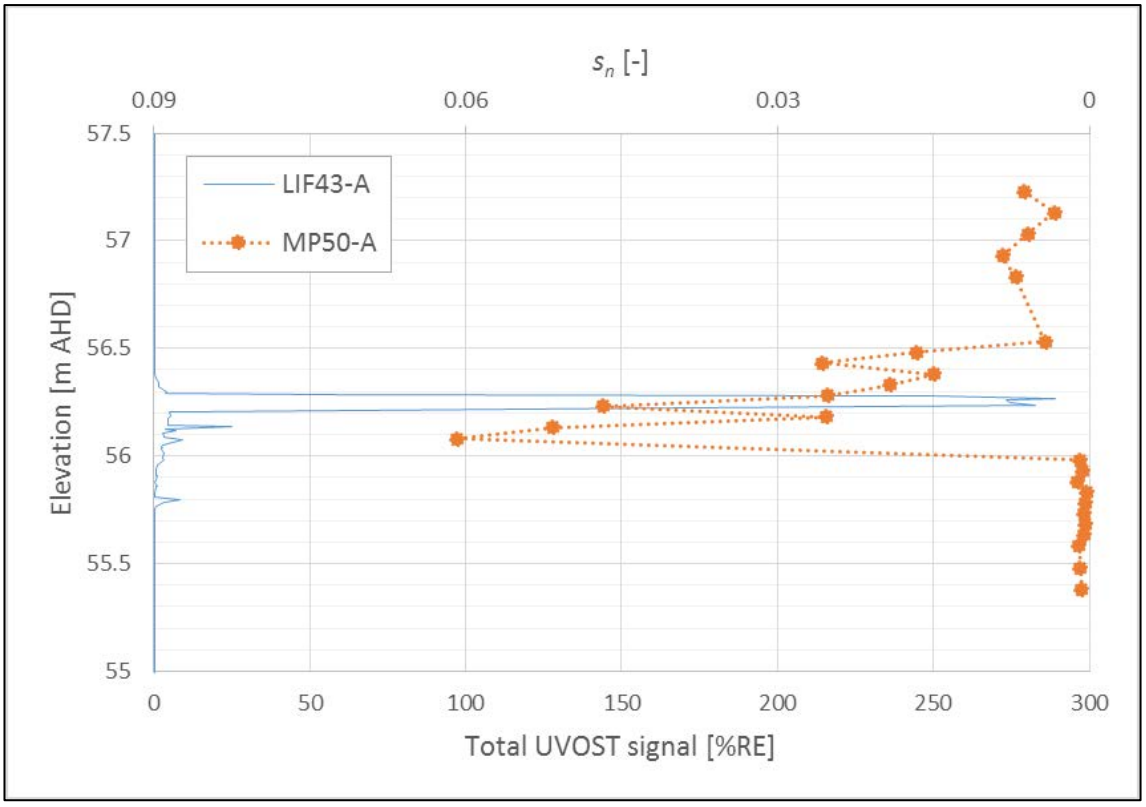


Fig. 6.18. LIF signal versus S_n profile in area A.

Therefore, besides of possible small-scale heterogeneities and errors associated to the elevation survey, two hypotheses arose: (i) the LIF probe was not able to detect relatively high values of S_n in some circumstances (e.g. residual LNAPL); (ii) the core sampling procedure induced LNAPL redistribution across the core and the S_n values obtained were artificially high.

In area A, the S_n profile obtained at MP77-A depicted in Fig. 6.16(a) was similar in shape to MP50-A, thus corroborating the presence of LNAPL above the LIF43-A peak, although not above 56.6 m AHD. Thus, a similar LNAPL-impacted interval was suggested by LIF and coring after discarding S_n values above 56.6 m AHD and considering that low LIF responses over the LIF peak were also indicative of LNAPL presence. In other areas, the answer was probably between both hypotheses, since the two methods have been reported to present differences with alternative techniques of fluorescence logging and coring. In particular, differences can be appreciated in logs taken with fluorescence

probes such as UVOST® and OIP (McCall et al., 2018) and also between analytical results from conventional and cryogenic coring (Kiaalhosseini, 2016).

Fig. 6.16(a) depicts the displacement of LNAPL mass after a rise in z_{aw} of 2.723 m (from 56.142 m AHD on 17/05/2016 when MP50-A was collected to 58.865 m AHD on 16/08/2016 when MP77-A was collected). The displacement was smaller than those recorded in areas B and C with similar pairs of monitoring wells. Limited vertical displacement under presumed unconfined LNAPL conditions and differences in T_n estimations through skimming and baildown testing (presumably influenced by z_{aw}) have been hypothesised to be caused by the presence of a preferential migration pathway (Gatsios et al., 2018b).

Besides of the increment in z_{aw}, a sequential LNAPL mass recovery trial took place at PB29-A between the collection of MP50-A and MP77-A (Gatsios, 2018; Gatsios et al., 2018b). The application of water-enhanced recovery explained the appearance of positive S_n values smeared below 56.00 m AHD at MP77-A. This LNAPL mass did not vertically migrate back to the original near-equilibrium elevations, suggesting that it may have become entrapped. The measured deep S_n values reached a peak of 1.4 %, a remarkable amount considering that the absolute maximum was 6 % and the highest measurement of potential S_{nr} was 0.8 %. This high value could have been due to the dynamic pressure gradient applied. LNAPL specific mass did not considerably change after the end of LNAPL mass recovery trial, making clear that not only the recovery well and immediate surroundings should be monitored to adequately evaluate the performance of such remediation systems.

Fig. 6.16(a) and (c) depict the relationship between core analysis and soil gas measurements at MP50-A and PB33-A, respectively. Peak values were found at similar elevations with both methods, although the upper limit of quantification of the soil gas measurement device (5 % by volume) was reached at MP50-A throughout a wide interval (from 56.10 to 56.50 m AHD and two more measurements around 56.85 m AHD). The range of positive readings was also similar between the two methods, thus supporting the definition of the interval impacted by LNAPL. Since soil gas measurements were performed on the cores, these measurements could have also

been affected by LNAPL redistribution and other errors derived from the sampling procedure. Higher measurements of soil gas at shallow depths may be due to a higher sensitivity to LNAPL constituents partitioned into the gas phase.

6.4.3.3 Integration of LNAPL distribution profiles and hydrostratigraphic data

The comparison of MP50-A, LIF43-A, and MP77-A with HPT73-A provided some insight into the link between LNAPL distribution and the geological profile. Fig. 6.19 shows that LNAPL was present in areas of relatively low HPT P and EC, generally indicators of coarse-grained materials. More specifically, HPT P was lower than 185 kPa in the interval 56–56.5 m AHD, where the highest values of S_n at MP50-A were congregated. The LIF peak was also found in this interval, getting greatly attenuated following a slight increment (from 166 to 173 kPa) in HPT P downwards. This increase reached an HPT P peak of 182 kPa at 56.12 m AHD that could be linked to the peaks in LIF43-A and MP50-A.

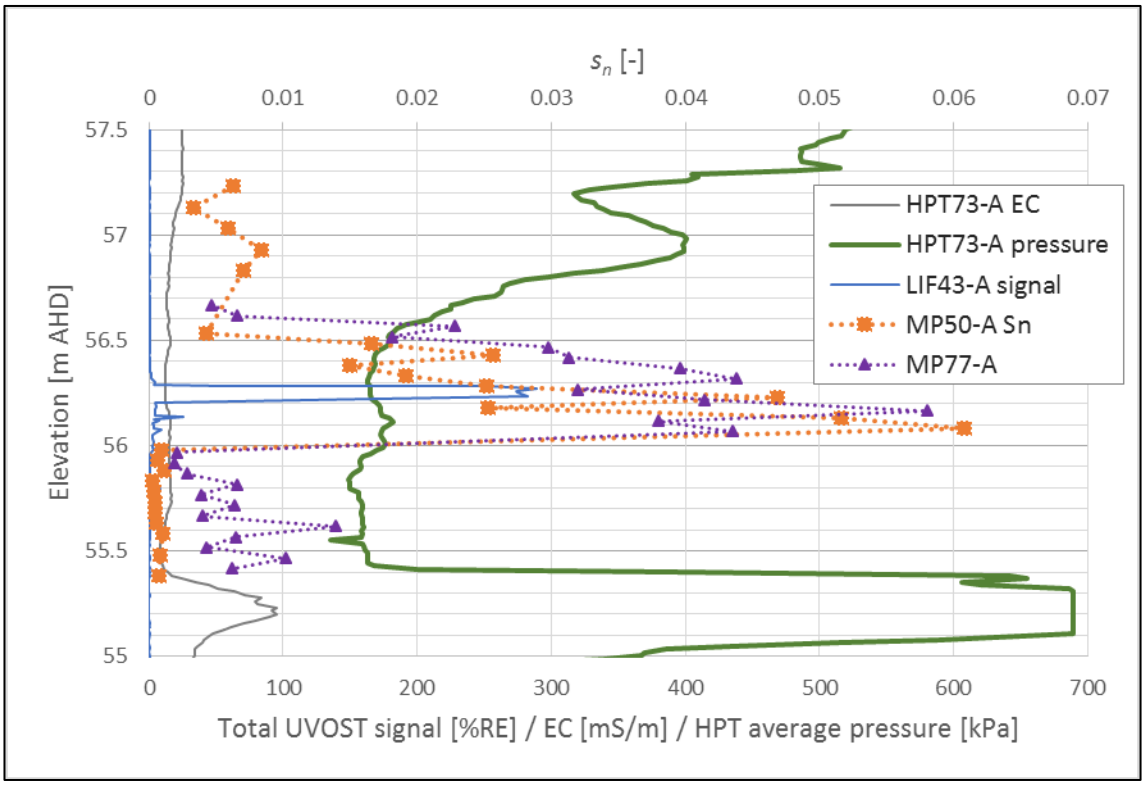


Fig. 6.19. Comparison of LNAPL distribution profiles (MP50-A, LIF43-A, MP70-A) with HPT73-A.

An exaggeration of the x-axis in Fig. 6.19 led to a better inspection of the EC log. Fig. 6.20 shows low EC values in the interval 56.10–56.45 m AHD, coincident with the highest values of S_n and the second fluorescence peak which were relatively more coherent with the in-well fluid levels at PB29-A (z_{an}: 56.229 m AHD; z_{aw}: 56.142 m AHD; z_{nw}:

55.898 m AHD) than the main LIF peak. z_{nw} was measured just below a relative minimum of EC at approximately 55.95 m AHD. The elevation difference between the fluid levels and the signs of LNAPL in the formation could have been influenced by the entry pressure of the medium.

The EC log revealed a relative minimum in EC in the interval 56.20–56.40 m AHD, coincident with the peak in fluorescence and its attenuation upwards. Therefore, it is likely that this strip of low EC values (around 12 mS/m) acted as a preferential migration pathway of LNAPL in area A. Alternatively, low EC could have been caused by the presence of LNAPL in the pore space, although low HPT P were also observed in this interval.

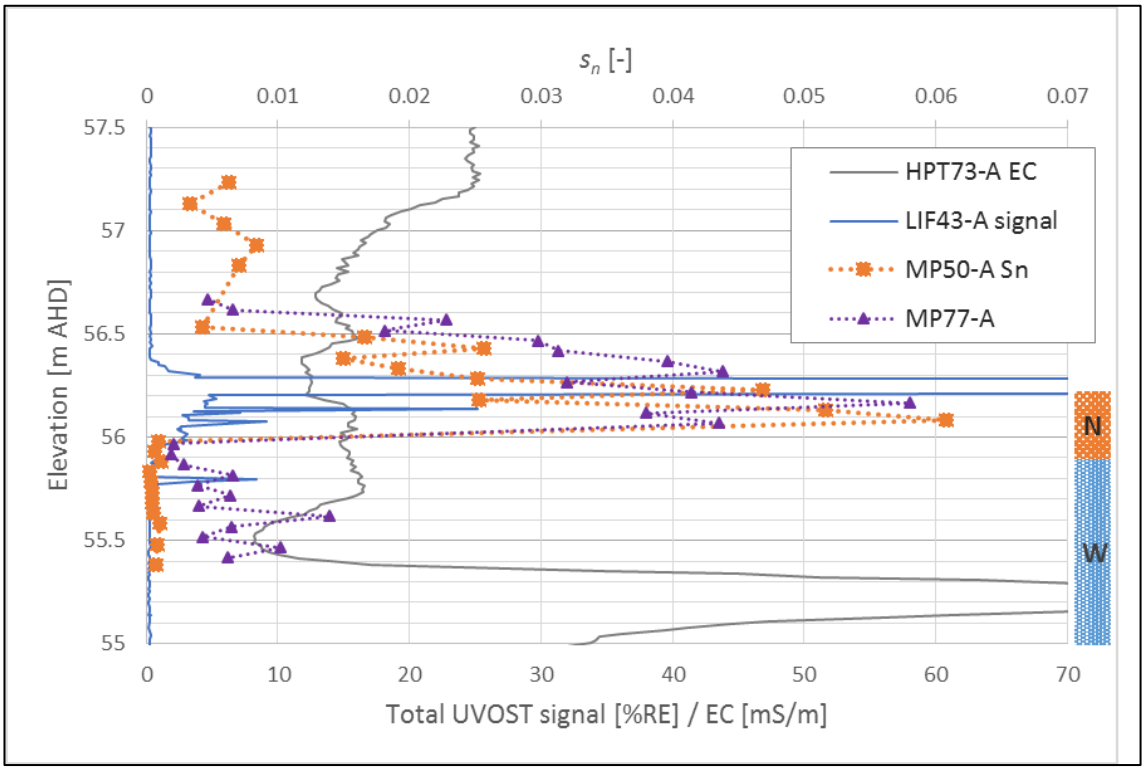


Fig. 6.20. Closer look at the HPT73-A EC log (the columns at the right side represent the fluid columns at PB29-A: ***W*** stands for water and ***N*** for LNAPL).

As illustrated in Fig. 6.19, the interval of low HPT P below 200 kPa (with a relatively constant flow rate; see Appendix D: HPT profiles) extended down to an elevation of 55.4 m AHD, where an abrupt rise took place and the HPT probe reached the upper limit of quantification for HPT P (689.48 kPa). Thus, the high HPT P values suggested the

presence of a clay lens, corroborated by an increase in EC up to the absolute maximum of almost 100 mS/m.

The increase in HPT P and EC above 56.5 m AHD was more gradual with EC records below 25 mS/m and HPT P values below the upper limit of quantification. There were S_n values up to 0.8 % in this interval as well as positive soil gas measurements up to 57.3 m AHD when a relative peak of HPT P (515.72 kPa) was reached. EC also reached a maximum at 57.2 m AHD.

The HPT log helped to elucidate the constrained displacement of LNAPL mass between MP50-A and MP77-A after a rise in z_{aw}. LNAPL vertical migration was apparently constrained to some extent by materials with an HPT P value of 200 kPa at 56.60 m AHD, where the value of S_n dropped at MP77-A.

As depicted in Fig. 6.20, more LNAPL mass got into the strip of low EC between 56.20 and 56.40 m AHD during the rise in z_{aw}. However, low amounts were able to migrate following an increase in EC up to 16 mS/m at 56.48 m AHD. This observation contrasted to Fig. 6.6 showing some LIF peaks at EC values over 15–20 mS/m in area C. In addition, the HPT log also revealed that the LNAPL could not overcome the entry pressure of the clay lens below 55.40 m AHD. Therefore, this was the limit of the LNAPL smearing impact induced by the use of skimmer plus drawdown during the LNAPL mass recovery trial, proving that HPT logging could be a useful tool to evaluate the application of water-enhanced recovery systems.

6.4.3.4 Inspection of low LIF signal values

Inspection of multi-wavelength waveforms, relative LIF signals, lifetime data, and logarithmic scales in the representation of total LIF signal was conducted to enhance the identification of the interval impacted with LNAPL, including less-mobile LNAPL. More specifically, the relative LIF signal at 350 nm accompanied by long lifetimes could be used to infer LNAPL presence even when LIF response is minimal due to the predominant response of petrol in this wavelength channel. A hypothesis was that this approach could improve the evaluation of the confining contact elevation assuming that LNAPL could be smeared up to the top of the aquifer, but not easily above it. Nevertheless, this assumption could be not met in a heterogeneous system like the

petrol station site, where the aquitard presented large amounts of coarse-grained materials and probably infiltration pathways.

In particular, Fig. 6.21 demonstrates that the relative LIF signal at 350 nm was over 25 % up to 56.4 m AHD and then it dropped to approximately 20 %. Despite this abrupt drop in LIF response, LNAPL could presumably migrate upwards as corroborated by pairs of cores collected adjacent to LIF43-A. Similar changes were also observed in the other wavelength channels, especially at 450 nm and 500 nm. On the contrary, these two ratios were lower in the LNAPL-impacted interval. Furthermore, positive anomalies were found at elevations as high as 57.46 m AHD. However, lifetime data did not corroborate these observations. Thus, there were no clear evidences of residual LNAPL according to these data. This could have been explained by absence of residual LNAPL in contact with the LIF probe, limited performance of the system given a decrease of S_n in increasingly finer-grained materials, or reduced lifetime due to oxygen quenching and/or NSZD in the vadose zone.

On the other hand, LIF47-A suggested a different LNAPL-impacted interval with the 350-nm relative LIF signal being over 20 % up to 56.80 m AHD. There were some peaks around 57.5 m AHD which could not be discriminated from natural fluorescence of the geological medium because of the high 350-nm relative LIF signals and very low 500-nm signal at shallow depths. In summary, there was not a unique interpretation of the confining contact elevation in area A, with possible limits at a wide range of 56.4–56.8 m AHD or even up to 57.5 m AHD.

Fig. 6.22 shows LIF lifetime profiles (calculated as the average of lifetimes from the four wavelength channels weighted by peak intensity values) from area A. Along the other features of the multi-wavelength waveform, LIF43-A suggested a 0.6-m interval impacted with LNAPL from 55.75 m AHD up to 56.35 m AHD, while LIF47-A exhibited long lifetimes between 55.9 and 56.30 m AHD and possibly up to 56.65 m AHD. LIF47-A revealed discontinuities at 56.15 m AHD and above 56.30 m AHD, which could have represented intervals of entrapped and residual LNAPL.

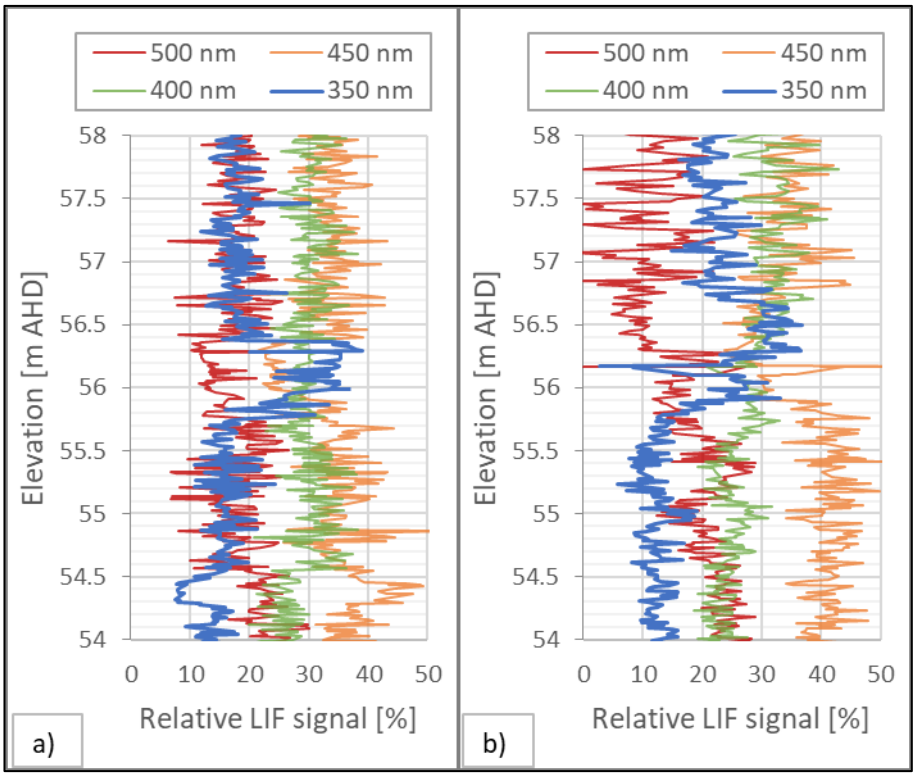


Fig. 6.21. Relative LIF signals for every wavelength channel at (a) LIF43-A and (b) LIF47-A.

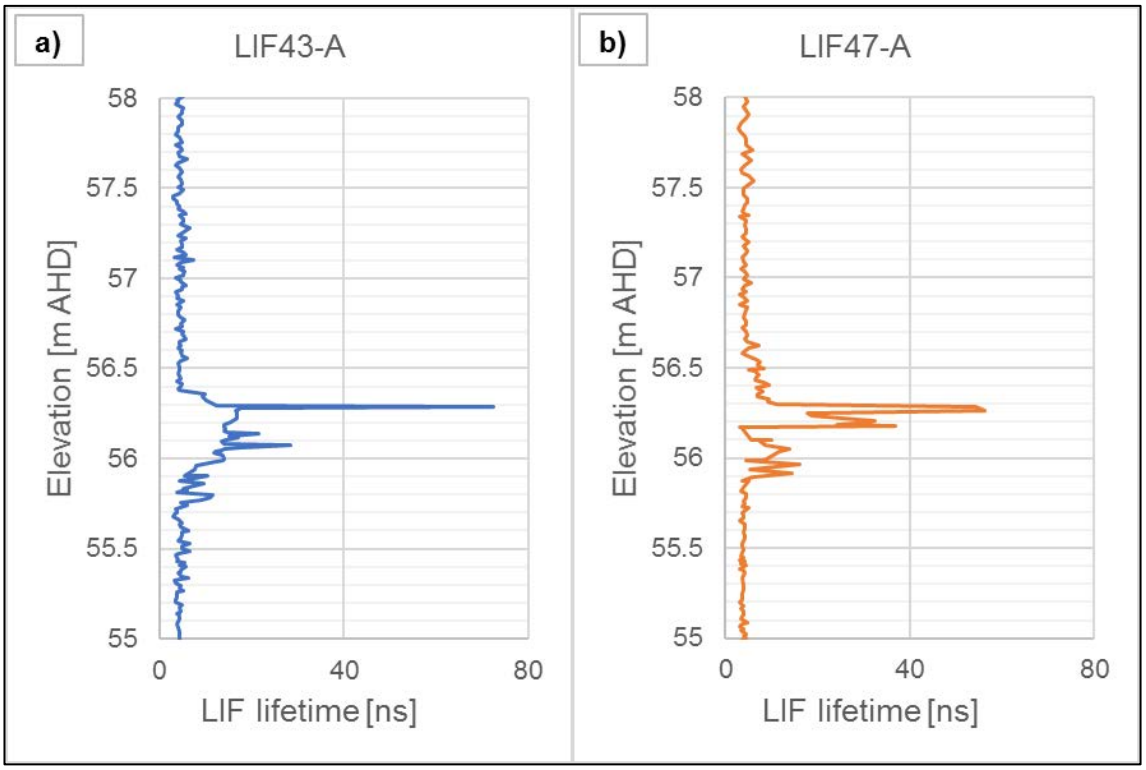


Fig. 6.22. Average LIF lifetime profiles at (a) LIF43-A and (b) LIF47-A.

Representing the total LIF signal in a logarithmic scale, as depicted in Fig. 6.23, resulted in practically the same estimations of the LNAPL-impacted interval as inferred through

relative LIF signals, including the abrupt drop in LIF response at LIF43-A above the peak values contrasting with the gradual decrease in LIF47-A. Fig. 6.23 also shows relatively good agreement with the LNAPL-impacted interval inferred from measurements of S_n through coring, including the identification in LIF43-A of features such as the S_n peak of 2.56 % at 56.431 m AHD. Total LIF signals did not contribute to identify the potential presence of LNAPL above 56.8 m AHD. Observations of residual LNAPL above 56.8 m AHD in cores could have been due to redistribution of LNAPL mass across the cores during the extraction process, since they were not corroborated by the analysis of neighbouring cores collected in August 2016.

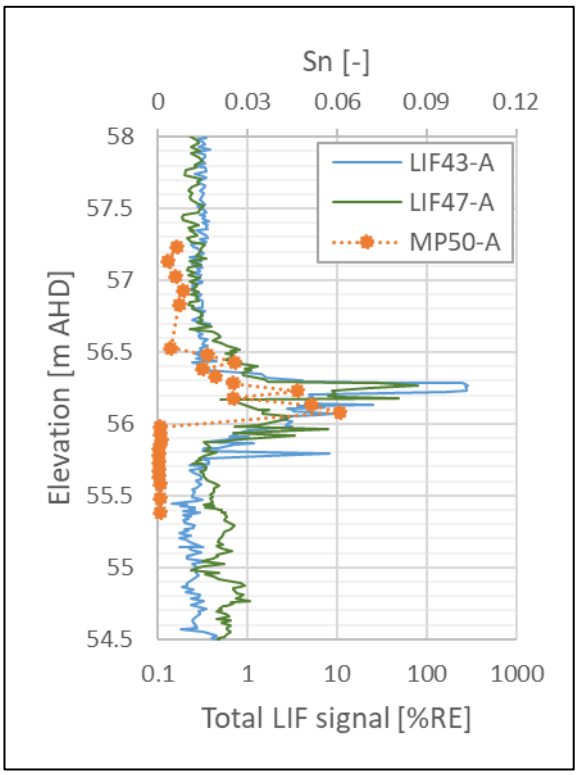


Fig. 6.23. Total LIF signals from area A in a logarithmic scale.

6.4.3.5 Summary of results and proposed model scenarios

It was not expected that a VEQ model assuming homogeneous conditions could predict the LNAPL distribution in area A. A two- or three-layer model would be needed to incorporate the strip of low EC values around 56.20–56.35 m AHD where the LIF43-A peak was found. This pathway was expected to have a great control on LNAPL mobility and its migration into the well and therefore pose a complex relationship between LNAPL mobility and the fluid pressures in the formation. The material above this

preferential pathway should be finer-grained than in the rest of the profile as suggested by an increase in HPT P and the inverse shark-fin shape of the S_n distribution.

The LNAPL thickness used for the model predictions should be 0.3 m, coherent with b_n at PB29-A, although the effects of values from 0.1 m (the width of the fluorescence peak) to 0.5–0.75 m (approximately the range where LIF suggested LNAPL presence) could be explored if the model predictions could not match the field observations.

6.4.4 Petrol station site. Area B

6.4.4.1 Analysis of twin LIF logs

Four LIF profiles (LIF51-B, LIF52-B, LIF53-B, and LIF71-B) were collected at less than 3 m from PB27-B. As mentioned in section 6.2.2, LIF53-B showed no appreciable LNAPL contamination, but such lack of response could be expected because of its location near monitoring wells with absence of in-well LNAPL. For instance, the core from PB35-B did not present any response to the soil gas screening measurements and only a maximum b_n of 0.002 m was measured after three years of monitoring. In addition, LIF52-B only exhibited a narrow peak of 5.2 %RE (roughly 0.01-m wide) and indicated the presence of LNAPL in an interval of approximately 0.1 m (from 56.497 m AHD to 56.601 m AHD). This impact was quite shallow compared to the surrounding LIF profiles where most of the fluorescence response was found at lower elevations. Nevertheless, the elevation of this peak corresponded to the shallowest signals of more than 0.5 %RE recorded at LIF51-B.

LIF51-B and LIF71-B showed substantial responses as depicted in Fig. 6.24. LIF52-B was located between LIF71-B and LIF51-B and between LIF71-B and PB27-B, thus evidencing the small-scale heterogeneity at the petrol station site. LIF51-B was the second highest fluorescence peak and the second highest cumulative LIF signal at the petrol station site as illustrated in Fig. 6.2. These observations were coherent with PB27-B being the well generally presenting the second highest T_n value in the petrol station site between 2015 and 2018. The signal peaks at LIF51-B were more than three times higher than at LIF71-B. The main two peaks at LIF51-B were found around 55.90 m AHD and 56.05 m AHD, being the later coincident with the stronger signals at LIF71-B (between 56.05 m AHD and 56.20 m AHD).

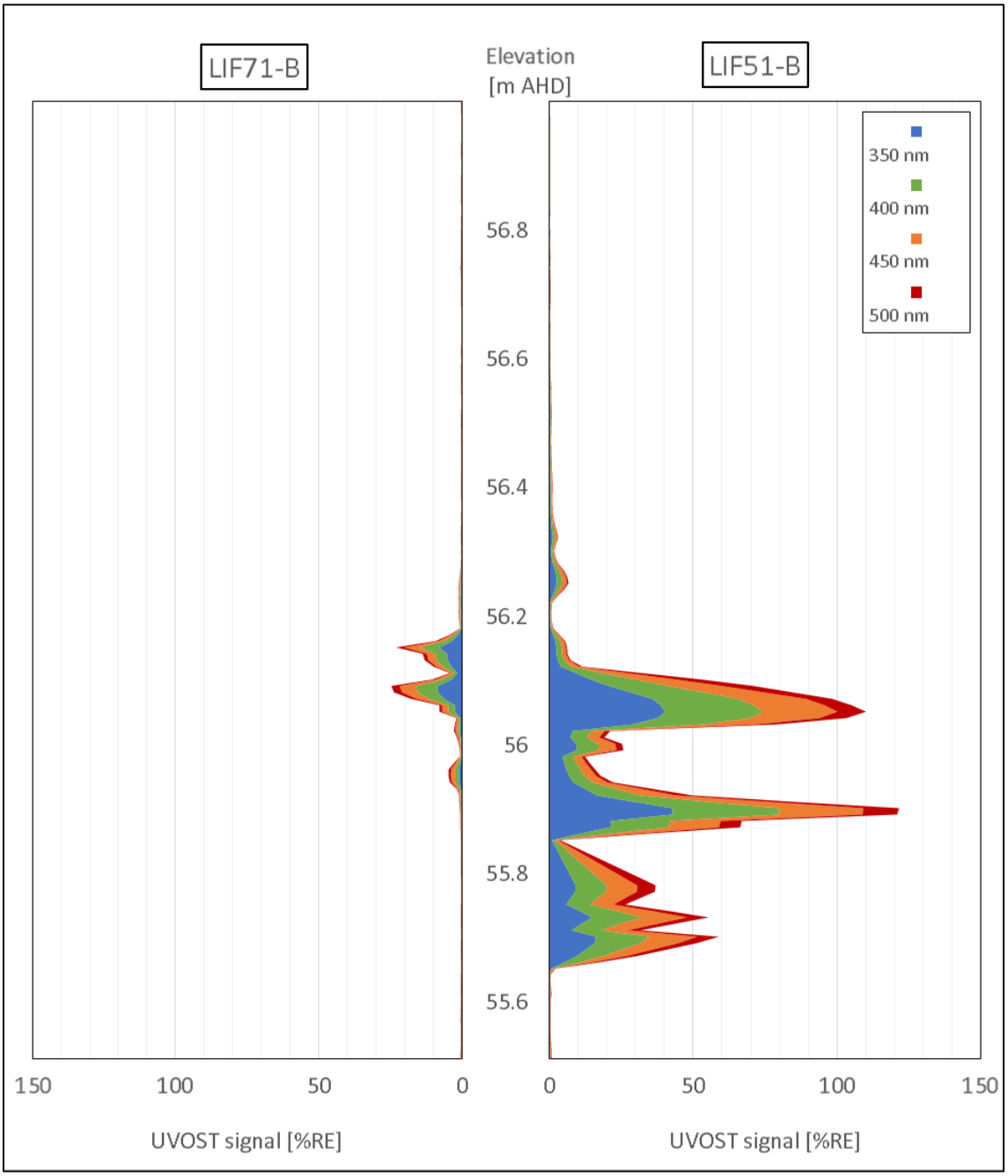


Fig. 6.24. Butterfly plot of LIF51-B and LIF71-B (interpolated values).

Above 56.20 m AHD, the fluorescence response was weaker at both LIF51-B and LIF71-B, suggesting the potential presence of residual LNAPL with a peak of almost 7 %RE at LIF51-B. However, LIF71-B was around 1 %RE at the same elevations. As regards the entrapped LNAPL, the signal at LIF71-B decreased below 56.05 m AHD and was negligible below 55.92 m AHD. As described in section 6.3, LIF51-B signal diminished right under 55.85 m AHD, but it was then followed by fluorescence peaks corresponding to long-term entrapment. This entrapped LNAPL could not be seen in the surrounding

LIF profiles. A reason could have been the two total fluids pumping tests that took place at PB27-B on 19/05/2015 and 20/05/2015, although the induced drawdown on z_{aw} was of just 0.01 m. A similar test was conducted at PB29-A on 21/05/2015, but there was not such an indication of entrapped LNAPL.

6.4.4.2 Correspondence between conventional methods and adjacent LIF logs

In-well fluid levels at PB27-B were z_{an} = 56.231 m AHD and z_{nw} = 55.897 m AHD, being z_{aw} = 56.143 m AHD and b_n = 0.334 m on 17/05/2016. In-well fluid elevations were very similar one month before (z_{aw} = 56.183 m AHD and b_n = 0.319 m on 28/04/2016) and some days later (less than 0.02 m difference before conducting a baildown test on 20/05/2016 and less than 0.03 m afterwards), suggesting quasi-equilibrium conditions.

As depicted in Fig. 6.25, the S_n profile obtained at MP58-B on 19/05/2016 vaguely resembled a shark fin, although uncertainties regarding this shape arose as a consequence of the lack of samples between 55.30 m AHD and 55.90 m AHD and the loss or redistribution of fluids during the coring process. Estimation of S_n at MP58-B presented more uncertainties than at MP50-A or MP44-C.

The better sampling resolution offered by the LIF probe at LIF51-B suggested that some LNAPL could exist between 55.65 m AHD and 55.85 m AHD. Assuming certain degree of subsurface homogeneity, this LNAPL was presumably entrapped (even if more than a 50 %RE was reached) given the elevation difference in comparison to in-well fluid levels as measured at PB27-B. LIF responses over 100 %RE and S_n values higher than 4 % were recorded within the b_n elevation range. Accordingly, there was reasonably good agreement between the three measurement methods (LIF, core analysis, in-well fluid levels), especially when considering strong LIF signals only. In addition, the screening soil gas measurements at MP58-B as illustrated in Fig. 6.26(a) presented a higher degree of correlation with S_n than in other cores such as MP44-C and MP50-A.

Furthermore, low S_n values between 0.6 % and 1.2 % possibly corresponding to residual LNAPL between 56.25 m AHD and 56.40 m AHD were also detected by LIF with responses between 1.2 and 6.8 %RE. Thus, an increment in LIF signal from 6.8 %RE to 113.2 %RE (a 16.6-fold increase) was comparable to an increment in S_n from 1.2 % to 8.6 % (a 7.2-fold increase).

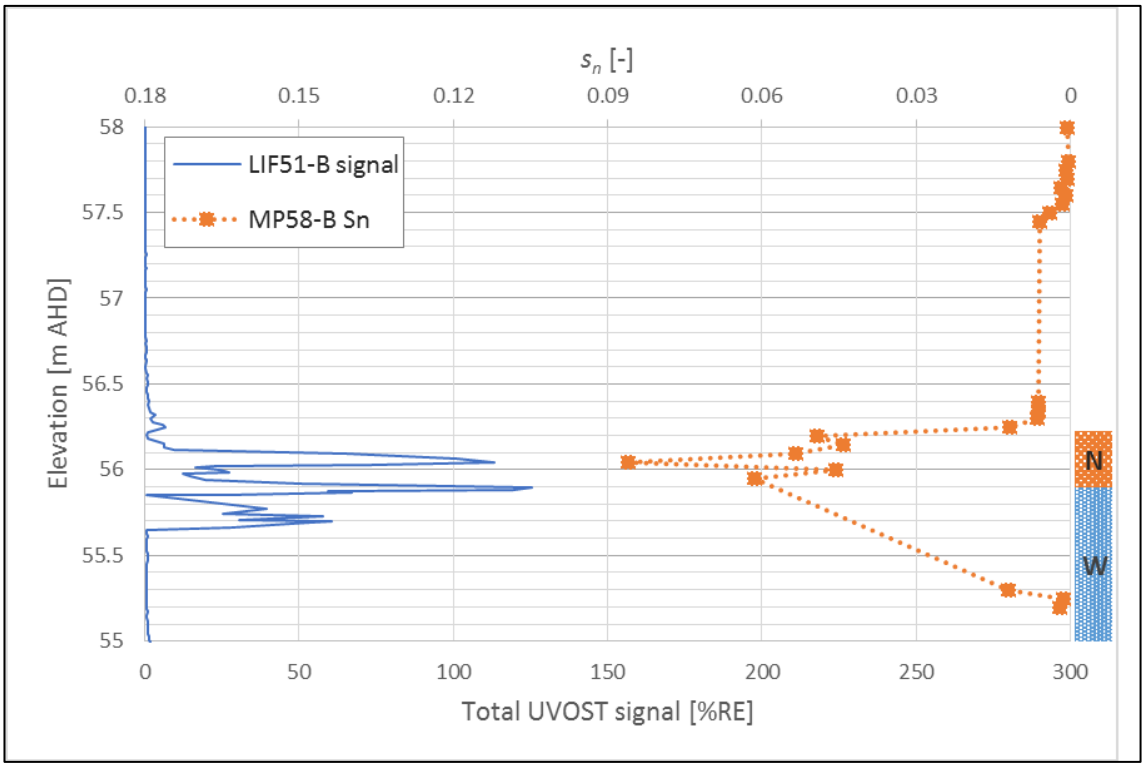


Fig. 6.25. LNAPL distribution profile (LIF and S_n) in area B in wells surrounding PB27-B (the columns at the right side represent the fluid columns at PB27-B: ***W*** stands for water and ***N*** for LNAPL).

Moreover, there were some remarkable differences between LIF51-B and MP58-B. A S_{ne} value of more than 1 % at 55.3 m AHD was not clearly identified by LIF (less than 1 %RE response). Likewise, core analysis identified positive S_{nr} values around 57.50 m AHD not detected by LIF. A similar discrepancy was also found in area A, although it was stronger in that case. Nevertheless, the presence of residual LNAPL was not clearly supported by the collection of twin cores, so it could have been due to errors associated to the coring process. Another discrepancy was that the absolute S_n peak corresponded to a relative fluorescence peak at 56.05 m AHD, while the main fluorescence peak was found at 55.90 m AHD and coring could have missed it or correspond to a S_n value of 6 %.

On 31/08/2016, a new core was collected at MP76-B. As illustrated in Fig. 6.26(a), the main S_n peak decreased from 8.61 % to 5.22 %. Most of LNAPL mass migrated upwards, although not as much as it could be expected from the rise of z_{aw}, likely because of non-equilibrium conditions and limited mobility. PB27-B did not exhibit LNAPL mobility at the end of the mass recovery trial from June 2016 and z_{aw} was 56.521 m AHD at PB27-B on 4/07/2016, coherent with the MP76-B profile.

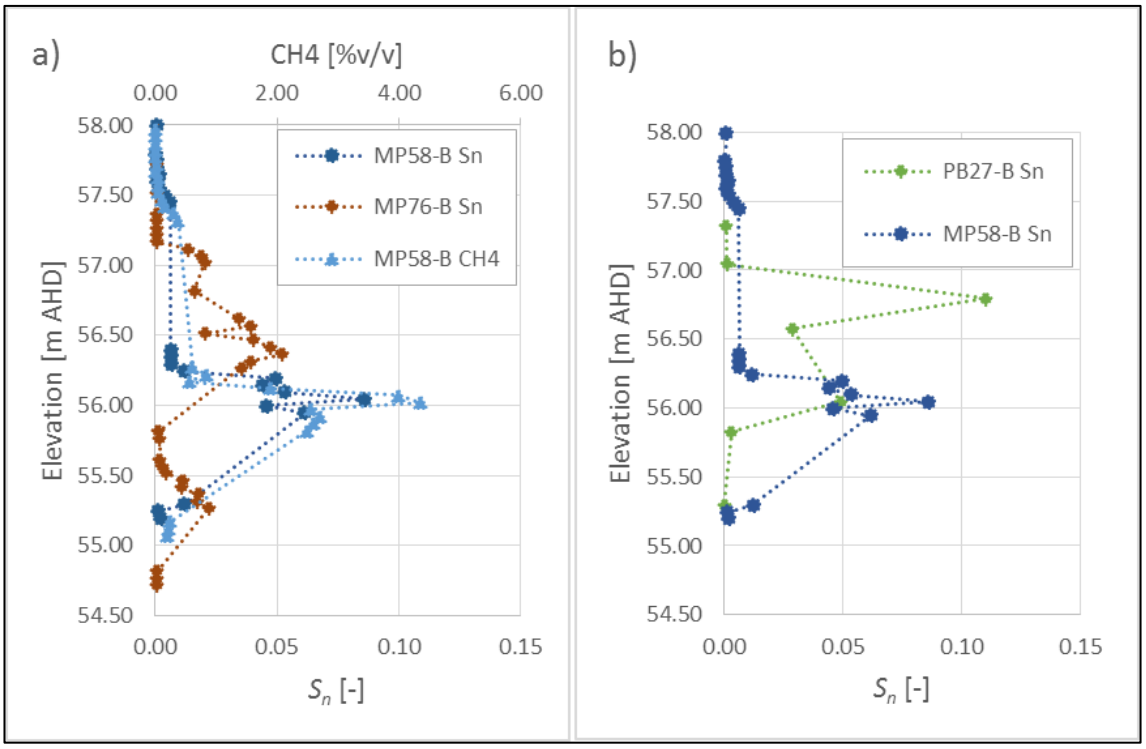


Fig. 6.26. Comparison of core analysis (S_n and TPH concentration) at PB33-A, MP50-A, and MP77-A, including soil gas measurements at PB33-A and MP50-A.

6.4.4.3 Integration of LNAPL distribution profiles and hydrostratigraphic data

As it can be inferred from Fig. 6.27, vertical migration of LNAPL was inhibited by finer-grained material represented by HPT pressure rising from 200 kPa at 56.1 m AHD to more than 500 kPa at 56.6 m AHD. This change explained the change in shape of the S_n profile from MP58-B to MP76-B and the fact of having more percentage of LNAPL mass above the S_n maximum at 56.367 m AHD.

A closer look at the EC log is depicted in Fig. 6.28. Most of S_n values and fluorescence response was found in intervals with an EC value of approximately 12 mS/m, same as the presumed preferential pathway identified in area A. EC dropped above 56.2 m AHD. Consequently, the decrease in S_n above that elevation at MP58-B was linked to the vertical distribution of fluid pressures in the formation and not to the existence of a lens of finer-grained material. In fact, the maximum S_n estimated at MP76-B was coincident with this drop in EC. A geological feature likely affecting the LNAPL distribution at MP76-B was the peak in EC with more than 40 mS/m right above 57 m AHD probably impeding the migration of LNAPL mass.

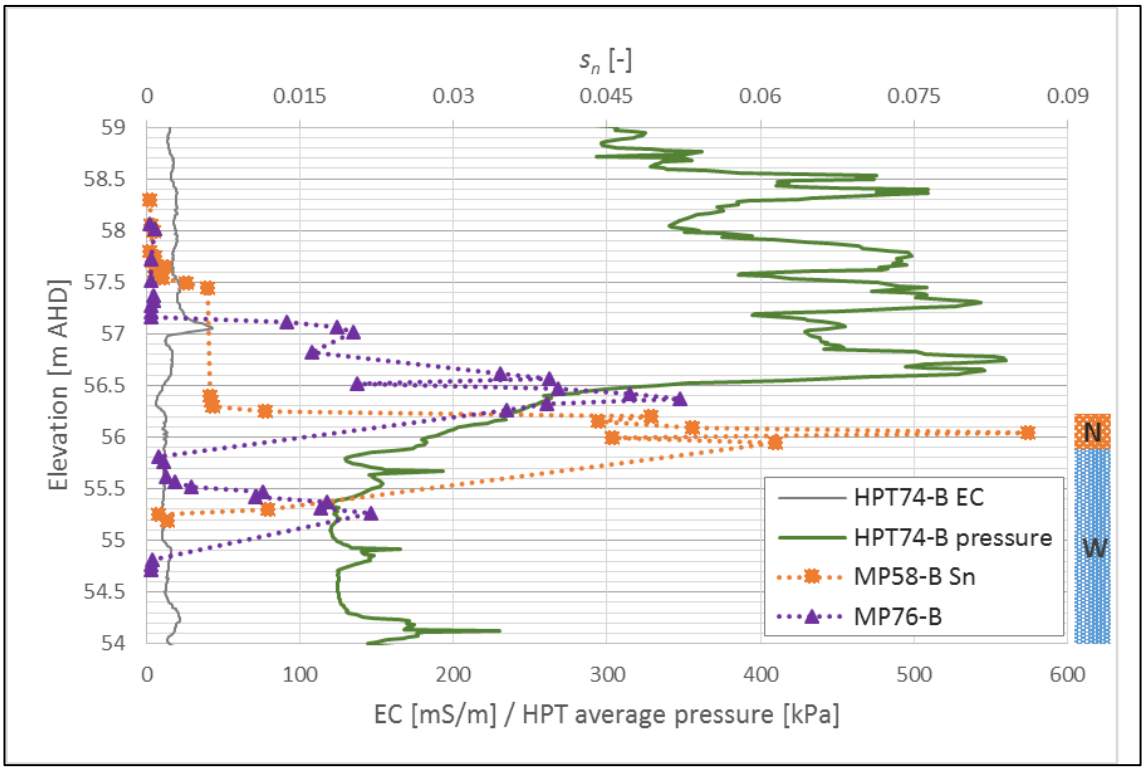


Fig. 6.27. LNAPL distribution before and after the LNAPL mass recovery trial (the columns at the right side represent the fluid columns at PB27-B: ***W*** stands for water and ***N*** for LNAPL).

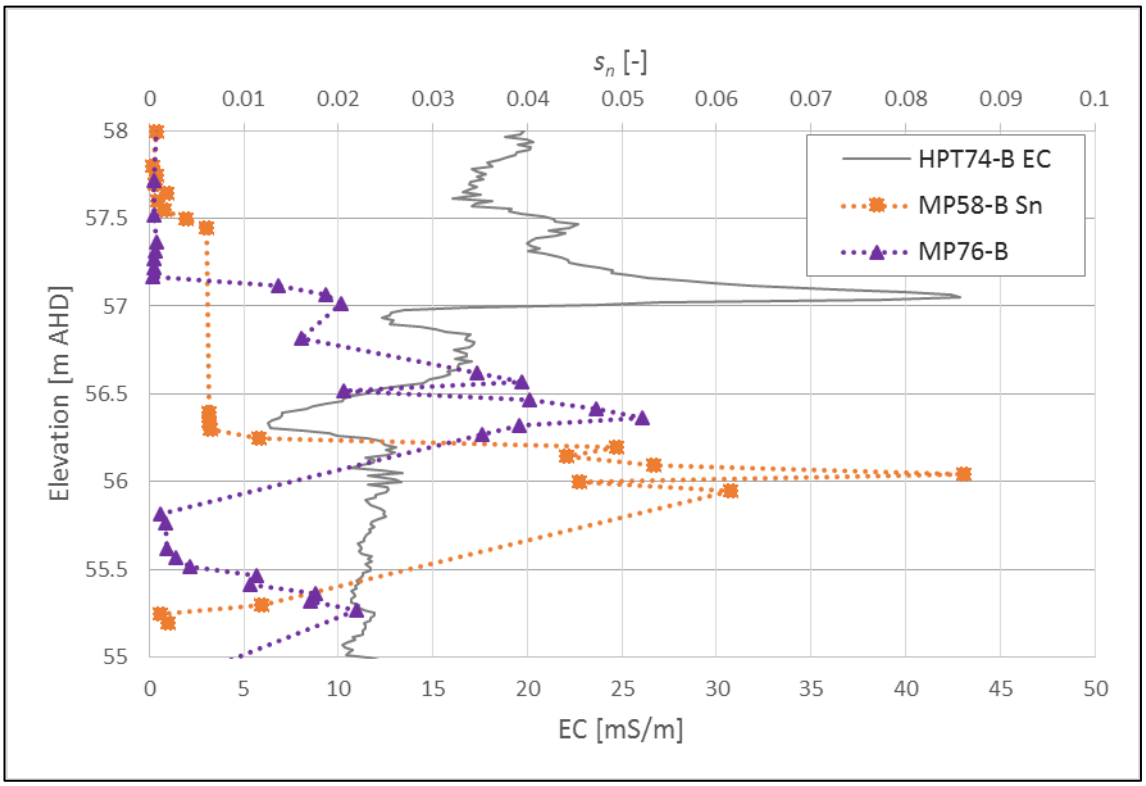


Fig. 6.28. Closer look at the EC log at HPT74-B.

After the LNAPL mass recovery trial, a previously unrecorded S_n peak of 2.2 % appeared at 55.267 m AHD, most likely due to the induced water drawdowns or have existed before the mass recovery trial. A similar peak of 1.4 % appeared at MP77-A in area A. Therefore, this LNAPL mass was probably entrapped after the induced water drawdown ceased, since it did not migrate upwards to the elevation where LNAPL was initially found.

6.4.4.4 Inspection of low LIF signal values

As shown in Fig. 6.29, the 350-nm channel contributed with more than 20 % to the total signal of LIF51-B up to 56.6 m AHD and did not reach a relative minimum up to 56.8 m AHD, with increases in the 450-nm and 500-nm channels. Regarding LIF71-B, the relative LIF signal at 350 nm decreased below 20 % above 56.4 m AHD. Despite the low fluorescence levels recorded at LIF52-B, the log suggested the presence of LNAPL between 56.4 and 56.8 m AHD. LIF52-B also reflected a decrease with depth regarding the contribution of the 350-nm and 400-nm channels and an increase with depth of the 450-nm and 500-nm channels. This could have influenced the LIF signature of LNAPL in area B.

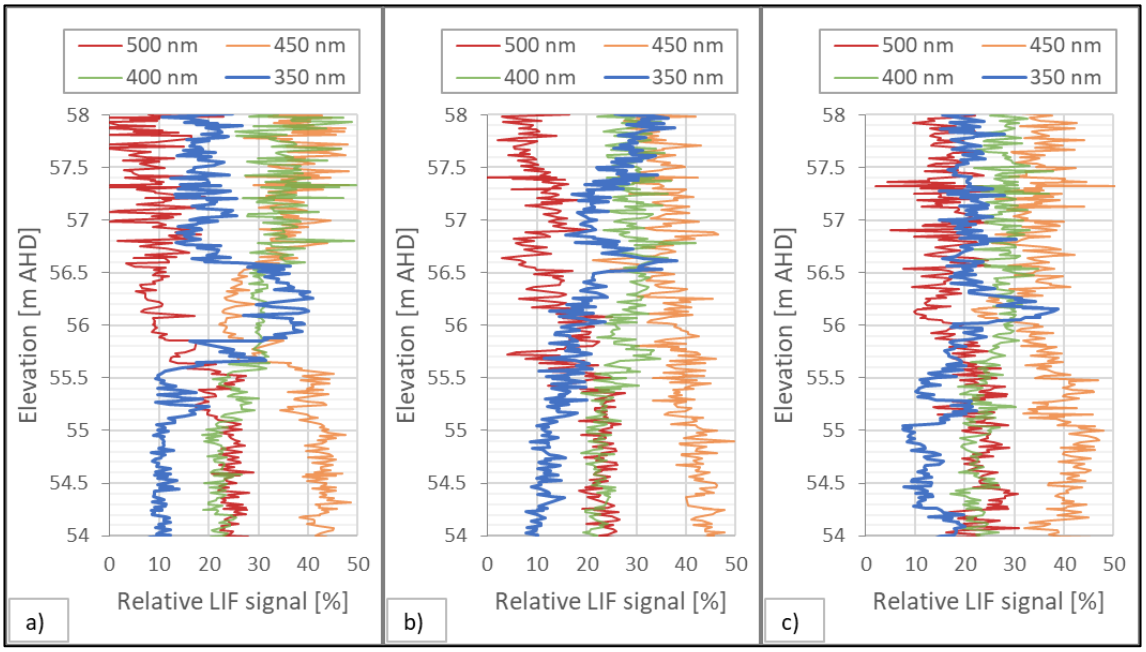


Fig. 6.29. Relative LIF signals at every wavelength channel at (a) LIF51-B, (b) LIF52-B, and (c) LIF71-B.

Some increments in the relative LIF signal at 350 nm at high elevations could be interpreted as a sign of LNAPL presence, although this kind of anomalies generally corresponded to single records and could have been caused by changes in the natural fluorescence of the geological medium or other issues. For instance, in the case of LIF71-B there was an increment in the 350-nm relative LIF signal at 56.8 m AHD. As shown in Fig. 6.30, LIF lifetime data could not unambiguously be used to interpret these anomalies in relative LIF signal, even if LIF lifetime exhibited subtle increments for instance at 56.8 m AHD and 57.8 m AHD at LIF71-B. Reduced lifetimes may be related to oxygen quenching processes, which may exist in the vadose zone.

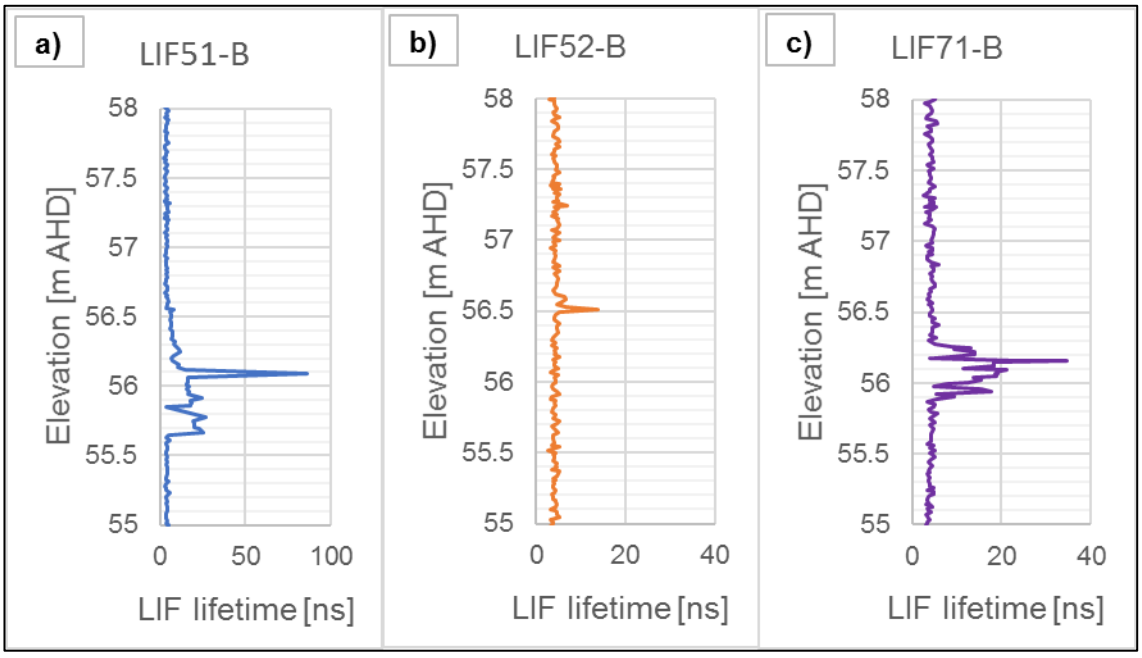


Fig. 6.30. Average LIF lifetime profiles at (a) LIF51-B, (b) LIF52-B, and (c) LIF71-B. Note the different scale in the x-axis.

Nevertheless, LIF lifetime profiles corroborated the existence of LNAPL-impacted intervals between 55.65 and 56.55 m AHD at LIF51-B (thus an interval of 0.9 m, although LNAPL below 55.85 m AHD could have been entrapped and LNAPL above 56.2 m AHD could have been residual according to discontinuities where LIF lifetime was negligible. Therefore, this profile was consistent with the b_n value around 0.32 m at PB27-B), between 56.5 and 56.6 m AHD at LIF52-B, and between 55.85 and 56.3 m AHD at LIF71-B (with discontinuities around 56.0 and 56.2 m AHD).

The three logs exhibited a positive anomaly in the 350-nm relative LIF signal at approximately 55.2 m AHD. As shown in Fig. 6.31, this anomaly was not observed in total LIF signals at logarithmic scale, being actually associated to a decrease in fluorescence response at LIF51-B and LIF52-B. LNAPL existence around 55.2 m AHD was not supported by the analysis of lifetime data either.

LIF logs did not contradict other methods applied to evaluate confined LNAPL conditions, but the interpretation of LIF data for this purpose could be misleading without considering additional lines of evidence.

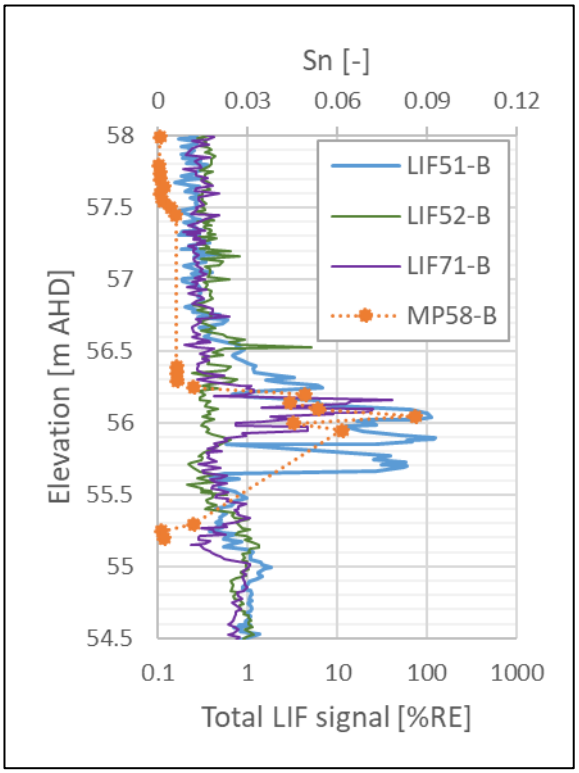


Fig. 6.31. Total LIF signals from area B in a logarithmic scale.

6.4.4.5 Summary of results and proposed model scenarios

A multi-layered model could be necessary to correctly predict the LNAPL distribution in area B, especially in the low range of S_n values. Field observations indicated intervals with finer-grained material above 56.4 m AHD and below 55.7-55.9 m AHD. Furthermore, the analysis of LIF profiles recommended using fine layering in order to imitate the fluorescence profiles. At the same time, the lack of response at LIF52-B suggested that differences between the LNAPL distribution at PB27-B and adjacent wells could not be discarded. The medium was anisotropic and radial flow assumptions were

not expected to be met during mass recovery operations. Nevertheless, an equivalent homogeneous VEQ model could be able to predict T_n under certain circumstances. Using a b_n value around 0.32 m was supported by in-well fluid levels, core analysis, and partly LIF data, although positive LIF signals were found within wider intervals (for instance, around 0.45 m at LIF71-B according to lifetime data) and the effects of this magnitude should be explored.

6.4.5 Petrol station site. Area C

6.4.5.1 Analysis of twin LIF logs

Three LIF profiles (LIF56-C, LIF57-C, and LIF68-C) were obtained less than 3 m away from PB40-C. LIF57-C was 1.8 m Northeast of PB40-C and presented the third highest fluorescence peak in the petrol station site (reaching 120 %RE) and the fourth largest integral LIF signal. On the contrary, LIF56-C and LIF68-C were South and Southwest of PB40-C, respectively, and suggested the existence of LNAPL contamination but with weaker signals.

As depicted in Fig. 6.32, most of LIF56-C was below 8 %RE, while LIF68-C peaks were over 20 %RE. PB40-C was closer to LIF68-C than LIF56-C, which was consistent with PB40-C exhibiting relatively high T_n compared to the surrounding wells. Both LIF56-C and LIF68-C responses were found at similar elevations, just slightly deeper at LIF56-C. In particular, both profiles detected the presence of LNAPL above 57.5 m AHD. Such shallow elevations suggested that LNAPL was under residual conditions.

Nevertheless, LIF57-C only showed strong signal below 57 m AHD as illustrated in Fig. 6.33 where LIF57-C is compared to LIF68-C. Despite the anomalous deep and shallow signals, no big differences were found in the multi-wavelength waveforms at LIF56-C, LIF57-C, and LIF68-C.

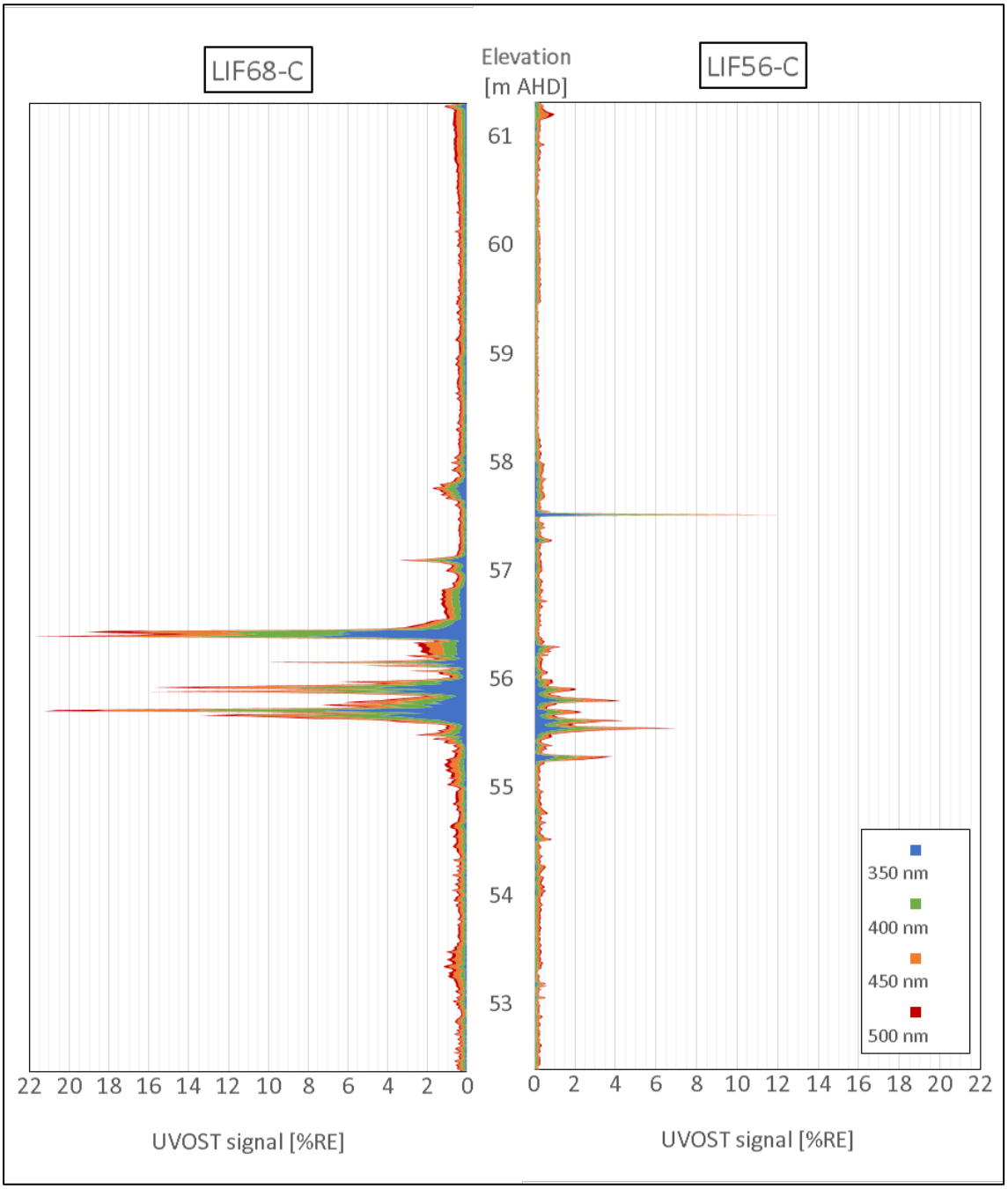


Fig. 6.32. Butterfly plot of LIF56-C and LIF68-C (interpolated values).

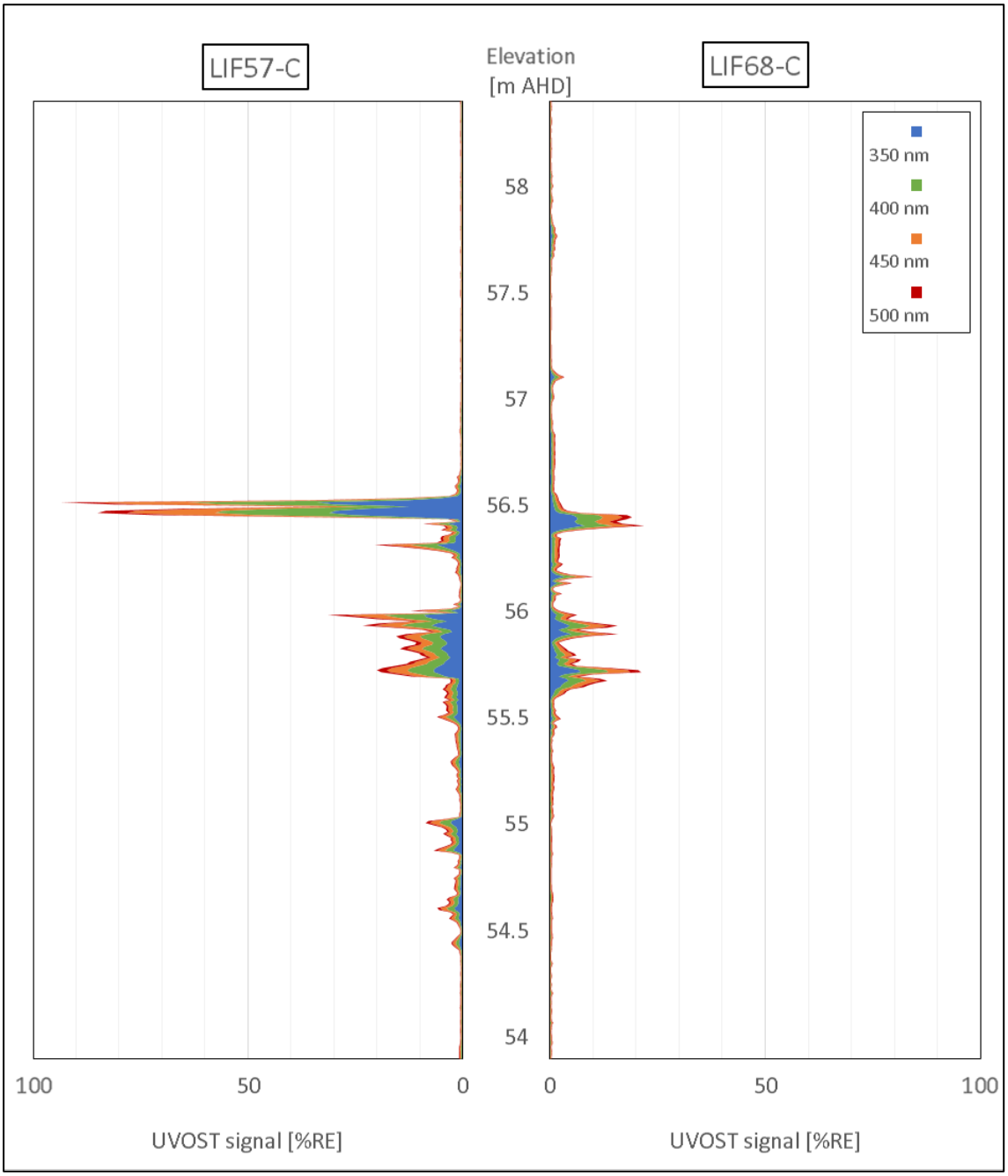


Fig. 6.33. Butterfly plot of LIF57-C and LIF68-C (interpolated values).

6.4.5.2 Correspondence between conventional methods and adjacent LIF logs

The distance between peaks reaching 20 %RE or more was in the range 0.735–0.801 m. Fig. 6.34 shows that b_n was within this range as measured at PB40-C on 16/05/2016 with z_{aw} being 56.152 m AHD, z_{an} equal to 56.354 m AHD, and z_{nw} equal to 55.585 m AHD. The rest of profiles in area C did not show more than one peak over 20 %RE.

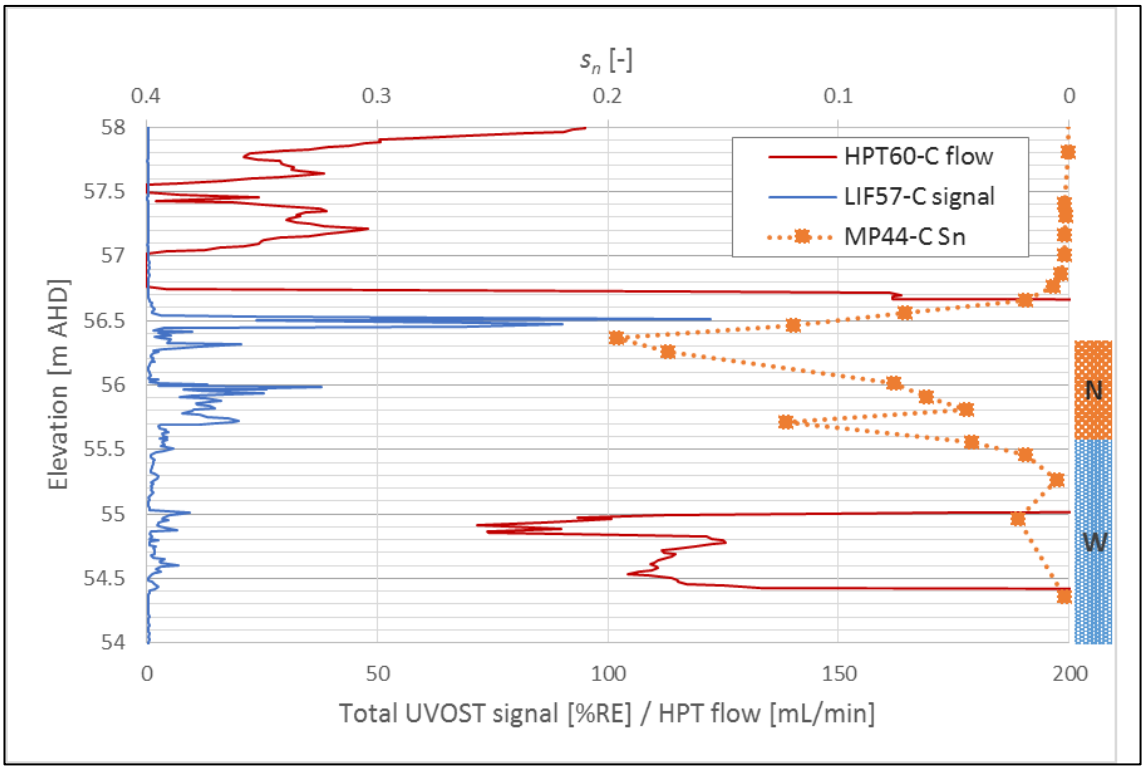


Fig. 6.34. Comparison of LIF57-C with MP44-C and in-well fluid levels (the columns at the right side represent the fluid columns at PB40-C: ***W*** stands for water and ***N*** for LNAPL).

Fig. 6.34 also shows that the MP44-C S_n profile was more similar to LIF57-C than to LIF68-C, even if it was at shorter distance from the later. Both MP44-C and LIF57-C displayed an absolute maximum just below an abrupt drop in HPT Q at 56.75 m AHD. The maximum S_n value of 19.6 % at MP44-C was higher than maximum S_n values found in area A and area B, in contrast to a maximum LIF signal that was deeper than in those areas. Area C generally showed lower T_n than area A and area B, and therefore LIF response presented better correlation with T_n than S_n.

This main peak in S_n and total LIF signal was followed by a decrease in these parameters and a relative maximum between 55.7 and 56.0 m AHD. In addition, both profiles suggested the existence of entrapped LNAPL around 55 m AHD but did not show evidences of residual LNAPL above 57 m AHD.

The lack of signs of LNAPL at shallow elevations at LIF57-C, MP44-C, and PB40-C (according to DGPs) contrasted to the screening soil gas measurements as illustrated in Fig. 6.35(a) and the rest of LIF profiles and cores in area C, including LIF66-C, LIF69-C, PB13-C as shown in Fig. 6.35(b), and PB39-C as shown in Fig. 6.35(c–d). The soil gas

measurements at MP44-C were anomalously high compared to those at MP50-A and MP58-B, probably because the samples were analysed one day after collecting them in plastic bags, not the same day as in the area A and area B.

Fluorescence was lower at LIF66-C and LIF69-C than at LIF57-C. This fact was consistent with PB40-C exhibiting the highest T_n recorded in area C. As it was mentioned in section 6.3.2, LIF69-C only detected weak responses in the sandy aquifer (less than 2 %RE), with stronger signals (maximum of 15 %RE) likely corresponding to residual LNAPL (or other forms of non-recoverable or stationary LNAPL) within the aquitard. PB39-C was located 2.5 m away from LIF69-C and also found LNAPL above 58 m AHD as depicted in Fig. 6.35(c). However, TPH concentration at PB39-C was more than twice higher at 55.151 m AHD (11,250 mg/kg) than at 58.251 m AHD (5,018 mg/kg), but the fluorescence response at LIF69-C was negligible at 55.151 m AHD and it was lower than 1.40 %RE in the interval 55–57 m AHD, while it reached more than 15 %RE at 57.5 m AHD. The material was coarser in the sandy aquifer (according to HPT logs) than in the overlying media at LIF69-C. Accordingly, the material was not the cause for the low LIF signal in the aquifer.

Additionally, PB13-C was another core with a S_n profile similar to PB39-C in spite of being located 15 m away. PB13-C was collected on 07/08/2014 and z_{aw} was dipped at 58.354 m AHD at MP02. Accordingly, the S_n peak recorded at 55.37 m AHD and depicted in Fig. 6.35(b) corresponded to entrapped LNAPL or mobile LNAPL under non-equilibrium conditions. Fig. 6.35(b–d) also indicated that LNAPL reached extremely high elevations up to 59.5 m AHD due to fluctuations in z_{aw}. The fact that S_n around 59 m AHD was similar at PB13-C (collected in August 2014) and PB39-C (collected in August 2015) did not reveal any effects of mass depletion phenomena at PB39-C. The limited LNAPL migration exhibited between MP44-C and MP78-C along the presence of LNAPL mass in the aquitard up to 59.5 m AHD supported the existence of a leaky confining unit. Slow LNAPL migration within the aquitard could have been the reason behind the anomalous measurements of in-well fluid levels at high z_{aw} values as discussed in section 5.2.5, likely representing non-equilibrium conditions.

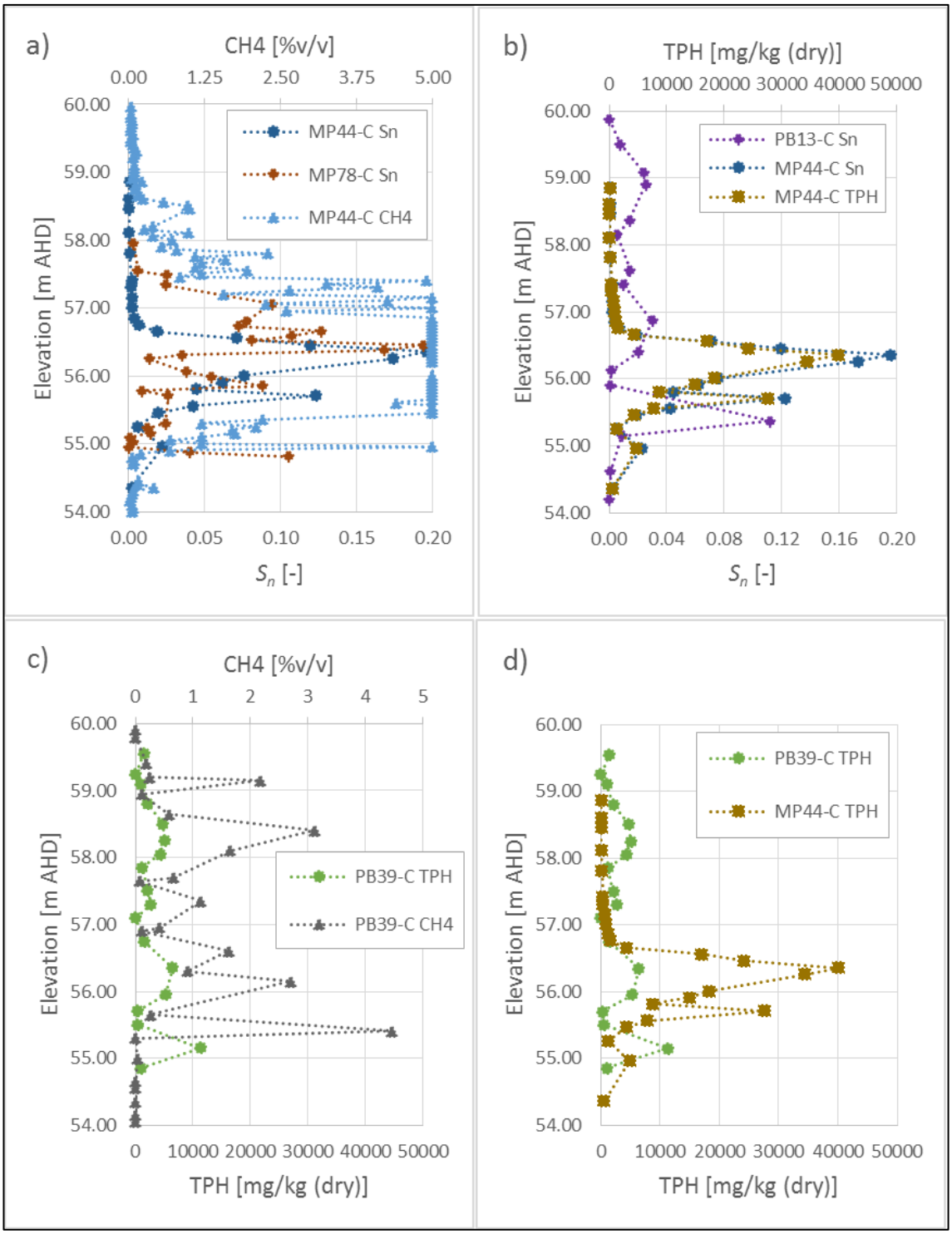


Fig. 6.35. Core analyses (S_n, TPH, and soil gas) in area C.

LIF66-C was next to PB13-C and also detected LNAPL at shallow depths, although with a signal strength lower than the LNAPL in the sandy aquifer. LIF66-C was similar to LIF68-C in terms of maximum signal, cumulative signal and impacted interval, despite being more than 8 m away from each other. However, the changes in signal magnitude at

LIF66-C were more abrupt than at LIF68-C and the corresponding HPT profiles (HPT63-C and HPT62-C, respectively) showed discrepancies.

6.4.5.3 Integration of LNAPL distribution profiles and hydrostratigraphic data

Fig. 6.36 reveals that there was vertical migration of LNAPL mass due to the increase in z_{aw} during the 2016 LNAPL mass recovery trial and LNAPL reached an elevation higher than 57.5 m AHD. Further migration was probably stopped by the fine-grained material represented by a peak in EC of 180 mS/m and a drop in HPT Q around 57.55–57.60 m AHD. Despite this vertical migration, the main S_n peak was still found at the same elevation (56.4 m AHD) and with similar magnitude (almost 20 %) as before the LNAPL mass recovery trial. EC was 17 mS/m at the elevation where the main S_n peak was found, a higher value than the 12 mS/m found in area A and area B. Similarly, HPT P was approximately 400 kPa in contrast to pressures frequently below 200 kPa measured in area A and area B.

HPT63-C (adjacent to LIF66-C and PB13-C) exhibited an abrupt change in HPT P and HPT Q at 58.3–58.4 m AHD, which was also accompanied by a relative maximum in EC. This could be caused by a capillary barrier decreasing gravity drainage of any overlying LNAPL. This was supported by the measurement of a S_n peak of 2 % at 59 m AHD. In addition, HPT63-C suggested the presence of a clay lens at 56 m AHD that could have constrained the vertical migration of LNAPL mass at PB13-C as depicted in Fig. 6.37.

The other four HPT profiles, (HPT59-C, HPT60-C, HPT61-C, and HPT62-C) presented an area of finer-grained material around 57 m AHD. Nonetheless, values of EC, HPT P, and HPT Q indicated that this lens was finer-grained and thicker at HPT60-C and HPT61-C than at other locations. More specifically, HPT60-C presented the lens with greater thickness as suggested by HPT Q and EC logs illustrated in Fig. 6.38. This could explain the absence of LNAPL at shallow elevations at LIF57-C due to the presence of this capillary barrier impeding vertical migration of LNAPL. EC peaks were similar at HPT60-C and HPT61-C (180 and 175 mS/m, respectively). Therefore, inspection of HPT Q logs contributed to improve the analysis of hydrostratigraphic information.

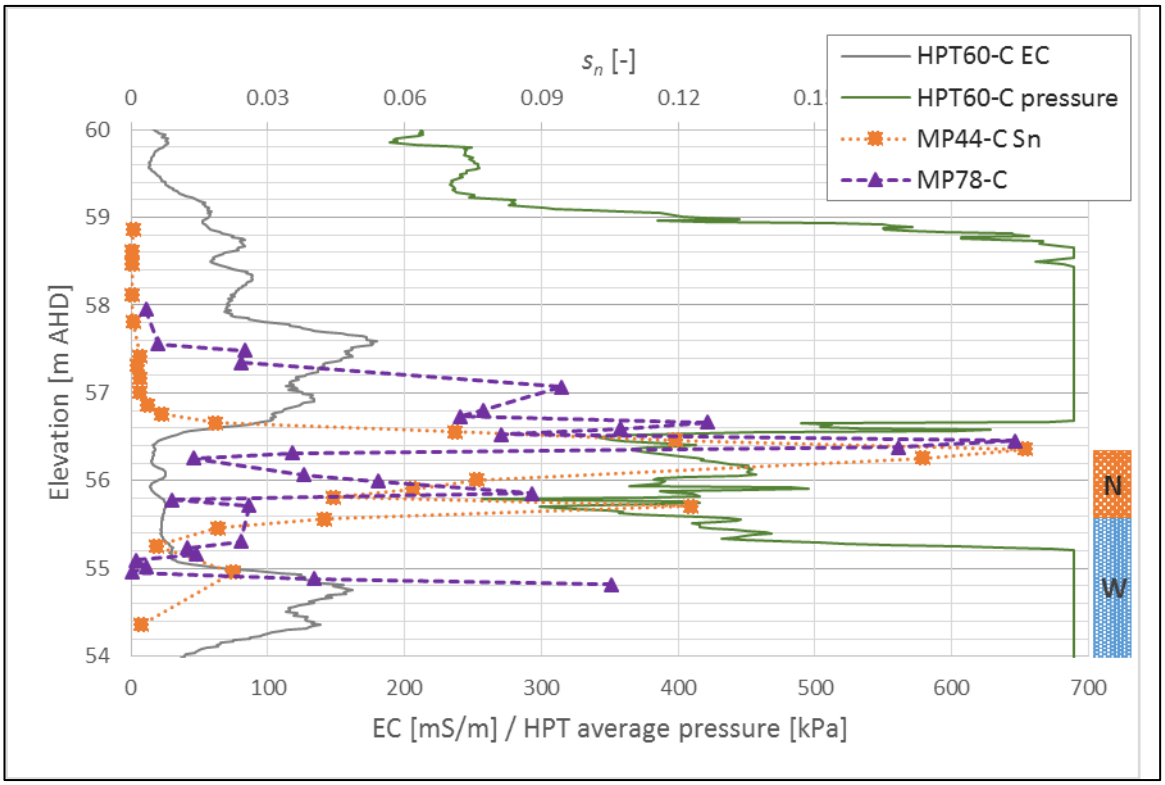


Fig. 6.36. S_n profile before and after the LNAPL mass recovery trial (the columns at the right side represent the fluid columns at PB40-C: ***W*** stands for water and ***N*** for LNAPL).

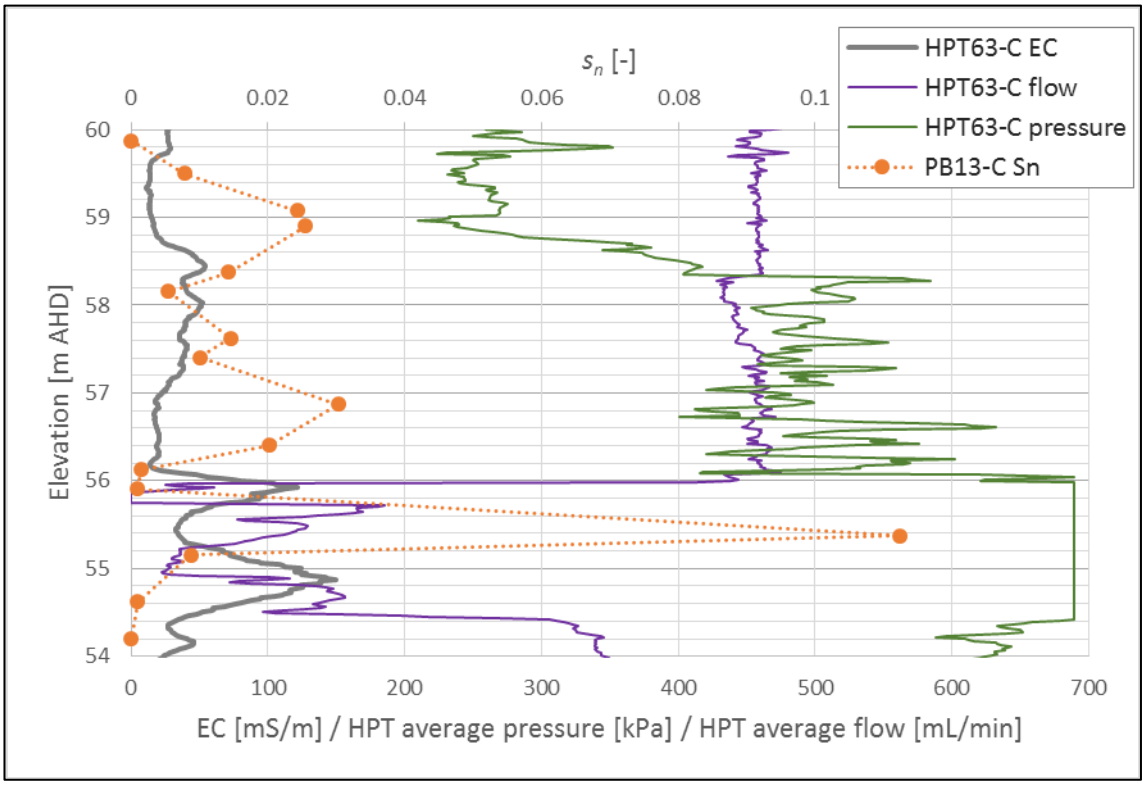


Fig. 6.37. LNAPL distribution at PB13-C and hydrostratigraphic barriers.

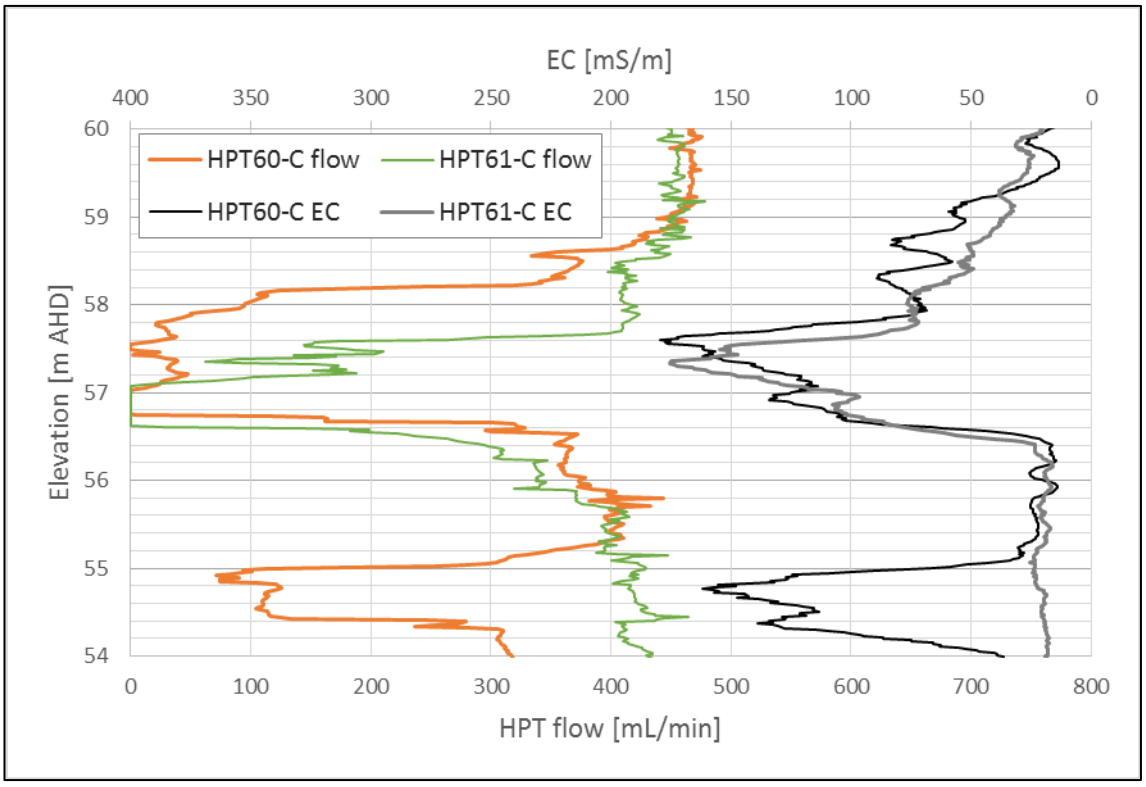


Fig. 6.38. Comparison of EC and HPT Q logs at HPT60-C and HPT61-C.

6.4.5.4 Inspection of low LIF signal values

As shown in Fig. 6.39, there were wide LNAPL-impacted intervals in area C. This was probably due to the proximity of area C to the UST compared to areas A and B. Relative LIF signals also suggested the existence of presumably entrapped and residual LNAPL in many logs according to their relationship with historical in-well fluid levels in area C. Some of the entrapped LNAPL could have been caused after conducting aquifer tests inducing considerable water table drawdown (z_{aw} lowered to 55.2 m AHD at PB39-C during WT15 for instance). It should also be noted that the coarsest-grained zone in the UST area (where the LNAPL release occurred in 2013) was between 54.0 and 55.0 m AHD according to HPT64. LNAPL likely migrated through finer-grained materials at higher elevations.

According to these observations, LNAPL was able to penetrate the confining aquitard most likely due to the large content in sands and the presence of associated preferential pathways, supporting the existence of leaky confined conditions more than ideal confined conditions. This aspect further complicated the analysis of the confining contact elevation through LIF in area C. For instance, positive anomalies of the 350-nm

relative signal were found at 57.6–58.0 m AHD at LIF56-C as well as around 57.6–58.0 and 59.0 m AHD at LIF68-C. LIF57-C was the only log exhibiting a sharp drop in 350-nm relative signal near the presumed confining contact elevation, around 56.8 m AHD.

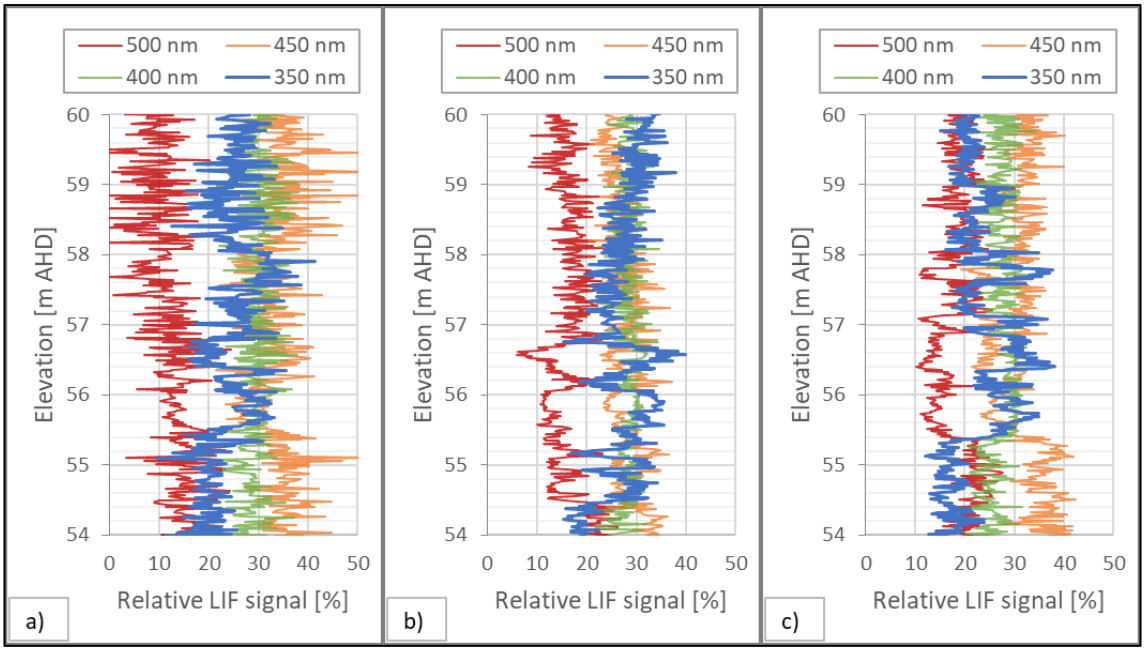


Fig. 6.39. Relative LIF signals at (a) LIF56-C, (b) LIF57-C, and (c) LIF68-C.

As in the case of areas A and B, the interpretation of these low LIF signals at high elevations presented some uncertainties that could be further investigated by inspecting lifetime data. Fig. 6.40 depicts lifetime profiles from LIF68-C at 350 nm and 450 nm. These measurements were not considered to corroborate the existence of LNAPL up to 59 m AHD due to the short LIF lifetimes recorded. Nevertheless, longer lifetimes were associated to the positive LIF response around 57.6–58.0 m AHD. LIF lifetime data corresponding to the 350-nm channel could present higher contrast with the natural fluorescence of the geological medium than lifetime data from other channels or average lifetime data. For instance, a long lifetime value could be found at 58.03 m AHD in the 350-nm channel but not easily distinguished from the lifetime of natural fluorescence in the 450-nm channel. There was a near-continuous interval of long lifetime between 55.4 and 56.6–56.8 m AHD that could have represented the mobile LNAPL interval (1.2–1.4 m wide).

In addition, Fig. 6.41 depicts relative LIF signals of more logs suggesting existence of LNAPL within the aquitard, therefore revealing its poor integrity. LIF69-C showed

anomalous LIF signatures above 57.2 m AHD, where there was an increase of the relative response at 350 nm accompanied by decreasing trends at 400 and 450 nm with constant contribution from the 500-nm channel. The LIF signature between 58.2 and 59 m AHD was not considered to be indicative of LNAPL contamination but of changes in the medium characteristics, possibly of anthropogenic nature. On the other hand, LIF66-C (adjacent to PB13-C), suggested the presence of an interval impacted by LNAPL only up to 56.6 m AHD, although patterns of confined LNAPL conditions were frequently observed in PB13-C DGPs at slightly lower elevations (around 56.4 m AHD). Finally, LIF65 was adjacent to the UST and exhibited a wide LNAPL-impacted interval and LNAPL signatures that could correspond to anthropogenic materials, for instance between 57.6 and 59.4 m AHD.

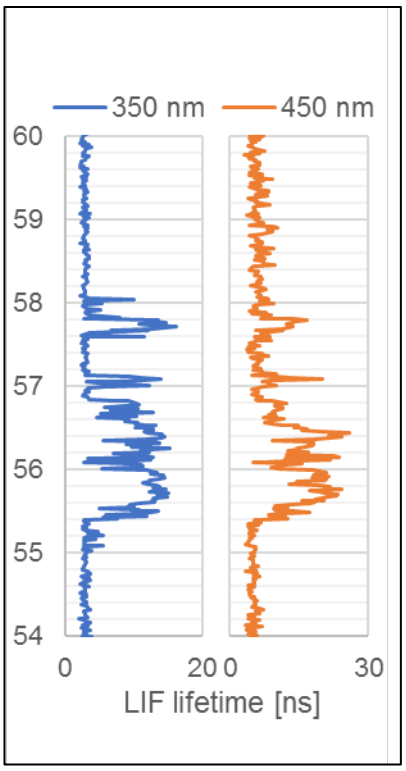


Fig. 6.40. Lifetime data from LIF68-C.

As depicted in Fig. 6.42, displaying total LIF signals in a logarithmic scale also facilitated the identification of some features such as residual LNAPL above 57.5 m AHD at LIF56-C and LIF68-C as well as relatively good agreement between the LNAPL-impacted intervals suggested by LIF57-C and MP44-C.

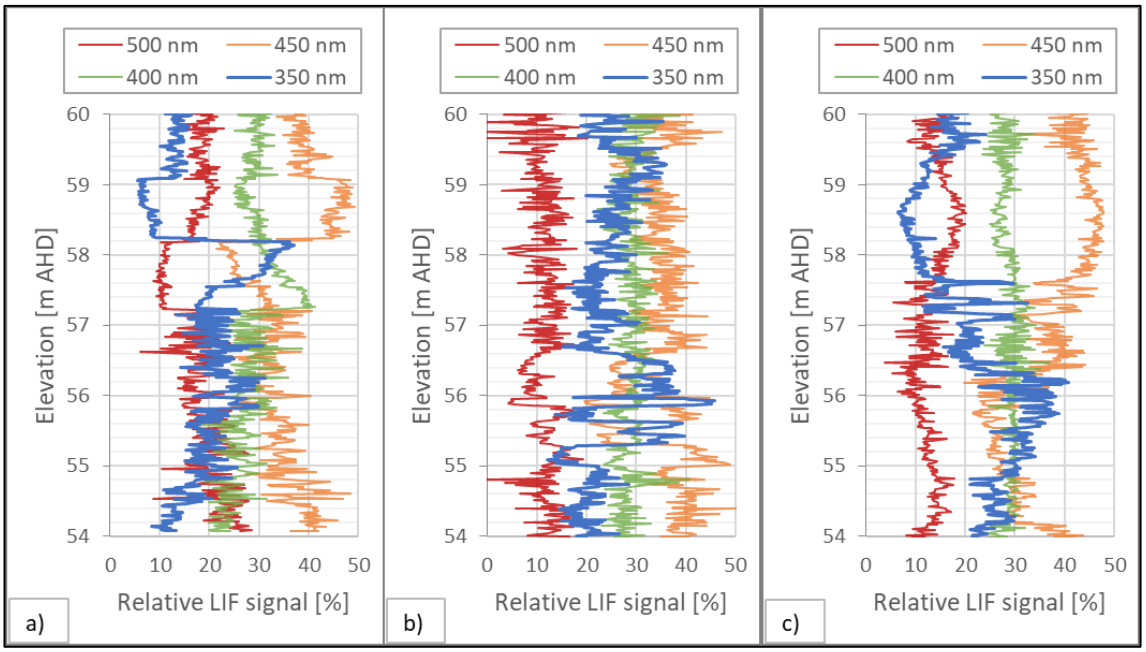


Fig. 6.41. Relative LIF signals at every wavelength channel at (a) LIF69-C, (b) LIF66-C, and (c) LIF65.

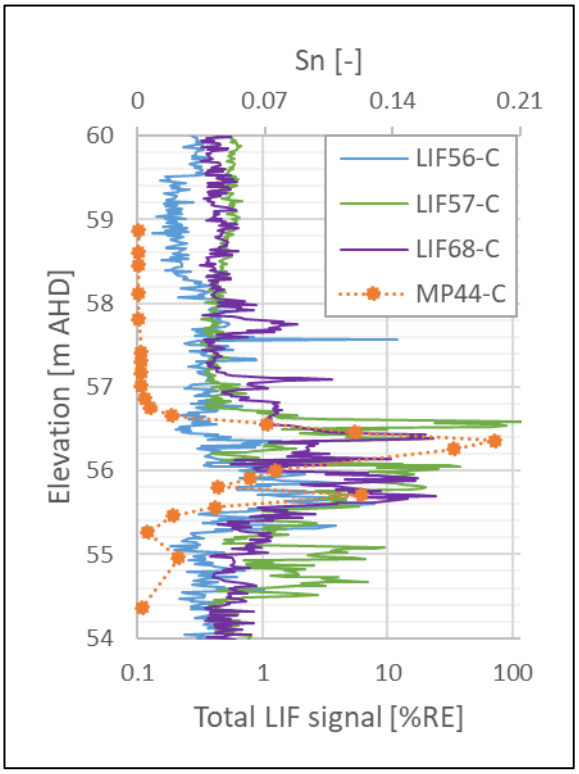


Fig. 6.42. Total LIF signals from area C in a logarithmic scale.

6.4.5.5 *Summary of results and proposed model scenarios*

It was not expected that a homogeneous VEQ model could capture all the details of the LNAPL distribution at PB40-C, although it could predict T_n to a certain extent. The main features that would require a multi-layered setting were:

1. finer-grained material around 56.0 m AHD causing a decrease in S_n between two peaks with more than 10 % S_n and more than 20 %RE;
2. an overlying aquitard and/or fining-upward sequence around 56.5–56.8 m AHD to simulate the decrease in S_n.

A b_n value between 0.75 and 0.80 m could adequately represent the field conditions according to measurement of in-well fluid levels. Analysis of cores and LIF profiles suggested that this value was reasonable.

6.4.6 Industrial site. Area T3/T4

6.4.6.1 *Preliminary compositional analysis*

Compositional analysis of samples from C66-T3 revealed minor BTEX and TMB concentrations (below 2.5 mg/kg). Therefore, PAH compounds such as naphthalene, 1-MN, 2-MN, and phenanthrene were predominant as depicted in Fig. 6.7 and expected from a diesel release. Fig. 6.43 showed good linear correlation (R^2 over 0.98) between concentrations of TPH, naphthalene, 1-MN, 2-MN, and phenanthrene when TPH concentration was over the limit of reporting (500 mg/kg).

One outlier was identified with nearly no PAH concentration but more than 20,000 mg/kg of TPH (not shown in Fig. 6.43). Closer inspection found out that the TPH value was doubled up, duplicating the value at 0.266 m AHD as shown in Fig. 6.44.

Fig. 6.44 also illustrated the correspondence between TPH concentration and S_n. The peak of almost 90,000 mg/kg corresponded to S_n of 40 %, while concentrations below 30,000 mg/kg resulted in S_n around 8–15 % with a minimum of 7.5 %. The S_n profile presented greater contrast between the two main peaks at 0.5 and 0.7 m AHD than the TPH profile.

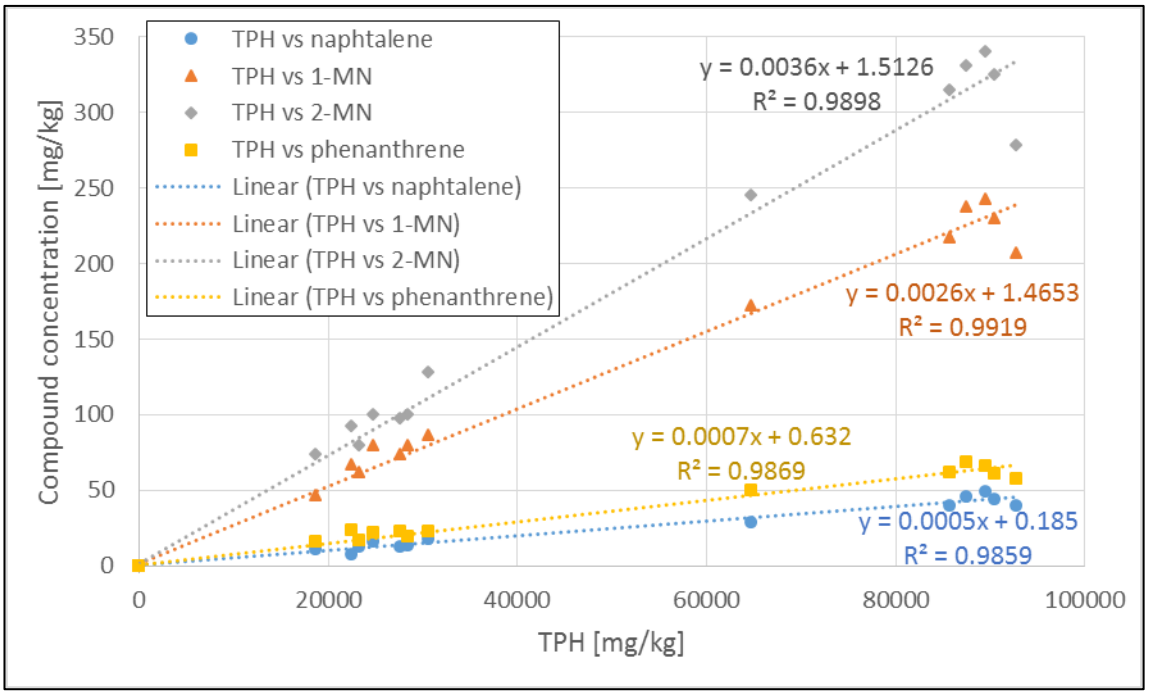


Fig. 6.43. Correlation between TPH concentrations and individual PAH compounds at C66-T3.

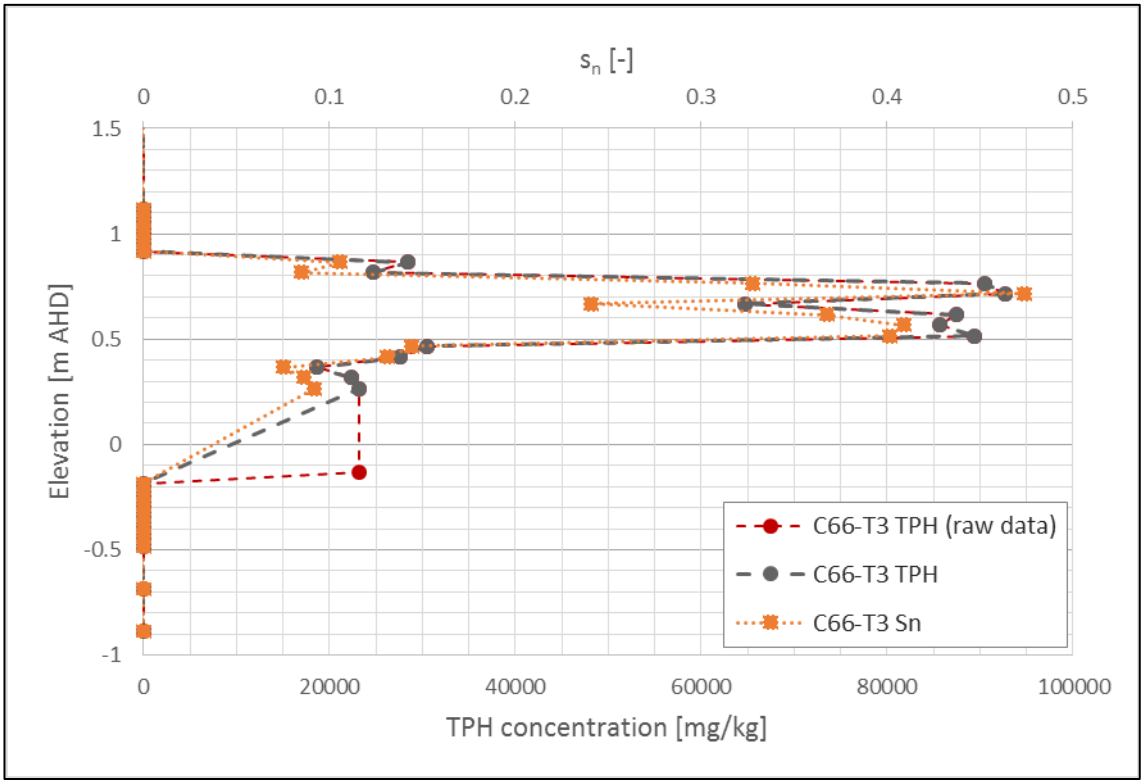


Fig. 6.44. Comparison between TPH and S_n profiles at C66-T3. The TPH value at -0.134 m AHD (presented as raw data) was doubled up and therefore removed.

6.4.6.2 Correspondence between conventional methods and near LIF logs

Four LIF profiles (LIF16-T3, LIF17-T3, LIF18-T3, and LIF19-T3) were taken at approximately 10 m from C66-T3. The LIF profiles were logged on 13/06/2016, almost

three months before coring C66-T3 on 08/09/2016. As depicted in Fig. 6.45, in-well fluid levels from previous years measured at 182-T3 (less than 5 m away from C66-T3) suggested that z_{aw} was likely a few centimetres lower in September than in June, corresponding to a greater b_n value (this observation was exaggerated in 2012 when the LNAPL repeatedly disappeared from the well in April and June despite b_n values over 0.14 m in March, May, and July).

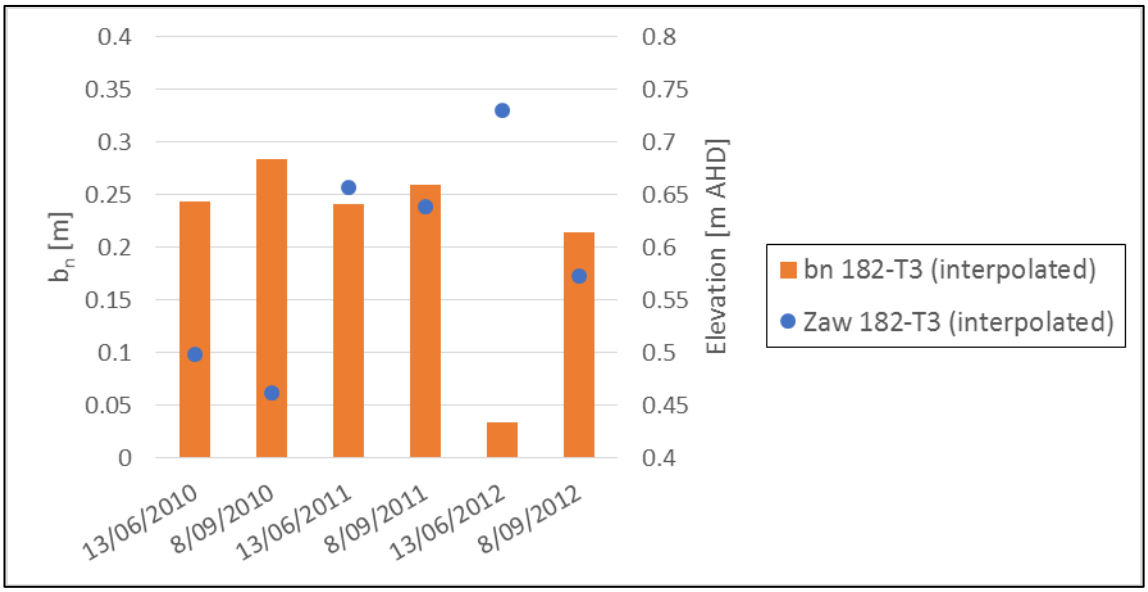


Fig. 6.45. Linearly interpolated z_{aw} and b_n values at 182-T3 (monthly monitored) in June and September during the period 2010–2012 (most recent data available).

As illustrated in Fig. 6.46, coring and LIF logging were consistent as regards the determination of the LNAPL-impacted interval despite the distance between both sites and the different sampling dates. According to C66-T3, the impacted interval was within a range of 0.7–1.1 m (containing 0.25–0.35 m with S_n over 15 %), while an impacted interval of 1.1 m was observed at LIF18-T3. This comparison exemplified the benefits of LIF logging over traditional coring in terms of sampling frequency and resolution.

In addition, the S_n profile at C66-T3 and the fluorescence response at LIF18-T3 revealed a similar pattern at the top 0.3 m of the LNAPL distribution profile. On the contrary, LIF18-T3 showed signals of a similar magnitude and even higher below 0.5 m AHD while the S_n estimations fell from 40 to 14 %.

Another LIF profile, LIF19-T3, did capture a decrease in fluorescence after the top 0.3 m of response as depicted in Fig. 6.47. However, this decrease in fluorescence was roughly

10 %, while S_n dropped two thirds. LIF19-T3 also detected signals under 25 %RE around -0.3 m AHD that could represent entrapped LNAPL. The dissimilarity in depths between LIF19-T3 and C66-T3 was probably due to variations in the LNAPL distribution at the scale of observation or fluid redistribution during the coring process.

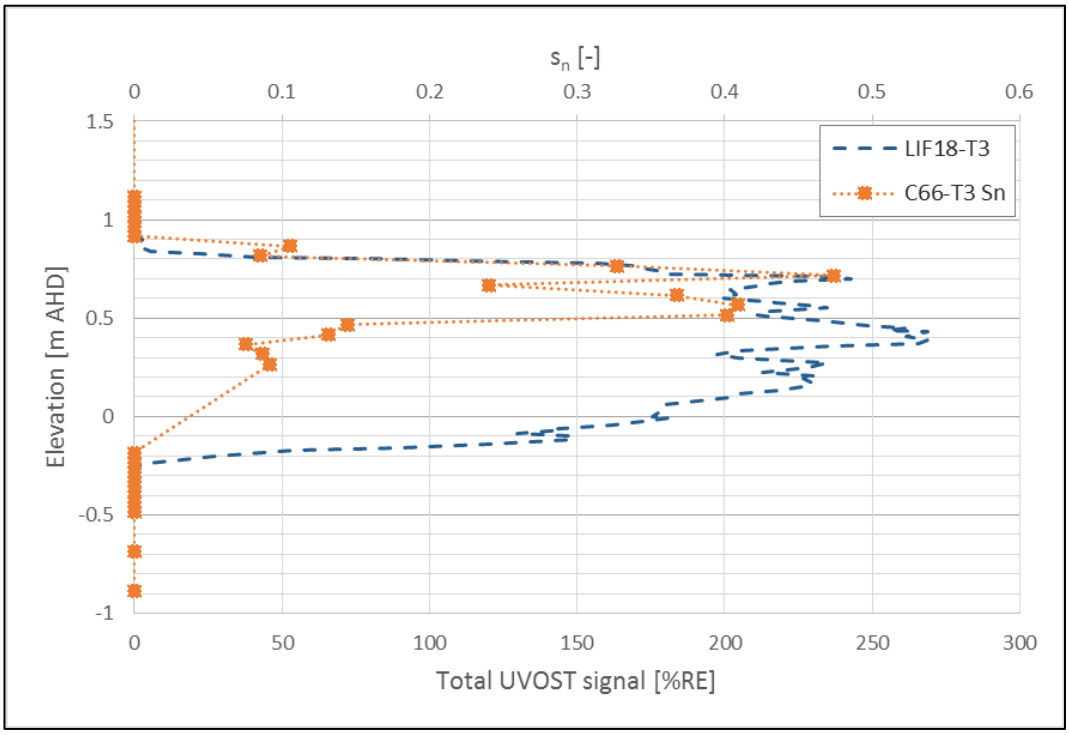


Fig. 6.46. S_n profile at C66-T3 versus LIF18-T3.

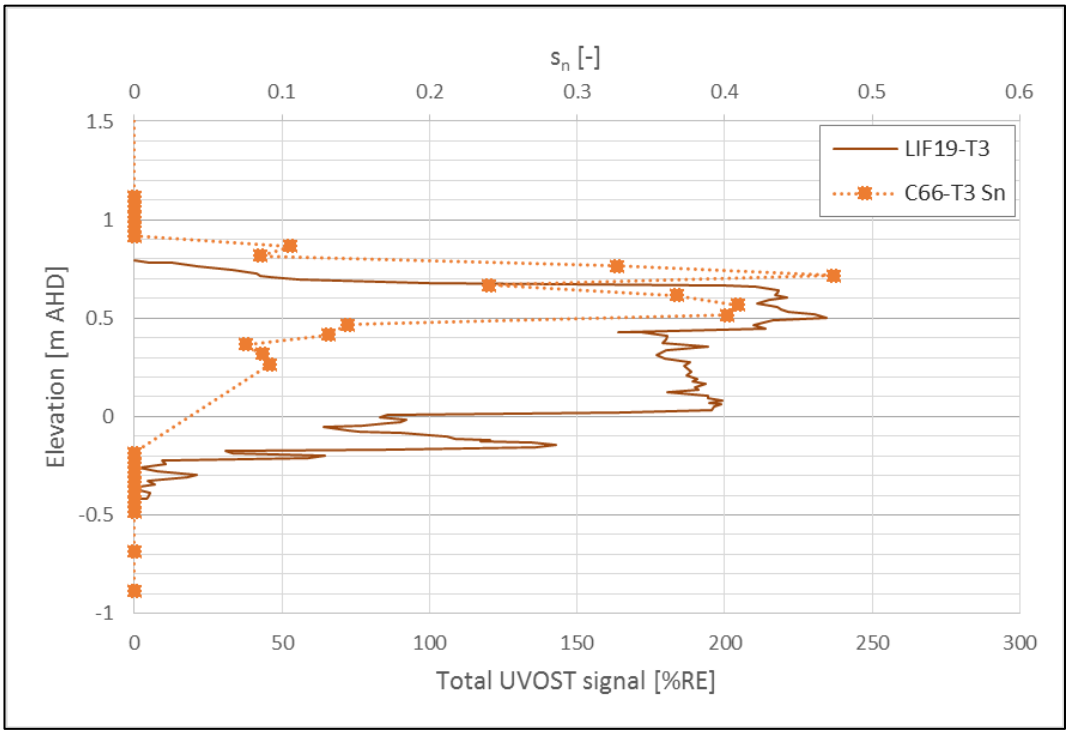


Fig. 6.47. S_n profile at C66-T3 versus LIF19-T3.

6.4.6.3 Comparison of LIF logs in the area of study. Relationship with T_n

Both LIF18-T3 and LIF19-T3 were located few meters West of C66-T3, presented signal maxima around 240–260 %RE and showed a relative peak of almost 150 %RE just below the main body of LNAPL mass. This peak was more clearly shown at LIF19-T3, where it occurred at -0.15 m AHD, although it could also be appreciated at LIF18-T3.

On the other hand, LIF16-T3 and LIF17-T3 were located East of C66-T3 and exhibited signal maxima around 350–370 %RE as illustrated in Fig. 6.48. Consequently, due to the geological homogeneity and similar multi-wavelength waveforms, higher S_n and T_n values could be expected East of C66-T3, although other factors such as the volume of near-immobile LNAPL in these areas could negatively influence the correlation between LIF response and T_n. LNAPL distribution at C66-T3 was more similar to LIF18-T3 and LIF19-T3 than to LIF16-T3 and LIF17-T3, whose main fluorescence peaks were detected at lower elevations. More specifically, LIF17-T3 displayed a larger impacted interval (1.8 m) and weak responses between 1.0 m AHD and 0.5 m AHD at the top of the profile in contrast to the S_n profile at C66-T3.

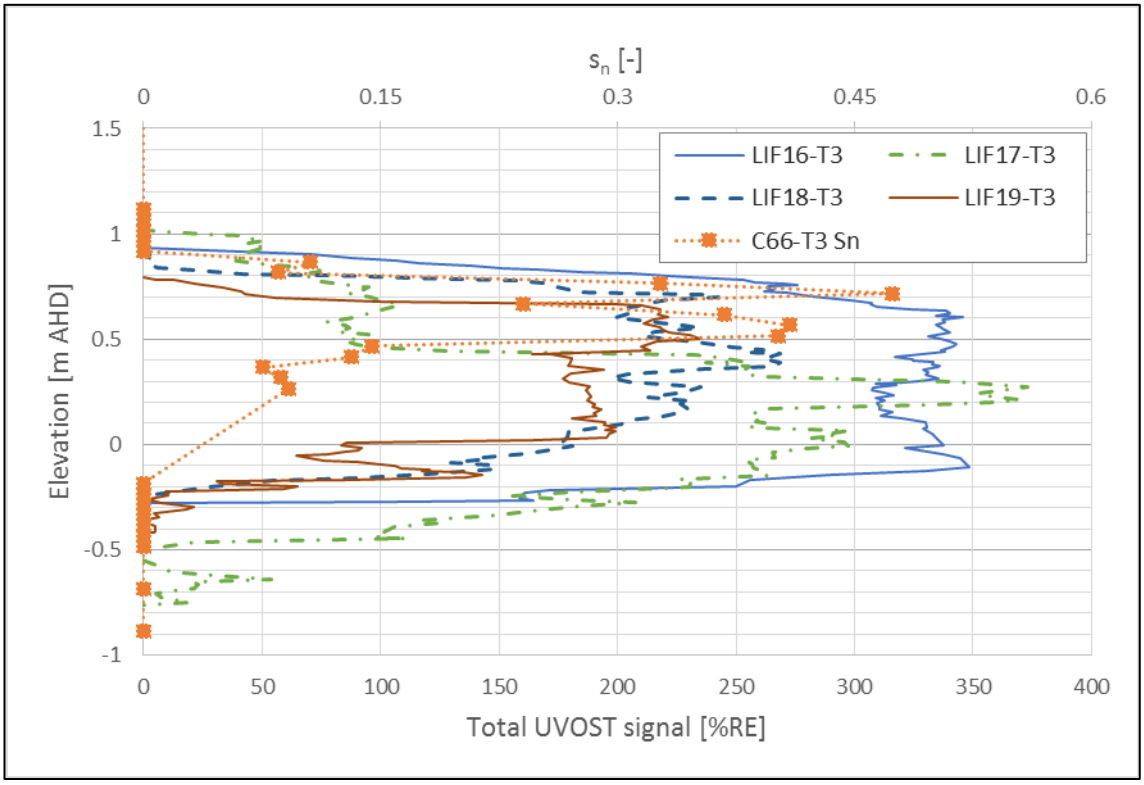


Fig. 6.48. Comparison of LIF and S_n profiles in area T3.

Despite these dissimilarities, the four LIF profiles from area T3 were relatively alike, even if there was a distance of 20 m between some of them as illustrated in map 12 (see Appendix B: Maps). This fact contrasted to the results from the HRSC campaign in the petrol station site and supported the existence of a higher degree of homogeneity at the industrial site in terms of hydrostratigraphy and LNAPL distribution.

The high fluorescence response typically found in the industrial site was due to the coarse-grained material compared to area C in the petrol station site and the presence of diesel instead of petrol as the LNAPL type. However, this high LIF signal was not necessarily linked to higher T_n values than those measured in the petrol station site. As further explained in section 7.4.5, baildown testing estimated a T_n between 0.07 and 0.08 m^2/day at NS7A-T4 in December 2005 (Johnston et al., 2010) and T_n values between 0.01 and 0.5 m^2/day were obtained in area T3 between 2009 and 2016 along consistent recovery rates through LNAPL skimming. Consistent chemical composition in the mobile LNAPL interval like in the case of the petrol station site was required to use peak LIF signal as an indicator of T_n, failing the application of such approach across sites or when different LNAPL types are found in the subsurface and relatively uniform characteristics cannot be expected.

6.4.6.4 Integration of LNAPL distribution profiles and hydrostratigraphic data

The HPT logs depicted in Fig. 6.49 corroborated the absence of materials as fine-grained as in the petrol station site. Nevertheless, the interval impacted by LNAPL was comparable to area A and area B, with HPT Q slightly over 450 mL/min and HPT P below 200 kPa, although reaching values under 150 kPa in the case of area T3. EC values were higher than in the petrol station site, but the observed shift with depth indicated that the reason probably was the contrast in S_w between the vadose and saturated zones as discussed in section 5.2.3. LNAPL mass at C66-T3 was found below an EC peak at 0.9 m AHD and most of it was above a minimum of HPT Q.

Given the coarse-grained material, it was expected that LNAPL could migrate upwards with little disturbance at least until HPT P increased over 200 kPa at 1.4 m AHD. Similar values of HPT P and HPT Q in area A did not lead to confined LNAPL conditions. In area T4, all the LNAPL mass was above z_{aw} at 050210/1-T4 after the water table quickly

dropped in February 2005 as illustrated in Fig. 6.50. This could have indicated absence of equilibrium conditions or effects of the entry pressure, aspect that was considered in the simulations presented in chapter 8.

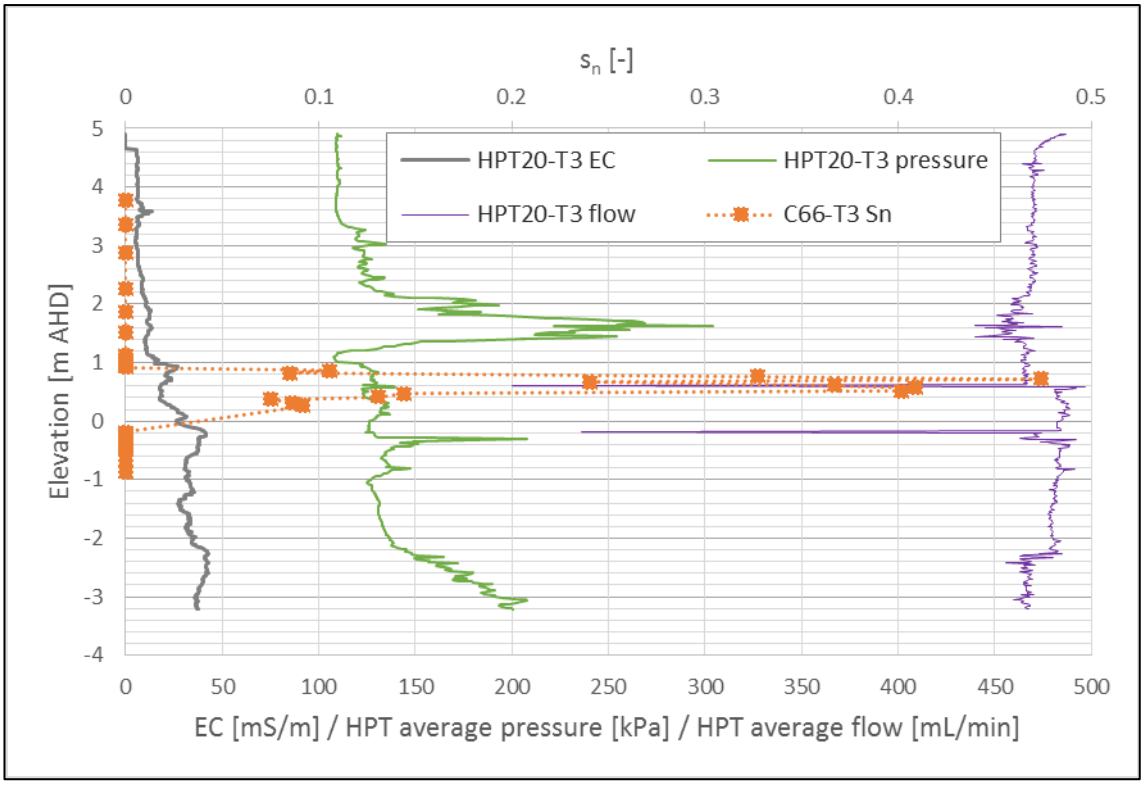


Fig. 6.49. HPT20-T3 and S_n profiles in area T3.

As regards other cores from area T4, the S_n profile at 040610/3-T4 was influenced by the stratigraphy, with the main body of LNAPL mass being within two lenses of coarser-grained sands (around 0.425–0.525 m AHD and 0.625–0.725 m AHD). The relative minimum in S_n between them also corresponded to a decrease in particle size at 0.575 m AHD as depicted in Fig. 6.51. In addition, coarser-grained sands above 0.85 m AHD could have influenced the absence of residual LNAPL.

Furthermore, both cores 040610/3-T4 and 040610/6-T4 revealed a decrease in S_n from more than 50 % above 0.5 m AHD (77.4 % in the case of 040610/3-T4) to less than 20 % when approaching 0.4 m AHD. Additionally, they exhibited a slight S_n increase at the lower interval of the LNAPL distribution. In core 040610/6-T4, this relative S_n peak was linked to the presence of coarser-grained sands around 0.19 m AHD. Lastly, an interval of isolated and potentially residual LNAPL at 040610/6-T4 (10.5 % at 0.885 m AHD) was also linked with an increase in particle size detected in multiple wells in area T4.

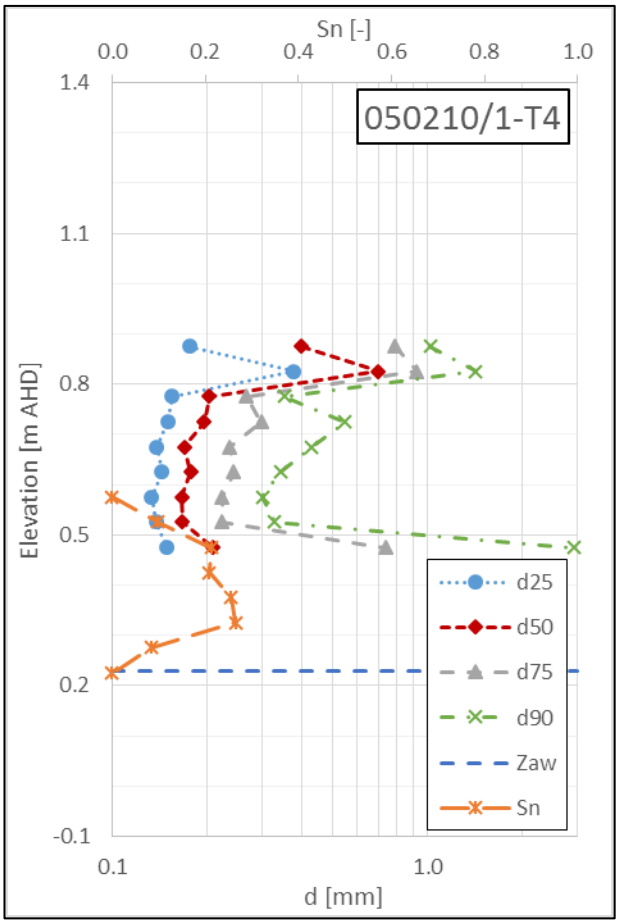


Fig. 6.50. Vertical profile of S_n and particle size at 050210/1-T4. *d25*, *d50*, *d75*, and *d90* stand for the 25th, 50th, 75th, and 90th percentiles of particle diameters, respectively. The value of z_{aw} corresponds to the date of coring (10/02/2005).

LNAPL mass was found at a similar elevation at C66-T3 in September 2016 (approximately between -0.2 and 0.9 m AHD) as in wells 040610/3-T4 and 040610/6-T4 collected in June 2004. C66-T3 presented a wider LNAPL-impacted interval than cores from area T4 (between 0.7 and 1.1 m in area T3 versus 0.55–0.85 m in area T4). C66-T3 exhibited lower S_n values than cores from area T4 (around 47 % instead of 77 % as found in area T4).

C66-T3, 040610/3-T4, and 040610/6-T4 were collected during periods of high water table conditions (September 2016 for C66-T3 and June 2004 for the other two cores) corresponding to low b_n values. For instance, b_n records were below 0.05 m in NS74-T4 (040610/3-T4) in June 2005. The three cores revealed high S_n values that would imply to have near-immobile LNAPL at saturations over 40 % in area T3 and over 50–60 % in T4 to present mobile LNAPL intervals of just 0.05 m. These values were not justified by the

subsurface materials nor the published literature. Therefore, b_n under equilibrium conditions was presumably greater than 0.05 m.

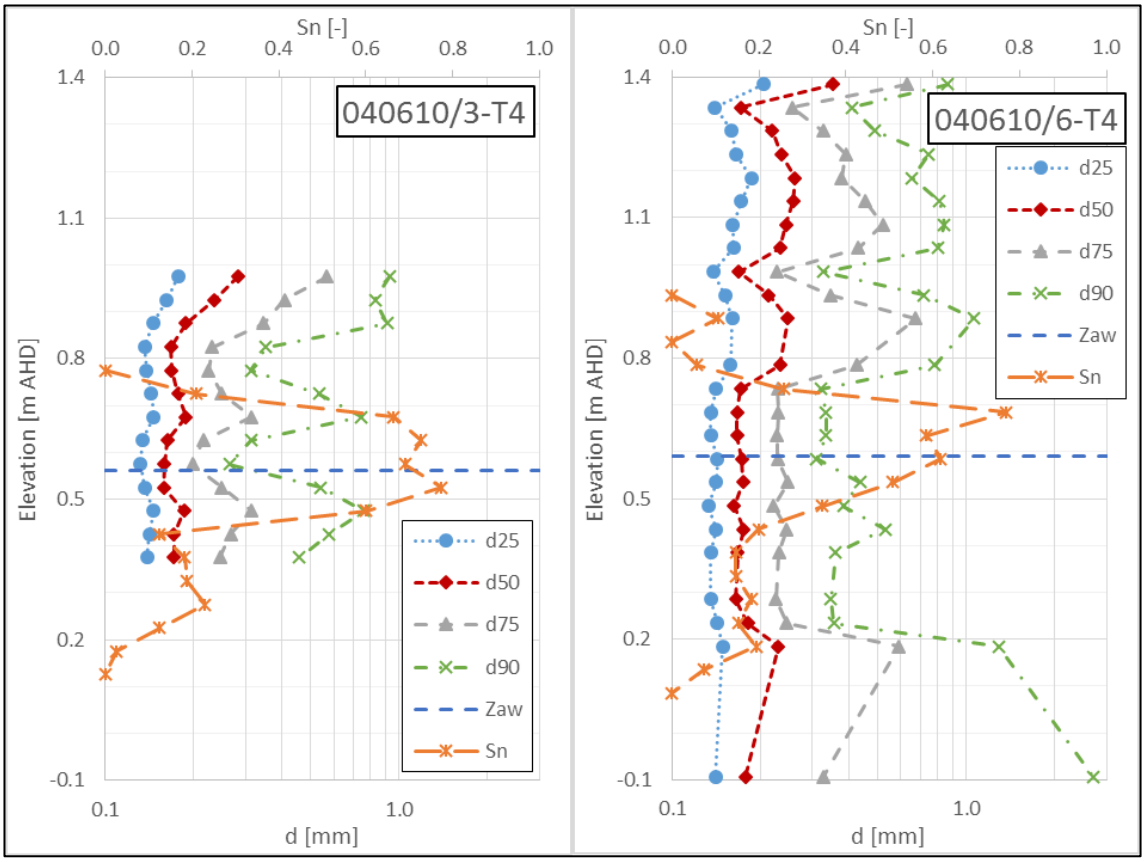


Fig. 6.51. Vertical profiles of S_n and particle size at 040610/3-T4 and 040610/6-T4. *d25*, *d50*, *d75*, and *d90* stand for the 25th, 50th, 75th, and 90th percentiles of particle diameters, respectively. The values of z_{aw} corresponds to the date of coring (10/06/2004).

NS7A-T4 presented a b_n value of 0.373 m with z_{aw} equal to 0.638 m AHD when the baildown test was conducted (01/12/2005). This b_n value was consistent with other records from previous and following days as inferred from the hydrograph in Fig. 5.34. Assuming a mobile LNAPL interval of 0.373 m with the LNAPL distribution inferred from the LIF campaign in June 2016 would imply to have entrapped LNAPL with fluorescence response over 180 %RE.

A mobile LNAPL interval of 0.373 m better resembled the S_n profiles measured at C66-T3 in September 2016 and in area T4 in June 2004, where LNAPL-impacted intervals with S_n over 15% were between 0.25 and 0.35 m at C66-T3, while intervals with S_n higher than 25% were between 0.20 and 0.30 m in area T4. Given the shape of the LNAPL distribution profiles, S_{ne}^{max} more likely corresponded to S_n values around 7.5–15 % in

area T3 and below 20 % in area T4. No evidences of a different value for S_{nr}^{max} were found in area T3, although the isolated mass of LNAPL at 040610/6-T4 (0.885 m AHD) could have suggested a value close to 10.5%.

6.4.6.5 Summary of results and proposed model scenarios

To sum up, the direct-push logs collected in area T3 were approximately 150 m North–Northeast from well NS7A-T4, where baildown testing was conducted in 01/12/2005 and retention parameters were estimated nearby. Therefore, the LNAPL distribution inferred from the HRSC campaign in 2016 could not be easily extrapolated to NS7A-T4 in order to build the model setting. Consequently, the model scenario was chosen to mainly follow information collected at NS7A-T4 and surrounding wells instead of the LIF profiles. A b_n value of 0.373 m was chosen to predict T_n on 01/12/2005, although a range between 0.04 m and 0.85 m (with maximum near-immobile S_n values up to 0.20) could be needed to predict the S_n profiles from area T4.

The LIF campaign still corroborated the subsurface characteristics inferred in section 5.2.3. It supported that the material should be coarser than in area A and area B. It also suggested using a scenario with two main layers (boundary around 0.4 m AHD), while using three layers corresponding to an upper facies, a diffuse boundary, and a lower facies, was discarded, since the potential contact between the first two model layers (1.2 m AHD) was above any evidence of LNAPL contamination, including historical maximum z_{an} values between 2004 and 2006.

6.5 Summary of results and conclusions

The application of LIF logging was highly beneficial for the characterisation of the petrol station site, even if LIF methods are commonly expected to provide stronger signals in coarser-grained materials and in the presence of fuels with more PAH molecules than petrol.

The main outcomes were:

- there was good agreement between the LIF campaign results and the existing CSM, suggesting that an initial LIF campaign could be an efficient approach to characterise sites similar to the petrol station site. Nevertheless, LIF profiling did

not detect new highly transmissive areas besides those already identified through the extensive monitoring network;

- unlike the core S_n values, LIF response was a good indicator of T_n considering one site with one type of LNAPL product. Therefore, LIF response was linked to the lumped concept of LNAPL mobility to a greater extent than S_n. In particular, signal maxima were a better indicator of T_n than integral LIF signal (integration of the whole profile) or the cumulative LIF signal (sum of all the data across the profile) used by other authors (Mulry and Lundy, 2013). LIF signal was not a clear indicator of T_n when considering different sites or different LNAPL types. Spatial variability in LNAPL composition or near-immobile LNAPL volumes could negatively influence the correlation between LIF response and T_n. Thus, the proposed approach is better suited for the characterisation of early-stage releases than for late-stage releases dominated by near-immobile LNAPL and NSZD phenomena;
- LIF allowed rapid identification of areas with long-term entrapment or residual LNAPL conditions because of the different multi-wavelength waveforms. These aspects were difficult to identify even after a long monitoring campaign through conventional methods. Other tools extensively reported in the literature like electrical resistivity methods and ground-penetrating radar (Atekwana and Atekwana, 2010) may need longer time to show a change in the geophysical signature (with high EC values associated to LNAPL attenuation processes). The ability of LIF systems to assess LNAPL weathering processes in heterogeneous media should be further investigated;
- the strongest LIF responses were commonly linked to relatively permeable materials according to HPT logging. Thus, this line of evidence suggested that HPT readings were not greatly affected by the presence of LNAPL despite the presumed decrease in k_{rw}. Nevertheless, fine-scale heterogeneity may complicate the integration of HRSC profiles collected in different locations. Therefore, systems combining multiple HRSC tools should be further developed;
- since heterogeneous conditions may generate complex LNAPL distributions even at fine scales, the design of a LIF campaign should ensure that appropriate

resolution is achieved in the horizontal plane as well. Interpretation of LIF data and delineation of subsurface LNAPL distributions should always consider the site hydrostratigraphy as suggested by other authors (Suthersan et al., 2017) as well as multiple lines of evidence. Three-dimensional representations of LIF data should be done and interpreted with caution;

- field logs supported that potential LNAPL contamination could be found even with signals weaker than the natural fluorescence of the geological medium. The use of relative LIF signals, lifetime data, and total LIF signal in logarithmic scale contributed to better identify intervals impacted by LNAPL with low LIF response. Accordingly, differences between b_n values and interval showing strong LIF response should not be directly linked to confined LNAPL conditions without other lines of evidence;
- the use of relative LIF signals may not enable clear determination of the confining contact elevation when the overlying aquitard is associated to leaky confined conditions. Consequently, relative LIF signals may serve as a metric to assess the aquitard integrity along other characterisation tools;
- in addition, the LIF probe was also able to detect anomalies associated to the location of the UST in the petrol station site, thus LIF could help to identify the location of the primary source of contamination if unknown;
- further investigation should be conducted in controlled environments to assess if LIF response is influenced by the different forms that LNAPL may exhibit in the saturated and unsaturated zones (including films, pendular rings, blobs or ganglia occluded by water, and mobile LNAPL with different degrees of wettability).

Fig. 6.52 illustrates some of these outcomes by comparing measurements of S_n and LIF response in area A (MP50-A and LIF43-A) and area C (MP44-C and LIF57-C) as well as the relative LIF signal from LIF43-A. Higher S_n values were measured in area C, while higher T_n and peak LIF signal were obtained in area A.

Regarding the core analysis, the S_n maximum was commonly located at the bottom of the LNAPL distribution profile. Decreasing S_n values were found upwards. Similar LNAPL distributions have been attributed in the past to falling water tables (Tomlinson et al.,

2012). However, in the case of the petrol station site, it was also possible to link this LNAPL redistribution to rising water tables by collecting pairs of cores before and after a rise in z_{aw}. The resulting LNAPL profile was partly due to finer-grained materials at the top of the aquifer.

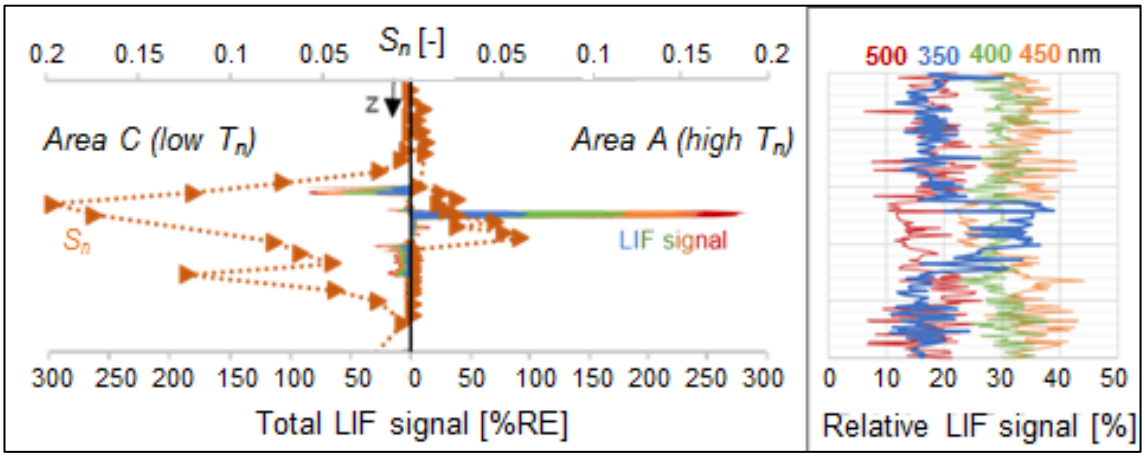


Fig. 6.52. Graphical representation of how peak LIF signal was correlated with T_n, unlike S_n. Relative LIF signals (the right panel depicts the case of area A) and lifetime data could be used to enhance the identification of the interval impacted with LNAPL through LIF logging.

Finally, the analysis of LIF and S_n profiles contributed to refine the modelling scenarios and provided information about aspects of the geological setting that could introduce errors and uncertainties further explored in chapter 8.

7 Quantification of subsurface parameters

7.1 Chapter structure

Chapter 7 investigates the variability of subsurface parameters required by the analytical models. It quantifies parameters ranges and most likely values in the modelling scenarios proposed for every area of study and simulated in chapter 8. These parameters included:

- Φ (from field measurements and literature values);
- k_{sw} (obtained from particle-size data, pumping tests, HPT logs, and literature values). It was assessed if DPIL readings were affected by LNAPL presence by comparing them to k_{sw} estimations from empirical correlations with particle-size data. The applicability of aquifer heterogeneity metrics such as logconductivity variance in stratified aquifers (as in the case of the petrol station site) was also evaluated. In addition, the most adequate d_E to adopt in the application of empirical correlations was investigated;
- retention parameters (laboratory measurements, derivations from particle-size data, and literature values);
- LNAPL properties (laboratory measurements and literature values);
- T_n (estimated through baildown testing, proposing alternative analysis and interpretation of baildown tests presented by Gatsios, 2018).

7.2 Literature values

7.2.1 Porosity

Table 7.1 summarises representative Φ ranges for sands (fine, medium and coarse) and silts from classic textbooks in hydrogeology and other references commonly used by researchers and practitioners. The lowest representative Φ value for sands (15 %) were given by de Marsily (1986) and Dassargues (2018), while the other consulted references presented minima between 20 % and 26 %. On the other side, maximum representative Φ values of sands ranged from 48 % to 53 %. Fine sands were considered to have a slightly higher Φ than medium and coarse sands by Todd and Mays (2005), while Bear (1972) gave a higher range for medium-to-coarse sand than for fine-to-medium sand.

Table 7.1. Representative ranges of Φ (in percentage) for silt and different types of sand according to multiple references. Average values are shown between parentheses. Carsel and Parrish (1988) reported θ_{ws} values. *One asterisk indicates that the value corresponds to sandy loam. **Two asterisks indicate that the value correspond to the sum of sands and loamy sands.

Silts/loam	Sands	Fine sands	Medium sands	Coarse sands	Reference
40–50	30–40	30–35	–	35–40	Bear (1972)
35–50 (40)	20–45 (35)	–	–	–	Custodio and Llamas (1983)
30–45	15–35	–	–	–	Dassargues (2018)
34–61	26–53	26–53	–	31–46	Domenico and Schwartz (1998)
35–50	25–50	–	–	–	Freeze and Cherry (1979), Fetter (2018)
–	15–48	–	–	–	Marsily (1986)
46	–	43	39	39	Todd and Mays (2005)
(41)*	(43)	–	–	–	Carsel and Parrish (1988)
29.8–54.4 (44.4)*	26.4–56.7 (40.7)**	–	–	–	Nemes et al. (2001)
28.5–54.0 (42.8)	30.6–51.4 (41.4)	–	–	–	API (2006)

Representative values of Φ for silts have been commonly reported to be higher than in the case of sands. The range spanned from a lower bound of 30 % as given by Dassargues (2018) to 61 % (Domenico and Schwartz, 1998).

Regarding the information obtained from databases and other references, the UNSODA (Nemes et al., 2001) and Carsel and Parrish (1988) databases were formed by agricultural soils and followed the USDA classification system. According to this classification, sands from the industrial site would still be classified as sands. In the case of the petrol station site, the sampled aquitard materials were sandy loam, the transition between the aquitard and the coarser-grained fractions of the aquifer were represented by loamy sand (and one sand sample), while the rest of the aquifer was comprised of sand and loamy sand.

Thus, 65 results from sand samples were retrieved from the UNSODA database (Nemes et al., 2001) with median, geometric and arithmetic mean Φ values of 41.40 %, 39.75 %, and 40.15 %, respectively, as well as a SD of 0.056. The database also included 17 samples of loamy sand (central Φ values of 43 % with SD equal to 0.065) and 61 samples of sandy loam (central Φ values between 43.3 % and 45.6 % and SD equal to 0.065). There were sandy loam Φ values below 30 % and sand Φ values over 53 %, contrasting to other ranges proposed in the literature.

Furthermore, Carsel and Parrish (1988) found an average θ_{ws} of 43 % in 246 sand samples, with a SD equal to 0.06 and a CV of 15.1 %. Samples of loamy sand and sandy loam exhibited slightly lower θ_{ws} values around 41 %, with SD of 0.09 and CV values between 21.6 % and 21 %, respectively. Typically, θ_{ws} is around 5–10 % lower than Φ because of the presence of entrapped air (van Genuchten et al., 1991), although the difference may be greater in LNAPL source zones undergoing methanogenesis (Amos and Mayer, 2006).

In addition, the API database (2006) followed the USCS classification. Sands from the industrial site commonly fell in the SP category. In the petrol station site, the aquitard materials were SM or ML, SM was characteristic of the transition zone, and multiple types of sand (SM, SW, and SP with different amounts of fines) formed the rest of the aquifer. Consequently, queries for ML (characteristic of the aquitard in the petrol station site), SM (characteristic of the transition zone in the petrol station site), SP (characteristic of the industrial site), and the sum of sand types (SM, SW, and SP; characteristic of the rest of the aquifer in the petrol station site) were created in the database.

The API database (2006) included 72 SM samples with an average Φ value of 42 % and SD equal to 0.045. A query for SP samples provided 25 results with an average Φ value of 41 % and SD equal to 0.054. The median and geometric mean were 40.36 % and 40.31 % in this case. These results were practically identical considering samples of any soil type (not just SP) containing less than 5 % of fines (same range, average Φ value of 39.6 %). In particular, a query for the sum of SM, SW, and SP resulted in 102 samples

with an average Φ value of 41 % and SD equal to 0.049. The API database included 80 ML samples with an average Φ value of 43 % and SD equal to 0.058.

7.2.2 Hydraulic conductivity

Table 7.2 summarises representative k_{sw} values for sands (fine, medium and coarse) and silts from classic textbooks in hydrogeology and other references commonly used by researchers and practitioners. Reviewed k_{sw} values from sediments exclusively reported as sands were within a range of five orders of magnitude, from 0.01 (Fetter, 2018; Dassargues, 2018) to 1,000 m/day (Freeze and Cherry, 1979; Dassargues, 2018), although Todd and Mays (2005) proposed representative values between 2.5 and 45 m/day. Values over 0.09–1 m/day were usually presented for coarse sands, while fine sand k_{sw} was below 20 m/day in all the reviewed references. There was a span of six orders of magnitude (from 0.0001 to 10 m/day) in k_{sw} values for silts. Thus, the adoption of k_{sw} values from the literature for calculations and modelling purposes may be accompanied by strong errors.

Table 7.2. Representative ranges of k_{sw} (in m/day) for different types of sand according to multiple references. Average values are shown between parentheses. The conversion of s^{-1} into day^{-1} was done with a factor of 10^5 instead of $8.64 \cdot 10^4$ for simplicity purposes. *Values marked with one asterisk corresponded to different types of fine sediments, for instance fine sand, silt or loess. **Two asterisks indicated coarse sands, sands mixed with gravels or from glacial outwash. Materials from Carsel and Parrish (1988), and Nemes et al. (2001) are consistent with those used for Φ values.

Silts/loam	Sands	Fine sands	Medium sands	Coarse sands	Reference
0.0001–1*	–	0.0001–1*	–	1–1000**	Bear (1972)
0.01–10	0.1–1000	–	–	–	Dassargues (2018)
0.0001–2	–	0.02–20	0.09–50	0.09–600	Domenico and Schwartz (1998)
0.001–0.1	–	0.01–1	–	1–100**	Fetter (2018)
0.001–1	0.1–1000	0.01–10*	–	–	Freeze and Cherry (1979)
0.0001–1*	–	0.0001–1*	–	1–10000**	Marsily (1986)
0.08	–	2.5	12	45	Todd and Mays (2005)
(1.06)	(7.128)	–	–	–	Carsel and Parrish (1988)

0.011–59.39 (4.12)	0.03–276.48 (11.93)	–	–	–	Nemes et al. (2001)
0.00001–137 (3.60)	0.0008–864 (38.0)	–	–	–	API (2006)

Regarding other references and databases, Carsel and Parrish (1988) reported average k_{sw} values of 1.06 m/day for sandy loam, 3.50 m/day for loamy sand, and 7.128 m/day for sand.

The UNSODA database (Nemes et al., 2001) had k_{sw} values for 99 sands samples presenting median, geometric, and arithmetic mean values of 9.01, 6.33, and 20.32 m/day, with SD equal to 39.18 m/day. In addition, it included 33 loamy sand samples (median, geometric, and arithmetic mean values of 3.1, 2.13, and 4.81 m/day, with SD equal to 6.24 m/day), and 83 sandy loam samples (median, geometric, and arithmetic mean values of 0.69, 0.91, and 4.12 m/day, with SD equal to 8.48 m/day). The average of 17.1 m/day shown in Table 7.2 corresponds to the sum of sand and loamy sand samples.

The API database (2006) included 88 sand samples (including SP, SW, and SM) with an average k_{sw} value of 38 m/day, but with much lower median and geometric mean values (0.56 and 0.81 m/day, respectively). The associated SD was 131 m/day. The value of SD was 19 m/day. There were only 14 SP samples with k_{sw} data. The median (2.253 m/day) and geometric mean (6.785 m/day) were clearly different to the arithmetic mean (125.144 m/day), although both were within the IQR this time (0.987–307.785 m/day). SD, MAD, and CV were 202.338 m/day, 2.635 m/day, and 162 %, respectively. Hence, samples from the API database were apparently biased towards high k_{sw} values. Similarly, there were 77 ML samples with an average k_{sw} value of 3.60 m/day, although the median and geometric mean values were 0.02 and 0.03 m/day, respectively.

Additionally, Johnston and Trefry (2009) chose a low k_{sw} of approximately 0.012 m/day as representative for modelling scenarios resembling subsurface conditions similar to area T4 and from the same geographic region. They built permeability fields using lognormal variances of 0.594 and 1.188.

Lastly, Gatsios (2018) and Gatsios et al. (2018a) considered k_{sw} values of 13 m/day in area A (although it should be increased up to 700 m/day to obtain T_n prediction through LDRM similar to field measurements), 8 m/day in area B, and 1.83 m/day in area C according to average HPT data. Furthermore, an additional intermediate layer of only 0.03 m/day was also considered in area C. It should be noted that this design in area C responded to assuming a value of zero S_n at 55.81 m AHD, representing a sample where the sleeve dimensions were not measured. However, this sample presented a positive TPH concentration value. S_n was calculated to be 4.44 % after assuming average sleeve dimensions from other samples.

7.2.3 Retention parameters

Table 7.3 summarises reference values of $vG\text{-}\alpha$, $vG\text{-}N$, and S_{wr} according to widely used literature sources.

Table 7.3. Typical retention parameters of sands according to literature sources. Estimations of S_{wr} from Carsel and Parrish (1988) were assumed to be the ratio between average residual and saturated water contents. Arithmetic means are given between parentheses.

Textural class	$vG\text{-}\alpha$ [m^{-1}]	$vG\text{-}N$ [-]	S_{wr} [-]	Reference
ML	0.05–2.50 (0.64)	1.34–4.50 (2.01)	0.005–0.900 (0.426)	API (2006)
SM	0.20–18.70 (1.65)	1.40–5.20 (2.55)	0.010–0.833 (0.344)	API (2006)
SP	0.31–5.15 (1.85)	1.74–8.00 (3.17)	0.020–0.486 (0.209)	API (2006)
Loam	3.6	1.56	0.181	Carsel and Parrish (1988)
Sandy loam	7.5	1.89	0.159	Carsel and Parrish (1988)
Loamy sand	12.4	2.28	0.139	Carsel and Parrish (1988)
Sand	14.5	2.68	0.105	Carsel and Parrish (1988)

A query for SP samples in the API database (API, 2006) generated 24 sets of values with a range of $vG\text{-}\alpha$ spanning more than one order of magnitude (median of 1.535 m^{-1} and geometric mean of 1.385 m^{-1}, SD of 1.329 m^{-1}), but still far below the arithmetic mean reported by Carsel and Parrish for sand samples (SD of 2.9 m^{-1}). Lower values were

obtained for finer-grained materials as it could be expected because of the higher air-entry pressures.

Regarding the API database range of $vG\text{-}N$, the obtained maximum equal to 8 could be considered as an outlier according to the criterium of Iglewicz and Hoaglin (1993), taking into account that the MAD was equal to 0.993 (SD of 1.421) and the median was 2.65 (geometric mean of 2.94), classifying as outliers any value over 7.804. This assumption made sense taking into consideration that the second and third highest values were only 5.54 and 4.56, respectively and the coefficient of determination (0.93) of the retention model of that sample was the second lowest obtained with the query. In general, lower values were observed for finer-grained materials, consistent with the literature.

The range of S_{wr} presented in API (2006) was very wide (spanning more than two orders of magnitude) and the average was twice as high as the value reported in Carsel and Parrish (1988). S_{wr} values were reported to be higher in finer-grained materials. Considering sands similar to those present in area T4, Steffy et al. (1997b) measured a S_{wr} value of 15.6 % in a diesel-water column, while Johnston and Trefry (2009) assumed a high S_{wr} of 28.87 % for modelling scenarios.

Furthermore, Yimsiri et al. (2018) conducted a laboratory experiment considering two drainage and imbibition stages in a three-phase (air-diesel-water) column. They obtained S_{wr} values 14.4 % and 10.7 % for Ottawa #3821 sands (fine poorly graded sands with a d_{50} of 0.422 mm, C_u of 1.48 and estimated k_{sw} of 15.552 m/day) as well as 10.2 % and 7.9 % for Ottawa #3820 sands (medium poorly graded sands with a d_{50} of 0.643 mm, C_u of 1.36 and estimated k_{sw} of 17.453 m/day). Therefore, sands from area T4 were relatively similar to Ottawa #3820 sands, although still fine grained. The diesel used in their experiments was comparable to the LNAPL found in area T4 according to its physical properties (ρ_n of 0.865 g/cm^3, η_n of 0.41 cP, and σ_{an} of 28.80 mN/m).

As concerns S_{nr} for diesel spills, Mercer and Cohen (1990) presented a value of 15 % for diesel and light fuel oil in soils. They also included retention factors of 0.025 and 0.040 L of middle distillate per litre of medium (fine to medium sand and silt to fine sand, respectively). This value divided by Φ yields S_{nr}. Therefore, S_{nr} ranges of 7–11 % and 11–18 % would be obtained for middle distillates considering a range of Φ of 35–65 % in

fine to medium sand and in silt to fine sand, respectively. Yimsiri et al. (2018) measured S_{nr} values of 3.8 % and 4.9 % for fine sands as well as 4.1 % and 4.6 % for medium sands. Lenhard et al. (2019) assumed a S_{nr}^{max} value of 10 % for a preliminary test of LNAPLTRANS at 050210/1-T4.

Regarding S_{nr} values for gasoline releases, values as high as 75 % have been reported for clays (Zytner et al., 1993) and as high as 60 % in sands (Hoag and Marley, 1986; Mercer and Cohen, 1990), more specifically in fine sands with d_{50} equal to 0.225 mm (Hoag and Marley, 1986). Hayden et al. (1997) employed gasoline and three soils with more than a 94 % of sand. They found strong differences in S_{nr} in air-dry systems (2.4–11 %) and systems with irreducible water content (0.71–1.5 %). Zalidis et al (1998) also employed gasoline in a soil with 25 % of fines, 50 % of fine sands and 25 % of medium sands. They measured S_{nr} to become near constant (1–4 %) when S_w was over 20 %. Van Geel and Roy (2002) used heptane and obtained S_{nr} values between 7.2–24.4 % in three phase systems. Gatsios et al. (2018a) predicted a S_{nr} values (assumed to be the same as S_{ne}) of 1 % in area A, 0–1 % in area B, and 3–4 % in area C after a calibration procedure.

Lastly, few studies have reported values of S_{ne} in cases of diesel contamination. Steffy et al. (1997b) estimated a $S_{ne}^{\max}$ of 45 % in a diesel water column packed with sands from a location relatively close and similar to area T4. Yimsiri et al. (2018) obtained S_{ne} values of 10.2 % and 6.7 % for fine sands and 4.6 % and 6.0 % for medium sands. Lenhard et al. (2019) assumed a S_{ne}^{max} value of 25 % for a preliminary test of LNAPLTRANS at 050210/1-T4, while Van Geel and Roy (2002) used heptane and obtained a S_{ne} value of 22 % in two-phase systems. This value could be considered more representative of cases of petrol contamination.

7.3 Petrol station site

7.3.1 Porosity

7.3.1.1 Laboratory measurements

In the petrol station site, estimations of Φ were obtained considering 183 measurements from cores MP50-A, MP77-A, PB27-B, MP58-B, MP76-B, MP44-C, and MP78-C, where S_n values were also measured. Alternatively, particle-size data were used to derive θ_{ws} values with RETC as presented in section 7.3.1.2.

As shown in section 5.2.1, the strong variability exhibited by Φ measurements from twin cores discouraged the assignation of different Φ values to specific subsurface layers or areas of study. Therefore, the analysis of Φ measures of spread and central values aggregated all the Φ values. Table 7.4 summarises some measures of spread and central values of Φ from the 183 estimations corresponding to cores collected in the petrol station site. A wide range between 30.5 and 72.0 % was found. The 5th, 95th, and 98th percentiles were 36.1, 59.5, and 62.5 %, respectively.

Table 7.4. Statistics of Φ measurements from the petrol station site.

	N	MIN	Q1	M	GEO-MEAN	MEAN	Q3	MAX	CVR
Φ [%]	183	30.5	41.6	44.4	44.9	45.4	47.4	72.0	9.71

Thus, maximum values were considerably higher than those reported in the literature as presented in section 7.2.1, with maxima around 61 % as given by Domenico and Schwartz (1998). The maximum was also higher than measurements from the industrial site as presented in section 7.4.1. Discrepancies could have been due to an inappropriate representation of this type of depositional environment in databases and other literature, measurement errors or other specific characteristics of the petrol station site. Assuming a ρ_s value of 2.65 kg/m^3 (representative of quartz particles) was presumably not a strong source of error since the subsurface materials consisted of silica sands and ρ_s measurements in 14 samples fell within a range of 2.52–2.69 kg/m^3 with both arithmetic and geometric means equal to 2.66 kg/m^3.

Nevertheless, Φ values over 66.8 % resulted in robust Z-scores over 3.5 and therefore could be labelled as outliers according to the Iglewicz and Hoaglin (1993) criterium (since MAD was 0.043). Removing the two measurements over this value (71.7 % from PB27-B at 57.325 m AHD and 72.0 % from MP78-C at 56.210 m AHD), the Φ maximum was 62.9 %, closer to values reported in the literature.

Fig. 7.1 illustrates the probability distribution of the 183 Φ measurements, which depicts the extreme nature of Φ values over 70 % and a relatively symmetrical distribution around central values of 44–45 % (skewness of 0.78 after removing the two suspected outliers; 1.10 without filtering data), despite some peaks (especially around 31–32 %

and 59–60 % and therefore out of the IQR) suggesting the potential presence of several populations.

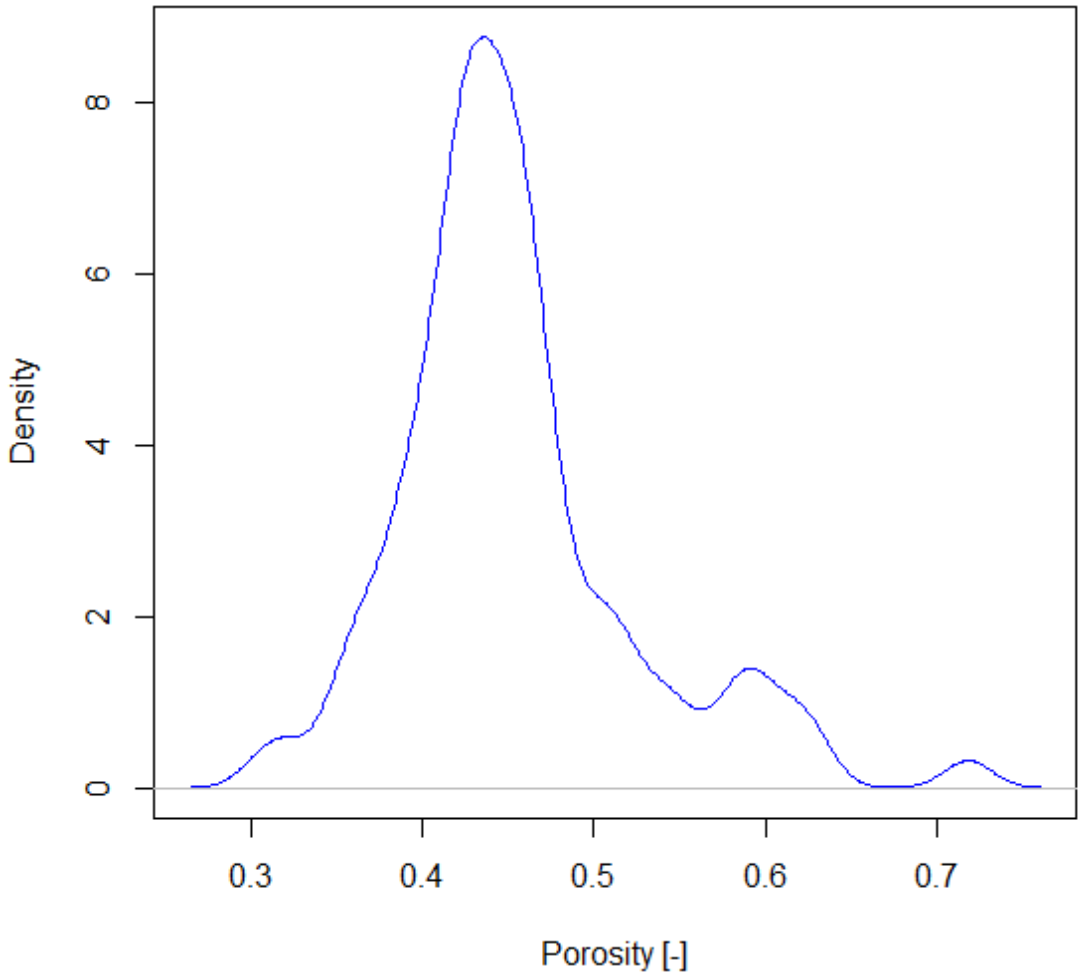


Fig. 7.1. Density trace of 183 Φ measurements from MP50-A, MP77-A, PB27-B, MP58-B, MP76-B, MP44-C, and MP78-C.

7.3.1.2 Neural network predictions

Neural network predictions of θ_{ws} only considered 25 samples. The main difference with core measurements of Φ was the estimation of a much narrower range (37.7–39.1 %) and lower variability (CVR of 2.13 % versus 9.71 %) as shown in Table 7.5. This was most likely due to only using textural classes as input data for the predictions and extreme values were likely missed. Nevertheless, considering that θ_{ws} is typically 5–10 % lower than Φ (van Genuchten et al., 1991), the obtained range was in a close agreement with the IQR of Φ measurements from cores.

Fig. 7.2 compares the distributions of θ_{ws}, calculated with RETC, and Φ, measured in cores, clearly illustrating the accumulation of θ_{ws} values around 38.4 %, while the central values of Φ measurements were between 44.4 and 45.4 %.

Table 7.5. Statistics of θ_{ws} values predicted with RETC in the petrol station site.

	N	MIN	Q1	M	GEO-MEAN	MEAN	Q3	MAX	CVR
Φ [%]	25	37.7	37.9	38.4	38.4	38.4	39.0	39.1	2.13

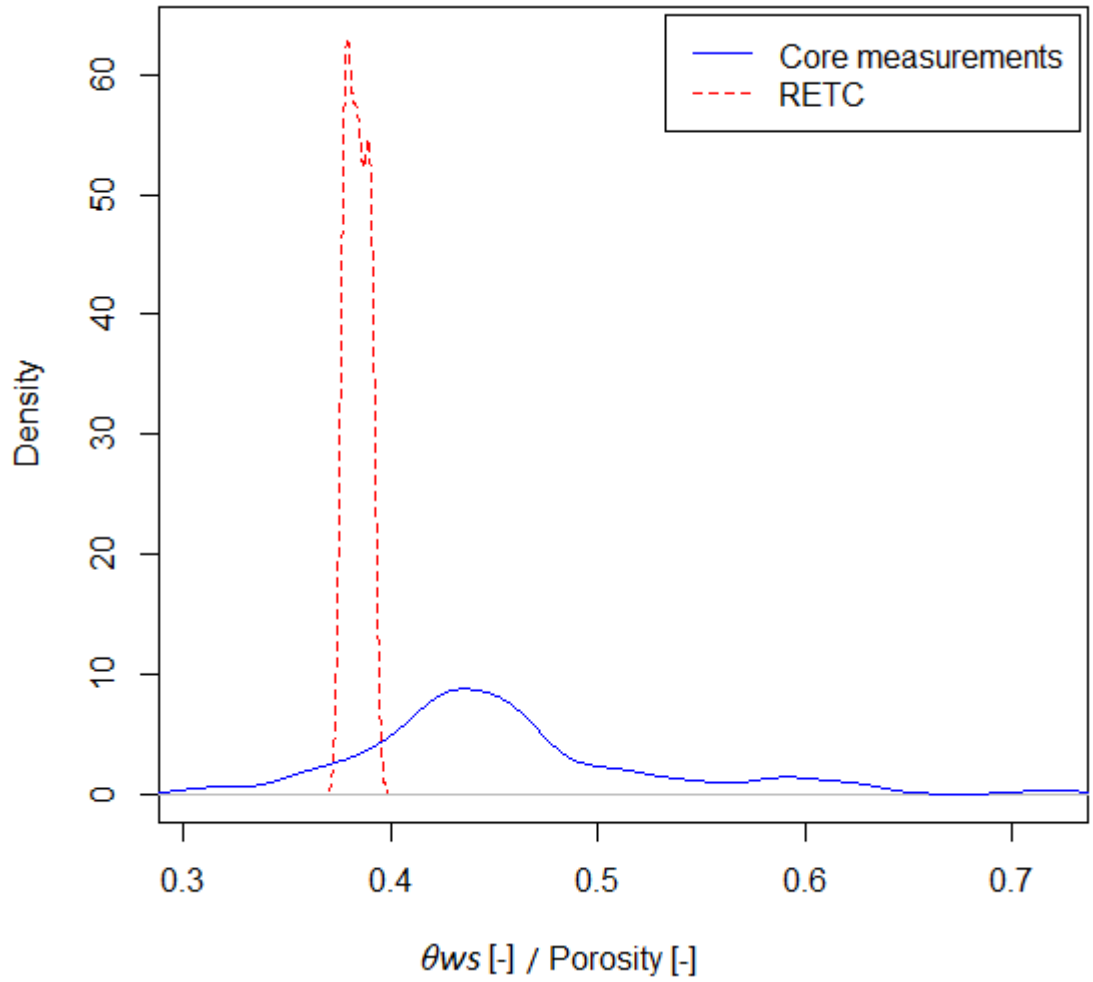


Fig. 7.2. Density trace of RETC predictions of θ_{ws} versus core measurements of Φ.

7.3.1.3 Reference values and ranges

The relative similarity in Φ ranges between areas A, B, and C along the strong variability exhibited by adjacent cores at the same depths discouraged the assignation of specific Φ values for each area or geological material. As summarised in Table 7.6, one reference Φ value of 45 % corresponding to the central values of core measurements was

considered for the base-case scenarios in the petrol station site. The most likely range was assumed to be represented by the IQR of the core measurements (41.6–47.4 %), while the extended range considered the minimum (30.5 %) and maximum (62.9 %) field values after removing two extremely high measurements classified as potential outliers. The conservative range was based in a minimum of 15 % from the literature (de Marsily, 1986; Dassargues, 2018) and the maximum field value without excluding potential outliers (72.0 %).

Table 7.6. Reference Φ values and ranges [%] for the petrol station site.

Reference value	Most likely range	Extended range	Conservative range
45	41.6–47.4	30.5–62.9	15–72

7.3.2 Hydraulic conductivity

7.3.2.1 Section structure

Section 7.3.2 investigates the variability of k_{sw} in the petrol station site as quantified through the following methods:

1. literature values assigned to the geological materials identified in chapter 4.9;
2. empirical correlations with particle-size data;
3. neural network predictions;
4. aquifer test analysis;
5. HPT logging.

A report has been prepared focusing on the analysis of aquifer testing data (Bekele et al., 2019). The estimation of k_{sw} was justified for the purposes shown below:

- comparison of HPT logging to conventional techniques, including aquifer testing and multiple methods based on particle-size data, addressing (i) the applicability of the quantification model proposed by HPT providers, and (ii) any potential effects derived from the presence of LNAPL;
- assessment of the use of logconductivity variance estimations as measures of aquifer heterogeneity, considering aggregated data and discriminating by location;

- evaluation of two possible effective diameters (d_{VS} and d_{UU}) in the empirical correlations of Slicher, Terzaghi, Kozeny–Carman, and Barr as well as the application on the collected field data sets of a model recently developed by Wang et al. (2017);
- suggestion of representative values and ranges for the materials considered in the modelling scenarios.

7.3.2.2 Empirical correlations with particle-size data

A total of 16 empirical models (15 implemented in HydrogeoSieveXL v2.3 by Devlin, 2015, and one recently developed by Wang et al., 2017) were used to derive k_{sw} values from particle-size data corresponding to 25 samples collected in the petrol station site. Predictions of k_{sw} through empirical correlations may be associated to uncertainties but imply a relatively low cost and are unaffected by the presence of LNAPL. As explained in section 4.7, different ways of determining d_E in some models have been proposed and therefore the use of two alternatives (d_{VS} and d_{UU}) was evaluated. These results were used to investigate k_{sw} variability (and aquifer heterogeneity metrics), the consistency with HPT measurements, and to contribute to define representative k_{sw} values and ranges for the analytical models.

Some empirical correlations, including many implemented by Devlin (2015), were not always applicable using particle-size data from the petrol station site. This was mainly due to the presence of fine-grained fractions. More specifically, Barr and Alyamani and Sen were the only methods whose applicable conditions were met in the 25 samples, while Sauerbrei and Krumbein and Monk could be applied 24 times. On the contrary, the restrictive application criteria of the simplified Hazen formula, Zunker, and Zamarin were not met by any sample (and Chapuis by only one sample). Slichter applicability depends on the effective diameter d_E and thus there were discrepancies between the use of d_{VS} (only applicable nine times) and d_{UU} (applicable 19 times). The other methods were only applied between four and nine times.

Fig. 7.3 illustrates the commonly low k_{sw} values obtained through empirical models in the petrol station site due to the numerous samples representing finer-grained intervals. Some boxplots represented relatively high k_{sw} values because the associated methods

(Hazen, Terzaghi, Beyer, Kozeny–Carman, and USBR) could be only applied to the coarsest-grained samples and therefore invalidated a direct comparison to the other methods (Slichter, Sauerbrei, Barr, Alyamani and Sen, and Krumbein and Monk). The use of d_{UU} considerably increased the k_{sw} estimations and variability through Terzaghi and Kozeny–Carman compared to using d_{VS}. Hazen and Beyer also exhibited relatively wide distributions due to the high k_{sw} values obtained in the coarser-grained samples.

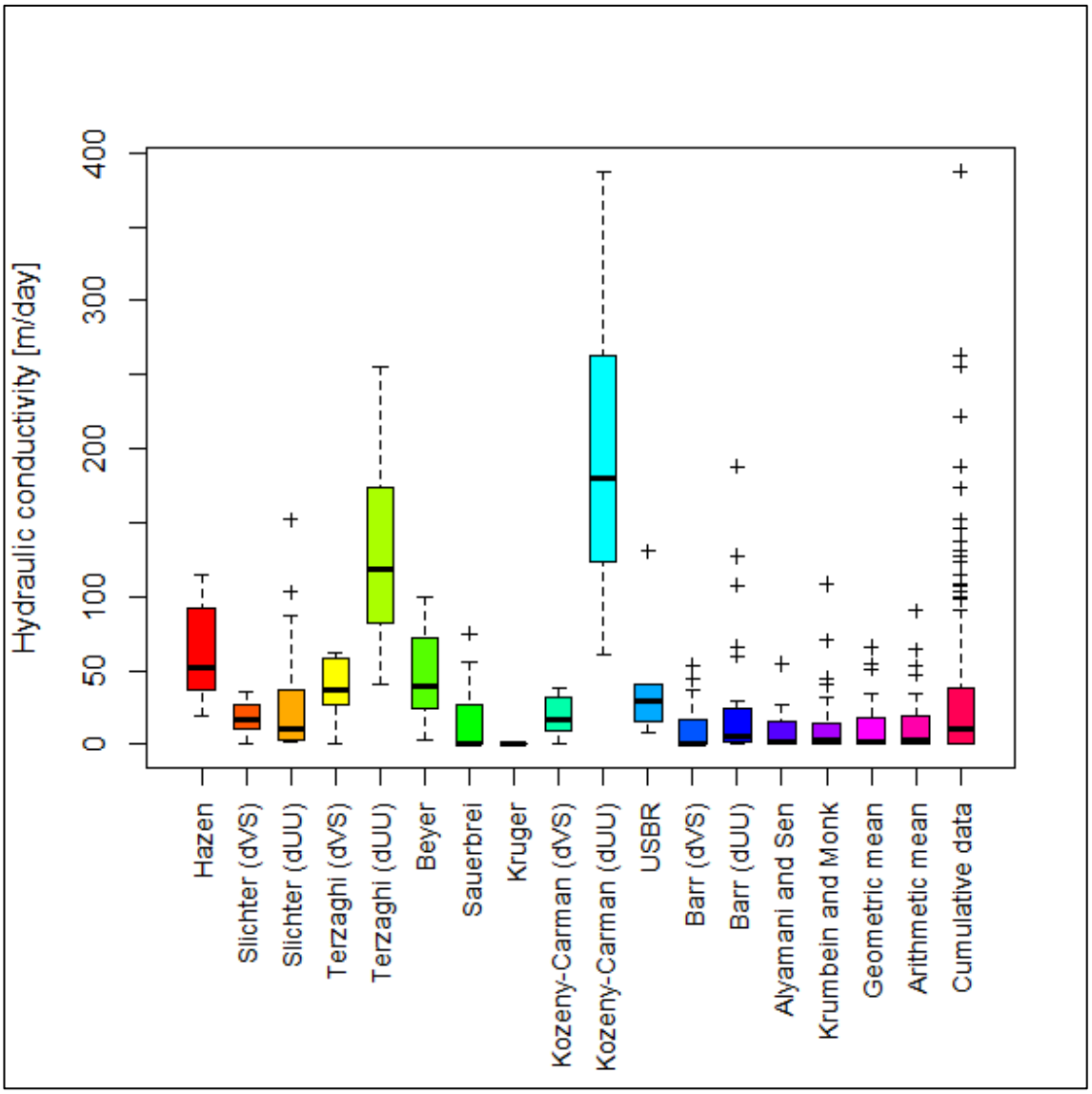


Fig. 7.3. Boxplots of k_{sw} predictions through multiple empirical correlations in the petrol station site.

Consequently, the study of representative values and ranges of k_{sw} had to consider the distinct subsurface materials, assumed to be as follows: fine sands with fines (a total of seven samples, five above 56.8 m AHD, and two between 55 and 55.15 m AHD), and fine

(five samples, four between 55.9 and 56.8 m AHD, and a similar one at 53.16 m AHD), medium (seven samples between 55.15 and 55.8 m AHD), and coarse sands low in fines (six samples between 53.8 m AHD and 54.8 m AHD). These four materials were representative of the overlying aquitard and relatively fine-grained lenses, the transition interval between the aquitard and the coarser-grained sections of the aquifer, the upper half of the aquifer and the lower half of the aquifer. Furthermore, a notable spatial variability existed in the petrol station site, but the limited number of samples discouraged the analysis of samples corresponding to specific locations and thus similar samples were grouped and analysed together.

Fig. 7.4 depicts the distributions of cumulative k_{sw} data from the four materials (named 'aquitard', 'transition', 'upper aquifer', and 'lower aquifer' hereafter for readability purposes). It can be seen the increasing k_{sw} with depth and the wide k_{sw} range found at the petrol station site, practically spanning six orders of magnitude. When only one type of material was considered, the range spanned between two and four orders of magnitude.

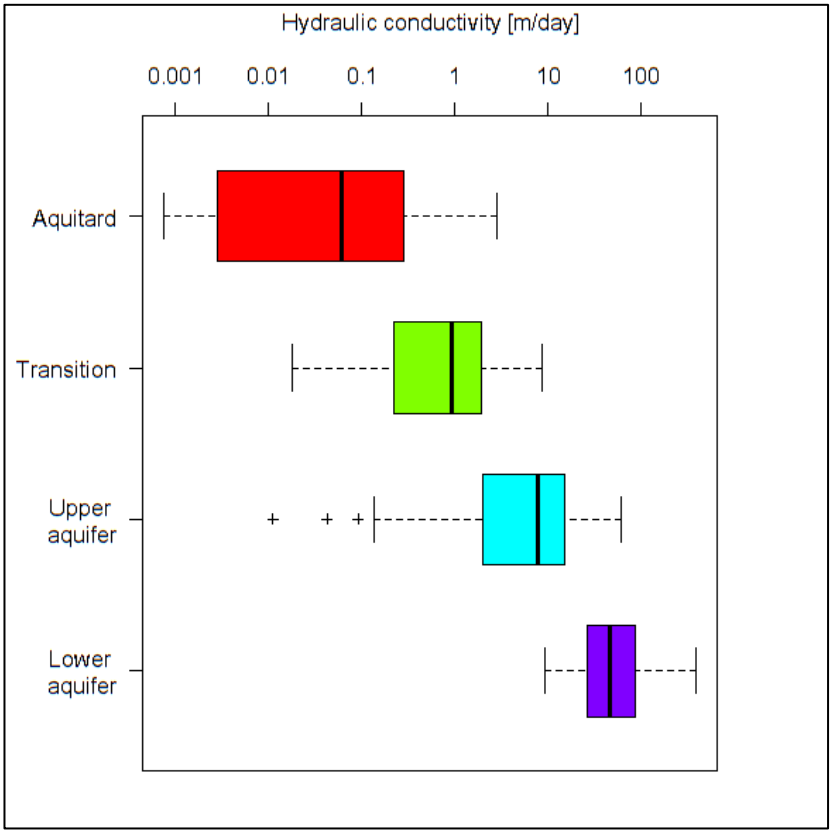


Fig. 7.4. Boxplots of k_{sw} predictions considering all the empirical methods applied in four main subsurface materials of the petrol station site.

Table 7.7 summarises statistics from the four data sets corresponding to distinct geological materials. The greater variability in the predictions of k_{sw} as given by coefficients of variation was associated to the finer-grained materials, partially due to scale effects and the lower degree of precision and accuracy of most of the empirical correlations with fine-grained materials. On the contrary, the lowest spread was linked to the lower section of the aquifer. In addition, it was notable the difference between the absolute k_{sw} maximum (387.6 m/day) and the 95th percentile (189.4 m/day) in the lower aquifer. The wide k_{sw} ranges obtained could be used for a quick definition of best- and worst-case scenarios in modelling and cost-benefit analyses.

Table 7.7. Statistics of empirical k_{sw} estimations [m/day] for the four main subsurface materials from the petrol station site and the aggregated data.

Statistic	Cumulative data	Aquitard	Transition	Upper aquifer	Lower aquifer
n	205	36	31	58	80
MIN	0.0008	0.0008	0.0179	0.0112	9.187
p5	0.0037	0.001	0.0244	0.1299	15.45
Q1	0.4723	0.0029	0.2227	2.04	26.91
MEDIAN	9.963	0.0617	0.9424	7.798	45.84
GEOMEAN	3.478	0.0358	0.6613	3.771	48.97
MEAN	29.99	0.3187	1.639	10.59	68.39
MODE	3.3448	0.0297	0.5814	2.3922	35.0036
Q3	37.73	0.2647	1.97	15.29	86.55
p95	126.6	1.464	6.968	31.59	189.4
MAX	387.6	2.892	8.649	60.87	387.6
SD	51.39	0.6327	2.159	11.87	65.03
MAD	14.65	0.0894	1.168	10.23	33.46
NIQ	27.62	0.1941	1.295	9.82	44.21
CV	171.4	198.5	131.7	112.2	95.08
CVR	147.1	144.8	123.9	131.2	72.99
SKEWNESS	3.332	2.711	2.01	1.789	2.365
KURTOSIS	14.78	7.114	3.272	4.088	6.943

As the boxplots suggested, k_{sw} distributions were right skewed as commonly observed in k_{sw} fields. The kurtosis of cumulative data was 14.78, far from the value of 3 associated to normal distributions. As shown in Table 7.7, kurtosis decreased when hydrostratigraphic units were examined separately. A similar approach was used by other authors such as Meerschaert et al. (2013) to demonstrate that non-Gaussian fields

in logconductivity may reflect the aggregation of data from hydrostratigraphic units with distinct multi-Gaussian distributions. In the case of the petrol station site, however, logconductivity followed a left-skewed multimodal distribution (skewness of -0.932) and did not fit a Gaussian distribution after segregating data by hydrofacies either, although these statistics could have been affected by the aggregation of different empirical correlations. Further analyses for HPT data are presented in section 7.3.2.4. Nevertheless, non-Gaussian phenomena are typically observed in the study of k_{sw} (Guadagnini et al., 2018) and other environmental data (Reimann and Filzmoser, 2000).

The logconductivity variance of the aggregated values from empirical correlations was 9.714 and therefore the petrol station site could be defined as highly heterogeneous (Gómez-Hernández et al., 2017). This value was greater than others reported in the literature, for instance the variance of 5.9 in the highly heterogeneous MADE site (Bohling et al., 2016). Nevertheless, the logconductivity variance value of 9.714 was obtained after combining different predictive methods and ignoring effects of stratification and data aggregation. Discrepancies in measurements of logconductivity with different methods have been found by other authors (Rehfeldt et al., 1992; Hess et al., 1992b; Bohling et al., 2012). In the case of the MADE site, Rehfeldt et al. (1992) found the highest variance associated to flowmeter measurements, followed by particle-size analyses and slug testing. An updated analysis by Bianchi et al. (2011) calculated practically the same variance with flowmeter and Hazen formula. Finally, Bohling et al. (2012) predicted a higher variance for DPP measurements than for DPIL and flowmeter. Individual methods may also predict different variances due to the testing conditions and limits of quantification.

Regarding the data aggregation effects, when the four geological materials were considered individually, the resulting logconductivity variance was 6.685 in the aquitard materials, 2.663 in the transition zone with fine sands, 3.795 in the medium sands of the upper aquifer, and only 0.655 in the coarse sands of the lower part of the aquifer. Thus, the average of the variance in the aquifer was 2.371 excluding fine-grained lenses and estimating that the three coarser-grained strata had a similar size (around 1 m of thickness). According to the empirical correlations, the logconductivity variance was over 2.6 in the interval where mobile LNAPL was commonly found, as inferred from the

variance of the transition zone of fine sands low in fines. This value was enough to produce a greatly heterogeneous LNAPL distribution and mobility in the petrol station site, as evidenced by the coexistence of wells with the highest T_n values and others with non-recoverable LNAPL within 2 m. To sum up, the contrasts in variance reflected heteroscedastic phenomena and exposed the complications of comparing sites according to this metric.

Fig. 7.5 collates k_{sw} ranges and geometric means as predicted through several empirical correlations in the petrol station site. Only ranges and geometric means were represented due to the few data points available (in some cases only one sample, so one values was given instead of a range). Considering the methods separately, the variability in k_{sw} was also high, with k_{sw} ranges spanning six orders the magnitude in Barr using d_{VS}, and generally between three and five orders of magnitude in the other methods. Discriminating by method and geological material, k_{sw} ranges decreased to one or two orders of magnitude except in the cases of Barr with d_{VS} and Alyamani and Sen in the upper aquifer. The maximum k_{sw} value was predicted by Kozeny–Carman with d_{UU}, which was one order of magnitude lower when d_{VS} was employed. Due to the shape of the grading curves and the presence of samples with little fines (between 15 % and 25 %), Barr with d_{VS} and Alyamani and Sen predicted lower minimum k_{sw} values in samples from the upper aquifer than in the transition between the confining aquitard and the coarser-grained aquifer.

Fig. 7.6 depicts the measured profiles of k_{sw} according to the empirical correlations most commonly applied in the petrol station site, as well as the geometric mean of all the methods implemented in HydrogeoSieveXL. These k_{sw} profiles were consistent with the CSM. Fig. 7.6(a) illustrates the strong contrasts in permeability across the stratigraphic profile and the distinctively high permeability of the materials found at the lower half of the aquifer (below 55 m AHD) where the maximum represented values almost reached 200 m/day, although the geometric mean of all the methods was 100 m/day and Kozeny–Carman with d_{UU} predicted a k_{sw} near 400 m/day. Predictions from Krumbein and Monk were similar to the geometric mean of all the methods.

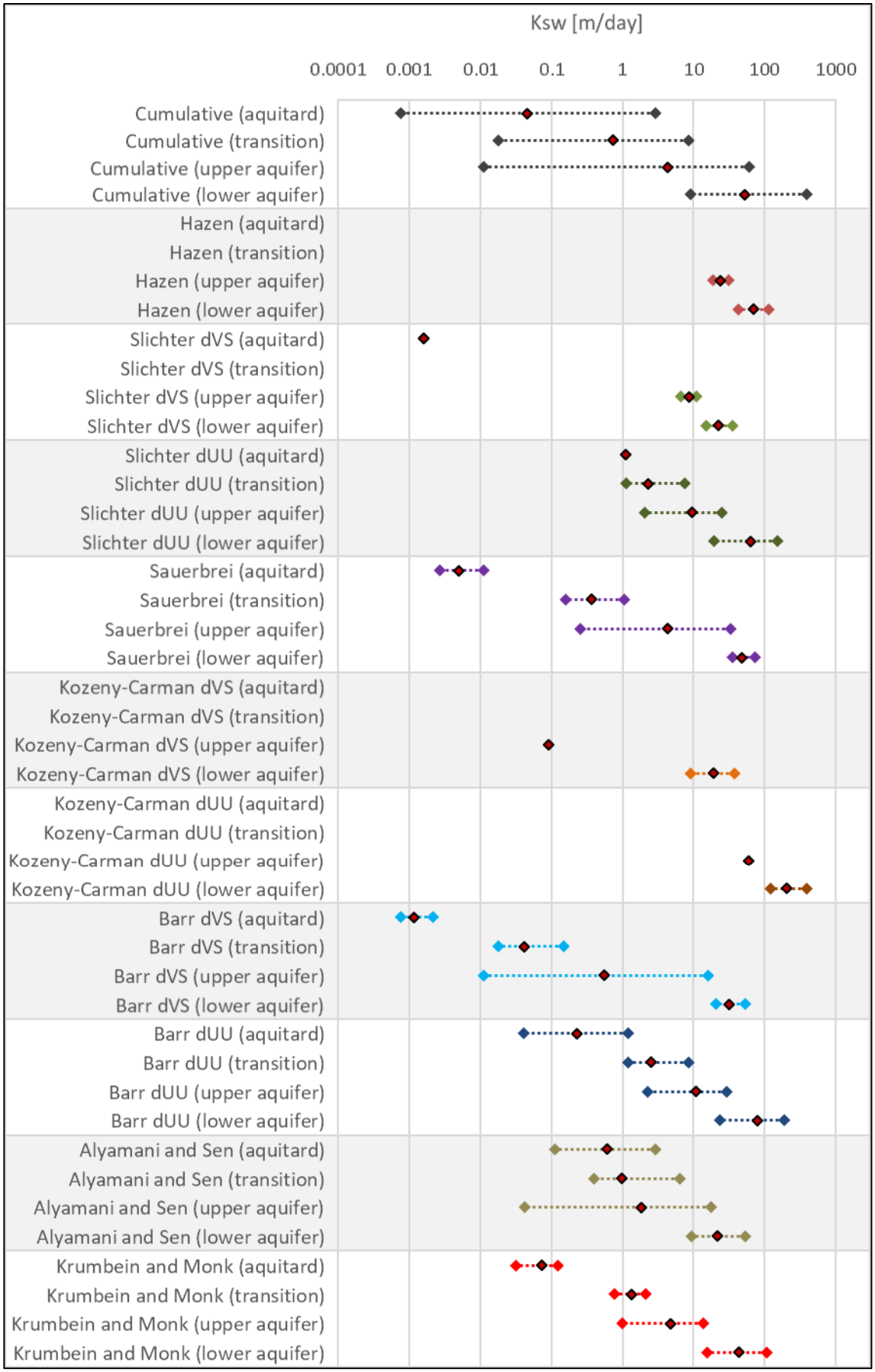


Fig. 7.5. Range and geometric mean of empirical k_{sw} predictions discriminating by material.

The approach of Wang et al. (2017) was also tested (as shown in Fig. 7.35 also including data from the industrial site). The maximum k_{sw} value obtained through Wang et al. (2017) was 65 m/day. In addition, k_{sw} estimations commonly found between Sauerbrei and the geometric mean of all the other implemented methods. The coefficient of determination between Wang et al. (2017) and the geometric mean of the other methods was 0.944, although the correlation decreased specific geological materials were considered, especially in the finer-grained intervals where the coefficient dropped below 0.5 as it could be expected because of the lack of accuracy associated to this range of particle sizes.

Slichter with d_{UU}, Barr with d_{UU}, Sauerbrei, and Alyamani and Sen (very sensitive to the shape of the grading curve) exhibited a maximum at 54.71 m AHD, while other methods (including Slichter and Barr with d_{VS}) calculated the maximum at 54.207 m AHD, the sample with less fines and more gravel. This illustrated the influence of choosing different d_E values. Furthermore, using d_{VS} in Slichter and Barr for these coarse-grained materials produced extremely high values of k_{sw}, most likely overestimating it. Slichter and Barr predicted similar k_{sw} values, being the difference lower than between both d_E options in the same method.

As depicted in Fig. 7.6(b), k_{sw} values were considerably lower at the aquitard (samples above 56.8 m AHD) and at the fine-grained lens around 55 m AHD, exhibiting a k_{sw} minimum of 0.0007 m/day obtained through Barr with d_{VS}. Comparisons with other empirical correlations suggested that the use of d_{VS} in Barr led to an underestimation of k_{sw}, since the minimum value obtained with other methods not employing d_{VS} was 0.003 m/day and the lowest value of the geometric mean was 0.018 m/day, after excluding methods that implemented d_{VS} or d_{UU}. Consequently, there was a k_{sw} range of approximately four orders of magnitude in the petrol station site considering geometric means of all the implemented correlations.

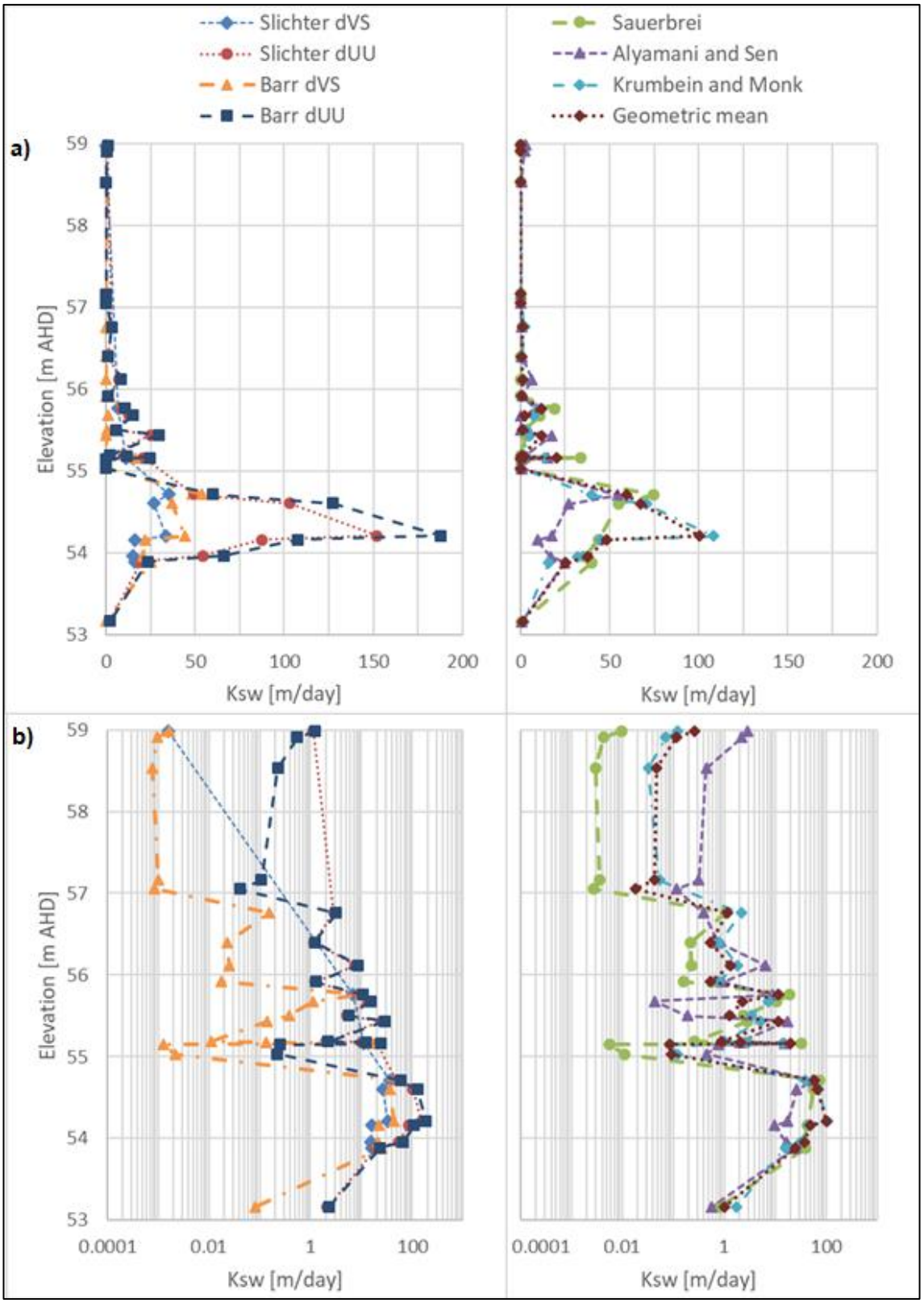


Fig. 7.6. Predicted values of k_{sw} derived from particle-size data in the petrol station site considering (a) linear, and (b) logarithmic scales. Values correspond to Slichter and Barr using d_{VS} and d_{UU}, Sauerbrei, Alyamani and Sen, Krumbein and Monk, and the geometric mean of all the methods implemented in HydrogeoSieveXL.

Slichter could not be applied in most of these fine-grained samples. Using d_{UU} enabled its application in the underlying transition zone with fine sands (samples between 55.9 and 56.8 m AHD) where k_{sw} values ranged between 0.02 and 8.65 m/day (comprising more than two orders of magnitude of k_{sw} variation), with geometric means of the empirical correlations ranging between 0.39 and 1.04 m/day (k_{sw} values within a factor of 3). These samples corresponded to elevations where LNAPL was normally found.

7.3.2.3 Neural network predictions

Artificial neural networks implemented in the RETC software through the Rosetta Lite module were used to derive k_{sw} values from particle-size data corresponding to 25 samples collected in the petrol station site. Predictions of k_{sw} through neural networks may be associated to uncertainties but imply a relatively low cost and are unaffected by the presence of LNAPL. These results were used to investigate the consistency of k_{sw} estimates with HPT measurements, and to contribute to define representative k_{sw} values and ranges for the analytical models.

As illustrated in Fig. 7.7, the use of RETC produced a narrow range of k_{sw} of less than two orders of magnitude (0.42–12.56 m/day). Furthermore, ignoring the values corresponding to aquitard materials, the minimum k_{sw} value was 2.12 m/day and therefore all the predictions fell in the same order of magnitude. Comparisons with the geometric mean of the empirical correlations suggested that maximum k_{sw} values were likely underestimated and minima overpredicted.

Average k_{sw} value was 0.58 m/day in the aquitard materials, 3.25 m/day in the transition zone, 5.77 m/day in the upper aquifer materials, and 11.58 m/day in the lower aquifer. Thus, neural network predictions of k_{sw} were reasonable, but exhibited a small range. The reason could have been due to the lack of predictors, since only texture percentages were employed and thus predicted k_{sw} values were not found in the extremes. Nevertheless, RETC produced k_{sw} values that could be used in preliminary and screening analyses.

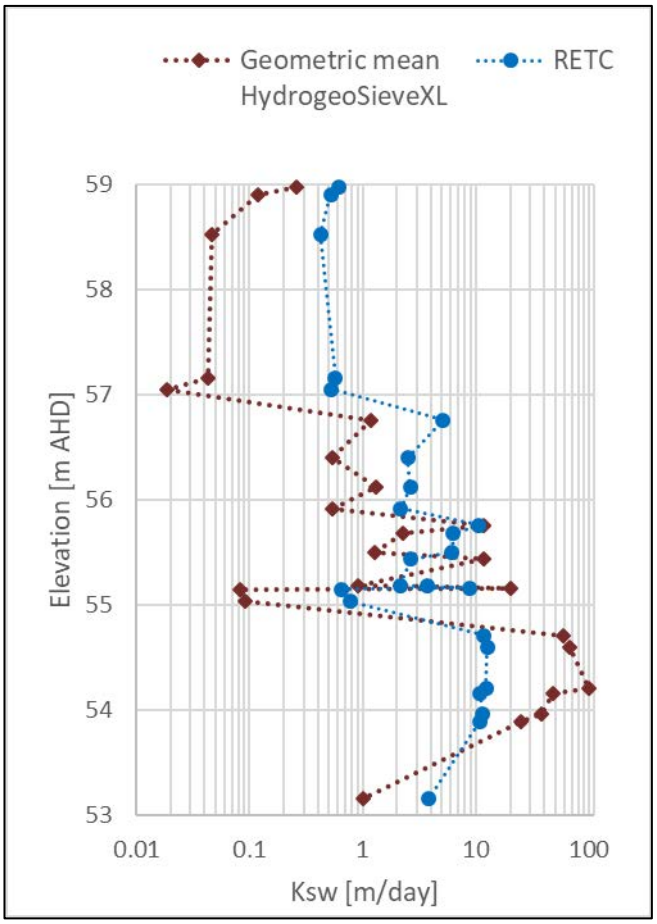


Fig. 7.7. Neural network predictions of k_{sw} compared to the geometric mean of multiple empirical correlations in the petrol station site.

7.3.2.4 Aquifer test analysis

Numerous hydraulic tests were conducted in the petrol station site to infer the aquifer and LNAPL hydrogeologic conditions and quantify effective k_{sw} values (representing a large support scale) derived from T_w estimations.

WT28 and WT29 were conducted at PB29-A and observations were collected in area A and surrounding wells. Assuming isotropic conditions, it could be estimated that these aquifer tests represented an area of more than 400 m^2 (being 11.8 m the distance between PB29-A and PB27-B where induced drawdown was observed). Similarly, WT30 (conducted in area C) exhibited a radius of influence of more than 19 m and therefore the support scale corresponded to an area greater than 1,200 m^2 assuming isotropic conditions. Thus, the support scale of aquifer tests was clearly larger than in HPT logging and methods based on particle-size data.

Table 7.8 summarises estimations of T_w, k_{sw}, and specific storage through the distance–drawdown method. There was a low variability associated to k_{sw} values, with all of them falling in half an order of magnitude. These k_{sw} values were representative of sands according to the literature values presented in section 7.2. T_w values were reasonable according to the CSM, being higher in area A than in area C and higher for aquifer tests conducted at PB40-C than for tests conducted at PB13-C or PB39-C. Thus, these T_w values were also consistent with T_n (higher in area A, being PB40-C likely the most productive well in area C).

Table 7.8. Estimations of T_w, k_{sw}, and specific storage by the distance–drawdown method in the petrol station site.

Test ID	Pumping well ID	T_w [m^2/day]	k_{sw} [m/day]	Specific storage [-]
WT1	PB13-C	3	1.3	0.008
WT15	PB39-C	5.9–7	1.7–2	0.01–0.019
WT27	PB40-C	14	4.4	0.04
WT28	PB29-A	25	6	0.12
WT29	PB29-A	27	6.5	0.05
WT30	PB40-C	10	2.9	0.011

As shown in Fig. 7.8, however, WT29 predictions did not respond to a good model fit, while others (WT27 for instance) exhibited a more ideal behaviour. The gap between the drawdown observed at the pumping well and the trend formed by observation wells in distance–drawdown plots of WT15 suggested the existence of well losses (Villanueva-Martínez and Iglesias-López, 1984). The apparent absence of a loglinear distance–drawdown patterns in WT15 could have been caused by anisotropic conditions. It should be noted that tests conducted in the same wells did not necessarily present identical distance–drawdown plots.

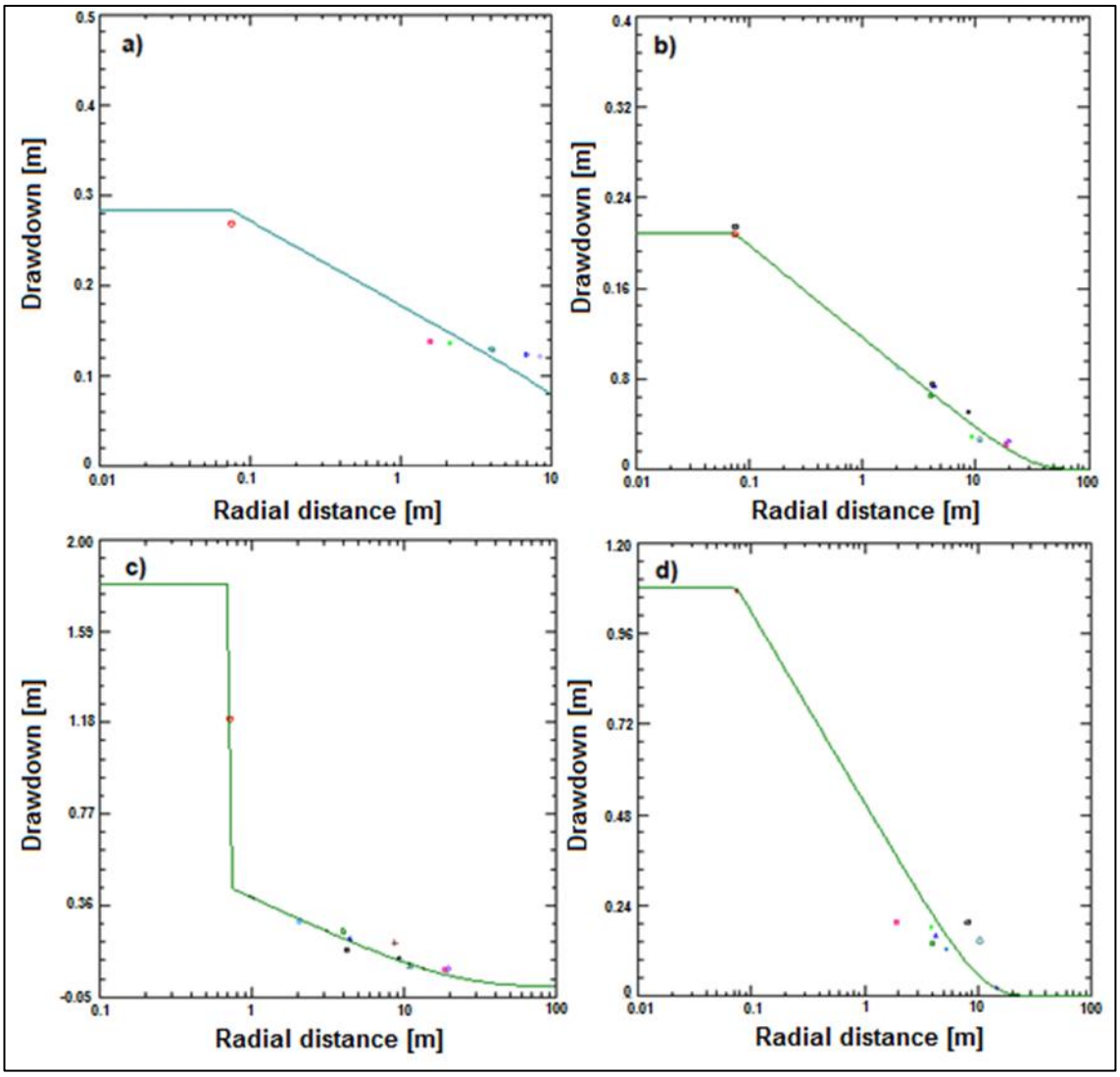


Fig. 7.8. Distance–drawdown plots at (a) WT29, (b) WT27, (c) WT30, and (d) WT15 (adapted after Bekele et al., 2019).

As illustrated in Fig. 7.9, there were also some discrepancies for instance between WT28 and WT29. The models generally fitted observed data better in WT28 than in WT29. WT28 predicted a lower T_w value at PB29-A than in the observation wells. The highest T_w value was estimated at MP38 (well without in-well LNAPL), although the model fit was done with only two points (not shown). In addition, T_w values from wells with low T_n such as MP01 and PB28 were higher than in PB29-A. On the contrary, area A showed greater T_w than MP01 and PB28, consistent with the higher T_n commonly found in area A. Discrepancies between T_w and T_n measurements could be expected and due to differences in LNAPL mass, the different scales relevant to groundwater and LNAPL flow,

and measurement errors. Thus, the analysis of WT28 and WT29 exposed limitations of aquifer testing to identify potential locations for the installation of production wells.

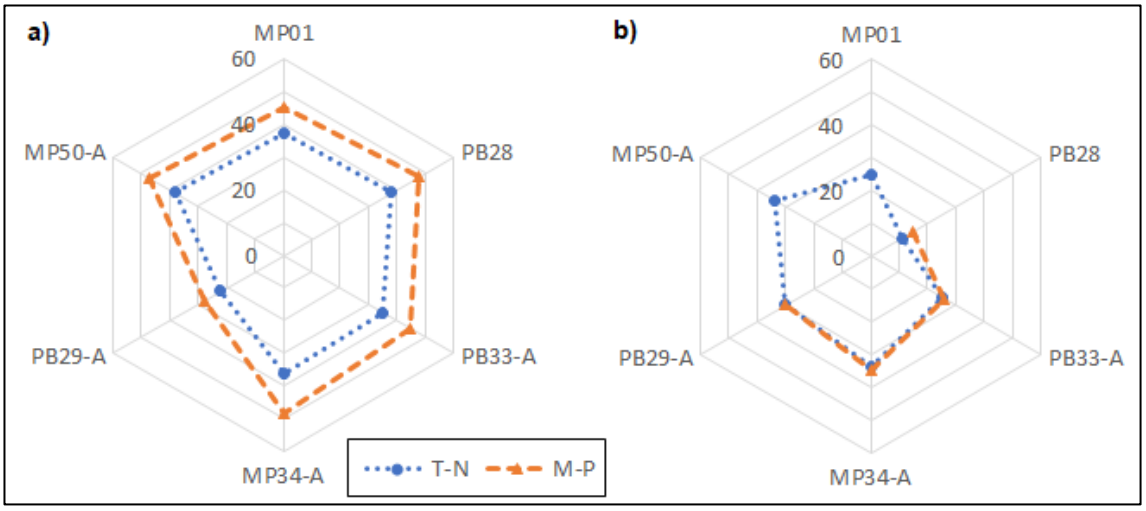


Fig. 7.9. Estimations of T_w in m^2/day through Tartakovsky–Neuman (T–N) and Moench–Prickett (M–P) during (a) WT28 and (b) WT29. Observation wells with only two measurements are not included.

Table 7.9 summarises T_w, k_{sw}, and S predictions obtained through aquifer testing. Relatively low predictions of T_w and k_{sw} could have been affected by the presence of LNAPL and finer-grained lenses. Nevertheless, aquifer testing commonly produced defensible estimates similar to RETC predictions and just in some cases lower than empirical correlations and HPT logs.

Exceptions included an extreme value of T_w measured at PB12-C in WT1 (77.94 m^2/day according to Hantush and 143.4 m^2/day with the method of Cooper and Jacob). The analysis of WT15, WT27, and WT30 suggested a lower T_w value (2–11 m^2/day) closer to the rest of observations. The extreme value could have been due to measurement errors, considering that the models were fitted to more data points in the other tests than in WT1, where five records were measured. A few measurements presenting poor model fits are not included in Table 7.9 due to the presumably bad quality of the predictions. LNAPL contamination likely exaggerated measurement errors due to the relative loss of accuracy dipping fluid interfaces under pumping conditions. Further research in improved field measurement methods (for instance involving automatic logging of fluid pressures) is encouraged.

Table 7.9. Estimations of T_w, k_{sw}, and S through aquifer testing in the petrol station site.

Test ID	Well ID	T_w [m²/day]	k_{sw} [m/day]	S [-]	Well type
WT1	PB13-C	0.727–1.911	0.4–1.03	0.053–0.093	Pumped
WT1	PB12-C	77.94–143.4	27–49.5	0.017–0.028	Observation
WT1	MP02	5.71	3	0.001	Observation
WT2	PB13-C	0.13–0.7	0.07–0.38	0.016–0.14	Pumped
WT15	PB39-C	4–4.6	1.1	0.008–0.014	Pumped
WT15	MP07-C	5.8–16	1.6–4.4	0.000–0.008	Observation
WT15	PB11-C	9–26	6–7	0.009–0.01	Observation
WT15	MP03-C	14–33	4–9.5	0.004–0.01	Observation
WT15	PB12-C	8–11	3–4	0.005–0.01	Observation
WT15	MP08-C	35	10	0.002	Observation
WT15	PB40-C	29–35	8–10	0.002–0.01	Observation
WT15	MP41-C	29–30	8–9	0.001–0.01	Observation
WT27	PB40-C	11–17	3–5	0.000–0.01	Pumped
WT27	MP07-C	1.4–11	0.4–3.5	0.000–0.06	Observation
WT27	MP08-C	0.9–17.4	0.3–5	0.000–0.03	Observation
WT27	MP41-C	9–23	3–7	0.005–0.03	Observation
WT27	PB12-C	3–11	0.73–3	0.002–0.015	Observation
WT27	PB39-C	11–26	3.4–7	0.003–0.02	Observation
WT28	PB29-A	22–28	5–6	0.19–0.3	Pumped
WT28	MP01	37–45	9–10	0.023–1	Observation
WT28	MP34-A	36–48	9–10	0.06–1	Observation
WT28	MP50-A	38–47	9–10	0.11–1	Observation
WT28	PB28	38–48	9–10	0.017–0.04	Observation
WT28	PB33-A	35–45	8–10	0.04–0.5	Observation
WT29	PB29-A	30	7	0.1	Pumped
WT29	MP01	25	6	0.04	Observation
WT29	MP34-A	34–35	7–8	0.1–0.2	Observation
WT29	MP50-A	34	8	0.2	Observation
WT29	PB28	11–15	2.7–3	0.09	Observation
WT29	PB33-A	25–26	5.5–6	0.12–0.46	Observation
WT30	PB40-C	7	2.1	0.02	Pumped
WT30	MP07-C	7.3	2.2	0.03	Observation
WT30	MP08-C	6	1.8	0.02	Observation
WT30	MP41-C	15	1.8	0.016	Observation
WT30	PB05	9.5	6.4	0.007	Observation
WT30	PB12-C	2	1.1	0.006	Observation
WT30	PB13-C	5	3.5	0.01	Observation
WT30	PB26	7.6	5	0.004	Observation
WT30	PB39-C	11	3.2	0.017	Observation

Another potential source of error could have been the uncertain determination of the aquifer thickness for each well. Table 7.9 presents k_{sw} values computed for the aquifer thicknesses estimated in Bekele et al. (2019) according to stratigraphic descriptions of extracted cores. For WT28 and WT29, the aquifer thickness was assumed to be 4.2 m, as inferred from the core collected at PB33-A. As depicted in Fig. 5.26, HPT73-A, HPT72, and HPT74-B logs showed increases in HPT P and EC below approximately 53.5 m AHD, being possible to use the direct-push rig down to 51.6 m AHD. The initial z_{aw} was 56.5 m AHD in WT28 and WT29, therefore HPT logs suggested a saturated aquifer thickness between 3 and 4.9 m. Consequently, the determination of the aquifer thickness could have led to errors in the prediction of k_{sw} around 25 %, but the value of 4.2 m was reasonable.

Regarding the aquifer tests conducted in area C, the determination of the saturated aquifer thicknesses was more uncertain in area C than in areas A and B due to the stratigraphic heterogeneity as revealed by stratigraphic columns and the HPT logs collected in Fig. 5.27. Thus, HPT logs may also be useful for this purpose because of the typically greater number of HPT logs compared to collected cores and the greater vertical resolution. Nevertheless, in some situations it may be complicated to discriminate which intervals contribute to groundwater and LNAPL flow exclusively according to HPT logs, for instance at PB13-C and HPT63-C where a saturated aquifer thickness of 1.85 m was determined (and assumed to be the same at MP02) after visual inspection of the PB13-C core.

7.3.2.5 HPT logging

A total of 10 HPT profiles were logged in the petrol station site to investigate the subsurface hydrostratigraphy and quantify k_{sw}. HPT logging was compared to the methods presented in the previous sections to assess the quantification model and elucidate if LNAPL had a clear impact on HPT readings. In addition, the application of logconductivity variance as a measure of aquifer heterogeneity was investigated.

As illustrated in Fig. 7.10, in average HPT logging predicted considerably lower k_{sw} values around area C and the UST location than in areas A, B, and surroundings. Fig. 7.10 shows arithmetic means of HPT72, HPT73-A, HPT74-B, and HPT75 representing areas A and B,

and of HPT59-C, HPT60-C, HPT61-C, HPT62-C, HPT63-C, and HPT64 representing area C and the UST location.

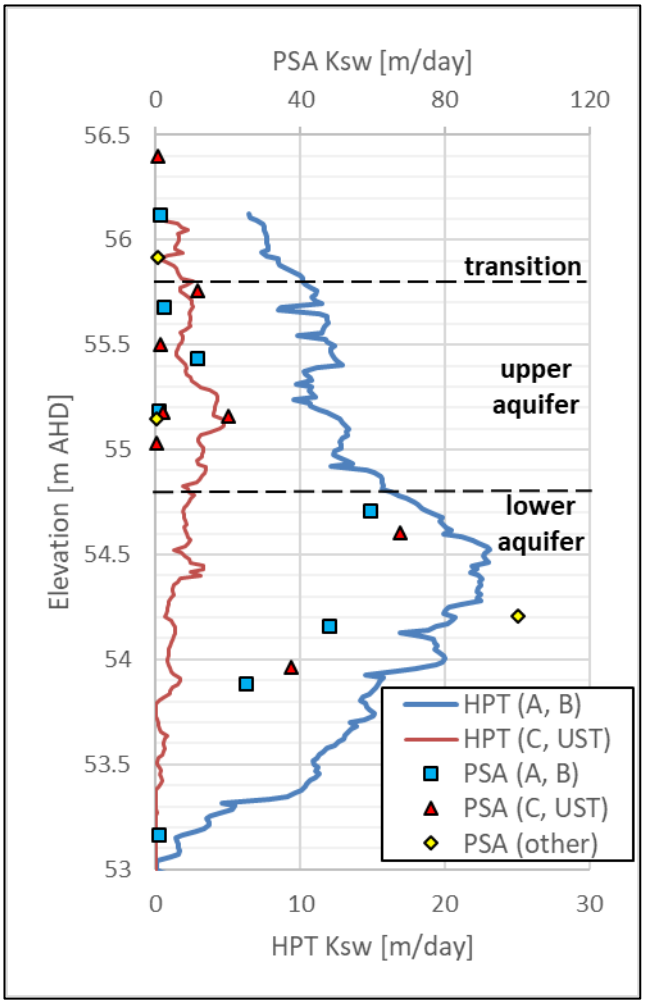


Fig. 7.10. Averages of k_{sw} estimated through HPT and geometric means of k_{sw} from empirical correlations implemented in HydrogeoSieveXL (PSA in the graph) in areas A, B, and surroundings (A, B), areas C and UST (C, UST), and other locations (ML15 and ML32). Aquifer zones considered in the analysis of empirical correlations (transition, upper aquifer, and lower aquifer) are separated with dashed lines.

Furthermore, the two k_{sw} profiles were clearly distinct. The arithmetic mean of k_{sw} in areas A and B gradually decreased from 23 m/day at 54.52 m AHD to 6 m/day at 56.12 m AHD. This trend was consistent with the fining-upward sequence and the three aquifer zones (transition, upper aquifer, lower aquifer) suggested by particle-size analysis. Consequently, it was also consistent with the geometric mean of k_{sw} values estimated through empirical correlations in section 7.3.2.2. The arithmetic mean of k_{sw}

in areas C and the UST did not present so consistent trends, exhibiting an average of 1 m/day and a maximum of 5 m/day at 55.12 m AHD.

Moreover, the average HPT response in areas C and the UST was relatively low despite particle-size analyses predicting some k_{sw} values higher in area C (for instance 68 m/day at 54.60 m AHD) than others in areas A and B. In addition, empirical correlations produced a much higher range of k_{sw} than HPT logging, while the artificial neural networks generated the narrowest k_{sw} range as described in section 7.3.2.3. Most of the empirical correlations estimated k_{sw} maxima considerably higher than HPT, especially in the lower aquifer. Consequently, the application of d_{VS} instead of d_{UU} generally resulted in k_{sw} values closer to HPT predictions. Alyamani and Sen was one of the methods predicting the lowest k_{sw} estimations, with only one sample over 25 m/day (corresponding to PB27-B at 54.71 m AHD, where HPT74-B recorded some of the maximum k_{sw} values in the petrol station site, but still below 30 m/day and likely affected by the upper limit of quantification of HPT k_{sw}).

For the comparison with aquifer testing, estimates of k_{sw} through HPT logging were integrated to calculate T_w values. Aquifer tests conducted at PB29-A (WT28 and WT29) were compared to the average of HPT72, HPT73-A, HPT74-B, and HPT75. On the other hand, aquifer tests conducted at PB13-C, PB39-C, and PB40-C were compared to the average of HPT64 and all the HPT profiles collected in area C.

WT28 and WT29 predicted T_w values between 11 and 48 m^2/day, with the distance–drawdown method estimating T_w as 25–27 m^2/day. HPT logs corresponding to the same intrinsic area of influence (with a slightly different water-saturated thickness) estimated T_w values between 23 and 56 m^2/day, with an average of 43 m^2/day. In area C, aquifer testing predicted T_w values between 0.1 and 143 m^2/day. Excluding values from wells presenting these extreme values, the T_w range was measured between 0.7 and 35 m^2/day. In addition, the distance–drawdown method resulted in T_w values between 3 and 14 m^2/day. HPT logs from area C and the UST location produced a T_w range of 0.4–11 m^2/day, with an average of 5 m^2/day.

Therefore, T_w estimations from aquifer testing and HPT logging did not exhibit strong discrepancies as it has also been found by Bohling et al. (2012) in the MADE site. In the

case of the petrol station site, HPT produced slightly greater estimations in the coarser-grained areas (A, B, and surroundings) and slightly lower T_w values in the finer-grained areas (C and surroundings).

Nevertheless, aquifer testing estimated effective T_w values as averages with unknown weighting over unknown aquifer volumes (Leven and Dietrich, 2006) and therefore discrepancies with the integration of a few HPT logs could be expected. The distinct nature of both methods could be used to assess the connectivity of the permeability field. For instance, the distance–drawdown method predicted an effective k_{sw} value around 6–7 m/day in the tests conducted at PB29-A (WT27 and WT28), while HPT logs from areas A, B, and surroundings predicted a geometric mean of k_{sw} equal to 4 m/day. The higher value of the effective k_{sw} suggested the presence of preferential flow paths (Knudby and Carrera, 2005; Bianchi et al., 2011), which was consistent with the hypothesis of having a preferential migration pathway at PB29-A, although it could not be directly measured. Furhter differences between HPT and aquifer testing were due to differences in the support scale, the quantification method, possibly LNAPL influence, and the limited number of HPT profiles and their location. The measured aquifer thickness was lower in the case of HPT due to the prediction of k_{sw} only in the water-saturated zone (excluding the capillary fringe) and the lower z_{aw} during the HRSC campaign compared to z_{aw} during the aquifer tests.

Thus, one limitation of HPT logging is that the k_{sw} quantification model should only be applied in the water-saturated zone. However, mobile LNAPL mass is predominantly accumulated at the top of the aquifer and therefore collecting HPT logs at low water table conditions may limit the delineation of relevant hydrostratigraphic features. As it can be seen in Fig. 7.11, which collates the 10 HPT profiles of k_{sw} collected in the petrol station site, HPT logging could not be used to quantify k_{sw} corresponding to some intervals of interest for model scenarios and features such as a potential preferential migration pathway suggested by LIF and baildown testing around 56.20–56.35 m AHD in PB29-A, since z_{aw} was around 56.15–56.16 m AHD during the HRSC campaign (HPT P, HPT Q and EC values did not clearly detect this feature though). Accordingly, this investigation suggested that HPT logging should be ideally conducted at high z_{aw} conditions in LNAPL impacted sites.

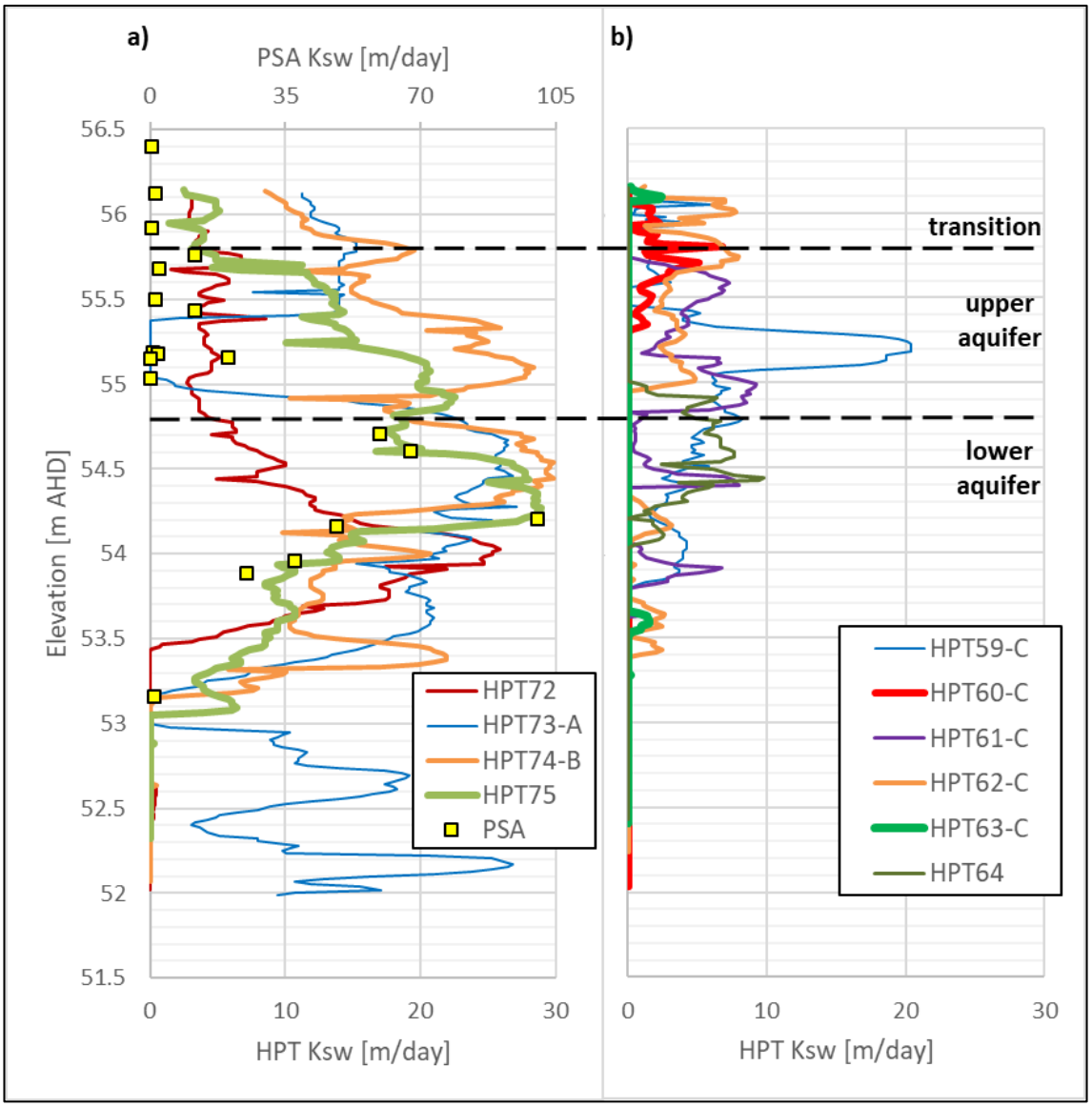


Fig. 7.11. HPT predictions of k_{sw} in (a) areas A, B, and surroundings, and (b) area C and UST. PSA refers to the geometric mean of k_{sw} estimated through empirical correlations implemented in HydrogeoSieveXL. Aquifer zones considered in the analysis of empirical correlations (transition, upper aquifer, lower aquifer) are separated with dashed lines.

Nevertheless, the potential impact of LNAPL presence on HPT readings due to the associated decrease in k_{rw} was not clearly reflected in Fig. 7.11. The decrease in HPT k_{sw} in the transition zone was consistent with particle-size analysis and stronger gradients in HPT k_{sw} were observed in intervals not impacted by LNAPL contamination (for instance, the lower aquifer). Thus, there were no evidences against the quantification of k_{sw} through HPT logging in LNAPL contaminated sites specifically related to the multiphase nature of the system.

Furthermore, Fig. 7.11 shows that the highest k_{sw} values in the transition zone (top of the aquifer) generally corresponded to HPT73-A (adjacent to PB29-A) followed by HPT74-B (adjacent to PB27-B), HPT62-C, and HPT59-C (adjacent to PB40-C). Therefore, they were consistent with the high T_n values commonly measured in these locations. Values of k_{sw} in these four logs at 56.05 m AHD were 12.2, 10.1, 6.1, and 6.1 m/day, respectively. The maximum k_{sw} value in the petrol station site was 29.9 m/day as estimated at HPT74-B at 54.45 and 54.54 m AHD. The maximum k_{sw} in area C was 20.4 m/day at HPT59-C at 55.2 m AHD, considerably higher than any prediction from other HPT profiles in area C. These values could be considered representative of the coarsest-grained materials in the petrol station site. HPT logging could not adequately quantify k_{sw} in fine-grained materials as found at HPT73-A between 55.05 and 55.4 m AHD and in many logs from area C where the lower limit of k_{sw} quantification was reached.

HPT logs visibly demonstrated the subsurface heterogeneity causing distinct profiles over distances of a few meters. Even if assuming layer-cake geological environments (such as the used in the analysis of particle-size data considering an aquitard, transition zone, upper aquifer, and lower aquifer) were useful for some interpretations, they also had important limitations as revealed by the comparison of specific HPT profiles. Several HPT logs did not reflect a fining-upward sequence, but distinct patterns explaining the complex LNAPL distributions found in the subsurface. More specifically, HPT72 (located between areas A and B) and HPT75 (North–East of area A) revealed lower k_{sw} values (between 3 and 4 m/day in average) in the transition zone than HPT logs closer to PB29-A and PB27-B and therefore contributed to elucidate the reasons behind the limited presence and mobility of LNAPL in these regions as suggested by LIF logging, in-well fluid levels and hydraulic testing.

Moreover, the three HPT logs adjacent to PB40-C (HPT59-C, HPT60-C, and HPT62-C) were dissimilar. The maximum k_{sw} record was more than twice as high in HPT59-C than in HPT60-C and HPT62-C. In addition, HPT59-C reflected a generally more transmissive aquifer than the other two logs, with HPT60-C being collected in the least transmissive location and HPT62-C showing higher k_{sw} values than HPT59-C in the transition zone where LNAPL was commonly found according to in-well fluid levels. As a consequence,

calibrating Q/P data with k_{sw} values from nearby wells (for instance, the calibration of distinct profiles such as HPT59-C and HPT62-C with the same particle-size data set from MP44-C) introduces errors due to fine-scale heterogeneity. Alternative approaches such as the application of the HRK tool (combination of DPIL and DPP) would reduce these errors by quantifying k_{sw} in the same vertical profile.

Table 7.10 shows statistics of HPT k_{sw} estimates in several regions of interest, including HPT73-A (adjacent to PB29-A), HPT74-B (adjacent to PB27-B), the sum of these two logs plus HPT72 and HPT75 due to their proximity (column 'Areas A, B'), wells adjacent to PB40-C (HPT59-C, HPT60-C, and HPT62-C as well as the sum of all of them in the column 'PB40-C'), the sum of all the HPT logs found in area C and the UST location (column 'Areas C, UST'), and the sum of all the HPT logs in the petrol station site (column 'total').

Table 7.10. Summary statistics of HPT k_{sw} estimates in the petrol station site. HPT72 and HPT75 were included in the analysis of areas A and B due to their proximity. The data set used for the analysis of PB40-C included data from HPT59-C, HPT60-C, and HPT62-C.

Statistic	Total	Areas A, B	Areas C, UST	HPT73-A	HPT74-B	PB40-C	HPT59-C	HPT60-C	HPT62-C
n	2599	1070	1529	272	269	785	256	271	258
MIN	0.0305	0.0305	0.0305	0.0305	0.0305	0.0305	0.0305	0.0305	0.0305
p5	0.0305	0.0305	0.0305	0.0305	0.0305	0.0305	0.0305	0.0305	0.0305
Q1	0.0305	2.56	0.0305	8.382	0.0549	0.0305	0.0305	0.0305	0.0305
MEDIAN	0.4281	10.36	0.0305	14.02	13.72	0.0305	1.509	0.0305	0.0305
GEO-MEAN	0.476	3	0.1312	6.281	3.191	0.1827	0.4382	0.0612	0.2419
MEAN	5.219	10.84	1.288	13.82	13.22	1.582	2.965	0.3598	1.493
MODE	0.088	0.6241	0.0313	13.538	13.612	0.0404	0.1681	0.0318	0.081
Q3	7.698	18.29	1.494	20.73	20.73	2.277	4.267	0.0305	2.634
p95	23.47	26.82	6.706	25.91	28.35	6.706	13.94	2.097	6.7
MAX	29.87	29.87	20.42	27.13	29.87	20.42	20.42	6.822	7.934
SD	7.745	9.052	2.662	8.255	9.82	3.064	4.487	0.8902	2.084
MAD	0.5895	11.68	0	9.49	12.2	0	2.192	0	0
NIQ	5.684	11.66	1.085	9.151	15.32	1.666	3.141	0	1.93
CV	148.4	83.52	206.8	59.73	74.28	193.7	151.3	247.4	139.6
CVR	137.7	112.7	0	67.68	88.96	0	145.3	0	0
SKEW-NESS	1.512	0.3546	3.431	-0.269	-0.021	3.513	2.374	3.592	1.43
KURTO-SIS	1.155	-1.111	16.37	-1.032	-1.225	15.81	5.834	15.68	1.163

Thus, Table 7.10 reflects that all the considered sets of data contained more than 5 % of values below the lower limit of k_{sw} quantification (determined at 0.03048 m/day). Furthermore, more than 25 % of all the values in the petrol station site and more than 50 % of values from HPT logs adjacent to PB40-C were below this limit.

These low values also affected the k_{sw} distribution, as reflected by the values of skewness and kurtosis, which exhibited a strong contrast between areas A, B and surroundings, and area C. The assignation of a constant value to all the measurements below the HPT lower limit of quantification of k_{sw} implied a decrease in measures of spread and a subtle increase in central values.

Table 7.11 summarises the same set of statistics after removing non-detects from the HPT logs. Due to the finer-grained materials, HPT logging could not quantify k_{sw} more often in area C than in areas A and B. Removing k_{sw} values below the low limit of quantification resulted in an increase in the central values of HPT k_{sw} that could be considered to be representative of the aquifer materials and an increase in the measures of spread in the finer-grained areas. Non-detects mainly corresponded to intervals of negligible groundwater and LNAPL flow and therefore it was valuable to count on statistics exclusively representing groundwater and LNAPL transmissive zones.

For other purposes like matrix diffusion studies, a better characterisation of low-permeability zones could be essential and more important than for the present investigation. In such scenarios, the HPT system could be modified to better address these materials (Liu et al., 2017) and methods to adequately deal with censored data should be used (Helsel et al., 2020).

Fig. 7.12 illustrates the probability distribution of k_{sw} as estimated through HPT logging in the petrol station site before and after removing non-detect data. The cumulative probability plot after removing non-detects as shown in Fig. 7.12(b) approached a normal distribution much better than the unfiltered data represented in Fig. 7.12(a). As reflected by curve flexures, filtered data still departed from Gaussianity in many intervals, especially at low (around a 20 % of data) and high k_{sw} values, as expected due to the quantification limitations of HPT technology.

Table 7.11. Summary statistics of HPT k_{sw} estimates in the petrol station site excluding non-detects. The columns refer to the same HPT logs as the unfiltered data.

Statistic	Total	Areas A, B	Areas C, UST	HPT73 -A	HPT74 -B	PB40- C	HPT59 -C	HPT60 -C	HPT62 -C
n	1341	843	498	238	201	312	141	48	123
MIN	0.0549	0.0549	0.0872	0.0579	0.0549	0.1554	0.1554	0.2227	0.2126
p5	0.762	2.658	0.471	3.612	7.62	0.5262	1.341	0.5094	0.4131
Q1	3.272	6.706	1.54	11.05	11.89	1.6	2.377	1.034	1.584
MEDIAN	7.315	13.72	3.048	15.24	17.07	2.988	3.962	1.537	2.702
GEO-MEAN	6.257	10.3	2.692	13.45	15.22	2.753	3.853	1.537	2.35
MEAN	10.09	13.75	3.89	15.79	17.68	3.934	5.359	1.889	3.099
MODE	3.0907	12.673	1.6933	13.554	12.983	1.8159	3.3366	1.3615	2.6072
Q3	15.54	20.27	5.486	21.03	24.08	4.722	6.096	2.294	3.887
p95	26.21	27.43	8.532	25.95	28.65	9.281	18.59	4.125	7.127
MAX	29.87	29.87	20.42	27.13	29.87	20.42	20.42	6.822	7.934
SD	8.204	8.004	3.424	6.836	7.079	3.802	4.881	1.284	2.045
MAD	7.788	9.942	2.486	7.682	8.134	2.17	3.028	0.847	1.744
NIQ	9.098	10.05	2.926	7.4	9.038	2.314	2.757	0.9342	1.707
CV	81.33	58.22	88.03	43.29	40.04	96.64	91.08	67.97	65.99
CVR	106.5	72.48	81.58	50.41	47.66	72.63	76.41	55.11	64.56
SKEW-NESS	0.7155	0.1762	2.339	-0.253	-0.02	2.642	1.947	1.646	0.756
KURTO-SIS	-0.688	-1.039	7.792	-0.794	-0.753	7.949	3.038	3.15	-0.292

The comparison of these filtered data with a lognormal distribution (not shown) revealed good agreement except for high k_{sw} values over 20–25 m/day (around a 20 % of the total set of data). These extreme values of the probability distribution were close to the HPT limits of quantification (0.03–25 m/day). These effects are depicted in Fig. 7.12(c), after transforming filtered data into natural logarithms. Fig. 7.12 also illustrated that the untransformed k_{sw} distribution were right-skewed, while the untransformed k_{sw} distribution was left skewed.

The variance of unfiltered and filtered k_{sw} were 60.0 and 67.3 $(m/day)^2$, while the variance of unfiltered and filtered logconductivity was 7.7 and 1.3, respectively, and therefore exposed the relevance of reporting the strata and the method used to quantify this metric of aquifer heterogeneity. The unfiltered variance was lower than the value obtained after combining multiple empirical correlations (9.7), but also represented a highly heterogeneous site.

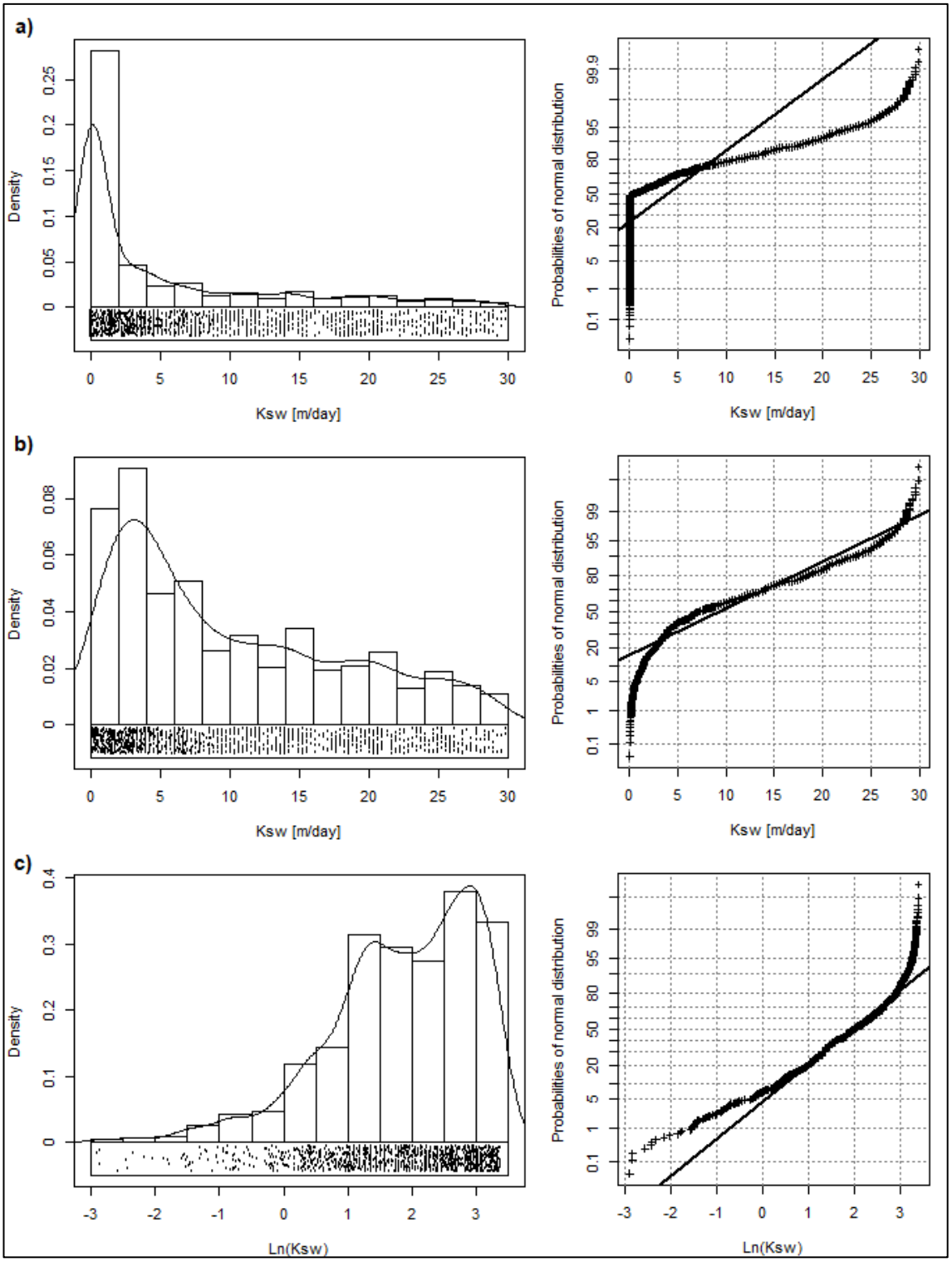


Fig. 7.12. Histogram, density trace, and one-dimensional scatterplot (left panels), as well as cumulative probability plots (right panels) of (a) cumulative HPT k_{sw} data from the petrol station site, (b) same data excluding non-detects, and (c) log-transformed data excluding non-detects.

The decision of including aquitards in the quantification of logconductivity variance through HPT could lead to the classification of the aquifer in different categories (highly heterogeneous considering the aquitards or mildly heterogeneous without them) and therefore suggested further investigation. It should be noted that the calibration between natural logarithms of Q/P and k_{sw} following the quantification model of McCall (2010) was not linear. Therefore, the variance of Ln*(*Q/P*)* and Ln*(k_{sw})* differed from each other, unlike other cases such as the linear calibration procedure conducted by Bohling et al. (2012).

Probability distributions also revealed multiple peaks suggesting the coexistence of distinct populations. However, the complex stratigraphy found across the site according to HPT logs discouraged the segregation of the cumulative data according to horizontal strata that should be present across the entire site. The analysis of smaller regions and individual HPT logs was more illustrative of these differences. For instance, Fig. 7.13 shows that logconductivity was closer to a normal distribution in area C than in areas A and B, where excluding further low k_{sw} values could contribute to yield a quasi-Gaussian distribution. Logconductivity variance of filtered k_{sw} data was similar in both zones (0.9). However, unfiltered data resulted in logconductivity variances of 6.4 and 4.7, respectively.

In the case of for HPT59-C, HPT60-C, and HPT62-C, the three HPT logs adjacent to PB40-C, logconductivity variances were 0.7, 0.5, and 0.7 for filtered data, and 6.2, 2.3, and 5.1 for unfiltered data, respectively. Thus, these values referred to the vertical variability of k_{sw} in the investigated profiles. Summing up the three HPT logs, logconductivity variance was 0.8 for filtered data, and 5.2 for unfiltered data.

The logconductivity variance of filtered data from HPT73-A and HPT74-B was 0.5 and 0.6, respectively. It should be noted that some logs such as HPT73-A presented finer-grained lenses with k_{sw} values below the lower limit of quantification within the aquifer itself, not just as possible aquitards underlying or overlying the aquifer. Thus, HPT73-A was a good example to illustrate the change in vertical variability in different hydrostratigraphic units.

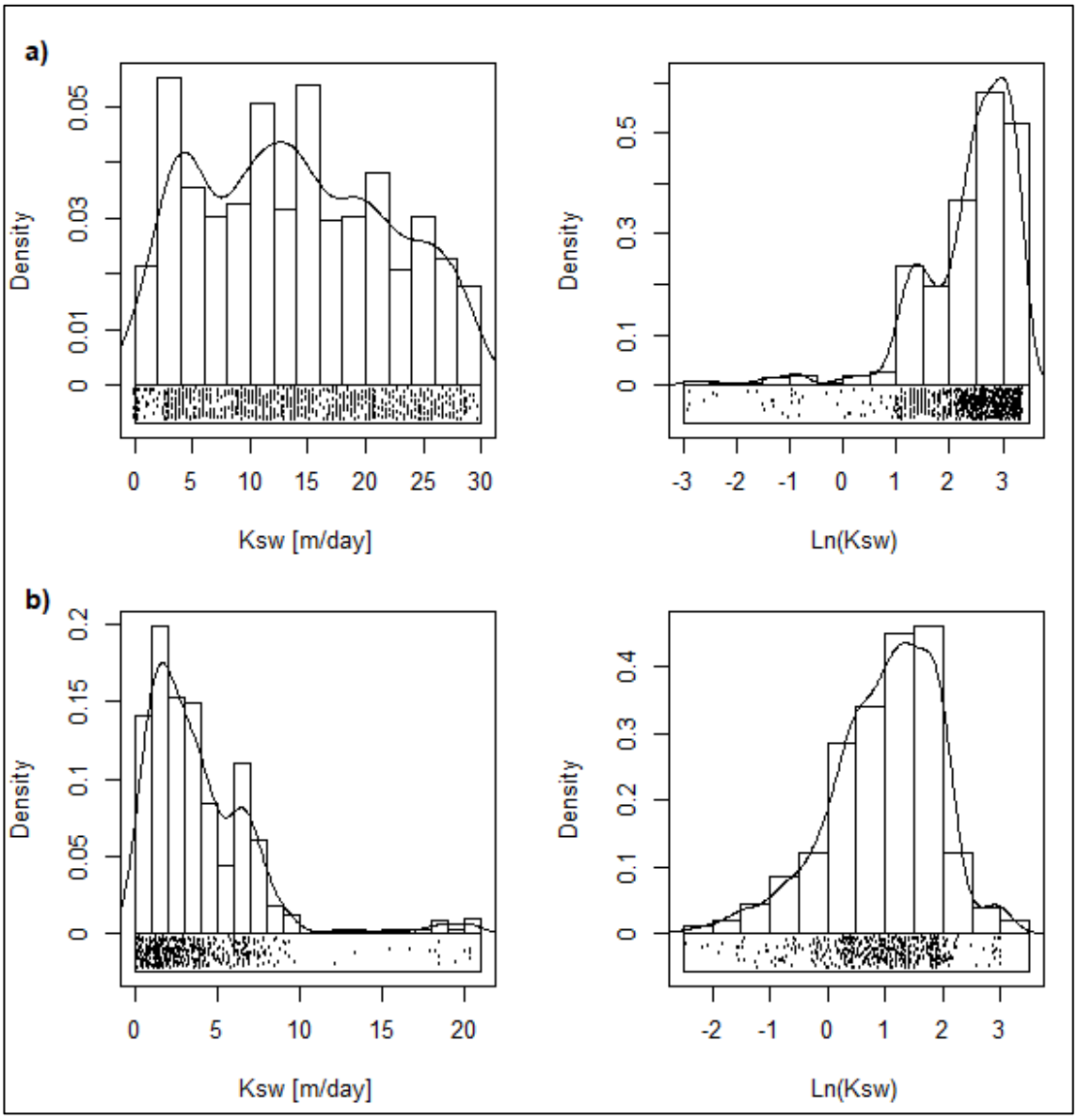


Fig. 7.13. Histogram, density trace, and one-dimensional scatterplot untransformed (left panels) and transformed (right panels) k_{sw} data in (a) areas A, B and surroundings, and (b) areas C and UST.

Table 7.12 shows a range of estimated logconductivity variances for segregated intervals from 0.08 at the top 0.74 m of the HPT log to 0.73 at the intermediate interval bounded by finer-grained lenses (which presented a variance of 0 due to the HPT lower limit of quantification of k_{sw}). Thus, these values suggested heteroscedasticity and also contrasted with the logconductivity variance of 4.52 considering the entire HPT profile. This was because the value of 4.52 did not represent the variance of a uniform medium, but the variance derived from the combination of multiple strata whose intra-variance was relatively lower. In a similar fashion, Bohling et al. (2012) partially attributed the

higher variance obtained with DPP than with DPIL and flowmeter to the supposition that DPP better captured the contrast between the upper and lower zones of the investigated aquifer (without discriminating by hydrofacies). The variance of unfiltered data from HPT73-A (4.52) suggested a high degree of heterogeneity even without considering bounding aquitards.

Table 7.12. Logconductivity variance in different hydrostratigraphic intervals at HPT73-A.

Elevation interval [m AHD]	Logconductivity variance	Description of the interval
51.990–56.120	4.52	Entire stratigraphic profile
55.388–56.120	0.08	Upper transmissive interval
55.038–55.373	0.00	Upper finer-grained lens
53.163–55.023	0.73	Intermediate transmissive interval
52.996–53.148	0.00	Lower finer-grained lens
51.990–52.980	0.35	Lower transmissive interval
51.990–56.120	0.51	Entire profile excluding non-detects
51.990–56.120	0.43	Weighted average variance of segregated intervals
51.990–56.120	0.49	Weighted average variance excluding non-detects

Thus, results from Table 7.12 and the rest of the section demonstrated several limitations of using a unique value of logconductivity variance to report aquifer heterogeneity. Alternative approaches could also report additional metrics more robust to non-Gaussian phenomena (MAD, IQR) and consider the average variance of distinct strata (which were weighted according to the thickness of the considered intervals) as presented in Table 7.12. Comparing sites according to these metrics could be especially meaningful when aquifers with similar structures and depositional environments are considered.

7.3.2.6 Reference values and ranges

Reference k_{sw} values for single-layer scenarios summarised in Table 7.13 were chosen as the average of HPT predictions from nearby HPT logs (HPT73-A in area A, HPT74-B in area B, and the IDW interpolation of HPT59-C, HPT60-C, and HPT62-C at PB40-C in area C) above z_{nw} as measured on 19–20/05/2016 (55.905 m AHD at PB29-A, 55.912 m AHD at PB27-B, and 55.600 m AHD at PB40-C). In area C, the average k_{sw} predicted at HPT59-C, HPT60-C, and HPT62-C were 1.54, 1.91, and 4.92 m/day, respectively. Thus, values from HPT59-C and HPT60-C were closer to the assumption of 1.83 m/day in

Gatsios et al. (2018a), although HPT62-C was the closest log to PB40-C. Values of k_{sw} above z_{aw} could have been slightly lower due to the fining-upward sequence. This was presumably more important in area B and less relevant in area A according to the Q/P logs shown in chapter 5.

Table 7.13. Reference values and ranges of k_{sw} [m/day] for the analytical models in the petrol station site.

Reference value(s)	Most likely range	Extended range	Conservative range
12.4 (area A), 10.3 (area B), 3.0 (area C)	0.76–26.21	0.02–100	0.0001–10000

For multi-layered scenarios in area A, the maximum k_{sw} field prediction (387.6 m/day) was assigned to a potential preferential migration pathway (around 56.20–56.35 m AHD) since a high k_{sw} value could be necessary to estimate T_n according to preliminary simulations (Gatsios et al., 2018a). Finer-grained materials were presumably found above 56.35 m AHD due to the transition between the aquifer and the aquitard. Nevertheless, Q/P values just above 56.35 m AHD were still higher than 5 mL/(kPa·min) and a k_{sw} value similar to the reference value in area B (10 m/day) was chosen.

For multi-layered scenarios in areas B and C, a value of 0.04 m/day (as the geometric mean of empirical correlations) was adopted for aquitard materials representing leaky confining layers and intervals with negligible LIF response when LIF suggested a greater impacted interval than b_n., for instance between 56.05 and 56.20 m AHD in area C. In area B, this low value was assigned below 55.85 m AHD because LNAPL was presumably entrapped in this interval according to in-well fluid levels. Nevertheless, the true k_{sw} was possibly higher according to HPT logging and entrapment was likely associated to capillary barriers with distinct retention parameters.

Regarding the k_{sw} ranges employed in the sensitivity analysis, same values were used for the entire site. The most likely range was chosen as the 5 %-trimmed range of HPT predictions after excluding non-detects (0.76–26.21 m/day). Empirical correlations exhibited a much greater variability and the corresponding IQR was already wider than the proposed most likely range. The range produced by the geometric mean of all the

empirical correlations was assumed as an extended range of k_{sw} (0.02–100 m/day). Finally, the conservative range comprised nine orders of magnitude, including a minimum k_{sw} of only 10^{-5} m/day corresponding to the API (2006) database and a maximum k_{sw} of 10,000 m/day. This conservative range was not likely representative of the petrol station site subsurface materials but contributed to test the robustness of the sensitivity analysis methodology.

7.3.3 Retention parameters

7.3.3.1 Predictions derived from particle-size data

Methods applied to estimate retention parameters (vG-α, vG-N, and S_{wr}) in the petrol station site included those proposed by Ghanbarian et al. (2010), Benson et al. (2014), multiple variants to calculate vG-α (Ellithy, Lenhard–Rawls, Lenhard–API, MS–Rawls, MS–API) and neural network predictions (Schaap et al., 2001) as implemented in RETC (van Genuchten et al., 1991). Predicted values and estimated vG retention curves are included in Appendix F: Retention curves.

As summarised in Table 7.14, the employed methods produced a wide vG-α range from 0.07 to 14.49 m^{-1}. The assumption of constant vG-α values taken from the literature resulted in the higher predictions, although Lenhard–Rawls and Benson also predicted vG-α values over 8 m^{-1}. On the other hand, the minimum vG-α values corresponded to MS–API and Benson.

As given by CVR values and also illustrated in Fig. 7.14, Benson and Ellithy exhibited the greatest variability. Due to the models employed, Benson generated the same distributions (in terms of CV, CVR, skewness, and kurtosis) for the drainage and imbibition curves, although around different central values. Despite the variability and the content in fines in the samples from the petrol station site, Benson generated reasonable vG-α ranges comparing them with other methods. RETC also predicted intermediate vG-α values with an IQR between 2.86 and 4.27 m^{-1}. Lenhard predicted considerably higher vG-α values than MS. Similarly, the use of h_{min} values from Rawls resulted in much higher estimations of vG-α than considering API samples. Benson produced slightly higher vG-α values for the imbibition period than for the drainage period as supported by multiphase theory. Nevertheless, estimations for both paths

were within the ranges proposed by other methods. Thus, the choice of the method may have a greater influence on the estimation of retention parameters than the path (drainage and imbibition) considered in Benson.

Table 7.14. Statistics of $vG\text{-}\alpha$ estimates [m^{-1}] in the petrol station site.

Statistic	Ellithy	Lenhard –Rawls	Lenhard –API	MS– Rawls	MS–API	Drainage	Imbibition	RETC
n	25	25	25	25	25	25	25	25
MIN	3.831	5.344	0.6647	0.6153	0.0743	0.1787	0.2631	0.94
p5	3.831	5.517	1.301	0.6462	0.1447	0.2344	0.345	1.178
Q1	3.831	7.752	1.393	0.8155	0.2125	0.3922	0.5773	2.86
MEDIAN	9.944	8.617	1.781	1.915	0.429	1.308	1.925	3.69
GEO-MEAN	8.719	8.172	1.618	1.646	0.3258	1.213	1.786	3.231
MEAN	9.869	8.372	1.668	1.885	0.3695	2.247	3.307	3.473
Q3	14.49	9.845	1.887	2.698	0.5115	3.271	4.814	4.27
p95	14.49	9.954	2.23	2.836	0.5508	6.646	9.783	4.688
MAX	14.49	9.977	2.305	2.854	0.5974	8.825	12.99	4.71
SD	4.318	1.741	0.3926	0.8492	0.1636	2.399	3.531	1.086
MAD	6.742	1.821	0.5126	1.161	0.1929	1.532	2.255	0.9044
NIQ	7.902	1.552	0.3662	1.396	0.2216	2.134	3.141	1.045
CV	43.75	20.79	23.53	45.06	44.27	106.8	106.8	31.27
CVR	67.8	21.13	28.78	60.62	44.95	117.1	117.1	24.51
SKEW-NESS	-0.3242	-0.7378	-0.2441	-0.3729	-0.2407	1.204	1.204	-0.9733
KURTO-SIS	-1.457	-1.107	-0.2662	-1.508	-1.608	0.3791	0.3791	-0.0659

As depicted in Fig. 7.15, $vG\text{-}\alpha$ estimations were commonly lower in finer-grained samples than in coarser-grained samples. Thus, the lowest $vG\text{-}\alpha$ values belonged to aquitard materials which could be interpreted as a sign of their higher air-entry pressure. Furthermore, above 55 m AHD, the methods of Lenhard–API, Benson (drainage and imbibition), and MS–Rawls predicted similar $vG\text{-}\alpha$ values. On the contrary, MS–API produced considerably lower $vG\text{-}\alpha$ values, while RETC and especially Lenhard–Rawls resulted in clearly higher $vG\text{-}\alpha$ predictions.

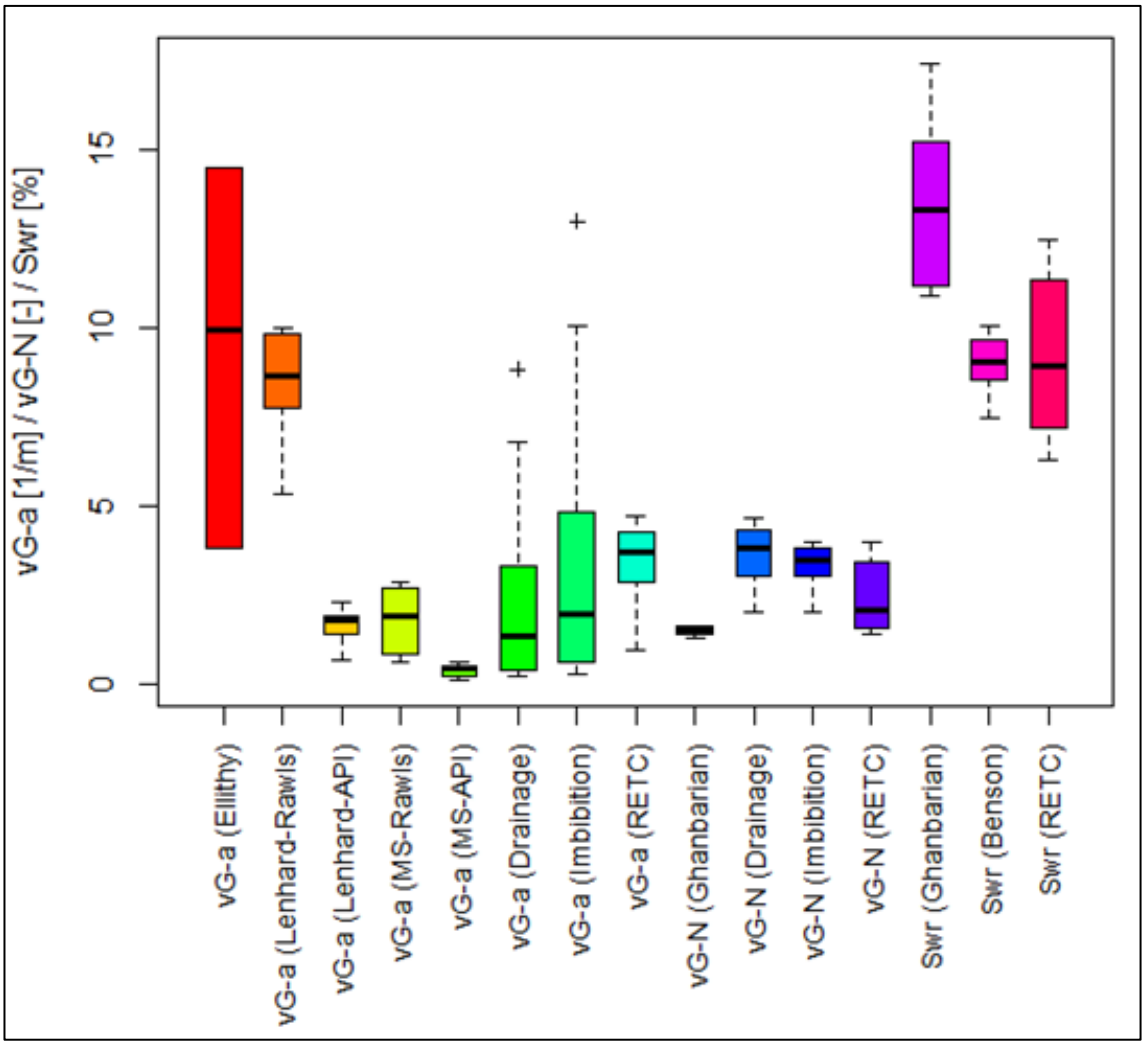


Fig. 7.14. Boxplots of *vG-α*, *vG-N*, and S_{wr} predictions in the petrol station site.

In the lower aquifer (below 55 m AHD), there was not a great increase in *vG-α* for most of the methods despite the coarser-grained and more uniform materials found in this interval. A clear exception was Benson, which predicted much greater *vG-α* values due to the lower C_u associated to lower aquifer materials. The dependence of Benson on C_u caused similar profiles to those of k_{sw} as obtained through empirical correlations and presented in 7.3.2.

Aggregating data from all the methods, Fig. 7.16 and Table 7.15 present the considerably lower *vG-α* values measured in the aquitard materials, where the median was out of the IQR of the other intervals. The transition and upper aquifer materials exhibited very similar *vG-α* distributions with just slightly higher values in the upper aquifer. The lower aquifer presented the highest *vG-α* values, partially reflecting the high estimations of Benson in these materials. Distributions of *vG-α* within every layer were right skewed.

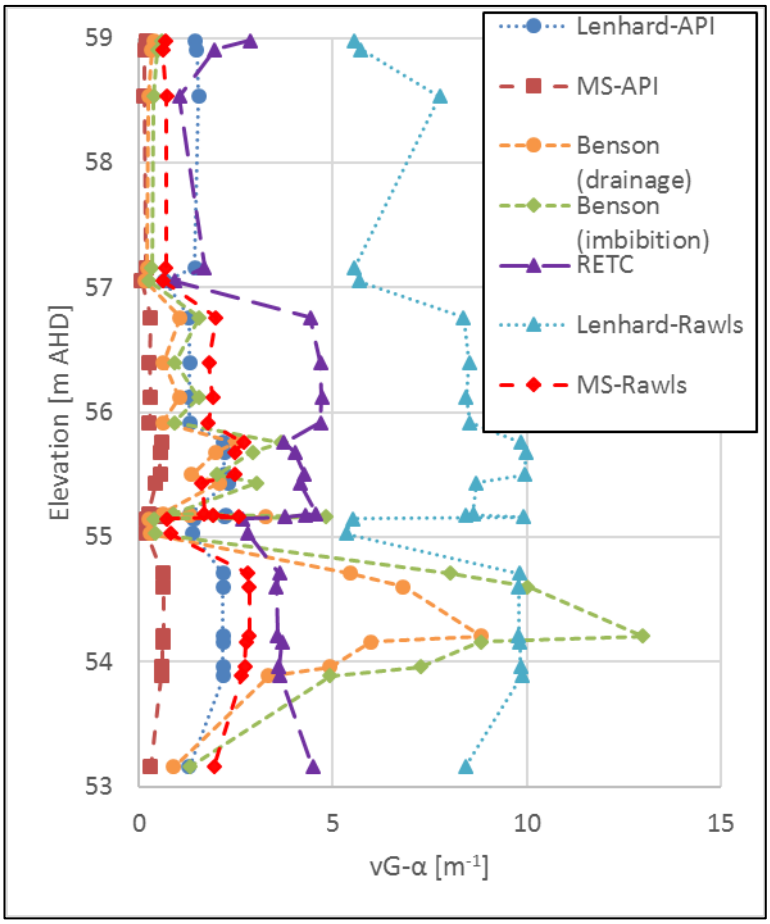


Fig. 7.15. Profiles of *vG-α* estimations according to multiple methods.

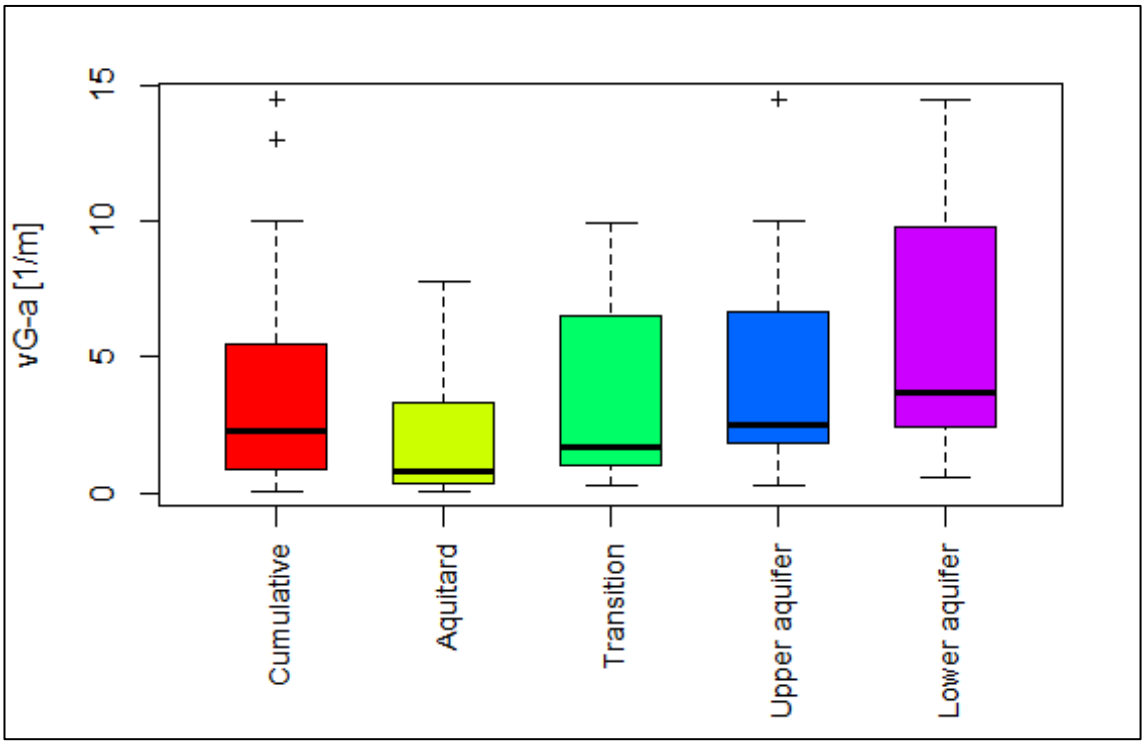


Fig. 7.16. Values of *vG-α* aggregating data from all the methods and discriminating by type of material.

Table 7.15. Statistics of vG-α [m^{-1}] of aggregated data and discriminating by type of material.

Statistic	Cumulative data	Aquitard materials	Transition materials	Upper aquifer	Lower aquifer
n	200	56	40	56	48
MIN	0.0743	0.0743	0.2769	0.262	0.5871
p5	0.262	0.1742	0.295	0.5358	0.6166
Q1	0.8741	0.3354	1.024	1.854	2.536
MEDIAN	2.271	0.7673	1.679	2.53	3.67
GEOMEAN	2.128	0.9443	2.024	2.797	4.16
MEAN	3.863	1.825	3.574	4.267	6.009
Q3	5.477	3.103	5.627	5.72	9.801
p95	9.98	5.587	9.944	9.966	14.49
MAX	14.49	7.752	9.944	14.49	14.49
SD	3.837	1.966	3.529	3.79	4.556
MAD	2.465	0.8862	1.803	2.313	4.506
NIQ	3.412	2.051	3.412	2.866	5.386
CV	99.33	107.7	98.74	88.81	75.82
CVR	108.6	115.5	107.4	91.43	122.8
SKEWNESS	1.207	1.151	0.8267	1.083	0.6316
KURTOSIS	0.4927	0.1824	-1.021	-0.0098	-0.9507

Regarding vG-N, it was also commonly higher in the coarser-grained materials as illustrated in Fig. 7.17. Benson generally predicted slightly greater vG-N values for the drainage path than for the imbibition path, although this relationship was lost in few samples from the aquitard. RETC generally estimated lower but reasonable vG-N values, arising the largest differences between RETC and Benson in the transition materials.

On the other hand, the fractal approach of Ghanbarian did not exhibit much sensitivity to the distinct subsurface materials and produced a practically constant and low vG-N value across the profile. Thus, the method was probably not suitable for the case of the petrol station site due to the relatively low clay content. The fractal model has been reported to produce reasonable estimates for loamy sand, sandy loam, and loam materials (Huang and Zhang, 2005). In the petrol station site, estimations in such samples were in a close agreement with RETC predictions, although the applicability of the method in this environment was questionable. Table 7.13 summarises central values and ranges of vG-N estimations from the methods of Benson and RETC in different materials. Ghanbarian estimates were not included in this set of data and Benson

drainage and imbibition parameters were averaged before aggregating them to RETC predictions.

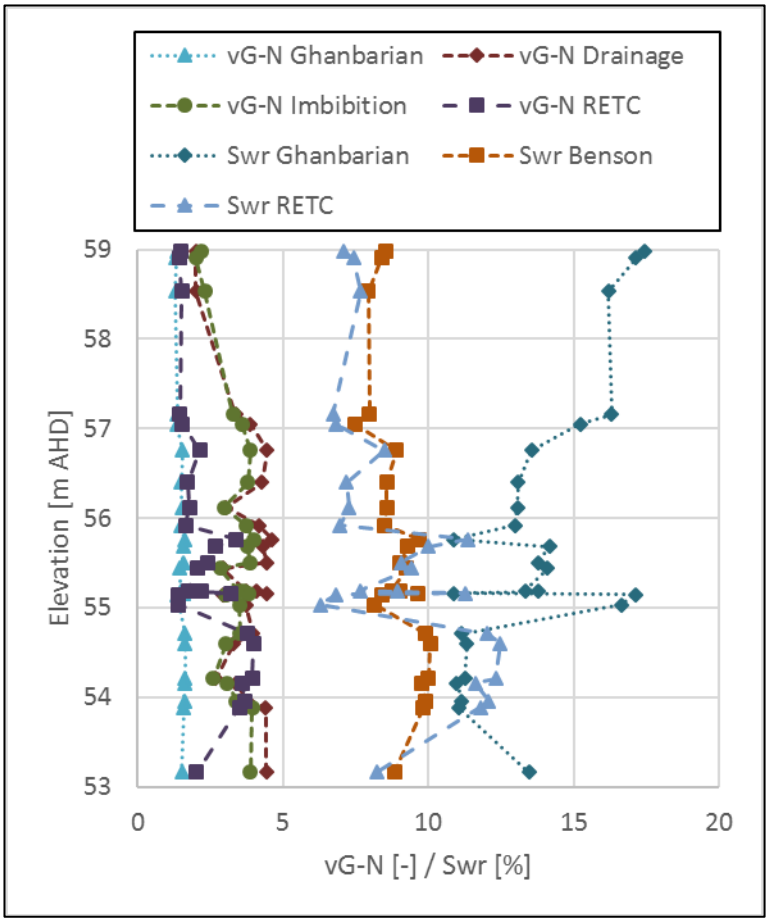


Fig. 7.17. Profiles of $vG\text{-}N$ and S_{wr} in the petrol station site.

Table 7.16. Central values and ranges of $vG\text{-}N$ [-] (cumulative and by type of material aggregating estimations through RETC and averages of Benson drainage and imbibition paths) and S_{wr} [%] (aggregation of estimations through RETC and Ghanbarian) in the petrol station site.

Statistic	Cumulative data ($vG\text{-}N$)	Aquitard materials	Transition materials	Upper aquifer	Lower aquifer	Cumulative S_{wr} data
n	50	14	10	14	12	50
MIN	1.414	1.414	1.658	1.734	2.637	6.276
p5	1.44	1.415	1.679	1.941	2.93	6.82
Q1	2.03	1.453	1.845	2.459	3.428	8.597
MEDIAN	3.188	1.766	2.572	3.298	3.637	11.3
GEOMEAN	2.743	2.006	2.664	3.063	3.56	10.89
MEAN	2.926	2.152	2.86	3.184	3.584	11.33
Q3	3.778	2.788	4.015	3.983	3.827	13.43
p95	4.155	3.652	4.151	4.206	4.068	16.91
MAX	4.305	3.739	4.157	4.305	4.174	17.43

Regarding S_{wr}, the three methods (Ghanbarian, Benson, and RETC) generated reasonable estimates, with Ghanbarian producing the highest S_{wr} values and Benson exhibiting the lowest variability due to the assumption of constant θ_{wr}. Ghanbarian was the only method predicting greater S_{wr} values in finer-grained materials. Table 7.13 presents values and ranges of aggregated S_{wr} estimations through the approaches of Ghanbarian, and RETC.

7.3.3.2 Reference values and ranges

The same reference values were used for base-case scenarios in areas A, B, and C due to the low number of samples and the similar values obtained regardless of the location. As shown in Table 7.17, the geometric mean of $vG\text{-}\alpha$ (aggregating all the methods), $vG\text{-}N$ (combining RETC and the average of Benson drainage and imbibition paths), and S_{wr} (combining RETC and Ghanbarian) were assumed as reference values. Nevertheless, slightly lower $vG\text{-}\alpha$ values were expected in area C than in areas A and B, for instance. For multi-layered scenarios, Q1 and Q3 values of aggregated $vG\text{-}\alpha$ and $vG\text{-}N$ data were used to represent coarser- and finer-grained materials.

Table 7.17. Reference values and ranges of retention parameters for the analytical models.

Parameter	Reference value(s)	Most likely range	Extended range	Conservative range
$vG\text{-}\alpha$ [m^{-1}]	2.13	0.87–5.48	0.26–9.98	0.05–18.70
$vG\text{-}N$ [-]	2.74	2.03–3.78	1.68–4.15	1.34–8.00
S_{wr} [%]	10.89	8.60–13.43	6.28–17.43	0.5–83.3
S_{nr} [%]	1.2	0.8–4	0.6–24.4	0–75
S_{ne} [%]	0.1 (area A), 1.2 (area B), 3.3 (area C)	1–4.4	0.1–22	0–75

Regarding the ranges of $vG\text{-}\alpha$, the most likely range was assumed to be the IQR of aggregated data, which was close to the IQR of transition materials and similar to the IQR of upper aquifer materials. The extended range was chosen as the 5 %-trimmed range and finally the conservative range was represented by extreme measurements found in the API database (API, 2006).

Regarding *vG-N*, the most likely range was defined according to the IQR of aggregated data and the extended range according to 5 %-trimmed data from the transition materials. The conservative range was again represented by data from API (2006).

In the case of S_{wr}, ranges were chosen considering the IQR, the field range, and a wide conservative range with data from API (2006).

Field estimations of S_{nr} and S_{ne} were considerably lower than those measured in laboratory studies. This discrepancy has already been reported by other authors (Adamski et al., 2003). Inspection of vertical profiles of field S_n measurements suggested S_{nr} values between 0.8 % and 2.6 % in area A, between 0.6 % and 1.2 % in area B, and around 1.8 % in area C. A value of 1.2 % was initially assigned to all the base-case scenarios due to the uncertainty in area A and B and the presumably limited influence of this parameter in the simulation of area C. The most likely range comprised the minimum of these estimations in area A (0.8 %) and the maximum used by Gatsios et al. (2018a). The extended range considered the minimum in area B (0.6 %) and the maximum obtained by Van Geel and Roy (2002) in a laboratory study using heptane. The conservative range was assumed to be as wide as 0–75 % according to the minimum used by Gatsios et al. (2018a) and, on the other side, high measurements in clays, most likely overpredictions, at laboratory scale (Zytner et al., 1993). It should be noted that similar extremely high S_{nr} values (up to 60 % in sands, as also measured by Zytner et al., 1993) have been reported by other authors, including popular references such as Hoag and Marley (1986) which is included in the review of Mercer and Cohen (1990).

In terms of S_{ne}, specific values were defined in area A, B, and C due to their potential impact on the model predictions. Coring suggested values as low as 0.1 % in area A, around 1.2 % in area B (although entrapped mass was potentially missed by coring as indicated by LIF logging), and between 2.2 % and 4.4 % in area C (an average of 3.3 % was assumed as the reference value). The most likely range was chosen as the minimum used by Gatsios et al. (2018a) in the lower layer (1 %) and the potential maximum in area C according to field estimations (4.4 %), the extended range considered the field minimum (0.1 %) and the value of 22 % reported by Van Geel and Roy (2002) in a

heptane–water system, while the conservative range was the same used in the analysis of S_{nr}.

7.3.4 LNAPL properties

The API database (API, 2006) included physical properties of five gasoline samples. Measurements were collected at multiple temperatures, being around 25 °C the lowest temperature with η_n measurements. Ranges and average values are presented in Table 7.18 along typical values for gasoline LNAPLs from other popular references (Mercer and Cohen, 1990; Johnston, 2010).

Table 7.18. Ranges and geometric means (between parenthesis) of LNAPL physical properties in gasoline samples from API (2006) and representative values of gasoline reported by Mercer and Cohen (1990) and Johnston (2010).

Statistic	ρ_n [g/cm^3]	η_n [cP]	σ_{an} [mN m^{-1}]	σ_{nw} [mN m^{-1}]
Mercer and Cohen (1990)	0.732	0.45	21	50
Johnston (2010)	0.733	0.48	20.5	22.9
API (2006) at any temperature	0.7–0.81	0.36–0.66	21.8–24.52	15.6–34.7
API (2006) at around 25 °C	0.73–0.80 (0.77)	0.41–0.66 (0.55)	21.8–24.52 (23.22)	15.6–34.7 (21.25)

Measurements of η_n in LNAPL samples from areas A, B, and C, resulted in values of 0.48, 0.42, and 0.41 cP, respectively, consistent with the literature. Thus, these values were selected for the base-case scenarios as shown in Table 7.19. The most likely range was chosen to comprise these three measurements and the geometric mean of API (2006) data collected at 25 °C. The extended and conservative ranges were very similar and considered 5 %-trimmed and full ranges from API (2006) considering measurements at any temperature.

Similarly, measurements of ρ_n in LNAPL samples from areas A, B, and C, resulted in values of 0.72, 0.73, and 0.73 g/cm^3, respectively, again consistent with the literature and these measurements were adopted as reference values. As described in section 4.3.3, 22 additional LNAPL samples were collected in 10 wells on 05/12/2014 to measure ρ_n, obtaining an average of 0.739 g/cm^3 and a range of 0.725–0.805 g/cm^3. The

maximum value corresponded to PB12-C, while the second and third highest ρ_n values were 0.760 g/cm^3 at PB09-B and 0.747 g/cm^3 at MP03-C, respectively. Thus, the most likely range considered the minimum and second maximum estimations from the petrol station site, the extended range comprised p5 and p75 of measurements from API (2006), and the conservative range was defined according to the API (2006) range.

Table 7.19. Reference values and ranges of LNAPL properties for model testing.

Parameter	Reference value(s)	Most likely range	Extended range	Conservative range
ρ_n [g/cm^3]	0.72 (area A), 0.73 (area B and C)	0.72–0.76	0.717–0.79	0.7–0.81
η_n [cP]	0.48 (area A), 0.42 (area B), 0.41 (area C)	0.4–0.55	0.37–0.65	0.36–0.66
σ_{an} [mN m^{-1}]	23.38	23–24.23	21.8–24.32	20.5–24.52
σ_{nw} [mN m^{-1}]	20.51	18.5–21.37	17.52–34.7	15.6–50

In the case of σ_{an} and σ_{nw}, geometric means from API (2006) were assumed as reference values. For σ_{an}, the API range was very narrow, which provoked that the three considered ranges were relatively similar. Greater variability was exhibited by σ_{nw}, both in the database and in other references such as Mercer and Cohen (1990), where a high σ_{nw} of 50 mN m^{-1} was presented. API (2006) presented three samples with σ_{an} higher than σ_{nw} and two where σ_{nw} was higher than σ_{an}. The most likely range was defined by central values of the median and arithmetic mean (18.5 and 21.37 mN m^{-1}, respectively).

7.3.5 LNAPL transmissivity

7.3.5.1 Section structure

T_n values and uncertainties associated to four baildown tests conducted during the HRSC campaign and close dates were assessed, since these T_n values were outputs of the analytical models. Alternative interpretations of cut-off times, drawdown adjustments, and J-ratios for each test and their effects were evaluated. In addition, the sensitivity of the T_n estimates to different values of specific yield, which was assumed to be 0.175 in Gatsios (2018) but could be as high as 0.231, was explored.

For every test, the following elements are discussed: (i) values used by Gatsios (2018) for the estimation of T_n, effects of different values of (ii) cut-off time, (iii) LNAPL specific yield, (iv) J-ratio and (v) drawdown adjustment, and (vi) summary of reasonable lower and upper bound T_n values. The lower and upper bound T_n values presented in Table 7.20 could be inferred from the analyses conducted in this section.

Table 7.20. Lower and upper bound Tn values according to alternative interpretations.

Bailed well	Date	Lower bound Tn value [m²/day]	T_n [m²/day] (Gatsios, 2018)	Upper bound T_n value [m²/day]
PB29-A	19/05/2016	1.459	1.510 (±0.093)	2.894
PB27-B	20/05/2016	0.262	0.572 (±0.011)	0.724
PB40-C	06/04/2016	0.258	0.577 (±0.025)	0.671
PB40-C	14/06/2016	0.061	0.304 (±0.008)	0.346

7.3.5.2 Baildown test at PB29-A

Gatsios (2018) selected a cut-off time of 1.95 min, a drawdown adjustment of -0.0012 m, and a J-ratio of -0.250, predicting a T_n value of 1.510 m²/day. As depicted in Fig. 7.18, z_{aw} became relatively constant (4.93–4.94 m bgl) since the fourth measurement, which was the interval chosen for the analysis by Gatsios (2018).

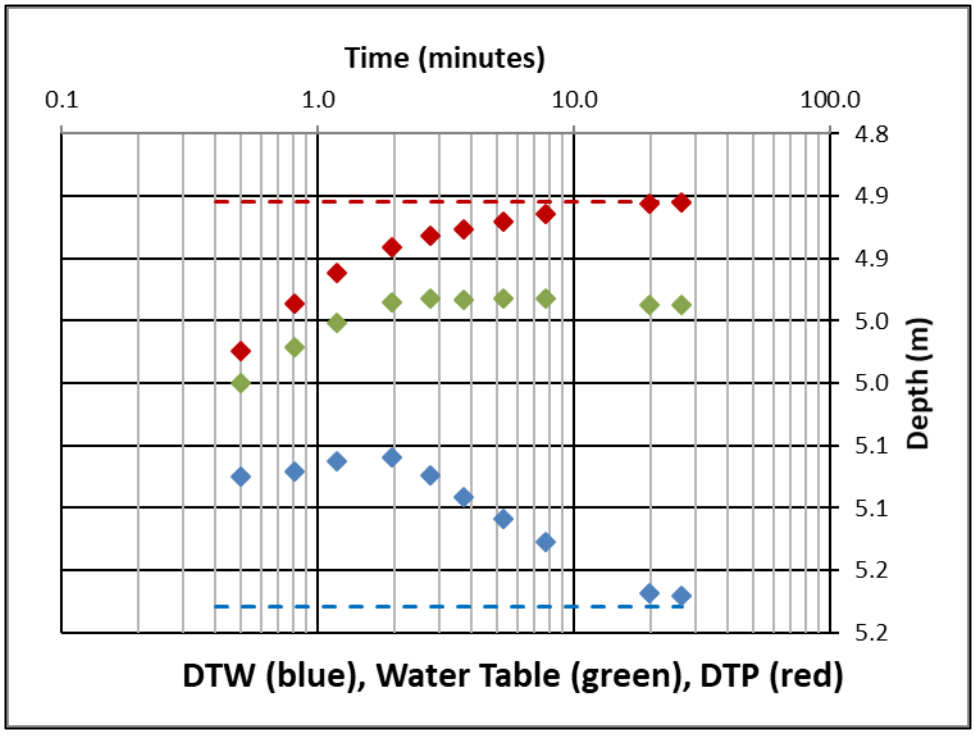


Fig. 7.18. Fluid interfaces during baildown test at PB29-A.

Consequently, this cut-off time only excluded the first two discharge measurements. However, as shown in Fig. 7.19, the third discharge measurement (0.329 m^3/day at 0.05 m) did not follow the same trend as the observations used in the analysis. This third measurement was not considered for the calculation of drawdown adjustment (-0.0012 m; illustrated by a dashed red line in Fig. 7.19), nor the J-ratio (-0.250 as depicted in Fig. 7.20, value consistent with constant z_{aw} conditions).

Thus, changing the cut-off time to 2 min to also exclude the third discharge measurement from the analysis produced a slightly lower T_n (1.459 instead of 1.510 m^2/day) with a slightly lower error associated to the linear regression (0.085 instead of 0.093 m^2/day). Consequently, the choice of this cut-off time did not lead to a different T_n estimation.

Similarly, using a LNAPL specific yield of 0.231 resulted in a subtle increase of T_n from 1.510 to 1.569 m^2/day. According to the default LNAPL specific yield of 0.175, the initial LNAPL volume in the filter pack was 0.56 L, amount that entered the well in less than 1.95 min. However, considering a LNAPL specific yield of 0.231, the initial LNAPL volume was 0.73 L, value not reached at 1.95 min. Therefore, these observations supported the choice of a greater cut-off time.

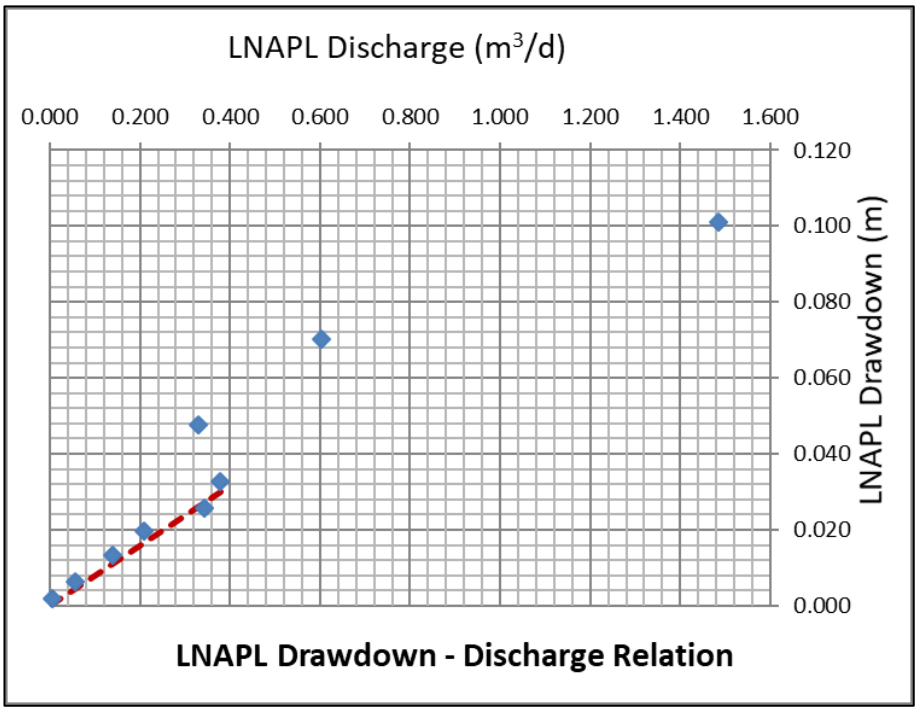


Fig. 7.19. DvD plot at PB29-A (Gatsios, 2018).

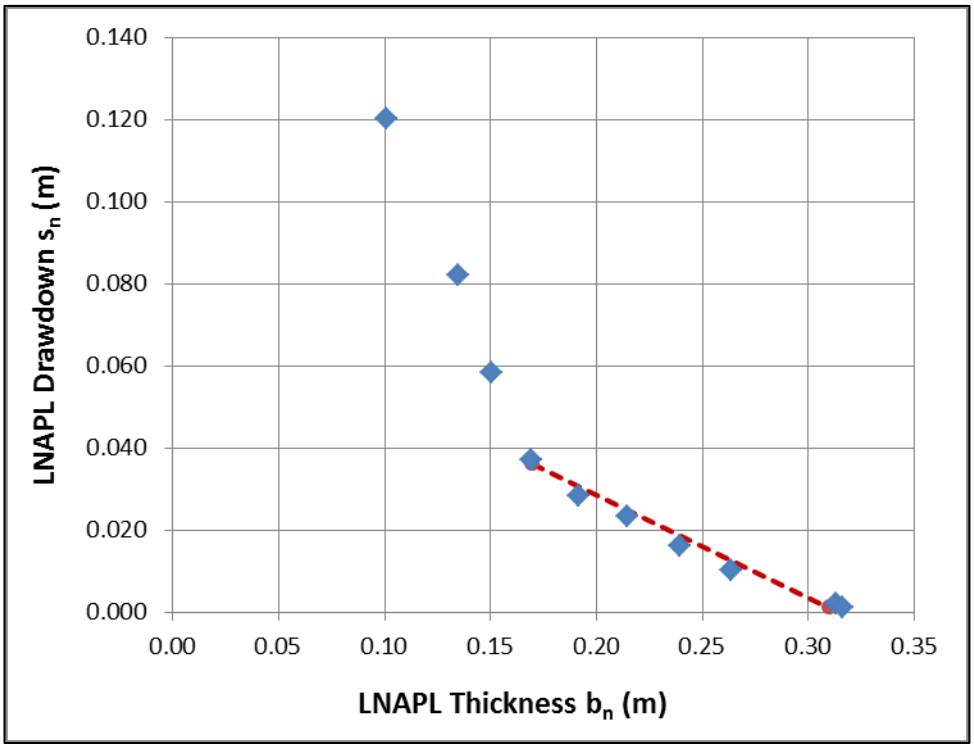


Fig. 7.20. Estimation of J-ratio at PB29-A (Gatsios, 2018).

Considering no cut-off time would produce a higher T_n of 1.770 m^2/day, but Fig. 7.20 exposed the existence of two intervals with different J-ratios. Using linear regression on the later six measurements, a J-ratio of -0.215 was predicted instead of -0.250 as estimated by Gatsios (2018). This change produced a T_n value of 1.756 instead of 1.510 m^2/day. If the last two measurements were excluded from the prediction of the J-ratio due to their low drawdown, a similar J-ratio of -0.253 was obtained.

Greater differences were found when alternative drawdown adjustments were applied. For instance, using a drawdown adjustment one order of magnitude lower (-0.00012 m), the prediction of T_n increased from 1.510 to 2.395 m^2/day. As depicted in Fig. 7.21, there was good fit of the Bouwer and Rice curve to the measured data after applying the new correction.

A reasonable upper bound of T_n equal to 2.894 m^2/day could be obtained considering a drawdown adjustment of -0.00012 m, a J-ratio of -0.215, and 0.231 as LNAPL specific yield. The lower bound T_n value estimated through these alternative interpretations was 1.459 m^2/day. These bound values were within a factor of 2 from the initial T_n estimation. It should be noted that the repetition of baildown tests applying other two

different initial drawdowns on the same date produced a T_n range between 1.29 and 2.06 m^2/day. These experiments were reported in Gatsios (2018) and are not repeated here.

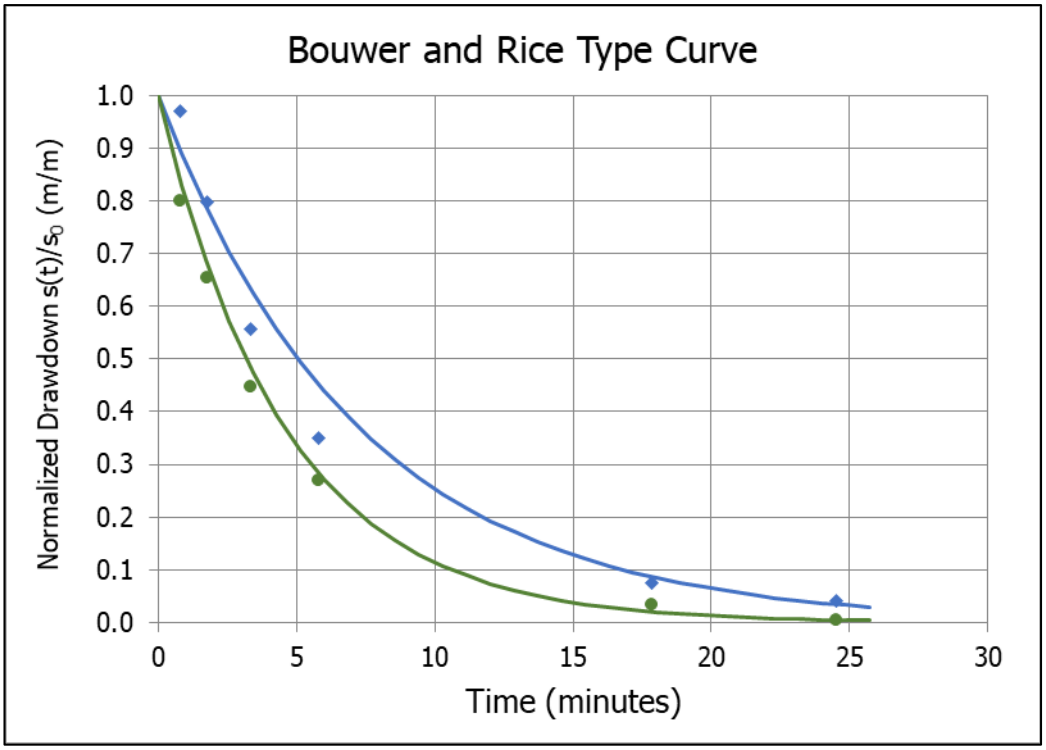


Fig. 7.21. Bouwer and Rice curves fitted to measured data considering drawdown adjustments of -0.0012 m (blue squares) and -0.00012 m (green circles).

7.3.5.3 Baildown test at PB27-B

Gatsios (2018) selected a cut-off time of 11 min, a drawdown adjustment of -0.002 m, and a J-ratio of -0.256, predicting a T_n value of 0.572 m^2/day. As depicted in Fig. 7.22, z_{aw} was practically constant the entire test (4.84–4.85 m bgl).

Applying a cut-off time of 11 min left the last five discharge measurements for the estimation of T_n. As depicted in Fig. 7.23, however, the last four discharge measurements followed a distinct trend and using a greater cut-off time could be justified. Nevertheless, using a cut-off time of 12 min predicted practically the same T_n (0.575 instead of 0.572 m^2/day) due to the great fit of the Bouwer and Rice solution (errors of 0.016 and 0.011 m^2/day, respectively).

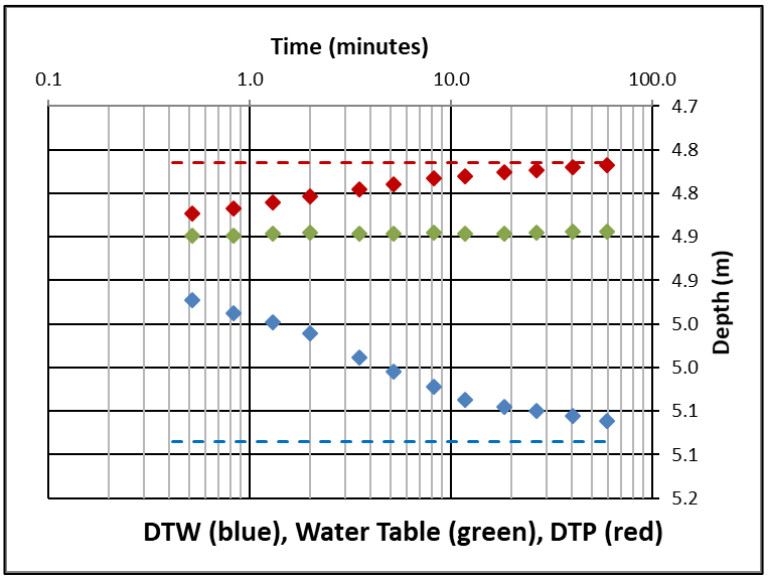


Fig. 7.22. Fluid interfaces during baildown test at PB27-B.

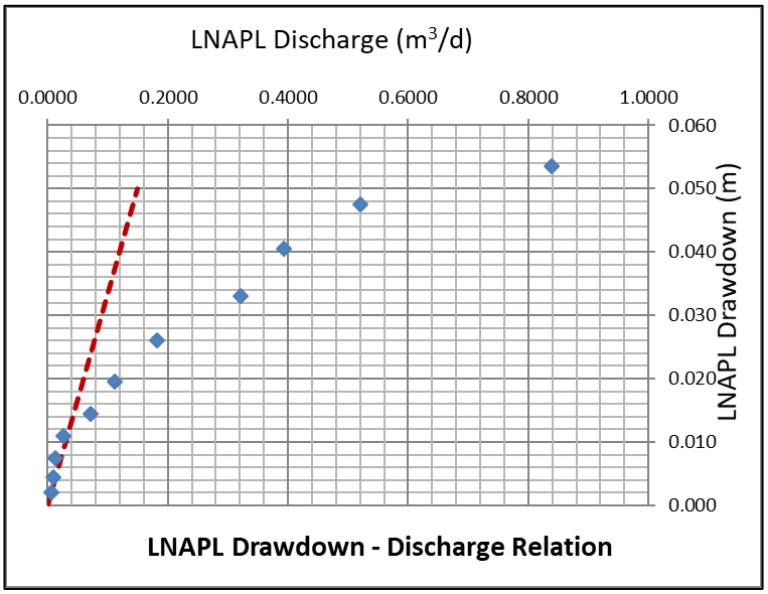


Fig. 7.23. DvD plot at PB27-B (after Gatsios, 2018).

In addition, using a LNAPL specific yield of 0.231 resulted in a subtle increase of T_n from 0.572 to 0.594 m^2/day. According to the default LNAPL specific yield of 0.175, the initial LNAPL volume in the filter pack was 0.55 L, amount that entered the well in 2 min. Similarly, a LNAPL specific yield of 0.231 resulted in an initial LNAPL volume of 0.73 L, value reached in less than 3.5 min. Consequently, the effects of applying a cut-off time of 3.5 min were also investigated, obtaining a T_n value of 0.611 m^2/day, increasing up to 0.697 m^2/day when no cut-off time was considered.

As illustrated in Fig. 7.24, practically the entire set of data was employed to estimate the J-ratio value of -0.256 due to the linearity of the relationship between LNAPL drawdown and b_n exhibited during the full test. Using linear regression for its estimation, a value of -0.278 was obtained, thus slightly decreasing the value of T_n from 0.572 to 0.526 m^2/day. Considering only the last four measurements, the J-ratio was -0.330 and T_n dropped to 0.443 m^2/day.

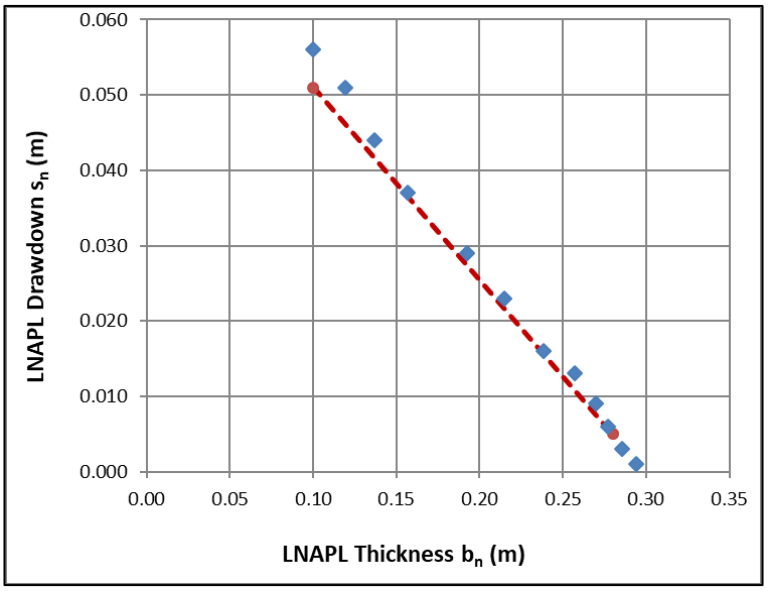


Fig. 7.24. Estimation of J-ratio at PB27-B (Gatsios, 2018).

Regarding the drawdown adjustment, the value of 0.002 m resulted in a great model fit. The choice of not applying a drawdown adjustment caused a decrease in T_n down to 0.358 m^2/day resulting in a worse model fit.

Thus, a reasonable upper bound T_n value of 0.724 m^2/day was obtained considering a LNAPL specific yield of 0.231 and no cut-off time. A lower bound T_n value of 0.262 m^2/day could be obtained using a cut-off time of 12 min, no drawdown adjustment, and a J-ratio of -0.330. This lower bound value was not within a factor of two comparing it to the initial T_n estimation. Nevertheless, as already presented in Gatsios (2018), practically the same T_n value (0.56 instead of 0.57 m^2/day) was obtained after repeating the baildown test on the same date with a different initial drawdown.

7.3.5.4 Baildown test at PB40-C on 06/04/2016

Gatsios (2018) selected a cut-off time of 4.2 min, a drawdown adjustment of 0.004 m, and a J-ratio of -0.258, predicting a T_n value of 0.577 m^2/day. As depicted in Fig. 7.25,

z_{aw} became constant (5.04–5.05 m bgl) since the third measurement collected at 2.3 min.

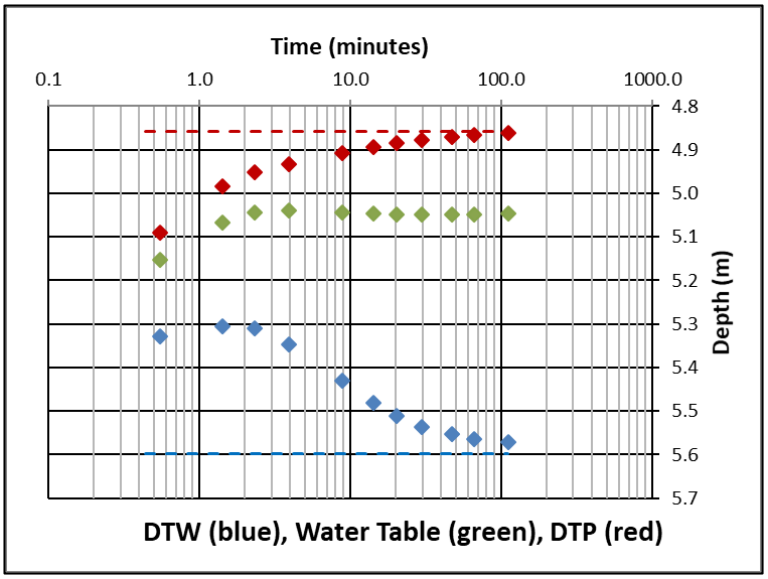


Fig. 7.25. Fluid interfaces during baildown test at PB40-C on 06/04/2016.

The cut-off time of 4.2 min excluded the first three discharge measurements in the estimation of T_n. As supported by Fig. 7.26, alternative interpretations could have only excluded the first two discharge measurements (cut-off time of 3 min), or only analyse the last three discharge measurements in a similar fashion to the baildown test at PB27-B (cut-off time of 30 min). These interpretations produced T_n values equal to 0.630 and 0.591 m^2/day, respectively.

Using a LNAPL specific yield of 0.231 instead of 0.175, T_n slightly increased from 0.577 to 0.603 m^2/day. According to both LNAPL specific yield values, the same amount of LNAPL initially contained in the filter pack (1.27–1.68 L) had entered the well between the third and fourth measurements (or second and third discharge points), supporting a cut-off time of 3 min.

Only excluding the first discharge measurement (cut-off time of 2 min) would additionally imply losing linearity in the estimation of J-ratio as shown in Fig. 7.27. A J-ratio value of -0.258 was assumed by Gatsios (2018). Applying linear regression to the last seven measurements (after 4.2 min), the J-ratio was calculated to be -0.242, causing a subtle increase in T_n from 0.577 to 0.616 m^2/day.

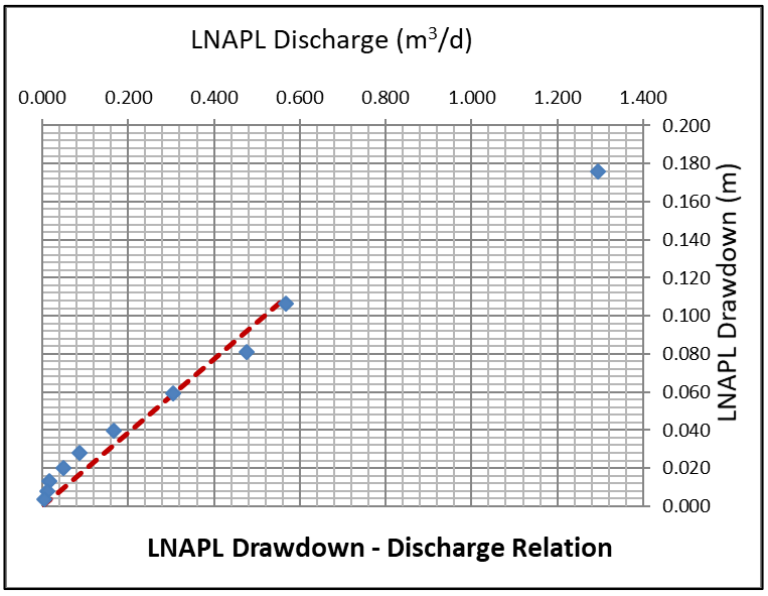


Fig. 7.26. DvD plot at PB40-C on 06/04/2016 (after Gatsios, 2018).

The drawdown adjustment of 0.004 m corresponded to predictions considering the last three measurements. Removing the adjustment resulted in a worse model fit and a lower T_n value of 0.347 m^2/day. If only the three last measurements were used, the model fit was good and a T_n value of 0.258 m^2/day was predicted.

Thus, according to these alternative interpretations, a reasonable upper bound T_n value of 0.671 m^2/day could be estimated considering a cut-off time of 3 min, LNAPL specific yield of 0.231 and J-ratio equal to -0.242. Similarly, a lower bound T_n value of 0.258 m^2/day corresponded to a cut-off time of 30 min and no drawdown adjustment.

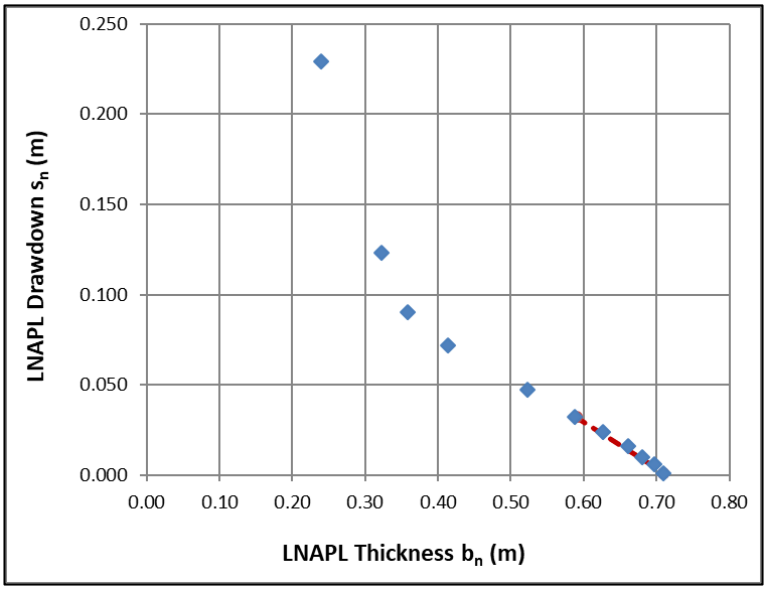


Fig. 7.27. Estimation of J-ratio at PB40-C on 06/04/2016 (Gatsios, 2018).

7.3.5.5 Baildown test at PB40-C on 14/06/2016

Gatsios (2018) selected a cut-off time of 0.7 min, a drawdown adjustment of 0.0224 m, and a J-ratio of -0.256, predicting a T_n value of 0.304 m^2/day. As depicted in Fig. 7.25, z_{aw} was practically constant the entire test (4.84–4.86 m bgl).

The cut-off time of 0.7 min only excluded the first discharge measurement in the estimation of T_n. This first discharge value clearly represented borehole effects and did not follow the same trend as the rest of values illustrated in Fig. 7.29. An alternative interpretation could only consider the last five discharge measurements in the analysis, thus applying a cut-off time of 15 min. This interpretation predicted the same T_n value (0.302 instead 0.304 m^2/day).

Using the default value of LNAPL specific yield (0.175), the initial LNAPL volume in the filter pack was calculated to be 0.91 L, amount that did not enter the well until the last five measurements, therefore supporting the cut-off time of 15 min. Using a LNAPL specific yield of 0.231, LNAPL volume at the filter pack increased to 1.20 L and suggested the increase of the cut-off time to 25 min, producing a slightly higher T_n value of 0.317 m^2/day. Keeping the cut-off time at 0.7 min with a LNAPL specific yield of 0.231 resulted again in a T_n value of 0.317 m^2/day.

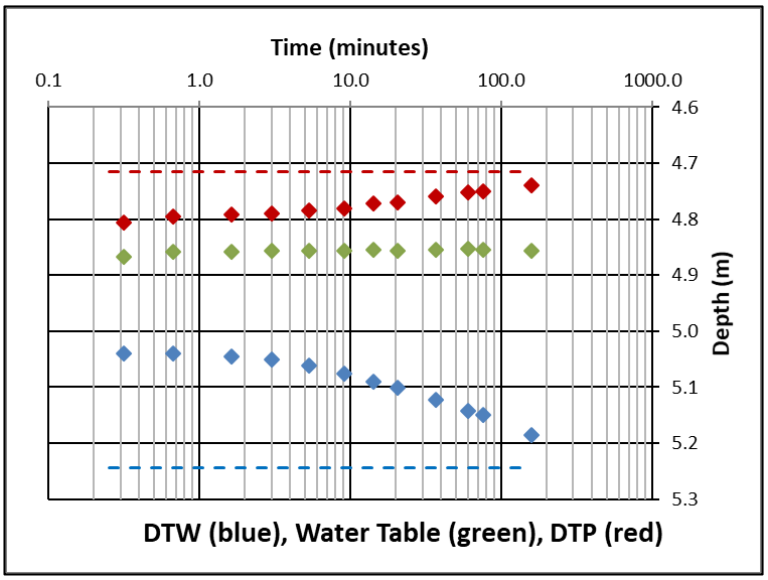


Fig. 7.28. Fluid interfaces during baildown test at PB40-C on 14/06/2016.

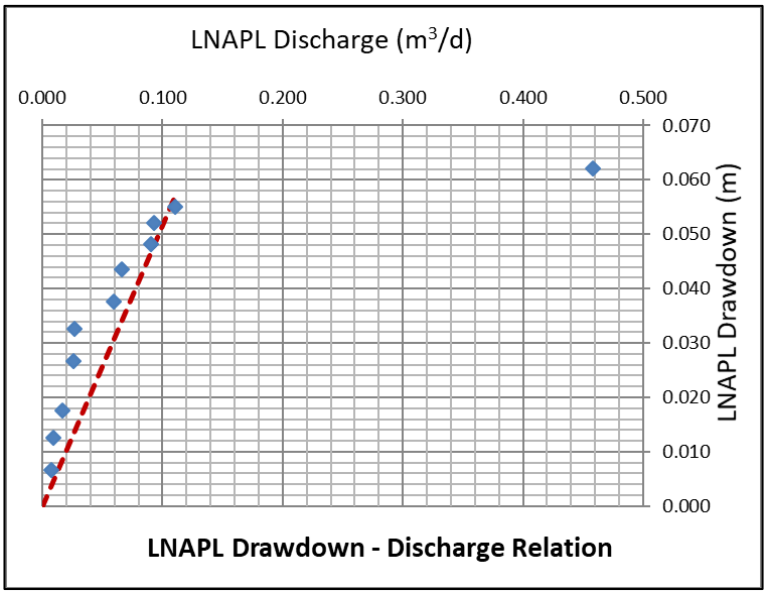


Fig. 7.29. DvD plot at PB40-C on 14/06/2016 (after Gatsios, 2018).

Linear regression of all the measurements except the first one, produced a J-ratio of -0.279 instead of -0.256 as estimated by Gatsios (2018) and illustrated in Fig. 7.30, resulting in a slightly lower T_n value (0.279 instead of 0.304 m^2/day). Using only the last four measurements, a J-ratio of -0.235 was predicted, corresponding to a T_n value of 0.332 m^2/day when the cut-off time was set at 25 min.

Not applying a drawdown adjustment resulted in a considerably lower T_n value (0.103 instead of 0.304 m^2/day), but with a worse model fit. Setting the cut-off time at 25 min caused a greater decrease in T_n, which dropped to 0.066 m^2/day.

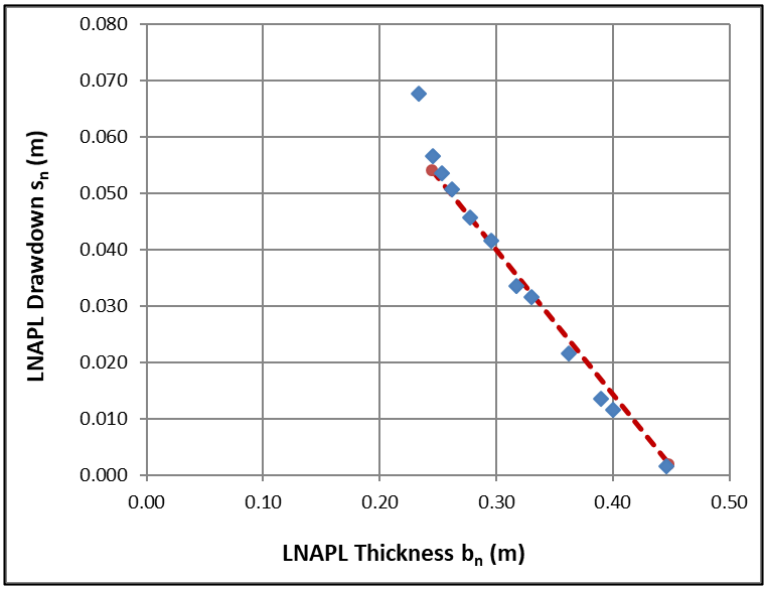


Fig. 7.30. Estimation of J-ratio at PB40-C on 14/06/2016 (Gatsios, 2018).

Thus, according to these alternative interpretations, the T_n value estimated by Gatsios (2018) was quite robust, only exhibiting a higher sensitivity to the drawdown adjustment. A reasonable upper bound T_n value of 0.346 m^2/day could be estimated considering a cut-off time of 25 min, LNAPL specific yield of 0.231 and J-ratio equal to -0.235. Similarly, a lower bound T_n value of 0.061 m^2/day could be estimated considering a cut-off time of 25 min, J-ratio equal to -0.279, and no drawdown adjustment.

In conclusion, the greatest potential errors in the calculation of T_n were commonly related to the drawdown adjustment estimation. Thus, further research on developing a better understanding of non-equilibrium conditions and more robust approaches to predict T_n from in-well fluid levels is encouraged.

7.4 Industrial site

7.4.1 Porosity

7.4.1.1 Laboratory measurements

A summary of statistics from 99 Φ measurements conducted in areas T3 and areas T4 is presented in Table 7.21. In area T4, only Φ measurements from samples with particle-size data were considered, thus the statistics represented the same set of data used in the application of RETC in section 7.4.1.2 and the derivation of values of k_{sw} and retention parameters. Analyses including samples without particle-size data explicitly mentioned it. Half of the values were within the range 48.30–53.21 % as indicated by the IQR, while only a 10 % of values fell out of the range 44.06–57.43 %. Spread statistics derived from field data were lower than in the literature (as expected since field data correspond to only one site). None of the values resulted in a robust Z-score over 3.5, hence no outliers were detected according to the Iglewicz and Hoaglin (1993) criterium.

In area T4, there were 53 additional samples without particle-size data. Some of the main statistics of the full set of 119 samples from area T4 are summarised in Table 7.22. The extended set of data presented a similar Φ range, with the same maximum value, but a slightly lower minimum of 40.11 % instead of 41.13 %. The addition of samples with relatively low Φ was reflected in a reduction in the first quartile (44.94 % versus 49.43 %) and central values (falling from approximately 51 % to 49 %).

Table 7.21. Summary of statistics of Φ measurements from samples with particle-size data in areas T3 and T4. Limits for the identification of outliers were computed according to Iglewicz and Hoaglin (1993).

Statistic	Areas T3-T4	Area T4	C66-T3	040610/1-T4	040610/3-T4	040610/6-T4	050210/1-T4
n	99	66	33	20	13	24	9
MIN	0.4113	0.4113	0.4267	0.4415	0.4868	0.4415	0.4113
p5	0.4406	0.4604	0.4301	0.4738	0.5049	0.4734	0.4294
Q1	0.4830	0.4943	0.4574	0.4821	0.5321	0.4972	0.4830
MEDIAN	0.5132	0.5170	0.5000	0.4981	0.5472	0.5170	0.5283
GEOMEAN	0.5079	0.5167	0.4908	0.5028	0.5549	0.5134	0.5039
MEAN	0.5096	0.5182	0.4923	0.5038	0.5565	0.5142	0.5061
MODE	0.5159	0.5236	0.5112	0.4929	0.5400	0.5182	0.5262
Q3	0.5321	0.5377	0.5181	0.5189	0.5849	0.5321	0.5321
p95	0.5743	0.5840	0.5560	0.5560	0.6226	0.5504	0.5570
MAX	0.6566	0.6566	0.5613	0.5811	0.6566	0.5585	0.5736
SD	0.0414	0.0399	0.0397	0.0323	0.0433	0.0274	0.0486
MAD	0.0364	0.0336	0.0408	0.0280	0.0336	0.0252	0.0280
NIQ	0.0364	0.0322	0.0450	0.0273	0.0392	0.0259	0.0364
CV	8.1320	7.6910	8.0540	6.4050	7.7800	5.3200	9.5960
CVR	7.0940	6.4930	8.1540	5.6160	6.1350	4.8700	5.2950
SKEWNESS	0.2004	0.3911	-0.0790	0.6019	0.6436	-0.6066	-0.6010
KURTOSIS	0.7468	1.4070	-1.1220	0.0279	-0.0885	0.1058	-0.8210
OUTLIER LIMITS	0.3243	0.3428	0.2884	0.3530	0.3730	0.3863	0.3832
	0.7021	0.6912	0.7116	0.6432	0.7214	0.6477	0.6734

The largest decreases were observed at 040610/3-T4 and 050210/1-T4, where central values were between 46–47 % considering all the samples. This was due to the large number of samples added (16 and 15 samples without particle-size data from 040610/3-T4 and 050210/1-T4, respectively), and the low Φ values associated to these samples. These low Φ values are further explored later in this section.

In addition, maximum measured Φ values were clearly higher than those proposed in section 7.2.1. This discrepancy could be due to a lack of representation of this type of depositional environment in databases and other literature, measurement errors, or other specific characteristics of the industrial site.

Table 7.22. Statistics of Φ measurements in area T4 including samples without particle-size data. NS7A-T4 refers to the combination of data from 040610/3-T4 and 050210/1-T4.

Statistic	Area T4	NS7A-T4	040610/1-T4	040610/3-T4	040610/6-T4	050210/1-T4
n	119	53	31	29	35	24
MIN	0.4011	0.4011	0.4105	0.4158	0.4219	0.4011
Q1	0.4494	0.4454	0.4675	0.4414	0.4737	0.4486
MEDIAN	0.4910	0.4848	0.4910	0.4984	0.5004	0.4683
GEOMEAN	0.4886	0.4816	0.4889	0.4945	0.4992	0.4665
MEAN	0.4891	0.4575	0.4906	0.4891	0.5094	0.4564
Q3	0.5256	0.5283	0.5038	0.5396	0.5210	0.4896
MAX	0.6566	0.6566	0.6362	0.6566	0.5585	0.5736

Beach sands may display high Φ values up to 57 % (Atkins and McBride, 1992), and occasionally over 60 % caused by the presence of oversized pores. In the industrial site, oversized pores could have been caused by shell fragments as mentioned in stratigraphic logs.

As concerns the quality of the measurements, one source of error could have been to assume a constant ρ_s of 2.65 kg/m^3. Despite some experiments corroborated the adequacy of using a ρ_s value of 2.65 kg/m^3, the following paragraphs discuss the effects of considering a different ρ_s.

Subsurface sands in the industrial site also consisted of biogenic material and minor amounts of feldspar and ρ_s could have exhibited some variability causing a few anomalously high estimations of Φ. The density of aragonite, a common source of carbonate sands, is 2.9 kg/m^3, while other shells have been reported to have a density of 2.4 kg/m^3 (Soulsby, 1997). With this ρ_s, the extreme Φ value of 65.66 % at 040610/3-T4 would still be 62.08 %.

Steffy et al. (1997a, 1998), Johnston et al. (1998), and Johnton and Trefry (2009) considered similar sands from the same geographic region. Steffy et al. (1997a) reported a Φ value of 49 % and a ρ_b of 1.33 kg/m^3, therefore inferring a ρ_s value of approximately 2.6 kg/m^3, almost the density of quartz. Johnston et al. (1998) similarly assumed a ρ_s of

2.65 kg/m^3 and thus obtained Φ values over 60 %, although they were typically found around 51 % like the measurements in areas T3 and T4. Johnston and Trefry (2009) chose a Φ value of 55 % as representative for their modelling study, a high value according to measurements from areas T3 and T4 as well as those reported by Johnston et al. (1998).

Nevertheless, Steffy et al. (1998) reported a Φ value of 40 % and a ρ_b of 1.38 kg/m^3, therefore inferring a low ρ_s value of 2.3 kg/m^3. With this ρ_s, the extreme Φ value of 65.66 % at 040610/3-T4 would become 60.43 %, while the second highest value of 60 % (also at 040610/3-T4, directly below the sample producing the absolute maximum in Φ) would become 53.91 %, falling within ranges given by Domenico and Schwartz (1998) and the UNSODA database (Nemes et al., 2001).

As a consequence, the maximum value of area T4 was seen as not generally representative of the subsurface conditions and the $\mathrm{p}95$ was assumed to better reflect values of Φ in the high range. Assumptions of quartz density being identical to ρ_s in sands from beach depositional environments may potentially induce errors in experimental and modelling studies. Cementation effects were also ignored.

As illustrated in Fig. 7.31(a) for samples with particle-size data, Φ was similar in areas T3 and T4. Differences were not substantial (average value of 49.23 % in T3 versus 51.82 % in T4) and practically disappeared after also considering samples without particle-size data.

Kurtosis of both distributions was different (platykurtic in the case of T3 and leptokurtic for T4) and data from T4 was more concentrated around central values than data from T3. This difference was due to the likely existence of an underlying bimodal distribution (not so clear in T4) as suggested by the density trace of T3.

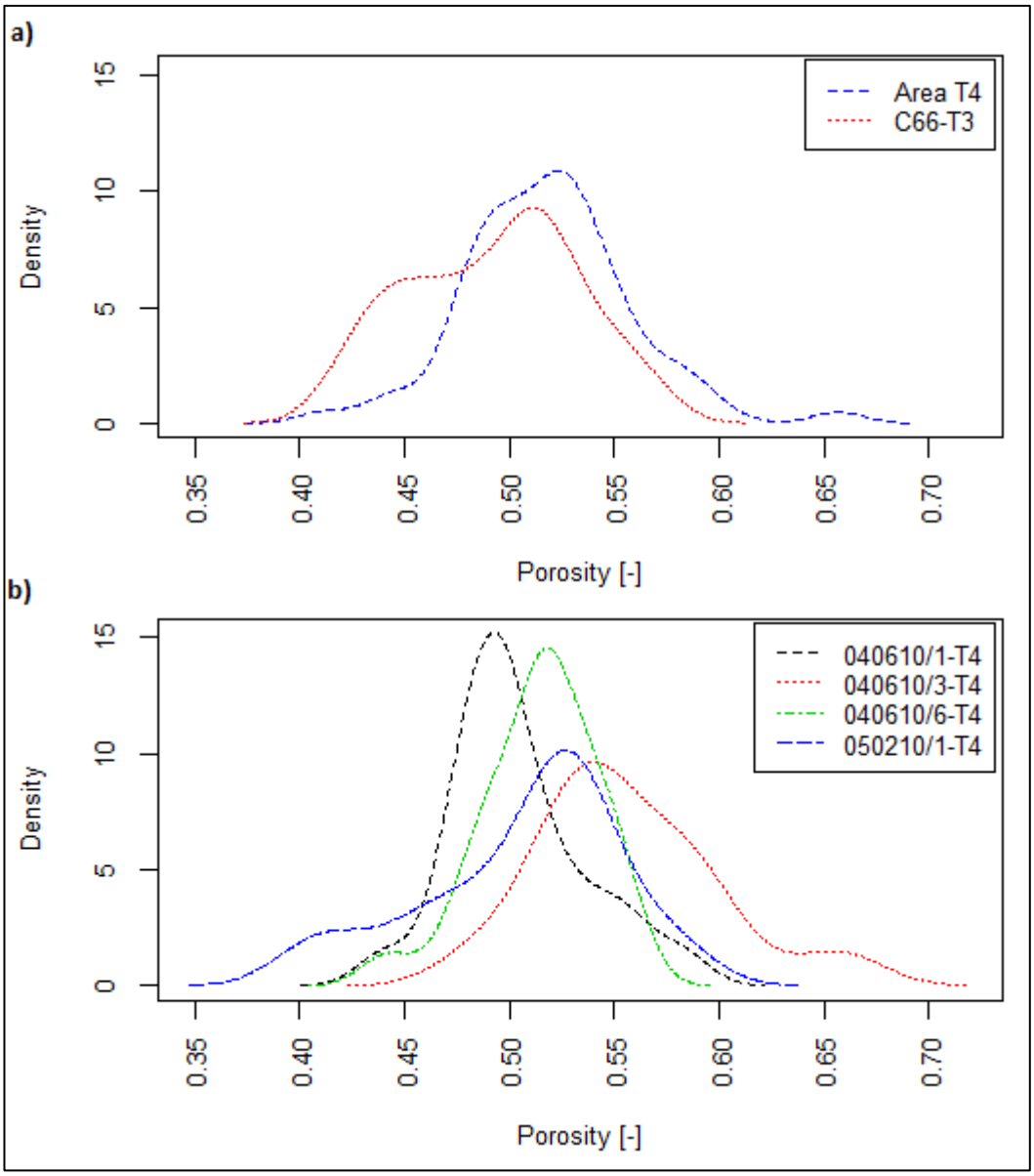


Fig. 7.31. (a) Density traces of Φ data from areas T3 and T4; (b) comparison between cores in T4.

In the case of area T4, the IQR was 49.43–53.77 % and the 5 %-trimmed range was 46.04–58.40 %. However, 040610/3-T4 exhibited a considerably different IQR with a mode of 54.00 % as shown in Fig. 7.31(b). Core 050210/1-T4 exhibited the second highest median and mode values as well as the greatest differences between robust and more sensitive estimators. However, these two cores, 040610/3-T4 and 050210/1-T4, only counted with a small number of samples (13 and 9, respectively) as depicted in Fig. 5.33. Furthermore, these samples (except one) represented a short interval mainly above 0.4 m AHD. It likely corresponded to a different facies than deeper data from other cores and yielded relatively high Φ values.

Consequently, the same type of analysis was performed discriminating data above 0.4 m AHD (proposed as an upper layer for model scenarios) and below such elevation (lower layer) as shown in Table 7.23 and Fig. 7.32. The sum of data from the top layer at 040610/3-T4 and 050210/1-T4 (named as NS7A-T4 in Table 7.23 and Fig. 7.32) exhibited a slightly higher Φ than the total of area T4. The mode and median of both sets of data was 53 % in spite of these differences, while the mode and median of the bottom layer was 48 % accounting for all the data from area T4.

Table 7.23. Summary of Φ measurements in area T4 discriminating between layers.

Statistic	Area T4 (top layer)	Area T4 (bottom layer)	NS7A-T4 (top layer)	040610/1-T4 (top layer)	040610/6-T4 (top layer)	040610/1-T4 (bottom layer)	040610/6-T4 (bottom layer)	040610/3-T4 (top layer)
n	53	13	21	13	19	7	5	12
MIN	0.4113	0.4415	0.4113	0.4415	0.4906	0.4755	0.4415	0.5170
p5	0.4725	0.4596	0.4566	0.4664	0.4940	0.4755	0.4475	0.5232
Q1	0.5057	0.4755	0.5283	0.4981	0.5113	0.4774	0.4717	0.5321
MEDIAN	0.5283	0.4830	0.5321	0.5019	0.5208	0.4792	0.4830	0.5509
GEOMEAN	0.5250	0.4844	0.5358	0.5115	0.5226	0.4871	0.4801	0.5610
MEAN	0.5265	0.4848	0.5382	0.5126	0.5229	0.4873	0.4808	0.5623
MODE	0.5261	0.4808	0.5317	0.4990	0.5170	0.4783	0.4829	0.5412
Q3	0.5472	0.4906	0.5698	0.5321	0.5377	0.4925	0.4868	0.5849
p95	0.5849	0.5185	0.6000	0.5653	0.5517	0.5102	0.5140	0.6255
MAX	0.6566	0.5208	0.6566	0.5811	0.5585	0.5170	0.5208	0.6566
SD	0.0393	0.0199	0.0512	0.0360	0.0196	0.0150	0.0286	0.0396
MAD	0.0336	0.0112	0.0336	0.0280	0.0168	0.0056	0.0168	0.0308
NIQ	0.0308	0.0112	0.0308	0.0252	0.0196	0.0112	0.0112	0.0392
CV	7.4670	4.1020	9.5050	7.0150	3.7440	3.0790	5.9420	7.0390
CVR	6.3540	2.3170	6.3090	5.5740	3.2230	1.1670	3.4750	5.5850
SKEWNESS	0.1842	-0.0382	-0.2162	0.0973	0.1219	0.9325	0.0261	0.9604
KURTOSIS	1.9510	0.1047	0.7346	-0.5116	-1.1340	-0.6790	-1.5160	0.0323

Despite the low number of samples, it could also be seen that 040610/1-T4 and 040610/6-T4 distributions corresponding to the bottom layer were similar, where the lower Φ hump at 040610/6-T4 was due to a single measurement at -0.1 m AHD.

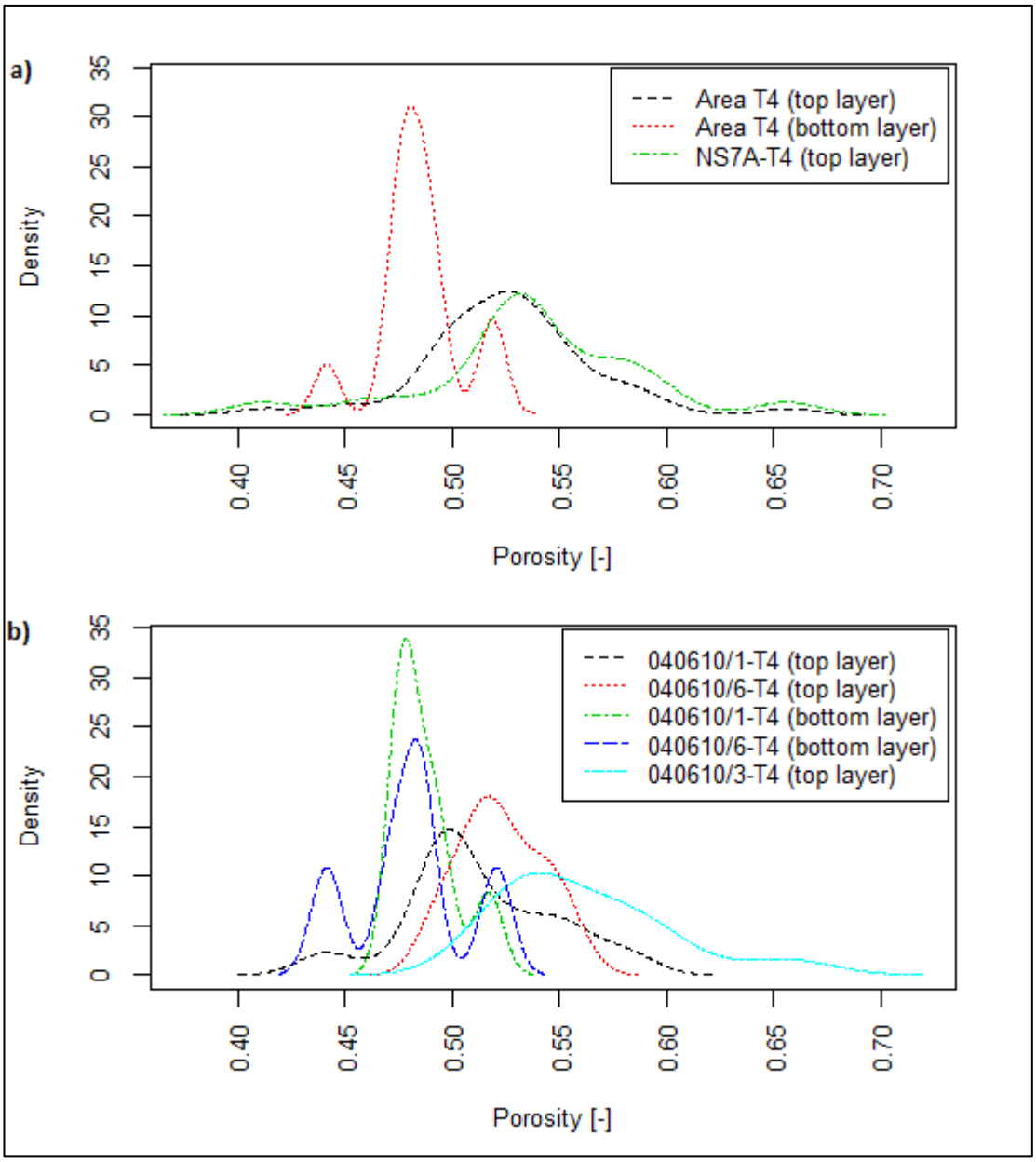


Fig. 7.32. Density traces discriminating layers using (a) cumulative data and (b) data from individual cores. NS7A-T4 density trace groups data from 040610/3-T4 and 050210/1-T4.

When also samples without particle-size data were considered, there was a better representation of the lower facies. Table 7.24 summarises statistics of Φ discriminating by hydrofacies also including samples without particle-size data. Central values of Φ were frequently more than 5 % higher in the upper layer (50–56 %) than in the lower layer (44–48 %). The minimum of 40.11 % corresponded to the lower layer at 050210/1-T4, while the minimum at the upper layer was just slightly higher (41.13 %). On the contrary, the Φ maximum was noticeably higher in the upper layer (65.66 %) than in the lower layer (52.08 %).

Table 7.24. Statistics of Φ discriminating by hydrofacies including samples without particle-size data. NS7A-T4 refers to the combination of data from 040610/3-T4 and 050210/1-T4.

Location	N	MIN	Q1	M	GEO-MEAN	MEAN	Q3	MAX
Area T4 (upper layer)	59	0.4113	0.5	0.5250	0.5233	0.5267	0.5453	0.6566
NS7A-T4 (upper layer)	24	0.4113	0.5151	0.5311	0.5285	0.5321	0.5585	0.6566
040610/1-T4 (upper layer)	14	0.4415	0.4981	0.5215	0.5195	0.5038	0.5462	0.6362
040610/3-T4 (upper layer)	13	0.5170	0.5321	0.5595	0.5583	0.5472	0.5849	0.6566
040610/6-T4 (upper layer)	21	0.4703	0.5094	0.5204	0.5199	0.5208	0.5321	0.5585
050210/1-T4 (upper layer)	11	0.4113	0.4585	0.4974	0.4953	0.5094	0.5302	0.5736
Area T4 (lower layer)	60	0.4011	0.4392	0.4576	0.4568	0.4511	0.4770	0.5208
NS7A-T4 (lower layer)	29	0.4011	0.4320	0.4465	0.4459	0.4488	0.4555	0.5119
040610/1-T4 (lower layer)	17	0.4105	0.4461	0.4660	0.4651	0.4755	0.4792	0.5170
040610/3-T4 (lower layer)	16	0.4158	0.4318	0.4487	0.4480	0.4434	0.4530	0.5119
040610/6-T4 (lower layer)	14	0.4219	0.4481	0.4705	0.4697	0.4703	0.4858	0.5208
050210/1-T4 (lower layer)	13	0.4011	0.4373	0.4437	0.4434	0.4488	0.4555	0.4642

7.4.1.2 Neural network predictions

There was a relatively constant gap of 0.05–0.07 (rarely 0.08) between measured Φ values and RETC predictions of θ_{ws} as illustrated in Fig. 7.33. Therefore, the gap was consistent with the typical difference between θ_{ws} and Φ of 5–10 % due to air entrapment phenomena (van Genuchten et al., 1991). Thus, the θ_{ws} range was practically as wide as the Φ range, which was not the case of the petrol station site. The better agreement in the industrial site was due to the inclusion of ρ_b values as input data for the predictions, not just textural classes.

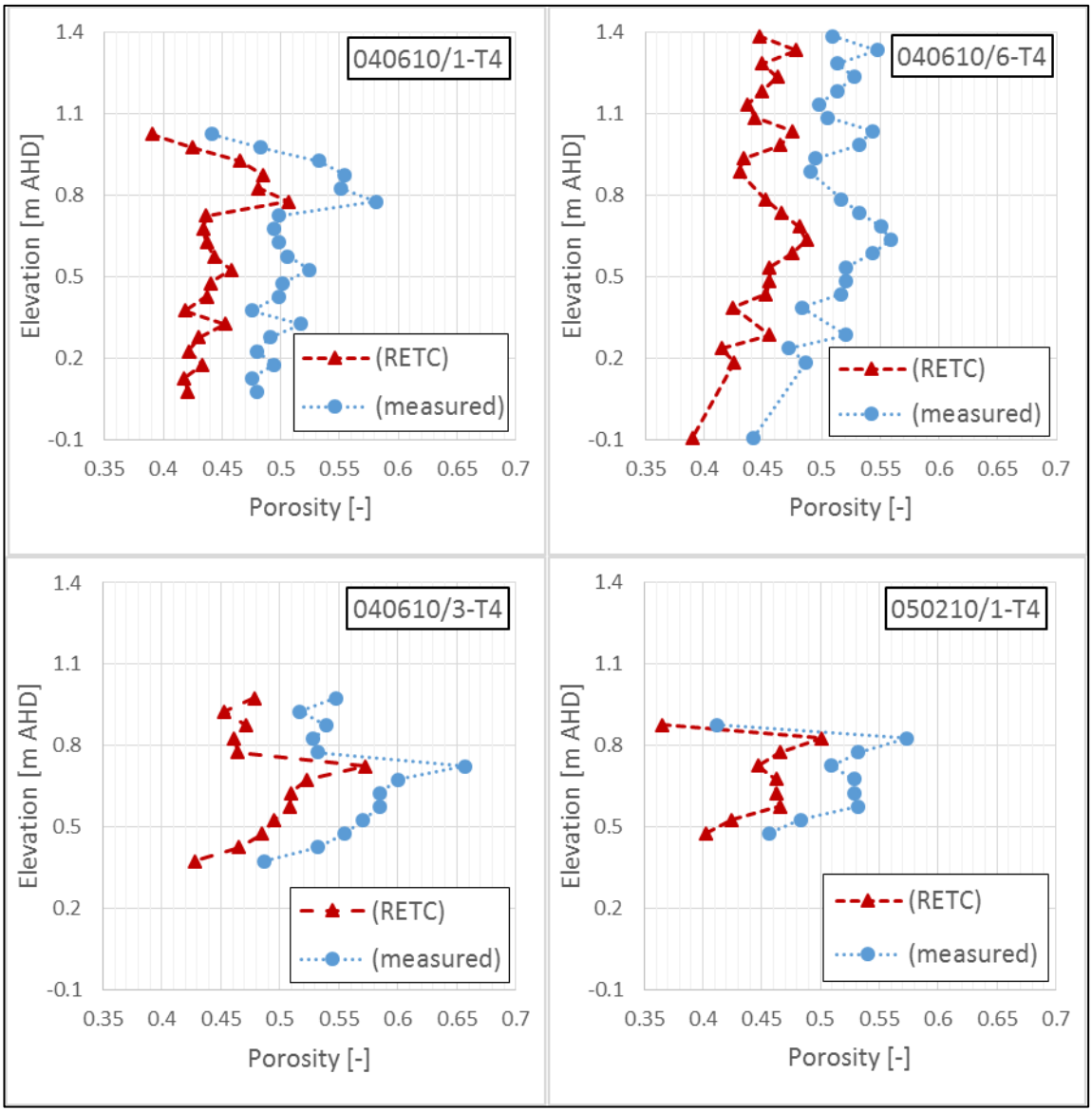


Fig. 7.33. Measured Φ values and RETC predictions of θ_{ws} used as proxies of Φ in area T4.

7.4.1.3 Reference values and ranges

Table 7.25 presents reference values and ranges of Φ for the model scenarios. Initial reference value of Φ for single-layer scenarios was assumed to be 49 %, representative of central values for the entire data set of area T4 including samples without particle-size data. The entire data set was considered instead of samples from only 040610/3-T4 and 050210/1-T4 or other specific locations because of the relatively low number of samples.

A conservative range between 15 % and 65.66 % was defined with a lower limit from the literature (15 %) by de Marsily (1986) and Dassargues (2018). The upper limit corresponded to an extremely high measurement of 65.66 % from area T4.

Table 7.25. Reference values and ranges of Φ [%] for the analytical models.

Reference value(s)	Most likely range	Extended range	Conservative range
49 (one layer), 53 (upper layer), 46 (lower layer)	45–53	40.11–57.43	15–65.66

A more realistic range (the 'extended range') considered to be characteristic of areas T3/T4 presumably went from the minimum field value (40.11 %) to a value around the p95 (57.43 %). The choice of the absolute minimum was consistent with literature values, while the use of p95 substituted the extreme value of 65.66 %, anomalously high compared to literature data and measurements from other cores in areas T3 and T4. Lastly, the most likely range was assumed to be 45–53 %, corresponding to the IQR of area T4 including all the samples.

In the case of two-layer scenarios, a Φ value of 53 % was expected to reflect the top layer material. This Φ represented central values of the upper layer in area T4 and also the combination of 040610/3-T4 and 050210/1-T4. As concerns the lower layer, a representative value of 46 % was chosen, consistent with literature values and the exploratory data analysis. Preliminary tests at 050210/1-T4 as presented in Lenhard et al. (2019) employed a Φ value of 50 % for the upper layer and 43 % for the lower layer, considering all the samples from 050210/1-T4, but not the adjacent core 040610/3-T4 or the rest of area T4.

7.4.2 Hydraulic conductivity

7.4.2.1 Empirical correlations with particle-size data

Some of the empirical correlations implemented by Devlin (2015) could not be employed in the analysis of the 66 samples collected between 040610/1-T4, 040610/3-T4, 040610/6-T4 and 050210/1-T4 due to their limited range of applicable conditions. For instance, requirements for the simplified Hazen formula and Krüger were very restrictive (including specific values of Φ, T, and/or coefficients of uniformity higher than 5) and could not be used in area T4.

Similarly, Terzaghi, Kozeny–Carman, Zamarin and the USBR formula were derived for coarser soils than the material generally found in area T4. Consequently, the first three

methods could be applied to four samples, while USBR was valid in nine cases. Additionally, requirements for Chapuis included coefficients of uniformity over 2 and could be employed for the analysis of 22 samples only. The rest of formulas were always applicable (Devlin, 2015), except Hazen in one sample.

Boxplots and summary statistics of k_{sw} values estimated with these 13 empirical correlations are presented in Fig. 7.34 and Table 7.26 (for values and graphs of specific samples see Appendix E: Particle-size data and correlations with hydraulic conductivity). Methods are identified through an ID as stated in Table 4.8. A logarithmic representation was more convenient since the distribution of k_{sw} was clearly right-skewed as expected.

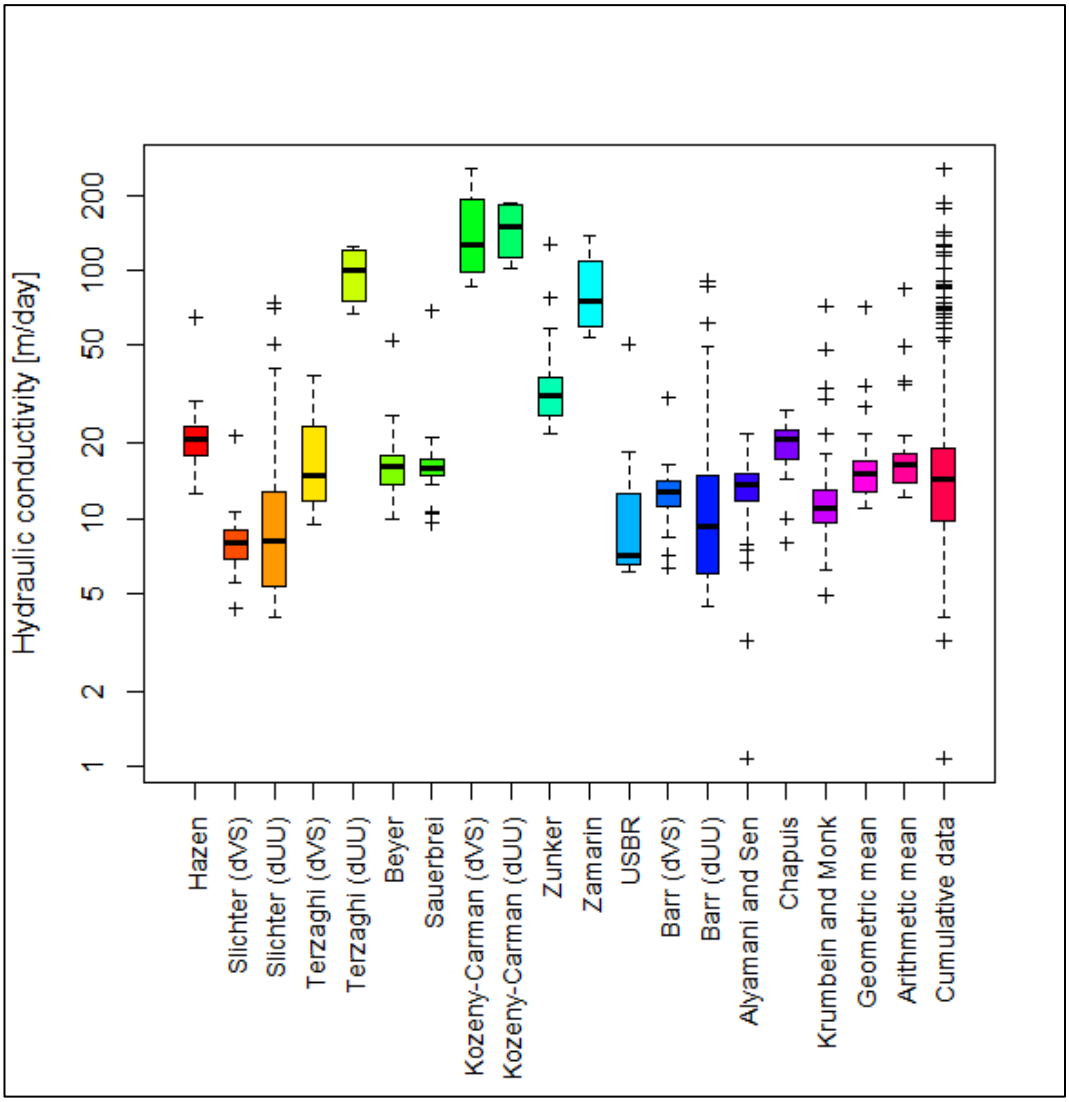


Fig. 7.34. Boxplots of k_{sw} predictions through multiple empirical correlations. Terzaghi, Kozeny–Carman and Zamarin boxplots correspond to only four data points, USBR to nine and Chapuis to 22.

Table 7.26. Statistics from HydrogeoSieveXL estimations. ID indicates the empirical method. *G* and *A* refer to geometric and arithmetic means including averages of results with d_{VS} and d_{UU}.

ID	N	MIN	Q1	M	GEO-MEAN	MEAN	Q3	MAX	CVR
Total	710	1.078	9.782	14.36	14.53	18.7	19.12	255.8	47.99
G	66	11.03	12.75	15.02	15.3	16.15	16.87	71.18	20.18
A	66	12.14	13.88	16.36	16.85	18.07	18.17	83.86	19.92
1	65	12.54	17.97	21	20.79	21.4	23.32	64.46	18.86
3 (d_{VS})	66	4.326	6.915	8.031	7.976	8.162	9.004	21.46	18.79
3 (d_{UU})	66	3.979	5.317	8.124	9.1	12.22	12.72	74.19	60.69
4 (d_{VS})	4	9.405	13.52	14.9	16.72	19.17	20.55	37.46	27.37
4 (d_{UU})	4	67.26	79.67	101.1	95.43	98.44	119.9	124.3	29.69
5	66	10	13.72	16.3	16.06	16.59	17.86	52.24	17.38
6	66	9.601	14.79	15.8	16.05	16.63	17.22	68.76	12.65
8 (d_{VS})	4	85.88	106.6	128.5	137.5	149.7	171.5	255.8	33.2
8 (d_{UU})	4	101	119.9	152.5	143.9	148.5	181.1	187.9	29.97
9	66	21.77	25.85	31.2	32	33.84	37.27	127.4	28.54
10	4	54.01	61.53	75.69	80.31	85.77	99.93	137.7	32.65
11	9	6.046	6.464	7.123	10.14	13.59	12.59	50.51	18.08
12 (d_{VS})	66	6.323	11.18	12.7	12.57	12.86	14.11	30.65	17.21
12 (d_{UU})	66	4.43	5.989	9.306	10.46	14.37	14.83	90.98	62.5
13	66	1.078	11.68	13.79	12.65	13.34	15.21	21.98	17.86
14	22	7.926	17.67	20.76	18.84	19.51	22.5	27.33	13.6
15	66	4.892	9.671	10.94	11.86	13.34	13.11	71.96	20.73

Despite the big range obtained with k_{sw} values spanning two orders of magnitude (1.078–255.8 m/day), the IQR (9.782–19.12 m/day) and the 5 %-trimmed range (5.436–43.865 m/day) were relatively narrow. The cumulative data from all the empirical models in area T4 (710 samples considering both d_{VS} and d_{UU}) exhibited a mode of 14.677 m/day. Wider ranges have been commonly reported in the literature, for instance comprising six orders of magnitude (Vienken, 2011).

Furthermore, when all the empirical correlations were combined, the logconductivity variance was 0.403, while the variance of every individual method did not generally exceed 0.2. Two exceptions were Slichter and Barr when d_{UU} was used as d_E, resulting in

variances of 0.461 and 0.494. The low variance estimations suggested that the aquifer was mildly heterogeneous in terms of k_{sw} distribution (Bohling et al., 2012; Gómez-Hernández et al., 2017), in a similar way to other research sites such as Borden and Cape Cod with logconductivity variances of 0.29 and 0.26, respectively (Bohling et al., 2012). Johnston and Trefry (2009) considered lognormal permeability variances of 0.594 and 1.188 for modelling subsurface conditions resembling a location relatively similar to area T4 and in the same geographic region.

The geometric and arithmetic mean of the results obtained with the 13 methods were similar in most of the cases. This was due to the consistent predictions obtained by multiple methods. Beyer, Sauerbrei, and Alyamani and Sen were generally in close agreement with the geometric and arithmetic mean values despite few clear underestimations of k_{sw} by Alyamani and Sen in infrequent gap-graded samples (for instance at 0.575 m AHD in 040610/1-T4, and to a certain extent in coarser textures). This was due to the high sensitivity of Alyamani and Sen to the shape of the grading curve (Odong, 2007). On the other hand, Hazen and Zunker predicted higher values, while Krumbein and Monk were generally below the geometric and arithmetic means. Hazen, Beyer, Terzaghi with d_{VS} and USBR have been found to generate similar distributions in previous studies (Vienken, 2011).

In the case of the industrial site, only Hazen and Beyer distributions were close, although with higher predictions in the case of Hazen. Terzaghi and USBR distributions were wider and considerably lower in the case of USBR. Slichter and USBR presented the lowest geometric mean and median values, which was consistent with outcomes from previous works (Cheng and Chen, 2007; Odong, 2007).

In addition, Fig. 7.35 illustrates the application of the approach of Wang et al. (2017) compared to the geometric mean of the methods implemented in HydrogeoSieveXL. Unlike the case of the petrol station site, the coefficient of determination between both parameters in the industrial site was relatively low (0.699 versus 0.944 in the petrol station site), partially due to differences in terms of layering between both sites. In general, Wang overpredicted k_{sw} compared to the geometric mean in the industrial site.

Compared to Hazen, Wang produced lower k_{sw} values, although there was higher correlation (R^2=0.855).

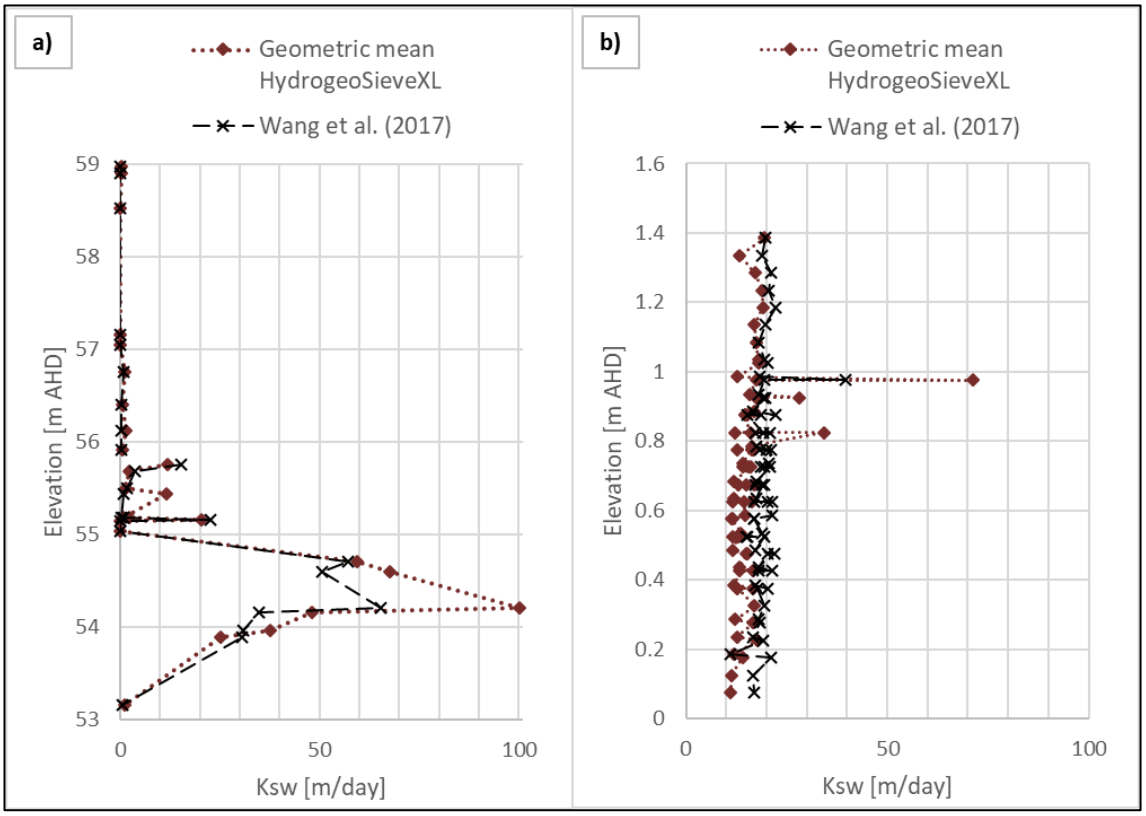


Fig. 7.35. Comparison of predictions with the approach of Wang et al. (2017) versus the geometric mean of multiple empirical methods in (a) the petrol station site and (b) the industrial site.

The two minimum k_{sw} values found in area T4 were obtained with the formula of Alyamani and Sen and were suspected outliers. Additionally, low k_{sw} values in the range 3.979-6.0 m/day were mainly linked to the use of d_{UU} in Slichter and Barr, with both methods, respectively predicting 35 % and 26 % of values below 6 m/day. On the contrary, using d_{VS} yielded 5 % of values below 6 m/day with Slichter and none with Barr. All the other methods predicted k_{sw} values over 6 m/day except an estimation of 4.892 m/day with Krumbein and Monk at -0.095 m AHD in 040610/6-T4. Consequently, a minimum value within the p5-p25 range (5.436–9.782) was considered to be more representative than the absolute minimum of 1.078 m/day.

Regarding additional discrepancies between the use of d_{VS} and d_{UU} in Slichter and Barr, both methods usually resulted in higher values when d_{UU} was employed in moderately

well sorted sands. On the contrary, uniform sands implied a lower prediction of k_{sw} with d_{UU} in most of the cases. Since Slichter and Barr frequently generated k_{sw} values below the arithmetic and geometric means of the 13 methods, the use of d_{UU} was more consistent with the other methods in moderately well sorted sands low in fines, while d_{VS} could be preferred in uniform sands low in fines as inferred from Fig. 7.36.

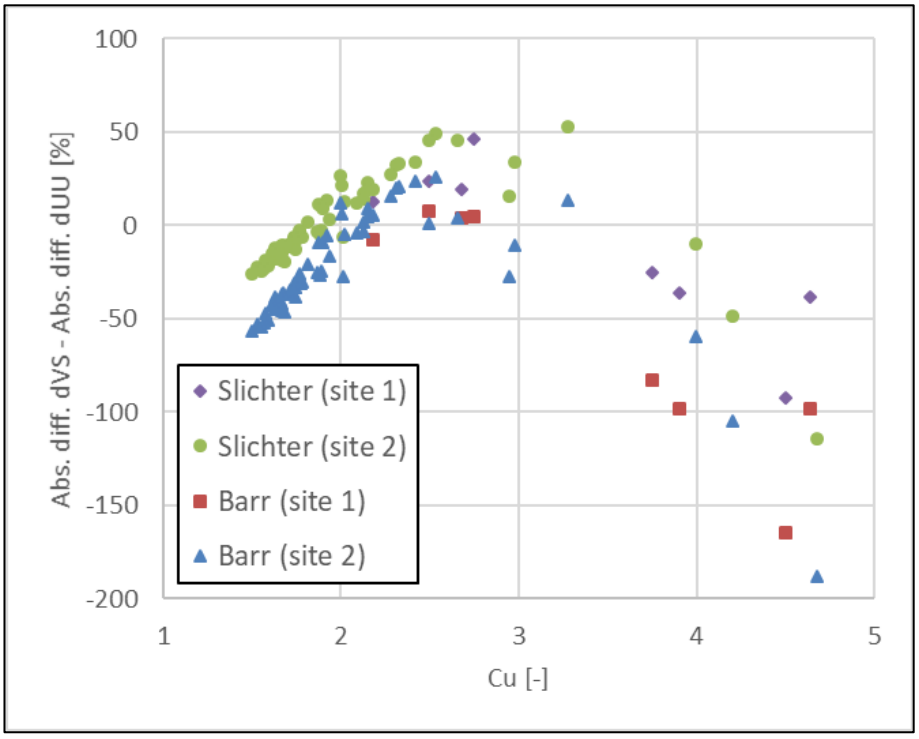


Fig. 7.36. Absolute differences between the use of d_{VS} and d_{UU} in Slichter and Barr compared to the geometric mean of other methods in the petrol station site (site 1) and the industrial site (site 2). Samples corresponding to C_u values over 5 (found at the petrol station site) did not follow any clear trend (not shown).

More specifically, Slichter with d_{UU} was closer to the geometric mean of all the methods (excluding those where both d_E options could be used) when C_u was between 1.9 and 3.9 in all the cases except one with a C_u equal to 2.01 (95.5 % of 20 cases). Additionally, d_{UU} was apparently a better choice than d_{VS} in six cases with C_u over 1.8, while other three samples with C_u over 1.8 showed the opposite behaviour. Similarly, Barr with d_{UU} was closer to the geometric mean of all the methods in a 70 % of cases when C_u was between 1.95 and 3.9. When C_u was higher than 3.9, predictions from Slichter and Barr with d_{UU} experimented greater increments than with d_{VS} resulting in an overestimation of k_{sw} as given by the geometric mean of the other methods.

In addition, Terzaghi apparently followed the same pattern, while Kozeny–Carman produced lower k_{sw} with d_{UU} than with d_{VS}, consistent with several measurements from the petrol station site and the example given by Devlin (2017b) where the use of d_{UU} in Kozeny–Carman overestimated the value of k_{sw} in poorly sorted sands. Nonetheless, there were exceptions to this rule as expected since non-uniform sorting had an impact on the quantification of d_E.

Furthermore, the choice of d_E apparently had a strong influence on spreading statistics. For instance, the greatest CVR values were computed for the methods of Slichter and Barr with d_{UU} while using d_{VS} in these methods resulted in a low variability.

According to the Iglewicz and Hoaglin (1993) criterium applied to the cumulative data from all the empirical models (710 samples considering both d_{VS} and d_{UU}), k_{sw} values over 50.119 m/day resulted in robust Z-scores over 3.5 (since MAD was equal to 6.891 m/day) and could be considered as outliers, including the few values (only four samples) calculated with Terzaghi (using d_{UU}), Kozeny–Carman (using both d_{VS} and d_{UU}) and Zamarin. In particular, Kozeny–Carman generated the maximum values in the entire data set. Nonetheless, although these values were most likely overestimated, the four samples corresponded to relatively coarse textures and represented intervals of high k_{sw}.

Therefore, it was important to account for the sample location and the corresponding type of geology. Values of k_{sw} from individual wells in area T4 discriminating between two layers (above and below 0.4 m AHD) are summarised in Table 7.27, where NS7A-T4 refers to the sum of data from 040610/3-T4 and 050210/1-T4. Additionally, a graphical representation of the data through boxplots is included as Fig. 7.37.

The two layers were in good agreement and the median of each layer was within the IQR of the other layer. Therefore, same values and ranges of k_{sw} were assumed to be representative of both layers. Nonetheless, the highest predictions of k_{sw} belonged to the top layer (above 0.4 m AHD), with 040610/1-T4 and 050210/1-T4 producing the highest values, while the bottom layer at 040610/6-T4 was apparently the least conductive.

Table 7.27. Summary statistics of k_{sw} predictions in area T4 discriminating by location (well and/or layer). *Layer 1* refers to the top layer and *Layer 2* to the bottom layer.

	N	MIN	p5	Q1	M	GEO-MEAN	MODE	Q3	p95	MAX
Layer 1 (total)	577	1.078	5.493	9.916	14.86	15.08	14.32	19.85	50.29	255.8
Layer 2 (total)	133	4.263	4.892	9.378	12.71	12.35	12.79	16.67	26.24	37.28
NS7A-T4 (total)	233	3.211	5.435	9.208	13.74	13.58	14.08	18.1	35.1	178.8
040610/1 (total)	225	1.078	6.155	10.87	15.55	17.1	14.59	22.96	73.74	255.8
040610/3 (total)	133	3.979	5.656	9.276	12.74	12.46	13.81	16.27	26.86	44.92
050210/1 (total)	100	3.211	5.449	9.195	14.73	15.22	14.02	20.25	77.73	178.8
040610/6 (total)	252	4.326	5.303	10	13.94	13.37	13.74	17.76	27.88	49.61
040610/1 (layer 1)	152	1.078	6.999	11.29	16.81	19.21	13.81	28.16	95.51	255.8
040610/1 (layer 2)	73	4.263	4.868	10.52	14.19	13.43	14.20	17.22	29.23	37.28
040610/6 (layer 1)	202	4.591	5.387	10.91	14.74	14	14.32	18.83	27.91	49.61
040610/6 (layer 2)	50	4.326	5.068	7.09	11.44	11.09	11.14	14.84	25.76	33.78

Since the empirical correlations of k_{sw} and particle-size data were based on d_E values, there was generally good spatial correlation between k_{sw} predictions and the particle-size diameters measured at each location in Fig. 5.33. More specifically, the highest k_{sw} predictions could be linked to the presence of lenses of coarser material.

For instance, the greatest k_{sw} (computed as the geometric mean of the 13 methods) was 71.18 m/day and corresponded to a sample with the highest d_{25} value as measured by sieve analysis (040610/1-T4 at 0.975 m AHD). This was assumed to be a representative k_{sw} value for coarse-grained lenses.

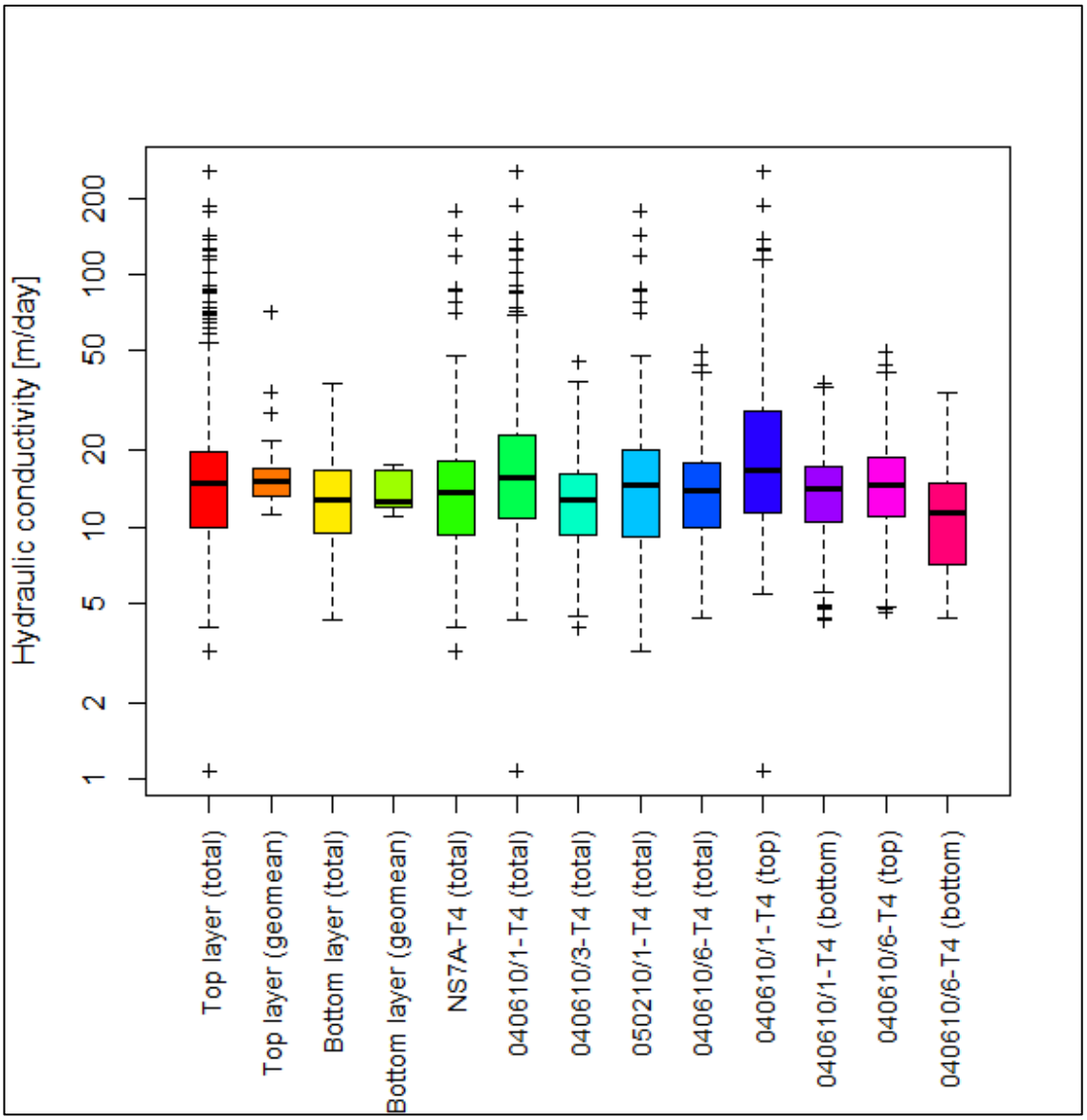


Fig. 7.37. Boxplots of k_{sw} predictions discriminating by location (well and layer). NS7A-T4 refers to the sum of data from 040610/3-T4 and 050210/1-T4.

7.4.2.2 Neural network predictions

Boxplots and summary statistics of the neural network predictions conducted with RETC are shown in Fig. 7.38 and Table 7.28. In both, NS7A-T4 refers to the sum of data from 040610/3-T4 and 050210/1-T4.

The obtained range of k_{sw} (4.206–15.74 m/day) was narrower than in the case of empirical correlations. Furthermore, the 5 %-trimmed range (9.672–14.99 m/day) was practically within the IQR of the empirical correlations (9.782–19.12 m/day). Moreover, the lowest p25 for any of the considered sets was 9.573 m/day, while the highest Q3 was 14.68 m/day, thus almost within the IQR of the empirical correlations as well.

Table 7.28. Summary statistics of k_{sw} predictions obtained with RETC. *Layer 1* refers to the top layer (above 0.4 m AHD), while *Layer 2* refers to the bottom layer (below 0.4 m AHD).

	N	MIN	p5	Q1	M	GEO-MEAN	MODE	Q3	p95	MAX
Area T4 (total)	66	4.206	9.672	12.73	13.73	13.01	13.72	14.34	14.99	15.74
Layer 1 (total)	53	4.206	9.548	12.58	13.69	12.87	14.06	14.35	14.99	15.74
Layer 2 (total)	13	10.85	11.37	13.33	13.77	13.55	13.74	14.25	14.95	15
NS7A-T4 (total)	22	4.206	8.487	11.15	13.15	11.92	13.60	13.85	14.93	15
040610/1 (total)	20	9.966	11.88	13.31	14.04	13.69	14.23	14.62	15.09	15.74
040610/3 (total)	13	4.206	6.743	9.573	12.58	10.92	13.71	13.08	14.54	15
050210/1 (total)	9	10.75	11.74	13.52	13.69	13.53	13.05	14.05	14.78	14.96
040610/6 (total)	24	10.85	11.72	12.84	13.73	13.49	14.03	14.37	14.82	15.03
040610/1 (layer 1)	13	9.966	11.17	12.26	14.3	13.56	14.50	14.68	15.33	15.74
040610/1 (layer 2)	7	13.27	13.29	13.55	14.01	13.94	14.01	14.16	14.72	14.92
040610/6 (layer 1)	19	11.74	12.17	13.06	13.86	13.69	14.19	14.39	14.86	15.03
040610/6 (layer 2)	5	10.85	11.03	11.72	13.46	12.77	13.72	13.64	14.37	14.56

Therefore, both approaches were relatively consistent with each other in spite of the absence of high extreme values in RETC and the prediction of slightly lower k_{sw} compared to HydrogeoSieveXL (the median, geometric mean, and mode were just 0.6, 1.5, and 1.0 m/day lower, respectively). This absence of extreme high predictions contributed to produce a slightly left-skewed distribution.

As expected, considerably lower deviations were associated to RETC predictions (CVR and CV values of 8.83 % and 14.23 %, respectively, for the full set of data with RETC instead of 47.99 % and 110.58 % with HydrogeoSieveXL) because of the combination of multiple methods in HydrogeoSieveXL. In addition, much of the variability in k_{sw} was due

to changes in ρ_b as illustrated in Fig. 7.39. The variance of k_{sw} was 3.526 (m/day)^2, while natural logarithms presented an extremely low value of 0.035 (m/day)^2. This reduction supported the hypothesis that determining aquifer heterogeneity by the variance of the natural logarithm of k_{sw} must account for other aspects, including the k_{sw} estimation method. In particular, alternative approaches should be followed to determine aquifer heterogeneity when predicted k_{sw} values do not resemble a logarithmic distribution.

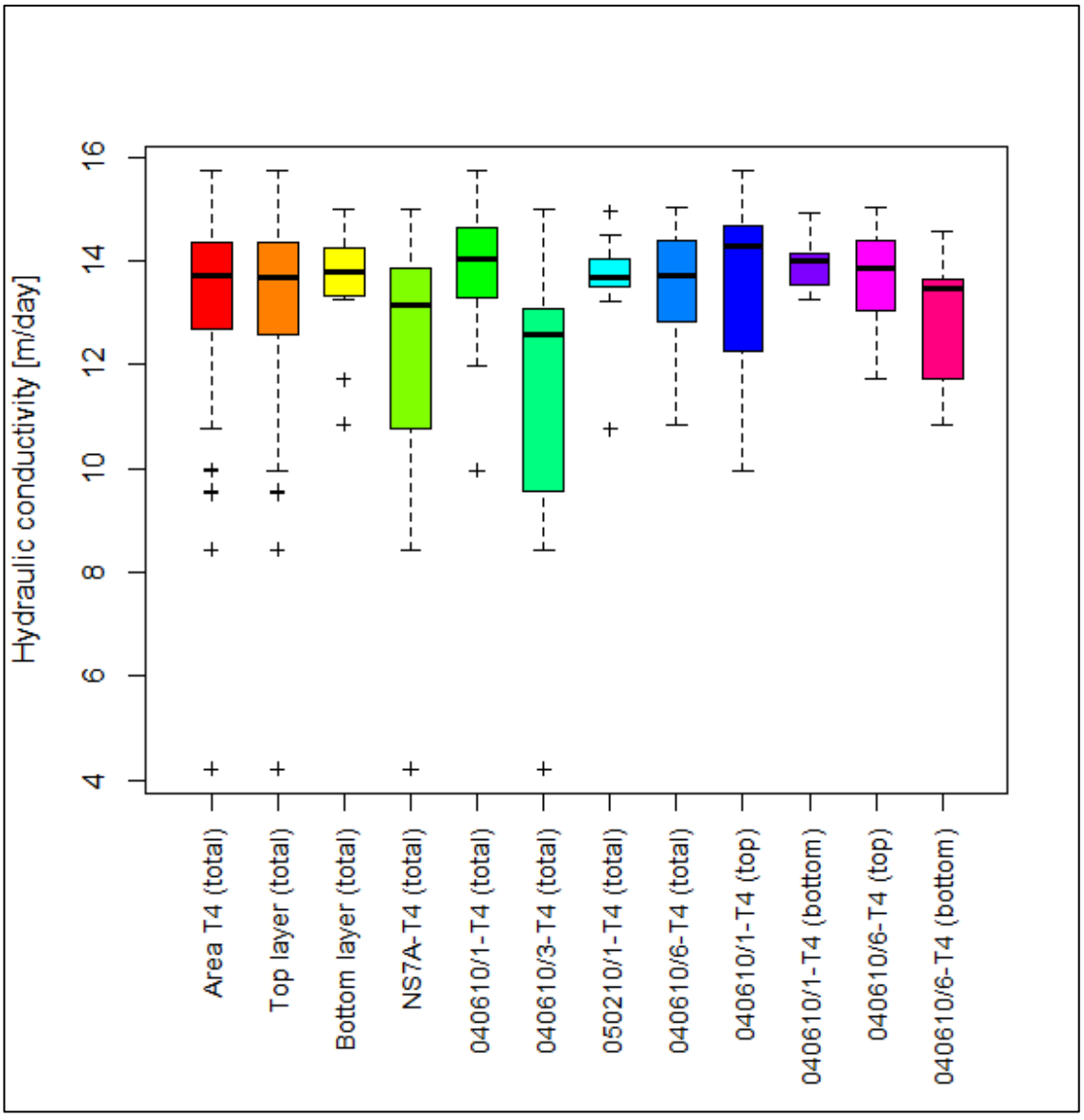


Fig. 7.38. Boxplots of k_{sw} predictions obtained with RETC.

Both layers produced similar central values and exhibited greater dispersion in the upper layer, although not so clearly in the case of empirical models. Additionally, it was also more evident that k_{sw} was predicted to be lower at 040610/3-T4 than in other locations,

with the median of 040610/3-T4 falling out of the IQR of 050210/1-T4 despite the short distance between them.

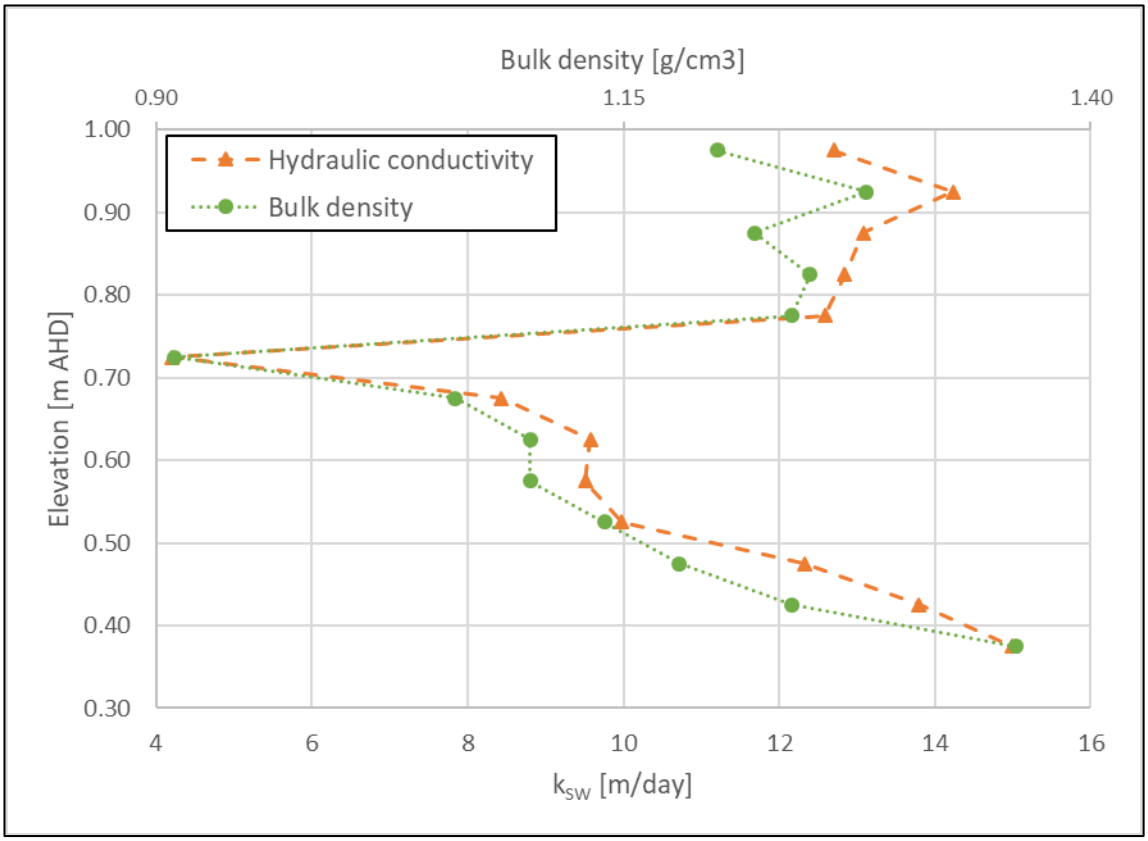


Fig. 7.39. Influence of ρ_b on k_{sw} (core 040610/3-T4).

7.4.2.3 Permeameter measurements

Measurements with a constant-head permeameter in five cores from a different area of the industrial site yielded k_{sw} values from approximately 3 to 115 m/day. A 0.25-m core apparently corresponding to the top layer provided high k_{sw} values from almost 50 m/day to the maximum of 115 m/day with a mean of 67.9 m/day throughout the core.

Since permeameter measurements were conducted in triplicate with different hydraulic gradients, the maximum of 115 m/day corresponded to a specific hydraulic gradient, while the average of the three tests at the same elevation was around 87 m/day. Analogously, the minimum of 3 m/day corresponded to an average of approximately 4 m/day.

Measurements in the other five cores (one from the upper layer and other three from the lower layer) did not exceed 25 m/day, obtaining an average of 7.9 m/day on the

other core corresponding to the top layer. Averages of 8.17, 11.0, and 14.4 m/day were estimated in the other locations.

Despite the distance between these samples and areas T3 and T4 (around 450 m and 300 m, respectively), the permeameter measurements supported the potential existence of high k_{sw} values in the top layer as predicted from particle-size data. Furthermore, permeameter measurements normally refer to vertical k_{sw}, commonly lower than horizontal k_{sw} (Song et al., 2009). Constant-head permeameter measurements in samples low in fines (less than 2 %) have been reported to include errors between 5 and 10 %, which are expected to be higher in finer-grained materials (Rosas et al., 2014).

7.4.2.4 HPT logging

Summary statistics for every log at HPT20-T3 and k_{sw} predictions across the whole industrial site are presented in Table 7.29. Density traces are depicted in Fig. 7.40. Estimated k_{sw} values were within a range of 10.06–30.48 m/day with an IQR of 17.83–27.13 m/day at HPT20-T3. Therefore, minimum values were consistent with other methods applied in other areas (similar to minima obtained with various empirical correlations as well as the p25 of 9.782 m/day obtained from geometric mean of all the empirical correlations and a p5 of 9.672 m/day from the neural network predictions in area T4). Estimations derived from particle-size data were still able to predict lower k_{sw} values that were likely in the industrial site according to permeameter measurements.

Considering all the HPT profiles in the industrial site, the range of k_{sw} got expanded to 5.182–45.72 m/day (still less than one order of magnitude) with a narrow IQR of 16.46–23.77 m/day, therefore lower than at HPT20-T3. The minimum value was above the assumed HPT method lower limit of quantification of 0.03 m/day and was consistent with other techniques. Therefore, this lower limit of quantification did not directly affect the comparison of HPT predictions with those derived from particle-size analysis in the industrial site.

Nonetheless, central values from the combination of all the HPT logs were generally higher (up to 10 m/day difference) than estimations from most of methods using sieve analysis data, although similar to Hazen estimates. Good correlation between Hazen and

direct-push estimations has already been reported in the literature (Butler et al., 2007), but it was shown in section 7.4.2.1 that Hazen formula usually produced higher k_{sw} values than the geometric mean of the 13 empirical correlations combined. Comparing Hazen estimates to measurements with an air permeameter, Eggleston and Rojstaczer (2001) found that Hazen generally overestimated k_{sw} and underestimated its variability in their set of samples, which was consistent with the pattern exhibited by Hazen and HPT estimates in the industrial site. The IQR was also slightly higher than those obtained from particle-size analysis and most of permeameter measurements. Nevertheless, Cheng and Chen (2007) indicated that empirical correlations such as Hazen could underestimate k_{sw} compared to the analysis of pumping test data. Therefore, HPT logging should not be assumed to overestimate k_{sw} without further evidence.

Table 7.29. Summary statistics of HPT logs at HPT20-T3 discriminating between saturated (excluding the capillary fringe) and vadose zones.

Statistic	k_{sw} [m/day] (all HPT logs)	HPT average pressure [kPa]	Corrected HPT pressure [kPa]	k_{sw} [m/day]	k_{sw} [m/day] (vad. zone)	EC [mS/m] (sat. zone)	EC [mS/m] (vad. zone)	C. press. [kPa] (sat. zone)	C. press. [kPa] (vad. zone)
n	1992	534	534	247	287	247	270	247	287
MIN	5.182	107.6	2.33	10.06	4.852	17.54	4.99	3.94	2.33
p5	11.58	109.3	3.946	13.5	7.985	19.18	5.709	5.07	3.669
Q1	16.46	120.6	5.518	17.83	18.43	31.02	6.322	6.96	4.425
MEDIAN	20.42	129.8	16.88	21.03	21.28	34.04	8.43	17.19	16.52
GEOMEAN	20.15	135.9	15.01	20.97	20.61	33.12	8.975	15.94	14.25
MEAN	21.4	139	25.23	21.62	22.2	33.75	9.906	21.48	28.47
MODE	20.81	129.6	5.667	20.82	29.93	32.52	6.363	8.382	5.013
Q3	23.77	141.9	27.68	27.13	29.81	37.95	11.54	29.12	25.18
p95	45.72	207.4	92.52	28.96	30.99	42.05	21.81	54.79	126.2
MAX	45.72	303.9	198.6	30.48	33.88	42.95	27.02	94.4	198.6
SD	7.908	32.66	30.56	5.162	7.462	6.086	4.995	16.59	38.48
MAD	5.423	14.77	16.78	7.23	11.11	5.352	3.432	15.64	17.81
NIQ	5.423	15.77	16.43	6.891	8.439	5.133	3.871	16.43	15.39
CV	36.96	23.49	121.1	23.88	33.61	18.03	50.43	77.25	135.2
CVR	26.55	11.38	99.41	34.38	52.23	15.72	40.71	90.99	107.8
SKEWNESS	1.49	1.886	2.645	-0.023	-0.457	-0.770	1.629	1.22	2.176
KURTOSIS	2.733	3.791	7.752	-1.14	-0.837	0.357	2.099	1.162	4.081

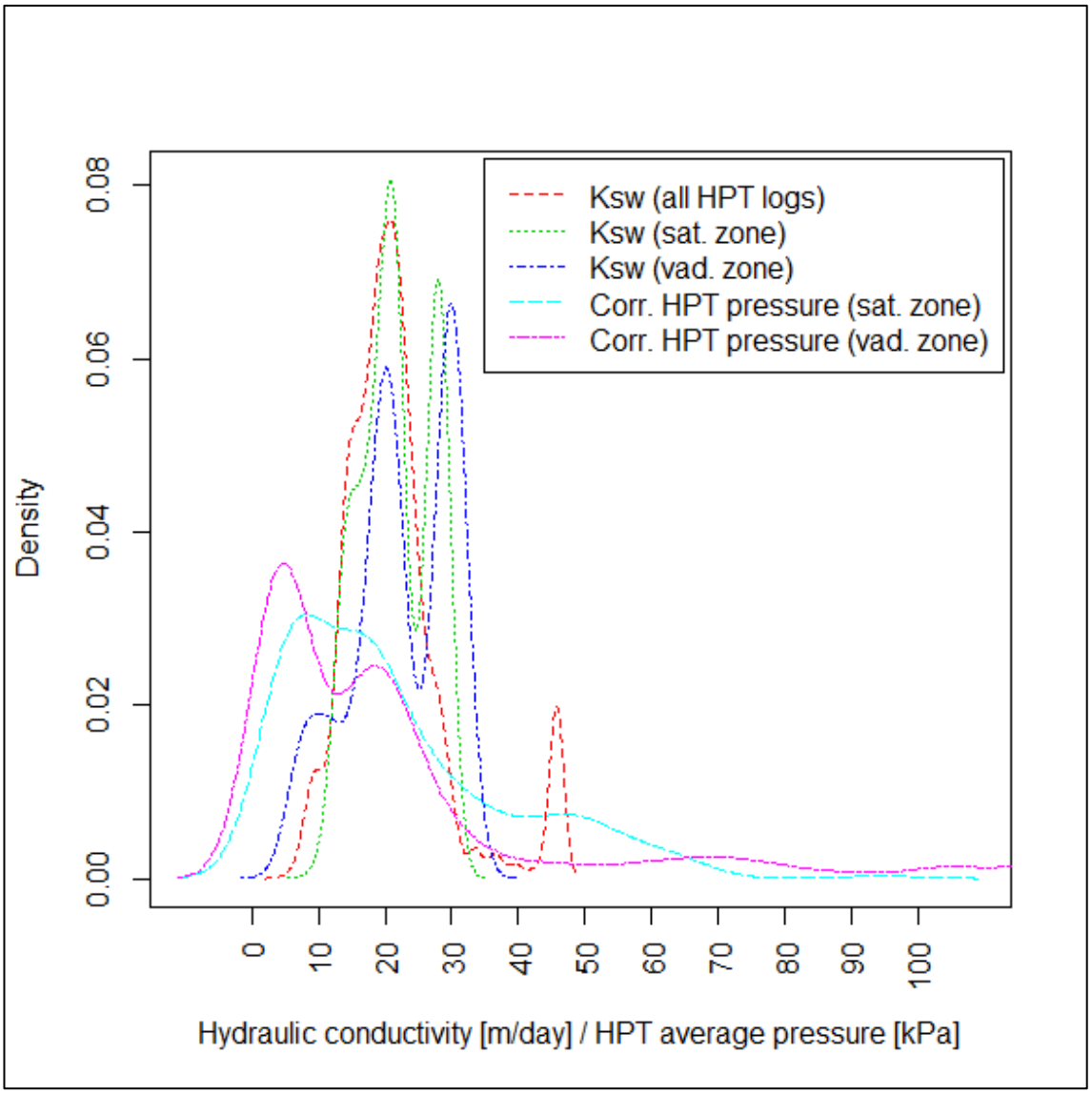


Fig. 7.40. Density traces of k_{sw} and corrected HPT pressure below the presumed water table and in the vadose zone at HPT20-T3. 'k_{sw} (all HPT logs)' corresponds to all the available HPT data from the industrial site in the saturated zone.

Underestimations of the true k_{sw} could be expected from HPT logging, since the method could be negatively influenced by the presence of LNAPL, while estimations derived from particle-size data were independent from the existence of LNAPL and potential bioclogging. As in the case of the petrol station site, observations from the industrial site did not suggest that LNAPL presence influenced HPT readings nor its applicability in LNAPL contaminated sites because of multifluid and bioclogging effects.

Furthermore, almost 25 % of the predictions were over the HPT method upper limit of approximately 25 m/day. More specifically, more than 5 % of values were equal to the

maximum of 45.72 m/day and that value could be considered an artefact derived from corrected HPT pressures of 0 kPa (such corrected HPT pressures of 0 kPa were most likely not due to a wrong correction of hydrostatic pressure, but to anomalous records of HPT pressure like in the clear example of HPT32-T5D9 at 0.9 m AHD shown in Fig. 5.38). Therefore, HPT logging could not adequately quantify highly transmissive intervals in the industrial site with the pre-existing quantification model, although could allow a quick qualitative identification of fine-layering conditions in the subsurface and provided a set of generally reasonable k_{sw} values. The existence of highly transmissive intervals was supported by permeameter measurements.

Values of k_{sw} from the saturated zone at HPT20-T3 presented a variance of 24.647 $(m/day)^2$, decreasing to 0.06 when natural logarithms were taken (similar to the value obtained with RETC). Logconductivity variance was also extremely low (0.12) when all the HPT logs collected in the industrial site were considered. These values reflected the relative homogeneity of the aquifer. Corrected values of pressure at HPT20-T3 had a variance of 933.86 kPa^2 (1.00 in natural logarithms) with their arithmetic mean decreasing from 139.0 kPa before the correction to 25.234 kPa. The variance of HPT P and k_{sw} parameters differed due to the non-linear quantification model.

Despite the right-skewed distributions of corrected HPT pressures depicted in Fig. 7.40, the resulting distributions of k_{sw} presented a much higher symmetry and the use of logarithms on HPT data to define the permeability field could not be justified. These observations reinforced that lognormality should always be evaluated despite frequent lognormal distributions being reported in the literature (Bohling et al., 2012), although non-Gaussianity in the lognormal distribution has been shown to not always strongly affect solute transport predictions (Fiori et al., 2015b). Besides of the variance of logconductivity, more robust metrics such as IQR, MAD, NIQ, CVR, and 5 %-trimmed ranges could be used to report the aquifer heterogeneity of field sites which are not completely Gaussian. These observations also supported that the method used to quantify k_{sw} should always be communicated when reporting values of variance as a measure of heterogeneity or to allow the development of permeability fields in stochastic simulations. Other authors have also found that the variance of logconductivity vary with the calibration method (Bohling et al., 2016).

In addition, values of k_{sw} in the vadose zone at HPT20-T3 exhibited a similar distribution to k_{sw} estimates from the saturated zone (excluding the capillary fringe), being both quantified following the same formula and not needing correction for hydrostatic pressure in the vadose zone. This good agreement was unexpected due to the unsaturated conditions affecting k_{rw}, thus the values could be concentrated around the same central values partly because of the quantification procedure. Future research should focus on further assessing the quantification models and their ranges of application in water-saturated and multifluid systems.

Despite the uncertainty around the estimations in the vadose zone, k_{sw} was found to be slightly higher than below the water table, which was consistent with higher predictions of k_{sw} above 0.4 m AHD than at greater depths as derived from sieve analysis data. Vadose zone predictions also included some of the lowest values (below 10 m/day), principally because of the finer-grained layer detected above 1.2 m AHD (see section 5.3.4).

As depicted in Fig. 7.41, estimations of k_{sw} through HPT logging were within the range obtained through empirical correlations and were therefore considered reasonable. Furthermore, predictions of k_{sw} in the vadose zone were consistent with other methods and results from the saturated zone and assigned low k_{sw} values to the finer-grained layer found above 1.20 m AHD at HPT20-T3. The small decrease in k_{sw} according at 0.6 m AHD in HPT20-T3 was almost coincident with a wide k_{sw} range obtained with empirical correlations at 0.575 m AHD which corresponded to a gap-graded sample in 040610/1-T4. A lens of k_{sw} values over 30 m/day was detected at 1.0–1.2 m AHD in area T3, while minimum values obtained from particle-size data were also higher above 0.9–1.0 m AHD. Differences between HPT logging and empirical methods could have been derived from hydrostratigraphic contrasts between areas T3 and T4.

Nevertheless, due to the high degree of geological homogeneity found in the industrial site, it could be inferred that the HPT system possibly overestimated k_{sw} compared to the geometric mean of 13 empirical models combined, being in the same range of Hazen's formula estimations. However, HPT predicted values were reasonable and empirical correlations have been found to underestimate k_{sw} in some scenarios (Cheng

and Chen, 2007). Neural network predictions with RETC were appreciably lower and were contained in a very narrow range.

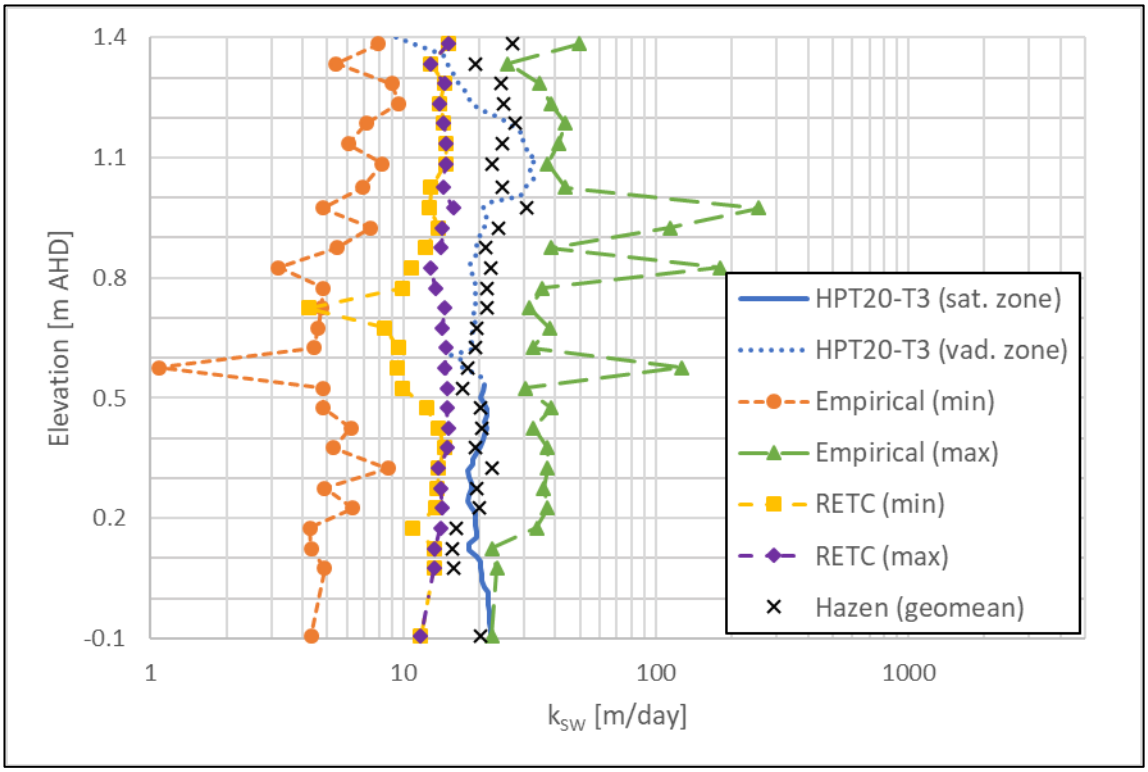


Fig. 7.41. Comparison of k_{sw} estimates from HPT logging at HPT20-T3 versus empirical correlations and neural network predictions in four cores from area T4. Samples from 040610/6-T4 were combined with samples from the other cores collected 0.1 m deeper.

7.4.2.5 Reference values and ranges

The absence of HPT logs in area T4 favoured the use of k_{sw} estimates derived from particle-size data in area T4 as most likely values for the model scenarios. Table 7.30 summarises reference values and ranges for the model scenarios in area T4. A reference value of 14 m/day was selected for NS7A-T4 (sum of data from 040610/3-T4 and 050210/1-T4), representative of central values of the empirical models and within 5 %-trimmed ranges of neural network predictions and HPT logging (except for 040610/6-T4 that was slightly higher than the neural network predictions).

Table 7.30. Reference values and ranges of k_{sw} [m/day] for the analytical models.

Reference value(s)	Most likely range	Extended range	Conservative range
14 (NS7A-T4)	5.44–43.87	4–87	0.01–255.8

The most likely range was assumed to be the 5 %-trimmed range obtained through empirical correlations since it represented the variability found with multiple methods consistent with each other, including HPT logging. The 5 %-trimmed range was chosen instead of the IQR due to the strong variability of k_{sw} and the uncertainties exposed by the comparison of all the methods.

The extended range was taken from average permeameter measurements. Finally, a minimum of 0.01 m/day was chosen for the conservative range as it has been reported as a minimum of k_{sw} in fine sands (Fetter, 2018). The other extreme of the range corresponded to the maximum obtained with empirical correlations, already representing k_{sw} from coarse sands (Domenico and Schwartz, 1998).

7.4.3 Retention parameters

7.4.3.1 Predictions derived from particle-size data

As presented in section 7.3.3, the method of Ghanbarian et al. (2010) was not very sensitive to the low clay contents in the petrol station site. Similarly, it was not expected that this approach would perform satisfactorily in the sands from the industrial site. The reason was that the empirical formula used to compute fractal dimensions and derive $vG\text{-}N$ has been reported to frequently show a low R^2 with sand samples (Huang and Zhang, 2005). In fact, forcing a low fractal dimension of 2 (related to coarse-grained soils) still resulted in a value of $vG\text{-}N$ lower than expected for sands with practically no fines. Therefore, this fractal approach could not adequately predict the retention curve in fine sands with contents of clay and silt below 5 %.

Nevertheless, the method was applied in every sample to gain insight on the range of $vG\text{-}\alpha$ that could be found in the subsurface. Fig. 7.42 illustrates the wide $vG\text{-}\alpha$ range of more than one order of magnitude derived only from modifications of the approach of Ghanbarian et al. (2010).

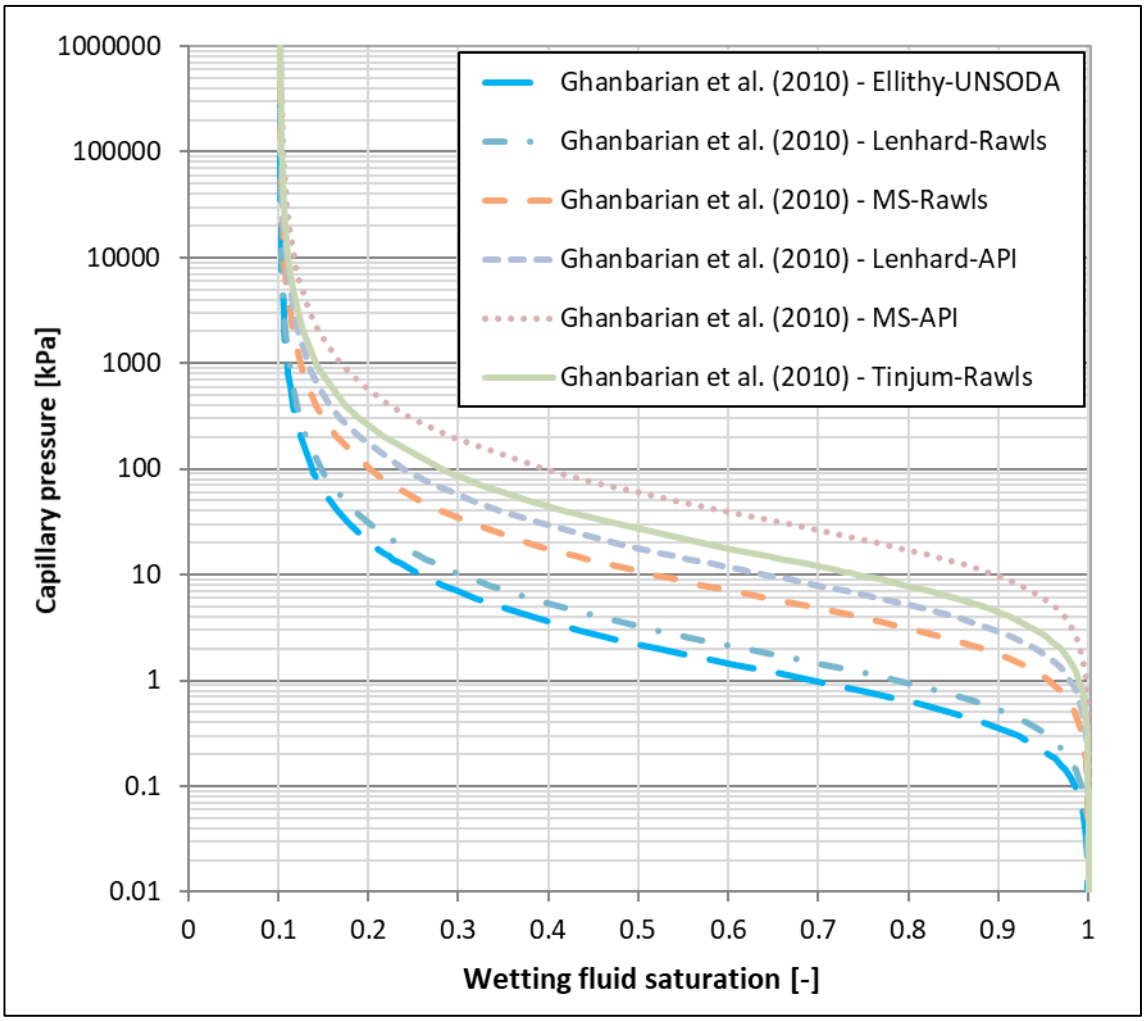


Fig. 7.42. Effects of the method used to predict $vG\text{-}\alpha$ in Ghanbarian et al. (2010) at 040610/3-T4 (1.025 m AHD). *Ellithy* refers to Ellithy (2017), *Lenhard* to Lenhard et al. (1989b), *MS* to Morel-Seytoux et al. (1996) and *Tinjum* to Tinjum et al. (1999). Initial values of h_{min} were taken as geometric means of sands from *Rawls* (Rawls et al., 1982) and SP samples from the *API* database (API, 2006).

The weak sensitivity of the fractal dimension to variations in clay content within the ranges found in the industrial site and the fact that all the samples represented the same type of soil in the USDA and USCS classifications produced practically constant values of both $vG\text{-}\alpha$ and $vG\text{-}N$ with the method of Ghanbarian et al. (2010) as shown in Fig. 7.43. Consequently, this fractal approach could not be used to characterise any variability in the retention parameters between sand samples with low contents of clays and silts.

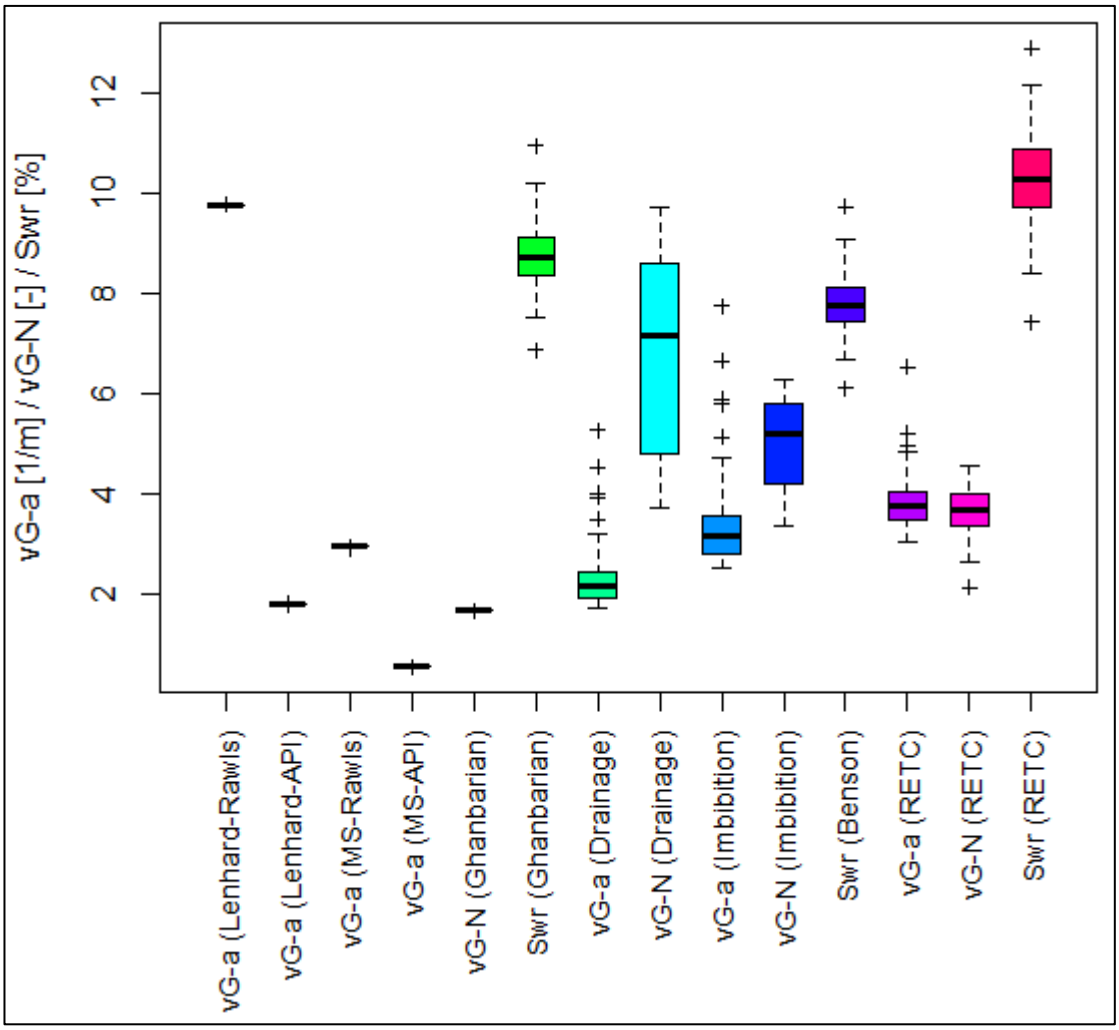


Fig. 7.43. Box-plots of retention parameters. *Lenhard* and *MS* refer to the methods of Lenhard et al. (1989b) and Morel-Seytoux et al. (1996) to estimate $vG\text{-}\alpha$. *Rawls* and *API* refer to Rawls et al. (1982) and API (2006) as sources of h_{min}. *Ghanbarian*, *Benson,* and *RETC* refer to the methods of Ghanbarian et al. (2010), Benson et al. (2014), and Schaap et al. (2001), respectively. Benson et al. (2014) produced *Drainage* and *Imbibition* parameters.

More specifically, a narrow $vG\text{-}\alpha$ range of 9.761–9.781 m^{-1} (median of 9.764 m^{-1}, geometric mean of 9.765 m^{-1}) was obtained through the method of Lenhard et al. (1989b) taking the h_{min} value from Rawls et al. (1982). These values were considerably higher than any predictions through the methods off Benson et al. (2014) or van Genuchten et al. (1991) and only surpassed by the constant value of 14.5 m^{-1} taken from Carsel and Parrish (1988) by Ellithy (2017). On the other hand, the method of Morel-Seytoux et al. (1996) with a h_{min} value taken from API (2006) resulted in an extremely low range of 0.525–0.536 m^{-1} (geometric mean of 0.534 m^{-1}).

Better predictions were apparently obtained combining the method of Lenhard et al. (1989b) with values from API (2006), which generated a geometric mean of 1.776 m^{-1} closer to the low range of vG-α values produced through Benson et al. (2014) for the drainage path. Finally, combining the method of Morel-Seytoux et al. (1996) and displacement pressures from Rawls et al. (1982) predicted a geometric mean of vG-α equal to 2.934 m^{-1}, consistent with ranges obtained through Benson et al. (2014) and neural network predictions presented in Table 7.31.

Table 7.31. Summary statistics of retention parameters in area T4.

Statistic	Benson et al. (2014) – Drainage vG-α [m^{-1}]	Benson et al. (2014) – Drainage vG-N [-]	Benson et al. (2014) – Imbibition vG-α [m^{-1}]	Benson et al. (2014) – Imbibition vG-N [-]	Benson et al. (2014) – S_{wr} [-]	RETC – vG-α [m^{-1}]	RETC – vG-N [-]	RETC – S_{wr} [-]
n	66	66	66	66	66	66	66	66
MIN	1.711	3.717	2.519	3.347	0.0609	3.04	2.11	0.0742
p5	1.748	4.029	2.574	3.566	0.0685	3.255	2.674	0.0857
Q1	1.886	4.805	2.776	4.183	0.0744	3.462	3.339	0.0973
M	2.123	7.15	3.125	5.18	0.0774	3.745	3.643	0.1025
GEO-MEAN	2.215	6.579	3.26	4.926	0.0774	3.797	3.597	0.1023
MEAN	2.284	6.843	3.361	5.001	0.0776	3.834	3.633	0.1027
MODE	1.9084	8.4569	2.8091	5.7177	0.0726	3.5040	3.9189	0.1014
Q3	2.409	8.551	3.546	5.771	0.0809	4.015	3.98	0.1086
p95	3.811	9.196	5.61	6.033	0.0869	4.912	4.307	0.1165
MAX	5.25	9.714	7.727	6.249	0.0973	6.51	4.551	0.1289
SD	0.6616	1.836	0.9738	0.8432	0.0060	0.5719	0.4885	0.0095
MAD	0.3925	2.36	0.5777	0.9956	0.0053	0.4151	0.4772	0.0087
NIQ	0.3877	2.777	0.5706	1.178	0.0048	0.4096	0.475	0.0084
CV	28.97	26.83	28.97	16.86	7.675	14.92	13.45	9.2040
CVR	18.49	33.01	18.49	19.22	6.791	11.08	13.1	8.4810
SKEW-NESS	2.444	-0.2206	2.444	-0.3744	0.3354	1.959	-0.6903	-0.2631
KUR-TOSIS	6.627	-1.477	6.627	-1.26	1.247	5.766	0.3615	0.6978

Values of vG-α predicted with RETC (IQR of 3.462–4.015 m^{-1}) and the method of Benson et al. (2014) were in a closer agreement with SP samples from the API database (API,

2006) than with the mean reported by Carsel and Parrish (1988). RETC commonly predicted slightly higher values than the method of Benson et al. (2014).

The later computed a lower $vG\text{-}\alpha$ for the drainage path than the imbibition path as expected. More specifically, the full range of values experimented an increase of 47 % in the imbibition path due to the method formulas. The IQR of the drainage path was 1.886–2.409 m^{-1} while the imbibition path presented an IQR of 2.776–3.546 m^{-1}. Limitations of the empirical relationships derived in identical values of CVR, skewness and kurtosis for both paths.

Regarding $vG\text{-}N$, a geometric mean of 1.646 and a narrow range of 1.637–1.649 were obtained with the method of Ghanbarian et al. (2010), clearly below estimates from the method of Benson et al. (2014) and neural network predictions as well as reported values in the API database (API, 2006) and Carsel and Parrish (1988).

In general, $vG\text{-}N$ values were lower with RETC (IQR between 3.339 and 3.980) than with the method of Benson et al. (2014) and lower for the imbibition path (IQR of 4.183–5.771) than for the drainage path (IQR equal to 4.805–8.551). These values were consistent with the API database (API, 2006), although slightly higher in the case of the drainage path. In addition, the estimated $vG\text{-}N$ ranges through these two methods were usually over the average given by Carsel and Parrish (1988).

Values of $vG\text{-}N$ corresponding to the drainage path exhibited a greater spread than those from the imbibition path. Furthermore, RETC estimations exhibited a lower degree of variability than the empirical method. This apparently low variability was also observed in the prediction of k_{sw} with RETC.

Finally, S_{wr} predictions with the three methods were in a relatively close agreement, exhibiting a combined range equal to 6.09–12.89 %. These values were consistent with Carsel and Parrish (1988) and API (2006), although S_{wr} values as high as those found in the API database were not identified in the industrial site.

Benson et al. (2014) and Ghanbarian et al. (2010) as presented by Ellithy (2017) assumed constant θ_{wr} values of 4 % and 4.5 %, respectively. Therefore, the distribution of S_{wr} was directly linked to the variability in Φ and both methods presented the same CVR,

skewness and kurtosis and the S_{wr} range was consequently a 12.5 % higher in the case of Ghanbarian et al. (2010).

RETC predicted a S_{wr} range of 7.42–12.89 % with a narrow IQR of 9.73–10.86 %, which was not too distant from physical measurements between 10.7 % and 15.7 % by Steffy et al. (1997b) and Yimsiri et al. (2018) in relatively similar sands. In this case and due to the limitations of the other methods, RETC presented a higher variability in the prediction of S_{wr}, although it was also influenced by measurements of ρ_b.

Fig. 7.44 illustrates the variability of retention parameters with elevation as exemplified with estimations from RETC in area T4. The proposed bottom layer below 0.4 m AHD exhibited a slightly lower variability than the interval between 0.4 and 1.05 m AHD. In general, central values of $vG\text{-}\alpha$ were slightly lower in the bottom layer, while $vG\text{-}N$ and S_{wr} were slightly higher. Extreme values of retention parameters were obtained at 040610/3-T4 (0.725 m AHD), although such anomaly was not identified in other cores or through other methods like Benson et al. (2014). Likely the reason was the extremely low measurement of ρ_b (0.91 g/cm^3) employed by RETC but not by other methods. Additionally, only two samples resulted in S_{wr} predictions over 12 %.

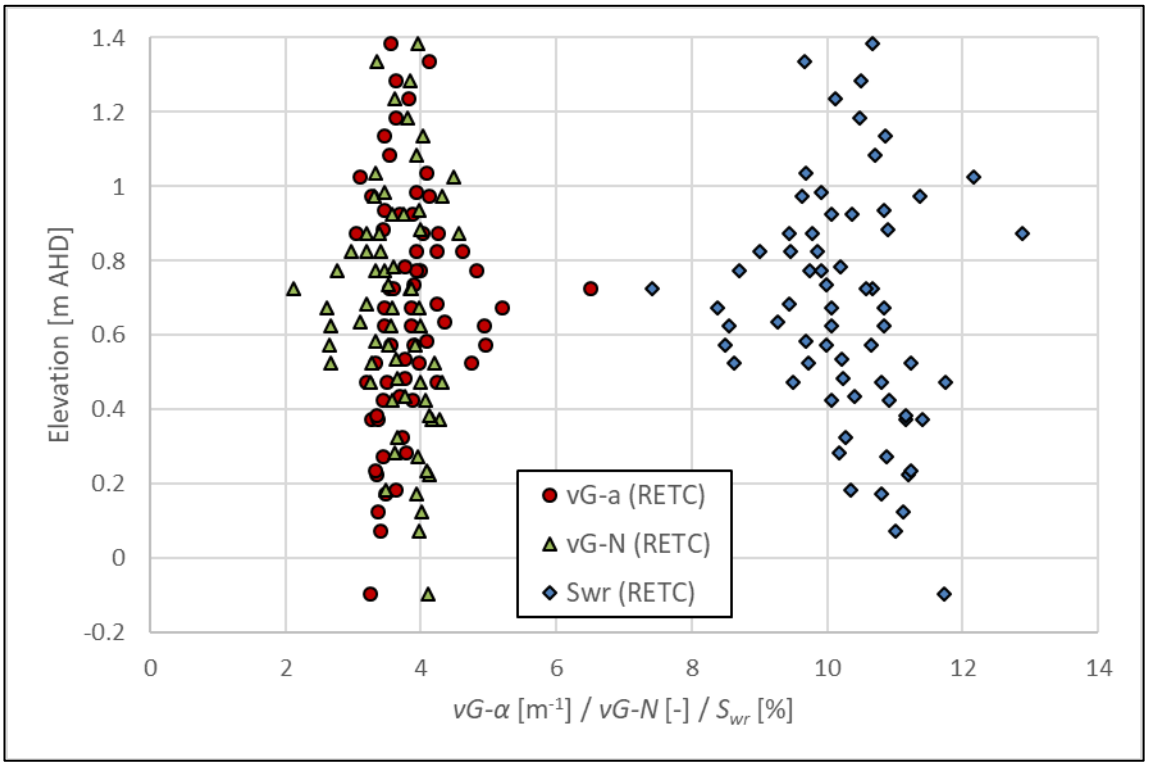


Fig. 7.44. Retention parameters as estimated through RETC versus elevation in area T4.

Fig. 7.45 depicts the density traces of retention parameters discriminating between two layers (above and below 0.4 m AHD) in area T4. In Fig. 7.45, drainage and imbibition parameters were combined and subsequently averaged with the neural network predictions to obtain values assumed as a reference for the modelling scenarios. Nevertheless, similar patterns to the use of only RETC predictions were observed between the two layers (slightly lower $vG\text{-}\alpha$ and higher $vG\text{-}N$ at the bottom layer).

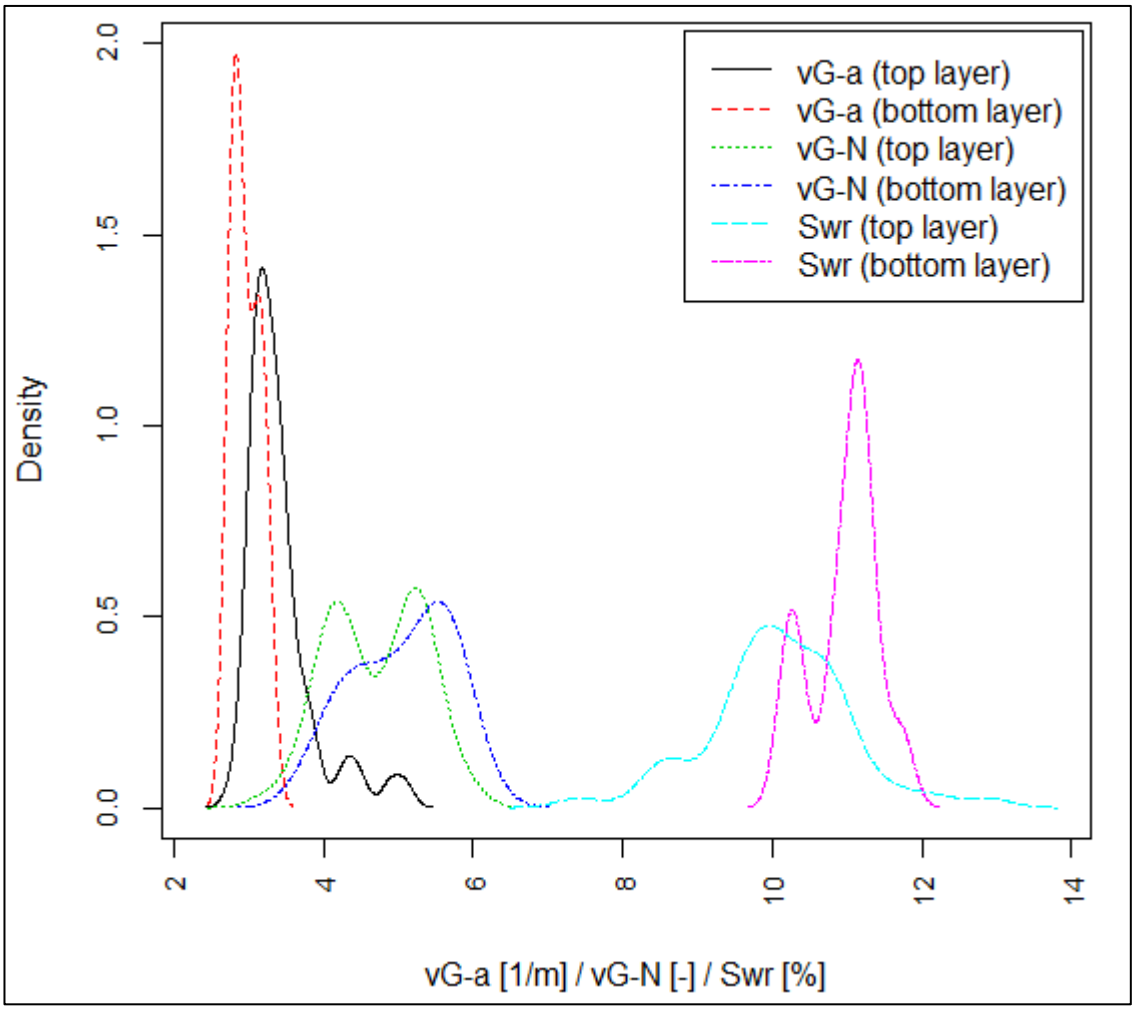


Fig. 7.45. Density traces of retention parameters discriminating between two layers in area T4.

As shown in Table 7.32, new ranges resulting from the averaging procedure were 2.744–5.093 m^{-1} for $vG\text{-}\alpha$ and 3.246–5.955 for $vG\text{-}N$, consistent with experimental measurements and the API database (API, 2006). S_{wr} values were solely taken from RETC due to their proximity to experimental measurements and because of limitations of other approaches.

Table 7.32. Summary statistics of retention parameters discriminating between two layers and different locations in area T4. G refers to the geometric mean.

	Site	N	MIN	p5	Q1	M	G	MODE	Q3	p95	MAX
vG-α [m^{-1}]	Area T4	66	2.744	2.809	3.077	3.212	3.301	3.149	3.444	4.329	5.093
	Layer 1	53	2.802	3.000	3.125	3.314	3.390	3.180	3.529	4.411	5.093
	Layer 2	13	2.744	2.752	2.827	2.905	2.961	2.832	3.158	3.223	3.288
	NS7A-T4	22	2.802	2.855	3.091	3.316	3.393	3.161	3.546	4.459	5.093
	040610/1	20	2.744	2.757	3.069	3.182	3.327	3.145	3.439	4.385	4.884
	040610/6	24	2.782	2.832	3.076	3.233	3.198	3.250	3.355	3.544	3.751
	040610/1 (layer 1)	13	2.971	3.034	3.125	3.325	3.513	3.208	3.833	4.569	4.884
	040610/6 (layer 1)	19	2.965	3.031	3.124	3.262	3.275	3.288	3.360	3.578	3.751
	040610/1 (layer 2)	7	2.744	2.748	2.832	3.049	3.006	3.145	3.170	3.256	3.288
	040610/6 (layer 2)	5	2.782	2.791	2.827	2.862	2.922	2.835	2.996	3.125	3.158
vG-N [-]	Area T4	66	3.246	3.821	4.203	4.869	4.733	5.258	5.318	5.661	5.955
	Layer 1	53	3.246	3.773	4.186	4.843	4.665	5.230	5.258	5.526	5.903
	Layer 2	13	3.915	4.110	4.448	5.069	5.019	5.533	5.628	5.780	5.955
	NS7A-T4	22	3.246	3.804	4.362	4.970	4.753	5.136	5.277	5.506	5.903
	040610/1	20	3.676	3.741	4.205	4.427	4.684	4.247	5.329	5.898	5.955
	040610/6	24	3.909	3.926	4.165	4.956	4.755	5.291	5.288	5.555	5.628
	040610/1 (layer 1)	13	3.676	3.717	4.139	4.313	4.521	4.147	5.317	5.575	5.895
	040610/6 (layer 1)	19	3.909	3.981	4.154	4.843	4.705	5.286	5.242	5.507	5.565
	040610/1 (layer 2)	7	4.240	4.279	4.410	4.979	5.002	4.467	5.661	5.867	5.955
	040610/6 (layer 2)	5	3.915	4.100	4.838	5.069	4.950	5.331	5.498	5.602	5.628
Swr [-]	Layer 1	53	0.074	0.085	0.097	0.101	0.101	0.099	0.107	0.115	0.129
	Layer 2	13	0.102	0.102	0.108	0.111	0.110	0.111	0.112	0.115	0.117
	NS7A-T4	22	0.074	0.084	0.091	0.099	0.098	0.099	0.103	0.117	0.129
	040610/1	20	0.087	0.094	0.102	0.108	0.106	0.110	0.110	0.114	0.122
	040610/6	24	0.093	0.095	0.100	0.103	0.103	0.103	0.107	0.112	0.117
	040610/1 (layer 1)	13	0.087	0.092	0.097	0.107	0.104	0.108	0.108	0.117	0.122
	040610/6 (layer 1)	19	0.093	0.094	0.098	0.102	0.102	0.110	0.106	0.109	0.109
	040610/1 (layer 2)	7	0.103	0.104	0.108	0.110	0.110	0.103	0.112	0.113	0.114
	040610/6 (layer 2)	5	0.102	0.102	0.104	0.112	0.109	0.113	0.112	0.116	0.117

Further distinction between drainage and imbibition parameters was not made because differences between both paths as exclusively predicted with Benson et al. (2014) were generally lower than differences with other methods.

7.4.3.2 Laboratory measurements

Laboratory measurements of retention parameters on 5-cm cores from 040610/2-T4 (adjacent to 040610/1-T4) are summarised in Table 7.33 for drainage paths and Table 7.34 for imbibition paths. Retention data fitted with six soil hydraulic models are included in Appendix F: Retention curves.

Table 7.33. Drainage retention parameters estimated at 040610/2-T4.

Elevation [m AHD]	S_{wr} [-]	*vG-α* [m^{-1}]	*vG-N* [-]
1.036	0.143	5.56	3.598
0.586	0.266	2.17	5.764
0.086	0.618	1.18	5.893

Table 7.34. Imbibition retention parameters estimated at 040610/2-T4.

Elevation [m AHD]	S_{wi} [-]	S_{wr} [-]	*vG-α* [m^{-1}]	*vG-N* [-]
1.036	0.901	0.093	12.74	2.222
0.586	0.883	0.249	3.46	3.859
0.086	0.952	0.610	2.18	3.416

The vG model predictions were in a relatively close agreement with the measured data, although more complicated bimodal models generally provided the best fitting. The pattern shown by measured data at high S_w values was not very well represented by B–C predictions in many cases.

Laboratory measurements resulted in ranges of *vG-α*, *vG-N*, and S_{wr} between 1.18 and 12.74 m^{-1}, 2.222 and 5.893, and 9.3 % and 61.8 %, respectively. The sample at 1.036 m AHD was observed to be coarser-grained than the others, while the sample at 0.086 m AHD was finer-grained than the others. Therefore, there was an expected increase of S_{wr} and an expected decrease of *vG-α* with grain size, although S_{wr} presented a very wide range with much higher values than those predicted with other methods or found in the literature. The B–C model also resulted in S_{wr} values up to 55.8 %.

Nevertheless, 16 additional samples from other areas of the industrial site resulted in ranges of *vG-α*, *vG-N*, and S_{wr} between 2.05 and 10.72 m^{-1} (IQR of 2.48–4.92 m^{-1}), 1.96 and 6.91 (IQR of 2.95–5.34), and 6.8 % and 32.2 %, respectively. Arithmetic and geometric means of S_{wr} were 19.4 % and 17.5 %. Thus, the *vG-α* and S_{wr} ranges at 040610/2-T4 were extremely wide compared to the rest of the industrial site.

Regarding the values obtained at 1.036 m AHD, the experimental values of S_{wr} were consistent with other methods deriving retention parameters from hydrogeological data at a similar elevation in the adjacent well of 040610/1-T4. The range between the experimental drainage and the imbibition curves could contain all the other S_{wr} estimations since both curves showed a strong contrast as illustrated in Fig. 7.46.

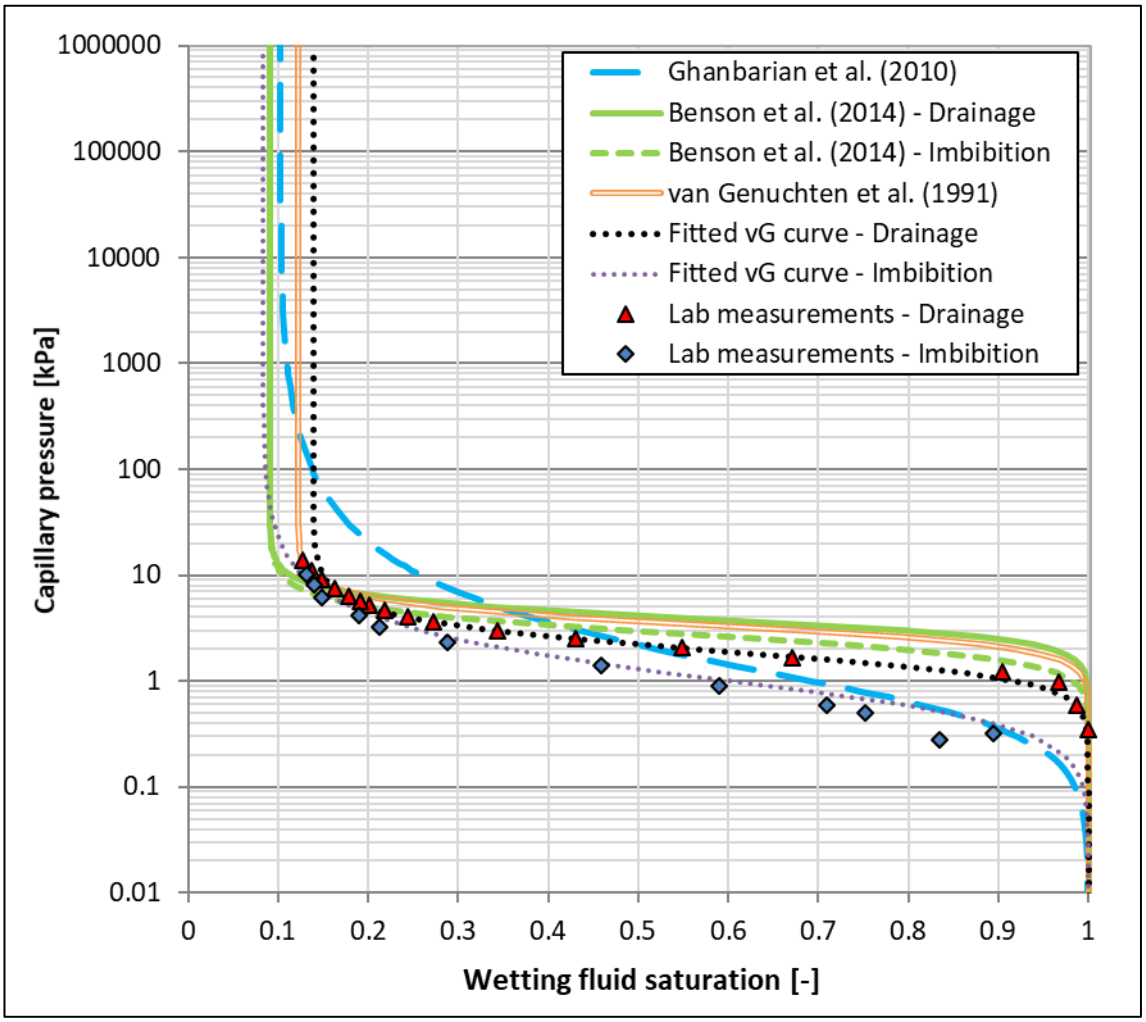


Fig. 7.46. Experimental measurements of P_c–S relationships at 040610/2-T4 (1.036 m AHD) and retention curves derived from hydrogeological data at 040610/1-T4 (1.025 m AHD).

In particular, the difference between the drainage and imbibition curves was more notable in the case of experimental measurements than using the method of Benson et al. (2014).

In addition, the experimental retention curves presented $vG\text{-}\alpha$ values higher than curves obtained through the methods of Benson et al. (2014) and RETC (van Genuchten et al., 1991), although the difference was small in the case of the experimental drainage curve that presented good agreement with the other methods. The effect of different values of $vG\text{-}\alpha$ is shown in Fig. 7.46, where the experimental retention curves exhibited a lower entry pressure than all the other curves, except the one predicted according to the method of Ghanbarian et al. (2010).

The method of Ghanbarian et al. (2010) as presented by Ellithy (2017) simply used default values of S_{wr} and $vG\text{-}\alpha$ from Carsel and Parrish (1988) since the prediction of $vG\text{-}\alpha$ according to the method of Lenhard et al. (1989b) presented in Ghanbarian et al. (2010) required a h_{min} value from the B–C model. Therefore, Ellithy (2017) assumed a high $vG\text{-}\alpha$ of 14.5 m^{-1}, similar to the value from the imbibition curve measured in the laboratory. In the case of area T4, data from 040610/2-T4 could be employed.

Thus, using a fitted h_{min} value of 1.150 kPa from 040610/2-T4 (1.036 m AHD) in the method of Lenhard et al. (1989b) produced a $vG\text{-}\alpha$ of 6.044 m^{-1} as illustrated in Fig. 7.47. Adding the fitted $vG\text{-}N$ value of 3.501 from 040610/2-T4 (1.036 m AHD) in the prediction of $vG\text{-}\alpha$ following Lenhard et al. (1989b) resulted in an estimation of 6.411 m^{-1} (not shown in Fig. 7.47) On the other hand, inferring $vG\text{-}\alpha$ through the method of Morel-Seytoux et al. (1996) from the same air-entry pressure resulted in a low value of 1.819 m^{-1} which only described well experimental data corresponding to the highest values of S_w. Lastly, the method of Tinjum et al. (1997) was not oriented to sands but to compacted clays and produced an unrealistic $vG\text{-}\alpha$ of 0.641 m^{-1}.

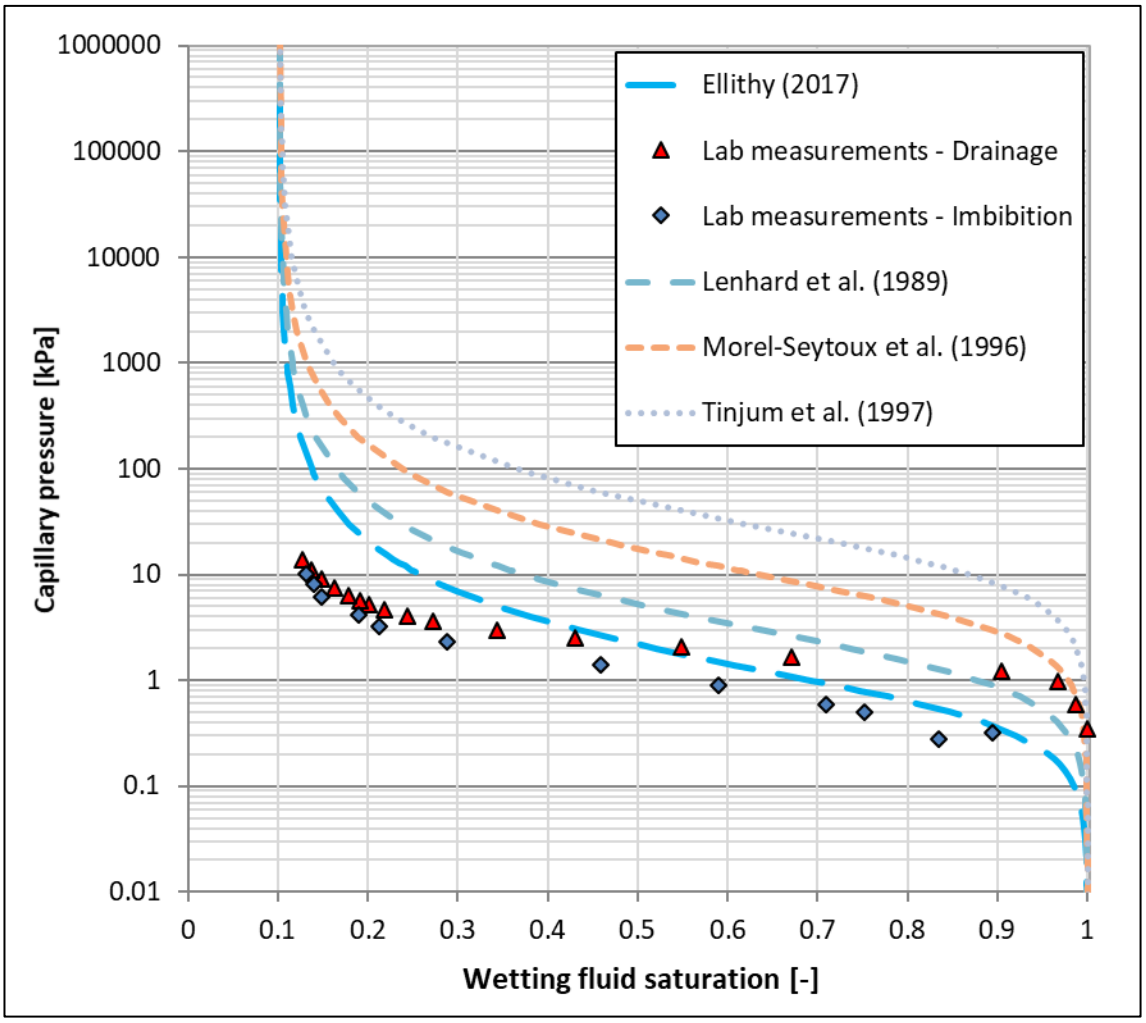


Fig. 7.47. Retention curves obtained in the laboratory and following the method of Ghanbarian et al. (2010) with different determinations of *vG-α*, including the default of Ellithy (2017).

Nevertheless, the curve obtained through the fractal approach of Ghanbarian et al. (2010) could not adequately fit the experimental imbibition curve because of the low *vG-N* value (1.65), while the other methods resulted in *vG-N* values slightly higher than the experimental measurements, especially for the imbibition curve. Ghanbarian et al. (2010) initially found that their method was more reliable than neural network predictions from Rosetta (Schaap et al., 2001) in terms of computing wetting fluid contents, while neural network predictions were more accurate in the estimation of *vG-N* (still overestimating it) and none of the methods generated reliable values of *vG-α*

after evaluating the options of Lenhard et al. (1989b) and Tinjum et al. (1997) in specific datasets. They did not discriminate between drainage and imbibition paths.

In addition, other empirical methods have been reported to produce low $vG\text{-}N$ values, for instance when C_u is high (Benson et al., 2014), suggesting that $vG\text{-}N$ may be kept over 2 in the case of sands if the predicted $vG\text{-}N$ is unreasonable. As depicted in Fig. 7.48, using an intermediate $vG\text{-}N$ value of 3.2 in the curve of Ghanbarian et al. (2010) resulted in better fitting of the laboratory data for the imbibition path.

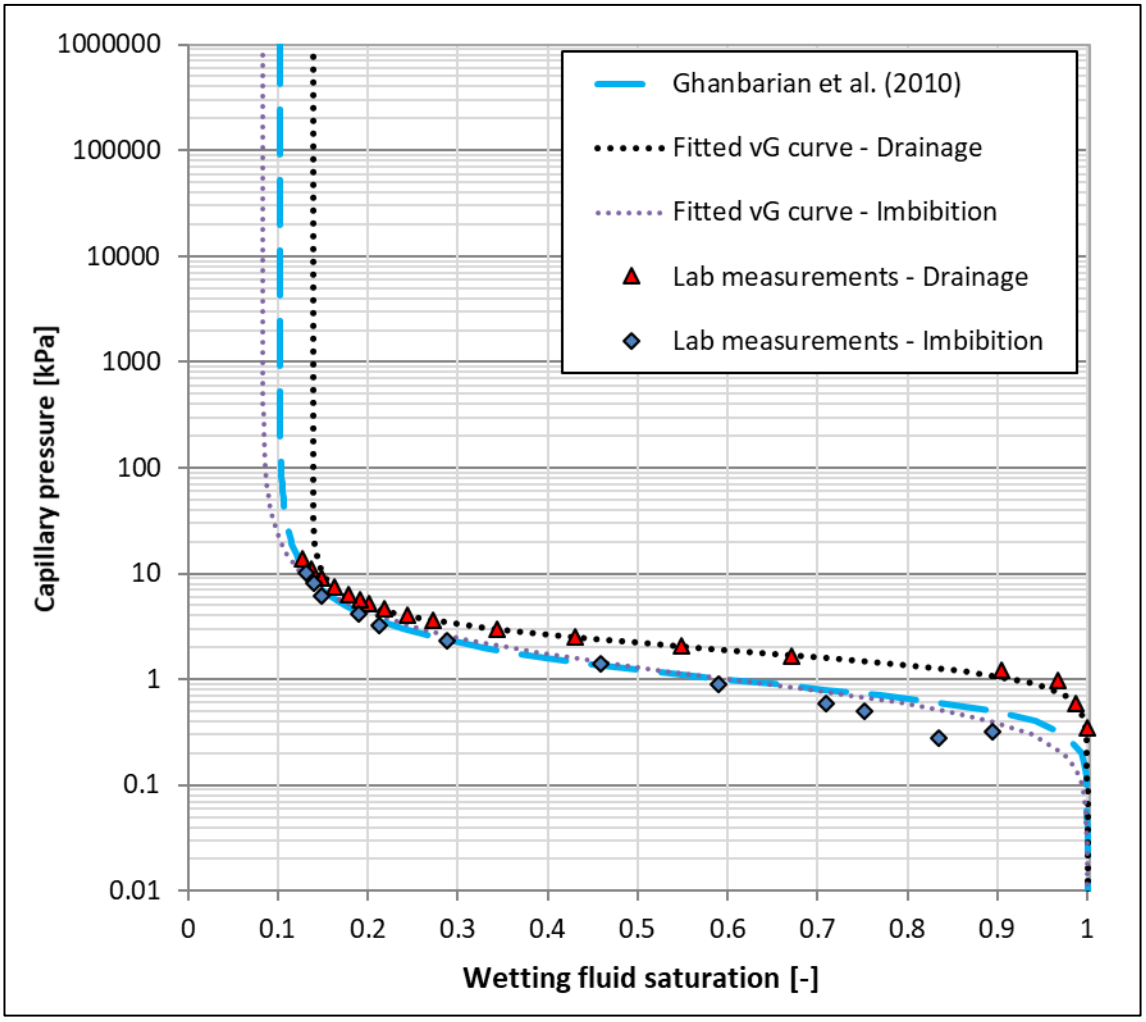


Fig. 7.48. Experimental retention curves at 040610/2-T4 (1.036 m AHD) versus Ghanbarian at 040610/1-T4 (1.025 m AHD), forcing $vG\text{-}N$ to be 3.2 instead of 1.6468.

Regarding the retention parameters measured at 0.586 m AHD, S_{wr} values were considerably higher than those obtained in section 7.4.3.1. However, Fig. 7.49 shows that the experiment finished before S_w became constant, rising uncertainties in the estimation of S_{wr}.

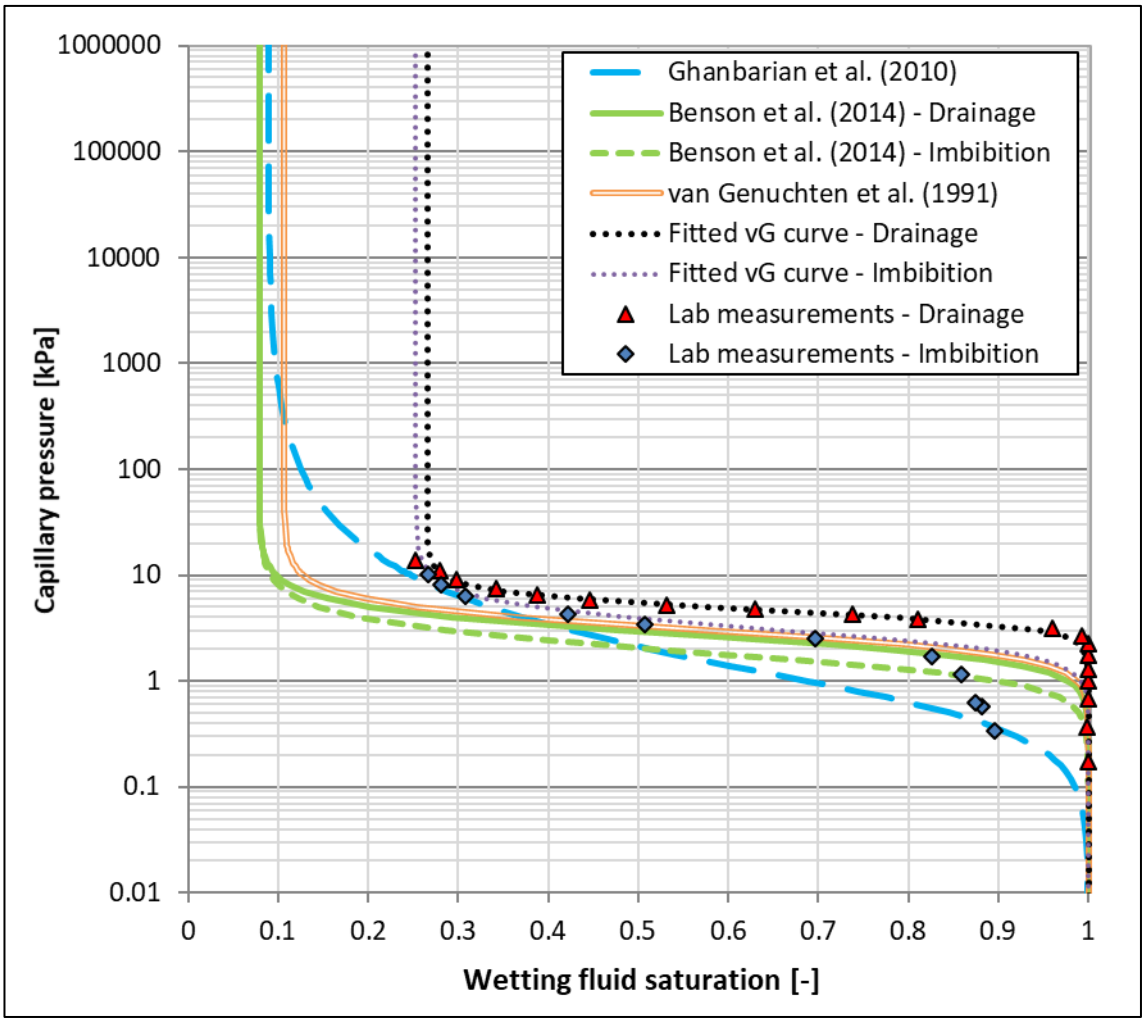


Fig. 7.49. Experimental measurements of P_c–S relationships at 040610/2-T4 (0.586 m AHD) and retention curves derived from hydrogeological data at 040610/1-T4 (0.575 m AHD).

Analogously to the previous case, the vG-N value estimated through Ghanbarian et al. (2010) was possibly underestimated, while the experimental range of vG-α contained the estimations of Benson et al. (2014) and RETC.

In addition, measurements along the imbibition path could not be adequately fitted by any of the vG curves without considering entrapment of the non-wetting fluid. Fig. 7.50 depicts the better fit obtained when assuming around 10 % of entrapped air.

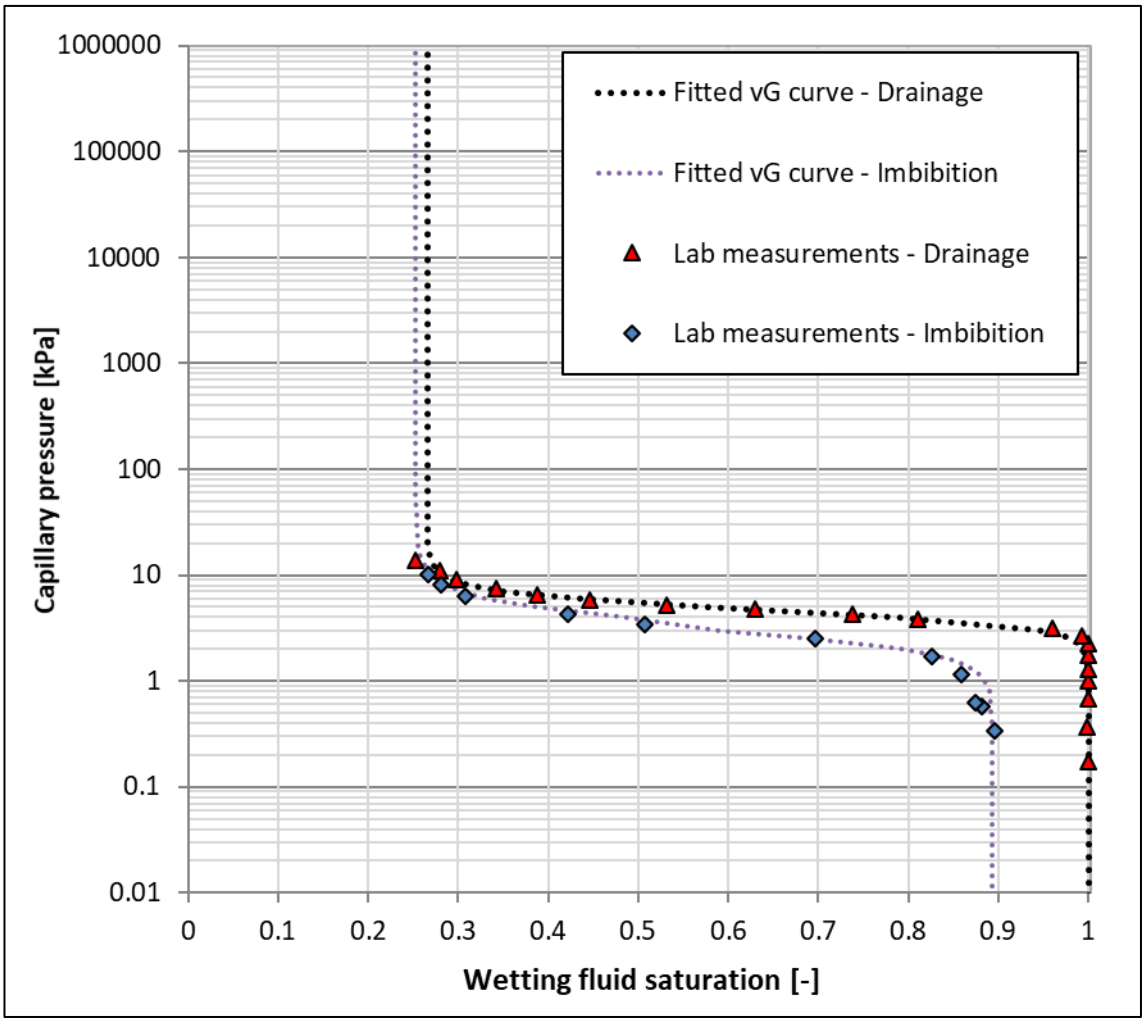


Fig. 7.50. Fitted vG curve considering entrapment of the non-wetting fluid along the imbibition path at 040610/2-T4 (0.586 m AHD).

Lastly, the measurements at 0.086 m AHD produced an unreasonably high S_{wr} prediction. Fig. 7.51 shows that the experiment finished in a relatively early stage and assuming such a high S_{wr} could be misleading. Therefore, S_{wr} estimations from the other methods were considered more representative of the subsurface conditions. In addition, $vG\text{-}N$ was probably underestimated through the method of Ghanbarian et al. (2010) and a range of $vG\text{-}\alpha$ values should be considered, in particular to account for hysteretic effects.

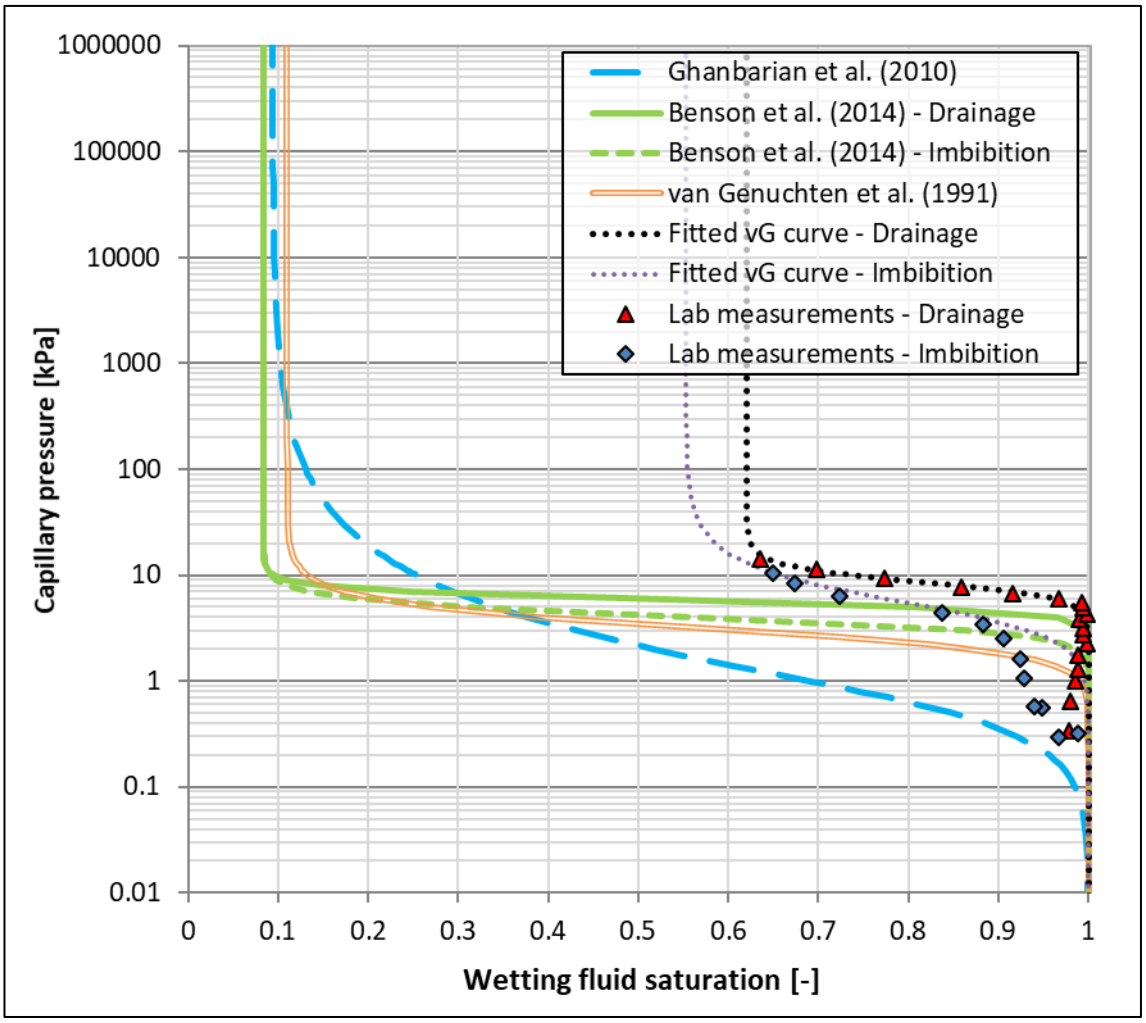


Fig. 7.51. Experimental measurements of P_c–S relationships at 040610/2-T4 (0.086 m AHD) and retention curves derived from particle-size data at 040610/1-T4 (0.075 m AHD).

7.4.3.3 Reference values and ranges

Table 7.35 presents reference values and ranges of retention parameters from area T4. Regarding *vG-α* and *vG-N*, the average of predictions from RETC and the method of Benson et al. (2014) resulted in ranges (shown in Table 7.32) consistent with the experimental measurements and the API database (API, 2006), although the experimental measurements exhibited a wider range and *vG-N* predictions were still slightly higher than laboratory measurements and the API database in some cases.

Furthermore, predictions from particle-size data were generally closer to laboratory measurements of the drainage path, while preliminary tests presented in Lenhard et al. (2019) showed that there could be a better agreement with field observations at 050210/1-T4 using imbibition parameters. Geometric means of the sets of data of

Benson et al. (2014) and RETC considering one and two model layers were taken as reference values.

Table 7.35. Reference values and ranges of retention parameters for the analytical models.

Parameter	Reference value(s)	Most likely range	Extended range	Conservative range
***vG-α* [m^{-1}]**	3.30 (one layer), 3.39 (top layer), 2.96 (bottom layer)	2.809–4.329	1.711–7.727	1.18–14.5
***vG-N* [-]**	4.73 (one layer), 4.67 (top layer), 5.02 (bottom layer)	3.821–5.661	2.11–6.91	1.74–9.714
S_{wr} [%]	10.1 (one layer), 9.8 (top layer), 11.0 (bottom layer)	8.6–11.7	6.8–15.6	2.0–48.6
S_{nr} [%]	10	7–15	3.8–18	0–45
S_{ne} [%]	15	7.5–20	6.7–25	0–45

The relatively narrow 5 %-trimmed ranges from Table 7.32 were considered to represent the most likely range of *vG-α* and *vG-N* since they were in a close agreement with the IQR of every method and the experimental measurements from the industrial site (considering the whole site and not only the 3 samples from area T4).

Additionally, the extended range of *vG-α* considered the methods of van Genuchten et al. (1991) and Benson et al. (2014) separately and the conservative range accounted for experimental measurements and literature values.

As concerns *vG-N*, the extended range included laboratory measurements from the industrial site, but not estimations for the drainage path from Benson et al. (2014), since this method probably overestimated *vG-N*. Therefore, the upper limit of the conservative range (9.714) corresponded to a value derived from particle-size data from the industrial site, higher than the maximum equal to 8 found in the API database (API, 2006).

Regarding S_{wr}, the reference value was assumed to be 10 % as already considered in preliminary tests published by Lenhard et al. (2019). This value was almost coincident with the geometric mean of RETC estimations (10.5 %). The most likely range was taken as the 5 %-trimmed range of RETC estimations. The extended range was defined by experimental measurements from field samples, being the upper limit of 15.6 % taken from the measurement in similar sands by Steffy et al. (1997b). The conservative range corresponded to the wide range shown in the API database (API, 2006). Laboratory measurements up to 61.8 % were not considered representative of subsurface conditions.

In terms of S_{nr}, the value of 10.5 % inferred from the S_n distribution at 040610/6-T4 (0.885 m AHD) was assumed as a reference value for the modelling scenarios. A most likely range of 7–15 % was derived from data reported by Mercer and Cohen (1990) for middle distillates in fine to medium sands, diesel and light fuel in soils. The extended range of 3.8–18 % considered the studies of Yimsiri et al. (2018) and Mercer and Cohen (1990), while the conservative range of 0–45 % assumed an upper $S_{nr}^{\max}$ equal to the $S_{ne}^{\max}$ reported by Steffy et al. (1997b) and a lower limit assuming that no residual LNAPL was formed.

Values of S_{ne} are typically higher than S_{nr} (Mercer and Cohen, 1990; Yimsiri et al., 2018). In the case of the industrial site, a S_{ne} of 15 % was assumed as a reference value taking into consideration the S_n profiles from areas T3 and T4. The most likely range (7.5–20 %) was also based on field observations of S_n profiles inferring plausible intervals of near-immobile LNAPL. The extended range was defined with measurements from Yimsiri et al. (2018) and the value of 25 % assumed in Lenhard et al. (2019) for the simulation of 050210/1-T4. Finally, the conservative range assumed a value of 0 % as the lower limit due to the narrow impacted interval compared to in-well fluid levels, while an upper limit of 45 % was selected, as measured by Steffy et al. (1997b) in sands similar to those found in areas T3/T4. Yimsiri et al. (2018) measured lower S_{ne} in medium sands than in fine sands as expected, although obtained relatively similar S_{nr} in both media.

7.4.4 LNAPL properties

Table 7.36 collects data for ρ_n, η_n, σ_{an}, and σ_{nw} from Mercer and Cohen (1990), API (2006), and field measurements in areas T3/T4. The row 'Area T4' refers to measurements exclusively from 040610/3-T4, 040610/6-T4, and 050210/1-T4 or adjacent wells. Both ρ_n and η_n were higher than in the petrol station site, as expected due to the presence of diesel instead of petrol.

Table 7.36. Literature values of diesel physical properties and statistical summary of field measurements from areas T3/T4. Values between parentheses represent averages.

Source/statistic	ρ_n [mg/cm^3]	η_n [cP]	σ_{an} [mN m^{-1}]	σ_{nw} [mN m^{-1}]
Mercer and Cohen (1990)	800-850	1.1-3.5	25	50
API (2006)	850	0.95	25.86	14.06
Johnston (2010)	832, 832	2.76, 4	22.3, 21.6	26.9, 27.5
Area T4	868–874 (872)	6.21–10.15 (8.18)	28.7	12.1–16.2 (14.15)
n	27	10	10	10
MIN	846.00	3.54	26.70	5.20
p5	849.80	3.54	26.79	5.25
Q1	859.50	3.83	27.30	7.85
MEDIAN	868.00	5.68	27.75	9.80
GEOMEAN	865.00	5.61	27.94	9.40
MEAN	865.10	6.03	27.96	10.03
MODE	870.37	4.71	27.59	8.66
Q3	871.00	7.17	28.62	11.98
p95	873.00	10.03	29.36	15.43
MAX	885.00	10.15	29.90	16.20
SD	8.85	2.47	0.98	3.68
MAD	7.41	2.88	1.11	3.19
NIQ	8.53	2.47	0.98	3.06
CV	1.02	40.99	3.50	36.66
CVR	0.85	50.68	4.01	32.53
SKEWNESS	-0.27	0.54	0.48	0.20
KURTOSIS	-0.36	-1.31	-0.93	-1.38

All the data corresponded to the period 2004–2005 (2004–2007 in the case of ρ_n) and temperature of 20 °C, except one sample of a diesel/gasoline mixture at 24–27 °C from API (2006) and the values for two types of diesel in Johnston (2010), where the first set of values correspond to a temperature of 25 °C and the second set was measured at

15 °C. It should also be noted that ρ_n was monitored in a regular basis, obtaining a total of 124 estimations across 26 wells in area T4 and 1 well in area T3. One average value was computed for each well to avoid the underrepresentation of some wells in the analysis presented in Table 7.36.

Field data of ρ_n, η_n, and σ_{an} were generally higher than values from Mercer and Cohen (1990), API (2006), and Johnston (2010), although still in close agreement. The shift from literature values could be explained by the LNAPL weathering process.

In contrast, the Mercer and Cohen (1990) value of σ_{nw} was around five times higher than field measurements. However, the API database (API, 2006) supported the results obtained in the field, providing a value near 50 mN m^{-1} for σ_{aw}, not σ_{nw}. In addition, tension measurements of unleaded 91 octane gasoline and unweathered diesel were conducted in the laboratory obtaining σ_{nw} values of 16.1 and 18.4 mN/m, respectively (19.4 and 26.9 mN/m for σ_{an}). Steffy et al. (1997b) also measured a σ_{nw} of 17 mN/m (σ_{an} of 25 mN/m). Therefore, using tabulated values from a popular reference such as Mercer and Cohen (1990) for this parameter may introduce errors. No outliers were identified according to the Iglewicz and Hoaglin (1993) criterium.

Histogram, density trace, scatterplot, and boxplot of ρ_n as measured in 27 wells from areas T3/T4 (26 wells from T4 and one from T3) are displayed in Fig. 7.52. This graphical representation facilitated the identification if two clusters of ρ_n values as 854–862 mg/cm^3 and 865–874 mg/cm^3, being 870 mg/cm^3 the mode of the entire data set. Extreme values below or over these ranges were not frequent. More specifically, measurements from 040610/3-T4, 040610/6-T4, and 050210/1-T4 or adjacent wells resulted in a range of ρ_n between 868 and 874 mg/cm^3, with averages of 870, 872, and 873 mg/cm^3 in three wells. Therefore, these monitoring points exhibited typical ρ_n values of areas T3/T4.

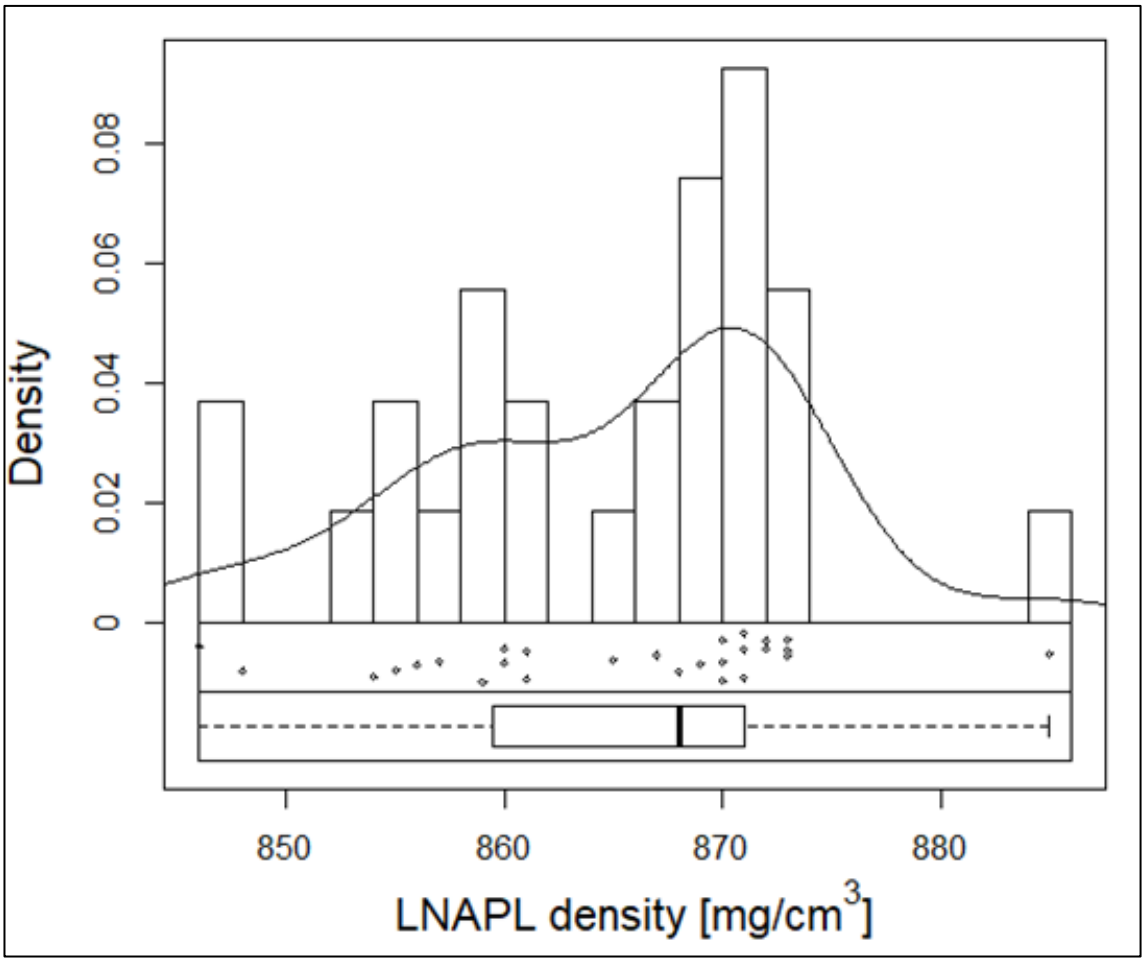


Fig. 7.52. ρ_n measurements from 27 wells in areas T3/T4 (minimum of 846 mg/cm^3 and maximum of 885 mg/cm^3).

Density traces of η_n, σ_{an}, and σ_{nw} as measured in the field are illustrated in Fig. 7.53. The distribution of η_n was apparently multimodal due to a few extreme high values, including the record of 10.15 cP from 040610/3-T4. This value represented an absolute maximum in area T4 despite the normal value in ρ_n (869–873 mg/cm^3 with an average of 872 mg/cm^3). A well adjacent to 040610/6-T4 presented a value of 6.21 cP, lower than the measurement at 040610/3-T4. Thus, this value was taken with caution and values within the IQR (3.83–7.17 cP), including the geometric mean of 5.61 cP and the measurement of 6.21 cP at 040610/6-T3, were considered to possibly represent the subsurface conditions at 040610/3-T4.

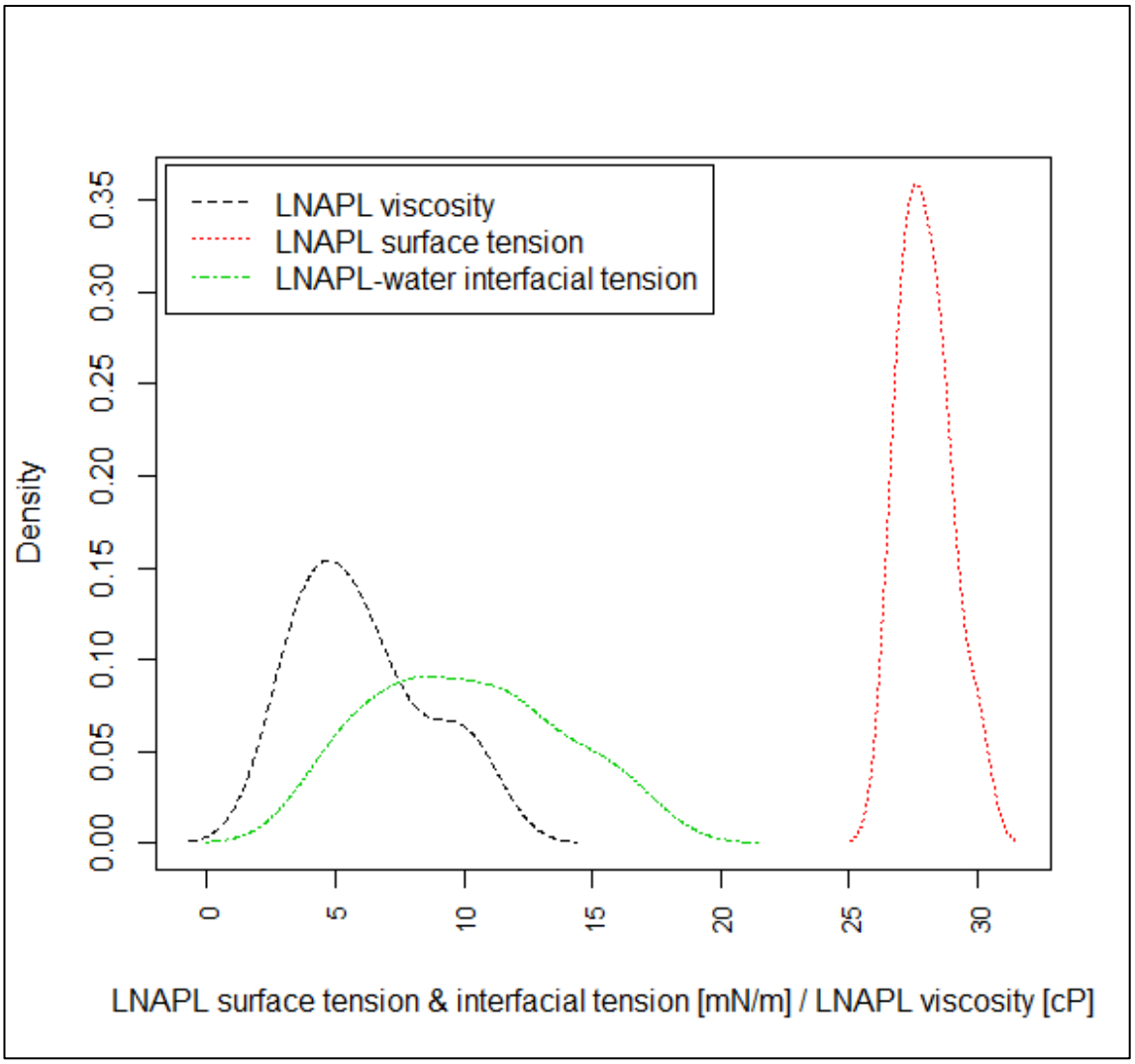


Fig. 7.53. Density traces of η_n, σ_{an}, and σ_{nw} as measured in area T4.

Measurements of σ_{an} exhibited a narrower distribution than the other physical properties and therefore it was expected to introduce a lower degree of variability into the model. Despite this, the two records from 040610/3-T4 and a well adjacent to 040610/6-T4 fell out of the IQR (27.30–28.62 mN/m) with a value of 28.7 mN/m.

Finally, σ_{nw} values from 040610/3-T4 (16.2 mN/m) and 040610/6-T4 (12.1 mN/m) fell out of the IQR from area T4 (7.85–11.98 mN/m) as well. In a similar way to η_n, the σ_{nw} value measured at 040610/3-T4 also represented an absolute maximum in area T4. Thus, the geometric mean value was employed instead of 16.1 mN/m or 12.1 mN/m if the initial predictions were not accurate enough.

In conclusion, ρ_n was likely within a range of 854–874 mg/cm^3 in the locations of concern, although the IQR for the complete dataset was 859.5–871 mg/cm^3. The most

likely value for the modelling scenarios was 872 mg/cm^3 (870 mg/cm^3 considering the full dataset), while the field range considering not only averages but all the measurements was 842–888 mg/cm^3.

Regarding η_n, preliminary model runs employed values of 5.61 cP (geometric mean), 6.21 cP (recorded at 040610/6-T4) and 10.15 cP (as measured at 040610/3-T4). The measurement from 040610/3-T4 represented an absolute maximum in area T4.

Analogously, several values of σ_{nw} were initially considered, including the geometric mean of 9.40 mN/m, 12.1 mN/m as recorded at 040610/6-T4, and 16.2 mN/m as measured at 040610/3-T4. The IQRs of η_n and σ_{nw} were extended to incorporate measurements from 040610/3-T4 and 040610/6-T4 in the extended ranges.

As concerns σ_{an}, the most likely value was assumed to be 28.7 mN/m as measured at 040610/3-T4 and a well adjacent to 040610/6-T4, while values within both the IQR (27.30–28.62 mN/m) and the field range (26.70–29.90 mN/m) were considered possible. Most likely values and potential ranges of data are summarised in Table 7.37.

Table 7.37. Reference values and ranges of LNAPL properties for model testing.

Parameter	Reference value(s)	Most likely range	Extended range	Conservative range
ρ_n [mg/cm^3]	872	859.5–874	846–885	800–888
η_n [cP]	5.61 (geomean), 6.21 (040610/6-T4), 10.15 (040610/3-T4)	3.83–7.17	3.54–10.03	0.95–10.15
σ_{an} [mN m^{-1}]	28.70	27.30–28.70	26.79–29.36	21.6–29.90
σ_{nw} [mN m^{-1}]	9.40 (geomean), 12.1 (040610/6-T4), 16.2 (040610/3-T4)	7.85–11.98	5.25–15.43	5.20–50

7.4.5 LNAPL transmissivity

A total of six baildown tests conducted in four wells of area T4 on 26/05/2004, 23/11/2004, and 01/12/2005 resulted in a range of T_n values between 0.026 and 0.111 m^2/day. T_n was obtained from the regression of b_n and *DTN* measurements, leading to two different sets of results due to the influence of z_{aw} fluctuations during the test on both measured parameters. The use of b_n resulted in a slightly better coefficient of determination for the regression model and generated lower T_n values (average of 0.060 m^2/day and median of 0.059 m^2/day instead of an average of 0.079 m^2/day and a median of 0.088 m^2/day when *DTN* values were employed). The predicted errors fell from 0.002 m^2/day with *DTN* to 0.001 m^2/day with b_n.

However, in the case of the baildown test conducted at 040610/3-T4 on 01/12/2005, z_{aw} remained practically stable during the test and there was practically no discrepancy between both methods (0.078 m^2/day using *DTN* and 0.072 m^2/day using b_n).

There was an increase in T_n between 26/05/2004 and 23/11/2004 as inferred by tests repeated at two wells on both dates. The average value increased from 0.037 m^2/day to 0.111 m^2/day considering *DTN* and from 0.039 m^2/day to 0.053 m^2/day considering b_n. This phenomenon was accompanied by slight drops in z_{aw} (0.020–0.025 m) and unexpectedly b_n (0.002–0.051 m).

Thus, the reasons behind these observations and the apparent increase in T_n were probably linked to other aspects such as the migration of LNAPL altering physical properties near the wells or the field estimation procedure of b_n and T_n. Regarding the baildown test at 040610/3-T4, z_{aw} was clearly lower (around 0.5–0.8 m) than on the tests from November 2004, although b_n was similar (less than 30 % difference), making the range 0.072–0.078 m^2/day consistent with the other measurements.

7.5 Summary of results and conclusions

In conclusion, HPT logging enabled rapid collection of large sets of high-resolution data across the industrial site and the petrol station site on real time. HPT logging enabled quantification of k_{sw} within reasonable ranges, although likely missing low and highly transmissive pathways and predicting central values of k_{sw} more than a third higher than the geometric mean of empirical correlations in the industrial site, where HPT

predictions were similar to those from Hazen method Thus, this line of evidence suggested that HPT readings were not greatly affected by LNAPL presence and bioclogging processes, since LNAPL mass and biomass should decrease the k_{sw} predictions from HPT, but not from empirical correlations. HPT also presented an acceptable agreement with estimations of k_{sw} and T_w through aquifer testing in the petrol station site, although certain metrics suggested the existence of preferential migration pathways in the subsurface.

Regarding the two applied d_E values, the most adequate d_E option was possibly linked to the C_u value of the sample, at least for sediments with C_u below 5. The model of Wang et al. (2017) performed well in the two sites, producing k_{sw} estimates close to the geometric mean of all the other empirical correlations considered. RETC predictions of k_{sw} were less accurate, most likely due to the limited input data provided.

Logconductivity variance as measured with HPT was extremely low (0.12) in the industrial site and could have been affected by non-Gaussianity in the probabilistic distribution of k_{sw}. Nevertheless, this value reflected the relatively homogeneous conditions of the subsurface. On the contrary, the HPT logconductivity variance was 7.7 in the petrol station site, although highly variable depending on the set of data considered. Thus, the variance within individual hydrostratigraphic units should also be reported and considered for stochastic modelling purposes.

Regarding the prediction of retention parameters, the variability between methods was commonly greater than the difference between considering drainage and imbibition paths in Benson et al. (2014). In addition, the fractal method of Ghanabarian et al. (2010) did not perform satisfactorily due to the lack of sensitivity to the clay contents found in the industrial site and even in the petrol station site.

Alternative interpretations of the baildown tests presented in Gatsios (2018) were explored and some improvements to the estimation of T_n through baildown testing were suggested. Measurement of T_n was particularly sensitive to drawdown adjustments. Therefore, improved methods to deal with non-equilibrium conditions deserve further investigation.

8 Evaluation of multiphase analytical models

8.1 Chapter structure

Chapter 8 briefly evaluates and compares two analytical models (LDRM and LNAPLTRANS) used to predict LNAPL distribution and T_n from in-well fluid levels and subsurface parameters. Input values were selected in according to analyses presented in previous chapters.

Section 8.2 tests capabilities of LDRM and LNAPLTRANS in base-case scenarios considering estimations of LNAPL distribution profiles, V_n, and T_n using Burdine and Mualem relative permeability models. Section 8.3 investigates the effects of layering in LNAPL distribution and mobility. In section 8.4, a sensitivity analysis of the two analytical models is performed considering the effects on V_n and T_n. Thus, the underlying assumptions of both models were compared. Implications of the uncertainty associated to the determination of hydrogeological settings and input parameters were explored. Section 8.5 presents a summary of results and conclusions from the chapter.

A paper titled 'Testing an analytical model for predicting subsurface LNAPL distributions from current and historic fluid levels in monitoring wells: a preliminary test considering hysteresis' published in Water is associated to the contents of this chapter. Its object was to test the capability of LNAPLTRANS to predict S_n distributions against field data from 050210/1-T4. In addition, it discussed the effects of using imbibition retention parameters instead of drainage ones as it is commonly done.

8.2 Base-case scenarios

8.2.1 Summary of base-case scenarios

Input values used for the base-case scenarios in areas A, B, C, and T4 are included in Table 8.1. Details of the sources of data can be found in the previous chapters, especially chapter 7. These values were considered reasonable and used to investigate the capabilities of the models, although they did not necessarily correspond to true nor optimal subsurface values. For instance, the presence of biomass and EPS may influence multiple properties including the retention characteristics of the system, but the methods employed did not account for this aspect.

Table 8.1. Details of base-case scenarios in areas A, B, C, and T4.

Area	A	B	C	T4
Φ [-]	45			49
k_{sw} [m/day]	12.4	10.3	3.0	14
$vG\text{-}\alpha$ [m^{-1}]	2.13			3.30
$vG\text{-}N$ [-]	2.74			4.73
S_{wr} [%]	10.9			10.1
S_{nr}^{max} [%]	1.2			10
S_{ne}^{max} [%]	0.1	1.2	3.3	15
ρ_n [mg/cm^3]	0.72	0.73	0.73	0.872
η_n [cP]	0.48	0.42	0.41	10.15
σ_{an} [mN/m]	23.38			28.70
σ_{nw} [mN/m]	20.51			16.2
z_{an} [m AHD]	56.229	56.232	56.356	0.317
z_{nw} [m AHD]	55.905	55.912	55.6	-0.355
z_{an}^{max} [m AHD]	57.25	57.13	59.0	0.482
z_{nw}^{min} [m AHD]	55.55	55.0	54.3	-0.530
T_n [m^2/day]	1.29–2.894	0.262–0.724	0.061–0.671	0.026–0.111

The base-scenario for area T4 represented a far more homogeneous system than the petrol station site (areas A, B, and C). Furthermore, LNAPL physical properties in area T4 corresponded to diesel, while only petrol was present in areas A, B, and C.

The base-case scenarios for both area T4 and area C represented systems with high b_n values (0.672 and 0.756 m, respectively) and relatively low T_n, while base-case scenarios for area A and area B reflected lower b_n values (0.324 and 0.320 m, respectively) and higher T_n, especially in area A.

8.2.2 Calibration issues

In addition to these base-case scenarios, Gatsios (2018) and Gatsios et al. (2018a) conducted LDRM simulations in areas A, B, and C. Values of S_{nr} between 0 and 4 % were chosen according to interpretations of field data and a calibration procedure to better match the vertical profiles of S_n measured through coring. Reasonable results were obtained in areas B and C, although the predicted LNAPL distribution in area B

corresponded to a typical shark fin shape and did not reflect the fining-upward characteristics of the stratigraphic profile.

Consequently, it was tested whether the set of parameters employed in Gatsios et al. (2018a) was robustly calibrated and could predict T_n in multiple dates. T_n values from baildown tests periodically conducted in area B were used for this purpose.

Table 8.2 shows that the simulation presented by Gatsios et al. (2018a) with in-well fluid levels from 20/05/2016 yielded the highest LDRM T_n prediction among all the dates considered. However, considerably higher T_n values were measured in the field in other days, with the four highest values corresponding to baildown tests conducted in 2015. A decrease in T_n with time at similar z_{aw} was reasonable due to formation of near-immobile LNAPL and NSZD processes, although other phenomena such as migration of LNAPL mass could reverse this relationship.

Table 8.2. T_n values at PB27-B measured through baildown testing (Gatsios, 2018) and predicted with LDRM using input parameters from Gatsios et al. (2018a). Baildown tests on 20/05/2016 and 14/06/2016 were conducted twice obtaining almost identical results (Gatsios, 2018).

Date	z_{aw} [m AHD]	b_n [m]	Field T_n [m^2/day]	LDRM T_n [m^2/day]
06/05/2015	56.250	0.350	0.91	0.17
06/05/2015	56.250	0.350	0.96	0.17
08/07/2015	56.185	0.360	1.33	0.3
20/07/2015	56.207	0.287	1.38	0.16
05/04/2016	56.201	0.311	0.414	0.2
20/05/2016	56.144	0.320	0.572	0.33
01/06/2016	56.279	0.236	0.664	0.03
14/06/2016	56.399	0.185	0.204	0.0

Fig. 8.1 illustrates the poor correlation between field measurements of T_n and LDRM simulations in area B. In general, LDRM predicted higher T_n for larger b_n values (as it would be expected in homogeneous scenarios), while this relation was weaker in the case of baildown testing. In addition to errors inherent to both methods, discrepancies in the estimation of T_n could have been due to the layering design and the temporal variation of certain subsurface characteristics, for instance LNAPL properties (due to NSZD) and retention parameters (due to hysteretic effects).

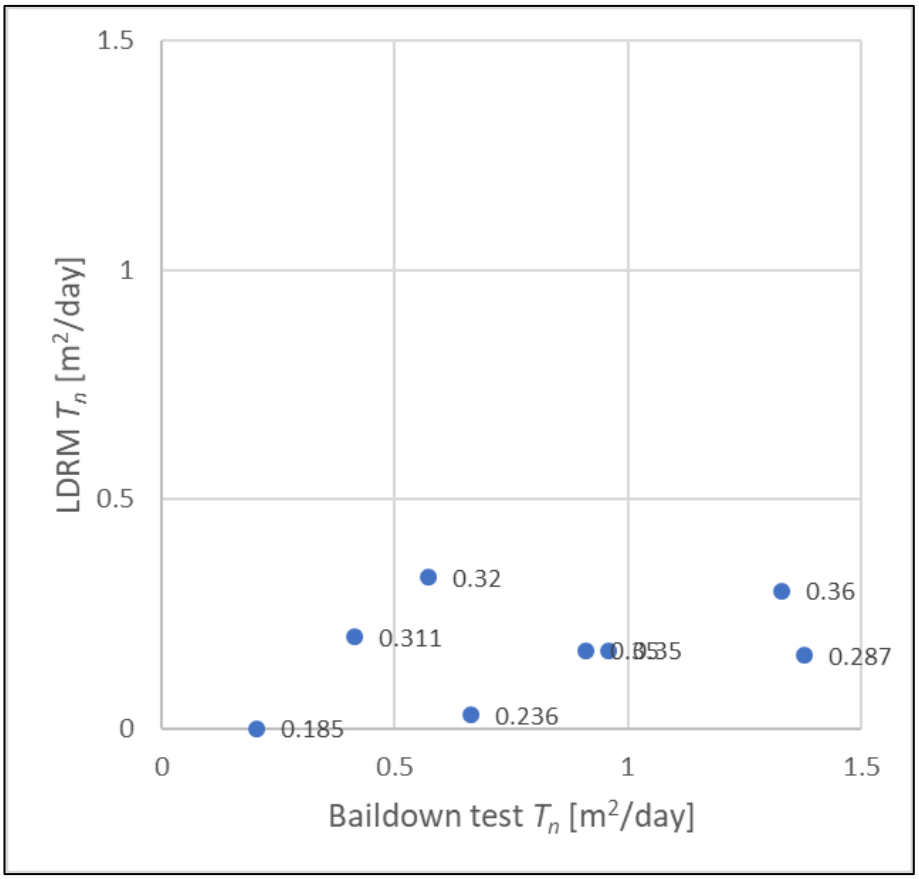


Fig. 8.1. Comparison of T_n values from baildown testing and LDRM simulations in area B according to the input parameter set used in Gatsios et al. (2018a). Dot labels correspond to the initial value of b_n [m] when baildown tests were conducted.

Therefore, the ability of a model and set of input parameters to adequately predict V_n and T_n at one specific instant (according to one core and one baildown test) should not lead to assume that the model equations and set of input parameters correctly represent subsurface conditions.

8.2.3 Relative permeability models and residual LNAPL saturation options

Before the comparison between LNAPLTRANS and LDRM, the effects of different options to predict S_{nr} and k_{rn} in LDRM were evaluated. Table 8.3 summarises LDRM predictions of V_n and free T_n in areas A, B, C, and T4.

The relative permeability model selection (Burdine or Mualem) was much more influential in the results than the different options to represent S_{nr}. The relative permeability model greatly influenced the prediction of T_n as well as the prediction of V_n to a certain extent.

Table 8.3. LDRM predictions of V_n [m] and free T_n [m^2/day] with different models of k_{rn} and S_{nr}.

		Burdine			Mualem		
		Constant S_{nr} (user defined)	Constant S_{nr} (with f-factor)	Variable S_{nr} (with f-factor)	Constant S_{nr} (user defined)	Constant S_{nr} (with f-factor)	Variable S_{nr} (with f-factor)
A	**Total V_n**	0.012	0.014	0.011	0.021	0.03	0.023
	Free V_n	0.009	0.008	0.008	0.018	0.018	0.018
	Free T_n	0.010	0.013	0.010	0.189	0.211	0.201
B	**Total V_n**	0.010	0.012	0.009	0.018	0.025	0.019
	Free V_n	0.007	0.007	0.007	0.015	0.015	0.015
	Free T_n	0.007	0.009	0.007	0.143	0.159	0.152
C	**Total V_n**	0.074	0.106	0.083	0.130	0.183	0.145
	Free V_n	0.067	0.063	0.064	0.123	0.107	0.112
	Free T_n	0.095	0.149	0.126	0.861	0.942	0.913
T4	**Total V_n**	0.107	0.116	0.083	0.121	0.137	0.099
	Free V_n	0.063	0.061	0.064	0.077	0.072	0.076
	Free T_n	0.051	0.054	0.049	0.114	0.116	0.113

Fig. 8.2 depicts how the relative permeability model influenced more the vertical S_n distribution than the approach adopted to determine S_{nr}. Similarly, Fig. 8.2 also shows that these effects were larger in area T4 than in area C (area C was similar to areas A and B in this regard). Using Mualem, V_n values were practically twice as high as with Burdine in areas A, B, and C, while differences were commonly below 20 % in area T4.

Burdine predictions were generally closer to measurements of S_n through coring, although LDRM overestimated the maximum S_n values compared to these field measurements.

Nevertheless, multiphase analytical models should predict somewhat greater S_n values than field measurements, since coring may miss the absolute S_n peak and samples were 5-cm wide, thus TPH concentration values were averaged within this interval. Loss and redistribution of fluids during coring could have created further discrepancies with model predictions.

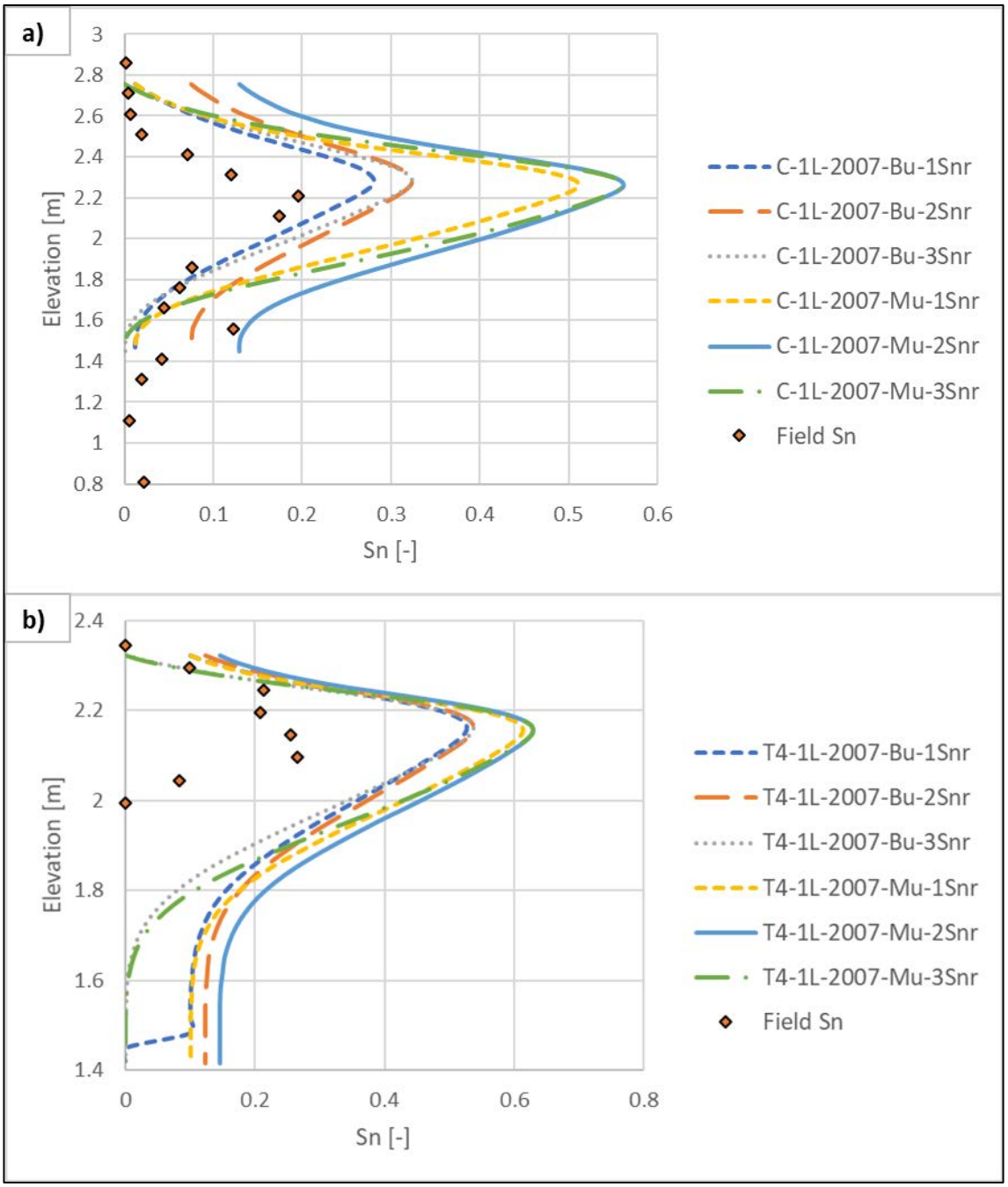


Fig. 8.2. Effects of S_{nr} and relative permeability models on S_n profiles in (a) area C and (b) area T4.

Fig. 8.3 illustrates the S_{nr} values predicted according to the three options implemented in LDRM and the relative permeability models of Burdine and Mualem. Calculating S_{nr} through a f-factor (methods 2*Snr* and *3Snr*) of 0.23—as measured by Johnston and Adamski (2005) for sands from the same geographic region where the industrial site was located—resulted in greater S_{nr} values than those adopted according to field observations (method *1Snr*). The difference between these methods to determine S_{nr}

was smaller in the industrial site than in the petrol station site due to the distinct subsurface material of the petrol station site, where a different f-factor should be used.

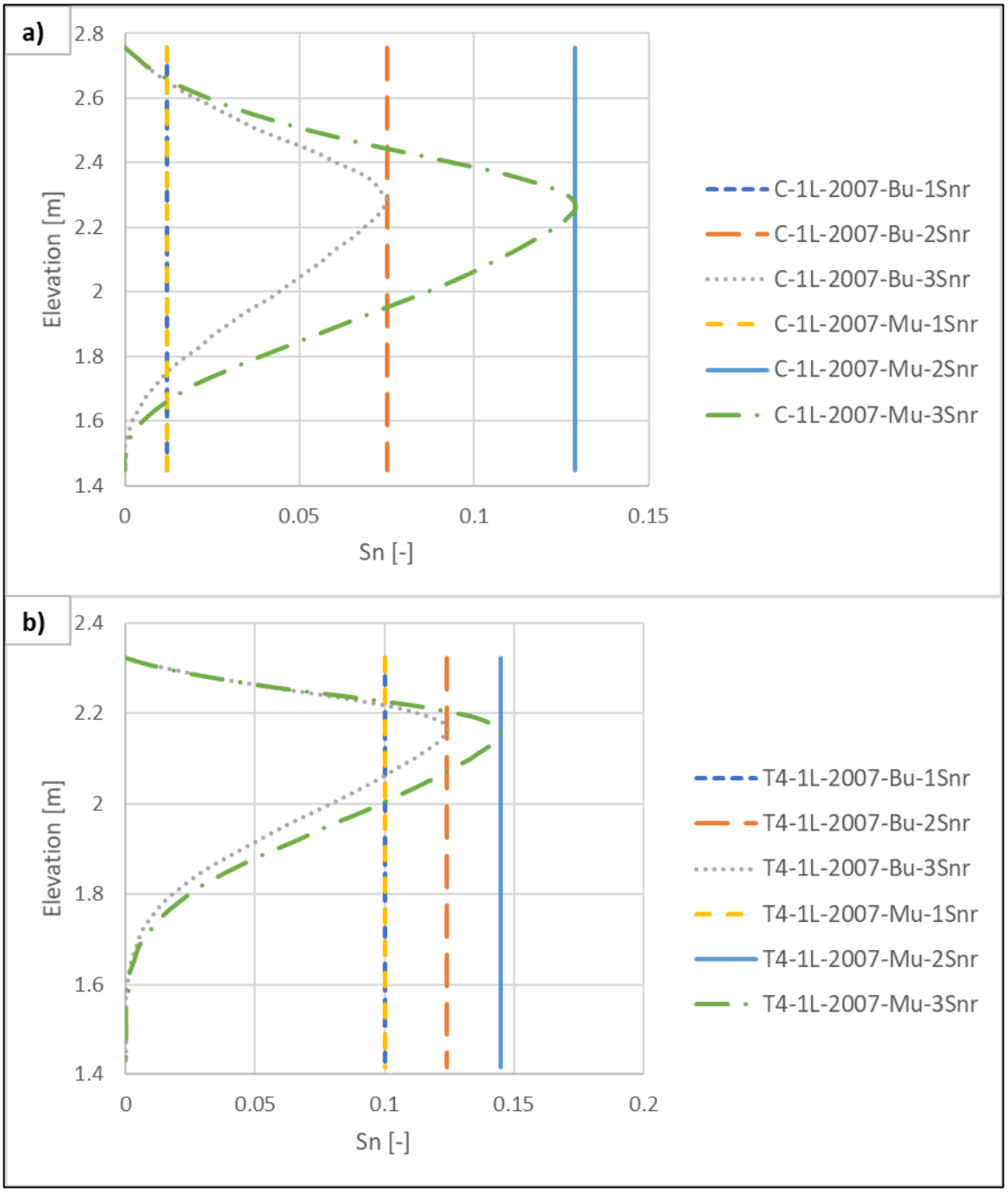


Fig. 8.3. Effects of S_{nr} and relative permeability models on S_{nr} profiles in (a) area C and (b) area T4.

8.2.4 Comparison between LNAPLTRANS and LDRM

8.2.4.1 Petrol station site. Area C

According to the results from section 8.2.2, both Mualem and Burdine relative permeability models were considered in LDRM for the comparison of S_n profiles with

LNAPLTRANS. A constant S_{nr} value was generally assumed in LDRM for the quantitative comparison of V_n and T_n predictions through LNAPLTRANS and LDRM.

Fig. 8.4 illustrates the application of LNAPLTRANS and LDRM in area C. LNAPLTRANS predicted a LNAPL distribution similar to those obtained through LDRM with Burdine, especially when a variable S_{nr} was defined as a function of the f-factor. Thus, the match between field measurements of S_n and LNAPLTRANS predictions (using Mualem relative permeability model) was similar to that obtained through LDRM with Burdine and considerably better than LDRM with Mualem (shown in Fig. 8.2).

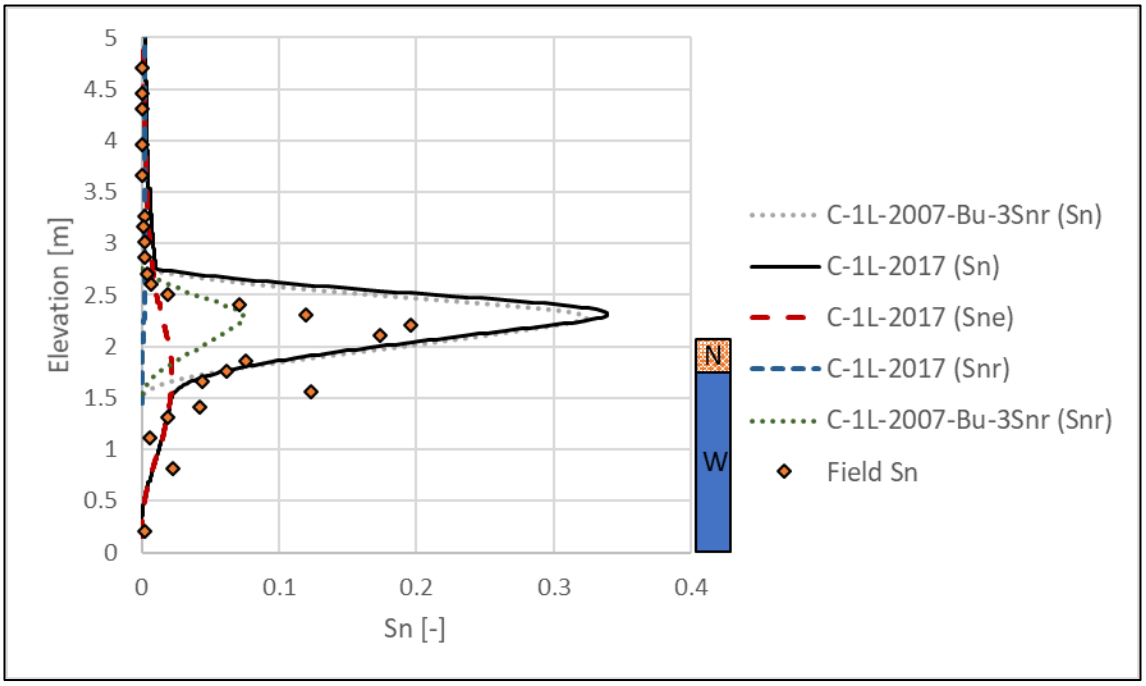


Fig. 8.4. Comparison between field S_n measurements and predictions of S_n, S_{nr}, and S_{ne} through LNAPLTRANS and LDRM in area C. Blue (*W*) and orange (*N*) columns represent in-well water and LNAPL fluid columns, respectively.

Furthermore, considering historic fluid levels in LNAPLTRANS produced relatively good match between the model predictions of entrapped LNAPL and field measurements of S_{ne} below 1.5 m (where a S_{ne}^{max} of 3.3 % was assumed). Moreover, Fig. 8.4 depicts the differences in the approaches followed by Lenhard et al., (2017) and Jeong and Charbeneau (2014) to predict S_{ne} and S_{nr} distributions (both parameters are assumed to be identical in LDRM), and how LDRM predicted the distribution of near-immobile LNAPL as a function of S_n, while LNAPLTRANS accounted for historic fluid levels and distinguished S_{ne} and S_{nr}. LNAPLTRANS did not predict high S_{nr} values in area C.

The discrepancy between field measurements and modelling results above z_{an} was likely related to the combined effect of parameter estimation errors and modelling errors. Some parameters that could have explained this discrepancy included a higher vG-α in the formation—as expected for imbibition conditions; see Lenhard et al. (2019) for a detailed discussion—or a narrower mobile LNAPL interval. For instance, inspection of LIF57-C revealed an interval of approximately 0.15 m above 56 m AHD with negligible LIF response. Considering z_{an} to be 0.15 m lower than the value from the base-case scenario improved the match of LNAPLTRANS predictions with field observations of S_n as depicted in Fig. 8.5.

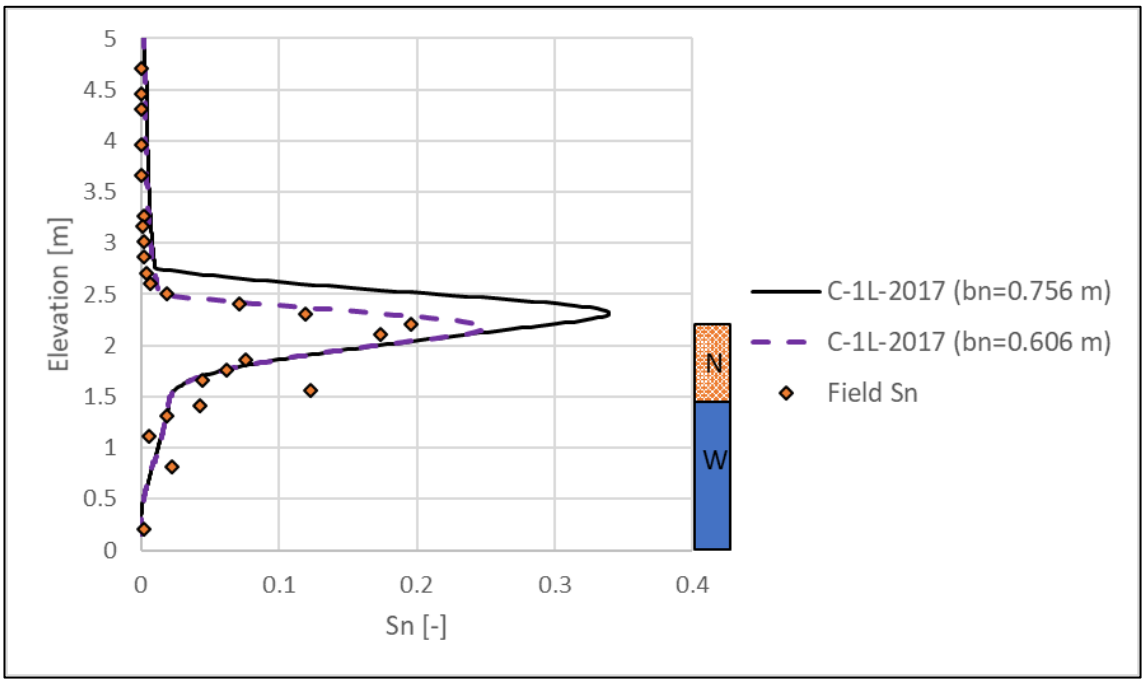


Fig. 8.5. LNAPLTRANS prediction of LNAPL distribution considering a lower b_n value. Blue (*W*) and orange (*N*) columns represent in-well water and LNAPL fluid columns, respectively (b_n = 0.756 m).

8.2.4.2 Petrol station site. Areas A and B

Fig. 8.6 shows the S_n distributions predicted by LNAPLTRANS in areas A and B. LNAPLTRANS produced lower S_n values than LDRM. Maximum predicted S_n were similar to the maximum measurements in the field, especially in the case of area A. Nevertheless, the analytical models did not capture the decrease in S_n above these maximum values, most likely due to the fining-upward sequence of the aquifer, thus requiring the design of multi-layered scenarios (discussed in section 8.3.2). LNAPLTRANS

did not predict any residual LNAPL in areas A and B. Some entrapped LNAPL was observed in area B in both the saturated zone and the unsaturated zone. Positive S_n values measured in cores above 2.5 m were not corroborated by other cores collected in adjacent locations and thus could have been caused by fluid redistribution during the coring process.

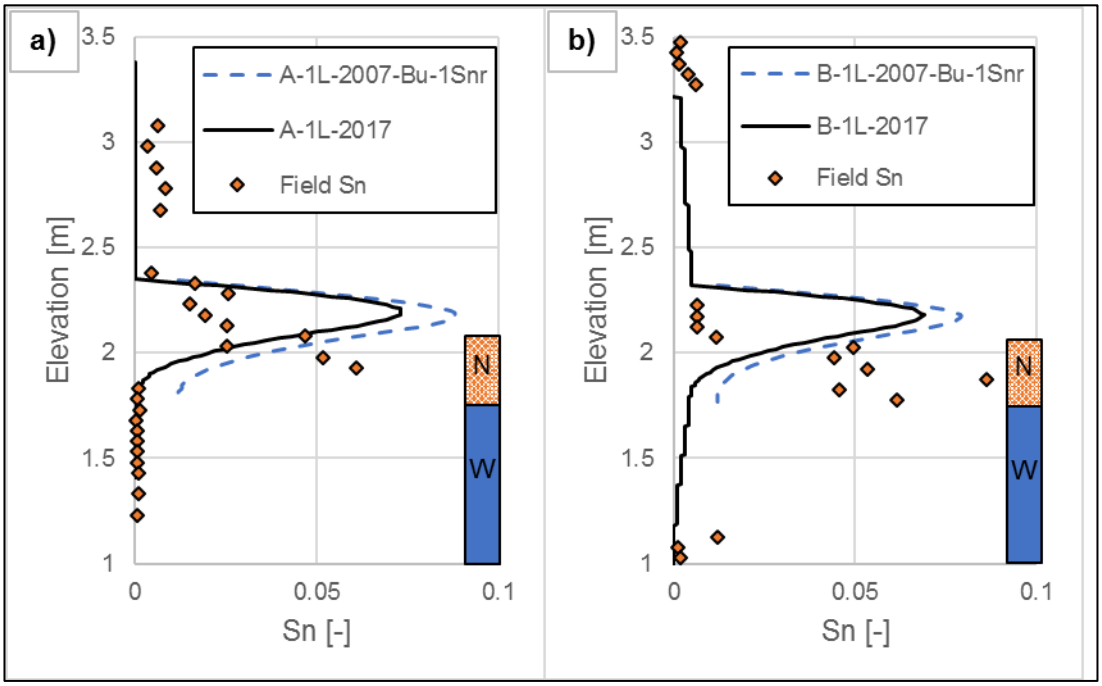


Fig. 8.6. Comparison of field S_n measurements with LNAPLTRANS and LDRM predictions in (a) area A and (b) area B. Blue (*W*) and orange (*N*) columns represent in-well water and LNAPL fluid columns, respectively.

8.2.4.3 Industrial site. Area T4

Finally, Fig. 8.7 depicts the S_n, S_{ne}, and S_{nr} predictions through LNAPLTRANS in area T4. As in areas A and B, the values were lower than those calculated with LDRM and the match with field measurements was considerably better.

The modelled LNAPL distribution was similar to that obtained by Lenhard et al. (2019) in a preliminary test with imbibition parameters and considering two layers. However, in this case only one layer was considered, and retention parameters were derived from particle-size data and did not necessarily represented an imbibition path. It should be noted that most of particle-size data corresponded to the upper layer as defined by Lenhard et al. (2019), which exhibited greater values of vG-α than the lower layer, although still considerably lower than the measurement in the laboratory for the

imbibition path (12.74 m^{-1}). Another important element was the calculation of entrapped LNAPL mass in the unsaturated zone with LNAPLTRANS. This difference with the simulations in the petrol station site was due to the lower water table fluctuations experienced in the industrial site.

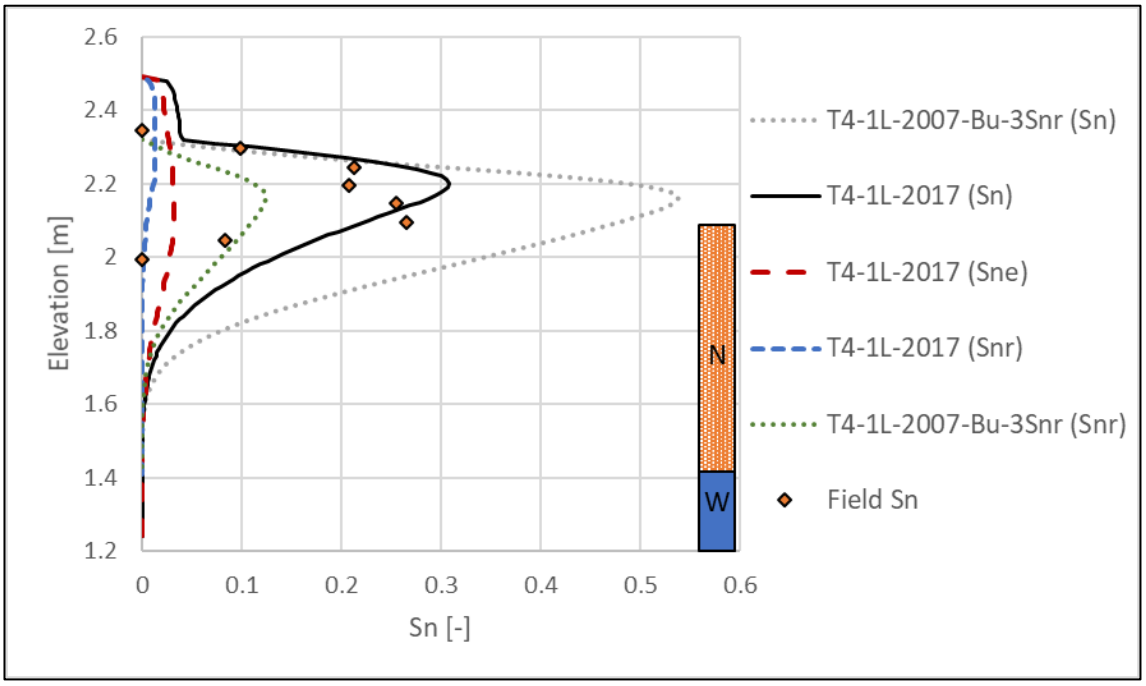


Fig. 8.7. Comparison of field S_n measurements with LNAPLTRANS and LDRM predictions of S_n, S_{nr}, and S_{ne} in area T4. The blue (*W*) and orange (*N*) columns represent in-well water and LNAPL fluid columns, respectively.

8.2.4.4 Model predictions of T_n

Table 8.4 shows that LNAPLTRANS, as LDRM (see Table 8.3), generally produced extremely low T_n values. LDRM was more accurate (better match with field measurements) in areas C and T4 than in areas A and B, and considerably more accurate with the relative permeability model of Mualem than with Burdine, despite better predicting S_n values with Burdine. Similarly, LNAPLTRANS produced a more reasonable T_n value in area C than in the other areas, although it was still lower than the value obtained through baildown testing. Additionally, it should be noted that baildown testing measures recoverable T_n, not the higher free T_n as calculated through LDRM. Thus, there was a strong discrepancy between the predictions of S_n and T_n in the base-case scenarios. These issues were further investigated by testing multi-layered scenarios (section 8.3) and performing a sensitivity analysis (section 8.4).

Table 8.4. LNAPLTRANS predictions of V_n [m] and free T_n [m^2/day] in areas A, B, C, and T4.

	Area A	Area B	Area C	Area T4
Total V_n	0.008	0.010	0.101	0.045
Free V_n	0.008	0.007	0.080	0.033
Free T_n	0.00008	0.00003	0.05311	0.00003

8.3 Layering implications on LNAPL distribution and recoverability

8.3.1 Comparison with preliminary tests in area T4

A multi-layered scenario for a preliminary test in area T4 has already been presented in Lenhard et al. (2019). First, the input parameters from this multi-layered scenario and the single-layer base-case scenario were compared.

One main difference between both scenarios was the value of vG-α. Lenhard et al. (2019) obtained a better match with field measurements of S_n using imbibition parameters (vG-α and vG-N equal to 12.74 m^{-1} and 2.220 instead of 5.56 m^{-1} and 3.598 during drainage in the upper sand and equal to 3.46 m^{-1} and 3.859 instead of 2.17 m^{-1} and 5.764 during drainage in the lower sand), while a vG-α value of 3.30 m^{-1} has been assumed in the base-case scenario.

Replacing the vG-α value of the base-case scenario with a value of 12.74 m^{-1} as presented by Lenhard et al. (2019) produced a more reasonable estimation of T_n (free T_n equal to 0.188 m^2/day and recoverable T_n equal to 0.151 m^2/day). Nevertheless, this modification resulted in worse agreement with field measurements of S_n as illustrated in Fig. 8.8.

An additional issue in area T4 was the extremely high values of certain LNAPL properties (η_n and σ_{nw}) measured at NS7A-T4 compared to the rest of the area. Using geometric means of η_n and σ_{nw} as input data, the estimation of free T_n increased from 3x10^{-5} m^2/day to 0.05 m^2/day, mainly caused by the change in σ_{nw}. Recoverable T_n was still as low as 0.0007 m^2/day and the prediction of S_n was worse than using the initial set of input parameters of the base-case scenario as depicted in Fig. 8.8.

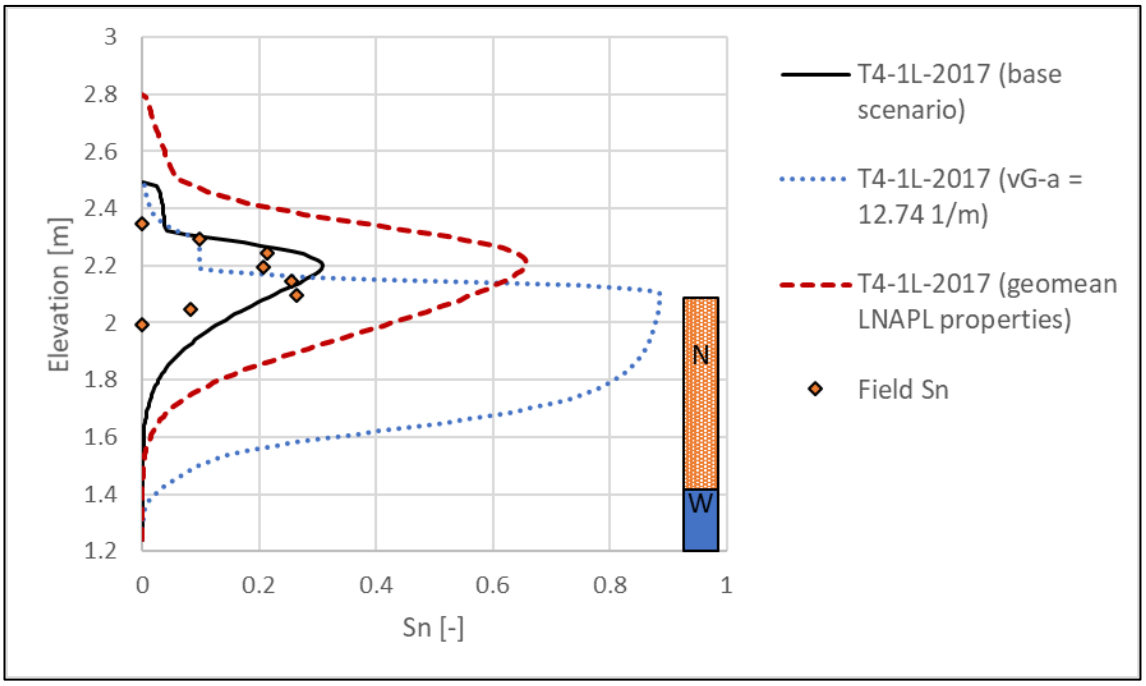


Fig. 8.8. LNAPLTRANS predictions of LNAPL distribution considering a higher $vG\text{-}\alpha$ value. Blue (W) and orange (N) columns represent in-well water and LNAPL fluid columns, respectively.

Fig. 8.9 depicts the prediction of S_n through LNAPLTRANS and LDRM in the multi-layered scenario, where the interface between layers corresponded to a model elevation of 2.17 m (0.4 m AHD). As shown in Fig. 8.9, this interface caused an abrupt change in S_n as predicted with LNAPLTRANS (simulation T4-2L-2017). Thus, the model fit with field S_n measurements below 2.05 m was improved in the multi-layered scenario using LNAPLTRANS.

Furthermore, the model fit with LNAPLTRANS (simulation T4-2L-2017) was also better than with LDRM in the multi-layered scenario (simulation T4-2L-2007-Bu-1Snr) and the simulation with imbibition parameters presented by Lenhard et al. (2019). One reason behind the improved fit with field measurements of S_n compared to LDRM was the stronger contrast observed between layers in the case of LNAPLTRANS (simulation T4-2L-2017).

LDRM did not exhibit such an abrupt change in S_n in the interface between layers despite employing practically the same input values, presumably due to the different sensitivity of the model to the parameters varying between layers LNAPLTRANS simulations as presented in Lenhard et al. (2019) exhibited greater contrast between layers when

drainage retention parameters were employed and only in S_{nr} and S_{ne} when imbibition retention parameters were selected (not shown; see Lenhard et al., 2019).

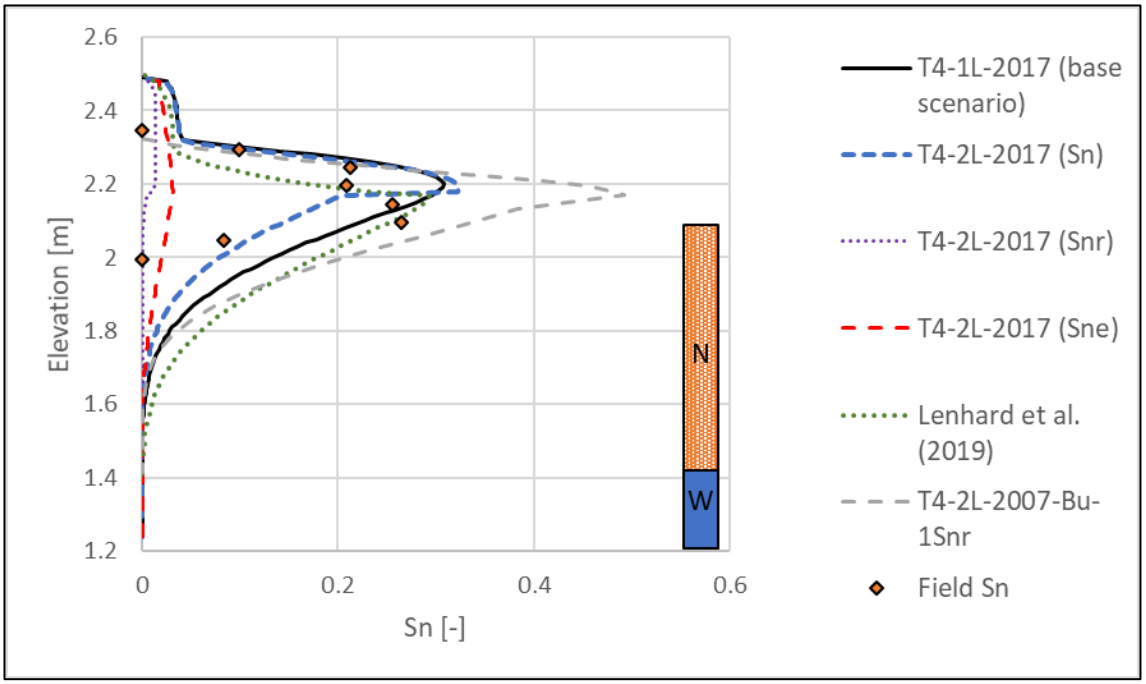


Fig. 8.9. Single-layer versus multi-layered scenarios in area T4. The prediction of S_n from Lenhard et al. (2019) correspond to the use of imbibition retention parameters in LNAPLTRANS.

Predictions of free T_n through LDRM in the multi-layered scenario produced a value of 0.03 m^2/day, consistent with the field measurements through baildown testing, although lower than in the single-layer base-case scenarios. Therefore, the improved fit with field measurements of S_n in multi-layered scenarios was not accompanied by more accurate prediction of T_n.

8.3.2 LNAPL distribution predictions in fining-upward sequences

One of the main advantages of designing multi-layered scenarios in LNAPLTRANS and LDRM was the gained precision in the prediction of S_n profiles in vertically heterogeneous media. Nonetheless, the simulation of LNAPL distribution in areas A and B was problematic in both LDRM and LNAPLTRANS due to the fining-upward sequence yielding S_n profiles where the peak value is deeper than most of the LNAPL mass (which could be seen as an inverse shark fin).

Fig. 8.10 illustrates the simulation of LNAPL distribution in area A with LDRM, which is used as an example to discuss this issue with fining-upward sequences. Three layers

were considered for simulation A-3L-2007-Bu-1Snr with layer interfaces at 2.05 and 2.20 m (56.20 and 56.35 m AHD). Same values of fluid properties, Φ, and S_{wr} (as defined for the single-layer base-case scenario) were set in the three layers, while $vG\text{-}\alpha$ values of 0.87, 2.13, and 5.47 m^{-1} were assigned to the top, intermediate, and lower layers, respectively. $vG\text{-}N$ values in these layers were 2.03, 3.78, and 2.74, respectively.

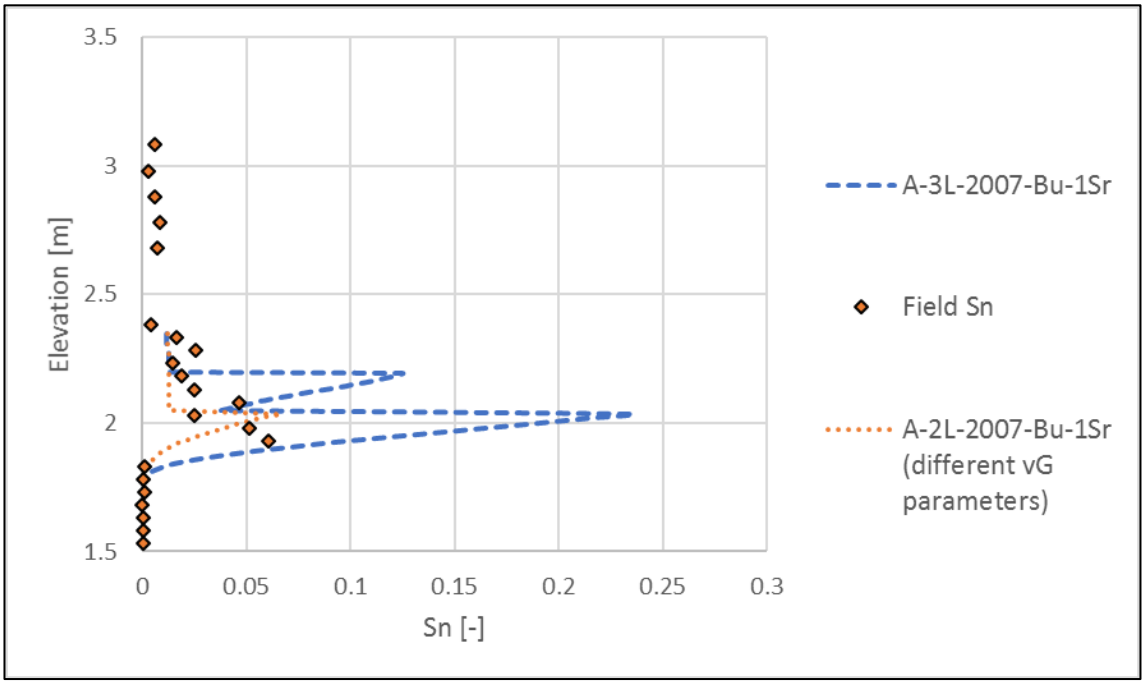


Fig. 8.10. LDRM prediction of LNAPL distribution in multi-layered scenarios of area A.

The decrease of $vG\text{-}\alpha$ in the upper layers aimed to represent the fining-upward sequence observed in the field, while the high $vG\text{-}N$ value of the intermediate layer was selected assuming a lower breadth of the pore-size distribution between 56.20 and 56.35 m AHD, where extremely high LIF response was detected during the HRSC campaign. However, the model prediction of LNAPL distribution resembled a sequence of shark fins due to the intra-homogeneity within every layer.

Enabling subsurface properties to exhibit vertical variation within single layers could greatly improve the representation of fining- and coarsening-upward sequences. A similar approach was explored in the analytical model developed by Al Awar (2008) after implementing linear interpolation of values defined at the layer boundaries.

The multi-layered scenario allowed definition of different S_{nr} values in each layer with LDRM. Thus, a value of 1.2 % was assigned to the top layer as in the base-case scenario.

For the intermediate and lower layers, the S_{ne} value of 0.1 % inferred from the analysis of field data was adopted as the input S_{nr} in LDRM. This contributed to a better match with field measurements of S_n above 2.20 m and below 1.80 m.

Fig. 8.10 also shows that varying the vG retention parameters could improve the prediction of S_n distribution as estimated through coring, even defining only two layers as in the case of simulation A-2L-2007.

The three-layer model (A-3L-2007) was modified to eliminate the intermediate layer, only keeping one interface at 2.05 m. The $vG\text{-}\alpha$ value at the lower layer was decreased to 2.797 m^{-1}, while the other parameters were the same as in A-3L-2007. Nevertheless, the two-layer model prediction did not capture the effects of the fining-upward sequence either.

In addition, the estimation of T_n was not accurate despite employing multiple layers and assigning high k_{sw} values, especially at the intermediate layer where an extremely high value of 387.6 m/day was selected. This value was used to test the hypothesis of a preferential migration pathway being located at this elevation.

The three-layer scenario yielded a T_n value of 0.31 m^2/day, while field measurements suggested a range of 1.3–2.9 m^2/day. Improved T_n estimations could be obtained with other input values and the Mualem relative permeability model but were accompanied by worse prediction of the vertical LNAPL distribution. This issue was also reported by Gatsios (2018) and Gatsios et al. (2018a).

8.4 Sensitivity analysis

8.4.1 Summary of parameter ranges

Area C was selected to illustrate the sensitivity analysis, since predictions of LNAPL distribution and T_n were considered more representative of subsurface conditions than in other areas.

Table 8.5 summarises the input data sets employed in the computation of sensitivity indices as defined by Hoffman and Gardner (1983). Simulation outputs are included in Appendix G: Computation of sensitivity indices.

Table 8.5. Summary of input values corresponding to most likely ('-1', '+1'), extended ('-2', '+2'), and conservative ranges ('-3', '+3') for the computation of sensitivity indices in area C.

	-3	-2	-1	Base-case value	+1	+2	+3
Φ [-]	15.0	30.5	41.6	45	47.4	62.9	72.0
k_{sw} [m/day]	0.0001	0.02	0.76	3.0	26.21	100	10000
vG-α [m^{-1}]	0.05	0.26	0.87	2.13	5.48	9.98	18.70
vG-N [-]	2.001	2.5	2.66	2.74	3.78	4.15	8.00
S_{wr} [%]	0.5	6.28	8.60	10.9	13.43	17.43	83.3
S_{nr}^{max} [%]	0	0.6	0.8	1.2	4	24.4	75
S_{ne}^{max} [%]	0	0.1	1	3.3	4.4	22	75
ρ_n [mg/cm^3]	0.70	0.717	0.72	0.73	0.76	0.79	0.81
η_n [cP]	0.36	0.37	0.40	0.41	0.55	0.65	0.66
σ_{an} [mN/m]	20.50	21.80	23.00	23.38	24.23	24.32	24.52
σ_{nw} [mN/m]	15.60	17.52	18.50	20.51	21.37	34.70	50.00
b_n [m]	0.400	0.606	0.734	0.756	0.778	0.906	1.100

The values showed in Table 8.5 were selected according to the discussion presented in previous chapters, especially chapter 7. Regarding the b_n ranges, a variation of 0.022 m was assumed for the most likely range. This value likely accounted for manual errors during dipping and was identical to the drawdown adjustment applied in a baildown test at PB40-C in June 2016. The extended range considered a variation of 0.15 m, which was similar to the case explored in section 8.2.4.1 and greater than any adjustment correction applied in baildown tests from area C under natural water table fluctuations (Gatsios, 2018). The conservative range was defined as 0.4–1.1 m.

The relative permeability model of Burdine with a constant user-defined S_{nr} value was selected in LDRM. Ranges of *vG-N* were modified to constrain the lower limit of the conservative range to a value of 2, so it could be employed as an input in the Burdine relative permeability model of LDRM. Accounting for three possible ranges allowed to evaluate the robustness of the sensitivity analysis procedure.

8.4.2 Computation of sensitivity indices

8.4.2.1 Sensitivity indices with different ranges

Computed SI values are summarised in Table 8.6, Table 8.7, Table 8.8, and Table 8.9.

Table 8.6. Sensitivity indices of V_n with LDRM.

	SI_1	SI_2	SI_3	Rank(SI_1)	Rank(SI_2)	Rank(SI_3)
Φ [-]	0.1154	0.5192	0.7899	6	6	6
k_{sw} [m/day]	0.0000	0.0000	0.0000	10	10	10
$vG\text{-}\alpha$ [m^{-1}]	0.8543	0.9585	0.9693	1	1	1
$vG\text{-}N$ [-]	0.4250	0.5538	0.9583	2	5	2
S_{wr} [%]	0.0395	0.1154	0.7683	9	8	7
S_{nr}^{max} [%]	0.1910	0.6321	0.8496	5	3	5
ρ_n [mg/cm^3]	0.2963	0.4819	0.6383	3	7	8
η_n [cP]	0.0000	0.0000	0.0000	10	10	10
σ_{an} [mN/m]	0.0519	0.0909	0.1410	8	9	9
σ_{nw} [mN/m]	0.2333	0.7475	0.9000	4	2	3
b_n [m]	0.1139	0.5701	0.8889	7	4	4

Table 8.7. Sensitivity indices of V_n with LNAPLTRANS.

	SI_1	SI_2	SI_3	Rank(SI_1)	Rank(SI_2)	Rank(SI_3)
Φ [-]	0.6835	0.5152	0.7917	2	5	4
k_{sw} [m/day]	0	0	0	11	11	11
$vG\text{-}\alpha$ [m^{-1}]	0.8607	0.9855	1.0000	1	1	1
$vG\text{-}N$ [-]	0.1167	0.1636	0.3687	6	8	9
S_{wr} [%]	0.0421	0.0955	0.6753	10	10	6
S_{nr}^{max} [%]	0.0610	0.3289	0.6158	9	7	8
S_{ne}^{max} [%]	0.1763	0.5959	0.8347	5	2	3
ρ_n [mg/cm^3]	0.2936	0.4870	0.6346	3	6	7
η_n [cP]	0	0	0	11	11	11
σ_{an} [mN/m]	0.0715	0.1434	0.2214	8	9	10
σ_{nw} [mN/m]	0.1859	0.5859	0.7441	4	3	5
b_n [m]	0.1121	0.5352	0.8416	7	4	2

Table 8.8. Sensitivity indices of T_n with LDRM.

	SI_1	SI_2	SI_3	Rank(SI_1)	Rank(SI_2)	Rank(SI_3)
Φ [-]	0.0000	0.0000	0.0000	11	11	11
k_{sw} [m/day]	0.9709	0.9997	1.0000	2	2	1
vG-α [m^{-1}]	0.9929	1.0000	1.0000	1	1	1
vG-N [-]	0.7508	0.8716	0.9991	3	4	3
S_{wr} [%]	0.1010	0.2115	0.9573	9	9	6
S_{nr}^{max} [%]	0.2137	0.7656	0.9532	7	6	7
ρ_n [mg/cm^3]	0.3810	0.6330	0.7891	4	7	8
η_n [cP]	0.2784	0.4286	0.4537	6	8	9
σ_{an} [mN/m]	0.0208	0.0619	0.0825	10	10	10
σ_{nw} [mN/m]	0.3566	0.9205	0.9902	5	3	4
b_n [m]	0.1905	0.7753	0.9818	8	5	5

Table 8.9. Sensitivity indices of T_n with LNAPLTRANS.

	SI_1	SI_2	SI_3	Rank(SI_1)	Rank(SI_2)	Rank(SI_3)
Φ [-]	0.0000	0.0000	0.0000	11	11	11
k_{sw} [m/day]	0.9710	0.9998	1.0000	2	2	1
vG-α [m^{-1}]	1.0000	1.0000	1.0000	1	1	1
vG-N [-]	0.0796	0.0893	0.3903	9	9	9
S_{wr} [%]	0.0017	0.0041	0.1323	10	10	10
S_{nr}^{max} [%]	0.0811	0.4846	0.9092	8	6	6
S_{ne}^{max} [%]	0.0000	0.0000	0.0000	11	11	11
ρ_n [mg/cm^3]	0.7709	0.9569	0.9929	3	4	5
η_n [cP]	0.2728	0.4309	0.4545	6	8	8
σ_{an} [mN/m]	0.2541	0.4654	0.6473	7	7	7
σ_{nw} [mN/m]	0.5499	0.9843	0.9990	4	3	4
b_n [m]	0.3125	0.9355	1.0000	5	5	1

The three ranges reasonable agreed in the ranking of the most influential parameters on V_n and T_n predictions. Therefore, the sensitivity analysis methodology was quite

robust regarding the range selection with few exceptions. Ranks frequently coincided or varied between one and three positions. The only exceptions sometimes were S_{wr}, ρ_n (because of the maximum values adopted in their conservative ranges), and b_n (which most likely range was very narrow compared to the conservative range).

Some of these extreme values were adopted from references and databases commonly used by researchers and practitioners, for instance very high values of S_{nr} and σ_{nw} in Mercer and Cohen (1990), S_{wr} in the API database (API, 2006), or $vG\text{-}\alpha$ in Carsel and Parrish (1988). Therefore, their selection was considered acceptable.

8.4.2.2 Sensitivity ranking

V_n was more sensitive to $vG\text{-}\alpha$ than to other parameters in both LDRM and LNAPLTRANS as depicted in Fig. 8.11. According to average *SI* values (average between the three considered ranges), other main sources of variability in estimations of V_n through the two models were Φ and σ_{nw}. Depending on the considered ranges, ρ_n and b_n could also be key parameters for the prediction of V_n.

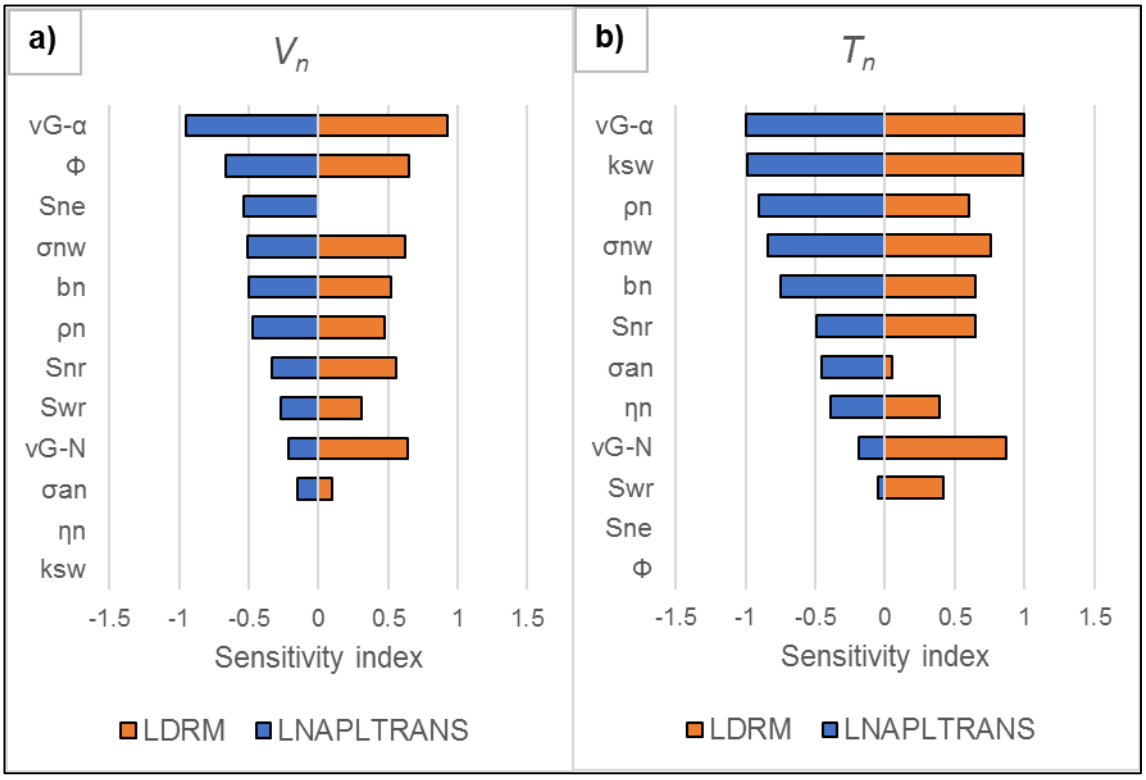


Fig. 8.11. Tornado diagram of sensitivity indices corresponding to calculations of (a) V_n and (b) T_n through LNAPLTRANS and LDRM. For illustrative purposes, *SI* values for LNAPLTRANS are given as negative quantities.

In the case of LNAPLTRANS S_{ne}^{max} was the third most influential parameter, while LDRM was much more sensitive to $vG\text{-}N$ and S_{nr}. In LNAPLTRANS, there was greater variability propagated by S_{ne}^{max} than S_{nr}^{max}, aspect that could not be explored in LDRM because of the identical definition of both near-immobile fractions. As it could be expected, the values of k_{sw} and η_n did not influence the estimation of V_n.

Regarding the evaluation of T_n, it was remarkable the strong sensitivity to a greater number of input parameters, including $vG\text{-}\alpha$, k_{sw}, ρ_n, σ_{nw}, and b_n as well as $vG\text{-}N$ in the case of LDRM. Furthermore, S_{nr}^{max} was more influential in the estimation of T_n than in the prediction of V_n. S_{ne}^{max} and Φ did not make any impact on T_n as it could be expected.

8.4.2.3 Effect of the perturbations

The relationship between the perturbations applied to the reference input parameters and the resulting output values was generally non-linear due to the influence of most of these parameters in the definition of the (non-linear) retention curve. In contrast, the impact of k_{sw} on T_n estimations was linear, since T_n is commonly defined as a linear function of k_{sw} and k_{sw} does not explicitly affect the retention curve.

In the case of σ_{nw}, ρ_n, and S_{wr}, a positive perturbation caused a decrease of V_n in LDRM and LNAPLTRANS, while a positive relationship existed between V_n and the rest of parameters (except with the uncorrelated k_{sw} and η_n). In addition to these parameters (σ_{nw}, ρ_n, and S_{wr}), η_n was also inversely correlated with T_n, consistent with the definition of T_n.

However, LDRM and LNAPLTRANS exhibited an opposite behaviour after perturbations in near-immobile S_n values. In LDRM, there was direct relationship between S_{nr} and T_n, while it was inverse in LNAPLTRANS considering changes in S_{nr}^{max}. The reason behind this discrepancy was the different approach followed in the estimation of free V_n and therefore T_n. Furthermore, the non-linear influence of $vG\text{-}N$ on T_n was reflected by a direct relationship considering the most likely range and extended range in LNAPLTRANS but an inverse correlation when the conservative range was employed.

The sensitivity analysis highlighted the importance of a good characterisation and improved representation of subsurface parameters, especially those related to the

retention curve and σ_{nw} as well as k_{sw} in the evaluation of T_n. Large errors in b_n may also greatly influence model predictions. Thus, robust methods to deal with non-equilibrium conditions are also needed.

8.4.3 Analysis of best- and worst-case scenarios

Best- and worst-case scenarios were defined according to the lower and upper limits of the most likely range in area C, accounting for the sign of change induced by every parameter. S_{nr}^{max}, S_{ne}^{max}, and $vG\text{-}N$ were not altered due to their distinct behaviour in LNAPLTRANS and LDRM. More conservative ranges yielded unrealistic predictions of V_n and T_n due to the strong variability exhibited by subsurface properties. The best-case scenario referred to the one with lower V_n (and T_n) values, while the worst-case scenario was assumed to be the one with larger V_n.

As shown in Table 8.10, good agreement existed between the predictions of total V_n, free V_n, and free T_n through LDRM and LNAPLTRANS. However, the comparison between scenarios revealed the strong uncertainties typically associated to the duration, cost, and effectiveness of management strategies in remediation projects. There was a change in free and total V_n of more than one order of magnitude between the considered scenarios. Furthermore, T_n was negligible in the best-case scenario and unrealistically high in the worst-case scenario, reflecting the great sensitivity of T_n to input parameters compared to V_n. It is therefore essential to estimate T_n with field-based methods to better assess LNAPL recoverability and the applicability of LNAPL mass recovery methods according to the project remediation objectives.

Table 8.10. LDRM and LNAPLTRANS predictions of V_n [m] and free T_n [m^2/day] in best- and worst-case scenarios as defined in area C.

	LDRM		LNAPLTRANS	
	Worst-case	**Best-case**	**Worst-case**	**Best-case**
Total V_n	0.196	0.012	0.263	0.019
Free V_n	0.187	0.006	0.229	0.006
Free T_n	6.742	0.000	12.60	0.000

8.5 Summary of modelling results and conclusions

Multiphase analytical models represent a simple and practical way to investigate scenarios accounting for the strong field variability of many subsurface parameters, although numerical, stochastic, and inverse approaches may be required for more accurate prediction of complex LNAPL distributions and T_n. For instance, the effects of fining-upward sequences on LNAPL distribution may not be captured even in multi-layered scenarios due to the homogeneity assumed within every layer in analytical models.

According to the field scenarios considered, field S_n measurements through coring were commonly in better agreement with predictions of S_n with LNAPLTRANS than with LDRM. Furthermore, considering different relative permeability models and alternative definitions of S_{nr} resulted in clearly distinct predictions of S_n and T_n through LDRM.

Despite the relatively adequate prediction of S_n, T_n was clearly underestimated in most of the scenarios in comparison to field measurements through baildown testing. Using the Mualem relative permeability model resulted in better estimations of T_n, although not adequately matching field S_n data.

Model outputs were associated to a strong uncertainty due to the variability of subsurface parameters used as inputs. For instance, a good fit of LNAPLTRANS with field observations of S_n was achieved in area T4 after selecting retention parameters derived from particle-size data and presumably more representative of draining conditions. However, Lenhard et al. (2019) showed that imbibition parameters measured in the laboratory resulted in better S_n estimations than using measurements of drainage paths.

V_n predictions were mostly sensitive to the retention parameters (especially $vG\text{-}\alpha$), followed by σ_{nw}. T_n predictions also exhibited the largest sensitivity to $vG\text{-}\alpha$, followed by k_{sw}, $vG\text{-}N$, and σ_{nw}. The relative permeability model is another aspect strongly determining the model outputs. Changes in S_{nr} and S_{ne} affect LNAPLTRANS and LDRM predictions of free V_n and T_n in opposite ways. Thus, the sensitivity analysis highlighted the importance of a good characterisation and improved representation of subsurface parameters, especially those related to the retention curve and σ_{nw} as well as k_{sw} in the evaluation of T_n.

9 Conclusions and future lines of research

9.1 Conclusions

Main conclusions from the thesis are presented in the following paragraphs. Further details about specific outcomes from every chapter can be found in sections 5.2.7, 5.3.5 (confinement), 6.5 (LIF logging), 7.5 (DPIL and k_{sw}), and 8.5 (modelling).

HRSC approaches represent a step forward in the effective investigation of LNAPL contaminated sites and may provide valuable information even in challenging environments such as relatively fine-grained materials with presence of light fuels. HRSC tools such as LIF and HPT allow rapid collection of high-resolution data in subsurface systems and therefore may detect important LNAPL distribution and hydrostratigraphic features overlooked by conventional methods, for instance masses of entrapped and residual LNAPL or variable boundaries between hydrostratigraphic units.

Nevertheless, LIF and HPT should be complemented with other techniques, since non-unique interpretations of HRSC logs may exist due to their qualitative or semi-quantitative nature. Investigators should always aim to evaluate multiple lines of evidence to take well-informed decisions while reducing and better acknowledging CSM uncertainty.

Due to project limitations in terms of budget, time, expertise, and availability of certain techniques, some of these approaches may be prioritised over others. For this purpose, investigators should consider site-specific conditions and the project characteristics. If active remediation operations are expected, the investment in HRSC approaches may contribute to design effective management strategies and reduce financial risks, eventually resulting in cost savings (Dyment and Kady, 2019) and better protection of human health and the environment. LIF and DPIL may be more efficient than coring and well installations for investigating the hydrostratigraphic profile and contaminant distribution across the site, even if improvements are still needed to increase the horizontal resolution and temporal resolution of measurements.

Continuous coring can still be used to quantify multiple subsurface parameters with different degrees of accuracy (including stratigraphic characteristics, LNAPL and total

liquid saturations during the coring event, k_{sw} and retention parameters derived from particle-size data or laboratory tests, and biogeochemical conditions with improved coring methods), although loss of material and pore fluids may represent an issue. Correlations based on particle-size data are highly uncertain, but not very costly if cores are already being collected for any other purpose, for instance to determine retention parameters.

Regarding other techniques explored in previous chapters, hydraulic testing (pumping tests, baildown tests, LNAPL mass recovery trials) provide information on the hydrogeologic characteristics of the aquifer and LNAPL body in the well and its radius of influence at the time of the test. Under confined conditions, they may also help to elucidate the confining contact elevation. However, pumping tests may be problematic because of the waste generated and the estimations of k_{sw} represent effective parameters over large support scales. Baildown testing is a convenient method to estimate T_n, although not free of errors and uncertainties. Some of the estimates in the petrol station site were greatly sensitive to the drawdown adjustment.

Single-well DGPs also offer valuable in-well information which may be easily accessible if long-term monitoring programs exist. Their analysis may be enhanced considering periods of monotonic z_{aw} fluctuations and using automatic logging systems. In the case of multi-well DGPs, investigators should first determine periods without field data to avoid misleading definition of LNAPL transmissive zones. In-well fluid level data should be examined to identify measurement errors and periods likely affected by non-equilibrium phenomena or poor hydraulic connection between the well and the formation.

Discrepancies between b_n and strong LIF signals should not lead to assume confined or perched LNAPL conditions without additional evidences. The use of lifetime logs, relative LIF signals, and total LIF signals at logarithmic scales may contribute to better identification of LNAPL-impacted intervals and the elevation of confining units, although leaky confined conditions may limit the applicability of this approach. These LIF metrics may be useful to assess aquitard integrity. Methods to subtract natural fluorescence of

the geological medium according to multi-wavelength waveforms may further enable the identification of intervals impacted by LNAPL with low LIF signal.

Furthermore, LIF response may work as an indicator of LNAPL mobility even when there is poor correlation with S_n. More specifically, maximum LIF signals may be more meaningful for the assessment of T_n than integral LIF signals. LIF logging may also assist in the rapid identification of long-term entrapped and residual LNAPL masses because of the multi-waveform wavelengths associated to distinct subsurface features. Spatial variability in LNAPL composition or near-immobile LNAPL volumes could negatively influence the correlation between LIF response and T_n. Thus, the proposed approach is better suited for the characterisation of early-stage releases than for late-stage releases dominated by near-immobile LNAPL and NSZD phenomena.

The DPIL system may produce reasonable estimates of k_{sw} in sandy materials without applying a site-specific calibration. Furthermore, LNAPL contamination does not necessarily have a negative impact on DPIL readings as supported by two lines of evidence. First, the intervals where LNAPL was found did not consistently exhibit lower Q/P values than other parts of the profiles. Second, there was acceptable agreement between k_{sw} estimations from DPIL (presumably affected by the decrease in k_{rw} caused by the presence of LNAPL mass in the pores) and empirical correlations based on particle-size data (unaffected by LNAPL contamination), with DPIL even overpredicting k_{sw} compared to the geometric mean of empirical correlations in the clean sands of the industrial site. Therefore, DPIL may be a useful tool in LNAPL contaminated systems. However, DPIL presumably underestimates the variability of k_{sw} and thus the application of multiple methods is encouraged.

Moreover, metrics of aquifer heterogeneity such as the logconductivity variance as measured with DPIL systems may strongly vary depending on the subsurface layering. Thus, the variance within individual hydrostratigraphic units should also be reported and considered for stochastic modelling purposes.

Multiphase analytical models represent a simple and practical way to investigate subsurface scenarios accounting for the strong field variability of multiple parameters, although numerical, stochastic, and inverse approaches may be required for more

accurate prediction of complex LNAPL distributions and T_n. For instance, the simulation of fining-upward sequences may not be satisfactory even in multi-layered scenarios due to the homogeneity assumed within every layer in analytical models.

According to the field scenarios considered, V_n predictions are mostly sensitive to the retention parameters (especially $vG\text{-}\alpha$), followed by σ_{nw}. T_n predictions also exhibit the largest sensitivity to $vG\text{-}\alpha$, followed by k_{sw}, $vG\text{-}N$, and σ_{nw}. The relative permeability model is another element strongly determining the model outputs. Changes in S_{nr} and S_{ne} affect LNAPLTRANS and LDRM predictions of T_n in opposite ways. Thus, the sensitivity analysis highlighted the importance of a good characterisation of retention parameters σ_{nw}, and b_n as well as k_{sw} in the evaluation of T_n.

9.2 Limitations and future lines of research

One of the typical limitations of field-based research is the semi-controlled nature of the experiments. Thus, testing hypotheses and outcomes from this thesis in other sites against a wider range of conditions is encouraged to gain better understanding of subsurface phenomena. Furthermore, future laboratory experiments may further elucidate the effects of some specific factors explored throughout the thesis. Some of these factors could be the influence of LNAPL presence (different LNAPL types at different degrees of S_n) on DPIL readings or the ability of LIF sensors to monitor LNAPL weathering in heterogeneous media.

Nevertheless, experiments at laboratory scale may not capture the full complexity of field settings. Accordingly, the reasons behind discrepancies between laboratory and field studies should be further investigated. Laboratory experiments should be more representative of field conditions accounting for aspects only occasionally considered in the literature such as complex pore geometries, mixed-wetting conditions, biological processes, and three-phase systems under non-equilibrium conditions.

Non-equilibrium conditions are an important issue found in the field that may affect VEQ modelling predictions, estimation of T_n through baildown testing, interpretation of DGPs, and the representativeness of CSMs in general. Therefore, more robust approaches to deal with non-equilibrium conditions are needed.

Further research on the characterisation (in laboratory, field, and modelling studies) of near-immobile S_n fractions and retention parameters should be conducted, since strong discrepancies have been reported between laboratory and field scales despite being a vital element in modelling predictions and the design of remediation strategies. In addition, the range of applicability of existing and new relative permeability models should be investigated and model formulations could be enhanced to respond in a consistent way to changes in S_{nr} and S_{ne}. Macro-scale models should better represent phenomena observed at pore scale in a practical manner.

Models should be able to account for heterogeneous conditions commonly found in the field. Thus, the implementation of layering capabilities in multiphase analytical models has been beneficial for predictions of LNAPL distribution and mobility in certain cases. Further refined approaches could incorporate vertical variation of subsurface properties within any layer to better represent coarsening- and fining-upward sequences in simple models as already implemented by Al Awar (2008). On the other hand, stochastic approaches from other disciplines will most likely be increasingly adopted in the near future to simulate multifluid systems and account for the associated uncertainties.

The development and evaluation of HRSC approaches is a promising area of research necessary for the study of many subsurface systems. Future HRSC approaches should exhibit a more quantitative nature and better integrate scale-appropriate measurements in time and space (in both vertical and horizontal planes). Current three-dimensional representations of LIF data should be done and interpreted with caution because of these reasons. In addition, HRSC approaches should facilitate the assessment not just of hydrostratigraphic characteristics and LNAPL distribution but also NSZD rates, specific mass transfer processes, and risks to human health and the environment.

These lines of research would lead to better understanding of subsurface systems and more effective and sustainable management of LNAPL contaminated sites in the future.

10 References

Abbasian, F., Lockington, R., Mallavarapu, M., Naidu, R. (2015). A comprehensive review of aliphatic hydrocarbon biodegradation by bacteria. Applied Biochemistry and Biotechnology, 176(3), 670–699.

Abriola, L.M., Pinder, G.F. (1985). A multiphase approach to the modeling of porous media contamination by organic compounds: 1. Equation development. Water Resources Research, 21(1), 11–18.

Adadevoh, J.S., Ramsburg, C.A., Ford, R.M. (2018). Chemotaxis increases the retention of bacteria in porous media with residual NAPL entrapment. Environmental Science & Technology, 52(13), 7289–7295.

Adamski, M., Kremesec, V., Charbeneau, R.J. (2003). Residual saturation: What is it? How is it measured? How should we use it? [Paper presentation]. Petroleum Hydrocarbons and Organic Chemicals in Ground Water: Prevention, Assessment, and Remediation Conference and Exposition, Costa Mesa, CA, United States.

Adamski, M., Kremesec, V., Kolhatkar, R., Pearson, C., Rowan, B. (2005). LNAPL in fine-grained soils: Conceptualization of saturation, distribution, recovery, and their modeling. Groundwater Monitoring & Remediation, 25(1), 100–112.

Adamson, D.T., Chapman, S., Mahler, N., Newell, C., Parker, B., Pitkin, S., Rossi, M., Singletary, M. (2014). Membrane interface probe protocol for contaminants in low-permeability zones. Groundwater, 52(4), 550–565.

Adamson, D.T., Chapman, S.W., Farhat, S.K., Parker, B.L., de Blanc, P., Newell, C.J. (2015). Characterization and source history modeling using low-k zone profiles at two source areas. Groundwater Monitoring & Remediation, 35(2), 52–69.

Agaoglu, B., Copty, N.K., Scheytt, T., Hinkelmann, R. (2015). Interphase mass transfer between fluids in subsurface formations: A review. Advances in Water Resources, 79, 162–194.

Ahmed, W., Palmier, C., Atteia, O., Class, H. (2018). Multiphase simulation model for validating the estimate of light non-aqueous phase liquids (LNAPL) transmissivity using bail-down test. Arabian Journal for Science and Engineering, 1–9.

Al Awar, Z.R. (2008). Adapting, optimizing, and evaluating a model for the remediation of LNAPL in heterogeneous soil environments [Doctoral dissertation, The University of Texas at Austin].

Al-Raoush, R.I., Willson, C.S. (2005). A pore-scale investigation of a multiphase porous media system. Journal of Contaminant Hydrology, 77(1–2), 67–89.

Aldstadt, J., St. Germain, R., Grundl, T., Schweitzer, R. (2002). An in situ laser-induced fluorescence system for polycylic aromatic hydrocarbon-contaminated sediments. U.S. Environmental Protection Agency.

Alexander, M., Berg, S.J., Illman, W.A. (2011). Field study of hydrogeologic characterization methods in a heterogeneous aquifer. Groundwater, 49(3), 365–382.

Alexandra, R., Gerhard, J.I., Kueper, B.H. (2012). Hydraulic displacement of dense nonaqueous phase liquids for source zone stabilization. Groundwater, 50(5), 765–774.

Alfaro Soto, M., Chang, H.K. (2015). Behavior of LNAPL in soils with multimodal pore-size distribution. In D. Manzanal, A.O. Sfriso (Eds.), From fundamentals to applications in geotechnics (pp. 2284–2291). IOS Press.

Alfaro Soto, M., Lenhard, R., Chang, H.K., van Genuchten, M.Th. (2019). Determination of specific LNAPL volumes in soils having a multimodal pore-size distribution. Journal of Environmental Management, 237, 576–584.

Algreen, M., Kalisz, M., Stalder, M., Martac, E., Krupanek, J., Trapp, S., Bartke, S. (2015). Using pre-screening methods for an effective and reliable site characterization at megasites. Environmental Science and Pollution Research, 22(19), 14673–14686.

Alizadeh, A.H., Piri, M. (2014). Three-phase flow in porous media: A review of experimental studies on relative permeability. Reviews of Geophysics, 52(3), 468–521.

Alostaz, M.D., Biggar, K., Donahue, R., Hall, G. (2008). Soil type effects on petroleum contamination characterization using ultraviolet induced fluorescence excitation-emission matrices (EEMs) and parallel factor analysis (PARAFAC). Journal of Environmental Engineering and Science, 7(6), 661–675.

Alvarez, P.J., Heathcote, R.C., Powers, S.E. (1998). Caution against interpreting gasoline release dates based on BTEX ratios in ground water. Groundwater Monitoring & Remediation, 18(4), 69–76.

Alvarez, P.J.J., Illman, W.A. (2006). Bioremediation and natural attenuation: process fundamentals and mathematical models. John Wiley & Sons.

Alvarez-Acosta, C., Lascano, R.J., Stroosnijder, L. (2012). Test of the Rosetta pedotransfer function for saturated hydraulic conductivity. Open Journal of Soil Science, 2(3), 203–212.

American Petroleum Institute (2006). API Interactive LNAPL Guide version 2.0.4.

American Petroleum Institute (2016). LNAPL transmissivity workbook: a tool for baildown test analysis—user guide (API Publication 4762).

Amos, R.T., Mayer, K.U. (2006). Investigating the role of gas bubble formation and entrapment in contaminated aquifers: Reactive transport modelling. Journal of Contaminant Hydrology, 87(1–2), 123–154.

Anderson, W.G. (1987). Wettability literature survey-part 4: Effects of wettability on capillary pressure. Journal of Petroleum Technology, 39(10), 1–283.

Andersson, J.T., Achten, C. (2015). Time to say goodbye to the 16 EPA PAHs? Toward an up-to-date use of PACs for environmental purposes. Polycyclic Aromatic Compounds, 35(2–4), 330–354.

Annable, M.D., Hatfield, K., Cho, J., Klammler, H., Parker, B.L., Cherry, J.A., Rao, P.S.C. (2005). Field-scale evaluation of the passive flux meter for simultaneous measurement of groundwater and contaminant fluxes. Environmental Science & Technology, 39(18), 7194–7201.

Apitz, S.E., Theriault, G.A., Lieberman, S.H. (1992). Optimization of the optical characteristics of a fiber-optic-guided laser fluorescence technique for the in-situ evaluation of fuels in soils. In T. Vo-Dinh (Ed.), Environmental and process monitoring technologies (vol. 1637, pp. 241-254). International Society for Optics and Photonics.

Aral, M.M., Liao, B. (2000). LNAPL thickness interpretation based on bail-down tests. Ground Water, 38(5), 696–701.

Aral, M.M., Liao, B. (2002). Effect of groundwater table fluctuations on LNAPL thickness in monitoring wells. Environmental Geology, 42(2–3), 151–161.

Archie, G.E. (1942). The electrical resistivity log as an aid in determining some reservoir characteristics. Transactions of the AIME, 146(01), 54–62.

Armstrong, R.T., McClure, J.E., Berrill, M.A., Rücker, M., Schlüter, S., Berg, S. (2016). Beyond Darcy's law: The role of phase topology and ganglion dynamics for two-fluid flow. Physical Review E, 94(4), Article 043113.

Arshadi, M., De Paolis Kaluza, M.C., Miller, E.L., Abriola, L.M. (2020). Subsurface source zone characterization and uncertainty quantification using discriminative random fields. Water Resources Research, 56(3), Article e2019WR026481.

Artiola, J., Pepper, I.L., Brusseau, M.L. (2004). Environmental monitoring and characterization. Elsevier.

Arya, L.M., Leij, F.J., van Genuchten, M.T., Shouse, P.J. (1999). Scaling parameter to predict the soil water characteristic from particle-size distribution data. Soil Science Society of America Journal, 63(3), 510–519.

Askarani, K.K. (2019). Thermal monitoring of natural source zone depletion [Doctoral dissertation, Colorado State University].

ASTM International (2009). Standard practice for description and identification of soils (visual-manual procedure) (D2488 - 09a).

ASTM International (2013). Standard guide for estimation of LNAPL transmissivity (E2856 - 13).

Atekwana, E.A., Atekwana, E.A. (2010). Geophysical signatures of microbial activity at hydrocarbon contaminated sites: a review. Surveys in Geophysics, 31(2), 247–283.

Atekwana, E.A., Sauck, W.A., Werkema Jr, D.D. (2000). Investigations of geoelectrical signatures at a hydrocarbon contaminated site. Journal of Applied Geophysics, 44(2–3), 167–180.

Atekwana, E.A., Slater, L.D. (2009). Biogeophysics: A new frontier in Earth science research. Reviews of Geophysics, 47(4), Article RG4004.

Atkins, J.E., McBride, E.F. (1992). Porosity and packing of Holocene river, dune, and beach sands. AAPG Bulletin, 76(3), 339–355.

Atteia, O., Palmier, C., Schäfer, G. (2019). On the influence of groundwater table fluctuations on oil thickness in a well related to an LNAPL contaminated aquifer. Journal of Contaminant Hydrology, 223, Article 103476.

Babak, O., Deutsch, C.V. (2009). Statistical approach to inverse distance interpolation. Stochastic Environmental Research and Risk Assessment, 23(5), 543–553.

Baedecker, M.J., Cozzarelli, I.M., Eganhouse, R.P., Siegel, D.I., Bennett, P.C. (1993). Crude oil in a shallow sand and gravel aquifer-III. Biogeochemical reactions and mass balance modeling in anoxic groundwater. Applied Geochemistry, 8(6), 569–586.

Baedecker, M.J., Eganhouse, R.P., Bekins, B.A., Delin, G.N. (2011). Loss of volatile hydrocarbons from an LNAPL oil source. Journal of Contaminant Hydrology, 126(3–4), 140–152.

Baedecker, M.J., Eganhouse, R.P., Qi, H., Cozzarelli, I.M., Trost, J.J., Bekins, B.A. (2018). Weathering of oil in a surficial aquifer. Groundwater, 56(5), 797–809.

Ballestero, T.P., Fiedler, F.R., Kinner, N.E. (1994). An investigation of the relationship between actual and apparent gasoline thickness in a uniform sand aquifer. Groundwater, 32(5), 708–718.

Barth, G.R., Hill, M.C., Illangasekare, T.H., Rajaram, H. (2001). Predictive modeling of flow and transport in a two-dimensional intermediate-scale, heterogeneous porous medium. Water Resources Research, 37(10), 2503–2512.

Basu, N.B., Fure, A.D., Jawitz, J.W. (2008a). Simplified contaminant source depletion models as analogs of multiphase simulators. Journal of Contaminant Hydrology, 97, 87–99.

Basu, N.B., Rao, P.S.C., Falta, R.W., Annable, M.D., Jawitz, J.W., Hatfield, K. (2008b). Temporal evolution of DNAPL source and contaminant flux distribution: Impacts of source mass depletion. Journal of Contaminant Hydrology, 95, 93–109.

Batu, V. (2012). An assessment of the Huntley (2000) baildown tests data analysis method. Groundwater, 50(4), 500–503.

Baveye, P.C. (2020). “Soil biofilms”: Misleading description of the spatial distribution of microbial biomass in soils. Soil Ecology Letters, 2(1), 2–5.

Bear, J. (1972). Dynamics of fluids in porous media. Elsevier.

Bear, J., Ryzhik, V. (1998). On the displacement of NAPL lenses and plumes in a phreatic aquifer. Transport in Porous Media, 33(3), 227–255.

Bear, J., Ryzhik, V., Braester, C., Entov, V. (1996). On the movement of an LNAPL lens on the water table. Transport in Porous Media, 25(3), 283–311.

Beckett, G.D., Huntley, D. (2015). LNAPL transmissivity: A twisted parameter. Groundwater Monitoring & Remediation, 35, 20–24.

Beckett, G.D., Lyverse, M.A. (2002). A protocol for performing field tasks and follow-up analytical evaluation for LNAPL transmissivity using well baildown procedures.

Behroozmand, A.A., Keating, K., Auken, E. (2015). A review of the principles and applications of the NMR technique for near-surface characterization. Surveys in Geophysics, 36(1), 27–85.

Bekele, D.N., Naidu, R., Bowman, M., Chadalavada, S. (2013). Vapor intrusion models for petroleum and chlorinated volatile organic compounds: Opportunities for future improvements. Vadose Zone Journal, 12(2), 1–13.

Bekele, E.B., García-Rincón, J., Rayner, J.L., McLaughlan, R.G., Gatsios, E., Paiva Lago, G. (2019). Groundwater pumping test analyses for a gasoline contaminated site at Donnybrook, Western Australia. Commonwealth Scientific and Industrial Research Organisation.

Bekins, B.A., Hostettler, F.D., Herkelrath, W.N., Delin, G.N., Warren, E., Essaid, H.I. (2005). Progression of methanogenic degradation of crude oil in the subsurface. Environmental Geosciences, 12(2), 139–152.

Béland-Pelletier, C., Fraser, M., Barker, J., Ptak, T. (2011). Estimating contaminant mass discharge: A field comparison of the multilevel point measurement and the integral pumping investigation approaches and their uncertainties. Journal of Contaminant Hydrology, 122(1–4), 63–75.

Bennett, D.H., James, A.L., McKone, T.E., Oldenburg, C.M. (1998). On uncertainty in remediation analysis: Variance propagation from subsurface transport to exposure modeling. Reliability Engineering and System Safety, 62(1–2), 117–129.

Bense, V.F., Read, T., Bour, O., Le Borgne, T., Coleman, T., Krause, S., Chalari, A., Mondanos, M., Ciocca, F., Selker, J.S. (2016). Distributed temperature sensing as a downhole tool in hydrogeology. Water Resources Research, 52(12), 9259–9273.

Benson, C.H., Chiang, I., Chalermyanont, T., Sawangsuriya, A. (2014). Estimating van Genuchten parameters α and n for clean sands from particle size distribution data. In M. Iskander, J.E. Garlanger, M.H. Hussein (Eds.), From soil behavior fundamentals to innovations in geotechnical engineering: honoring Roy E. Olson (pp. 410–427). American Society of Civil Engineers.

Benson, D.A., Meerschaert, M.M., Revielle, J. (2013). Fractional calculus in hydrologic modeling: A numerical perspective. Advances in Water Resources, 51, 479–497.

Berg, S.J., Illman, W.A. (2015). Comparison of hydraulic tomography with traditional methods at a highly heterogeneous site. Groundwater, 53(1), 71–89.

Berkowitz, B. (1995). Analysis of fracture network connectivity using percolation theory. Mathematical Geology, 27(4), 467–483.

Berkowitz, B. (2002). Characterizing flow and transport in fractured geological media: A review. Advances in Water Resources, 25(8–12), 861–884.

Berkowitz, B., Cortis, A., Dentz, M., Scher, H. (2006). Modeling Non-fickian transport in geological formations as a continuous time random walk. Reviews of Geophysics, 44, Article RG2003.

Beven, K. (1993). Prophecy, reality and uncertainty in distributed hydrological modelling. Advances in Water Resources, 16(1), 41–51.

Bianchi, M., Zheng, C., Wilson, C., Tick, G.R., Liu, G., Gorelick, S.M. (2011). Spatial connectivity in a highly heterogeneous aquifer: From cores to preferential flow paths. Water Resources Research, 47, Article W05524.

Binley, A., Hubbard, S.S., Huisman, J.A., Revil, A., Robinson, D.A., Singha, K., Slater, L.D. (2015). The emergence of hydrogeophysics for improved understanding of subsurface processes over multiple scales. Water resources research, 51(6), 3837–3866.

Blunt, M.J. (2000). An empirical model for three-phase relative permeability. SPE Journal, 5(04), 435–445.

Blunt, M.J. (2017). Multiphase flow in permeable media: A pore-scale perspective. Cambridge University Press.

Boadu, F.K. (2000). Hydraulic conductivity of soils from grain-size distribution: new models. Journal of Geotechnical and Geoenvironmental Engineering, 126(8), 739–746.

Bohling, G., Liu, G., Knobbe, S., Reboulet, E.C., Butler, J.J. (2011, December). A modified approach for direct-push hydraulic profiling in formations of moderate to high hydraulic conductivity [Conference session]. AGU Fall Meeting, San Francisco, CA, United States.

Bohling, G.C., Butler Jr., J.J. (2010). Inherent limitations of hydraulic tomography. Groundwater, 48(6), 809–824.

Bohling, G.C., Liu, G., Dietrich, P., Butler, J.J. (2016). Reassessing the MADE direct-push hydraulic conductivity data using a revised calibration procedure. Water Resources Research, 52(11), 8970–8985.

Bohling, G.C., Liu, G., Knobbe, S.J., Reboulet, E.C., Hyndman, D.W., Dietrich, P., Butler, J.J. (2012). Geostatistical analysis of centimeter-scale hydraulic conductivity variations at the MADE site. Water Resources Research, 48(2), Article W02525.

Bonnet, E., Bour, O., Odling, N.E., Davy, P., Main, I., Cowie, P., Berkowitz, B. (2001). Scaling of fracture systems in geological media. Reviews of Geophysics, 39(3), 347–383.

Borgonovo, E. (2010). Sensitivity analysis with finite changes: An application to modified EOQ models. European Journal of Operational Research, 200(1), 127–138.

Borgonovo, E., Plischke, E. (2016). Sensitivity analysis: a review of recent advances. European Journal of Operational Research, 248(3), 869–887.

Bouchard, D., Hunkeler, D., Madsen, E.L., Buscheck, T., Daniels, E., Kolhatkar, R., DeRito, C.M., Aravena, R., Thomson, N.R. (2018). Application of diagnostic tools to evaluate remediation performance at petroleum hydrocarbon-impacted sites. Groundwater Monitoring & Remediation, 38(4), 88–98.

Bouwer, H. (1989). The Bouwer and Rice Slug Test—An Update. Groundwater, 27(3), 304–309.

Bouwer, H., Rice, R.C. (1976). A slug test for determining hydraulic conductivity of unconfined aquifers with completely or partially penetrating wells. Water Resources Research, 12(3), 423–428.

Bradford, S.A., Abriola, L.M., Leij, F.J. (1997). Wettability effects on two-and three-fluid relative permeabilities. Journal of Contaminant Hydrology, 28(1–2), 171–191.

Bradford, S.A., Abriola, L.M., Rathfelder, K.M. (1998). Flow and entrapment of dense nonaqueous phase liquids in physically and chemically heterogeneous aquifer formations. Advances in Water Resources, 22(2), 117–132.

Carles Brangarí, A., Sanchez-Vila, X., Freixa, A., Romaní, A.M., Rubol, S., Fernàndez-Garcia, D. (2017). A mechanistic model (BCC-PSSICO) to predict changes in the hydraulic properties for bio-amended variably saturated soils. Water Resources Research, 53(1), 93–109.

Broholm, M.M., Janniche, G.S., Mosthaf, K., Fjordbøge, A.S., Binning, P.J., Christensen, A.G., Grosen, B., Jørgensen, T.H., Keller, C., Wealthall, G., Kerrn-Jespersen, H. (2016). Characterization of chlorinated solvent contamination in limestone using innovative FLUTe® technologies in combination with other methods in a line of evidence approach. Journal of Contaminant Hydrology, 189, 68–85.

Brooks, R.H., Corey, A.T. Hydraulic properties of porous media (Hydrology papers no. 3). Colorado State University.

Brusseau, M.L., DiFilippo, E.L., Marble, J.C., Oostrom, M. (2008). Mass-removal and mass-flux-reduction behavior for idealized source zones with hydraulically poorly-accessible immiscible liquid. Chemosphere, 71(8), 1511–1521.

Brusseau, M.L., Rao, P.S.C., Gillham, R.W. (1989). Sorption nonideality during organic contaminant transport in porous media. Critical Reviews in Environmental Science & Technology, 19(1), 33–99.

Bujewski, G., Rutherford, B. (1997). The rapid optical screening tool (ROST) laser-induced fluorescence (LIF) system for screening of petroleum hydrocarbons in subsurface soils (EPA/600/R-97/020). U.S. Environmental Protection Agency.

Burdine, N. (1953). Relative permeability calculations from pore size distribution data. Journal of Petroleum Technology, 5(3), 71–78.

Butler Jr., J.J. (1988). Pumping tests in nonuniform aquifers—The radially symmetric case. Journal of Hydrology, 101(1–4), 15–30.

Butler Jr., J.J. (2019). The design, performance, and analysis of slug tests (2nd ed.). CRC Press.

Butler Jr., J.J., Bohling, G.C., Hyder, Z., McElwee, C.D. (1994). The use of slug tests to describe vertical variations in hydraulic conductivity. Journal of Hydrology, 156(1–4), 137–162.

Butler Jr., J.J., Dietrich, P., Wittig, V., Christy, T. (2007). Characterizing hydraulic conductivity with the direct-push permeameter. Groundwater, 45(4), 409–419.

Butler Jr., J.J., Healey, J.M. (1998). Relationship between pumping-test and slug-test parameters: Scale effect or artifact? Groundwater, 36(2), 305–312.

Butler Jr., J.J., Healey, J.M., McCall, G.W., Garnett, E.J., Loheide, S.P. (2002). Hydraulic tests with direct-push equipment. Groundwater, 40(1), 25–36.

Butler Jr., J.J., McElwee, C.D., Liu, W. (1996). Improving the quality of parameter estimates obtained from slug tests. Groundwater, 34(3), 480–490.

Butler, J.J. (2005). Hydrogeological methods for estimation of spatial variations in hydraulic conductivity. In Y. Rubbin, S.S. Hubbard (Eds.), Hydrogeophysics (pp., 23–58). Springer.

Camps-Roach, G., O'Carroll, D.M., Newson, T.A., Sakaki, T., Illangasekare, T.H. (2010). Experimental investigation of dynamic effects in capillary pressure: Grain size dependency and upscaling. Water Resources Research, 46(8), Article W08544.

Carrera, J. (1993). An overview of uncertainties in modelling groundwater solute transport. Journal of Contaminant Hydrology, 13(1–4), 23–48.

Carrera, J., Alcolea, A., Medina, A., Hidalgo, J., Slooten, L.J. (2005). Inverse problem in hydrogeology. Hydrogeology Journal, 13(1), 206–222.

Carrera, J., Sánchez-Vila, X., Benet, I., Medina, A., Galarza, G., Guinerà, J. (1998). On matrix diffusion: Formulations, solution methods and qualitative effects. Hydrogeology Journal, 6(1), 178–190.

Carsel, R.F., Parrish, R.S. (1988). Developing joint probability distributions of soil water retention characteristics. Water resources research, 24(5), 755–769.

Carstea, E.M., Popa, C.L., Baker, A., Bridgeman, J. (2020). In situ fluorescence measurements of dissolved organic matter: A review. Science of the Total Environment, 699, Article 134361.

Chapelle, F.H. (2000). The significance of microbial processes in hydrogeology and geochemistry. Hydrogeology Journal, 8(1), 41–46.

Chaplin, B.P., Delin, G.N., Baker, R.J., Lahvis, M.A. (2002). Long-term evolution of biodegradation and volatilization rates in a crude oil-contaminated aquifer. Bioremediation Journal, 6(3), 237–255.

Chapman, S.W., Parker, B.L. (2005). Plume persistence due to aquitard back diffusion following dense nonaqueous phase liquid source removal or isolation. Water Resources Research, 41(12), 1–16.

Chapuis, R.P. (2012). Predicting the saturated hydraulic conductivity of soils: a review. Bulletin of Engineering Geology and the Environment, 71(3), 401–434.

Chapuis, R.P., Aubertin, M. (2003). On the use of the Kozeny Carman equation to predict the hydraulic conductivity of soils. Canadian Geotechnical Journal, 40(3), 616–628.

Charbeneau, R., Kirkman, A., Adamski, M. (2013). Discussion of "An assessment of the Huntley (2000) baildown test data analysis method". Groundwater, 51(5), 657–659.

Charbeneau, R.J. (2007a). LNAPL Distribution and Recovery Model (LDRM). Volume 1: distribution and recovery of petroleum hydrocarbon liquids in porous media (API Publication 4760). American Petroleum Institute.

Charbeneau, R.J. (2007b). LNAPL Distribution and Recovery Model (LDRM). Volume 2: user and parameter selection guide (API Publication 4760). American Petroleum Institute.

Charbeneau, R.J., Johns, R.T., Lake, L.W., McAdams III, M.J. (2000). Free-product recovery of petroleum hydrocarbon liquids. Ground Water Monitoring and Remediation, 20(3), 147–158.

Chatzis, I., Morrow, N.R., Lim, H.T. (1983). Magnitude and detailed structure of residual oil saturation. Society of Petroleum Engineers Journal, 23(02), 311–326.

Cheng, C., Chen, X. (2007). Evaluation of methods for determination of hydraulic properties in an aquifer–aquitard system hydrologically connected to a river. Hydrogeology Journal, 15(4), 669–678.

Cherry, J.A., Gillham, R.W., Anderson, E.G., Johnson, P.E. (1983). Migration of contaminants in groundwater at a landfill: A case study: 2. Groundwater monitoring devices. Journal of Hydrology, 63(1–2), 31–49.

Cherry, J.A., Parker, B.L., Keller, C. (2007). A new depth-discrete multilevel monitoring approach for fractured rock. Groundwater Monitoring & Remediation, 27(2), 57–70.

Childs, E.C., Collis-George, N. (1950). The permeability of porous materials. Proceedings of the Royal Society of London. Series A. Mathematical and Physical Sciences, 201(1066), 392–405.

Chompusri, S., Rivett, M.O., Mackay, R. (2002). LNAPL redistribution on a fluctuating water table: column experiments. In S.F. Thornton, S.E. Oswald (Eds.), Groundwater quality: natural and enhanced restoration of groundwater pollution (IAHS Publication no. 275, pp. 225–231). IAHS Press.

Christ, J.A., Ramsburg, C.A., Pennell, K.D., Abriola, L.M. (2006). Estimating mass discharge from dense nonaqueous phase liquid source zones using upscaled mass transfer coefficients: An evaluation using multiphase numerical simulations. Water Resources Research, 42(11), Article W11420.

Ciriello, V., Edery, Y., Guadagnini, A., Berkowitz, B. (2015). Multimodel framework for characterization of transport in porous media. Water Resources Research, 51, 3384–3402.

Cirpka, O. A., Valocchi, A. J. (2016). Debates—Stochastic subsurface hydrology from theory to practice: Does stochastic subsurface hydrology help solving practical problems of contaminant hydrogeology? Water Resources Research, 52(12), 9218–9227.

Contaminated Land: Applications in Real Environments (2014). An illustrated handbook of LNAPL transport and fate in the subsurface. Environment Agency.

Cohen, G.J., Jousse, F., Luze, N., Höhener, P., Atteia, O. (2016). LNAPL source zone delineation using soil gases in a heterogeneous silty-sand aquifer. Journal of Contaminant Hydrology, 192, 20–34.

Cooper Jr, H.H., Jacob, C.E. (1946). A generalized graphical method for evaluating formation constants and summarizing well-field history. Eos, Transactions American Geophysical Union, 27(4), 526–534.

Corapcioglu, M.Y., Tuncay, K., Lingarn, R., Kambham, K.K. (1994). Analytical expressions to estimate the free product recovery in oil-contaminated aquifers. Water Resources Research, 30(12), 3301–3311.

Corey, A.T. (1994). Mechanics of immiscible fluids in porous media (3rd ed.). Water Resources Publication.

Corey, A.T., Brooks, R.H. (1999). Brooks-Corey relationships. In M.Th. van Genuchten, F.J. Leji, L. Wu (Eds.), Proceedings of the International Workshop on Characterization and Measurement of the Hydraulic Properties of Unsaturated Porous Media. U.S. Department of Agriculture; University of California.

Cormican, A., Devlin, J.F., Divine, C. (2020. Grain size analysis and permeametry for estimating hydraulic conductivity in engineered porous media. Groundwater Monitoring & Remediation, 40(2), 65–72.

Costa, A. (2006). Permeability-porosity relationship: A reexamination of the Kozeny-Carman equation based on a fractal pore-space geometry assumption. Geophysical Research Letters, 33(2), Article L02318.

Cozzarelli, I.M., Baedecker, M.J., Eganhouse, R.P., Goerlitz, D.F. (1994). The geochemical evolution of low-molecular-weight organic acids derived from the degradation of petroleum contaminants in groundwater. Geochimica et Cosmochimica Acta, 58(2), 863–877.

Cozzarelli, I.M., Herman, J.S., Baedecker, M.J., Fischer, J.M. (1999). Geochemical heterogeneity of a gasoline-contaminated aquifer. Journal of Contaminant Hydrology, 40(3), 261–284.

Cozzarelli, I.M., Schreiber, M.E., Erickson, M.L., Ziegler, B.A. (2015). Arsenic cycling in hydrocarbon plumes: secondary effects of natural attenuation. Groundwater, 54(1), 35–45.

CRC CARE (2018, December). Ignore soil pollution at humanity's peril [Press release]. https://www.crccare.com/news/ignore-soil-pollution-at-humanity-s-peril

Custodio, E., Llamas, M.R. (1976). Hidrología subterránea. Omega.

Cvetkovic, V., Fiori, A., Dagan, G. (2014). Solute transport in aquifers of arbitrary variability: A time-domain random walk formulation. Water Resources Research, 50(7), 5759–5773.

Dagan, G. (1986). Statistical theory of groundwater flow and transport: Pore to laboratory, laboratory to formation, and formation to regional scale. Water Resources Research, 22(9S), 120S–134S.

Dagan, G., Fiori, A., Jankovic, I. (2013). Upscaling of flow in heterogeneous porous formations: Critical examination and issues of principle. Advances in Water Resources, 51, 67–85.

Dalton, M.G., Huntsman, B.E., Bradbury, K. (2006). Acquisition and interpretation of water-level data. In D.M. Nielsen (Ed.), Practical handbook of environmental site characterization and ground-water monitoring (2nd ed.). CRC Press.

D'Aniello, A. (2017). The flow behaviour of elemental mercury DNAPL in porous media [Doctoral dissertation, Università degli Studi di Napoli Federico II].

Darcy, H. (1856). The public fountains of the city of Dijon. Dalmont.

Das, D.B., Hassanizadeh, S.M. (Eds.). (2005). Upscaling multiphase flow in porous media. Springer.

Das, N., Chandran, P. (2011). Microbial degradation of petroleum hydrocarbon contaminants: an overview. Biotechnology Research International, 2011, 2–13.

Dassargues, A. (2018). Hydrogeology: groundwater science and engineering. CRC Press.

Davis, G.B., Trefry, M.G., Patterson, B.M. (2009). Petroleum vapour model comparison (CRC CARE Technical Report 9). Cooperative Research Centre for Contamination Assessment and Remediation of the Environment.

de Blanc, P., Farhat, S.K. (2018, October–November). A new tool for determining LNAPL volume and extent [Conference session]. 25th IPEC: International Petroleum Environmental Conference, Denver, CO, United States.

de Dreuzy, J.R. (2008). Modélisation des écoulements et du transport dans les milieux fortement hétérogènes et fracturés. Université de Rennes 1.

de Marsily, G. (1986). Quantitative hydrogeology. Paris School of Mines.

de Marsily, G., Combes, P., Goblet, P. (1992). Comment on 'Ground-water models cannot be validated', by LF Konikow JD Bredehoeft. Advances in Water Resources, 15(6), 367–369.

de Marsily, G., Delay, F., Gonçalvès, J., Renard, P., Teles, V., Violette, S. (2005). Dealing with spatial heterogeneity. Hydrogeology Journal, 13(1), 161–183.

De Miguel, E., Barrio-Parra, F., Elío, J., Izquierdo-Díaz, M., García-González, J.E., Mazadiego, L.F., Medina, R. (2018). Applicability of radon emanometry in lithologically discontinuous sites contaminated by organic chemicals. Environmental Science and Pollution Research, 25(20), 20255-20263.

Dell'Arciprete, D., Vassena, C., Baratelli, F., Giudici, M., Bersezio, R., Felletti, F. (2014). Connectivity and single/dual domain transport models: Tests on a point-bar/channel aquifer analogue. Hydrogeology Journal, 22(4), 761–778.

Delle Site, A. (2001). Factors affecting sorption of organic compounds in natural sorbent/water systems and sorption coefficients for selected pollutants. A review. Journal of Physical and Chemical Reference Data, 30(1), 187–439.

Delshad, M., Pope, G.A. (1989). Comparison of the three-phase oil relative permeability models. Transport in Porous Media, 4(1), 59–83.

Devlin, J.F. (2015). HydrogeoSieveXL: an Excel-based tool to estimate hydraulic conductivity from grain-size analysis. Hydrogeology Journal, 23(4), 837–844.

Devlin, J.F. (2017a). Erratum to: HydrogeoSieveXL: an Excel-based tool to estimate hydraulic conductivity from grain-size analysis. Hydrogeology Journal, 25(2), 599–599.

Devlin, J.F. (2017b). Reply to Comment on "HydrogeoSieveXL: an Excel-based tool to estimate hydraulic conductivity from grain-size analysis": technical note published in Hydrogeology Journal (2015) 23:837–844, by JF Devlin. Hydrogeology Journal, 25(2), 593–596.

Devlin, J.F. (2018). Reply to Comment on 'Reply to Comment on "HydrogeoSieveXL: an Excel-based tool to estimate hydraulic conductivity from grain-size analysis": technical note published in Hydrogeology Journal (2015) 23:837–844, by JF Devlin': article published in Hydrogeology Journal (2017) 25:593–596, by JF Devlin. Hydrogeology Journal, 26(1), 359–360.

Devlin, J.F., McElwee, C.D. (2007). Effects of measurement error on horizontal hydraulic gradient estimates. Groundwater, 45(1), 62–73.

Diamantopoulos, E., Durner, W., (2012). Dynamic nonequilibrium of water flow in porous media: A review. Vadose Zone Journal, 11(3), Article vzj2011-0197.

Dietrich, P., Butler Jr., J.J., Faiß, K. (2008). A rapid method for hydraulic profiling in unconsolidated formations. Groundwater, 46(2), 323–328.

Dietrich, P., Leven, C. (2009). Direct push-technologies. In R. Kirsch (Ed.), Groundwater geophysics—a tool for hydrogeology (2nd ed., pp., 347–366). Springer.

Dietze, M., Dietrich, P. (2012). Evaluation of vertical variations in hydraulic conductivity in unconsolidated sediments. Groundwater, 50(3), 450–456.

DiFilippo, E.L., Brusseau, M.L. (2011). Assessment of a simple function to evaluate the relationship between mass flux reduction and mass removal for organic-liquid contaminated source zones. Journal of Contaminant Hydrology, 123, 104–113.

Dillard, L.A., Essaid, H.I., Herkelrath, W.N. (1997). Multiphase flow modeling of a crude-oil spill site with a bimodal permeability distribution. Water Resources Research, 33(7), 1617–1632.

Dobson, R., Schroth, M.H., Zeyer, J. (2007). Effect of water-table fluctuation on dissolution and biodegradation of a multi-component, light nonaqueous-phase liquid. Journal of Contaminant Hydrology, 94, 235–248.

Dogan, M., Van Dam, R.L., Bohling, G.C., Butler Jr., J.J., Hyndman, D.W. (2011). Hydrostratigraphic analysis of the MADE site with full-resolution GPR and direct-push hydraulic profiling. Geophysical Research Letters, 38(6), Article L06405.

Dogan, M., van Dam, R.L., Liu, G., Meerschaert, M.M., Butler Jr., J.J., Bohling, G.C., Benson, D.A., Hyndman, D.W. (2014). Predicting flow and transport in highly heterogeneous alluvial aquifers. Geophysical Research Letters, 41, 7560–7565.

Doherty, J. (2015). Calibration and uncertainty analysis for complex environmental models. Watermark Numerical Computing.

Domenico, P.A., Schwartz, F.W. (1998). Physical and chemical hydrogeology. Wiley.

Douglas, R.K., Nawar, S., Alamar, M.C., Coulon, F., Mouazen, A.M. (2017). Almost 25 years of chromatographic and spectroscopic analytical method development for petroleum hydrocarbons analysis in soil and sediment: state-of-the-art, progress and trends. Critical Reviews in Environmental Science & Technology, 47(16), 1497–1527.

Drake, S.S., O'Carroll, D.M., Gerhard, J.I. (2013). Wettability contrasts between fresh and weathered diesel fuels. Journal of Contaminant Hydrology, 144, 46–57.

Durner, W. (1994). Hydraulic conductivity estimation for soils with heterogeneous pore structure. Water Resources Research, 30(2), 211–223.

Durnford, D., Brookman, J., Billica, J., Milligan, J. (1991). LNAPL distribution in a cohesionless soil: A field investigation and cryogenic sampler. Groundwater Monitoring & Remediation, 11(3), 115–122.

Dyment, S., Kady, T. (2019). Part, 2: To HRSC or not? Cost vs. benefits. LUSTLine, 85, 13–28.

Ebrahimi, F., Lenhard, R.J., Nakhaei, M., Nassery, H.R. (2019). An approach to optimize the location of LNAPL recovery wells using the concept of a LNAPL specific yield. Environmental Science and Pollution Research, 26(28), 28714–28724.

Eggleston, J., Rojstaczer, S. (2001). The value of grain-size hydraulic conductivity estimates: Comparison with high resolution in-situ field hydraulic conductivity. Geophysical Research Letters, 28(22), 4255–4258.

Eichert, J., McAlexander, B., Lyverse, M., Michalski, P., Sihota, N. (2017). Spatial and temporal variation in natural source zone depletion rates at a former oil refinery. Vadose Zone Journal, 16(10), 1–16.

Einarson, M., Fure, A., St. Germain, R.W., Chapman, S., Parker, B.L. (2016). Direct Push Optical Screening Tool for High Resolution, Real-Time Mapping of Chlorinated Solvent DNAPL Architecture (ESTCP Project ER-201121). Environmental Security Technology Certification Program.

Einarson, M., Fure, A., St. Germain, R.W., Chapman, S., Parker, B.L. (2018). DyeLIF™: A new direct-push laser-induced fluorescence sensor system for chlorinated solvent DNAPL and other non-naturally fluorescing NAPLs. Groundwater Monitoring & Remediation, 38(3), 28–42.

Einarson, M.D., Cherry, J.A. (2002). A new multilevel ground water monitoring system using multichannel tubing. Groundwater Monitoring & Remediation, 22(4), 52–65.

Ellithy, G. (2017). A spreadsheet for estimating soil water characteristic curves (SWCC) (ERDC/GSL-TN-17–1). U.S. Army Engineer Research and Development Center.

Enemark, T., Peeters, L.J., Mallants, D., Batelaan, O. (2019). Hydrogeological conceptual model building and testing: A review. Journal of Hydrology, 569, 310–329.

Essaid, H.I., Bekins, B.A., Cozzarelli, I.M. (2015). Organic contaminant transport and fate in the subsurface: Evolution of knowledge and understanding. Water Resources Research, 51, 4861–4902.

Essaid, H.I., Bekins, B.A., Herkelrath, W.N., Delin, G.N. (2011). Crude oil at the Bemidji site: 25 years of monitoring, modeling, and understanding. Groundwater, 49(5), 706–726.

Essaid, H.I., Herkelrath, W.N., Hess, K.M. (1993). Simulation of fluid distributions observed at a crude oil spill site incorporating hysteresis, oil entrapment, and spatial variability of hydraulic properties. Water Resources Research, 29(6), 1753–1770.

Falta, R.W. (2008). Methodology for comparing source and plume remediation alternatives. Ground Water, 46(2), 272–285.

Falta, R.W., Javandel, I., Pruess, K., Witherspoon, P.A. (1989). Density-driven flow of gas in the unsaturated zone due to the evaporation of volatile organic compounds. Water Resources Research, 25(10), 2159–2169.

Farr, A.M., Houghtalen, R.J., McWhorter, D.B. (1990). Volume estimation of light nonaqueous phase liquids in porous media. Ground Water, 28(1), 48–56.

Farthing, M.W., Seyedabbasi, M.A., Imhoff, P.T., Miller, C.T. (2012). Influence of porous media heterogeneity on nonaqueous phase liquid dissolution fingering and upscaled mass transfer. Water Resources Research, 48(8), Article W08507.

Feenstra, S., Mackay, D.M., Cherry, J.A. (1991). A method for assessing residual NAPL based on organic chemical concentrations in soil samples. Groundwater Monitoring & Remediation, 11(2), 128–136.

Fernàndez-Garcia, D., Gómez-Hernández, J.J. (2007). Impact of upscaling on solute transport: Traveltimes, scale dependence of dispersivity, and propagation of uncertainty. Water Resources Research, 43, Article W02423.

Fernàndez-Garcia, D., Trinchero, P., Sanchez-Vila, X. (2010). Conditional stochastic mapping of transport connectivity. Water Resources Research, 46, Article W10515.

Fetter, C.W. (2018). Applied Hydrogeology (4th ed.). Waveland Press.

Filippini, M., Parker, B.L., Dinelli, E., Wanner, P., Chapman, S.W., Gargini, A. (2020). Assessing aquitard integrity in a complex aquifer–aquitard system contaminated by chlorinated hydrocarbons. Water Research, Article 115388.

Fingas, M.F. (2015). Oil and petroleum evaporation. Handbook of Oil Spill Science and Technology, 2(3), 205–223.

Fiori, A., Bellin, A., Cvetkovic, V., De Barros, F.P.J., Dagan, G. (2015a). Stochastic modeling of solute transport in aquifers: From heterogeneity characterization to risk analysis. Water Resources Research, 51(8), 6622–6648.

Fiori, A., Volpi, E., Zarlenga, A., Bohling, G.C. (2015b). Gaussian or non-Gaussian logconductivity distribution at the MADE site: What is its impact on the breakthrough curve? Journal of Contaminant Hydrology, 179, 25–34.

Flemming, H.C., Wingender, J. (2010). The biofilm matrix. Nature Reviews Microbiology, 8(9), 623–633.

Flores Orozco, A., Kemna, A., Oberdörster, C., Zschornack, L., Leven, C., Dietrich, P., Weiss, H. (2012). Delineation of subsurface hydrocarbon contamination at a former hydrogenation plant using spectral induced polarization imaging. Journal of Contaminant Hydrology, 136, 131–144.

Forsythe, G.E., Moler, C.B., Malcolm, M.A. (1977). Computer methods for mathematical computations. Prentice Hall.

Francisca, F.M., Montoro, M.A. (2014). Influence of particle size distribution and wettability on the displacement of LNAPL in saturated sandy soils. Journal of Environmental Engineering, 141(6), Article 04014091.

Fredlund, D.G., Xing, A. (1994). Equations for the soil-water characteristic curve. Canadian Geotechnical Journal, 31(4), 521–532.

Freeze, R.A., Cherry, J.A. (1979). Groundwater. Prentice Hall.

French, H.K., Kästner, M., van der Zee, S.E. (2014). New approaches for low-invasive contaminated site characterization, monitoring and modelling. Environmental Science and Pollution Research, 21, 8893–8896.

Fritsch, F.N., Carlson, R.E. (1980). Monotone piecewise cubic interpolation. SIAM Journal on Numerical Analysis, 17(2), 238–246.

Frollini, E., Petitta, M. (2018). Free LNAPL volume estimation by pancake model and vertical equilibrium model: comparison of results, limitations, and critical points. Geofluids, 2018, Article 8234167.

Fure, A.D., Jawitz, J.W., Annable, M.D. (2006). DNAPL source depletion: Linking architecture and flux response. Journal of Contaminant Hydrology, 85, 118–140.

Gallego, J.L., Loredo, J., Llamas, J.F., Vázquez, F., Sánchez, J. (2001). Bioremediation of diesel-contaminated soils: evaluation of potential in situ techniques by study of bacterial degradation. Biodegradation, 12(5), 325–335.

García-Rincón, J., Gatsios, E., Rayner, J.L., Lenhard, R.J. (2018, May). Comparison of analytical models to estimate LNAPL distribution and transmissivity in a heterogeneous site [Poster presentation]. New Zealand 5th Contaminated Land Conference, Christchurch, New Zealand.

García-Rincón, J., Gatsios, E., Rayner, J.L., McLaughlan, R.G., Davis, G.B. (2020). Laser-induced fluorescence logging as a high-resolution characterisation tool to assess LNAPL mobility. Science of the Total Environment, 725, Article 138480.

Garg, S., Newell, C.J., Kulkarni, P.R., King, D.C., Adamson, D.T., Renno, M.I., Sale, T. (2017). Overview of natural source zone depletion: Processes, controlling factors, and composition change. Groundwater Monitoring & Remediation, 37(3), 62–81.

Gatsios, E. (2018). Evaluation of LNAPL distribution and mobility in heterogeneous porous media under water table fluctuations [Doctoral dissertation, University of Technology Sydney].

Gatsios, E., García-Rincón, J., Rayner, J.L. (2018a, September). LNAPL transmissivity: comparison of theoretical, field and modelling estimations in a multi-layered aquifer in Western Australia [Paper presentation]. 6th International Conference on Industrial and Hazardous Waste Management, Chania, Greece.

Gatsios, E., García-Rincón, J., Rayner, J.L., McLaughlan, R.G., Davis, G.B. (2018b). LNAPL transmissivity as a remediation metric in complex sites under water table fluctuations. Journal of Environmental Management, 215, 40–48.

Gee, G.W., Or, D. (2002). Particle-size analysis. In J.H. Dane, G.C. Topp (Eds.), Methods of soil analysis: part 4—physical methods (no. 5, pp. 255–293), Soil Science Society of America.

Gelhar, L.W., Welty, C., Rehfeldt, K.R. (1992). A critical review of data on field-scale dispersion in aquifers. Water Resources Research, 28(7), 1955–1974.

Geoprobe (2015). Geoprobe Hydraulic Profiling Tool (HPT) system, standard operating procedure (Technical bulletin no. MK3137).

Gerhard, J.I., Kueper, B.H. (2003). Influence of constitutive model parameters on the predicted migration of DNAPL in heterogeneous porous media. Water Resources Research, 39(10), SBH41–SBH413.

Ghanbarian, B., Liaghat, A., Huang, G.H., van Genuchten, M.Th. (2010). Estimation of the van Genuchten soil water retention properties from soil textural data. Pedosphere, 20(4), 456–465.

Gierczak, R.F.D., Devlin, J.F., Rudolph, D.L. (2006). Combined use of field and laboratory testing to predict preferred flow paths in an heterogeneous aquifer. Journal of Contaminant Hydrology, 82(1–2), 75–98.

Gillham, R.W., Sudicky, E.A., Cherry, J.A., Frind, E.O. (1984). An advection-diffusion concept for solute transport in heterogeneous unconsolidated geological deposits. Water Resources Research, 20(3), 369–378.

Gómez-Hernández, J.J., Butler, J.J., Fiori, A., Bolster, D., Cvetkovic, V., Dagan, G., Hyndman, D. (2017). Introduction to special section on modeling highly heterogeneous aquifers: Lessons learned in the last, 30 years from the MADE experiments and others. Water Resources Research, 53(4), 2581–2584.

Gómez-Hernández, J.J., Gorelick, S.M. (1989). Effective groundwater model parameter values: Influence of spatial variability of hydraulic conductivity, leakance, and recharge. Water Resources Research, 25(3), 405–419.

Gottlieb, J., Dietrich, P. (1995). Identification of the permeability distribution in soil by hydraulic tomography. Inverse Problems, 11(2), 353–360.

Gray, W.G., Miller, C.T. (2004). Examination of Darcy's law for flow in porous media with variable porosity. Environmental Science & Technology, 38(22), 5895–5901.

Griffin, T.W., Watson, K.W. (2002). A comparison of field techniques for confirming dense nonaqueous phase liquids. Groundwater Monitoring & Remediation, 22(2), 48–59.

Gringarten, A.C. (2008). From straight lines to deconvolution: The evolution of the state of the art in well test analysis. SPE Reservoir Evaluation Engineering, 11(01) 41–62.

Grundl, T.J., Aldstadt, J.H., Harb, J.G., St. Germain, R.W., Schweitzer, R.C. (2003). Demonstration of a method for the direct determination of polycyclic aromatic hydrocarbons in submerged sediments. Environmental Science & Technology, 37(6), 1189–1197.

Guadagnini, A., Riva, M., Neuman, S.P. (2018). Recent advances in scalable non-Gaussian geostatistics: The generalized sub-Gaussian model. Journal of Hydrology, 562, 685–691.

Gueting, N., Vienken, T., Klotzsche, A., van der Kruk, J., Vanderborght, J., Caers, J., Vereecken, H., Englert, A. (2017). High resolution aquifer characterization using crosshole GPR full-waveform tomography: Comparison with direct-push and tracer test data. Water Resources Research, 53(1), 49–72.

Gupta, P.K., Yadav, B., Yadav, B.K. (2019). Assessment of LNAPL in subsurface under fluctuating groundwater table using 2D sand tank experiments. Journal of Environmental Engineering, 145(9), Article 04019048.

Hadley, P.W., Newell, C. (2014). The new potential for understanding groundwater contaminant transport. Groundwater, 52(2), 174–186.

Haggerty, R., Gorelick, S.M. (1995). Multiple-rate mass transfer for modeling diffusion and surface reactions in media with pore-scale heterogeneity. Water Resources Research, 31(10), 2383–2400.

Haitjema, H.M., Anderson, M.P. (2015). Darcy velocity is not a velocity. Groundwater, 54(1), 1–1.

Halihan, T., Sefa, V., Sale, T., Lyverse, M. (2017). Mechanism for detecting NAPL using electrical resistivity imaging. Journal of Contaminant Hydrology, 205, 57–69.

Hamby, D.M. (1994). A review of techniques for parameter sensitivity analysis of environmental models. Environmental Monitoring and Assessment, 32(2), 135–154.

Hamby, D.M. (1995). A comparison of sensitivity analysis techniques. Health Physics, 68(2), 195–204.

Hampton, D.R. (1989). Laboratory investigation of the relationship between actual and apparent product thickness in sands. In S.M. Testa (Ed.), Environmental concerns in the petroleum industry (pp. 31–55).

Hampton, D.R. (2003). Improving bail-down testing of free product wells [Paper presentation]. Petroleum Hydrocarbons and Organic Chemicals in Ground Water: Prevention, Assessment, and Remediation Conference and Exposition, Costa Mesa, CA, United States.

Hantush, M.S. (1960). Modification of the theory of leaky aquifers. Journal of Geophysical Research, 65(11), 3713–3725.

Hantush, M.S. (1964). Hydraulics of wells. Advances in Hydroscience, 1, 281–432.

Hartsock, J. (2014). Evaluating the effectiveness of pre-remedial LNAPL recovery modeling using the 'LNAPL distribution and recovery model' at two active remediation sites [Master's thesis, Emporia State University].

Harvey, C., Gorelick, S.M. (2000). Rate-limited mass transfer or macrodispersion: Which dominates plume evolution at the Macrodispersion Experiment (MADE) site? Water Resources Research, 36(3), 637–650.

Hassanizadeh, M. (1986). Derivation of basic equations of mass transport in porous media, Part 2. Generalized Darcy's and Fick's laws. Advances in Water Resources, 9(4), 207–222.

Hassanizadeh, M., Gray, W.G. (1979). General conservation equations for multi-phase systems: 1. Averaging procedure. Advances in Water Resources, 2, 131–144.

Hassanizadeh, S.M., Gray, W.G. (1990). Mechanics and thermodynamics of multiphase flow in porous media including interphase boundaries. Advances in Water Resources, 13(4), 169–186.

Hassanizadeh, S.M., Gray, W.G. (1993). Thermodynamic basis of capillary pressure in porous media. Water Resources Research, 29(10), 3389–3405.

Hatfield, K., Annable, M., Cho, J., Rao, P.S.C., Klammler, H. (2004). A direct passive method for measuring water and contaminant fluxes in porous media. Journal of Contaminant Hydrology, 75, 155–181.

Hawkins, A.M. (2013). Processes controlling the behavior of LNAPLs at groundwater surface water interfaces [Master's thesis, Colorado State University].

Hawthorne, J.M. (2014). Site wide analysis of LNAPL distribution and hydrogeologic conditions using plume scale diagnostic gauge plots. Applied NAPL Science Review, 4(1).

Hawthorne, J.M. (2015, November). Selection of an optimal site-specific method for the measurement of LNAPL transmissivity [Conference session]. 22nd IPEC: International Petroleum Environmental Conference, Denver, CO, United States.

Hawthorne, J.M., Adamski, M., Garg, S., Kirkman, A. (2011). Confined LNAPL. Definition, conditions and terminology. Applied NAPL Science Review, 1(5).

Hawthorne, J.M., Helsel, D., Stone, C. (2015, November). LNAPL transmissivity data mining project mining project [Conference session]. 22nd IPEC: International Petroleum Environmental Conference, Denver, CO, United States.

Hayden, N.J., Voice, T.C., Wallace, R.B. (1997). Residual gasoline saturation in unsaturated soil with and without organic matter. Journal of Contaminant Hydrology, 25(3–4), 271–281.

He, L., Huang, G., Lu, H., Wang, S., Xu, Y. (2012). Quasi-Monte Carlo based global uncertainty and sensitivity analysis in modeling free product migration and recovery from petroleum-contaminated aquifers. Journal of Hazardous Materials, 219, 133–140.

Held, R.J., Illangasekare, T.H. (1995). Fingering of dense nonaqueous phase liquids in porous media: 1. Experimental investigation. Water Resources Research, 31(5), 1213–1222.

Helmig, R. (1997). Multiphase flow and transport processes in the subsurface: a contribution to the modeling of hydrosystems. Springer-Verlag.

Helsel, D.R., Hirsch, R.M., Ryberg, K.R., Archfield, S.A., Gilroy, E.J. (2020). Statistical methods in water resources (Book 4, Chapter A3). U.S. Geological Survey.

Herman, D.C., Lenhard, R.J., Miller, R.M. (1997). Formation and removal of hydrocarbon residual in porous media: effects of attached bacteria and biosurfactants. Environmental Science & Technology, 31(5), 1290–1294.

Hernández-Espriú, A., Martínez-Santos, P., Sánchez-León, E., Marín, L.E. (2012). Free-product plume distribution and recovery modeling prediction in a diesel-contaminated volcanic aquifer. Physics and Chemistry of the Earth, Parts A/B/C, 37, 43–51.

Hess, K.M., Herkelrath, W.N., Essaid, H.I. (1992a). Determination of subsurface fluid contents at a crude-oil spill site. Journal of Contaminant Hydrology, 10(1), 75-96.

Hess, K.M., Wolf, S.H., Celia, M.A. (1992b). Large-scale natural gradient tracer test in sand and gravel, Cape Cod, Massachusetts: 3. Hydraulic conductivity variability and calculated macrodispersivities. Water Resources Research, 28(8), 2011–2027.

Heyse, E., Augustijn, D., Suresh, P., Rao, C., Delfino, J.J. (2002). Nonaqueous phase liquid dissolution and soil organic matter sorption in porous media: Review of system similarities. Critical Reviews in Environmental Science & Technology, 32(4), 337–397.

Hill, M.C. (2006). The practical use of simplicity in developing ground water models. Groundwater, 44(6), 775–781.

Hillel, D. (1998). Environmental soil physics: Fundamentals, applications, and environmental considerations. Elsevier.

Hoag, G.E., Marley, M.C. (1986). Gasoline residual saturation in unsaturated uniform aquifer materials. Journal of Environmental Engineering, 112(3), 586–604.

Hoffman, F.O., Gardner, R.H. (1983). Evaluation of uncertainties in environmental radiological assessment models. In J.E. Till, H.R. Meyer (Eds.), Radiological assessments—a textbook on environmental dose assessment (NUREG/CR-3332, pp. 11-1–11-55). U.S. Nuclear Regulatory Comission.

Holmes, D. (2019). Advances in in-situ automatous LNAPL and water level monitoring by guided wire radar: detailed analysis of LNAPL behaviour and improved site understanding. In AquaConSoil 2019 proceedings—sustainable use and management of soil, sediment and water resources.

Horst, J., Welty, N., Stuetzle, R., Wenzel, R., St. Germain, R. (2018). Fluorescent dyes: a new weapon for conquering DNAPL characterization. Groundwater Monitoring & Remediation, 38(1), 19–25.

Houben, G.J. (2015). Hydraulics of water wells—head losses of individual components. Hydrogeology Journal, 23(8), 1659–1675.

Huang, G., Zhang, R. (2005). Evaluation of soil water retention curve with the pore–solid fractal model. Geoderma, 127(1–2), 52–61.

Hubbert, M.K. (1940). The theory of ground-water motion. The Journal of Geology, 48(8, Part 1), 785–944.

Hubbert, M.K. (1956). Darcy's law and the field equations of the flow of underground fluids. Hydrological Sciences Journal, 2(1), 23–59.

Hunkeler, D., Aravena, R. (2000). Determination of compound-specific carbon isotope ratios of chlorinated methanes, ethanes, and ethenes in aqueous samples. Environmental Science & Technology, 34(13), 2839–2844.

Hunt, J.R., Sitar, N., Udell, K.S. (1988). Nonaqueous phase liquid transport and cleanup: 1. Analysis of mechanisms. Water Resources Research, 24(8), 1247–1258.

Huntley, D. (2000). Analytic determination of hydrocarbon transmissivity from baildown tests. Ground Water, 38(1), 46–52.

Huntley, D., Beckett, G.D. (2002). Persistence of LNAPL sources: Relationship between risk reduction and LNAPL recovery. Journal of Contaminant Hydrology, 59, 3–26.

Huntley, D., Hawk, R.N., Corley, H.P. (1994a). Nonaqueous phase hydrocarbon in a fine-grained sandstone: 1. Comparison between measured and predicted saturations and mobility. Groundwater, 32(4), 626–634.

Huntley, D., Wallace, J.W., Hawk, R.N. (1994b). Nonaqueous phase hydrocarbon in a fine-grained sandstone: 2. Effect of local sediment variability on the estimation of hydrocarbon volumes. Groundwater, 32(5), 778–783.

Huo, L., Liu, G., Yang, X., Ahmad, Z., Zhong, H. (2020). Surfactant-enhanced aquifer remediation: Mechanisms, influences, limitations and the countermeasures. Chemosphere, Article 126620.

Huysmans, M., Dassargues, A. (2009). Application of multiple-point geostatistics on modelling groundwater flow and transport in a cross-bedded aquifer, Belgium. Hydrogeology Journal, 17, 1901–1911.

Hyde, K., Ma, W., Obal, T., Bradshaw, K., Carlson, T., Mamet, S., Siciliano, S.D. (2019). Incremental sampling methodology for petroleum hydrocarbon contaminated soils: volume estimates and remediation strategies. Soil and Sediment Contamination: An International Journal, 28(1), 51–64.

Hyder, Z., Butler Jr., J.J. (1995). Slug tests in unconfined formations: An assessment of the Bouwer and Rice technique. Groundwater, 33(1), 16–22.

Hyder, Z., Butler Jr., J.J., McElwee, C.D. (1993). An approximate technique for analysis of slug tests in wells (Open-file Report 93–44). Kansas Geological Survey.

Iglewicz, B., Hoaglin, D.C. (1993). How to detect and handle outliers (Vol. 16). ASQC Quality Press.

Illangasekare, T.H., Armbruster III, E.J., Yates, D.N. (1995). Non-aqueous-phase fluids in heterogeneous aquifers—experimental study. Journal of Environmental Engineering, 121(8), 571–579.

Illman, W.A., Craig, A.J., Liu, X. (2008). Practical issues in imaging hydraulic conductivity through hydraulic tomography. Groundwater, 46(1), 120–132.

Imhoff, P.T., Jaffé, P.R., Pinder, G.F. (1994). An experimental study of complete dissolution of a nonaqueous phase liquid in saturated porous media. Water Resources Research, 30(2), 307–320.

Ippisch, O., Vogel, H.J., & Bastian, P. (2006). Validity limits for the van Genuchten–Mualem model and implications for parameter estimation and numerical simulation. Advances in Water Resources, 29(12), 1780–1789.

Isaaks, E.H.S., Srivastava, M.R. (1989). An introduction to applied geostatistics. Oxford University Press.

Interstate Technology and Regulatory Council (2018a). LNAPL site management: LCSM evolution, decision process, and remedial technologies (LNAPL-3). https://lnapl-3.itrcweb.org

Interstate Technology and Regulatory Council (2018b). TPH risk evaluation at petroleum-contaminated sites (TPHRisk-1). https://tphrisk-1.itrcweb.org

Interstate Technology and Regulatory Council (2019). Implementing advanced site characterization tools (ASCT-1). https://asct-1.itrcweb.org

Jackson, S.J., Lin, Q., Krevor, S. (2020). Representative elementary volumes, hysteresis, and heterogeneity in multiphase flow from the pore to continuum scale. Water Resources Research, 56(6), Article e2019WR026396.

Jacob, C.E., Lohman, S.W. (1952). Nonsteady flow to a well of constant drawdown in an extensive aquifer. Eos, Transactions American Geophysical Union, 33(4), 559–569.

James, A.L., Oldenburg, C.M. (1997). Linear and Monte Carlo uncertainty analysis for subsurface contaminant transport simulation. Water Resources Research, 33(11), 2495–2508.

Jawitz, J.W., Fure, A.D., Demmy, G.G., Berglund, S., Rao, P.S.C. (2005). Groundwater contaminant flux reduction resulting from nonaqueous phase liquid mass reduction. Water Resources Research, 41(10), Article W10408.

Jeong, J., Charbeneau, R.J. (2014). An analytical model for predicting LNAPL distribution and recovery from multi-layered soils. Journal of Contaminant Hydrology, 156, 52–61.

Joanes, D.N., Gill, C.A. (1998). Comparing measures of sample skewness and kurtosis. Journal of the Royal Statistical Society: Series D, The Statistician, 47(1), 183–189.

Joekar-Niasar, V., Hassanizadeh, S.M. (2012). Analysis of fundamentals of two-phase flow in porous media using dynamic pore-network models: A review. Critical Reviews in Environmental Science & Technology, 42(18), 1895–1976.

Joekar-Niasar, V., Hassanizadeh, S.M., Dahle, H.K. (2010). Non-equilibrium effects in capillarity and interfacial area in two-phase flow: dynamic pore-network modelling. Journal of Fluid Mechanics, 655, 38–71.

Johnson, R.L., Brow, C.N., Johnson, R.O.B., Simon, H.M. (2013). Cryogenic core collection and preservation of subsurface samples for biomolecular analysis. Groundwater Monitoring & Remediation, 33(2), 38–43.

Johnson, P.C., Ettinger, R.A. (1991). Heuristic model for predicting the intrusion rate of contaminant vapors into buildings. Environmental Science & Technology, 25(8), 1445–1452.

Johnston, C.D. (2010). Selecting and assessing strategies for remediating LNAPL in soils and aquifers (CRC CARE Technical Report 18). Cooperative Research Centre for Contamination Assessment and Remediation of the Environment.

Johnston, C.D., Adamski, M. (2005, August). Relationship between initial and residual LNAPL saturation for different soil types [Paper presentation]. Petroleum Hydrocarbons and Organic Chemicals in Ground Water: Prevention, Assessment, and Remediation Conference and Exposition, Costa Mesa, CA, United States.

Johnston, C.D., Innes, N.L., Bastow, T.P. (2010). Hydraulic and structural controls on the spreading of diesel LNAPL near the interface with the marine environment. Commonwealth Scientific and Industrial Research Organisation.

Johnston, C.D., Rayner, J.L., Patterson, B.M., Davis, G.B. (1998). Volatilisation and biodegradation during air sparging of dissolved BTEX-contaminated groundwater. Journal of Contaminant Hydrology, 33(3–4), 377–404.

Johnston, C.D., Trefry, M.G. (2009). Characteristics of light nonaqueous phase liquid recovery in the presence of fine-scale soil layering. Water Resources Research, 45(5), Article W05412.

Jury, W.A., Spencer, W.F., Farmer, W.J. (1983). Behavior assessment model for trace organics in soil: I. Model description. Journal of Environmental Quality, 12(4), 558–564.

Kahraman, I. (2013). Analysis of a LNAPL recovery system using LDRM in a South Texas facility [Master's thesis, The University of Texas at Austin].

Kaluarachchi, J.J. (1996). Effect of subsurface heterogeneity on free-product recovery from unconfined aquifers. Journal of Contaminant Hydrology, 22(1–2), 19–37.

Kechavarzi, C., Soga, K., Illangasekare, T.H. (2005). Two-dimensional laboratory simulation of LNAPL infiltration and redistribution in the vadose zone. Journal of Contaminant Hydrology, 76(3–4), 211–233.

Keller, A.A., Chen, M. (2003). Effect of spreading coefficient on three-phase relative permeability of nonaqueous phase liquids. Water Resources Research, 39(10), Article 1288.

Keller, C.E., Cherry, J.A., Parker, B.L. (2014). New method for continuous transmissivity profiling in fractured rock. Groundwater, 52(3), 352–367.

Kemblowski, M.W., Chiang, C.Y. (1990). Hydrocarbon thickness fluctuations in monitoring wells. Groundwater, 28(2), 244–252.

Khudur, L.S., Ball, A.S. (2018). RemScan: A tool for monitoring the bioremediation of total petroleum hydrocarbons in contaminated soil. MethodsX, 5, 705–709.

Kiaalhosseini, S. (2016). Third-generation site characterization: cryogenic core collection, nuclear magnetic resonance, and electrical resistivity [Doctoral dissertation, Colorado State University].

Kiaalhosseini, S., Johnson, R.L., Rogers, R.C., Renno, M.I., Lyverse, M., Sale, T.C. (2016). Cryogenic core collection (C3) from unconsolidated subsurface media. Groundwater Monitoring & Remediation, 36(4), 41–49.

Kiaalhosseini, S., Kohn, B., Watson, A.T., Sale, T.C., Blotevogel, J. (2019). Magnetic resonance imaging of nonaqueous phase liquid distribution in unconsolidated soils using discriminatory freezing. Groundwater Monitoring & Remediation, 39(2), 71–75.

Kianinejad, A., Chen, X., DiCarlo, D.A. (2015). The effect of saturation path on three-phase relative permeability. Water Resources Research, 51(11), 9141–9164.

Kim, J., Corapcioglu, M.Y. (2003). Modeling dissolution and volatilization of LNAPL sources migrating on the groundwater table. Journal of Contaminant Hydrology, 65(1–2), 137–158.

Kimball, C.G., Hawthorne, J.M., Menatti, J.A., Rousseau, M. (2017, October–November). Light non-aqueous phase liquid transmissivity acceptance and use by the regulatory community [Conference session]. 24th IPEC: International Petroleum Environmental Conference, San Antonio, TX, United States.

Kindred, J.S., Celia, M.A. (1989). Contaminant transport and biodegradation: 2. Conceptual model and test simulations. Water Resources Research, 25(6), 1149–1159.

King, A.J., Readman, J.W., Zhou, J.L. (2007). Behaviour of polycyclic aromatic hydrocarbons in dissolved, colloidal, and particulate phases in sedimentary cores. International Journal of Environmental and Analytical Chemistry, 87(3), 211–225.

Kirkman, A.J. (2013). Refinement of Bouwer-Rice baildown test analysis. Groundwater Monitoring & Remediation, 33(1), 105–110.

Kirkman, A.J., Adamski, M., Hawthorne, J.M. (2013). Identification and assessment of confined and perched LNAPL conditions. Groundwater Monitoring & Remediation, 33, 75–86.

Kirkman, A.J., Hawthorne, J.M. (2014). Transmissivity—the emerging metric for LNAPL recoverability—Part 2: a tangible perspective on the hydraulic recovery endpoint. LUSTLine, 76, 15–20.

Kirkman, A.J., Koons, B. (2020). Unifying NAPL drawdown and transmissivity testing in unconfined, confined, perched, and fractured settings using the Z-Factor and MH principles. Groundwater Monitoring & Remediation, 40(1), 47–64.

Kitanidis, P.K. (2015). Persistent questions of heterogeneity, uncertainty, and scale in subsurface flow and transport. Water Resources Research, 51(8), 5888–5904.

Klammler, H., Hatfield, K., Guimarães, D.L., Annable, M.D., Newman, M., Cho, J., Peacock, A., Stucker, V., Ranville, J., Cabaniss, S.A., Rao, P.S.C. (2012). Contaminant discharge and uncertainty estimates from passive flux meter measurements. Water Resources Research, 48, Article W02512.

Klute, A. (1986). Water retention: laboratory methods. In A. Klute (Ed.), Methods of soil analysis: part 1—physical and mineralogical methods (no. 9, pp. 635–662).

Klute, A., Dirksen, C. (1986). Hydraulic conductivity and diffusivity: Laboratory methods. In A. Klute (Ed.), Methods of soil analysis: part 1—physical and mineralogical methods (no. 9, pp. 687–734).

Knight, R., Walsh, D.O., Butler Jr., J.J., Grunewald, E., Liu, G., Parsekian, A.D., Reboulet, E.C., Knobbe, S., Barrows, M. (2016). NMR logging to estimate hydraulic conductivity in unconsolidated aquifers. Groundwater, 54(1), 104–114.

Knudby, C., Carrera, J. (2005). On the relationship between indicators of geostatistical, flow and transport connectivity. Advances in Water Resources, 28(4), 405–421.

Köber, R., Hornbruch, G., Leven, C., Tischer, L., Großmann, J., Dietrich, P., Weiß, H., Dahmke, A. (2009). Evaluation of combined direct-push methods used for aquifer model generation. Groundwater, 47(4), 536–546.

Koch, J., Nowak, W. (2015). Predicting DNAPL mass discharge and contaminated site longevity probabilities: Conceptual model and high-resolution stochastic simulation. Water Resources Research, 51(2), 806–831.

Koch, J., Nowak, W. (2016). Identification of contaminant source architectures—A statistical inversion that emulates multiphase physics in a computationally practicable manner. Water Resources Research, 52(2), 1009–1025.

Kokkinaki, A., O'Carroll, D.M., Werth, C.J., Sleep, B.E. (2013). An evaluation of Sherwood–Gilland models for NAPL dissolution and their relationship to soil properties. Journal of Contaminant Hydrology, 155, 87–98.

Koltermann, C.E., Gorelick, S.M. (1995). Fractional packing model for hydraulic conductivity derived from sediment mixtures. Water Resources Research, 31(12), 3283–3297.

Koltermann, C.E., Gorelick, S.M. (1996). Heterogeneity in sedimentary deposits: A review of structure-imitating, process-imitating, and descriptive approaches. Water Resources Research, 32(9), 2617–2658.

Konikow, L.F., Bredehoeft, J.D. (1992). Ground-water models cannot be validated. Advances in Water Resources, 15(1), 75–83.

Kool, J.B., Parker, J.C. (1987). Development and evaluation of closed-form expressions for hysteretic soil hydraulic properties. Water Resources Research, 23(1), 105–114.

Kosugi, K.I. (1996). Lognormal distribution model for unsaturated soil hydraulic properties. Water Resources Research, 32(9), 2697–2703.

Kram, M.L., Keller, A.A. (2004). Complex NAPL site characterization using fluorescence part 2: Analysis of soil matrix effects on the excitation/emission matrix. Soil Sediment Contamination, 13(2), 119–134.

Kram, M.L., Keller, A.A., Rossabi, J., Everett, L.G. (2001a). DNAPL characterization methods and approaches, Part, 1: Performance comparisons. Groundwater Monitoring & Remediation, 21(4), 109–123.

Kram, M.L., Lieberman, S.H., Fee, J., Keller, A.A. (2001b). Use of LIF for Real-Time In-Situ Mixed NAPL Source Zone Detection. Groundwater Monitoring & Remediation, 21(1), 67–76.

Kruseman, G.P., de Ridder, N.A. (2000). Analysis and evaluation of pumping test data (2nd ed.). International Institute for Land Reclamation and Improvement.

Kueper, B.H., Frind, E.O. (1988). An overview of immiscible fingering in porous media. Journal of Contaminant Hydrology, 2(2), 95–110.

Kueper, B.H., Frind, E.O. (1991). Two-phase flow in heterogeneous porous media: 2. Model application. Water Resources Research, 27(6), 1059–1070.

Kueper, B.H., Redman, D., Starr, R.C., Reitsma, S., Mah, M. (1993). A field experiment to study the behavior of tetrachloroethylene below the water table: Spatial distribution of residual and pooled DNAPL. Groundwater, 31(5), 756–766.

Kueper, B.H., Stroo, H.F., Vogel, C.M., Ward, C.H. (Eds.). (2014). Chlorinated solvent source zone remediation. Springer.

Kuo, T., Chen, Y., Lin, C., Chen, J. (2016). Oil recovery from a fluctuating water table. Petroleum Science and Technology, 34(17–18), 1562–1567.

Lahvis, M.A., Hers, I., Davis, R.V., Wright, J., DeVaull, G.E. (2013). Vapor intrusion screening at petroleum UST sites. Groundwater Monitoring & Remediation, 33(2), 53–67.

Lakowicz, J.R. (2006). Principles of fluorescence spectroscopy (3rd ed.). Springer Science & Business Media.

Land, C.S. (1968). Calculation of imbibition relative permeability for two-and three-phase flow from rock properties. Society of Petroleum Engineers Journal, 8(02), 149–156.

Landrigan, P.J., Fuller, R., Acosta, N.J., Adeyi, O., Arnold, R., Baldé, A.B., Bertollini, R., Bose-O'Reilly, S., Boufford, J.I., Breysse, P.N., Chiles, T., Mahidol, C., Coll-Seck, A.M., Cropper, M.L., Fobil, J., Fuster, V., Greenstone, M., Haines, A., Hanrahan, D., ... Zhong, M. (2018). The Lancet Commission on pollution and health. The Lancet, 391(10119), 462–512.

Laspidou, C.S., Rittmann, B.E. (2002). A unified theory for extracellular polymeric substances, soluble microbial products, and active and inert biomass. Water Research, 36(11), 2711–2720.

Le Borgne, T., Bour, O., Riley, M.S., Gouze, P., Pezard, P.A., Belghoul, A., Lods, G., Le Provost, R., Greswell, R.B., Ellis, P.A., Isakov, E., Last, B.J. (2007). Comparison of alternative methodologies for identifying and characterizing preferential flow paths in heterogeneous aquifers. Journal of Hydrology, 345(3–4), 134–148.

Lefebvre, R., Boutin, A. (2006). Écoulement multiphase en milieux poreux, chapitre, 8: volume et transmissivité des liquides immiscibles dans les sols [Lecture notes]. Université du Québec; Institut National de la Recherche Scientifique—Eau Terre Environnement.

Lekmine, G., Bastow, T.P., Johnston, C.D., Davis, G.B. (2014). Dissolution of multi-component LNAPL gasolines: The effects of weathering and composition. Journal of Contaminant Hydrology, 160, 1–11.

Lemke, L.D., Abriola, L.M. (2006). Modeling dense nonaqueous phase liquid mass removal in nonuniform formations: Linking source-zone architecture and system response. Geosphere, 2(2), 74–82.

Lemke, L.D., Abriola, L.M., Lang, J.R. (2004). Influence of hydraulic property correlation on predicted dense nonaqueous phase liquid source zone architecture, mass recovery and contaminant flux. Water Resources Research, 40(12), 1–18.

Lenhard, R.J. (1992). Measurement and modeling of three-phase saturation-pressure hysteresis. Journal of Contaminant Hydrology, 9(3), 243–269.

Lenhard, R.J., Johnson, T.G., Parker, J.C. (1993). Experimental observations of nonaqueous-phase liquid subsurface movement. Journal of Contaminant Hydrology, 12(1–2), 79–101.

Lenhard, R.J., Oostrom, M., Dane, J.H. (2004). A constitutive model for air–NAPL–water flow in the vadose zone accounting for immobile, non-occluded (residual) NAPL in strongly water-wet porous media. Journal of Contaminant Hydrology, 73, 283-304.

Lenhard, R.J., Parker, J.C. (1988). Experimental validation of the theory of extending two-phase saturation-pressure relations to three-fluid phase systems for monotonic drainage paths. Water Resources Research, 24(3), 373–380.

Lenhard, R.J., Parker, J.C. (1990a). Estimation of free hydrocarbon volume from fluid levels in monitoring wells. Groundwater, 28(1), 57–67.

Lenhard, R.J., Parker, J.C. (1990b). Discussion of "Estimation of free hydrocarbon volume from fluid levels in monitoring wells," by RJ Lenhard and JC Parker, January-February 1990 issue, v. 28, no. 1, pp. 57–67 and "Volume estimation of light nonaqueous phase liquids in porous media," by AM Farr, RJ Houghtalen, and DB McWhorter, January-February 1990 issue, v. 28, no. 1, pp. 48–56. Groundwater, 28(5), 800–801.

Lenhard, R.J., Parker, J.C., Kaluarachchi, J.J. (1989a). A model for hysteretic constitutive relations governing multiphase flow: 3. Refinements and numerical simulations. Water Resources Research, 25(7), 1727–1736.

Lenhard, R.J., Parker, J.C., Mishra, S. (1989b). On the correspondence between Brooks-Corey and van Genuchten models. Journal of Irrigation and Drainage Engineering, 115(4), 744–751.

Lenhard, R.J., Rayner, J.L., Davis, G.B. (2017). A practical tool for estimating subsurface LNAPL distributions and transmissivity using current and historical fluid levels in groundwater wells: Effects of entrapped and residual LNAPL. Journal of Contaminant Hydrology, 205, 1–11.

Lenhard, R.J., Rayner, J.L., García-Rincón, J. (2019). Testing an analytical model for predicting subsurface LNAPL distributions from current and historic fluid levels in monitoring wells: A preliminary test considering hysteresis. Water, 11, Article 2404.

Lenhard, R.J., Sookhak Lari, K., Rayner, J.L., Davis, G.B. (2018). Evaluating an analytical model to predict subsurface LNAPL distributions and transmissivity from current and historic fluid levels in groundwater wells: Comparing results to numerical simulations. Groundwater Monitoring & Remediation, 38(1), 75–84.

Leong, E.C., Rahardjo, H. (1997). Review of soil-water characteristic curve equations. Journal of Geotechnical and Geoenvironmental Engineering, 123(12), 1106–1117.

Lessoff, S.C., Schneidewind, U., Leven, C., Blum, P., Dietrich, P., Dagan, G. (2010). Spatial characterization of the hydraulic conductivity using direct-push injection logging. Water Resources Research, 46(12), Article W12502.

Leven, C., Dietrich, P. (2006). What information can we get from pumping tests? Comparing pumping test configurations using sensitivity coefficients. Journal of Hydrology, 319(1–4), 199–215.

Leverett, M.C, Lewis, W.B. (1941). Steady flow of gas-oil-water mixtures through unconsolidated sands. Transactions of the AIME, 142(01), 107–116.

Li, J., Heap, A.D. (2014). Spatial interpolation methods applied in the environmental sciences: A review. Environmental Modelling Software, 53, 173–189.

Likos, W.J., Yao, J. (2014). Effects of constraints on van Genuchten parameters for modeling soil-water characteristic curves. Journal of Geotechnical and Geoenvironmental Engineering, 140(12), Article 06014013.

Linde, N., Ginsbourger, D., Irving, J., Nobile, F., Doucet, A. (2017). On uncertainty quantification in hydrogeology and hydrogeophysics. Advances in Water Resources, 110, 166–181.

Linde, N., Renard, P., Mukerji, T., Caers, J. (2015). Geological realism in hydrogeological and geophysical inverse modeling: A review. Advances in Water Resources, 86, 86–101.

Liu, G., Borden, R.C., Butler, J.J. (2019). Simulation assessment of direct push injection logging for high-resolution aquifer characterization. Groundwater, 57(4), 562–574.

Liu, G., Butler Jr., J.J., Bohling, G.C., Reboulet, E., Knobbe, S., Hyndman, D.W. (2009). A new method for high-resolution characterization of hydraulic conductivity. Water Resources Research, 45(8), Article W08202.

Liu, G., Butler, J.J., Reboulet, E., Knobbe, S. (2012). Hydraulic conductivity profiling with direct push methods. Grundwasser, 17(1), 19–29.

Liu, G., Knobbe, S., Butler Jr., J.J., Reboulet, E.C., Borden, R.C., Bohling, G. (2017, December). Direct push injection logging for high resolution characterization of low permeability zones [Conference session]. 2017 American Geophysical Union Fall Meeting, New Orleans, LA, United States.

Liu, H.H., Zhang, Y.Q., Zhou, Q., Molz, F.J. (2007). An interpretation of potential scale dependence of the effective matrix diffusion coefficient. Journal of Contaminant Hydrology, 90, 41–57.

Loke, M.H. (1999). Electrical imaging surveys for environmental and engineering studies. A practical guide [Lecture notes].

Lovley, D.R., Baedecker, M.J., Lonergan, D.J., Cozzarelli, I.M., Phillips, E.J., Siegel, D.I. (1989). Oxidation of aromatic contaminants coupled to microbial iron reduction. Nature, 339(6222), 297–300.

Lu, G.Y., Wong, D.W. (2008). An adaptive inverse-distance weighting spatial interpolation technique. Computers Geosciences, 34(9), 1044–1055.

Lu, J., Germain, R.S., Andrews, T. (2014). NAPL source identification utilizing data from laser induced fluorescence (LIF) screening tools. In R.D. Morrison, G. O'Sullivan (Eds.), Environmental forensics: Proceedings of the 2013 INEF Conference (pp. 77–97). Royal Society of Chemistry.

Lundegard, P.D., Johnson, P.C. (2006). Source zone natural attenuation at petroleum hydrocarbon spill sites—II: application to a former oil field. Groundwater Monitoring & Remediation, 26(4), 93–106.

Lundegard, P.D., Mudford, B.S. (1998). LNAPL volume calculation: Parameter estimation by nonlinear regression of saturation profiles. Groundwater Monitoring & Remediation, 18(3), 88–93.

Lundy, D.A. (2005, August). Laboratory study of filter-pack drainage during slug withdrawal tests with implications for free product baildown tests [Paper presentation]. Petroleum Hydrocarbons and Organic Chemicals in

Ground Water: Prevention, Assessment, and Remediation Conference and Exposition, Costa Mesa, CA, United States.

Lundy, D.A. (2006, November). Field measurement of LNAPL mobility and soil properties through parametric analysis of product bail-down tests [Paper presentation]. Petroleum Hydrocarbons and Organic Chemicals in Ground Water: Prevention, Assessment, and Remediation Conference and Exposition, Houston, TX, United States.

Lundy, D.A. (2014). An investigation of the relationship between lateral spreading and mass depletion of an LNAPL body in contact with groundwater at the Bemidji, MN crude oil release site [Doctoral dissertation, The University of Georgia].

Lundy, D.A., Zimmerman, L.M. (1996, May). Assessing the recoverability of LNAPL plumes for recovery system conceptual design [Paper presentation]. NGWA 10th National Outdoor Action Conference and Exposition, Las Vegas, NV, United States.

Ma, J., McHugh, T.E., Beckley, L., Lahvis, M.A., Devaull, G.E., Jiang, L. (2020). Vapor intrusion investigations and decision-making: A critical review. Environmental Science & Technology, 54(12), 7050–7069.

Ma, Y., Zheng, X., Anderson, S.H., Lu, J., Feng, X. (2014). Diesel oil volatilization processes affected by selected porous media. Chemosphere, 99, 192–198.

MacDonald, A.M., Barker, J.A., Davies, J. (2008). The bailer test: a simple effective pumping test for assessing borehole success. Hydrogeology Journal, 16(6), 1065–1075.

Mackay, D., Hathaway, E., de Sieyes, N., Zhang, H., Rasa, E., Paradis, C., Schmidt, R., Peng, J., Buscheck, T., Sihota, N. (2018). Comparing natural source zone depletion pathways at a fuel release site. Groundwater Monitoring & Remediation, 38(2), 24–39.

Mackay, D.M., Cherry, J.A. (1989). Groundwater contamination: Pump-and-treat remediation. Environmental Science & Technology, 23, 630–636.

Mackay, D.M., Freyberg, D.L., Roberts, P.V., Cherry, J.A. (1986). A natural gradient experiment on solute transport in a sand aquifer: 1. Approach and overview of plume movement. Water Resources Research, 22, 2017–2029.

Mahler, N., Sale, T., Smith, T., Lyverse, M. (2012a). Use of single-well tracer dilution tests to evaluate LNAPL flux at seven field sites. Groundwater, 50(6), 851–860.

Mahler, N., Sale, T., Lyverse, M. (2012b). A mass balance approach to resolving LNAPL stability. Groundwater, 50(6), 861–871.

Maji, R., Sudicky, E.A. (2008). Influence of mass transfer characteristics for DNAPL source depletion and contaminant flux in a highly characterized glaciofluvial aquifer. Journal of Contaminant Hydrology, 102(1–2), 105–119.

Maliva, R.G. (2016). Aquifer characterization techniques. Springer.

Mariethoz, G., Caers, J. (2014). Multiple-point geostatistics: stochastic modeling with training images. John Wiley & Sons.

Marinelli, F., Durnford, D.S. (1996). LNAPL thickness in monitoring wells considering hysteresis and entrapment. Groundwater, 34(3), 405–414.

Martínez-Santos, P., Martín-Loeches, M., García-Castro, N., Solera, D., Díaz-Alcaide, S., Montero, E., García-Rincón, J. (2017). A survey of domestic wells and pit latrines in rural settlements of Mali: implications of on-site sanitation on the quality of water supplies. International Journal of Hygiene and Environmental Health, 220(7), 1179–1189.

Matheron, G. (1967). Eléments pour une théorie des milieux poreux. Masson et Cie.

Matott, L.S., Babendreier, J.E., Purucker, S.T. (2009). Evaluating uncertainty in integrated environmental models: a review of concepts and tools. Water Resources Research, 45(6), Article W06421.

Matschullat, J., Ottenstein, R., Reimann, C. (2000). Geochemical background—can we calculate it? Environmental Geology, 39(9), 990–1000.

Mayer, A.S., Hassanizadeh, S.M. (Eds.). (2005). Soil and groundwater contamination: nonaqueous phase liquids: principles and observations. American Geophysical Union.

McAlexander, B.L., Tuggle, K.V. (2015). Estimating remediation and contaminant respiration emissions for alternatives comparisons at petroleum spill sites. Remediation Journal, 25(3), 53–67.

McBratney, A.B., Minasny, B., Cattle, S.R., Vervoort, R.W. (2002). From pedotransfer functions to soil inference systems. Geoderma, 109(1–2), 41–73.

McCall, W. (2010). Tech guide for calculation of estimated hydraulic conductivity (Est. K) log from HPT data. Geoprobe.

McCall, W. (2011). Application of Geoprobe HPT logging system for geo-environmental investigations (Technical Bulletin No. MK3184). Geoprobe.

McCall, W. (2013). HPT webinar: Using HPT logs for site characterization [Webinar]. Geoprobe.

McCall, W., Christy, T.M. (2020). The Hydraulic Profiling Tool (HPT) for hydrogeologic investigation of unconsolidated formations. Groundwater Monitoring & Remediation.

McCall, W., Christy, T.M., Evald, M.K. (2017). Applying the HPT-GWS for hydrostratigraphy, water quality and aquifer recharge investigations. Groundwater Monitoring & Remediation, 37(1), 78–91.

McCall, W., Christy, T.M., Pipp, D., Terkelsen, M., Christensen, A., Weber, K., Engelsen, P. (2014). Field application of the combined membrane-interface probe and hydraulic profiling tool (MiHpt). Groundwater Monitoring & Remediation, 34(2), 85–95.

McCall, W., Christy, T.M., Pipp, D.A., Jaster, B., White, J., Goodrich, J., Fontana, J., Doxtader, S. (2018). Evaluation and application of the optical image profiler (OIP) a direct push probe for photo-logging UV-induced fluorescence of petroleum hydrocarbons. Environmental Earth Sciences, 77(10), Article 374.

McCall, W., Nielsen, D.M., Farrington, S.P., Christy, T.M. (2005). Use of direct-push technologies in environmental site characterization and ground-water monitoring. In D.M. Nielsen (Ed.), Practical handbook of environmental site characterization and ground-water monitoring (2nd ed., pp., 345–471). Taylor & Francis.

McElwee, C.D., Bohling, G.C., Butler Jr., J.J. (1995). Sensitivity analysis of slug tests. Part 1. The slugged well. Journal of Hydrology, 164(1–4), 53–67.

McElwee, C.D., Engard, B.R., Wachter, B.J., Lyle, S.A., Healey, J., Devlin, J.F. (2011). Hydraulic tomography and high-resolution slug testing to determine hydraulic conductivity distributions (SERDP Project ER-1367). Strategic Environmental Research and Development Program.

McGenity, T.J., Timmis, K.N., Nogales, B. (Eds.). (2017). Hydrocarbon and lipid microbiology protocols—field studies. Springer-Verlag.

McMillan, L.A., Rivett, M.O., Wealthall, G.P., Zeeb, P., Dumble, P. (2018). Monitoring well utility in a heterogeneous DNAPL source zone area: Insights from proximal multilevel sampler wells and sampling capture-zone modelling. Journal of Contaminant Hydrology, 210, 15–30.

Meisenheimer, D.E., McClure, J.E., Rivers, M.L., Wildenschild, D. (2020). Exploring the effect of flow condition on the constitutive relationships for two-phase flow. Advances in Water Resources, 137, Article 103506.

Meerschaert, M.M., Dogan, M., Van Dam, R.L., Hyndman, D.W., Benson, D.A. (2013). Hydraulic conductivity fields: Gaussian or not? Water Resources Research, 49(8), 4730–4737.

Mercer, J.W., Cohen, R.M. (1990). A review of immiscible fluids in the subsurface: properties, models, characterization and remediation. Journal of Contaminant Hydrology, 6, 107–163.

Meyer, J.R., Parker, B.L., Arnaud, E., Runkel, A.C. (2016). Combining high resolution vertical gradients and sequence stratigraphy to delineate hydrogeologic units for a contaminated sedimentary rock aquifer system. Journal of Hydrology, 534, 505–523.

Miller, C.T., Bruning, K., Talbot, C.L., McClure, J.E., Gray, W.G. (2019). Nonhysteretic capillary pressure in two-fluid porous medium systems: definition, evaluation, validation, and dynamics. Water Resources Research, 55(8), 6825–6849.

Miller, C.T., Christakos, G., Imhoff, P.T., McBride, J.F., Pedit, J.A., Trangenstein, J.A. (1998). Multiphase flow and transport modeling in heterogeneous porous media: challenges and approaches. Advances in Water Resources, 21, 77–120.

Miller, C.T., Poirier-McNeil, M.M., Mayer, A.S. (1990). Dissolution of trapped nonaqueous phase liquids: Mass transfer characteristics. Water Resources Research, 26, 2783–2796.

Minasny, B., McBratney, A.B., Bristow, K.L. (1999). Comparison of different approaches to the development of pedotransfer functions for water-retention curves. Geoderma, 93(3–4), 225–253.

Moench, A.F. (1997). Flow to a well of finite diameter in a homogeneous, anisotropic water table aquifer. Water Resources Research, 33(6), 1397–1407.

Moench, A.F., Prickett, T.A. (1972). Radial flow in an infinite aquifer undergoing conversion from artesian to water table conditions. Water Resources Research, 8(2), 494–499.

Molnar, I.L., Gerhard, J.I., Willson, C.S., O'Carroll, D.M. (2020). Wettability effects on primary drainage mechanisms and NAPL distribution: a pore-scale study. Water Resources Research, 56(1), Article e2019WR025381.

Molz, F.J., Rajaram, H., Lu, S. (2004). Stochastic fractal-based models of heterogeneity in subsurface hydrology: Origins, applications, limitations, and future research questions. Reviews of Geophysics, 42, Article RG1002.

Monod, J. (1949). The growth of bacterial cultures. Annual Review of Microbiology, 3(1), 371–394.

Morel-Seytoux, H.J., Meyer, P.D., Nachabe, M., Tourna, J., van Genuchten, M.T., Lenhard, R.J. (1996). Parameter equivalence for the Brooks-Corey and van Genuchten soil characteristics: Preserving the effective capillary drive. Water Resources Research, 32(5), 1251–1258.

Morrison, R.D., Murphy, B.L. (Eds.). (2006). Environmental forensics: contaminant specific guide. Academic Press.

Mostafa, M., Van Geel, P.J. (2012). Validation of a relative permeability model for bioclogging in unsaturated soils. Vadose Zone Journal, 11(1).

Mualem, Y. (1974). A conceptual model of hysteresis. Water Resources Research, 10(3), 514–520.

Mualem, Y., Dagan, G. (1978). Hydraulic conductivity of soils: unified approach to the statistical models 1. Soil Science Society of America Journal, 42(3), 392–395.

Mulry, C.J., Lundy, D.A. (2013, March). LNAPL investigation and behavior in a saprolite aquifer. In P.T. Kostecki, E.J. Calabrese, C.M. Teaf, D.F. Ludwig (Eds.), Proceedings of the 23rd Annual International Conference on Soil, Water, Energy & Air (pp. 173–193).

Mumford, K.G., Mustafa, N., Gerhard, J.I. (2016). Probabilistic risk assessment of contaminant transport in groundwater and vapour intrusion following remediation of a contaminant source. Stochastic Environmental Research and Risk Assessment, 30(3), 1017-1031.

Mundle, K., Reynolds, D.A., West, M.R., Kueper, B.H. (2007). Concentration rebound following in situ chemical oxidation in fractured clay. Ground Water, 45, 692–702). doi:10.1111/j.1745–6584.2007.00359.x.

Murphy, F., Herkelrath, W.N. (1996). A sample-freezing drive shoe for a wire line piston core sampler. Groundwater Monitoring & Remediation, 16(3), 86–90.

Murphy, K.R., Stedmon, C.A., Graeber, D., Bro, R. (2013). Fluorescence spectroscopy and multi-way techniques: PARAFAC. Analytical Methods, 5(23), 6557–6566.

Naidu, R., Nandy, S., Megharaj, M., Kumar, R.P., Chadalavada, S., Chen, Z., Bowman, M. (2012). Monitored natural attenuation of a long-term petroleum hydrocarbon contaminated sites: a case study. Biodegradation, 23(6), 881–895.

National Environment Protection (Assessment of Site Contamination) Measure 1999.

Nemes, A.D., Schaap, M.G., Leij, F.J., Wösten, J.H. (2001). Description of the unsaturated soil hydraulic database UNSODA version 2.0. Journal of Hydrology, 251(3–4), 151–162.

Neuman, S.P. (1990). Universal scaling of hydraulic conductivities and dispersivities in geologic media. Water Resources Research, 26, 1749–1758.

Neuman, S.P. (1994). Generalized scaling of permeabilities: validation and effect of support scale. Geophysical Research Letters, 21, 349–352.

Neuman, S.P. (2003). Maximum likelihood Bayesian averaging of uncertain model predictions. Stochastic Environmental Research and Risk Assessment, 17, 291–305.

Neuman, S.P. (2005). Trends, prospects and challenges in quantifying flow and transport through fractured rocks. Hydrogeology Journal, 13, 124–147.

Neuman, S.P. (2020). Twenty lessons drawn from my subsurface hydrology career. Perspectives of Earth and Space Scientists, 1(1), Article, e2020CN000131.

Neuman, S.P., Di Federico, V. (2003). Multifaceted nature of hydrogeologic scaling and its interpretation. Reviews of Geophysics, 41(4–1), 4–31.

Neuman, S.P., Tartakovsky, D.M. (2009). Perspective on theories of non-Fickian transport in heterogeneous media. Advances in Water Resources, 32, 670–680.

Neuweiler, I., Papafotiou, A., Class, H., Helmig, R. (2011). Estimation of effective parameters for a two-phase flow problem in non-Gaussian heterogeneous porous media. Journal of Contaminant Hydrology, 120, 141–156.

Newell, C.J., Acree, S.D., Ross, R.R., Huling, S.G. (1995). Light nonaqueous phase liquids (EPA/540/S-95/500). U.S. Environmental Protection Agency.

Newell, C.J., Farhat, S.K., Adamson, D.T., Looney, B.B. (2011). Contaminant plume classification system based on mass discharge. Groundwater, 49(6), 914–919.

Ng, G.H.C., Bekins, B.A., Cozzarelli, I.M., Baedecker, M.J., Bennett, P.C., Amos, R.T. (2014). A mass balance approach to investigating geochemical controls on secondary water quality impacts at a crude oil spill site near Bemidji, MN. Journal of Contaminant Hydrology, 164, 1–15.

Nguyen, V.H., Sheppard, A.P., Knackstedt, M.A., & Pinczewski, W.V. (2006). The effect of displacement rate on imbibition relative permeability and residual saturation. Journal of Petroleum Science and Engineering, 52(1–4), 54–70.

Niessner, J., Hassanizadeh, S.M. (2008). A model for two-phase flow in porous media including fluid-fluid interfacial area. Water Resources Research, 44, Article W08439.

O'Carroll, D.M., Abriola, L.M., Polityka, C.A., Bradford, S.A., Demond, A.H. (2005). Prediction of two-phase capillary pressure–saturation relationships in fractional wettability systems. Journal of Contaminant Hydrology, 77(4), 247–270.

Odong, J. (2007). Evaluation of empirical formulae for determination of hydraulic conductivity based on grain-size analysis. Journal of American Science, 3(3), 54–60.

Oostrom, M., Dane, J.H., Wietsma, T.W. (2006a). A review of multidimensional, multifluid intermediate-scale experiments: Nonaqueous phase liquid dissolution and enhanced remediation. Vadose Zone Journal, 5, 570–598.

Oostrom, M., Hofstee, C., Wietsma, T.W. (2006b). Behavior of a viscous LNAPL under variable water table conditions. Soil and Sediment Contamination, 15, 543–564.

Oostrom, M., Lenhard, R.J. (1998). Comparison of relative permeability-saturation-pressure parametric models for infiltration and redistribution of a light nonaqueous-phase liquid in sandy porous media. Advances in Water Resources, 21(2), 145–157.

Oostrom, M., White, M.D., Lenhard, R.J., Van Geel, P.J., Wietsma, T.W. (2005). A comparison of models describing residual NAPL formation in the vadose zone. Vadose Zone Journal, 4(1), 163–174.

Or, D., Smets, B.F., Wraith, J.M., Dechesne, A., Friedman, S.P. (2007). Physical constraints affecting bacterial habitats and activity in unsaturated porous media–a review. Advances in Water Resources, 30(6–7), 1505–1527.

Oreskes, N., Shrader-Frechette, K., Belitz, K. (1994). Verification, validation, and confirmation of numerical models in the earth sciences. Science, 263(5147), 641–646.

Palmier, C., Cazals, F., Atteia, O. (2017). Bail-down test simulation at laboratory scale. Transport in Porous Media, 116(2), 567–583.

Palmier, C., Dodt, M., Atteia, O. (2016). Comparison of oil transmissivity methods using bail-down test data. Groundwater Monitoring & Remediation, 36(3), 73–83.

Pankow, J.F., Cherry, J.A. (Eds.). (1996). Dense chlorinated solvents and other DNAPLs in groundwater: History, behavior, and remediation. Waterloo Press.

Pannell, D.J. (1997). Sensitivity analysis of normative economic models: theoretical framework and practical strategies. Agricultural Economics, 16(2), 139–152.

Paradis, D., Lefebvre, R., Morin, R.H., Gloaguen, E. (2011). Permeability profiles in granular aquifers using flowmeters in direct-push wells. Groundwater, 49(4), 534–547.

Parker, B.L., Cherry, J.A., Chapman, S.W. (2004). Field study of TCE diffusion profiles below DNAPL to assess aquitard integrity. Journal of Contaminant Hydrology, 74(1–4), 197–230.

Parker, B.L., Cherry, J.A., Chapman, S.W. (2012). Discrete fracture network approach for studying contamination in fractured rock. AQUA mundi, 3, 101–116.

Parker, B.L., Gillham, R.W., Cherry, J.A. (1994). Diffusive disappearance of immiscible-phase organic liquids in fractured geologic media. Ground Water, 32, 805–819.

Parker, J.C., Lenhard, R.J. (1987). Model for hysteretic constitutive relations governing multiphase flow: 1. saturation-pressure relations. Water Resources Research, 23, 2187–2196.

Parker, J.C., Lenhard, R.J. (1990). Vertical integration of three-phase flow equations for analysis of light hydrocarbon plume movement. Transport in Porous Media, 5(2), 187–206.

Parker, J.C., Lenhard, R.J., Kuppusamy, T. (1987). Parametric model for constitutive properties governing multiphase flow in porous media. Water Resources Research, 23, 618–624.

Parker, J.C., Park, E. (2004). Modeling field-scale dense nonaqueous phase liquid dissolution kinetics in heterogeneous aquifers. Water Resources Research, 40, W051091–W0510912.

Parker, J.C., Waddill, D.W., Johnson, J.A. (1996). UST corrective action technologies: Engineering design of free product recovery systems (PB-96-153556/XAB). U.S. Environmental Protection Agency.

Pastrovich, L.D., Baradat, Y., Barthel, R., Chiarelli, A., Fussell, D.R. (1979). Protection of groundwater from oil pollution. Concawe.

Patterson, C. (2011). A history-dependent nonwetting phase trapping model for multiphase flow characteristic curves [Doctoral dissertation, Clemson University].

Payá Pérez, A., Rodríguez Eugenio, N. (2018). Status of local soil contamination in Europe: Revision of the indicator 'Progress in the management Contaminated Sites in Europe' (EUR, 29124 EN). Publications Office of the European Union.

Payne, F.C., Quinnan, J.A., Potter, S.T. (2008). Remediation hydraulics. CRC Press.

Pede, M.A.Z. (2009). Flutuação do lençol freático e sua implicação na recuperação de hidrocarbonetos: um estudo de caso [Doctoral dissertation, Universidade Estadual Paulista].

Pennington, A., Smith, J., Koons, B., Divine, C.E. (2016). Comparative evaluation of single-well LNAPL tracer testing at five sites. Groundwater Monitoring & Remediation, 36(2), 45–58.

Peters, C.A., Knightes, C.D., Brown, D.G. (1999). Long-term composition dynamics of PAH-containing NAPLs and implications for risk assessment. Environmental Science & Technology, 33(24), 4499–4507.

Petri, B.G., Fučík, R., Illangasekare, T.H., Smits, K.M., Christ, J.A., Sakaki, T., Sauck, C.C. (2015). Effect of NAPL source morphology on mass transfer in the vadose zone. Groundwater, 53(5), 685–698.

Pianosi, F., Beven, K., Freer, J., Hall, J.W., Rougier, J., Stephenson, D.B., Wagener, T. (2016). Sensitivity analysis of environmental models: A systematic review with practical workflow. Environmental Modelling Software, 79, 214–232.

Pickens, J.F., Cherry, J.A., Grisak, G.E., Merritt, W.F., Risto, B.A. (1978). A multilevel device for ground-water sampling and piezometric monitoring. Groundwater, 16(5), 322–327.

Pierce, A.A., Chapman, S.W., Zimmerman, L.K., Hurley, J.C., Aravena, R., Cherry, J.A., Parker, B.L. (2018). DFN-M field characterization of sandstone for a process-based site conceptual model and numerical simulations of TCE transport with degradation. Journal of Contaminant Hydrology, 212, 96–114.

Pinder, G.F., Gray, W.G. (2008). Essentials of multiphase flow and transport in porous media. John Wiley & Sons.

Powers, S.E., Abriola, L.M., Weber Jr, W.J. (1992). An experimental investigation of nonaqueous phase liquid dissolution in saturated subsurface systems: Steady state mass transfer rates. Water Resources Research, 28, 2691–2705.

Powers, S.E., Anckner, W.H., Seacord, T.F. (1996). Wettability of NAPL-contaminated sands. Journal of Environmental Engineering, 122(10), 889–896.

Powers, S.E., Loureiro, C.O., Abriola, L.M., Weber, W.J. (1991). Theoretical study of the significance of nonequilibrium dissolution of nonaqueous phase liquids in subsurface systems. Water Resources Research, 27, 463–477.

Ptak, T., Piepenbrink, M., Martac, E. (2004). Tracer tests for the investigation of heterogeneous porous media and stochastic modelling of flow and transport—a review of some recent developments. Journal of Hydrology, 294(1–3), 122–163.

Radcliffe, D.E., Šimůnek, J. (2010). Soil physics with HYDRUS: Modeling and applications. CRC Press.

Rao, P.S.C., Jawitz, J.W. (2003). Comment on "Steady state mass transfer from single-component dense nonaqueous phase liquids in uniform flow fields" by T. C. Sale and D. B. McWhorter. Water Resources Research, 39.

Rao, P.S.C., Jawitz, J.W., Enfield, C.G., Falta Jr, R.W., Annable, M.D., Wood, A.L. (2001). Technology integration for contaminated site remediation: clean-up goals and performance criteria. In S.F. Thornton, S.E. Oswald (Eds.), Groundwater quality: natural and enhanced restoration of groundwater pollution (IAHS Publication no. 275, pp. 571–578). IAHS Press.

Rau, G.C., Post, V.E., Shanafield, M., Krekeler, T., Banks, E.W., Blum, P. (2019). Error in hydraulic head and gradient time-series measurements: a quantitative appraisal. Hydrology & Earth System Sciences, 23(9), 3603–3629.

Rawls, W.J., Brakensiek, D.L., Saxtonn, K.E. (1982). Estimation of soil water properties. Transactions of the ASAE, 25(5), 1316–1320.

Rayner, J.L., Bekele, E., Donn, M., Bastow, T.P., Davis, G.B., Woodbury, R., Furness, A., Geste, Y. (2020). Australian case studies of light non-aqueous phase liquid (LNAPL) natural source zone depletion rates compared with conventional active recovery efforts (CRC CARE Technical Report 47). Cooperative Research Centre for Contamination Assessment and Remediation of the Environment.

Rehfeldt, K.R., Boggs, J.M., Gelhar, L.W. (1992). Field study of dispersion in a heterogeneous aquifer, 3. Geostatistical analysis of hydraulic conductivity. Water Resources Research, 28, 3309–3324.

Reimann, C., Filzmoser, P. (2000). Normal and lognormal data distribution in geochemistry: death of a myth. Consequences for the statistical treatment of geochemical and environmental data. Environmental Geology, 39(9), 1001–1014.

Reimann, C., Filzmoser, P., Garrett, R.G. (2005). Background and threshold: critical comparison of methods of determination. Science of the Total Environment, 346(1–3), 1–16.

Reimann, C., Filzmoser, P., Garrett, R.G., Dutter, R. (2008). Statistical data analysis explained: applied environmental statistics with R. Wiley.

Reimann, C., Garrett, R.G. (2005). Geochemical background—concept and reality. Science of the Total Environment, 350(1–3), 12–27.

Reischer, M., Christensen, A.G., De Weirdt, F., Bruns, S., Dideriksen, K. (2020). Capabilities of an optical direct push probe for 2D-subsurface imaging. Journal of Contaminant Hydrology, 232, Article 103636.

Ren, X.W., Santamarina, J.C. (2018). The hydraulic conductivity of sediments: A pore size perspective. Engineering Geology, 233, 48–54.

Renard, P. (2007). Stochastic hydrogeology: What professionals really need? Ground Water, 45, 531–541.

Renard, P., Allard, D. (2013). Connectivity metrics for subsurface flow and transport. Advances in Water Resources, 51, 168–196.

Renard, P., de Marsily, G. (1997). Calculating equivalent permeability: A review. Advances in Water Resources, 20, 253–278.

Renard, P., Glenz, D., Mejias, M. (2009). Understanding diagnostic plots for well-test interpretation. Hydrogeology Journal, 17(3), 589–600.

Reyenga, L., Hawthorne, M. (2017, October). High resolution mobile NAPL interval identification and transmissivity calculations for DNAPL [Conference session]. MGP 2017—7th International Symposium and Exhibition on the Redevelopment of Manufactured Gas Plant Sites, New Orleans, LA, United States.

Reynolds, C.A., Menke, H., Andrew, M., Blunt, M.J., Krevor, S. (2017). Dynamic fluid connectivity during steady-state multiphase flow in a sandstone. Proceedings of the National Academy of Sciences, 114(31), 8187–8192.

Richards, L.A. (1931). Capillary conduction of liquids through porous mediums. Physics, 1(5), 318–333.

Riha, B.D., Rossabi, J., Eddy-Dilek, C.A., Jackson, D., Keller, C. (2000, April). DNAPL characterization using the ribbon NAPL sampler: Methods and results. In Proceedings of the Second International Conference on Remediation of Chlorinated and Recalcitrant Compounds (pp. 33–40). Batelle.

Rivett, M., Sweeney, R. (2019). An introduction to natural source zone depletion at LNAPL sites (CL:AIRE Technical Bulletin 20). Contaminated Land: Applications in Real Environments.

Rivett, M., Wealthall, G. (2019). Light non-aqueous phase liquids: managing site complexities (Bulletin ECGEB No, 20). Royal Society of Chemistry.

Rivett, M.O. (1995). Soil-gas signatures from volatile chlorinated solvents: Borden field experiments. Groundwater, 33(1), 84–98.

Rivett, M.O. (2019, November). A review of the recent international LNAPL literature—are we missing out on something? [Conference session]. 2019 Year of Carbon meeting of Contaminated Land Group of The Geological Society, Birmingham, UK.

Rivett, M.O., Dearden, R.A., Wealthall, G.P. (2014). Architecture, persistence and dissolution of a 20 to 45 year old trichloroethene DNAPL source zone. Journal of Contaminant Hydrology, 170, 95–115.

Rivett, M.O., Wealthall, G.P., Dearden, R.A., McAlary, T.A. (2011). Review of unsaturated-zone transport and attenuation of volatile organic compound (VOC) plumes leached from shallow source zones. Journal of Contaminant Hydrology, 123(3–4), 130–156.

Riyis, M.T. (2019). Contribuição para investigação de áreas contaminadas com abordagem de alta resolução [Doctoral dissertation, Universidade Estadual Paulista].

Robert, T., Martel, R., Lefebvre, R., Lauzon, J.M., Morin, A. (2017). Impact of heterogeneous properties of soil and LNAPL on surfactant-enhanced capillary desaturation. Journal of Contaminant Hydrology, 204, 57–65.

Roberts, P.V., Goltz, M.N., Mackay, D.M. (1986). A natural gradient experiment on solute transport in a sand aquifer: 3. Retardation estimates and mass balances for organic solutes. Water Resources Research, 22, 2047–2058.

Rockhold, M.L., Yarwood, R.R., Niemet, M.R., Bottomley, P.J., Selker, J.S. (2002). Considerations for modeling bacterial-induced changes in hydraulic properties of variably saturated porous media. Advances in Water Resources, 25(5), 477–495.

Rodell, M., Famiglietti, J.S., Wiese, D.N., Reager, J.T., Beaudoing, H.K., Landerer, F.W., Lo, M.H. (2018). Emerging trends in global freshwater availability. Nature, 557(7707), 651–659.

Rodríguez, D.J., Kueper, B.H. (2013). Specification of matrix cleanup goals in fractured porous media. Groundwater, 51, 58–65.

Rogiers, B., Mallants, D., Batelaan, O., Gedeon, M., Huysmans, M., Dassargues, A. (2012). Estimation of hydraulic conductivity and its uncertainty from grain-size data using GLUE and artificial neural networks. Mathematical Geosciences, 44(6), 739–763.

Rojas, R., Feyen, L., Dassargues, A. (2008). Conceptual model uncertainty in groundwater modeling: Combining generalized likelihood uncertainty estimation and Bayesian model averaging. Water Resources Research, 44, Article W12418.

Rojas, R., Kahunde, S., Peeters, L., Batelaan, O., Feyen, L., Dassargues, A. (2010). Application of a multimodel approach to account for conceptual model and scenario uncertainties in groundwater modelling. Journal of Hydrology, 394, 416–435.

Rojo, F. (2009). Degradation of alkanes by bacteria. Environmental Microbiology, 11(10), 2477–2490.

Rosas, J., Lopez, O., Missimer, T.M., Coulibaly, K.M., Dehwah, A.H., Sesler, K., Lujan, L.R., Mantilla, D. (2014). Determination of hydraulic conductivity from grain-size distribution for different depositional environments. Groundwater, 52(3), 399–413.

Rosenzweig, R., Shavit, U., Furman, A. (2012). Water retention curves of biofilm-affected soils using xanthan as an analogue. Soil Science Society of America Journal, 76(1), 61–69.

Rovey, C.W., Cherkauer, D.S. (1995). Scale dependency of hydraulic conductivity measurements. Groundwater, 33(5), 769–780.

Rubin, Y., Hubbard, S.S. (Eds.). (2005). Hydrogeophysics. Springer Science & Business Media.

Sale, T. (2001). Methods for determining inputs to environmental petroleum hydrocarbon mobility and recovery models (API Publication No. 4711). American Petroleum Institute.

Sale, T., Hopkins, H., Kirkman, A. (2018). Managing risk at LNAPL sites. Frequently Asked Questions. 2nd edition (Soil and Groundwater Research Bulletin No. 18). American Petroleum Institute.

Sale, T., Kiaalhosseini, S., Olson, M., Johnson, R., Rogers, R. (2016). Third generation (3G) site characterization: Cryogenic core collection and high throughput core analysis-an addendum to basic research addressing contaminants in low permeability zones—a state of the science review (SERDP Project ER-1740). Strategic Environmental Research and Development Program.

Sale, T., Parker, B.L., Newell, C.J., Devlin, J.F. (2013). State-of-the-science review: Management of contaminants stored in low permeability zones (SERDP Project ER-1740). Strategic Environmental Research and Development Program.

Sale, T.C., McWhorter, D.B. (2001). Steady state mass transfer from single-component dense nonaqueous phase liquids in uniform flow fields. Water Resources Research, 37, 393–404.

Saleem, M. (2005). Assessment of the relation between the spilled LNAPL volume and its thickness in monitoring well considering the water table fluctuation history [Doctoral dissertation, King Fahd University of Petroleum & Minerals].

Saltelli, A., Annoni, P. (2010). How to avoid a perfunctory sensitivity analysis. Environmental Modelling Software, 25(12), 1508–1517.

Saltelli, A., Ratto, M., Andres, T., Campolongo, F., Cariboni, J., Gatelli, D., Saisana, M., Tarantola, S. (2008). Global sensitivity analysis: the primer. John Wiley & Sons.

Saltelli, A., Tarantola, S., Campolongo, F., Ratto, M. (2004). Sensitivity analysis in practice: a guide to assessing scientific models. John Wiley & Sons.

Sánchez-Vila, X., Carrera, J., Girardi, J.P. (1996). Scale effects in transmissivity. Journal of Hydrology, 183, 1–22.

Sánchez-Vila, X., Guadagnini, A., Carrera, J. (2006). Representative hydraulic conductivities in saturated groundwater flow. Reviews of Geophysics, 44, Article RG3002.

Saxton, K.E., Rawls, W., Romberger, J.S., Papendick, R.I. (1986). Estimating generalized soil-water characteristics from texture 1. Soil Science Society of America Journal, 50(4), 1031–1036.

Schaap, M.G., Leij, F.J. (1998a). Database-related accuracy and uncertainty of pedotransfer functions. Soil Science, 163(10), 765–779.

Schaap, M.G., Leij, F.J. (1998b). Using neural networks to predict soil water retention and soil hydraulic conductivity. Soil and Tillage Research, 47(1–2), 37–42.

Schaap, M.G., Leij, F.J., van Genuchten, M.Th. (1998). Neural network analysis for hierarchical prediction of soil hydraulic properties. Soil Science Society of America Journal, 62(4), 847–855.

Schaap, M.G., Leij, F.J., van Genuchten, M.Th. (2001). Rosetta: A computer program for estimating soil hydraulic parameters with hierarchical pedotransfer functions. Journal of Hydrology, 251(3–4), 163–176.

Schiegg, H.O. (1985). Considerations on water, oil and air in porous media. Water Science and Technology, 17(4–5), 467–476.

Schiegg, H.O., Schwille, F. (1991). Hydrocarbons in porous media. In J. Bear, M.Y. Corapcioglu (Eds.), Transport processes in porous media (pp. 69–201). Springer.

Schmelzbach, C., Tronicke, J., Dietrich, P. (2011). Three-dimensional hydrostratigraphic models from ground-penetrating radar and direct-push data. Journal of Hydrology, 398(3–4), 235–245.

Schöniger, A., Illman, W.A., Wöhling, T., Nowak, W. (2015). Finding the right balance between groundwater model complexity and experimental effort via Bayesian model selection. Journal of Hydrology, 531, 96–110.

Schulmeister, M.K., Butler Jr., J.J., Healey, J.M., Zheng, L., Wysocki, D.A., McCall, G.W. (2003). Direct-push electrical conductivity logging for high-resolution hydrostratigraphic characterization. Groundwater Monitoring & Remediation, 23(3), 52–62.

Schwille, F. (1984). Migration of organic fluids immiscible with water in the unsaturated zone. In B. Yaron, G. Dagan, J. Goldshmid (Eds.), Pollutants in porous media (pp., 27–48).

Segal, E., Shouse, P.J., Bradford, S.A., Skaggs, T.H., Corwin, D.L. (2009). Measuring particle size distribution using laser diffraction: implications for predicting soil hydraulic properties. Soil Science, 174(12), 639–645.

Seki, K. (2007). SWRC fit—a nonlinear fitting program with a water retention curve for soils having unimodal and bimodal pore structure. Hydrology and Earth System Sciences Discussions, 4(1), 407–437.

Selker, J.S., Thévenaz, L., Huwald, H., Mallet, A., Luxemburg, W., van De Giesen, N., Stejskal, M., Zeman, J., Westhoff, M., Parlange, M.B. (2006). Distributed fiber-optic temperature sensing for hydrologic systems. Water Resources Research, 42(12), Article W12202.

Sellwood, S.M., Healey, J.M., Birk, S., Butler Jr., J.J. (2005). Direct-push hydrostratigraphic profiling: Coupling electrical logging and slug tests. Groundwater, 43(1), 19–29.

Semple, K.T., Doick, K.J., Wick, L.Y., Harms, H. (2007). Microbial interactions with organic contaminants in soil: definitions, processes and measurement. Environmental Pollution, 150(1), 166–176.

Seyedabbasi, M.A., Newell, C.J., Adamson, D.T., Sale, T.C. (2012). Relative contribution of DNAPL dissolution and matrix diffusion to the long-term persistence of chlorinated solvent source zones. Journal of Contaminant Hydrology, 134, 69–81.

Sharma, P., Kostarelos, K., Lenschow, S., Christensen, A., de Blanc, P.C. (2020). Surfactant flooding makes a comeback: Results of a full-scale, field implementation to recover mobilized NAPL. Journal of Contaminant Hydrology, 230, Article 103602.

Sherry, A., Grant, R.J., Aitken, C.M., Jones, M., Head, I.M., Gray, N.D. (2014). Volatile hydrocarbons inhibit methanogenic crude oil degradation. Frontiers in Microbiology, 5(131), 1–9.

Sherwood Lollar, B., Slater, G.F., Sleep, B., Witt, M., Klecka, G.M., Harkness, M., Spivack, J. (2001). Stable carbon isotope evidence for intrinsic bioremediation of tetrachloroethene and trichloroethene at area 6, Dover Air Force Base. Environmental Science & Technology, 35(2), 261–269.

Siirila-Woodburn, E.R., Sanchez-Vila, X., Fernàndez-Garcia, D. (2015). On the formation of multiple local peaks in breakthrough curves. Water Resources Research, 51, 2128–2152.

Silva, O., Carrera, J., Dentz, M., Kumar, S., Alcolea, A., Willmann, M. (2009). A general real-time formulation for multi-rate mass transfer problems. Hydrology and Earth System Sciences, 13, 1399–1411.

Šimůnek, J., van Genuchten, M.Th., Šejna, M. (2012). The HYDRUS software package for simulating the two-and three-dimensional movement of water, heat, and multiple solutes in variably-saturated porous media. Technical manual, version 2.0. PC Progress.

Singh, A., Maichle, R. (2015). ProUCL Version 5.1.00 user guide-statistical software for environmental applications for data sets with and without nondetect observations (EPA/600/R-07/041). U.S. Environmental Protection Agency.

Skinner, A.M. (2013). LNAPL longevity as a function of remedial actions: tools for evaluating LNAPL remedies [Master's thesis, Colorado State University].

Slater, L. (2007). Near surface electrical characterization of hydraulic conductivity: From petrophysical properties to aquifer geometries—A review. Surveys in Geophysics, 28(2–3), 169–197.

Slater, L., Lesmes, D.P. (2002). Electrical-hydraulic relationships observed for unconsolidated sediments. Water Resources Research, 38(10), 31-1–31-13.

Sleep, B.E., Sehayek, L., Chien, C.C. (2000). A modeling and experimental study of light nonaqueous phase liquid (LNAPL) accumulation in wells and LNAPL recovery from wells. Water Resources Research, 36, 3535–3545.

Sleep, B.E., Sykes, J.F. (1989). Modeling the transport of volatile organics in variably saturated media. Water Resources Research, 25, 81–92.

Smith, T. (2008). Direct measurement of LNAPL flow using single well periodic mixing reactor tracer tests [Master's thesis, Colorado State University].

Soga, K., Page, J.W.E., Illangasekare, T.H. (2004). A review of NAPL source zone remediation efficiency and the mass flux approach. Journal of Hazardous Materials, 110(1–3), 13–27.

Song, J., Chen, X., Cheng, C., Wang, D., Lackey, S., Xu, Z. (2009). Feasibility of grain-size analysis methods for determination of vertical hydraulic conductivity of streambeds. Journal of Hydrology, 375(3–4), 428–437.

Song, X., Zhang, J., Zhan, C., Xuan, Y., Ye, M., Xu, C. (2015). Global sensitivity analysis in hydrological modeling: Review of concepts, methods, theoretical framework, and applications. Journal of Hydrology, 523, 739–757.

Sookhak Lari, K., Davis, G.B., Johnston, C.D. (2016a). Incorporating hysteresis in a multi-phase multi-component NAPL modelling framework; a multi-component LNAPL gasoline example. Advances in Water Resources, 96, 190–201.

Sookhak Lari, K., Davis, G.B., Rayner, J.L., Bastow, T.P., Puzon, G.J. (2019). Natural source zone depletion of LNAPL: A critical review supporting modelling approaches. Water Research, 157, 630–646.

Sookhak Lari, K., Johnston, C.D., Davis, G.B. (2016b). Gasoline multiphase and multicomponent partitioning in the vadose zone: Dynamics and risk longevity. Vadose Zone Journal, 15(3), 1–15.

Sookhak Lari, K., Johnston, C.D., Rayner, J.L., Davis, G.B. (2018). Field-scale multi-phase LNAPL remediation: Validating a new computational framework against sequential field pilot trials. Journal of Hazardous Materials, 345, 87–96.

Sookhak Lari, K., Rayner, J.L., Davis, G.B., Johnston, C.D. (2020). LNAPL recovery endpoints; lessons learnt through modelling, experiments and field trials. Groundwater Monitoring & Remediation.

Soriano-Disla, J.M., Janik, L.J., Allen, D.J., McLaughlin, M.J. (2017). Evaluation of the performance of portable visible-infrared instruments for the prediction of soil properties. Biosystems Engineering, 161, 24–36.

Soulsby, R. (1997). Dynamics of marine sands: a manual for practical applications. Thomas Telford.

St. Germain, R. (2011). Laser-induced fluorescence primer. Applied NAPL Science Review, 1(9).

St. Germain, R. (2014). Laser-induced fluorescence: theory and data interpretation [Webinar]. Montana Department of Environmental Quality Group.

Stauffer, P.H. (2006). Flux flummoxed: A proposal for consistent usage. Ground Water, 44, 125–128.

Steffy, D.A., Barry, D.A., Johnston, C.D. (1997a). Improved scaling technique for two-phase pressure-saturation relationships. Journal of Contaminant Hydrology, 28, 207–225.

Steffy, D.A., Barry, D.A., Johnston, C.D. (1997b). Influence of antecedent moisture content on residual LNAPL saturation. Soil and Sediment Contamination, 6(2), 113–147.

Steffy, D.A., Johnston, C.D., Barry, D.A. (1995). A field study of the vertical immiscible displacement of LNAPL associated with a fluctuating water table. In K. Kovar, J. Krásný (Eds.), Groundwater quality: remediation and protection (IAHS Publication no. 225, pp. 49–57). IAHS Press.

Steffy, D.A., Johnston, C.D., Barry, D.A. (1998). Numerical simulations and long-column tests of LNAPL displacement and trapping by a fluctuating water table. Soil and Sediment Contamination, 7, 325–356.

Stout, S.A., Douglas, G.S., Uhler, A.D. (2006). Automotive gasoline. In R.D. Morrison, B.L. Murphy (Eds.), Environmental forensics: contaminant specific guide (pp. 465–531). Academic Press.

Stout, S.A., Emsbo-Mattingly, S.D., Douglas, G.S., Uhler, A.D., McCarthy, K.J. (2015). Beyond, 16 priority pollutant PAHs: A review of PACs used in environmental forensic chemistry. Polycyclic Aromatic Compounds, 35(2–4), 285–315.

Sudicky, E.A. (1986). A natural gradient experiment on solute transport in a sand aquifer: Spatial variability of hydraulic conductivity and its role in the dispersion process. Water Resources Research, 22, 2069–2082.

Sudicky, E.A., Frind, E.O. (1982). Contaminant transport in fractured porous media: analytical solutions for a system of parallel fractures. Water Resources Research, 18, 1634–1642.

Sun, S. (2016). Transient water table influence upon Light Non-Aqueous Phase Liquids (LNAPLs) redistribution: laboratory and modelling studies [Doctoral dissertation, University of Birmingham].

Sundaram, B., Feitz, A., de Caritat, P., Plazinska, A., Brodie, R., Coram, J., Ransley, T. (2009). Groundwater sampling and analysis–a field guide (Record 2009/27). Geoscience Australia.

Suthersan, S.S., Horst, J., Schnobrich, M., Welty, N., McDonough, J. (2016). Remediation engineering: design concepts (2nd ed.). CRC Press.

Tartakovsky, D.M. (2013). Assessment and management of risk in subsurface hydrology: A review and perspective. Advances in Water Resources, 51, 247–260.

Tartakovsky, G.D., Neuman, S.P. (2007). Three-dimensional saturated-unsaturated flow with axial symmetry to a partially penetrating well in a compressible unconfined aquifer. Water Resources Research, 43(1), Article W01410.

Taylor, S.R., Moltyaner, G.L., Howard, K.W.F., Killey, R.W.D. (1987). A comparison of field and laboratory methods for determining contaminant flow parameters. Groundwater, 25(3), 321–330.

Telford, W.M., Geldart, L.P., Sheriff, R.E. (1990). Applied geophysics (2nd ed.). Cambridge University Press.

Teramoto, E.H., Chang, H.K. (2017). Field data and numerical simulation of btex concentration trends under water table fluctuations: Example of a jet fuel-contaminated site in Brazil. Journal of Contaminant Hydrology, 198, 37–47.

Teramoto, E.H., Isler, E., Polese, L., Baessa, M.P.M., Chang, H.K. (2019). LNAPL saturation derived from laser induced fluorescence method. Science of the Total Environment, 683, 762–772.

Teramoto, E.H., Vogt, C., Baessa, M.P.M., Polese, L., Soriano, A.U., Chang, H.K., Richnow, H.H. (2020). Dynamics of hydrocarbon mineralization characterized by isotopic analysis at a jet-fuel-contaminated site in subtropical climate. Science of the Total Environment, 234, Article 103684.

Testa, S.M., Paczkowski, M.T. (1989). Volume determination and recoverability of free hydrocarbon. Groundwater Monitoring & Remediation, 9(1), 120–128.

Theis, C.V. (1935). The relation between the lowering of the piezometric surface and the rate and duration of discharge of a well using ground-water storage. Eos, Transactions American Geophysical Union, 16(2), 519–524.

Tinjum, J.M., Benson, C.H., Blotz, L.R. (1997). Soil-water characteristic curves for compacted clays. Journal of Geotechnical and Geoenvironmental Engineering, 123(11), 1060–1069.

Todd, D. K., Mays, L. W. (2005). Groundwater hydrology (3rd ed.). John Wiley & Sons.

Tomlinson, D.W., Butler, W.A., Loper, J.R., Martin, H. (2012). Multiple lines of evidence approach for development of an LNAPL conceptual site model at a former waste oil facility. In Remediation of Chlorinated and Recalcitrant Compounds 2012. Eight International Conference on Remediation of Chlorinated and Recalcitrant Compounds. Batelle.

Tomlinson, D.W., Rivett, M.O., Wealthall, G.P., Sweeney, R.E. (2017). Understanding complex LNAPL sites: Illustrated handbook of LNAPL transport and fate in the subsurface. Journal of Environmental Management, 204, 748–756.

Total Petroleum Hydrocarbon Criteria Working Group (1998). Analysis of petroleum hydrocarbons in environmental media: volume 1. Amherst Scientific Publishers.

Tracy, M.K. (2015). Method comparison for analysis of LNAPL natural source zone depletion using CO_2 fluxes [Master's thesis, Colorado State University].

Trinchero, P., Sánchez-Vila, X., Fernàndez-Garcia, D. (2008). Point-to-point connectivity, an abstract concept or a key issue for risk assessment studies? Advances in Water Resources, 31, 1742–1753.

Troldborg, M., Nowak, W., Tuxen, N., Bjerg, P.L., Helmig, R., Binning, P.J. (2010). Uncertainty evaluation of mass discharge estimates from a contaminated site using a fully Bayesian framework. Water Resources Research, 46, Article W12552.

Trost, J.J., Christy, T.M., Bekins, B.A. (2018). A direct-push freezing core barrel for sampling unconsolidated subsurface sediments and adjacent pore fluids. Vadose Zone Journal, 17(1).

Tsai, Y.J., Chou, Y.C., Wu, Y.S., Lee, C.H. (2020). Noninvasive survey technology for LNAPL-contaminated site investigation. Journal of Hydrology, 587, Article 125002.

Urumović, K., Urumović Sr, K. (2016). The referential grain size and effective porosity in the Kozeny–Carman model. Hydrology and Earth System Sciences, 20(5), 1669–1680.

Urumović, K., Urumović Sr., K. (2017). Comment on "HydrogeoSieveXL: an Excel-based tool to estimate hydraulic conductivity from grain-size analysis": technical note published in Hydrogeology Journal (2015) 23:837–844, by JF Devlin. Hydrogeology Journal, 25(2), 589–591.

Urumović, K., Urumović Sr., K. (2018). Comment on 'Reply to Comment on "HydrogeoSieveXL: an Excel-based tool to estimate hydraulic conductivity from grain-size analysis": technical note published in Hydrogeology Journal (2015) 23:837–844, by JF Devlin': article published in Hydrogeology Journal (2017) 25:593–596, by JF Devlin. Hydrogeology Journal, 26(1), 357–358.

U.S. Environmental Protection Agency (2016, September). High-resolution site characterization (HRSC) webpage. https://clu-in.org/characterization/technologies/hrsc

Van Geel, P.J., Roy, S.D. (2002). A proposed model to include a residual NAPL saturation in a hysteretic capillary pressure–saturation relationship. Journal of Contaminant Hydrology, 58(1–2), 79–110.

Van Geel, P.J., Sykes, J.F. (1997). The importance of fluid entrapment, saturation hysteresis and residual saturations on the distribution of a lighter-than-water non-aqueous phase liquid in a variably saturated sand medium. Journal of Contaminant Hydrology, 25, 249–270.

van Genuchten, M.Th. (1980). A closed-form equation for predicting the hydraulic conductivity of unsaturated soils 1. Soil science society of America journal, 44(5), 892–898.

van Genuchten, M.Th., Leij, F.J., Yates, S.R. (1991). The RETC code for quantifying the hydraulic functions of unsaturated soils (EPA/600/2-91/065). U.S. Environmental Protection Agency.

van Hullebusch, E.D., Huguenot, D., Pechaud, Y., Simonnot, M.O., Colombano, S. (2020). Environmental soil remediation and rehabilitation. Springer.

Vandevivere, P., Baveye, P. (1992). Saturated hydraulic conductivity reduction caused by aerobic bacteria in sand columns. Soil Science Society of America Journal, 56(1), 1–13.

Vereecken, H., Schnepf, A., Hopmans, J. W., Javaux, M., Or, D., Roose, T., Vanderborght, J., Young, M.H., Amelung, W., Aitkenhead, M., Allison, S.D., Assouline, S., Baveye, P., Berli, M., Brüggemann, N., Finke, P., Flury, M., Gaiser, T., Govers, G., …, Young, I.M. (2016). Modeling soil processes: Review, key challenges, and new perspectives. Vadose Zone Journal, 15(5).

Vereecken, H., Weynants, M., Javaux, M., Pachepsky, Y., Schaap, M.G., Genuchten, M.Th. (2010). Using pedotransfer functions to estimate the van Genuchten–Mualem soil hydraulic properties: A review. Vadose Zone Journal, 9(4), 795–820.

Verginelli, I., Baciocchi, R. (2014). Vapor intrusion screening model for the evaluation of risk-based vertical exclusion distances at petroleum contaminated sites. Environmental Science & Technology, 48(22), 13263–13272.

Vienken, T. (2011). Critical evaluation of vertical high resolution methods for determining hydraulic conductivity [Doctoral dissertation, Eberhard Karls Universität Tübingen].

Vienken, T., Dietrich, P. (2011). Field evaluation of methods for determining hydraulic conductivity from grain size data. Journal of Hydrology, 400(1–2), 58–71.

Vienken, T., Dietrich, P. (2014). Comment on “Determination of hydraulic conductivity from grain-size distribution for different depositional environments” by J. Rosas, O. Lopez, T.M. Missimer, K.M. Coulibaly, A.H.A. Dehwah, K. Sesler, L.R. Lujan, and D. Mantilla. Groundwater, 52, no. 6.

Vienken, T., Leven, C., Dietrich, P. (2012). Use of CPT and other direct push methods for (hydro-) stratigraphic aquifer characterization—a field study. Canadian Geotechnical Journal, 49(2), 197–206.

Villanueva Martínez, M., Iglesias López, A. (1984). Pozos y acuíferos: técnicas de evaluación mediante ensayos de bombeo. Instituto Geológico y Minero de España.

Voss, C.I. (2011a). Editor’s message: Groundwater modeling fantasies—part, 1, adrift in the details. Hydrogeology Journal, 19(7), 1281–1284.

Voss, C.I. (2011b). Editor’s message: Groundwater modeling fantasies—part, 2, down to earth. Hydrogeology Journal, 19(8), 1455–1458.

Vuković, M., Soro, A. (1992). Determination of hydraulic conductivity of porous media from grain-size composition. Water Resources Publications.

Waddill, D.W., Parker, J.C. (1997a). A semianalytical model to predict recovery of light, nonaqueous phase liquids from unconfined aquifers. Ground Water, 35, 280–290.

Waddill, D.W., Parker, J.C. (1997b). Simulated recovery of light, nonaqueous phase liquid from unconfined heterogeneous aquifers. Ground Water, 35, 938–947.

Waddill, D.W., Parker, J.C. (1997c). Recovery of light, non-aqueous phase liquid from porous media: Laboratory experiments and model validation. Journal of Contaminant Hydrology, 27, 127–155.

Wang, J.P., François, B., Lambert, P. (2017). Equations for hydraulic conductivity estimation from particle size distribution: A dimensional analysis. Water Resources Research, 53(9), 8127–8134.

Wen, X.H., Gómez-Hernández, J.J. (1996). Upscaling hydraulic conductivities in heterogeneous media: An overview. Journal of Hydrology, 183, IX–XXXII.

Wentzel, A., Ellingsen, T.E., Kotlar, H.K., Zotchev, S.B., Throne-Holst, M. (2007). Bacterial metabolism of long-chain n-alkanes. Applied Microbiology and Biotechnology, 76(6), 1209–1221.

Wheatcraft, S.W., Tyler, S.W. (1988). An explanation of scale-dependent dispersivity in heterogeneous aquifers using concepts of fractal geometry. Water Resources Research, 24(4), 566–578.

Whitaker, S. (1967). Diffusion and dispersion in porous media. AIChE Journal, 13(3), 420–427.

Whitaker, S. (1986). Flow in porous media II: The governing equations for immiscible, two-phase flow. Transport in Porous Media, 1(2), 105–125.

Wiedemeier, T.H., Rifai, H.S., Newell, C.J., Wilson, J.T. (1999). Natural attenuation of fuels and chlorinated solvents in the subsurface. John Wiley & Sons.

Wildenschild, D., Sheppard, A.P. (2013). X-ray imaging and analysis techniques for quantifying pore-scale structure and processes in subsurface porous medium systems. Advances in Water Resources, 51, 217–246.

Willmann, M., Carrera, J., Sánchez-Vila, X., Vázquez-Suñé, E. (2007). On the meaning of the transmissivity values obtained from recovery tests. Hydrogeology Journal, 15(5), 833–842.

Wilson, J.L., Conrad, S.H., Mason, W.R., Peplinski, W., Hagan, E. (1990). Laboratory investigation of residual liquid organics from spills, leaks, and the disposal of hazardous wastes in groundwater (EPA/600/6-90/004). U.S. Environmental Protection Agency.

Wu, C.M., Yeh, T.C.J., Zhu, J., Lee, T.H., Hsu, N.S., Chen, C.H., Sancho, A.F. (2005). Traditional analysis of aquifer tests: Comparing apples to oranges? Water Resources Research, 41(9), Article W09402.

Xiao, B., Haslauer, C., Bohling, G. (2019). Comparison of multivariate spatial dependence structures of DPIL and flowmeter hydraulic conductivity data sets at the MADE site. Water, 11(7), Article 1420.

Yadav, B.K., Hassanizadeh, S.M. (2011). An overview of biodegradation of LNAPLs in coastal (semi)-arid environment. Water, Air, & Soil Pollution, 220(1–4), 225–239.

Yang, M., Annable, M.D., Jawitz, J.W. (2017). Field-scale forward and back diffusion through low-permeability zones. Journal of Contaminant Hydrology, 202, 47–58.

Yao, Y., Shen, R., Pennell, K.G., Suuberg, E.M. (2013). A review of vapor intrusion models. Environmental Science & Technology, 47(6), 2457–2470.

Yeh, T.C.J., Liu, S. (2000.) Hydraulic tomography: Development of a new aquifer test method. Water Resources Research, 36(8), 2095–2105.

Yeh, W.W.G. (1986). Review of parameter identification procedures in groundwater hydrology: the inverse problem. Water Resources Research, 22(2), 95–108.

Yimsiri, S., Euaapiwatch, S., Flores, G., Katsumi, T., Likitlersuang, S. (2018). Effects of water table fluctuation on diesel fuel migration in one-dimensional laboratory study. European Journal of Environmental and Civil Engineering, 22(3), 359–385.

Zalidis, G.C., Wallace, R.B., Voice, T.C. (1998). Influence of initial water saturation on the residual saturation of an organic liquid in the vadose zone. Water Resources Management, 12(2), 81–93.

Zapico, M.M., Vales, S., Cherry, J.A. (1987). A wireline piston core barrel for sampling cohesionless sand and gravel below the water table. Groundwater Monitoring & Remediation, 7(3), 74-82.

Zech, A., Arnold, S., Schneider, C., Attinger, S. (2015). Estimating parameters of aquifer heterogeneity using pumping tests–implications for field applications. Advances in Water Resources, 83, 137–147.

Zhang, C., Oostrom, M., Wietsma, T.W., Grate, J.W., Warner, M.G. (2011). Influence of viscous and capillary forces on immiscible fluid displacement: Pore-scale experimental study in a water-wet micromodel demonstrating viscous and capillary fingering. Energy Fuels, 25(8), 3493–3505.

Zhang, C., Yoon, H., Werth, C.J., Valocchi, A.J., Basu, N.B., Jawitz, J.W. (2008). Evaluation of simplified mass transfer models to simulate the impacts of source zone architecture on nonaqueous phase liquid dissolution in heterogeneous porous media. Journal of Contaminant Hydrology, 102(1–2), 49–60.

Zhang, Y., Schaap, M.G. (2017). Weighted recalibration of the Rosetta pedotransfer model with improved estimates of hydraulic parameter distributions and summary statistics (Rosetta3). Journal of Hydrology, 547, 39–53.

Zheng, C., Bianchi, M., Gorelick, S.M. (2011). Lessons learned from 25 years of research at the MADE site. Groundwater, 49(5), 649–662.

Zhou, D., Blunt, M. (1997). Effect of spreading coefficient on the distribution of light non-aqueous phase liquid in the subsurface. Journal of Contaminant Hydrology, 25(1–2), 1–19.

Zhou, H., Gómez-Hernández, J.J., Li, L. (2014). Inverse methods in hydrogeology: Evolution and recent trends. Advances in Water Resources, 63, 22–37.

Zhou, J.L., Siddiqui, E., Ngo, H.H., Guo, W. (2014). Estimation of uncertainty in the sampling and analysis of polychlorinated biphenyls and polycyclic aromatic hydrocarbons from contaminated soil in Brighton, UK. Science of the Total Environment, 497, 163–171.

Zhu, J., Sykes, J.F. (2000a). The influence of NAPL dissolution characteristics on field-scale contaminant transport in subsurface. Journal of Contaminant Hydrology, 41(1–2), 133–154.

Zhu, J., Sykes, J.F. (2000b). Stochastic simulations of NAPL mass transport in variably saturated heterogeneous porous media. Transport in Porous Media, 39(3), 289–314.

Zhu, J., Sykes, J.F. (2004). Simple screening models of NAPL dissolution in the subsurface. Journal of Contaminant Hydrology, 72(1–4), 245–258.

Zhu, J., Yeh, T.C.J. (2005). Characterization of aquifer heterogeneity using transient hydraulic tomography. Water Resources Research, 41(7), Article W07028.

Zhu, J.L., Parker, J.C., Lundy, D.A., & Zimmerman, L.M. (1993, November). Estimation of soil properties and free product volume from baildown tests [Paper presentation]. Petroleum Hydrocarbons and Organic Chemicals in Ground Water: Prevention, Detection and Restoration, Houston, TX, United States.

Zimmerman, D.A., de Marsily, G., Gotway, C.A., Marietta, M.G., Axness, C.L., Beauheim, R.L., Bras, R.L., Carrera, J., Dagan, G., Davies, P.B., Gallegos, D.P., Galli, A., Gómez-Hernández, J., Grindrod, P., Gutjahr, A.L., Kitanidis, P.K., Lavenue, A.M., McLaughlin, D., Neuman, S.P., ..., Rubin, Y. (1998). A comparison of seven geostatistically based inverse approaches to estimate transmissivities for modeling advective transport by groundwater flow. Water Resources Research, 34(6), 1373–1413.

Zinn, B., Harvey, C.F. (2003). When good statistical models of aquifer heterogeneity go bad: A comparison of flow, dispersion, and mass transfer in connected and multivariate Gaussian hydraulic conductivity fields. Water Resources Research, 39(3), Article 1051.

Zschornack, L., Bohling, G.C., Butler Jr., J.J., Dietrich, P. (2013). Hydraulic profiling with the direct-push permeameter: Assessment of probe configuration and analysis methodology. Journal of Hydrology, 496, 195–204.

Appendix A: Publications

Three co-authored peer-reviewed journal papers and a technical report are available online:

1. García-Rincón, J., Gatsios, E., Rayner, J.L., McLaughlan, R.G., Davis, G.B. (2020). Laser-induced fluorescence logging as a high-resolution characterisation tool to assess LNAPL mobility. Science of the Total Environment, 725, Article 138480. Impact factor (2019): 6.551.
   https://doi.org/10.1016/j.scitotenv.2020.138480
   https://www.sciencedirect.com/science/article/abs/pii/S0048969720319938
2. Lenhard, R.J., Rayner, J.L., García-Rincón, J. (2019). Testing an analytical model for predicting subsurface LNAPL distributions from current and historic fluid levels in monitoring wells: A preliminary test considering hysteresis. Water, 11, Article 2404. Impact factor (2018): 2.524.
   https://doi.org/10.3390/w11112404
   https://www.mdpi.com/2073-4441/11/11/2404
3. Bekele, E.B., García-Rincón, J., Rayner, J.L., McLaughlan, R.G., Gatsios, E., Paiva Lago, G. (2019). Groundwater pumping test analyses for a gasoline contaminated site at Donnybrook, Western Australia. Commonwealth Scientific and Industrial Research Organisation.
   https://doi.org/10.25919/5d72acbe6c512
   https://publications.csiro.au/publications/#publication/PIcsiro:EP196101
4. Gatsios, E., García-Rincón, J., Rayner, J.L., McLaughlan, R.G., Davis, G.B. (2018). LNAPL transmissivity as a remediation metric in complex sites under water table fluctuations. Journal of Environmental Management, 215, 40–48. Impact factor (2017): 4.005.
   https://doi.org/10.1016/j.jenvman.2018.03.026
   https://www.sciencedirect.com/science/article/pii/S0301479718302494

Other three documents can be found in this appendix:

1. a conference abstract titled ‘High-resolution vertical profiling in challenging subsurface settings’ presented in March 2020;
2. a conference paper titled ‘LNAPL transmissivity: comparison of theoretical, field and modelling estimations in a multi-layered aquifer in Western Australia’ presented in September 2018;
3. a conference poster titled ‘Comparison of analytical models to estimate LNAPL distribution and transmissivity in a heterogeneous site’ presented in May 2018.

HIGH RESOLUTION CHARACTERISATION CONFERENCE
Monday 2 March 2020
Sydney Australia

High-Resolution Vertical Profiling in Challenging Subsurface Settings

Jonás García-Rincón[1,2,3], Evangelos Gatsios[1,2,3], John L. Rayner[1,3], Robert G. McLaughlan[2,3]

[1]CSIRO Land and Water, Private bag No. 5, Wembley, WA 6913, AUSTRALIA
[2]University of Technology Sydney, 15 Broadway, Ultimo, NSW 2007, AUSTRALIA
[3]Cooperative Research Centre for Contamination Assessment and Remediation of the Environment (CRC CARE), Australia
Jonas.Garciarincon@csiro.au

Session Theme relevant to: Investigation

Keywords:
Heterogeneous fine-grained system, HPT, LIF, LNAPL Conceptual Site Model, LNAPL mobility

Overview:
High-resolution site characterisation (HRSC) tools such as Laser-Induce Fluorescence (LIF) and Hydraulic Profiling Tool (HPT) were used in a heterogeneous gasoline contaminated site where fluorescence response was not a good indicator of LNAPL saturation (S_n). However, HRSC outcomes were highly valuable and revealed a good agreement with the existing conceptual site model in terms of hydrostratigraphic features and LNAPL mobility. Thus, HRSC may be an efficient approach to investigate LNAPL contaminated sites even in challenging subsurface settings.

Background/Objectives:
LIF profiling is a popular HRSC method to delineate LNAPL contamination. However, it has been reported that the presence of light fuels and fine-grained materials may negatively impact its performance even if this is frequently the case in LNAPL contaminated sites. Our objective is to provide insight into the value offered by HPT and LIF technology when applied under unfavourable conditions where there is not more than a weak correlation between fluorescence response and S_n. The case of a heterogeneous fine-grained system contaminated with relatively fresh petrol in Western Australia was used to illustrate our findings.

Approach/Activities:
A HRSC field campaign including LIF and HPT logging was conducted in a heaviliy instrumentalised site with 85 monitoring points and where multiple baildown and mass recovery tests were conducted. The employed LIF system was the Ultraviolet Optical Screening Tool (UVOST®) by Dakota Technologies, which records fluorescence response in 4 wavelength channels: 350, 400, 450 and 500 nm. In practice, the use of fiber optics in UVOST® impedes detection of BTEX. Thus, light fuels with low PAH concentrations may be more difficult to detect. Multi-wavelength waveforms were analysed to improve the interpretation of LIF data and links with other parameters were explored.

Results/Lessons Learned:
HPT and LIF logging allowed to rapidly collect information about the site stratigraphy, LNAPL presence and anomalous conditions across the entire site. There was a good agreement between the HRSC outcomes and the existing LNAPL conceptual site model in terms of LNAPL mobility despite of the lack of correlation with S_n. Therefore, conducting a HRSC campaign could have been an approach with a better return on investigation than exclusively using traditional methods in sites similar to the case of study, where LNAPL mass recovery works could be required.

LNAPL TRANSMISSIVITY: COMPARISON OF THEORETICAL, FIELD AND MODELLING ESTIMATIONS IN A MULTI-LAYERED AQUIFER IN WESTERN AUSTRALIA

GATSIOS E.*,**,***, GARCÍA-RINCÓN J.*,**,*** AND RAYNER J. L.*,***

**CSIRO Land and Water, Private Bag No. 5, Wembley, WA 6913, AUSTRALIA*, *email: Evangelos.Gatsios@csiro.au*
***Faculty of Engineering and Information Technology, University of Technology Sydney, 15 Broadway, Ultimo, NSW 2007, AUSTRALIA*
****Cooperative Research Centre for Contamination Assessment and Remediation of the Environment (CRC CARE), AUSTRALIA*

SUMMARY: LNAPL transmissivity (T_n) is being increasingly adopted as an improved metric for predicting LNAPL recoverability. The objective of this study is to assess the ability of the API LNAPL Distribution and Recovery Model (LDRM) to estimate T_n at a heterogeneous gasoline contaminated site in Western Australia and develop a better understanding of subsurface conditions. LDRM was applied at three different areas exhibiting differences in the vertical LNAPL distribution and the stratigraphic profile. Field-based T_n values obtained through baildown testing and simplified theoretical estimations of T_n were used to evaluate and calibrate the model. In addition, cores, Hydraulic Profiling Tool (HPT) logs and Laser-Induced Fluorescence (LIF) profiles were collected to support the development of the conceptual site model. Results indicated there was good agreement between the different approaches to estimate T_n in two areas. LDRM simulations were not able to predict the T_n value in the third area, thus scenarios considering potentially higher LNAPL conductivities were examined. LDRM is a useful tool for the evaluation of T_n and LNAPL distribution in the subsurface, but it is strongly dependent on the field LNAPL and geological properties. Accordingly, additional efforts need to be conducted to establish detailed measurements of spatial variability to avoid misleading estimations that would negatively affect the design and predictions of the expected remediation performance.

1. INTRODUCTION

Petroleum hydrocarbons such as gasoline, diesel and jet fuel are among the most common and widespread contaminants in urban and industrial environments. These substances are frequently found as light non-aqueous phase liquids (LNAPLs) in the subsurface and pose potential risks to human

health and the environment.

LNAPL mobility depends on the fluid properties and the geological medium, which frequently exhibit a significant variability under field conditions (Al Awar 2008). LNAPL transmissivity (T_n), a measure of LNAPL mobility, is being increasingly adopted instead of in-well LNAPL thickness (b_n) as an improved metric for predicting LNAPL recoverability. T_n represents the volume of LNAPL that flows through a unit width of a medium per unit time for a unit drawdown, in an analogous way to groundwater transmissivity (Kirkman 2013). Baildown testing is commonly applied as a method for estimating T_n in the field (Hampton 2003). These T_n values can be used to calibrate analytical and numerical models and get estimations of field parameters (Zhu et al. 1993).

The API LNAPL Distribution and Recovery Model (LDRM) is a modelling tool to predict LNAPL saturation, distribution and recovery in the subsurface (Charbeneau 2007a). Up to three homogenous layers can be expressed by defining the soil parameters for each layer separately. Some basic assumptions that LDRM uses are: LNAPL is unconfined and at vertical equilibrium; there is a uniform radial distribution of LNAPL adjacent to a recovery well; all LNAPL within the radius of capture will be captured by the remediation well; LNAPL recovery is estimated with radial flow equations and hysteresis in the capillary pressure-saturation relationship is not explicitly considered (Charbeneau 2007b; Jeong & Charbeneau 2014). Other models have been recently developed to account for the effects of water table fluctuations (Lenhard et al. 2017) that may have a strong impact on T_n under field conditions (Gatsios et al. 2018).

The objective of this study is to assess the ability of LDRM to estimate T_n at a heterogeneous gasoline contaminated site in Western Australia and thereby validate the conceptual site model. Simplified theoretical and field-based T_n estimations were used to evaluate and calibrate the model.

2. MATERIALS AND METHODS

2.1. The field site of research

The study area comprises an operating petrol station located within a residential-commercial zone in country Western Australia. The local hydrogeology consists of a multi-layered unconsolidated aquifer system formed in a fluvial depositional environment. It presents discontinuous interbedded sands, silts and clays. In general, the stratigraphic profile consists of 3 main strata. A clayey silt layer (CL-ML) from 0 to approximately 4.5 m below ground underlain by a sandy (SW-SM) layer (fine and coarse sand with up to 30% of silt and clay) from approximately 4.5 m to 8 m and then heavy clays (CL) from approximately 8 m and below. A fining-upward sequence was observed in the sandy unit according to core logs. The study area typically experiences annual water table fluctuations of 2-3 m. The gasoline release occurred in 2013 and the exact amount of the released product remains unknown.

Three different areas within the LNAPL plume where subsurface characterisation and T_n studies have taken place since 2014 (Gatsios et al. 2018) were chosen. The tested wells were PB29 (area A), PB27 (area B) and PB40 (area C). The distance between the tested wells for area A and B is 12 m, with area C approximately 30 m away from the other two areas. Core logging, Hydraulic Profiling Tool (HPT) logs and Laser-Induced Fluorescence (LIF) profiles shown the differences in the stratigraphic profile and the vertical LNAPL distribution between the three research areas. The geological material in area C was generally finer textured than at the other two areas.

2.2. T_n estimations through baildown testing

The field T_n values were obtained through baildown testing under unconfined LNAPL conditions according to different lines of evidence such as diagnostic gauge plots, core logging, HPT profiles, baildown testing and hydrostratigraphs (Kirkman et al., 2013). More details have been previously reported

in the literature (Gatsios et al. 2016; Gatsios et al. 2018). It is considered to be a reasonable assumption that field-based methods provide T_n values within a factor of 2 (ASTM 2013; Gatsios 2018).

2.3. T_n estimations through LDRM simulations

LDRM was used to estimate LNAPL distributions and T_n in three areas (areas A, B and C) exhibiting differences in the vertical LNAPL distribution and the stratigraphic profile. The determination of input parameters was based on: 1) literature values and 2) field and laboratory estimates. The simulation at area A consisted of only one layer because of the relatively homogeneous stratigraphy, while three layers were considered at areas B and C as shown in Table 1. The Mualem relative permeability model was chosen (instead of Burdine's model) after calibrating the LNAPL distributions obtained by LDRM with LNAPL saturations from the field site.

Table 1. Input parameters for LDRM simulations.

Parameter	Area A	Area B	Area C	Source
Max. monitoring LNAPL thickness [m]	0.324	0.324	0.750	Measured data
Ground surface elevation [m]	61.087	60.993	61.282	Measured data
Water table elevation [m]	56.150	56.150	56.155	Measured data
Elevation of facies interface 1 [m]	-	56.600	56.055	Measured data
Elevation of facies interface 2 [m]	-	56.200	55.970	Measured data
LNAPL density [g/cm^3]	0.740	0.740	0.740	Measured data
LNAPL viscosity [cp]	0.480	0.480	0.480	Measured data
Air/water surface tension [dyne/cm]	65.000	65.000	65.000	(Johnston 2010)
Air/LNAPL surface tension [dyne/cm]	20.500	20.500	20.500	(Johnston 2010)
LNAPL/water interfacial tension [dyne/cm]	22.900	22.900	22.900	(Johnston 2010)
Characteristics for layer 1 (top)				
Porosity [-]	0.41	0.43	0.45	(API 2000)
Hydraulic conductivity [m/d]	13	8.00	1.83	Measured data (HPT)
Van Genuchten N [-]	3.17	2.20	1.38	(API 2000)
Van Genuchten α [m^{-1}]	1.85	0.29	3.55	(API 2000)
Irreducible water saturation [-]	0.209	0.34	0.34	(API 2000)
Residual LNAPL saturation [-]	0.010	0.010	0.03	Field data and calibration
Characteristics for layer 2 (intermediate)				
Porosity [-]	-	0.38	0.41	(API 2000)
Hydraulic conductivity [m/d]	-	8.00	0.03	Measured data (HPT)
Van Genuchten N [-]	-	3.55	3.55	(API 2000)
Van Genuchten α [m^{-1}]	-	1.38	1.38	(API 2000)
Irreducible water saturation [-]	-	0.19	0.19	(API 2000)
Residual LNAPL saturation [-]	-	0.00	0.00	Field data and calibration
Characteristics for layer 3 (bottom)				
Porosity [-]	-	0.40	0.41	(API 2000)
Hydraulic conductivity [m/d]	-	8.00	1.83	Measured data (HPT)
Van Genuchten N [-]	-	1.38	1.38	(API 2000)
Van Genuchten α [m^{-1}]	-	3.55	3.55	(API 2000)
Irreducible water saturation [-]	-	0.34	0.34	(API 2000)
Residual LNAPL saturation [-]	-	0.010	0.04	Field data and calibration

2.4. T_n estimations through a simplified theoretical approach

LNAPL conductivity (K_n) was evaluated as an average of the mobile LNAPL interval estimated from up to six subintervals to explore the effects of using simple constant values instead of models accounting for capillary pressure-saturation relationships across the whole vertical profile. In the case of having more than one subinterval, each of them corresponded to one LNAPL saturation field measured value. Equation 1 was used for the calculation of K_n [m/d]:

$$K_n = \frac{k_n \cdot k^* \cdot \rho_n \cdot g}{\mu_n} \qquad \text{[Equation 1]}$$

where k_n is the LNAPL relative permeability [-], k^* is the intrinsic permeability of the porous medium [m^2], ρ_n is the fluid density [kg/m^3], g is the acceleration due to gravity [m/d^2] and μ_n is the fluid viscosity [cp]. k_n was obtained as an output from LDRM (values taken from Gatsios 2018) and k^* was calculated according to the HPT hydraulic conductivity values and water properties (μ = 0.01 g/cm•s, ρ = 1 g/cm^3 and g = 980 cm/s^2).

T_n [m^2/d] was calculated according to Equation 2:

$$T_n = \int_{Z_{nw}}^{Z_{an}} k_n \cdot k^* \cdot \frac{\rho_n \cdot g}{\mu_n} dz \qquad \text{[Equation 2]}$$

where Z_{an} is the elevation of the LNAPL/air interface [m] and Z_{nw} is the elevation of the LNAPL/water interface [m] (since the mobile LNAPL interval was assumed to correspond to b_n).

3. RESULTS AND DISCUSSION

3.1. PB27 (area B)

Fig. 1 depicts the layers used in the LDRM simulations at area B. Fig. 2 illustrates the saturation and LNAPL relative permeability profiles after the calibration process. It can be seen that the predicted LNAPL saturation values using average van Genuchten parameters from the literature (API 2000) were consistent with the field measured LNAPL saturation values. The predicted LDRM T_n value was 0.32 m^2/d in agreement with the field measurement of 0.5 m^2/d.The simplified theoretical approach provided a T_n estimation of 0.35 m^2/d in the case of using six different intervals. Thus, the result was in a good agreement with the T_n estimates through LDRM simulation.

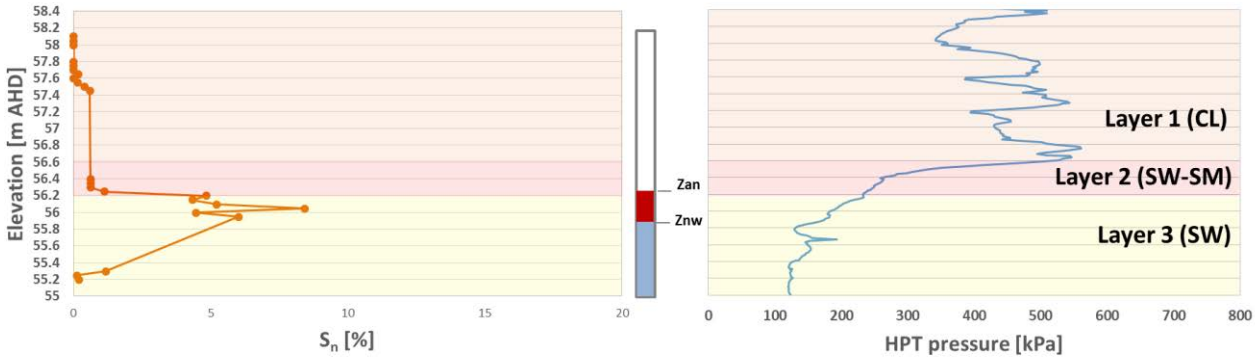


Fig. 1. The three layers used for the LDRM simulations at area B. LNAPL saturations (orange line), b_n (red colour) and one HPT pressure log (blue line) are depicted. CL corresponds to lean clay, SW to well-graded sand and SW-SM to well-graded sand with silt.

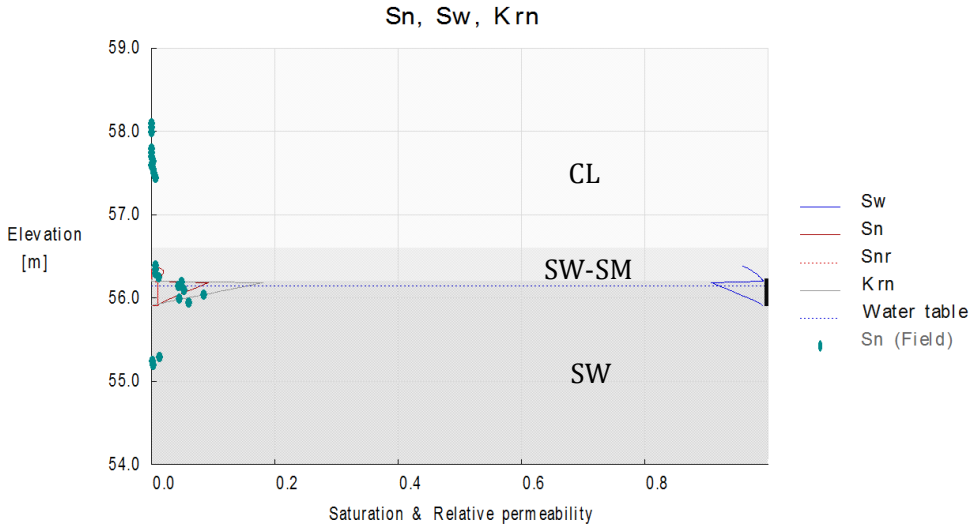


Fig. 2. LNAPL saturation (modelled and field data) and LNAPL relative permeability profiles using LDRM at area B.

3.2. PB40 (area C)

Fig. 3 presents the layers used in the LDRM simulations at area C. Fig. 4 depicts a good agreement between the simulated LNAPL saturation profile and the field measured LNAPL saturations. The predicted LDRM T_n value was 0.41 m^2/d in agreement with the field measurement of 0.40 m^2/d.

The simplified theoretical approach provided a T_n estimation of 0.38 m^2/d in the case of using six different intervals (see Fig. 5). A T_n of 0.44 m^2/d was found when different hydraulic conductivity values were assigned to each interval, although it has to be noted that these new values would also affect K_n.

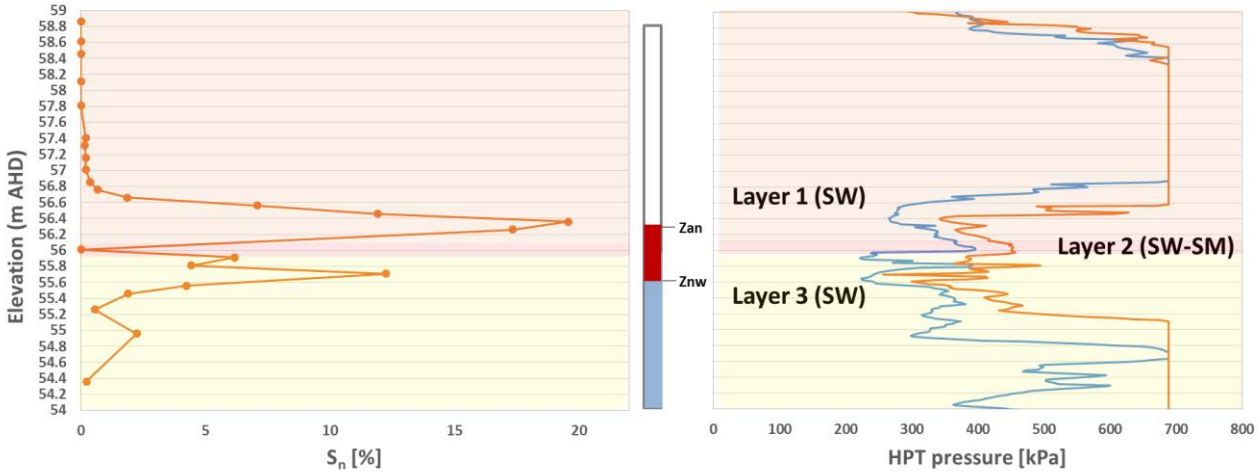


Fig. 3. The three layers used for the LDRM simulations at area C. LNAPL saturations (orange line; left panel), b_n (red colour) and two HPT pressure logs (blue and orange lines; right panel) are depicted. SW corresponds to well-graded sand and SW-SM to well-graded sand with silt.

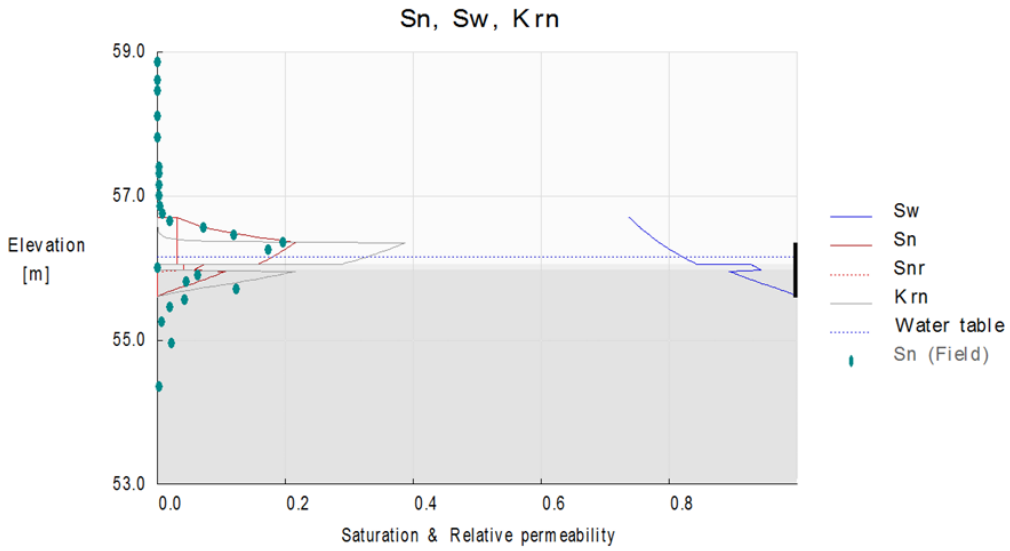


Fig. 4. LNAPL saturation (modelled and field data) and LNAPL relative permeability profiles using LDRM at area C.

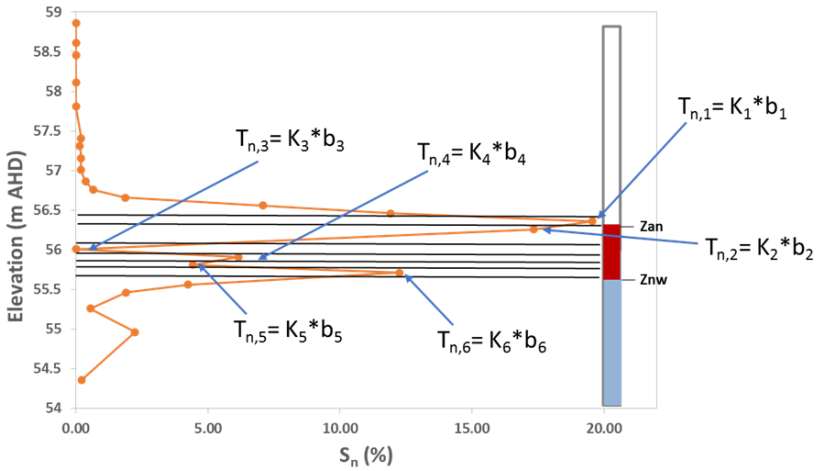


Fig. 5. Subintervals used for the T_n estimation through a simplified theoretical approach at area C.

3.3. PB29 (area A)

The simulation of area A with a homogenous sandy material (as indicated by the HPT profile and lithological descriptions) was unsuccessful, as it estimated a zero T_n output in contrast with the field measured value of 1.5 m^2/d. Thus, two scenarios (scenario A and scenario B) related to the potential presence of a preferential migration pathway (as suggested by the LIF signal) and/or higher LNAPL saturations were examined.

Scenario A (Fig. 6) was referred to the case that the field LNAPL saturation values used in the calibration of the model were not representative of the real field conditions, resulting in the calculation of inaccurate LNAPL relative permeability values. Poorly representative LNAPL saturation values can be related to errors in the sampling process, the chemical analysis or the existence of dynamic factors. The van Genuchten α parameter was increased to obtain higher LNAPL saturation and relative permeability values (Charbeneau 2007a). A sensitivity analysis of van Genuchten parameters related to scenario A showed that higher N values had a negative impact on T_n, while higher α values affected T_n positively. A higher van Genuchten N parameter represents a

more uniform pore-size distribution, i.e. more pores drain at a particular capillary pressure. An increase in α represents a decrease in the air-entry pressure and therefore a coarser-grained material. A new van Genuchten α value of 6.4 m^{-1}, still in the range of sandy materials (Carsel & Parrish 1988), provided a T_n value of 1.5 m^2/d.

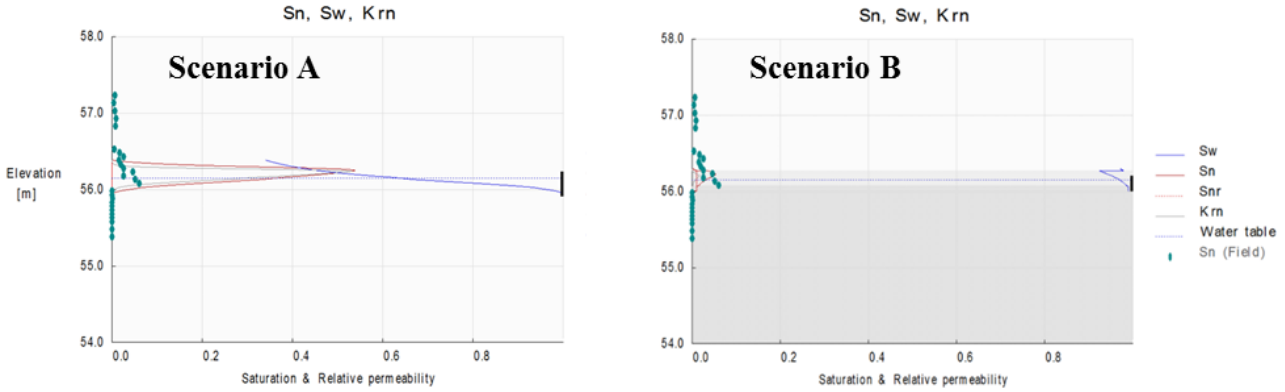


Fig. 6. LNAPL saturation (modelled and field data) and LNAPL relative permeability profiles using LDRM.

Scenario B simulated the existence of a preferential migration pathway (highly LNAPL transmissive zone). For this purpose the hydraulic conductivity was increased. However, a very high value of 700 m/d was necessary to reach a T_n value of 1.5 m^2/d. Although this high hydraulic conductivity value may be unrealistic (core logging did not reveal such a coarse material at this specific elevation), a preferential pathway due to a high pore connectivity (Deb & Shukla 2012) could explain the high T_n in this area.

4. CONCLUSIONS

In conclusion, LDRM is a useful tool for the evaluation of T_n and LNAPL distribution in the subsurface, but it is strongly dependent on the field characterisation and some of its assumptions are not necessarily met under field conditions. Accordingly, if the presence of preferential migration pathways or other heterogeneities are not identified, it may negatively affect the design and predictions of the expected remediation performance. Further research related to more recent analytical models that take into consideration the effect of residual saturation estimates and water table fluctuations is encouraged.

ACKNOWLEDGMENTS

This work was supported by the Cooperative Research Centre for Contamination Assessment and Remediation of the Environment (CRC CARE), whose activities are funded by the Australian Government's Cooperative Research Centres Programme. Author Evangelos Gatsios would like to thank the Public Benefit Foundation “Alexander S. Onassis” for its financial support. We are also grateful for the assistance of CSIRO Land and Water staff: Gabriel Paiva Lago and Robert Woodbury in the instrumentation, characterisation and monitoring of the field site; Trevor Bastow and Yasuko Geste in the chemical analysis of the samples; Elise Bekele and Michael Donn for their many valuable comments. We would also like to thank the site owners for their continued assistance and cooperation. Finally, we would like to express our sincere gratitude to Robert McLaughlan from University of Technology Sydney for his help and support.

REFERENCES

Al Awar, Z.R. 2008, Adapting, Optimizing, and Evaluating a Model for the Remediation of LNAPL in Heterogeneous Soil Environments [Ph.D. Thesis]: Austin, The University of Texas at Austin.

API 2000, API LNAPL Parameters Database, Version 2.0.

ASTM 2013, E2856-13, Standard Guide for Estimation of LNAPL Transmissivity, ASTM International, West Conshohocken, PA.

Carsel, R.F. & Parrish, R.S. 1988, Developing joint probability distributions of soil water retention characteristics, Water Resources Research, vol. 24, no. 5, pp. 755-69.

Charbeneau, R.J. 2007a, LNAPL Distribution and Recovery Model (LDRM). Volume 1: 754 Distribution and Recovery of Petroleum Hydrocarbon Liquids in Porous Media. API Publ. No. 755 4760. American Petroleum Institute. Washington, D.C.

Charbeneau, R.J. 2007b, LNAPL Distribution and Recovery Model (LDRM). Volume 2: User and Parameter Selection Guide: API Publ. No. 4760. American Petroleum Institute. Washington, D.C.

Deb, S.K. & Shukla, M.K. 2012, Variability of hydraulic conductivity due to multiple factors, American Journal of Environmental Science, vol. 8, no. 5, pp. 489-502.

Gatsios, E., Rayner, J.L. & McLaughlan, R.G. 2016, Use of LNAPL transmissivity to evaluate LNAPL recoverability in a fine grained aquifer in Western Australia. In Proc. 5th International Conference on Industrial and Hazardous Waste Management, Chania, Crete.

Gatsios, E. 2018, Evaluation of LNAPL Distribution and Mobility in Heterogeneous Porous Media under Water Table Fluctuations [Ph.D. Thesis]: Sydney, University of Technology Sydney.

Gatsios, E., García-Rincón, J., Rayner, J.L., McLaughlan, R.G. & Davis, G.B. 2018, LNAPL transmissivity as a remediation metric in complex sites under water table fluctuations, Journal of Environmental Management, vol. 215, pp. 40-48.

Hampton, D.R. 2003, Improving Bail-Down Testing of Free Product Wells. In Proc. Petroleum Hydrocarbons and Organic Chemicals in Ground Water, Prevention, Detection, and Remediation Conference and Exposition, National Ground Water Association, Costa Mesa, CA.

Huntley, D. 2000, Analytic Determination of Hydrocarbon Transmissivity from Baildown Tests, Ground Water, vol. 38, no. 1, pp. 46-52.

Jeong, J. & Charbeneau, R.J. 2014, An analytical model for predicting LNAPL distribution and recovery from multi-layered soils, Journal of Contaminant Hydrology, vol. 156, pp. 52-61.

Johnston, C.D. 2010, CRC CARE Tech. Report 18- Selecting and assessing strategies for remediating LNAPL in soils and aquifers.

Kirkman, A.J. 2013, Refinement of Bouwer-Rice Baildown Test Analysis, Groundwater Monitoring & Remediation, vol. 33, no. 1, pp. 105-10.

Kirkman, A.J., Adamski, M. & Hawthorne, J.M. 2013, Identification and Assessment of Confined and Perched LNAPL Conditions, Groundwater Monitoring & Remediation, vol. 33, no. 1, pp. 75-86.

Lenhard, R.J., Rayner, J.L. & Davis, G.B. 2017, A practical tool for estimating subsurface LNAPL distributions and transmissivity using current and historical fluid levels in groundwater wells: Effects of entrapped and residual LNAPL, Journal of Contaminant Hydrology, vol. 205, no. Supplement C, pp. 1-11.

Zhu, J.L., Parker, J.C., Lundy, D.A. & Zimmerman, L.M. 1993, Estimation of soil properties and free product volume from baildown tests. In Proc. Petroleum Hydrocarbons and Organic Chemicals in Ground Water, National Water Well Association, Dublin, OH.

Comparison of Analytical Models to Estimate LNAPL Distribution and Transmissivity in a Heterogeneous Site

Jonás García-Rincón[1,2,3], Evangelos Gatsios[1,2,3], John L. Rayner[1,3], Robert J. Lenhard[1,3]
[1]CSIRO Land and Water, Private Bag No. 5, Wembley, WA 6913, AUSTRALIA
[2]Faculty of Engineering and Information Technology, University of Technology Sydney, 15 Broadway, Ultimo, NSW 2007, AUSTRALIA
[3]Cooperative Research Centre for Contamination Assessment and Remediation of the Environment (CRC CARE), AUSTRALIA

CSIRO LAND AND WATER
www.csiro.au

Prediction of LNAPL distribution and transmissivity is critical to the cost effective management of contaminated sites both in terms of remediation endpoints and environmental risks. The challenge with all models is to efficiently generate the most realistic predictions with available datasets.

Introduction

LNAPL transmissivity (T_n) is being increasingly adopted as an improved metric for LNAPL recoverability. Two analytical tools to estimate LNAPL vertical distributions and T_n have been developed:

- API LNAPL Distribution and Recovery Model (LDRM);
- Lenhard, 2017 (Lenhard et al., 2017).

Both models differ in their formulation, notably in the definition of residual (S_r) and entrapped LNAPL saturations (S_e).

The objective of this study was to compare both models in scenarios that resemble a gasoline contaminated site consisting of a multi-layered unconsolidated aquifer system located in Western Australia.

Methods

Field data. Baildown tests were conducted in the field to estimate T_n (see Gatsios et al., 2018). Particle-size distributions were analysed with the RETC software to estimate van Genuchten parameters and hydraulic conductivity. LNAPL samples were collected to determine fluid density and viscosity.

Simulations. Multiple scenarios were simulated, including the hypothetical and field-based cases shown in Table 1. In these scenarios with relatively similar T_n estimations, different relative permeability models (Burdine and Mualem in LDRM and a modified Mualem equation in Lenhard, 2017) and maximum residual and entrapped LNAPL saturation values were applied to explore their effects on the models outputs.

A modified version of Lenhard, 2017 (Lenhard, 2018; personal communication) was employed to simulate the cases depicted in Fig. 1, where two sets of fluid interfaces and three lithological strata were represented to illustrate the capabilities of both models.

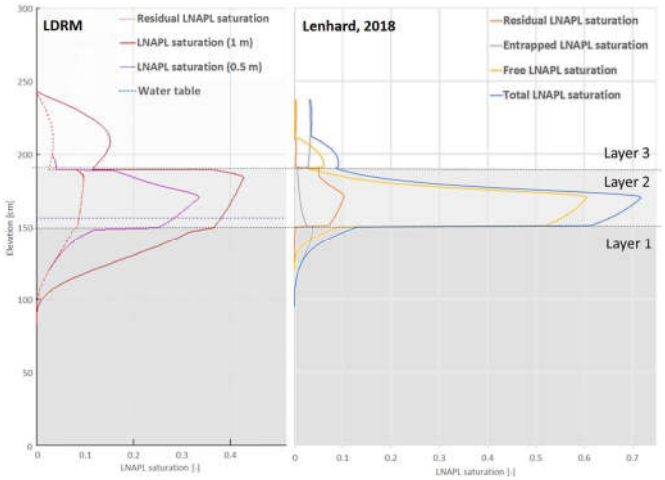


Figure 1: Vertical LNAPL distributions in a hypothetical 3-layer scenario (layer 1 is well-graded sand, layer 2 is loamy sand, layer 3 is well-graded sand with silt). In-well LNAPL thickness were decreased from 1 m to 0.5 m in LDRM, while 50 cm of fluctuations were applied in Lenhard, 2017.

Table 1: Input parameters and T_n estimations for two scenarios

	Scenario A (hypothetic)	Scenario B (field-based)
In-well LNAPL thickness [cm]	50	75
Van Genuchten a [cm^{-1}] / N [-]	0.124 / 2.28	0.036 / 3.32
Porosity [-]	0.41	0.45
Hydraulic conductivity [cm/day]	350	670
Tensions NAPL-water / air-NAPL [mN m^{-1}]	29 / 36	22.9 / 20.5
LNAPL density / LNAPL viscosity ratios [-]	0.73 / 0.8	0.74 / 0.48
T_n baildown testing [m^2/day]	x	0.3-0.58
T_n Burdine / Mualem / Lenhard (free T_n) (S_r=0.15) [m^2/day]	0.13 / 0.87 / 0.34 (0.43)	0.77 / 2.64 / 0.04 (0.17)
T_n Burdine / Mualem / Lenhard (free T_n) (S_r=0.01) [m^2/day]	0.05 / 0.83 / 0.49 (0.64)	0.50 / 2.48 / 0.08 (0.39)

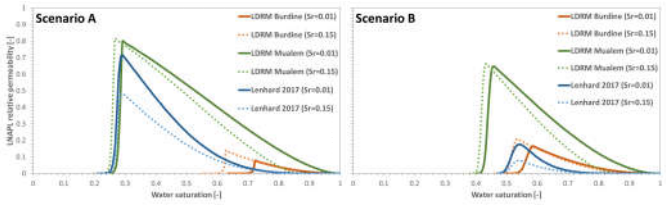


Figure 2: LNAPL relative permeability curves for different models for scenarios A and B. Decreasing LNAPL relative permeabilities at low water saturations correspond to the unsaturated zone.

Results

- Great variability in LNAPL distributions and T_n existed in the field site.
- The models differed in the estimated LNAPL distributions and T_n values (see Table 1), in some cases for more than one order of magnitude.
- A key element for these discrepancies is the applied relative permeability model and the integration limits (see Fig. 2).
- The Mualem relative permeability model resulted in higher T_n values and LNAPL saturations than Burdine. The modified Mualem equation in Lenhard, 2017 provided intermediate results or lower than Burdine.
- an increase in the maximum S_r values corresponded to the same specific LNAPL volume and lower T_n values in Lenhard, 2017, but different specific volumes and higher T_n values in LDRM.

Conclusions

- Analytical models are valuable tools for site management that need to be accompanied by a good understanding of the site conditions.
- Uncertainties associated to LNAPL distribution and T_n have direct implications to the expected remediation performance and project costs.
- Further research will be conducted in the laboratory to better understand residual and entrapped LNAPL saturations in three-phase systems.

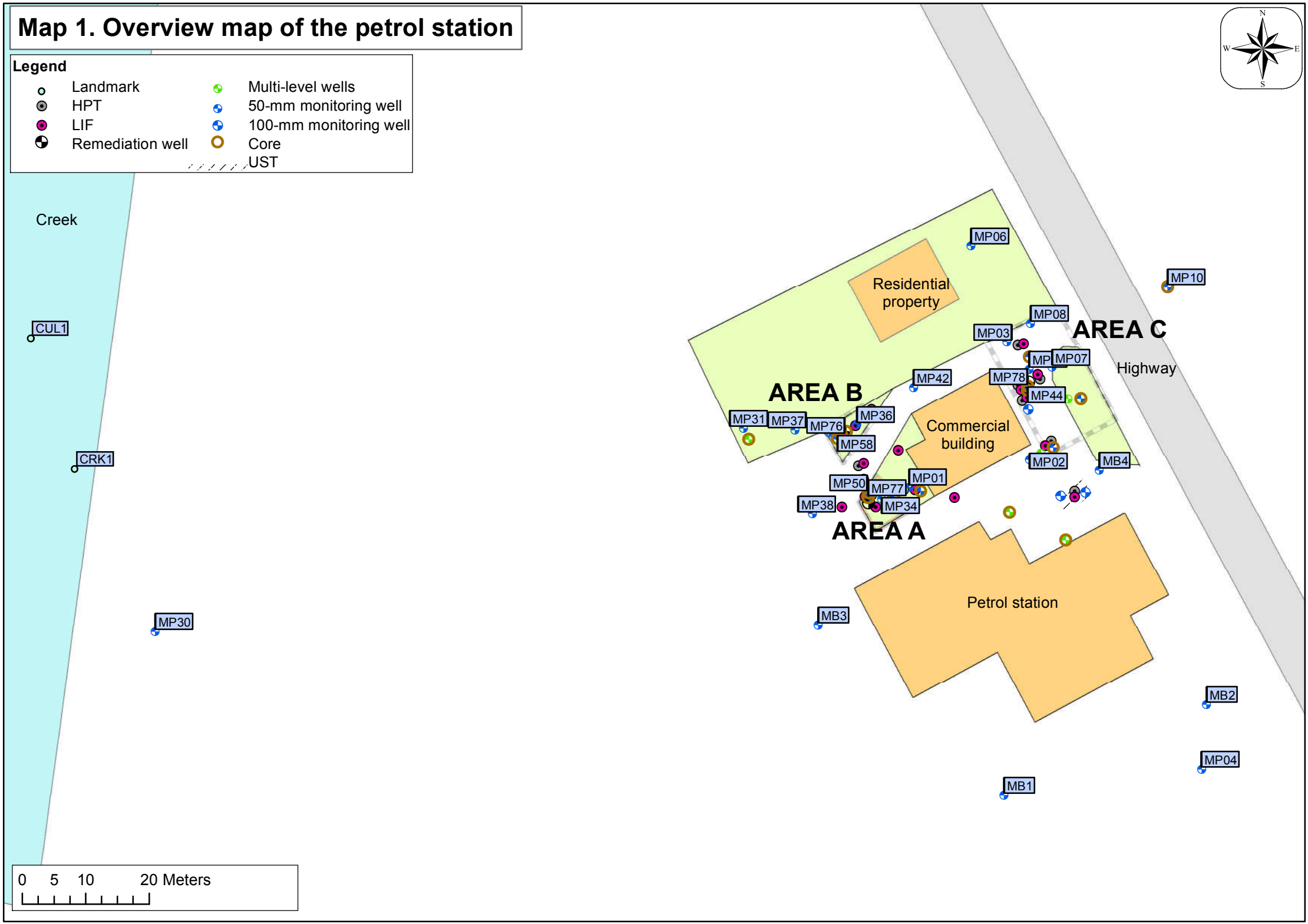
FOR FURTHER INFORMATION
Jonás García-Rincón
e Jonas.Garciarincon@csiro.au
w www.csiro.au/en/Research/LWF

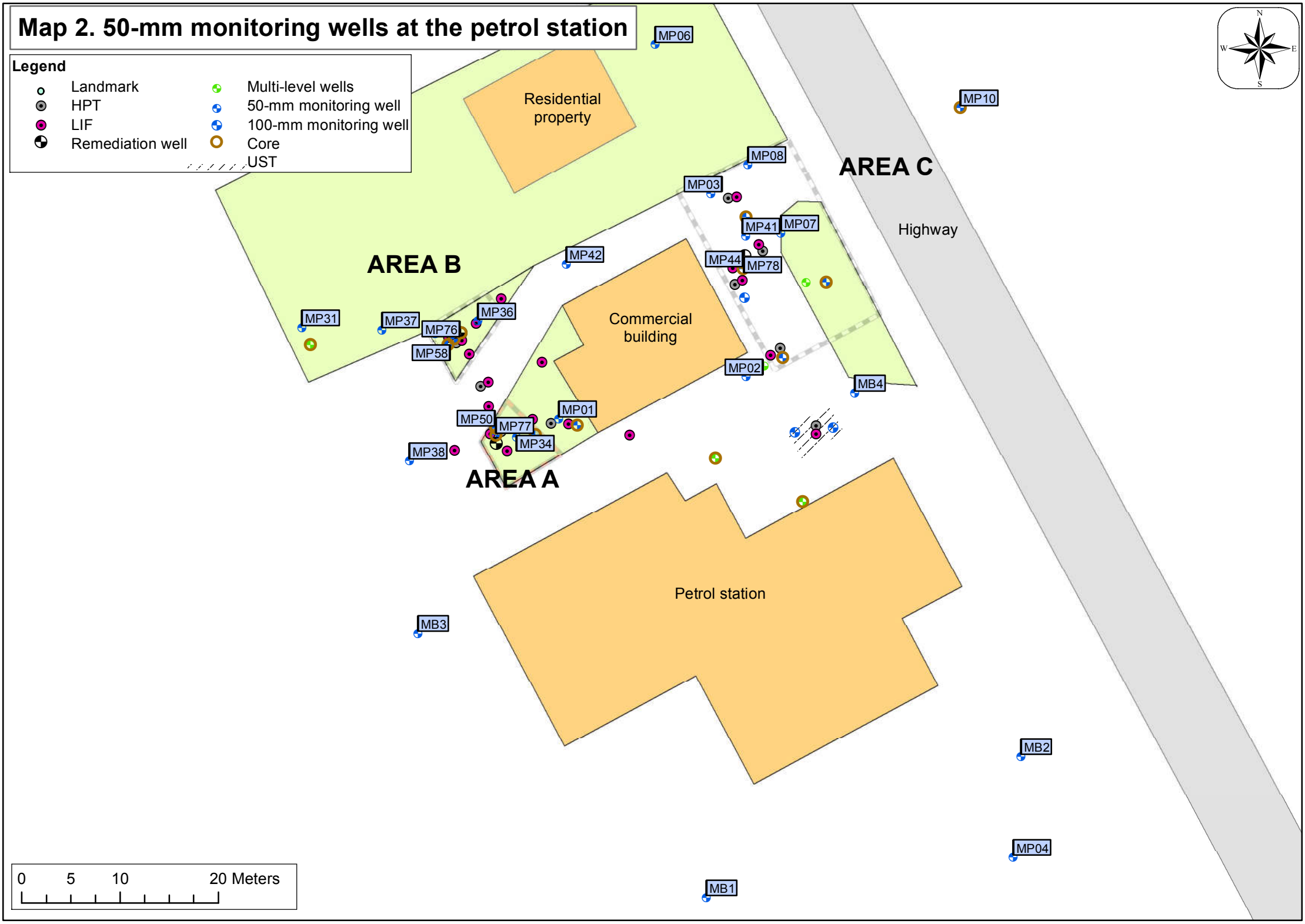
REFERENCES
Gatsios et al. in Enviro. Manage. 215:40-48, 2018. https://doi.org/10.1016/j.jenvman.2018.03.026
Lenhard et al. in Contam. Hydrol. 205:1-11, 2017. https://doi.org/10.1016/j.jconhyd.2017.06.002

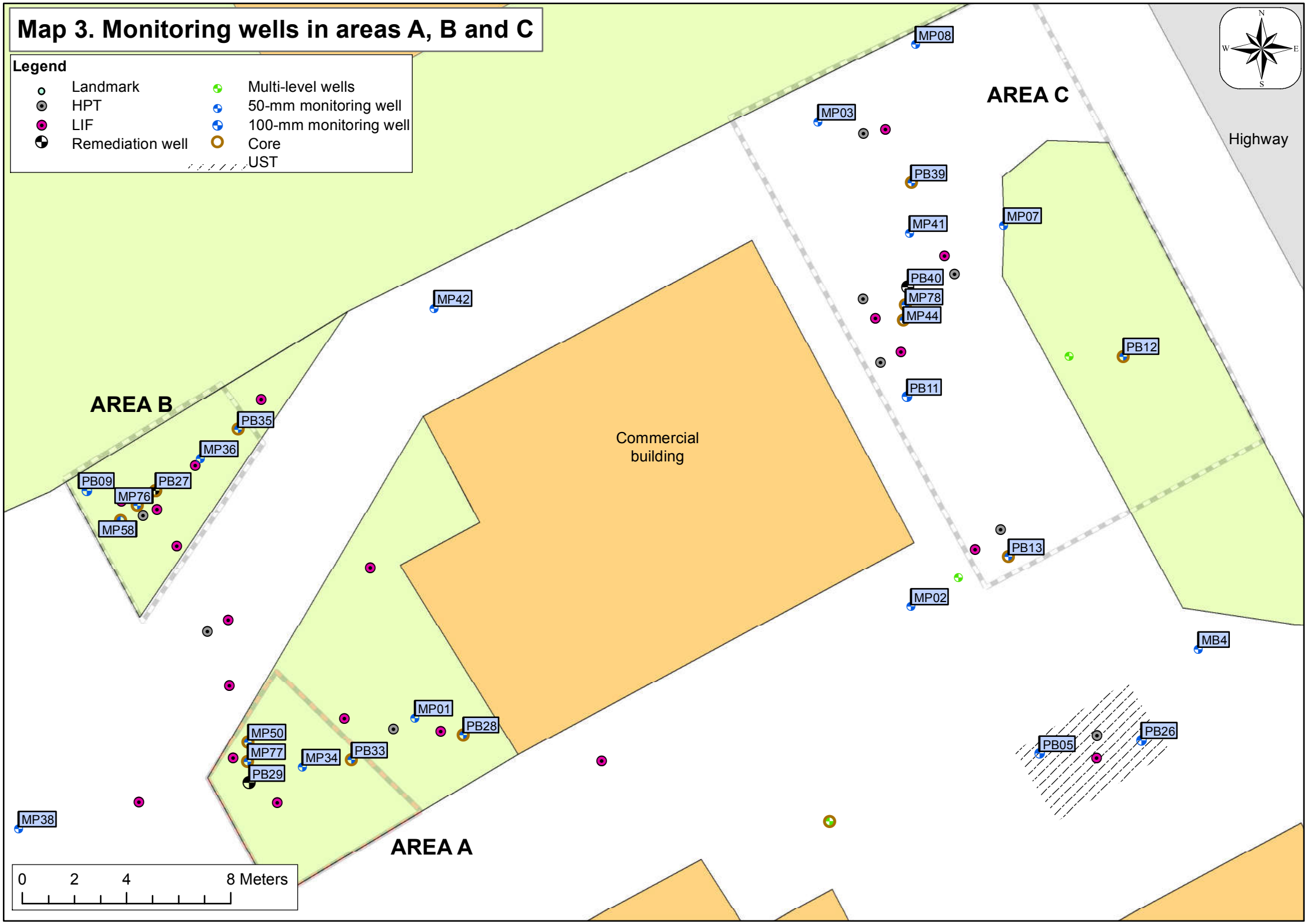
ACKNOWLEDGEMENTS
This research is financially supported jointly by CRC CARE and CSIRO Land and Water. The efforts of staff from CSIRO in the field program are appreciated. The support and assistance of the site owners is also greatly appreciated.

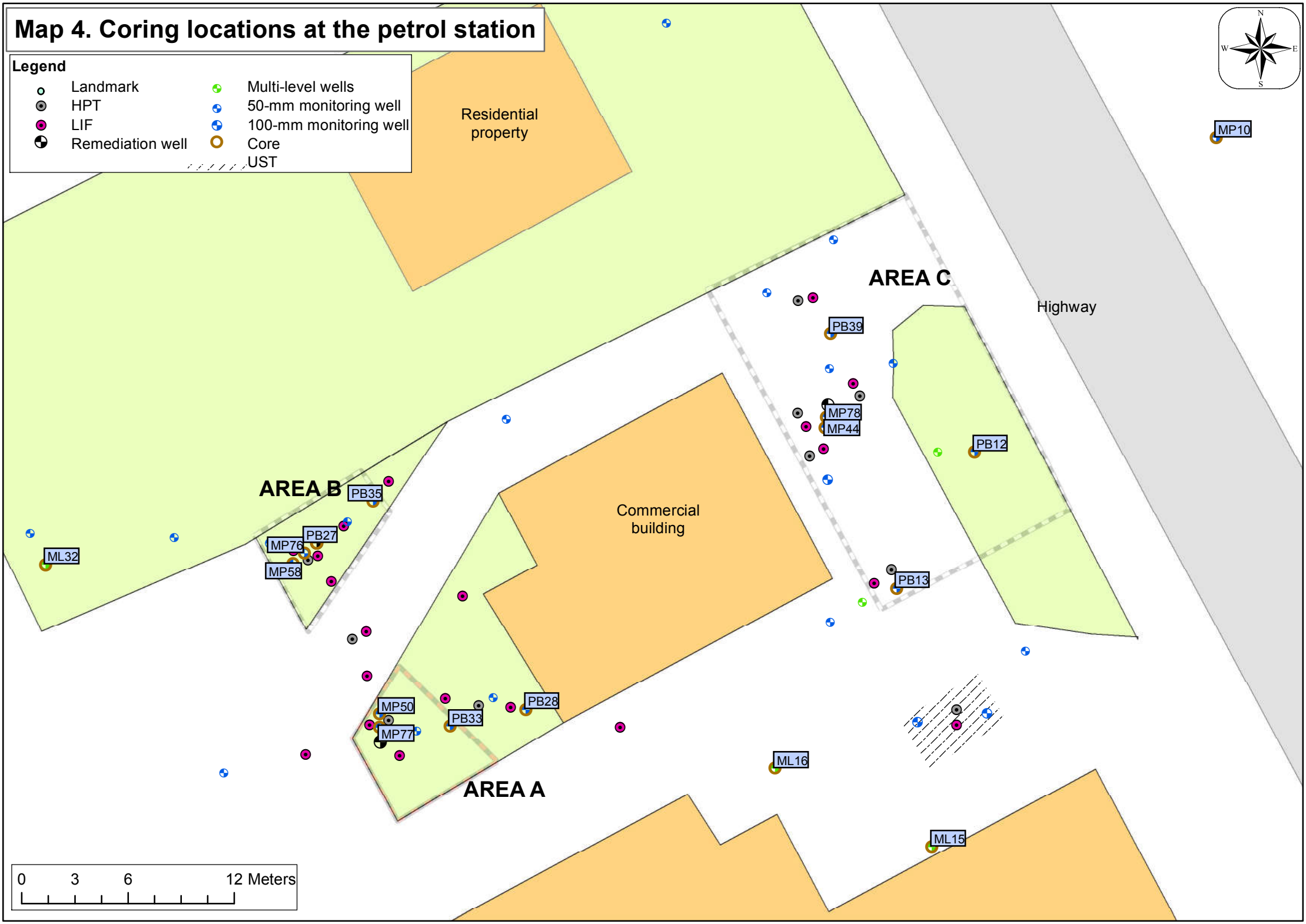
Appendix B: Maps

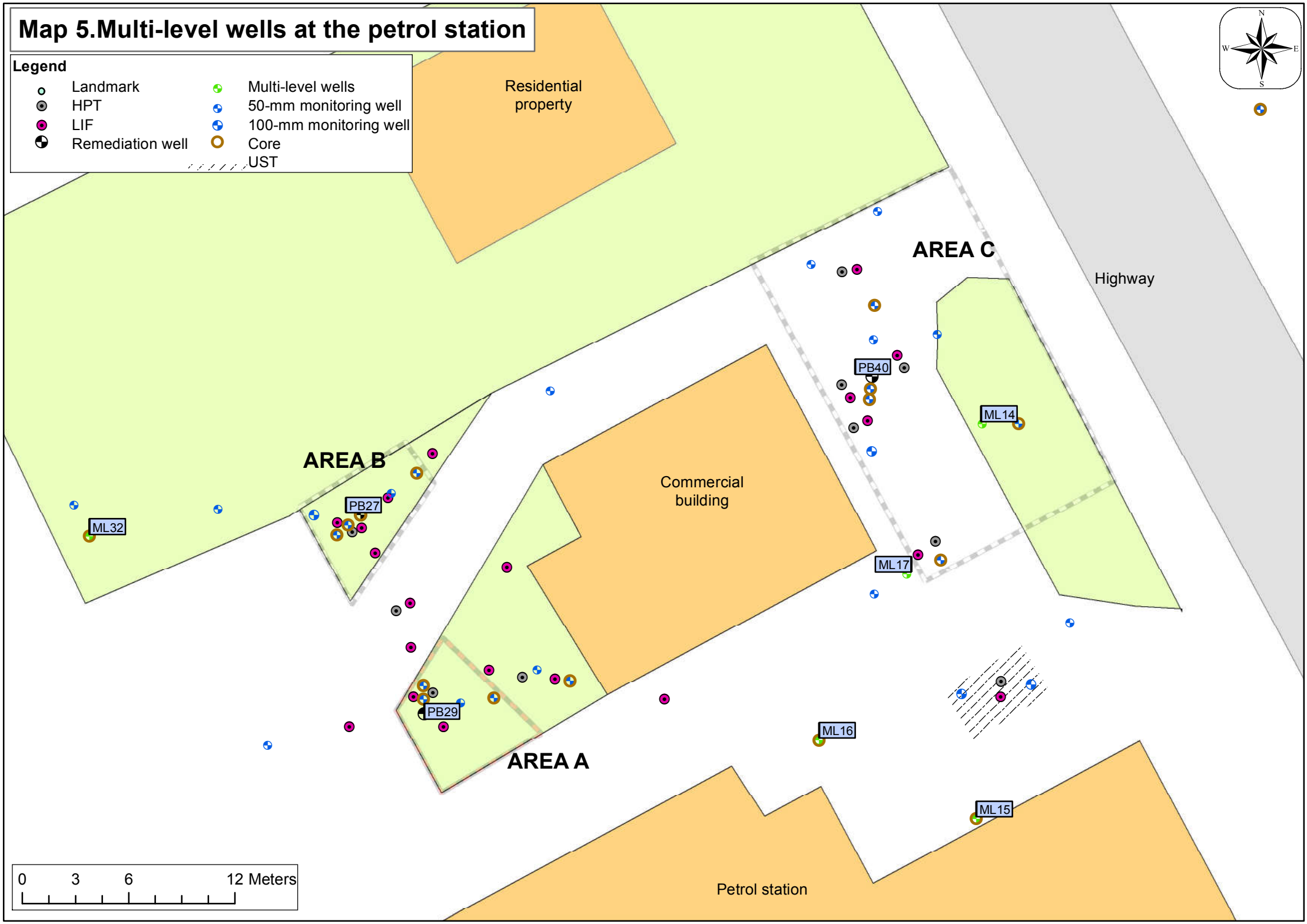
Map 1. Overview map of the petrol station

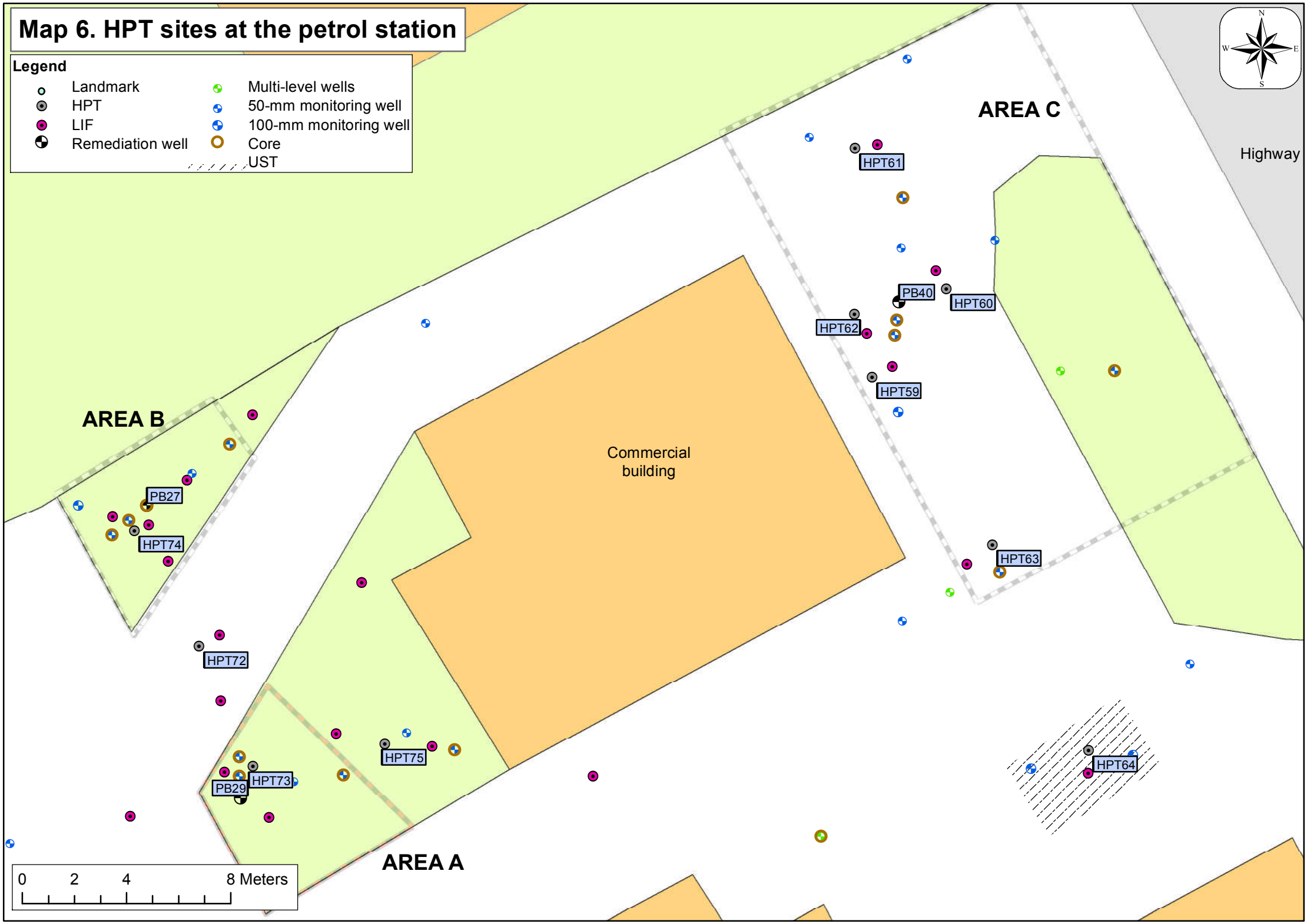


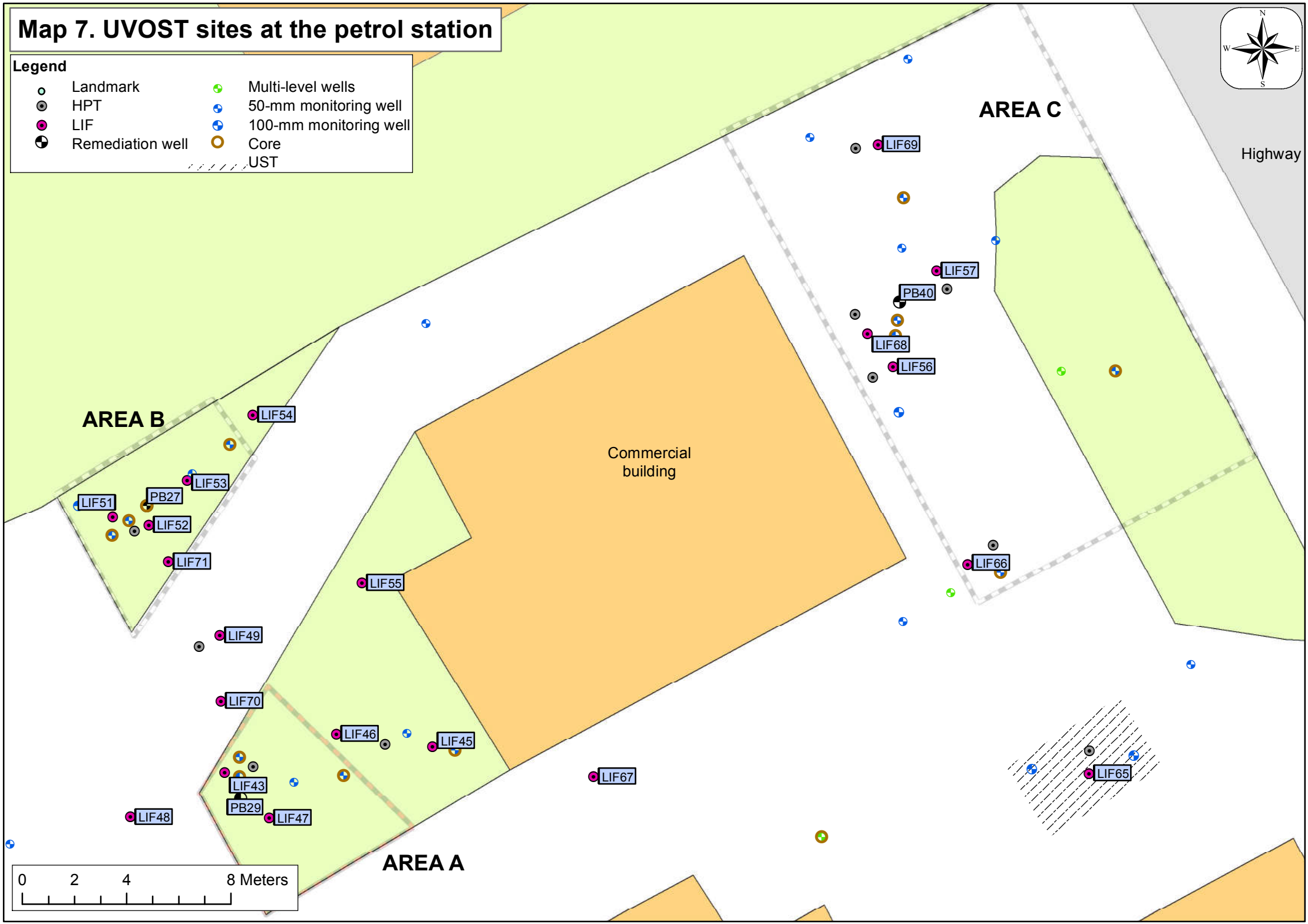

Map 2. 50-mm monitoring wells at the petrol station
Legend
Landmark
HPT
LIF
Remediation well
Multi-level wells
50-mm monitoring well
100-mm monitoring well
Core
UST
Residential property
AREA B
AREA C
AREA A
Highway
Commercial building
Petrol station
MP06
MP10
MP08
MP03
MP41
MP07
MP42
MP44
MP78
MP31
MP37
MP36
MP76
MP58
MP02
MB4
MP01
MP50
MP77
MP34
MP38
MB3
MB2
MP04
MB1
0
5
10
20 Meters
N
W
E
S

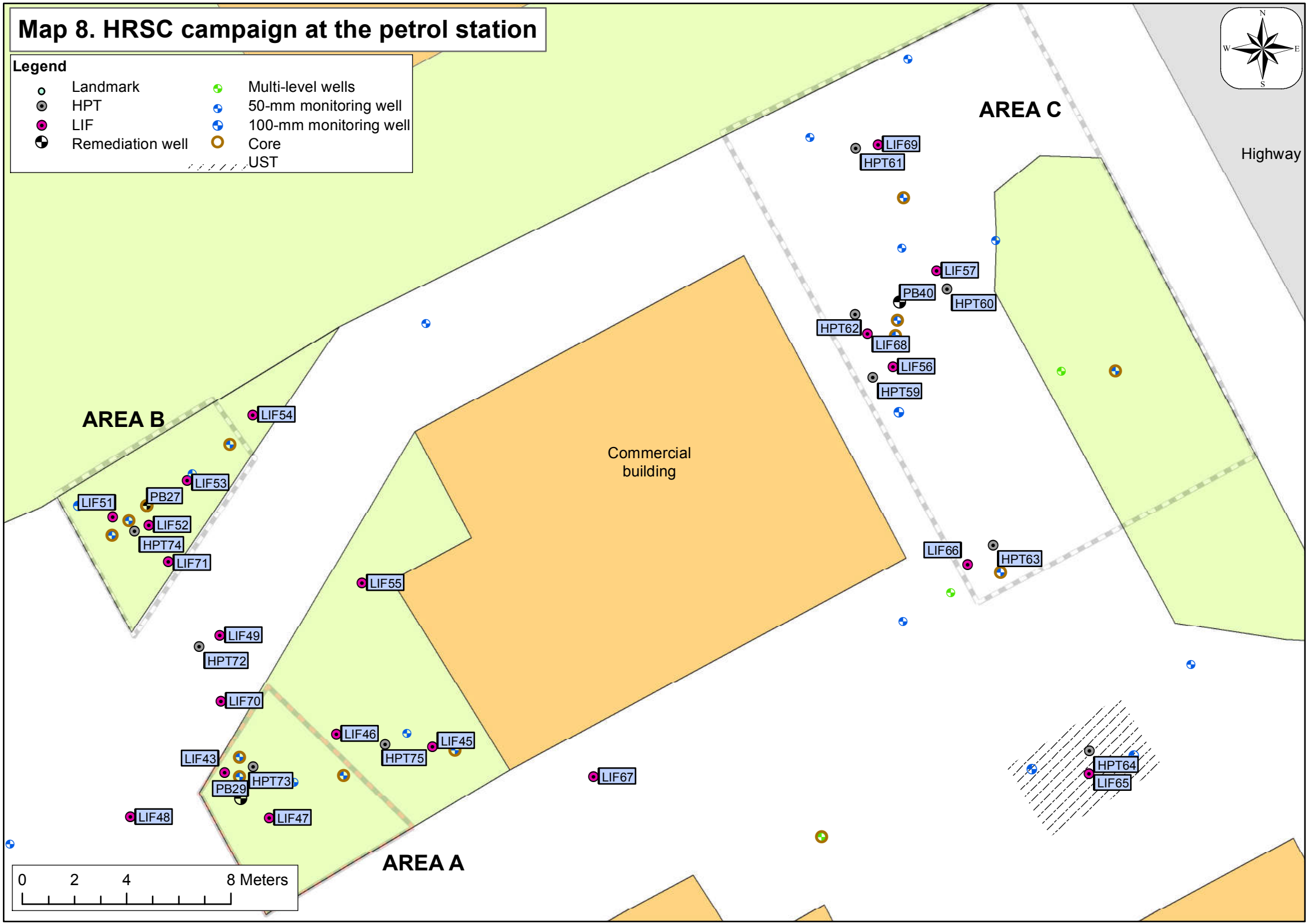

Map 3. Monitoring wells in areas A, B and C
Legend
Landmark
HPT
LIF
Remediation well
Multi-level wells
50-mm monitoring well
100-mm monitoring well
Core
UST
AREA A
AREA B
AREA C
Commercial building
Highway
MP08
MP03
PB39
MP41
MP07
PB40
MP78
MP44
MP42
PB12
PB11
PB35
MP36
PB09
PB27
MP76
MP58
PB13
MP02
MB4
MP01
PB28
MP50
MP77
MP34
PB33
PB29
PB05
PB26
MP38
0 2 4 8 Meters
N
W
E
S


Map 4. Coring locations at the petrol station
Legend
Landmark
HPT
LIF
Remediation well
Multi-level wells
50-mm monitoring well
100-mm monitoring well
Core
UST
Residential property
Highway
AREA C
AREA B
AREA A
Commercial building
MP10
PB39
MP78
MP44
PB12
PB35
PB27
MP76
MP58
ML32
PB13
MP50
PB33
PB28
MP77
ML16
ML15
0 3 6 12 Meters
N
W
E
S

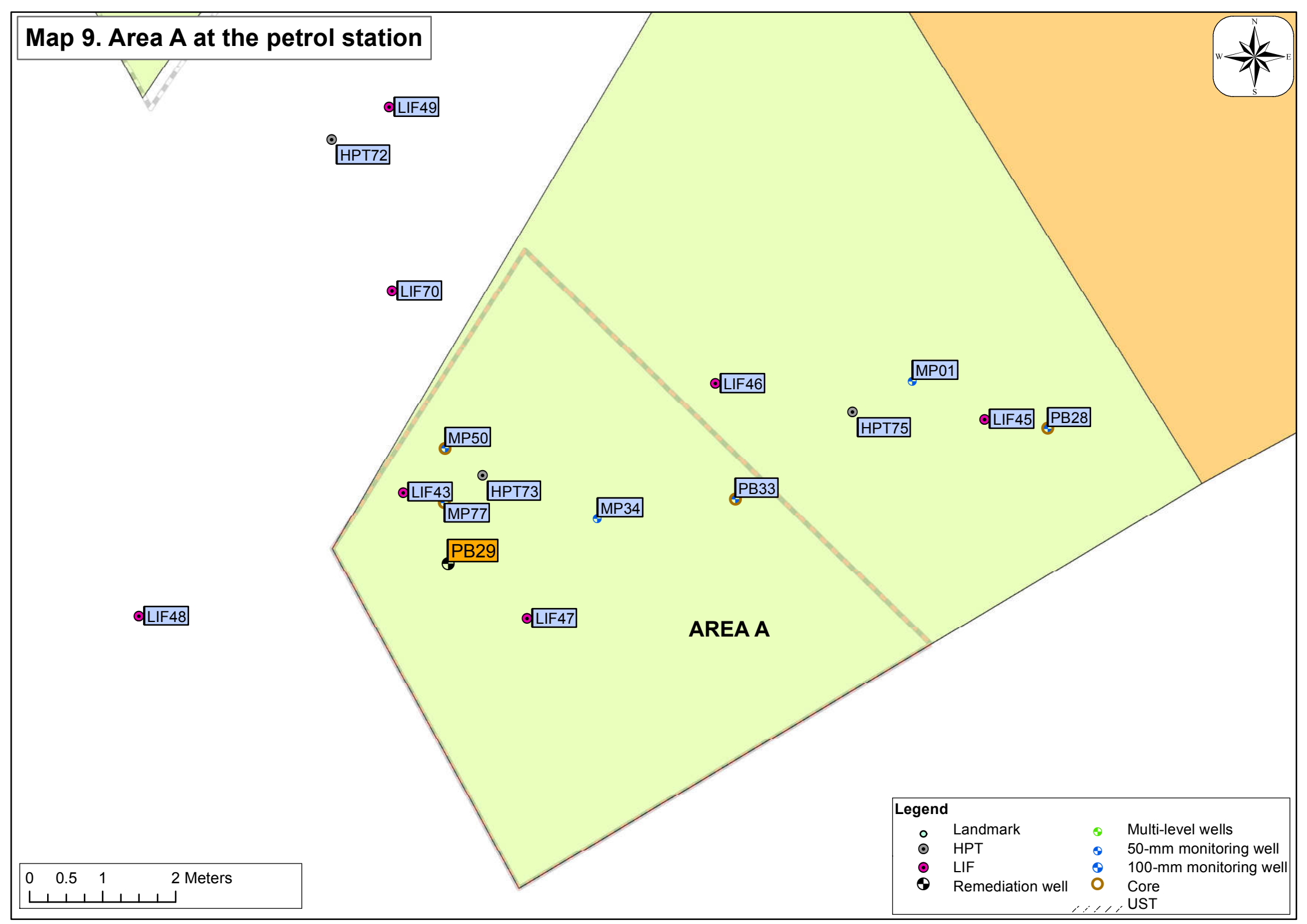

Map 5.Multi-level wells at the petrol station
Legend
Landmark
HPT
LIF
Remediation well
Multi-level wells
50-mm monitoring well
100-mm monitoring well
Core
UST
Residential property
AREA C
Highway
PB40
ML14
AREA B
PB27
ML32
Commercial building
ML17
PB29
ML16
AREA A
ML15
Petrol station
0 3 6 12 Meters
N
W
E
S

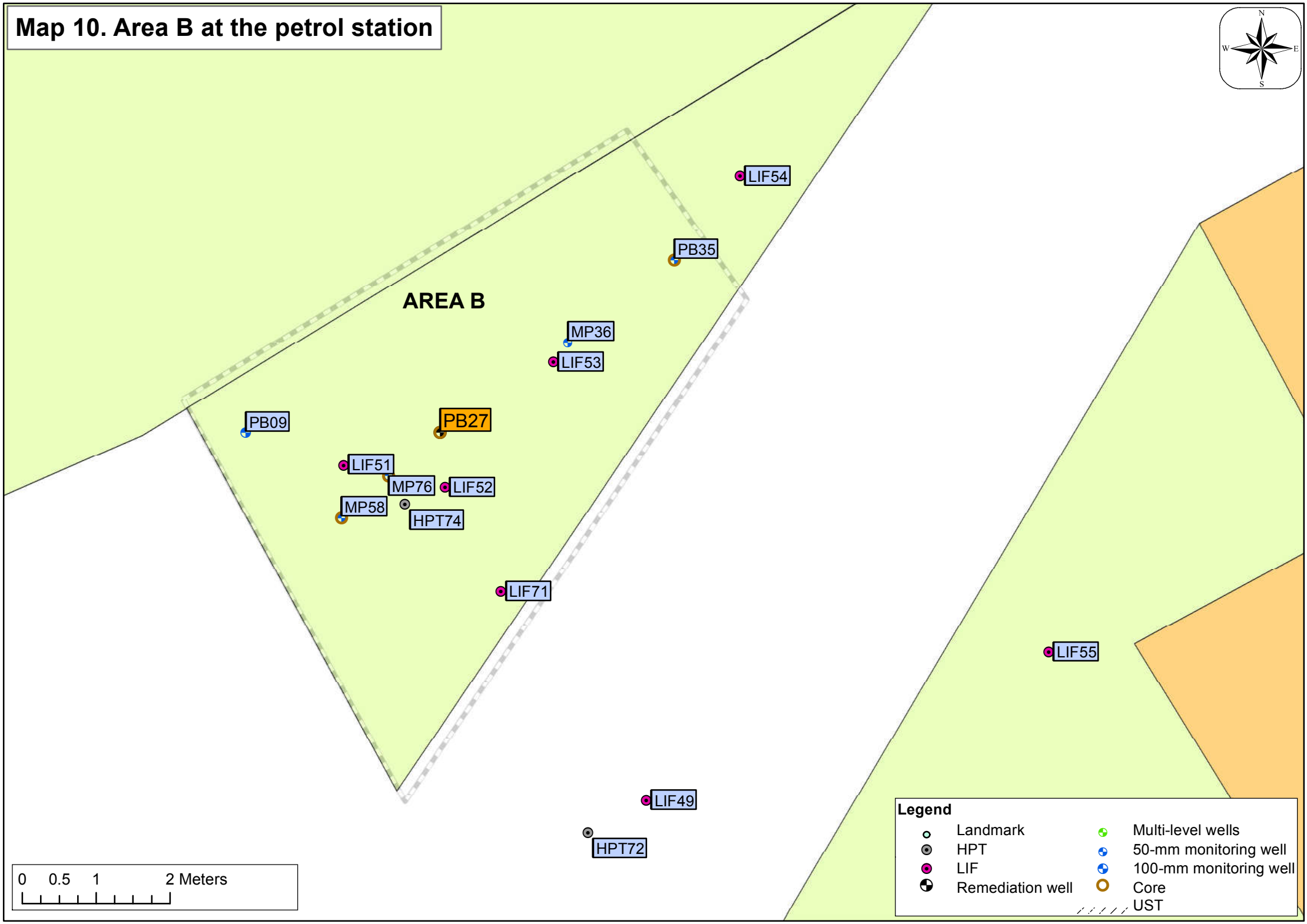

Map 6. HPT sites at the petrol station
Legend
Landmark
HPT
LIF
Remediation well
Multi-level wells
50-mm monitoring well
100-mm monitoring well
Core
UST
N
W
E
S
AREA C
Highway
HPT61
PB40
HPT60
HPT62
HPT59
AREA B
Commercial building
PB27
HPT74
HPT63
HPT72
HPT75
HPT64
PB29
HPT73
AREA A
0
2
4
8 Meters

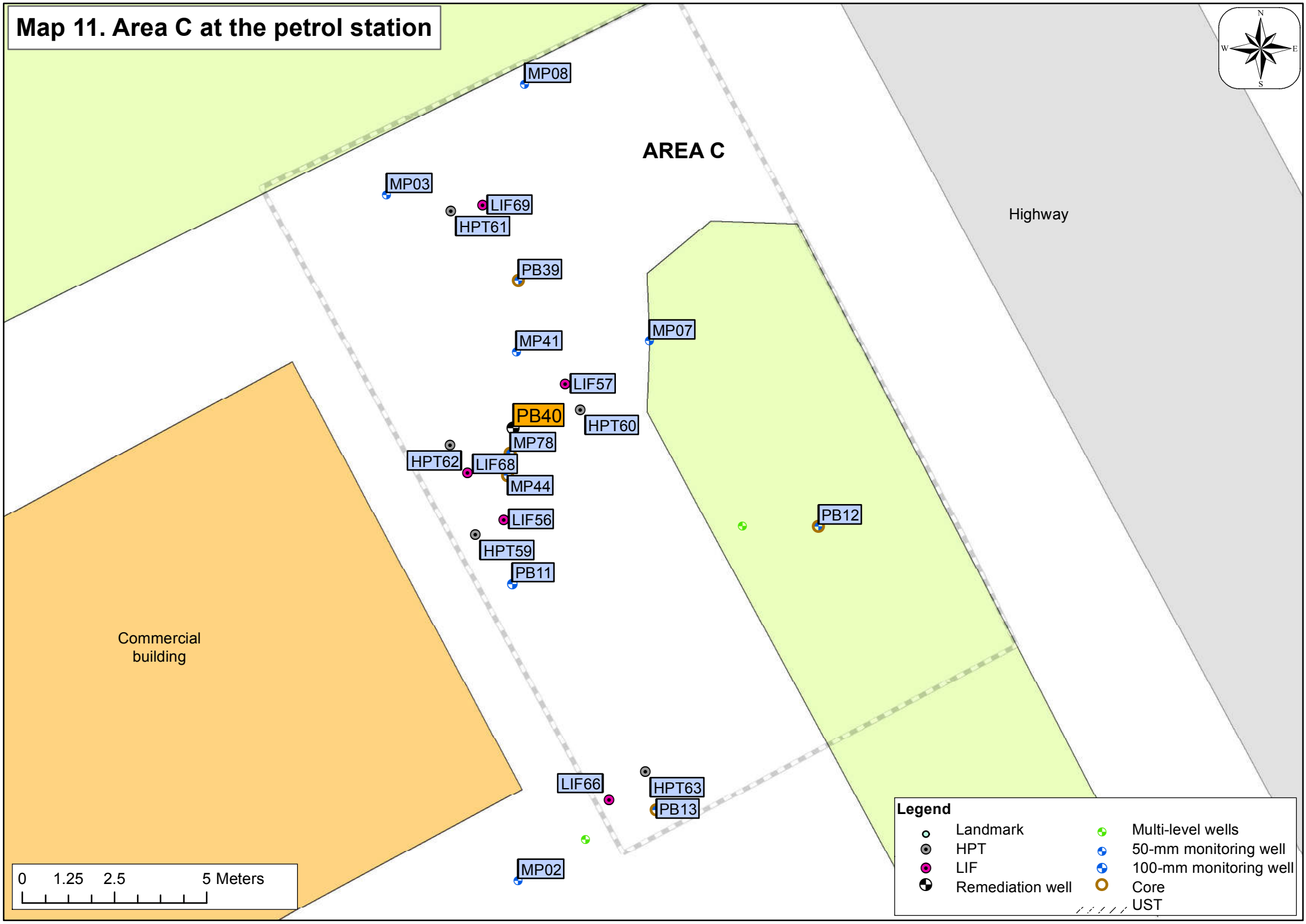

Map 7. UVOST sites at the petrol station
Legend
Landmark
HPT
LIF
Remediation well
Multi-level wells
50-mm monitoring well
100-mm monitoring well
Core
UST
N
W
E
S
AREA C
Highway
LIF69
LIF57
PB40
LIF68
LIF56
AREA B
LIF54
LIF53
LIF51
PB27
LIF52
LIF71
Commercial building
LIF55
LIF66
LIF49
LIF70
LIF46
LIF45
LIF67
LIF65
LIF43
PB29
LIF47
LIF48
AREA A
0
2
4
8 Meters


Map 8. HRSC campaign at the petrol station
Legend
Landmark
HPT
LIF
Remediation well
Multi-level wells
50-mm monitoring well
100-mm monitoring well
Core
UST
AREA C
Highway
LIF69
HPT61
LIF57
PB40
HPT60
HPT62
LIF68
LIF56
HPT59
AREA B
LIF54
Commercial building
LIF53
LIF51
PB27
LIF52
HPT74
LIF71
LIF55
LIF66
HPT63
LIF49
HPT72
LIF70
LIF46
LIF45
HPT75
LIF43
HPT73
PB29
LIF67
HPT64
LIF65
LIF48
LIF47
AREA A
0 2 4 8 Meters
N
W
E
S

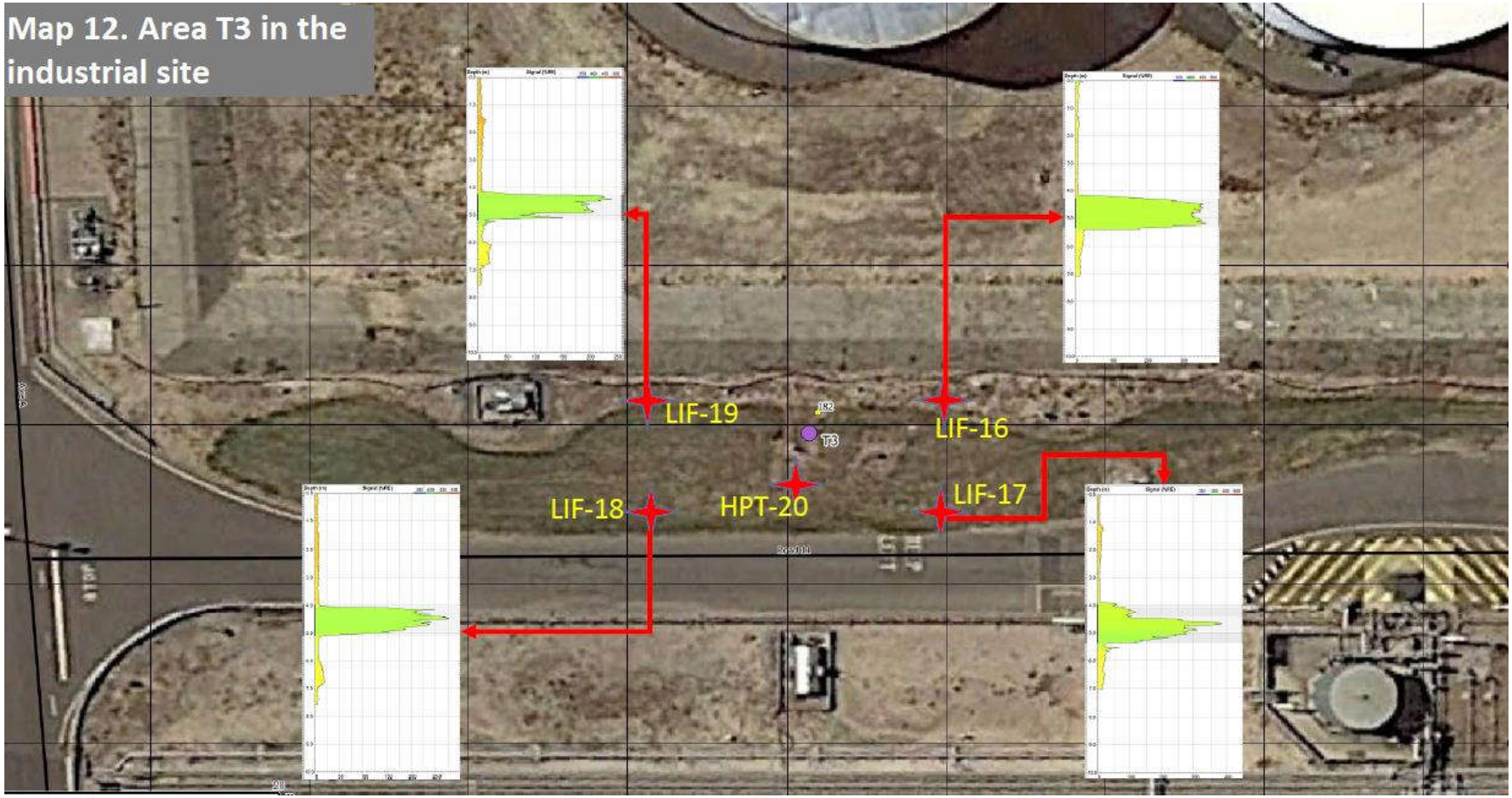
Map 9. Area A at the petrol station



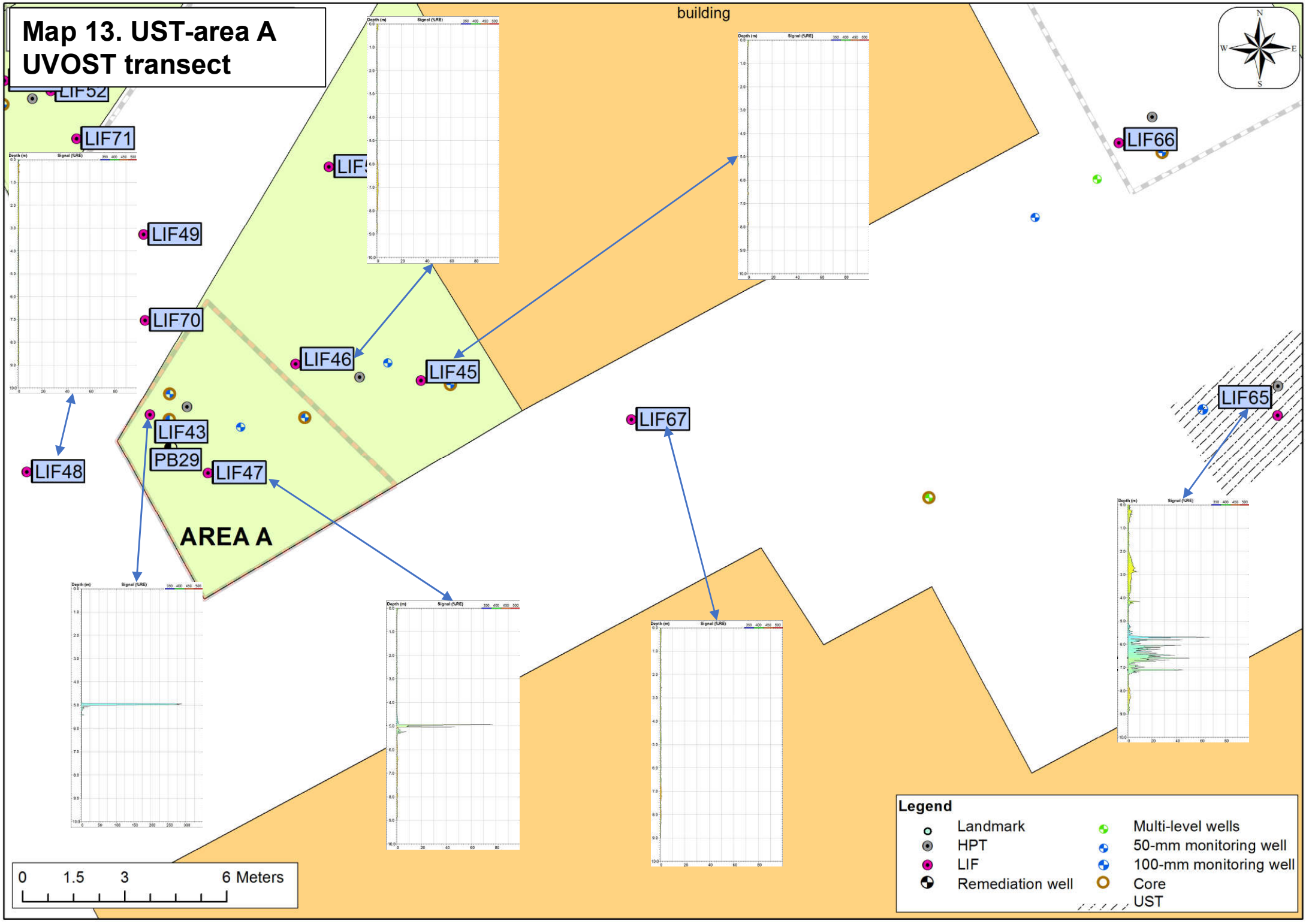

Map 10. Area B at the petrol station
N
W
E
S
AREA B
LIF54
PB35
MP36
LIF53
PB09
PB27
LIF51
MP76
LIF52
MP58
HPT74
LIF71
LIF55
LIF49
HPT72
0 0.5 1 2 Meters
Legend
Landmark
HPT
LIF
Remediation well
Multi-level wells
50-mm monitoring well
100-mm monitoring well
Core
UST


Map 11. Area C at the petrol station
AREA C
MP08
MP03
LIF69
HPT61
PB39
MP41
MP07
LIF57
PB40
HPT60
MP78
HPT62
LIF68
MP44
LIF56
HPT59
PB11
PB12
LIF66
HPT63
PB13
MP02
Highway
Commercial building
N
W
E
S
0 1.25 2.5 5 Meters
Legend
Landmark
HPT
LIF
Remediation well
Multi-level wells
50-mm monitoring well
100-mm monitoring well
Core
UST

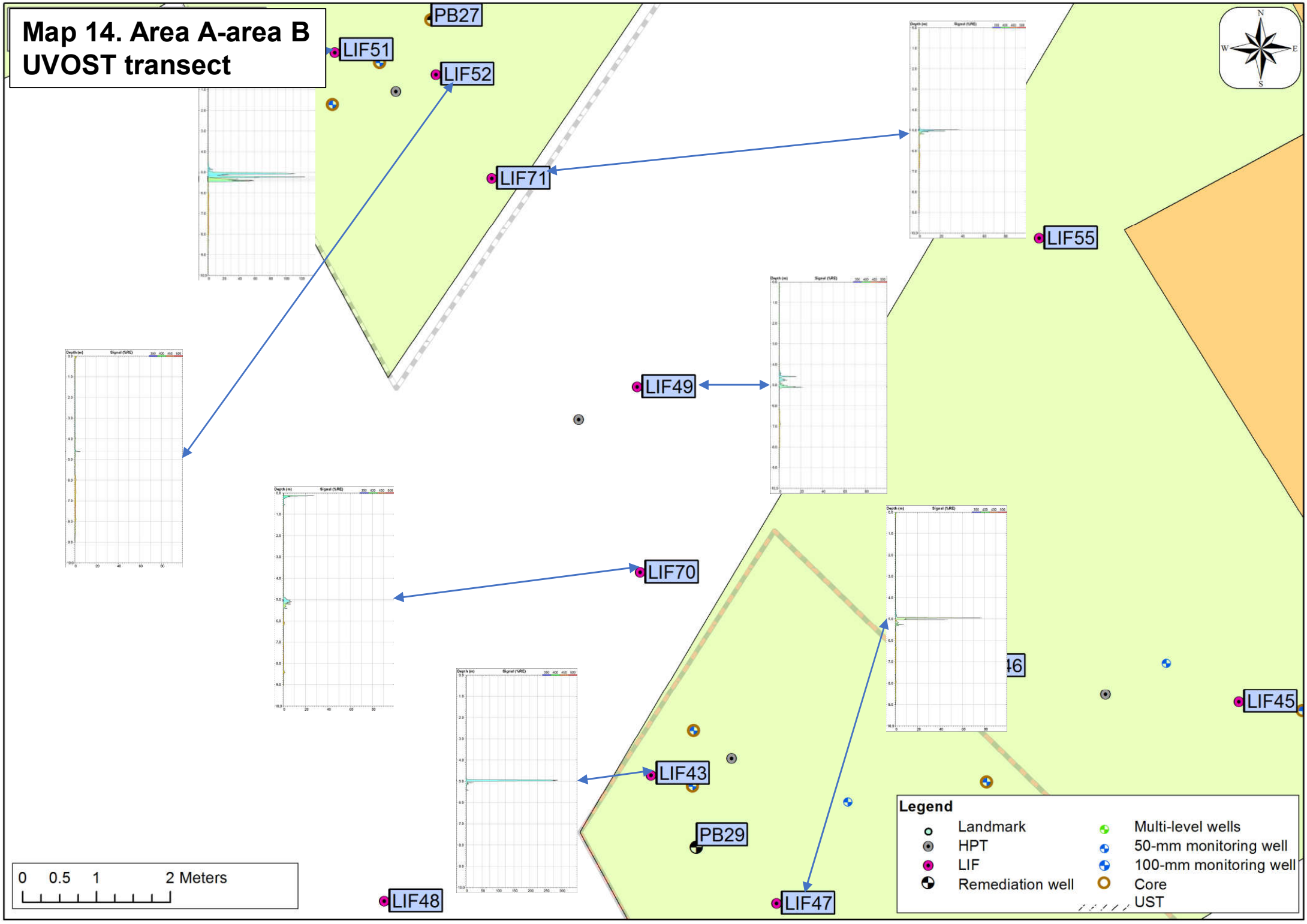
Map 12. Area T3 in the industrial site



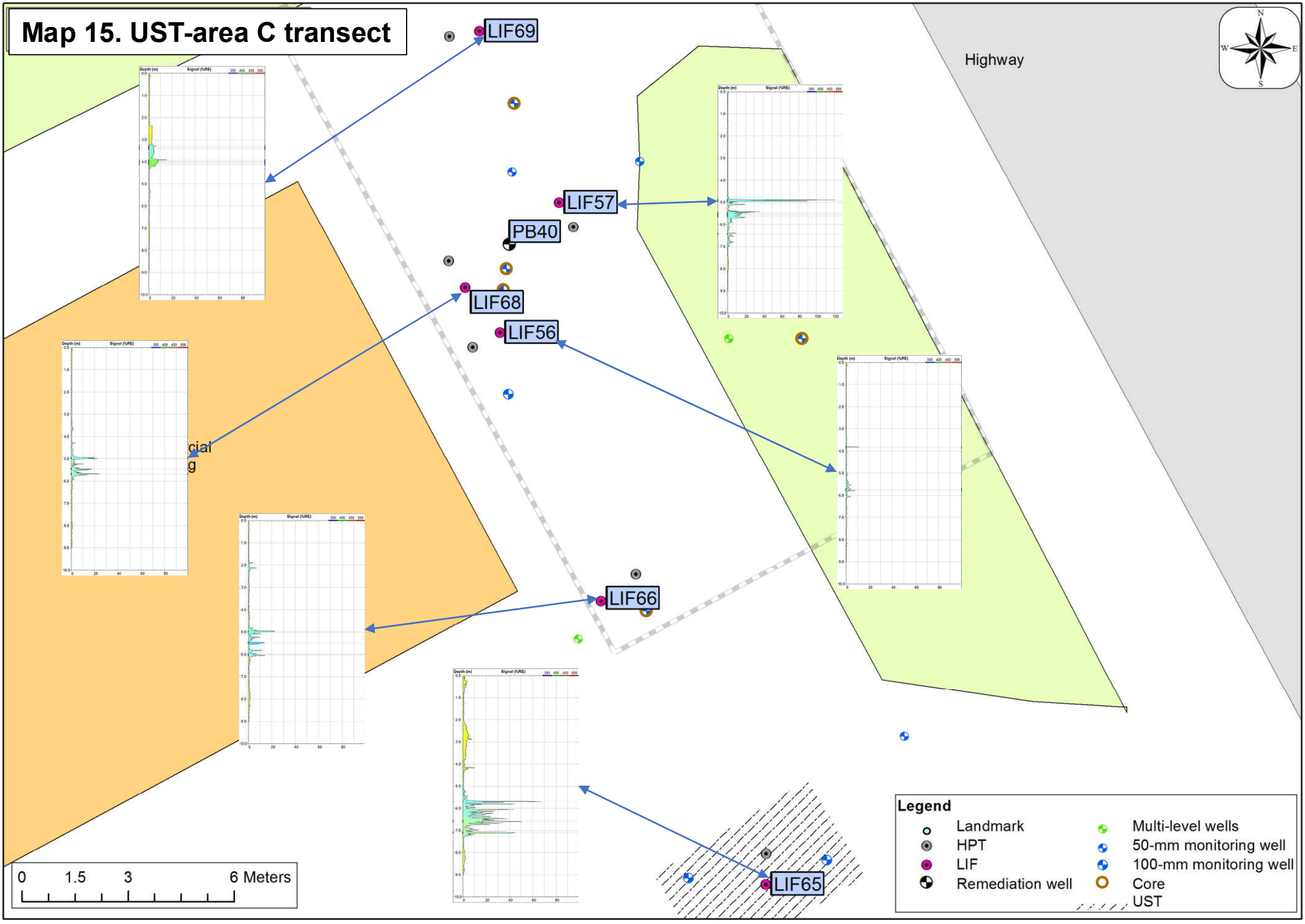
Map 13. UST-area A
UVOST transect

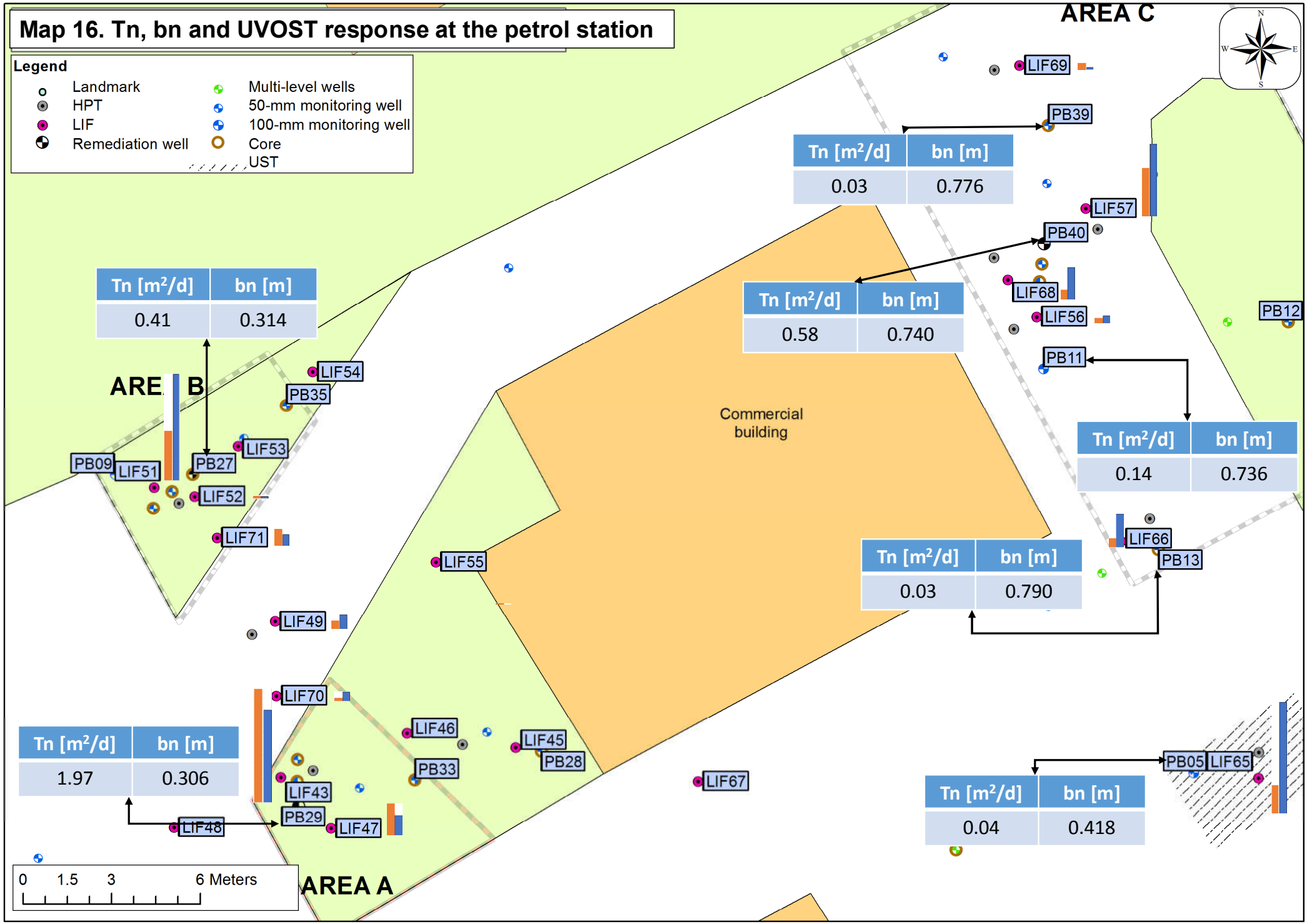


Map 14. Area A-area B
UVOST transect

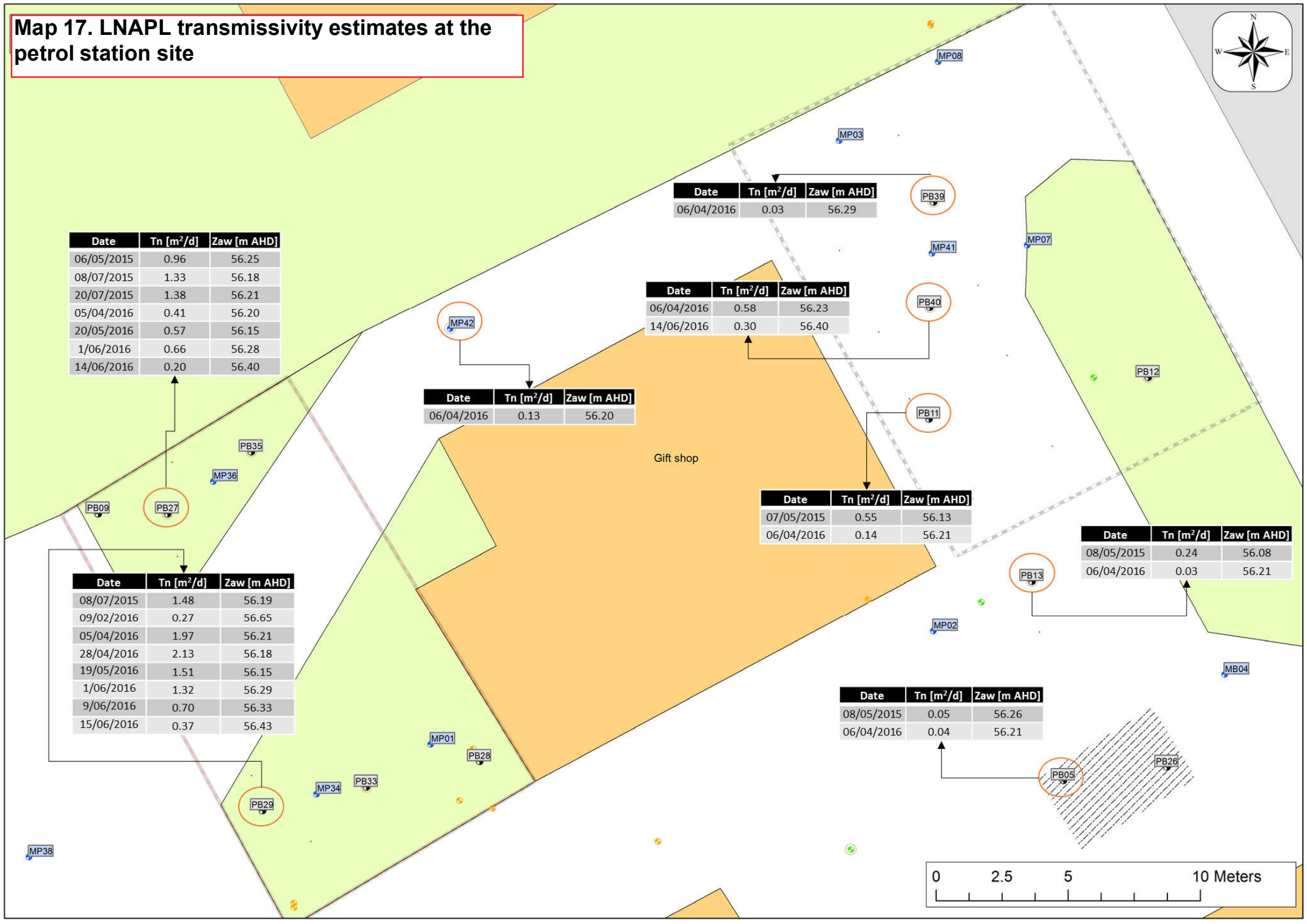


Map 15. UST-area C transect




Map 16. Tn, bn and UVOST response at the petrol station
Legend
Landmark
HPT
LIF
Remediation well
Multi-level wells
50-mm monitoring well
100-mm monitoring well
Core
UST
AREA C
LIF69
PB39
Tn [m²/d] bn [m]
0.03 0.776
LIF57
PB40
LIF68
LIF56
PB12
Tn [m²/d] bn [m]
0.58 0.740
PB11
Tn [m²/d] bn [m]
0.14 0.736
LIF66
PB13
Tn [m²/d] bn [m]
0.03 0.790
Tn [m²/d] bn [m]
0.41 0.314
AREA B
LIF54
PB35
LIF53
PB09
LIF51
PB27
LIF52
LIF71
Commercial building
LIF55
LIF49
LIF70
LIF46
LIF45
PB28
PB33
LIF43
PB29
LIF47
LIF48
Tn [m²/d] bn [m]
1.97 0.306
LIF67
PB05
LIF65
Tn [m²/d] bn [m]
0.04 0.418
0 1.5 3 6 Meters
AREA A

Map 17. LNAPL transmissivity estimates at the petrol station site



Date	Tn [m²/d]	Zaw [m AHD]
06/04/2016	0.03	56.29

Date	Tn [m²/d]	Zaw [m AHD]
06/05/2015	0.96	56.25
08/07/2015	1.33	56.18
20/07/2015	1.38	56.21
05/04/2016	0.41	56.20
20/05/2016	0.57	56.15
1/06/2016	0.66	56.28
14/06/2016	0.20	56.40

Date	Tn [m²/d]	Zaw [m AHD]
06/04/2016	0.58	56.23
14/06/2016	0.30	56.40

Date	Tn [m²/d]	Zaw [m AHD]
06/04/2016	0.13	56.20

Date	Tn [m²/d]	Zaw [m AHD]
07/05/2015	0.55	56.13
06/04/2016	0.14	56.21

Date	Tn [m²/d]	Zaw [m AHD]
08/05/2015	0.24	56.08
06/04/2016	0.03	56.21

Date	Tn [m²/d]	Zaw [m AHD]
08/07/2015	1.48	56.19
09/02/2016	0.27	56.65
05/04/2016	1.97	56.21
28/04/2016	2.13	56.18
19/05/2016	1.51	56.15
1/06/2016	1.32	56.29
9/06/2016	0.70	56.33
15/06/2016	0.37	56.43

Date	Tn [m²/d]	Zaw [m AHD]
08/05/2015	0.05	56.26
06/04/2016	0.04	56.21

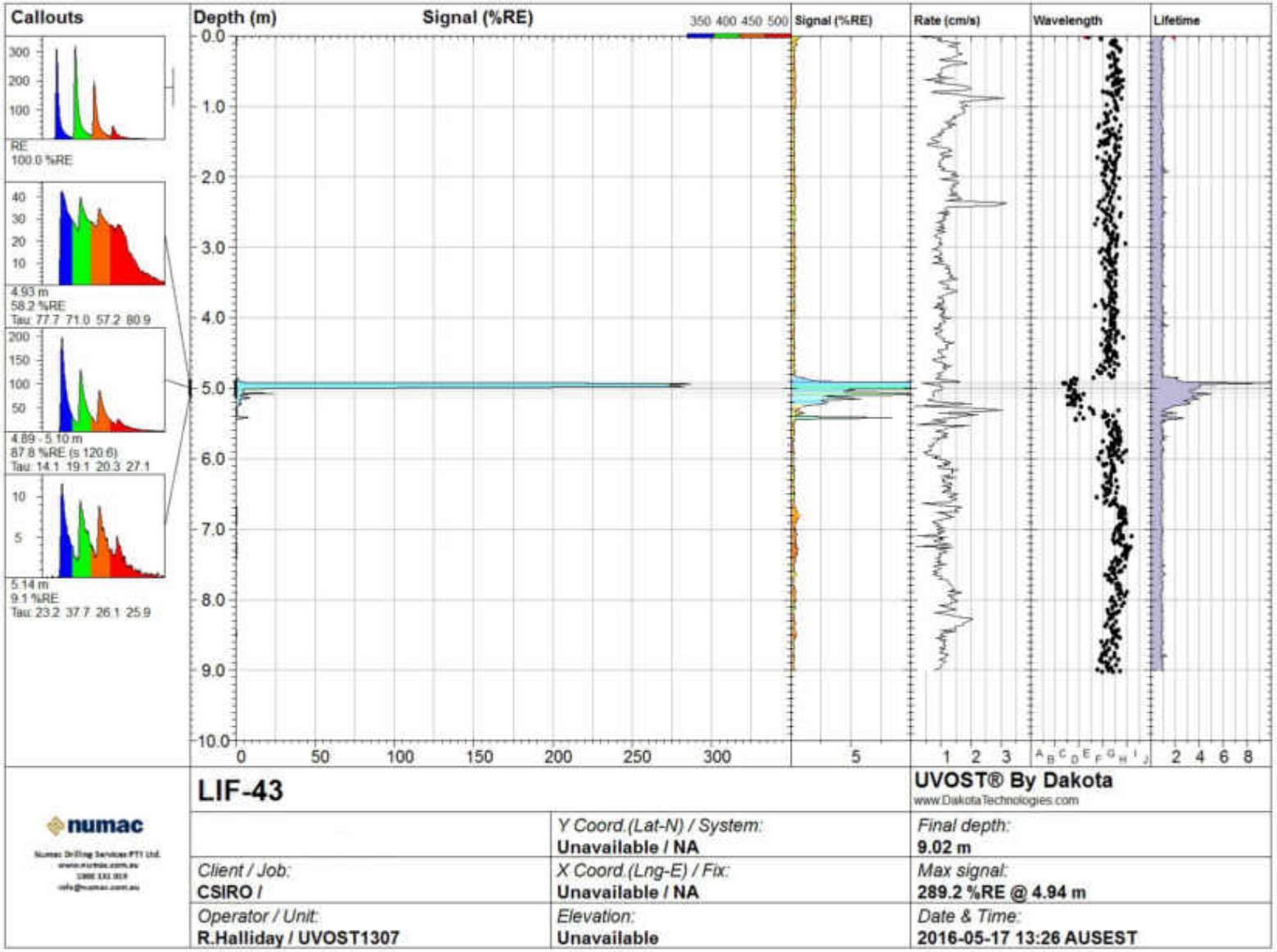
Appendix C: LIF profiles

Contents

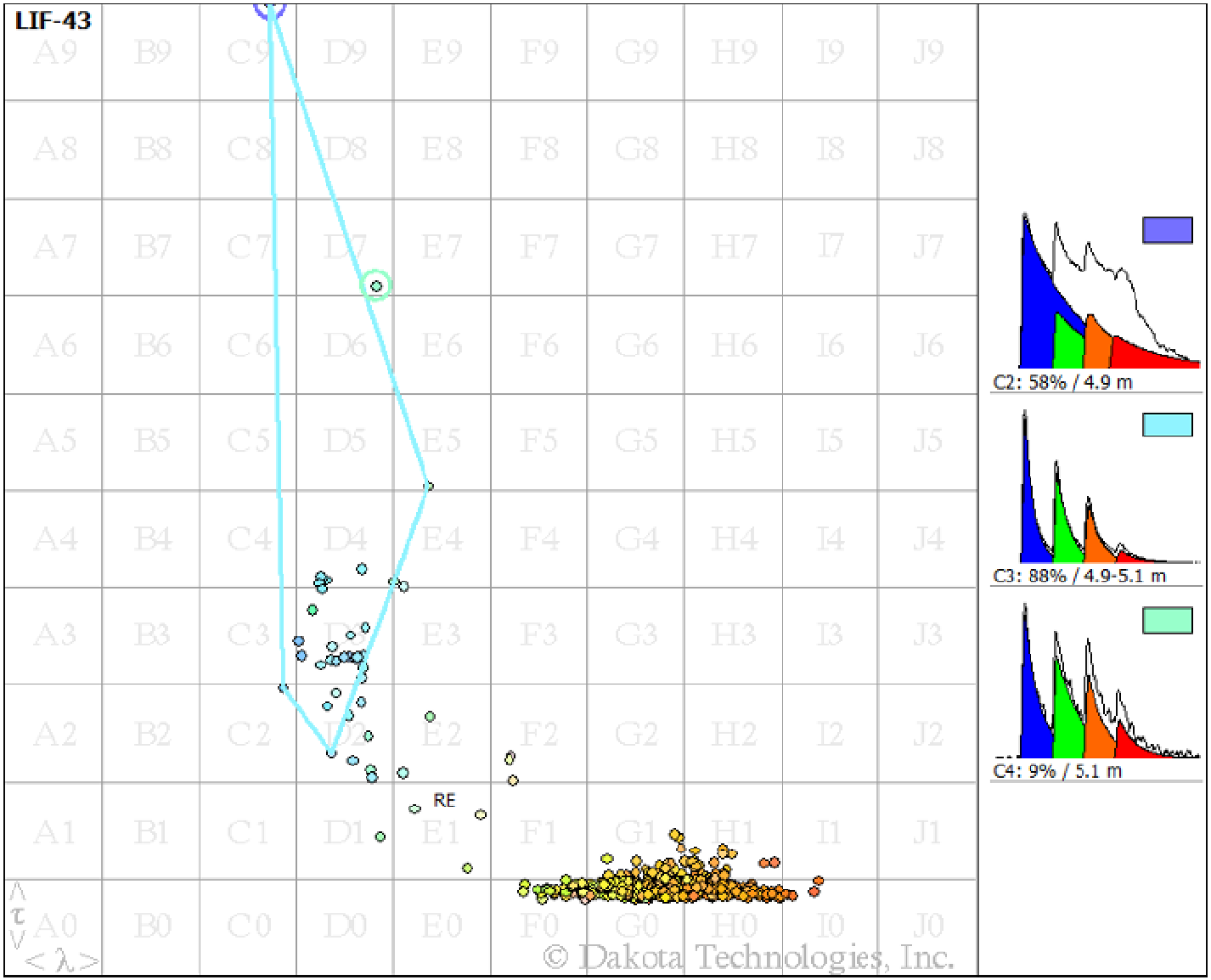
LIF profiles from the petrol station site C-2

LIF profiles from the industrial site.....C-43

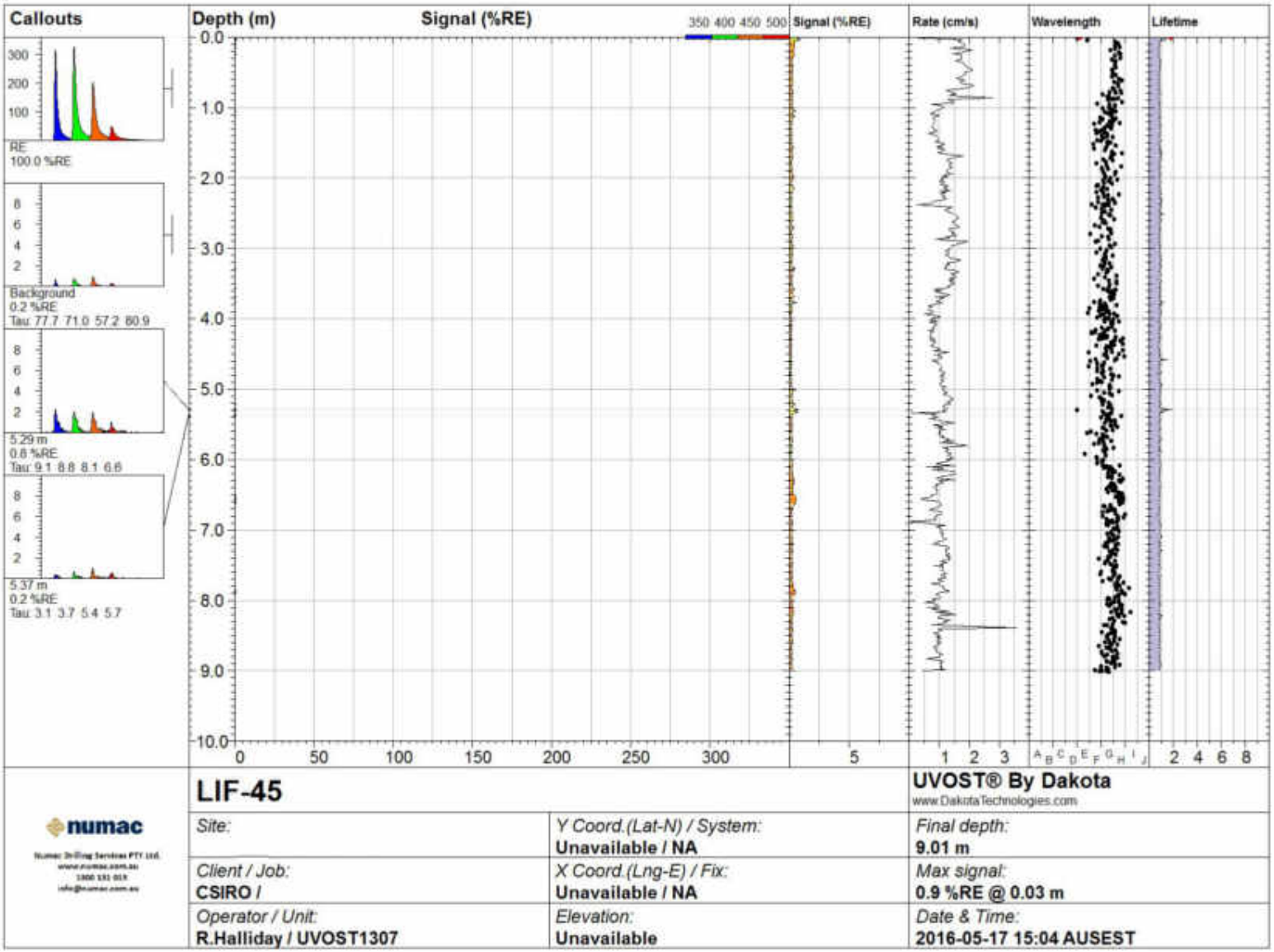
LIF profiles from the petrol station site


Callouts
Depth (m)
Signal (%RE)
350 400 450 500
Signal (%RE)
Rate (cm/s)
Wavelength
Lifetime
RE
100.0 %RE
4.93 m
58.2 %RE
Tau: 77.7 71.0 57.2 80.9
4.89 - 5.10 m
87.8 %RE (s 120.6)
Tau: 14.1 19.1 20.3 27.1
5.14 m
9.1 %RE
Tau: 23.2 37.7 26.1 25.9
LIF-43
UVOST® By Dakota
www.DakotaTechnologies.com
numac
Y Coord.(Lat-N) / System:
Unavailable / NA
Final depth:
9.02 m
Client / Job:
CSIRO /
X Coord.(Lng-E) / Fix:
Unavailable / NA
Max signal:
289.2 %RE @ 4.94 m
Operator / Unit:
R.Halliday / UVOST1307
Elevation:
Unavailable
Date & Time:
2016-05-17 13:26 AUSEST

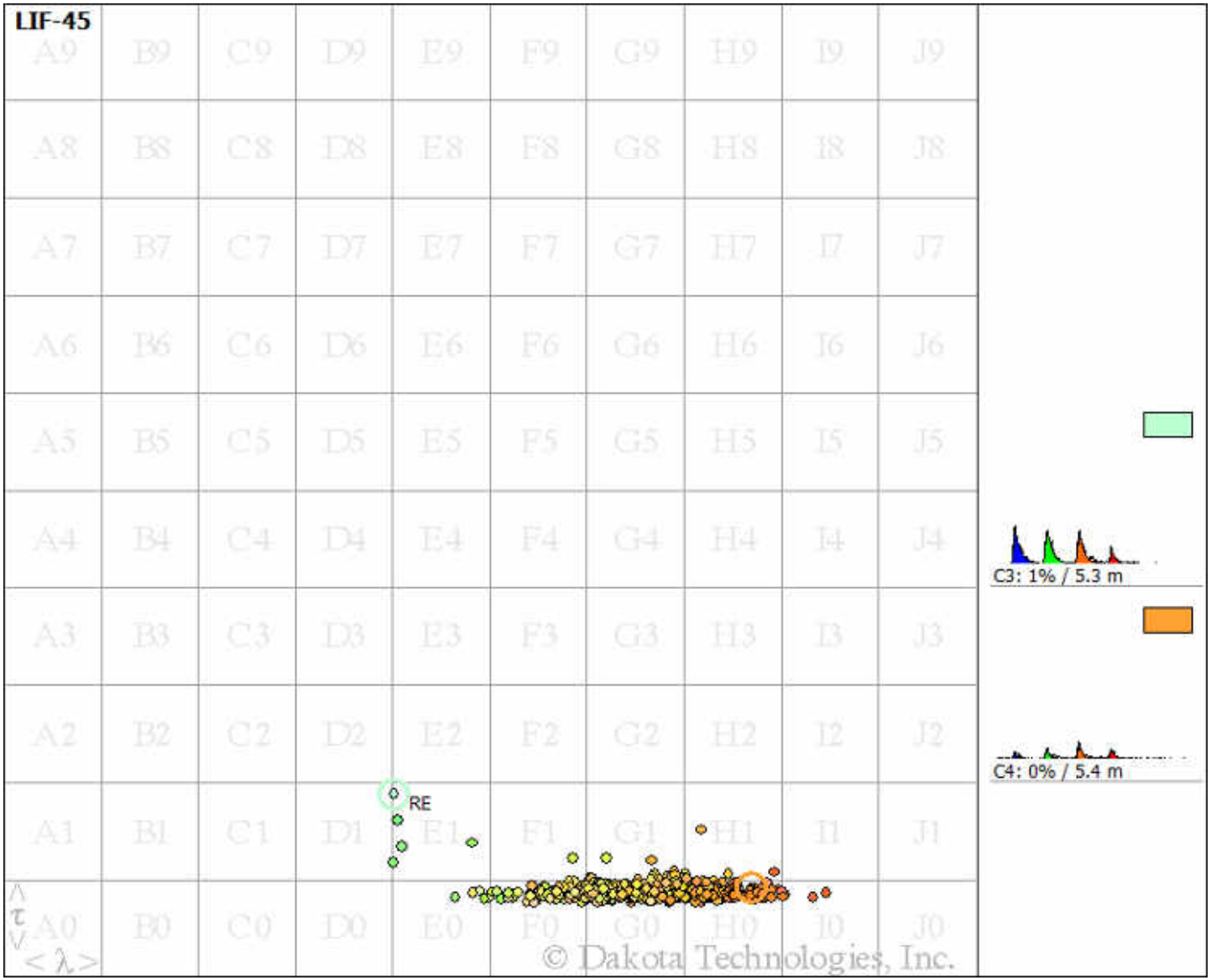
LIF43-A log



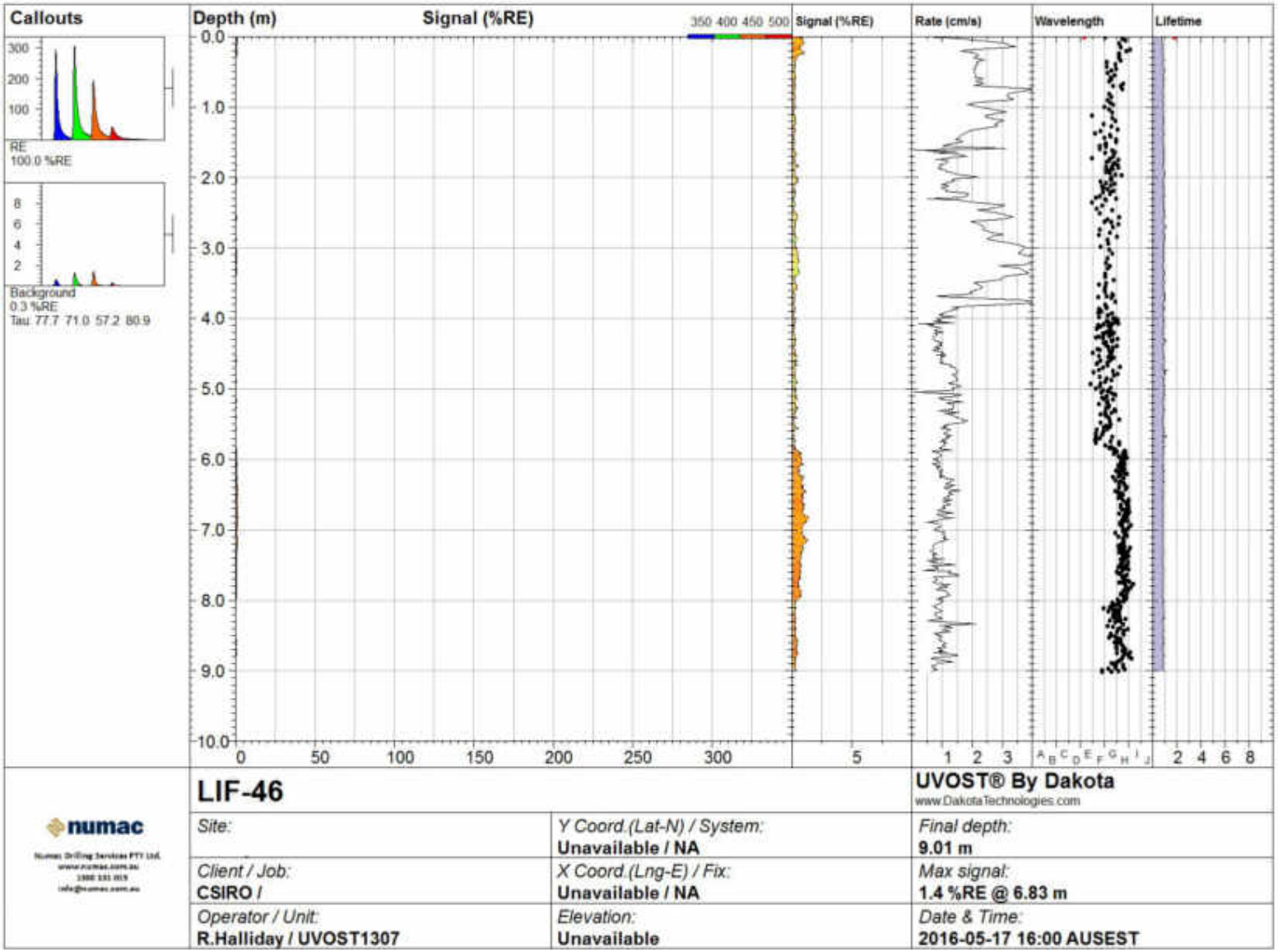
LIF43-A wavelength–lifetime matrix


Callouts
Depth (m)
Signal (%RE)
350 400 450 500
Signal (%RE)
Rate (cm/s)
Wavelength
Lifetime
RE
100.0 %RE
Background
0.2 %RE
Tau: 77.7 71.0 57.2 80.9
5.29 m
0.8 %RE
Tau: 9.1 8.8 8.1 6.6
5.37 m
0.2 %RE
Tau: 3.1 3.7 5.4 5.7
LIF-45
UVOST® By Dakota
www.DakotaTechnologies.com
numac
Site:
Y Coord.(Lat-N) / System:
Unavailable / NA
Final depth:
9.01 m
Client / Job:
CSIRO /
X Coord.(Lng-E) / Fix:
Unavailable / NA
Max signal:
0.9 %RE @ 0.03 m
Operator / Unit:
R.Halliday / UVOST1307
Elevation:
Unavailable
Date & Time:
2016-05-17 15:04 AUSEST

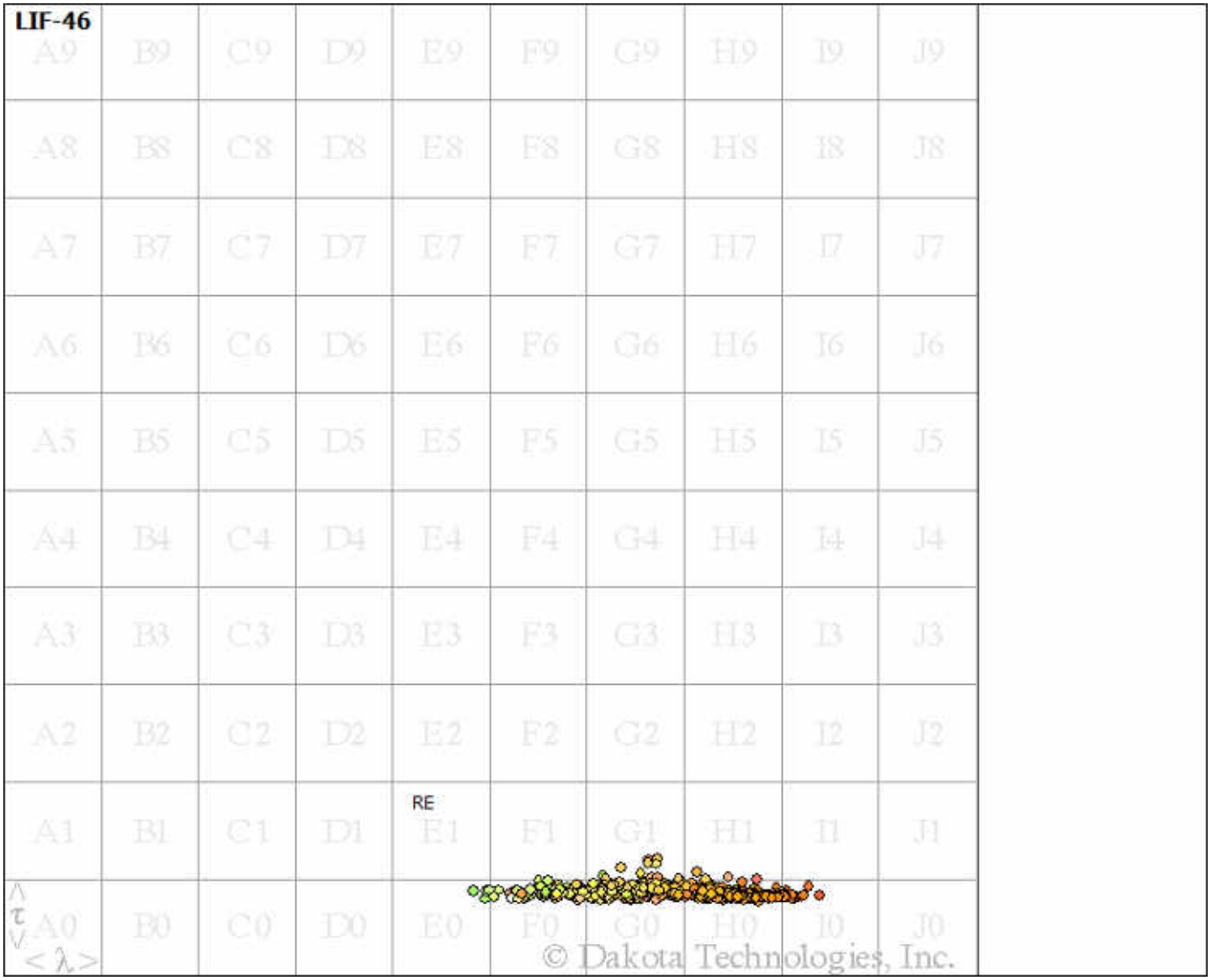
LIF45 log



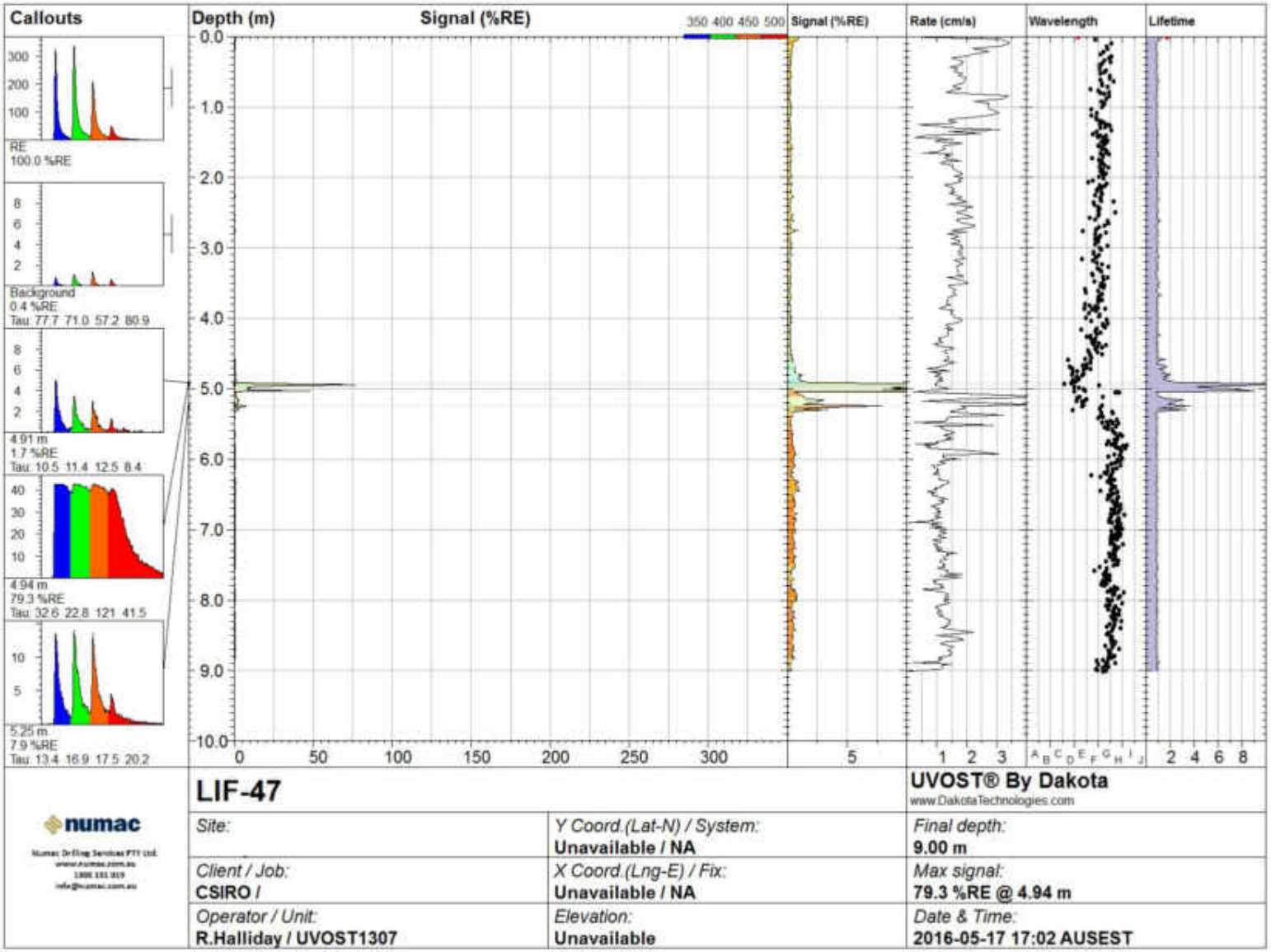
LIF45 wavelength–lifetime matrix


Callouts
300
200
100
RE
100.0 %RE
8
6
4
2
Background
0.3 %RE
Tau: 77.7 71.0 57.2 80.9
Depth (m)
Signal (%RE)
350 400 450 500
Signal (%RE)
Rate (cm/s)
Wavelength
Lifetime
0.0
1.0
2.0
3.0
4.0
5.0
6.0
7.0
8.0
9.0
10.0
0 50 100 150 200 250 300
5
1 2 3
A B C D E F G H I J
2 4 6 8
numac
LIF-46
UVOST® By Dakota
www.DakotaTechnologies.com
Site:
Y Coord.(Lat-N) / System:
Unavailable / NA
Final depth:
9.01 m
Client / Job:
CSIRO /
X Coord.(Lng-E) / Fix:
Unavailable / NA
Max signal:
1.4 %RE @ 6.83 m
Operator / Unit:
R.Halliday / UVOST1307
Elevation:
Unavailable
Date & Time:
2016-05-17 16:00 AUSEST

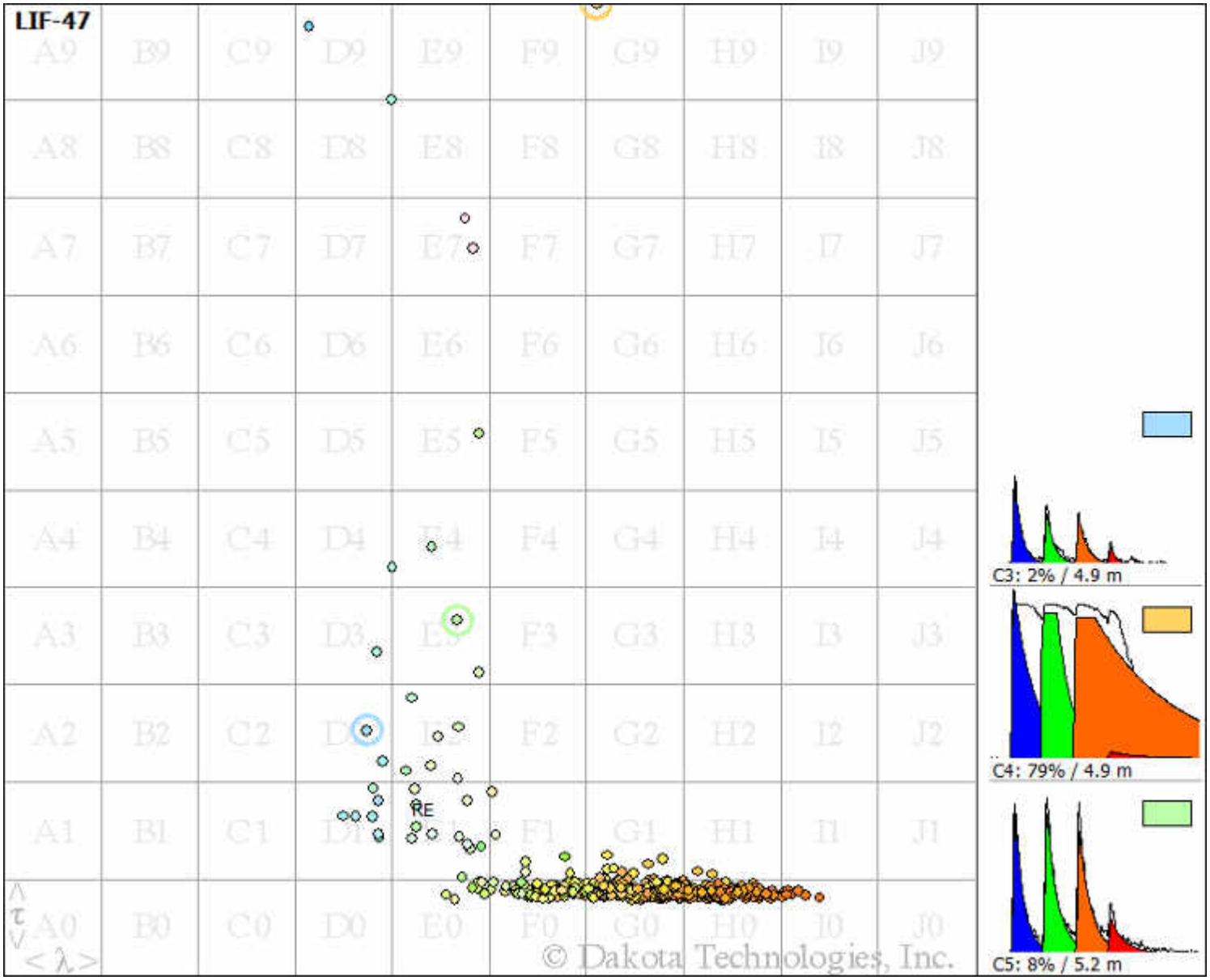
LIF46 log



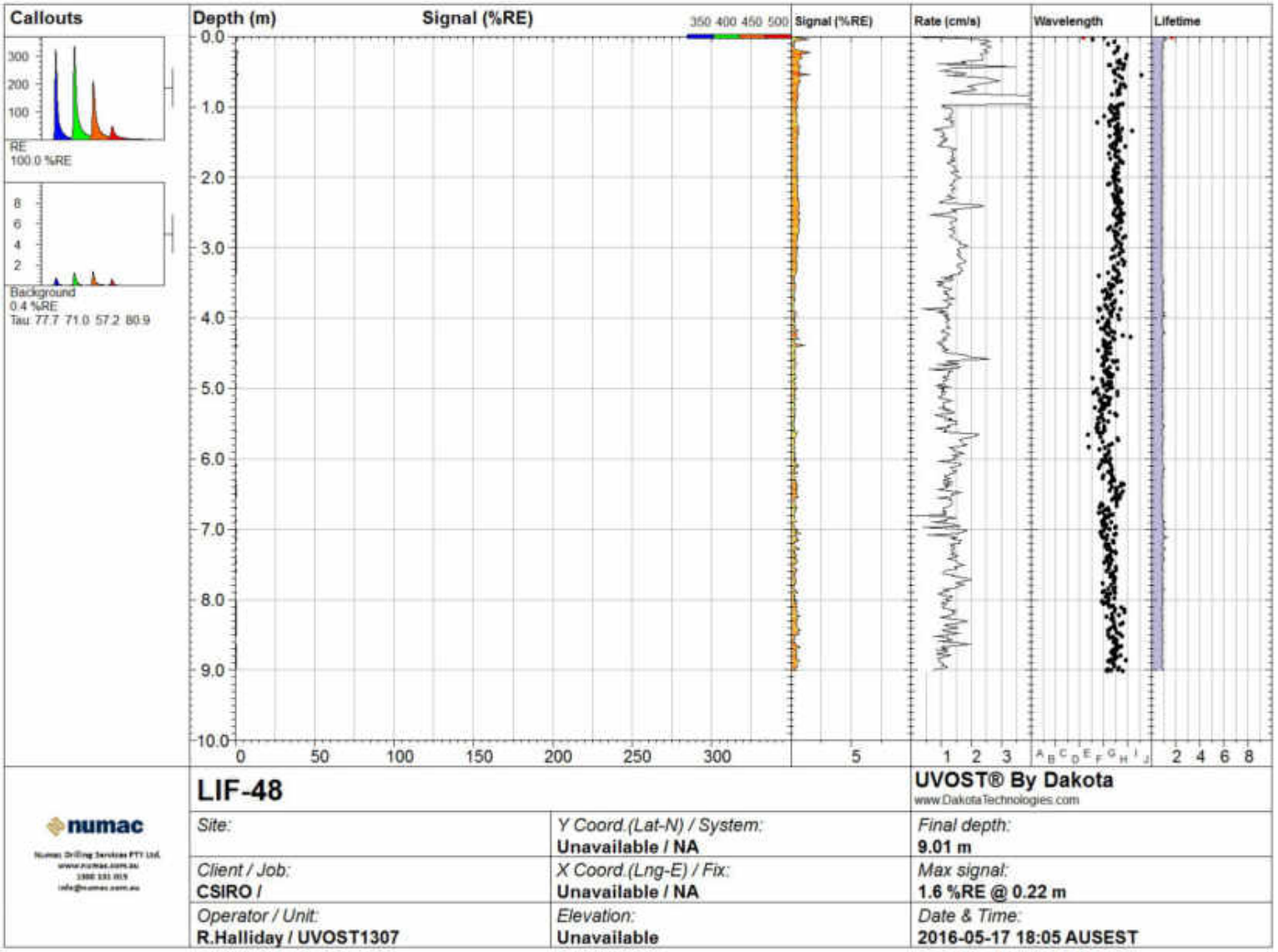
LIF46 wavelength–lifetime matrix


Callouts
Depth (m)
Signal (%RE)
350 400 450 500
Signal (%RE)
Rate (cm/s)
Wavelength
Lifetime
RE
100.0 %RE
Background
0.4 %RE
Tau: 77.7 71.0 57.2 80.9
4.91 m
1.7 %RE
Tau: 10.5 11.4 12.5 8.4
4.94 m
79.3 %RE
Tau: 32.6 22.8 121 41.5
5.25 m
7.9 %RE
Tau: 13.4 16.9 17.5 20.2
LIF-47
UVOST® By Dakota
www.DakotaTechnologies.com
numac
Site:
Y Coord.(Lat-N) / System:
Unavailable / NA
Final depth:
9.00 m
Client / Job:
CSIRO /
X Coord.(Lng-E) / Fix:
Unavailable / NA
Max signal:
79.3 %RE @ 4.94 m
Operator / Unit:
R.Halliday / UVOST1307
Elevation:
Unavailable
Date & Time:
2016-05-17 17:02 AUSEST

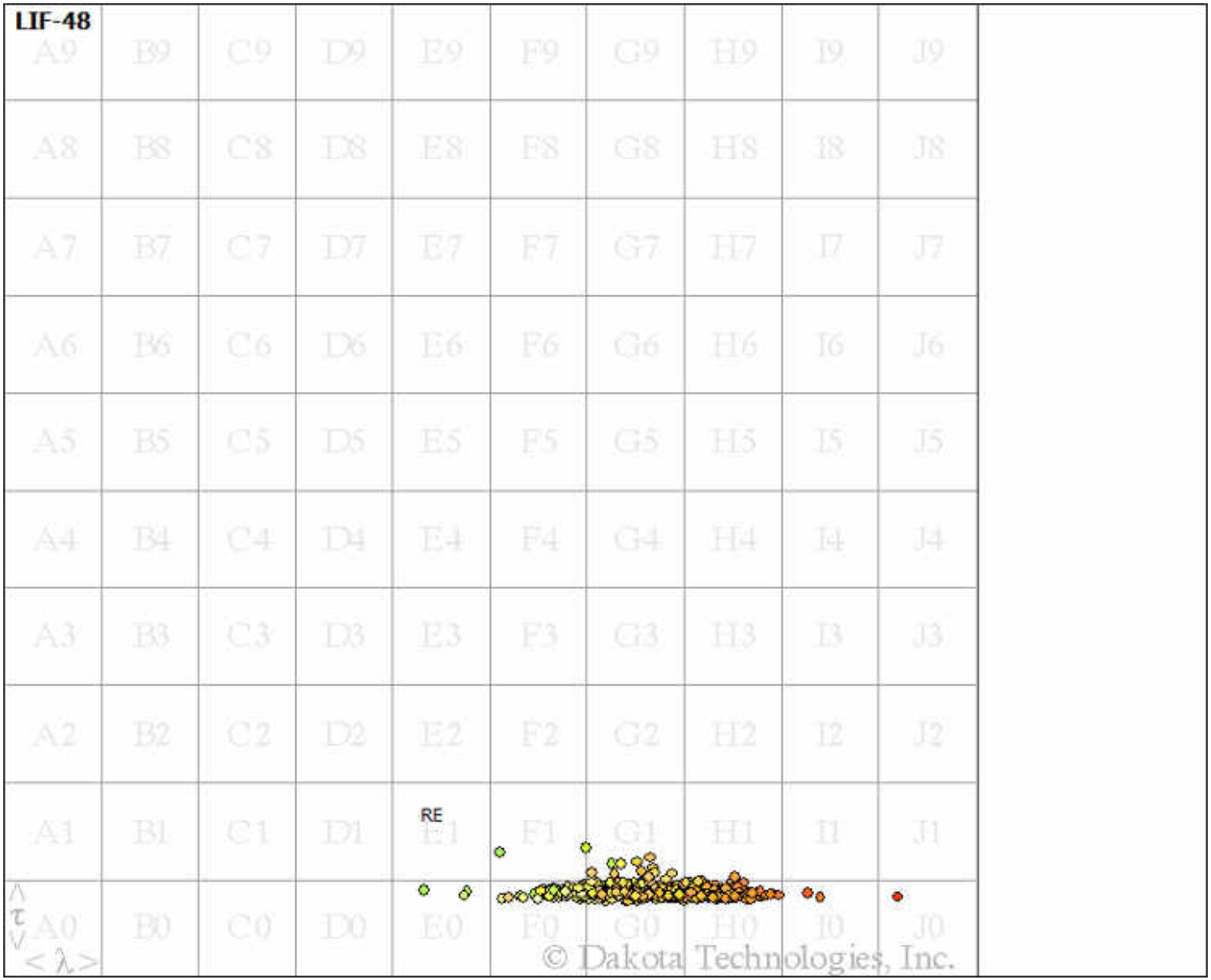
LIF47-A log



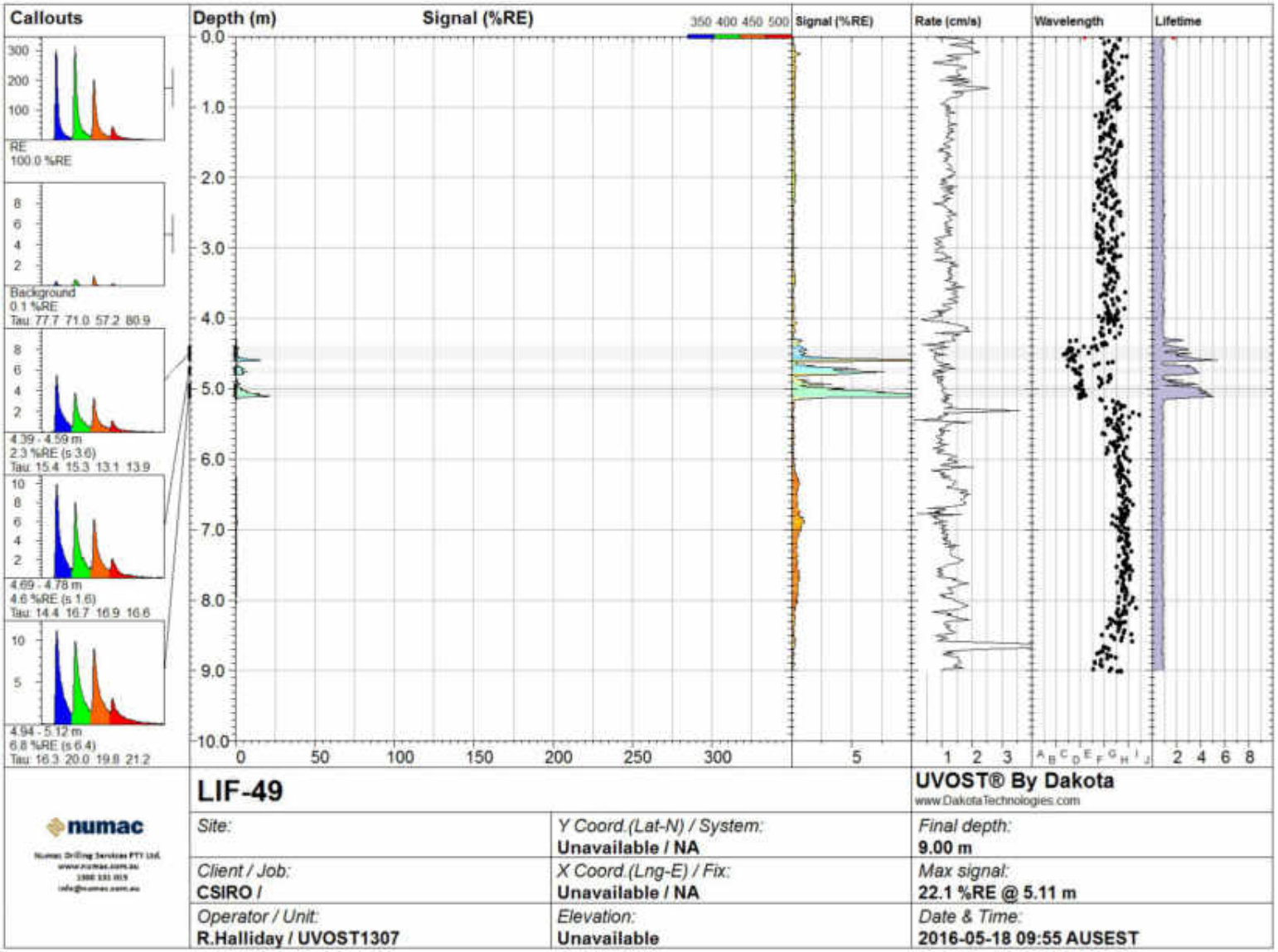
LIF47-A wavelength–lifetime matrix


Callouts
RE
100.0 %RE
Background
0.4 %RE
Tau: 77.7 71.0 57.2 80.9
Depth (m)
Signal (%RE)
350 400 450 500
Signal (%RE)
Rate (cm/s)
Wavelength
Lifetime
LIF-48
UVOST® By Dakota
www.DakotaTechnologies.com
numac
Site:
Y Coord.(Lat-N) / System:
Unavailable / NA
Final depth:
9.01 m
Client / Job:
CSIRO /
X Coord.(Lng-E) / Fix:
Unavailable / NA
Max signal:
1.6 %RE @ 0.22 m
Operator / Unit:
R.Halliday / UVOST1307
Elevation:
Unavailable
Date & Time:
2016-05-17 18:05 AUSEST

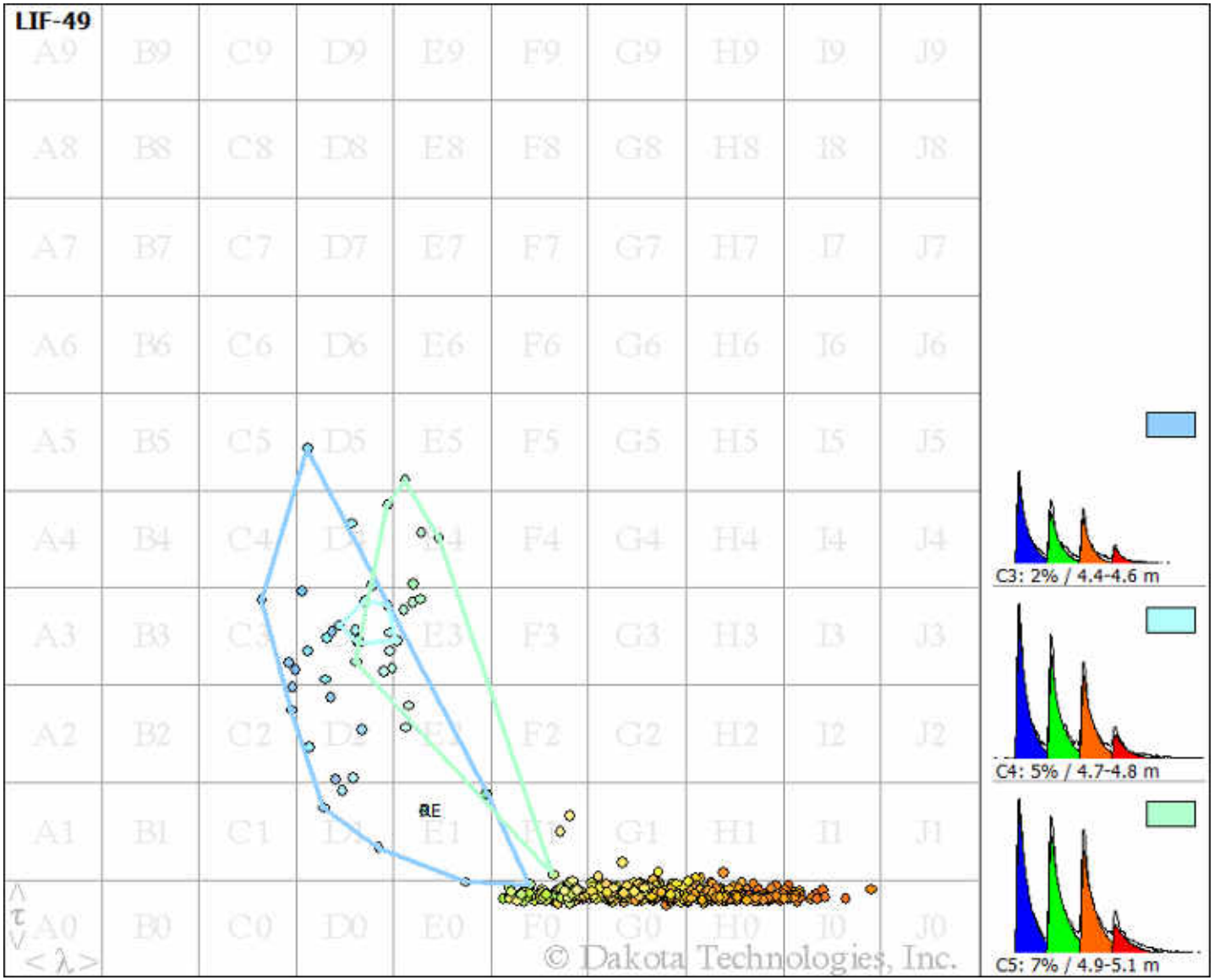
LIF48 log



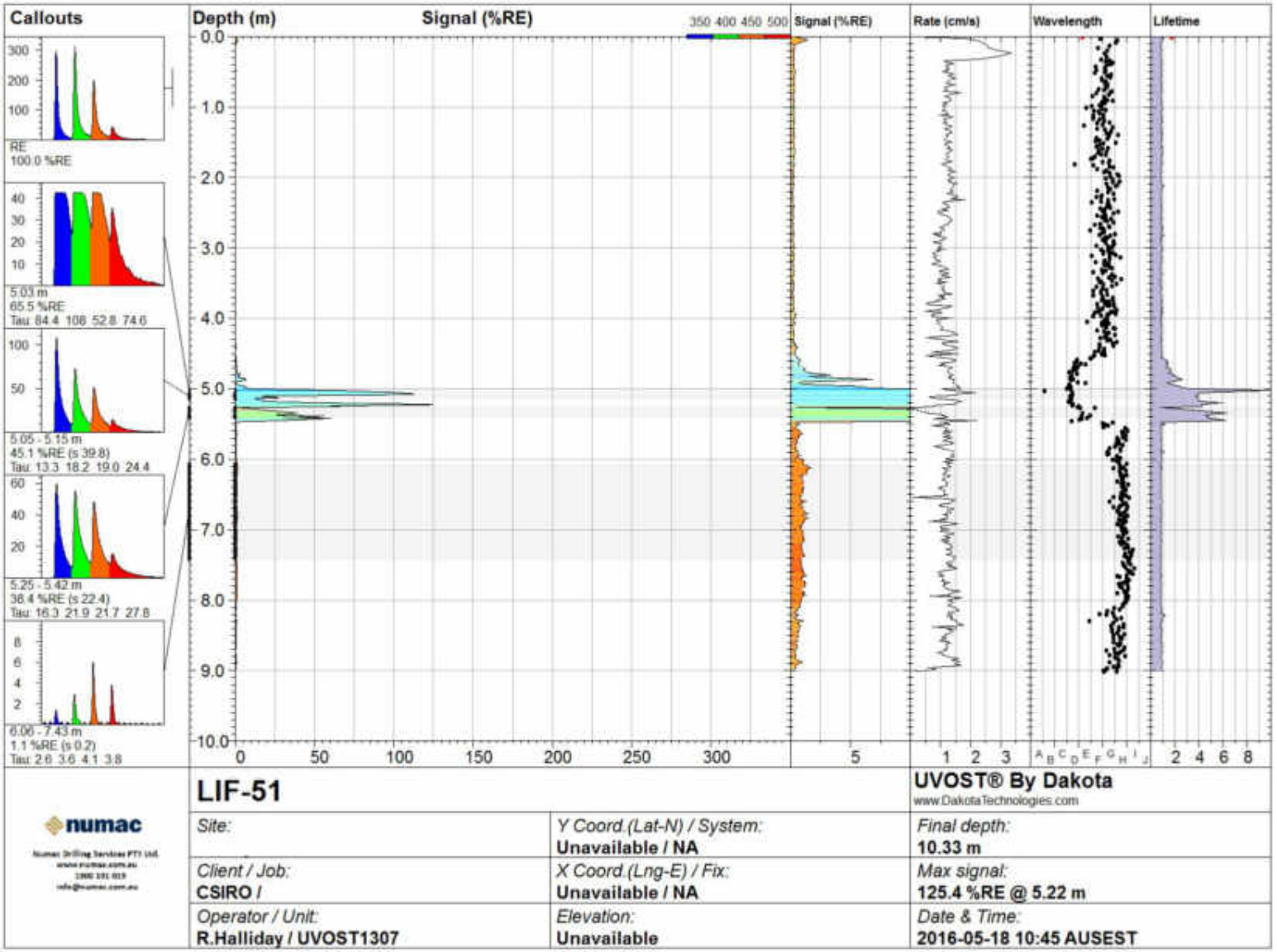
LIF48 wavelength–lifetime matrix


Callouts
Depth (m)
Signal (%RE)
350 400 450 500
Signal (%RE)
Rate (cm/s)
Wavelength
Lifetime
RE
100.0 %RE
Background
0.1 %RE
Tau: 77.7 71.0 57.2 80.9
4.39 - 4.59 m
2.3 %RE (s 3.6)
Tau: 15.4 15.3 13.1 13.9
4.69 - 4.78 m
4.6 %RE (s 1.6)
Tau: 14.4 16.7 16.9 16.6
4.94 - 5.12 m
6.8 %RE (s 6.4)
Tau: 16.3 20.0 19.8 21.2
LIF-49
UVOST® By Dakota
www.DakotaTechnologies.com
numac
Site:
Y Coord.(Lat-N) / System:
Unavailable / NA
Final depth:
9.00 m
Client / Job:
CSIRO /
X Coord.(Lng-E) / Fix:
Unavailable / NA
Max signal:
22.1 %RE @ 5.11 m
Operator / Unit:
R.Halliday / UVOST1307
Elevation:
Unavailable
Date & Time:
2016-05-18 09:55 AUSEST

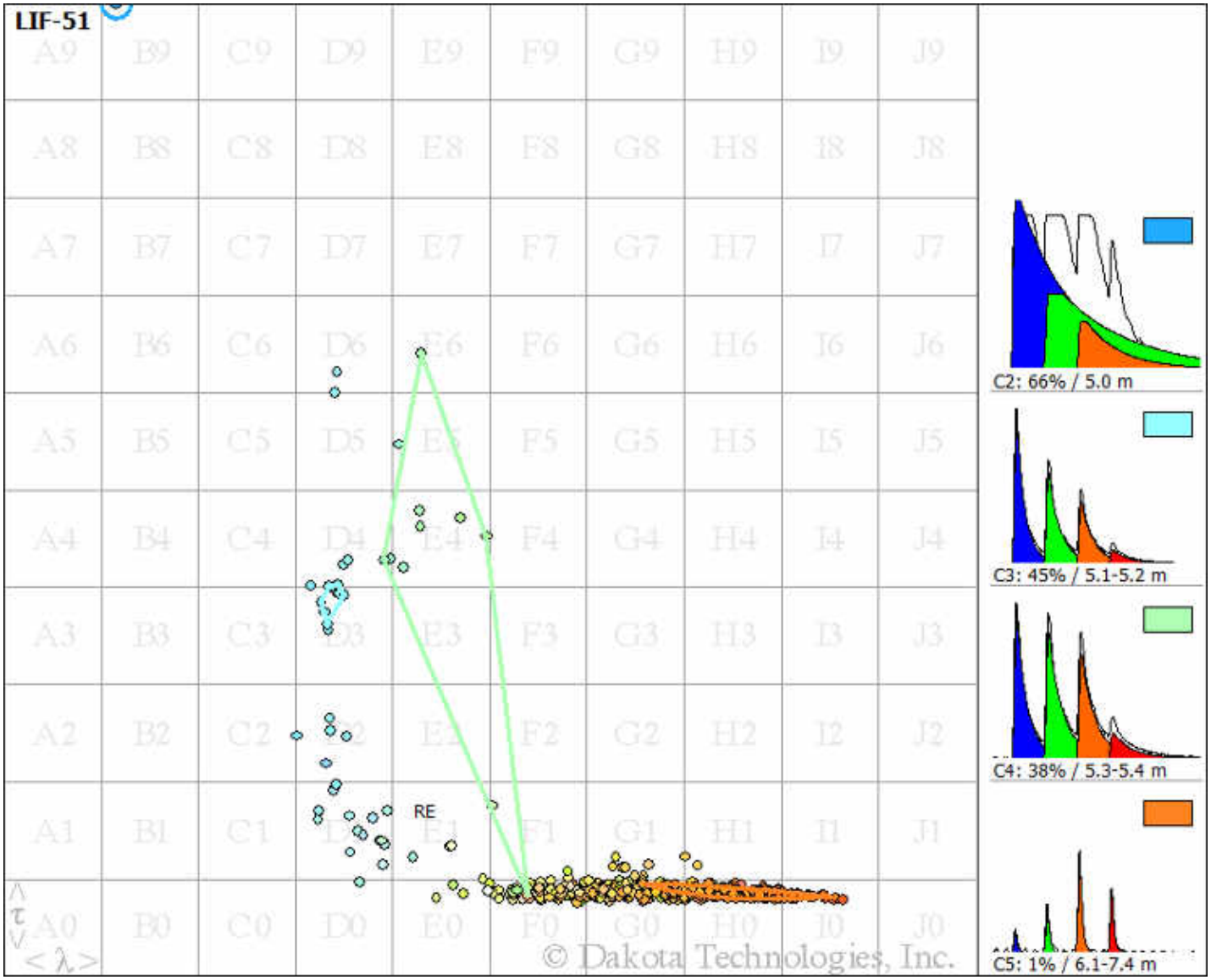
LIF49 log



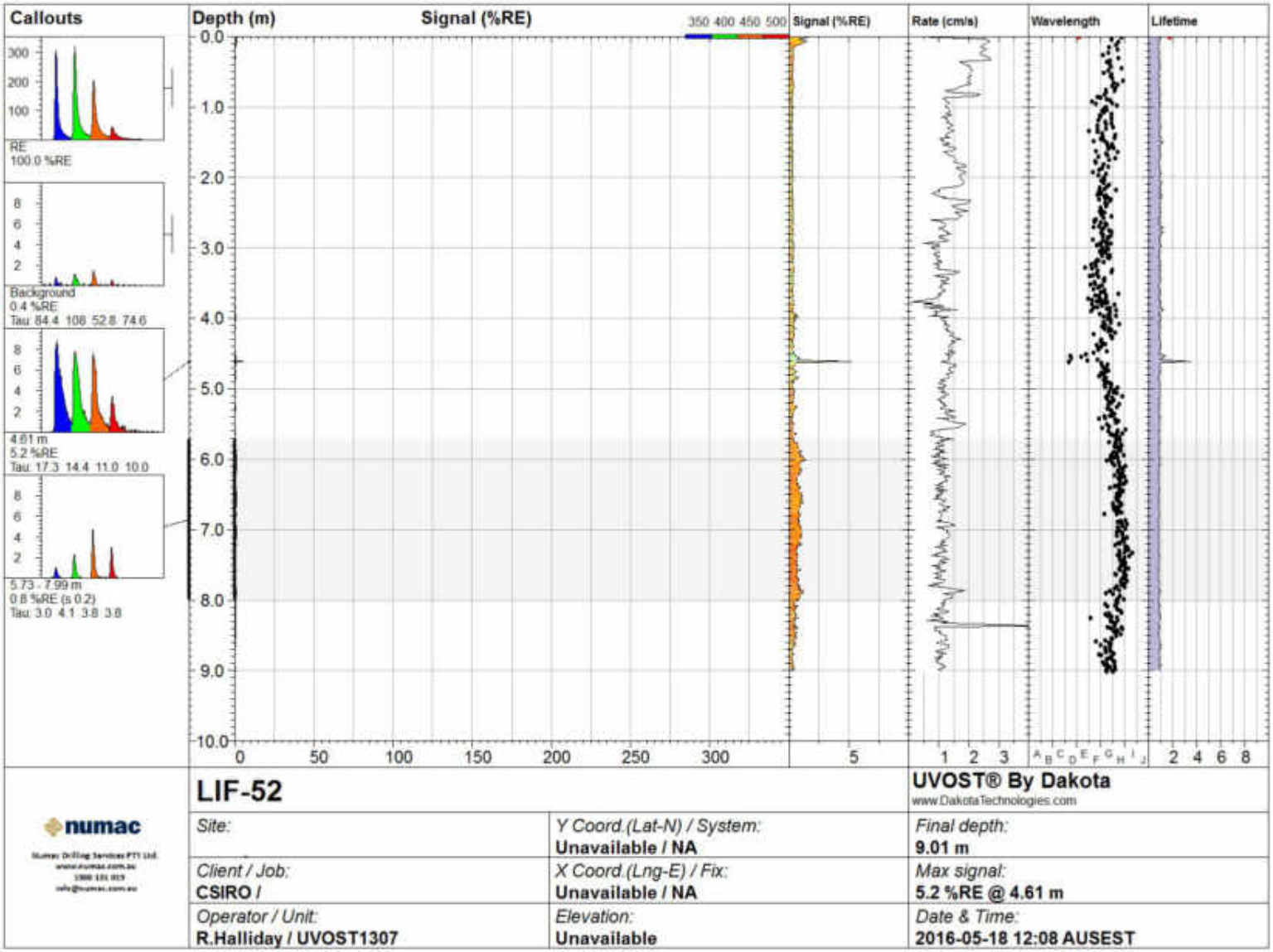
LIF49 wavelength–lifetime matrix


Callouts
Depth (m)
Signal (%RE)
350 400 450 500
Signal (%RE)
Rate (cm/s)
Wavelength
Lifetime
RE
100.0 %RE
5.03 m
65.5 %RE
Tau: 84.4 108 52.8 74.6
5.05 - 5.15 m
45.1 %RE (s 39.8)
Tau: 13.3 18.2 19.0 24.4
5.25 - 5.42 m
38.4 %RE (s 22.4)
Tau: 16.3 21.9 21.7 27.8
0.00 - 7.43 m
1.1 %RE (s 0.2)
Tau: 2.6 3.6 4.1 3.8
LIF-51
UVOST® By Dakota
www.DakotaTechnologies.com
numac
Site:
Y Coord.(Lat-N) / System:
Unavailable / NA
Final depth:
10.33 m
Client / Job:
CSIRO /
X Coord.(Lng-E) / Fix:
Unavailable / NA
Max signal:
125.4 %RE @ 5.22 m
Operator / Unit:
R.Halliday / UVOST1307
Elevation:
Unavailable
Date & Time:
2016-05-18 10:45 AUSEST

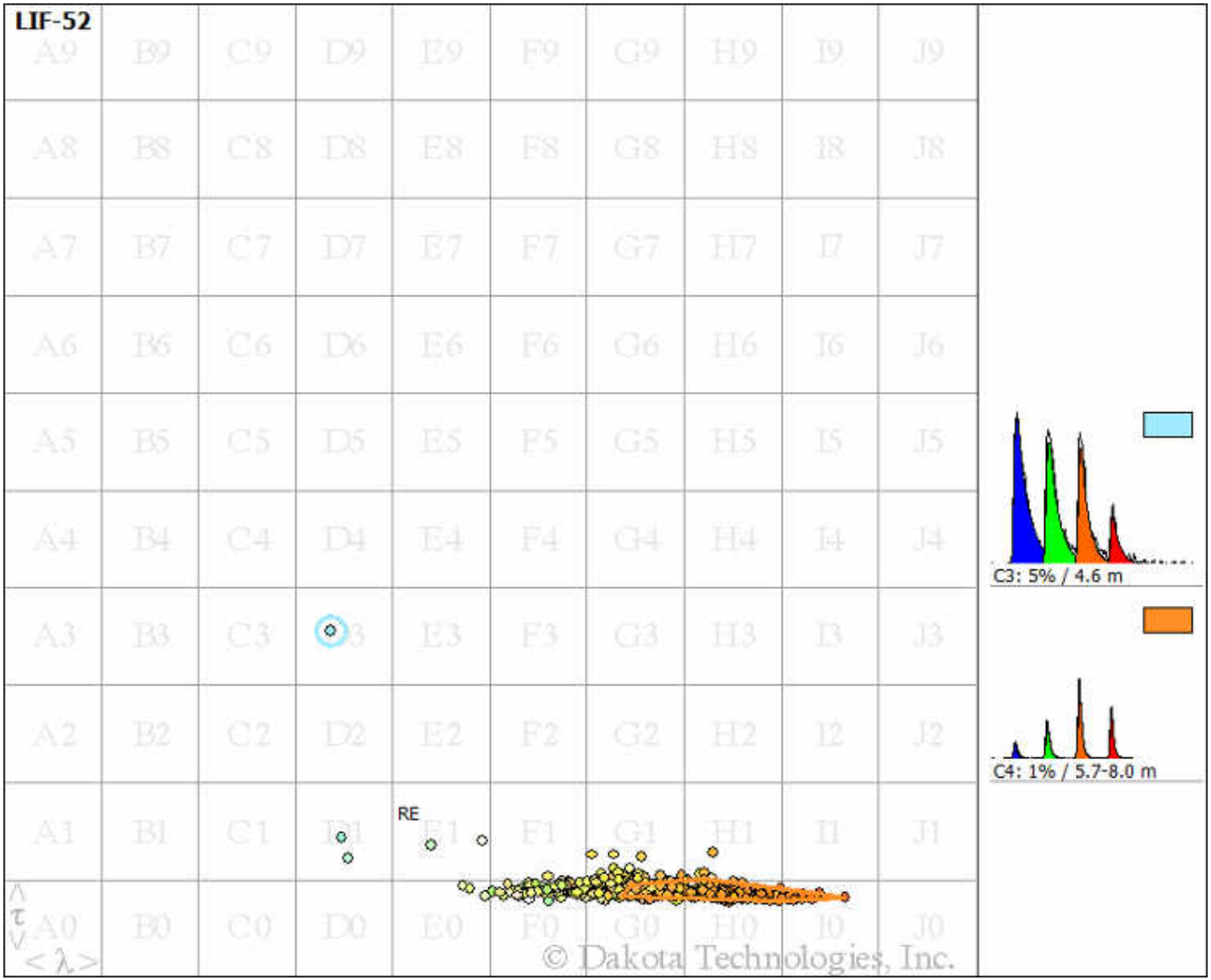
LIF51-B log



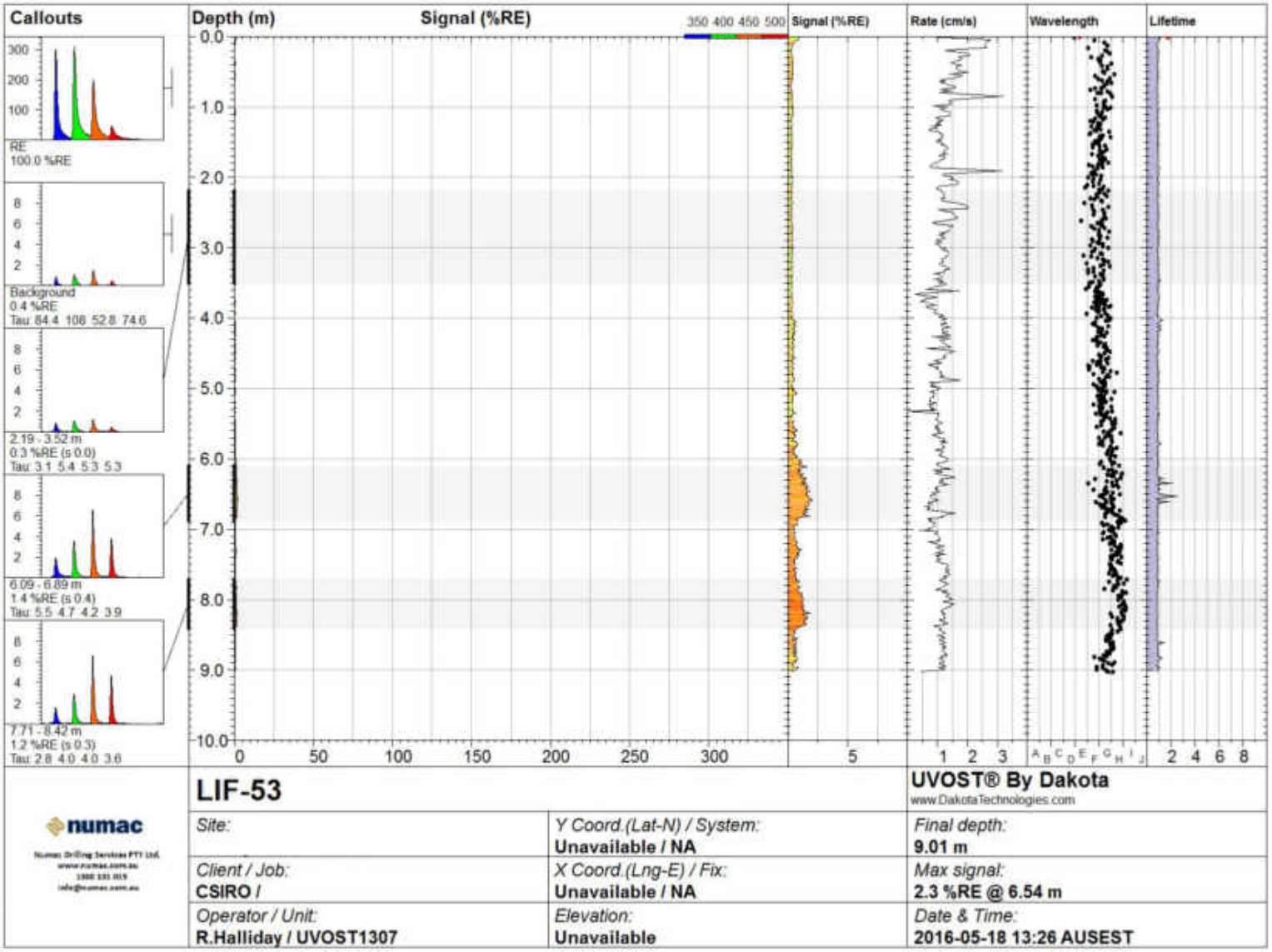
LIF51-B wavelength–lifetime matrix


Callouts
Depth (m)
Signal (%RE)
350 400 450 500
Signal (%RE)
Rate (cm/s)
Wavelength
Lifetime
RE
100.0 %RE
Background
0.4 %RE
Tau: 84.4 108 52.8 74.6
4.61 m
5.2 %RE
Tau: 17.3 14.4 11.0 10.0
5.73 - 7.99 m
0.8 %RE (s 0.2)
Tau: 3.0 4.1 3.8 3.8
LIF-52
UVOST® By Dakota
www.DakotaTechnologies.com
numac
Site:
Y Coord.(Lat-N) / System:
Unavailable / NA
Final depth:
9.01 m
Client / Job:
CSIRO /
X Coord.(Lng-E) / Fix:
Unavailable / NA
Max signal:
5.2 %RE @ 4.61 m
Operator / Unit:
R.Halliday / UVOST1307
Elevation:
Unavailable
Date & Time:
2016-05-18 12:08 AUSEST

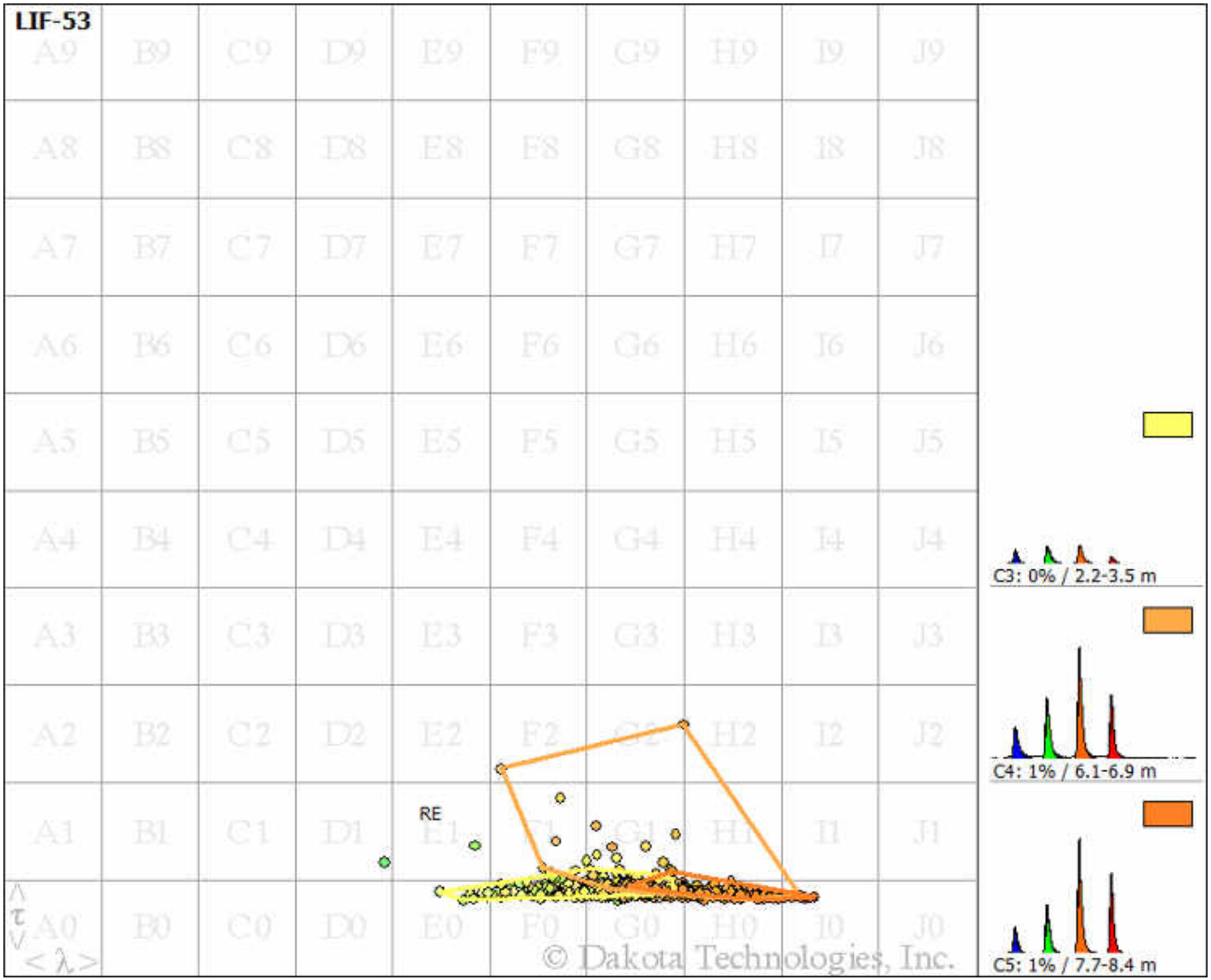
LIF52-B log



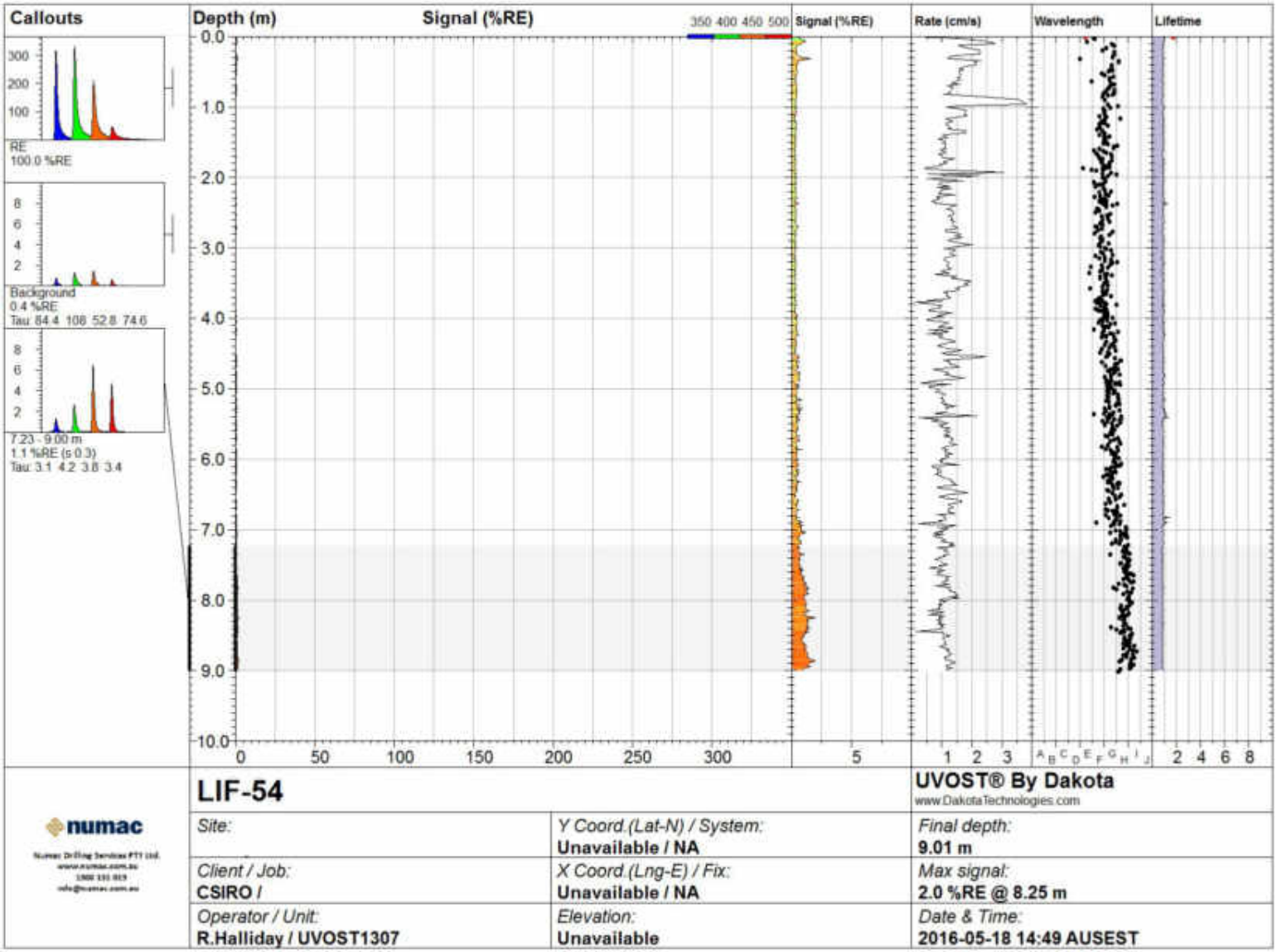
LIF52-B wavelength–lifetime matrix


Callouts
Depth (m)
Signal (%RE)
350 400 450 500
Signal (%RE)
Rate (cm/s)
Wavelength
Lifetime
RE
100.0 %RE
Background
0.4 %RE
Tau: 84.4 106 52.8 74.6
2.19 - 3.52 m
0.3 %RE (s 0.0)
Tau: 3.1 5.4 5.3 5.3
6.09 - 6.89 m
1.4 %RE (s 0.4)
Tau: 5.5 4.7 4.2 3.9
7.71 - 8.42 m
1.2 %RE (s 0.3)
Tau: 2.8 4.0 4.0 3.6
LIF-53
UVOST® By Dakota
www.DakotaTechnologies.com
numac
Site:
Y Coord.(Lat-N) / System:
Unavailable / NA
Final depth:
9.01 m
Client / Job:
CSIRO /
X Coord.(Lng-E) / Fix:
Unavailable / NA
Max signal:
2.3 %RE @ 6.54 m
Operator / Unit:
R.Halliday / UVOST1307
Elevation:
Unavailable
Date & Time:
2016-05-18 13:26 AUSEST

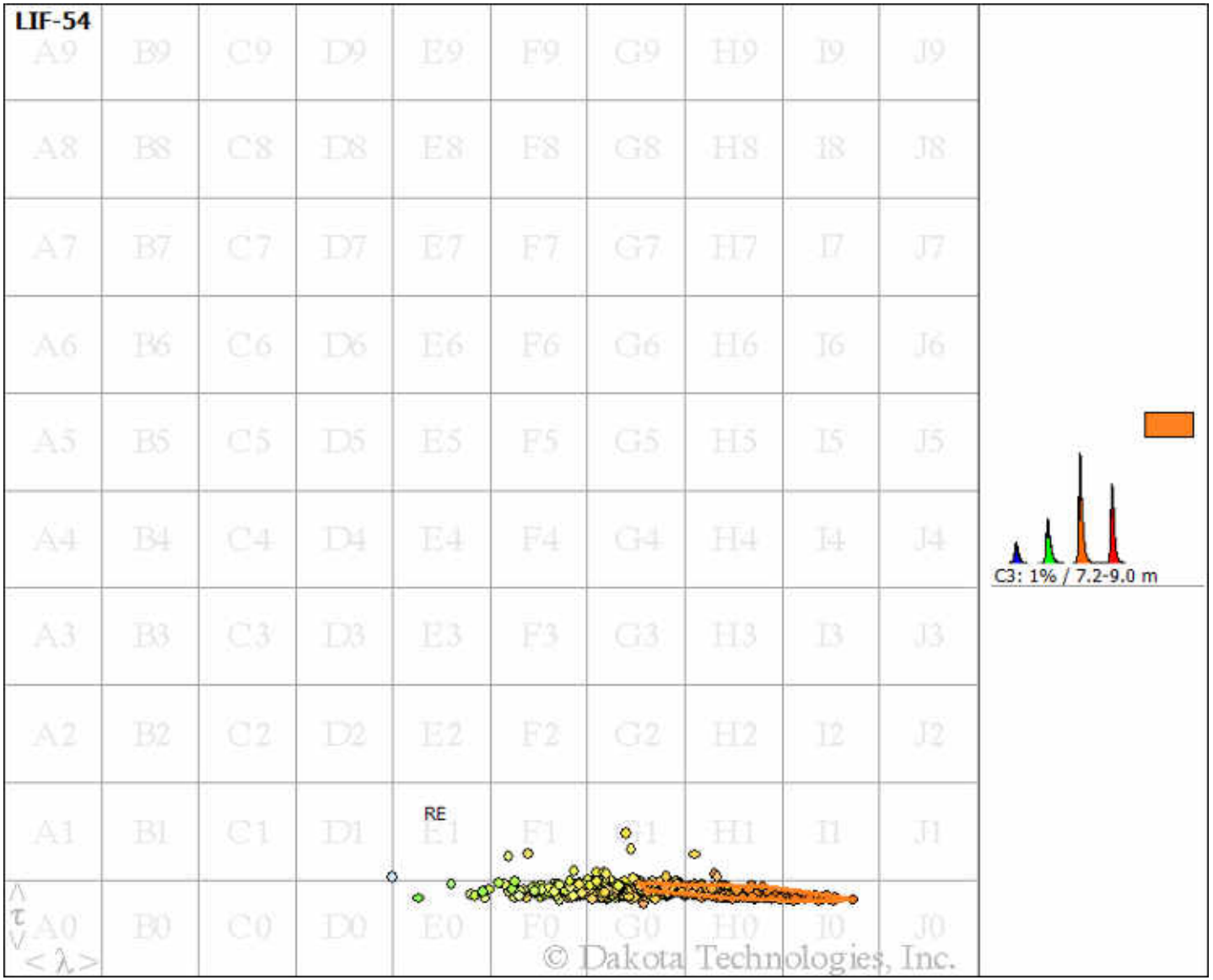
LIF53-B log



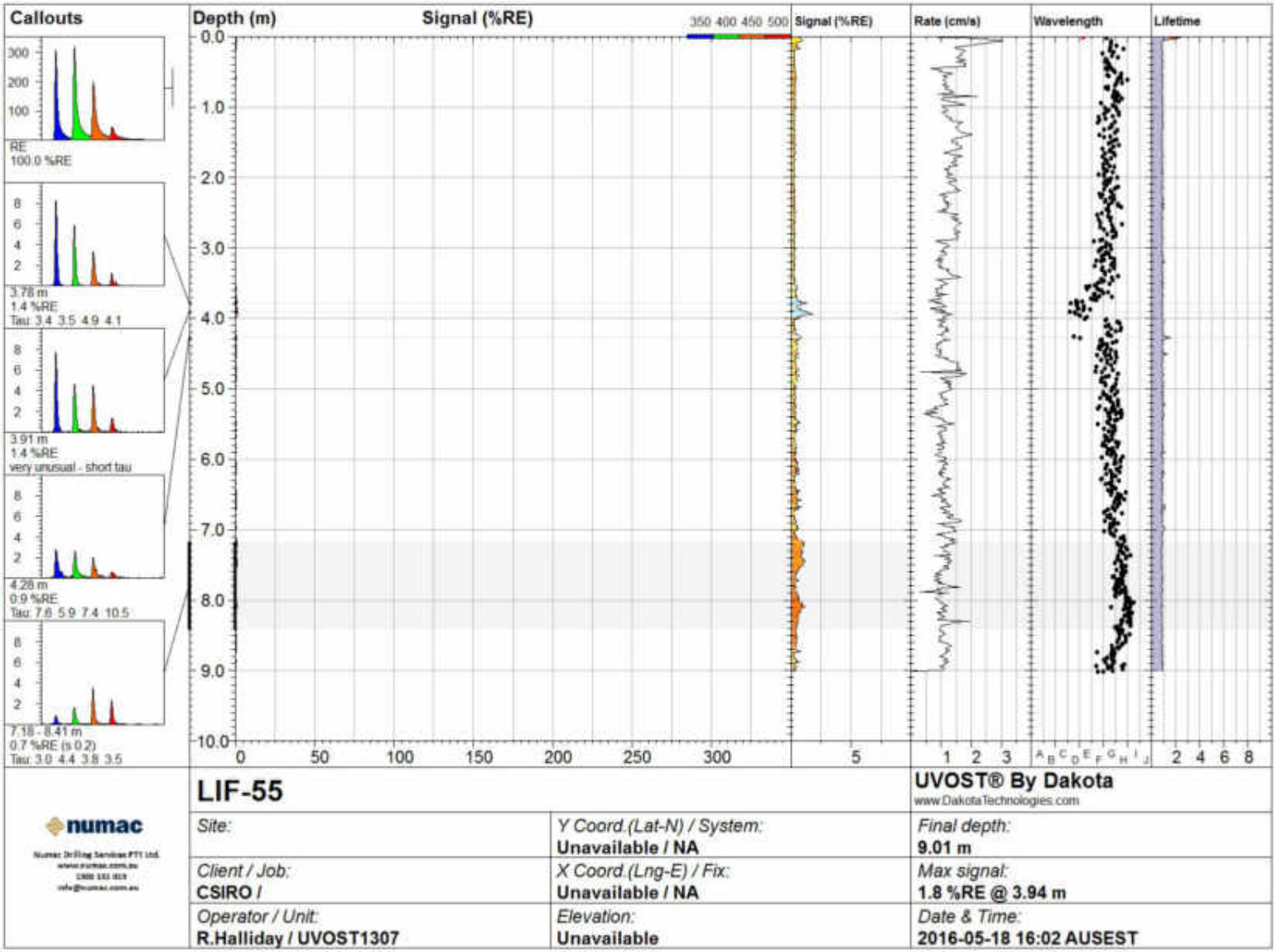
LIF53-B wavelength–lifetime matrix


Callouts
Depth (m)
Signal (%RE)
350 400 450 500
Signal (%RE)
Rate (cm/s)
Wavelength
Lifetime
RE
100.0 %RE
Background
0.4 %RE
Tau: 84.4 108 52.8 74.6
7.23 - 9.00 m
1.1 %RE (s 0.3)
Tau: 3.1 4.2 3.8 3.4
LIF-54
UVOST® By Dakota
www.DakotaTechnologies.com
numac
Site:
Y Coord.(Lat-N) / System:
Unavailable / NA
Final depth:
9.01 m
Client / Job:
CSIRO /
X Coord.(Lng-E) / Fix:
Unavailable / NA
Max signal:
2.0 %RE @ 8.25 m
Operator / Unit:
R.Halliday / UVOST1307
Elevation:
Unavailable
Date & Time:
2016-05-18 14:49 AUSEST

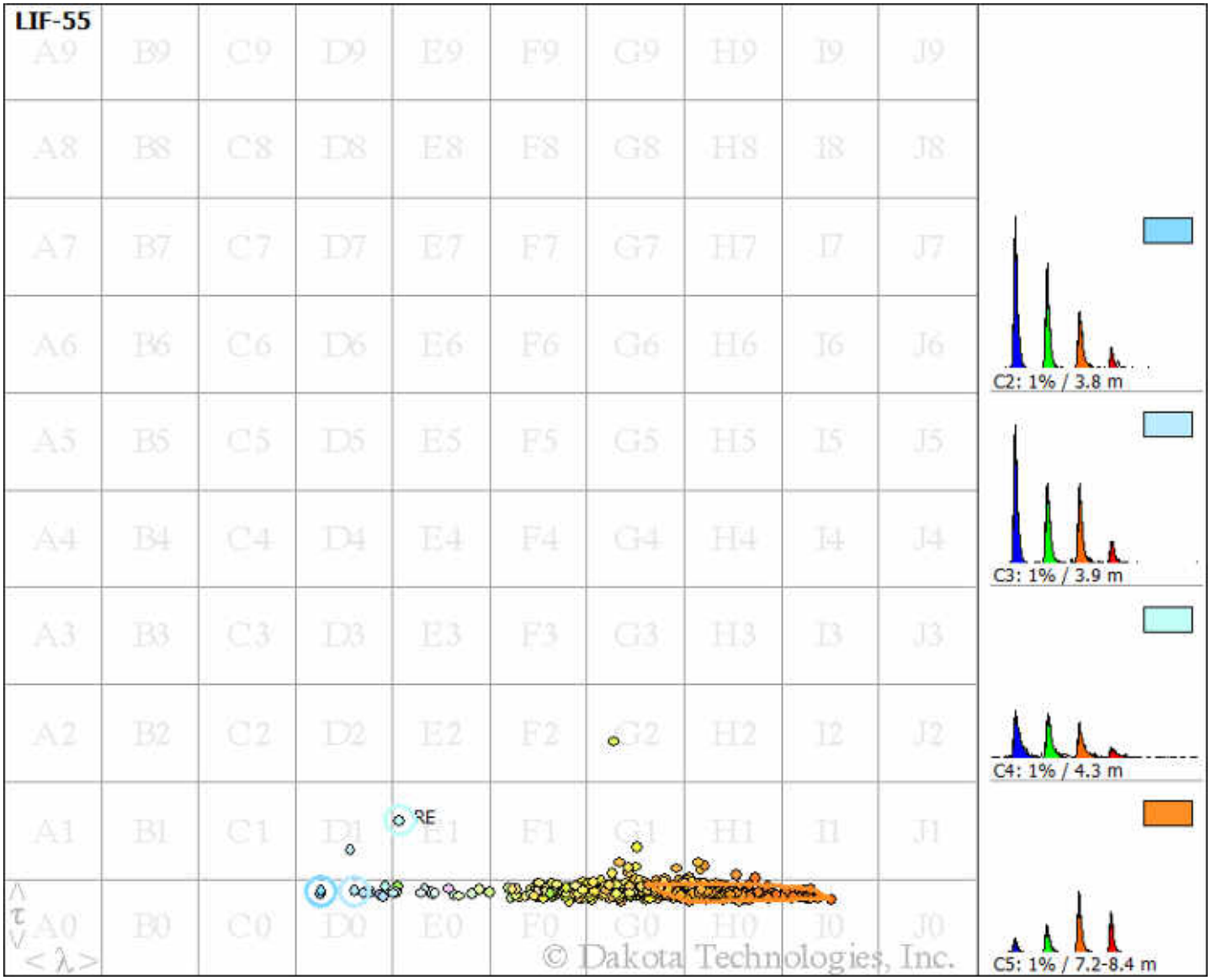
LIF54 log



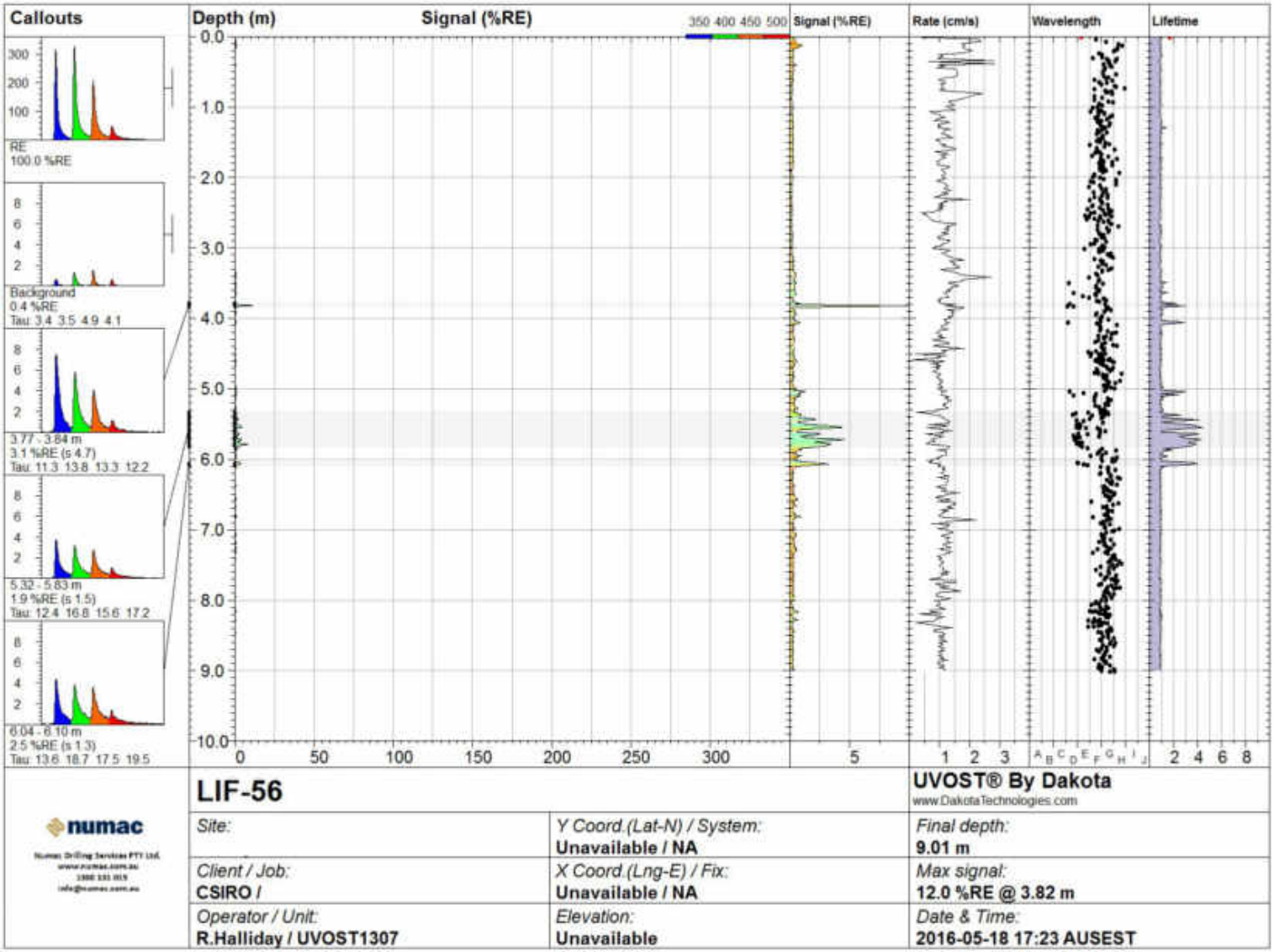
LIF54 wavelength–lifetime matrix


Callouts
Depth (m)
Signal (%RE)
350 400 450 500
Signal (%RE)
Rate (cm/s)
Wavelength
Lifetime
RE
100.0 %RE
3.78 m
1.4 %RE
Tau: 3.4 3.5 4.9 4.1
3.91 m
1.4 %RE
very unusual - short tau
4.28 m
0.9 %RE
Tau: 7.6 5.9 7.4 10.5
7.18 - 8.41 m
0.7 %RE (s 0.2)
Tau: 3.0 4.4 3.8 3.5
LIF-55
UVOST® By Dakota
www.DakotaTechnologies.com
numac
Site:
Y Coord.(Lat-N) / System:
Unavailable / NA
Final depth:
9.01 m
Client / Job:
CSIRO /
X Coord.(Lng-E) / Fix:
Unavailable / NA
Max signal:
1.8 %RE @ 3.94 m
Operator / Unit:
R.Halliday / UVOST1307
Elevation:
Unavailable
Date & Time:
2016-05-18 16:02 AUSEST

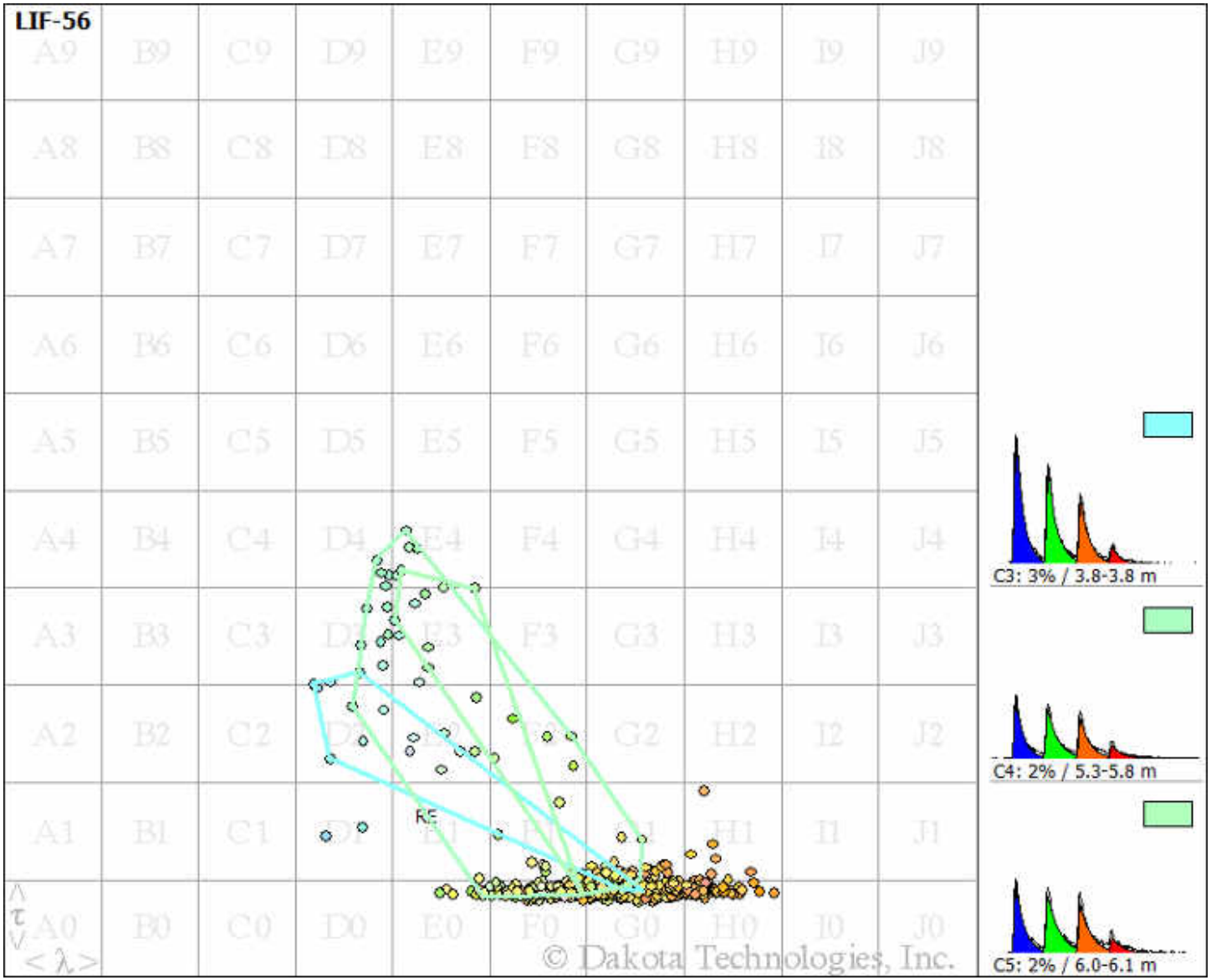
LIF55 log



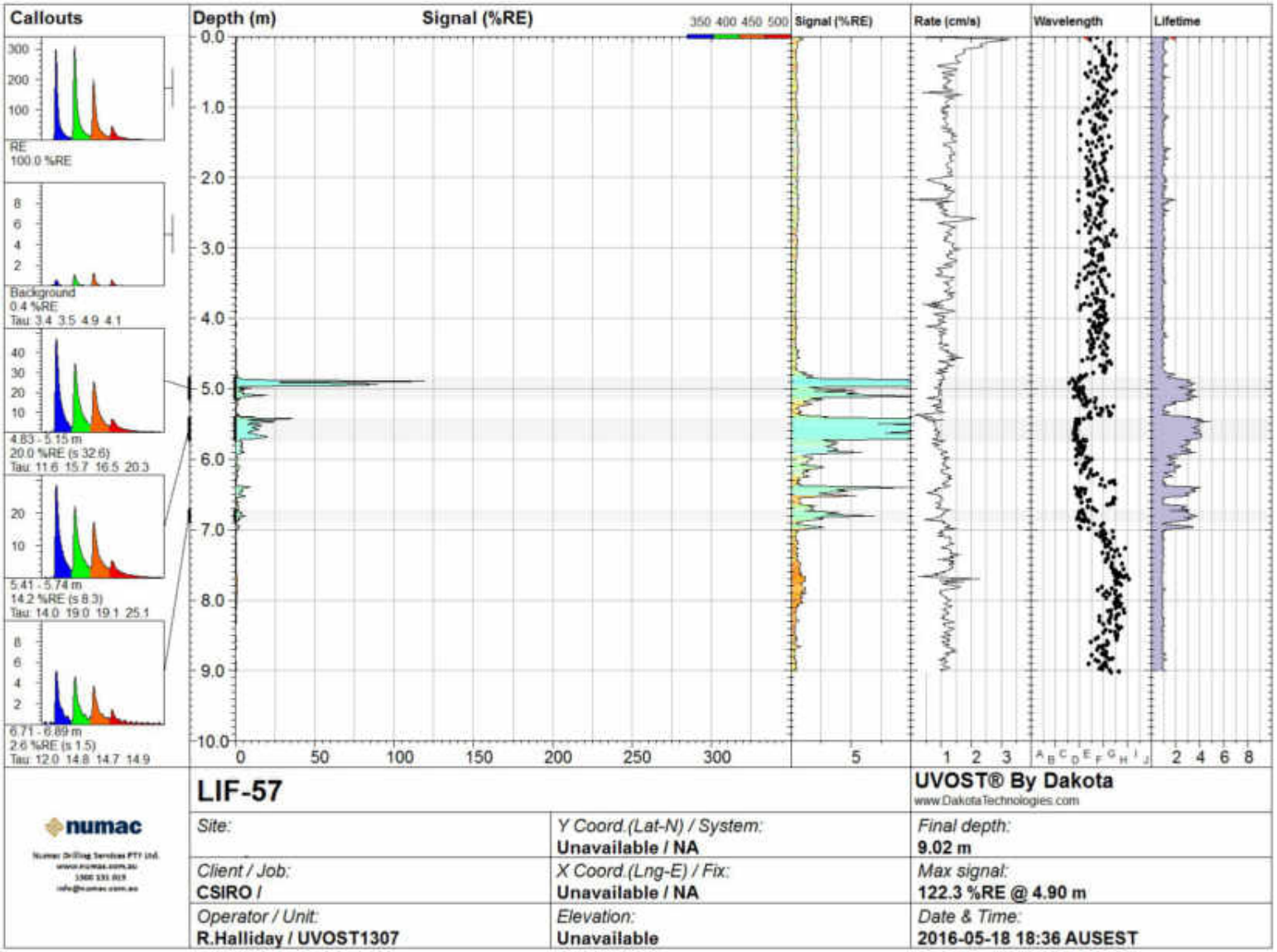
LIF55 wavelength–lifetime matrix


Callouts
Depth (m)
Signal (%RE)
350 400 450 500
Signal (%RE)
Rate (cm/s)
Wavelength
Lifetime
RE
100.0 %RE
Background
0.4 %RE
Tau: 3.4 3.5 4.9 4.1
3.77 - 3.84 m
3.1 %RE (s 4.7)
Tau: 11.3 13.8 13.3 12.2
5.32 - 5.83 m
1.9 %RE (s 1.5)
Tau: 12.4 16.8 15.6 17.2
6.04 - 6.10 m
2.5 %RE (s 1.3)
Tau: 13.6 18.7 17.5 19.5
LIF-56
UVOST® By Dakota
www.DakotaTechnologies.com
numac
Site:
Y Coord.(Lat-N) / System:
Unavailable / NA
Final depth:
9.01 m
Client / Job:
CSIRO /
X Coord.(Lng-E) / Fix:
Unavailable / NA
Max signal:
12.0 %RE @ 3.82 m
Operator / Unit:
R.Halliday / UVOST1307
Elevation:
Unavailable
Date & Time:
2016-05-18 17:23 AUSEST

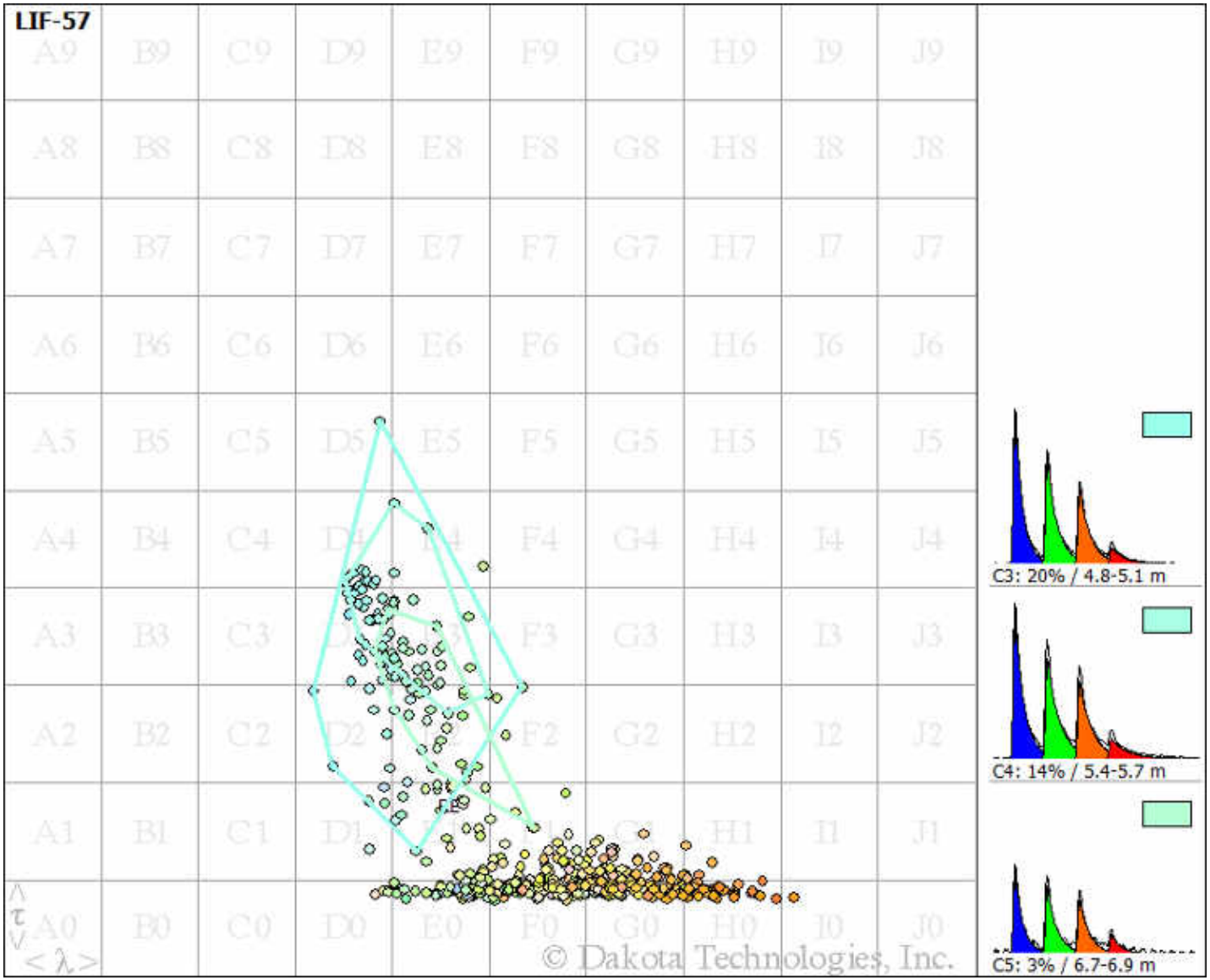
LIF56-C log



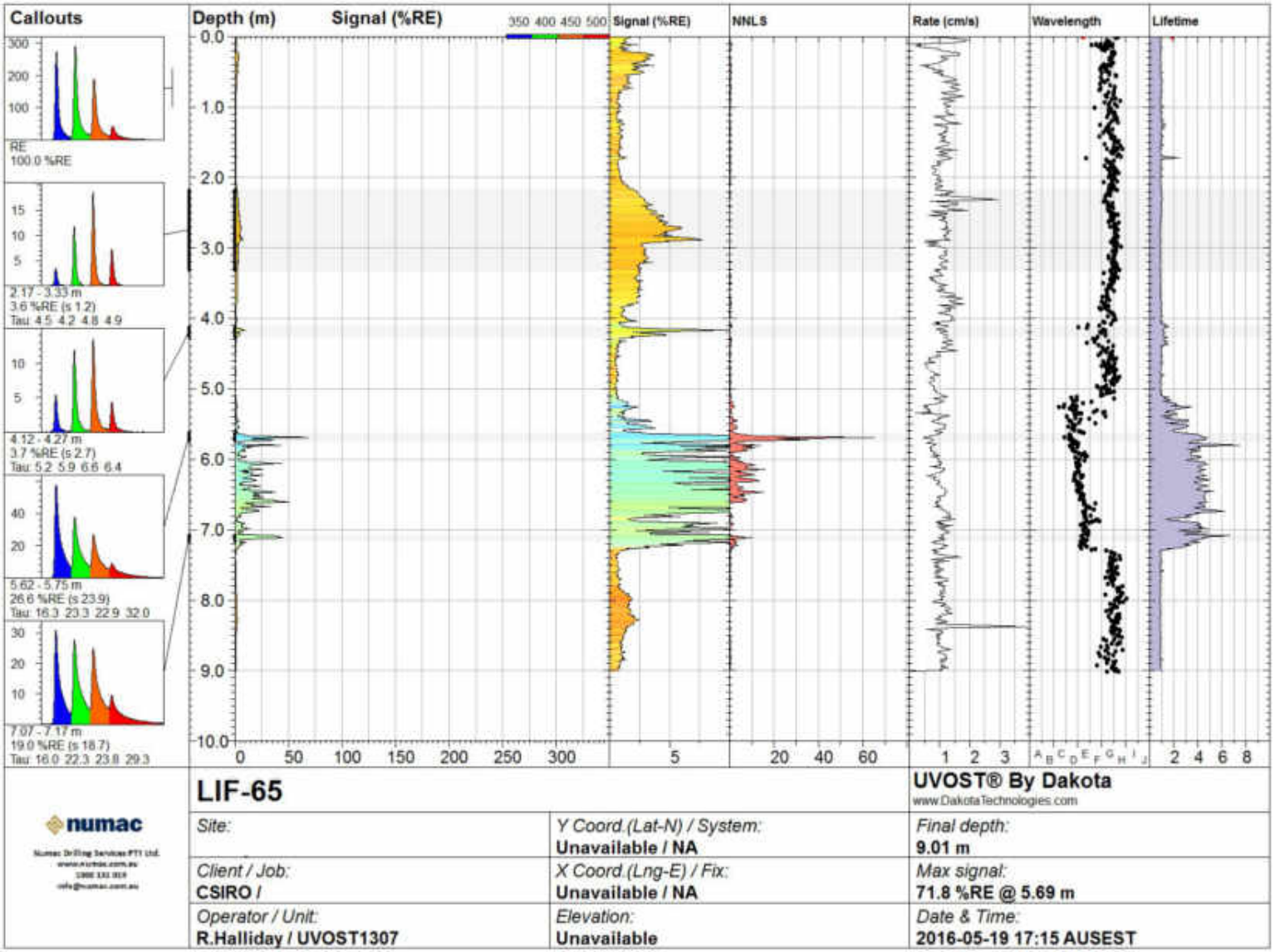
LIF56-C wavelength–lifetime matrix


Callouts
Depth (m)
Signal (%RE)
350 400 450 500
Signal (%RE)
Rate (cm/s)
Wavelength
Lifetime
RE
100.0 %RE
Background
0.4 %RE
Tau: 3.4 3.5 4.9 4.1
4.83 - 5.15 m
20.0 %RE (s 32.6)
Tau: 11.6 15.7 16.5 20.3
5.41 - 5.74 m
14.2 %RE (s 8.3)
Tau: 14.0 19.0 19.1 25.1
6.71 - 6.89 m
2.6 %RE (s 1.5)
Tau: 12.0 14.8 14.7 14.9
LIF-57
UVOST® By Dakota
www.DakotaTechnologies.com
numac
Site:
Y Coord.(Lat-N) / System:
Unavailable / NA
Final depth:
9.02 m
Client / Job:
CSIRO /
X Coord.(Lng-E) / Fix:
Unavailable / NA
Max signal:
122.3 %RE @ 4.90 m
Operator / Unit:
R.Halliday / UVOST1307
Elevation:
Unavailable
Date & Time:
2016-05-18 18:36 AUSEST

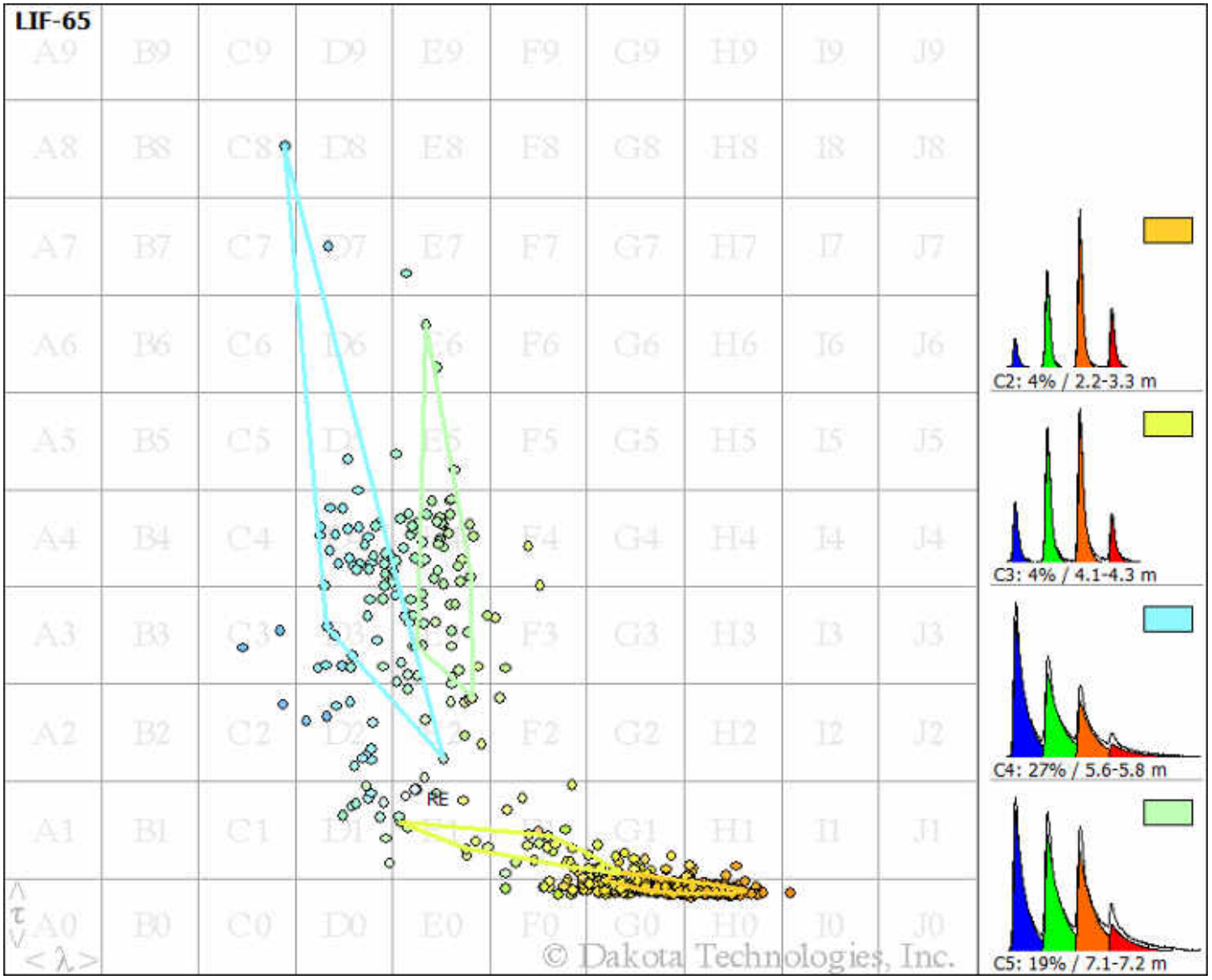
LIF57-C log



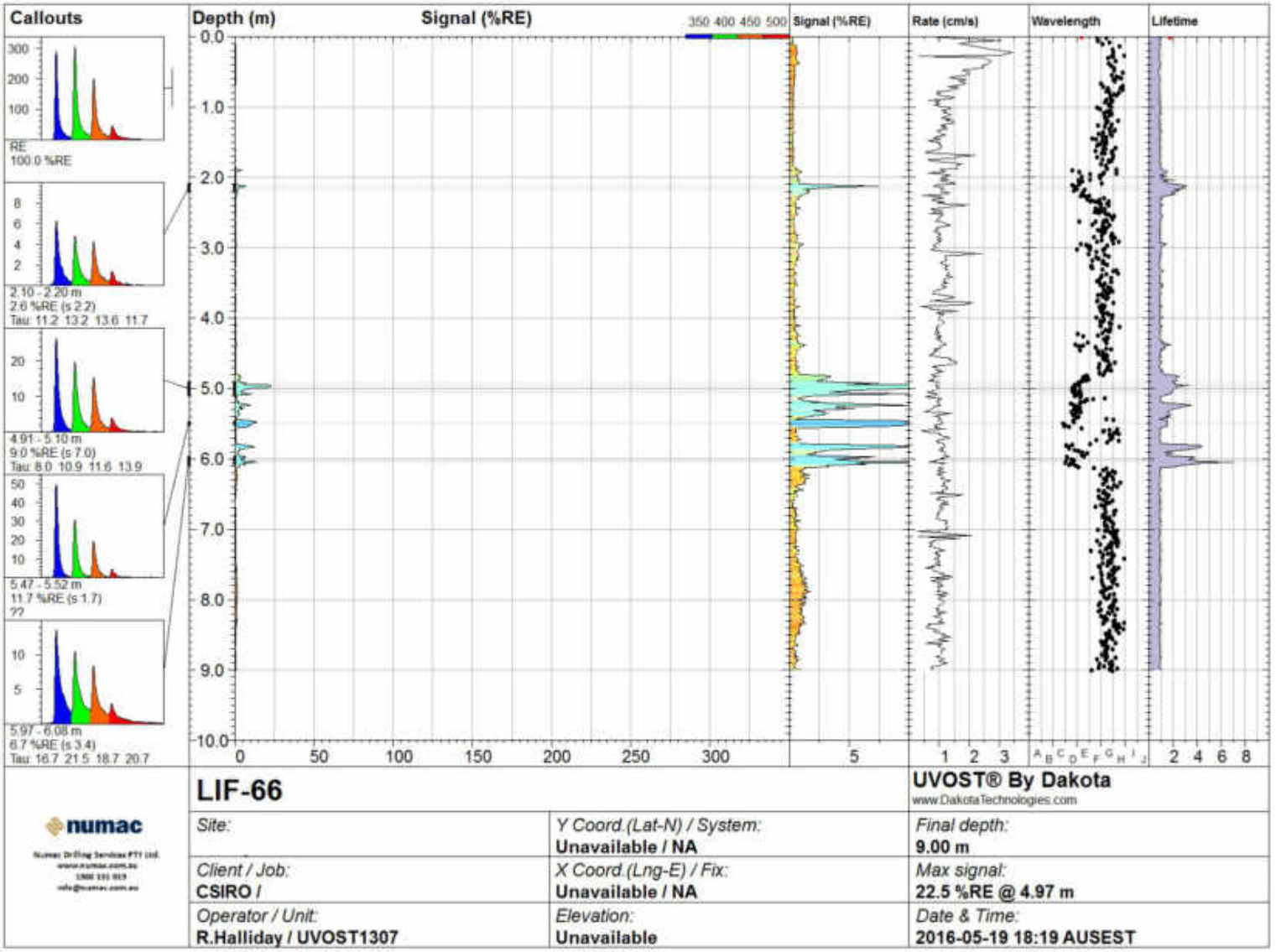
LIF57-C wavelength–lifetime matrix


Callouts
Depth (m)
Signal (%RE)
350 400 450 500
Signal (%RE)
NNLS
Rate (cm/s)
Wavelength
Lifetime
RE
100.0 %RE
2.17 - 3.33 m
3.6 %RE (s 1.2)
Tau: 4.5 4.2 4.8 4.9
4.12 - 4.27 m
3.7 %RE (s 2.7)
Tau: 5.2 5.9 6.6 6.4
5.62 - 5.75 m
26.6 %RE (s 23.9)
Tau: 16.3 23.3 22.9 32.0
7.07 - 7.17 m
19.0 %RE (s 18.7)
Tau: 16.0 22.3 23.8 29.3
LIF-65
UVOST® By Dakota
www.DakotaTechnologies.com
numac
Site:
Y Coord.(Lat-N) / System:
Unavailable / NA
Final depth:
9.01 m
Client / Job:
CSIRO /
X Coord.(Lng-E) / Fix:
Unavailable / NA
Max signal:
71.8 %RE @ 5.69 m
Operator / Unit:
R.Halliday / UVOST1307
Elevation:
Unavailable
Date & Time:
2016-05-19 17:15 AUSEST

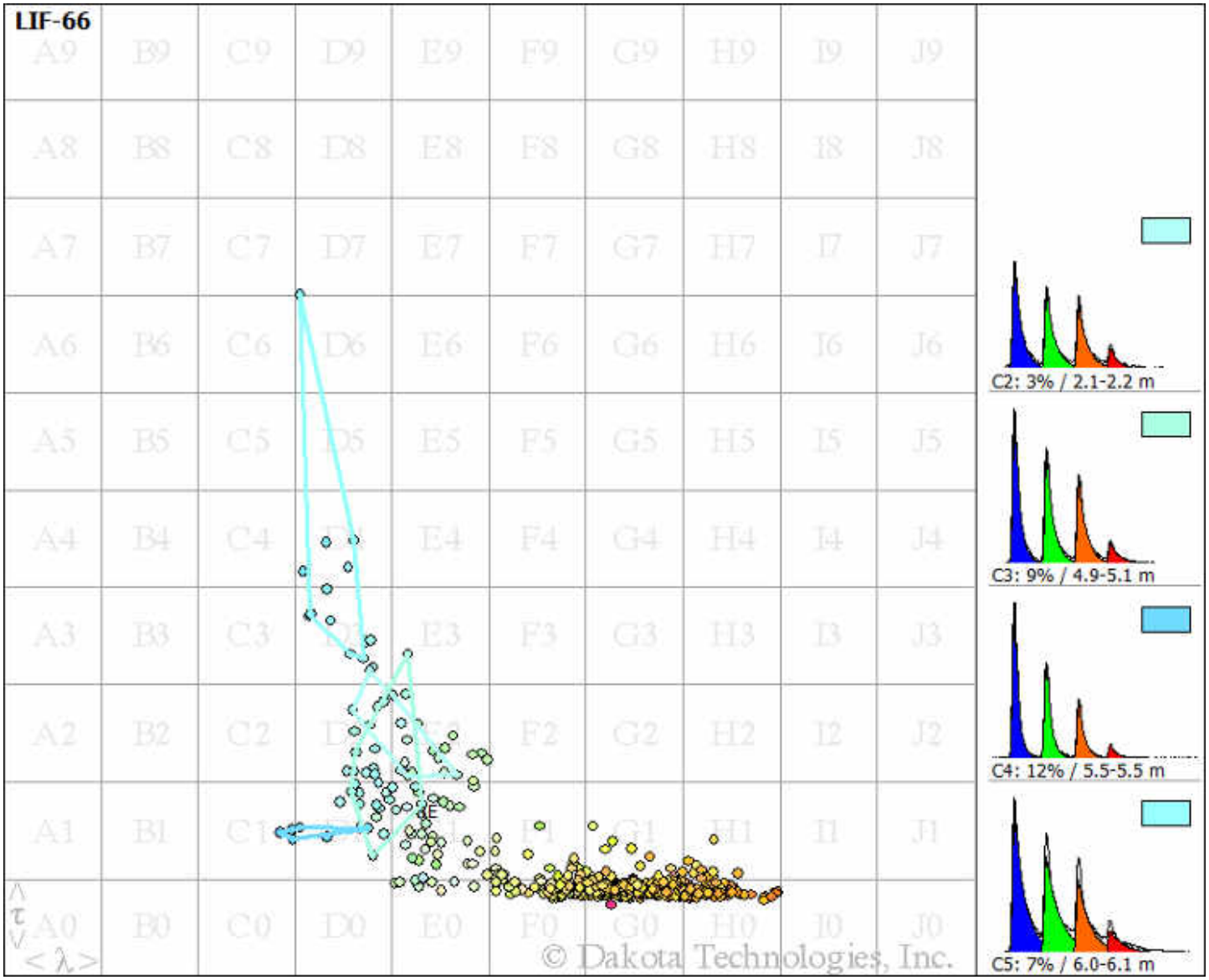
LIF65 log



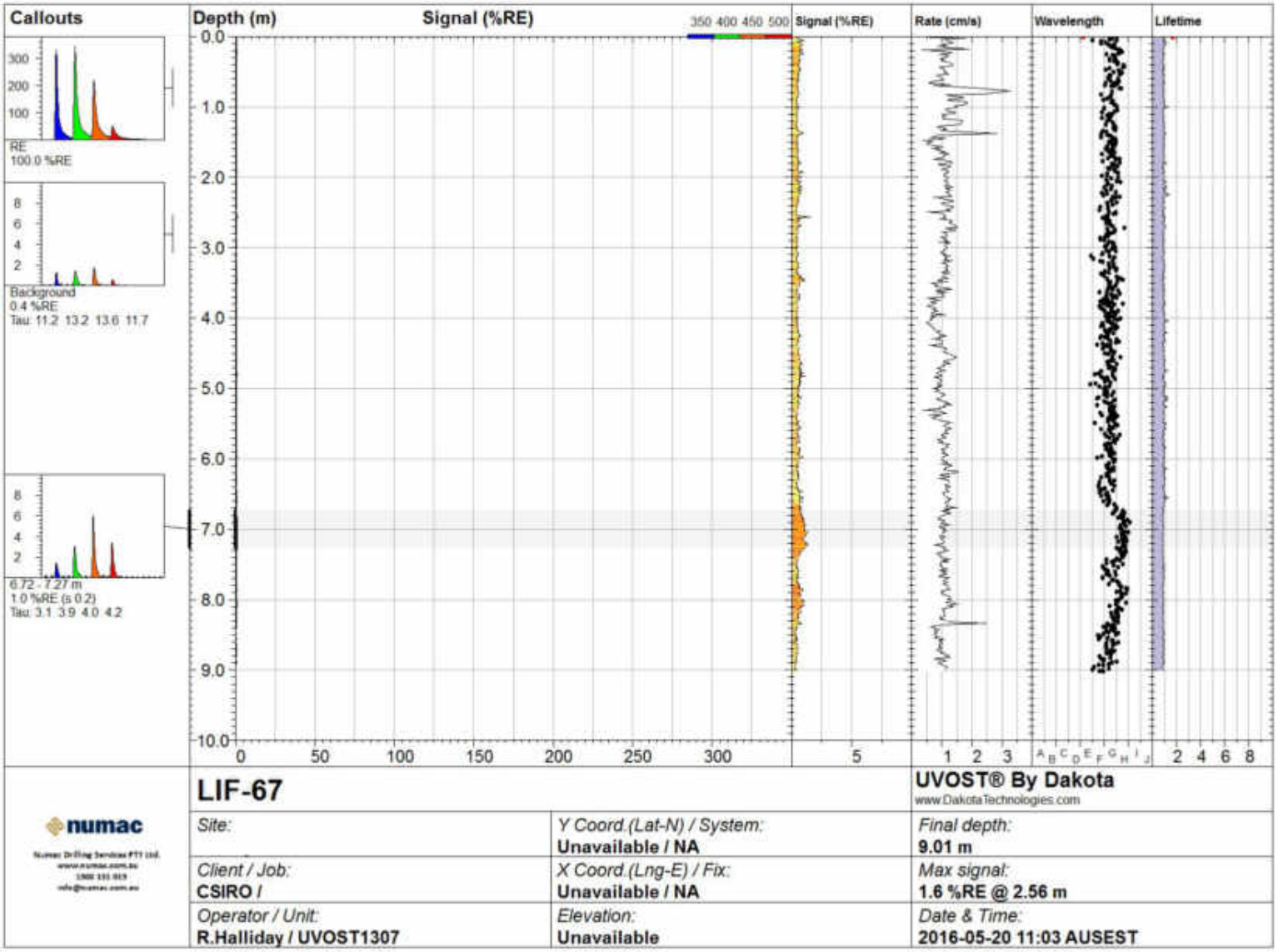
LIF65 wavelength–lifetime matrix


Callouts
Depth (m)
Signal (%RE)
350 400 450 500
Signal (%RE)
Rate (cm/s)
Wavelength
Lifetime
RE
100.0 %RE
2.10 - 2.20 m
2.6 %RE (s 2.2)
Tau: 11.2 13.2 13.6 11.7
4.91 - 5.10 m
9.0 %RE (s 7.0)
Tau: 8.0 10.9 11.6 13.9
5.47 - 5.52 m
11.7 %RE (s 1.7)
??
5.97 - 6.08 m
6.7 %RE (s 3.4)
Tau: 16.7 21.5 18.7 20.7
LIF-66
UVOST® By Dakota
www.DakotaTechnologies.com
numac
Site:
Y Coord.(Lat-N) / System:
Unavailable / NA
Final depth:
9.00 m
Client / Job:
CSIRO /
X Coord.(Lng-E) / Fix:
Unavailable / NA
Max signal:
22.5 %RE @ 4.97 m
Operator / Unit:
R.Halliday / UVOST1307
Elevation:
Unavailable
Date & Time:
2016-05-19 18:19 AUSEST

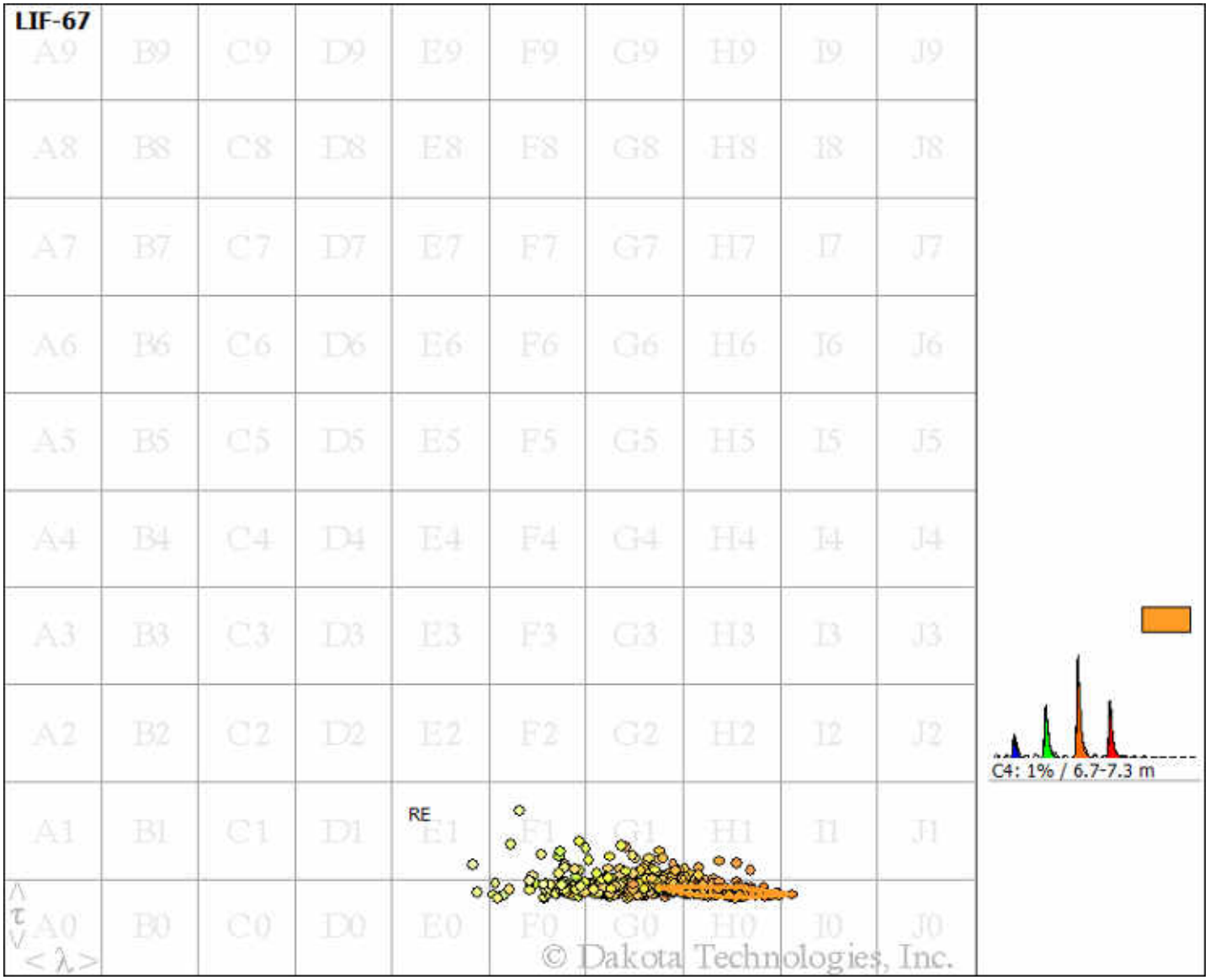
LIF66-C log



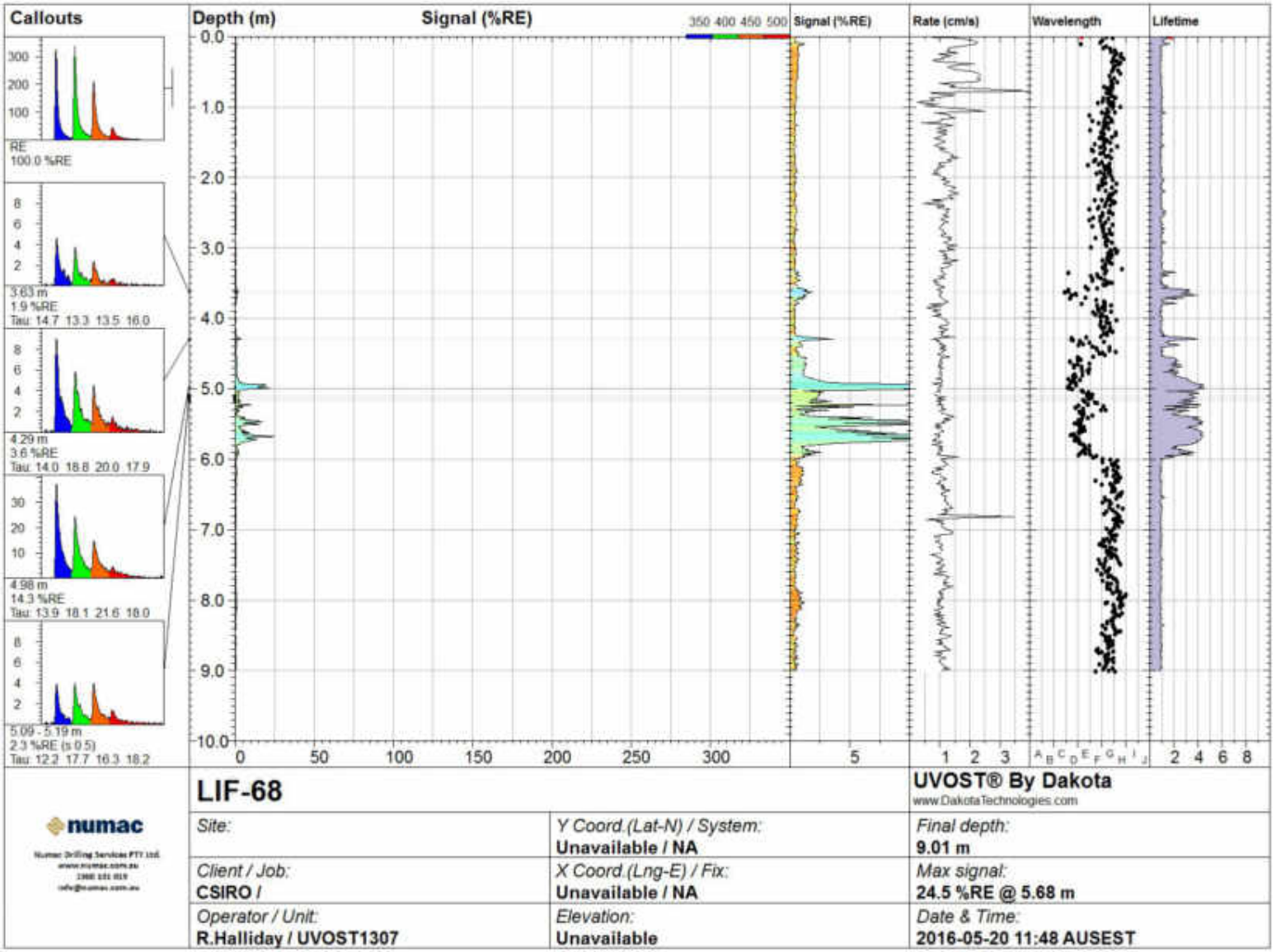
LIF66-C wavelength–lifetime matrix


Callouts
Depth (m)
Signal (%RE)
350 400 450 500
Signal (%RE)
Rate (cm/s)
Wavelength
Lifetime
RE
100.0 %RE
Background
0.4 %RE
Tau: 11.2 13.2 13.6 11.7
6.72 - 7.27 m
1.0 %RE (s 0.2)
Tau: 3.1 3.9 4.0 4.2
LIF-67
UVOST® By Dakota
www.DakotaTechnologies.com
numac
Site:
Y Coord.(Lat-N) / System:
Unavailable / NA
Final depth:
9.01 m
Client / Job:
CSIRO /
X Coord.(Lng-E) / Fix:
Unavailable / NA
Max signal:
1.6 %RE @ 2.56 m
Operator / Unit:
R.Halliday / UVOST1307
Elevation:
Unavailable
Date & Time:
2016-05-20 11:03 AUSEST

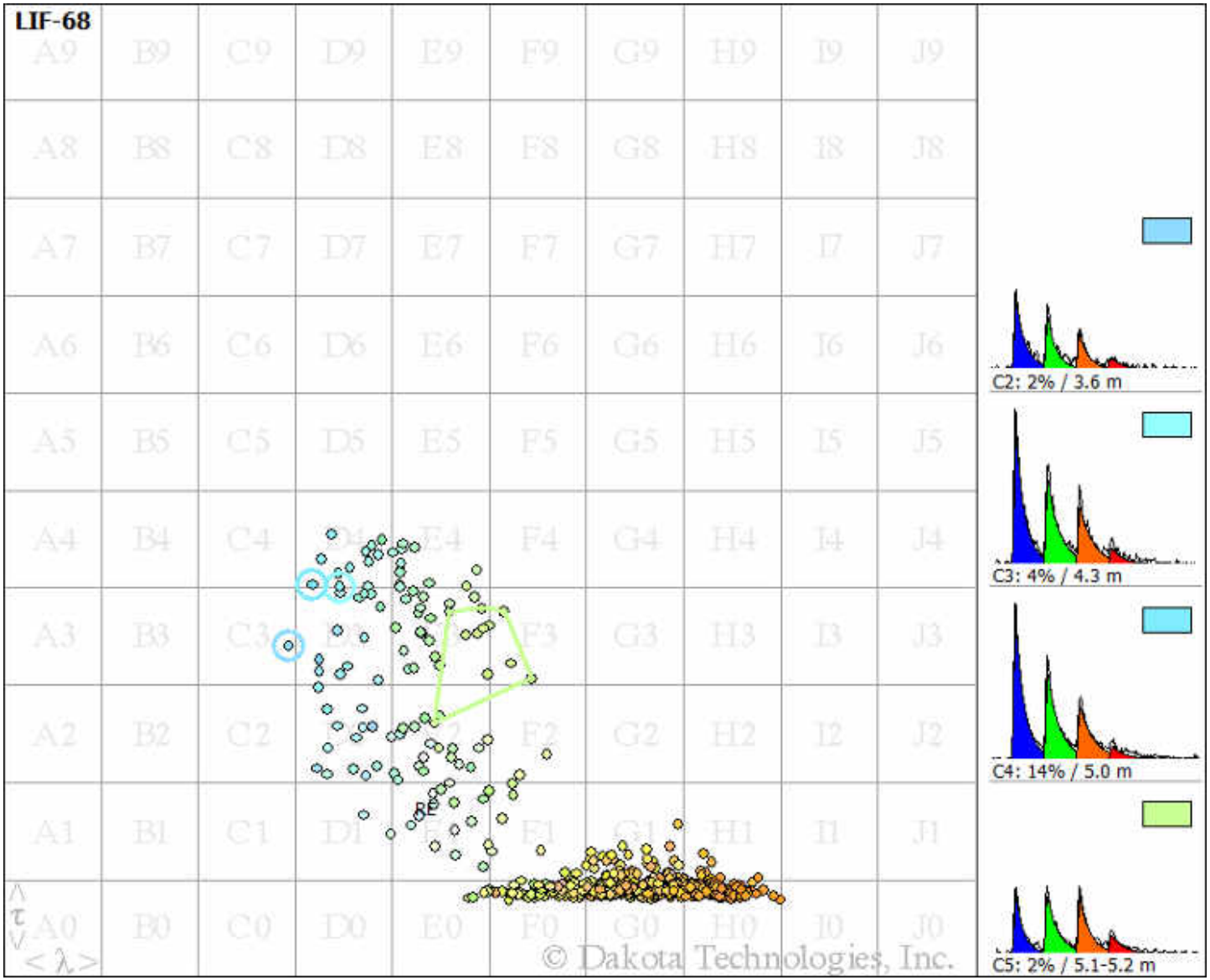
LIF67 log



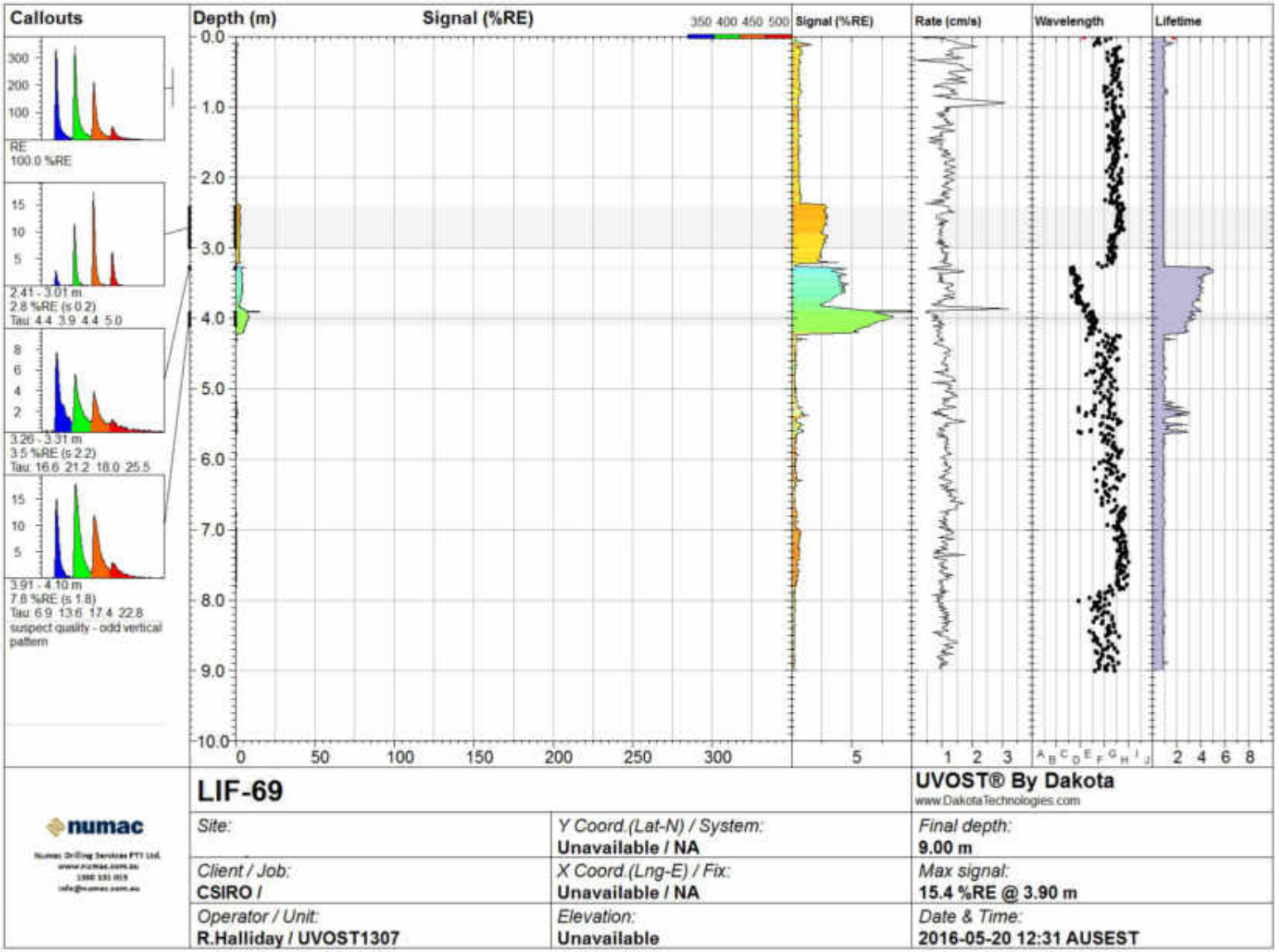
LIF67 wavelength–lifetime matrix


Callouts
Depth (m)
Signal (%RE)
350 400 450 500
Signal (%RE)
Rate (cm/s)
Wavelength
Lifetime
RE
100.0 %RE
3.63 m
1.9 %RE
Tau: 14.7 13.3 13.5 16.0
4.29 m
3.6 %RE
Tau: 14.0 18.6 20.0 17.9
4.98 m
14.3 %RE
Tau: 13.9 18.1 21.6 18.0
5.09 - 5.19 m
2.3 %RE (s 0.5)
Tau: 12.2 17.7 16.3 18.2
LIF-68
UVOST® By Dakota
www.DakotaTechnologies.com
numac
Site:
Y Coord.(Lat-N) / System:
Unavailable / NA
Final depth:
9.01 m
Client / Job:
CSIRO /
X Coord.(Lng-E) / Fix:
Unavailable / NA
Max signal:
24.5 %RE @ 5.68 m
Operator / Unit:
R.Halliday / UVOST1307
Elevation:
Unavailable
Date & Time:
2016-05-20 11:48 AUSEST

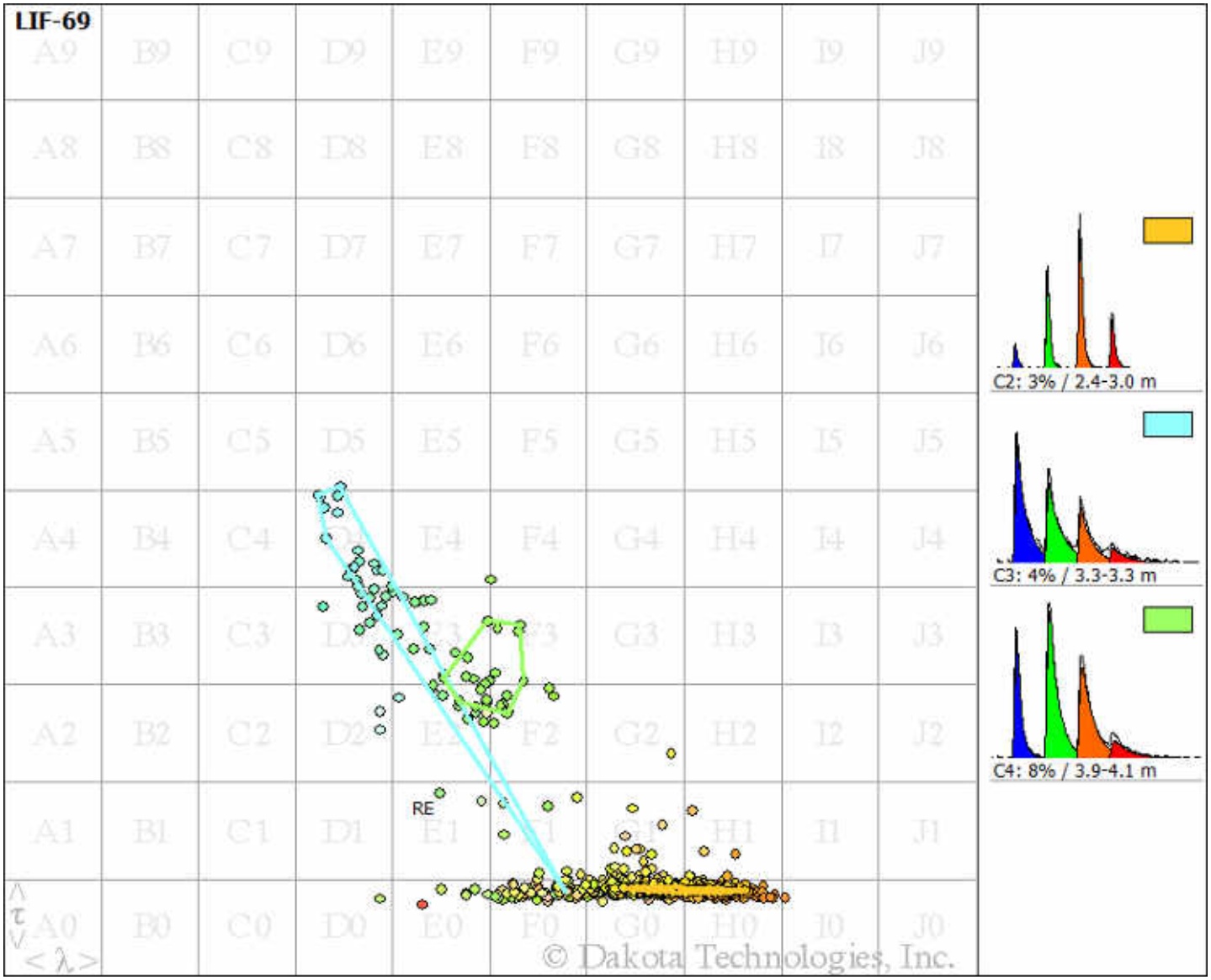
LIF68-C log



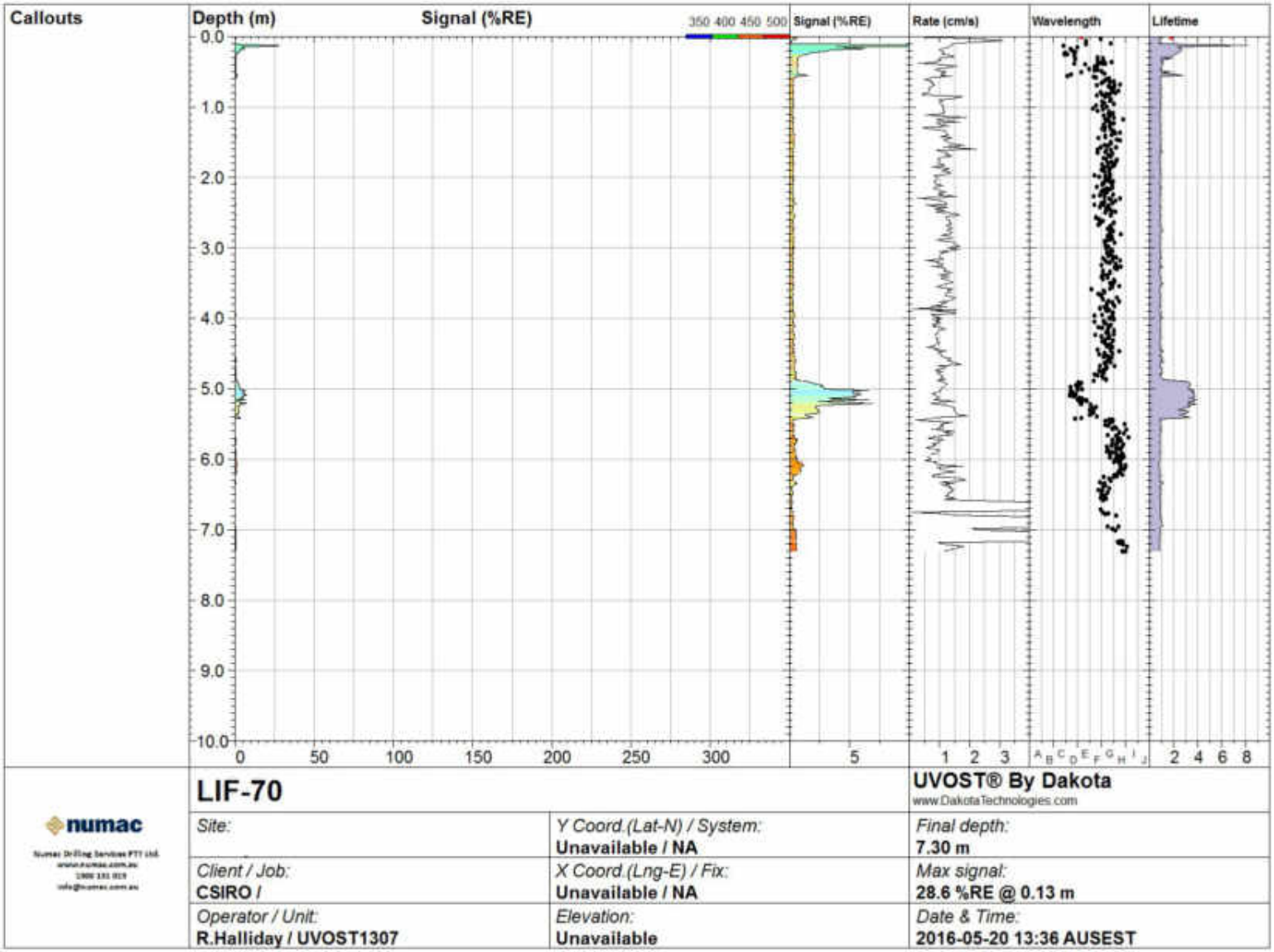
LIF68-C wavelength–lifetime matrix


Callouts
Depth (m)
Signal (%RE)
350 400 450 500
Signal (%RE)
Rate (cm/s)
Wavelength
Lifetime
RE
100.0 %RE
2.41 - 3.01 m
2.8 %RE (s 0.2)
Tau: 4.4 3.9 4.4 5.0
3.26 - 3.31 m
3.5 %RE (s 2.2)
Tau: 16.6 21.2 18.0 25.5
3.91 - 4.10 m
7.8 %RE (s 1.8)
Tau: 6.9 13.6 17.4 22.8
suspect quality - odd vertical pattern
LIF-69
UVOST® By Dakota
www.DakotaTechnologies.com
numac
Site:
Y Coord.(Lat-N) / System:
Unavailable / NA
Final depth:
9.00 m
Client / Job:
CSIRO /
X Coord.(Lng-E) / Fix:
Unavailable / NA
Max signal:
15.4 %RE @ 3.90 m
Operator / Unit:
R.Halliday / UVOST1307
Elevation:
Unavailable
Date & Time:
2016-05-20 12:31 AUSEST

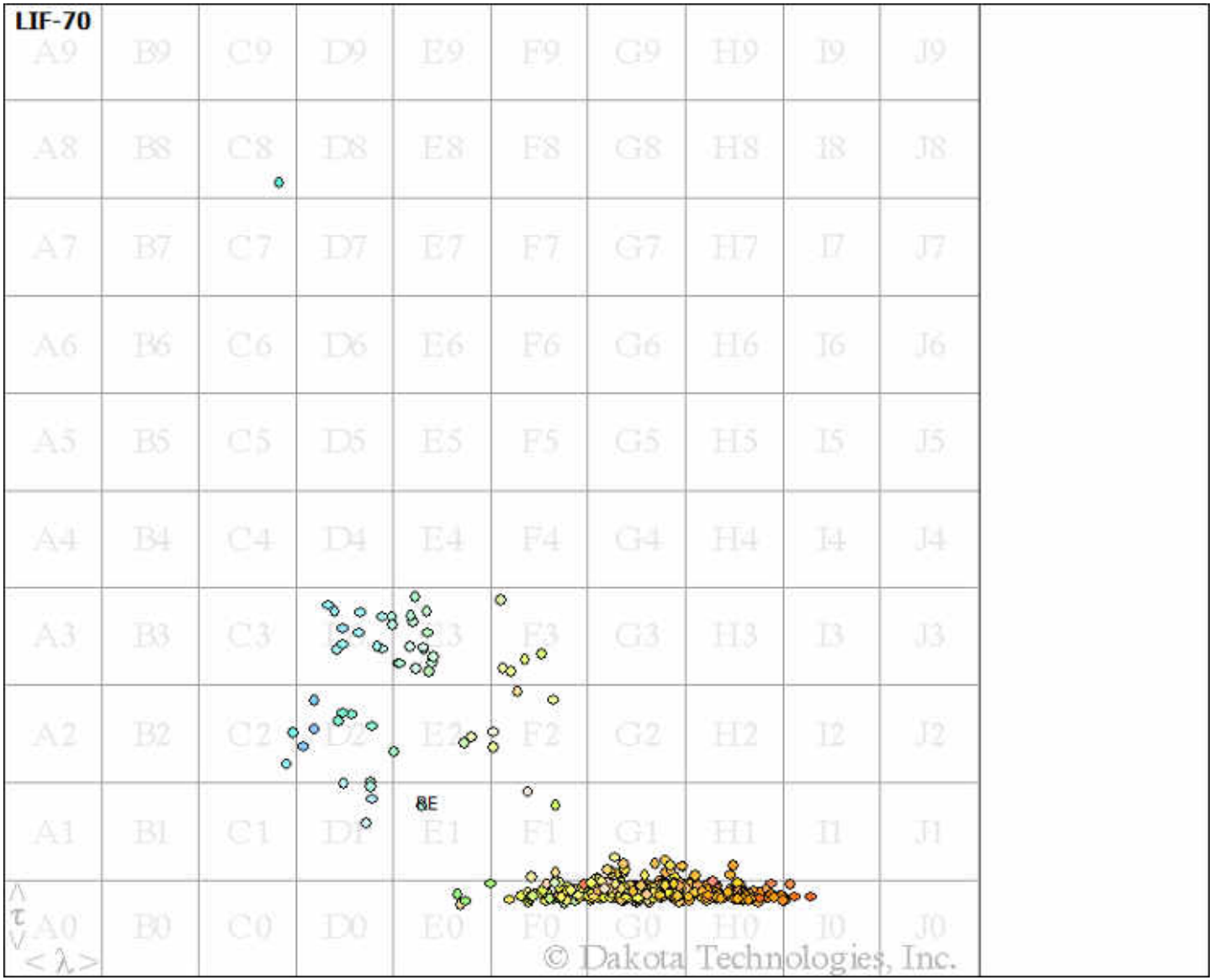
LIF69-C log



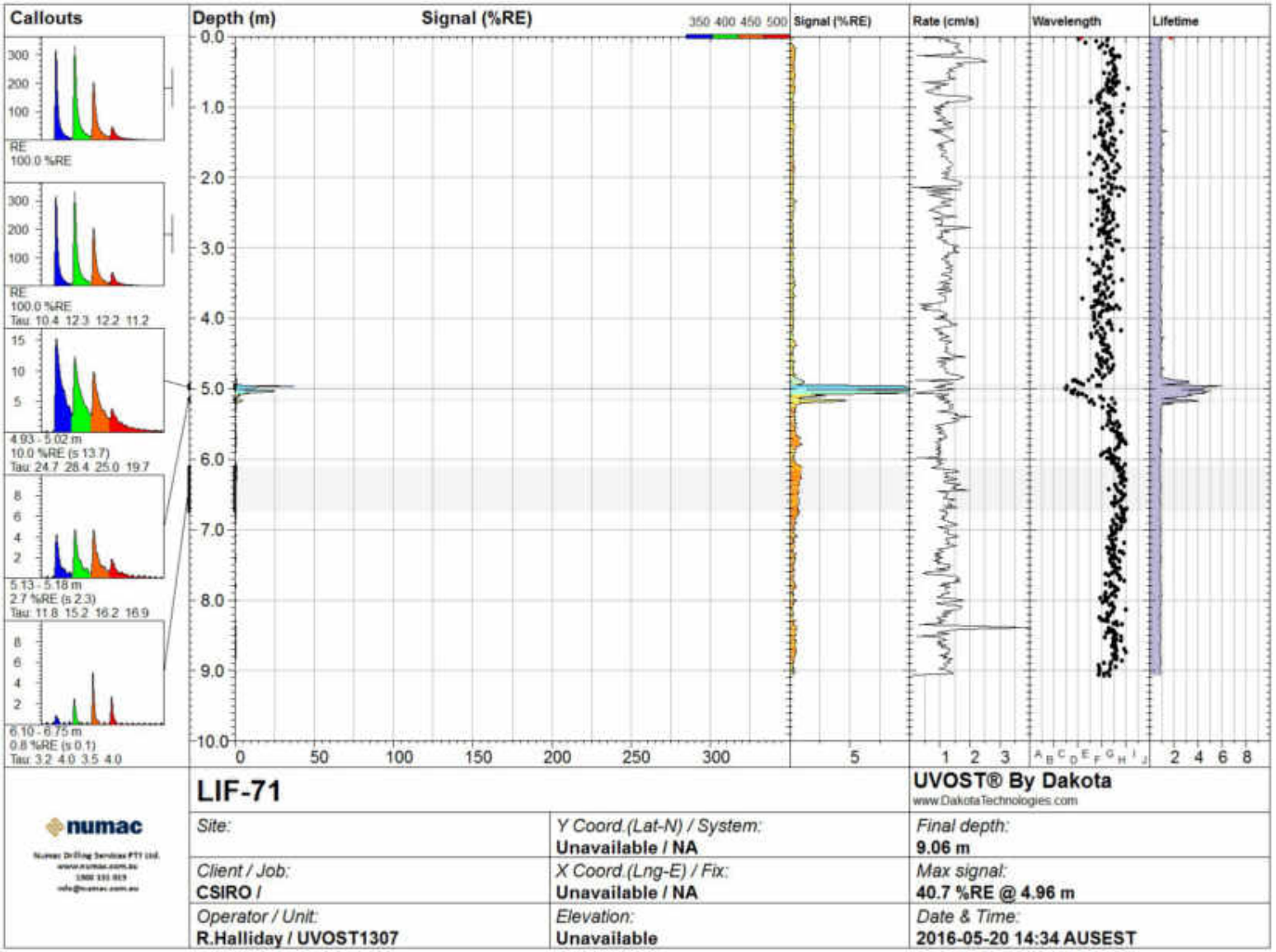
LIF69-C wavelength–lifetime matrix


Callouts
Depth (m)
Signal (%RE)
350 400 450 500
Signal (%RE)
Rate (cm/s)
Wavelength
Lifetime
0.0
1.0
2.0
3.0
4.0
5.0
6.0
7.0
8.0
9.0
10.0
0 50 100 150 200 250 300
5
1 2 3
A B C D E F G H I J
2 4 6 8
numac
LIF-70
UVOST® By Dakota
www.DakotaTechnologies.com
Site:
Y Coord.(Lat-N) / System:
Unavailable / NA
Final depth:
7.30 m
Client / Job:
CSIRO /
X Coord.(Lng-E) / Fix:
Unavailable / NA
Max signal:
28.6 %RE @ 0.13 m
Operator / Unit:
R.Halliday / UVOST1307
Elevation:
Unavailable
Date & Time:
2016-05-20 13:36 AUSEST

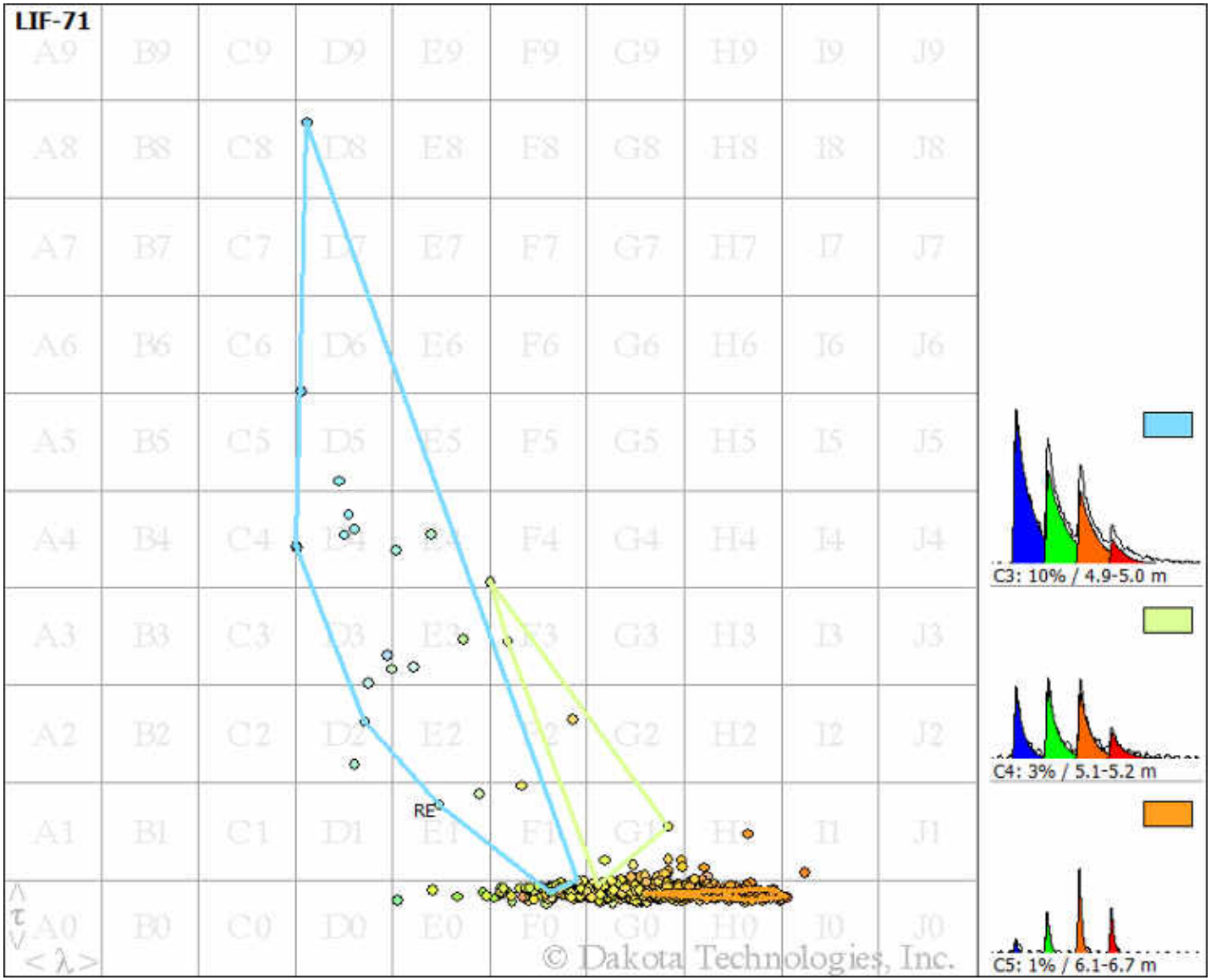
LIF70 log



LIF70 wavelength–lifetime matrix

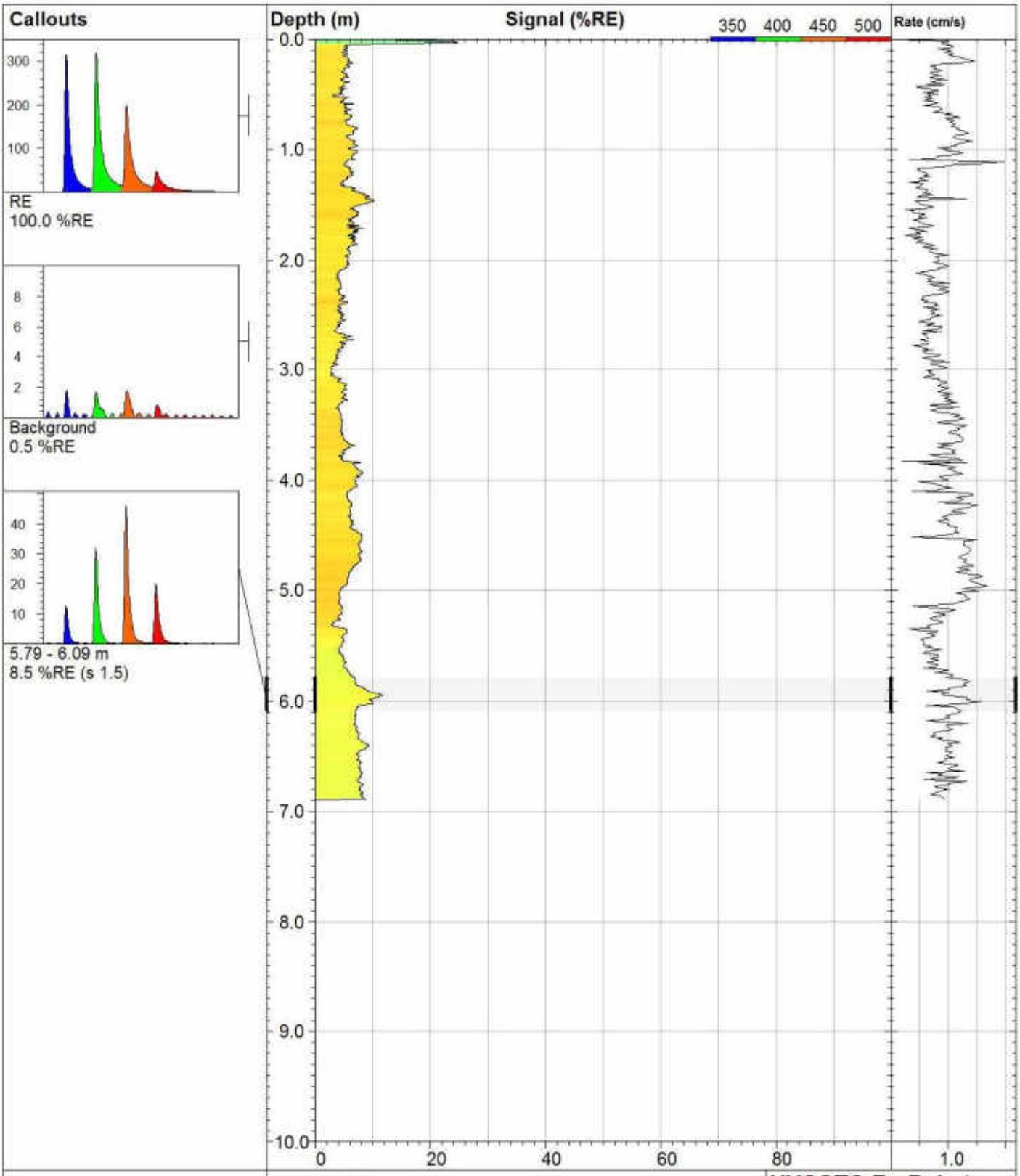

Callouts
Depth (m)
Signal (%RE)
350 400 450 500
Signal (%RE)
Rate (cm/s)
Wavelength
Lifetime
RE
100.0 %RE
RE
100.0 %RE
Tau: 10.4 12.3 12.2 11.2
4.93 - 5.02 m
10.0 %RE (s 13.7)
Tau: 24.7 28.4 25.0 19.7
5.13 - 5.18 m
2.7 %RE (s 2.3)
Tau: 11.8 15.2 16.2 16.9
6.10 - 6.75 m
0.8 %RE (s 0.1)
Tau: 3.2 4.0 3.5 4.0
LIF-71
UVOST® By Dakota
www.DakotaTechnologies.com
numac
Site:
Y Coord.(Lat-N) / System:
Unavailable / NA
Final depth:
9.06 m
Client / Job:
CSIRO /
X Coord.(Lng-E) / Fix:
Unavailable / NA
Max signal:
40.7 %RE @ 4.96 m
Operator / Unit:
R.Halliday / UVOST1307
Elevation:
Unavailable
Date & Time:
2016-05-20 14:34 AUSEST

LIF71-B log



LIF71-B wavelength–lifetime matrix

LIF profiles from the industrial site



numac

Numac Drilling Services PTY Ltd.
www.numac.com.au
1300 131 019
info@numac.com.au

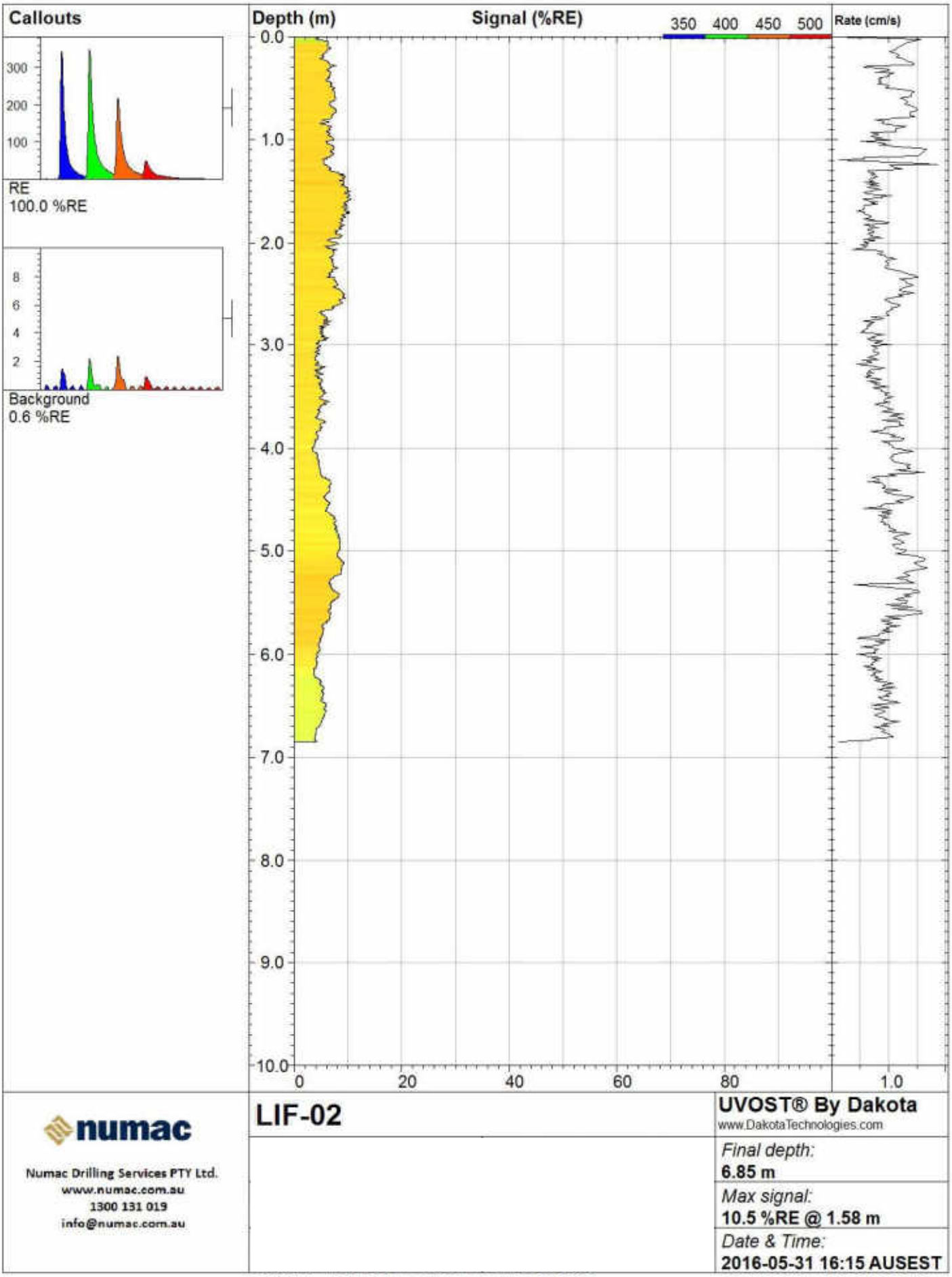
LIF-01

UVOST® By Dakota
www.DakotaTechnologies.com

Final depth:
6.89 m

Max signal:
24.8 %RE @ 0.03 m

Date & Time:
2016-05-31 15:36 AUSEST



numac

Numac Drilling Services PTY Ltd.
www.numac.com.au
1300 131 019
info@numac.com.au

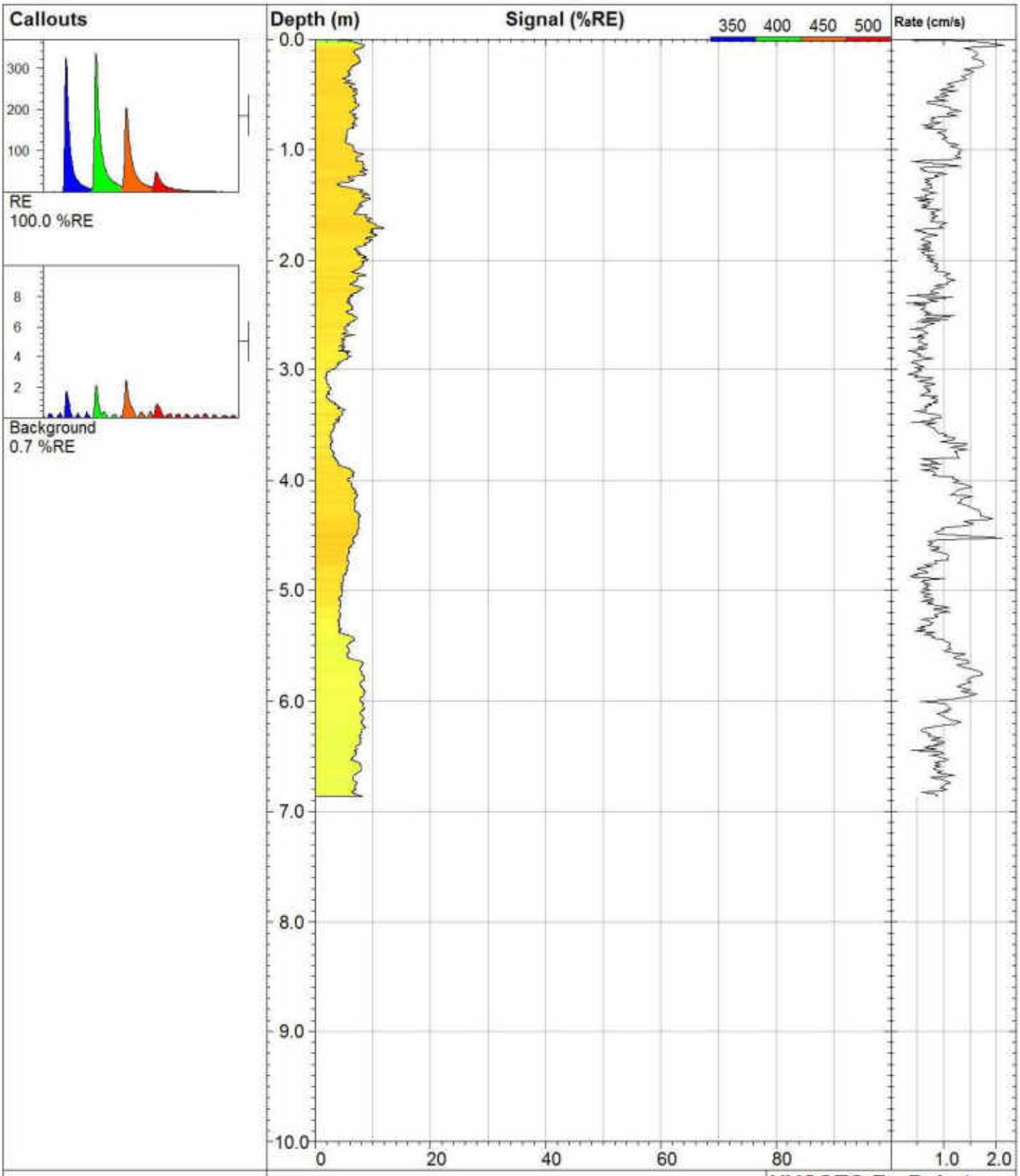
LIF-02

UVOST® By Dakota
www.DakotaTechnologies.com

Final depth:
6.85 m

Max signal:
10.5 %RE @ 1.58 m

Date & Time:
2016-05-31 16:15 AUSEST



numac

Numac Drilling Services PTY Ltd.
www.numac.com.au
1300 131 019
info@numac.com.au

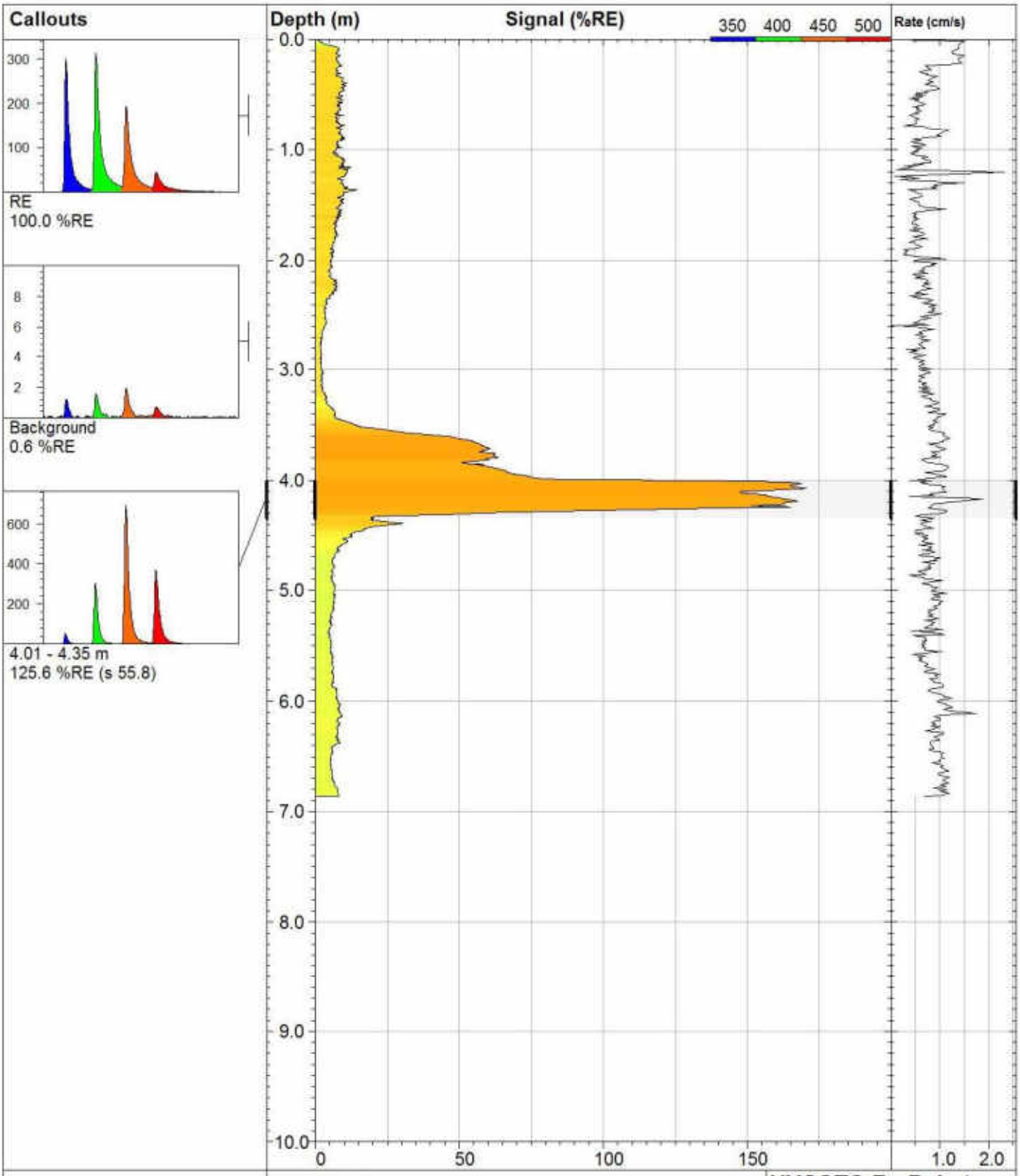
LIF-03

UVOST® By Dakota
www.DakotaTechnologies.com

Final depth:
6.86 m

Max signal:
12.0 %RE @ 1.71 m

Date & Time:
2016-05-31 16:48 AUSEST



numac

Numac Drilling Services PTY Ltd.
www.numac.com.au
1300 131 019
info@numac.com.au

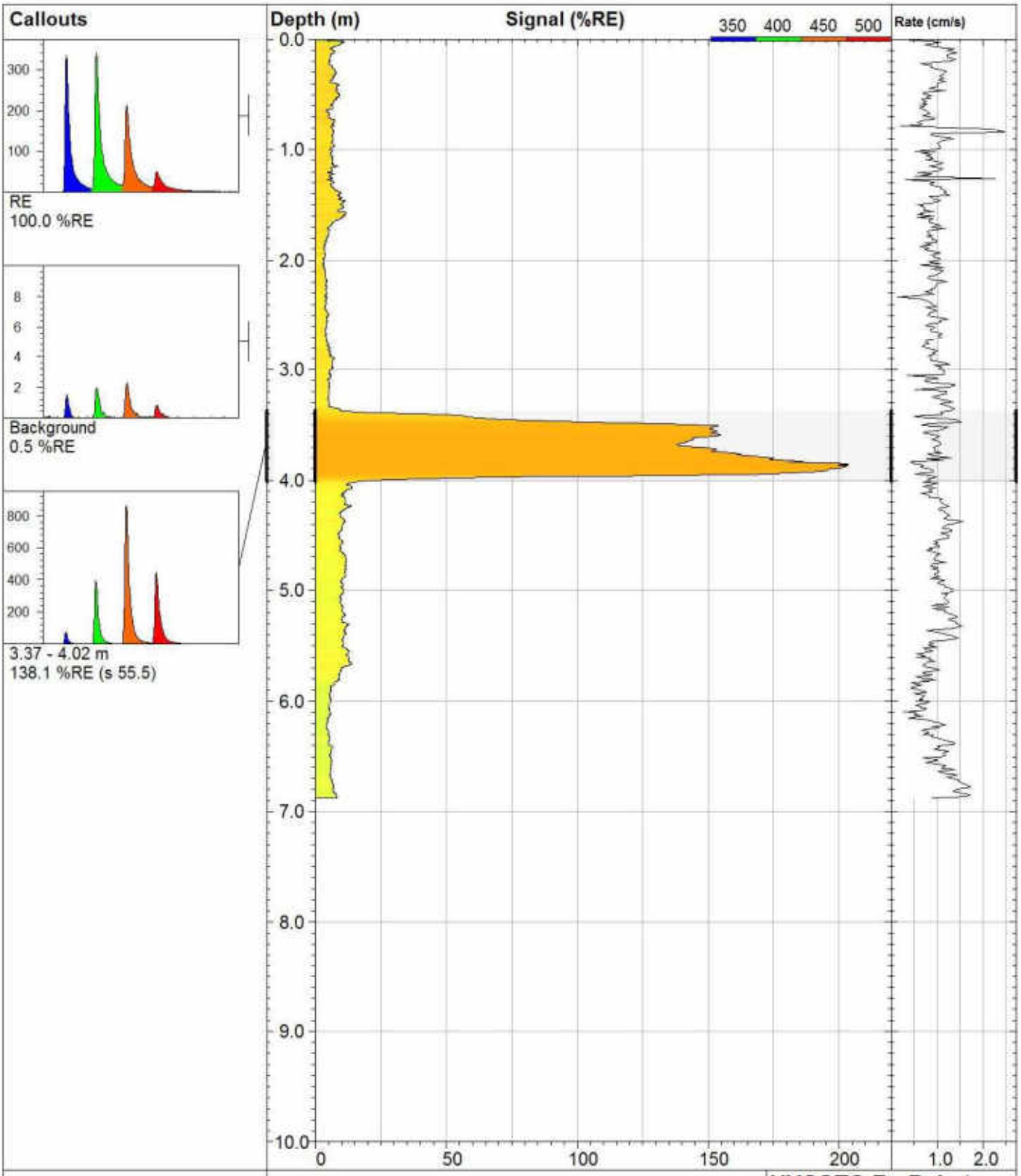
LIF-04

UVOST® By Dakota
www.DakotaTechnologies.com

Final depth:
6.87 m

Max signal:
170.6 %RE @ 4.07 m

Date & Time:
2016-05-31 17:33 AUSEST



numac
Numac Drilling Services PTY Ltd.
www.numac.com.au
1300 131 019
info@numac.com.au

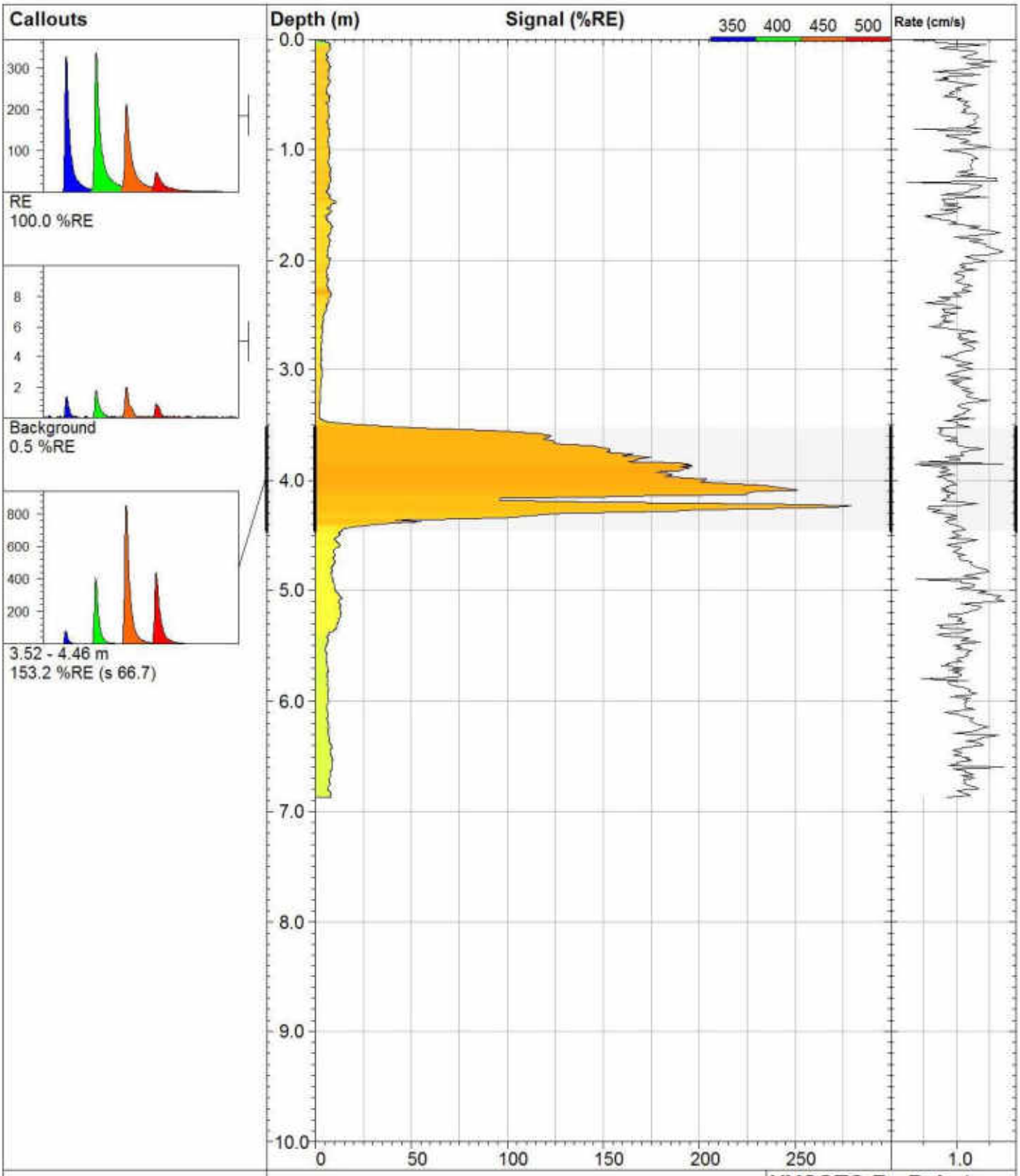
LIF-05

UVOST® By Dakota
www.DakotaTechnologies.com

Final depth:
6.88 m

Max signal:
203.7 %RE @ 3.86 m

Date & Time:
2016-06-01 11:00 AUSEST



numac
Numac Drilling Services PTY Ltd.
www.numac.com.au
1300 131 019
info@numac.com.au

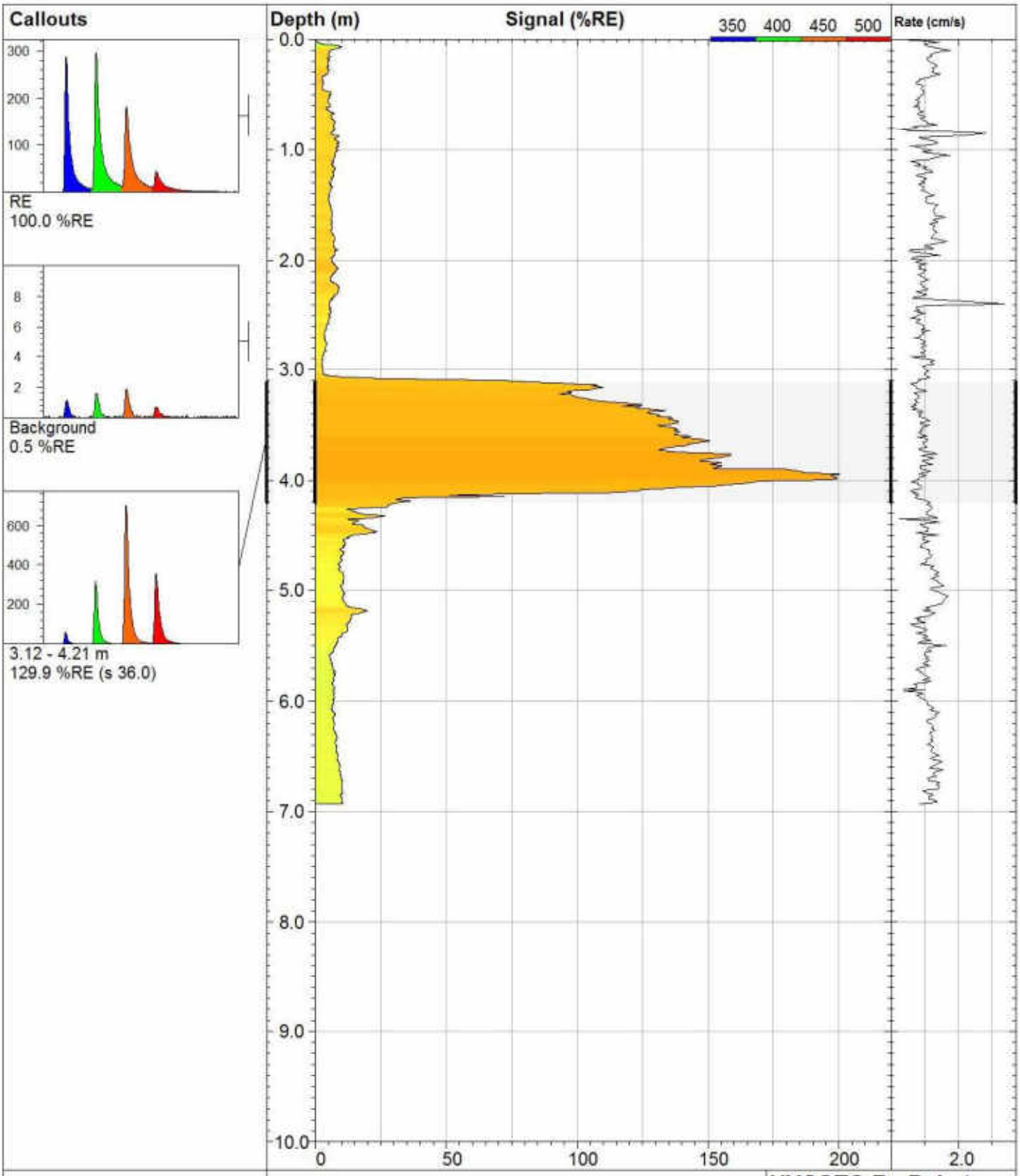
LIF-07

UVOST® By Dakota
www.DakotaTechnologies.com

Final depth:
6.88 m

Max signal:
279.5 %RE @ 4.23 m

Date & Time:
2016-06-01 12:07 AUSEST



numac

Numac Drilling Services PTY Ltd.
www.numac.com.au
1300 131 019
info@numac.com.au

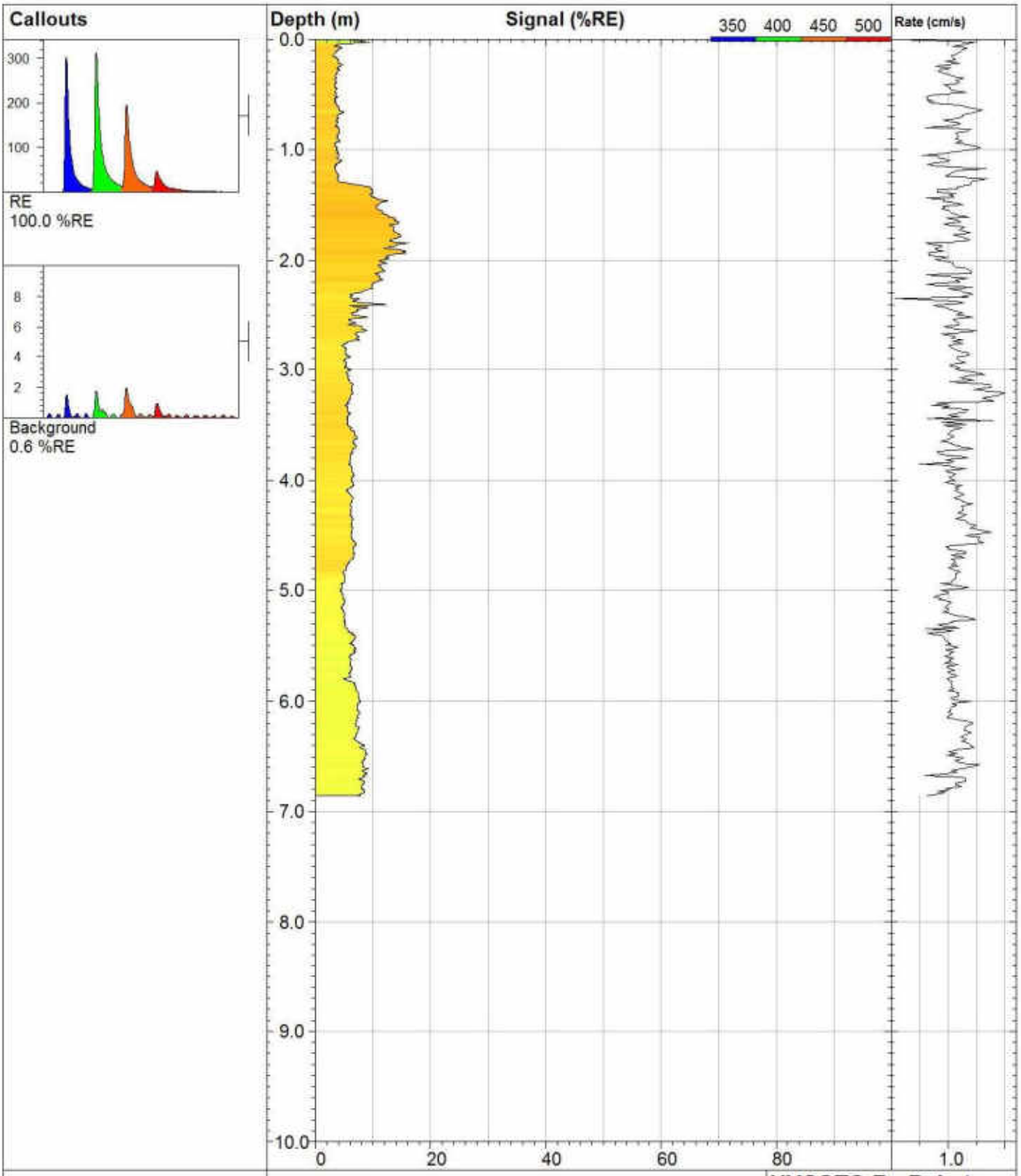
LIF-08

UVOST® By Dakota
www.DakotaTechnologies.com

Final depth:
6.94 m

Max signal:
200.3 %RE @ 3.95 m

Date & Time:
2016-06-01 12:37 AUSEST



numac

Numac Drilling Services PTY Ltd.
www.numac.com.au
1300 131 019
info@numac.com.au

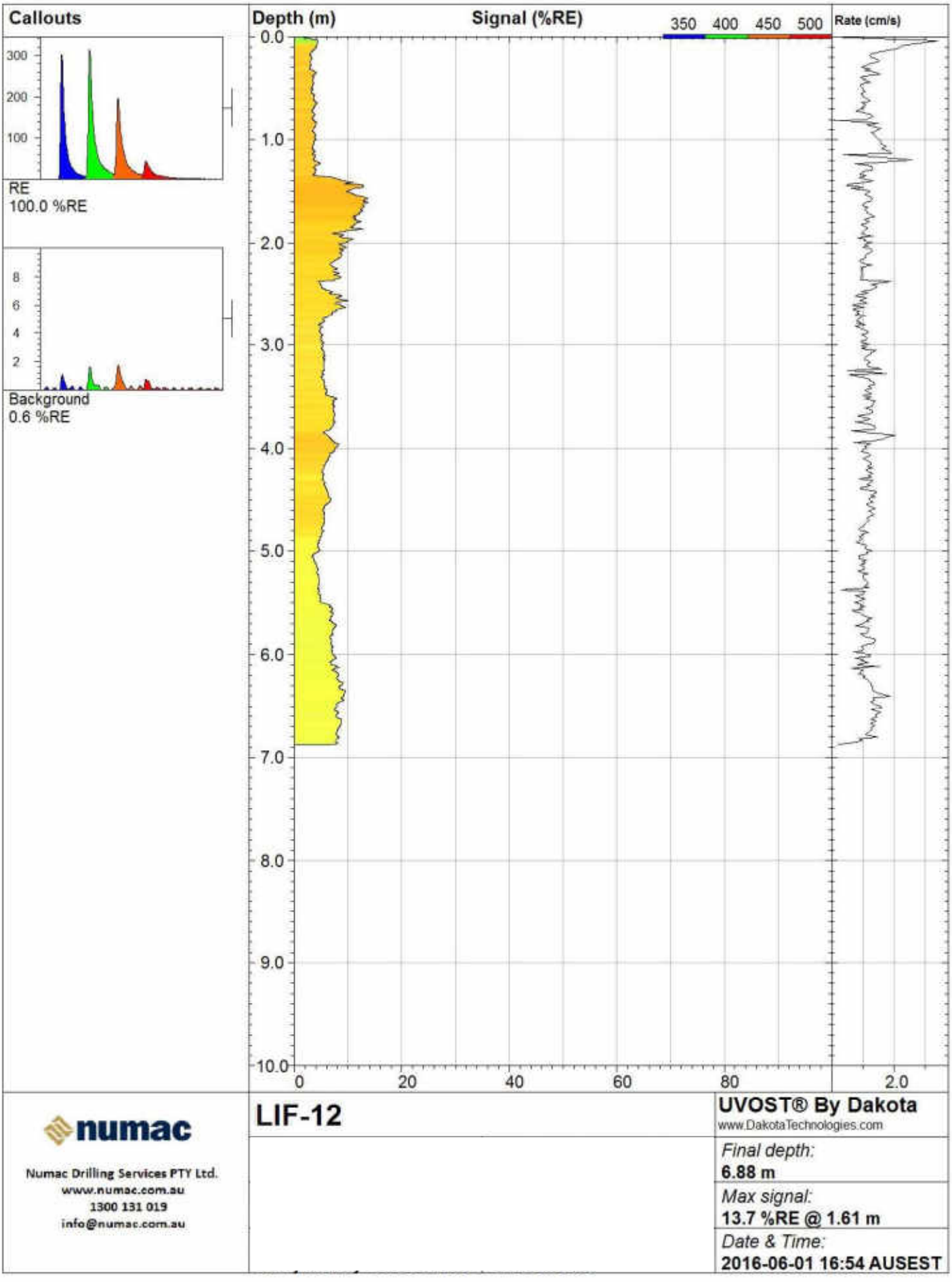
LIF-11

UVOST® By Dakota
www.DakotaTechnologies.com

Final depth:
6.85 m

Max signal:
16.2 %RE @ 1.85 m

Date & Time:
2016-06-01 16:24 AUSEST



numac

Numac Drilling Services PTY Ltd.
www.numac.com.au
1300 131 019
info@numac.com.au

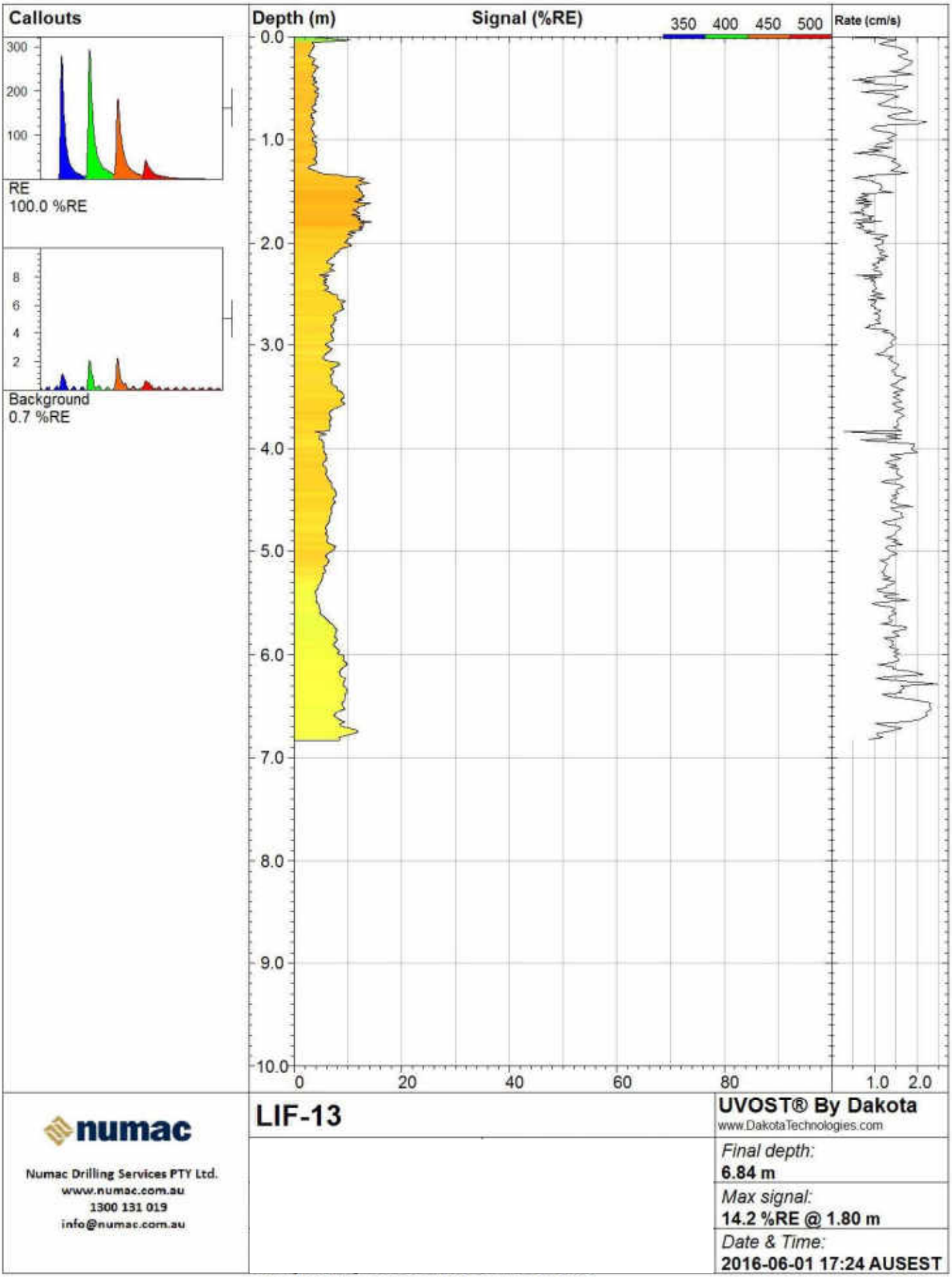
LIF-12

UVOST® By Dakota
www.DakotaTechnologies.com

Final depth:
6.88 m

Max signal:
13.7 %RE @ 1.61 m

Date & Time:
2016-06-01 16:54 AUSEST



numac

Numac Drilling Services PTY Ltd.
www.numac.com.au
1300 131 019
info@numac.com.au

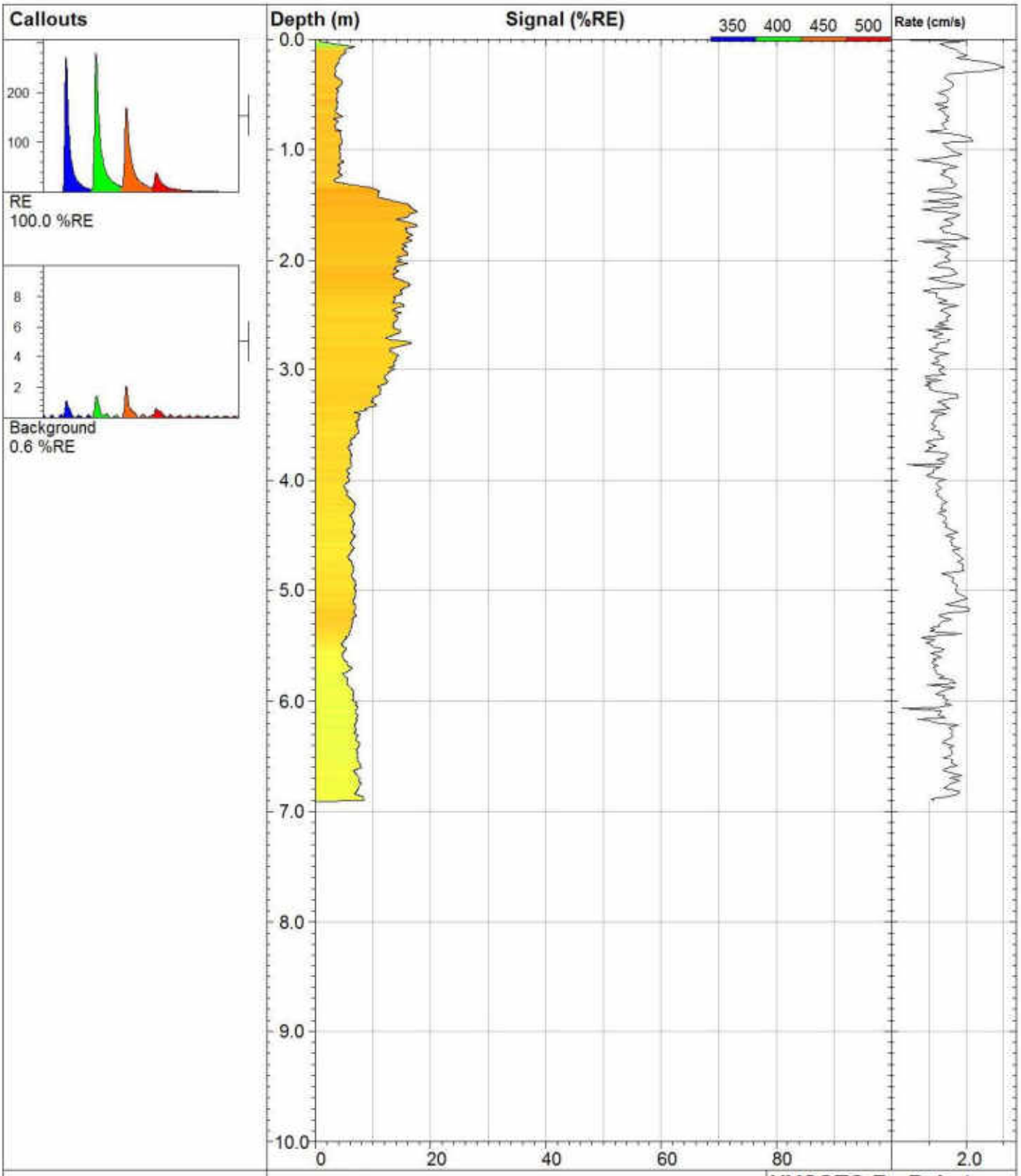
LIF-13

UVOST® By Dakota
www.DakotaTechnologies.com

Final depth:
6.84 m

Max signal:
14.2 %RE @ 1.80 m

Date & Time:
2016-06-01 17:24 AUSEST



numac

Numac Drilling Services PTY Ltd.
www.numac.com.au
1300 131 019
info@numac.com.au

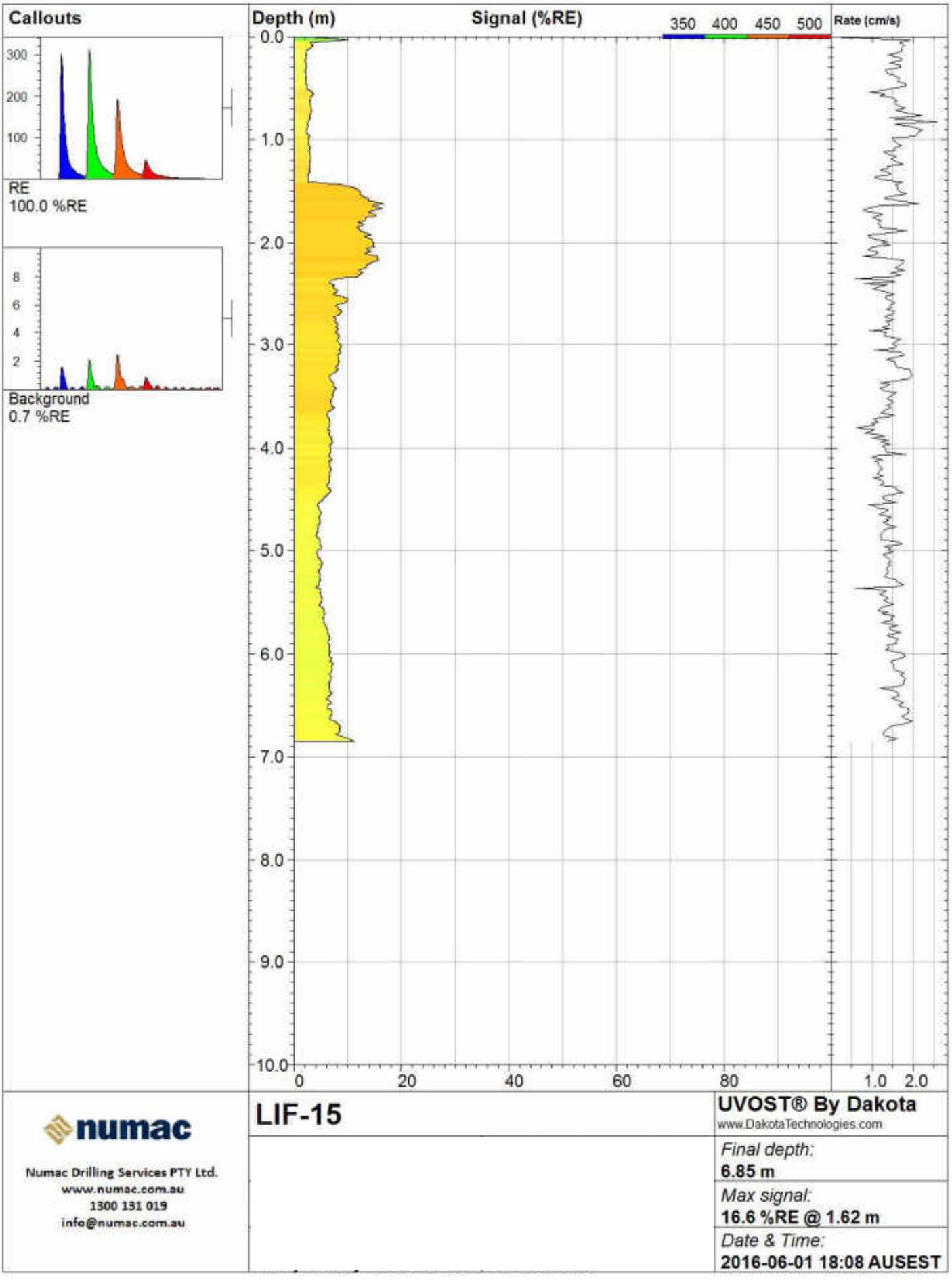
LIF-14

UVOST® By Dakota
www.DakotaTechnologies.com

Final depth:
6.91 m

Max signal:
17.7 %RE @ 1.56 m

Date & Time:
2016-06-01 17:46 AUSEST



numac

Numac Drilling Services PTY Ltd.
www.numac.com.au
1300 131 019
info@numac.com.au

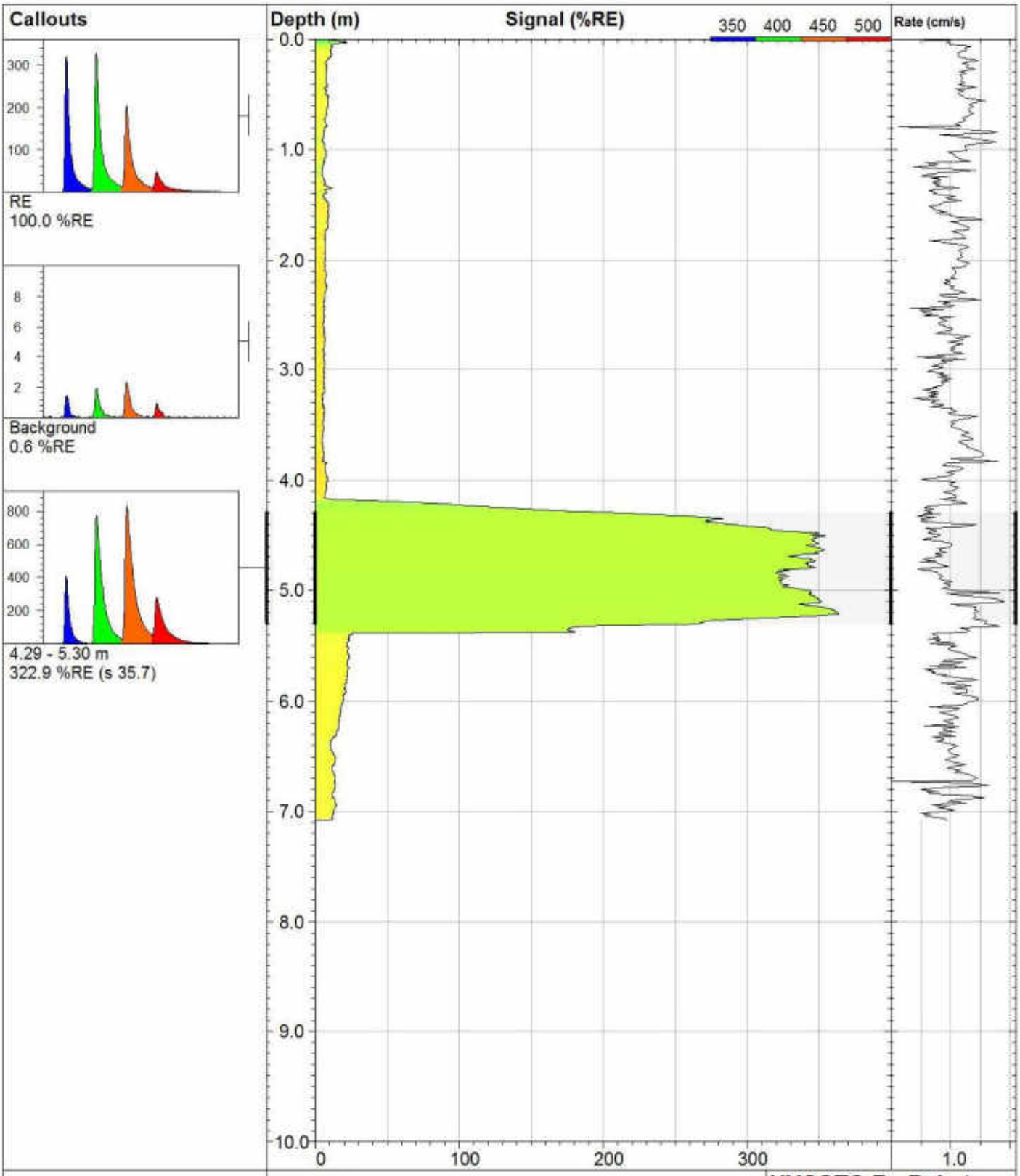
LIF-15

UVOST® By Dakota
www.DakotaTechnologies.com

Final depth:
6.85 m

Max signal:
16.6 %RE @ 1.62 m

Date & Time:
2016-06-01 18:08 AUSEST



numac

Numac Drilling Services PTY Ltd.
www.numac.com.au
1300 131 019
info@numac.com.au

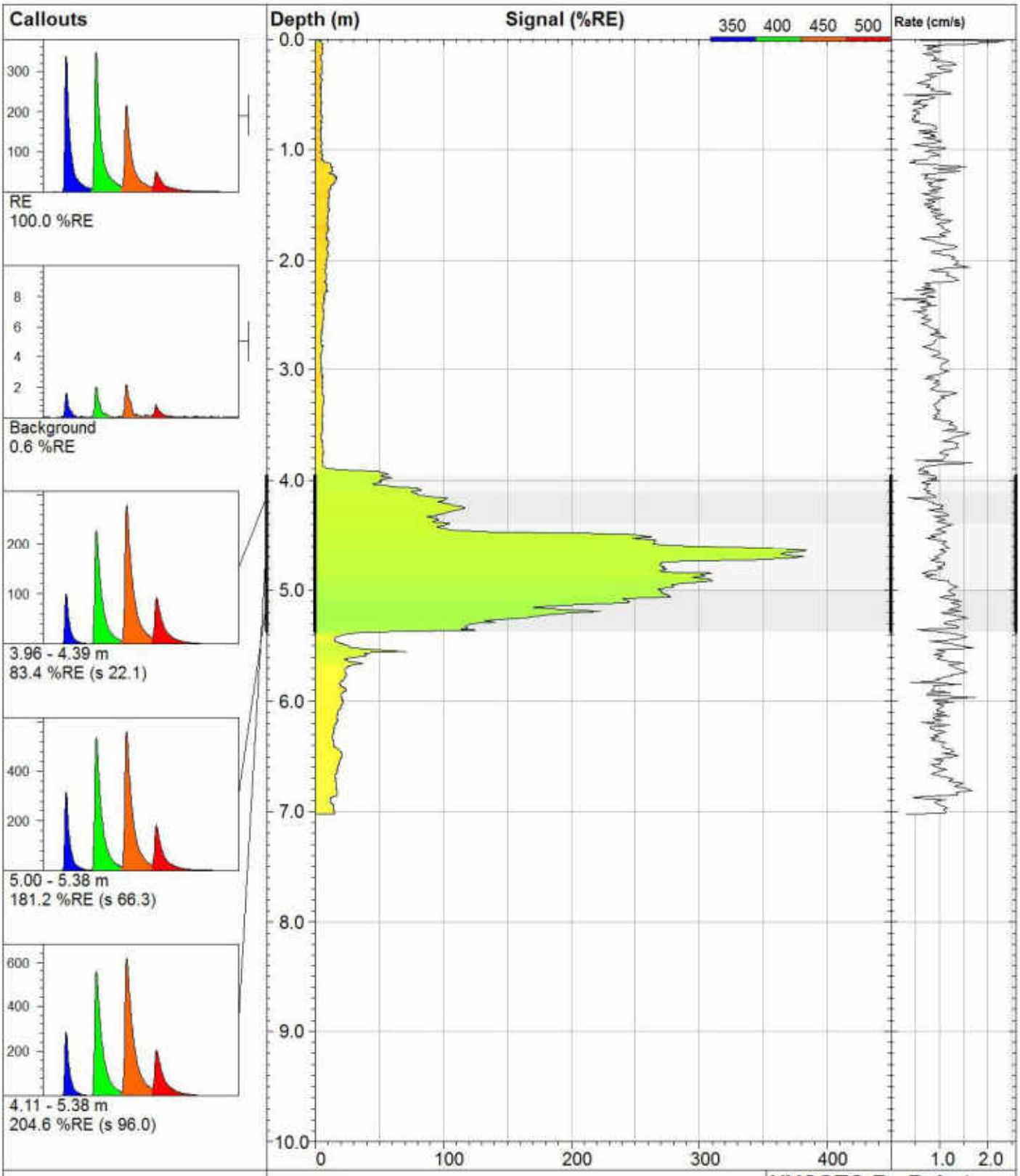
LIF-16

UVOST® By Dakota
www.DakotaTechnologies.com

Final depth:
7.08 m

Max signal:
363.7 %RE @ 5.21 m

Date & Time:
2016-06-13 13:26 AUSEST



numac
Numac Drilling Services PTY Ltd.
www.numac.com.au
1300 131 019
info@numac.com.au

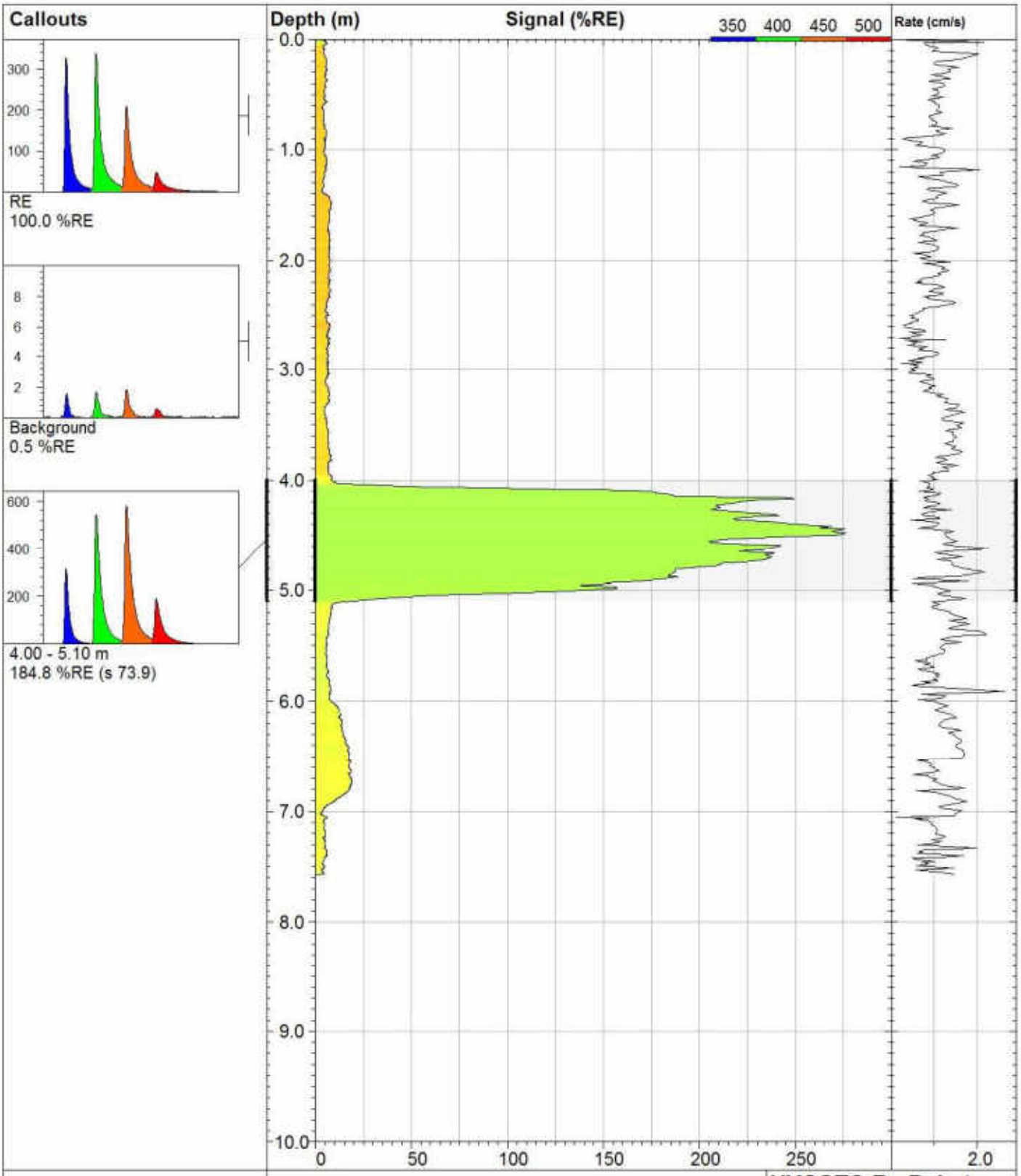
LIF-17

UVOST® By Dakota
www.DakotaTechnologies.com

Final depth:
7.02 m

Max signal:
384.2 %RE @ 4.64 m

Date & Time:
2016-06-13 14:06 AUSEST



numac

Numac Drilling Services PTY Ltd.
www.numac.com.au
1300 131 019
info@numac.com.au

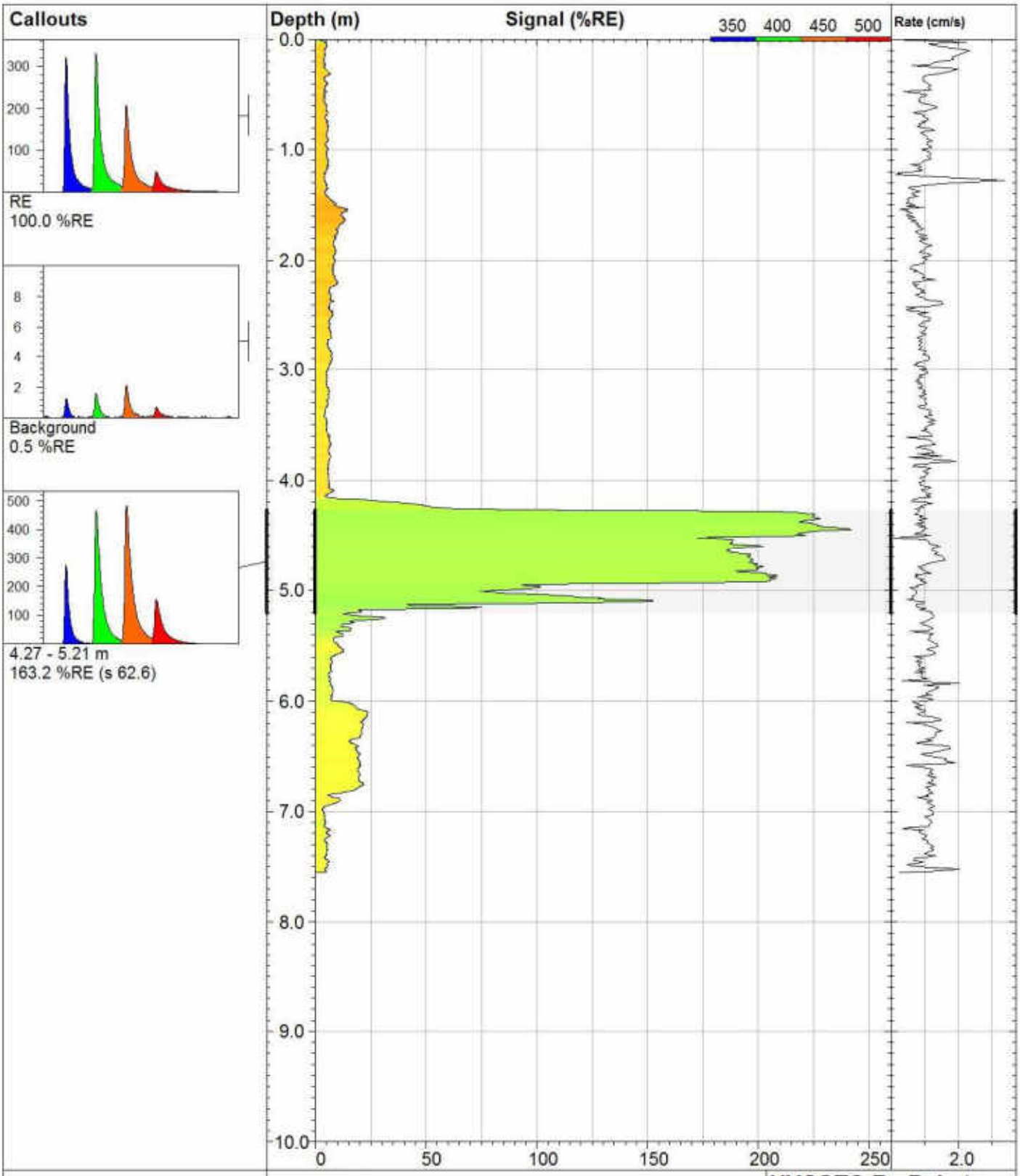
LIF-18

UVOST® By Dakota
www.DakotaTechnologies.com

Final depth:
7.57 m

Max signal:
276.1 %RE @ 4.48 m

Date & Time:
2016-06-13 14:41 AUSEST



numac
Numac Drilling Services PTY Ltd.
www.numac.com.au
1300 131 019
info@numac.com.au

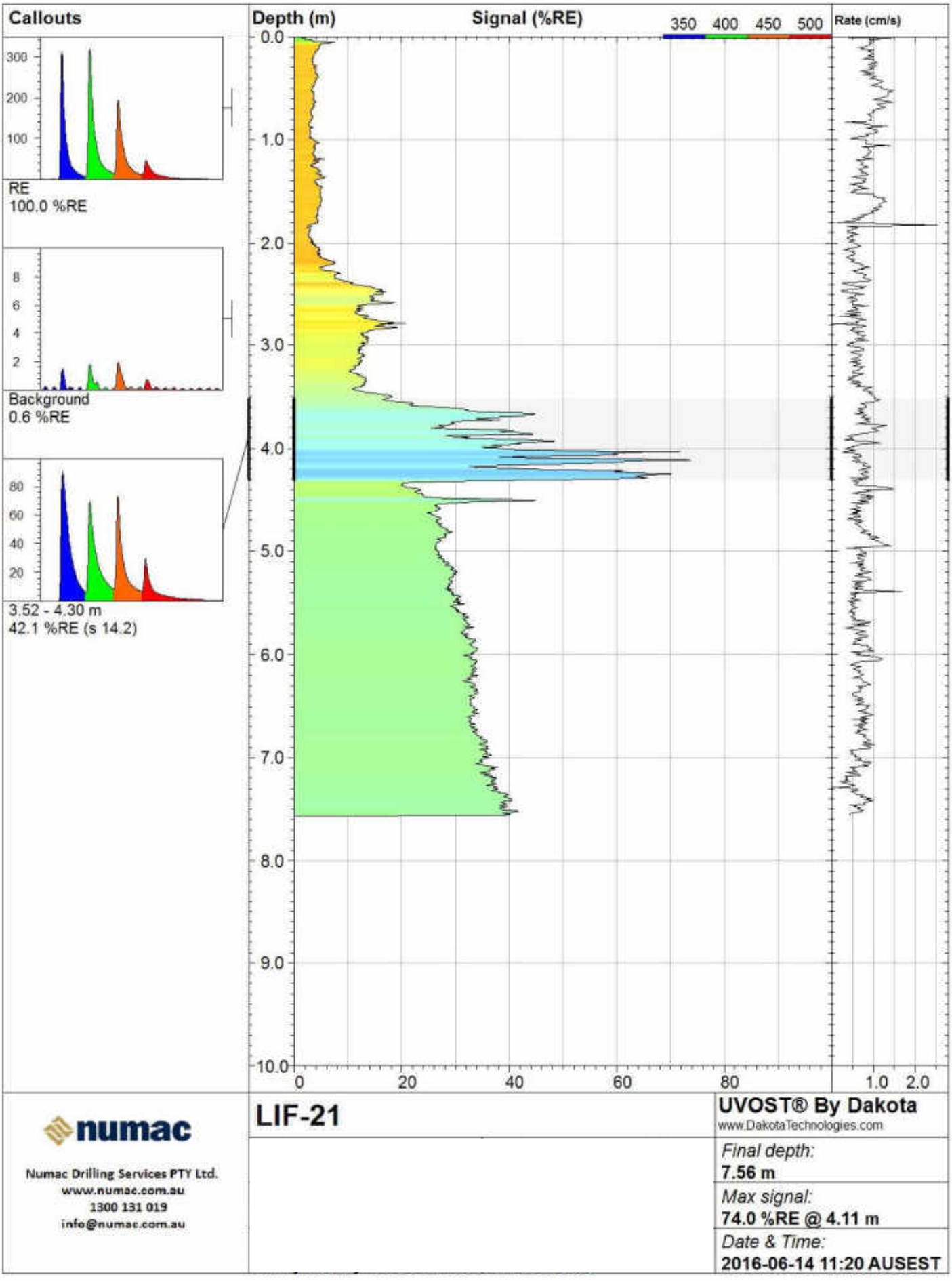
LIF-19

UVOST® By Dakota
www.DakotaTechnologies.com

Final depth:
7.55 m

Max signal:
242.2 %RE @ 4.45 m

Date & Time:
2016-06-13 15:12 AUSEST



numac
Numac Drilling Services PTY Ltd.
www.numac.com.au
1300 131 019
info@numac.com.au

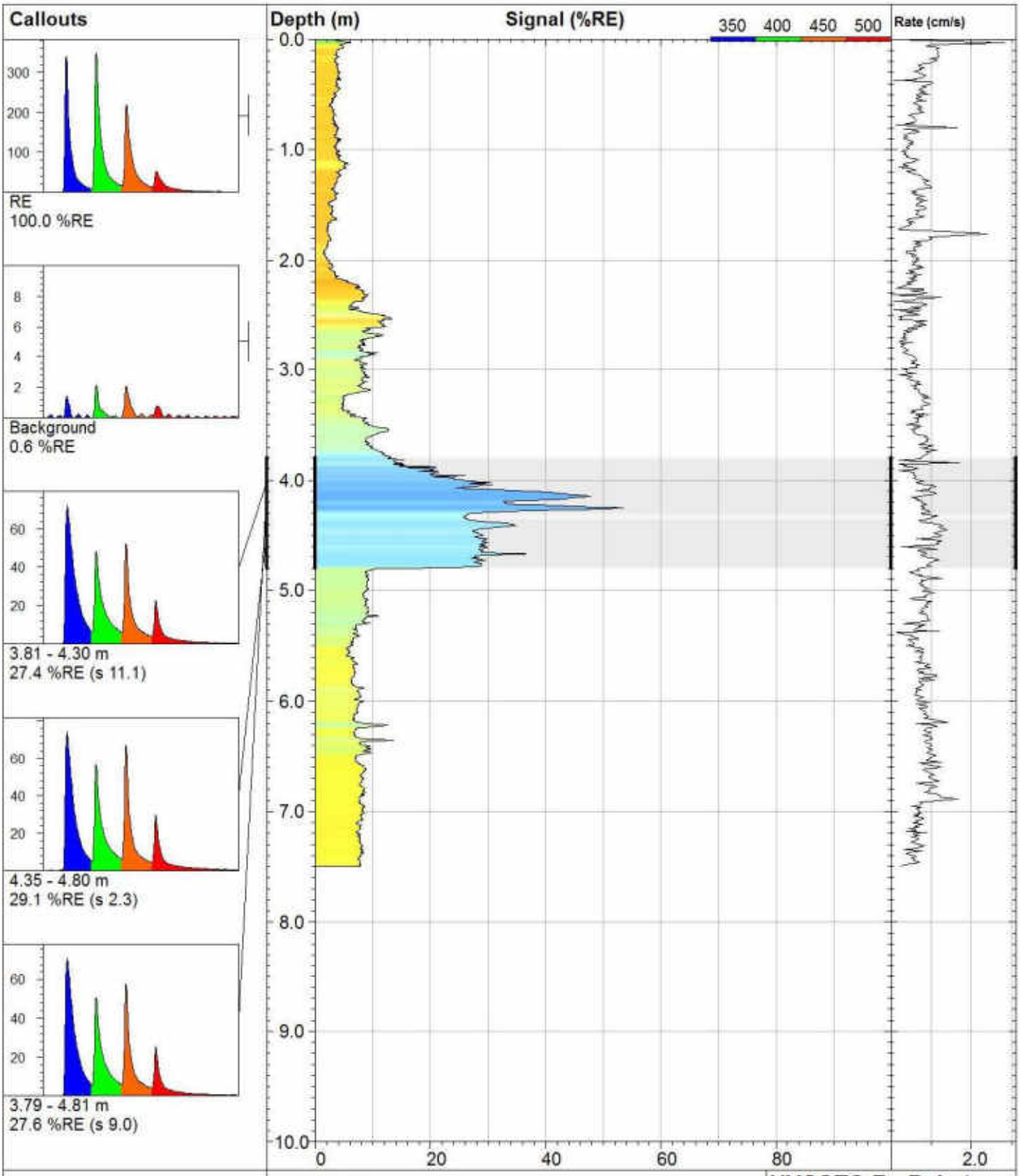
LIF-21

UVOST® By Dakota
www.DakotaTechnologies.com

Final depth:
7.56 m

Max signal:
74.0 %RE @ 4.11 m

Date & Time:
2016-06-14 11:20 AUSEST



numac

Numac Drilling Services PTY Ltd.
www.numac.com.au
1300 131 019
info@numac.com.au

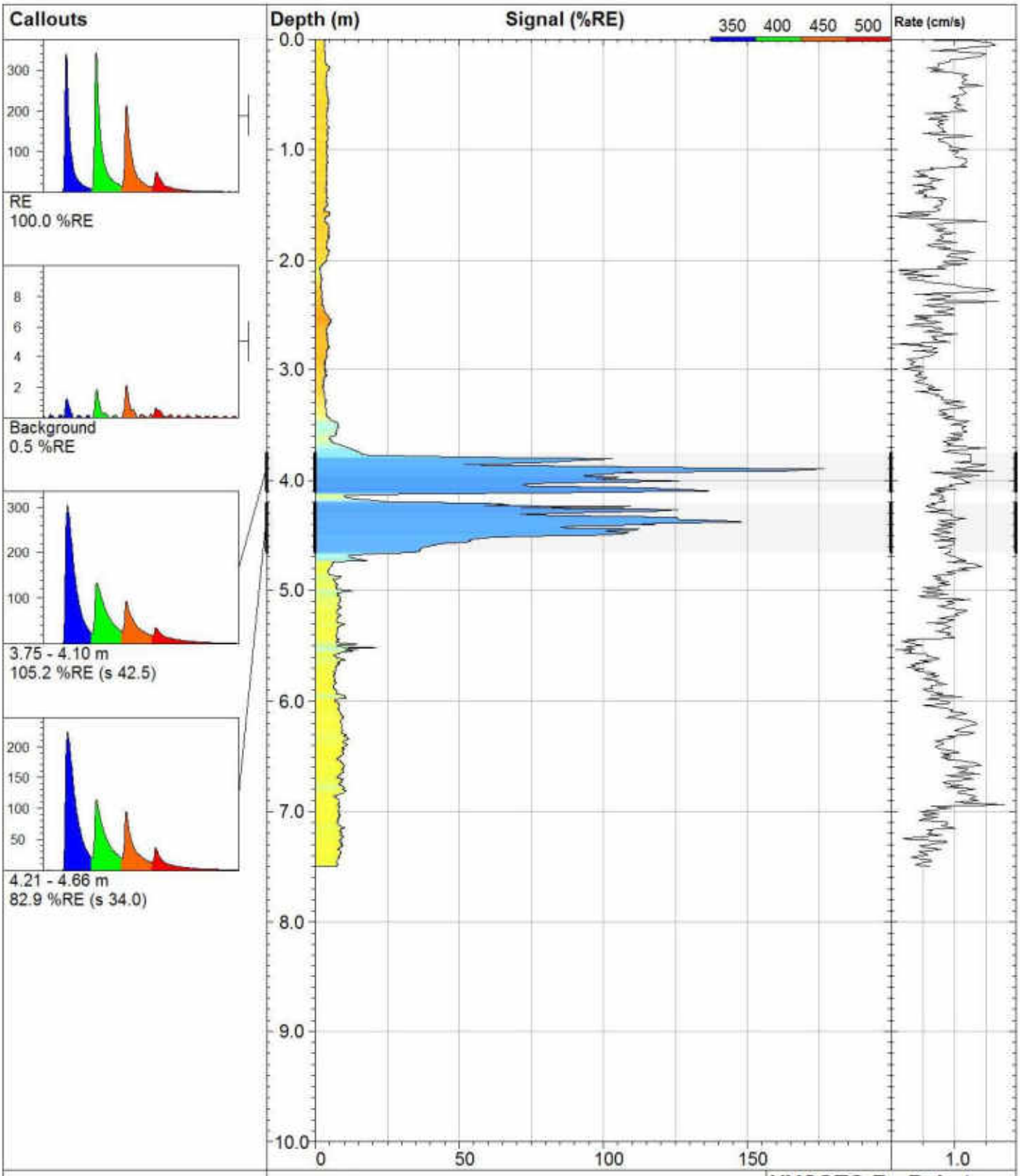
LIF-22

UVOST® By Dakota
www.DakotaTechnologies.com

Final depth:
7.50 m

Max signal:
53.5 %RE @ 4.25 m

Date & Time:
2016-06-14 12:07 AUSEST



numac
Numac Drilling Services PTY Ltd.
www.numac.com.au
1300 131 019
info@numac.com.au

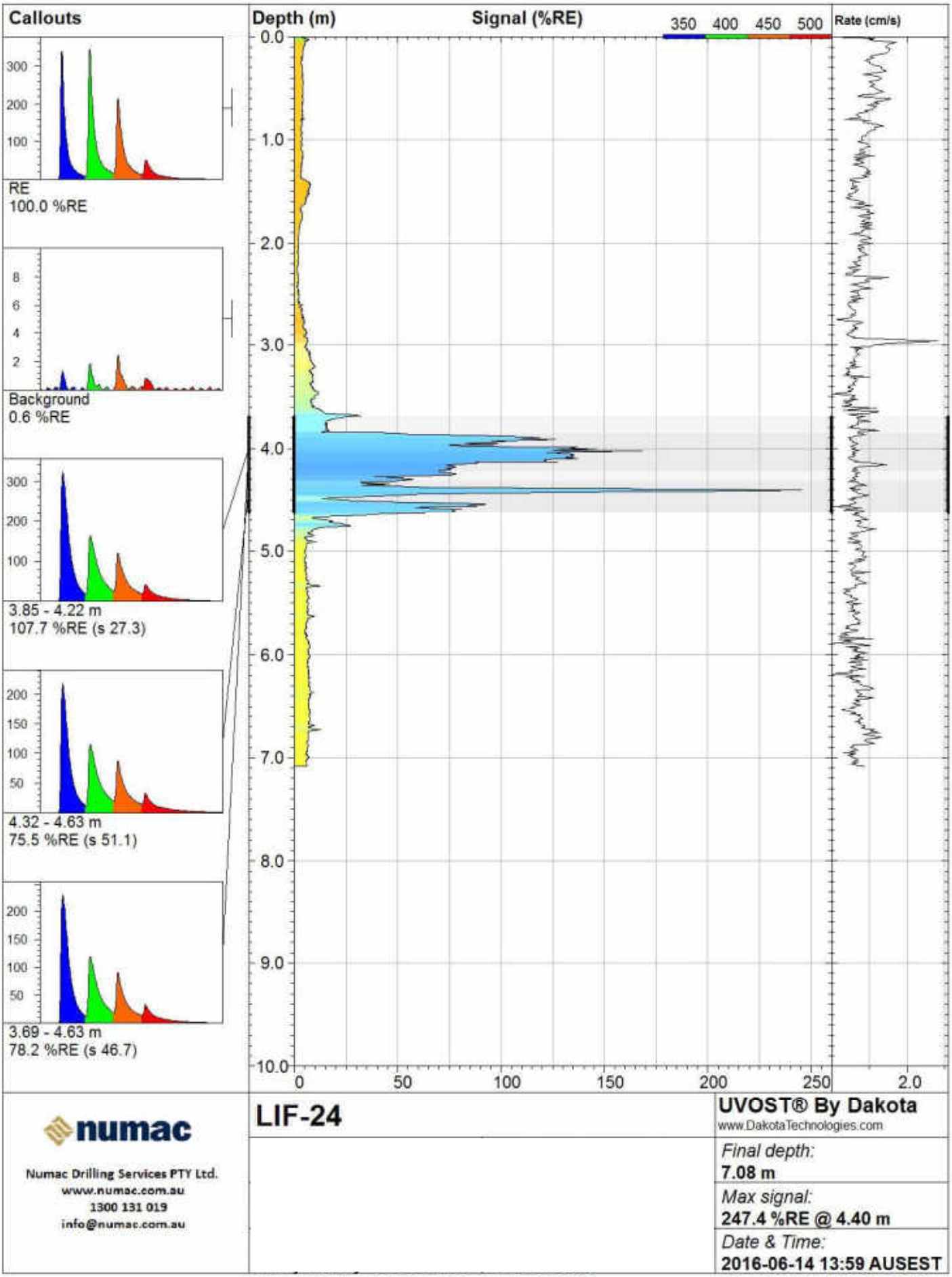
LIF-23

UVOST® By Dakota
www.DakotaTechnologies.com

Final depth:
7.50 m

Max signal:
179.5 %RE @ 3.90 m

Date & Time:
2016-06-14 12:51 AUSEST



numac

Numac Drilling Services PTY Ltd.
www.numac.com.au
1300 131 019
info@numac.com.au

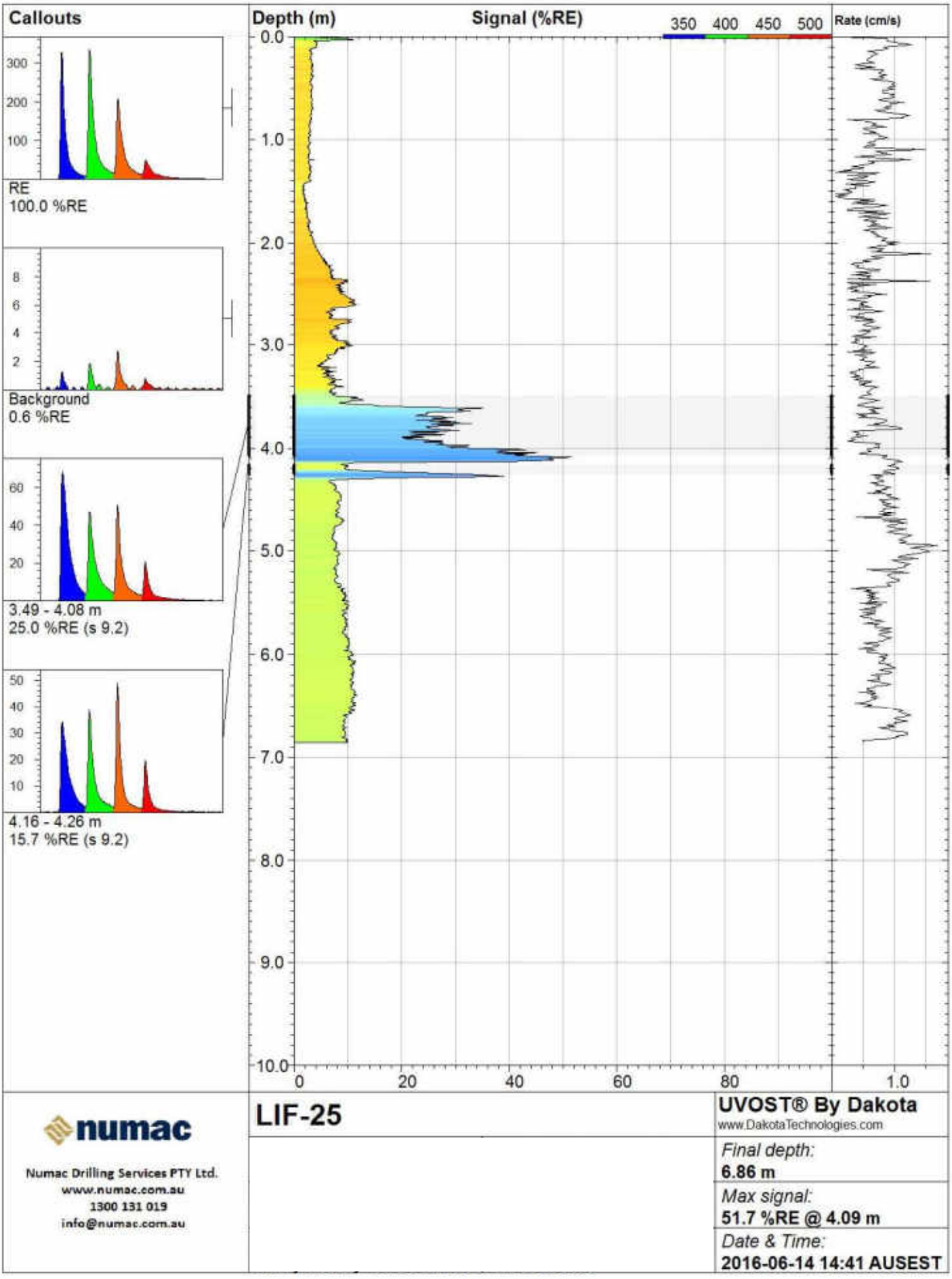
LIF-24

UVOST® By Dakota
www.DakotaTechnologies.com

Final depth:
7.08 m

Max signal:
247.4 %RE @ 4.40 m

Date & Time:
2016-06-14 13:59 AUSEST



numac

Numac Drilling Services PTY Ltd.
www.numac.com.au
1300 131 019
info@numac.com.au

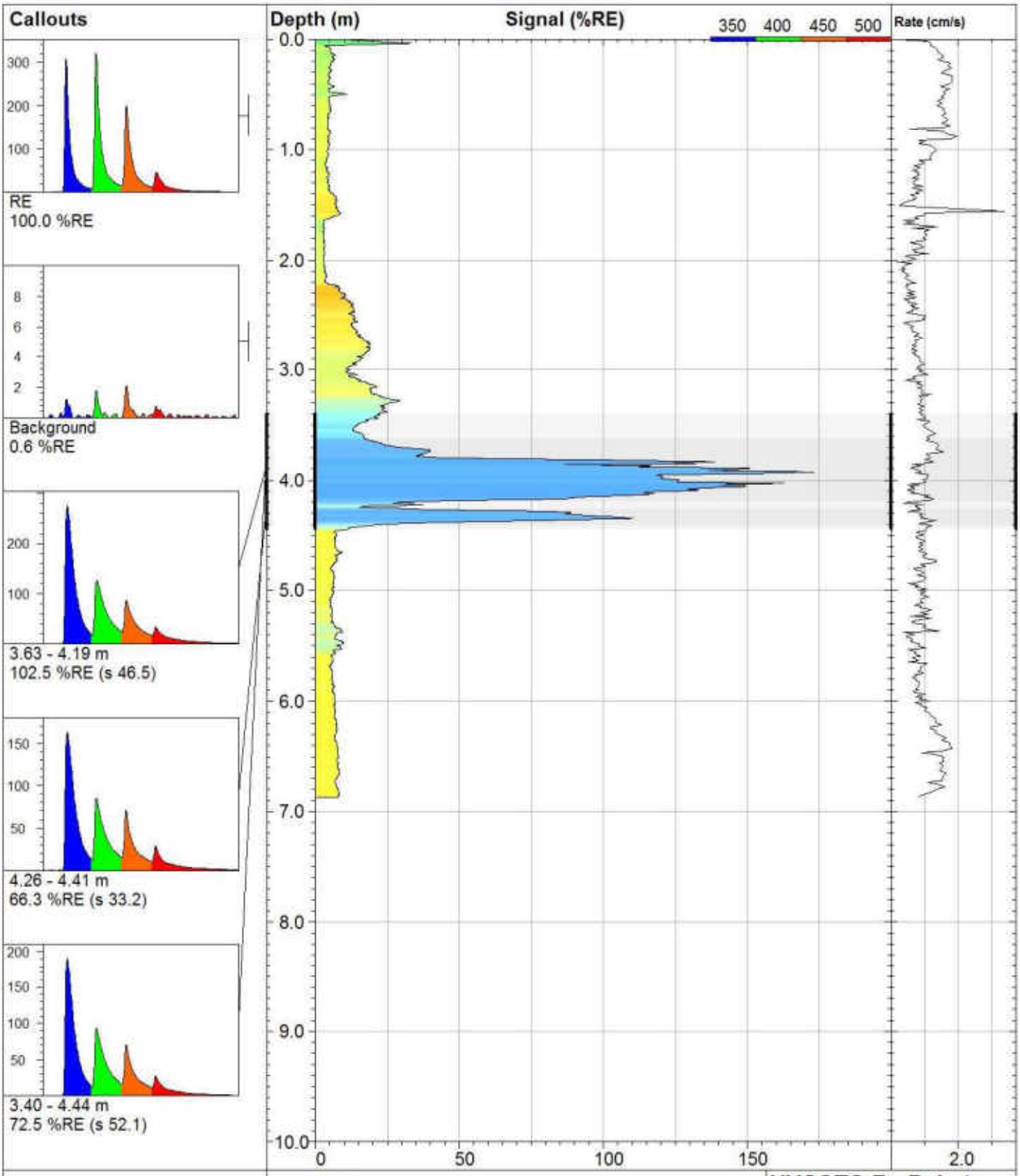
LIF-25

UVOST® By Dakota
www.DakotaTechnologies.com

Final depth:
6.86 m

Max signal:
51.7 %RE @ 4.09 m

Date & Time:
2016-06-14 14:41 AUSEST



numac
Numac Drilling Services PTY Ltd.
www.numac.com.au
1300 131 019
info@numac.com.au

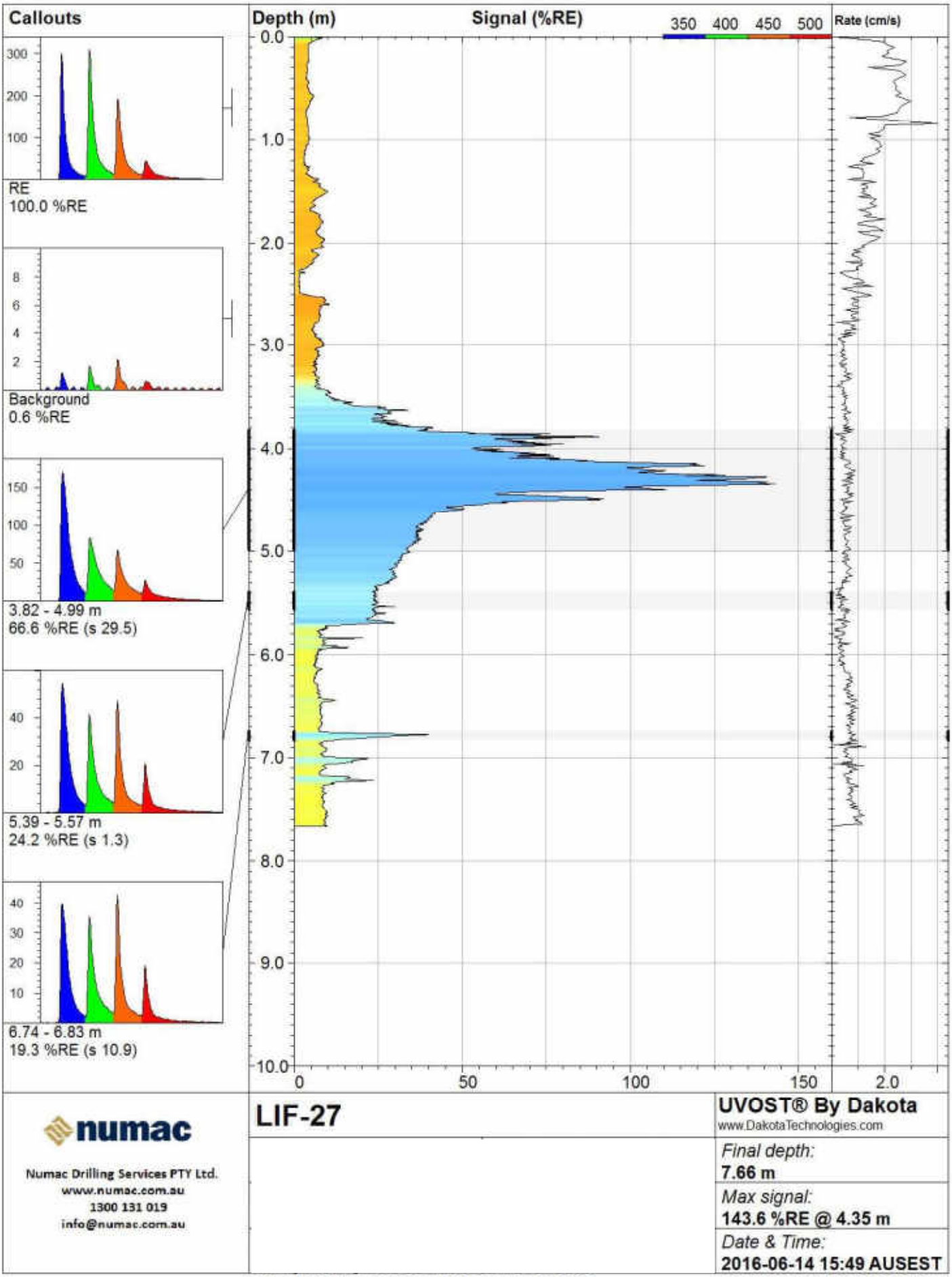
LIF-26

UVOST® By Dakota
www.DakotaTechnologies.com

Final depth:
6.87 m

Max signal:
173.4 %RE @ 3.93 m

Date & Time:
2016-06-14 15:17 AUSEST



numac

Numac Drilling Services PTY Ltd.
www.numac.com.au
1300 131 019
info@numac.com.au

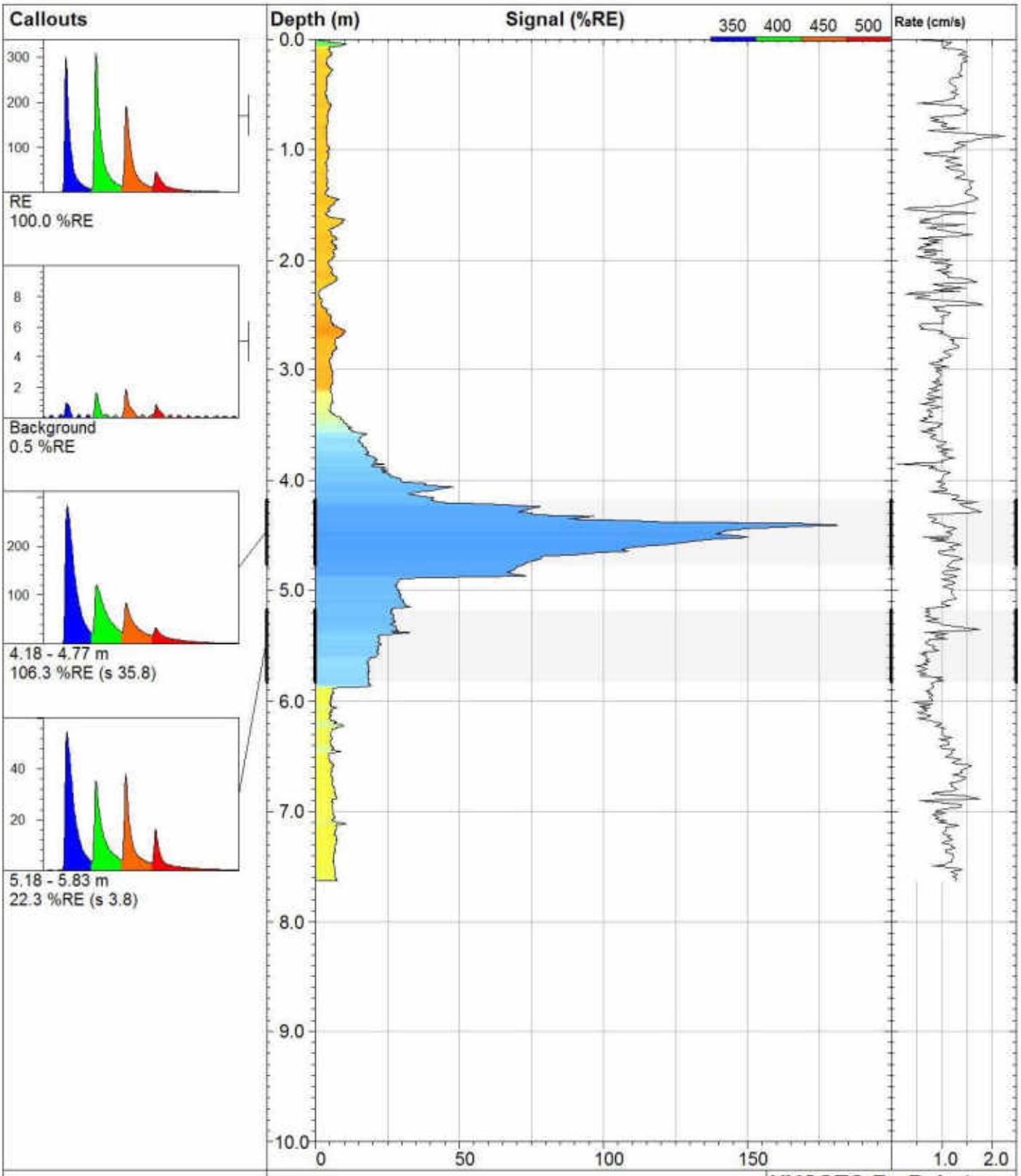
LIF-27

UVOST® By Dakota
www.DakotaTechnologies.com

Final depth:
7.66 m

Max signal:
143.6 %RE @ 4.35 m

Date & Time:
2016-06-14 15:49 AUSEST



numac
Numac Drilling Services PTY Ltd.
www.numac.com.au
1300 131 019
info@numac.com.au

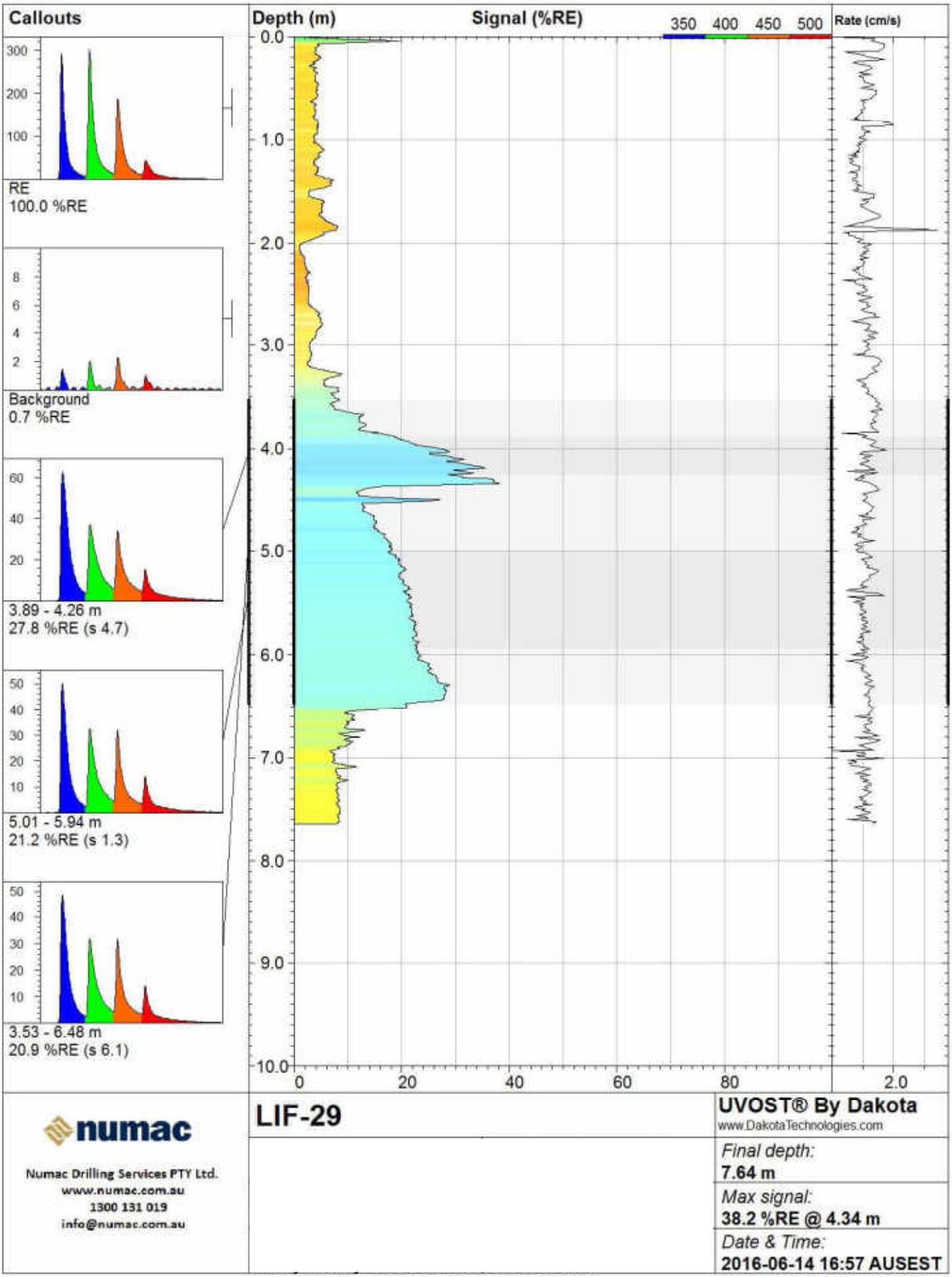
LIF-28

UVOST® By Dakota
www.DakotaTechnologies.com

Final depth:
7.62 m

Max signal:
181.1 %RE @ 4.41 m

Date & Time:
2016-06-14 16:28 AUSEST



numac
Numac Drilling Services PTY Ltd.
www.numac.com.au
1300 131 019
info@numac.com.au

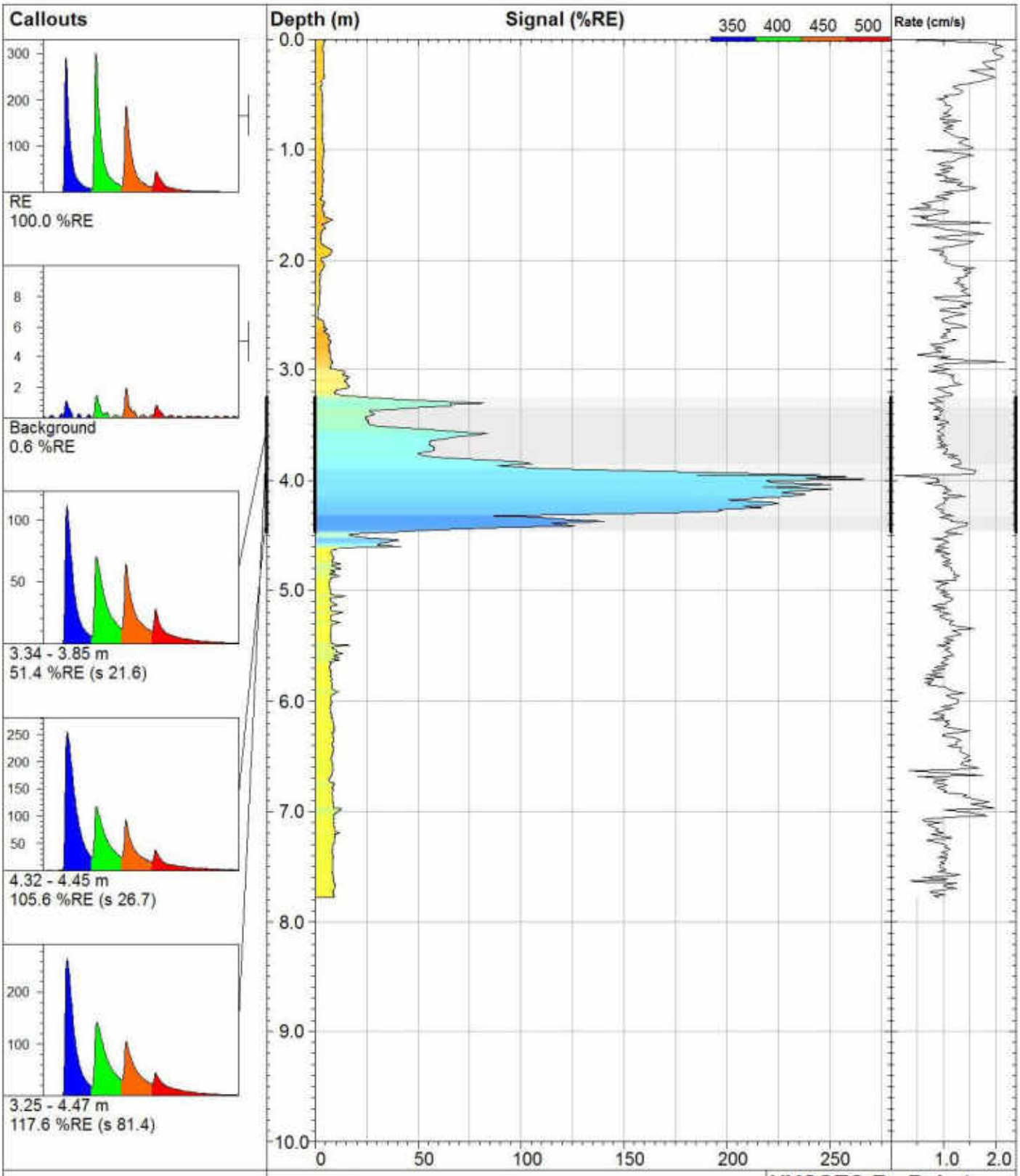
LIF-29

UVOST® By Dakota
www.DakotaTechnologies.com

Final depth:
7.64 m

Max signal:
38.2 %RE @ 4.34 m

Date & Time:
2016-06-14 16:57 AUSEST



numac
Numac Drilling Services PTY Ltd.
www.numac.com.au
1300 131 019
info@numac.com.au

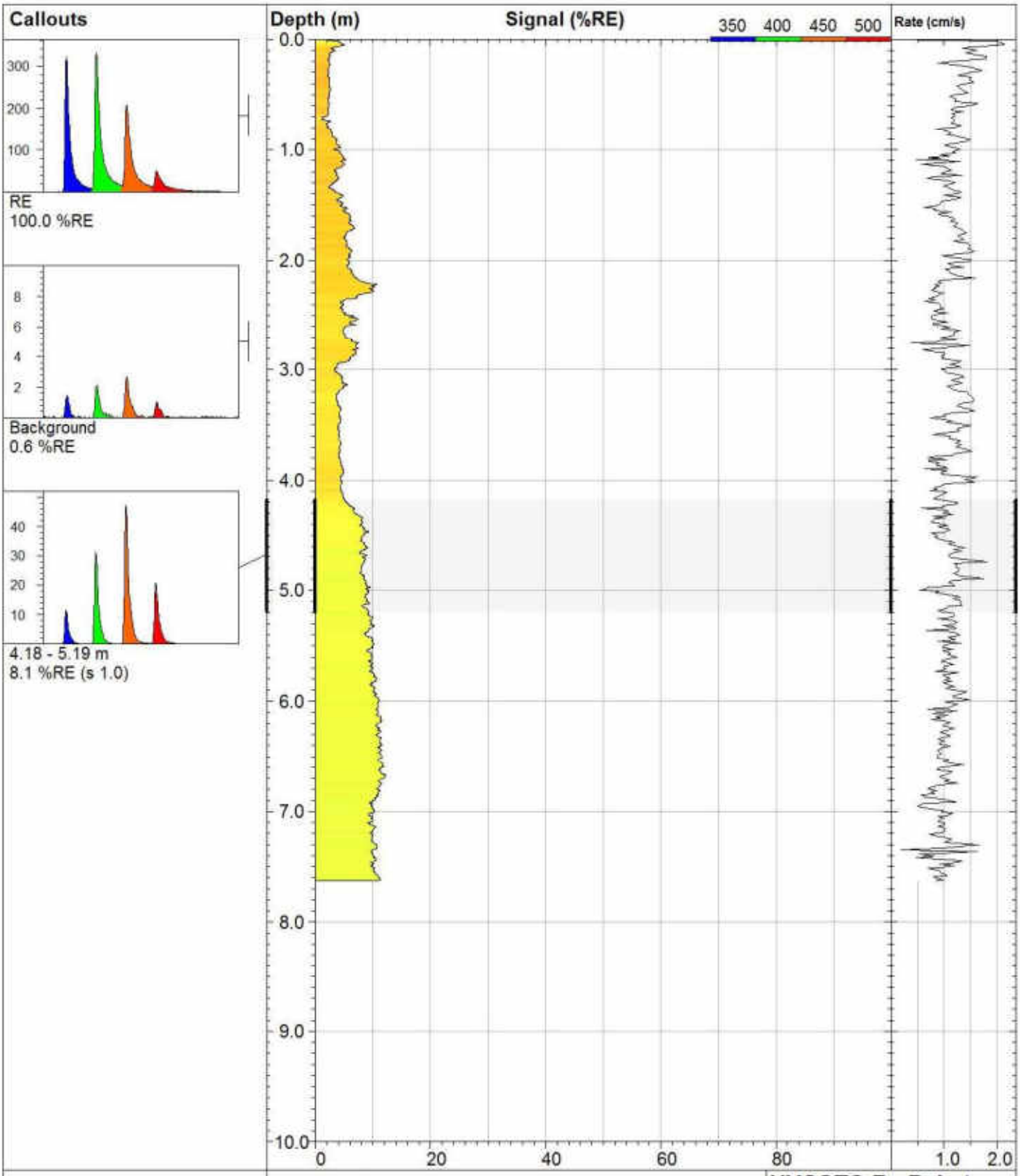
LIF-30

UVOST® By Dakota
www.DakotaTechnologies.com

Final depth:
7.78 m

Max signal:
268.1 %RE @ 3.99 m

Date & Time:
2016-06-14 17:32 AUSEST



numac

Numac Drilling Services PTY Ltd.
www.numac.com.au
1300 131 019
info@numac.com.au

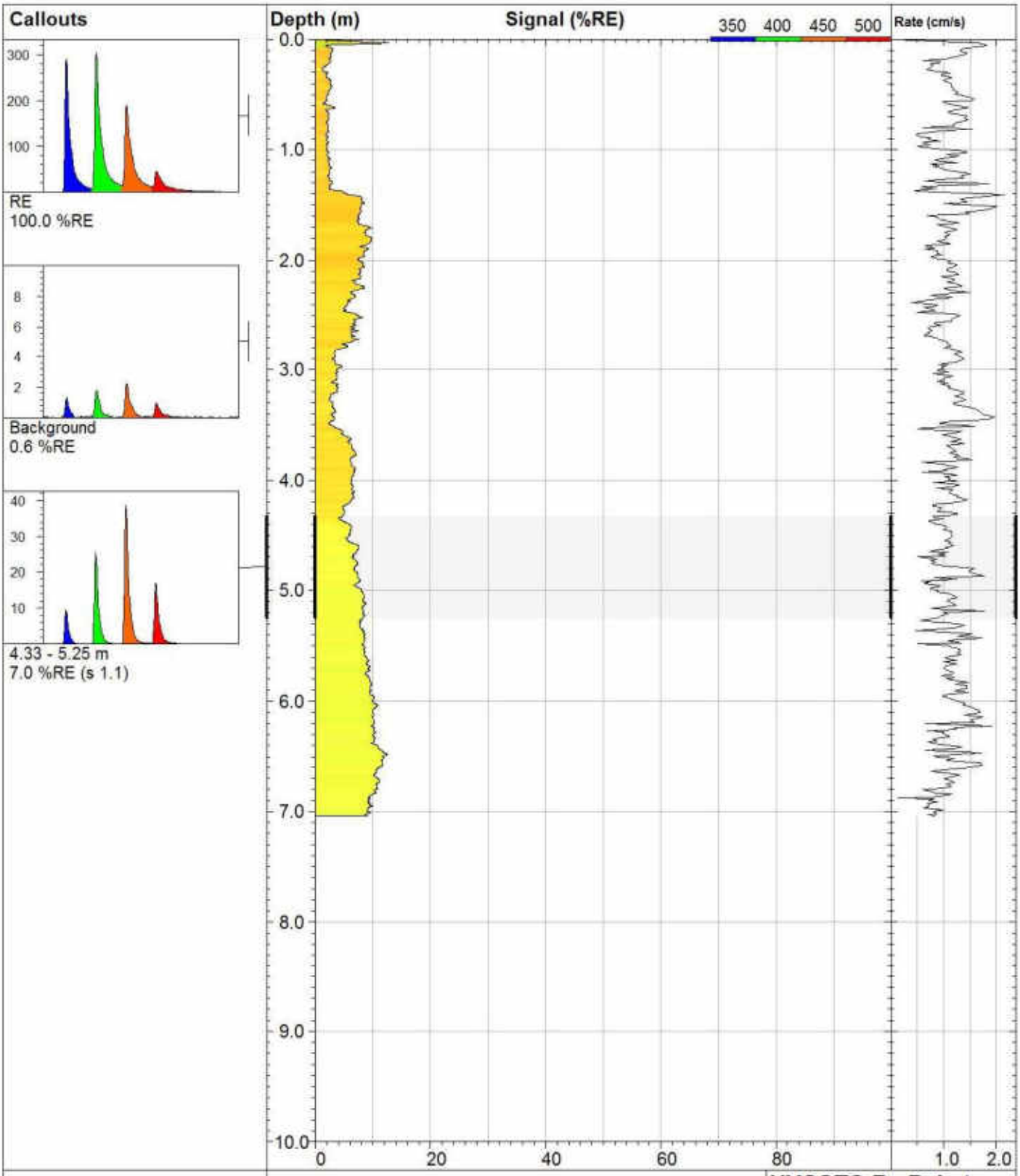
LIF-34

UVOST® By Dakota
www.DakotaTechnologies.com

Final depth:
7.63 m

Max signal:
12.2 %RE @ 6.67 m

Date & Time:
2016-06-15 14:13 AUSEST



numac

Numac Drilling Services PTY Ltd.
www.numac.com.au
1300 131 019
info@numac.com.au

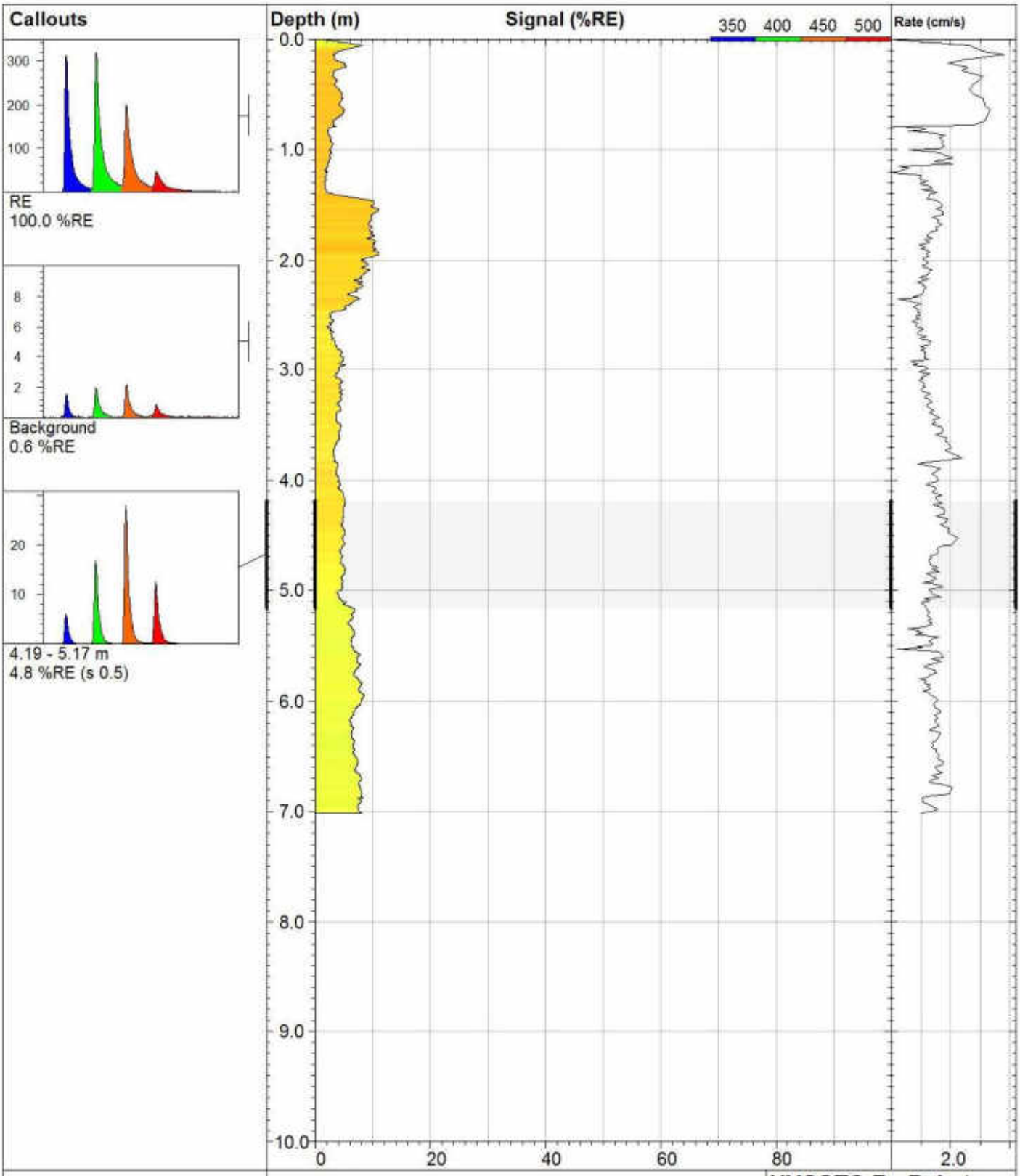
LIF-35

UVOST® By Dakota
www.DakotaTechnologies.com

Final depth:
7.04 m

Max signal:
12.9 %RE @ 0.03 m

Date & Time:
2016-06-15 14:42 AUSEST



numac

Numac Drilling Services PTY Ltd.
www.numac.com.au
1300 131 019
info@numac.com.au

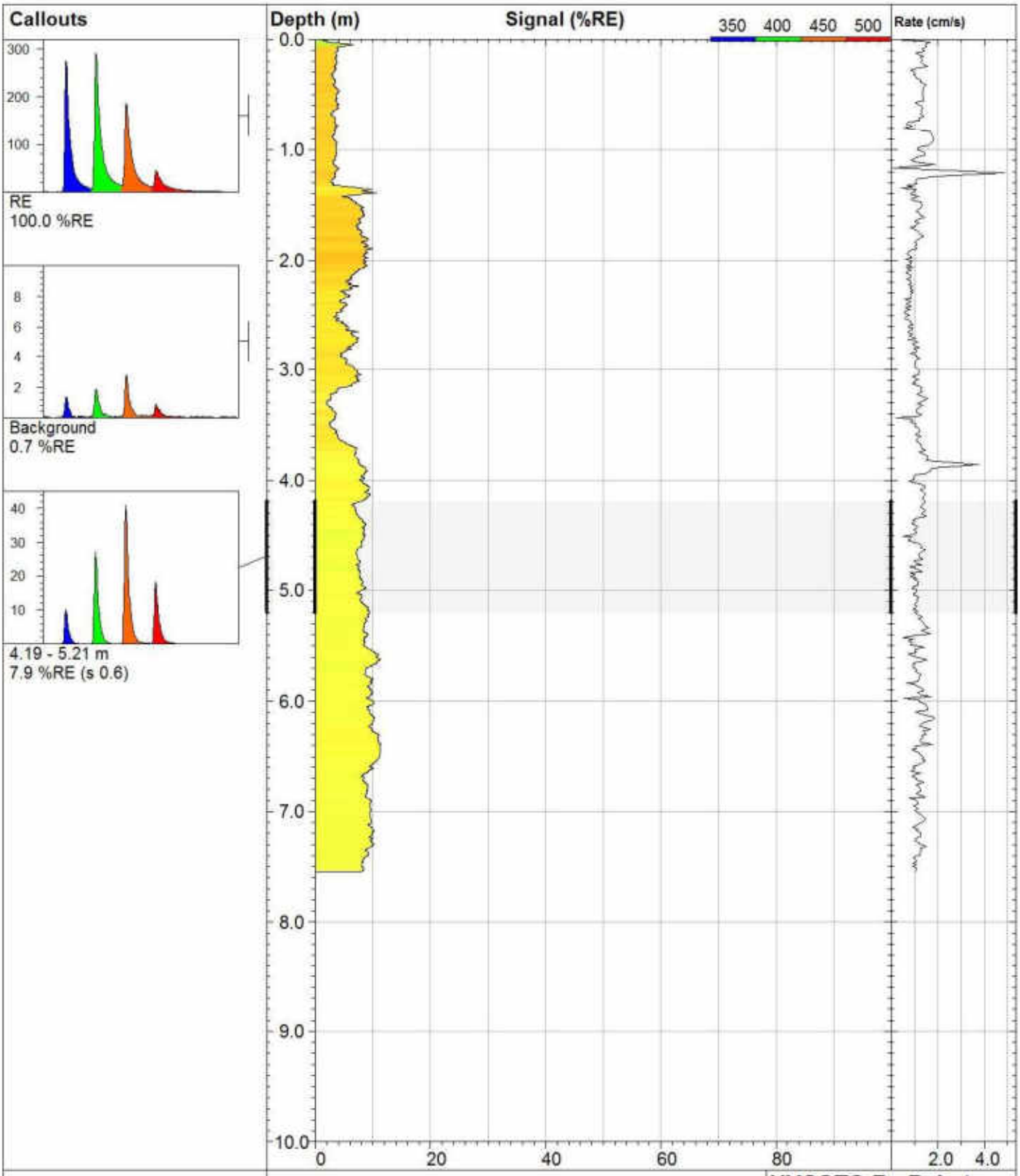
LIF-36

UVOST® By Dakota
www.DakotaTechnologies.com

Final depth:
7.02 m

Max signal:
11.0 %RE @ 1.54 m

Date & Time:
2016-06-15 15:10 AUSEST



numac

Numac Drilling Services PTY Ltd.
www.numac.com.au
1300 131 019
info@numac.com.au

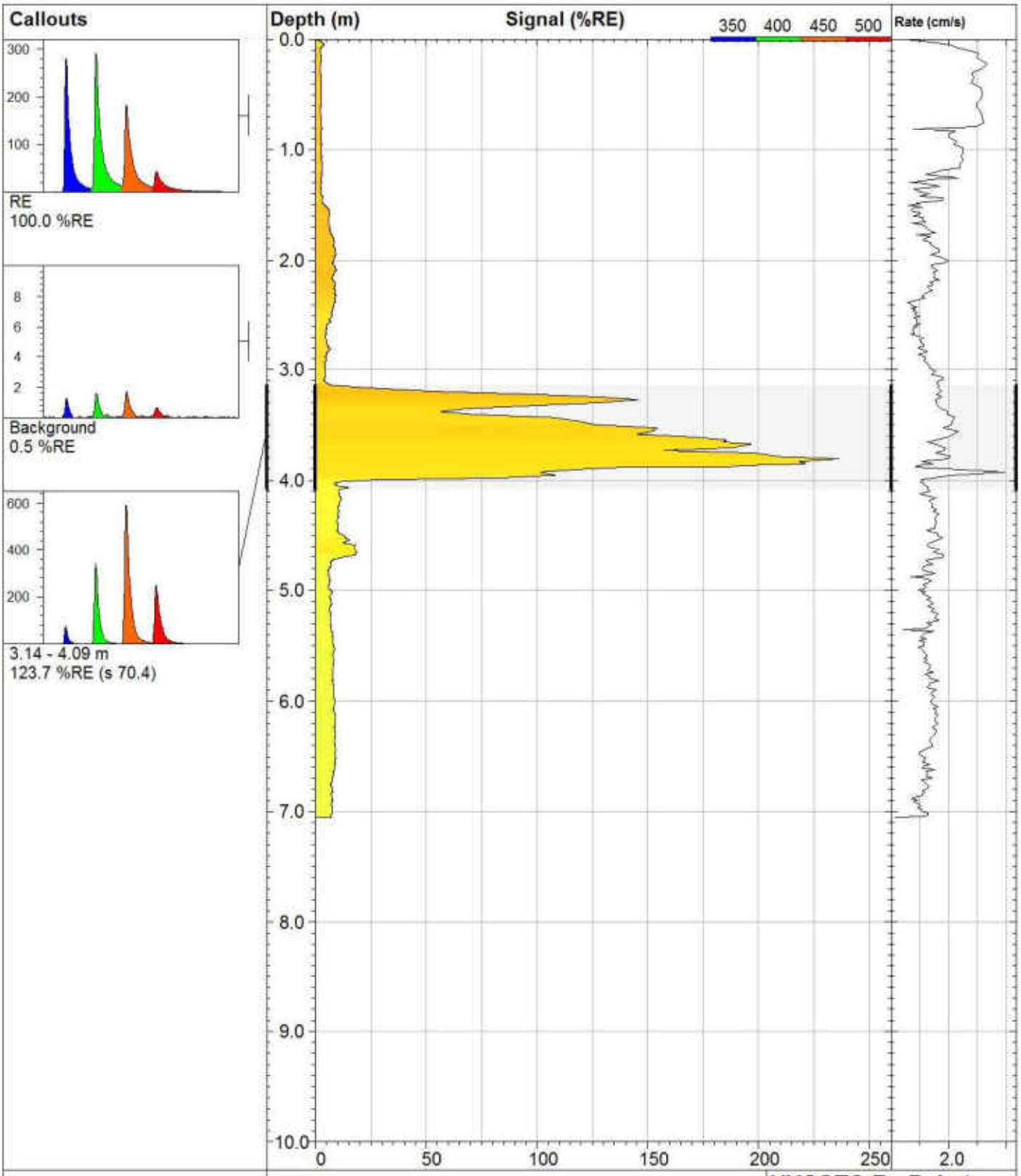
LIF-37

UVOST® By Dakota
www.DakotaTechnologies.com

Final depth:
7.54 m

Max signal:
11.3 %RE @ 5.62 m

Date & Time:
2016-06-15 15:37 AUSEST



numac

Numac Drilling Services PTY Ltd.
www.numac.com.au
1300 131 019
info@numac.com.au

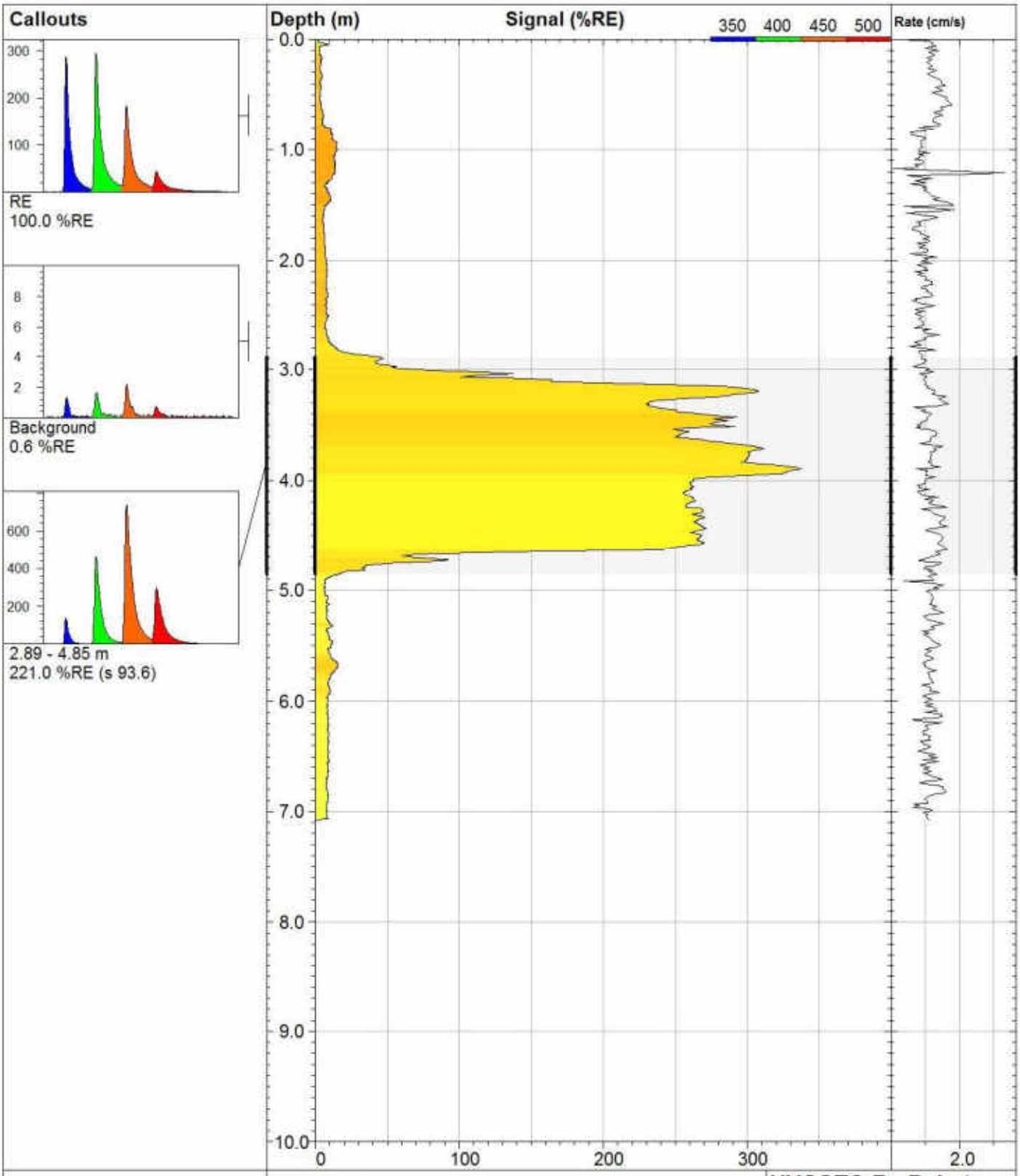
LIF-38

UVOST® By Dakota
www.DakotaTechnologies.com

Final depth:
7.05 m

Max signal:
236.5 %RE @ 3.81 m

Date & Time:
2016-06-15 16:00 AUSEST



numac
Numac Drilling Services PTY Ltd.
www.numac.com.au
1300 131 019
info@numac.com.au

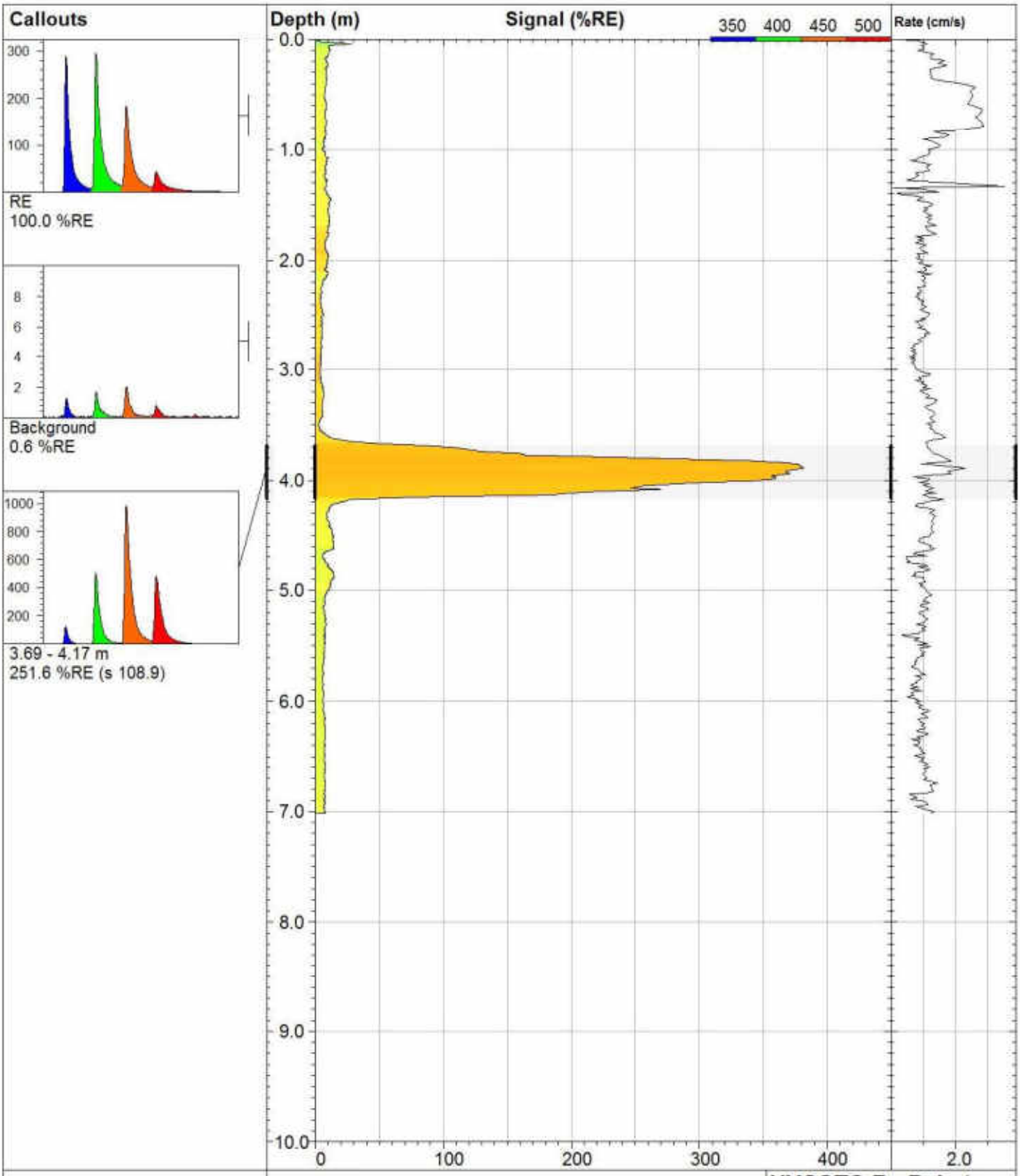
LIF-39

UVOST® By Dakota
www.DakotaTechnologies.com

Final depth:
7.07 m

Max signal:
337.6 %RE @ 3.90 m

Date & Time:
2016-06-15 16:31 AUSEST



numac
Numac Drilling Services PTY Ltd.
www.numac.com.au
1300 131 019
info@numac.com.au

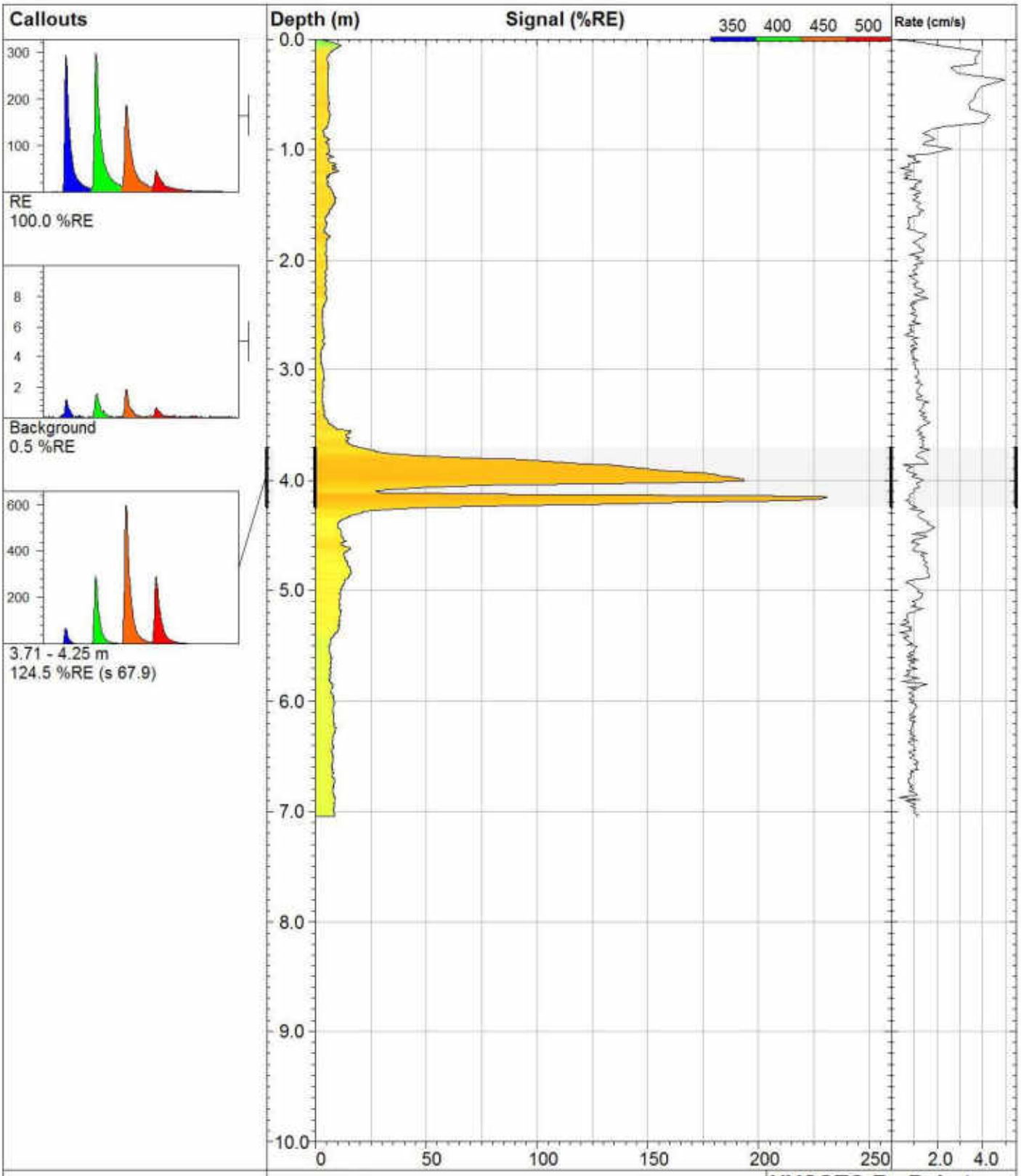
LIF-40

UVOST® By Dakota
www.DakotaTechnologies.com

Final depth:
7.02 m

Max signal:
381.9 %RE @ 3.89 m

Date & Time:
2016-06-15 17:08 AUSEST



numac
Numac Drilling Services PTY Ltd.
www.numac.com.au
1300 131 019
info@numac.com.au

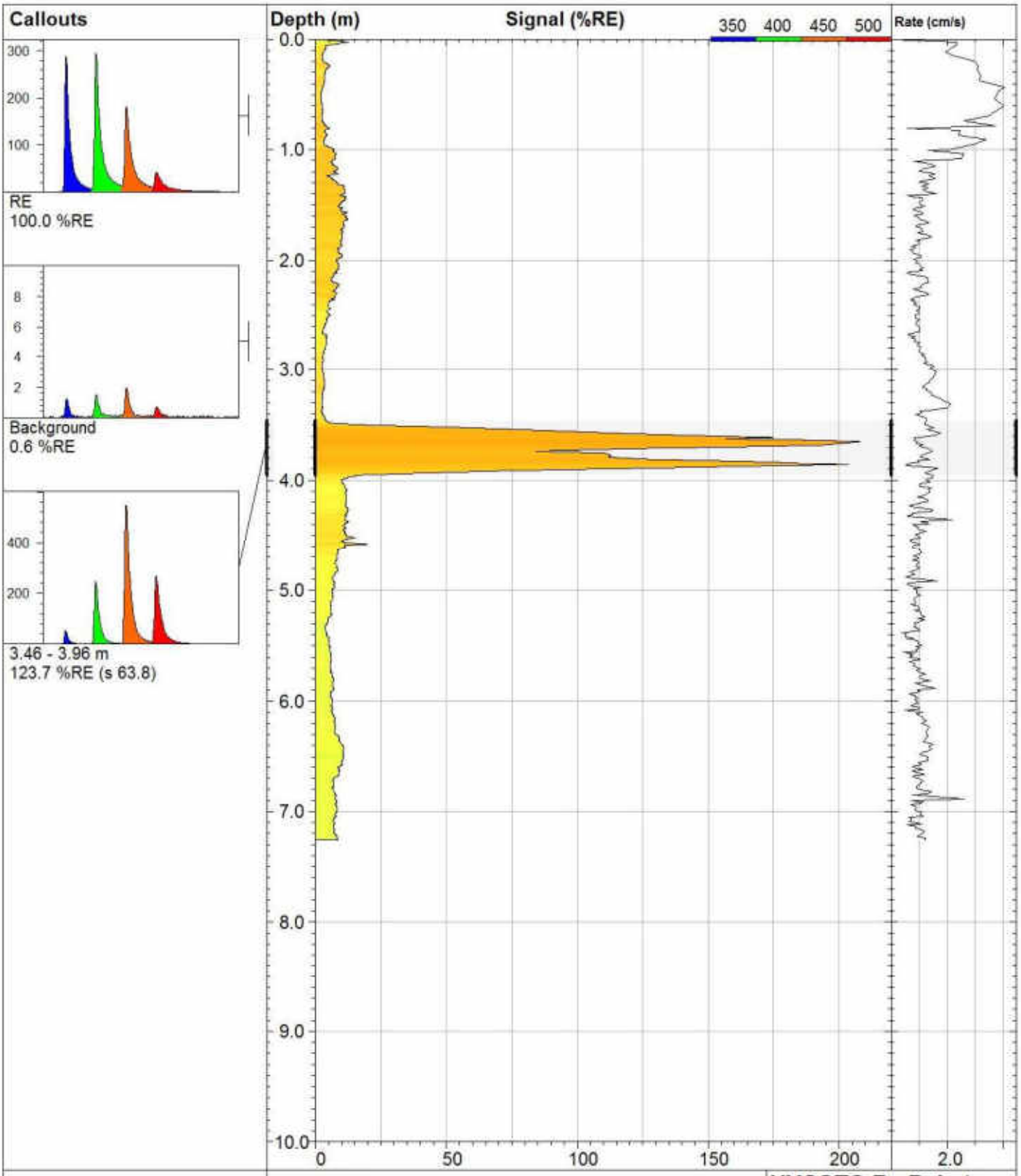
LIF-41

UVOST® By Dakota
www.DakotaTechnologies.com

Final depth:
7.05 m

Max signal:
231.2 %RE @ 4.15 m

Date & Time:
2016-06-15 17:40 AUSEST



numac
Numac Drilling Services PTY Ltd.
www.numac.com.au
1300 131 019
info@numac.com.au

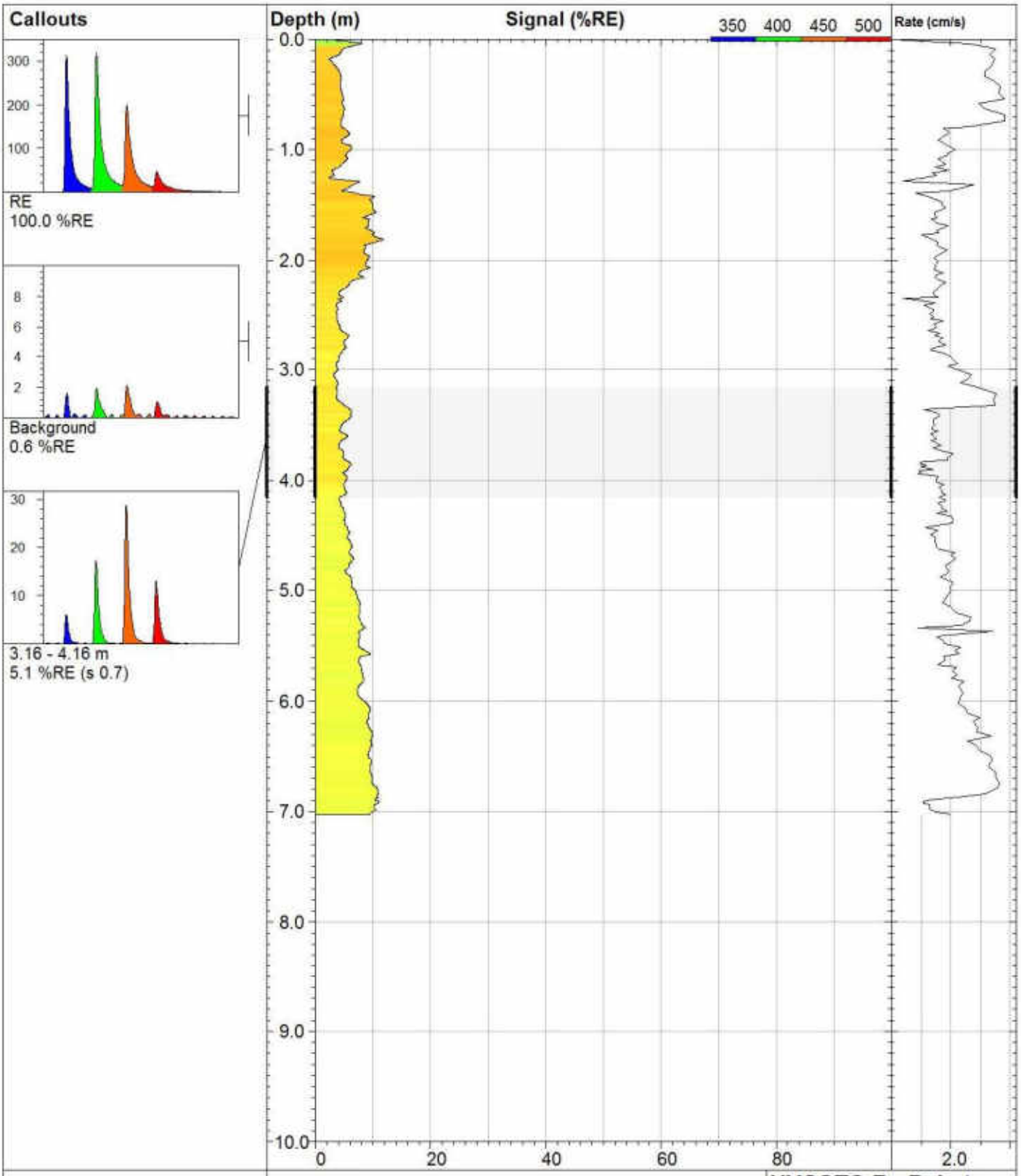
LIF-42

UVOST® By Dakota
www.DakotaTechnologies.com

Final depth:
7.26 m

Max signal:
207.9 %RE @ 3.65 m

Date & Time:
2016-06-15 18:03 AUSEST



numac

Numac Drilling Services PTY Ltd.
www.numac.com.au
1300 131 019
info@numac.com.au

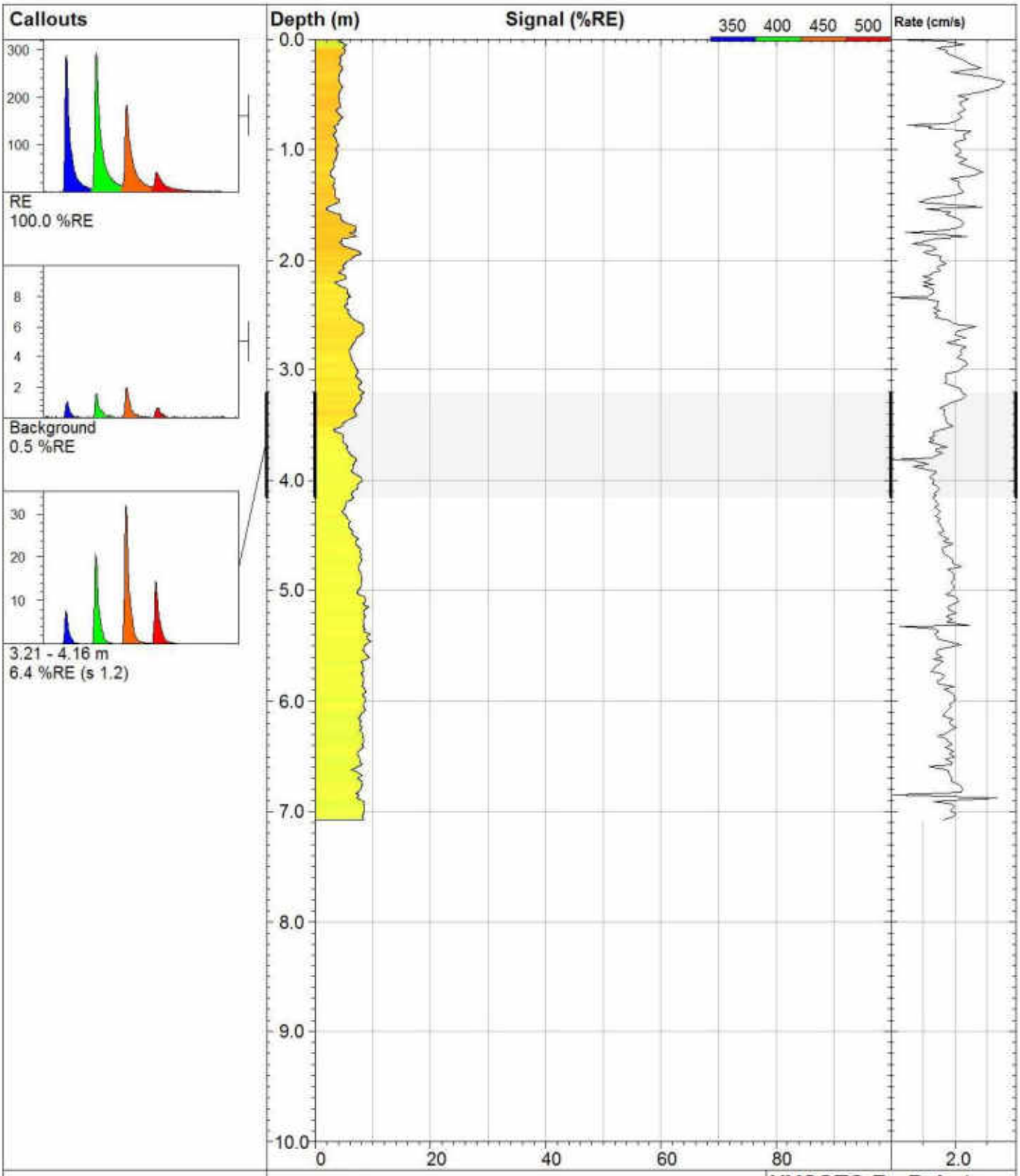
LIF-43

UVOST® By Dakota
www.DakotaTechnologies.com

Final depth:
7.03 m

Max signal:
11.9 %RE @ 1.81 m

Date & Time:
2016-06-16 12:27 AUSEST



numac

Numac Drilling Services PTY Ltd.
www.numac.com.au
1300 131 019
info@numac.com.au

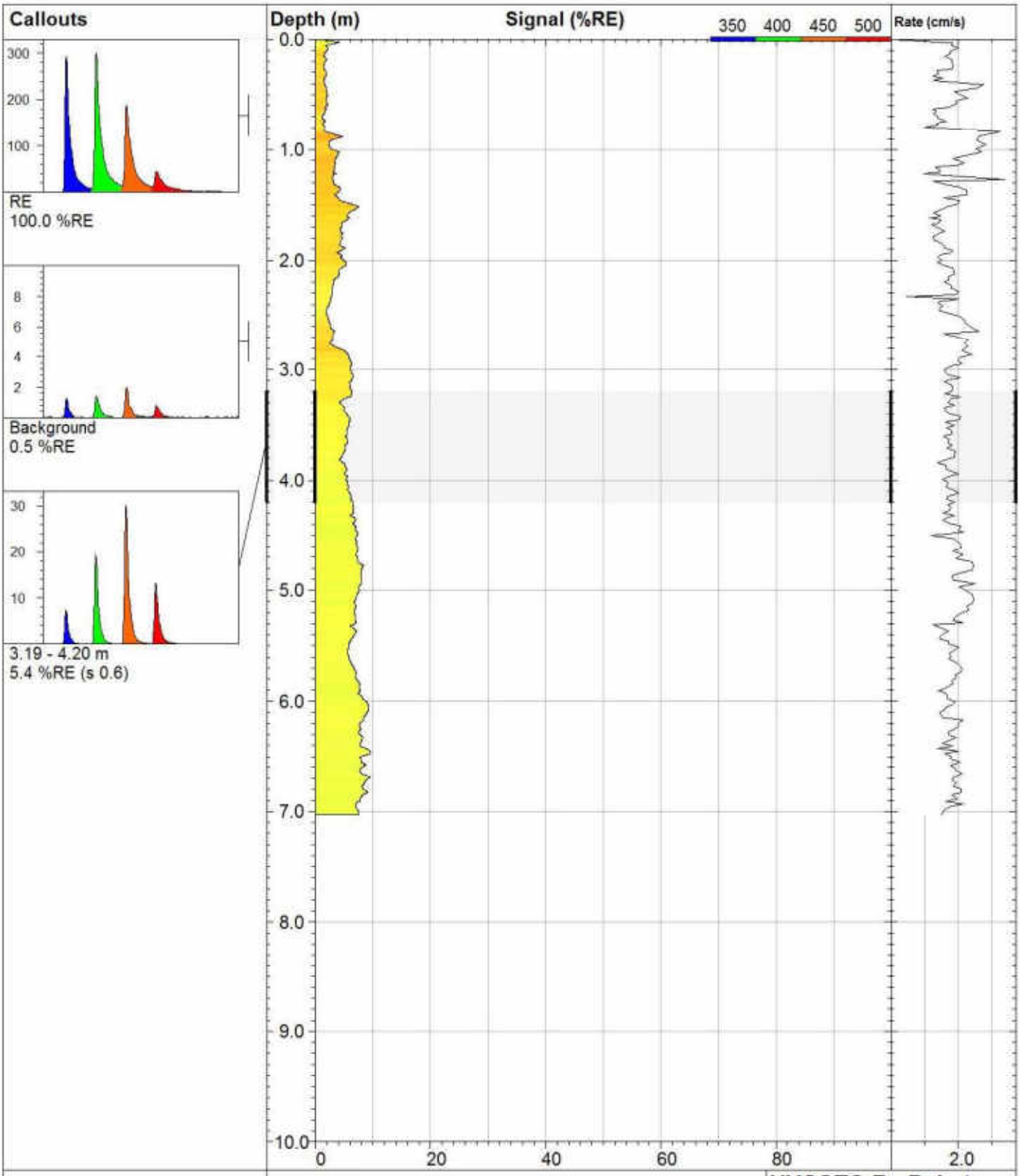
LIF-44

UVOST® By Dakota
www.DakotaTechnologies.com

Final depth:
7.08 m

Max signal:
9.6 %RE @ 5.46 m

Date & Time:
2016-06-16 12:50 AUSEST



numac

Numac Drilling Services PTY Ltd.
www.numac.com.au
1300 131 019
info@numac.com.au

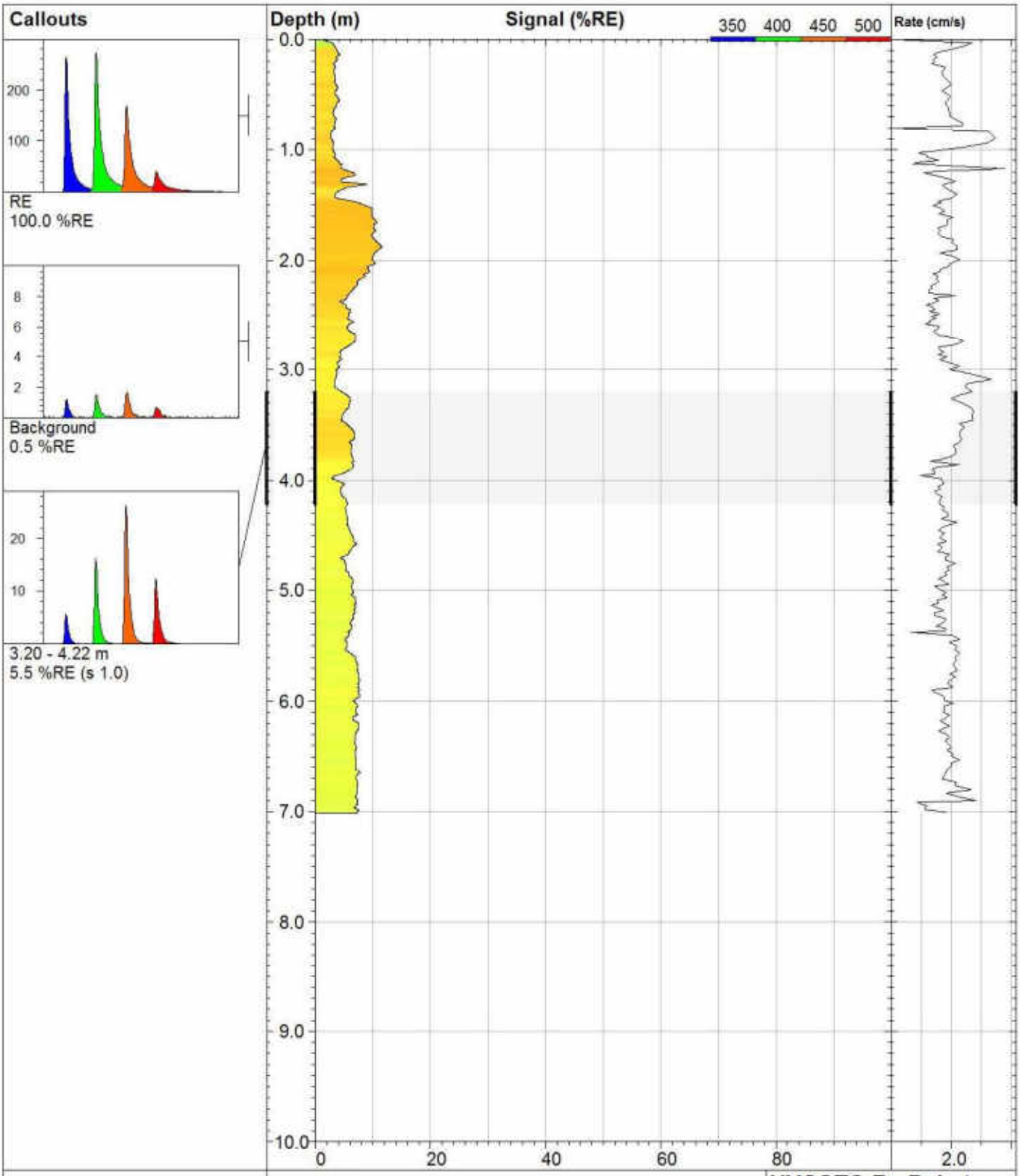
LIF-45

UVOST® By Dakota
www.DakotaTechnologies.com

Final depth:
7.03 m

Max signal:
9.6 %RE @ 6.47 m

Date & Time:
2016-06-16 13:18 AUSEST



numac

Numac Drilling Services PTY Ltd.
www.numac.com.au
1300 131 019
info@numac.com.au

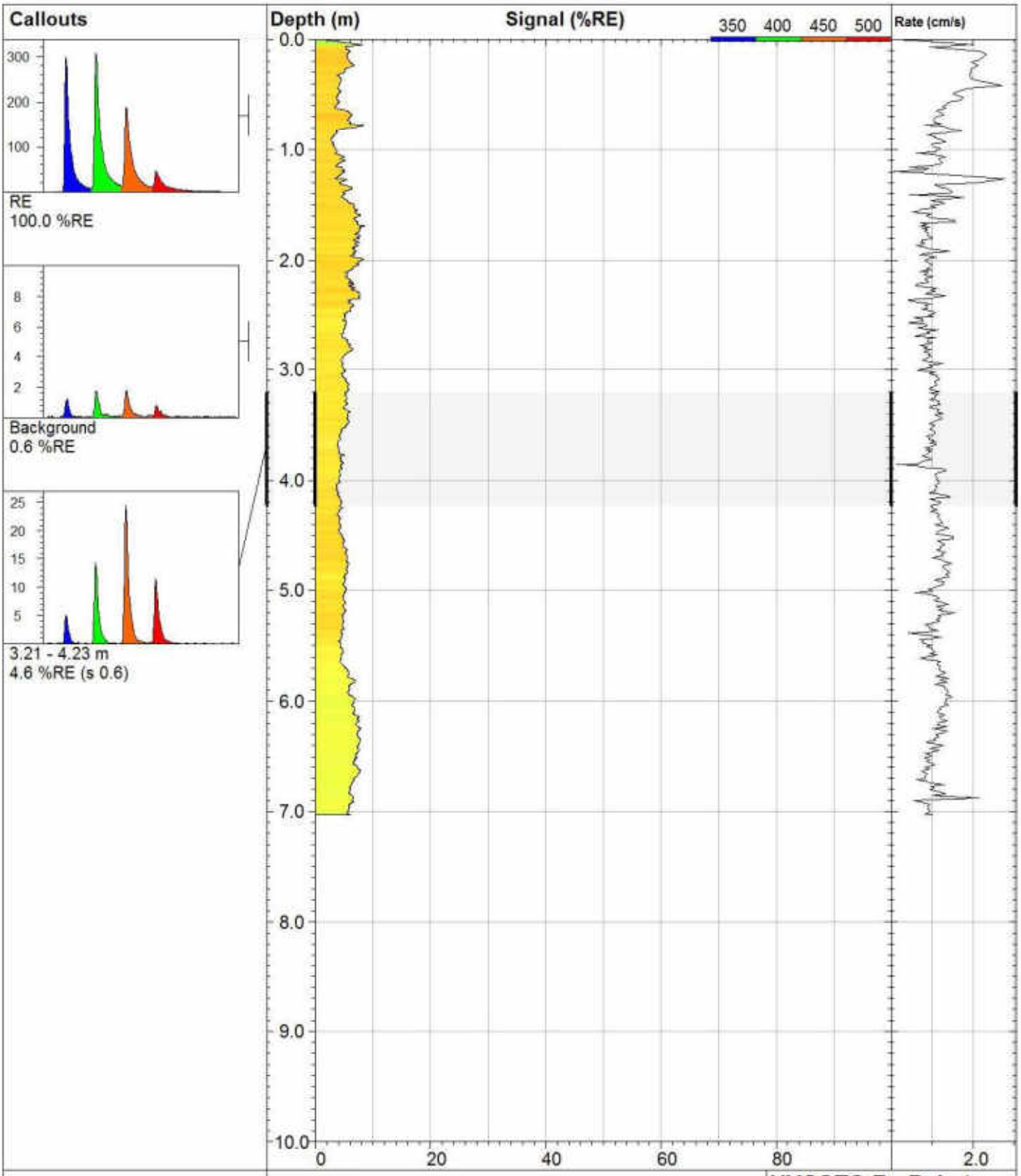
LIF-46

UVOST® By Dakota
www.DakotaTechnologies.com

Final depth:
7.02 m

Max signal:
11.6 %RE @ 1.88 m

Date & Time:
2016-06-16 13:41 AUSEST



numac

Numac Drilling Services PTY Ltd.
www.numac.com.au
1300 131 019
info@numac.com.au

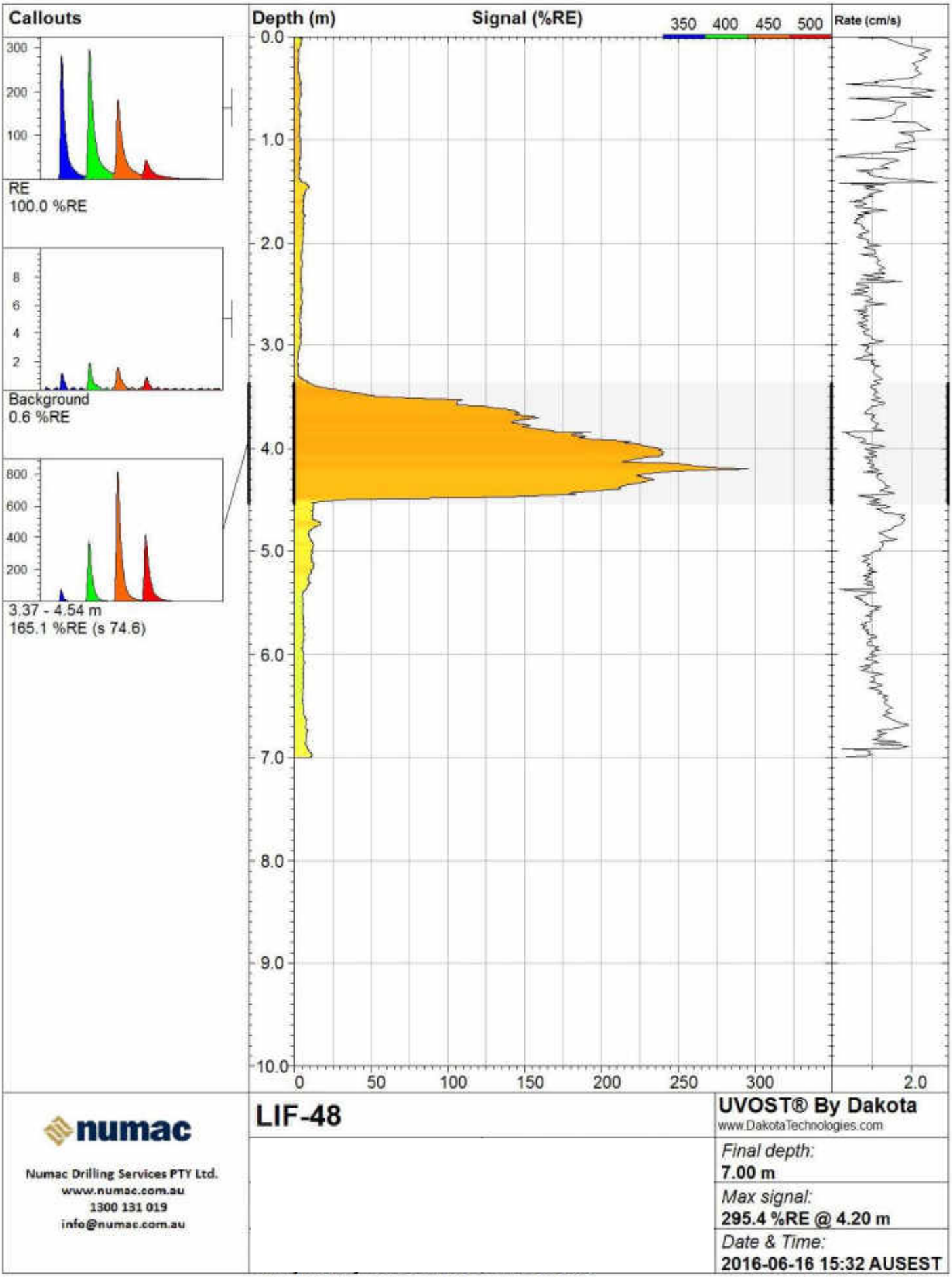
LIF-47

UVOST® By Dakota
www.DakotaTechnologies.com

Final depth:
7.03 m

Max signal:
8.6 %RE @ 1.69 m

Date & Time:
2016-06-16 15:03 AUSEST



numac

Numac Drilling Services PTY Ltd.
www.numac.com.au
1300 131 019
info@numac.com.au

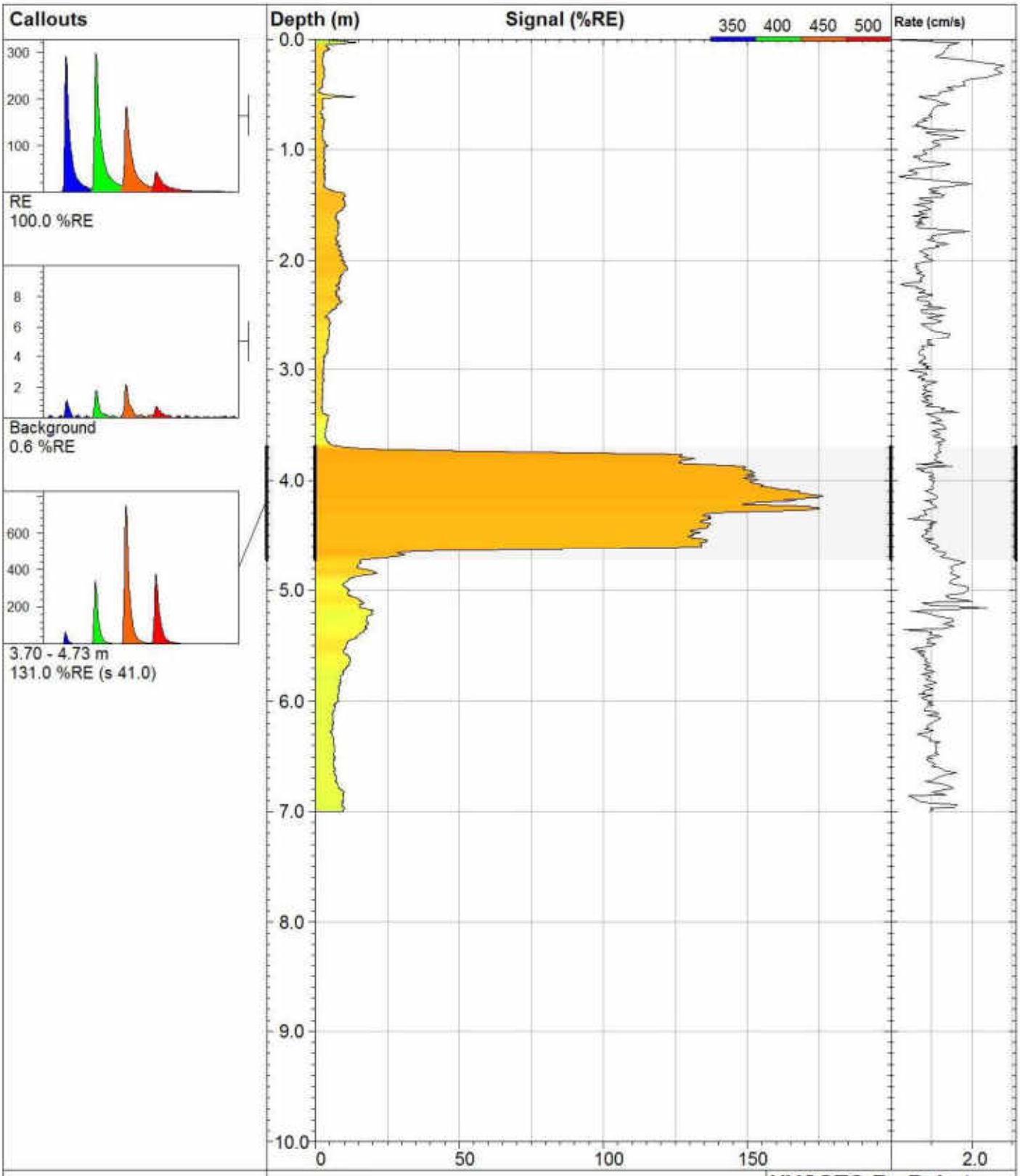
LIF-48

UVOST® By Dakota
www.DakotaTechnologies.com

Final depth:
7.00 m

Max signal:
295.4 %RE @ 4.20 m

Date & Time:
2016-06-16 15:32 AUSEST



numac

Numac Drilling Services PTY Ltd.
www.numac.com.au
1300 131 019
info@numac.com.au

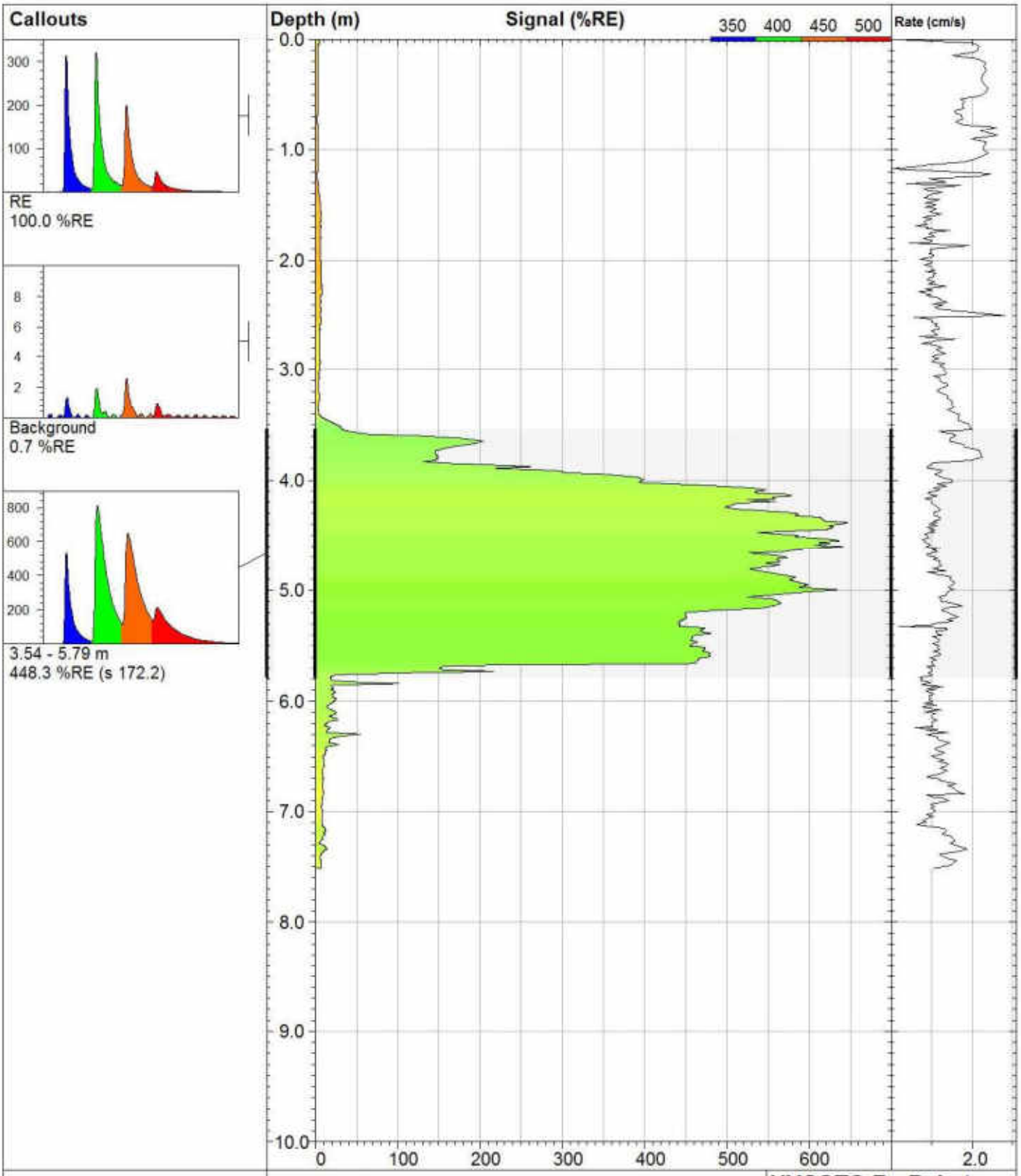
LIF-49

UVOST® By Dakota
www.DakotaTechnologies.com

Final depth:
7.00 m

Max signal:
176.3 %RE @ 4.14 m

Date & Time:
2016-06-16 16:02 AUSEST



numac
Numac Drilling Services PTY Ltd.
www.numac.com.au
1300 131 019
info@numac.com.au

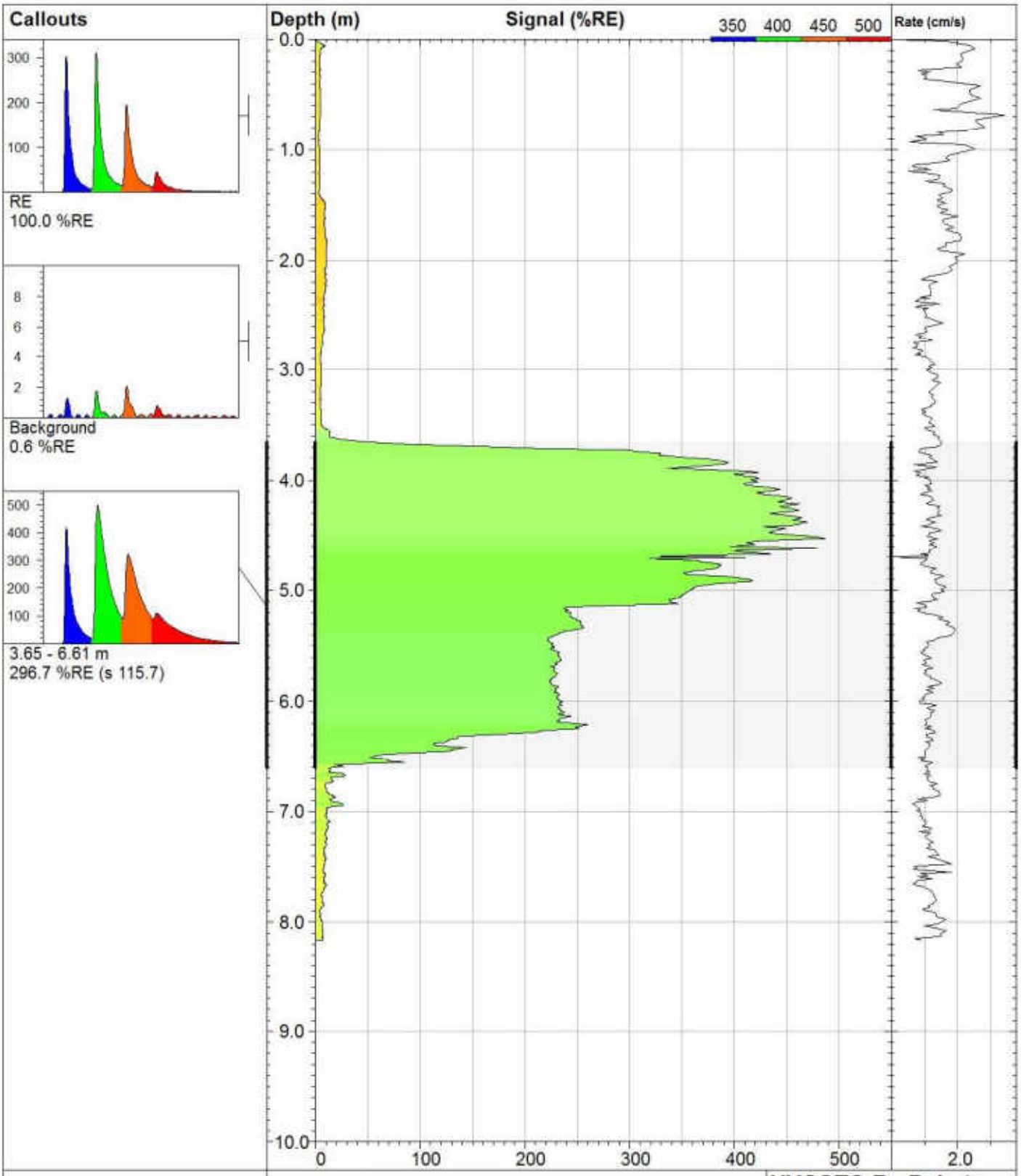
LIF-51

UVOST® By Dakota
www.DakotaTechnologies.com

Final depth:
7.52 m

Max signal:
646.5 %RE @ 4.38 m

Date & Time:
2016-06-16 18:11 AUSEST



numac
Numac Drilling Services PTY Ltd.
www.numac.com.au
1300 131 019
info@numac.com.au

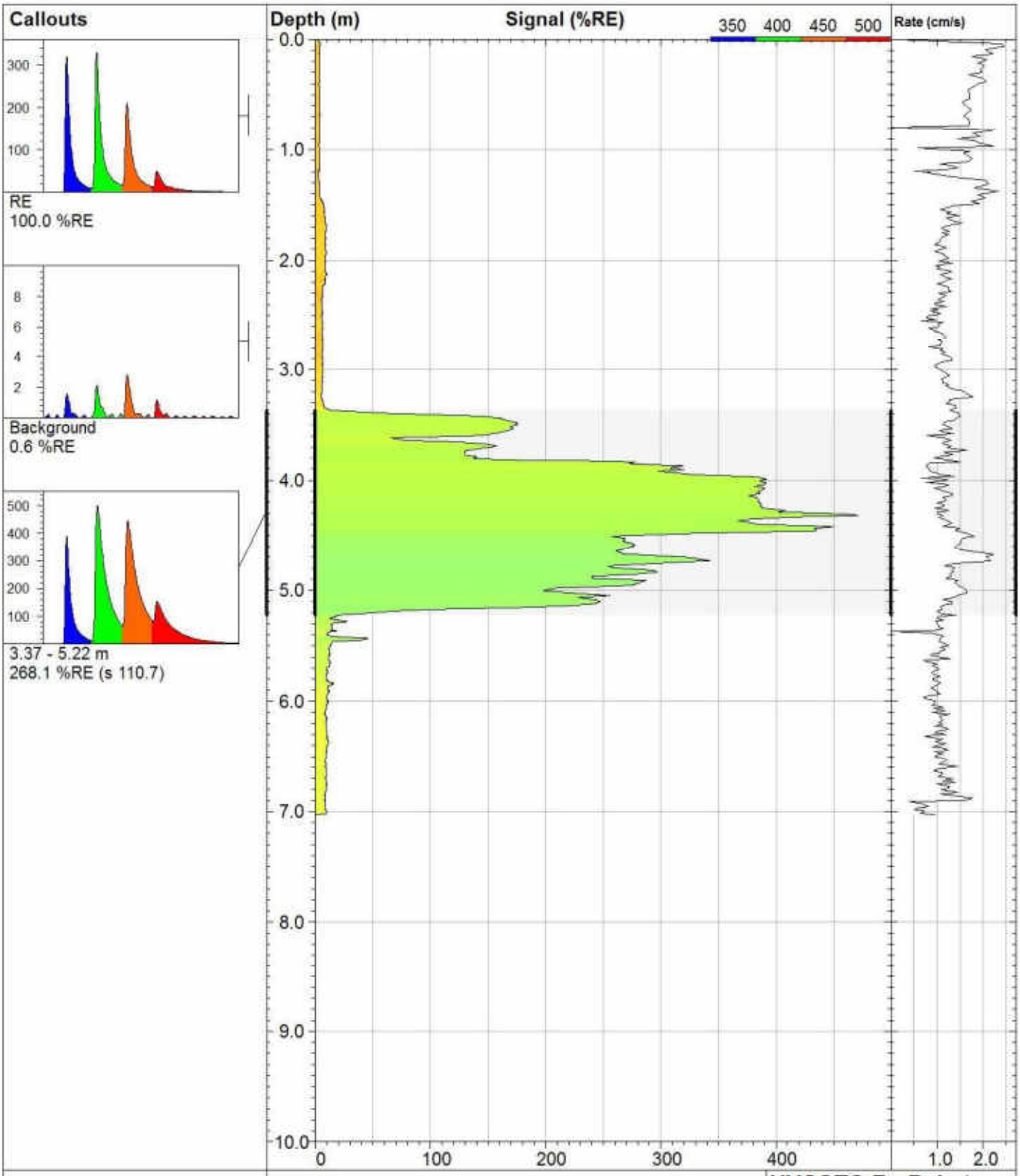
LIF-52

UVOST® By Dakota
www.DakotaTechnologies.com

Final depth:
8.16 m

Max signal:
486.5 %RE @ 4.53 m

Date & Time:
2016-06-16 18:35 AUSEST



numac

Numac Drilling Services PTY Ltd.
www.numac.com.au
1300 131 019
info@numac.com.au

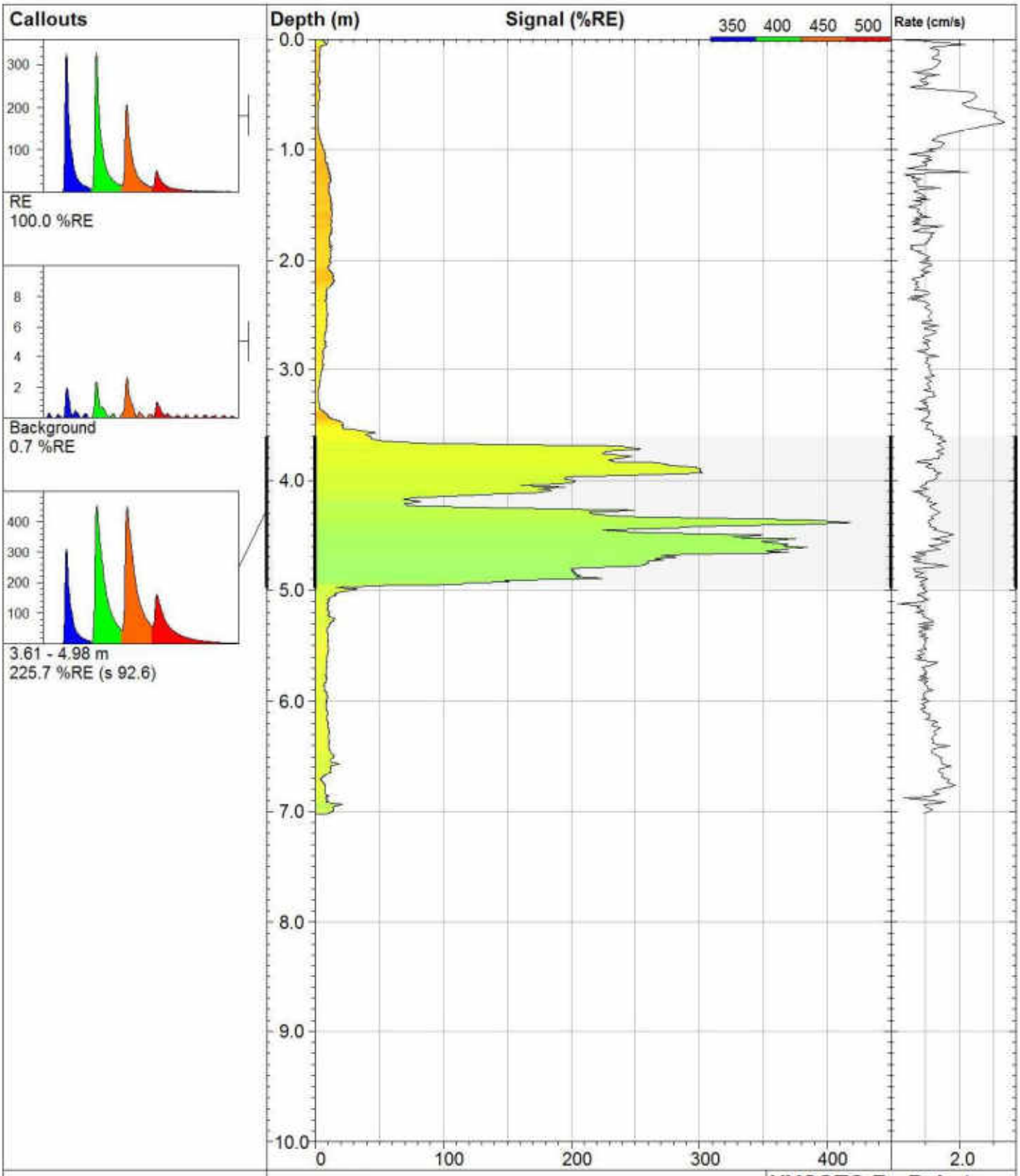
LIF-53

UVOST® By Dakota
www.DakotaTechnologies.com

Final depth:
7.03 m

Max signal:
471.8 %RE @ 4.32 m

Date & Time:
2016-06-17 10:29 AUSEST



numac

Numac Drilling Services PTY Ltd.
www.numac.com.au
1300 131 019
info@numac.com.au

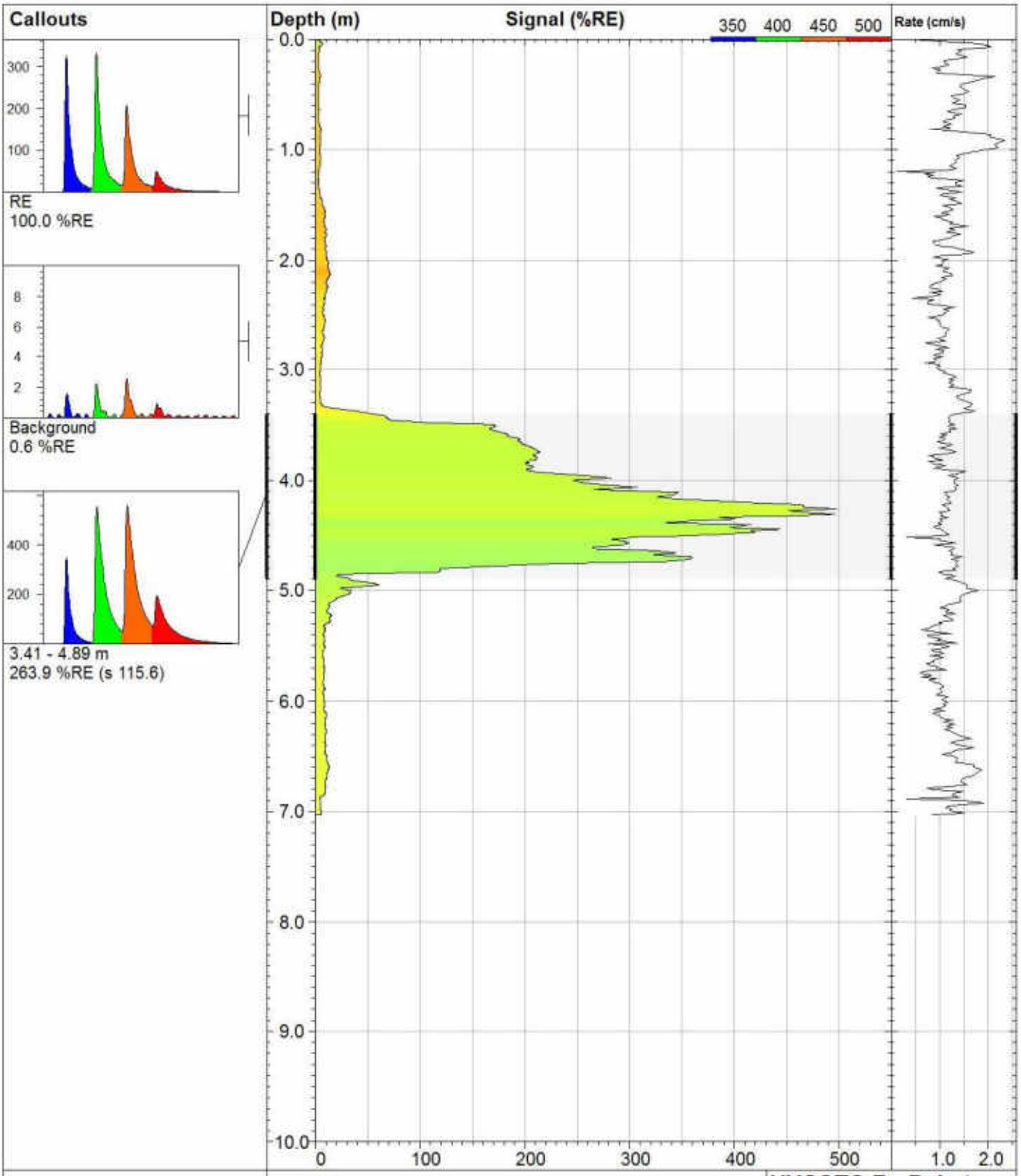
LIF-54

UVOST® By Dakota
www.DakotaTechnologies.com

Final depth:
7.02 m

Max signal:
418.6 %RE @ 4.38 m

Date & Time:
2016-06-17 11:01 AUSEST



numac

Numac Drilling Services PTY Ltd.
www.numac.com.au
1300 131 019
info@numac.com.au

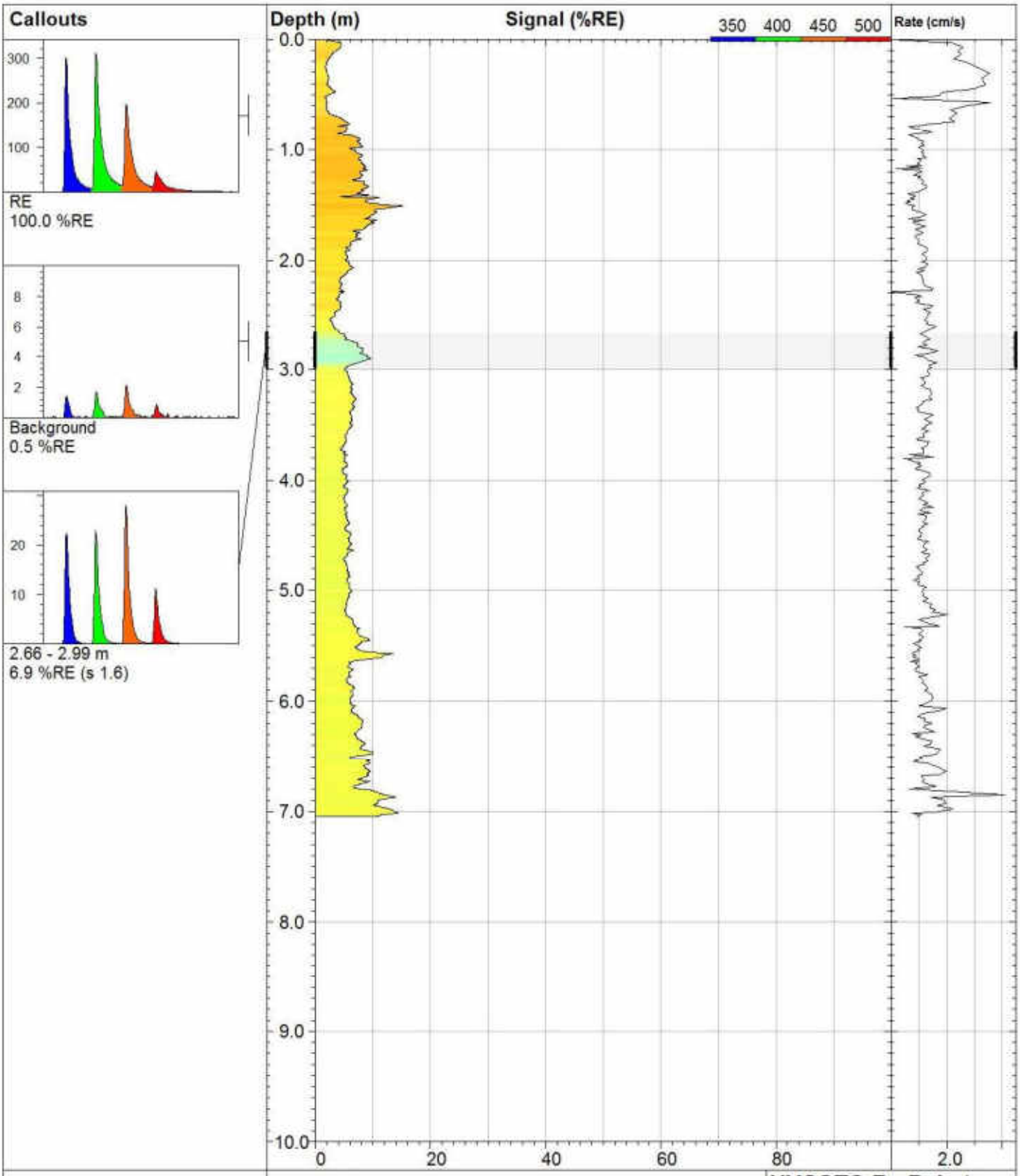
LIF-55

UVOST® By Dakota
www.DakotaTechnologies.com

Final depth:
7.03 m

Max signal:
497.8 %RE @ 4.26 m

Date & Time:
2016-06-17 11:34 AUSEST



numac
Numac Drilling Services PTY Ltd.
www.numac.com.au
1300 131 019
info@numac.com.au

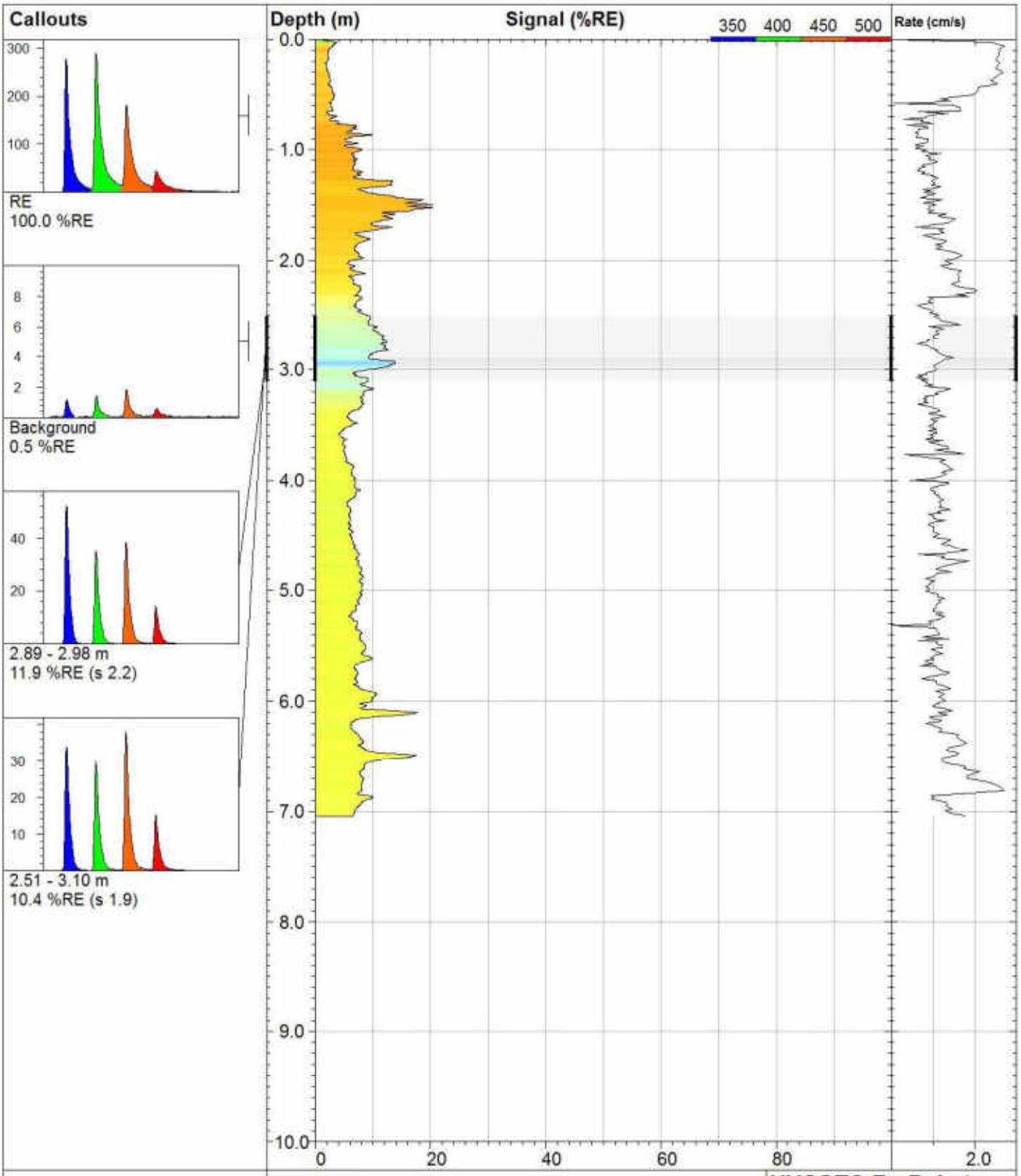
LIF-57

UVOST® By Dakota
www.DakotaTechnologies.com

Final depth:
7.04 m

Max signal:
15.1 %RE @ 1.51 m

Date & Time:
2016-06-17 15:45 AUSEST



numac

Numac Drilling Services PTY Ltd.
www.numac.com.au
1300 131 019
info@numac.com.au

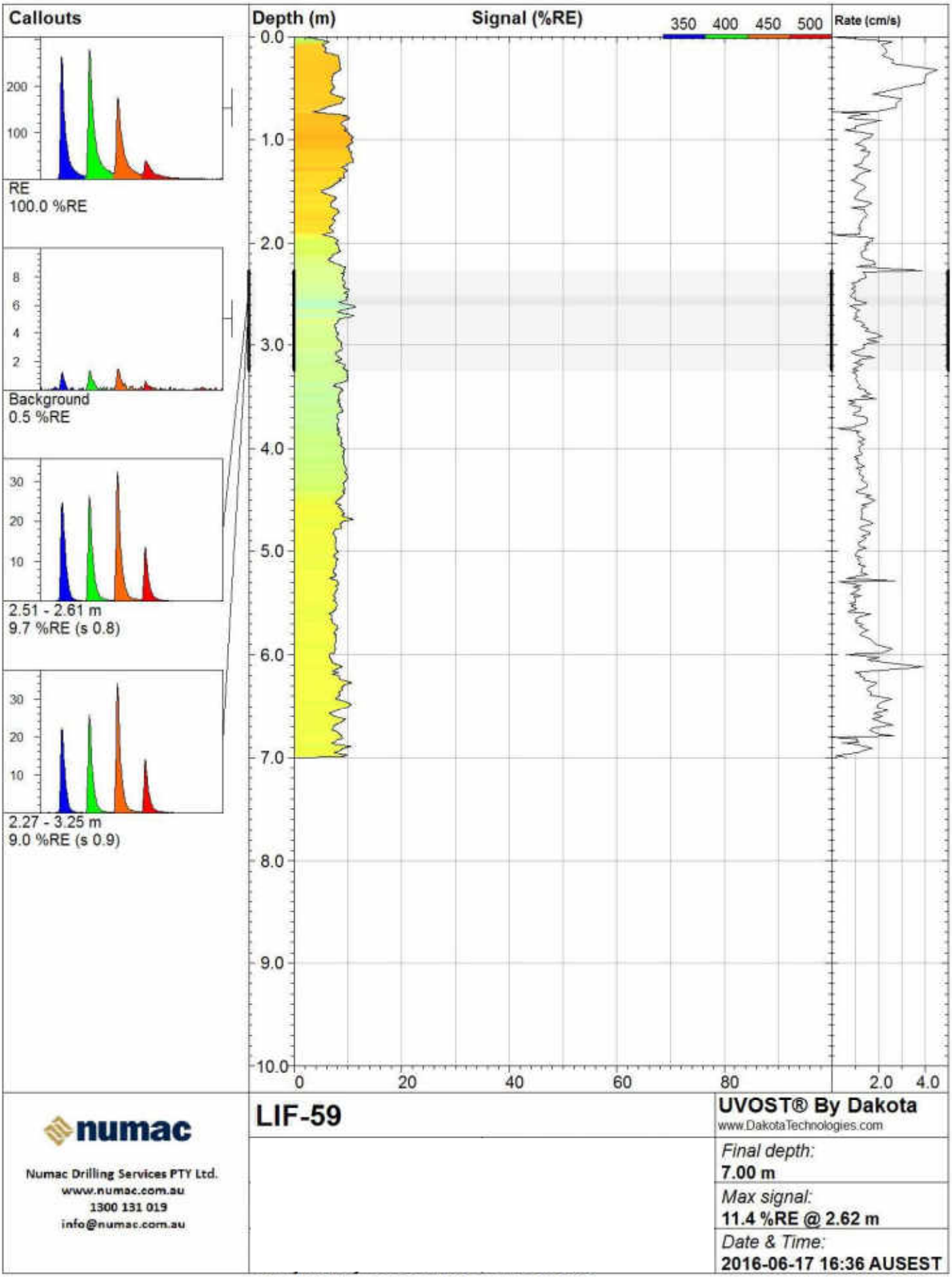
LIF-58

UVOST® By Dakota
www.DakotaTechnologies.com

Final depth:
7.05 m

Max signal:
20.6 %RE @ 1.53 m

Date & Time:
2016-06-17 16:08 AUSEST



numac

Numac Drilling Services PTY Ltd.
www.numac.com.au
1300 131 019
info@numac.com.au

LIF-59

UVOST® By Dakota
www.DakotaTechnologies.com

Final depth:
7.00 m

Max signal:
11.4 %RE @ 2.62 m

Date & Time:
2016-06-17 16:36 AUSEST

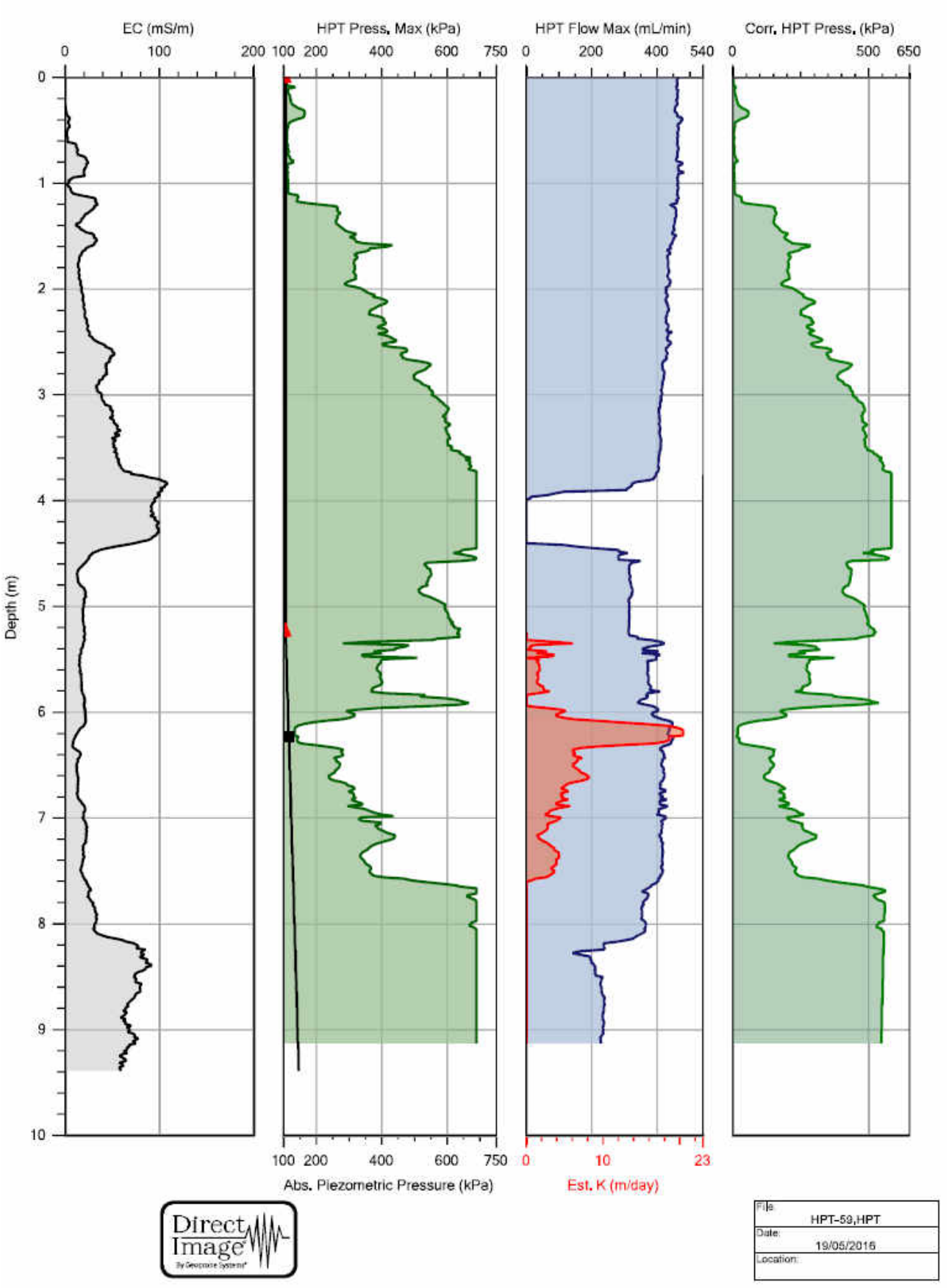
Appendix D: HPT profiles

Contents

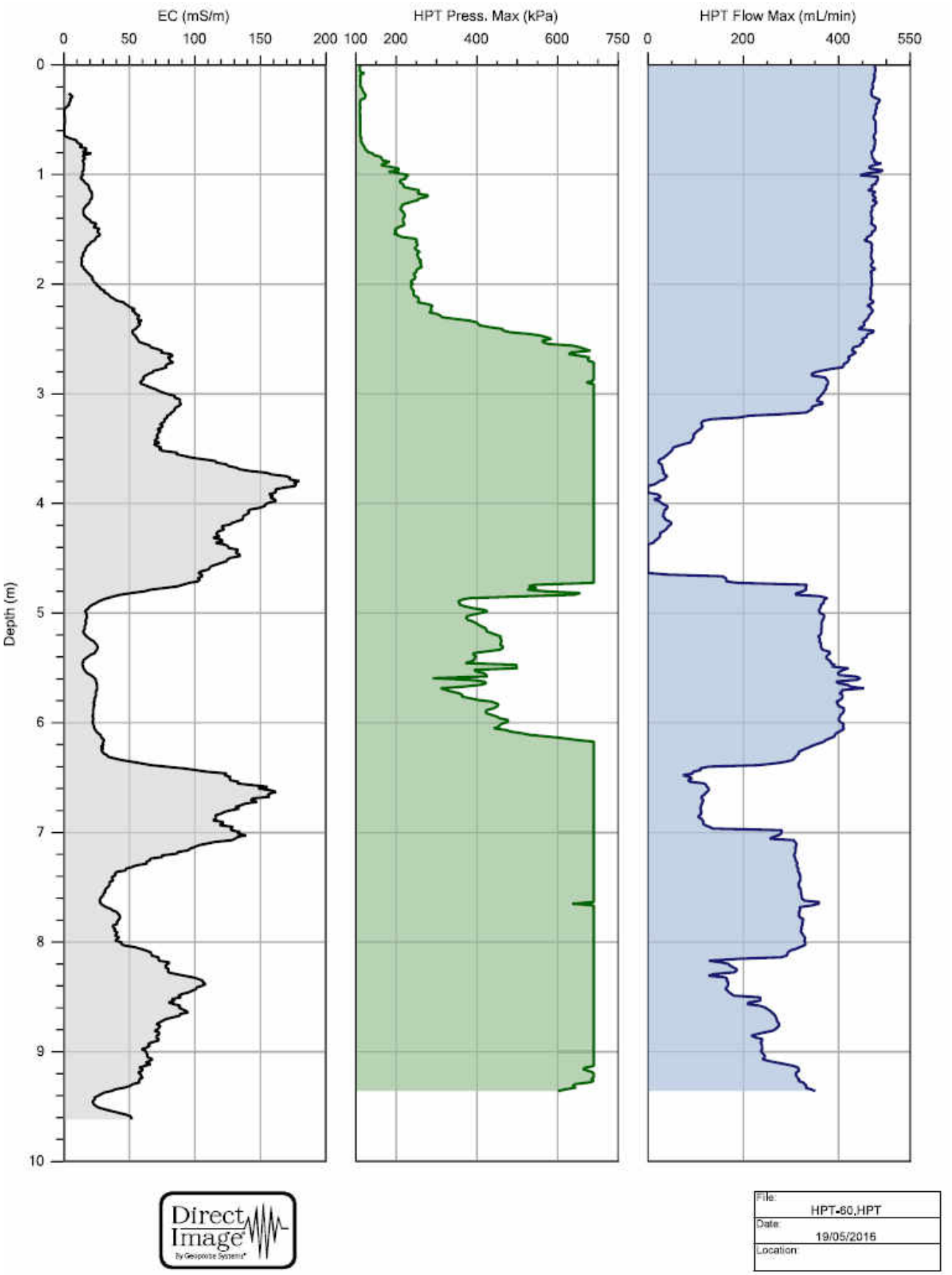
HPT profiles from the petrol station site D-3
HPT59 ..... D-4
HPT60 ..... D-5
HPT61 ..... D-6
HPT62 ..... D-7
HPT63 ..... D-8
HPT64 ..... D-9
HPT72 ..... D-10
HPT73 ..... D-11
HPT74 ..... D-12
HPT75 ..... D-13
HPT profiles from the industrial site D-14
HPT09 ..... D-15
HPT10 ..... D-16
HPT20 ..... D-17
HPT31 ..... D-18
HPT32 ..... D-19
HPT33 ..... D-20
HPT50 ..... D-21
HPT56 ..... D-22

HPT profiles from the petrol station site

HPT59


EC (mS/m)
0
100
200
HPT Press. Max (kPa)
100
200
400
600
750
HPT Flow Max (mL/min)
0
200
400
540
Corr. HPT Press. (kPa)
0
500
650
Depth (m)
0
1
2
3
4
5
6
7
8
9
10
100
200
400
600
750
Abs. Piezometric Pressure (kPa)
0
10
23
Est. K (m/day)
Direct Image
File:
HPT-59.HPT
Date:
19/05/2016
Location:

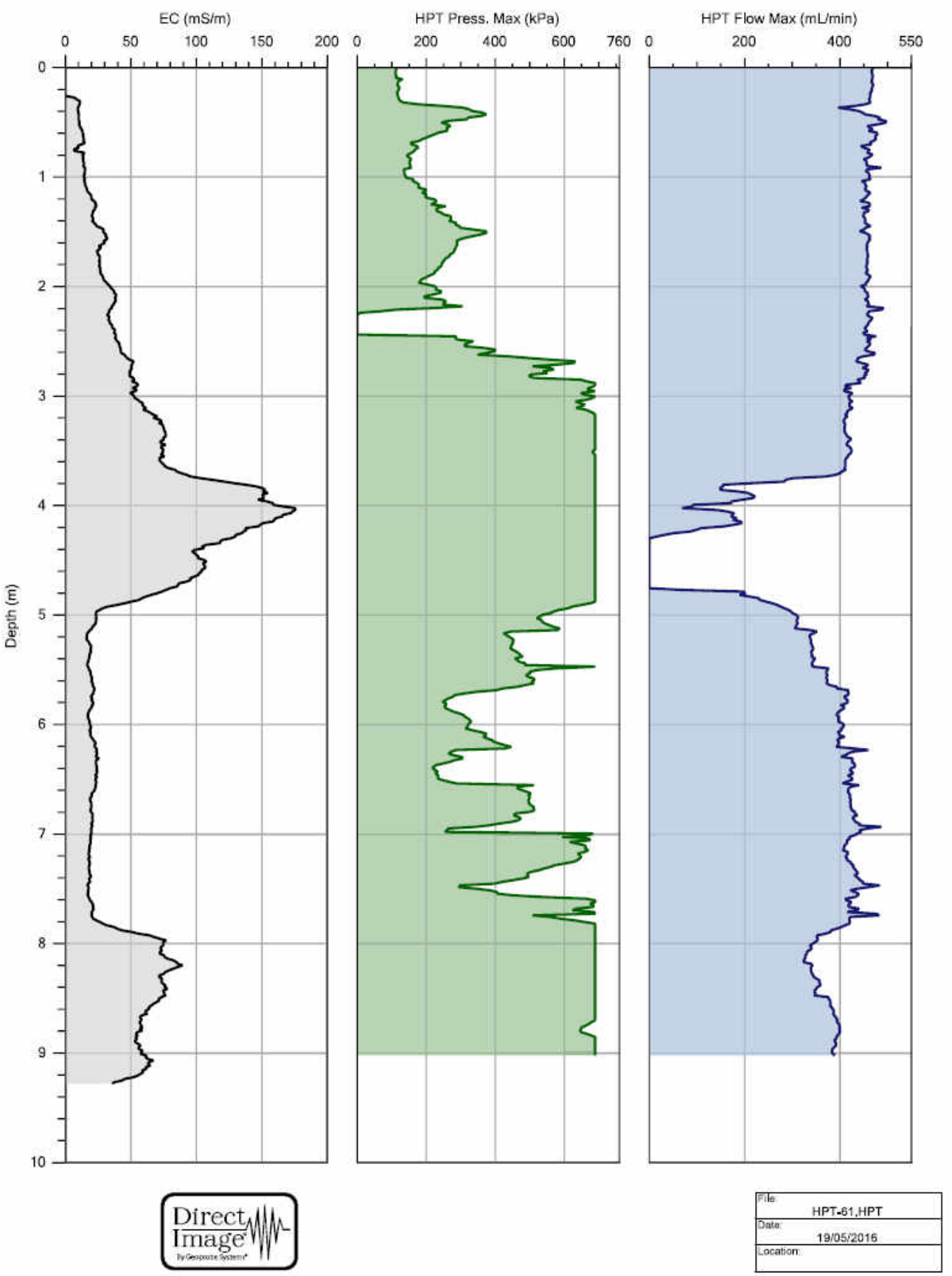
HPT60



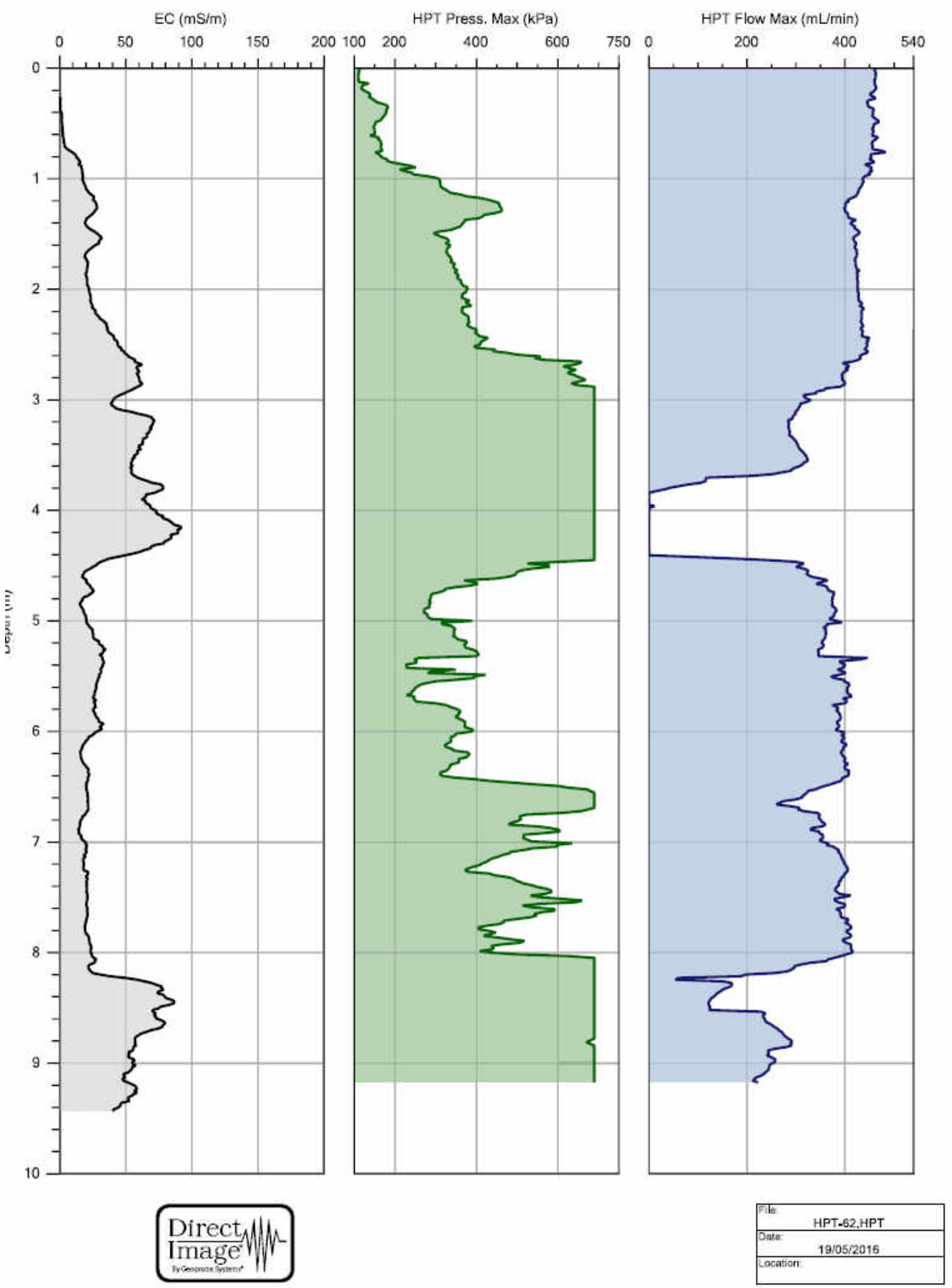
Direct Image
By Geoprobe Systems®

File:	HPT-60.HPT
Date:	19/05/2016
Location:	

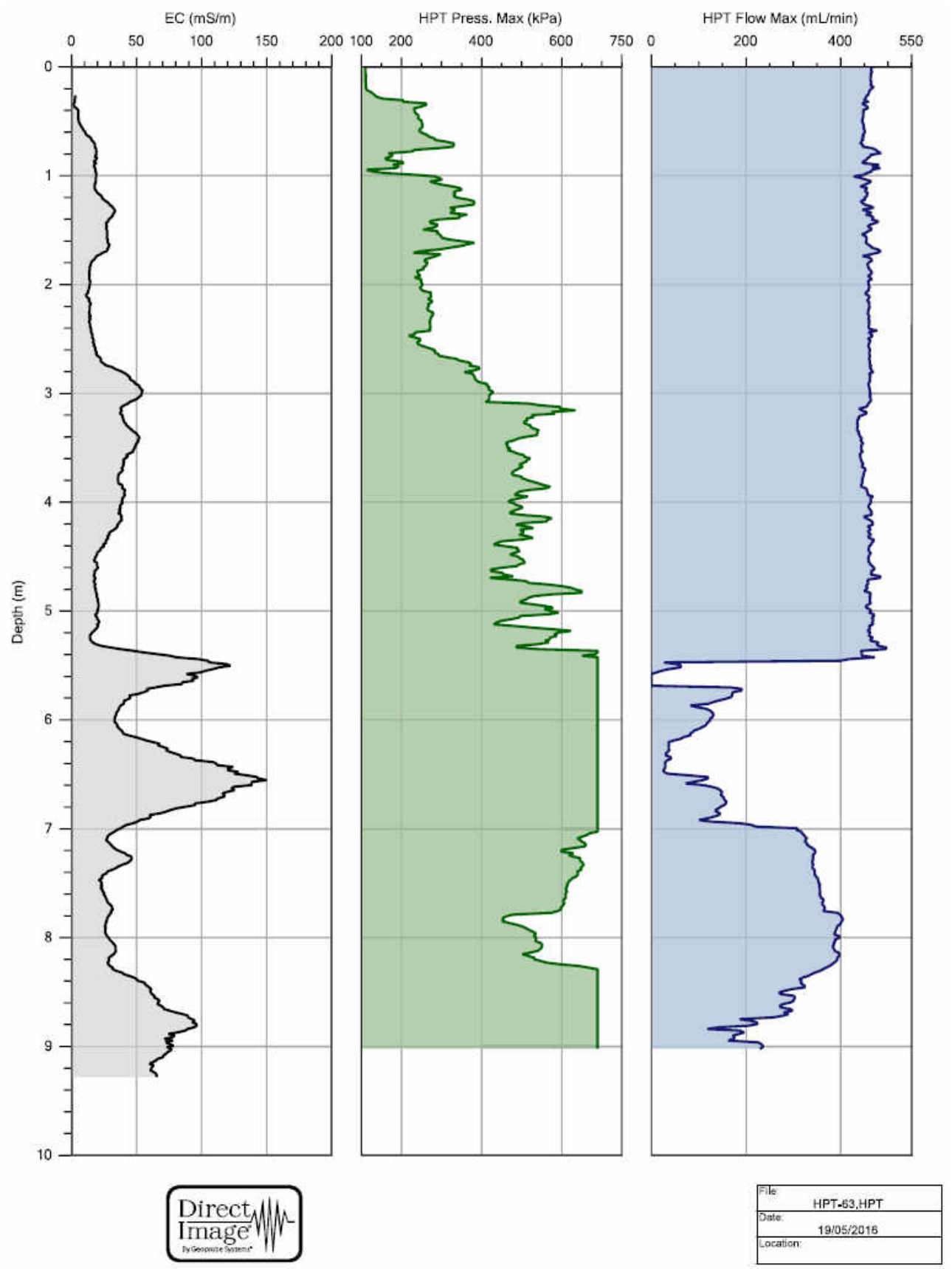
HPT61


EC (mS/m)
0
50
100
150
200
HPT Press. Max (kPa)
0
200
400
600
760
HPT Flow Max (mL/min)
0
200
400
550
Depth (m)
0
1
2
3
4
5
6
7
8
9
10
Direct Image
File:
HPT-61.HPT
Date:
19/05/2016
Location:

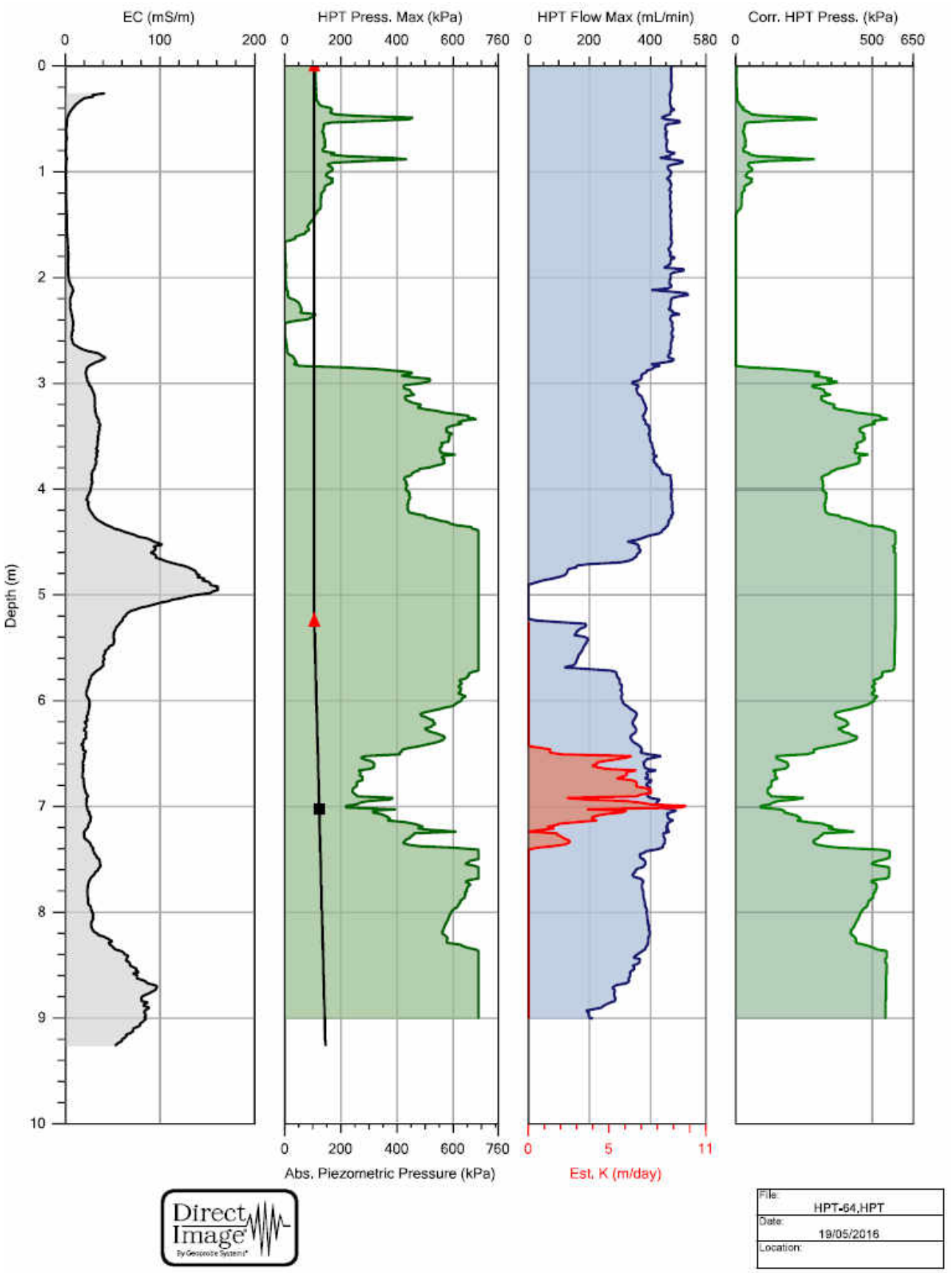
HPT62


EC (mS/m)
0
50
100
150
200
HPT Press. Max (kPa)
100
200
400
600
750
HPT Flow Max (mL/min)
0
200
400
540
0
1
2
3
4
5
6
7
8
9
10
Direct Image
File:
HPT-62.HPT
Date:
19/05/2016
Location:

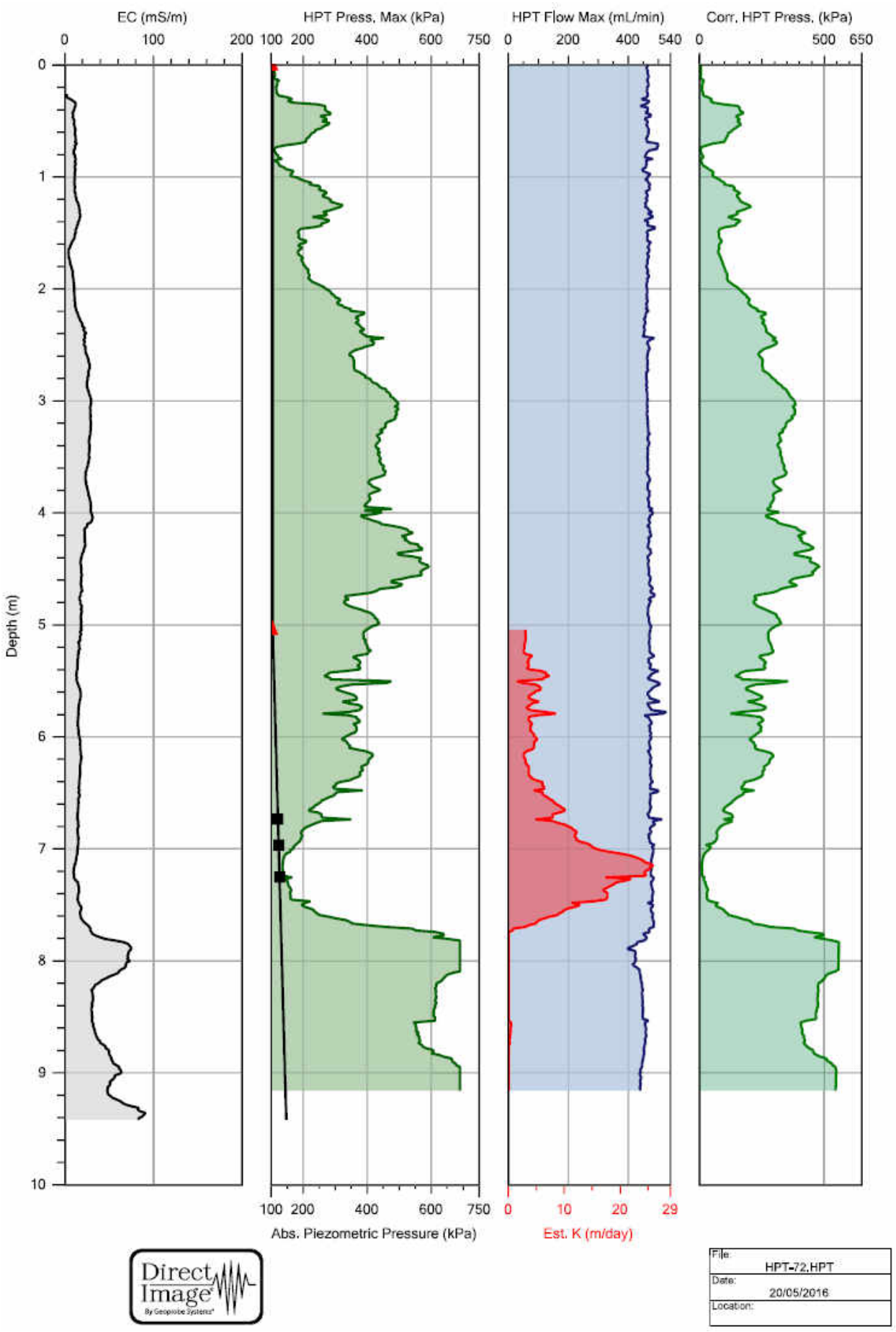
HPT63


EC (mS/m)
0
50
100
150
200
HPT Press. Max (kPa)
100
200
400
600
750
HPT Flow Max (mL/min)
0
200
400
550
Depth (m)
0
1
2
3
4
5
6
7
8
9
10
Direct Image
By Geoprobe Systems
File:
HPT-63.HPT
Date:
19/05/2016
Location:

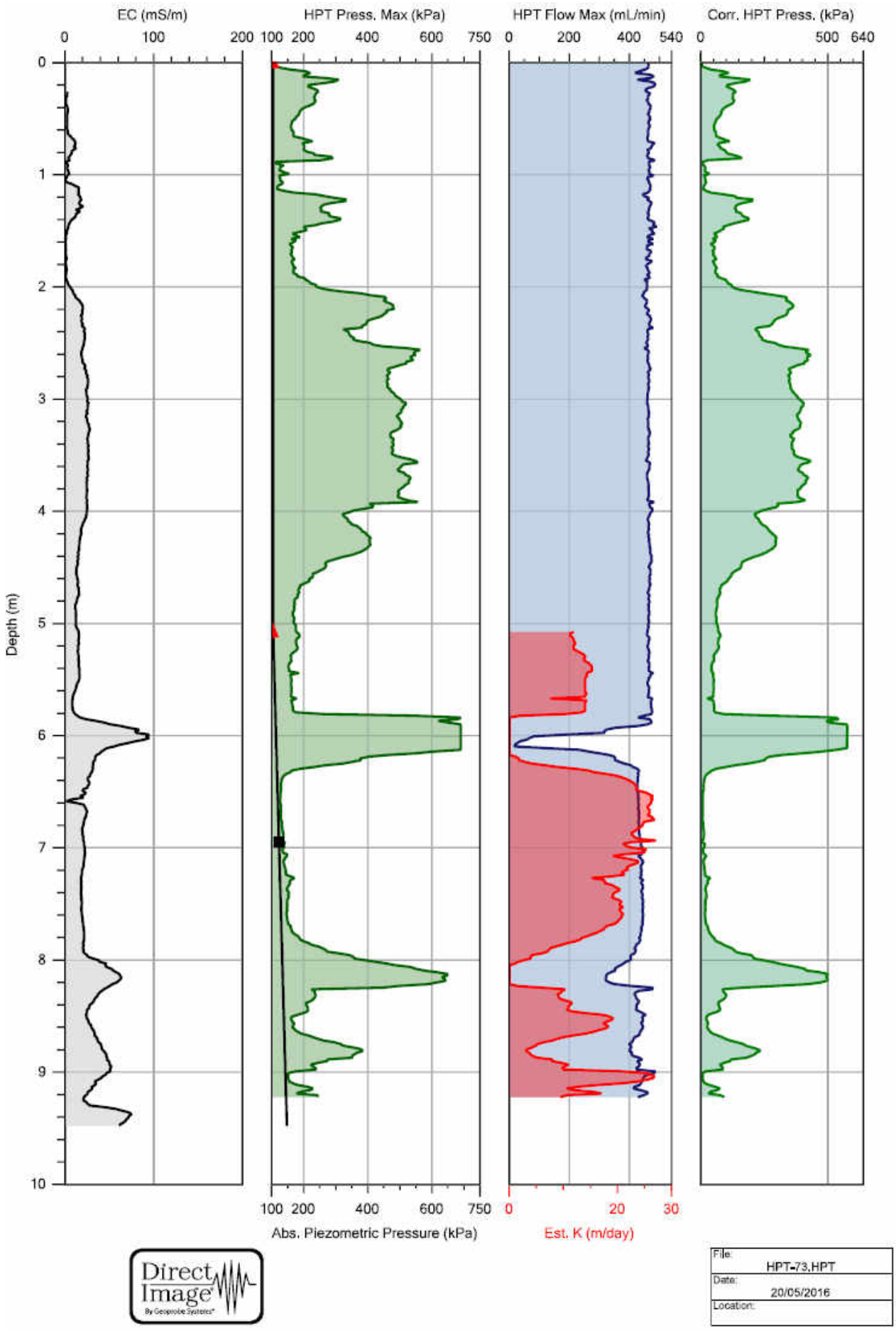
HPT64


EC (mS/m)
0
100
200
HPT Press. Max (kPa)
0
200
400
600
760
HPT Flow Max (mL/min)
0
200
400
580
Corr. HPT Press. (kPa)
0
500
650
Depth (m)
0
1
2
3
4
5
6
7
8
9
10
0
200
400
600
760
Abs. Piezometric Pressure (kPa)
0
5
11
Est. K (m/day)
Direct Image
By Geoprobe Systems
File:
HPT-64.HPT
Date:
19/05/2016
Location:

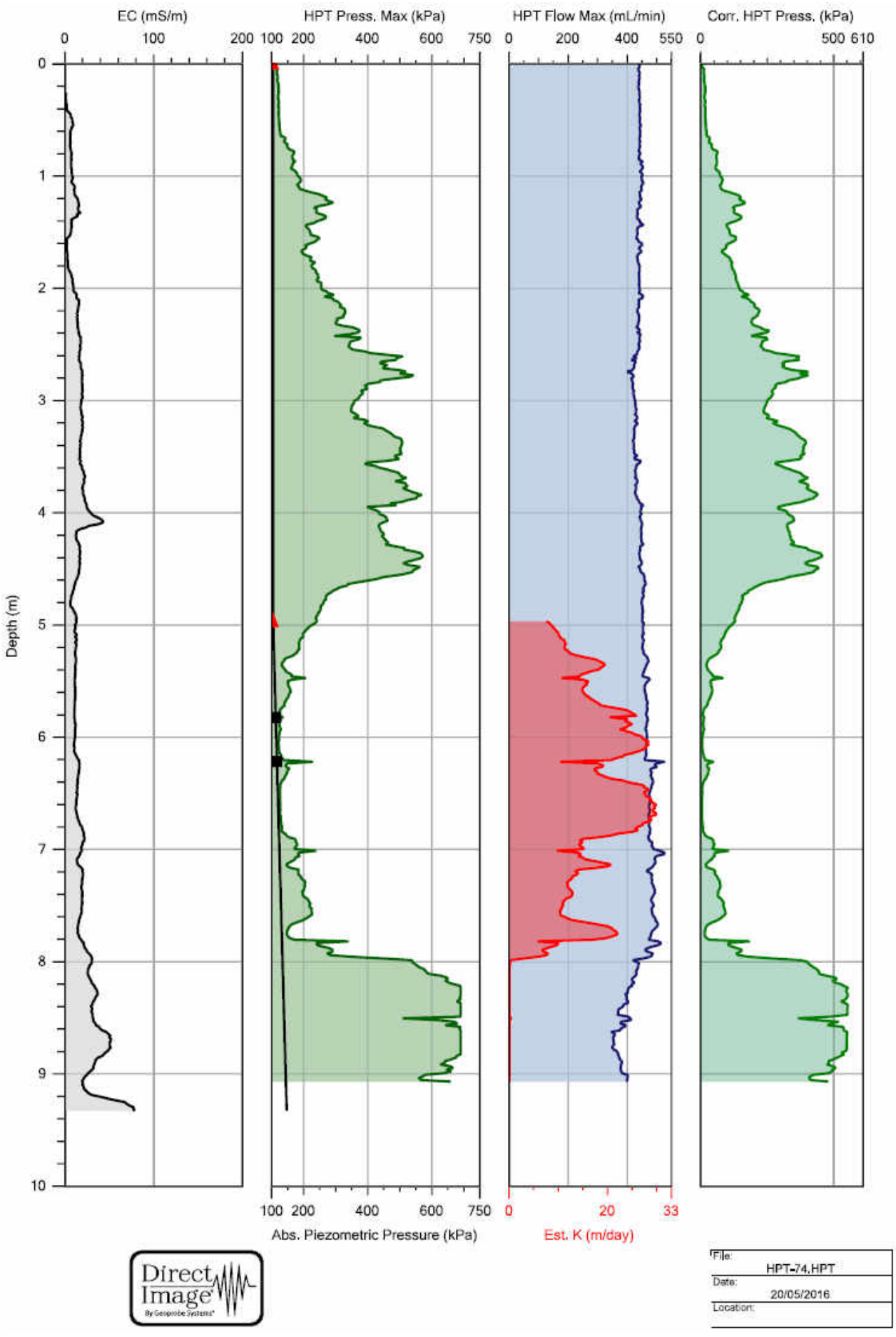
HPT72


EC (mS/m)
0
100
200
HPT Press, Max (kPa)
100
200
400
600
750
HPT Flow Max (mL/min)
0
200
400
540
Corr. HPT Press. (kPa)
0
500
650
Depth (m)
0
1
2
3
4
5
6
7
8
9
10
100
200
400
600
750
Abs. Piezometric Pressure (kPa)
0
10
20
29
Est. K (m/day)
Direct Image
By Geoprobe Systems
File:
HPT-72.HPT
Date:
20/05/2016
Location:

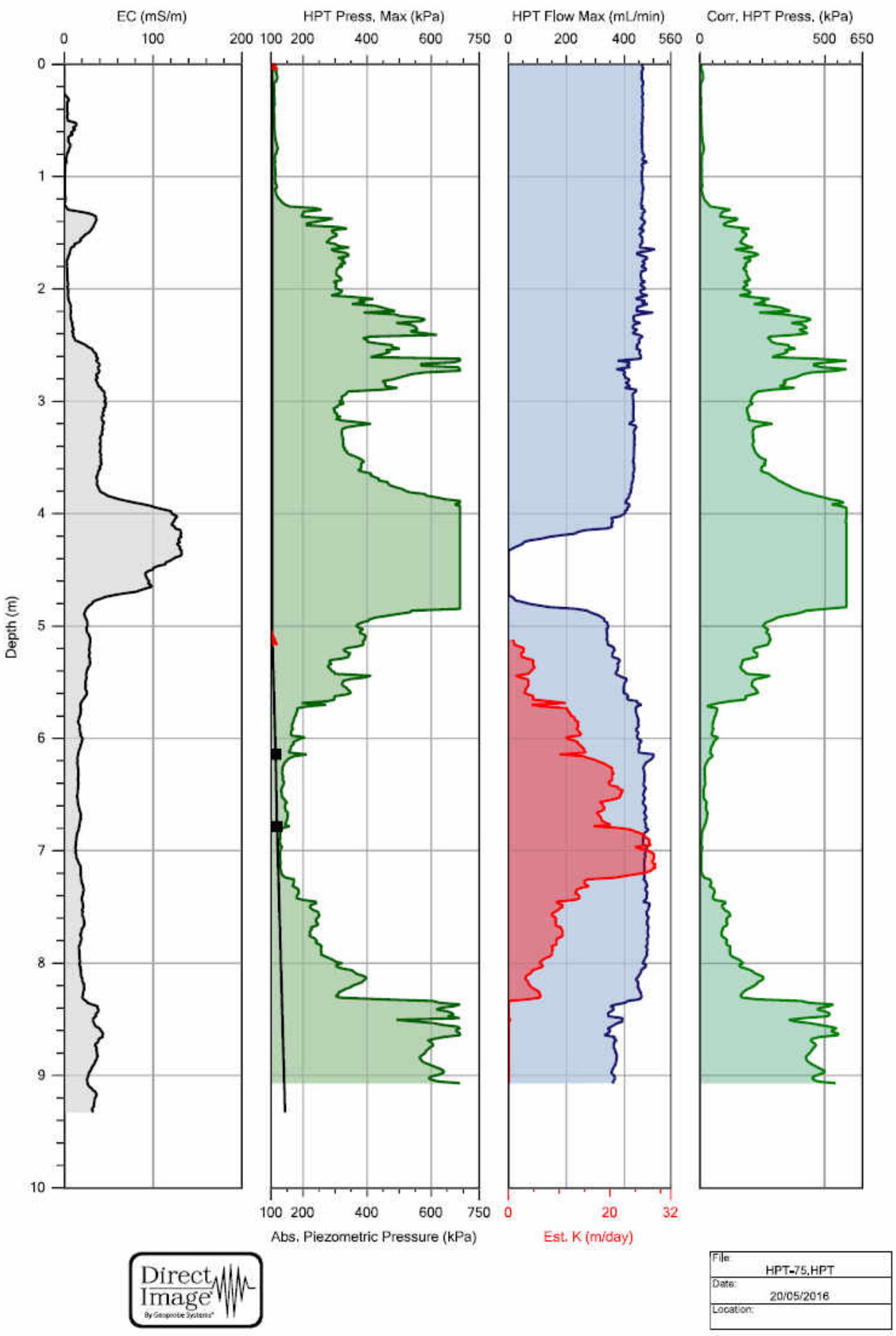
HPT73


EC (mS/m)
0
100
200
HPT Press. Max (kPa)
100
200
400
600
750
HPT Flow Max (mL/min)
0
200
400
540
Corr. HPT Press. (kPa)
0
500
640
Depth (m)
0
1
2
3
4
5
6
7
8
9
10
100
200
400
600
750
Abs. Piezometric Pressure (kPa)
0
20
30
Est. K (m/day)
Direct Image
By Geoprobe Systems
File:
HPT-73.HPT
Date:
20/05/2016
Location:

HPT74

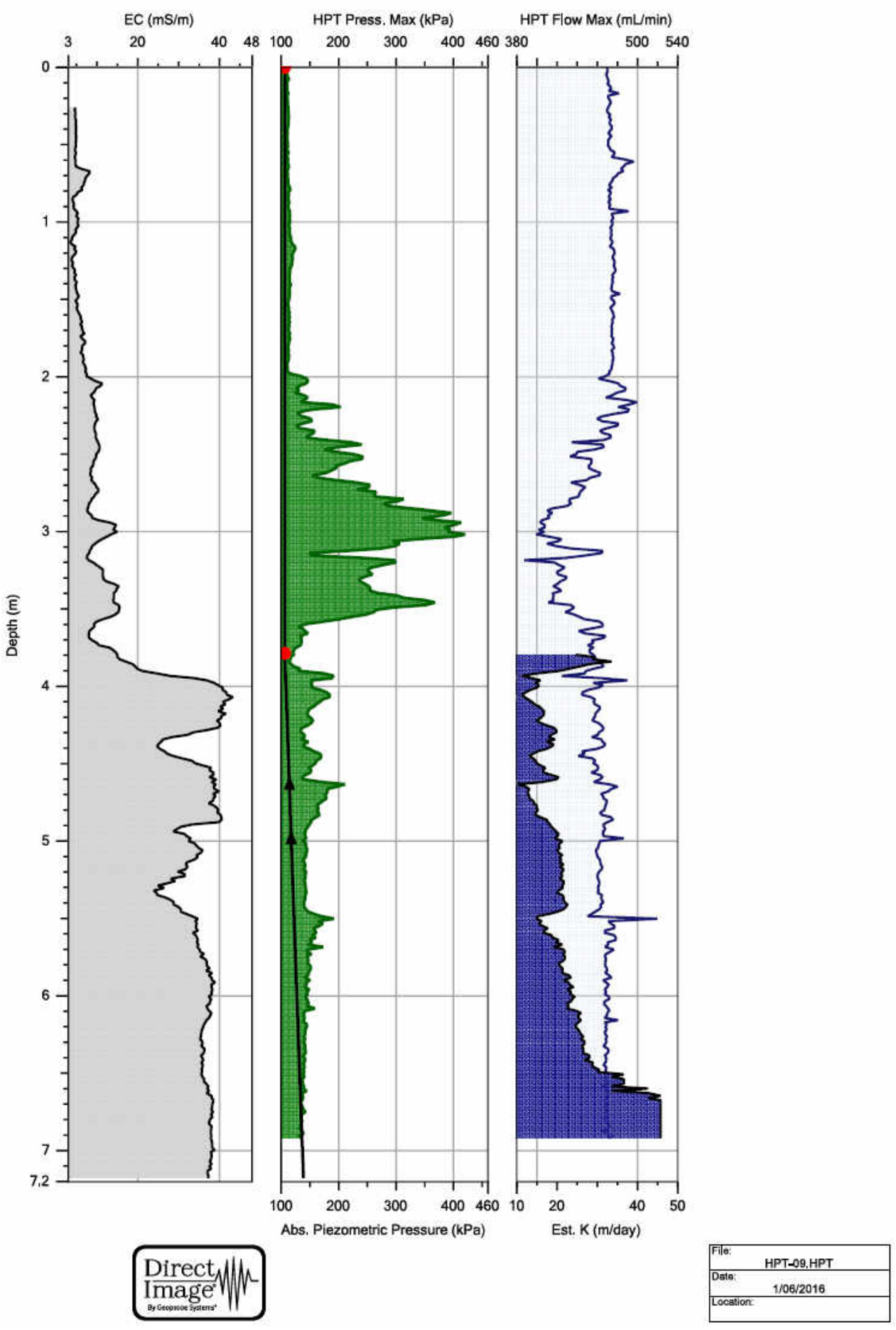

EC (mS/m)
0
100
200
HPT Press. Max (kPa)
100
200
400
600
750
HPT Flow Max (mL/min)
0
200
400
550
Corr. HPT Press. (kPa)
0
500
610
Depth (m)
0
1
2
3
4
5
6
7
8
9
10
100
200
400
600
750
Abs. Piezometric Pressure (kPa)
0
20
33
Est. K (m/day)
Direct Image
By Geoprobe Systems
File:
HPT-74.HPT
Date:
20/05/2016
Location:

HPT75

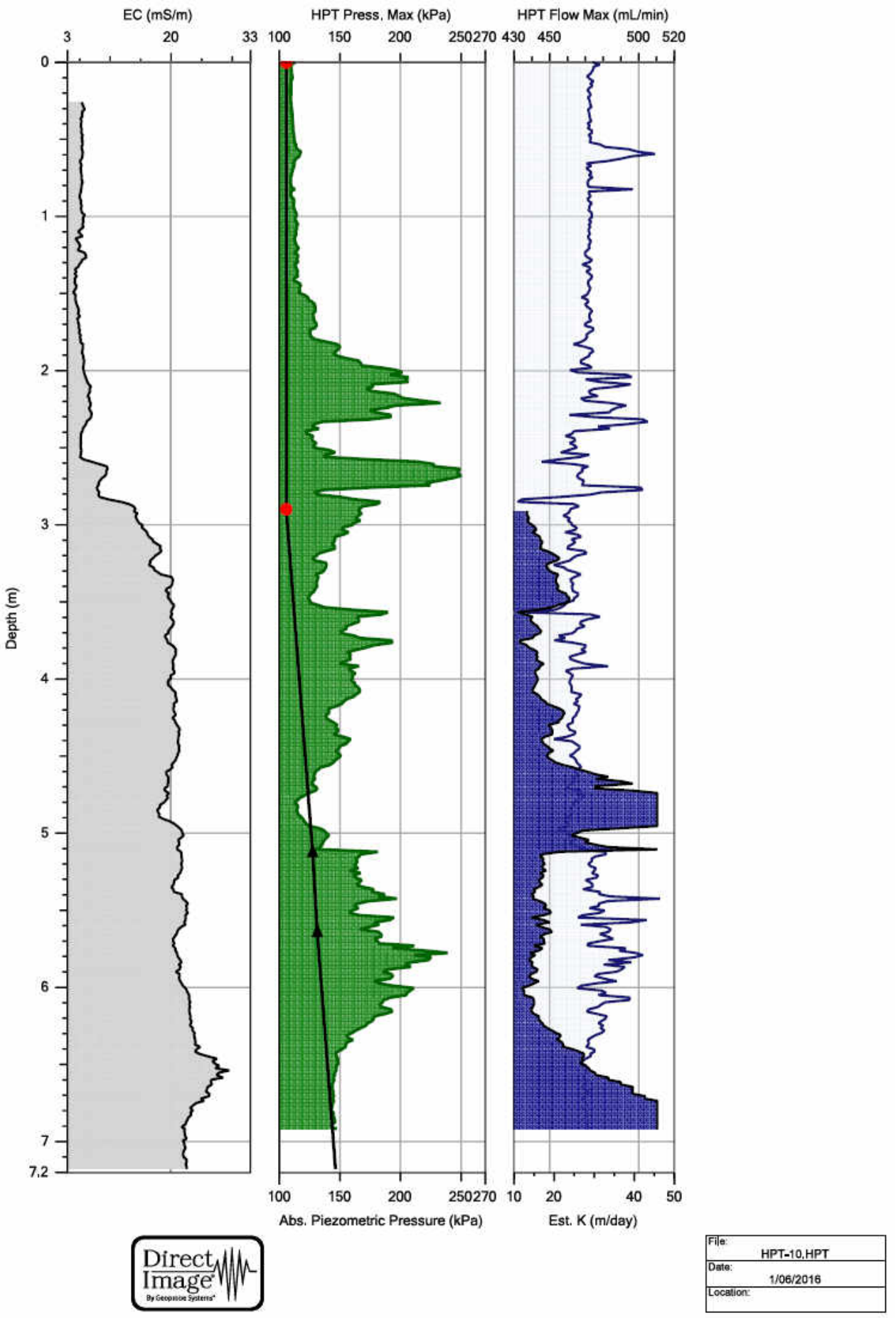

EC (mS/m)
0
100
200
HPT Press, Max (kPa)
100
200
400
600
750
HPT Flow Max (mL/min)
0
200
400
560
Corr. HPT Press. (kPa)
0
500
650
Depth (m)
0
1
2
3
4
5
6
7
8
9
10
100
200
400
600
750
Abs. Piezometric Pressure (kPa)
0
20
32
Est. K (m/day)
Direct Image
By Geoprobe Systems
File:
HPT-75.HPT
Date:
20/05/2016
Location:

HPT profiles from the industrial site

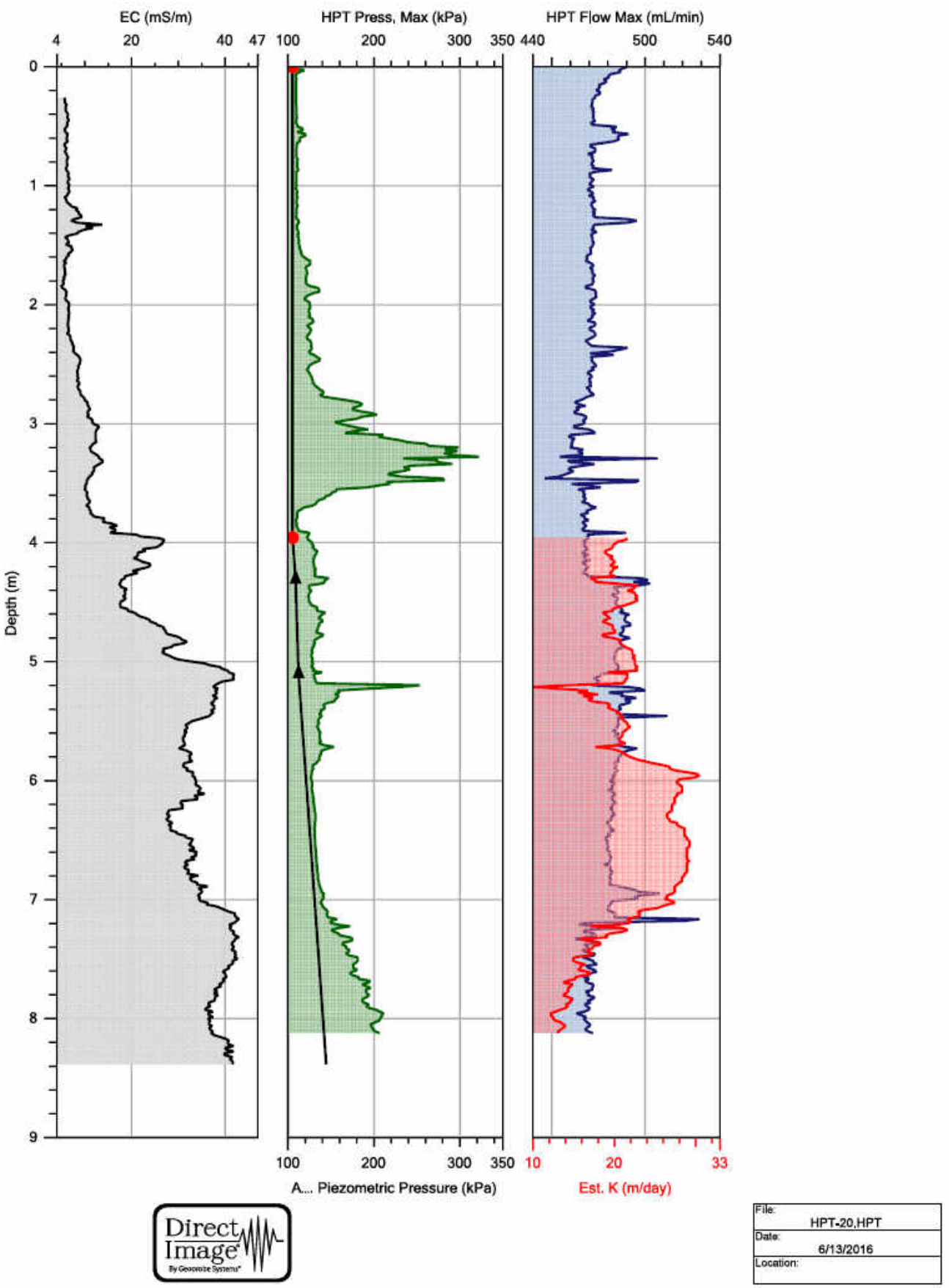
HPT09


EC (mS/m)
3
20
40
48
HPT Press. Max (kPa)
100
200
300
400
460
HPT Flow Max (mL/min)
380
500
540
Depth (m)
0
1
2
3
4
5
6
7
7.2
100
200
300
400
460
Abs. Piezometric Pressure (kPa)
10
20
40
50
Est. K (m/day)
Direct Image
By Geoprobe Systems
File:
HPT-09.HPT
Date:
1/06/2016
Location:

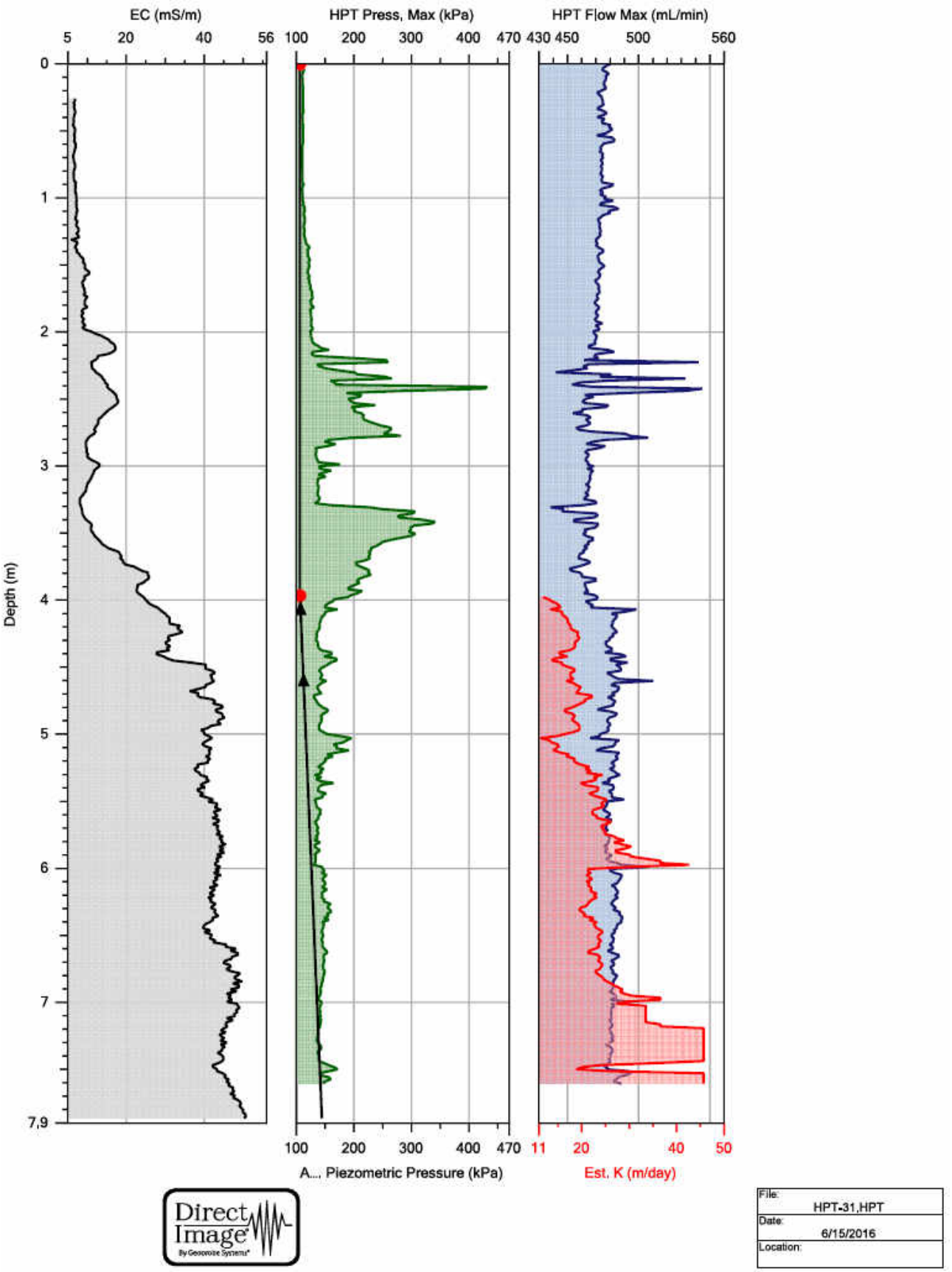
HPT10


EC (mS/m)
3
20
33
HPT Press. Max (kPa)
100
150
200
250270
HPT Flow Max (mL/min)
430
450
500
520
Depth (m)
0
1
2
3
4
5
6
7
7.2
100
150
200
250270
Abs. Piezometric Pressure (kPa)
10
20
40
50
Est. K (m/day)
Direct Image
By Geoprobe Systems
File:
HPT-10.HPT
Date:
1/06/2016
Location:

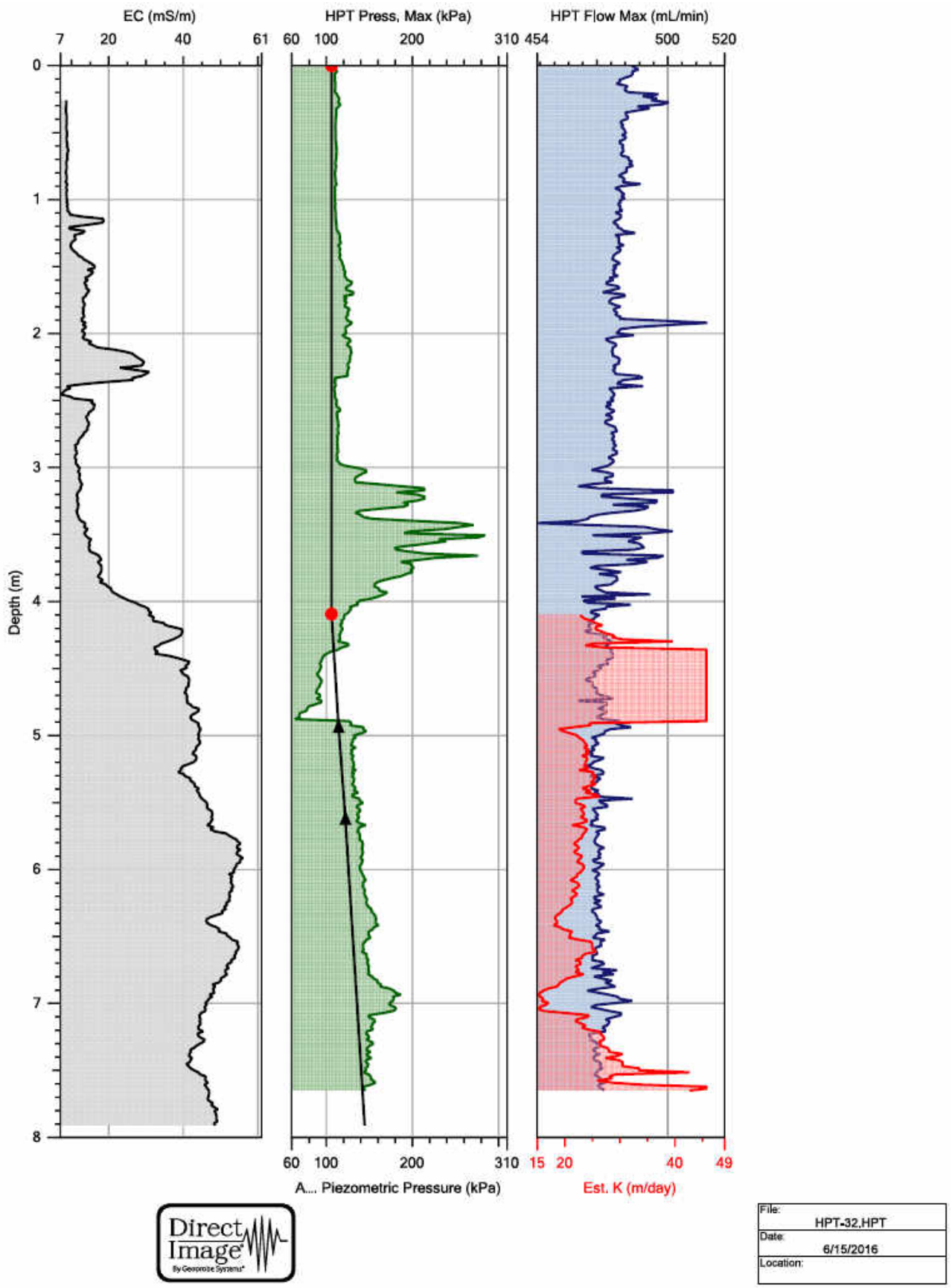
HPT20


EC (mS/m)
4
20
40
47
HPT Press, Max (kPa)
100
200
300
350
HPT Flow Max (mL/min)
440
500
540
Depth (m)
0
1
2
3
4
5
6
7
8
9
100
200
300
350
A... Piezometric Pressure (kPa)
10
20
33
Est. K (m/day)
Direct Image
By Geoprobe Systems
File:
HPT-20.HPT
Date:
6/13/2016
Location:

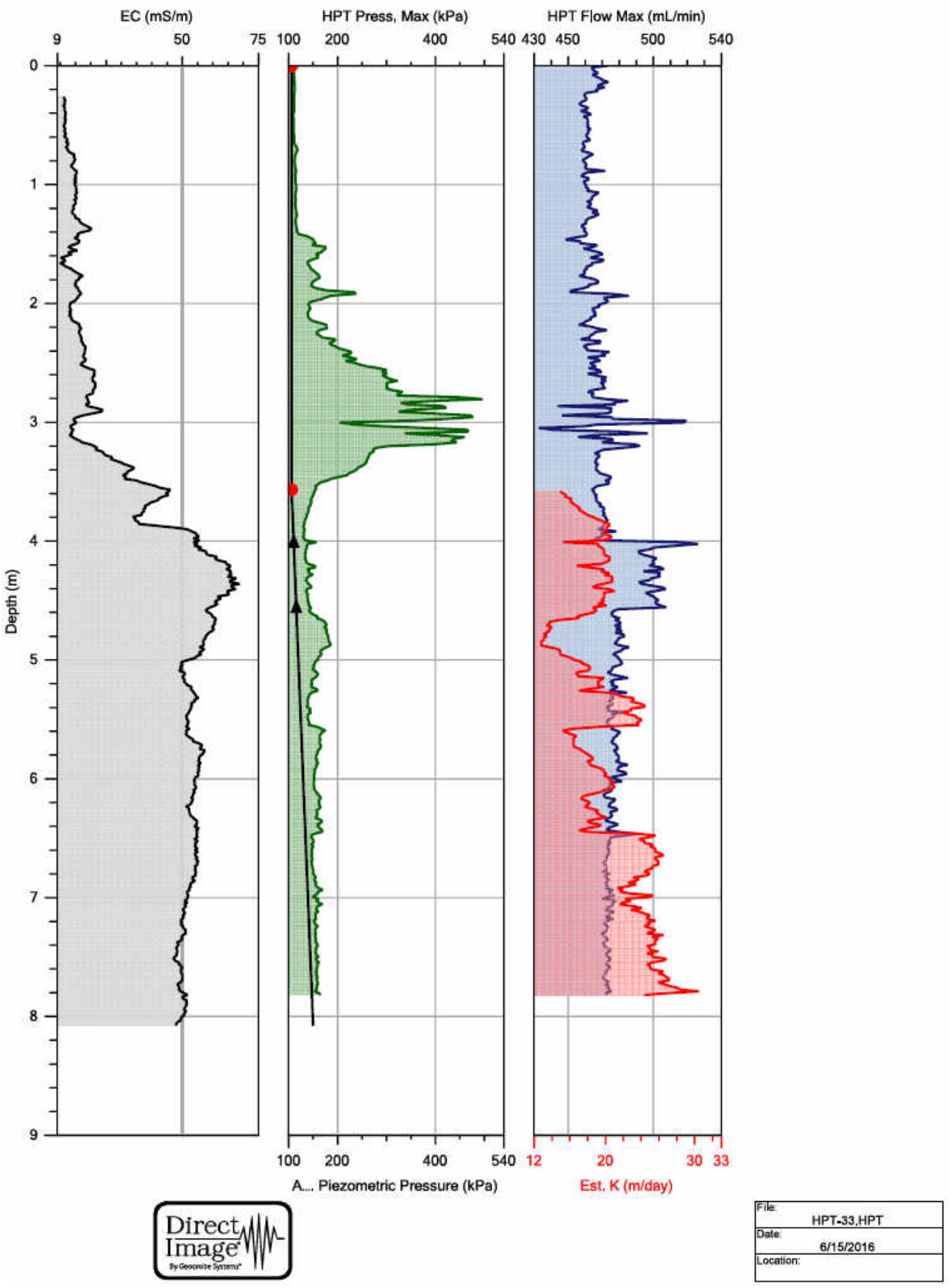
HPT31


EC (mS/m)
5
20
40
56
HPT Press, Max (kPa)
100
200
300
400
470
HPT Flow Max (mL/min)
430
450
500
560
Depth (m)
0
1
2
3
4
5
6
7
7,9
100
200
300
400
470
A... Piezometric Pressure (kPa)
11
20
40
50
Est. K (m/day)
Direct Image
By Geoprobe Systems
File:
HPT-31.HPT
Date:
6/15/2016
Location:

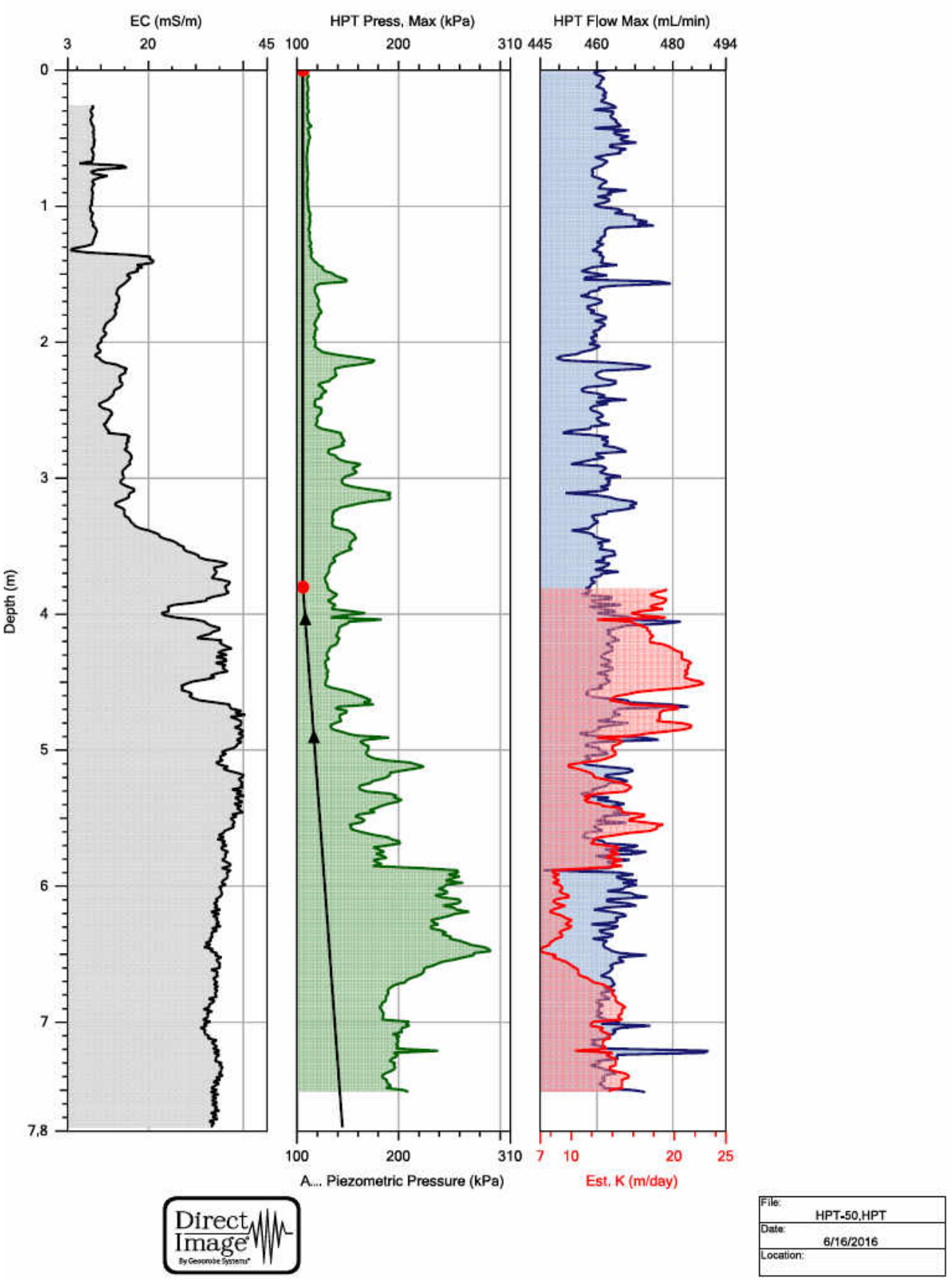
HPT32


EC (mS/m)
7 20 40 61
HPT Press, Max (kPa)
60 100 200 310
HPT Flow Max (mL/min)
454 500 520
Depth (m)
0 1 2 3 4 5 6 7 8
60 100 200 310
A... Piezometric Pressure (kPa)
15 20 40 49
Est. K (m/day)
Direct Image
By Geoprobe Systems
File: HPT-32.HPT
Date: 6/15/2016
Location:

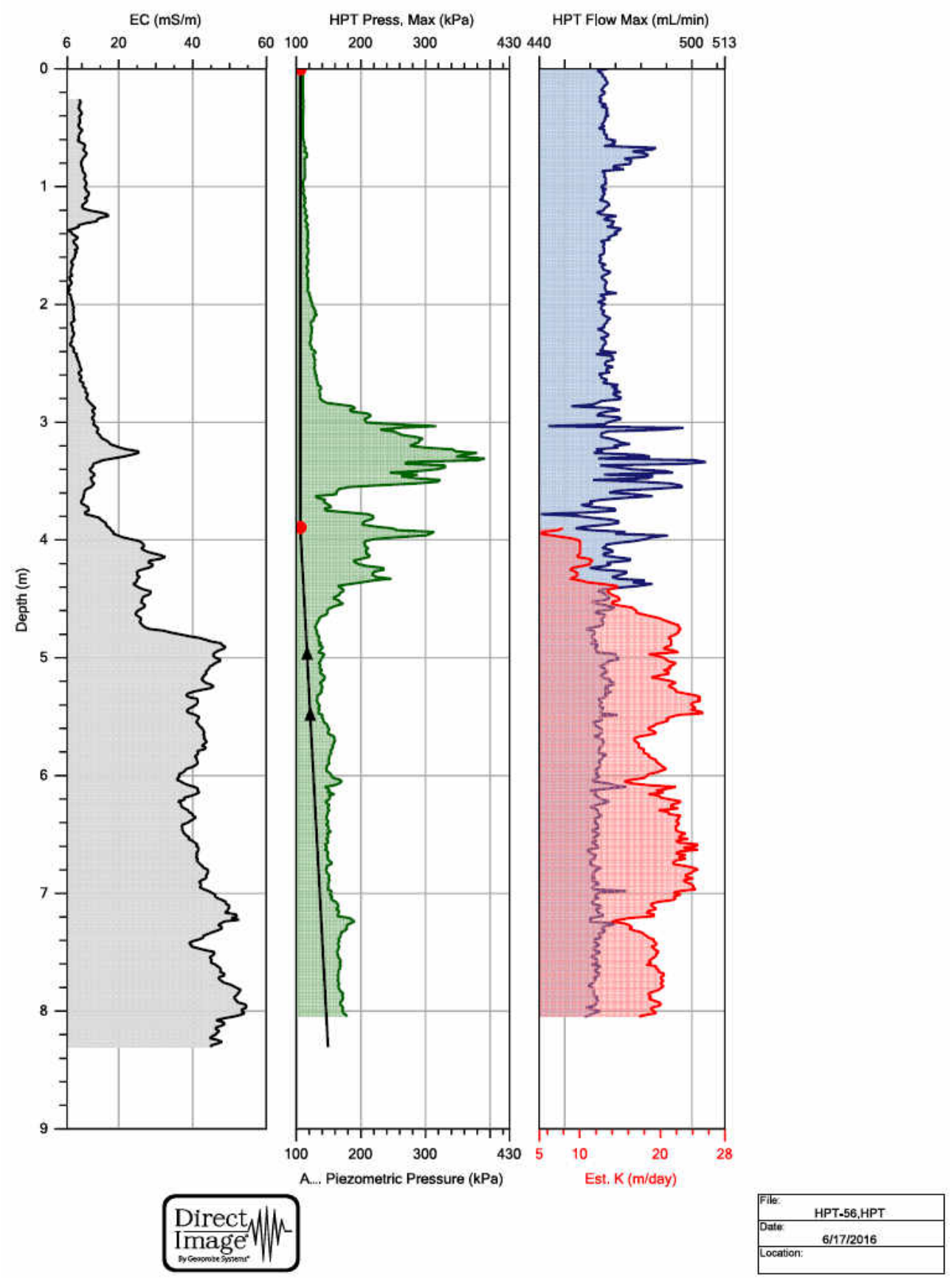
HPT33


EC (mS/m)
9
50
75
HPT Press, Max (kPa)
100
200
400
540
HPT Flow Max (mL/min)
430
450
500
540
Depth (m)
0
1
2
3
4
5
6
7
8
9
100
200
400
540
A... Piezometric Pressure (kPa)
12
20
30
33
Est. K (m/day)
Direct Image
By Geoprobe Systems
File:
HPT-33.HPT
Date:
6/15/2016
Location:

HPT50


EC (mS/m)
3
20
45
HPT Press, Max (kPa)
100
200
310
HPT Flow Max (mL/min)
445
460
480
494
Depth (m)
0
1
2
3
4
5
6
7
7,8
100
200
310
A... Piezometric Pressure (kPa)
7
10
20
25
Est. K (m/day)
Direct Image
By Geoprobe Systems
File:
HPT-50.HPT
Date:
6/16/2016
Location:

HPT56


EC (mS/m)
6
20
40
60
HPT Press. Max (kPa)
100
200
300
430
HPT Flow Max (mL/min)
440
500
513
Depth (m)
0
1
2
3
4
5
6
7
8
9
100
200
300
430
A... Piezometric Pressure (kPa)
5
10
20
28
Est. K (m/day)
Direct Image
By Geoprobe Systems
File:
HPT-56.HPT
Date:
6/17/2016
Location:

Appendix E: Particle-size data and correlations with hydraulic conductivity

Contents

Particle-size data from the petrol station site E-5

Well PB13-C. Elevation 58.980 m AHD. E-6

Well PB12-C. Elevation 58.906 m AHD. E-8

Well PB13-C. Elevation 58.530 m AHD. E-10

Well MP44-C. Elevation 57.160 m AHD. E-12

Well PB39-C. Elevation 57.051 m AHD. E-14

Well MP44-C. Elevation 56.760 m AHD. E-16

Well PB39-C. Elevation 56.401 m AHD. E-18

Well PB27-B. Elevation 56.120 m AHD. E-20

Well ML32. Elevation 55.917 m AHD. E-22

Well MP44-C. Elevation 55.760 m AHD. E-24

Well MP50-A. Elevation 55.681 m AHD. E-26

Well PB39-C. Elevation 55.501 m AHD. E-28

Well PB28. Elevation 55.436 m AHD. E-30

Well MP50-A. Elevation 55.186 m AHD. E-32

Well PB13-C. Elevation 55.180 m AHD. E-34

Well MP44-C. Elevation 55.160 m AHD. E-36

Well ML15. Elevation 55.147 m AHD. E-38

Well PB13-C. Elevation 55.030 m AHD. E-40

Well PB27-B. Elevation 54.710 m AHD. E-42

Well PB39-C. Elevation 54.601 m AHD. E-44

Well ML15. Elevation 54.207 m AHD. E-46

Well PB27-B. Elevation 54.160 m AHD. E-48

Well MP44-C. Elevation 53.960 m AHD. E-50

Well MP50-A. Elevation 53.886 m AHD. E-52

Well PB27-B. Elevation 53.160 m AHD. E-54

Particle-size data from the industrial site E-56

Well 040610/1-T4. Elevation 1.025 m AHD. E-57

Well 040610/1-T4. Elevation 0.975 m AHD. E-59

Well 040610/1-T4. Elevation 0.925 m AHD. E-61

Well 040610/1-T4. Elevation 0.875 m AHD. E-63

Well 040610/1-T4. Elevation 0.825 m AHD. E-65

Well 040610/1-T4. Elevation 0.775 m AHD. E-67
Well 040610/1-T4. Elevation 0.725 m AHD. E-69
Well 040610/1-T4. Elevation 0.675 m AHD. E-71
Well 040610/1-T4. Elevation 0.625 m AHD. E-73
Well 040610/1-T4. Elevation 0.575 m AHD. E-75
Well 040610/1-T4. Elevation 0.525 m AHD. E-77
Well 040610/1-T4. Elevation 0.475 m AHD. E-79
Well 040610/1-T4. Elevation 0.425 m AHD. E-81
Well 040610/1-T4. Elevation 0.375 m AHD. E-83
Well 040610/1-T4. Elevation 0.325 m AHD. E-85
Well 040610/1-T4. Elevation 0.275 m AHD. E-87
Well 040610/1-T4. Elevation 0.225 m AHD. E-89
Well 040610/1-T4. Elevation 0.175 m AHD. E-91
Well 040610/1-T4. Elevation 0.125 m AHD. E-93
Well 040610/1-T4. Elevation 0.075 m AHD. E-95
Well 040610/3-T4. Elevation 0.975 m AHD. E-97
Well 040610/3-T4. Elevation 0.925 m AHD. E-99
Well 040610/3-T4. Elevation 0.875 m AHD. E-101
Well 040610/3-T4. Elevation 0.825 m AHD. E-103
Well 040610/3-T4. Elevation 0.775 m AHD. E-105
Well 040610/3-T4. Elevation 0.725 m AHD. E-107
Well 040610/3-T4. Elevation 0.675 m AHD. E-109
Well 040610/3-T4. Elevation 0.625 m AHD. E-111
Well 040610/3-T4. Elevation 0.575 m AHD. E-113
Well 040610/3-T4. Elevation 0.525 m AHD. E-115
Well 040610/3-T4. Elevation 0.475 m AHD. E-117
Well 040610/3-T4. Elevation 0.425 m AHD. E-119
Well 040610/3-T4. Elevation 0.375 m AHD. E-121
Well 050210/1-T4. Elevation 0.875 m AHD. E-123
Well 050210/1-T4. Elevation 0.825 m AHD. E-125
Well 050210/1-T4. Elevation 0.775 m AHD. E-127
Well 050210/1-T4. Elevation 0.725 m AHD. E-129
Well 050210/1-T4. Elevation 0.675 m AHD. E-131
Well 050210/1-T4. Elevation 0.625 m AHD. E-133

Well 050210/1-T4. Elevation 0.575 m AHD. E-135
Well 050210/1-T4. Elevation 0.525 m AHD. E-137
Well 050210/1-T4. Elevation 0.475 m AHD. E-139
Well 040610/6-T4. Elevation 1.385 m AHD. E-141
Well 040610/6-T4. Elevation 1.335 m AHD. E-143
Well 040610/6-T4. Elevation 1.285 m AHD. E-145
Well 040610/6-T4. Elevation 1.235 m AHD. E-147
Well 040610/6-T4. Elevation 1.185 m AHD. E-149
Well 040610/6-T4. Elevation 1.135 m AHD. E-151
Well 040610/6-T4. Elevation 1.085 m AHD. E-153
Well 040610/6-T4. Elevation 1.035 m AHD. E-155
Well 040610/6-T4. Elevation 0.985 m AHD. E-157
Well 040610/6-T4. Elevation 0.935 m AHD. E-159
Well 040610/6-T4. Elevation 0.885 m AHD. E-161
Well 040610/6-T4. Elevation 0.785 m AHD. E-163
Well 040610/6-T4. Elevation 0.735 m AHD. E-165
Well 040610/6-T4. Elevation 0.685 m AHD. E-167
Well 040610/6-T4. Elevation 0.635 m AHD. E-169
Well 040610/6-T4. Elevation 0.585 m AHD. E-171
Well 040610/6-T4. Elevation 0.535 m AHD. E-173
Well 040610/6-T4. Elevation 0.485 m AHD. E-175
Well 040610/6-T4. Elevation 0.435 m AHD. E-177
Well 040610/6-T4. Elevation 0.385 m AHD. E-179
Well 040610/6-T4. Elevation 0.285 m AHD. E-181
Well 040610/6-T4. Elevation 0.235 m AHD. E-183
Well 040610/6-T4. Elevation 0.185 m AHD. E-185
Well 040610/6-T4. Elevation -0.095 m AHD. E-187

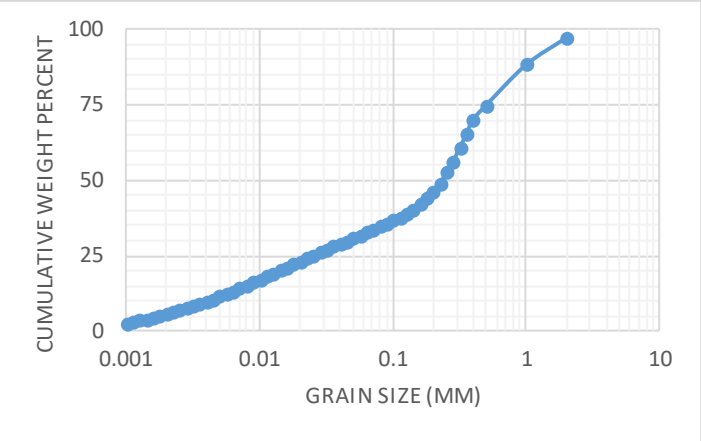
Particle-size data from the petrol station site

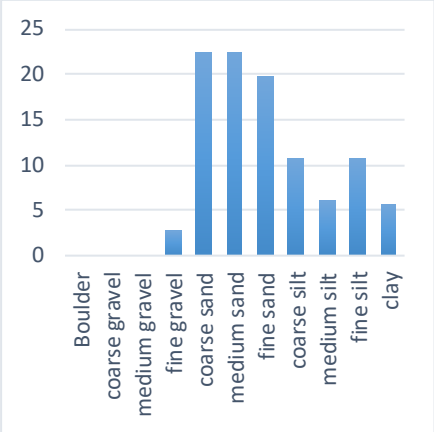
Well PB13-C. Elevation 58.980 m AHD.

Grain Size Analysis Report

Mass Sample (g): 100 T (oC) 20

Poorly sorted sand with fines



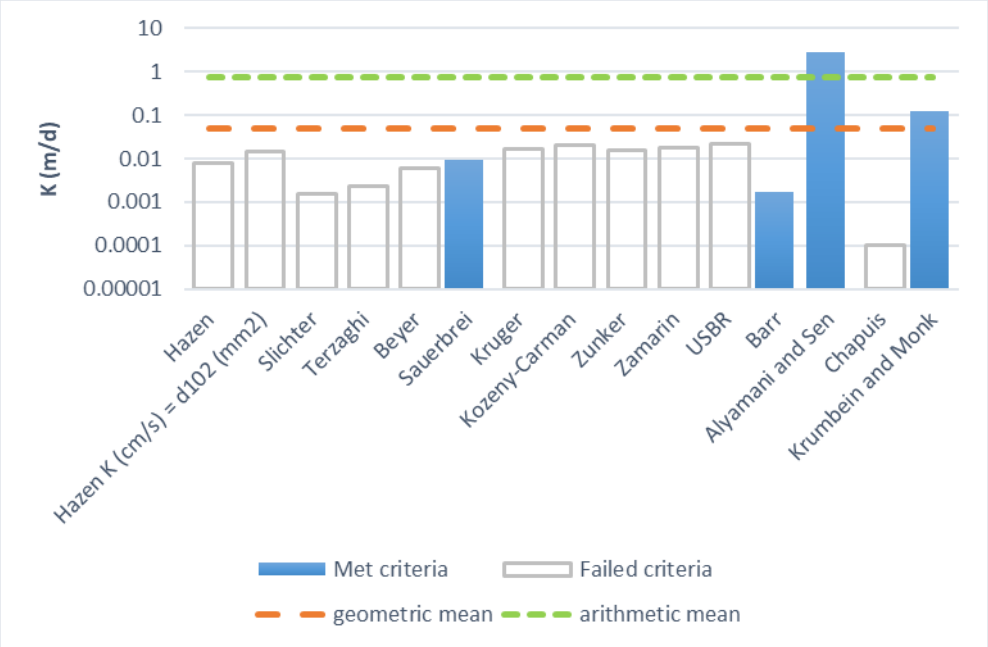


Sieve opening (ps) di (mm)	Mass of retained (mr) (g)	mass fraction (mf)	Percent Passing (pp)
2	2.8	0.028	97.2
1	8.9	0.089	88.3
0.5	13.4	0.134	74.9
0.39905	4.69155	0.04692	70.2084
0.35566	4.78948	0.04789	65.419
0.31698	4.66457	0.04665	60.7544
0.28251	4.35559	0.04356	56.3988
0.25179	3.90848	0.03908	52.4903
0.2244	3.39071	0.03391	49.0996
0.2	2.85644	0.02856	46.2432
0.17825	2.35518	0.02355	43.888
0.15887	1.92928	0.01929	41.9587
0.14159	1.58597	0.01586	40.3727
0.12619	1.33931	0.01339	39.0334
0.11247	1.17083	0.01171	37.8626
0.10024	1.06961	0.0107	36.793
0.08934	1.01417	0.01014	35.7788
0.07962	0.98854	0.00989	34.7903
0.07096	0.97841	0.00978	33.8119
0.06325	0.97392	0.00974	32.838
0.05637	0.96993	0.0097	31.868
0.05024	0.96438	0.00964	30.9037

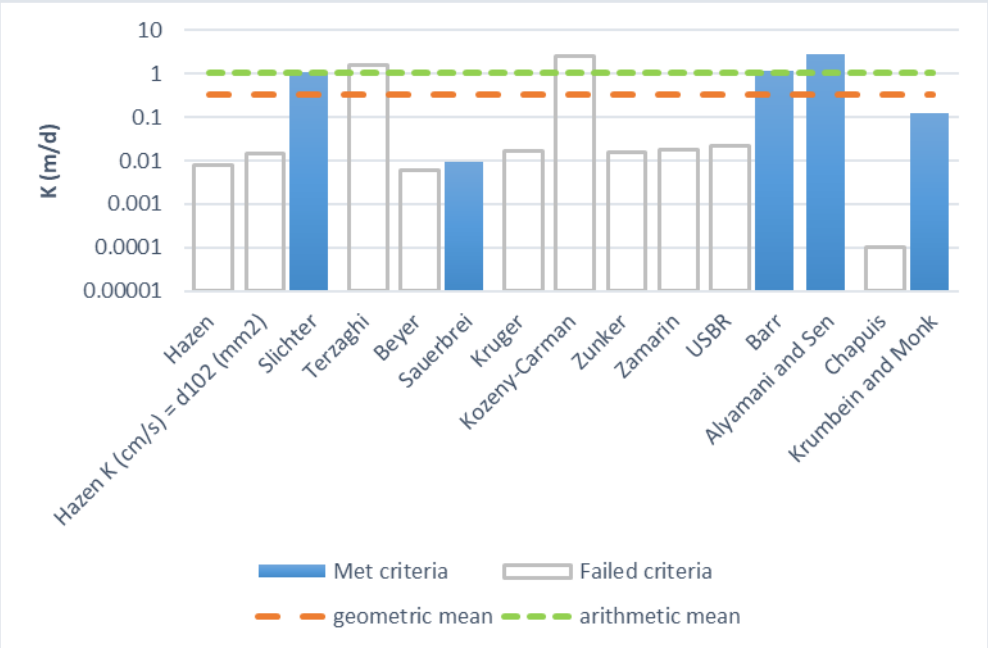
Effective Grain Diameters (mm)		Other Useful Parameters	
d10	0.004	Uniformity Coef.	76.75
d17	0.010	n computed	0.26
d20	0.014	g (cm/s^2)	980.00
d50	0.232	ρ (g/cm^3)	0.9981
d60	0.311	μ (g/cm s)	0.0098
de (Kruger)	0.010	ρg/μ (1/cm s)	9.9327E+04
de (Kozeny)	0.010	tau (Sauerbrei)	1.053
de (Zunker)	0.010	$d_{geometric\ mean}$	0.109
de (Zamarin)	0.010	σ_ϕ	3.156
Io (Alyameni	-0.053		

mm	0	% in sample
>64	Boulder	
16 - 64	coarse gravel	
8 - 16	medium gravel	
2 - 8	fine gravel	2.8
0.5 - 2	coarse sand	22.3
0.25 - 0.5	medium sand	22.40967394
0.063 - 0.25	fine sand	19.65236318
0.016 - 0.063	coarse silt	10.60656098
0.008 - 0.016	medium silt	5.988126062
0.002 - 0.008	fine silt	10.6334017
<0.002	clay	5.609874139

Slichter, Terzaghi, Kozeny-Carman and Barr with d_{VS}:



Slichter, Terzaghi, Kozeny-Carman and Barr with d_{UU}:

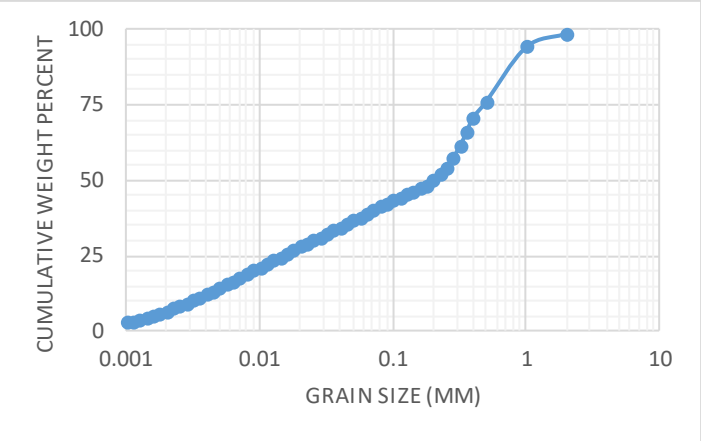


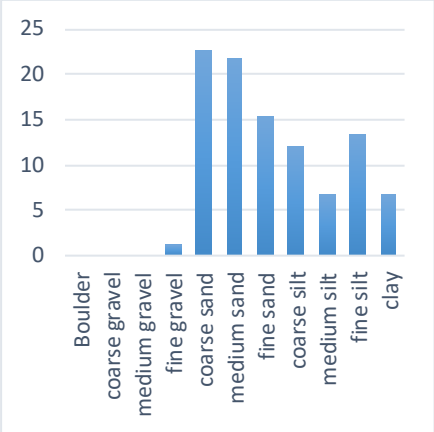
Well PB12-C. Elevation 58.906 m AHD.

Grain Size Analysis Report

Mass Sample (g): 100 T (oC) 20

Poorly sorted sand with fines





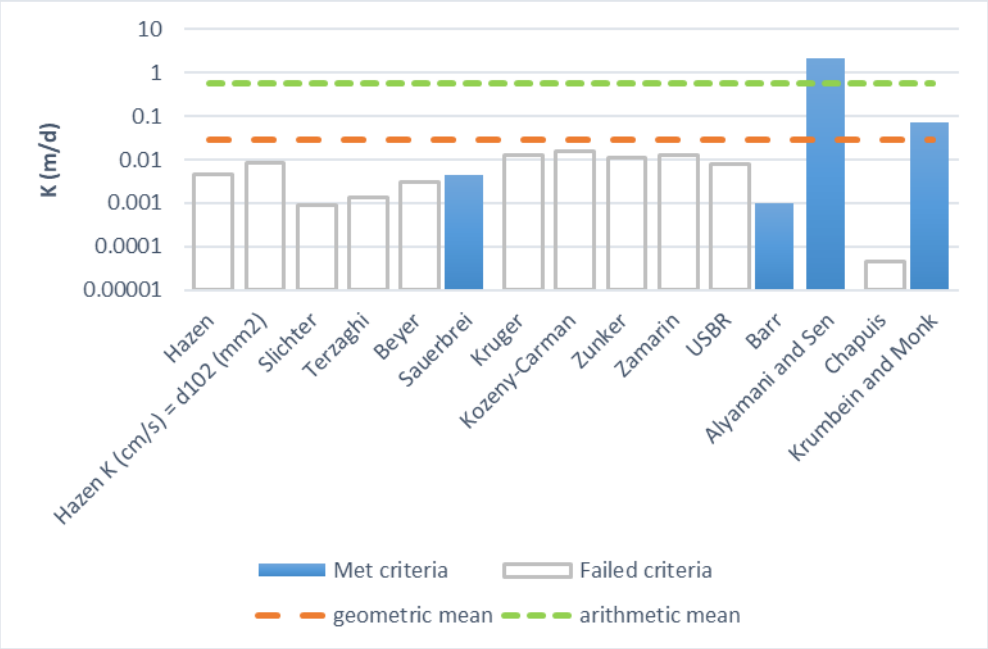
Sieve opening (ps) di (mm)	Mass of retained (mr) (g)	mass fraction (mf)	Percent Passing (pp)
2	1.3	0.013	98.7
1	4.4	0.044	94.3
0.5	18.1	0.181	76.2
0.39905	5.24096	0.05241	70.959
0.35566	4.99937	0.04999	65.9597
0.31698	4.51374	0.04514	61.4459
0.28251	3.88396	0.03884	57.562
0.25179	3.18451	0.03185	54.3775
0.2244	2.51264	0.02513	51.8648
0.2	1.92691	0.01927	49.9379
0.17825	1.46998	0.0147	48.4679
0.15887	1.16142	0.01161	47.3065
0.14159	0.98539	0.00985	46.3211
0.12619	0.92281	0.00923	45.3983
0.11247	0.93673	0.00937	44.4616
0.10024	0.9919	0.00992	43.4697
0.08934	1.05951	0.0106	42.4102
0.07962	1.11822	0.01118	41.2919
0.07096	1.15606	0.01156	40.1359
0.06325	1.17017	0.0117	38.9657
0.05637	1.16385	0.01164	37.8019
0.05024	1.14344	0.01143	36.6584

Effective Grain Diameters (mm)	
d10	0.003
d17	0.007
d20	0.009
d50	0.201
d60	0.304
de (Kruger)	0.009
de (Kozeny)	0.009
de (Zunker)	0.009
de (Zamarin)	0.009
Io (Alyameni	-0.046

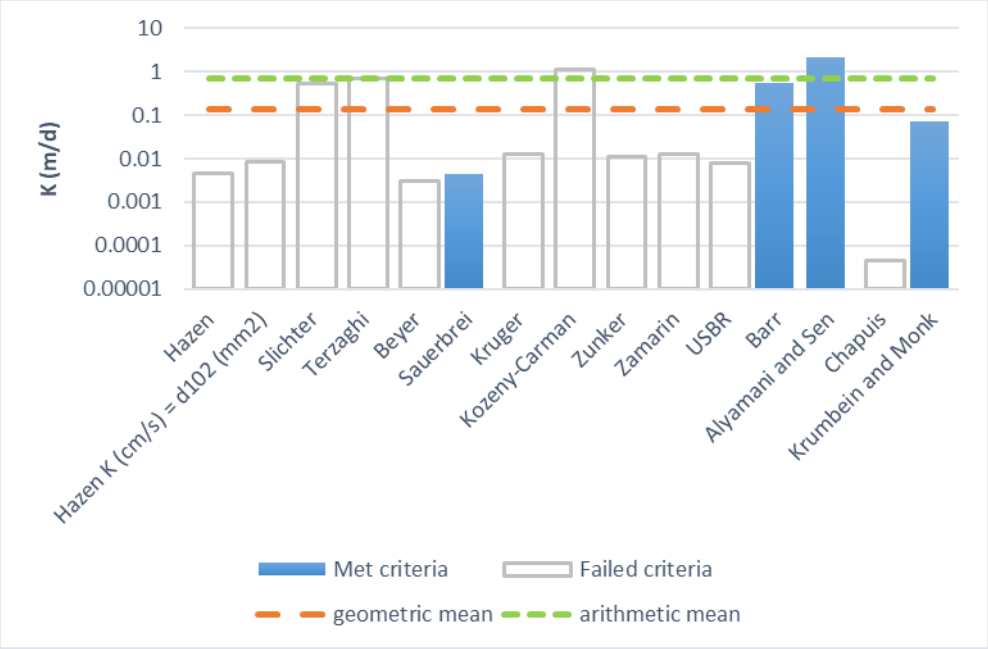
Other Useful Parameters	
Uniformity Coef.	98.34
n computed	0.26
g (cm/s^2)	980.00
ρ (g/cm^3)	0.9981
μ (g/cm s)	0.0098
ρg/μ (1/cm s)	9.9327E+04
tau (Sauerbrei)	1.053
$d_{geometric\ mean}$	0.084
σ_ϕ	3.179

mm	0	% in sample
>64	Boulder	
16 - 64	coarse gravel	
8 - 16	medium gravel	
2 - 8	fine gravel	1.3
0.5 - 2	coarse sand	22.5
0.25 - 0.5	medium sand	21.82253613
0.063 - 0.25	fine sand	15.41174843
0.016 - 0.063	coarse silt	12.06074699
0.008 - 0.016	medium silt	6.808345697
0.002 - 0.008	fine silt	13.43532924
<0.002	clay	6.66129351

Slichter, Terzaghi, Kozeny-Carman and Barr with d_{VS}:



Slichter, Terzaghi, Kozeny-Carman and Barr with d_{UU}:

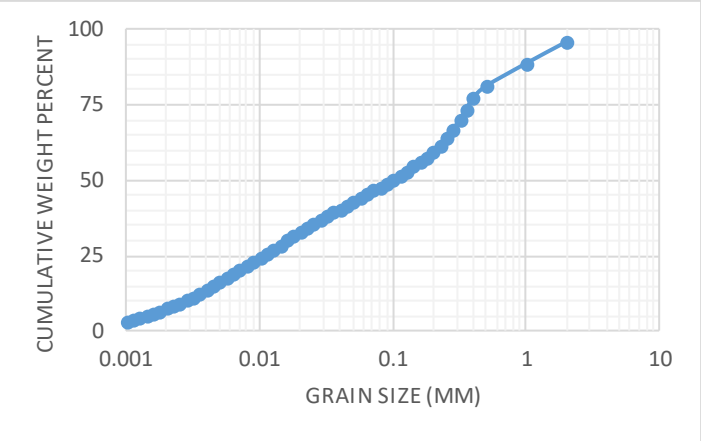


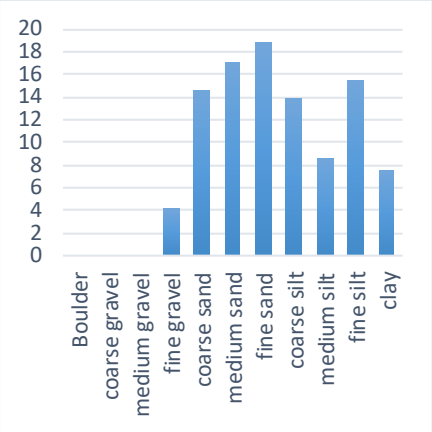
Well PB13-C. Elevation 58.530 m AHD.

Grain Size Analysis Report

Mass Sample (g): 100 T (oC) 20

Poorly sorted sand with fines



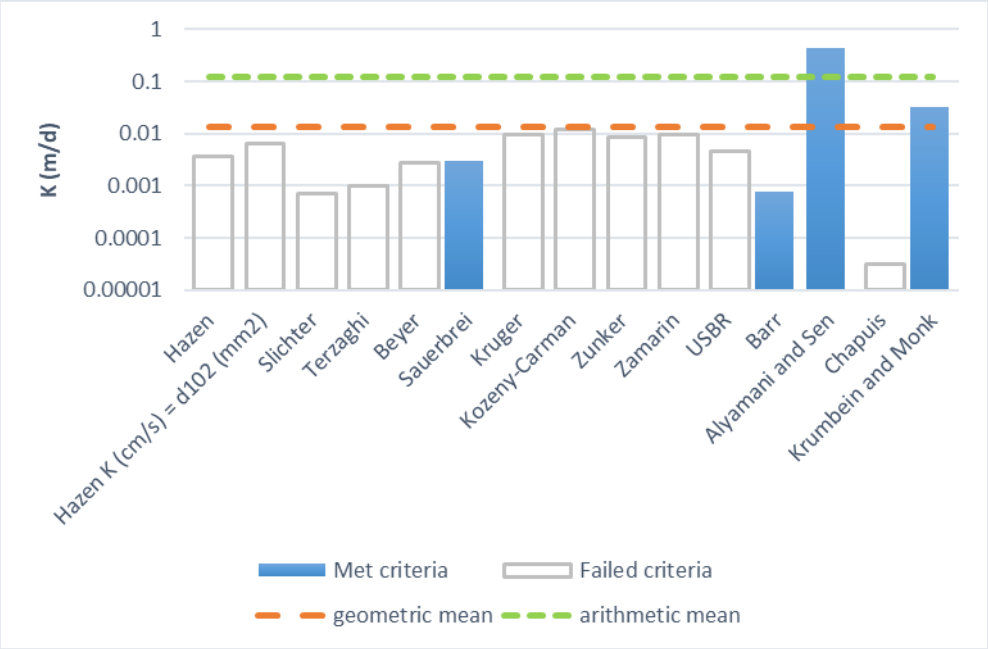


Sieve opening (ps) di (mm)	Mass of retained (mr) (g)	mass fraction (mf)	Percent Passing (pp)
2	4.2	0.042	95.8
1	7.1	0.071	88.7
0.5	7.5	0.075	81.2
0.39905	3.85174	0.03852	77.3483
0.35566	3.73363	0.03734	73.6146
0.31698	3.48702	0.03487	70.1276
0.28251	3.1657	0.03166	66.9619
0.25179	2.80587	0.02806	64.156
0.2244	2.45335	0.02453	61.7027
0.2	2.13451	0.02135	59.5682
0.17825	1.86901	0.01869	57.6992
0.15887	1.66768	0.01668	56.0315
0.14159	1.5228	0.01523	54.5087
0.12619	1.42926	0.01429	53.0794
0.11247	1.36948	0.01369	51.71
0.10024	1.3316	0.01332	50.3784
0.08934	1.30362	0.01304	49.0747
0.07962	1.27883	0.01279	47.7959
0.07096	1.25396	0.01254	46.542
0.06325	1.22883	0.01229	45.3131
0.05637	1.20656	0.01207	44.1066
0.05024	1.18969	0.0119	42.9169

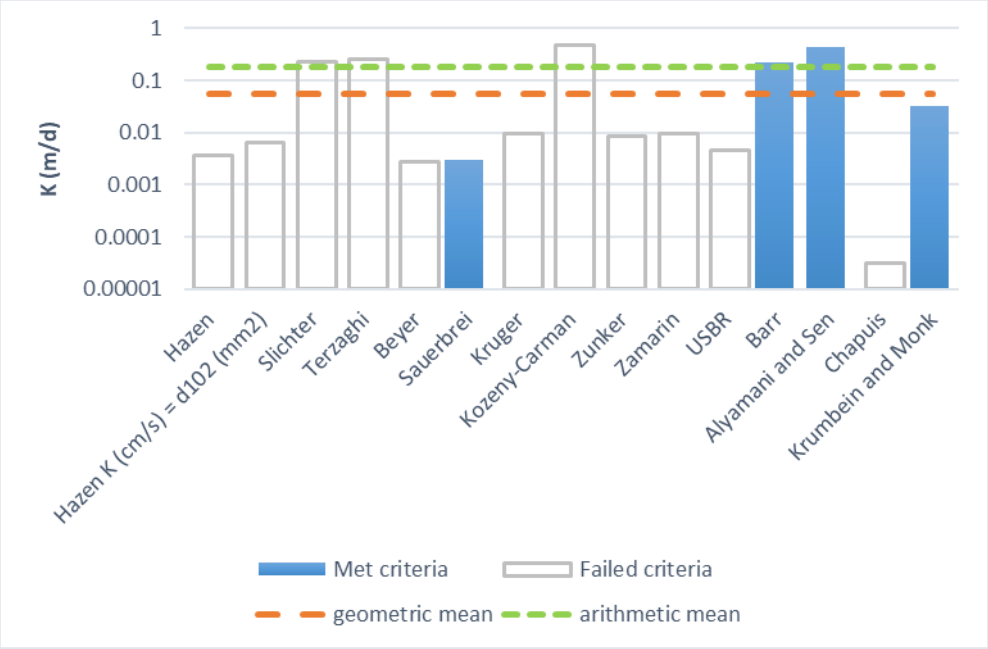
Effective Grain Diameters (mm)		Other Useful Parameters	
d10	0.003	Uniformity Coef.	75.41
d17	0.005	n computed	0.26
d20	0.007	g (cm/s^2)	980.00
d50	0.097	ρ (g/cm^3)	0.9981
d60	0.205	μ (g/cm s)	0.0098
de (Kruger)	0.007	ρg/μ (1/cm s)	9.9327E+04
de (Kozeny)	0.007	tau (Sauerbrei)	1.053
de (Zunker)	0.007	$d_{geometric\ mean}$	0.064
de (Zamarin)	0.007	σ_ϕ	3.360
Io (Alyameni	-0.021		

mm	0	% in sample
>64	Boulder	
16 - 64	coarse gravel	
8 - 16	medium gravel	
2 - 8	fine gravel	4.2
0.5 - 2	coarse sand	14.6
0.25 - 0.5	medium sand	17.04395798
0.063 - 0.25	fine sand	18.84291951
0.016 - 0.063	coarse silt	13.83520851
0.008 - 0.016	medium silt	8.581524584
0.002 - 0.008	fine silt	15.37491508
<0.002	clay	7.521474331

Slichter, Terzaghi, Kozeny-Carman and Barr with d_{VS}:



Slichter, Terzaghi, Kozeny-Carman and Barr with d_{UU}:

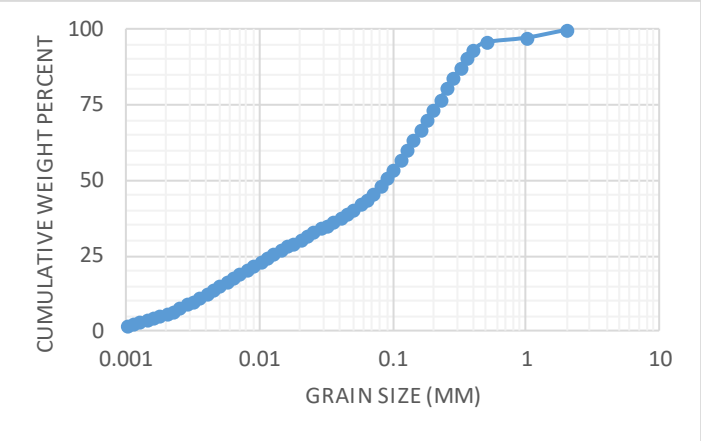


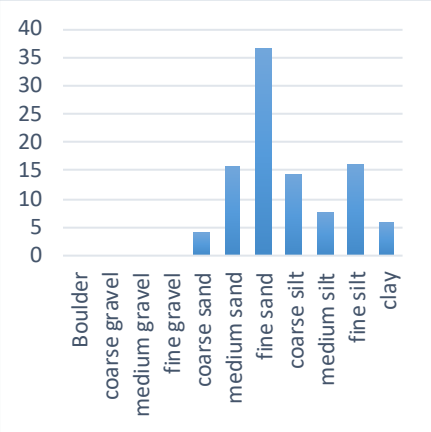
Well MP44-C. Elevation 57.160 m AHD.

Grain Size Analysis Report

Mass Sample (g): 100 T (oC) 20

Poorly sorted sand with fines





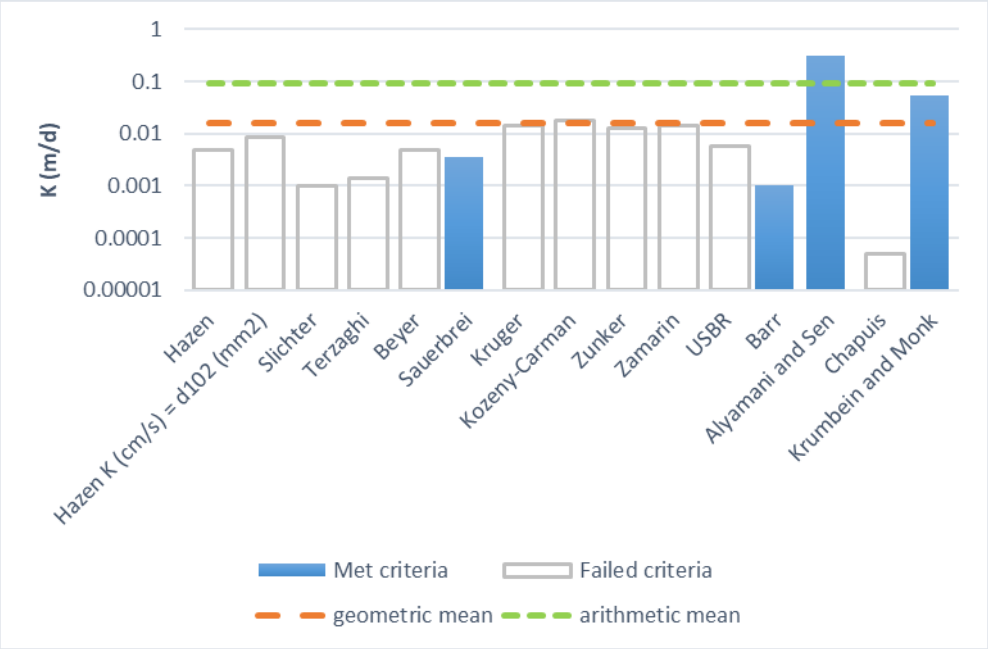
Sieve opening (ps) di (mm)	Mass of retained (mr) (g)	mass fraction (mf)	Percent Passing (pp)
2	0	0	100
1	2.6	0.026	97.4
0.5	1.5	0.015	95.9
0.39905	2.65754	0.02658	93.2425
0.35566	2.95502	0.02955	90.2874
0.31698	3.17796	0.03178	87.1095
0.28251	3.32634	0.03326	83.7831
0.25179	3.4196	0.0342	80.3635
0.2244	3.4684	0.03468	76.8951
0.2	3.48501	0.03485	73.4101
0.17825	3.47654	0.03477	69.9336
0.15887	3.44642	0.03446	66.4872
0.14159	3.39094	0.03391	63.0962
0.12619	3.30642	0.03306	59.7898
0.11247	3.1833	0.03183	56.6065
0.10024	3.02137	0.03021	53.5851
0.08934	2.81994	0.0282	50.7652
0.07962	2.58777	0.02588	48.1774
0.07096	2.33838	0.02338	45.8391
0.06325	2.08376	0.02084	43.7553
0.05637	1.84675	0.01847	41.9085
0.05024	1.63254	0.01633	40.276

Effective Grain Diameters (mm)	
d10	0.003
d17	0.006
d20	0.008
d50	0.086
d60	0.127
de (Kruger)	0.009
de (Kozeny)	0.009
de (Zunker)	0.009
de (Zamarin)	0.009
Io (Alyameni	-0.018

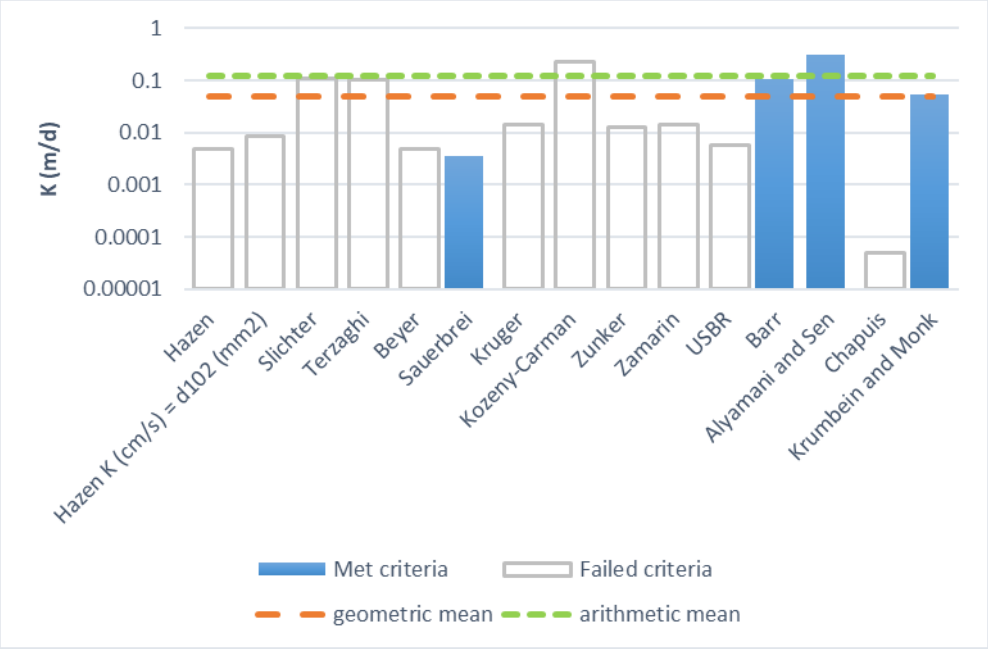
Other Useful Parameters	
Uniformity Coef.	40.08
n computed	0.26
g (cm/s^2)	980.00
ρ (g/cm^3)	0.9981
μ (g/cm s)	0.0098
ρg/μ (1/cm s)	9.9327E+04
tau (Sauerbrei)	1.053
$d_{geometric\ mean}$	0.051
σ_ϕ	2.642

mm	0	% in sample
>64	Boulder	
16 - 64	coarse gravel	
8 - 16	medium gravel	
2 - 8	fine gravel	0
0.5 - 2	coarse sand	4.1
0.25 - 0.5	medium sand	15.53646095
0.063 - 0.25	fine sand	36.60824294
0.016 - 0.063	coarse silt	14.45314201
0.008 - 0.016	medium silt	7.587886819
0.002 - 0.008	fine silt	15.94655244
<0.002	clay	5.767714841

Slichter, Terzaghi, Kozeny-Carman and Barr with d_{VS}:



Slichter, Terzaghi, Kozeny-Carman and Barr with d_{UU}:

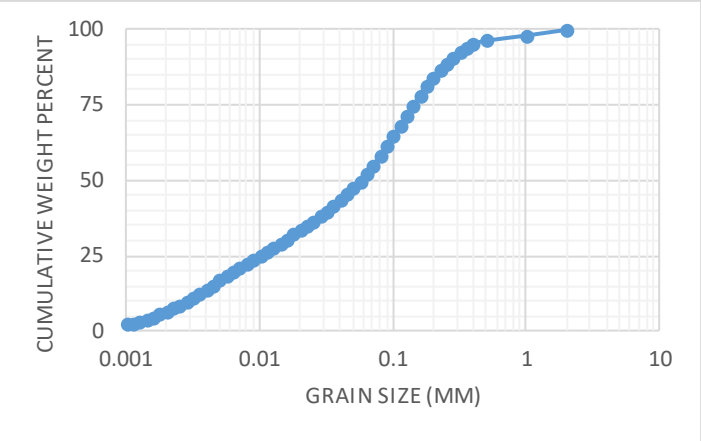


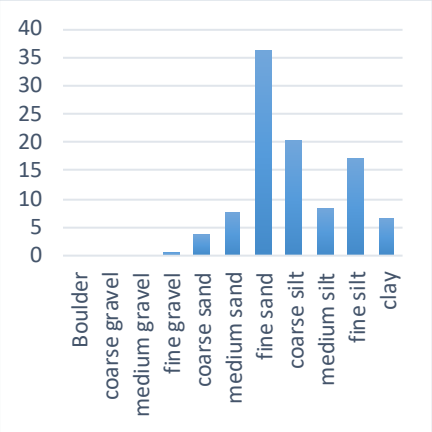
Well PB39-C. Elevation 57.051 m AHD.

Grain Size Analysis Report

Mass Sample (g): 100 T (oC) 20

Poorly sorted sandy silt with fines





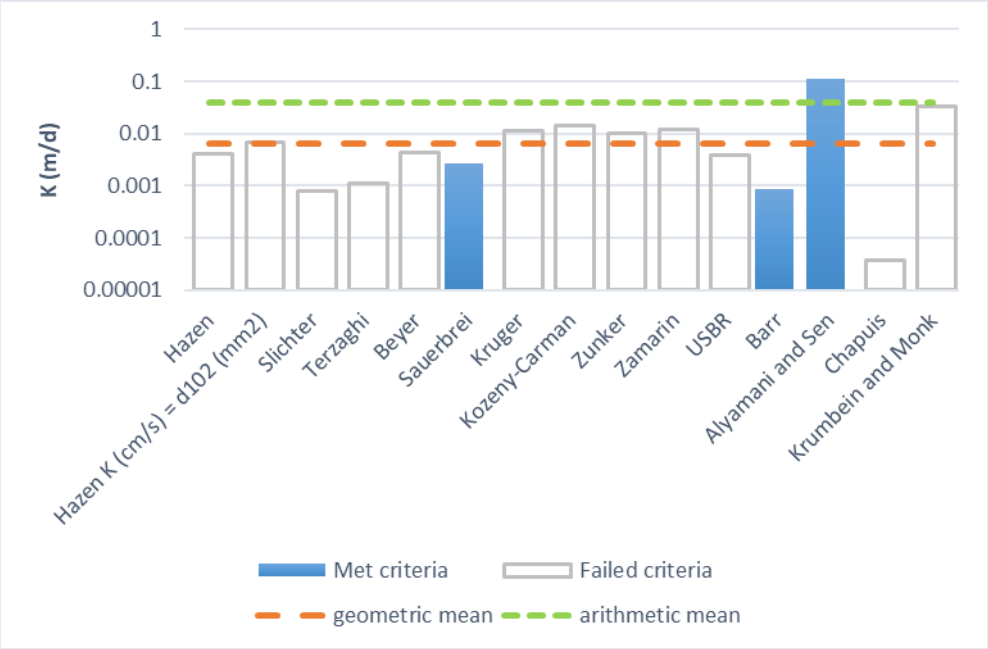
Sieve opening (ps) di (mm)	Mass of retained (mr) (g)	mass fraction (mf)	Percent Passing (pp)
2	0.2	0.002	99.8
1	1.9	0.019	97.9
0.5	1.7	0.017	96.2
0.39905	1.0052	0.01005	95.1948
0.35566	1.28667	0.01287	93.9081
0.31698	1.54204	0.01542	92.3661
0.28251	1.78708	0.01787	90.579
0.25179	2.03552	0.02036	88.5435
0.2244	2.28393	0.02284	86.2595
0.2	2.53284	0.02533	83.7267
0.17825	2.77538	0.02775	80.9513
0.15887	2.99749	0.02997	77.9538
0.14159	3.1901	0.0319	74.7637
0.12619	3.33077	0.03331	71.433
0.11247	3.40961	0.0341	68.0233
0.10024	3.41387	0.03414	64.6095
0.08934	3.34337	0.03343	61.2661
0.07962	3.20454	0.03205	58.0616
0.07096	3.01292	0.03013	55.0487
0.06325	2.78543	0.02785	52.2632
0.05637	2.55053	0.02551	49.7127
0.05024	2.3199	0.0232	47.3928

Effective Grain Diameters (mm)	
d10	0.003
d17	0.005
d20	0.007
d50	0.057
d60	0.085
de (Kruger)	0.008
de (Kozeny)	0.008
de (Zunker)	0.008
de (Zamarin)	0.008
Io (Alyameni	-0.011

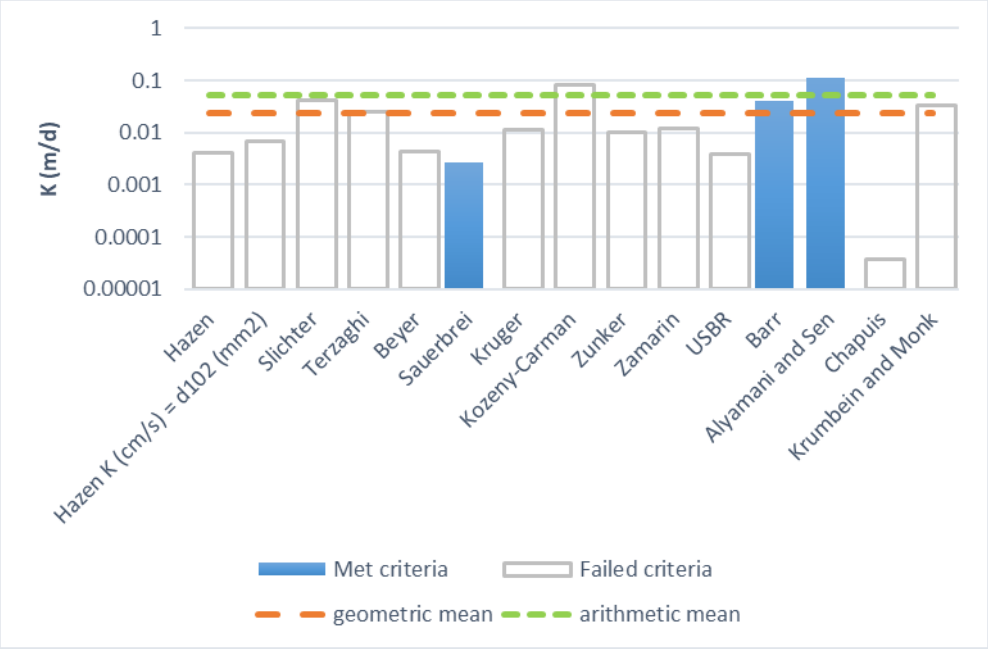
Other Useful Parameters	
Uniformity Coef.	30.09
n computed	0.26
g (cm/s^2)	980.00
ρ (g/cm^3)	0.9981
μ (g/cm s)	0.0098
ρg/μ (1/cm s)	9.9327E+04
tau (Sauerbrei)	1.053
$d_{geometric\ mean}$	0.038
σ_ϕ	2.551

mm	0	% in sample
>64	Boulder	
16 - 64	coarse gravel	
8 - 16	medium gravel	
2 - 8	fine gravel	0.2
0.5 - 2	coarse sand	3.6
0.25 - 0.5	medium sand	7.656525261
0.063 - 0.25	fine sand	36.28024676
0.016 - 0.063	coarse silt	20.28183878
0.008 - 0.016	medium silt	8.403529383
0.002 - 0.008	fine silt	17.09766319
<0.002	clay	6.48019663

Slichter, Terzaghi, Kozeny-Carman and Barr with d_{VS}:



Slichter, Terzaghi, Kozeny-Carman and Barr with d_{UU}:

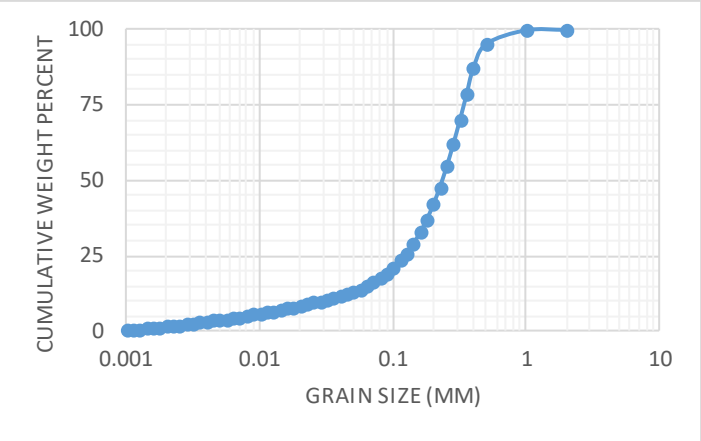


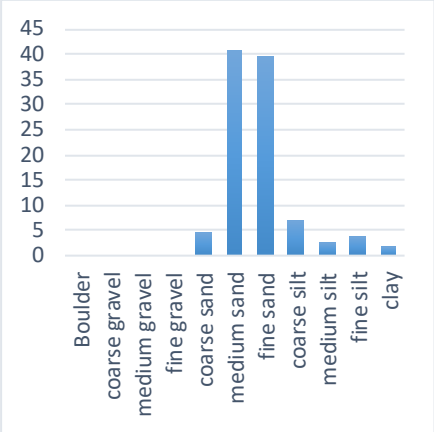
Well MP44-C. Elevation 56.760 m AHD.

Grain Size Analysis Report

Mass Sample (g): 100 T (oC) 20

Poorly sorted sand low in fines



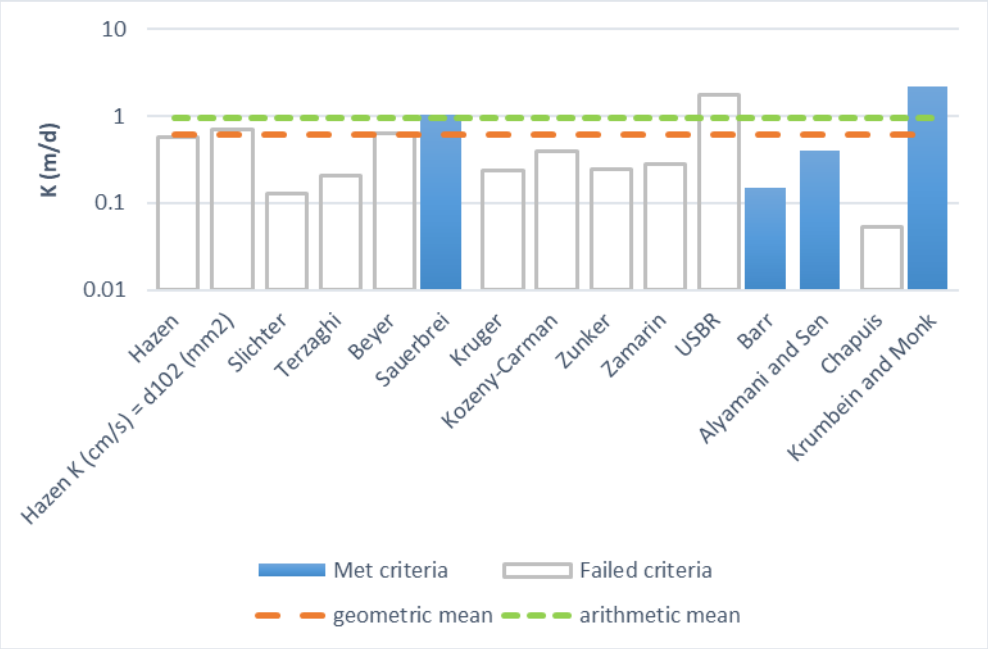


Sieve opening (ps) di (mm)	Mass of retained (mr) (g)	mass fraction (mf)	Percent Passing (pp)
2	0	0	100
1	0.1	0.001	99.9
0.5	4.6	0.046	95.3
0.39905	8.31811	0.08318	86.9819
0.35566	8.56151	0.08562	78.4204
0.31698	8.45841	0.08458	69.962
0.28251	8.05787	0.08058	61.9041
0.25179	7.42779	0.07428	54.4763
0.2244	6.66331	0.06663	47.813
0.2	5.84025	0.0584	41.9728
0.17825	5.02664	0.05027	36.9461
0.15887	4.28487	0.04285	32.6612
0.14159	3.62371	0.03624	29.0375
0.12619	3.07429	0.03074	25.9633
0.11247	2.61032	0.0261	23.3529
0.10024	2.2316	0.02232	21.1213
0.08934	1.9124	0.01912	19.2089
0.07962	1.64159	0.01642	17.5673
0.07096	1.40855	0.01409	16.1588
0.06325	1.20375	0.01204	14.955
0.05637	1.02997	0.0103	13.9251
0.05024	0.88065	0.00881	13.0444

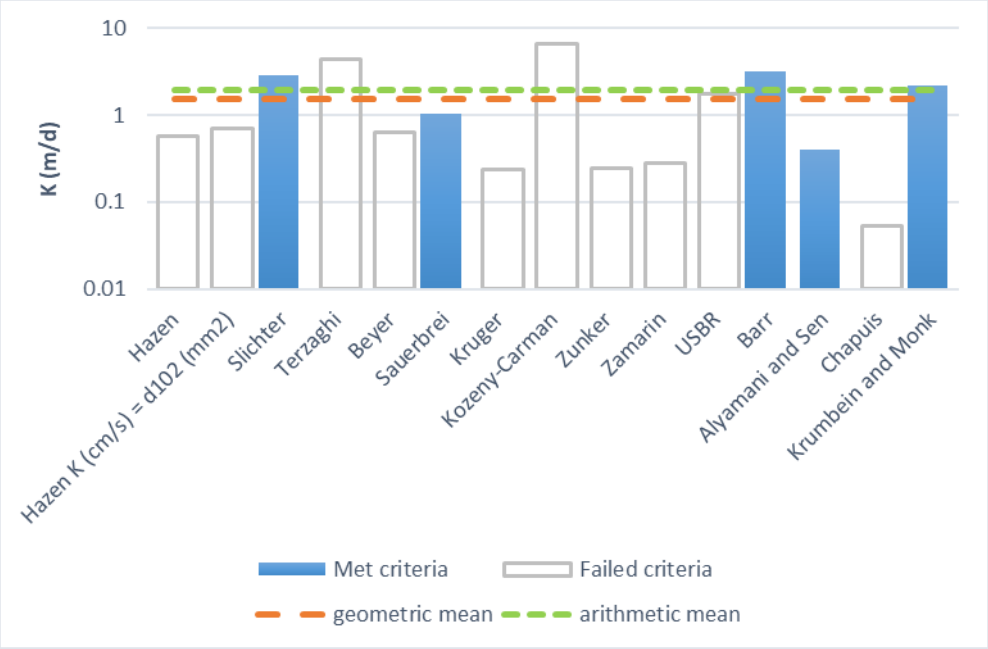
Effective Grain Diameters (mm)		Other Useful Parameters	
d10	0.029	Uniformity Coef.	9.61
d17	0.076	n computed	0.30
d20	0.094	g (cm/s^2)	980.00
d50	0.233	ρ (g/cm^3)	0.9981
d60	0.275	μ (g/cm s)	0.0098
de (Kruger)	0.032	ρg/μ (1/cm s)	9.9327E+04
de (Kozeny)	0.032	tau (Sauerbrei)	1.053
de (Zunker)	0.032	$d_{geometric\ mean}$	0.158
de (Zamarin)	0.032	σ_ϕ	1.527
Io (Alyameni	-0.023		

mm	0	% in sample
>64	Boulder	
16 - 64	coarse gravel	
8 - 16	medium gravel	
2 - 8	fine gravel	0
0.5 - 2	coarse sand	4.7
0.25 - 0.5	medium sand	40.82368852
0.063 - 0.25	fine sand	39.52127725
0.016 - 0.063	coarse silt	6.940409777
0.008 - 0.016	medium silt	2.526201338
0.002 - 0.008	fine silt	3.8983205
<0.002	clay	1.590102612

Slichter, Terzaghi, Kozeny-Carman and Barr with d_{VS}:



Slichter, Terzaghi, Kozeny-Carman and Barr with d_{UU}:

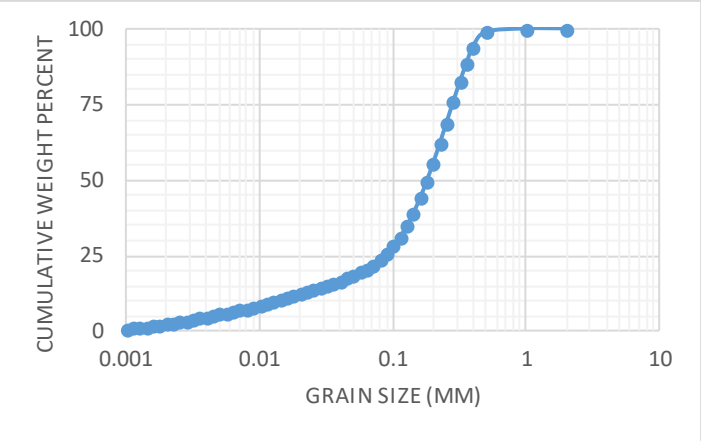


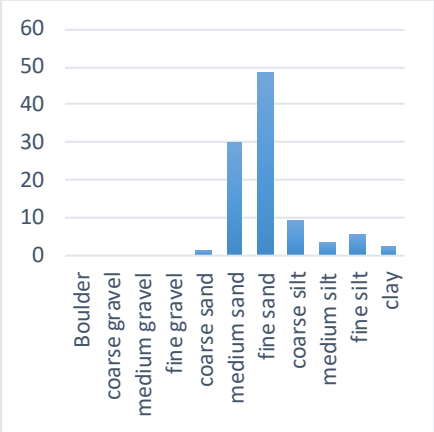
Well PB39-C. Elevation 56.401 m AHD.

Grain Size Analysis Report

Mass Sample (g): 100 T (oC) 20

Poorly sorted sand low in fines



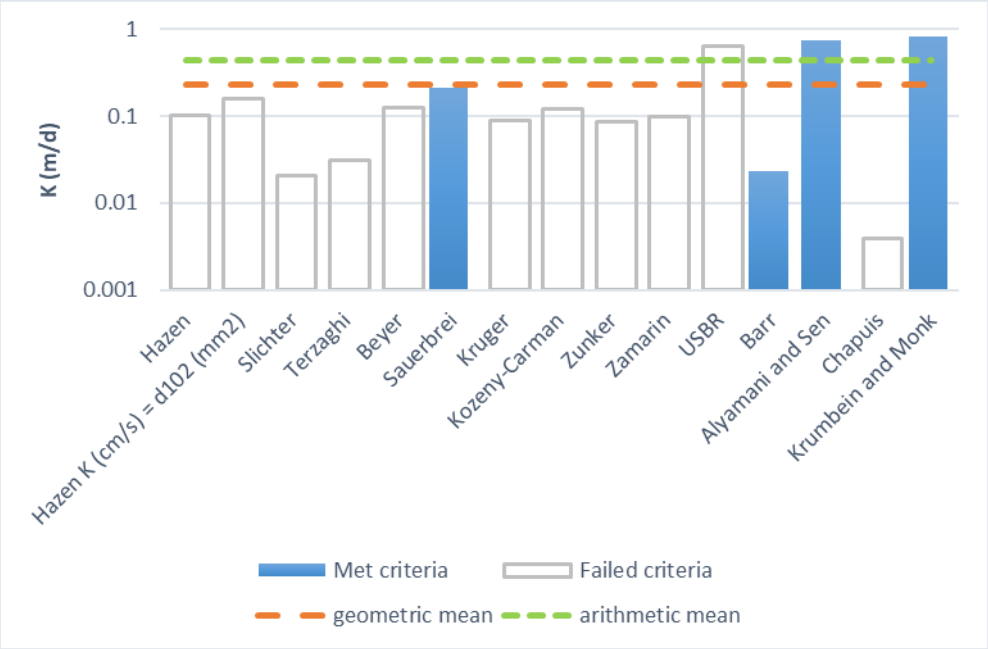


Sieve opening (ps) di (mm)	Mass of retained (mr) (g)	mass fraction (mf)	Percent Passing (pp)
2	0	0	100
1	0	0	100
0.5	1.1	0.011	98.9
0.39905	4.76901	0.04769	94.131
0.35566	5.55301	0.05553	88.578
0.31698	6.19379	0.06194	82.3842
0.28251	6.6202	0.0662	75.764
0.25179	6.82377	0.06824	68.9402
0.2244	6.79337	0.06793	62.1468
0.2	6.5483	0.06548	55.5985
0.17825	6.11987	0.0612	49.4787
0.15887	5.56591	0.05566	43.9128
0.14159	4.92327	0.04923	38.9895
0.12619	4.26392	0.04264	34.7256
0.11247	3.60781	0.03608	31.1178
0.10024	3.00836	0.03008	28.1094
0.08934	2.4744	0.02474	25.635
0.07962	2.0235	0.02023	23.6115
0.07096	1.65955	0.0166	21.952
0.06325	1.37417	0.01374	20.5778
0.05637	1.16529	0.01165	19.4125
0.05024	1.01412	0.01014	18.3984

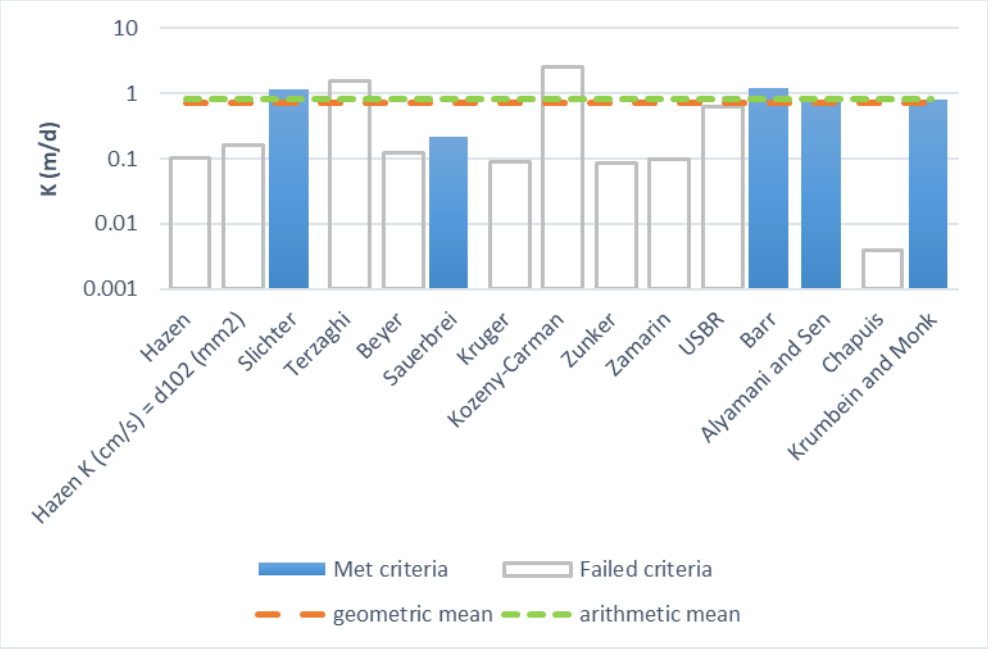
Effective Grain Diameters (mm)		Other Useful Parameters	
d10	0.014	Uniformity Coef.	15.89
d17	0.042	n computed	0.27
d20	0.060	g (cm/s^2)	980.00
d50	0.180	ρ (g/cm^3)	0.9981
d60	0.216	μ (g/cm s)	0.0098
de (Kruger)	0.022	ρg/μ (1/cm s)	9.9327E+04
de (Kozeny)	0.022	tau (Sauerbrei)	1.053
de (Zunker)	0.022	$d_{geometric\ mean}$	0.115
de (Zamarin)	0.022	σ_ϕ	1.787
Io (Alyameni	-0.028		

mm	0	% in sample
>64	Boulder	
16 - 64	coarse gravel	
8 - 16	medium gravel	
2 - 8	fine gravel	0
0.5 - 2	coarse sand	1.1
0.25 - 0.5	medium sand	29.95977961
0.063 - 0.25	fine sand	48.36242466
0.016 - 0.063	coarse silt	9.079375889
0.008 - 0.016	medium silt	3.579541041
0.002 - 0.008	fine silt	5.568188062
<0.002	clay	2.350690738

Slichter, Terzaghi, Kozeny-Carman and Barr with d_{VS}:



Slichter, Terzaghi, Kozeny-Carman and Barr with d_{UU}:

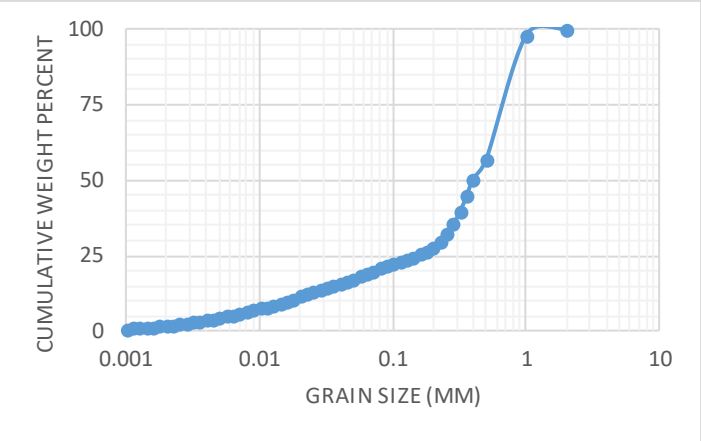


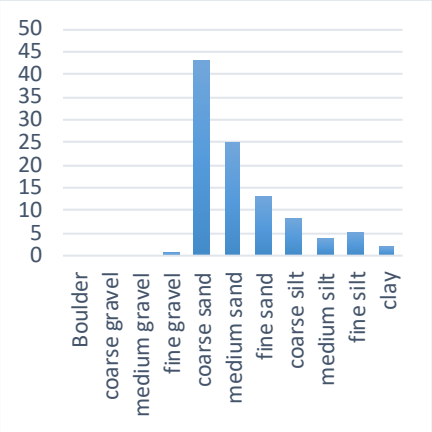
Well PB27-B. Elevation 56.120 m AHD.

Grain Size Analysis Report

Mass Sample (g): 100 T (oC) 20

Poorly sorted sand low in fines





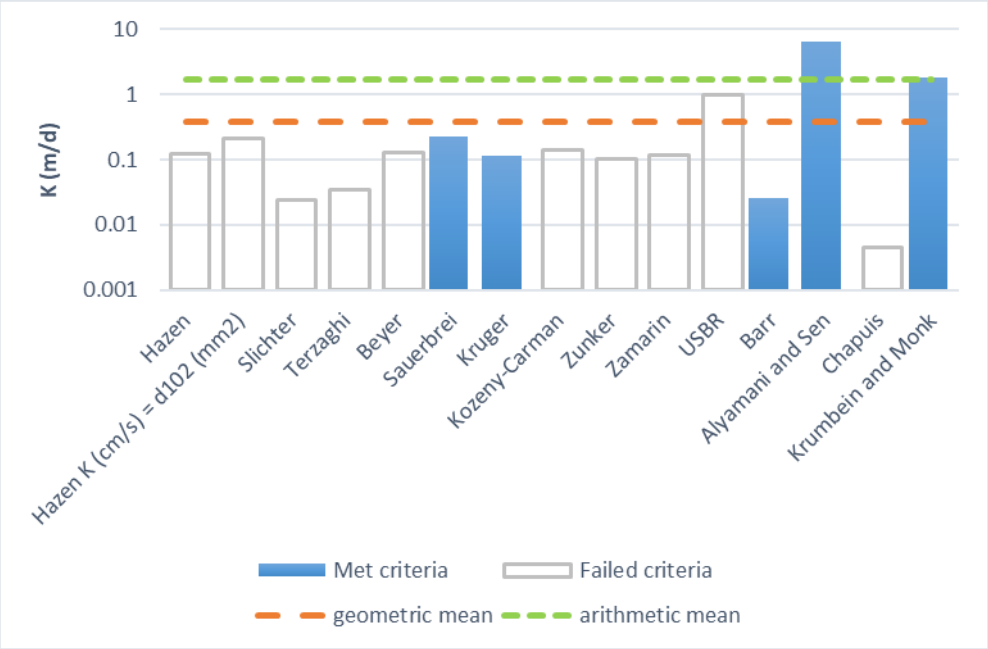
Sieve opening (ps) di (mm)	Mass of retained (mr) (g)	mass fraction (mf)	Percent Passing (pp)
2	0.1	0.001	99.9
1	2.1	0.021	97.8
0.5	41.1	0.411	56.7
0.39905	6.33477	0.06335	50.3652
0.35566	5.82234	0.05822	44.5429
0.31698	5.06179	0.05062	39.4811
0.28251	4.1927	0.04193	35.2884
0.25179	3.29821	0.03298	31.9902
0.2244	2.4864	0.02486	29.5038
0.2	1.81077	0.01811	27.693
0.17825	1.30429	0.01304	26.3887
0.15887	0.97307	0.00973	25.4157
0.14159	0.78785	0.00788	24.6278
0.12619	0.71964	0.0072	23.9082
0.11247	0.72453	0.00725	23.1837
0.10024	0.76492	0.00765	22.4187
0.08934	0.81241	0.00812	21.6063
0.07962	0.84825	0.00848	20.7581
0.07096	0.86376	0.00864	19.8943
0.06325	0.85875	0.00859	19.0356
0.05637	0.83875	0.00839	18.1968
0.05024	0.81022	0.0081	17.3866

Effective Grain Diameters (mm)	
d10	0.016
d17	0.048
d20	0.072
d50	0.396
d60	0.540
de (Kruger)	0.026
de (Kozeny)	0.026
de (Zunker)	0.026
de (Zamarin)	0.026
Io (Alyameni	-0.079

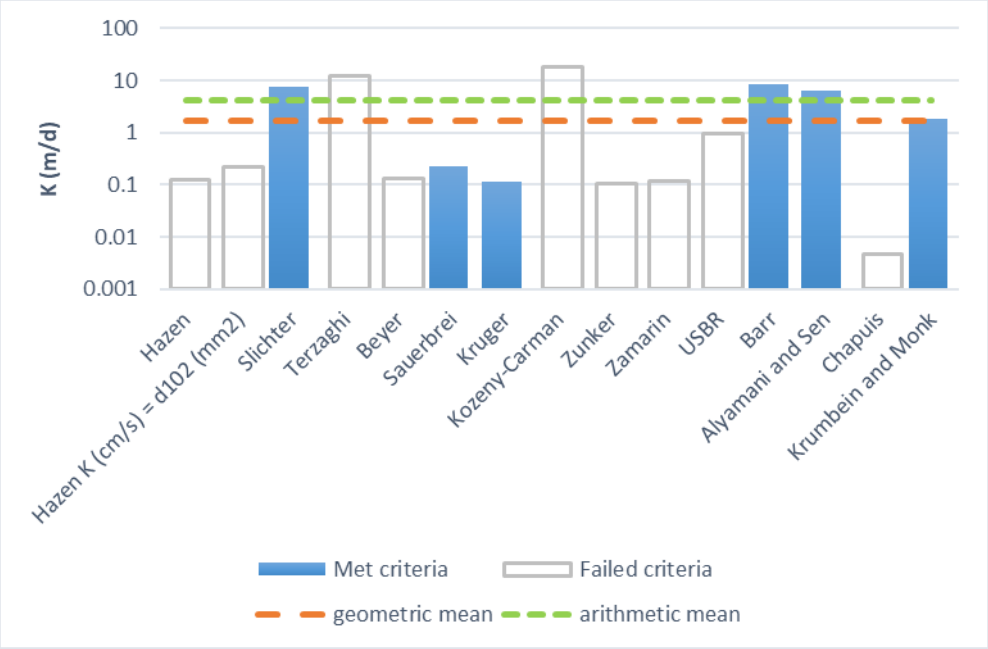
Other Useful Parameters	
Uniformity Coef.	34.33
n computed	0.26
g (cm/s^2)	980.00
ρ (g/cm^3)	0.9981
μ (g/cm s)	0.0098
ρg/μ (1/cm s)	9.9327E+04
tau (Sauerbrei)	1.053
$d_{geometric\ mean}$	0.226
σ_ϕ	2.209

mm	0	% in sample
>64	Boulder	
16 - 64	coarse gravel	
8 - 16	medium gravel	
2 - 8	fine gravel	0.1
0.5 - 2	coarse sand	43.2
0.25 - 0.5	medium sand	24.70980778
0.063 - 0.25	fine sand	12.95461901
0.016 - 0.063	coarse silt	8.275235966
0.008 - 0.016	medium silt	3.820685917
0.002 - 0.008	fine silt	5.050278973
<0.002	clay	1.889372348

Slichter, Terzaghi, Kozeny-Carman and Barr with d_{VS}:



Slichter, Terzaghi, Kozeny-Carman and Barr with d_{UU}:

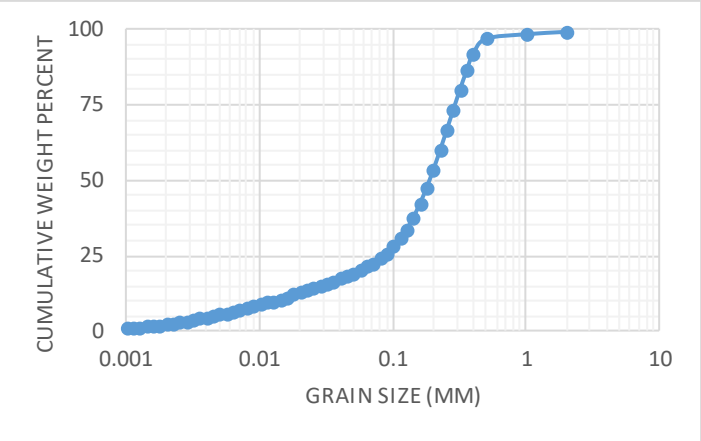


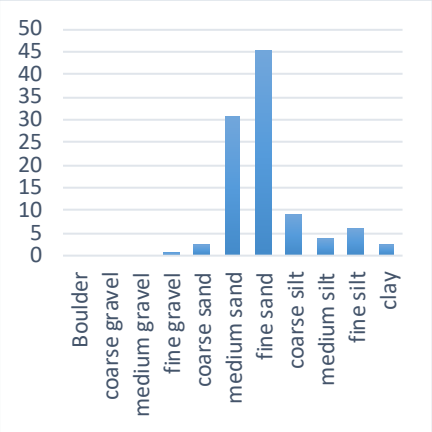
Well ML32. Elevation 55.917 m AHD.

Grain Size Analysis Report

Mass Sample (g): 100 T (oC) 20

Poorly sorted sand low in fines



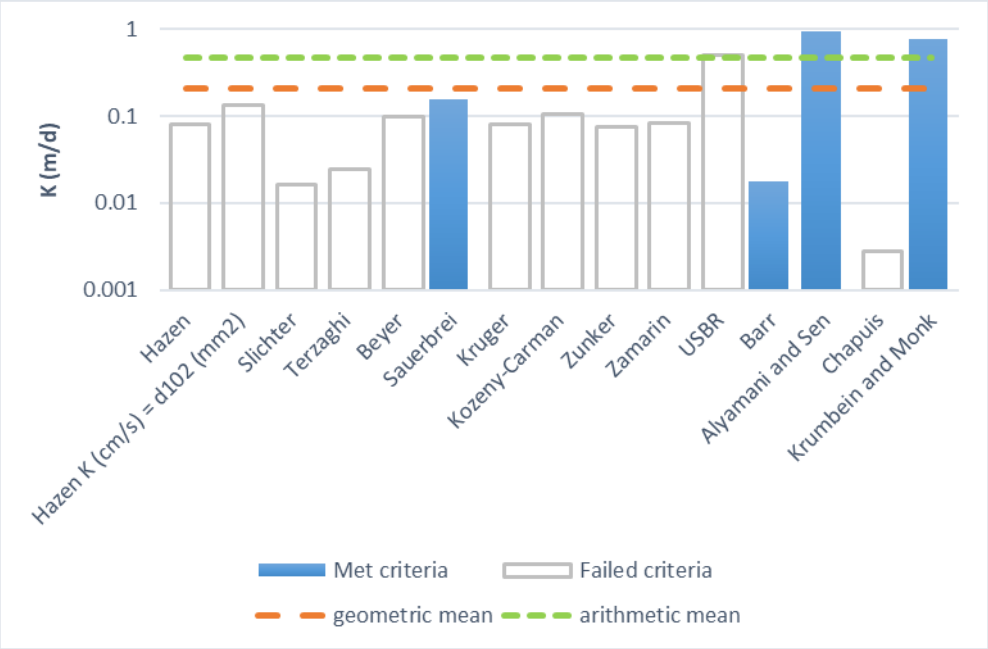


Sieve opening (ps) di (mm)	Mass of retained (mr) (g)	mass fraction (mf)	Percent Passing (pp)
2	0.6	0.006	99.4
1	0.8	0.008	98.6
0.5	1.5	0.015	97.1
0.39905	4.98553	0.04986	92.1145
0.35566	5.73104	0.05731	86.3834
0.31698	6.32015	0.0632	80.0633
0.28251	6.68397	0.06684	73.3793
0.25179	6.81235	0.06812	66.567
0.2244	6.69973	0.067	59.8672
0.2	6.37181	0.06372	53.4954
0.17825	5.86836	0.05868	47.6271
0.15887	5.2552	0.05255	42.3719
0.14159	4.57233	0.04572	37.7995
0.12619	3.89502	0.03895	33.9045
0.11247	3.24236	0.03242	30.6622
0.10024	2.66576	0.02666	27.9964
0.08934	2.17061	0.02171	25.8258
0.07962	1.76973	0.0177	24.056
0.07096	1.46152	0.01462	22.5945
0.06325	1.23304	0.01233	21.3615
0.05637	1.07605	0.01076	20.2854
0.05024	0.9701	0.0097	19.3153

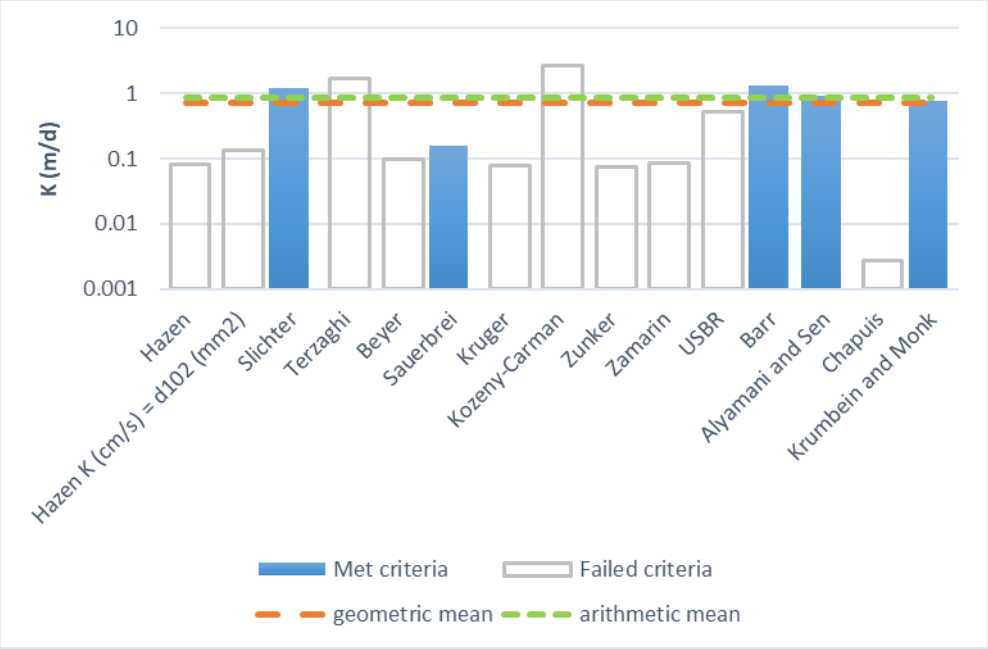
Effective Grain Diameters (mm)		Other Useful Parameters	
d10	0.012	Uniformity Coef.	18.18
d17	0.037	n computed	0.26
d20	0.055	g (cm/s^2)	980.00
d50	0.187	ρ (g/cm^3)	0.9981
d60	0.225	μ (g/cm s)	0.0098
de (Kruger)	0.021	ρg/μ (1/cm s)	9.9327E+04
de (Kozeny)	0.021	tau (Sauerbrei)	1.053
de (Zunker)	0.021	$d_{geometric\ mean}$	0.117
de (Zamarin)	0.021	σ_ϕ	1.870
Io (Alyameni	-0.031		

mm	0	% in sample
>64	Boulder	
16 - 64	coarse gravel	
8 - 16	medium gravel	
2 - 8	fine gravel	0.6
0.5 - 2	coarse sand	2.3
0.25 - 0.5	medium sand	30.53303903
0.063 - 0.25	fine sand	45.20547163
0.016 - 0.063	coarse silt	9.254775623
0.008 - 0.016	medium silt	3.8061239
0.002 - 0.008	fine silt	5.919820726
<0.002	clay	2.380769093

Slichter, Terzaghi, Kozeny-Carman and Barr with d_{VS}:



Slichter, Terzaghi, Kozeny-Carman and Barr with d_{UU}:

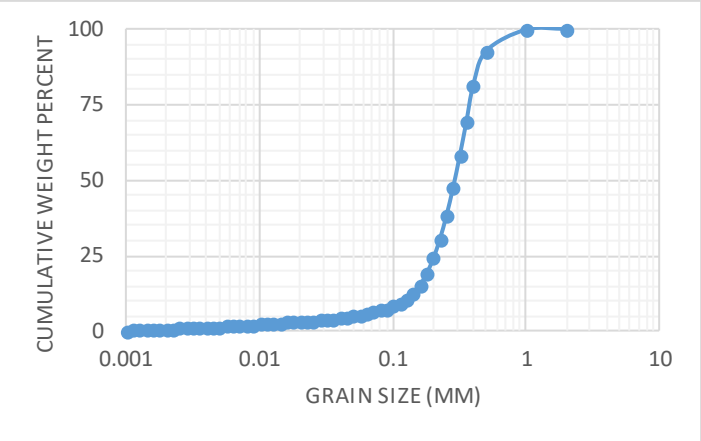


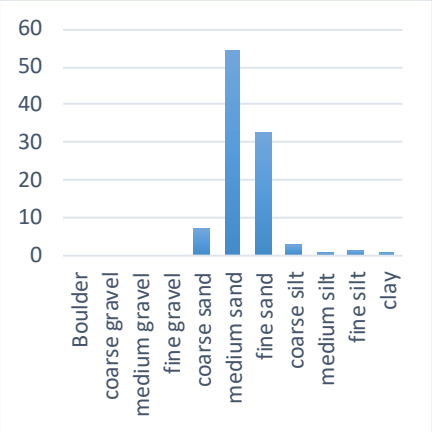
Well MP44-C. Elevation 55.760 m AHD.

Grain Size Analysis Report

Mass Sample (g): 100 T (oC) 20

Moderately well sorted sand low in fines



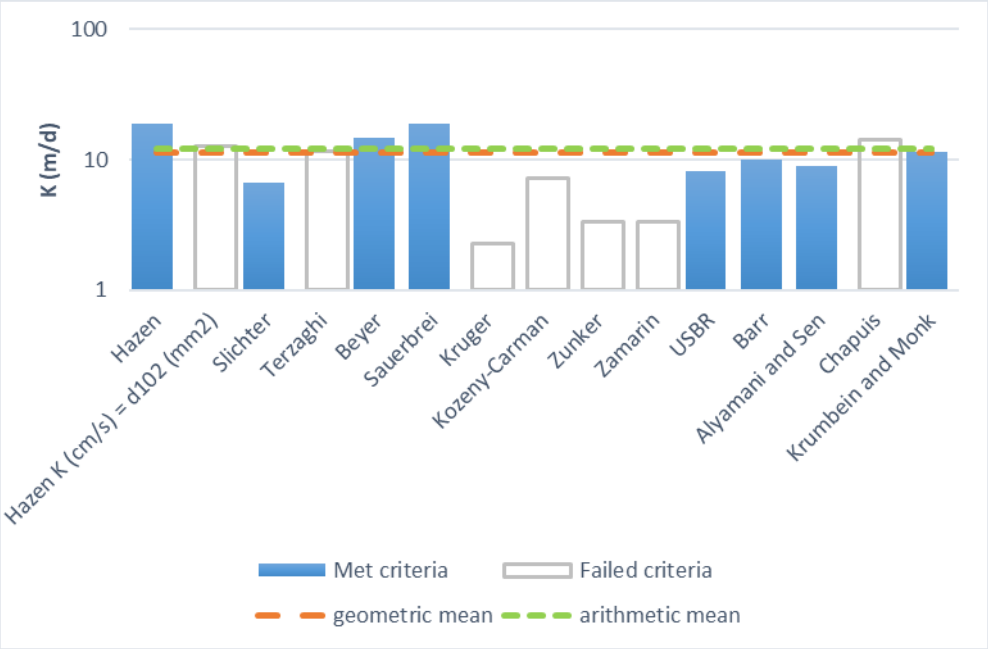


Sieve opening (ps) di (mm)	Mass of retained (mr) (g)	mass fraction (mf)	Percent Passing (pp)
2	0	0	100
1	0.2	0.002	99.8
0.5	7.1	0.071	92.7
0.39905	11.5512	0.11551	81.1488
0.35566	11.7145	0.11715	69.4343
0.31698	11.3312	0.11331	58.1031
0.28251	10.4864	0.10486	47.6167
0.25179	9.28228	0.09282	38.3344
0.2244	7.88298	0.07883	30.4515
0.2	6.41966	0.0642	24.0318
0.17825	5.01503	0.05015	19.0168
0.15887	3.78223	0.03782	15.2345
0.14159	2.74455	0.02745	12.49
0.12619	1.95552	0.01956	10.5345
0.11247	1.37495	0.01375	9.15951
0.10024	0.98914	0.00989	8.17038
0.08934	0.74472	0.00745	7.42565
0.07962	0.60228	0.00602	6.82338
0.07096	0.52179	0.00522	6.30159
0.06325	0.47159	0.00472	5.83
0.05637	0.43321	0.00433	5.39679
0.05024	0.3945	0.00395	5.00228

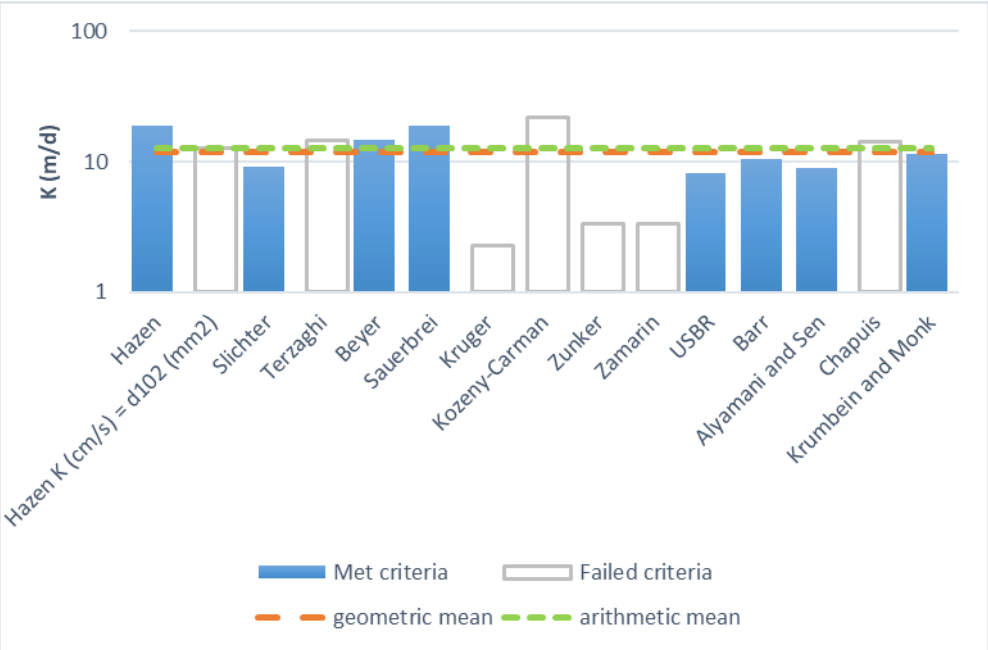
Effective Grain Diameters (mm)		Other Useful Parameters	
d10	0.121	Uniformity Coef.	2.68
d17	0.168	n computed	0.41
d20	0.183	g (cm/s^2)	980.00
d50	0.290	ρ (g/cm^3)	0.9981
d60	0.323	μ (g/cm s)	0.0098
de (Kruger)	0.072	ρg/μ (1/cm s)	9.9327E+04
de (Kozeny)	0.072	tau (Sauerbrei)	1.053
de (Zunker)	0.072	$d_{geometric\ mean}$	0.241
de (Zamarin)	0.072	σ_ϕ	0.909
Io (Alyameni	0.078		

mm	0	% in sample
>64	Boulder	
16 - 64	coarse gravel	
8 - 16	medium gravel	
2 - 8	fine gravel	0
0.5 - 2	coarse sand	7.3
0.25 - 0.5	medium sand	54.36556511
0.063 - 0.25	fine sand	32.50443917
0.016 - 0.063	coarse silt	2.82215834
0.008 - 0.016	medium silt	0.898187639
0.002 - 0.008	fine silt	1.441267052
<0.002	clay	0.668382687

Slichter, Terzaghi, Kozeny-Carman and Barr with d_{VS}:



Slichter, Terzaghi, Kozeny-Carman and Barr with d_{UU}:

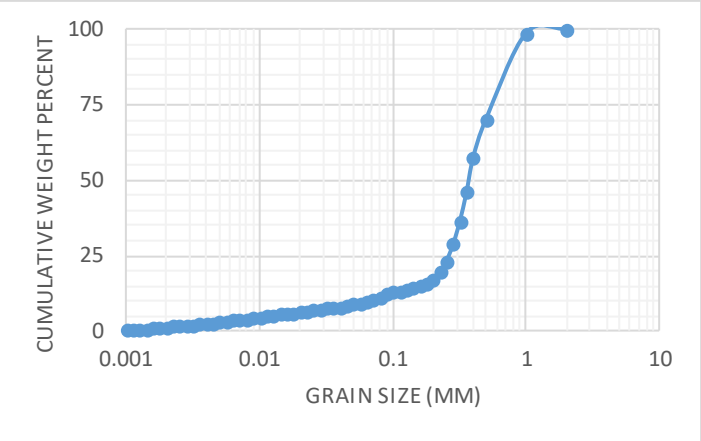


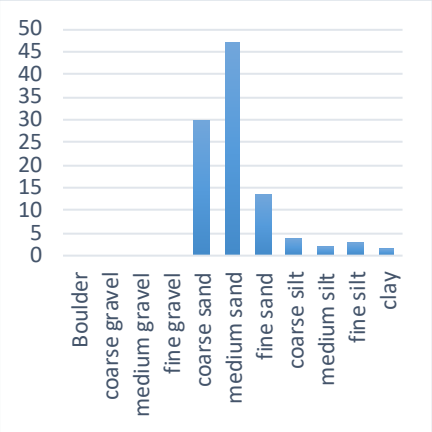
Well MP50-A. Elevation 55.681 m AHD.

Grain Size Analysis Report

Mass Sample (g): 100 T (oC) 20

Poorly sorted sand low in fines



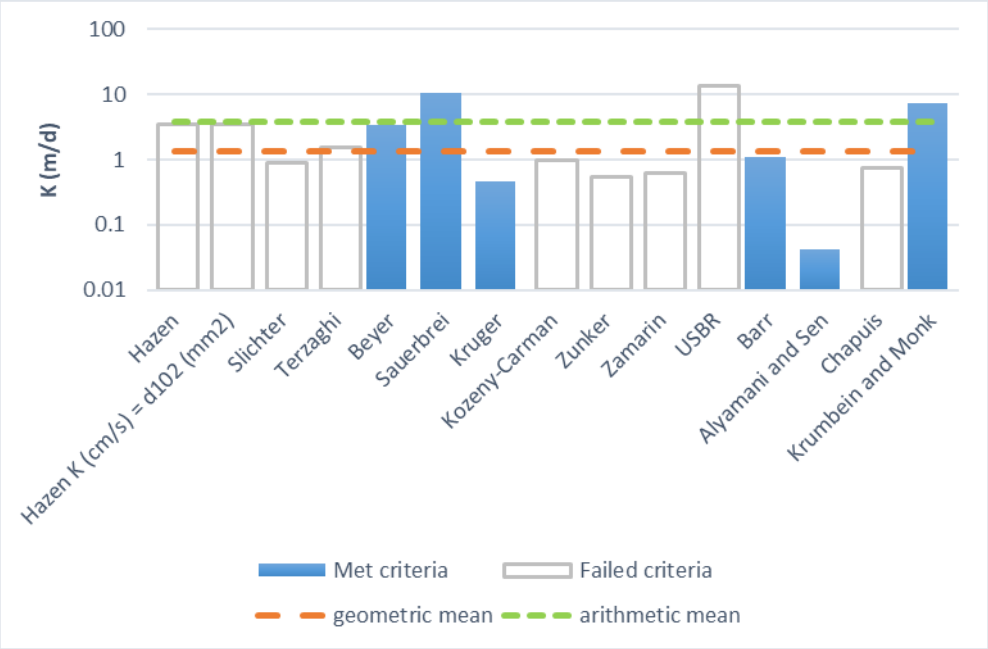


Sieve opening (ps) di (mm)	Mass of retained (mr) (g)	mass fraction (mf)	Percent Passing (pp)
2	0	0	100
1	1.3	0.013	98.7
0.5	28.4	0.284	70.3
0.39905	12.9077	0.12908	57.3923
0.35566	11.4613	0.11461	45.931
0.31698	9.5569	0.09557	36.3741
0.28251	7.52265	0.07523	28.8514
0.25179	5.52976	0.0553	23.3216
0.2244	3.79841	0.03798	19.5232
0.2	2.41847	0.02418	17.1048
0.17825	1.43277	0.01433	15.672
0.15887	0.82629	0.00826	14.8457
0.14159	0.52023	0.0052	14.3255
0.12619	0.43894	0.00439	13.8865
0.11247	0.48735	0.00487	13.3992
0.10024	0.58578	0.00586	12.8134
0.08934	0.67914	0.00679	12.1343
0.07962	0.73299	0.00733	11.4013
0.07096	0.73477	0.00735	10.6665
0.06325	0.68841	0.00688	9.97811
0.05637	0.61043	0.0061	9.36768
0.05024	0.51605	0.00516	8.85164

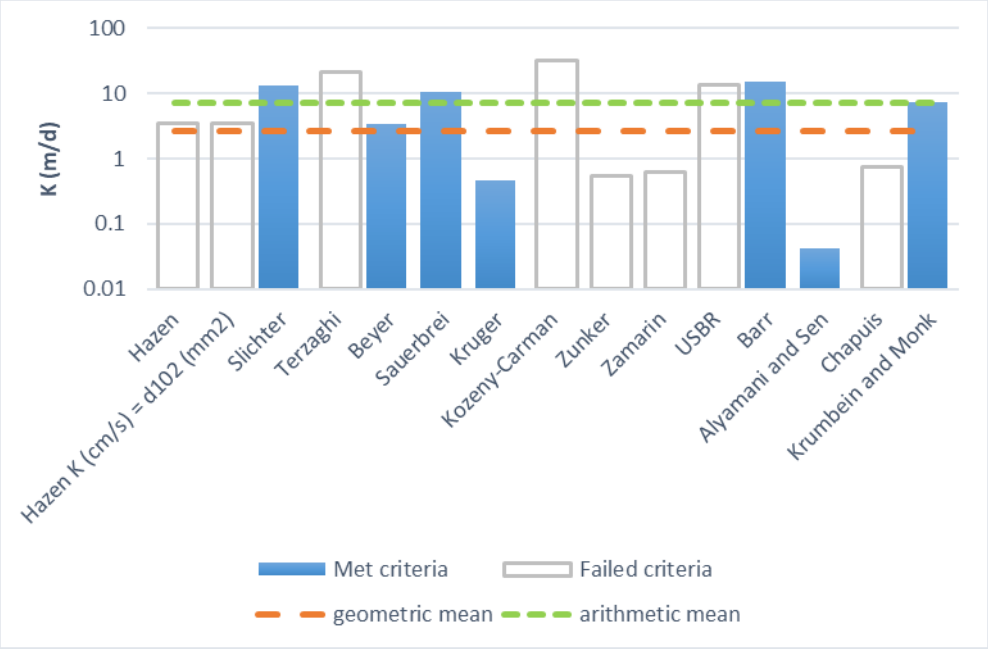
Effective Grain Diameters (mm)		Other Useful Parameters	
d10	0.063	Uniformity Coef.	6.61
d17	0.198	n computed	0.33
d20	0.228	g (cm/s^2)	980.00
d50	0.371	ρ (g/cm^3)	0.9981
d60	0.419	μ (g/cm s)	0.0098
de (Kruger)	0.042	ρg/μ (1/cm s)	9.9327E+04
de (Kozeny)	0.041	tau (Sauerbrei)	1.053
de (Zunker)	0.041	$d_{geometric\ mean}$	0.278
de (Zamarin)	0.041	σ_ϕ	1.459
Io (Alyameni	-0.013		

mm	0	% in sample
>64	Boulder	
16 - 64	coarse gravel	
8 - 16	medium gravel	
2 - 8	fine gravel	0
0.5 - 2	coarse sand	29.7
0.25 - 0.5	medium sand	46.97835333
0.063 - 0.25	fine sand	13.34353967
0.016 - 0.063	coarse silt	3.855933287
0.008 - 0.016	medium silt	1.82188227
0.002 - 0.008	fine silt	2.958918166
<0.002	clay	1.341373282

Slichter, Terzaghi, Kozeny-Carman and Barr with d_{VS}:



Slichter, Terzaghi, Kozeny-Carman and Barr with d_{UU}:

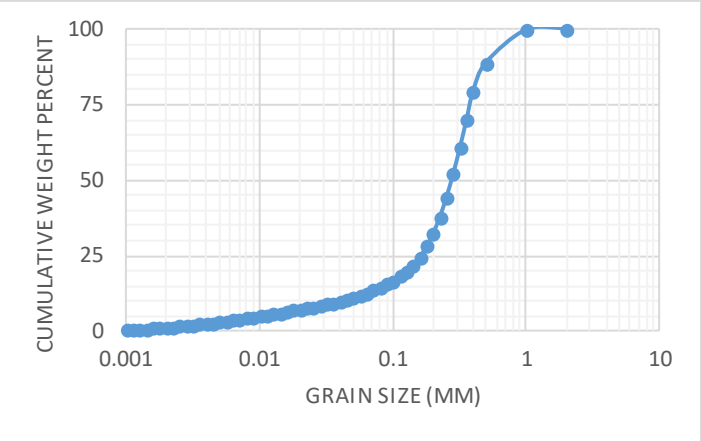


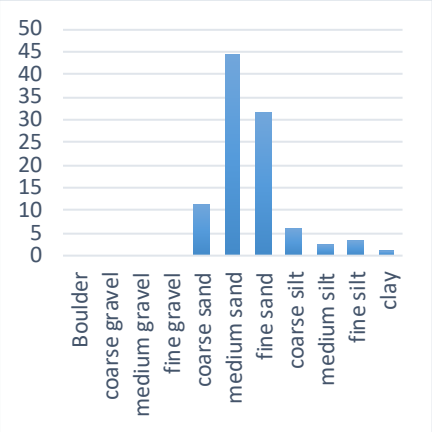
Well PB39-C. Elevation 55.501 m AHD.

Grain Size Analysis Report

Mass Sample (g): 100 T (oC) 20

Poorly sorted sand low in fines





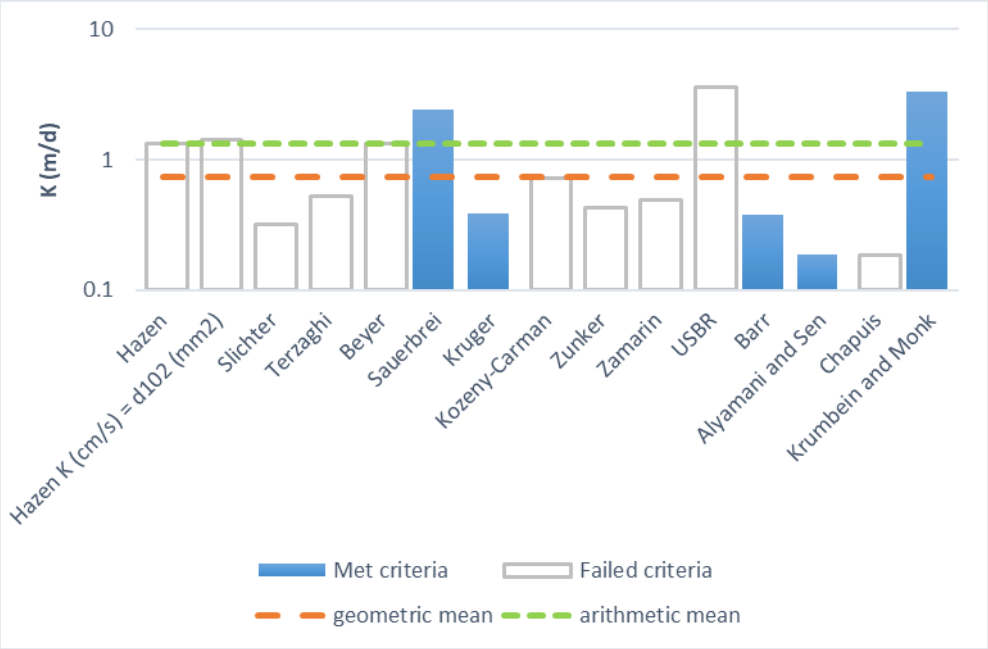
Sieve opening (ps) di (mm)	Mass of retained (mr) (g)	mass fraction (mf)	Percent Passing (pp)
2	0	0	100
1	0.4	0.004	99.6
0.5	10.8	0.108	88.8
0.39905	9.48001	0.0948	79.32
0.35566	9.57131	0.09571	69.7487
0.31698	9.2372	0.09237	60.5115
0.28251	8.55517	0.08555	51.9563
0.25179	7.60999	0.0761	44.3463
0.2244	6.53151	0.06532	37.8148
0.2	5.42002	0.0542	32.3948
0.17825	4.36692	0.04367	28.0279
0.15887	3.45334	0.03453	24.5745
0.14159	2.69147	0.02691	21.8831
0.12619	2.11458	0.02115	19.7685
0.11247	1.68685	0.01687	18.0816
0.10024	1.3932	0.01393	16.6884
0.08934	1.19175	0.01192	15.4967
0.07962	1.05345	0.01053	14.4432
0.07096	0.95123	0.00951	13.492
0.06325	0.865	0.00865	12.627
0.05637	0.78708	0.00787	11.8399
0.05024	0.71105	0.00711	11.1289

Effective Grain Diameters (mm)	
d10	0.041
d17	0.103
d20	0.128
d50	0.275
d60	0.315
de (Kruger)	0.039
de (Kozeny)	0.039
de (Zunker)	0.039
de (Zamarin)	0.039
Io (Alyameni	-0.018

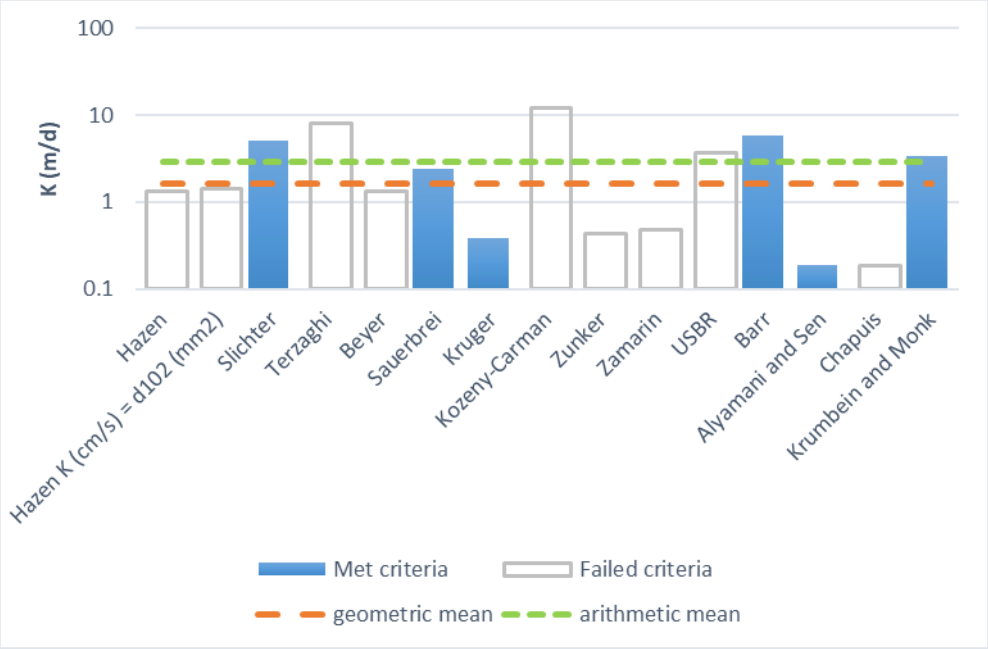
mm	0	% in sample
>64	Boulder	
16 - 64	coarse gravel	
8 - 16	medium gravel	
2 - 8	fine gravel	0
0.5 - 2	coarse sand	11.2
0.25 - 0.5	medium sand	44.45368329
0.063 - 0.25	fine sand	31.71931717
0.016 - 0.063	coarse silt	5.801868572
0.008 - 0.016	medium silt	2.275327575
0.002 - 0.008	fine silt	3.291343153
<0.002	clay	1.258460237

Other Useful Parameters	
Uniformity Coef.	7.75
n computed	0.32
g (cm/s^2)	980.00
ρ (g/cm^3)	0.9981
μ (g/cm s)	0.0098
ρg/μ (1/cm s)	9.9327E+04
tau (Sauerbrei)	1.053
$d_{geometric\ mean}$	0.194
σ_ϕ	1.510

Slichter, Terzaghi, Kozeny-Carman and Barr with d_{VS}:



Slichter, Terzaghi, Kozeny-Carman and Barr with d_{UU}:

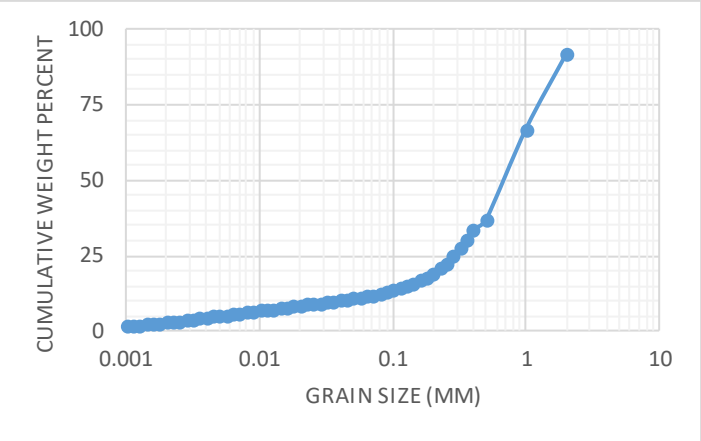


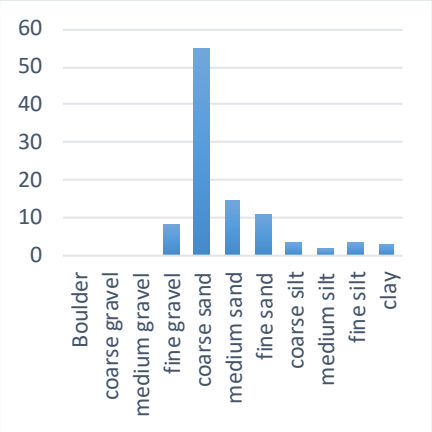
Well PB28. Elevation 55.436 m AHD.

Grain Size Analysis Report

Mass Sample (g): 100 T (oC) 20

Poorly sorted sand with fines



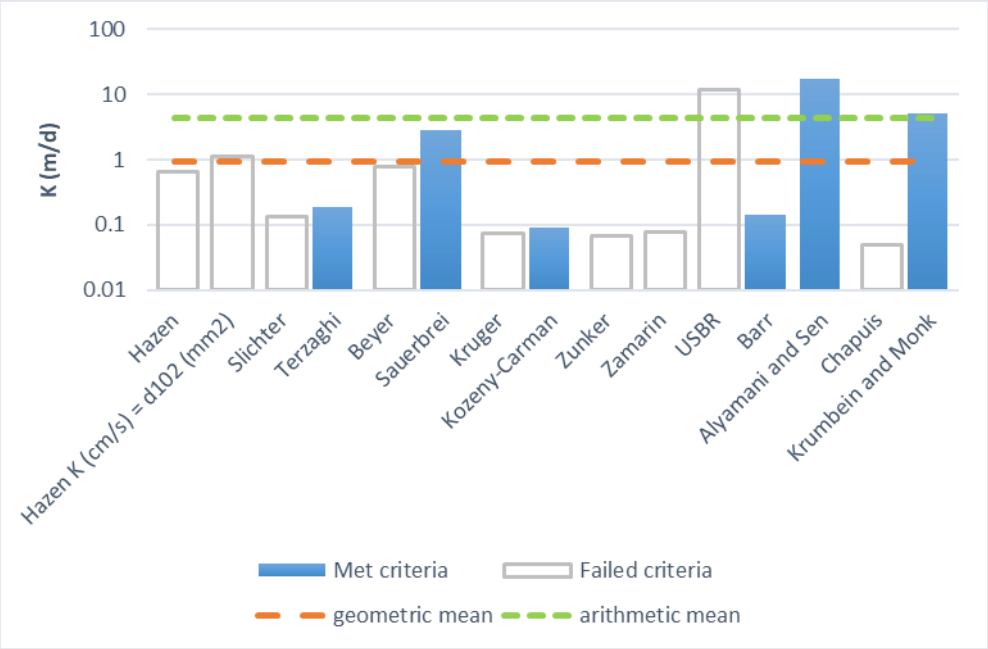


Sieve opening (ps) di (mm)	Mass of retained (mr) (g)	mass fraction (mf)	Percent Passing (pp)
2	8.4	0.084	91.6
1	24.6	0.246	67
0.5	30	0.3	37
0.39905	3.31601	0.03316	33.684
0.35566	3.19048	0.0319	30.4935
0.31698	2.94282	0.02943	27.5507
0.28251	2.62373	0.02624	24.927
0.25179	2.26675	0.02267	22.6602
0.2244	1.91544	0.01915	20.7448
0.2	1.59381	0.01594	19.151
0.17825	1.31878	0.01319	17.8322
0.15887	1.09968	0.011	16.7325
0.14159	0.92846	0.00928	15.804
0.12619	0.80298	0.00803	15.0011
0.11247	0.70782	0.00708	14.2932
0.10024	0.63554	0.00636	13.6577
0.08934	0.57602	0.00576	13.0817
0.07962	0.52432	0.00524	12.5574
0.07096	0.47742	0.00477	12.0799
0.06325	0.43378	0.00434	11.6462
0.05637	0.39508	0.00395	11.2511
0.05024	0.36099	0.00361	10.8901

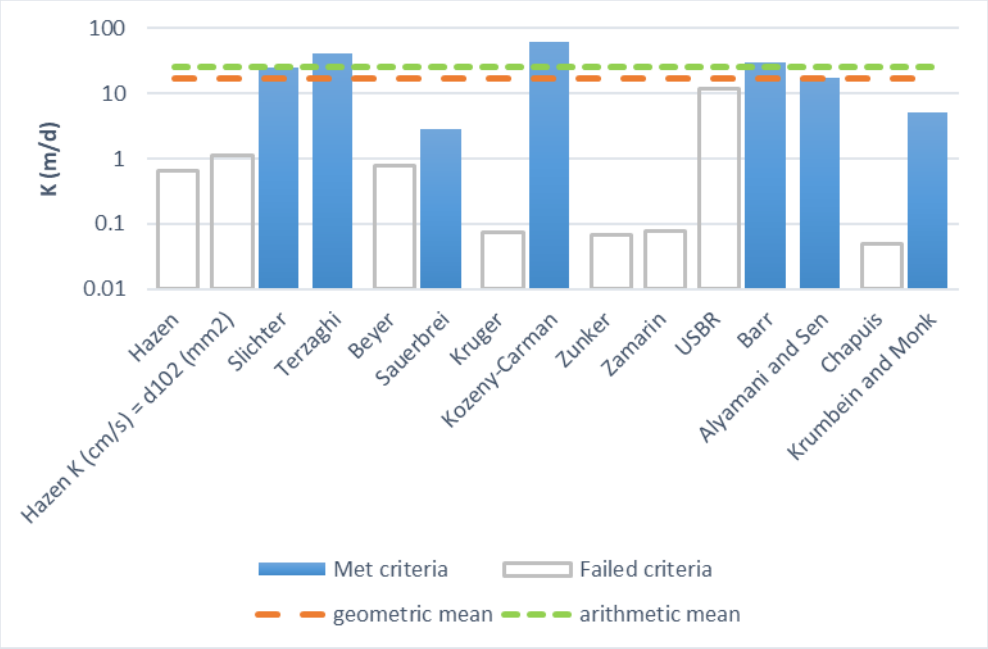
Effective Grain Diameters (mm)		Other Useful Parameters	
d10	0.036	Uniformity Coef.	24.29
d17	0.164	n computed	0.26
d20	0.213	g (cm/s^2)	980.00
d50	0.717	ρ (g/cm^3)	0.9981
d60	0.883	μ (g/cm s)	0.0098
de (Kruger)	0.021	ρg/μ (1/cm s)	9.9327E+04
de (Kozeny)	0.020	tau (Sauerbrei)	1.053
de (Zunker)	0.020	$d_{geometric\ mean}$	0.380
de (Zamarin)	0.020	σ_ϕ	2.213
Io (Alyameni	-0.134		

mm	0	% in sample
>64	Boulder	
16 - 64	coarse gravel	
8 - 16	medium gravel	
2 - 8	fine gravel	8.4
0.5 - 2	coarse sand	54.6
0.25 - 0.5	medium sand	14.33978237
0.063 - 0.25	fine sand	11.01406201
0.016 - 0.063	coarse silt	3.405589215
0.008 - 0.016	medium silt	1.676417771
0.002 - 0.008	fine silt	3.65148094
<0.002	clay	2.912667696

Slichter, Terzaghi, Kozeny-Carman and Barr with d_{VS}:



Slichter, Terzaghi, Kozeny-Carman and Barr with d_{UU}:

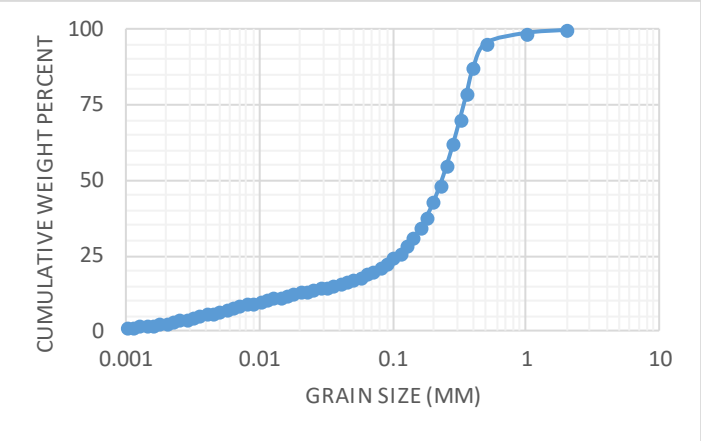


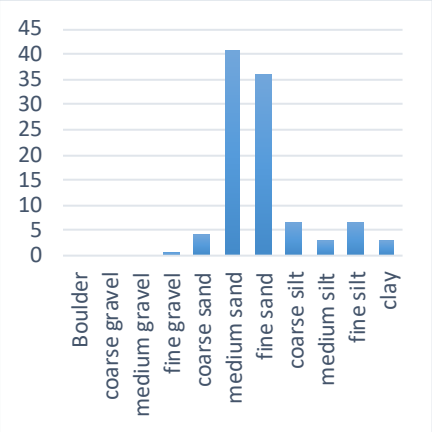
Well MP50-A. Elevation 55.186 m AHD.

Grain Size Analysis Report

Mass Sample (g): 100 T (oC) 20

Poorly sorted sand with fines



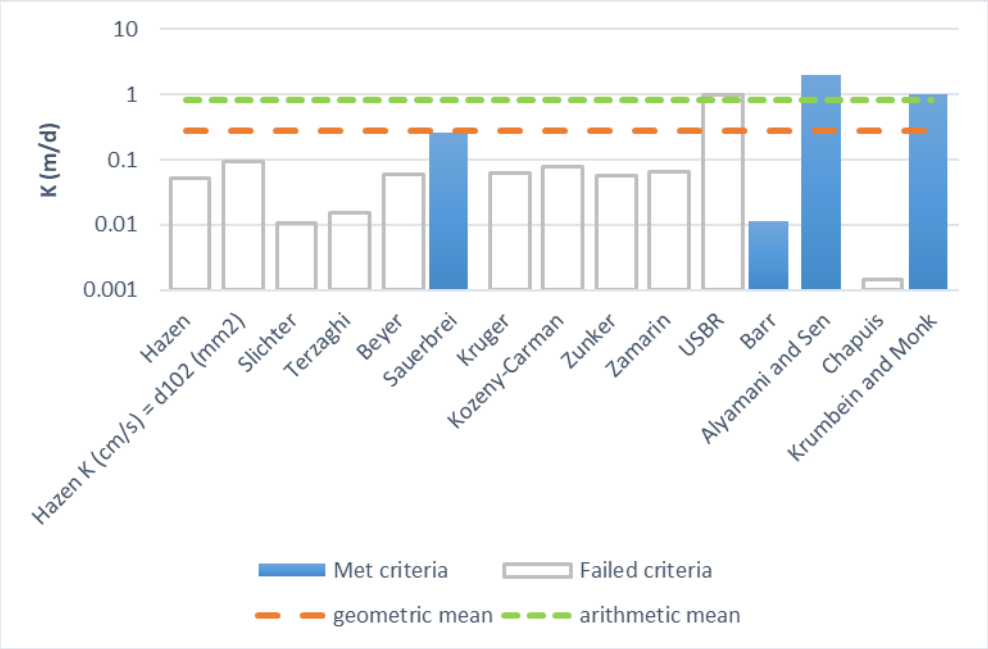


Sieve opening (ps) di (mm)	Mass of retained (mr) (g)	mass fraction (mf)	Percent Passing (pp)
2	0.4	0.004	99.6
1	1	0.01	98.6
0.5	3.3	0.033	95.3
0.39905	8.28132	0.08281	87.0187
0.35566	8.54253	0.08543	78.4761
0.31698	8.43677	0.08437	70.0394
0.28251	8.00976	0.0801	62.0296
0.25179	7.33032	0.0733	54.6993
0.2244	6.50021	0.065	48.1991
0.2	5.60367	0.05604	42.5954
0.17825	4.71895	0.04719	37.8765
0.15887	3.91932	0.03919	33.9571
0.14159	3.21973	0.0322	30.7374
0.12619	2.65669	0.02657	28.0807
0.11247	2.20397	0.02204	25.8768
0.10024	1.85809	0.01858	24.0187
0.08934	1.58786	0.01588	22.4308
0.07962	1.37478	0.01375	21.056
0.07096	1.20048	0.012	19.8555
0.06325	1.0498	0.0105	18.8057
0.05637	0.91986	0.0092	17.8859
0.05024	0.80349	0.00803	17.0824

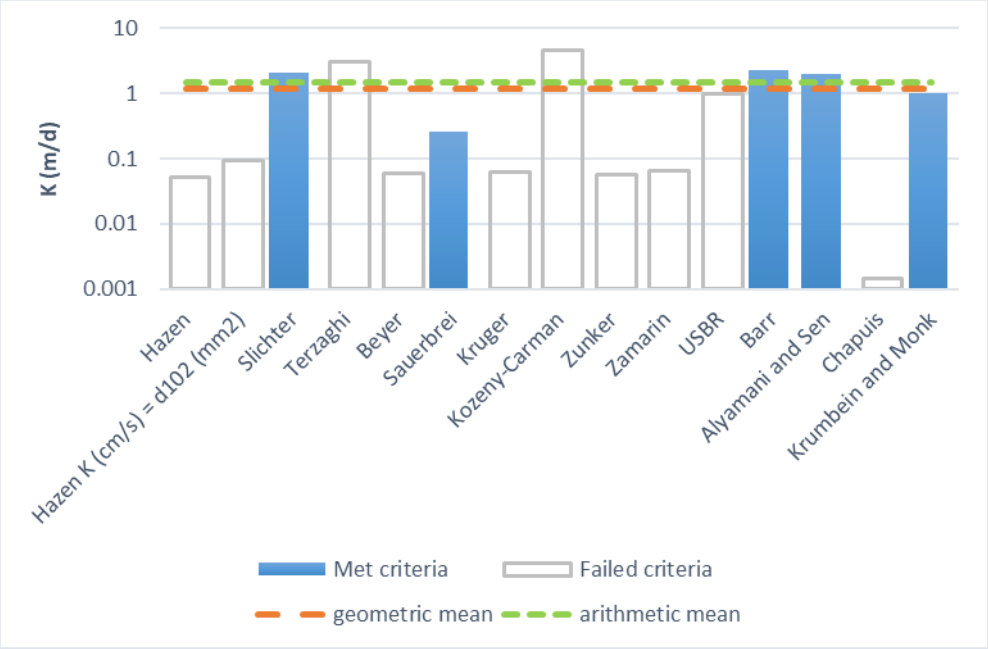
Effective Grain Diameters (mm)		Other Useful Parameters	
d10	0.010	Uniformity Coef.	26.61
d17	0.050	n computed	0.26
d20	0.072	g (cm/s^2)	980.00
d50	0.232	ρ (g/cm^3)	0.9981
d60	0.274	μ (g/cm s)	0.0098
de (Kruger)	0.019	ρg/μ (1/cm s)	9.9327E+04
de (Kozeny)	0.019	tau (Sauerbrei)	1.053
de (Zunker)	0.019	$d_{geometric\ mean}$	0.136
de (Zamarin)	0.019	σ_ϕ	1.882
Io (Alyameni	-0.045		

mm	0	% in sample
>64	Boulder	
16 - 64	coarse gravel	
8 - 16	medium gravel	
2 - 8	fine gravel	0.4
0.5 - 2	coarse sand	4.3
0.25 - 0.5	medium sand	40.60070756
0.063 - 0.25	fine sand	35.89354925
0.016 - 0.063	coarse silt	6.428912507
0.008 - 0.016	medium silt	3.017220057
0.002 - 0.008	fine silt	6.550490878
<0.002	clay	2.809119745

Slichter, Terzaghi, Kozeny-Carman and Barr with d_{VS}:



Slichter, Terzaghi, Kozeny-Carman and Barr with d_{UU}:

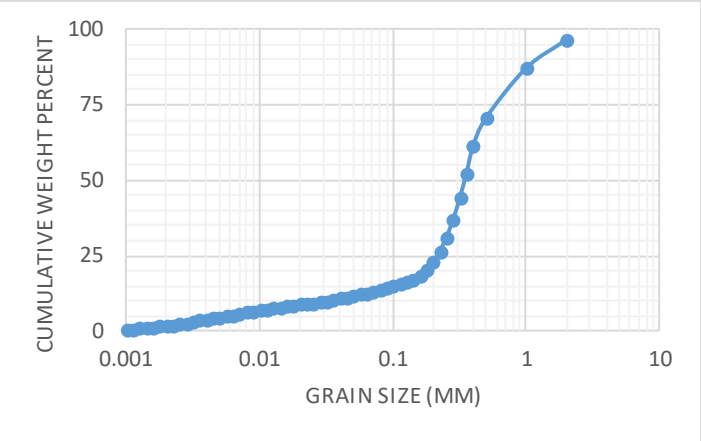


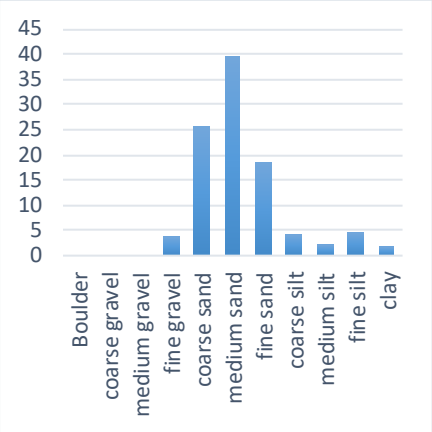
Well PB13-C. Elevation 55.180 m AHD.

Grain Size Analysis Report

Mass Sample (g): 100 T (oC) 20

Poorly sorted sand low in fines



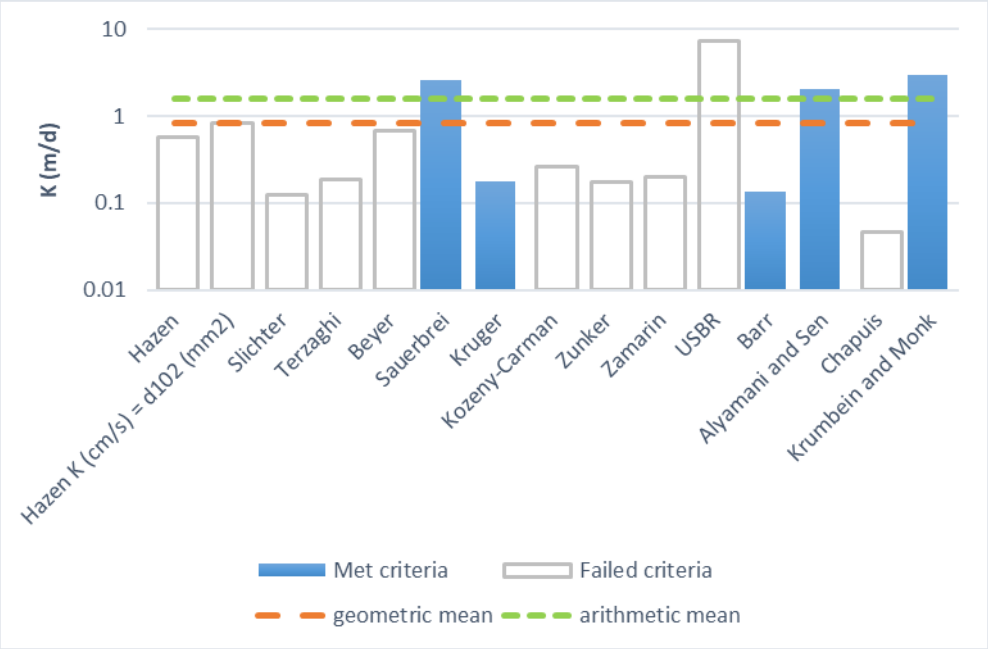


Sieve opening (ps) di (mm)	Mass of retained (mr) (g)	mass fraction (mf)	Percent Passing (pp)
2	3.8	0.038	96.2
1	9.3	0.093	86.9
0.5	16.4	0.164	70.5
0.39905	9.37201	0.09372	61.128
0.35566	8.94432	0.08944	52.1837
0.31698	8.12352	0.08124	44.0601
0.28251	7.0575	0.07058	37.0026
0.25179	5.84748	0.05847	31.1552
0.2244	4.6403	0.0464	26.5149
0.2	3.52558	0.03526	22.9893
0.17825	2.57451	0.02575	20.4148
0.15887	1.83411	0.01834	18.5807
0.14159	1.28943	0.01289	17.2912
0.12619	0.93773	0.00938	16.3535
0.11247	0.72858	0.00729	15.6249
0.10024	0.62583	0.00626	14.9991
0.08934	0.5853	0.00585	14.4138
0.07962	0.57506	0.00575	13.8387
0.07096	0.57086	0.00571	13.2678
0.06325	0.55877	0.00559	12.7091
0.05637	0.53466	0.00535	12.1744
0.05024	0.49881	0.00499	11.6756

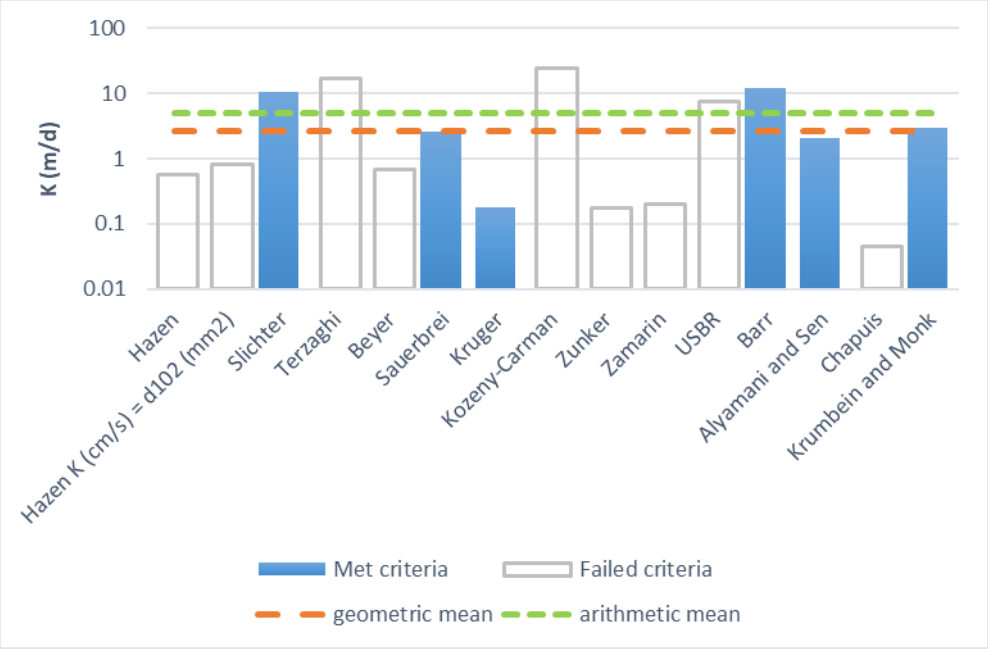
Effective Grain Diameters (mm)		Other Useful Parameters	
d10	0.031	Uniformity Coef.	12.76
d17	0.137	n computed	0.28
d20	0.174	g (cm/s^2)	980.00
d50	0.345	ρ (g/cm^3)	0.9981
d60	0.394	μ (g/cm s)	0.0098
de (Kruger)	0.030	ρg/μ (1/cm s)	9.9327E+04
de (Kozeny)	0.030	tau (Sauerbrei)	1.053
de (Zunker)	0.030	$d_{geometric\ mean}$	0.254
de (Zamarin)	0.030	σ_ϕ	2.005
Io (Alyameni	-0.048		

mm	0	% in sample
>64	Boulder	
16 - 64	coarse gravel	
8 - 16	medium gravel	
2 - 8	fine gravel	3.8
0.5 - 2	coarse sand	25.7
0.25 - 0.5	medium sand	39.344842
0.063 - 0.25	fine sand	18.44607945
0.016 - 0.063	coarse silt	4.20212377
0.008 - 0.016	medium silt	1.986472671
0.002 - 0.008	fine silt	4.670715131
<0.002	clay	1.84976698

Slichter, Terzaghi, Kozeny-Carman and Barr with d_{VS}:



Slichter, Terzaghi, Kozeny-Carman and Barr with d_{UU}:

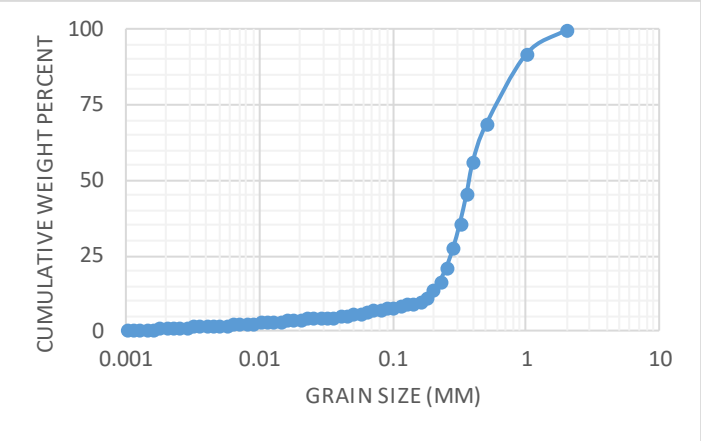


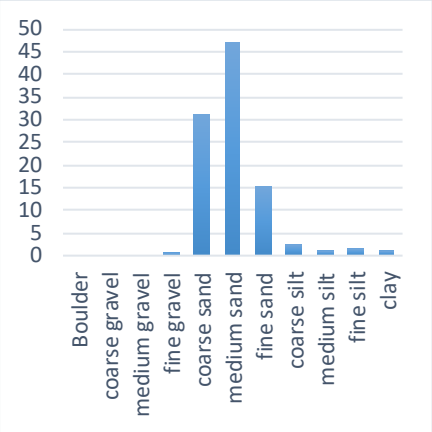
Well MP44-C. Elevation 55.160 m AHD.

Grain Size Analysis Report

Mass Sample (g): 100 T (oC) 20

Moderately well sorted sand low in fines





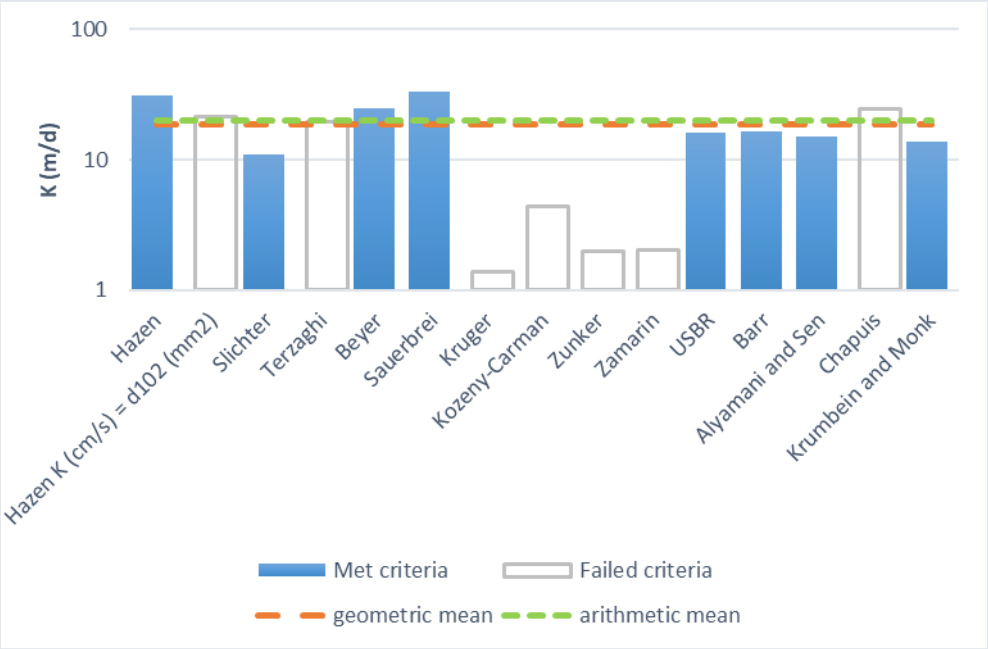
Sieve opening (ps) di (mm)	Mass of retained (mr) (g)	mass fraction (mf)	Percent Passing (pp)
2	0.4	0.004	99.6
1	8	0.08	91.6
0.5	23.2	0.232	68.4
0.39905	11.9833	0.11983	56.4167
0.35566	11.0763	0.11076	45.3405
0.31698	9.67461	0.09675	35.6658
0.28251	8.02571	0.08026	27.6401
0.25179	6.27978	0.0628	21.3604
0.2244	4.64288	0.04643	16.7175
0.2	3.22348	0.03223	13.494
0.17825	2.09583	0.02096	11.3982
0.15887	1.29079	0.01291	10.1074
0.14159	0.76526	0.00765	9.34211
0.12619	0.48497	0.00485	8.85714
0.11247	0.37186	0.00372	8.48528
0.10024	0.36285	0.00363	8.12244
0.08934	0.39991	0.004	7.72253
0.07962	0.44218	0.00442	7.28034
0.07096	0.46423	0.00464	6.81612
0.06325	0.4563	0.00456	6.35981
0.05637	0.42136	0.00421	5.93845
0.05024	0.3668	0.00367	5.57165

Effective Grain Diameters (mm)	
d10	0.156
d17	0.226
d20	0.244
d50	0.374
d60	0.429
de (Kruger)	0.056
de (Kozeny)	0.056
de (Zunker)	0.056
de (Zamarin)	0.056
Io (Alyameni	0.102

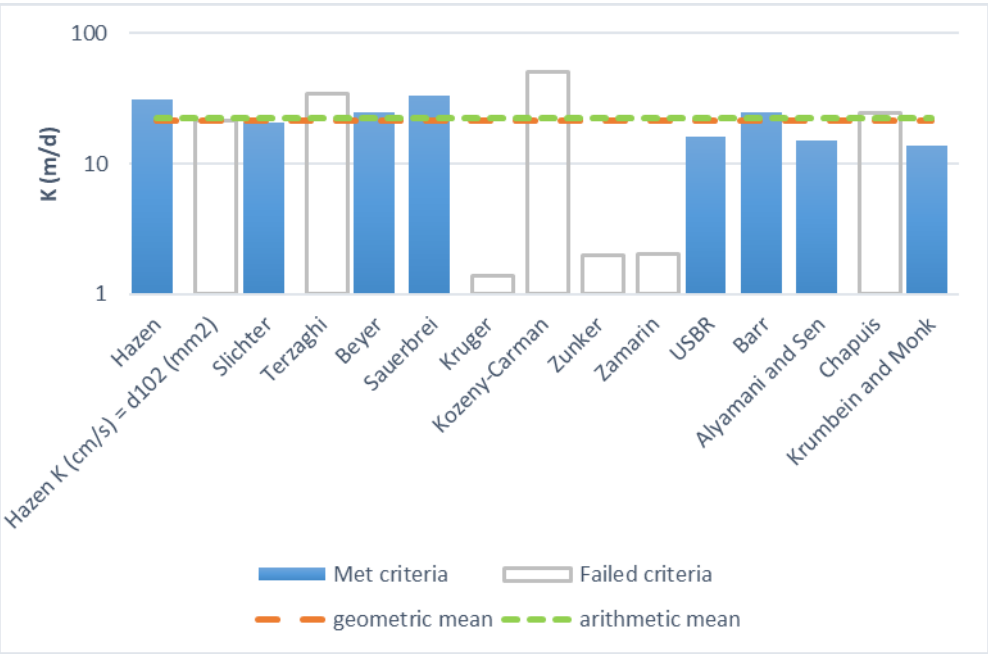
Other Useful Parameters	
Uniformity Coef.	2.74
n computed	0.41
g (cm/s^2)	980.00
ρ (g/cm^3)	0.9981
μ (g/cm s)	0.0098
ρg/μ (1/cm s)	9.9327E+04
tau (Sauerbrei)	1.053
$d_{geometric\ mean}$	0.334
σ_ϕ	1.267

mm	0	% in sample
>64	Boulder	
16 - 64	coarse gravel	
8 - 16	medium gravel	
2 - 8	fine gravel	0.4
0.5 - 2	coarse sand	31.2
0.25 - 0.5	medium sand	47.03964291
0.063 - 0.25	fine sand	15.00054569
0.016 - 0.063	coarse silt	2.518601866
0.008 - 0.016	medium silt	1.096113738
0.002 - 0.008	fine silt	1.694352506
<0.002	clay	1.050743289

Slichter, Terzaghi, Kozeny-Carman and Barr with d_{VS}:



Slichter, Terzaghi, Kozeny-Carman and Barr with d_{UU}:

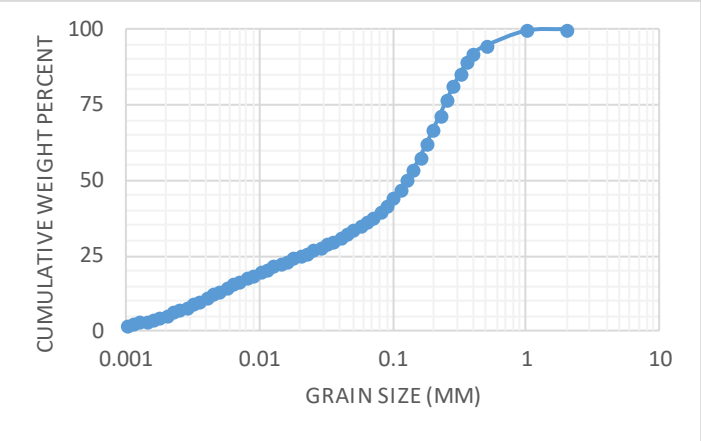


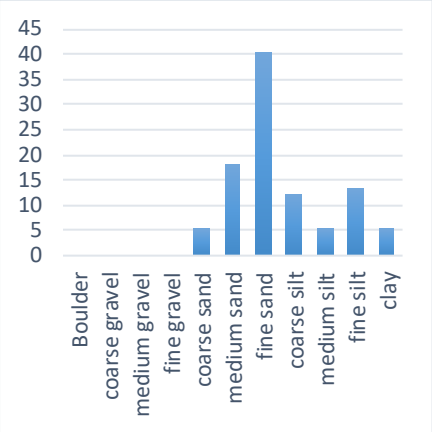
Well ML15. Elevation 55.147 m AHD.

Grain Size Analysis Report

Mass Sample (g): 100 T (oC) 20

Poorly sorted sand with fines





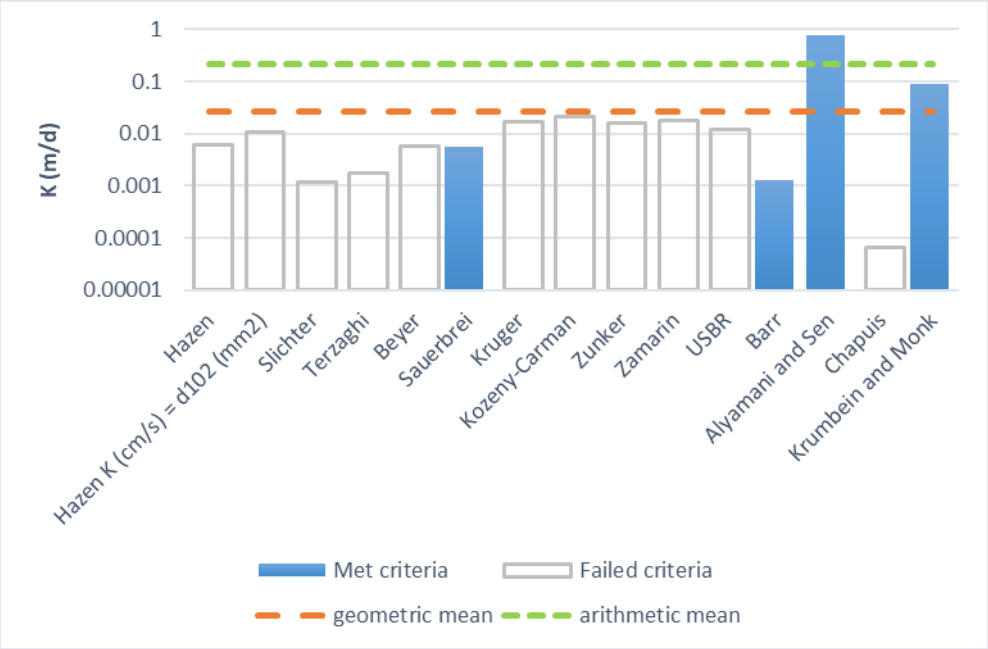
Sieve opening (ps) di (mm)	Mass of retained (mr) (g)	mass fraction (mf)	Percent Passing (pp)
2	0	0	100
1	0.5	0.005	99.5
0.5	4.9	0.049	94.6
0.39905	2.55959	0.0256	92.0404
0.35566	3.15128	0.03151	88.8891
0.31698	3.72128	0.03721	85.1678
0.28251	4.19759	0.04198	80.9703
0.25179	4.55672	0.04557	76.4135
0.2244	4.7611	0.04761	71.6524
0.2	4.80265	0.04803	66.8498
0.17825	4.68551	0.04686	62.1643
0.15887	4.43711	0.04437	57.7272
0.14159	4.08319	0.04083	53.644
0.12619	3.67386	0.03674	49.9701
0.11247	3.2328	0.03233	46.7373
0.10024	2.80709	0.02807	43.9302
0.08934	2.41346	0.02413	41.5168
0.07962	2.07268	0.02073	39.4441
0.07096	1.79346	0.01793	37.6506
0.06325	1.5723	0.01572	36.0783
0.05637	1.40826	0.01408	34.6701
0.05024	1.28618	0.01286	33.3839

Effective Grain Diameters (mm)	
d10	0.004
d17	0.007
d20	0.011
d50	0.126
d60	0.169
de (Kruger)	0.010
de (Kozeny)	0.010
de (Zunker)	0.010
de (Zamarin)	0.010
Io (Alyameni	-0.027

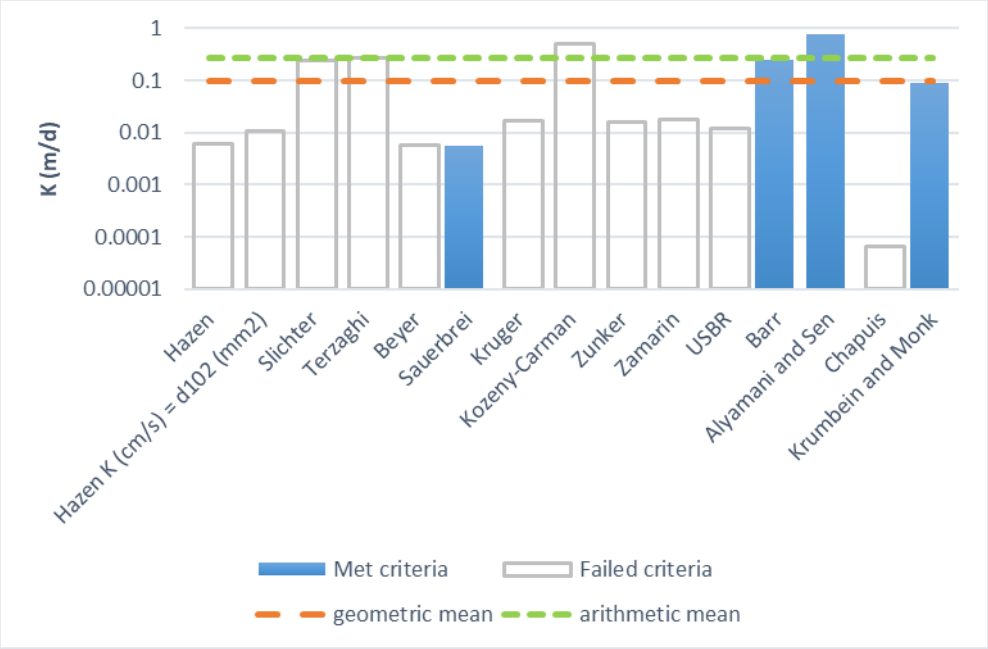
Other Useful Parameters	
Uniformity Coef.	47.87
n computed	0.26
g (cm/s^2)	980.00
ρ (g/cm^3)	0.9981
μ (g/cm s)	0.0098
ρg/μ (1/cm s)	9.9327E+04
tau (Sauerbrei)	1.053
$d_{geometric\ mean}$	0.065
σ_ϕ	2.620

mm	0	% in sample
>64	Boulder	
16 - 64	coarse gravel	
8 - 16	medium gravel	
2 - 8	fine gravel	0
0.5 - 2	coarse sand	5.4
0.25 - 0.5	medium sand	18.18646742
0.063 - 0.25	fine sand	40.33521616
0.016 - 0.063	coarse silt	11.93680322
0.008 - 0.016	medium silt	5.545985226
0.002 - 0.008	fine silt	13.12751457
<0.002	clay	5.468013397

Slichter, Terzaghi, Kozeny-Carman and Barr with d_{VS}:



Slichter, Terzaghi, Kozeny-Carman and Barr with d_{UU}:

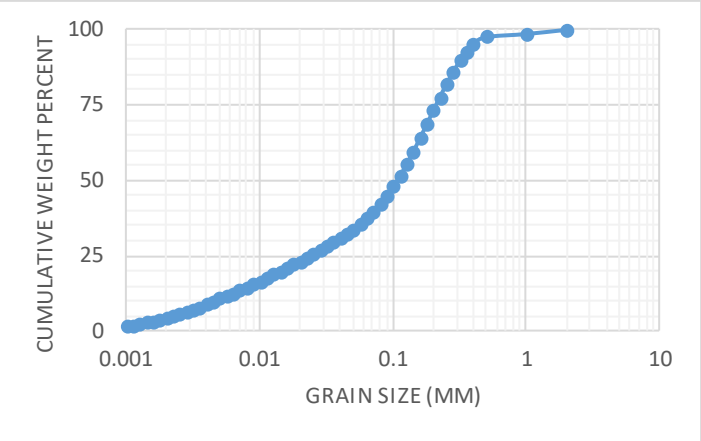


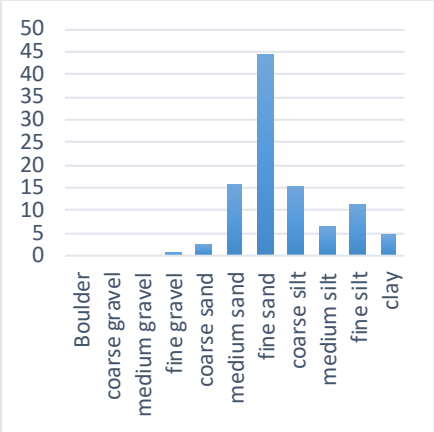
Well PB13-C. Elevation 55.030 m AHD.

Grain Size Analysis Report

Mass Sample (g): 100 T (oC) 20

Poorly sorted sand with fines



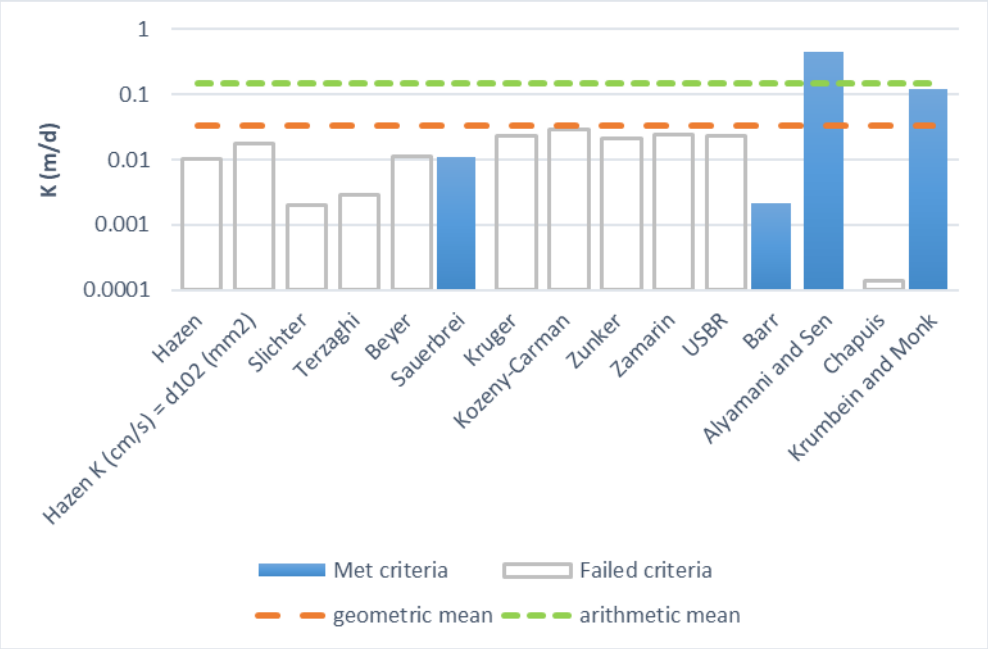


Sieve opening (ps) di (mm)	Mass of retained (mr) (g)	mass fraction (mf)	Percent Passing (pp)
2	0.1	0.001	99.9
1	1.4	0.014	98.5
0.5	1	0.01	97.5
0.39905	2.1405	0.02141	95.3595
0.35566	2.65411	0.02654	92.7054
0.31698	3.17106	0.03171	89.5343
0.28251	3.63395	0.03634	85.9004
0.25179	4.03085	0.04031	81.8695
0.2244	4.32862	0.04329	77.5409
0.2	4.51582	0.04516	73.0251
0.17825	4.58633	0.04586	68.4388
0.15887	4.5453	0.04545	63.8935
0.14159	4.401	0.04401	59.4925
0.12619	4.17364	0.04174	55.3188
0.11247	3.87383	0.03874	51.445
0.10024	3.53188	0.03532	47.9131
0.08934	3.16469	0.03165	44.7484
0.07962	2.79794	0.02798	41.9505
0.07096	2.45361	0.02454	39.4969
0.06325	2.14358	0.02144	37.3533
0.05637	1.88601	0.01886	35.4673
0.05024	1.67629	0.01676	33.791

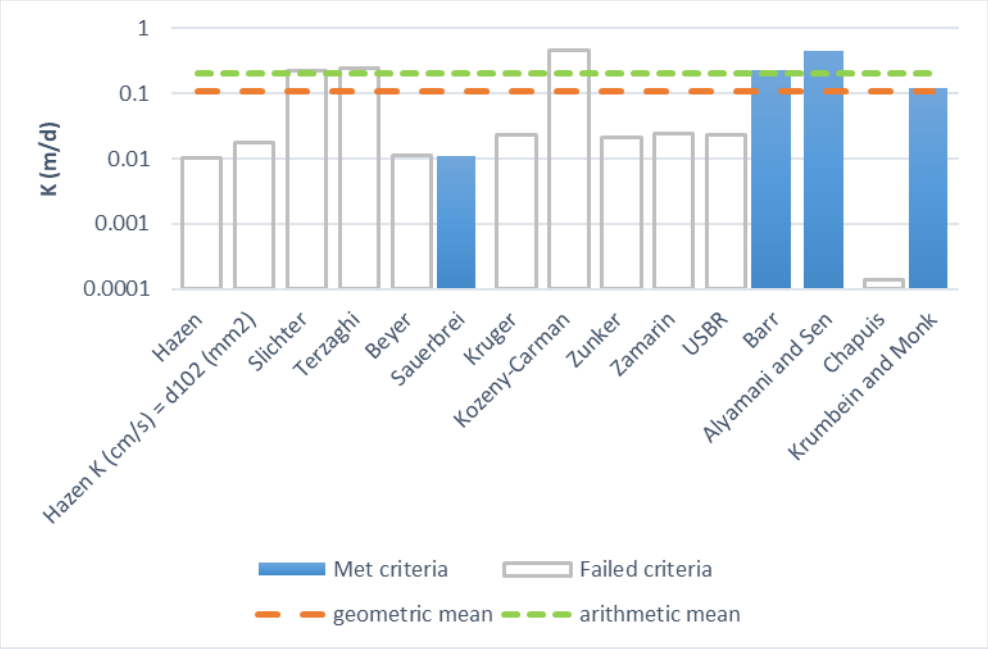
Effective Grain Diameters (mm)		Other Useful Parameters	
d10	0.005	Uniformity Coef.	31.52
d17	0.010	n computed	0.26
d20	0.014	g (cm/s^2)	980.00
d50	0.107	ρ (g/cm^3)	0.9981
d60	0.144	μ (g/cm s)	0.0098
de (Kruger)	0.012	ρg/μ (1/cm s)	9.9327E+04
de (Kozeny)	0.012	tau (Sauerbrei)	1.053
de (Zunker)	0.012	$d_{geometric\ mean}$	0.063
de (Zamarin)	0.012	σ_ϕ	2.345
Io (Alyameni	-0.021		

mm	0	% in sample
>64	Boulder	
16 - 64	coarse gravel	
8 - 16	medium gravel	
2 - 8	fine gravel	0.1
0.5 - 2	coarse sand	2.4
0.25 - 0.5	medium sand	15.63047381
0.063 - 0.25	fine sand	44.51622792
0.016 - 0.063	coarse silt	15.18720405
0.008 - 0.016	medium silt	6.49729243
0.002 - 0.008	fine silt	11.2158348
<0.002	clay	4.452966991

Slichter, Terzaghi, Kozeny-Carman and Barr with d_{VS}:



Slichter, Terzaghi, Kozeny-Carman and Barr with d_{UU}:

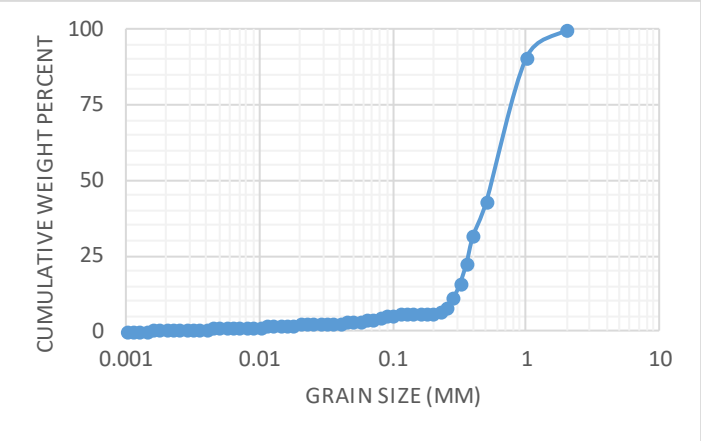


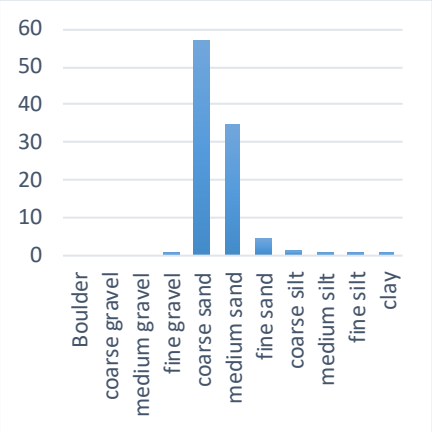
Well PB27-B. Elevation 54.710 m AHD.

Grain Size Analysis Report

Mass Sample (g): 100 T (oC) 20

Moderately well sorted sand low in fines





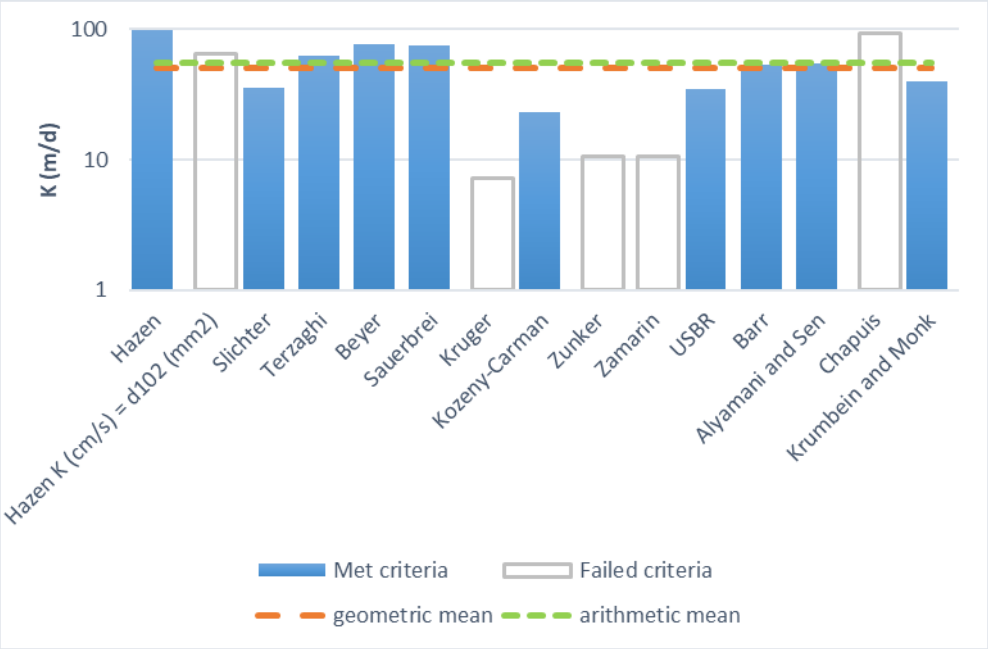
Sieve opening (ps) di (mm)	Mass of retained (mr) (g)	mass fraction (mf)	Percent Passing (pp)
2	0.4	0.004	99.6
1	9.3	0.093	90.3
0.5	47.6	0.476	42.7
0.39905	11.0541	0.11054	31.6459
0.35566	9.13266	0.09133	22.5133
0.31698	6.88597	0.06886	15.6273
0.28251	4.73994	0.0474	10.8873
0.25179	2.88164	0.02882	8.00571
0.2244	1.49719	0.01497	6.50851
0.2	0.59245	0.00592	5.91606
0.17825	0.11248	0.00112	5.80359
0.15887	0	0	5.80359
0.14159	0	0	5.80359
0.12619	0.00071	7.1E-06	5.80288
0.11247	0.09079	0.00091	5.71209
0.10024	0.25467	0.00255	5.45742
0.08934	0.39763	0.00398	5.0598
0.07962	0.46742	0.00467	4.59238
0.07096	0.47678	0.00477	4.11561
0.06325	0.43338	0.00433	3.68222
0.05637	0.35859	0.00359	3.32363
0.05024	0.2704	0.0027	3.05323

Effective Grain Diameters (mm)	
d10	0.273
d17	0.325
d20	0.342
d50	0.577
d60	0.682
de (Kruger)	0.127
de (Kozeny)	0.125
de (Zunker)	0.125
de (Zamarin)	0.126
Io (Alyameni	0.197

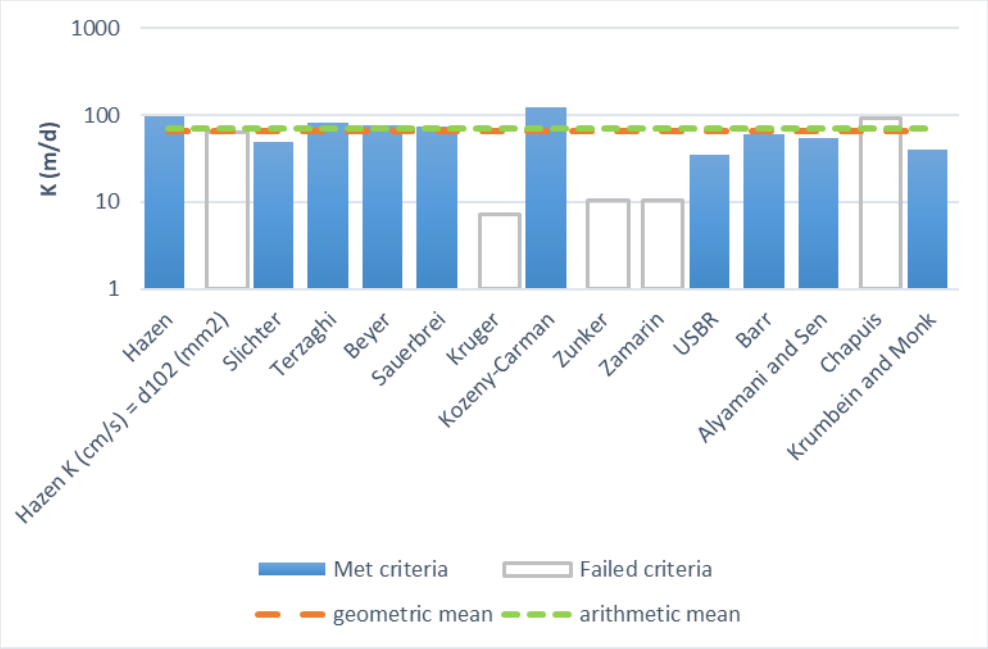
Other Useful Parameters	
Uniformity Coef.	2.50
n computed	0.42
g (cm/s^2)	980.00
ρ (g/cm^3)	0.9981
μ (g/cm s)	0.0098
ρg/μ (1/cm s)	9.9327E+04
tau (Sauerbrei)	1.053
$d_{geometric\ mean}$	0.483
σ_ϕ	1.008

mm	0	% in sample
>64	Boulder	
16 - 64	coarse gravel	
8 - 16	medium gravel	
2 - 8	fine gravel	0.4
0.5 - 2	coarse sand	56.9
0.25 - 0.5	medium sand	34.69429022
0.063 - 0.25	fine sand	4.323486557
0.016 - 0.063	coarse silt	1.56441481
0.008 - 0.016	medium silt	0.774623609
0.002 - 0.008	fine silt	0.983425976
<0.002	clay	0.359758828

Slichter, Terzaghi, Kozeny-Carman and Barr with d_{VS}:



Slichter, Terzaghi, Kozeny-Carman and Barr with d_{UU}:

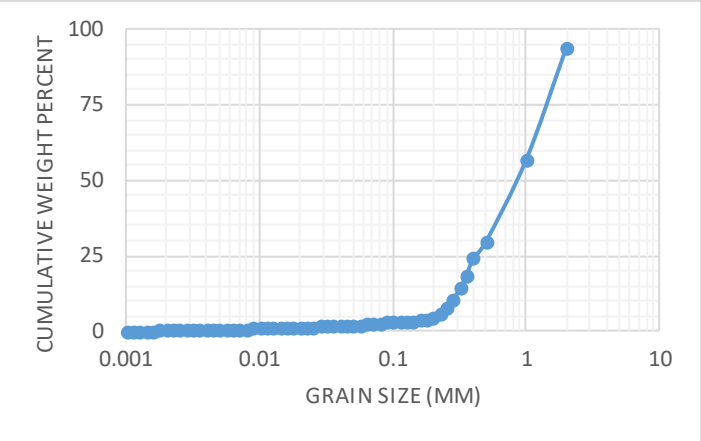


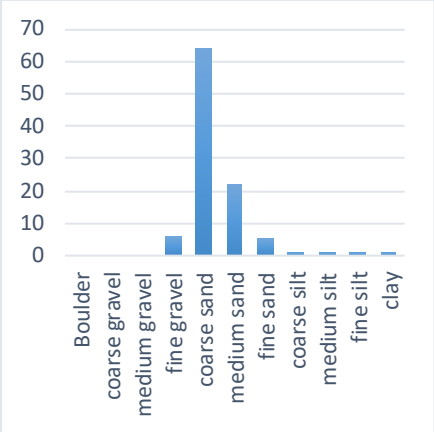
Well PB39-C. Elevation 54.601 m AHD.

Grain Size Analysis Report

Mass Sample (g): 100 T (oC) 20

Moderately well sorted sand low in fines





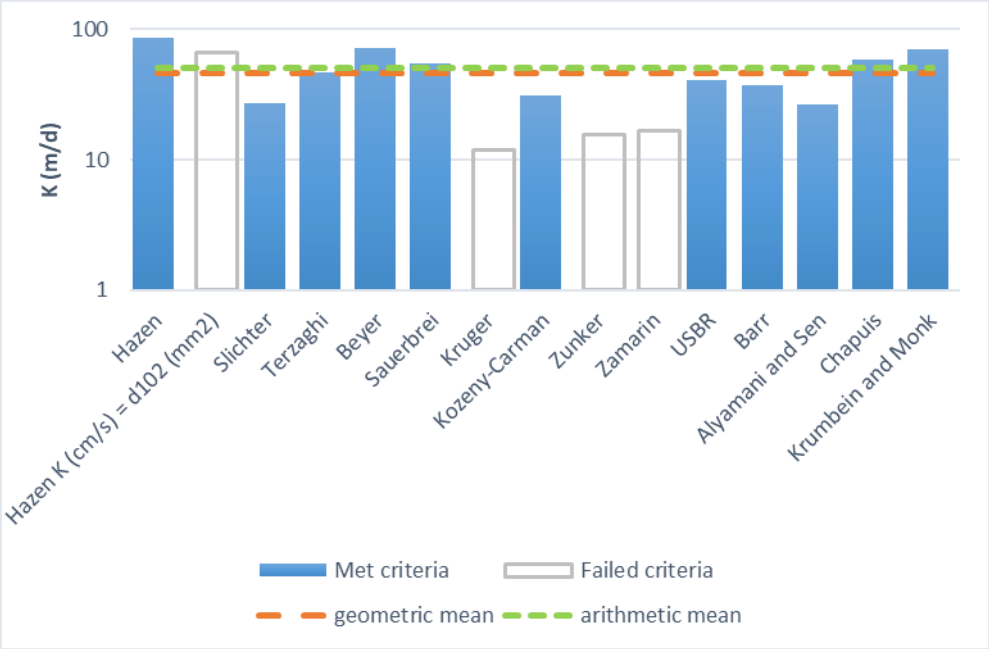
Sieve opening (ps) di (mm)	Mass of retained (mr) (g)	mass fraction (mf)	Percent Passing (pp)
2	5.9	0.059	94.1
1	37.1	0.371	57
0.5	27.1	0.271	29.9
0.39905	5.8891	0.05889	24.0109
0.35566	5.33437	0.05334	18.6765
0.31698	4.54126	0.04541	14.1353
0.28251	3.64797	0.03648	10.4873
0.25179	2.73439	0.02734	7.75291
0.2244	1.9074	0.01907	5.84551
0.2	1.21887	0.01219	4.62664
0.17825	0.70052	0.00701	3.92612
0.15887	0.35807	0.00358	3.56805
0.14159	0.16237	0.00162	3.40568
0.12619	0.08571	0.00086	3.31997
0.11247	0.08479	0.00085	3.23518
0.10024	0.12253	0.00123	3.11265
0.08934	0.16994	0.0017	2.9427
0.07962	0.20716	0.00207	2.73554
0.07096	0.22406	0.00224	2.51148
0.06325	0.21901	0.00219	2.29247
0.05637	0.19674	0.00197	2.09573
0.05024	0.16337	0.00163	1.93236

Effective Grain Diameters (mm)	
d10	0.277
d17	0.341
d20	0.366
d50	0.871
d60	1.081
de (Kruger)	0.181
de (Kozeny)	0.178
de (Zunker)	0.179
de (Zamarin)	0.180
Io (Alyameni	0.129

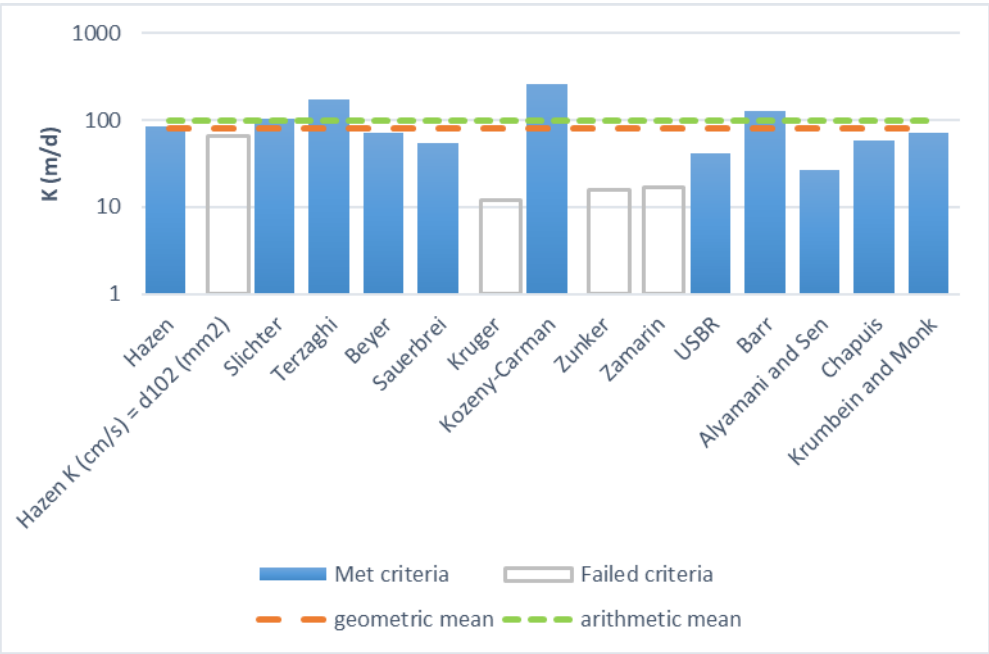
Other Useful Parameters	
Uniformity Coef.	3.90
n computed	0.38
g (cm/s^2)	980.00
ρ (g/cm^3)	0.9981
μ (g/cm s)	0.0098
ρg/μ (1/cm s)	9.9327E+04
tau (Sauerbrei)	1.053
$d_{geometric\ mean}$	0.677
σ_ϕ	1.091

mm	0	% in sample
>64	Boulder	
16 - 64	coarse gravel	
8 - 16	medium gravel	
2 - 8	fine gravel	5.9
0.5 - 2	coarse sand	64.2
0.25 - 0.5	medium sand	22.14708693
0.063 - 0.25	fine sand	5.460444568
0.016 - 0.063	coarse silt	0.992692552
0.008 - 0.016	medium silt	0.446221888
0.002 - 0.008	fine silt	0.58764976
<0.002	clay	0.265904304

Slichter, Terzaghi, Kozeny-Carman and Barr with d_{VS}:



Slichter, Terzaghi, Kozeny-Carman and Barr with d_{UU}:

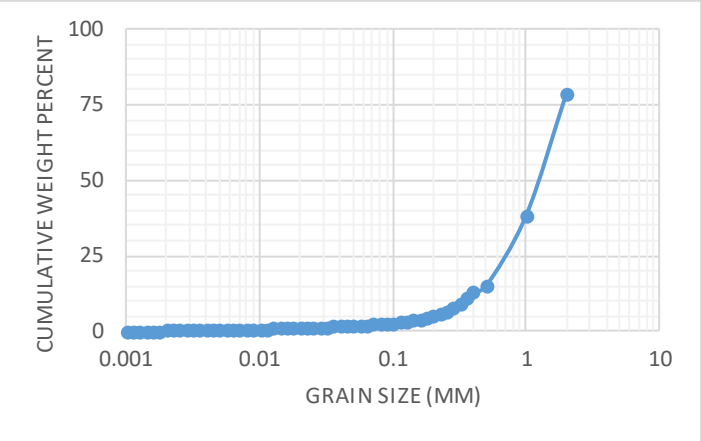


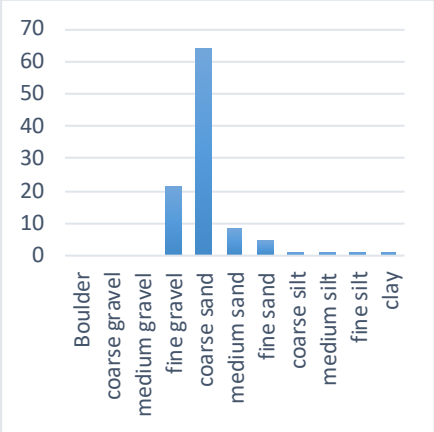
Well ML15. Elevation 54.207 m AHD.

Grain Size Analysis Report

Mass Sample (g): 100 T (oC) 20

Moderately well sorted gravelly sand low in fines



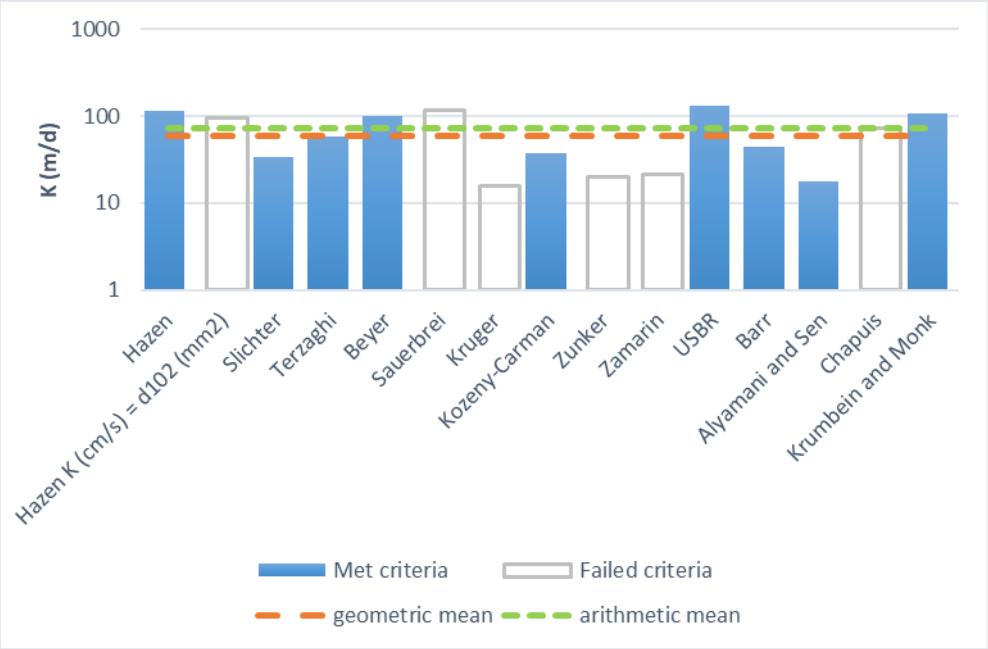


Sieve opening (ps) di (mm)	Mass of retained (mr) (g)	mass fraction (mf)	Percent Passing (pp)
2	21.4	0.214	78.6
1	40.2	0.402	38.4
0.5	23.4	0.234	15
0.39905	2.02316	0.02023	12.9768
0.35566	1.90891	0.01909	11.0679
0.31698	1.7174	0.01717	9.35054
0.28251	1.48328	0.01483	7.86726
0.25179	1.22818	0.01228	6.63908
0.2244	0.98216	0.00982	5.65692
0.2	0.76177	0.00762	4.89515
0.17825	0.57904	0.00579	4.31611
0.15887	0.44033	0.0044	3.87578
0.14159	0.34016	0.0034	3.53562
0.12619	0.27551	0.00276	3.26011
0.11247	0.23512	0.00235	3.02499
0.10024	0.21131	0.00211	2.81368
0.08934	0.1958	0.00196	2.61788
0.07962	0.18338	0.00183	2.4345
0.07096	0.17077	0.00171	2.26373
0.06325	0.15651	0.00157	2.10722
0.05637	0.14132	0.00141	1.9659
0.05024	0.12567	0.00126	1.84023

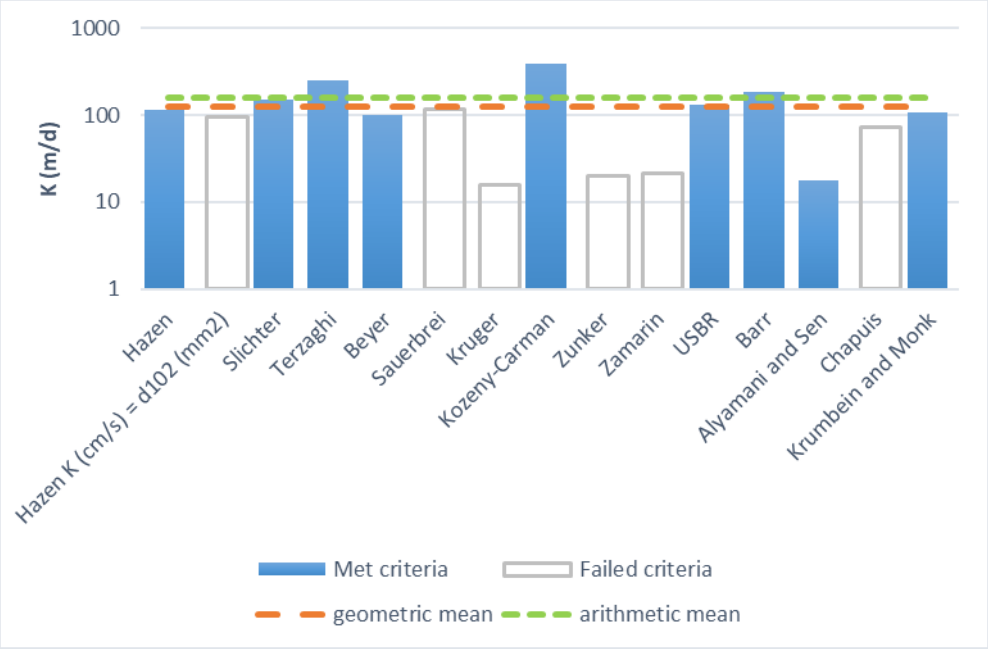
Effective Grain Diameters (mm)		Other Useful Parameters	
d10	0.332	Uniformity Coef.	4.64
d17	0.543	n computed	0.36
d20	0.607	g (cm/s^2)	980.00
d50	1.289	ρ (g/cm^3)	0.9981
d60	1.537	μ (g/cm s)	0.0098
de (Kruger)	0.217	ρg/μ (1/cm s)	9.9327E+04
de (Kozeny)	0.213	tau (Sauerbrei)	1.053
de (Zunker)	0.214	$d_{geometric\ mean}$	0.816
de (Zamarin)	0.215	σ_ϕ	1.050
Io (Alyameni	0.092		

mm	0	% in sample
>64	Boulder	
16 - 64	coarse gravel	
8 - 16	medium gravel	
2 - 8	fine gravel	21.4
0.5 - 2	coarse sand	63.6
0.25 - 0.5	medium sand	8.360922653
0.063 - 0.25	fine sand	4.531860982
0.016 - 0.063	coarse silt	1.033376154
0.008 - 0.016	medium silt	0.391867569
0.002 - 0.008	fine silt	0.483721767
<0.002	clay	0.198250874

Slichter, Terzaghi, Kozeny-Carman and Barr with d_{VS}:



Slichter, Terzaghi, Kozeny-Carman and Barr with d_{UU}:

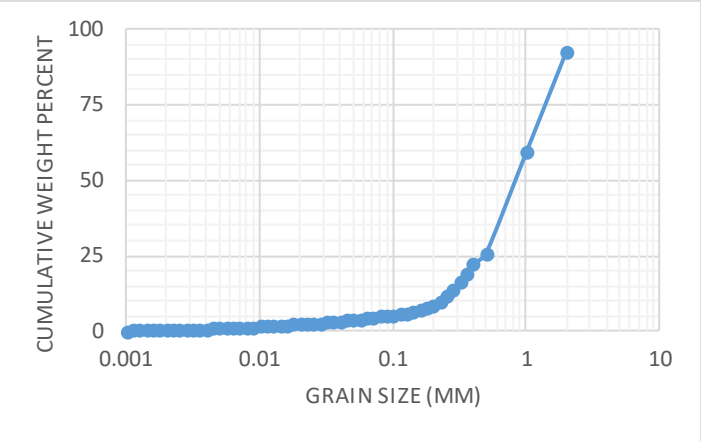


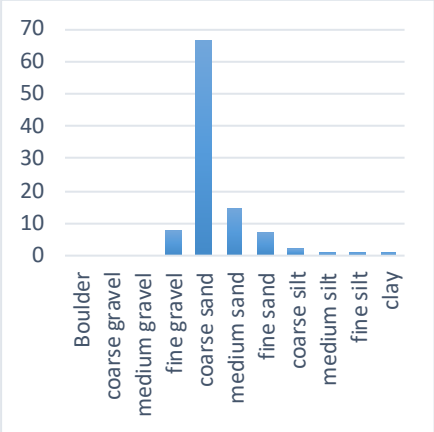
Well PB27-B. Elevation 54.160 m AHD.

Grain Size Analysis Report

Mass Sample (g): 100 T (oC) 20

Moderately well sorted sand low in fines





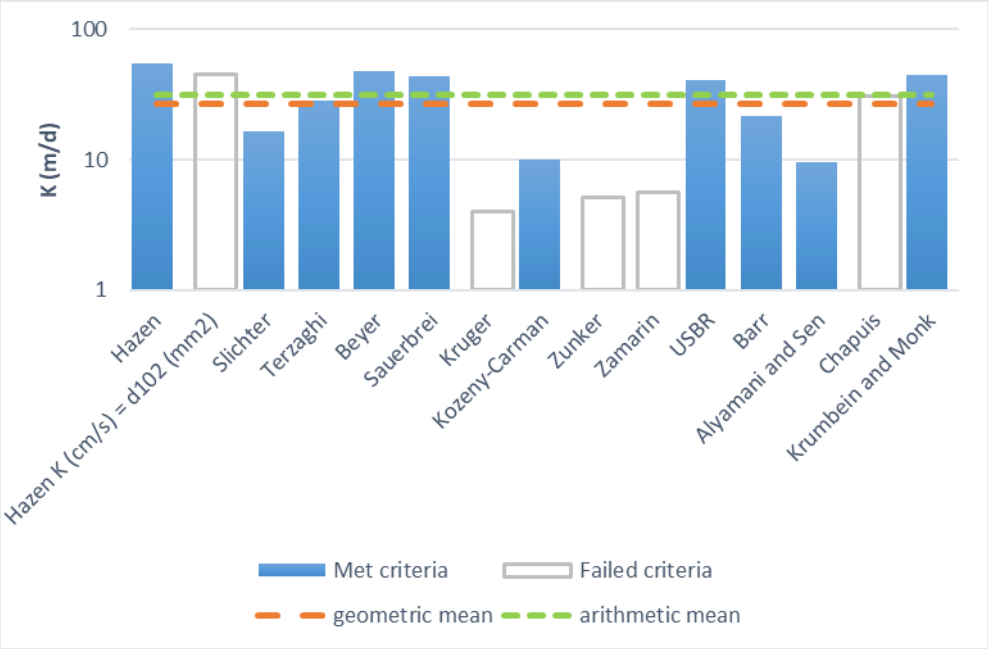
Sieve opening (ps) di (mm)	Mass of retained (mr) (g)	mass fraction (mf)	Percent Passing (pp)
2	7.6	0.076	92.4
1	33.3	0.333	59.1
0.5	33.2	0.332	25.9
0.39905	3.38112	0.03381	22.5189
0.35566	3.26383	0.03264	19.2551
0.31698	2.99012	0.0299	16.2649
0.28251	2.61249	0.02612	13.6524
0.25179	2.17131	0.02171	11.4811
0.2244	1.72427	0.01724	9.75687
0.2	1.30867	0.01309	8.4482
0.17825	0.9544	0.00954	7.4938
0.15887	0.68118	0.00681	6.81261
0.14159	0.48429	0.00484	6.32832
0.12619	0.36213	0.00362	5.96619
0.11247	0.29509	0.00295	5.67109
0.10024	0.26792	0.00268	5.40317
0.08934	0.26309	0.00263	5.14008
0.07962	0.26763	0.00268	4.87245
0.07096	0.27198	0.00272	4.60047
0.06325	0.27091	0.00271	4.32955
0.05637	0.26309	0.00263	4.06647
0.05024	0.24909	0.00249	3.81737

Effective Grain Diameters (mm)	
d10	0.228
d17	0.326
d20	0.366
d50	0.863
d60	1.027
de (Kruger)	0.109
de (Kozeny)	0.107
de (Zunker)	0.108
de (Zamarin)	0.108
Io (Alyameni	0.070

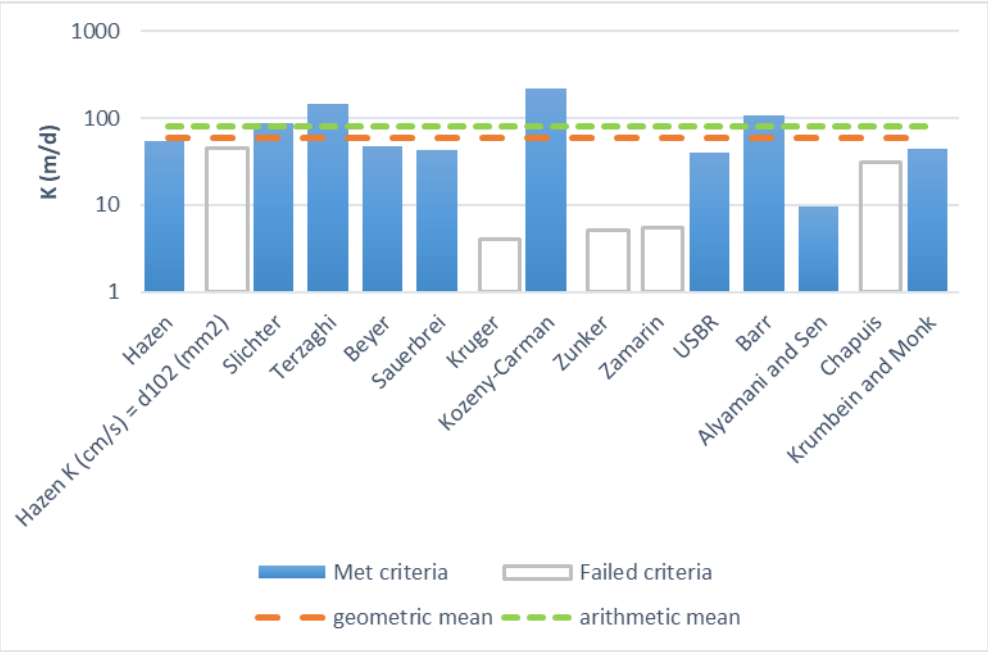
mm	0	% in sample
>64	Boulder	
16 - 64	coarse gravel	
8 - 16	medium gravel	
2 - 8	fine gravel	7.6
0.5 - 2	coarse sand	66.5
0.25 - 0.5	medium sand	14.41886376
0.063 - 0.25	fine sand	7.15158204
0.016 - 0.063	coarse silt	2.118578145
0.008 - 0.016	medium silt	0.760295267
0.002 - 0.008	fine silt	1.014368011
<0.002	clay	0.436312772

Other Useful Parameters	
Uniformity Coef.	4.50
n computed	0.37
g (cm/s^2)	980.00
ρ (g/cm^3)	0.9981
μ (g/cm s)	0.0098
ρg/μ (1/cm s)	9.9327E+04
tau (Sauerbrei)	1.053
$d_{geometric\ mean}$	0.626
σ_ϕ	1.318

Slichter, Terzaghi, Kozeny-Carman and Barr with d_{VS}:



Slichter, Terzaghi, Kozeny-Carman and Barr with d_{UU}:

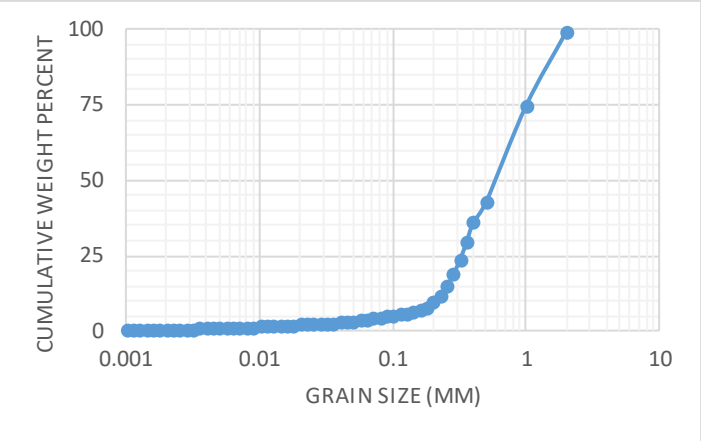


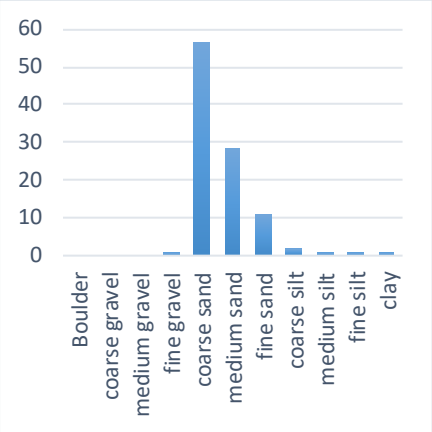
Well MP44-C. Elevation 53.960 m AHD.

Grain Size Analysis Report

Mass Sample (g): 100 T (oC) 20

Moderately well sorted sand low in fines



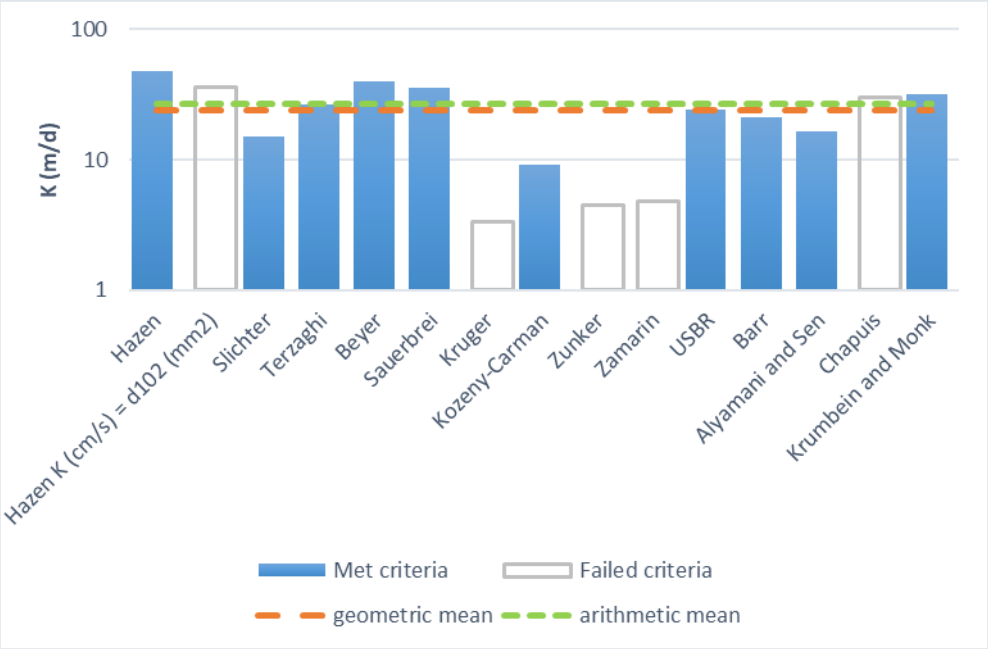


Sieve opening (ps) di (mm)	Mass of retained (mr) (g)	mass fraction (mf)	Percent Passing (pp)
2	0.7	0.007	99.3
1	24.4	0.244	74.9
0.5	32	0.32	42.9
0.39905	6.94683	0.06947	35.9532
0.35566	6.5142	0.06514	29.439
0.31698	5.79152	0.05792	23.6474
0.28251	4.90676	0.04907	18.7407
0.25179	3.94242	0.03942	14.7983
0.2244	3.0147	0.03015	11.7836
0.2	2.18938	0.02189	9.59418
0.17825	1.51468	0.01515	8.0795
0.15887	1.01591	0.01016	7.06359
0.14159	0.67343	0.00673	6.39017
0.12619	0.47363	0.00474	5.91654
0.11247	0.37334	0.00373	5.5432
0.10024	0.33879	0.00339	5.20442
0.08934	0.33613	0.00336	4.86828
0.07962	0.34165	0.00342	4.52663
0.07096	0.33984	0.0034	4.18679
0.06325	0.32394	0.00324	3.86284
0.05637	0.29507	0.00295	3.56778
0.05024	0.25649	0.00256	3.31129

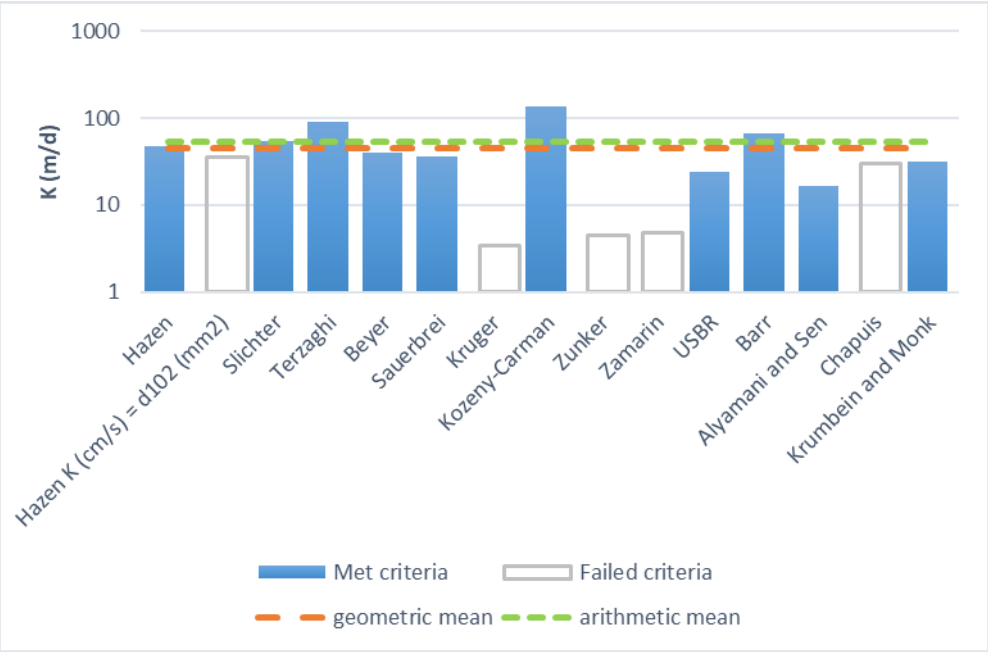
Effective Grain Diameters (mm)		Other Useful Parameters	
d10	0.205	Uniformity Coef.	3.75
d17	0.269	n computed	0.38
d20	0.291	g (cm/s^2)	980.00
d50	0.611	ρ (g/cm^3)	0.9981
d60	0.767	μ (g/cm s)	0.0098
de (Kruger)	0.095	ρg/μ (1/cm s)	9.9327E+04
de (Kozeny)	0.094	tau (Sauerbrei)	1.053
de (Zunker)	0.094	$d_{geometric\ mean}$	0.504
de (Zamarin)	0.095	σ_ϕ	1.248
Io (Alyameni	0.103		

mm	0	% in sample
>64	Boulder	
16 - 64	coarse gravel	
8 - 16	medium gravel	
2 - 8	fine gravel	0.7
0.5 - 2	coarse sand	56.4
0.25 - 0.5	medium sand	28.10173509
0.063 - 0.25	fine sand	10.93541995
0.016 - 0.063	coarse silt	1.767552332
0.008 - 0.016	medium silt	0.662229024
0.002 - 0.008	fine silt	0.84433965
<0.002	clay	0.588723949

Slichter, Terzaghi, Kozeny-Carman and Barr with d_{VS}:



Slichter, Terzaghi, Kozeny-Carman and Barr with d_{UU}:

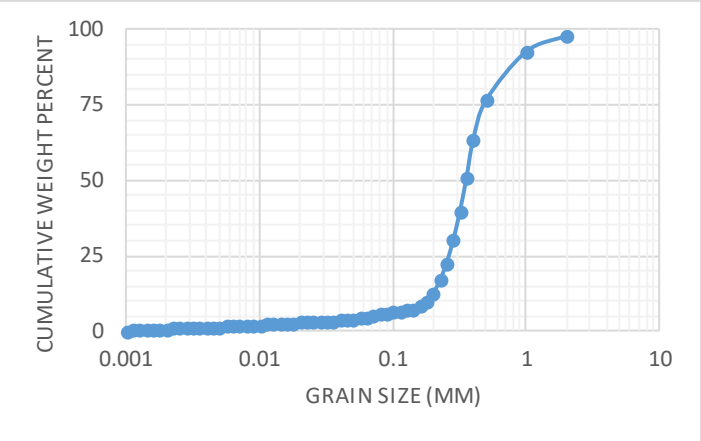


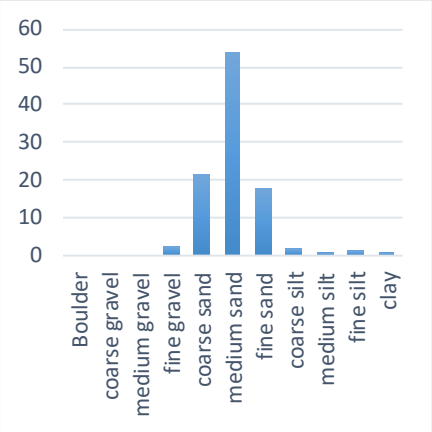
Well MP50-A. Elevation 53.886 m AHD.

Grain Size Analysis Report

Mass Sample (g): 100 T (oC) 20

Moderately well sorted sand low in fines



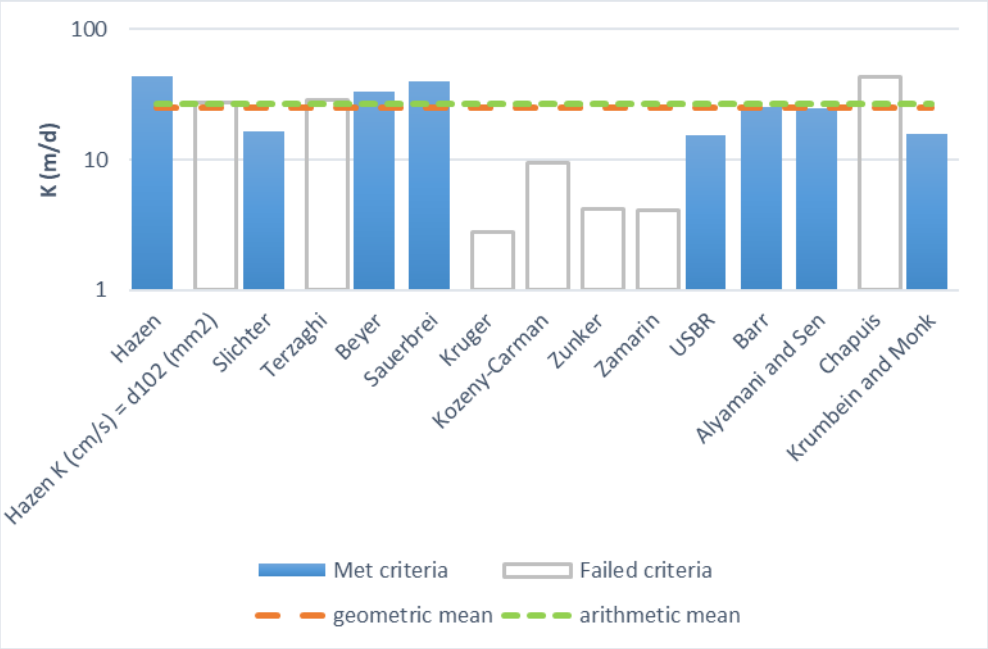


Sieve opening (ps) di (mm)	Mass of retained (mr) (g)	mass fraction (mf)	Percent Passing (pp)
2	2.5	0.025	97.5
1	5.2	0.052	92.3
0.5	16	0.16	76.3
0.39905	13.2118	0.13212	63.0882
0.35566	12.4732	0.12473	50.6151
0.31698	11.1396	0.1114	39.4754
0.28251	9.44911	0.09449	30.0263
0.25179	7.56501	0.07565	22.4613
0.2244	5.721	0.05721	16.7403
0.2	4.05665	0.04057	12.6836
0.17825	2.67857	0.02679	10.0051
0.15887	1.64904	0.01649	8.35604
0.14159	0.93759	0.00938	7.41845
0.12619	0.52472	0.00525	6.89373
0.11247	0.32731	0.00327	6.56641
0.10024	0.2779	0.00278	6.28851
0.08934	0.30598	0.00306	5.98254
0.07962	0.35928	0.00359	5.62326
0.07096	0.40104	0.00401	5.22222
0.06325	0.41313	0.00413	4.80909
0.05637	0.3927	0.00393	4.41638
0.05024	0.3452	0.00345	4.07118

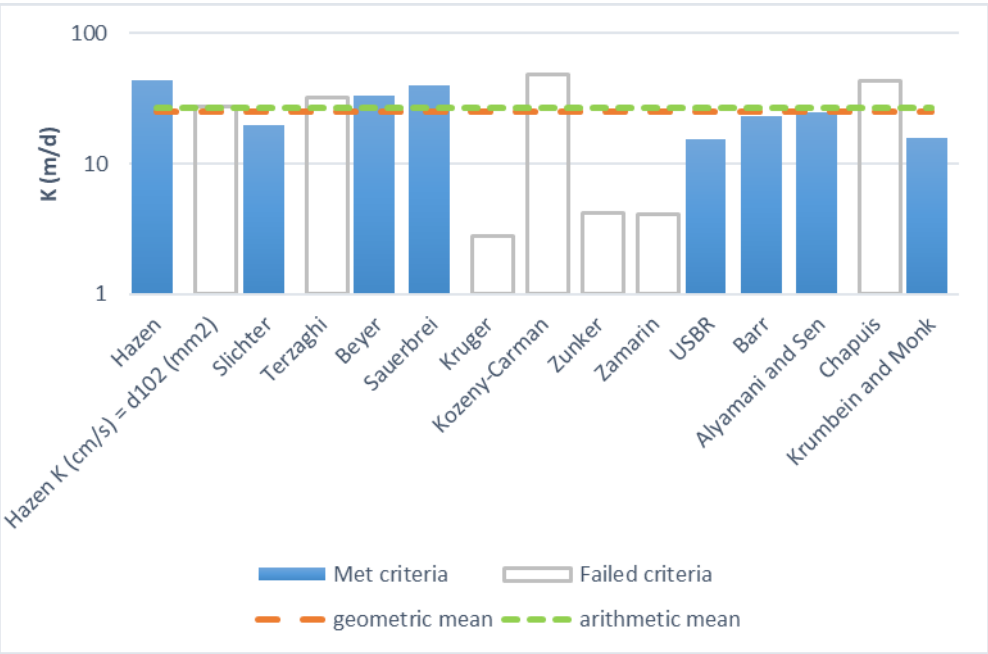
Effective Grain Diameters (mm)		Other Useful Parameters	
d10	0.178	Uniformity Coef.	2.18
d17	0.226	n computed	0.42
d20	0.240	g (cm/s^2)	980.00
d50	0.354	ρ (g/cm^3)	0.9981
d60	0.388	μ (g/cm s)	0.0098
de (Kruger)	0.076	ρg/μ (1/cm s)	9.9327E+04
de (Kozeny)	0.076	tau (Sauerbrei)	1.053
de (Zunker)	0.076	$d_{geometric\ mean}$	0.327
de (Zamarin)	0.076	σ_ϕ	1.121
Io (Alyameni	0.134		

mm	0	% in sample
>64	Boulder	
16 - 64	coarse gravel	
8 - 16	medium gravel	
2 - 8	fine gravel	2.5
0.5 - 2	coarse sand	21.2
0.25 - 0.5	medium sand	53.83870665
0.063 - 0.25	fine sand	17.65220547
0.016 - 0.063	coarse silt	1.982080152
0.008 - 0.016	medium silt	0.791544034
0.002 - 0.008	fine silt	1.258260146
<0.002	clay	0.777203545

Slichter, Terzaghi, Kozeny-Carman and Barr with d_{VS}:



Slichter, Terzaghi, Kozeny-Carman and Barr with d_{UU}:

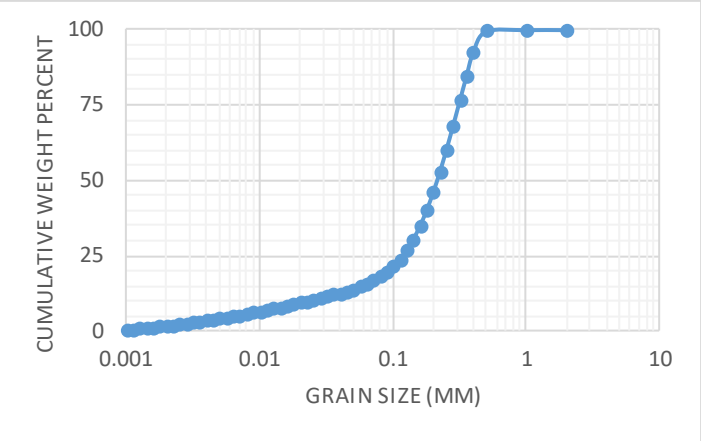


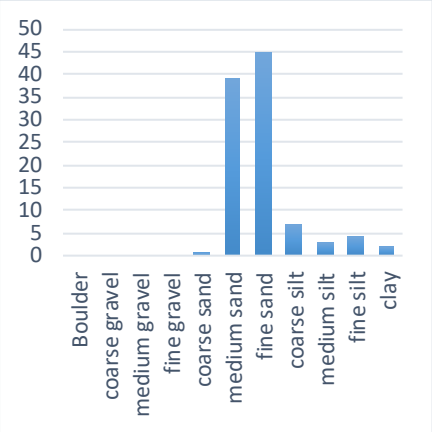
Well PB27-B. Elevation 53.160 m AHD.

Grain Size Analysis Report

Mass Sample (g): 100 T (oC) 20

Poorly sorted sand low in fines



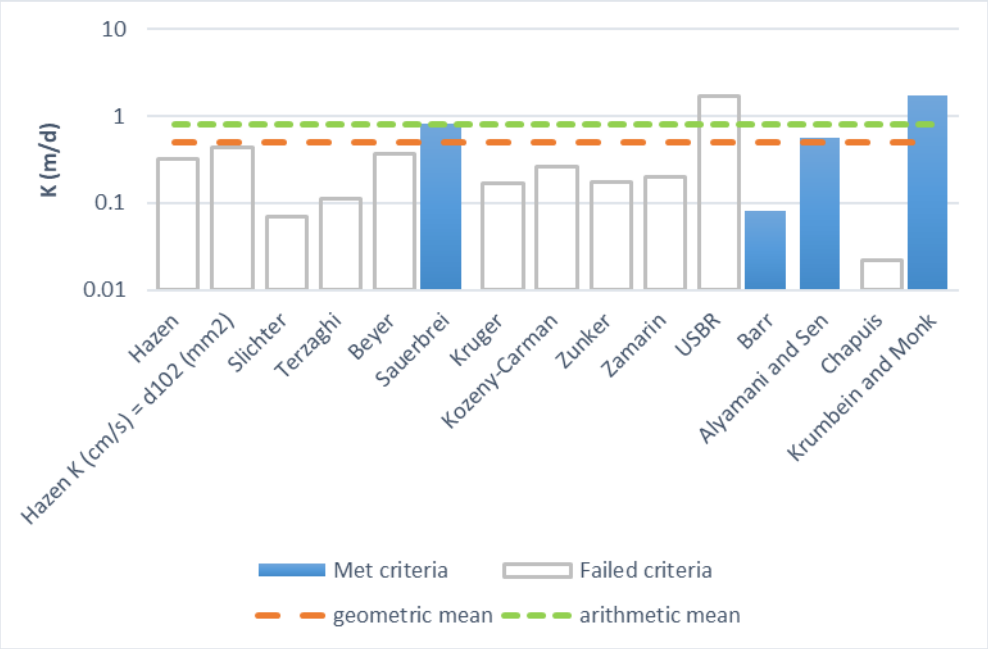


Sieve opening (ps) di (mm)	Mass of retained (mr) (g)	mass fraction (mf)	Percent Passing (pp)
2	0	0	100
1	0	0	100
0.5	0.5	0.005	99.5
0.39905	7.11335	0.07113	92.3867
0.35566	7.77186	0.07772	84.6148
0.31698	8.14194	0.08142	76.4729
0.28251	8.19262	0.08193	68.2802
0.25179	7.95024	0.0795	60.33
0.2244	7.46197	0.07462	52.868
0.2	6.78895	0.06789	46.0791
0.17825	5.99928	0.05999	40.0798
0.15887	5.177	0.05177	34.9028
0.14159	4.3591	0.04359	30.5437
0.12619	3.61689	0.03617	26.9268
0.11247	2.95099	0.02951	23.9758
0.10024	2.394	0.02394	21.5818
0.08934	1.93278	0.01933	19.649
0.07962	1.56523	0.01565	18.0838
0.07096	1.27968	0.0128	16.8041
0.06325	1.05918	0.01059	15.745
0.05637	0.89641	0.00896	14.8485
0.05024	0.77464	0.00775	14.0739

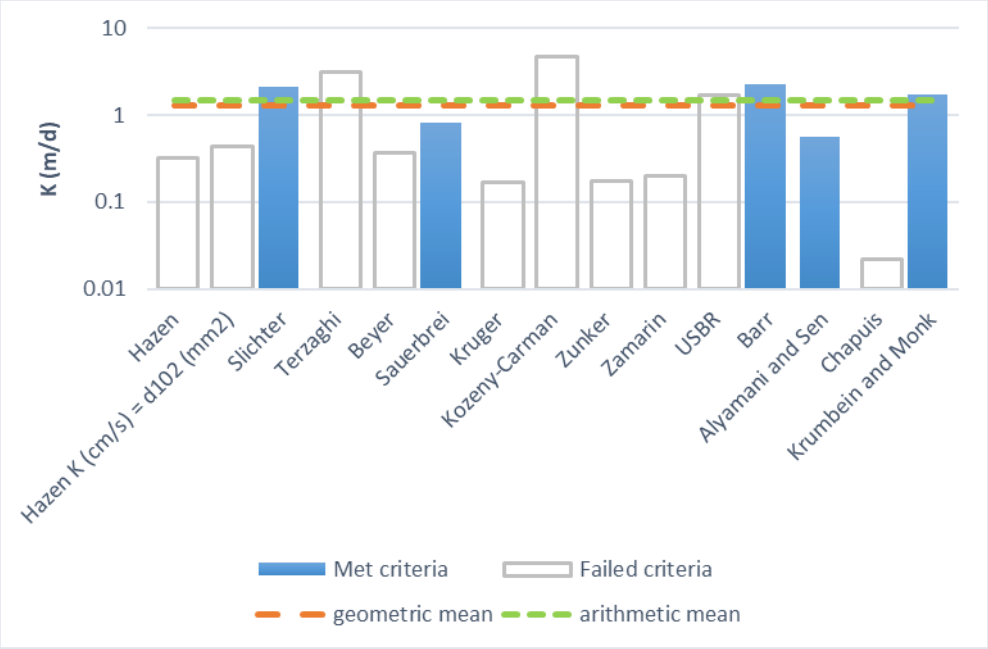
Effective Grain Diameters (mm)		Other Useful Parameters	
d10	0.022	Uniformity Coef.	11.19
d17	0.072	n computed	0.29
d20	0.091	g (cm/s^2)	980.00
d50	0.214	ρ (g/cm^3)	0.9981
d60	0.251	μ (g/cm s)	0.0098
de (Kruger)	0.028	ρg/μ (1/cm s)	9.9327E+04
de (Kozeny)	0.028	tau (Sauerbrei)	1.053
de (Zunker)	0.028	$d_{geometric\ mean}$	0.141
de (Zamarin)	0.028	σ_ϕ	1.532
Io (Alyameni	-0.026		

mm	0	% in sample
>64	Boulder	
16 - 64	coarse gravel	
8 - 16	medium gravel	
2 - 8	fine gravel	0
0.5 - 2	coarse sand	0.5
0.25 - 0.5	medium sand	39.17000243
0.063 - 0.25	fine sand	44.58504597
0.016 - 0.063	coarse silt	6.763142052
0.008 - 0.016	medium silt	2.827795867
0.002 - 0.008	fine silt	4.341089848
<0.002	clay	1.812923827

Slichter, Terzaghi, Kozeny-Carman and Barr with d_{VS}:



Slichter, Terzaghi, Kozeny-Carman and Barr with d_{UU}:



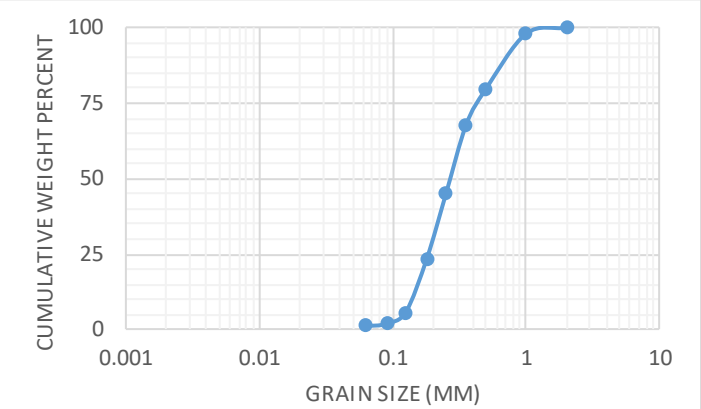
Particle-size data from the industrial site

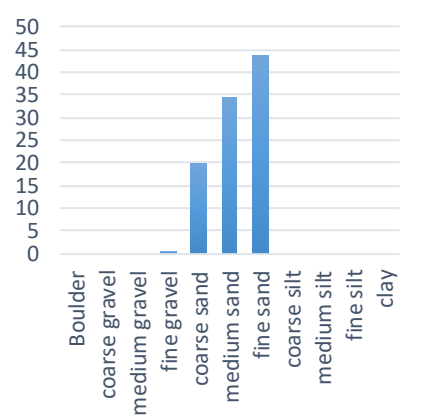
Well 040610/1-T4. Elevation 1.025 m AHD.

Grain Size Analysis Report

Mass Sample (g): 100 T (oC) 20

Moderately well sorted sand low in fines



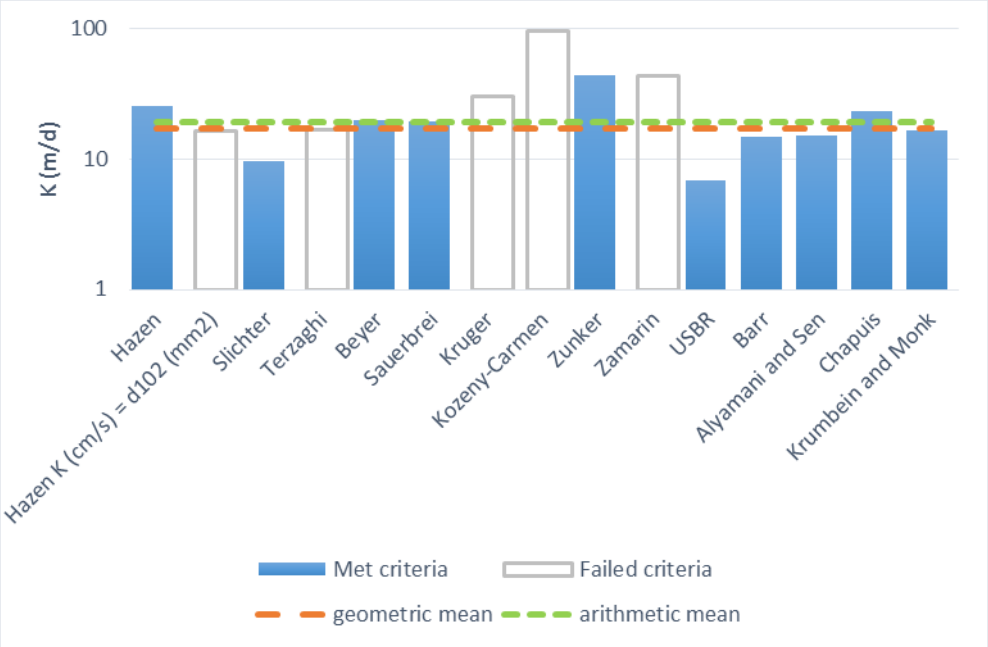


Sieve opening (ps) di (mm)	Mass of retained (mr) (g)	mass fraction (mf)	Percent Passing (pp)
2	0.0545	0.00054	99.9455
1	1.92098	0.01921	98.0245
0.5	18.2698	0.1827	79.7548
0.355	11.8529	0.11853	67.9019
0.25	22.9428	0.22943	44.9591
0.18	21.3351	0.21335	23.624
0.125	17.8474	0.17847	5.77657
0.09	3.85559	0.03856	1.92098
0.063	0.70845	0.00708	1.21253

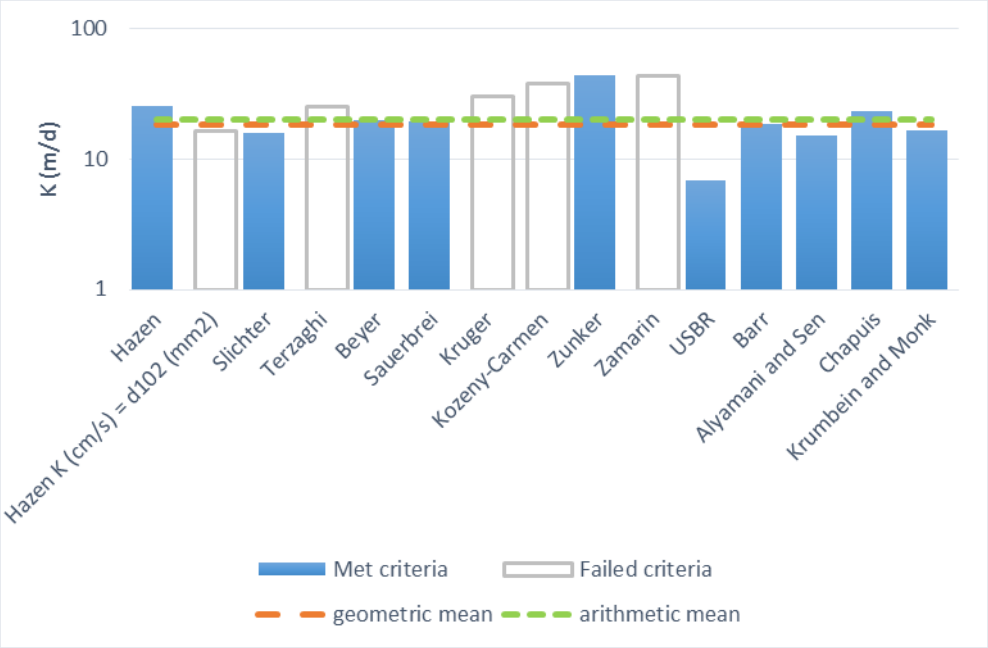
Effective Grain Diameters (mm)		Other Useful Parameters	
d10	0.138	Uniformity Coef.	2.31
d17	0.160	n computed	0.42
d20	0.169	g (cm/s^2)	980.00
d50	0.273	ρ (g/cm^3)	0.9981
d60	0.319	μ (g/cm s)	0.0098
de (Kruger)	0.256	ρg/μ (1/cm s)	9.9327E+04
de (Kozeny)	0.247	tau (Sauerbrei)	1.053
de (Zunker)	0.250	$d_{geometric\ mean}$	0.298
de (Zamarin)	0.253	σ_ϕ	0.943
Io (Alyameni	0.104		

mm	0	% in sample
>64	Boulder	
16 - 64	coarse gravel	
8 - 16	medium gravel	
2 - 8	fine gravel	0.054495913
0.5 - 2	coarse sand	20.19073569
0.25 - 0.5	medium sand	34.79564033
0.063 - 0.25	fine sand	43.74659401
0.016 - 0.063	coarse silt	
0.008 - 0.016	medium silt	
0.002 - 0.008	fine silt	
<0.002	clay	

Slichter, Terzaghi, Kozeny-Carman and Barr with d_{VS}:



Slichter, Terzaghi, Kozeny-Carman and Barr with d_{UU}:

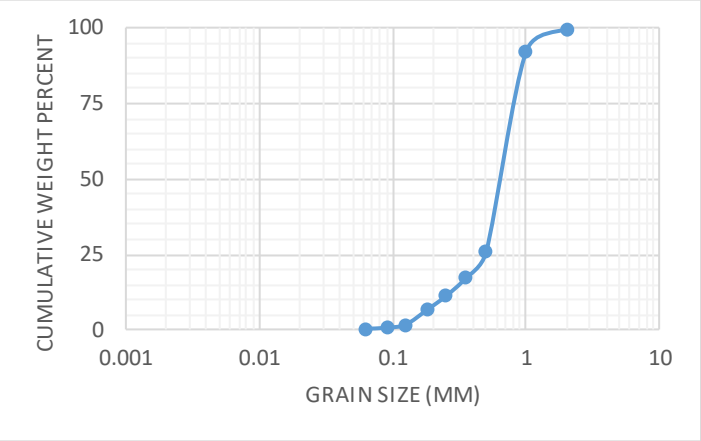


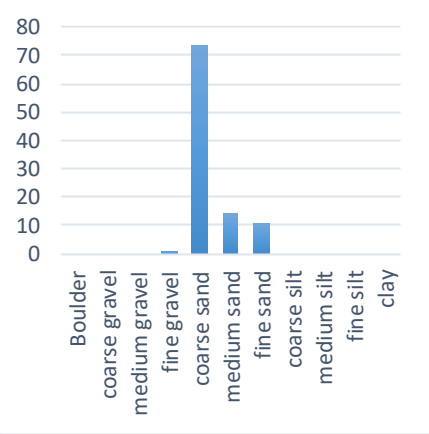
Well 040610/1-T4. Elevation 0.975 m AHD.

Grain Size Analysis Report

Mass Sample (g): 100 T (oC) 20

Moderately well sorted sand low in fines



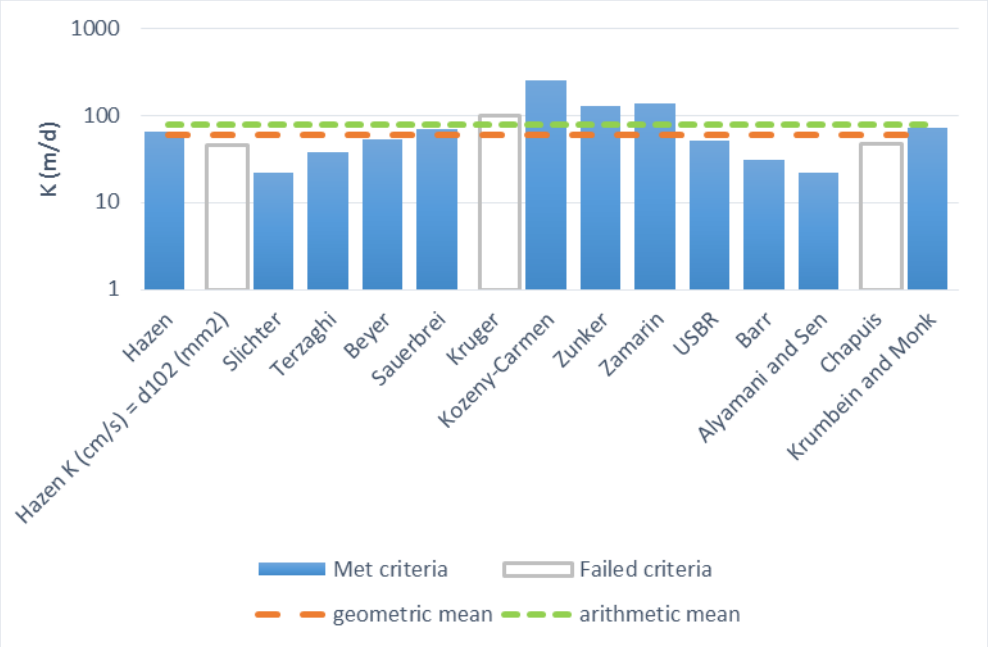


Sieve opening (ps) di (mm)	Mass of retained (mr) (g)	mass fraction (mf)	Percent Passing (pp)
2	0.26034	0.0026	99.7397
1	7.53446	0.07534	92.2052
0.5	66.4855	0.66485	25.7198
0.355	8.42266	0.08423	17.2971
0.25	6.07963	0.0608	11.2175
0.18	4.60949	0.04609	6.60796
0.125	4.80858	0.04809	1.79939
0.09	1.07963	0.0108	0.71975
0.063	0.26034	0.0026	0.45942

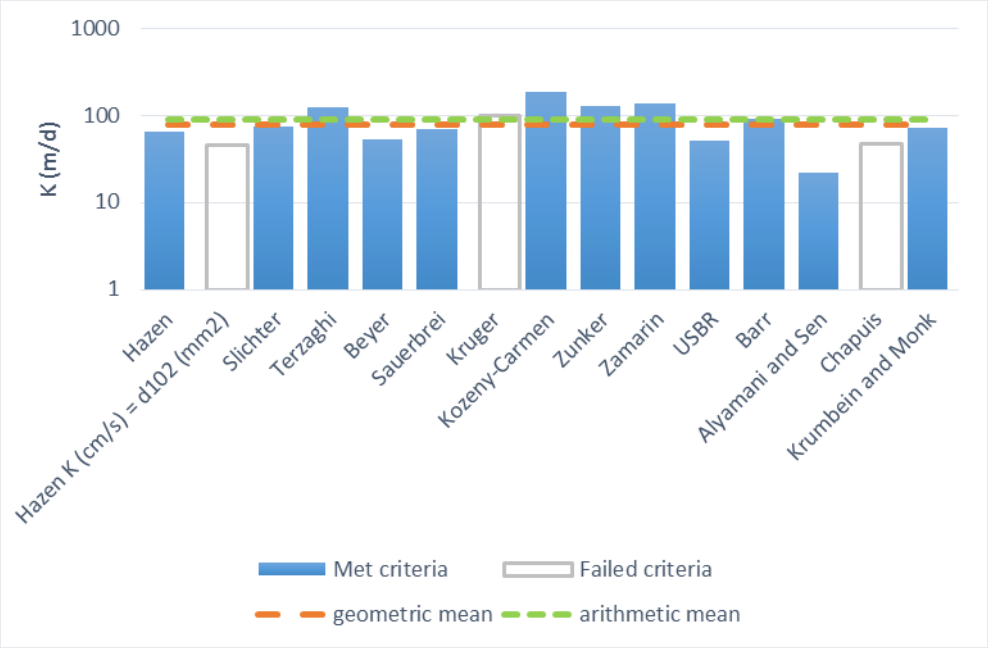
Effective Grain Diameters (mm)		Other Useful Parameters	
d10	0.232	Uniformity Coef.	3.27
d17	0.350	n computed	0.39
d20	0.402	g (cm/s^2)	980.00
d50	0.683	ρ (g/cm^3)	0.9981
d60	0.758	μ (g/cm s)	0.0098
de (Kruger)	0.500	ρg/μ (1/cm s)	9.9327E+04
de (Kozeny)	0.465	tau (Sauerbrei)	1.053
de (Zunker)	0.477	$d_{geometric\ mean}$	0.580
de (Zamarin)	0.489	σ_ϕ	0.841
Io (Alyameni	0.119		

mm	0	% in sample
>64	Boulder	
16 - 64	coarse gravel	
8 - 16	medium gravel	
2 - 8	fine gravel	0.260336907
0.5 - 2	coarse sand	74.01990812
0.25 - 0.5	medium sand	14.50229709
0.063 - 0.25	fine sand	10.75803982
0.016 - 0.063	coarse silt	
0.008 - 0.016	medium silt	
0.002 - 0.008	fine silt	
<0.002	clay	

Slichter, Terzaghi, Kozeny-Carman and Barr with d_{VS}:



Slichter, Terzaghi, Kozeny-Carman and Barr with d_{UU}:

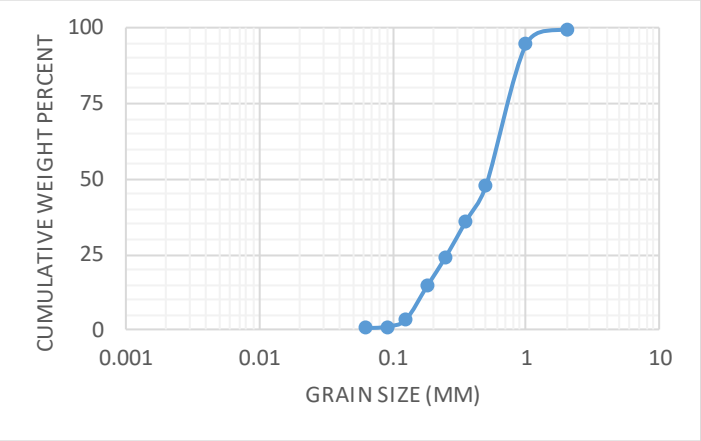


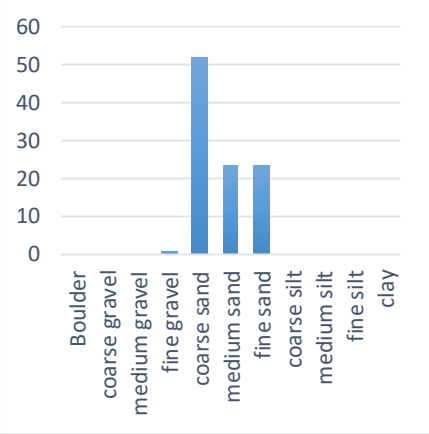
Well 040610/1-T4. Elevation 0.925 m AHD.

Grain Size Analysis Report

Mass Sample (g): 100 T (oC) 20

Moderately well sorted sand low in fines



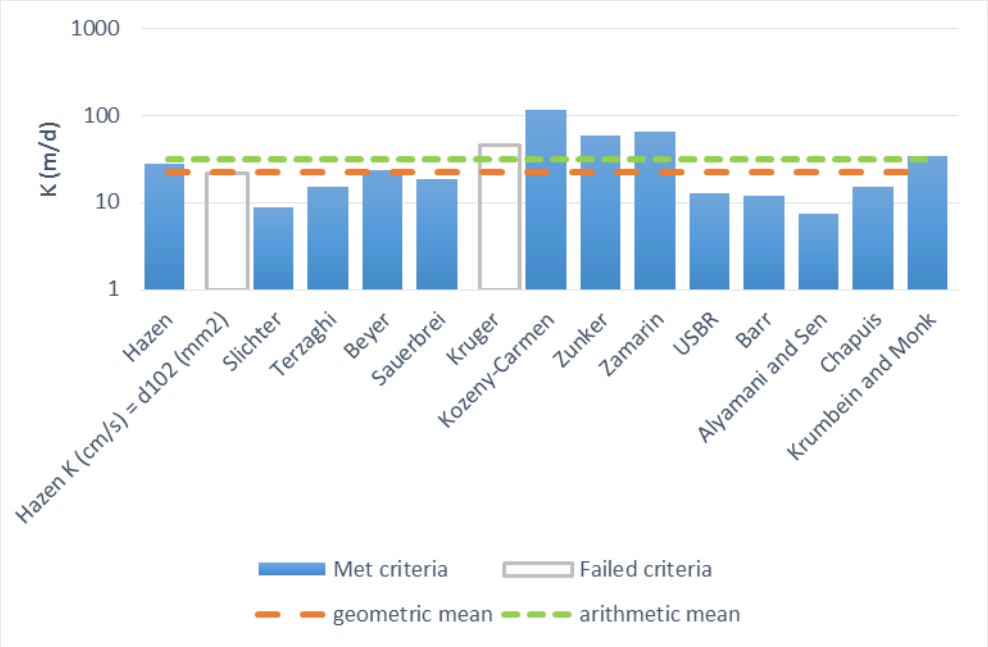


Sieve opening (ps) di (mm)	Mass of retained (mr) (g)	mass fraction (mf)	Percent Passing (pp)
2	0.23705	0.00237	99.7629
1	5.17998	0.0518	94.583
0.5	46.7779	0.46778	47.8051
0.355	11.5716	0.11572	36.2335
0.25	11.9403	0.1194	24.2932
0.18	9.85075	0.09851	14.4425
0.125	11.0272	0.11027	3.41528
0.09	2.34416	0.02344	1.07112
0.063	0.45654	0.00457	0.61457

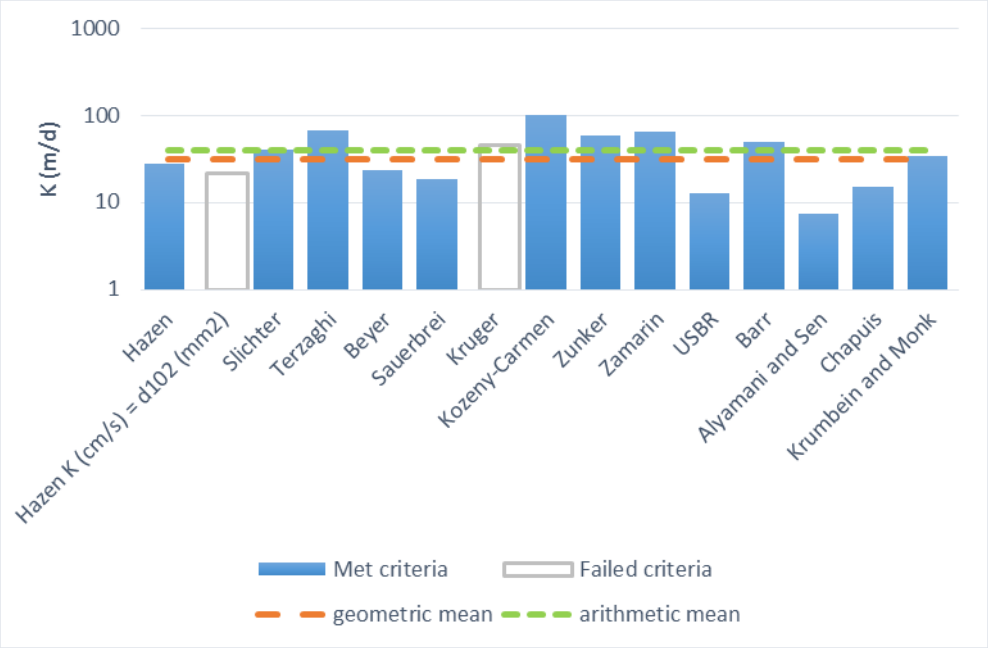
Effective Grain Diameters (mm)		Other Useful Parameters	
d10	0.158	Uniformity Coef.	3.99
d17	0.198	n computed	0.38
d20	0.219	g (cm/s^2)	980.00
d50	0.523	ρ (g/cm^3)	0.9981
d60	0.630	μ (g/cm s)	0.0098
de (Kruger)	0.359	ρg/μ (1/cm s)	9.9327E+04
de (Kozeny)	0.341	tau (Sauerbrei)	1.053
de (Zunker)	0.347	$d_{geometric\ mean}$	0.443
de (Zamarin)	0.353	σ_ϕ	1.012
Io (Alyameni	0.066		

mm	0	% in sample
>64	Boulder	
16 - 64	coarse gravel	
8 - 16	medium gravel	
2 - 8	fine gravel	0.237050044
0.5 - 2	coarse sand	51.95785777
0.25 - 0.5	medium sand	23.5118525
0.063 - 0.25	fine sand	23.6786655
0.016 - 0.063	coarse silt	
0.008 - 0.016	medium silt	
0.002 - 0.008	fine silt	
<0.002	clay	

Slichter, Terzaghi, Kozeny-Carman and Barr with d_{VS}:



Slichter, Terzaghi, Kozeny-Carman and Barr with d_{UU}:

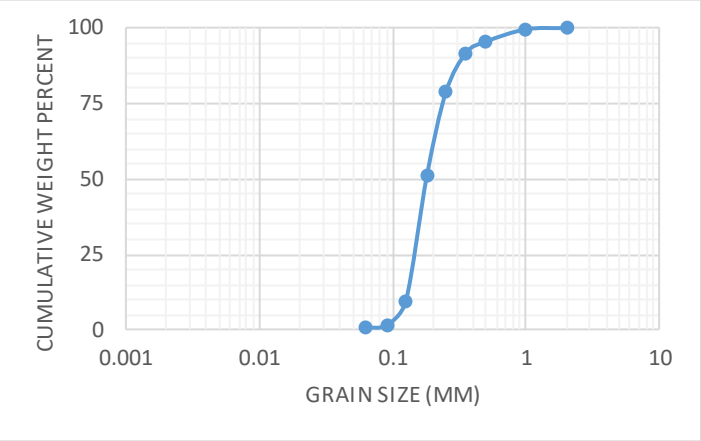


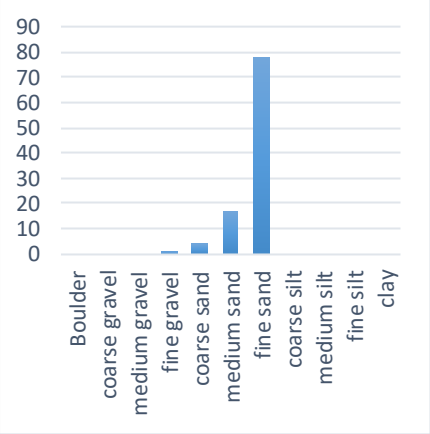
Well 040610/1-T4. Elevation 0.875 m AHD.

Grain Size Analysis Report

Mass Sample (g): 100 T (oC) 20

Uniform sand low in fines



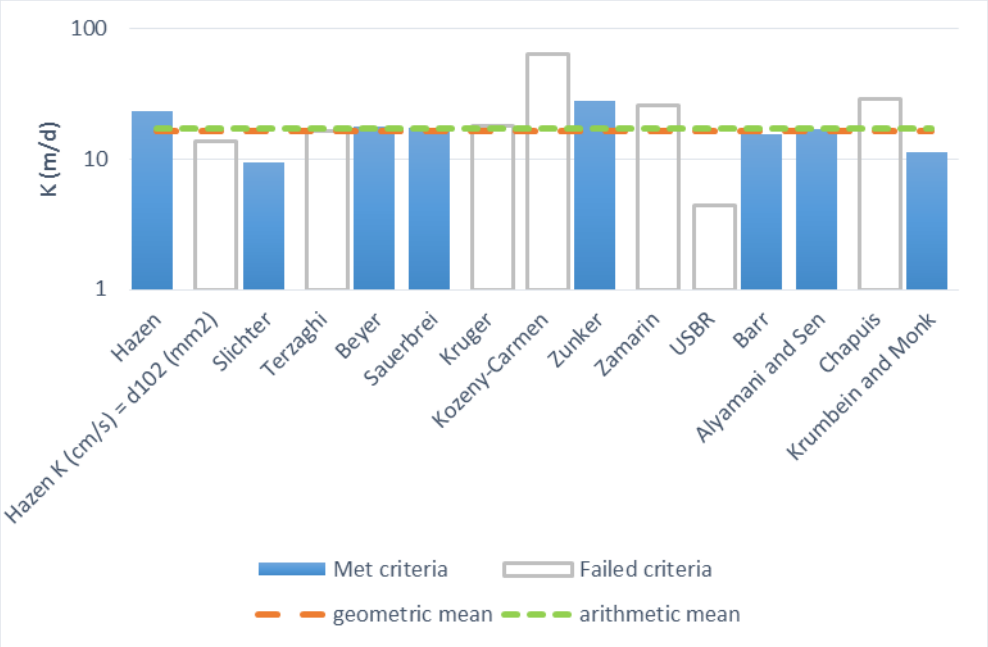


Sieve opening (ps) di (mm)	Mass of retained (mr) (g)	mass fraction (mf)	Percent Passing (pp)
2	0.01972	0.0002	99.9803
1	0.40418	0.00404	99.5761
0.5	4.07137	0.04071	95.5047
0.355	3.72634	0.03726	91.7784
0.25	13.0323	0.13032	78.7461
0.18	27.6025	0.27603	51.1435
0.125	41.6009	0.41601	9.54259
0.09	7.95544	0.07955	1.58715
0.063	0.76893	0.00769	0.81822

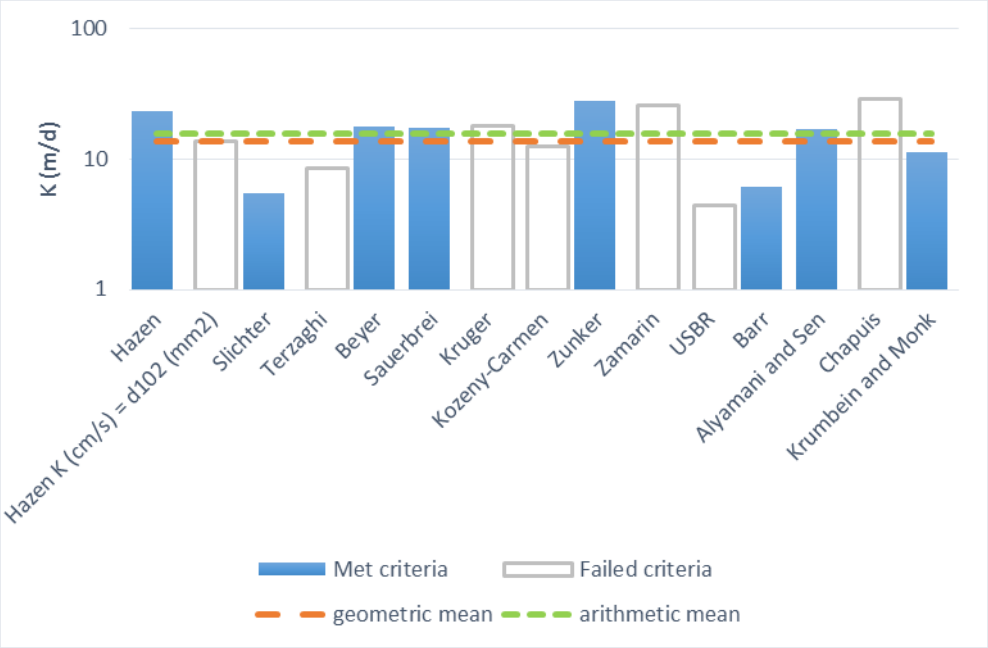
Effective Grain Diameters (mm)		Other Useful Parameters	
d10	0.126	Uniformity Coef.	1.61
d17	0.135	n computed	0.44
d20	0.139	g (cm/s^2)	980.00
d50	0.178	ρ (g/cm^3)	0.9981
d60	0.202	μ (g/cm s)	0.0098
de (Kruger)	0.184	ρg/μ (1/cm s)	9.9327E+04
de (Kozeny)	0.179	tau (Sauerbrei)	1.053
de (Zunker)	0.180	$d_{geometric\ mean}$	0.198
de (Zamarin)	0.182	σ_ϕ	0.615
Io (Alyameni	0.112		

mm	0	% in sample
>64	Boulder	
16 - 64	coarse gravel	
8 - 16	medium gravel	
2 - 8	fine gravel	0.019716088
0.5 - 2	coarse sand	4.47555205
0.25 - 0.5	medium sand	16.75867508
0.063 - 0.25	fine sand	77.92783912
0.016 - 0.063	coarse silt	
0.008 - 0.016	medium silt	
0.002 - 0.008	fine silt	
<0.002	clay	

Slichter, Terzaghi, Kozeny-Carman and Barr with d_{VS}:



Slichter, Terzaghi, Kozeny-Carman and Barr with d_{UU}:

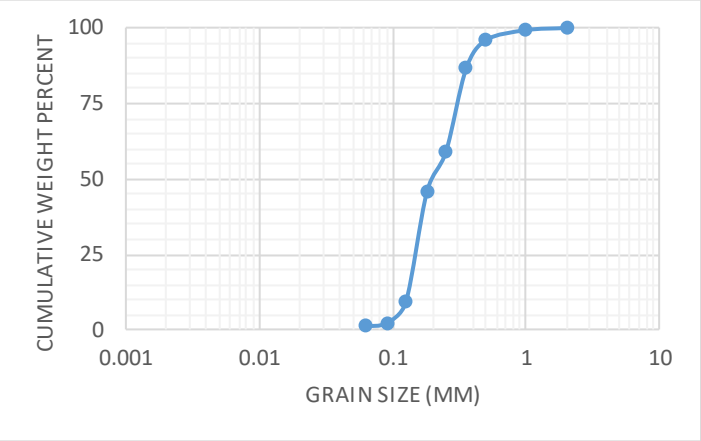


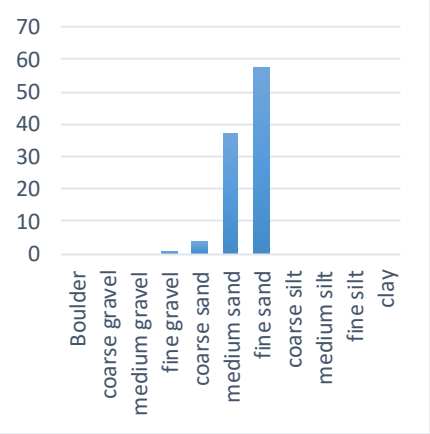
Well 040610/1-T4. Elevation 0.825 m AHD.

Grain Size Analysis Report

Mass Sample (g): 100 T (oC) 20

Moderately well sorted sand low in fines



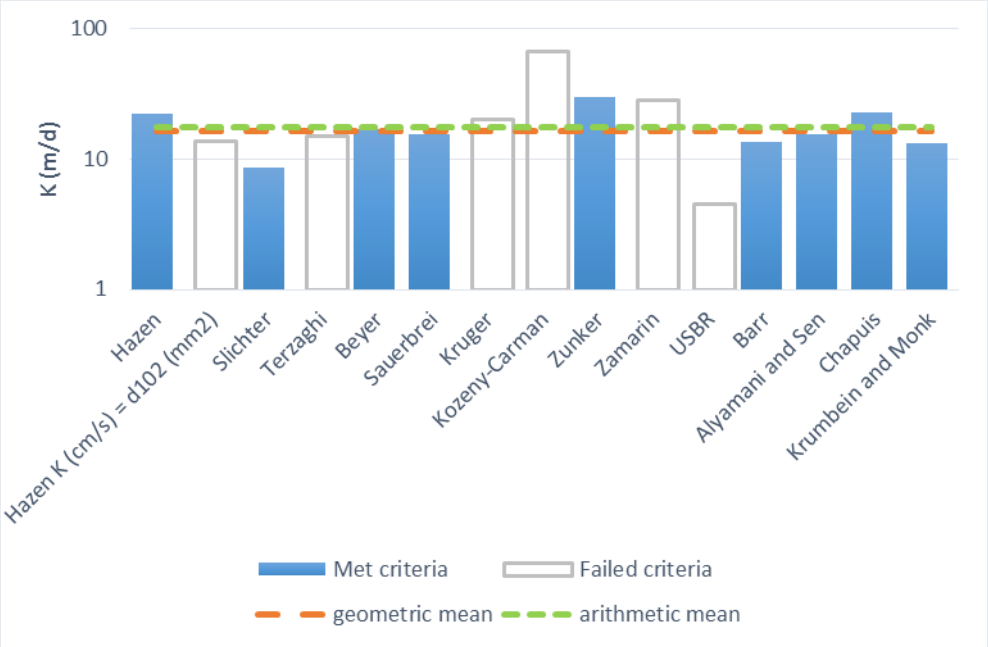


Sieve opening (ps) di (mm)	Mass of retained (mr) (g)	mass fraction (mf)	Percent Passing (pp)
2	0.01071	0.00011	99.9893
1	0.69623	0.00696	99.2931
0.5	3.28835	0.03288	96.0047
0.355	9.38303	0.09383	86.6217
0.25	27.6671	0.27667	58.9546
0.18	13.2498	0.1325	45.7048
0.125	36.5467	0.36547	9.1581
0.09	6.87661	0.06877	2.28149
0.063	1.03899	0.01039	1.2425

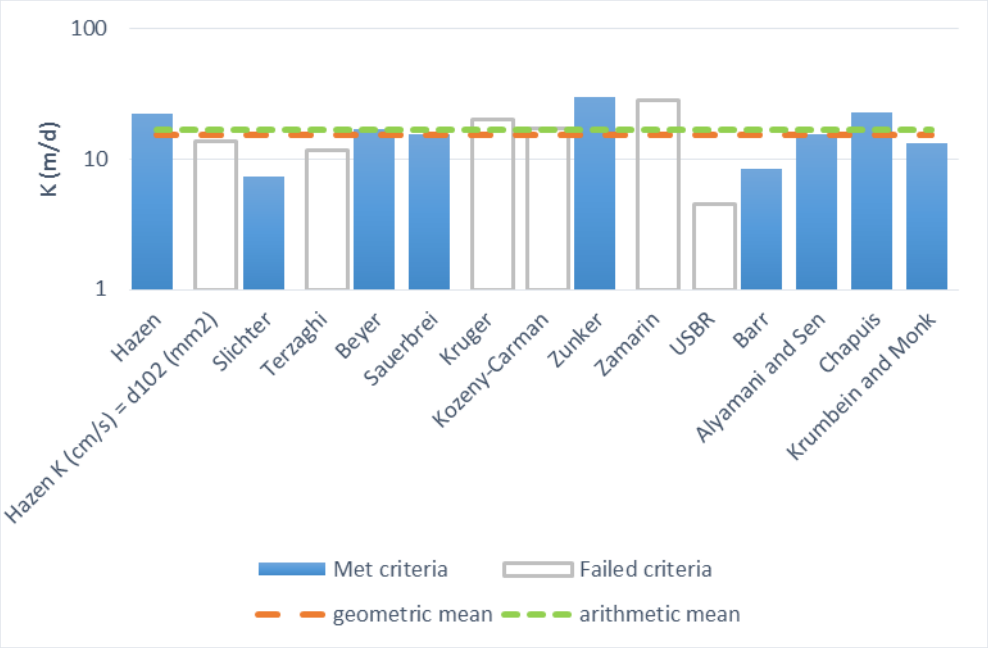
Effective Grain Diameters (mm)		Other Useful Parameters	
d10	0.126	Uniformity Coef.	2.01
d17	0.137	n computed	0.43
d20	0.141	g (cm/s^2)	980.00
d50	0.203	ρ (g/cm^3)	0.9981
d60	0.254	μ (g/cm s)	0.0098
de (Kruger)	0.201	ρg/μ (1/cm s)	9.9327E+04
de (Kozeny)	0.195	tau (Sauerbrei)	1.053
de (Zunker)	0.197	$d_{geometric\ mean}$	0.222
de (Zamarin)	0.199	σ_ϕ	0.674
Io (Alyameni	0.107		

mm	0	% in sample
>64	Boulder	
16 - 64	coarse gravel	
8 - 16	medium gravel	
2 - 8	fine gravel	0.010711225
0.5 - 2	coarse sand	3.984575835
0.25 - 0.5	medium sand	37.05012853
0.063 - 0.25	fine sand	57.71208226
0.016 - 0.063	coarse silt	
0.008 - 0.016	medium silt	
0.002 - 0.008	fine silt	
<0.002	clay	

Slichter, Terzaghi, Kozeny-Carman and Barr with d_{VS}:



Slichter, Terzaghi, Kozeny-Carman and Barr with d_{UU}:

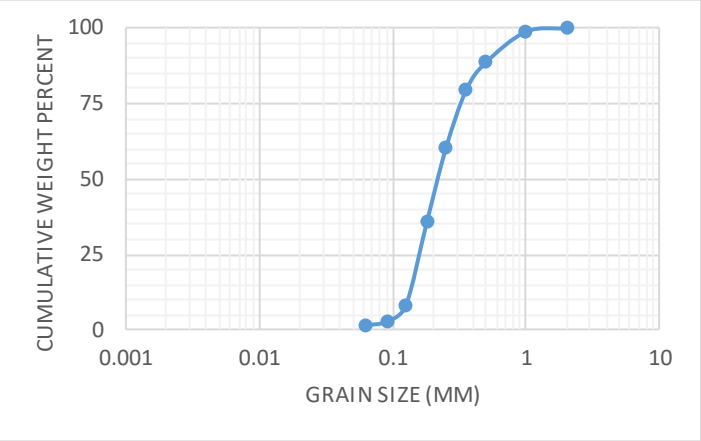


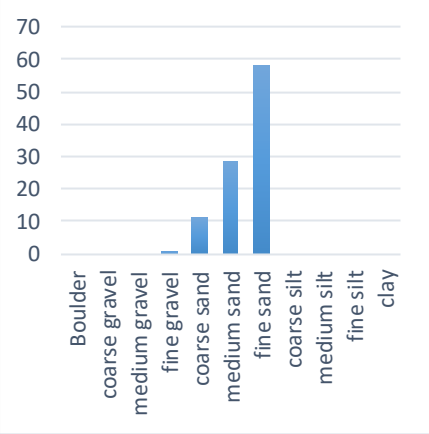
Well 040610/1-T4. Elevation 0.775 m AHD.

Grain Size Analysis Report

Mass Sample (g): 100 T (oC) 20

Uniform sand low in fines



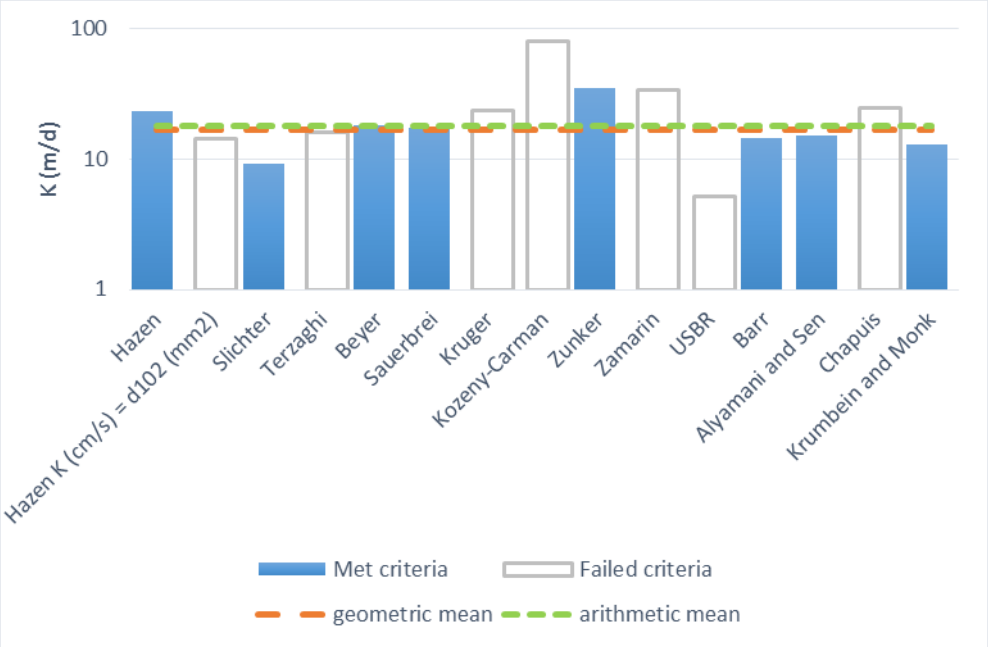


Sieve opening (ps) di (mm)	Mass of retained (mr) (g)	mass fraction (mf)	Percent Passing (pp)
2	0.10122	0.00101	99.8988
1	1.10335	0.01103	98.7954
0.5	10.1731	0.10173	88.6223
0.355	9.16085	0.09161	79.4615
0.25	19.2732	0.19273	60.1883
0.18	24.4154	0.24415	35.7729
0.125	27.7154	0.27715	8.0575
0.09	5.32443	0.05324	2.73307
0.063	1.1236	0.01124	1.60947

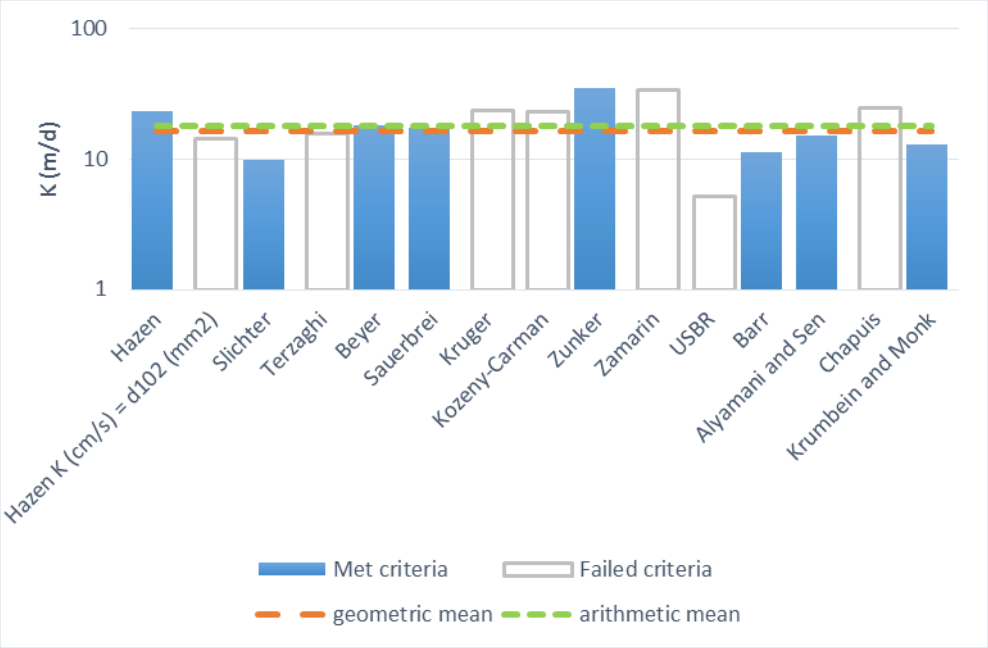
Effective Grain Diameters (mm)		Other Useful Parameters	
d10	0.129	Uniformity Coef.	1.94
d17	0.143	n computed	0.43
d20	0.149	g (cm/s^2)	980.00
d50	0.221	ρ (g/cm^3)	0.9981
d60	0.249	μ (g/cm s)	0.0098
de (Kruger)	0.218	ρg/μ (1/cm s)	9.9327E+04
de (Kozeny)	0.211	tau (Sauerbrei)	1.053
de (Zunker)	0.213	$d_{geometric\ mean}$	0.247
de (Zamarin)	0.216	σ_ϕ	0.848
Io (Alyameni	0.106		

mm	0	% in sample
>64	Boulder	
16 - 64	coarse gravel	
8 - 16	medium gravel	
2 - 8	fine gravel	0.10122482
0.5 - 2	coarse sand	11.27644498
0.25 - 0.5	medium sand	28.43405203
0.063 - 0.25	fine sand	58.57880352
0.016 - 0.063	coarse silt	
0.008 - 0.016	medium silt	
0.002 - 0.008	fine silt	
<0.002	clay	

Slichter, Terzaghi, Kozeny-Carman and Barr with d_{VS}:



Slichter, Terzaghi, Kozeny-Carman and Barr with d_{UU}:

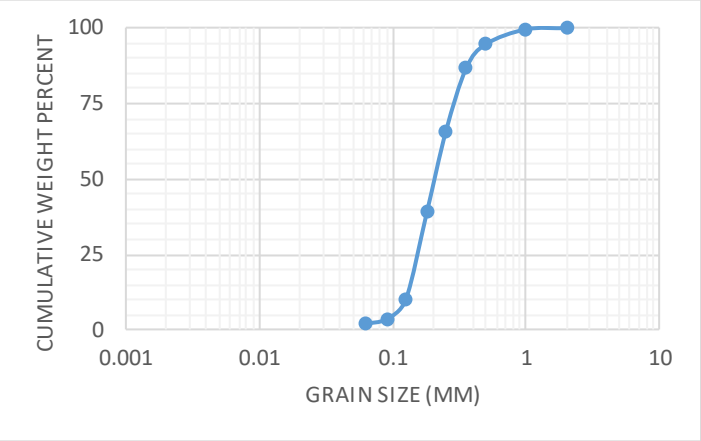


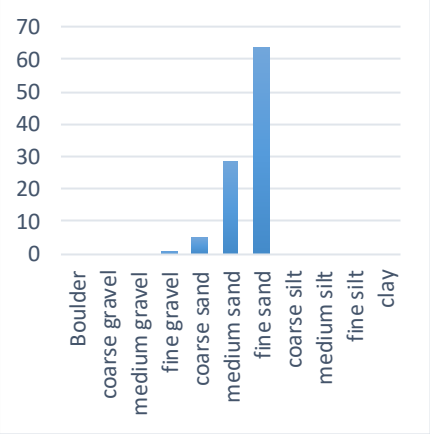
Well 040610/1-T4. Elevation 0.725 m AHD.

Grain Size Analysis Report

Mass Sample (g): 100 T (oC) 20

Uniform sand low in fines



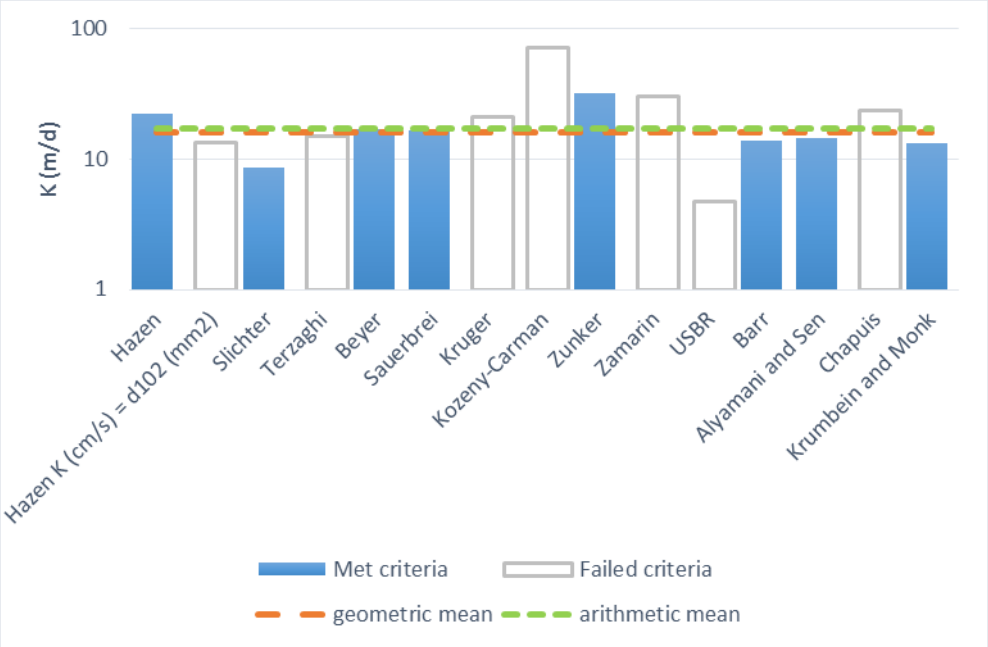


Sieve opening (ps) di (mm)	Mass of retained (mr) (g)	mass fraction (mf)	Percent Passing (pp)
2	0.07862	0.00079	99.9214
1	0.34816	0.00348	99.5732
0.5	4.88544	0.04885	94.6878
0.355	7.98518	0.07985	86.7026
0.25	20.9007	0.20901	65.8019
0.18	26.7633	0.26763	39.0386
0.125	28.9757	0.28976	10.0629
0.09	6.45777	0.06458	3.60512
0.063	1.48248	0.01482	2.12264

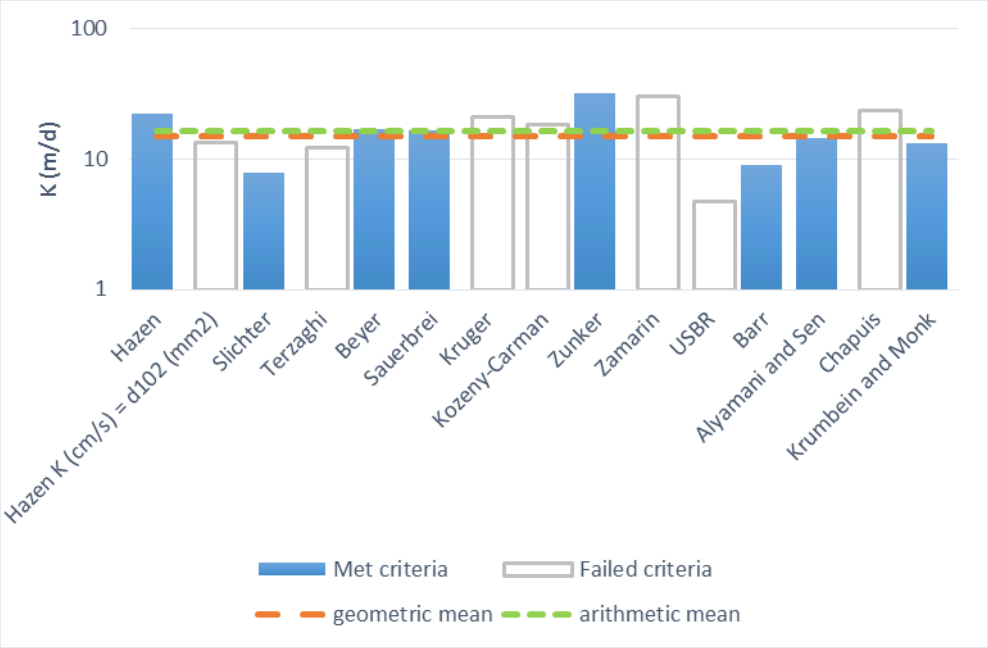
Effective Grain Diameters (mm)		Other Useful Parameters	
d10	0.125	Uniformity Coef.	1.88
d17	0.138	n computed	0.43
d20	0.144	g (cm/s^2)	980.00
d50	0.209	ρ (g/cm^3)	0.9981
d60	0.235	μ (g/cm s)	0.0098
de (Kruger)	0.205	ρg/μ (1/cm s)	9.9327E+04
de (Kozeny)	0.198	tau (Sauerbrei)	1.053
de (Zunker)	0.200	$d_{geometric\ mean}$	0.226
de (Zamarin)	0.203	σ_ϕ	0.702
Io (Alyameni	0.104		

mm	0	% in sample
>64	Boulder	
16 - 64	coarse gravel	
8 - 16	medium gravel	
2 - 8	fine gravel	0.078616352
0.5 - 2	coarse sand	5.233602875
0.25 - 0.5	medium sand	28.88589398
0.063 - 0.25	fine sand	63.67924528
0.016 - 0.063	coarse silt	
0.008 - 0.016	medium silt	
0.002 - 0.008	fine silt	
<0.002	clay	

Slichter, Terzaghi, Kozeny-Carman and Barr with d_{VS}:



Slichter, Terzaghi, Kozeny-Carman and Barr with d_{UU}:

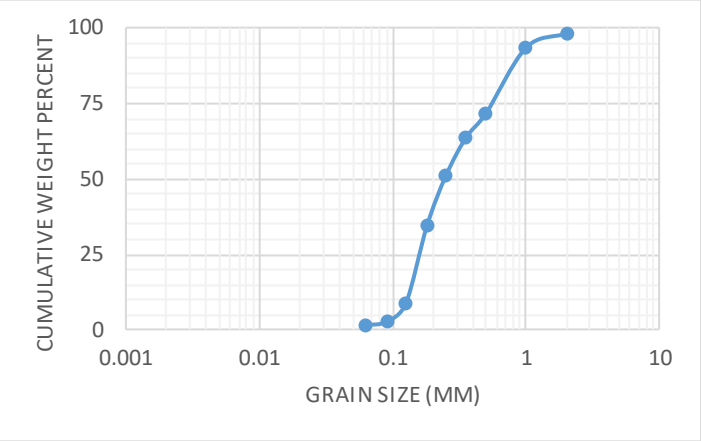


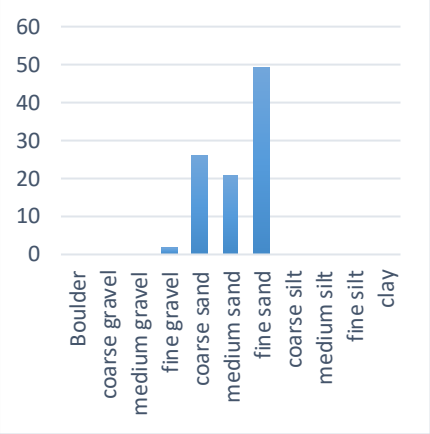
Well 040610/1-T4. Elevation 0.675 m AHD.

Grain Size Analysis Report

Mass Sample (g): 100 T (oC) 20

Moderately well sorted sand low in fines



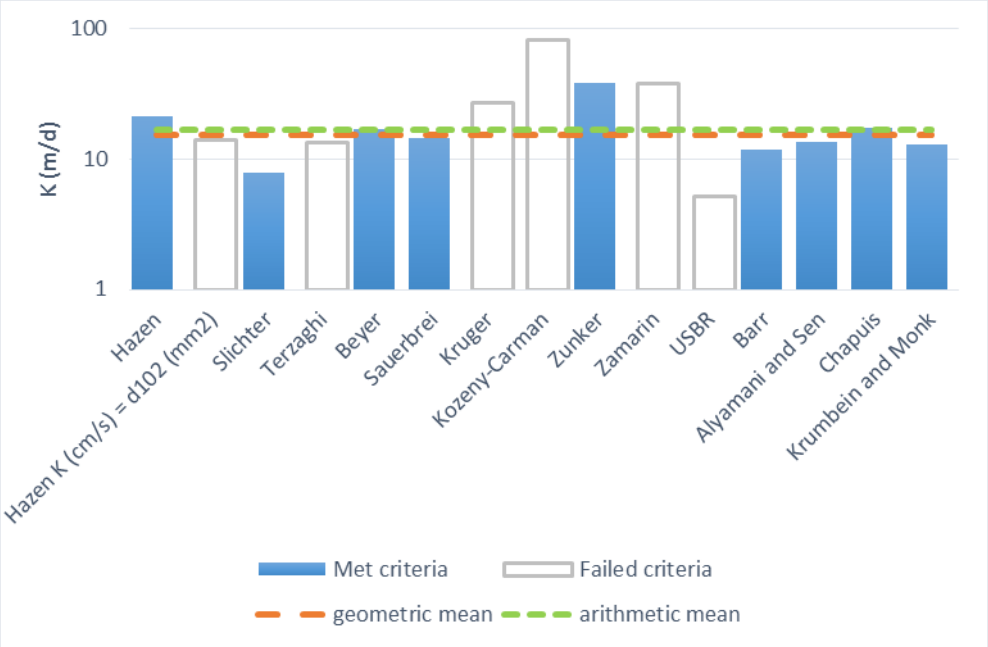


Sieve opening (ps) di (mm)	Mass of retained (mr) (g)	mass fraction (mf)	Percent Passing (pp)
2	1.83461	0.01835	98.1654
1	4.64586	0.04646	93.5195
0.5	21.7689	0.21769	71.7506
0.355	7.91347	0.07913	63.8372
0.25	12.7419	0.12742	51.0953
0.18	16.6667	0.16667	34.4286
0.125	25.7028	0.25703	8.72581
0.09	6.01497	0.06015	2.71084
0.063	1.08616	0.01086	1.62468

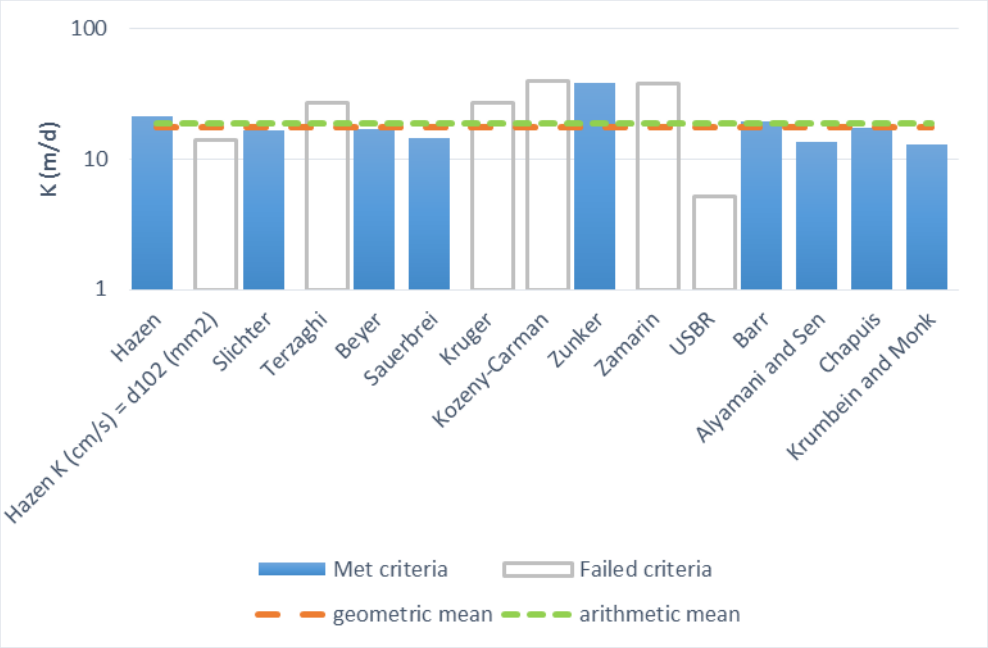
Effective Grain Diameters (mm)		Other Useful Parameters	
d10	0.128	Uniformity Coef.	2.53
d17	0.143	n computed	0.41
d20	0.149	g (cm/s^2)	980.00
d50	0.245	ρ (g/cm^3)	0.9981
d60	0.323	μ (g/cm s)	0.0098
de (Kruger)	0.245	ρg/μ (1/cm s)	9.9327E+04
de (Kozeny)	0.236	tau (Sauerbrei)	1.053
de (Zunker)	0.238	$d_{geometric\ mean}$	0.304
de (Zamarin)	0.242	σ_ϕ	1.175
Io (Alyameni	0.098		

mm	0	% in sample
>64	Boulder	
16 - 64	coarse gravel	
8 - 16	medium gravel	
2 - 8	fine gravel	1.834611172
0.5 - 2	coarse sand	26.41474991
0.25 - 0.5	medium sand	20.65534867
0.063 - 0.25	fine sand	49.47060971
0.016 - 0.063	coarse silt	
0.008 - 0.016	medium silt	
0.002 - 0.008	fine silt	
<0.002	clay	

Slichter, Terzaghi, Kozeny-Carman and Barr with d_{VS}:



Slichter, Terzaghi, Kozeny-Carman and Barr with d_{UU}:

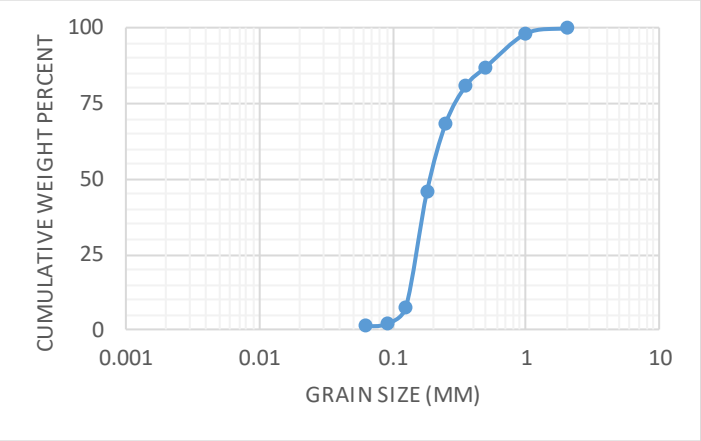


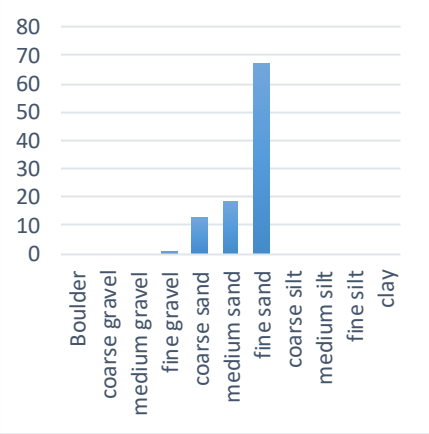
Well 040610/1-T4. Elevation 0.625 m AHD.

Grain Size Analysis Report

Mass Sample (g): 100 T (oC) 20

Uniform sand low in fines



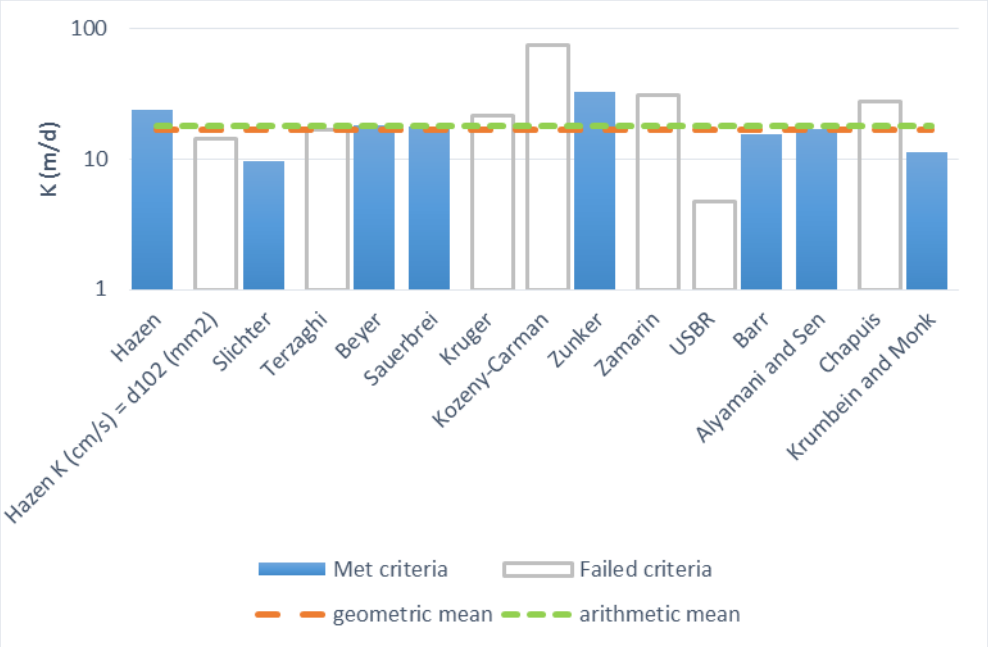


Sieve opening (ps) di (mm)	Mass of retained (mr) (g)	mass fraction (mf)	Percent Passing (pp)
2	0.06524	0.00065	99.9348
1	1.76142	0.01761	98.1733
0.5	11.0531	0.11053	87.1202
0.355	6.09506	0.06095	81.0252
0.25	12.4697	0.1247	68.5555
0.18	22.8239	0.22824	45.7316
0.125	38.2759	0.38276	7.45573
0.09	5.47064	0.05471	1.98509
0.063	0.78285	0.00783	1.20224

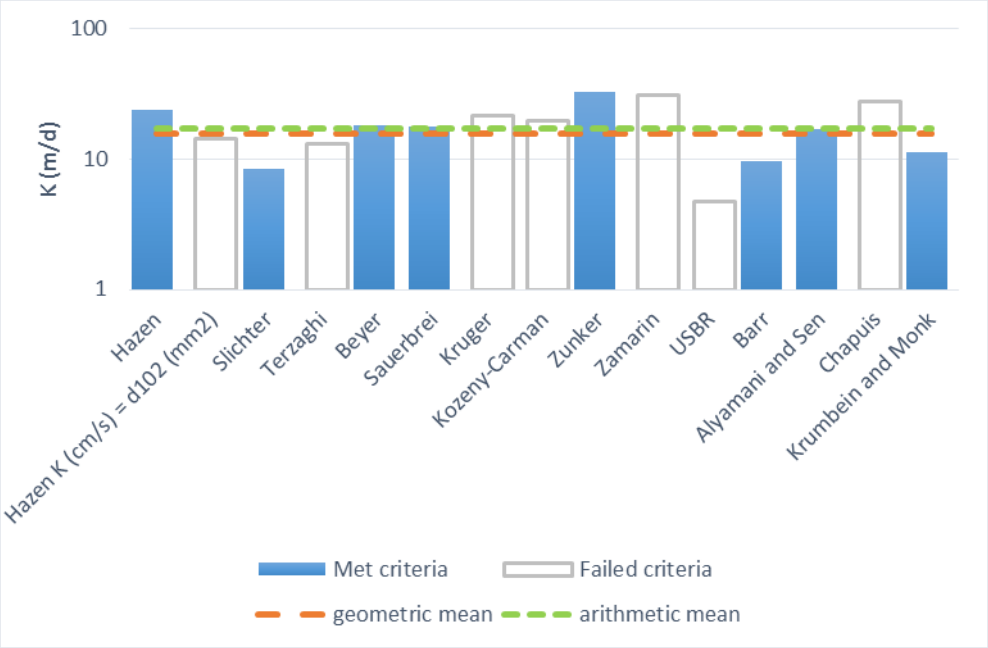
Effective Grain Diameters (mm)		Other Useful Parameters	
d10	0.129	Uniformity Coef.	1.74
d17	0.139	n computed	0.44
d20	0.143	g (cm/s^2)	980.00
d50	0.193	ρ (g/cm^3)	0.9981
d60	0.224	μ (g/cm s)	0.0098
de (Kruger)	0.204	ρg/μ (1/cm s)	9.9327E+04
de (Kozeny)	0.197	tau (Sauerbrei)	1.053
de (Zunker)	0.200	$d_{geometric\ mean}$	0.232
de (Zamarin)	0.202	σ_ϕ	0.858
Io (Alyameni	0.113		

mm	0	% in sample
>64	Boulder	
16 - 64	coarse gravel	
8 - 16	medium gravel	
2 - 8	fine gravel	0.065237651
0.5 - 2	coarse sand	12.81453868
0.25 - 0.5	medium sand	18.56477167
0.063 - 0.25	fine sand	67.35321528
0.016 - 0.063	coarse silt	
0.008 - 0.016	medium silt	
0.002 - 0.008	fine silt	
<0.002	clay	

Slichter, Terzaghi, Kozeny-Carman and Barr with d_{VS}:



Slichter, Terzaghi, Kozeny-Carman and Barr with d_{UU}:

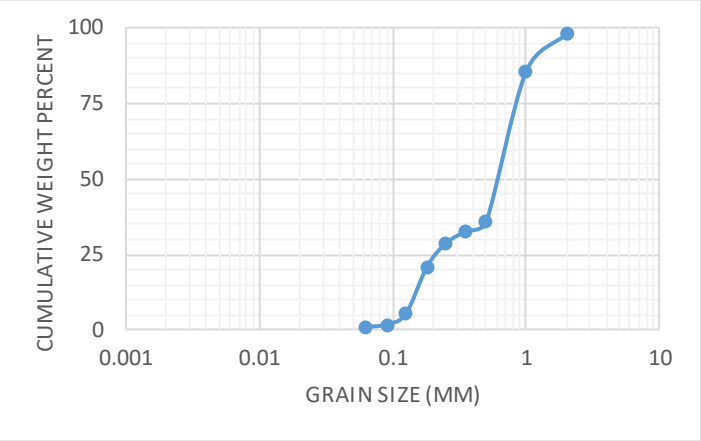


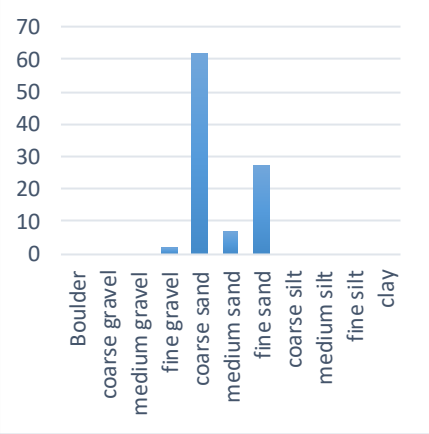
Well 040610/1-T4. Elevation 0.575 m AHD.

Grain Size Analysis Report

Mass Sample (g): 100 T (oC) 20

Poorly sorted sand low in fines



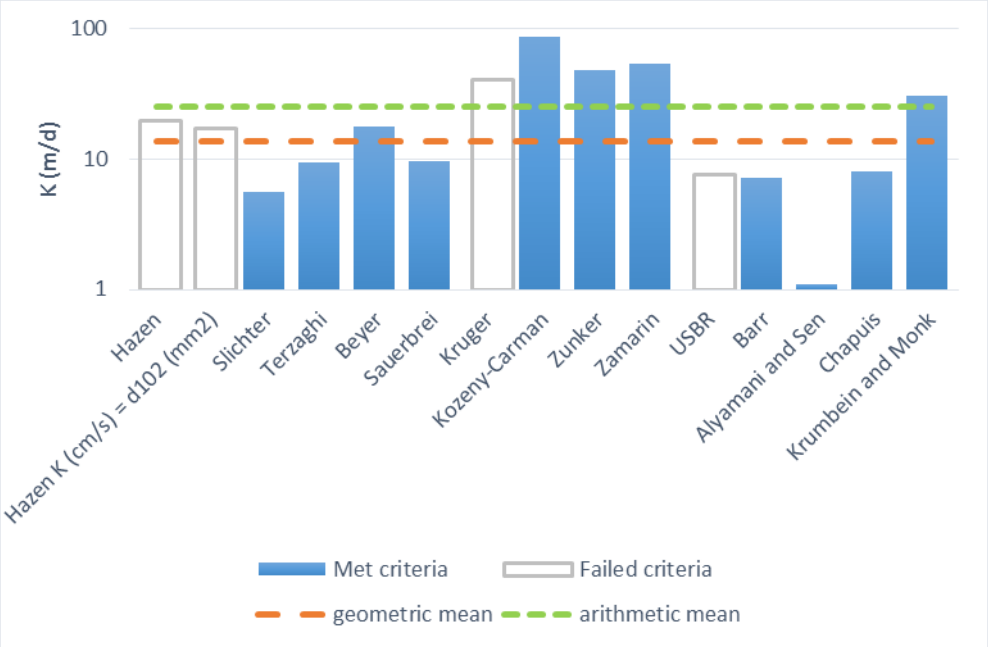


Sieve opening (ps) di (mm)	Mass of retained (mr) (g)	mass fraction (mf)	Percent Passing (pp)
2	2.08236	0.02082	97.9176
1	12.2878	0.12288	85.6299
0.5	49.8734	0.49873	35.7565
0.355	2.98283	0.02983	32.7737
0.25	4.11781	0.04118	28.6558
0.18	7.73849	0.07738	20.9174
0.125	15.6271	0.15627	5.29031
0.09	3.47997	0.0348	1.81034
0.063	0.75978	0.0076	1.05056

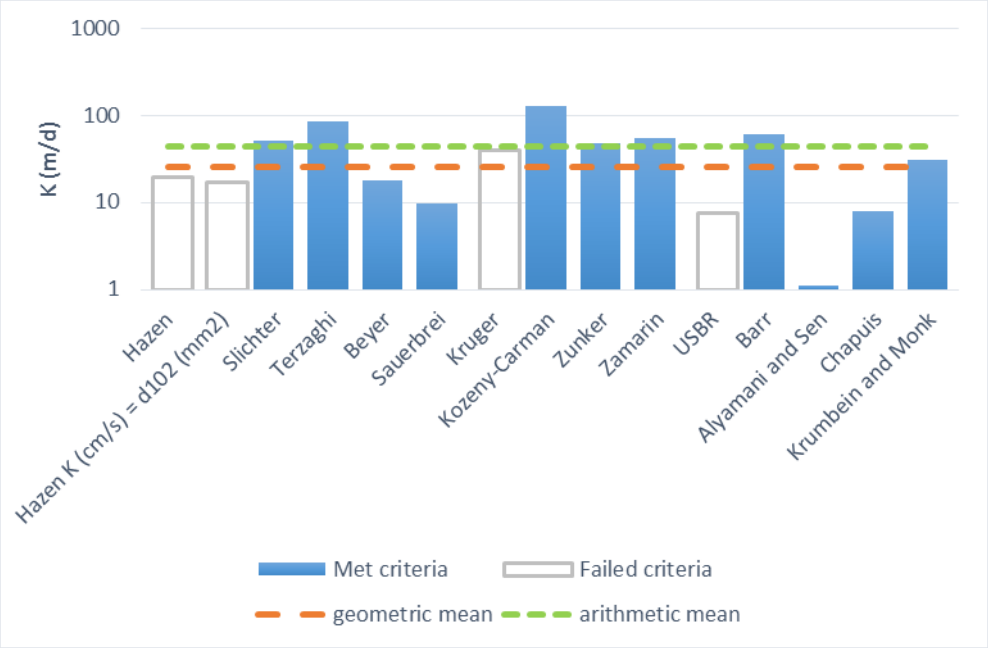
Effective Grain Diameters (mm)		Other Useful Parameters	
d10	0.142	Uniformity Coef.	5.25
d17	0.166	n computed	0.35
d20	0.177	g (cm/s^2)	980.00
d50	0.643	ρ (g/cm^3)	0.9981
d60	0.743	μ (g/cm s)	0.0098
de (Kruger)	0.362	ρg/μ (1/cm s)	9.9327E+04
de (Kozeny)	0.343	tau (Sauerbrei)	1.053
de (Zunker)	0.349	$d_{geometric\ mean}$	0.487
de (Zamarin)	0.356	σ_ϕ	1.233
Io (Alyameni	0.016		

mm	0	% in sample
>64	Boulder	
16 - 64	coarse gravel	
8 - 16	medium gravel	
2 - 8	fine gravel	2.082356252
0.5 - 2	coarse sand	62.16114811
0.25 - 0.5	medium sand	7.100647219
0.063 - 0.25	fine sand	27.60529031
0.016 - 0.063	coarse silt	
0.008 - 0.016	medium silt	
0.002 - 0.008	fine silt	
<0.002	clay	

Slichter, Terzaghi, Kozeny-Carman and Barr with d_{VS}:



Slichter, Terzaghi, Kozeny-Carman and Barr with d_{UU}:

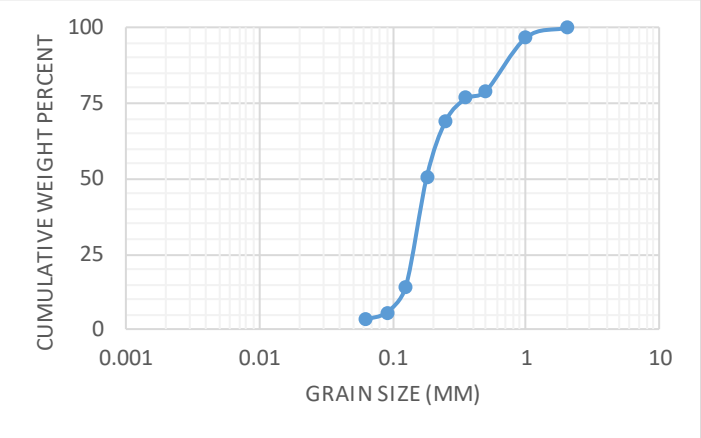


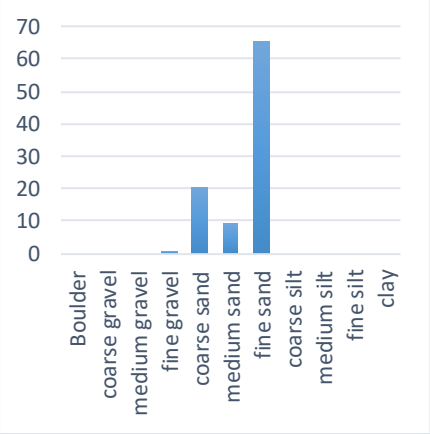
Well 040610/1-T4. Elevation 0.525 m AHD.

Grain Size Analysis Report

Mass Sample (g): 100 T (oC) 20

Uniform sand low in fines



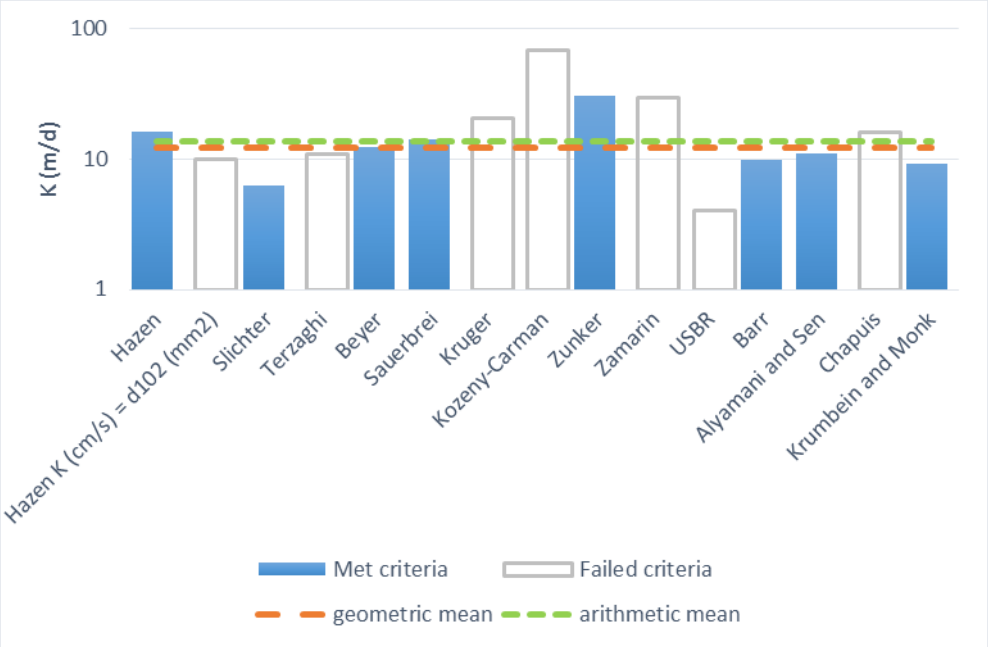


Sieve opening (ps) di (mm)	Mass of retained (mr) (g)	mass fraction (mf)	Percent Passing (pp)
2	0.07496	0.00075	99.925
1	3.18382	0.03184	96.7412
0.5	17.7113	0.17711	79.03
0.355	2.41048	0.0241	76.6195
0.25	7.39148	0.07391	69.228
0.18	18.4221	0.18422	50.8059
0.125	36.5273	0.36527	14.2786
0.09	8.54171	0.08542	5.73688
0.063	2.24269	0.02243	3.49419

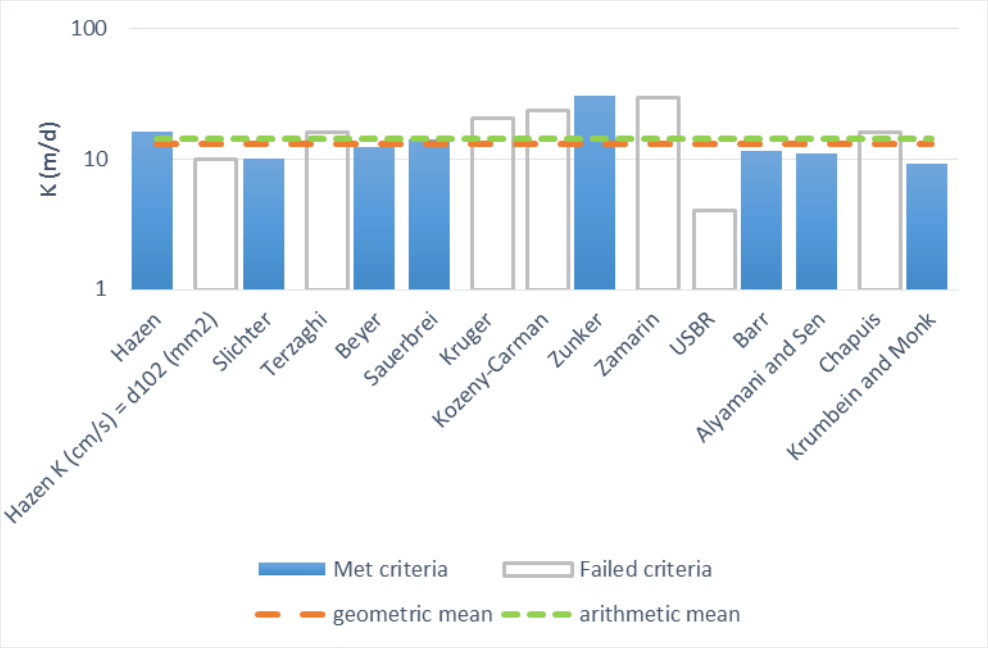
Effective Grain Diameters (mm)		Other Useful Parameters	
d10	0.107	Uniformity Coef.	2.00
d17	0.129	n computed	0.43
d20	0.134	g (cm/s^2)	980.00
d50	0.179	ρ (g/cm^3)	0.9981
d60	0.215	μ (g/cm s)	0.0098
de (Kruger)	0.204	ρg/μ (1/cm s)	9.9327E+04
de (Kozeny)	0.197	tau (Sauerbrei)	1.053
de (Zunker)	0.199	$d_{geometric\ mean}$	0.249
de (Zamarin)	0.202	σ_ϕ	1.120
Io (Alyameni	0.090		

mm	0	% in sample
>64	Boulder	
16 - 64	coarse gravel	
8 - 16	medium gravel	
2 - 8	fine gravel	0.074960927
0.5 - 2	coarse sand	20.89507409
0.25 - 0.5	medium sand	9.801960392
0.063 - 0.25	fine sand	65.73381156
0.016 - 0.063	coarse silt	
0.008 - 0.016	medium silt	
0.002 - 0.008	fine silt	
<0.002	clay	

Slichter, Terzaghi, Kozeny-Carman and Barr with d_{VS}:



Slichter, Terzaghi, Kozeny-Carman and Barr with d_{UU}:

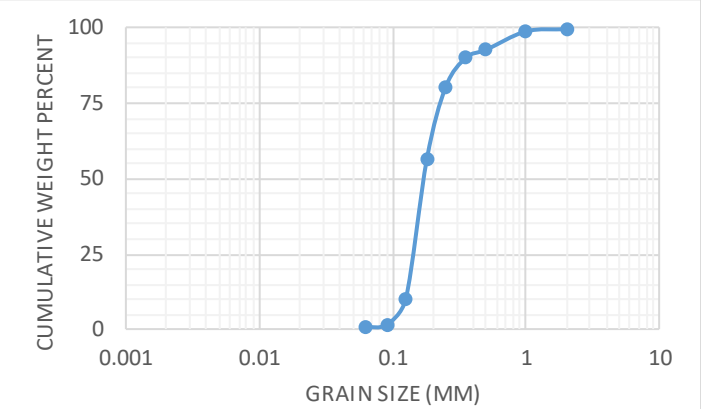


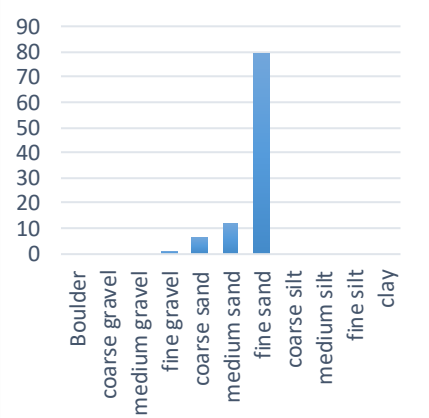
Well 040610/1-T4. Elevation 0.475 m AHD.

Grain Size Analysis Report

Mass Sample (g): 100 T (oC) 20

Uniform sand low in fines



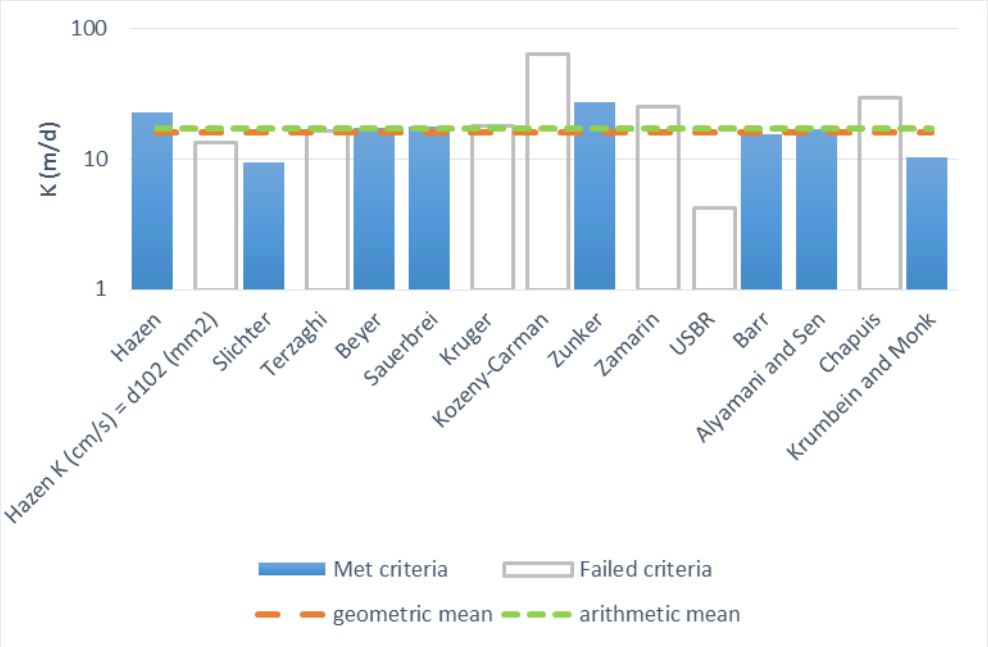


Sieve opening (ps) di (mm)	Mass of retained (mr) (g)	mass fraction (mf)	Percent Passing (pp)
2	0.50476	0.00505	99.4952
1	0.71429	0.00714	98.781
0.5	6.10476	0.06105	92.6762
0.355	2.57143	0.02571	90.1048
0.25	9.57143	0.09571	80.5333
0.18	23.9238	0.23924	56.6095
0.125	46.4095	0.4641	10.2
0.09	8.5619	0.08562	1.6381
0.063	0.74286	0.00743	0.89524

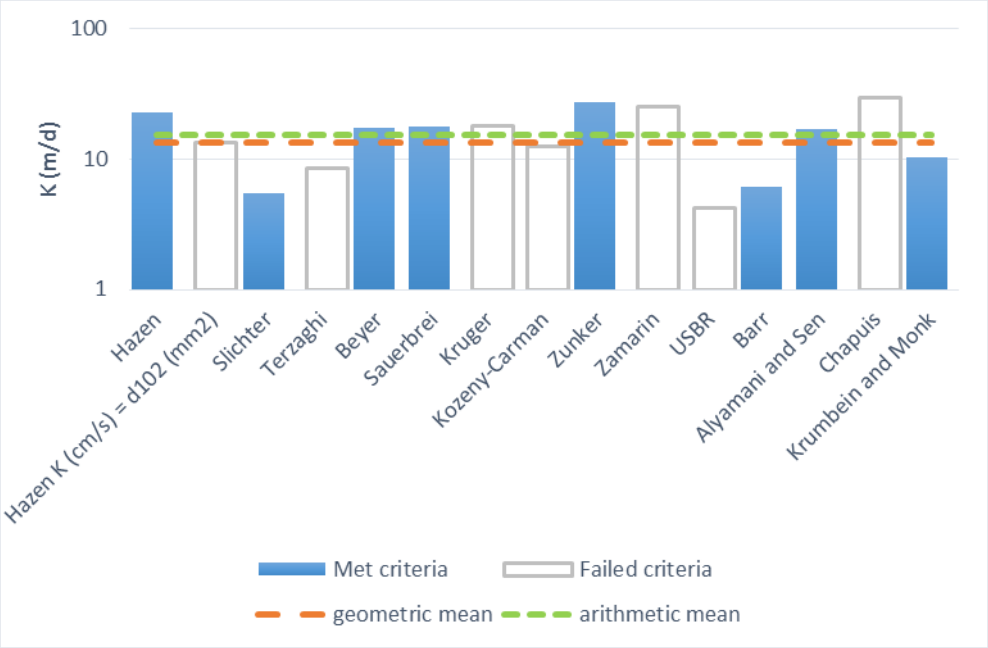
Effective Grain Diameters (mm)		Other Useful Parameters	
d10	0.124	Uniformity Coef.	1.53
d17	0.133	n computed	0.45
d20	0.137	g (cm/s^2)	980.00
d50	0.172	ρ (g/cm^3)	0.9981
d60	0.190	μ (g/cm s)	0.0098
de (Kruger)	0.181	ρg/μ (1/cm s)	9.9327E+04
de (Kozeny)	0.176	tau (Sauerbrei)	1.053
de (Zunker)	0.178	$d_{geometric\ mean}$	0.198
de (Zamarin)	0.179	σ_ϕ	0.696
Io (Alyameni	0.112		

mm	0	% in sample
>64	Boulder	
16 - 64	coarse gravel	
8 - 16	medium gravel	
2 - 8	fine gravel	0.504761905
0.5 - 2	coarse sand	6.819047619
0.25 - 0.5	medium sand	12.14285714
0.063 - 0.25	fine sand	79.63809524
0.016 - 0.063	coarse silt	
0.008 - 0.016	medium silt	
0.002 - 0.008	fine silt	
<0.002	clay	

Slichter, Terzaghi, Kozeny-Carman and Barr with d_{VS}:



Slichter, Terzaghi, Kozeny-Carman and Barr with d_{UU}:

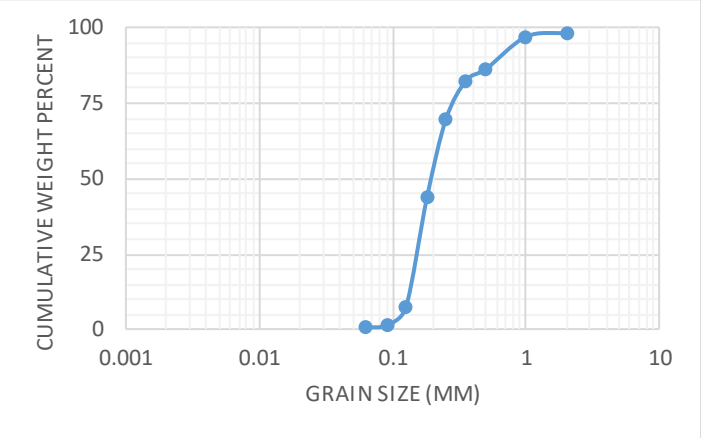


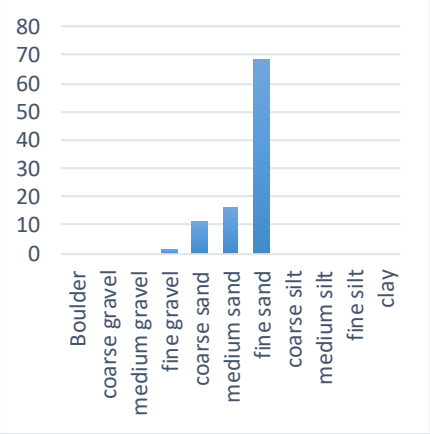
Well 040610/1-T4. Elevation 0.425 m AHD.

Grain Size Analysis Report

Mass Sample (g): 100 T (oC) 20

Uniform sand low in fines



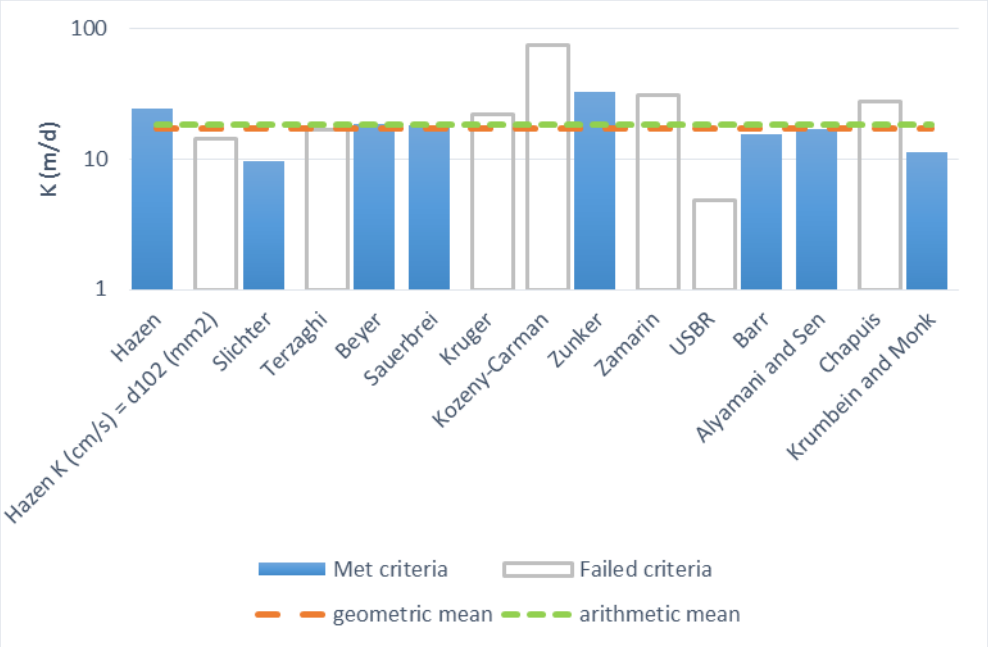


Sieve opening (ps) di (mm)	Mass of retained (mr) (g)	mass fraction (mf)	Percent Passing (pp)
2	1.71142	0.01711	98.2886
1	1.27648	0.01276	97.0121
0.5	10.7035	0.10703	86.3086
0.355	3.7916	0.03792	82.517
0.25	12.8688	0.12869	69.6483
0.18	25.9739	0.25974	43.6744
0.125	36.3937	0.36394	7.28064
0.09	5.86233	0.05862	1.41831
0.063	0.6146	0.00615	0.80371

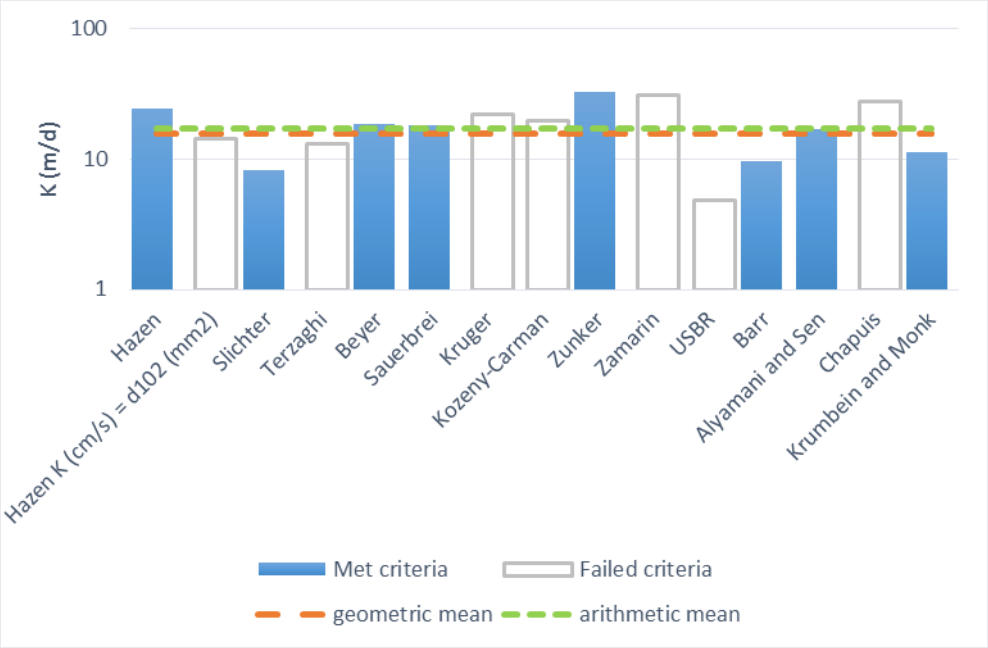
Effective Grain Diameters (mm)		Other Useful Parameters	
d10	0.129	Uniformity Coef.	1.73
d17	0.140	n computed	0.44
d20	0.144	g (cm/s^2)	980.00
d50	0.197	ρ (g/cm^3)	0.9981
d60	0.224	μ (g/cm s)	0.0098
de (Kruger)	0.205	ρg/μ (1/cm s)	9.9327E+04
de (Kozeny)	0.198	tau (Sauerbrei)	1.053
de (Zunker)	0.200	$d_{geometric\ mean}$	0.232
de (Zamarin)	0.202	σ_ϕ	0.852
Io (Alyameni	0.112		

mm	0	% in sample
>64	Boulder	
16 - 64	coarse gravel	
8 - 16	medium gravel	
2 - 8	fine gravel	1.711422088
0.5 - 2	coarse sand	11.97995461
0.25 - 0.5	medium sand	16.66036309
0.063 - 0.25	fine sand	68.84455371
0.016 - 0.063	coarse silt	
0.008 - 0.016	medium silt	
0.002 - 0.008	fine silt	
<0.002	clay	

Slichter, Terzaghi, Kozeny-Carman and Barr with d_{VS}:



Slichter, Terzaghi, Kozeny-Carman and Barr with d_{UU}:

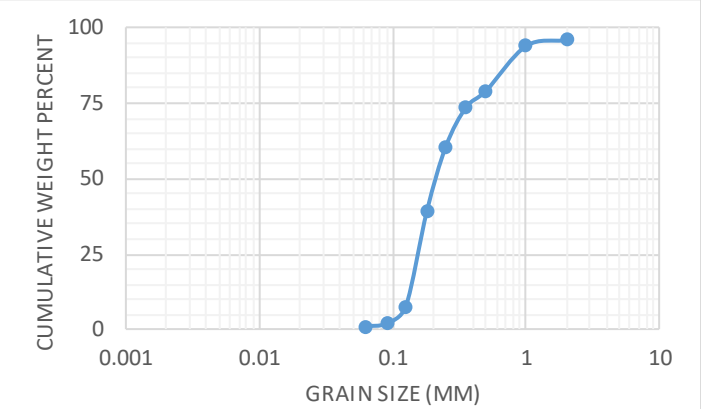


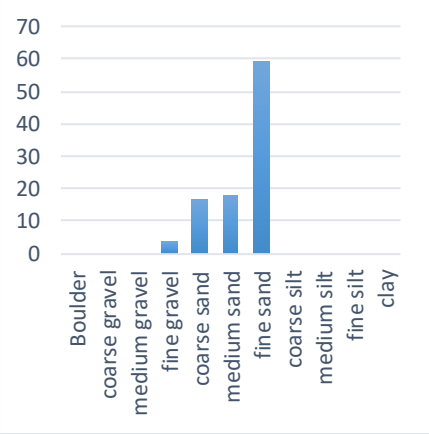
Well 040610/1-T4. Elevation 0.375 m AHD.

Grain Size Analysis Report

Mass Sample (g): 100 T (oC) 20

Uniform sand low in fines



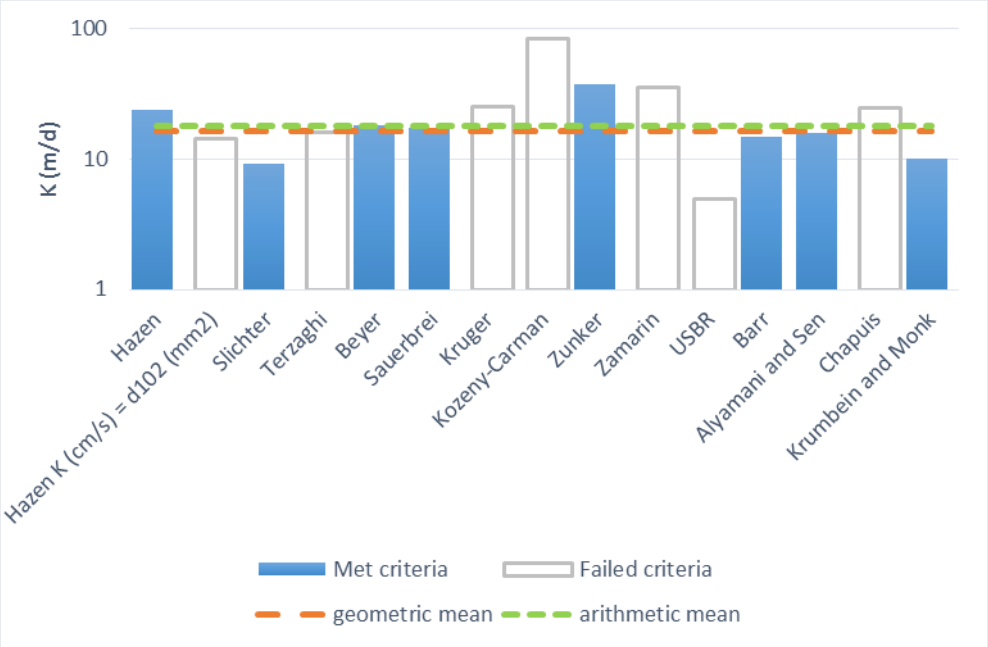


Sieve opening (ps) di (mm)	Mass of retained (mr) (g)	mass fraction (mf)	Percent Passing (pp)
2	4.14424	0.04144	95.8558
1	1.91995	0.0192	93.9358
0.5	14.8616	0.14862	79.0742
0.355	5.37778	0.05378	73.6964
0.25	12.9716	0.12972	60.7248
0.18	21.4293	0.21429	39.2955
0.125	31.6267	0.31627	7.66882
0.09	5.64524	0.05645	2.02358
0.063	0.84868	0.00849	1.1749

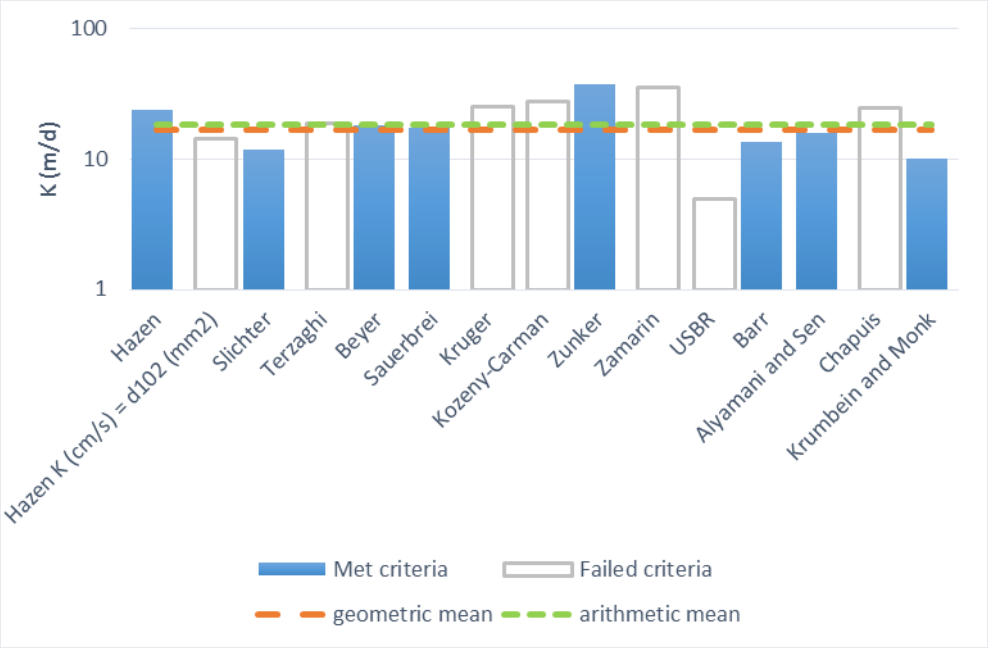
Effective Grain Diameters (mm)		Other Useful Parameters	
d10	0.129	Uniformity Coef.	1.92
d17	0.141	n computed	0.43
d20	0.146	g (cm/s^2)	980.00
d50	0.215	ρ (g/cm^3)	0.9981
d60	0.248	μ (g/cm s)	0.0098
de (Kruger)	0.224	ρg/μ (1/cm s)	9.9327E+04
de (Kozeny)	0.216	tau (Sauerbrei)	1.053
de (Zunker)	0.218	$d_{geometric\ mean}$	0.265
de (Zamarin)	0.221	σ_ϕ	1.146
Io (Alyameni	0.108		

mm	0	% in sample
>64	Boulder	
16 - 64	coarse gravel	
8 - 16	medium gravel	
2 - 8	fine gravel	4.144239654
0.5 - 2	coarse sand	16.78156086
0.25 - 0.5	medium sand	18.34941255
0.063 - 0.25	fine sand	59.54988962
0.016 - 0.063	coarse silt	
0.008 - 0.016	medium silt	
0.002 - 0.008	fine silt	
<0.002	clay	

Slichter, Terzaghi, Kozeny-Carman and Barr with d_{VS}:



Slichter, Terzaghi, Kozeny-Carman and Barr with d_{UU}:

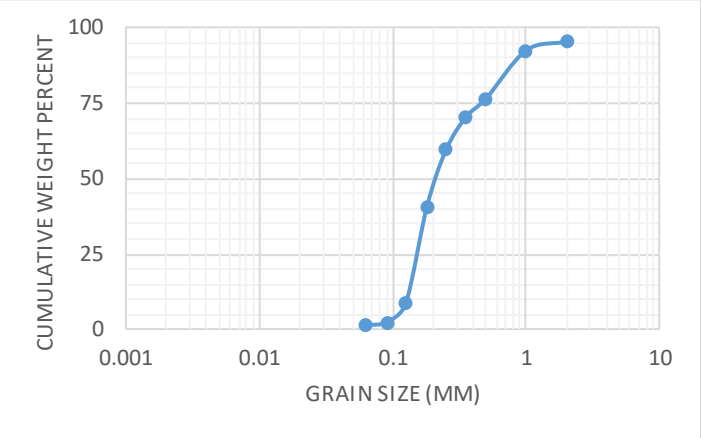


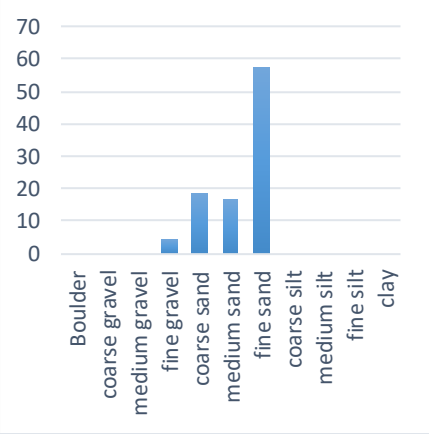
Well 040610/1-T4. Elevation 0.325 m AHD.

Grain Size Analysis Report

Mass Sample (g): 100 T (oC) 20

Moderately well sorted sand low in fines



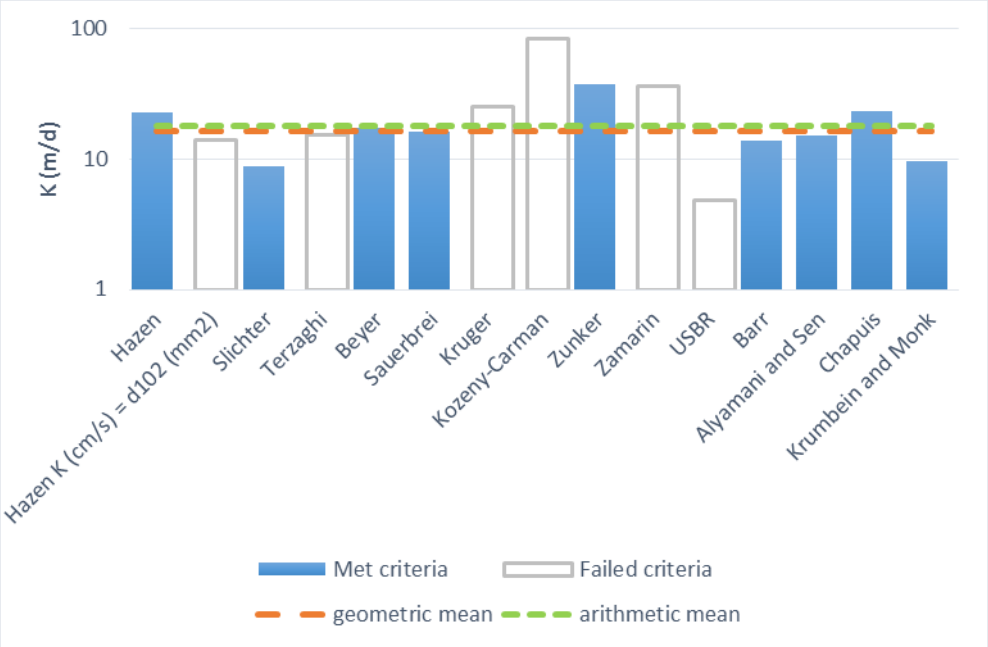


Sieve opening (ps) di (mm)	Mass of retained (mr) (g)	mass fraction (mf)	Percent Passing (pp)
2	4.67383	0.04674	95.3262
1	2.85887	0.02859	92.4673
0.5	15.9566	0.15957	76.5107
0.355	5.97606	0.05976	70.5346
0.25	11.0988	0.11099	59.4358
0.18	18.7462	0.18746	40.6896
0.125	31.9728	0.31973	8.71681
0.09	6.22385	0.06224	2.49296
0.063	0.99035	0.0099	1.5026

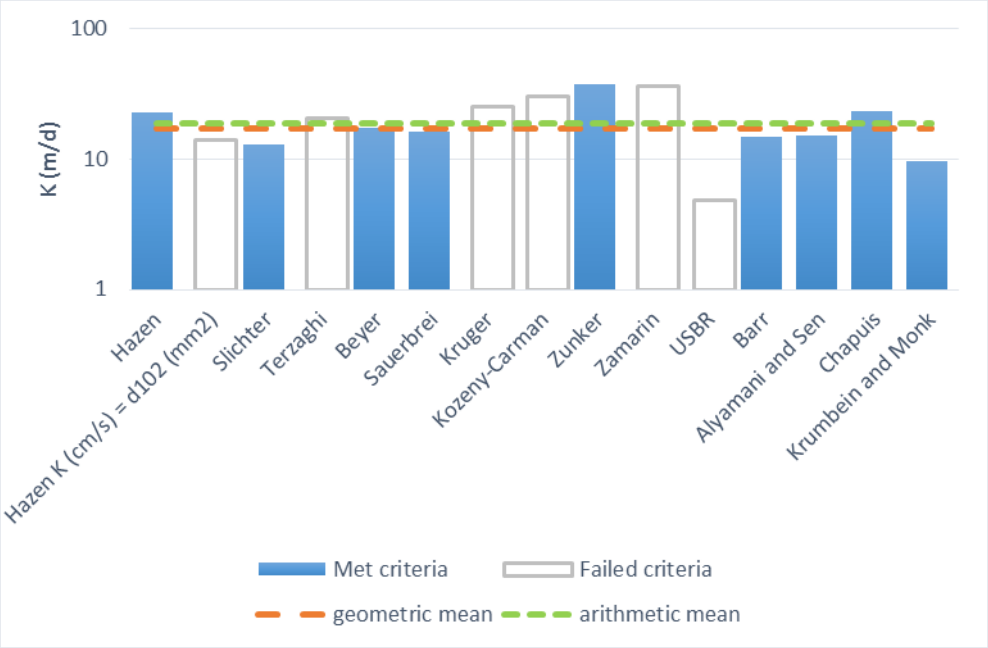
Effective Grain Diameters (mm)		Other Useful Parameters	
d10	0.127	Uniformity Coef.	2.01
d17	0.139	n computed	0.43
d20	0.144	g (cm/s^2)	980.00
d50	0.215	ρ (g/cm^3)	0.9981
d60	0.255	μ (g/cm s)	0.0098
de (Kruger)	0.226	ρg/μ (1/cm s)	9.9327E+04
de (Kozeny)	0.219	tau (Sauerbrei)	1.053
de (Zunker)	0.221	$d_{geometric\ mean}$	0.274
de (Zamarin)	0.224	σ_ϕ	1.238
Io (Alyameni	0.105		

mm	0	% in sample
>64	Boulder	
16 - 64	coarse gravel	
8 - 16	medium gravel	
2 - 8	fine gravel	4.673832936
0.5 - 2	coarse sand	18.81549445
0.25 - 0.5	medium sand	17.07484044
0.063 - 0.25	fine sand	57.93322822
0.016 - 0.063	coarse silt	
0.008 - 0.016	medium silt	
0.002 - 0.008	fine silt	
<0.002	clay	

Slichter, Terzaghi, Kozeny-Carman and Barr with d_{VS}:



Slichter, Terzaghi, Kozeny-Carman and Barr with d_{UU}:

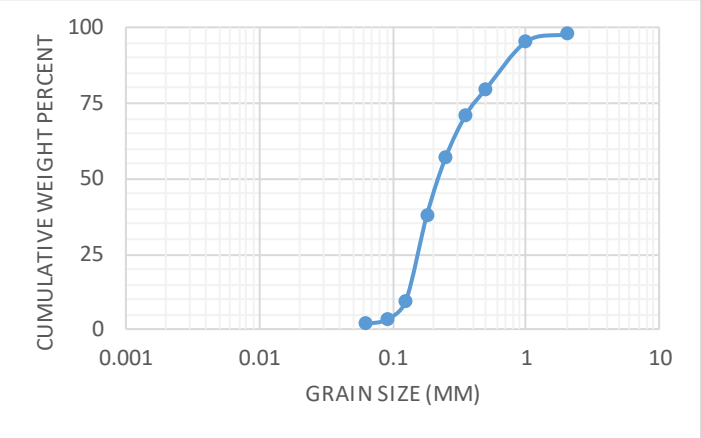


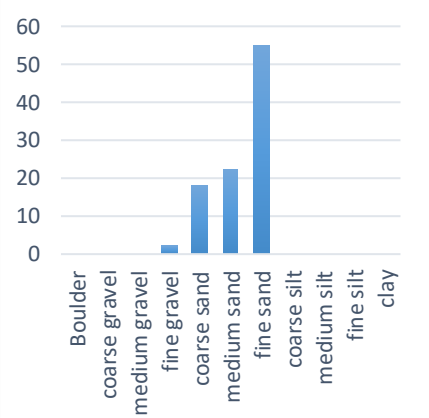
Well 040610/1-T4. Elevation 0.275 m AHD.

Grain Size Analysis Report

Mass Sample (g): 100 T (oC) 20

Moderately well sorted sand low in fines



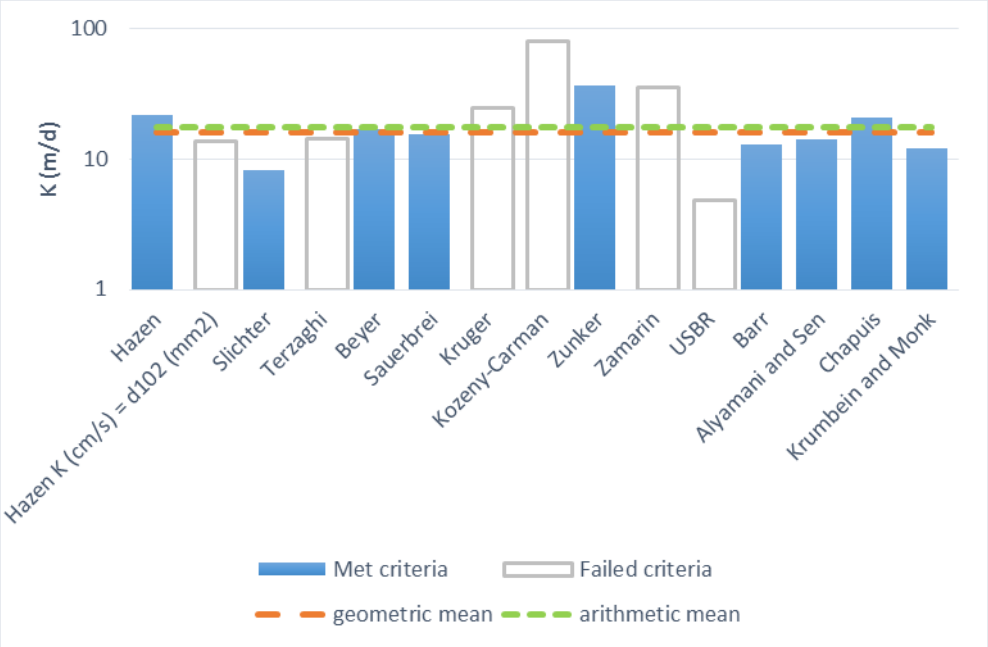


Sieve opening (ps) di (mm)	Mass of retained (mr) (g)	mass fraction (mf)	Percent Passing (pp)
2	2.20033	0.022	97.7997
1	2.43949	0.02439	95.3602
0.5	15.6223	0.15622	79.7379
0.355	8.44734	0.08447	71.2905
0.25	14.0342	0.14034	57.2563
0.18	19.3055	0.19305	37.9508
0.125	28.4703	0.2847	9.48053
0.09	6.15134	0.06151	3.32919
0.063	1.38716	0.01387	1.94203

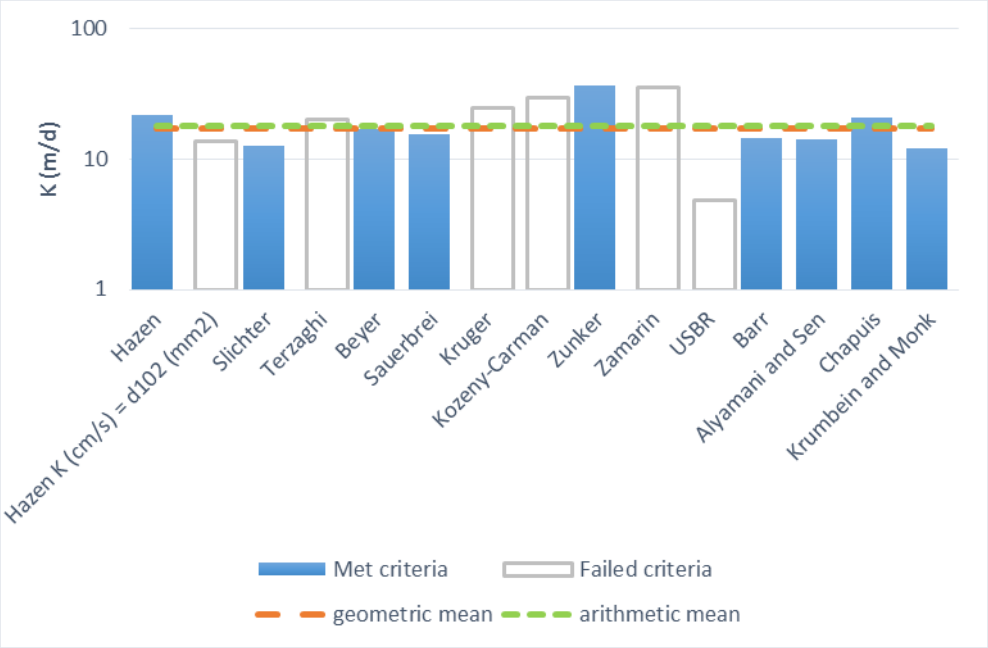
Effective Grain Diameters (mm)		Other Useful Parameters	
d10	0.126	Uniformity Coef.	2.15
d17	0.140	n computed	0.43
d20	0.145	g (cm/s^2)	980.00
d50	0.224	ρ (g/cm^3)	0.9981
d60	0.271	μ (g/cm s)	0.0098
de (Kruger)	0.227	ρg/μ (1/cm s)	9.9327E+04
de (Kozeny)	0.219	tau (Sauerbrei)	1.053
de (Zunker)	0.222	$d_{geometric\ mean}$	0.272
de (Zamarin)	0.224	σ_ϕ	1.054
Io (Alyameni	0.102		

mm	0	% in sample
>64	Boulder	
16 - 64	coarse gravel	
8 - 16	medium gravel	
2 - 8	fine gravel	2.200325265
0.5 - 2	coarse sand	18.06180044
0.25 - 0.5	medium sand	22.48158423
0.063 - 0.25	fine sand	55.31426385
0.016 - 0.063	coarse silt	
0.008 - 0.016	medium silt	
0.002 - 0.008	fine silt	
<0.002	clay	

Slichter, Terzaghi, Kozeny-Carman and Barr with d_{VS}:



Slichter, Terzaghi, Kozeny-Carman and Barr with d_{UU}:

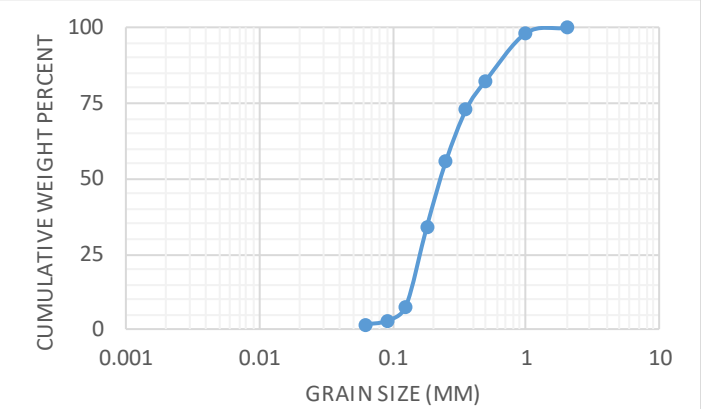


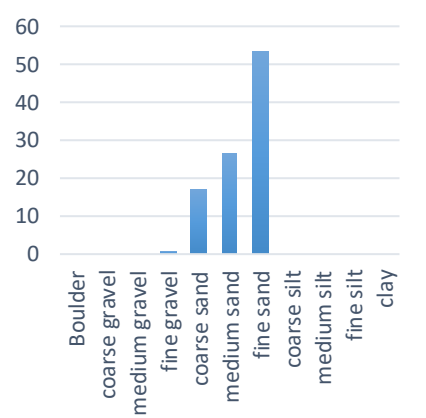
Well 040610/1-T4. Elevation 0.225 m AHD.

Grain Size Analysis Report

Mass Sample (g): 100 T (oC) 20

Moderately well sorted sand low in fines



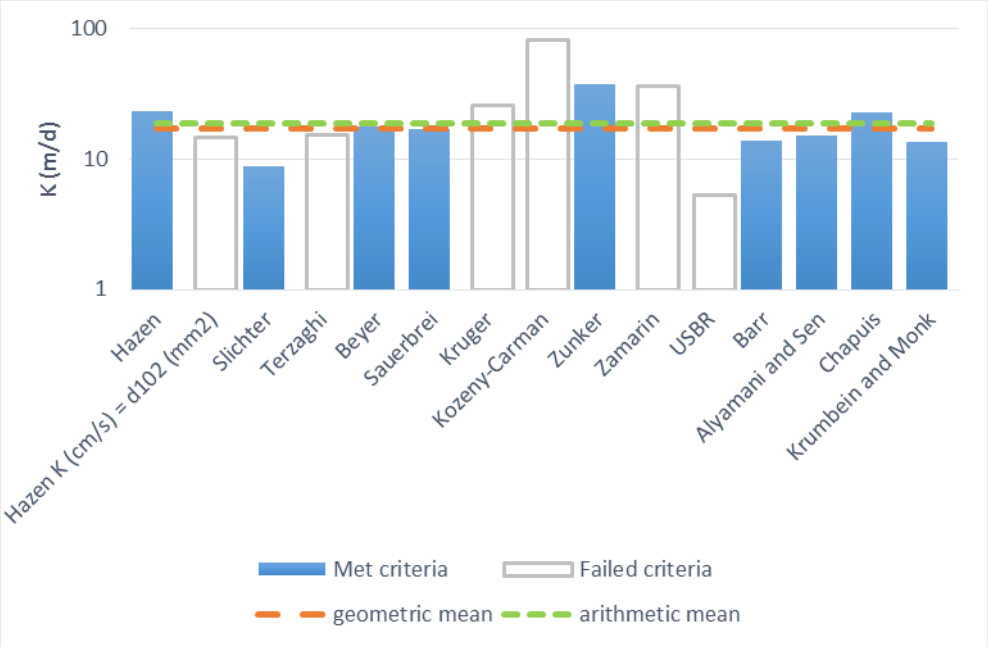


Sieve opening (ps) di (mm)	Mass of retained (mr) (g)	mass fraction (mf)	Percent Passing (pp)
2	0.10882	0.00109	99.8912
1	1.63985	0.0164	98.2513
0.5	15.6877	0.15688	82.5636
0.355	9.62908	0.09629	72.9345
0.25	17.1532	0.17153	55.7813
0.18	21.5603	0.2156	34.2211
0.125	26.545	0.26545	7.67601
0.09	4.77292	0.04773	2.90309
0.063	1.09013	0.0109	1.81297

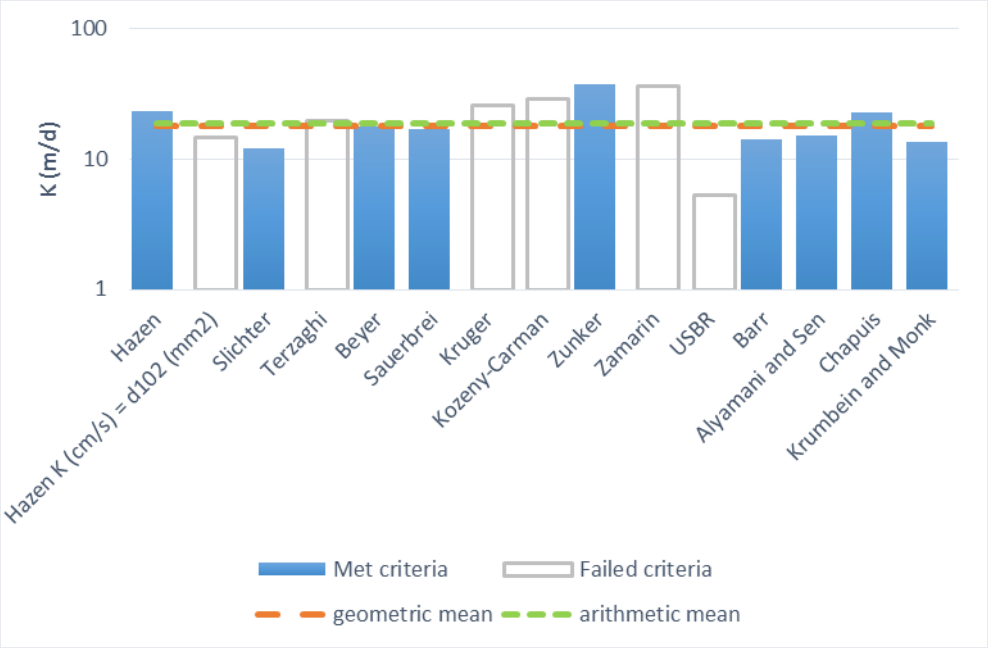
Effective Grain Diameters (mm)		Other Useful Parameters	
d10	0.130	Uniformity Coef.	2.12
d17	0.144	n computed	0.43
d20	0.151	g (cm/s^2)	980.00
d50	0.231	ρ (g/cm^3)	0.9981
d60	0.276	μ (g/cm s)	0.0098
de (Kruger)	0.230	ρg/μ (1/cm s)	9.9327E+04
de (Kozeny)	0.222	tau (Sauerbrei)	1.053
de (Zunker)	0.225	$d_{geometric\ mean}$	0.269
de (Zamarin)	0.228	σ_ϕ	0.953
Io (Alyameni	0.104		

mm	0	% in sample
>64	Boulder	
16 - 64	coarse gravel	
8 - 16	medium gravel	
2 - 8	fine gravel	0.108824505
0.5 - 2	coarse sand	17.32757378
0.25 - 0.5	medium sand	26.78226755
0.063 - 0.25	fine sand	53.96836589
0.016 - 0.063	coarse silt	
0.008 - 0.016	medium silt	
0.002 - 0.008	fine silt	
<0.002	clay	

Slichter, Terzaghi, Kozeny-Carman and Barr with d_{VS}:



Slichter, Terzaghi, Kozeny-Carman and Barr with d_{UU}:

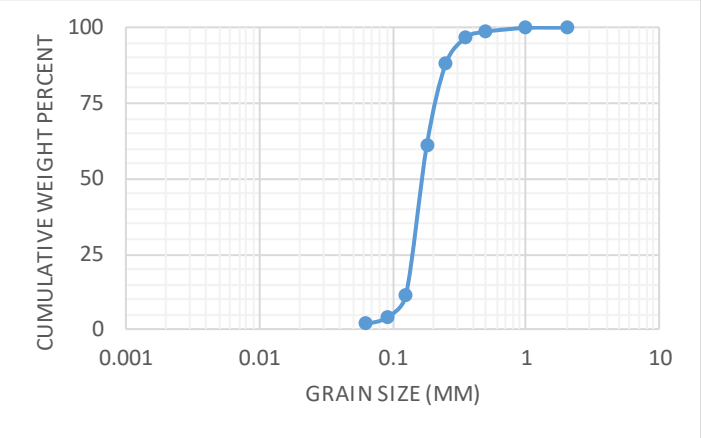


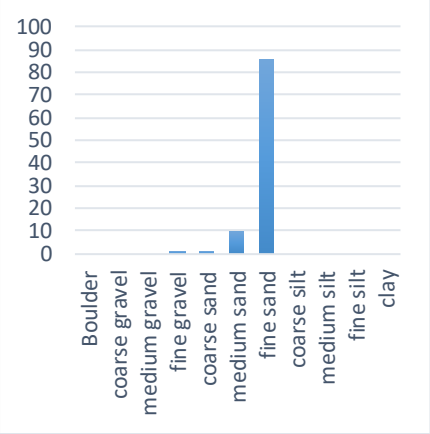
Well 040610/1-T4. Elevation 0.175 m AHD.

Grain Size Analysis Report

Mass Sample (g): 100 T (oC) 20

Uniform sand low in fines



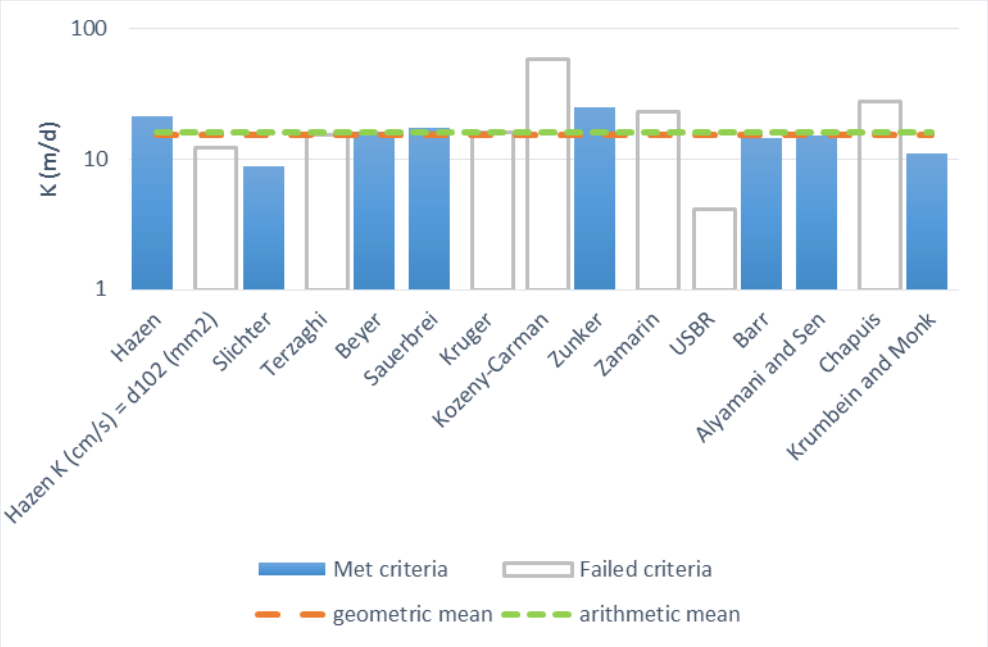


Sieve opening (ps) di (mm)	Mass of retained (mr) (g)	mass fraction (mf)	Percent Passing (pp)
2	0.01742	0.00017	99.9826
1	0.06967	0.0007	99.9129
0.5	1.24532	0.01245	98.6676
0.355	1.91588	0.01916	96.7517
0.25	8.5779	0.08578	88.1738
0.18	26.8571	0.26857	61.3167
0.125	50.0827	0.50083	11.234
0.09	7.23678	0.07237	3.99721
0.063	2.12488	0.02125	1.87233

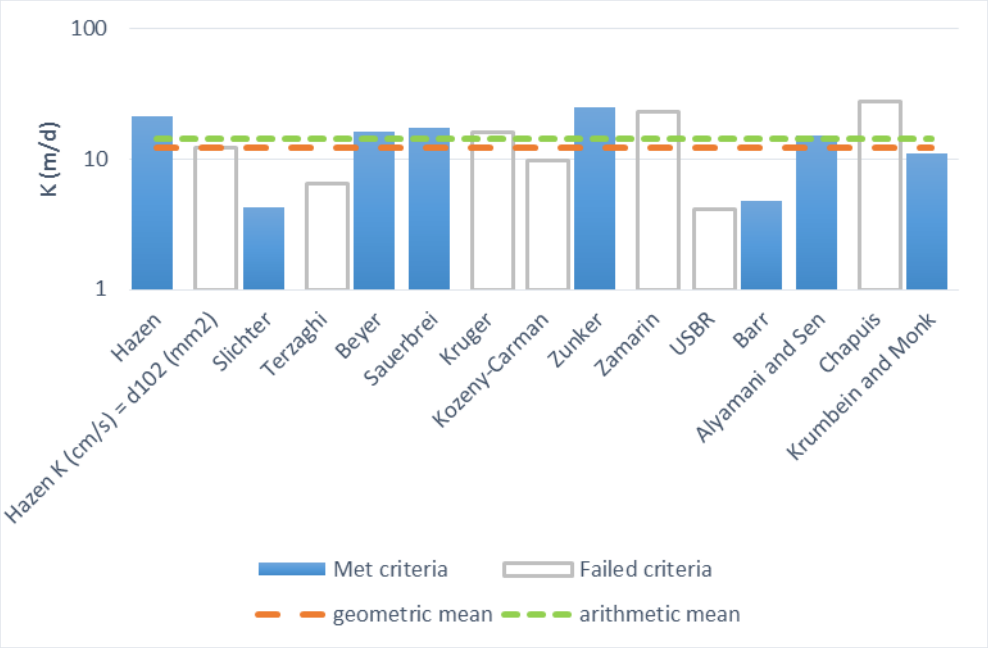
Effective Grain Diameters (mm)		Other Useful Parameters	
d10	0.119	Uniformity Coef.	1.50
d17	0.131	n computed	0.45
d20	0.135	g (cm/s^2)	980.00
d50	0.168	ρ (g/cm^3)	0.9981
d60	0.179	μ (g/cm s)	0.0098
de (Kruger)	0.172	ρg/μ (1/cm s)	9.9327E+04
de (Kozeny)	0.166	tau (Sauerbrei)	1.053
de (Zunker)	0.168	$d_{geometric\ mean}$	0.181
de (Zamarin)	0.170	σ_ϕ	0.494
Io (Alyameni	0.107		

mm	0	% in sample
>64	Boulder	
16 - 64	coarse gravel	
8 - 16	medium gravel	
2 - 8	fine gravel	0.017417051
0.5 - 2	coarse sand	1.314987373
0.25 - 0.5	medium sand	10.4937734
0.063 - 0.25	fine sand	86.30148916
0.016 - 0.063	coarse silt	
0.008 - 0.016	medium silt	
0.002 - 0.008	fine silt	
<0.002	clay	

Slichter, Terzaghi, Kozeny-Carman and Barr with d_{VS}:



Slichter, Terzaghi, Kozeny-Carman and Barr with d_{UU}:

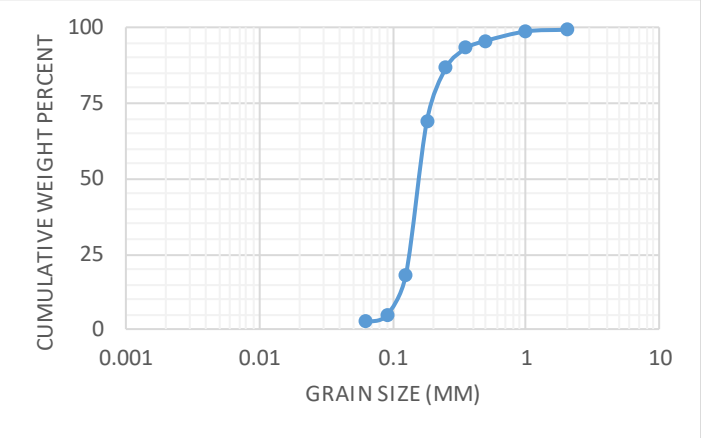


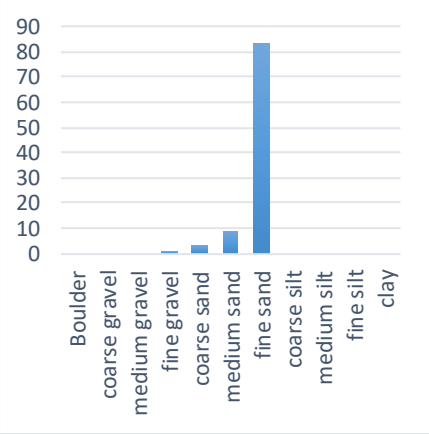
Well 040610/1-T4. Elevation 0.125 m AHD.

Grain Size Analysis Report

Mass Sample (g): 100 T (oC) 20

Uniform sand low in fines



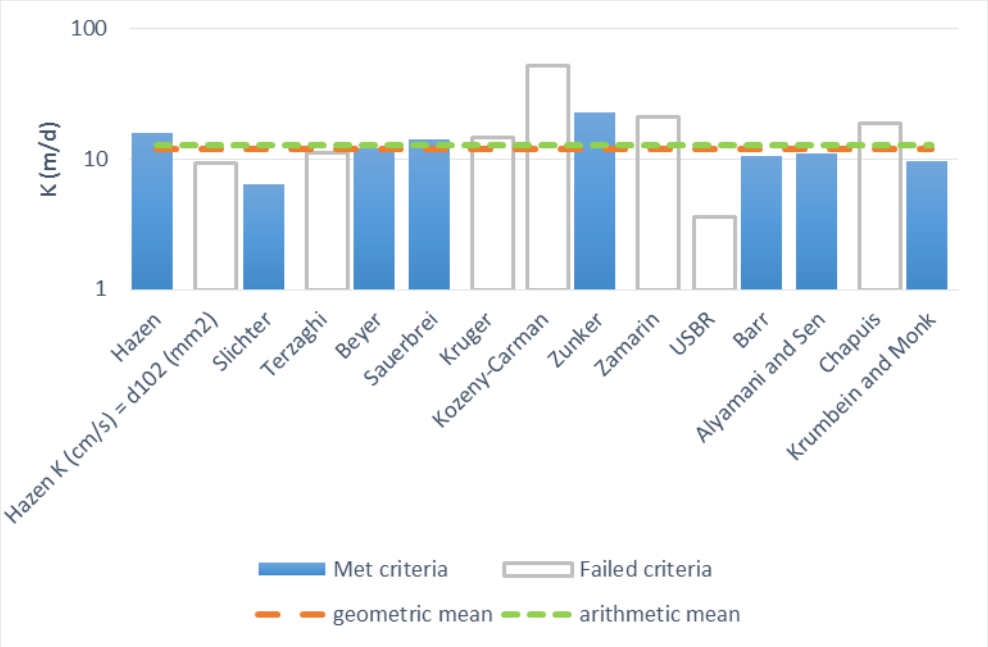


Sieve opening (ps) di (mm)	Mass of retained (mr) (g)	mass fraction (mf)	Percent Passing (pp)
2	0.69414	0.00694	99.3059
1	0.53395	0.00534	98.7719
0.5	3.10581	0.03106	95.6661
0.355	2.49177	0.02492	93.1743
0.25	6.52309	0.06523	86.6512
0.18	17.5047	0.17505	69.1466
0.125	51.1257	0.51126	18.0208
0.09	13.2776	0.13278	4.74326
0.063	2.1002	0.021	2.64305

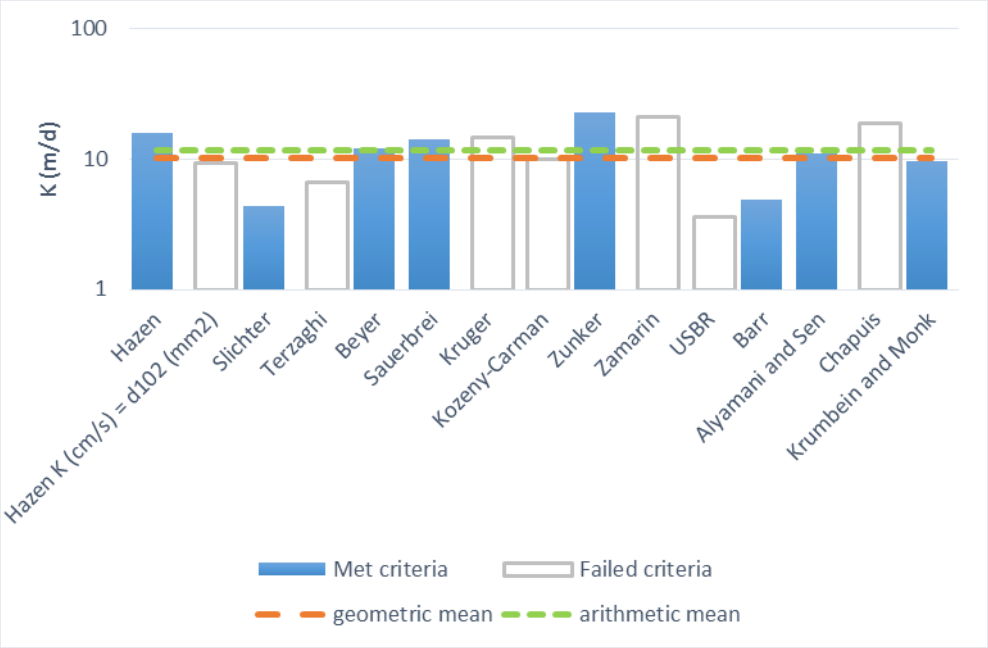
Effective Grain Diameters (mm)		Other Useful Parameters	
d10	0.104	Uniformity Coef.	1.64
d17	0.122	n computed	0.44
d20	0.127	g (cm/s^2)	980.00
d50	0.159	ρ (g/cm^3)	0.9981
d60	0.170	μ (g/cm s)	0.0098
de (Kruger)	0.167	ρg/μ (1/cm s)	9.9327E+04
de (Kozeny)	0.162	tau (Sauerbrei)	1.053
de (Zunker)	0.163	$d_{geometric\ mean}$	0.182
de (Zamarin)	0.165	σ_ϕ	0.606
Io (Alyameni	0.090		

mm	0	% in sample
>64	Boulder	
16 - 64	coarse gravel	
8 - 16	medium gravel	
2 - 8	fine gravel	0.694135445
0.5 - 2	coarse sand	3.639761502
0.25 - 0.5	medium sand	9.014861618
0.063 - 0.25	fine sand	84.00818724
0.016 - 0.063	coarse silt	
0.008 - 0.016	medium silt	
0.002 - 0.008	fine silt	
<0.002	clay	

Slichter, Terzaghi, Kozeny-Carman and Barr with d_{VS}:



Slichter, Terzaghi, Kozeny-Carman and Barr with d_{UU}:

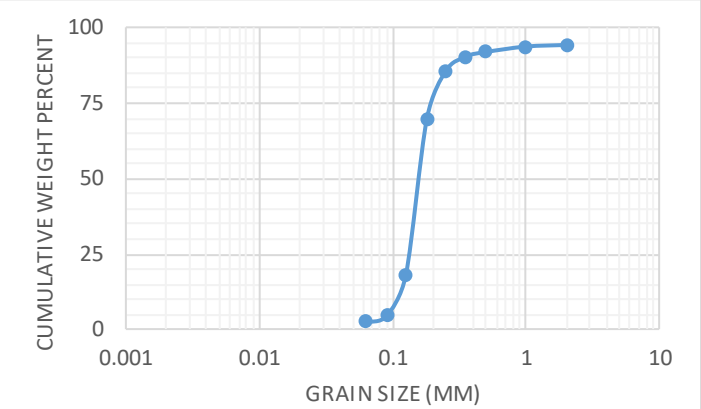


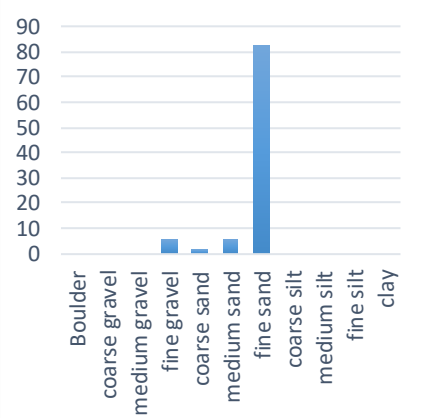
Well 040610/1-T4. Elevation 0.075 m AHD.

Grain Size Analysis Report

Mass Sample (g): 100 T (oC) 20

Uniform sand low in fines



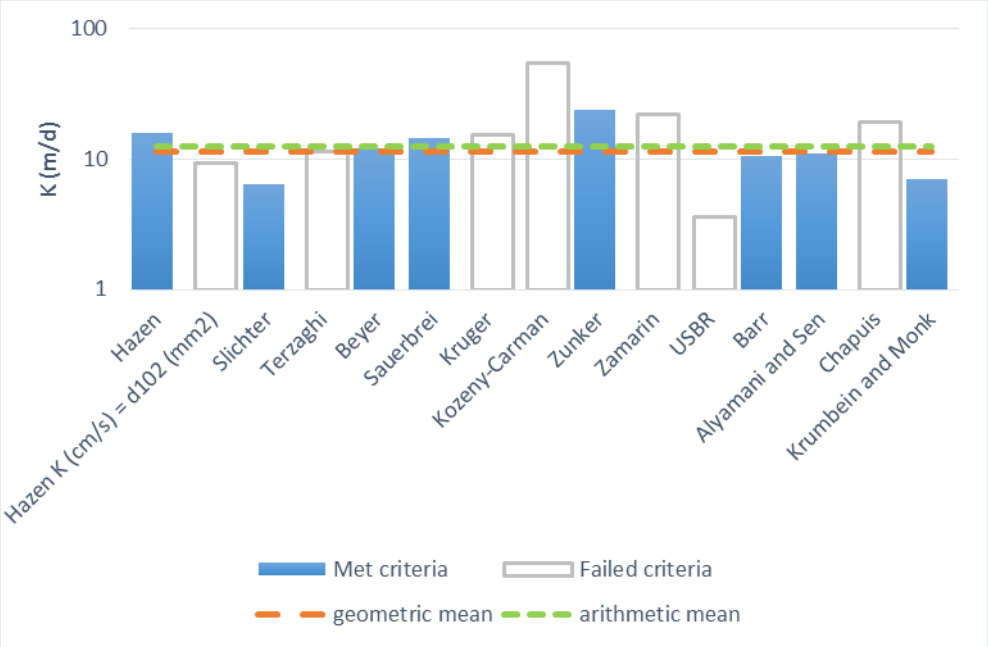


Sieve opening (ps) di (mm)	Mass of retained (mr) (g)	mass fraction (mf)	Percent Passing (pp)
2	5.72452	0.05725	94.2755
1	0.52438	0.00524	93.7511
0.5	1.80912	0.01809	91.942
0.355	1.49449	0.01494	90.4475
0.25	4.71071	0.04711	85.7368
0.18	15.8189	0.15819	69.9178
0.125	51.914	0.51914	18.0038
0.09	13.433	0.13433	4.57088
0.063	2.01014	0.0201	2.56074

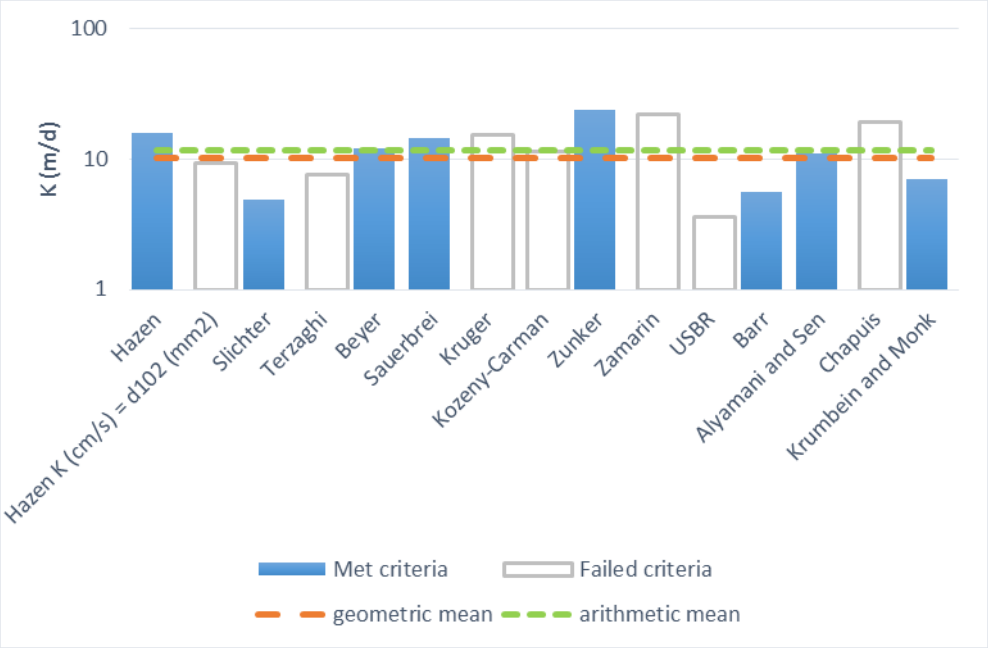
Effective Grain Diameters (mm)		Other Useful Parameters	
d10	0.104	Uniformity Coef.	1.63
d17	0.122	n computed	0.44
d20	0.127	g (cm/s^2)	980.00
d50	0.159	ρ (g/cm^3)	0.9981
d60	0.169	μ (g/cm s)	0.0098
de (Kruger)	0.170	ρg/μ (1/cm s)	9.9327E+04
de (Kozeny)	0.165	tau (Sauerbrei)	1.053
de (Zunker)	0.167	$d_{geometric\ mean}$	0.191
de (Zamarin)	0.169	σ_ϕ	0.931
Io (Alyameni	0.090		

mm	0	% in sample
>64	Boulder	
16 - 64	coarse gravel	
8 - 16	medium gravel	
2 - 8	fine gravel	5.724523685
0.5 - 2	coarse sand	2.333508128
0.25 - 0.5	medium sand	6.20520888
0.063 - 0.25	fine sand	83.17601818
0.016 - 0.063	coarse silt	
0.008 - 0.016	medium silt	
0.002 - 0.008	fine silt	
<0.002	clay	

Slichter, Terzaghi, Kozeny-Carman and Barr with d_{VS}:



Slichter, Terzaghi, Kozeny-Carman and Barr with d_{UU}:

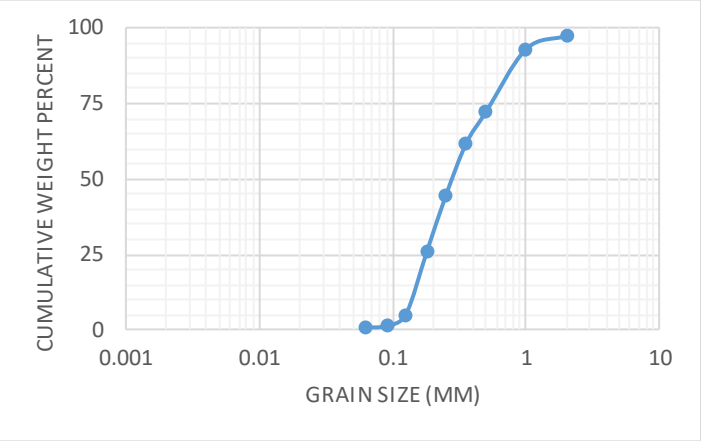


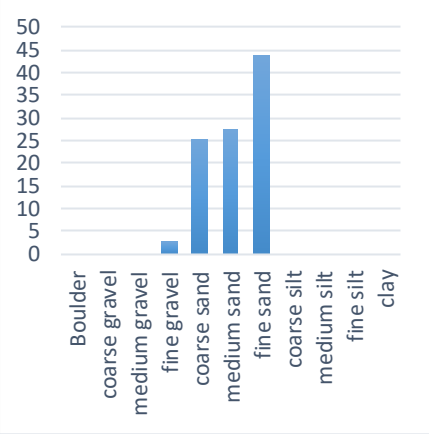
Well 040610/3-T4. Elevation 0.975 m AHD.

Grain Size Analysis Report

Mass Sample (g): 100 T (oC) 20

Moderately well sorted sand low in fines



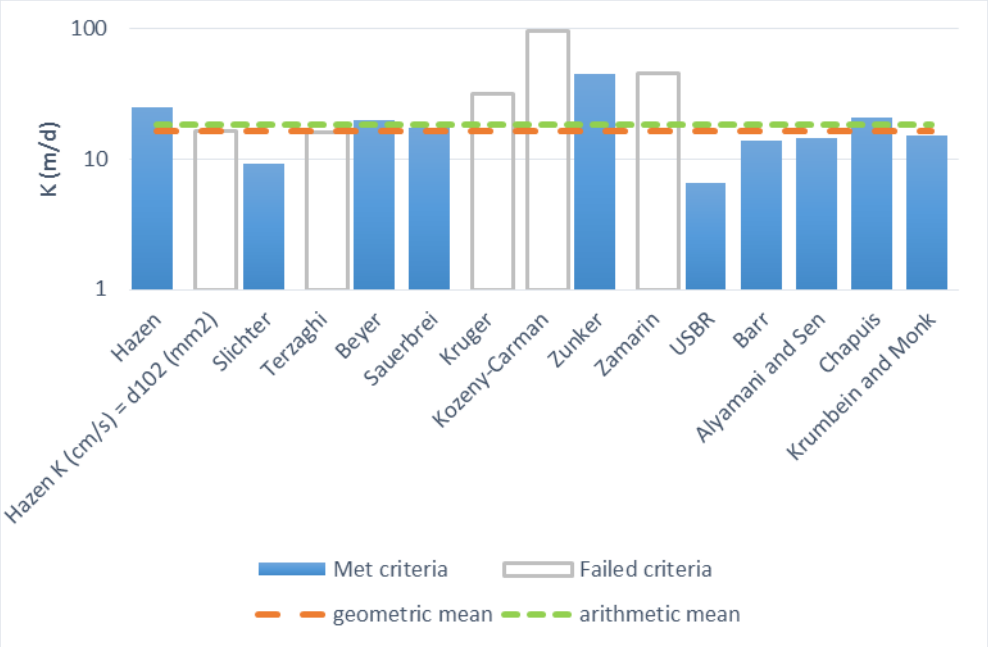


Sieve opening (ps) di (mm)	Mass of retained (mr) (g)	mass fraction (mf)	Percent Passing (pp)
2	2.64706	0.02647	97.3529
1	4.32353	0.04324	93.0294
0.5	20.8235	0.20824	72.2059
0.355	10.4118	0.10412	61.7941
0.25	17.2255	0.17225	44.5686
0.18	18.5882	0.18588	25.9804
0.125	20.8922	0.20892	5.08824
0.09	3.77451	0.03775	1.31373
0.063	0.48039	0.0048	0.83333

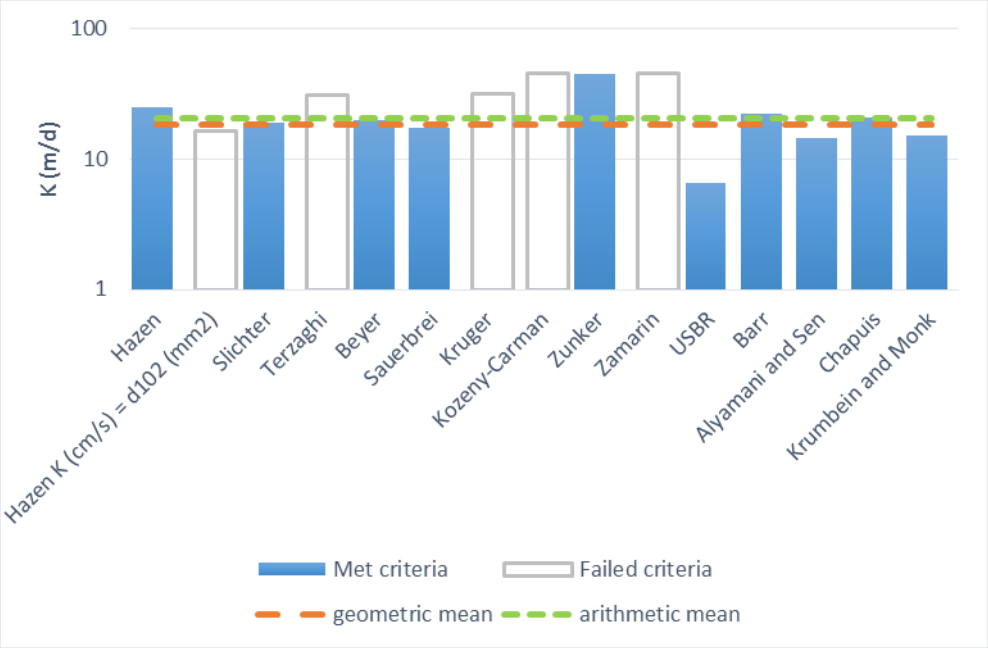
Effective Grain Diameters (mm)		Other Useful Parameters	
d10	0.138	Uniformity Coef.	2.49
d17	0.156	n computed	0.42
d20	0.164	g (cm/s^2)	980.00
d50	0.283	ρ (g/cm^3)	0.9981
d60	0.344	μ (g/cm s)	0.0098
de (Kruger)	0.265	ρg/μ (1/cm s)	9.9327E+04
de (Kozeny)	0.256	tau (Sauerbrei)	1.053
de (Zunker)	0.259	$d_{geometric\ mean}$	0.321
de (Zamarin)	0.262	σ_ϕ	1.125
Io (Alyameni	0.102		

mm	0	% in sample
>64	Boulder	
16 - 64	coarse gravel	
8 - 16	medium gravel	
2 - 8	fine gravel	2.647058824
0.5 - 2	coarse sand	25.14705882
0.25 - 0.5	medium sand	27.6372549
0.063 - 0.25	fine sand	43.73529412
0.016 - 0.063	coarse silt	
0.008 - 0.016	medium silt	
0.002 - 0.008	fine silt	
<0.002	clay	

Slichter, Terzaghi, Kozeny-Carman and Barr with d_{VS}:



Slichter, Terzaghi, Kozeny-Carman and Barr with d_{UU}:

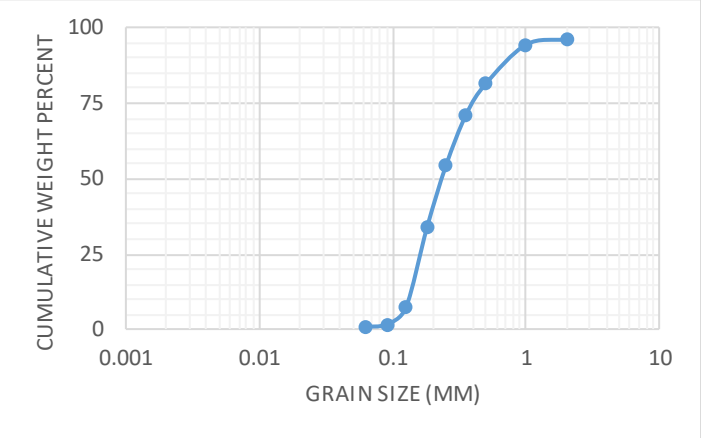


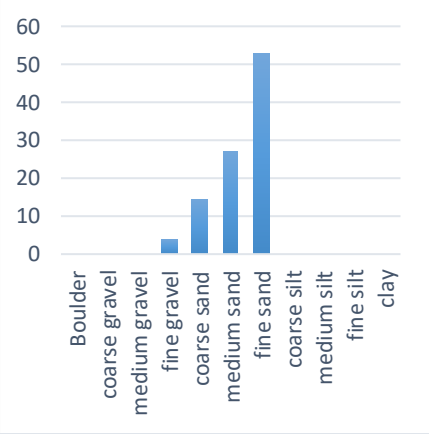
Well 040610/3-T4. Elevation 0.925 m AHD.

Grain Size Analysis Report

Mass Sample (g): 100 T (oC) 20

Moderately well sorted sand low in fines



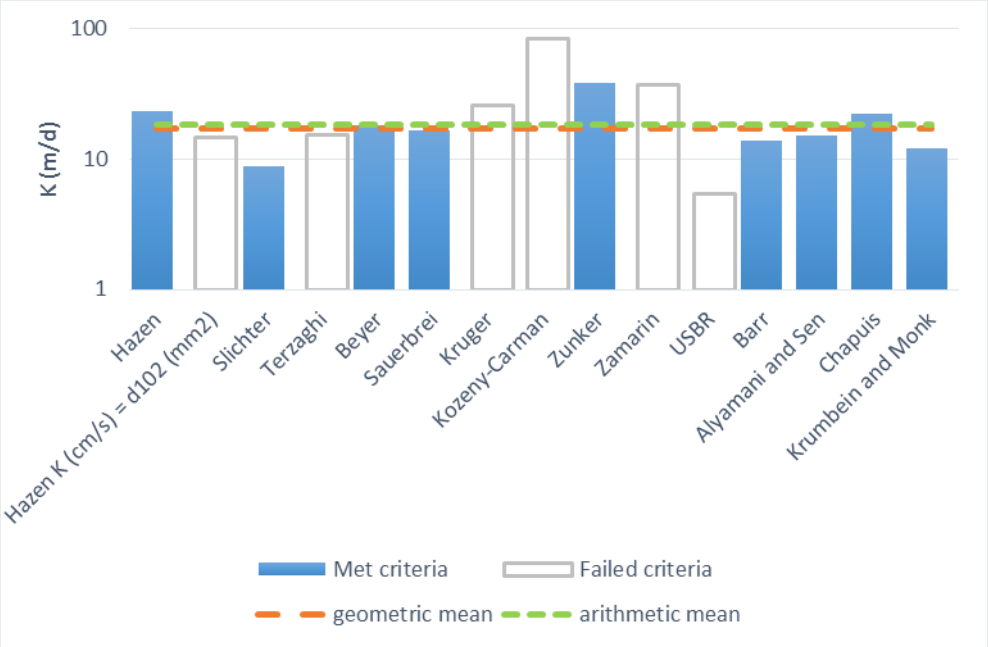


Sieve opening (ps) di (mm)	Mass of retained (mr) (g)	mass fraction (mf)	Percent Passing (pp)
2	3.85721	0.03857	96.1428
1	1.74517	0.01745	94.3976
0.5	12.8706	0.12871	81.527
0.355	10.2231	0.10223	71.3039
0.25	17.0154	0.17015	54.2885
0.18	20.5553	0.20555	33.7333
0.125	26.5245	0.26525	7.20873
0.09	5.46356	0.05464	1.74517
0.063	0.75359	0.00754	0.99157

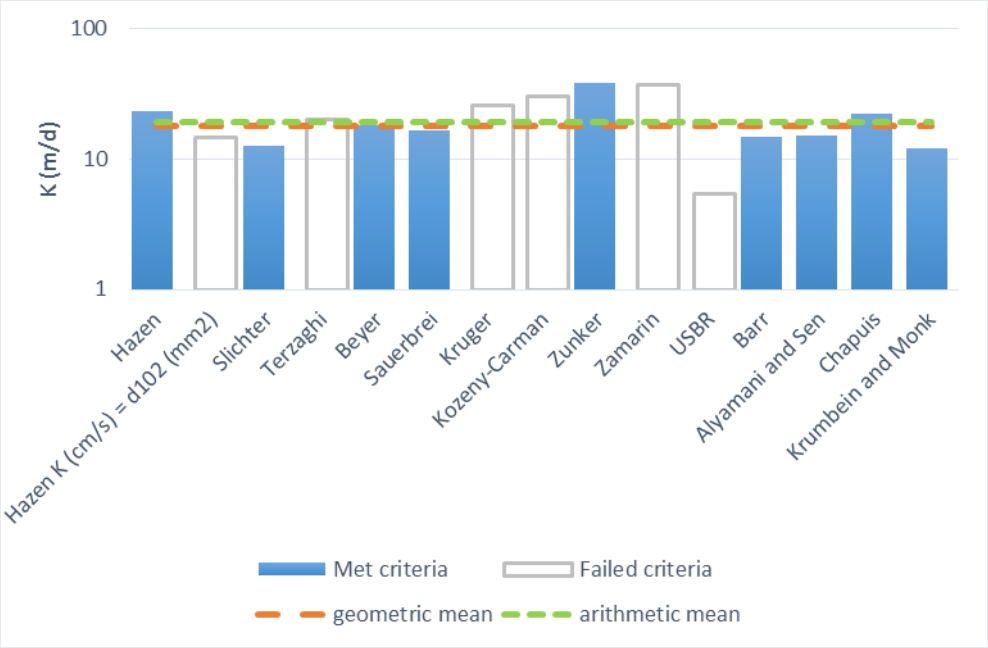
Effective Grain Diameters (mm)		Other Useful Parameters	
d10	0.131	Uniformity Coef.	2.18
d17	0.145	n computed	0.42
d20	0.152	g (cm/s^2)	980.00
d50	0.235	ρ (g/cm^3)	0.9981
d60	0.285	μ (g/cm s)	0.0098
de (Kruger)	0.233	ρg/μ (1/cm s)	9.9327E+04
de (Kozeny)	0.225	tau (Sauerbrei)	1.053
de (Zunker)	0.228	$d_{geometric\ mean}$	0.273
de (Zamarin)	0.231	σ_ϕ	1.060
Io (Alyameni	0.105		

mm	0	% in sample
>64	Boulder	
16 - 64	coarse gravel	
8 - 16	medium gravel	
2 - 8	fine gravel	3.857213684
0.5 - 2	coarse sand	14.61576599
0.25 - 0.5	medium sand	27.23847298
0.063 - 0.25	fine sand	53.29697571
0.016 - 0.063	coarse silt	
0.008 - 0.016	medium silt	
0.002 - 0.008	fine silt	
<0.002	clay	

Slichter, Terzaghi, Kozeny-Carman and Barr with d_{VS}:



Slichter, Terzaghi, Kozeny-Carman and Barr with d_{UU}:

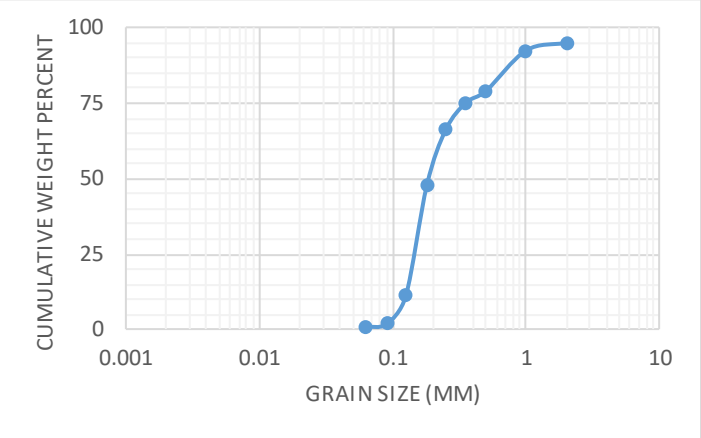


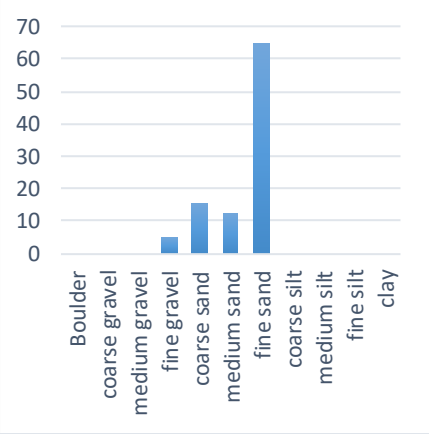
Well 040610/3-T4. Elevation 0.875 m AHD.

Grain Size Analysis Report

Mass Sample (g): 100 T (oC) 20

Uniform sand low in fines



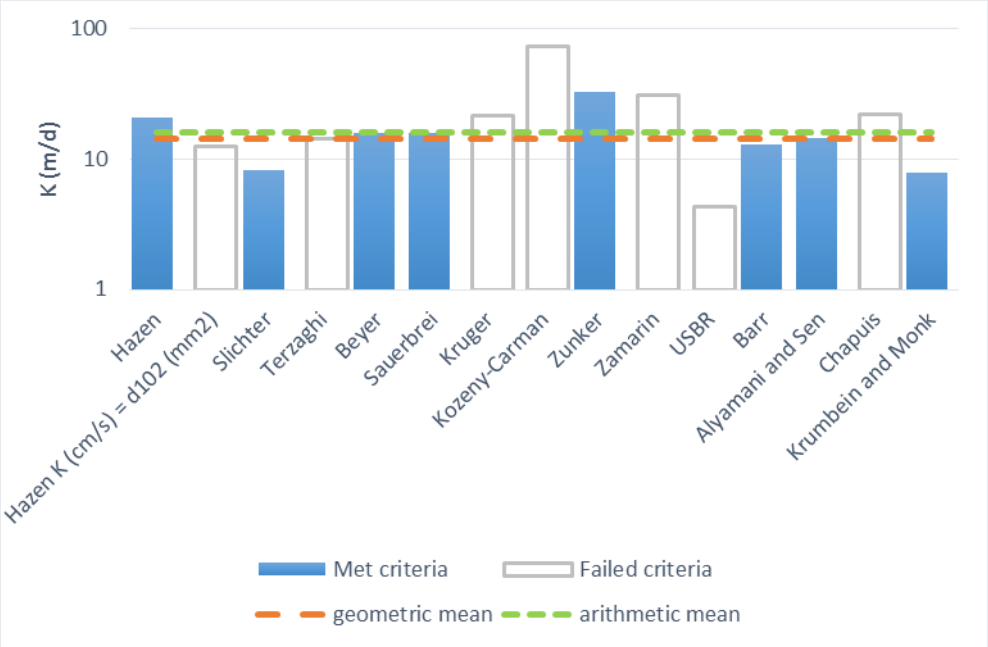


Sieve opening (ps) di (mm)	Mass of retained (mr) (g)	mass fraction (mf)	Percent Passing (pp)
2	5.02987	0.0503	94.9701
1	2.5053	0.02505	92.4648
0.5	13.413	0.13413	79.0518
0.355	3.81576	0.03816	75.2361
0.25	8.92272	0.08923	66.3134
0.18	18.4043	0.18404	47.909
0.125	36.7701	0.3677	11.1389
0.09	9.28888	0.09289	1.85007
0.063	0.85758	0.00858	0.99248

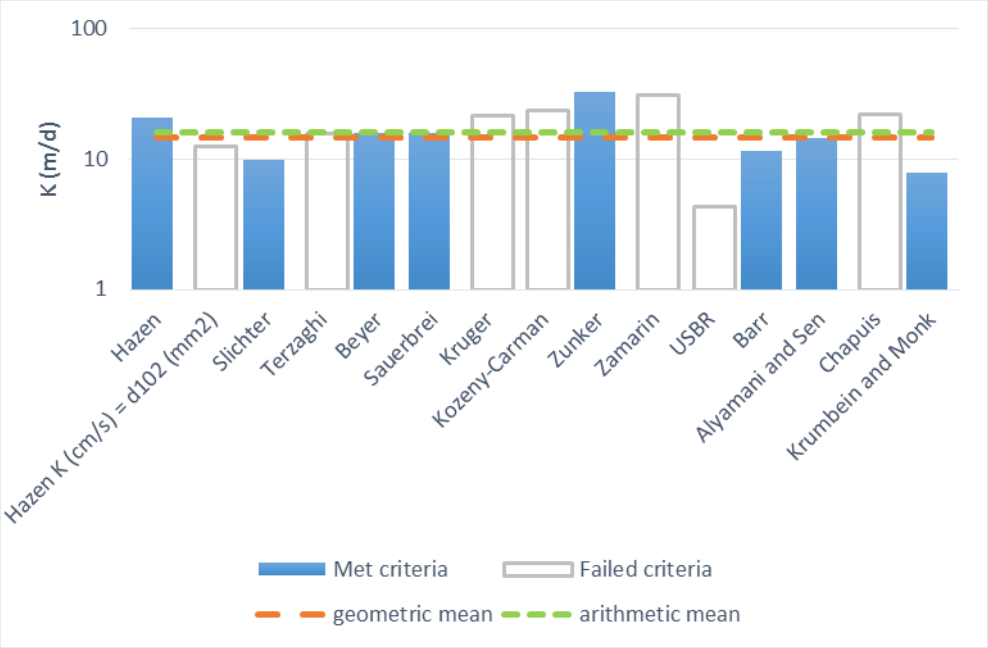
Effective Grain Diameters (mm)		Other Useful Parameters	
d10	0.121	Uniformity Coef.	1.87
d17	0.134	n computed	0.43
d20	0.138	g (cm/s^2)	980.00
d50	0.188	ρ (g/cm^3)	0.9981
d60	0.226	μ (g/cm s)	0.0098
de (Kruger)	0.207	ρg/μ (1/cm s)	9.9327E+04
de (Kozeny)	0.200	tau (Sauerbrei)	1.053
de (Zunker)	0.203	$d_{geometric\ mean}$	0.248
de (Zamarin)	0.205	σ_ϕ	1.244
Io (Alyameni	0.104		

mm	0	% in sample
>64	Boulder	
16 - 64	coarse gravel	
8 - 16	medium gravel	
2 - 8	fine gravel	5.029870881
0.5 - 2	coarse sand	15.91828869
0.25 - 0.5	medium sand	12.73848526
0.063 - 0.25	fine sand	65.32087107
0.016 - 0.063	coarse silt	
0.008 - 0.016	medium silt	
0.002 - 0.008	fine silt	
<0.002	clay	

Slichter, Terzaghi, Kozeny-Carman and Barr with d_{VS}:



Slichter, Terzaghi, Kozeny-Carman and Barr with d_{UU}:

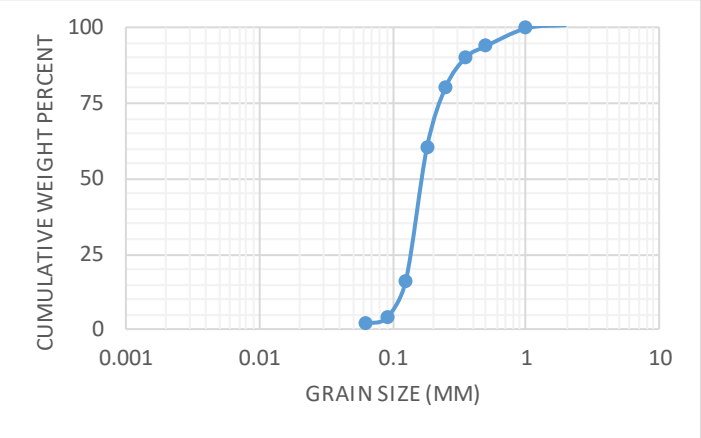


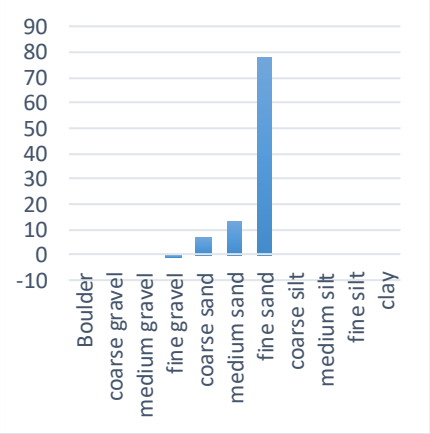
Well 040610/3-T4. Elevation 0.825 m AHD.

Grain Size Analysis Report

Mass Sample (g): 100 T (oC) 20

Uniform sand low in fines



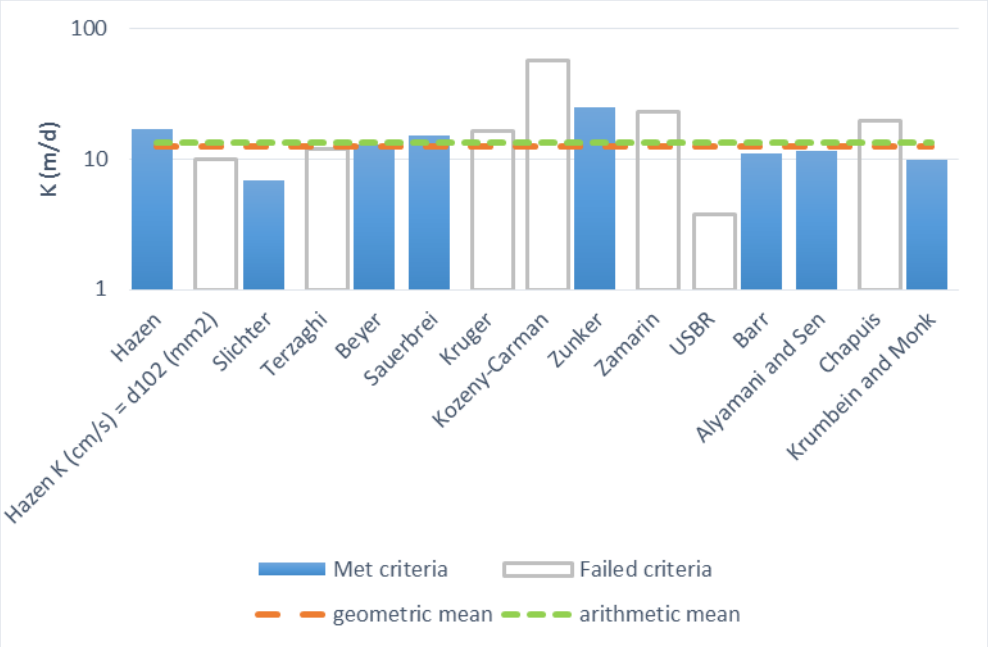


Sieve opening (ps) di (mm)	Mass of retained (mr) (g)	mass fraction (mf)	Percent Passing (pp)
2	-0.8567	-0.0086	100.857
1	1.06606	0.01066	99.7906
0.5	5.89187	0.05892	93.8987
0.355	3.67409	0.03674	90.2246
0.25	9.73729	0.09737	80.4873
0.18	20.2265	0.20227	60.2608
0.125	44.1081	0.44108	16.1527
0.09	12.2406	0.12241	3.91205
0.063	1.68475	0.01685	2.2273

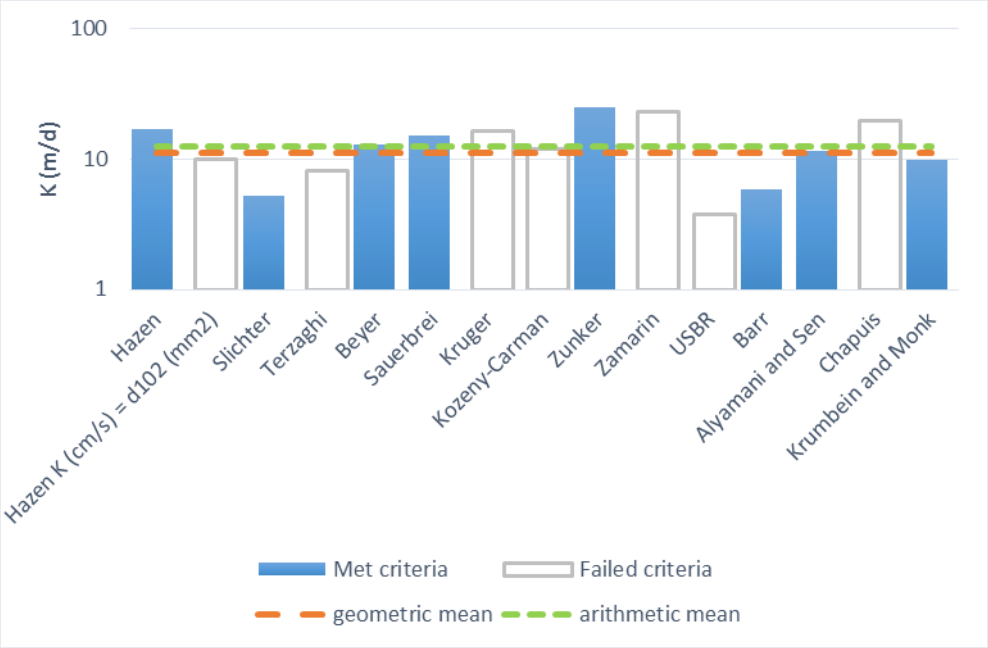
Effective Grain Diameters (mm)		Other Useful Parameters	
d10	0.107	Uniformity Coef.	1.67
d17	0.126	n computed	0.44
d20	0.130	g (cm/s^2)	980.00
d50	0.167	ρ (g/cm^3)	0.9981
d60	0.180	μ (g/cm s)	0.0098
de (Kruger)	0.176	ρg/μ (1/cm s)	9.9327E+04
de (Kozeny)	0.170	tau (Sauerbrei)	1.053
de (Zunker)	0.172	$d_{geometric\ mean}$	0.195
de (Zamarin)	0.174	σ_ϕ	0.707
Io (Alyameni	0.092		

mm	0	% in sample
>64	Boulder	
16 - 64	coarse gravel	
8 - 16	medium gravel	
2 - 8	fine gravel	-0.856653341
0.5 - 2	coarse sand	6.957928803
0.25 - 0.5	medium sand	13.41138397
0.063 - 0.25	fine sand	78.26004188
0.016 - 0.063	coarse silt	
0.008 - 0.016	medium silt	
0.002 - 0.008	fine silt	
<0.002	clay	

Slichter, Terzaghi, Kozeny-Carman and Barr with d_{VS}:



Slichter, Terzaghi, Kozeny-Carman and Barr with d_{UU}:

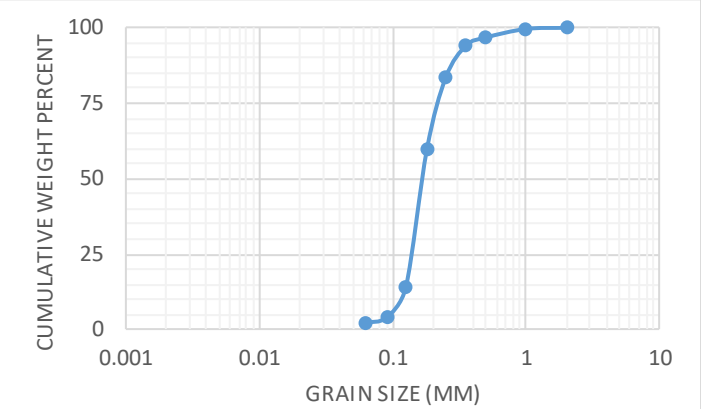


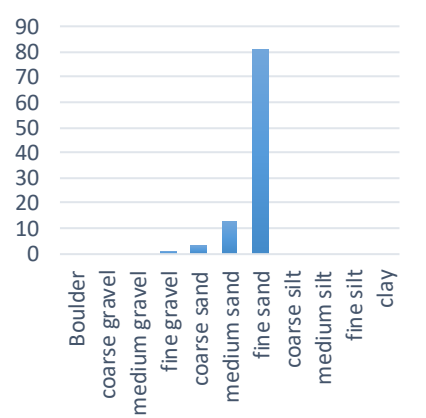
Well 040610/3-T4. Elevation 0.775 m AHD.

Grain Size Analysis Report

Mass Sample (g): 100 T (oC) 20

Uniform sand low in fines



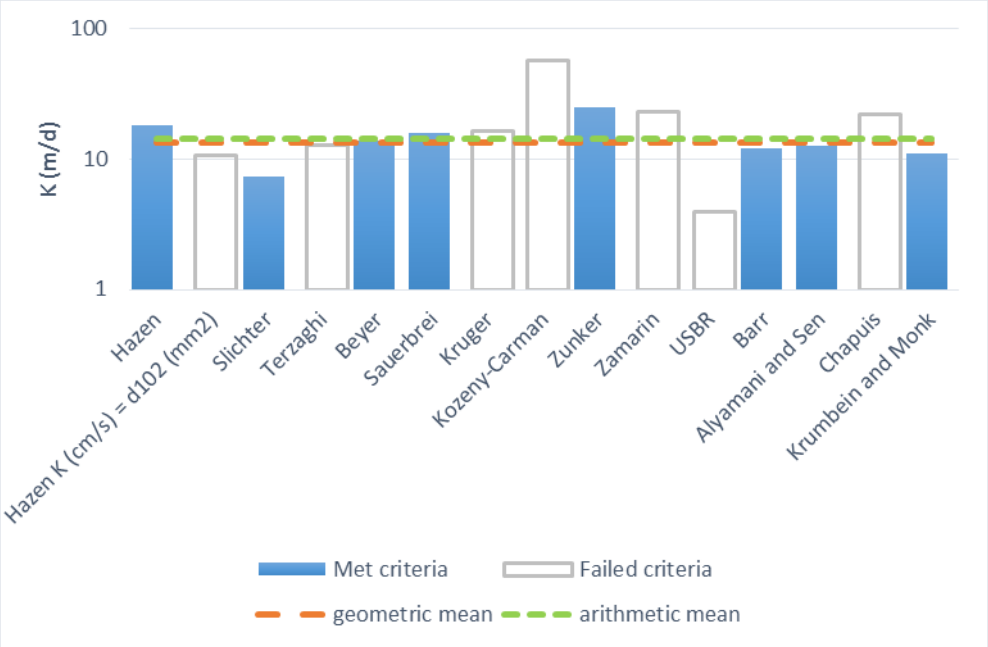


Sieve opening (ps) di (mm)	Mass of retained (mr) (g)	mass fraction (mf)	Percent Passing (pp)
2	0.03981	0.0004	99.9602
1	0.37818	0.00378	99.582
0.5	2.82643	0.02826	96.7556
0.355	2.64729	0.02647	94.1083
0.25	10.4797	0.1048	83.6286
0.18	23.8854	0.23885	59.7432
0.125	45.7604	0.4576	13.9829
0.09	9.96218	0.09962	4.0207
0.063	1.66202	0.01662	2.35868

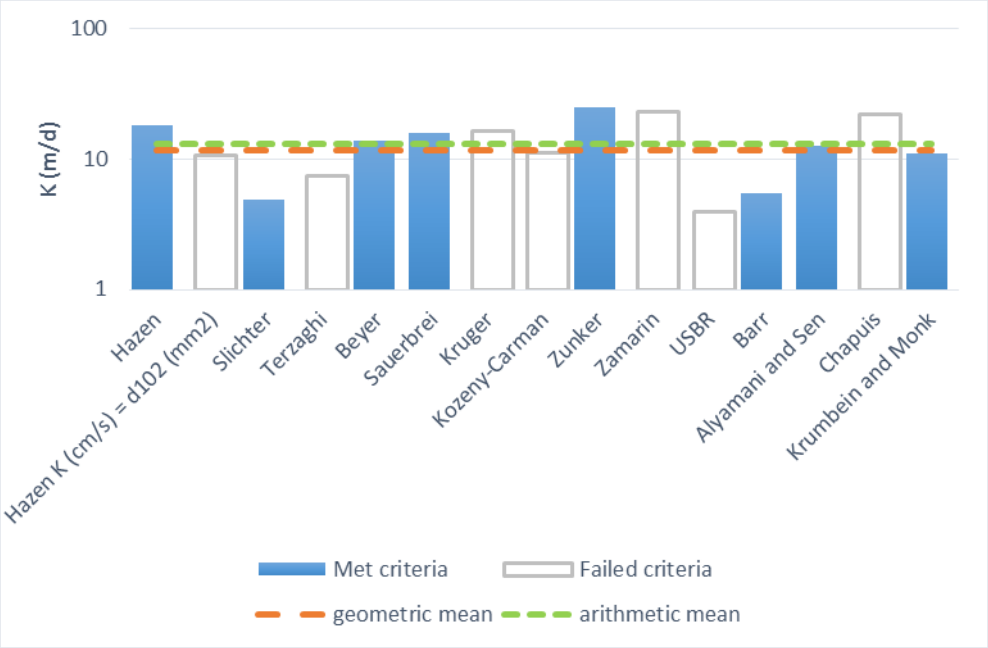
Effective Grain Diameters (mm)		Other Useful Parameters	
d10	0.111	Uniformity Coef.	1.63
d17	0.129	n computed	0.44
d20	0.132	g (cm/s^2)	980.00
d50	0.168	ρ (g/cm^3)	0.9981
d60	0.181	μ (g/cm s)	0.0098
de (Kruger)	0.175	ρg/μ (1/cm s)	9.9327E+04
de (Kozeny)	0.170	tau (Sauerbrei)	1.053
de (Zunker)	0.172	$d_{geometric\ mean}$	0.190
de (Zamarin)	0.174	σ_ϕ	0.568
Io (Alyameni	0.097		

mm	0	% in sample
>64	Boulder	
16 - 64	coarse gravel	
8 - 16	medium gravel	
2 - 8	fine gravel	0.039808917
0.5 - 2	coarse sand	3.204617834
0.25 - 0.5	medium sand	13.12699045
0.063 - 0.25	fine sand	81.26990446
0.016 - 0.063	coarse silt	
0.008 - 0.016	medium silt	
0.002 - 0.008	fine silt	
<0.002	clay	

Slichter, Terzaghi, Kozeny-Carman and Barr with d_{VS}:



Slichter, Terzaghi, Kozeny-Carman and Barr with d_{UU}:

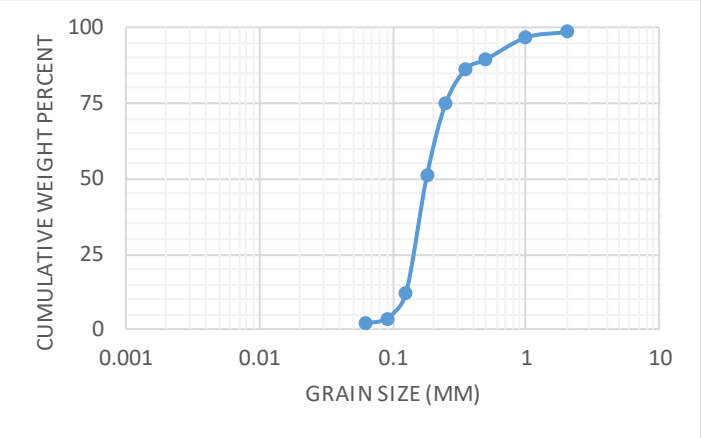


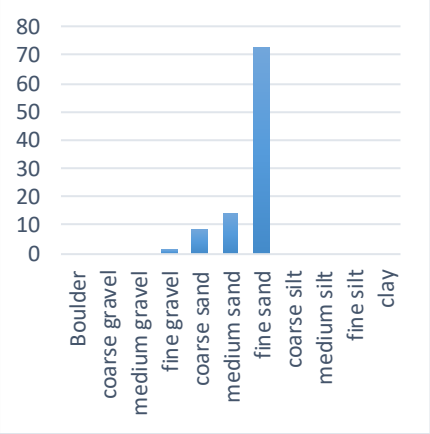
Well 040610/3-T4. Elevation 0.725 m AHD.

Grain Size Analysis Report

Mass Sample (g): 100 T (oC) 20

Uniform sand low in fines



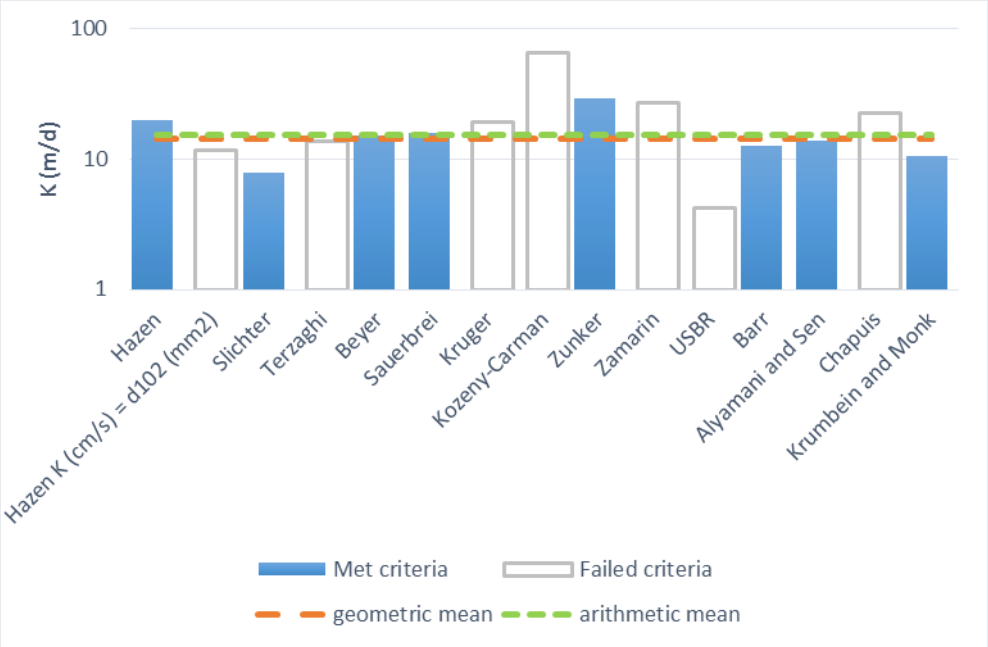


Sieve opening (ps) di (mm)	Mass of retained (mr) (g)	mass fraction (mf)	Percent Passing (pp)
2	1.48717	0.01487	98.5128
1	1.74961	0.0175	96.7632
0.5	7.25117	0.07251	89.5121
0.355	3.17846	0.03178	86.3336
0.25	11.217	0.11217	75.1166
0.18	24.0766	0.24077	51.04
0.125	39.2205	0.3922	11.8196
0.09	8.06765	0.08068	3.75194
0.063	1.55521	0.01555	2.19673

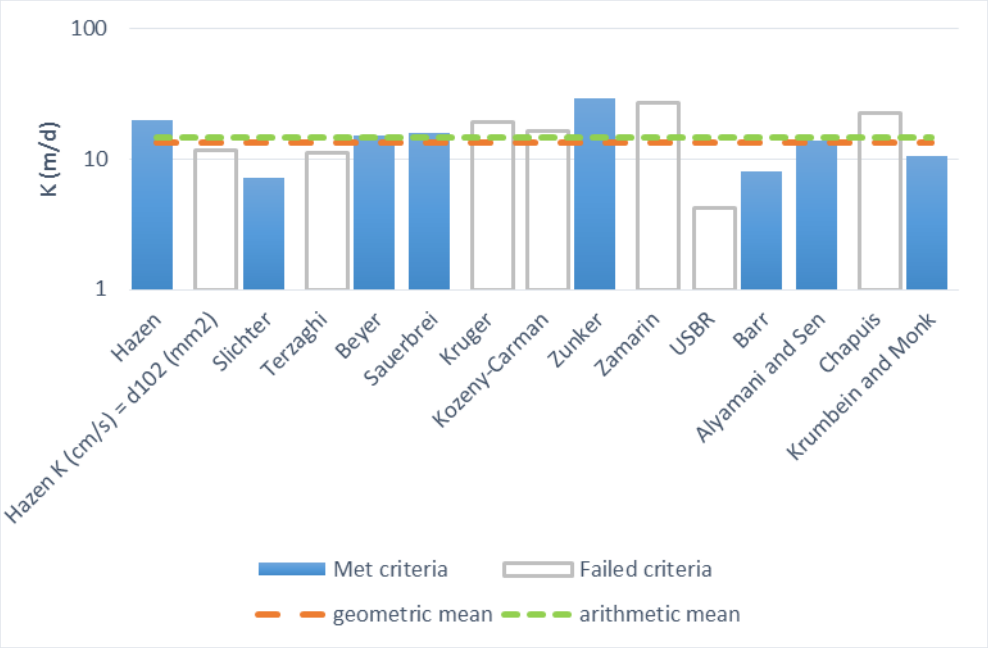
Effective Grain Diameters (mm)		Other Useful Parameters	
d10	0.117	Uniformity Coef.	1.76
d17	0.132	n computed	0.44
d20	0.136	g (cm/s^2)	980.00
d50	0.179	ρ (g/cm^3)	0.9981
d60	0.206	μ (g/cm s)	0.0098
de (Kruger)	0.192	ρg/μ (1/cm s)	9.9327E+04
de (Kozeny)	0.186	tau (Sauerbrei)	1.053
de (Zunker)	0.188	$d_{geometric\ mean}$	0.218
de (Zamarin)	0.190	σ_ϕ	0.822
Io (Alyameni	0.102		

mm	0	% in sample
>64	Boulder	
16 - 64	coarse gravel	
8 - 16	medium gravel	
2 - 8	fine gravel	1.487169518
0.5 - 2	coarse sand	9.000777605
0.25 - 0.5	medium sand	14.39541213
0.063 - 0.25	fine sand	72.91990669
0.016 - 0.063	coarse silt	
0.008 - 0.016	medium silt	
0.002 - 0.008	fine silt	
<0.002	clay	

Slichter, Terzaghi, Kozeny-Carman and Barr with d_{VS}:



Slichter, Terzaghi, Kozeny-Carman and Barr with d_{UU}:

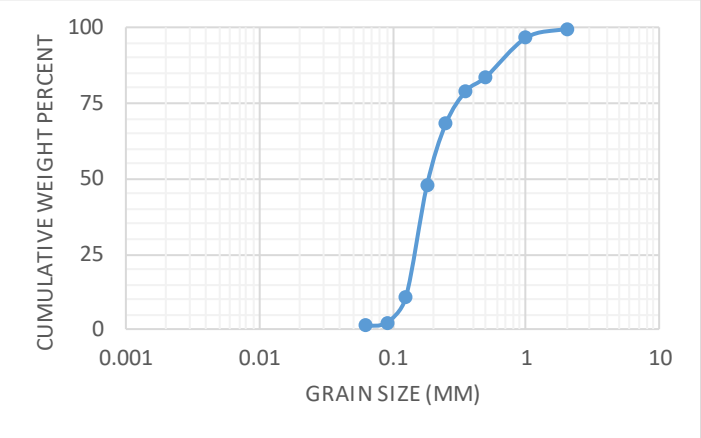


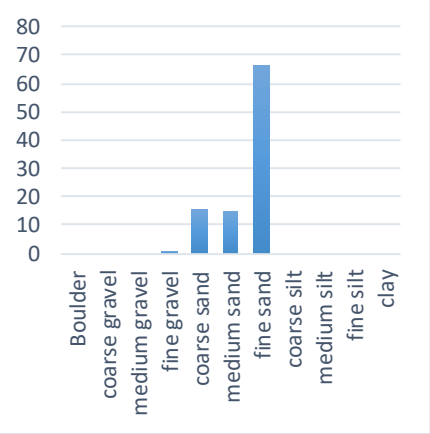
Well 040610/3-T4. Elevation 0.675 m AHD.

Grain Size Analysis Report

Mass Sample (g): 100 T (oC) 20

Uniform sand low in fines



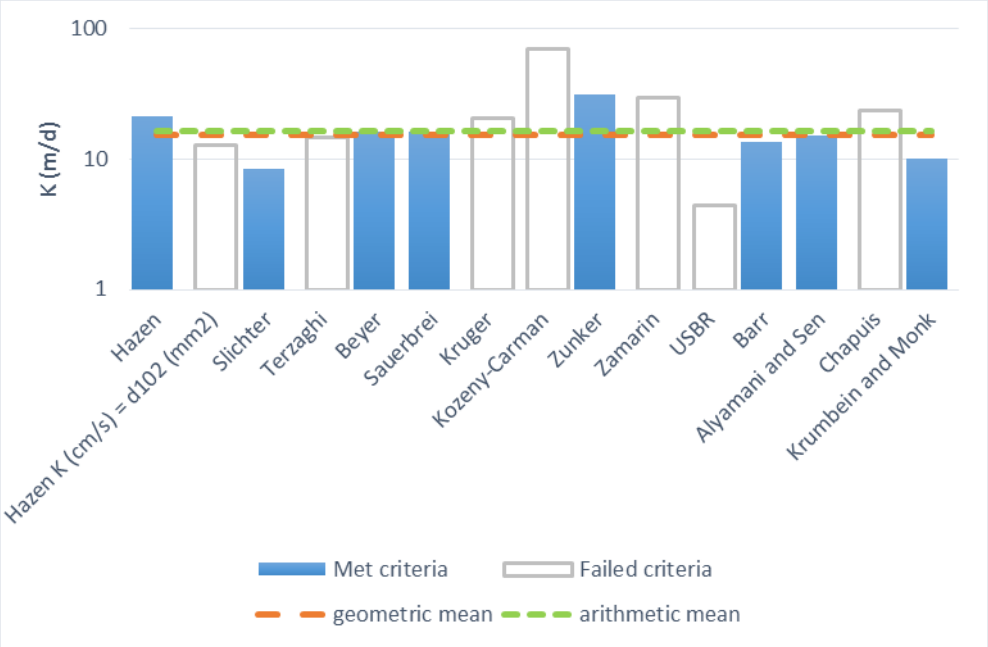


Sieve opening (ps) di (mm)	Mass of retained (mr) (g)	mass fraction (mf)	Percent Passing (pp)
2	0.37884	0.00379	99.6212
1	2.936	0.02936	96.6852
0.5	12.9752	0.12975	83.7099
0.355	4.60019	0.046	79.1097
0.25	10.8375	0.10838	68.2722
0.18	20.5385	0.20538	47.7337
0.125	37.0721	0.37072	10.6616
0.09	8.32093	0.08321	2.34068
0.063	1.09593	0.01096	1.24476

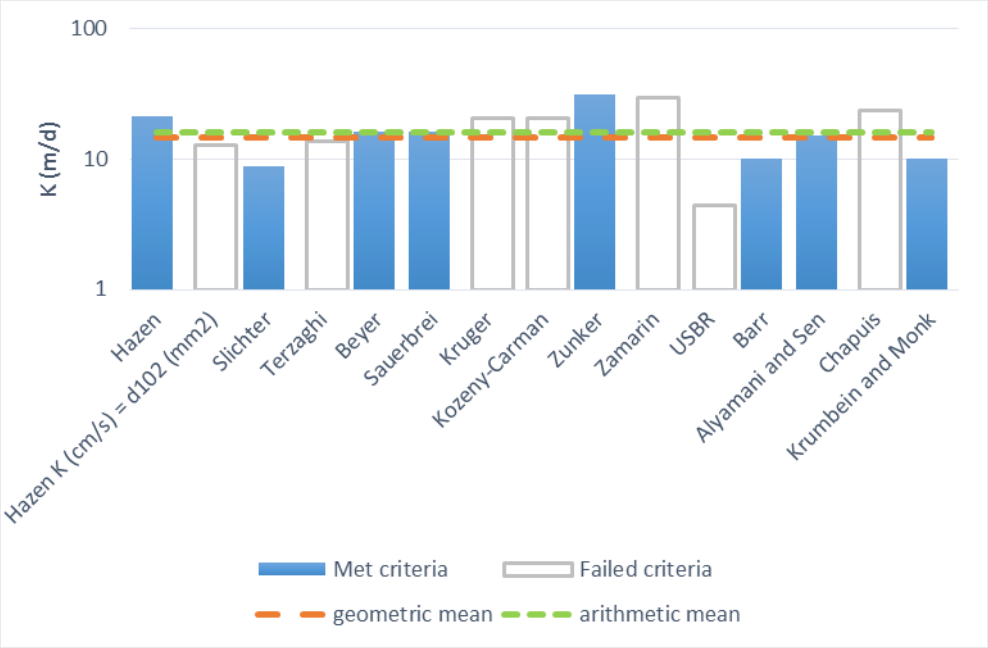
Effective Grain Diameters (mm)		Other Useful Parameters	
d10	0.122	Uniformity Coef.	1.81
d17	0.134	n computed	0.44
d20	0.139	g (cm/s^2)	980.00
d50	0.188	ρ (g/cm^3)	0.9981
d60	0.222	μ (g/cm s)	0.0098
de (Kruger)	0.202	ρg/μ (1/cm s)	9.9327E+04
de (Kozeny)	0.195	tau (Sauerbrei)	1.053
de (Zunker)	0.197	$d_{geometric\ mean}$	0.236
de (Zamarin)	0.199	σ_ϕ	0.972
Io (Alyameni	0.106		

mm	0	% in sample
>64	Boulder	
16 - 64	coarse gravel	
8 - 16	medium gravel	
2 - 8	fine gravel	0.378839129
0.5 - 2	coarse sand	15.9112434
0.25 - 0.5	medium sand	15.43769449
0.063 - 0.25	fine sand	67.02746584
0.016 - 0.063	coarse silt	
0.008 - 0.016	medium silt	
0.002 - 0.008	fine silt	
<0.002	clay	

Slichter, Terzaghi, Kozeny-Carman and Barr with d_{VS}:



Slichter, Terzaghi, Kozeny-Carman and Barr with d_{UU}:

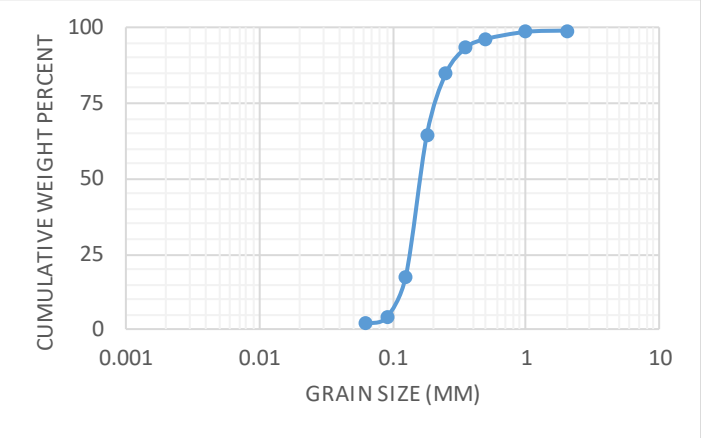


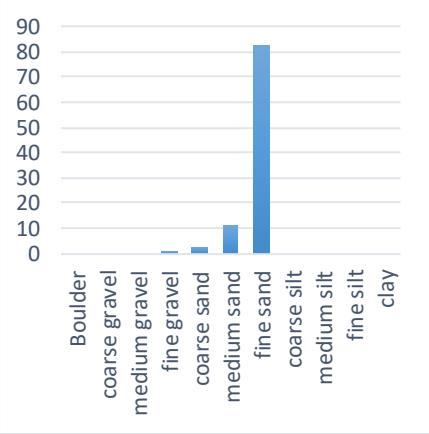
Well 040610/3-T4. Elevation 0.625 m AHD.

Grain Size Analysis Report

Mass Sample (g): 100 T (oC) 20

Uniform sand low in fines



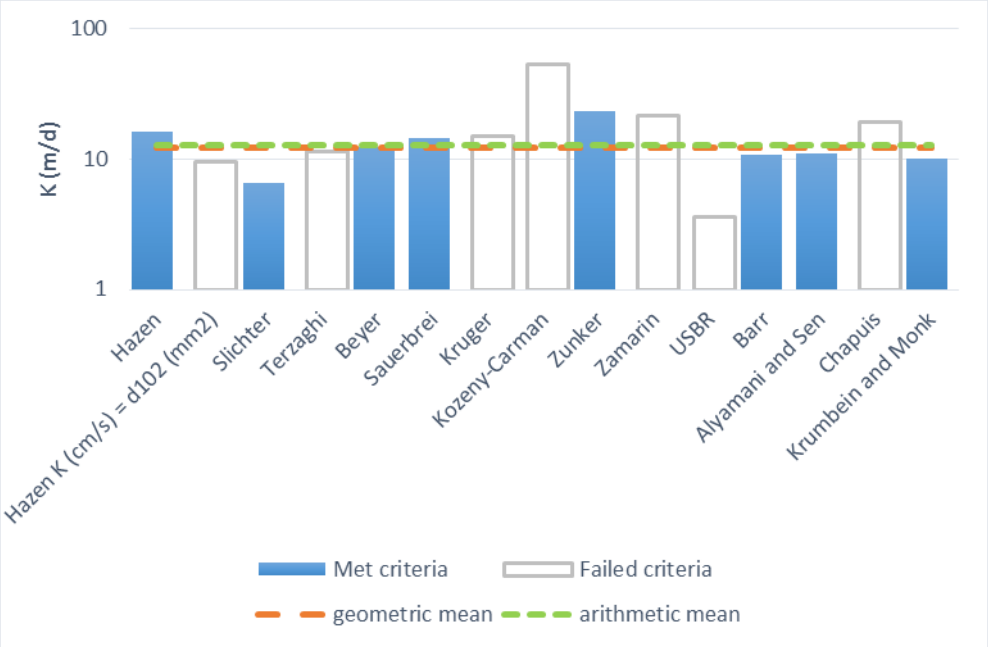


Sieve opening (ps) di (mm)	Mass of retained (mr) (g)	mass fraction (mf)	Percent Passing (pp)
2	0.95901	0.00959	99.041
1	0.42154	0.00422	98.6195
0.5	2.36063	0.02361	96.2588
0.355	2.85594	0.02856	93.4029
0.25	8.54674	0.08547	84.8561
0.18	20.234	0.20234	64.6222
0.125	46.9702	0.4697	17.652
0.09	13.5736	0.13574	4.07841
0.063	1.92855	0.01929	2.14986

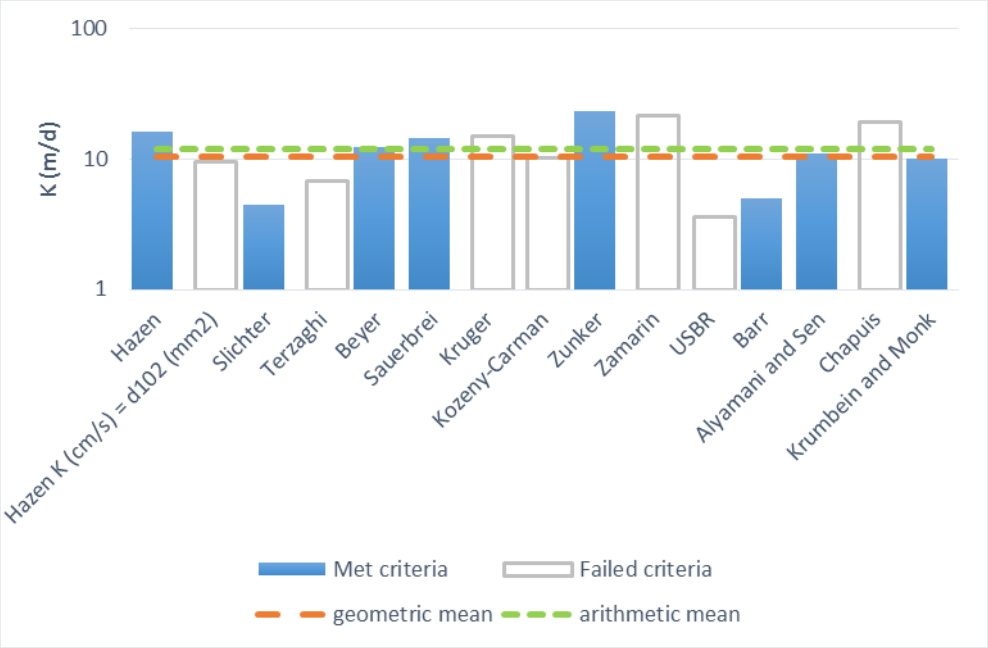
Effective Grain Diameters (mm)		Other Useful Parameters	
d10	0.105	Uniformity Coef.	1.66
d17	0.123	n computed	0.44
d20	0.128	g (cm/s^2)	980.00
d50	0.163	ρ (g/cm^3)	0.9981
d60	0.175	μ (g/cm s)	0.0098
de (Kruger)	0.169	ρg/μ (1/cm s)	9.9327E+04
de (Kozeny)	0.164	tau (Sauerbrei)	1.053
de (Zunker)	0.165	$d_{geometric\ mean}$	0.184
de (Zamarin)	0.167	σ_ϕ	0.597
Io (Alyameni	0.091		

mm	0	% in sample
>64	Boulder	
16 - 64	coarse gravel	
8 - 16	medium gravel	
2 - 8	fine gravel	0.959005164
0.5 - 2	coarse sand	2.782168827
0.25 - 0.5	medium sand	11.40267678
0.063 - 0.25	fine sand	82.7062915
0.016 - 0.063	coarse silt	
0.008 - 0.016	medium silt	
0.002 - 0.008	fine silt	
<0.002	clay	

Slichter, Terzaghi, Kozeny-Carman and Barr with d_{VS}:



Slichter, Terzaghi, Kozeny-Carman and Barr with d_{UU}:

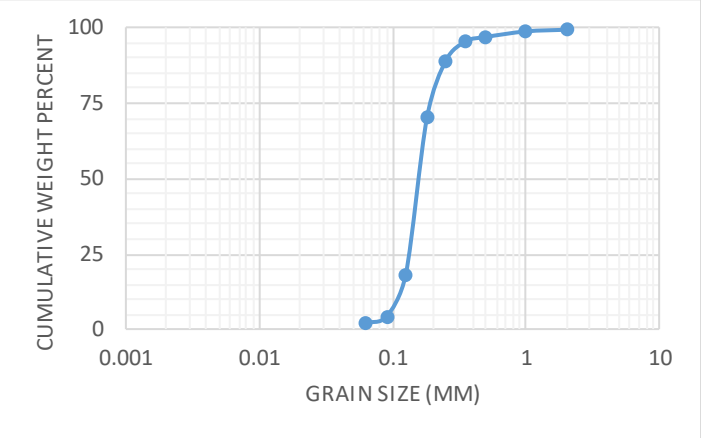


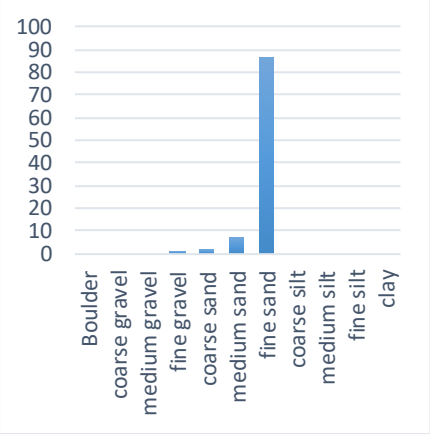
Well 040610/3-T4. Elevation 0.575 m AHD.

Grain Size Analysis Report

Mass Sample (g): 100 T (oC) 20

Uniform sand low in fines



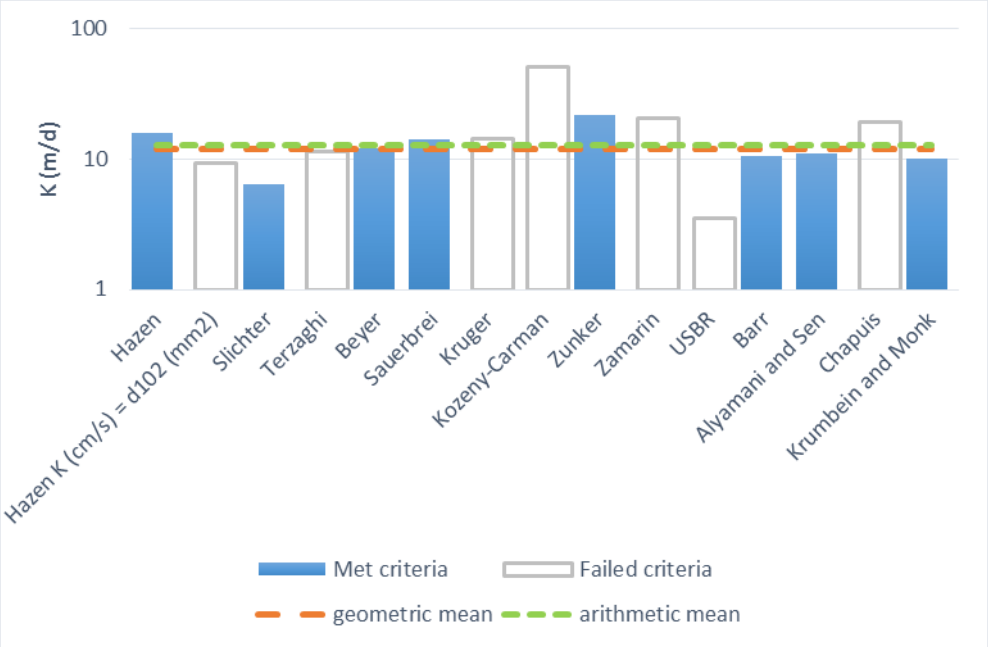


Sieve opening (ps) di (mm)	Mass of retained (mr) (g)	mass fraction (mf)	Percent Passing (pp)
2	0.68012	0.0068	99.3199
1	0.55543	0.00555	98.7645
0.5	1.83632	0.01836	96.9281
0.355	1.43958	0.0144	95.4886
0.25	6.3591	0.06359	89.1294
0.18	19.0093	0.19009	70.1202
0.125	51.8023	0.51802	18.3178
0.09	13.9538	0.13954	4.36409
0.063	1.89299	0.01893	2.47109

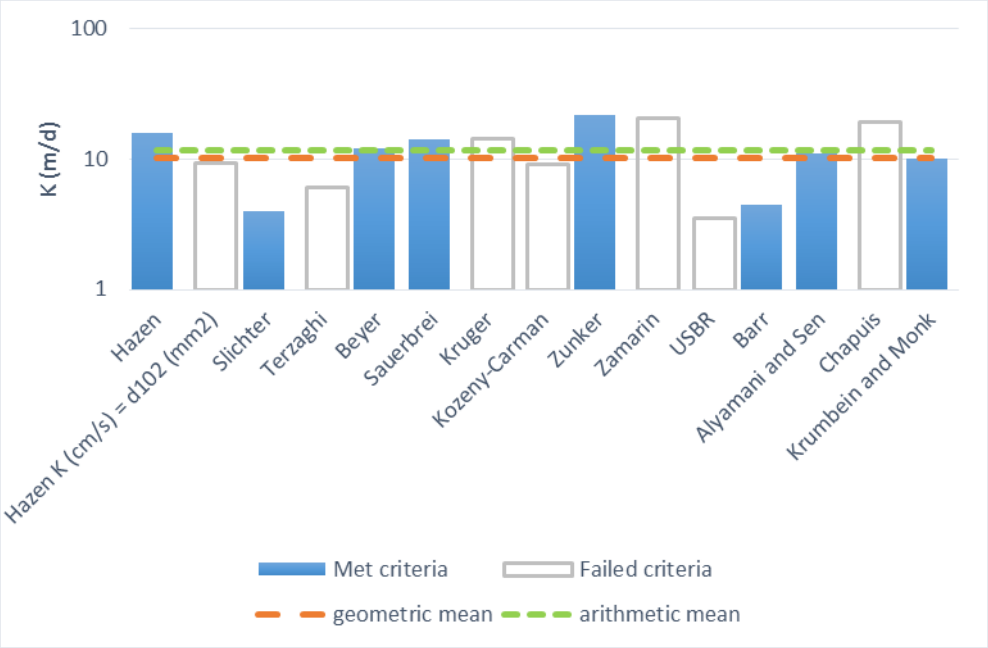
Effective Grain Diameters (mm)		Other Useful Parameters	
d10	0.104	Uniformity Coef.	1.63
d17	0.122	n computed	0.44
d20	0.127	g (cm/s^2)	980.00
d50	0.159	ρ (g/cm^3)	0.9981
d60	0.169	μ (g/cm s)	0.0098
de (Kruger)	0.164	ρg/μ (1/cm s)	9.9327E+04
de (Kozeny)	0.159	tau (Sauerbrei)	1.053
de (Zunker)	0.161	$d_{geometric\ mean}$	0.177
de (Zamarin)	0.162	σ_ϕ	0.530
Io (Alyameni	0.091		

mm	0	% in sample
>64	Boulder	
16 - 64	coarse gravel	
8 - 16	medium gravel	
2 - 8	fine gravel	0.680117887
0.5 - 2	coarse sand	2.391747903
0.25 - 0.5	medium sand	7.798685105
0.063 - 0.25	fine sand	86.65835411
0.016 - 0.063	coarse silt	
0.008 - 0.016	medium silt	
0.002 - 0.008	fine silt	
<0.002	clay	

Slichter, Terzaghi, Kozeny-Carman and Barr with d_{VS}:



Slichter, Terzaghi, Kozeny-Carman and Barr with d_{UU}:

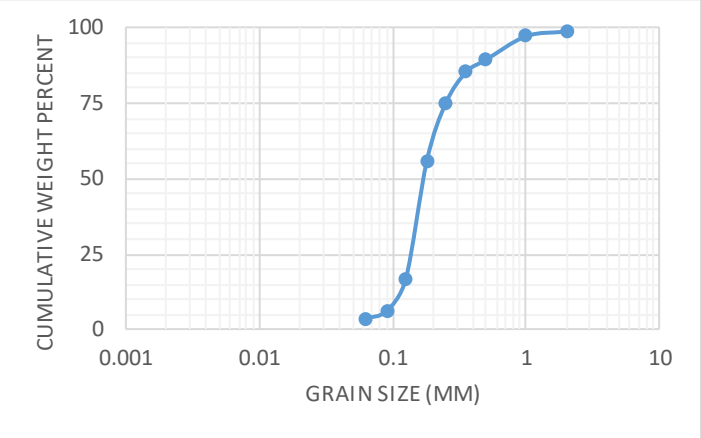


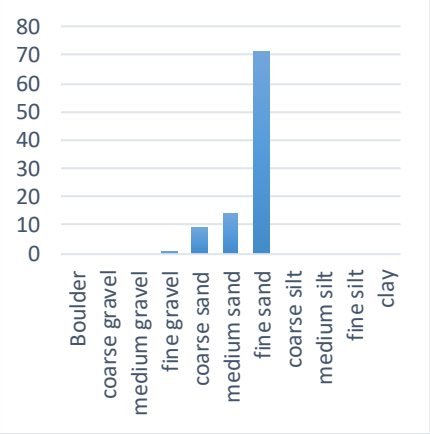
Well 040610/3-T4. Elevation 0.525 m AHD.

Grain Size Analysis Report

Mass Sample (g): 100 T (oC) 20

Uniform sand low in fines



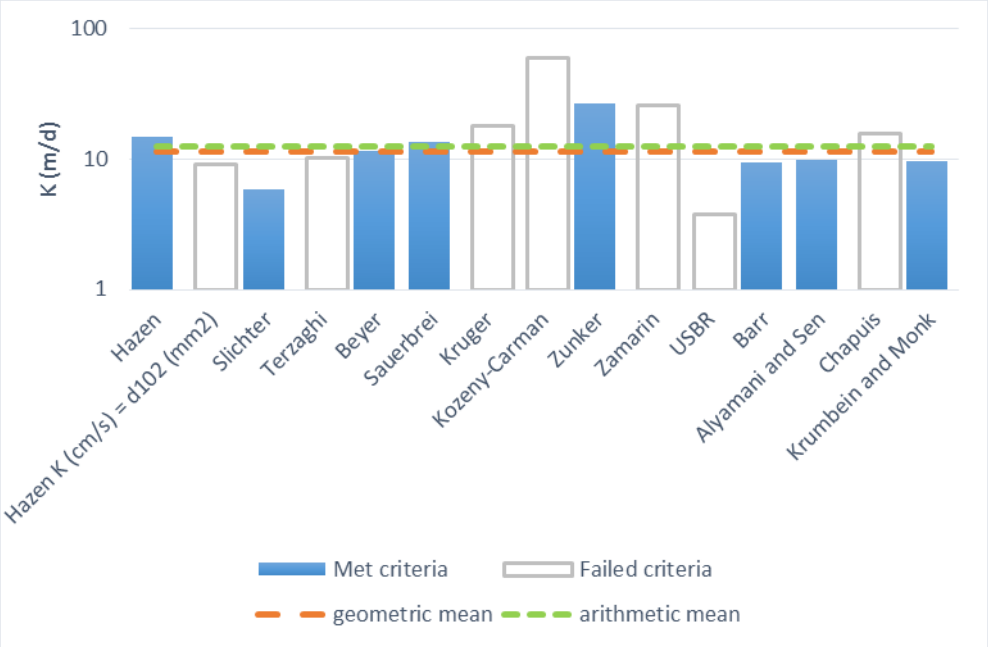


Sieve opening (ps) di (mm)	Mass of retained (mr) (g)	mass fraction (mf)	Percent Passing (pp)
2	1.28486	0.01285	98.7151
1	1.55823	0.01558	97.1569
0.5	7.79114	0.07791	89.3658
0.355	4.0596	0.0406	85.3062
0.25	10.2105	0.1021	75.0957
0.18	19.0951	0.19095	56.0005
0.125	39.2154	0.39215	16.7851
0.09	10.6206	0.10621	6.16457
0.063	2.36468	0.02365	3.79989

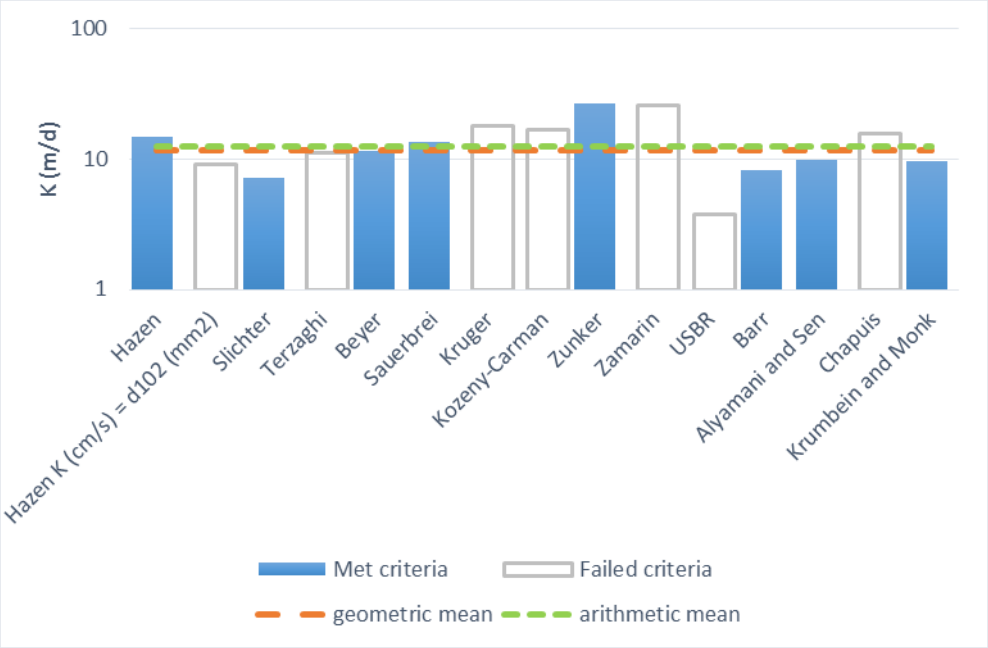
Effective Grain Diameters (mm)		Other Useful Parameters	
d10	0.103	Uniformity Coef.	1.90
d17	0.125	n computed	0.43
d20	0.130	g (cm/s^2)	980.00
d50	0.172	ρ (g/cm^3)	0.9981
d60	0.195	μ (g/cm s)	0.0098
de (Kruger)	0.189	ρg/μ (1/cm s)	9.9327E+04
de (Kozeny)	0.183	tau (Sauerbrei)	1.053
de (Zunker)	0.185	$d_{geometric\ mean}$	0.219
de (Zamarin)	0.187	σ_ϕ	0.899
Io (Alyameni	0.085		

mm	0	% in sample
>64	Boulder	
16 - 64	coarse gravel	
8 - 16	medium gravel	
2 - 8	fine gravel	1.284855112
0.5 - 2	coarse sand	9.349371241
0.25 - 0.5	medium sand	14.27009295
0.063 - 0.25	fine sand	71.29579005
0.016 - 0.063	coarse silt	
0.008 - 0.016	medium silt	
0.002 - 0.008	fine silt	
<0.002	clay	

Slichter, Terzaghi, Kozeny-Carman and Barr with d_{VS}:



Slichter, Terzaghi, Kozeny-Carman and Barr with d_{UU}:

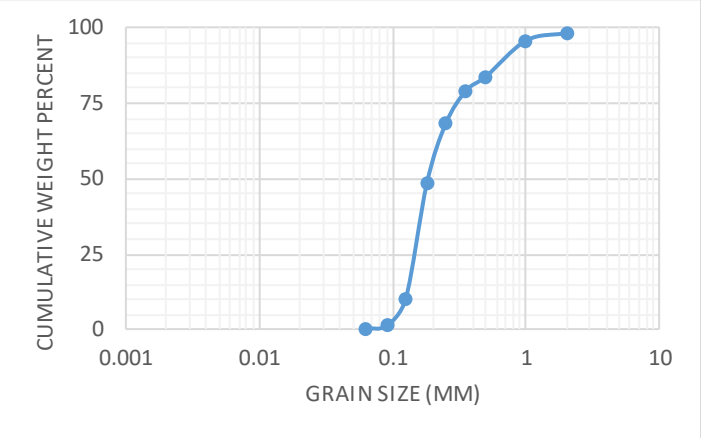


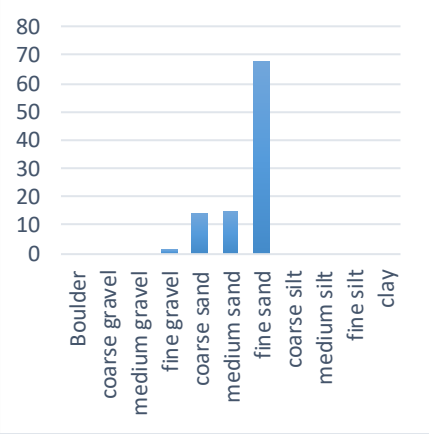
Well 040610/3-T4. Elevation 0.475 m AHD.

Grain Size Analysis Report

Mass Sample (g): 100 T (oC) 20

Uniform sand low in fines



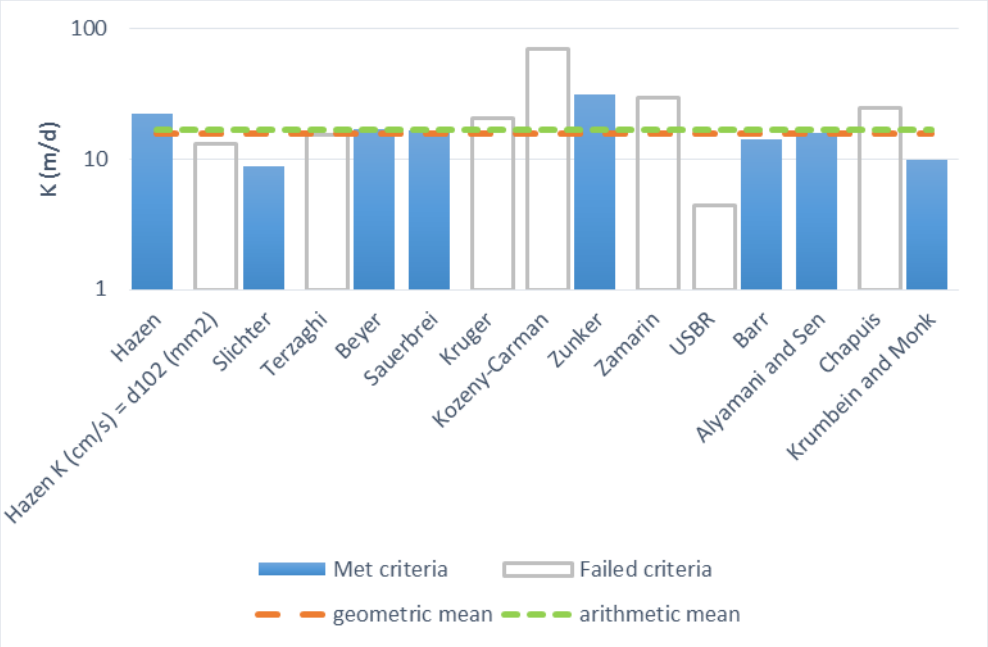


Sieve opening (ps) di (mm)	Mass of retained (mr) (g)	mass fraction (mf)	Percent Passing (pp)
2	1.82195	0.01822	98.1781
1	2.43271	0.02433	95.7453
0.5	11.8944	0.11894	83.8509
0.355	4.64803	0.04648	79.2029
0.25	10.8489	0.10849	68.354
0.18	19.8137	0.19814	48.5404
0.125	38.2505	0.38251	10.2899
0.09	9.03727	0.09037	1.25259
0.063	0.76605	0.00766	0.48654

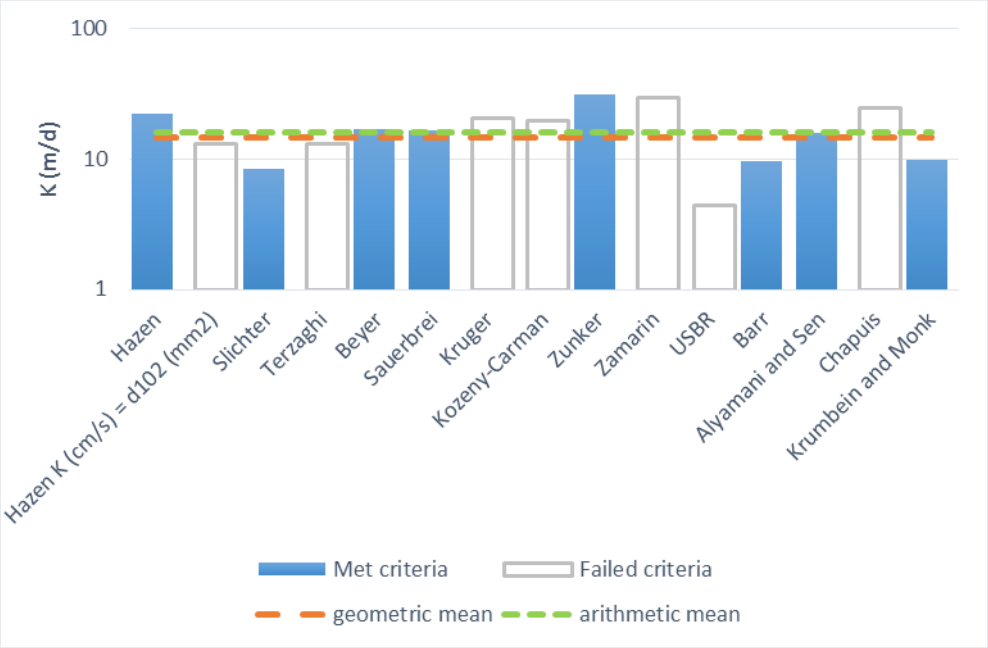
Effective Grain Diameters (mm)		Other Useful Parameters	
d10	0.124	Uniformity Coef.	1.78
d17	0.135	n computed	0.44
d20	0.139	g (cm/s^2)	980.00
d50	0.185	ρ (g/cm^3)	0.9981
d60	0.220	μ (g/cm s)	0.0098
de (Kruger)	0.199	ρg/μ (1/cm s)	9.9327E+04
de (Kozeny)	0.193	tau (Sauerbrei)	1.053
de (Zunker)	0.195	$d_{geometric\ mean}$	0.232
de (Zamarin)	0.197	σ_ϕ	0.968
Io (Alyameni	0.109		

mm	0	% in sample
>64	Boulder	
16 - 64	coarse gravel	
8 - 16	medium gravel	
2 - 8	fine gravel	1.82194617
0.5 - 2	coarse sand	14.32712215
0.25 - 0.5	medium sand	15.49689441
0.063 - 0.25	fine sand	67.86749482
0.016 - 0.063	coarse silt	
0.008 - 0.016	medium silt	
0.002 - 0.008	fine silt	
<0.002	clay	

Slichter, Terzaghi, Kozeny-Carman and Barr with d_{VS}:



Slichter, Terzaghi, Kozeny-Carman and Barr with d_{UU}:

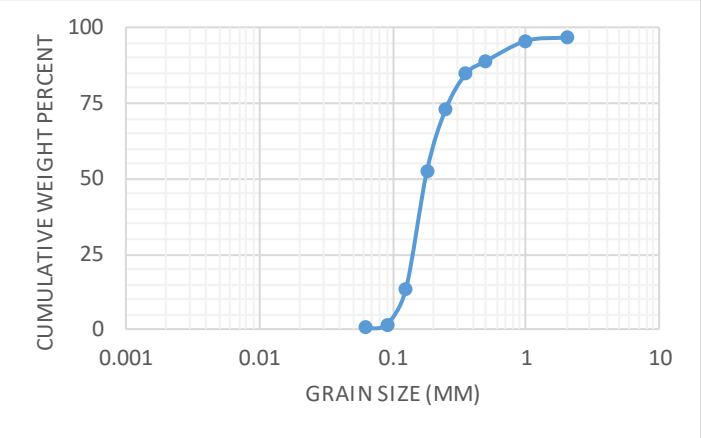


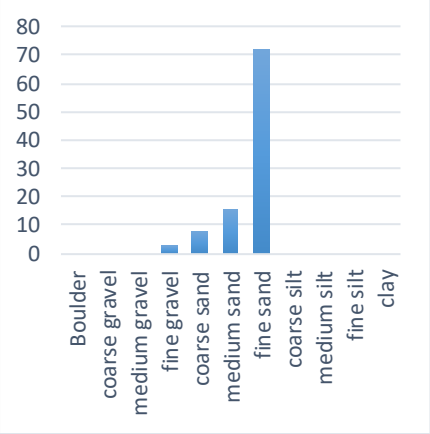
Well 040610/3-T4. Elevation 0.425 m AHD.

Grain Size Analysis Report

Mass Sample (g): 100 T (oC) 20

Uniform sand low in fines



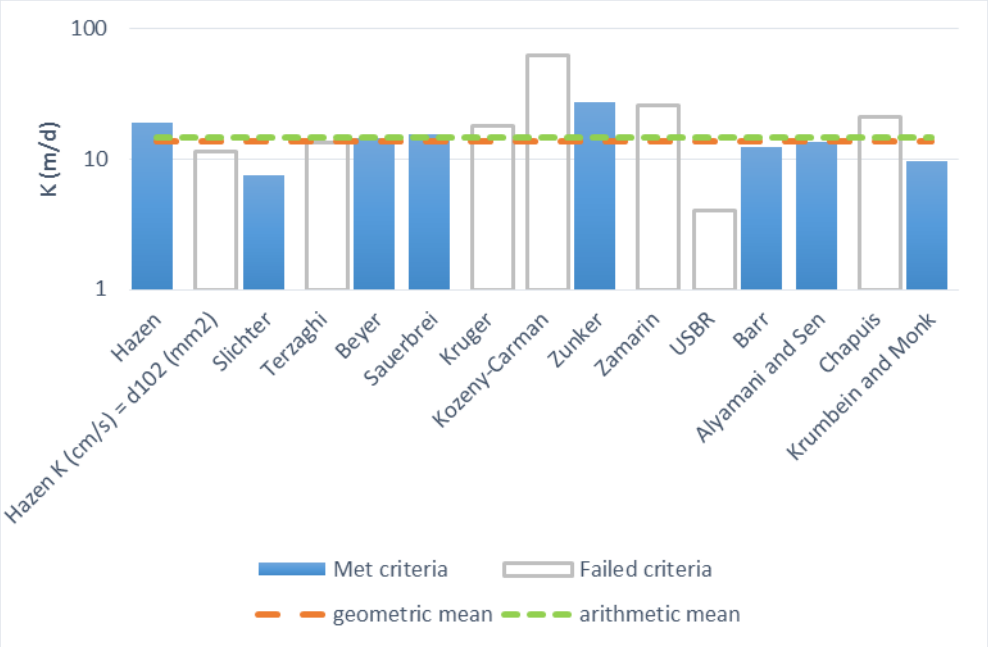


Sieve opening (ps) di (mm)	Mass of retained (mr) (g)	mass fraction (mf)	Percent Passing (pp)
2	3.25952	0.0326	96.7405
1	1.09685	0.01097	95.6436
0.5	6.69495	0.06695	88.9487
0.355	4.14942	0.04149	84.7993
0.25	11.6411	0.11641	73.1581
0.18	20.6229	0.20623	52.5352
0.125	39.2695	0.39269	13.2657
0.09	11.5584	0.11558	1.70737
0.063	1.11755	0.01118	0.58982

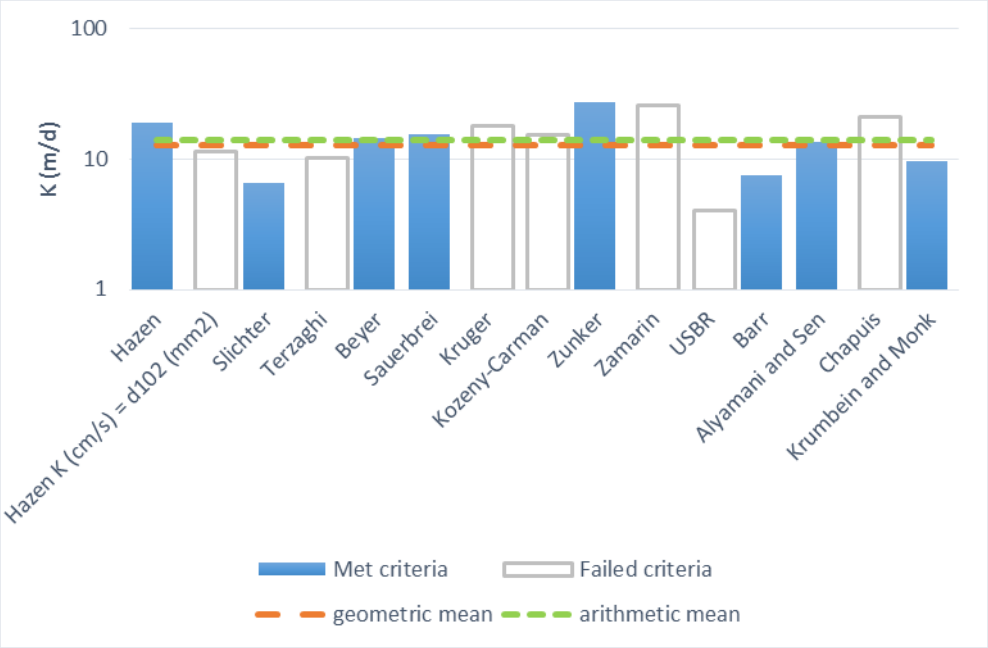
Effective Grain Diameters (mm)		Other Useful Parameters	
d10	0.115	Uniformity Coef.	1.78
d17	0.130	n computed	0.44
d20	0.134	g (cm/s^2)	980.00
d50	0.176	ρ (g/cm^3)	0.9981
d60	0.205	μ (g/cm s)	0.0098
de (Kruger)	0.187	ρg/μ (1/cm s)	9.9327E+04
de (Kozeny)	0.182	tau (Sauerbrei)	1.053
de (Zunker)	0.184	$d_{geometric\ mean}$	0.212
de (Zamarin)	0.185	σ_ϕ	0.851
Io (Alyameni	0.100		

mm	0	% in sample
>64	Boulder	
16 - 64	coarse gravel	
8 - 16	medium gravel	
2 - 8	fine gravel	3.259519868
0.5 - 2	coarse sand	7.791804636
0.25 - 0.5	medium sand	15.79056291
0.063 - 0.25	fine sand	72.5682947
0.016 - 0.063	coarse silt	
0.008 - 0.016	medium silt	
0.002 - 0.008	fine silt	
<0.002	clay	

Slichter, Terzaghi, Kozeny-Carman and Barr with d_{VS}:



Slichter, Terzaghi, Kozeny-Carman and Barr with d_{UU}:

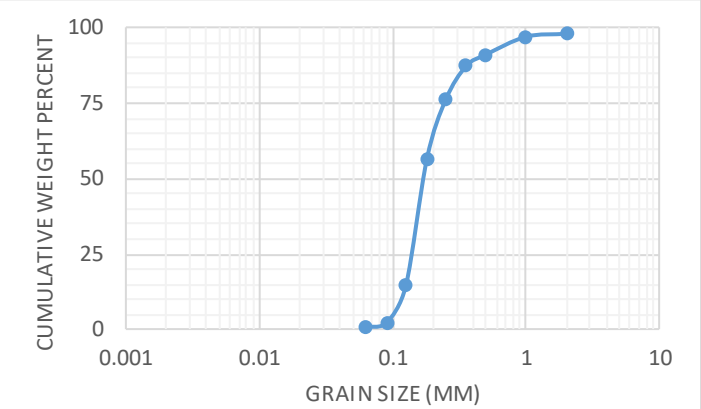


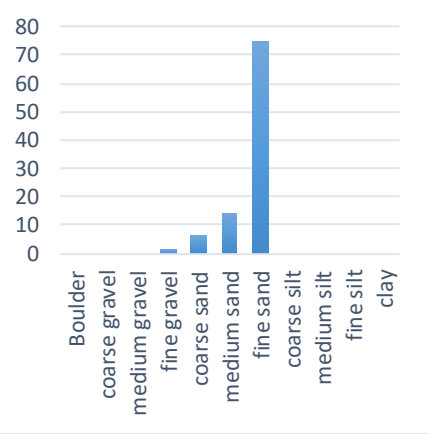
Well 040610/3-T4. Elevation 0.375 m AHD.

Grain Size Analysis Report

Mass Sample (g): 100 T (oC) 20

Uniform sand low in fines



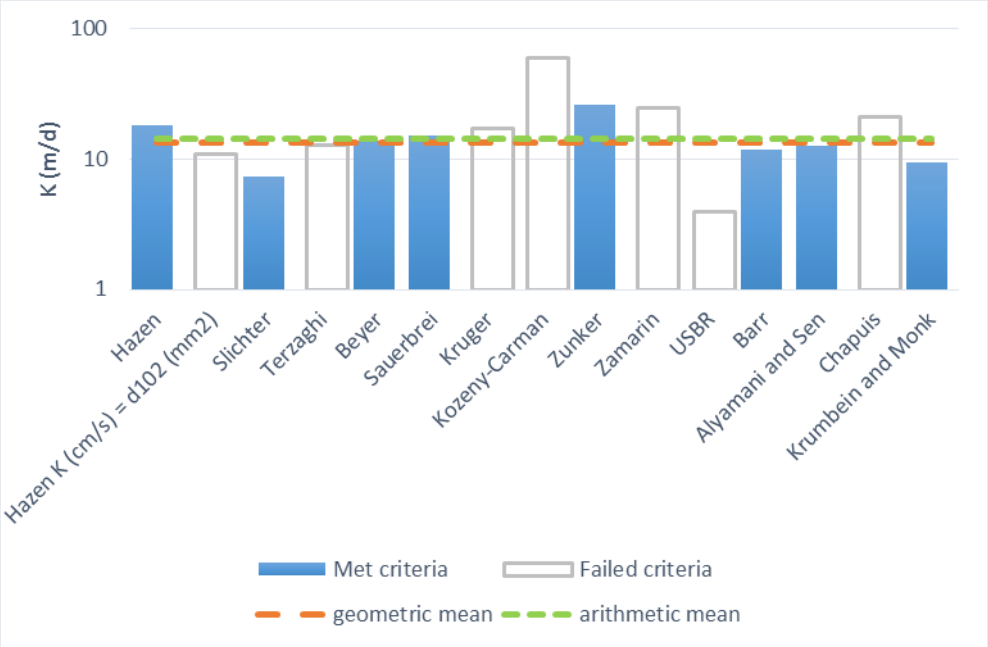


Sieve opening (ps) di (mm)	Mass of retained (mr) (g)	mass fraction (mf)	Percent Passing (pp)
2	2.04102	0.02041	97.959
1	0.94908	0.00949	97.0099
0.5	5.90877	0.05909	91.1011
0.355	3.79631	0.03796	87.3048
0.25	11.0011	0.11001	76.3037
0.18	19.7265	0.19727	56.5772
0.125	42.1267	0.42127	14.4505
0.09	12.1237	0.12124	2.32677
0.063	1.25523	0.01255	1.07154

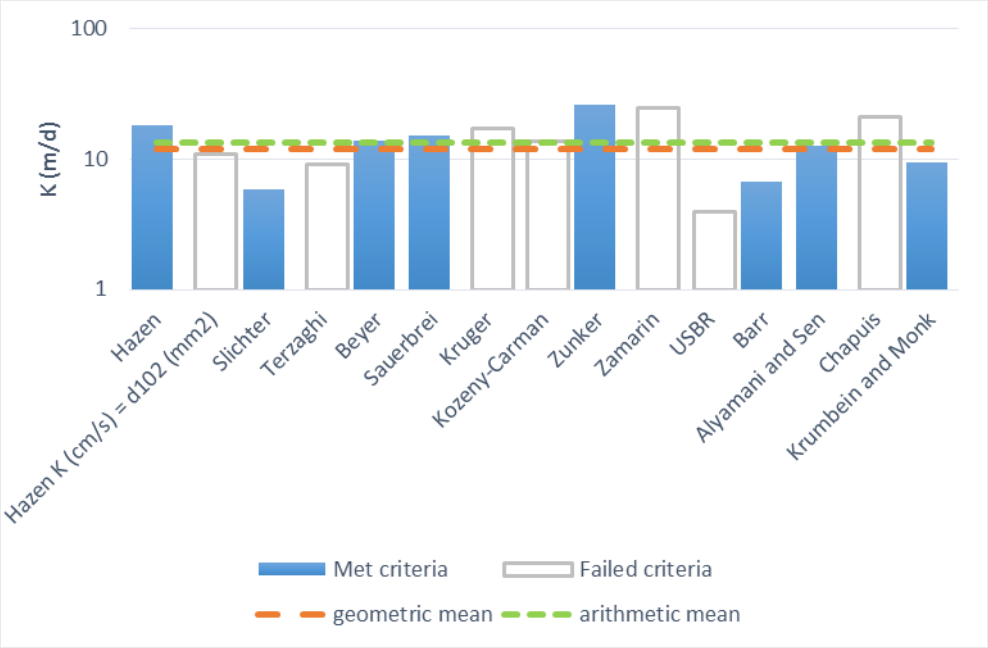
Effective Grain Diameters (mm)		Other Useful Parameters	
d10	0.112	Uniformity Coef.	1.71
d17	0.128	n computed	0.44
d20	0.132	g (cm/s^2)	980.00
d50	0.171	ρ (g/cm^3)	0.9981
d60	0.192	μ (g/cm s)	0.0098
de (Kruger)	0.182	ρg/μ (1/cm s)	9.9327E+04
de (Kozeny)	0.176	tau (Sauerbrei)	1.053
de (Zunker)	0.178	$d_{geometric\ mean}$	0.203
de (Zamarin)	0.180	σ_ϕ	0.805
Io (Alyameni	0.097		

mm	0	% in sample
>64	Boulder	
16 - 64	coarse gravel	
8 - 16	medium gravel	
2 - 8	fine gravel	2.041024594
0.5 - 2	coarse sand	6.857842637
0.25 - 0.5	medium sand	14.79742831
0.063 - 0.25	fine sand	75.23216655
0.016 - 0.063	coarse silt	
0.008 - 0.016	medium silt	
0.002 - 0.008	fine silt	
<0.002	clay	

Slichter, Terzaghi, Kozeny-Carman and Barr with d_{VS}:



Slichter, Terzaghi, Kozeny-Carman and Barr with d_{UU}:

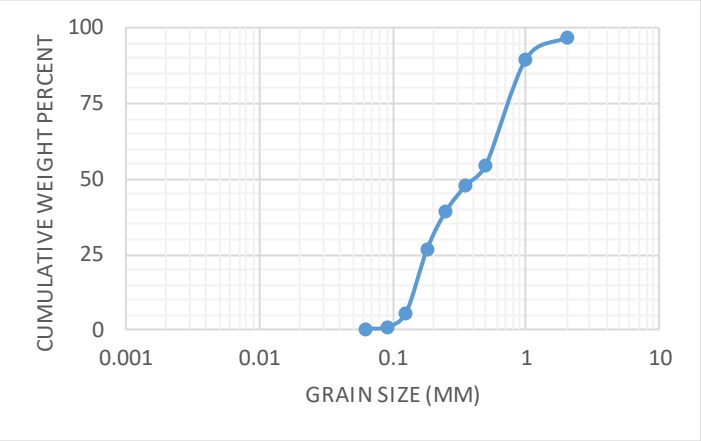


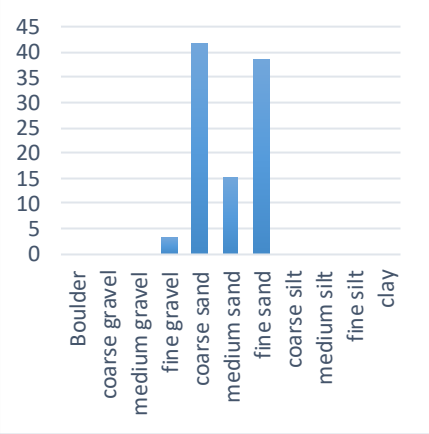
Well 050210/1-T4. Elevation 0.875 m AHD.

Grain Size Analysis Report

Mass Sample (g): 100 T (oC) 20

Moderately well sorted sand low in fines



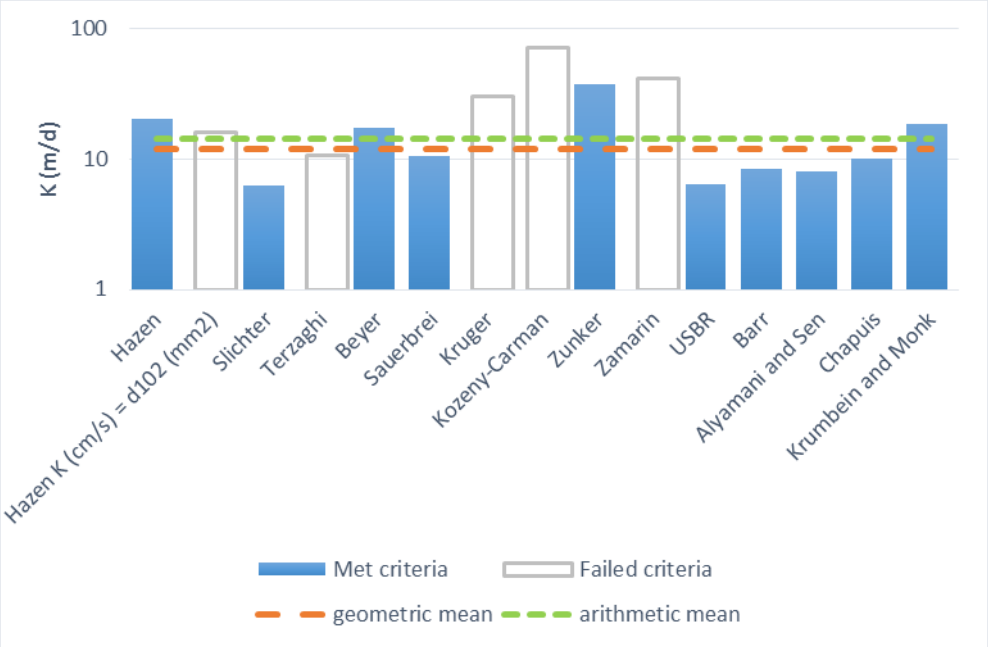


Sieve opening (ps) di (mm)	Mass of retained (mr) (g)	mass fraction (mf)	Percent Passing (pp)
2	3.20245	0.03202	96.7975
1	6.95	0.0695	89.8475
0.5	35.0992	0.35099	54.7483
0.355	6.74559	0.06746	48.0027
0.25	8.68751	0.08688	39.3152
0.18	12.7246	0.12725	26.5906
0.125	21.0715	0.21071	5.51912
0.09	4.58223	0.04582	0.93689
0.063	0.45141	0.00451	0.48548

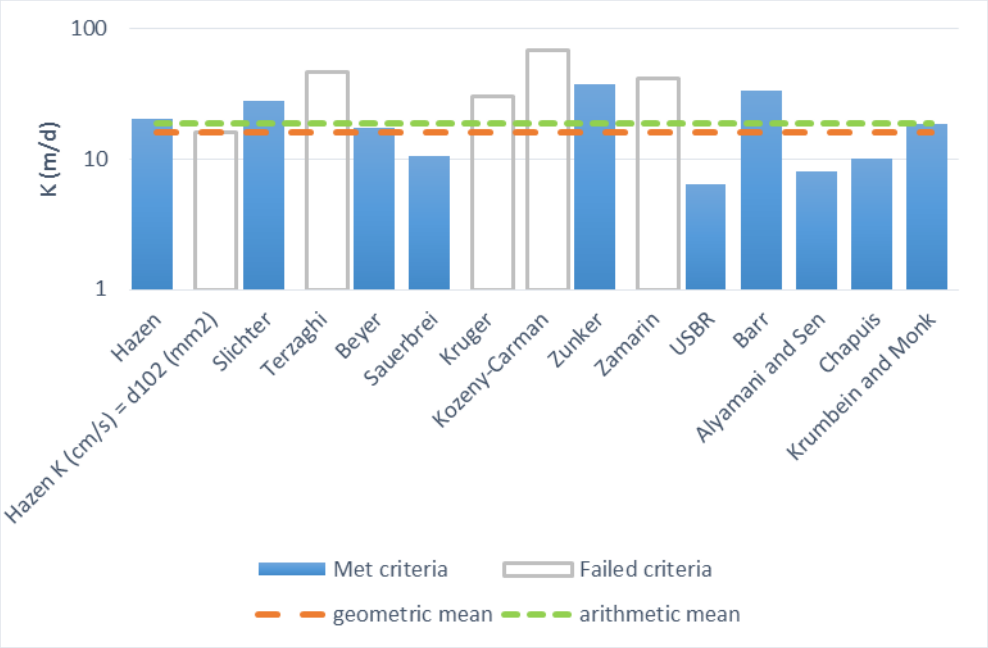
Effective Grain Diameters (mm)		Other Useful Parameters	
d10	0.137	Uniformity Coef.	4.21
d17	0.155	n computed	0.37
d20	0.163	g (cm/s^2)	980.00
d50	0.398	ρ (g/cm^3)	0.9981
d60	0.575	μ (g/cm s)	0.0098
de (Kruger)	0.293	ρg/μ (1/cm s)	9.9327E+04
de (Kozeny)	0.280	tau (Sauerbrei)	1.053
de (Zunker)	0.284	$d_{geometric\ mean}$	0.378
de (Zamarin)	0.288	σ_ϕ	1.230
Io (Alyameni	0.071		

mm	0	% in sample
>64	Boulder	
16 - 64	coarse gravel	
8 - 16	medium gravel	
2 - 8	fine gravel	3.202452943
0.5 - 2	coarse sand	42.0492292
0.25 - 0.5	medium sand	15.43309769
0.063 - 0.25	fine sand	38.82974193
0.016 - 0.063	coarse silt	
0.008 - 0.016	medium silt	
0.002 - 0.008	fine silt	
<0.002	clay	

Slichter, Terzaghi, Kozeny-Carman and Barr with d_{VS}:



Slichter, Terzaghi, Kozeny-Carman and Barr with d_{UU}:

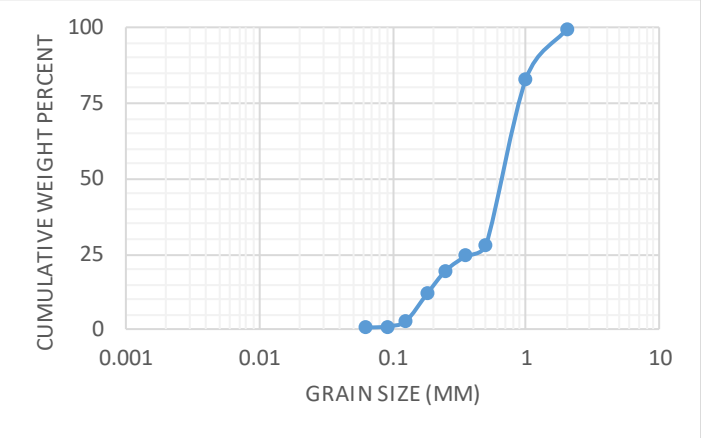


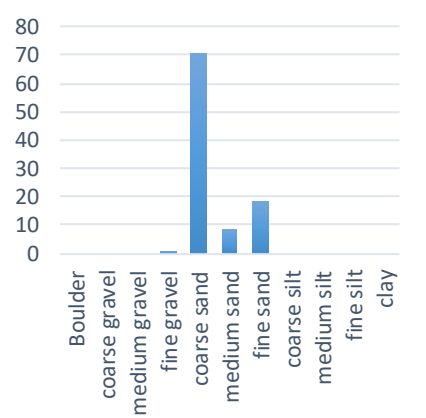
Well 050210/1-T4. Elevation 0.825 m AHD.

Grain Size Analysis Report

Mass Sample (g): 100 T (oC) 20

Moderately well sorted sand low in fines



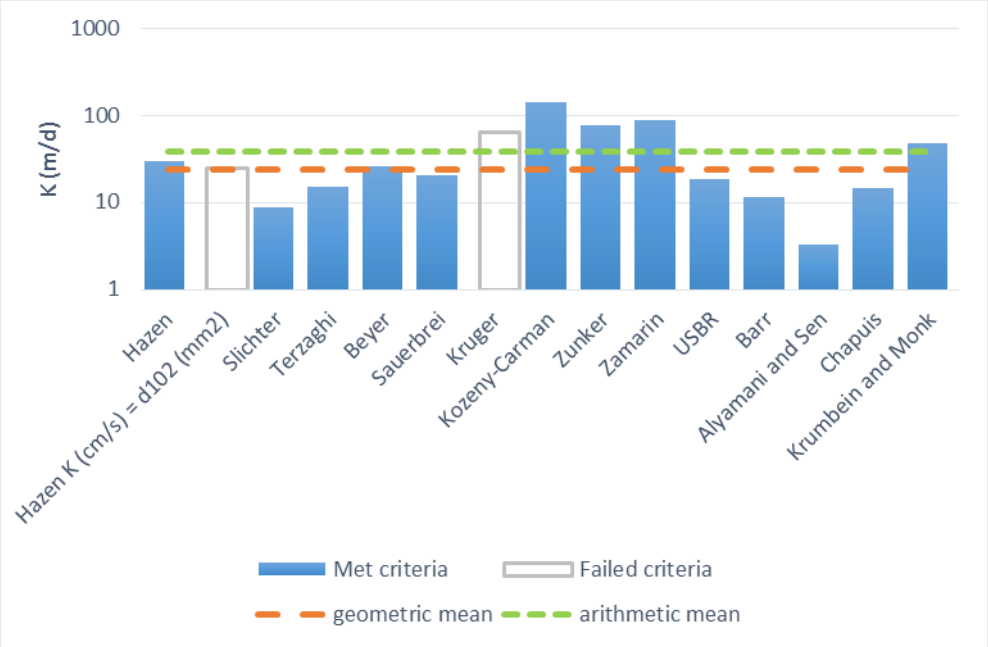


Sieve opening (ps) di (mm)	Mass of retained (mr) (g)	mass fraction (mf)	Percent Passing (pp)
2	0.6946	0.00695	99.3054
1	16.0878	0.16088	83.2176
0.5	55.09	0.5509	28.1276
0.355	3.6896	0.0369	24.438
0.25	4.83979	0.0484	19.5982
0.18	7.77504	0.07775	11.8231
0.125	9.00739	0.09007	2.81574
0.09	1.77011	0.0177	1.04563
0.063	0.37344	0.00373	0.67219

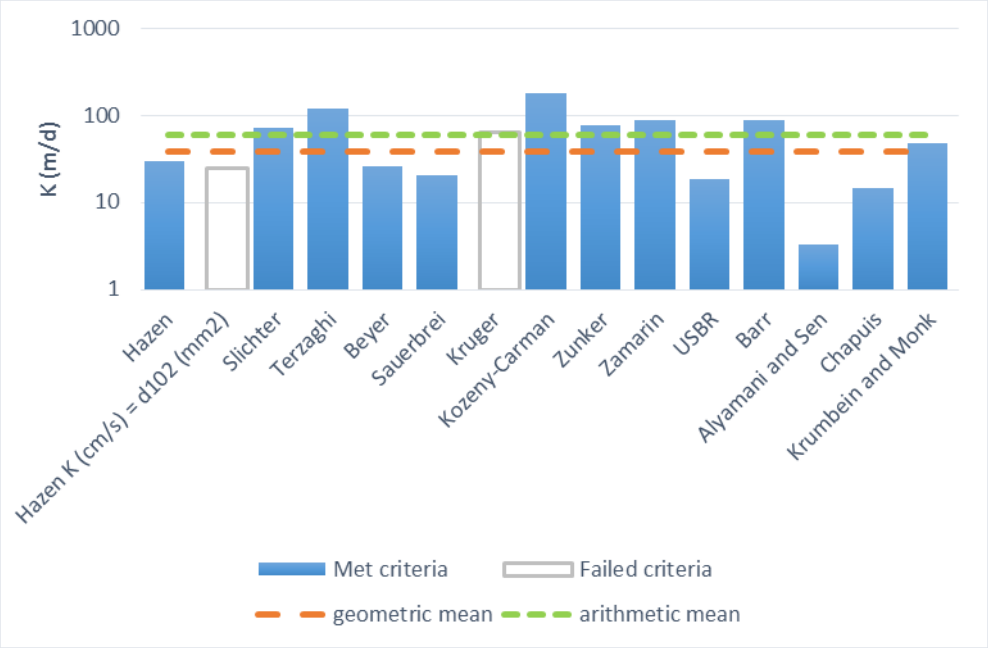
Effective Grain Diameters (mm)		Other Useful Parameters	
d10	0.169	Uniformity Coef.	4.67
d17	0.227	n computed	0.36
d20	0.259	g (cm/s^2)	980.00
d50	0.699	ρ (g/cm^3)	0.9981
d60	0.789	μ (g/cm s)	0.0098
de (Kruger)	0.444	ρg/μ (1/cm s)	9.9327E+04
de (Kozeny)	0.416	tau (Sauerbrei)	1.053
de (Zunker)	0.425	$d_{geometric\ mean}$	0.568
de (Zamarin)	0.434	σ_ϕ	1.120
Io (Alyameni	0.036		

mm	0	% in sample
>64	Boulder	
16 - 64	coarse gravel	
8 - 16	medium gravel	
2 - 8	fine gravel	0.694600045
0.5 - 2	coarse sand	71.17783255
0.25 - 0.5	medium sand	8.529389798
0.063 - 0.25	fine sand	18.92598402
0.016 - 0.063	coarse silt	
0.008 - 0.016	medium silt	
0.002 - 0.008	fine silt	
<0.002	clay	

Slichter, Terzaghi, Kozeny-Carman and Barr with d_{VS}:



Slichter, Terzaghi, Kozeny-Carman and Barr with d_{UU}:

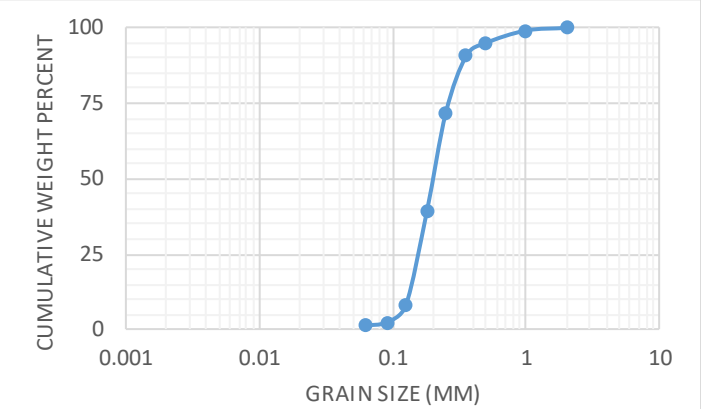


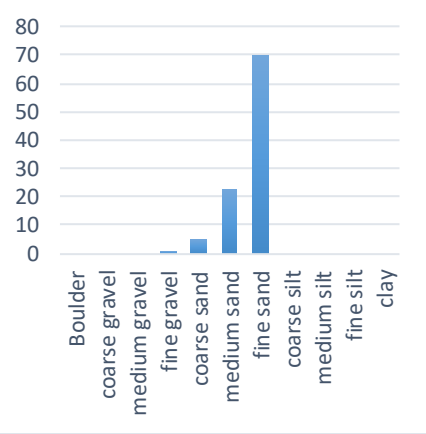
Well 050210/1-T4. Elevation 0.775 m AHD.

Grain Size Analysis Report

Mass Sample (g): 100 T (oC) 20

Uniform sand low in fines



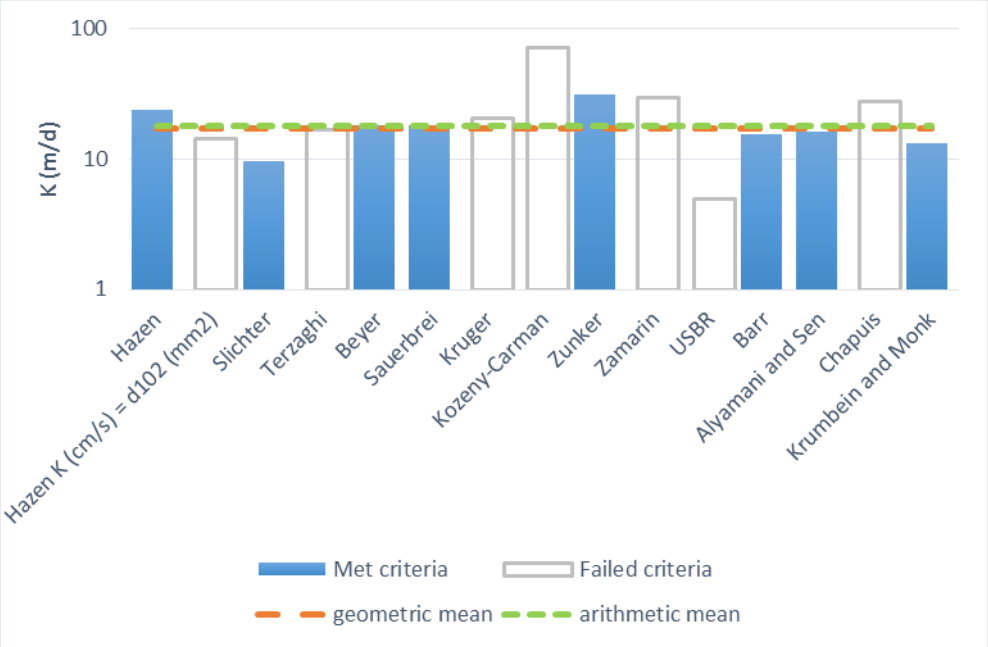


Sieve opening (ps) di (mm)	Mass of retained (mr) (g)	mass fraction (mf)	Percent Passing (pp)
2	0.09557	0.00096	99.9044
1	0.83891	0.00839	99.0655
0.5	4.12021	0.0412	94.9453
0.355	4.33259	0.04333	90.6127
0.25	18.6577	0.18658	71.955
0.18	32.7387	0.32739	39.2163
0.125	31.1989	0.31199	8.01742
0.09	5.59626	0.05596	2.42115
0.063	0.98758	0.00988	1.43358

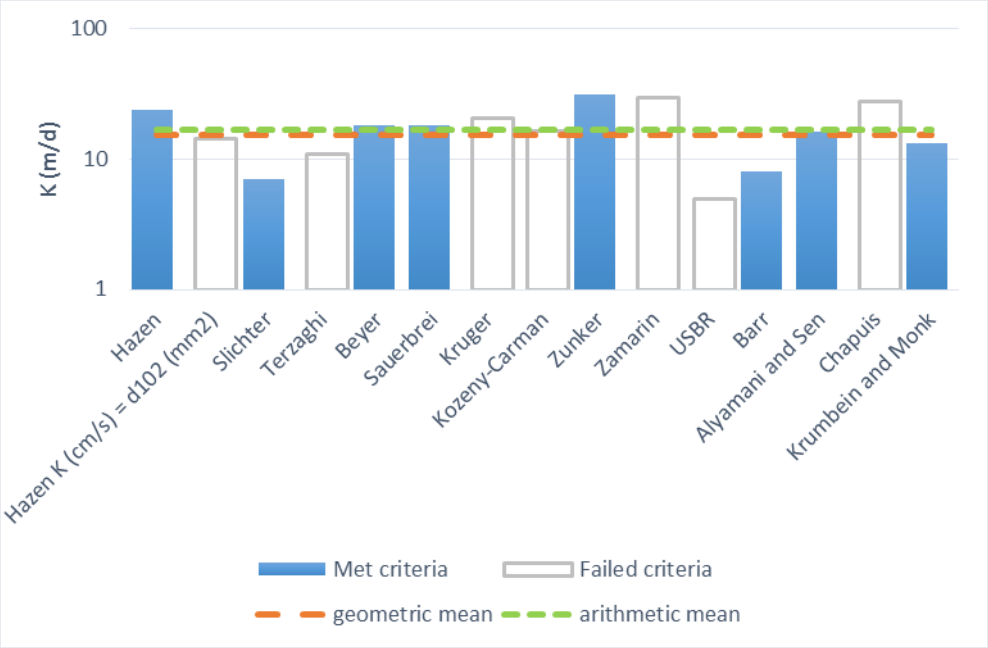
Effective Grain Diameters (mm)		Other Useful Parameters	
d10	0.128	Uniformity Coef.	1.75
d17	0.141	n computed	0.44
d20	0.146	g (cm/s^2)	980.00
d50	0.203	ρ (g/cm^3)	0.9981
d60	0.224	μ (g/cm s)	0.0098
de (Kruger)	0.200	ρg/μ (1/cm s)	9.9327E+04
de (Kozeny)	0.194	tau (Sauerbrei)	1.053
de (Zunker)	0.196	$d_{geometric\ mean}$	0.218
de (Zamarin)	0.198	σ_ϕ	0.640
Io (Alyameni	0.110		

mm	0	% in sample
>64	Boulder	
16 - 64	coarse gravel	
8 - 16	medium gravel	
2 - 8	fine gravel	0.095571838
0.5 - 2	coarse sand	4.959116491
0.25 - 0.5	medium sand	22.99033663
0.063 - 0.25	fine sand	70.52139747
0.016 - 0.063	coarse silt	
0.008 - 0.016	medium silt	
0.002 - 0.008	fine silt	
<0.002	clay	

Slichter, Terzaghi, Kozeny-Carman and Barr with d_{VS}:



Slichter, Terzaghi, Kozeny-Carman and Barr with d_{UU}:

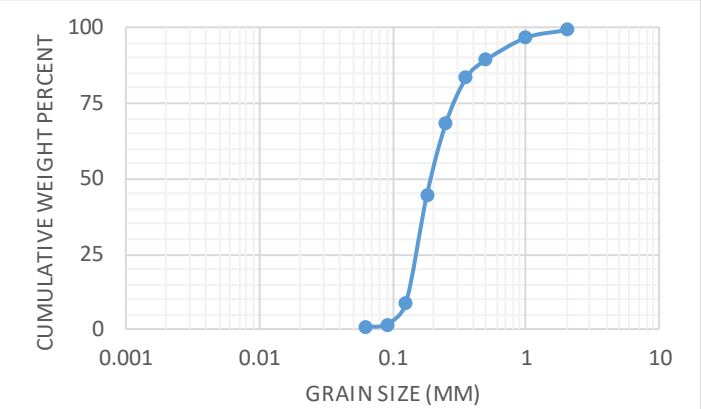


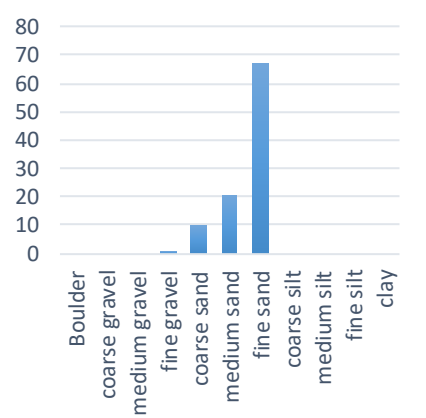
Well 050210/1-T4. Elevation 0.725 m AHD.

Grain Size Analysis Report

Mass Sample (g): 100 T (oC) 20

Uniform sand low in fines



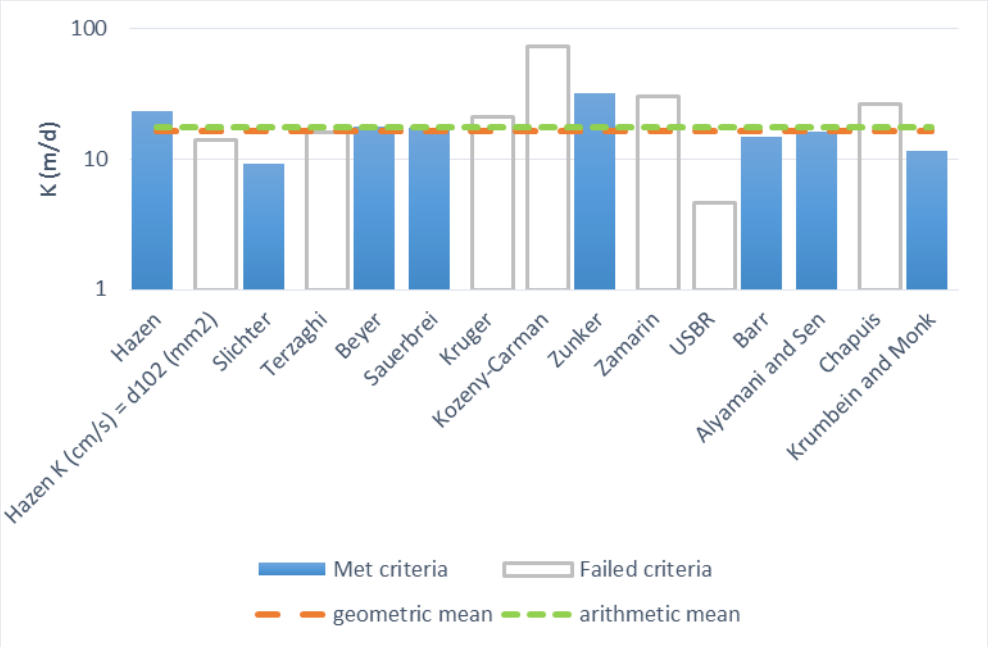


Sieve opening (ps) di (mm)	Mass of retained (mr) (g)	mass fraction (mf)	Percent Passing (pp)
2	0.83168	0.00832	99.1683
1	2.48559	0.02486	96.6827
0.5	7.39061	0.07391	89.2921
0.355	5.95407	0.05954	83.3381
0.25	14.9891	0.14989	68.3489
0.18	23.7312	0.23731	44.6177
0.125	35.989	0.35989	8.62867
0.09	6.88026	0.0688	1.74842
0.063	0.72772	0.00728	1.0207

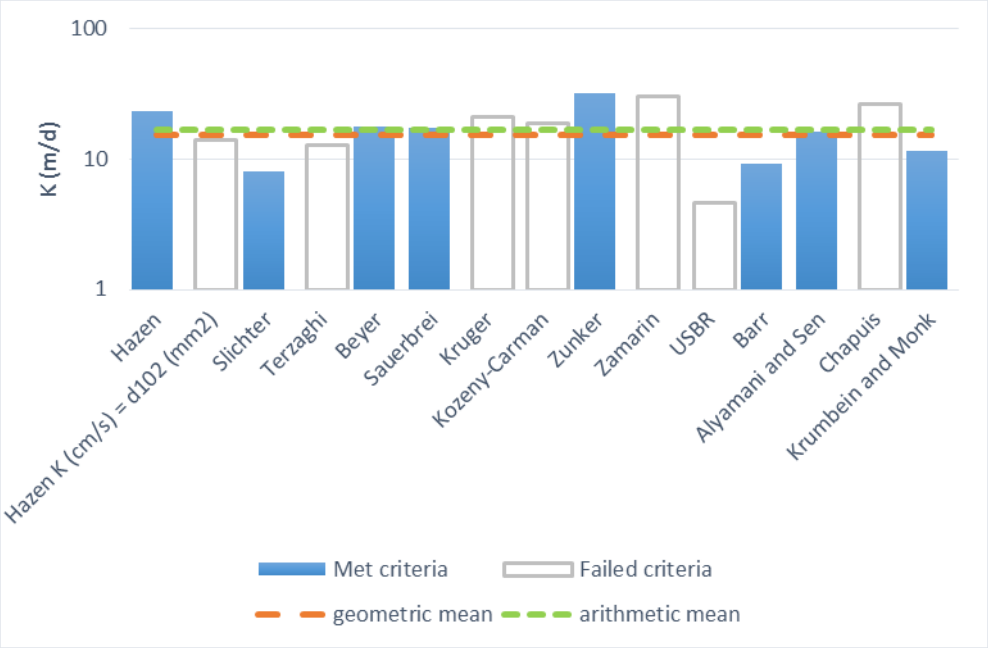
Effective Grain Diameters (mm)		Other Useful Parameters	
d10	0.127	Uniformity Coef.	1.77
d17	0.138	n computed	0.44
d20	0.142	g (cm/s^2)	980.00
d50	0.196	ρ (g/cm^3)	0.9981
d60	0.225	μ (g/cm s)	0.0098
de (Kruger)	0.202	ρg/μ (1/cm s)	9.9327E+04
de (Kozeny)	0.196	tau (Sauerbrei)	1.053
de (Zunker)	0.198	$d_{geometric\ mean}$	0.229
de (Zamarin)	0.200	σ_ϕ	0.824
Io (Alyameni	0.110		

mm	0	% in sample
>64	Boulder	
16 - 64	coarse gravel	
8 - 16	medium gravel	
2 - 8	fine gravel	0.831679425
0.5 - 2	coarse sand	9.876193176
0.25 - 0.5	medium sand	20.94320008
0.063 - 0.25	fine sand	67.32822985
0.016 - 0.063	coarse silt	
0.008 - 0.016	medium silt	
0.002 - 0.008	fine silt	
<0.002	clay	

Slichter, Terzaghi, Kozeny-Carman and Barr with d_{VS}:



Slichter, Terzaghi, Kozeny-Carman and Barr with d_{UU}:

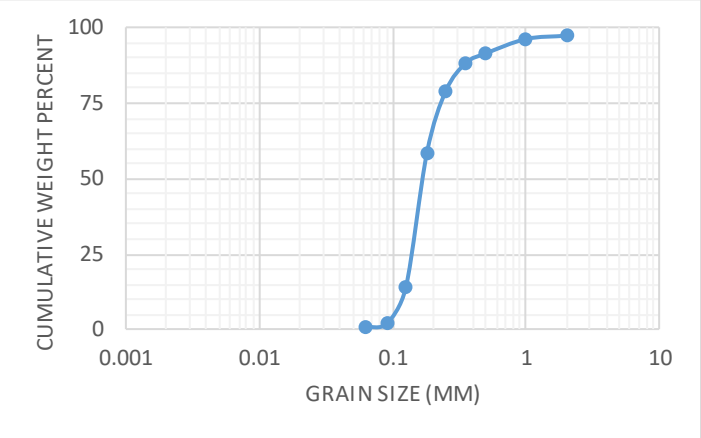


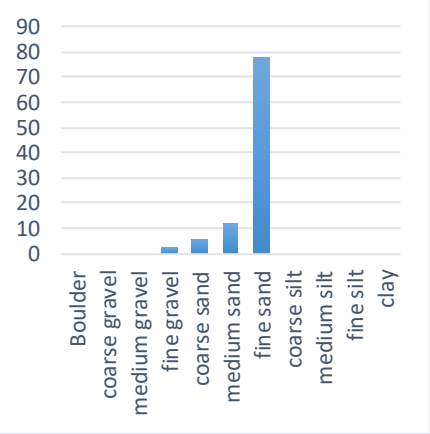
Well 050210/1-T4. Elevation 0.675 m AHD.

Grain Size Analysis Report

Mass Sample (g): 100 T (oC) 20

Uniform sand low in fines



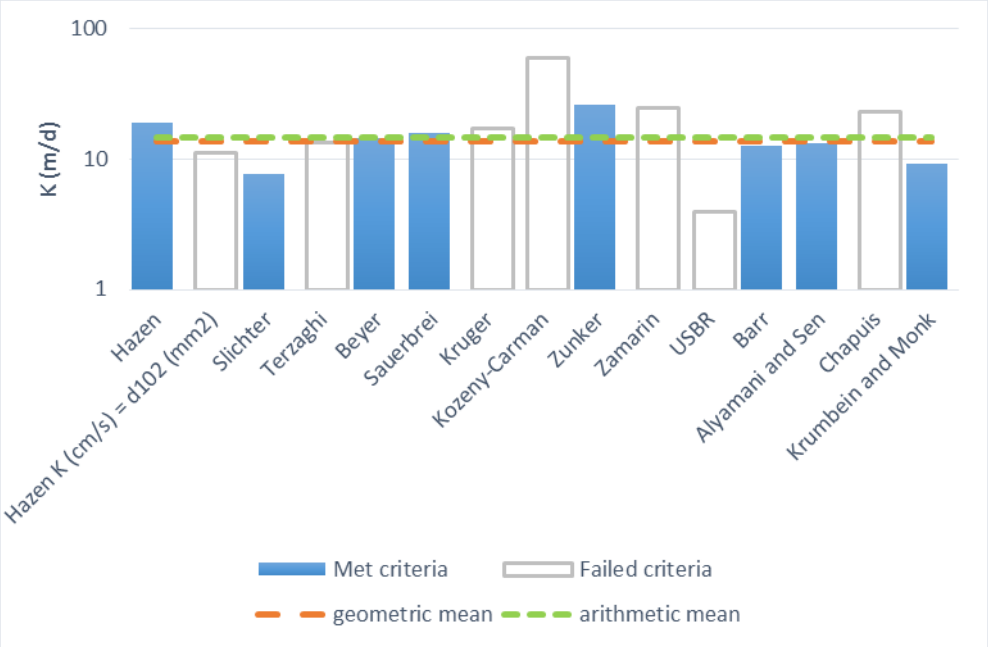


Sieve opening (ps) di (mm)	Mass of retained (mr) (g)	mass fraction (mf)	Percent Passing (pp)
2	2.67172	0.02672	97.3283
1	1.07058	0.01071	96.2577
0.5	4.74657	0.04747	91.5111
0.355	3.14543	0.03145	88.3657
0.25	9.23733	0.09237	79.1284
0.18	20.559	0.20559	58.5694
0.125	44.6613	0.44661	13.9081
0.09	11.9185	0.11919	1.98958
0.063	0.95689	0.00957	1.03269

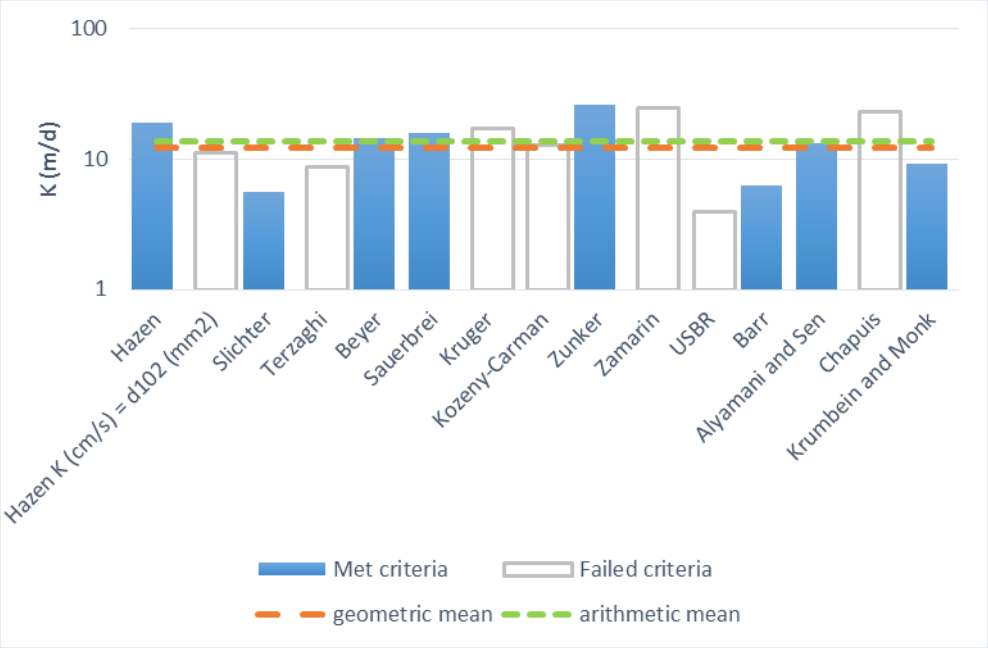
Effective Grain Diameters (mm)		Other Useful Parameters	
d10	0.114	Uniformity Coef.	1.63
d17	0.129	n computed	0.44
d20	0.133	g (cm/s^2)	980.00
d50	0.169	ρ (g/cm^3)	0.9981
d60	0.185	μ (g/cm s)	0.0098
de (Kruger)	0.180	ρg/μ (1/cm s)	9.9327E+04
de (Kozeny)	0.174	tau (Sauerbrei)	1.053
de (Zunker)	0.176	$d_{geometric\ mean}$	0.200
de (Zamarin)	0.178	σ_ϕ	0.790
Io (Alyameni	0.100		

mm	0	% in sample
>64	Boulder	
16 - 64	coarse gravel	
8 - 16	medium gravel	
2 - 8	fine gravel	2.671719564
0.5 - 2	coarse sand	5.817148271
0.25 - 0.5	medium sand	12.38275699
0.063 - 0.25	fine sand	78.09568925
0.016 - 0.063	coarse silt	
0.008 - 0.016	medium silt	
0.002 - 0.008	fine silt	
<0.002	clay	

Slichter, Terzaghi, Kozeny-Carman and Barr with d_{VS}:



Slichter, Terzaghi, Kozeny-Carman and Barr with d_{UU}:

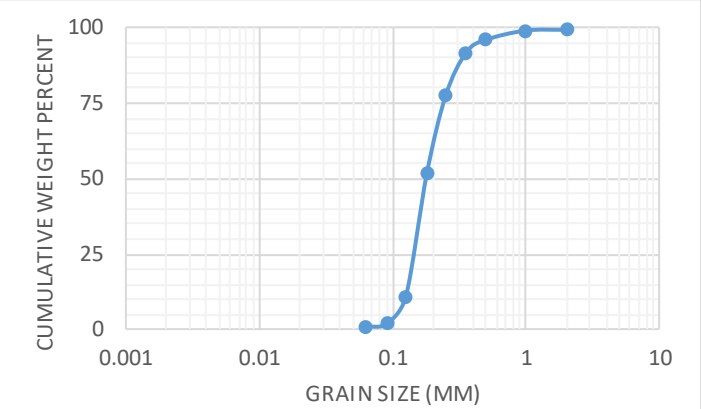


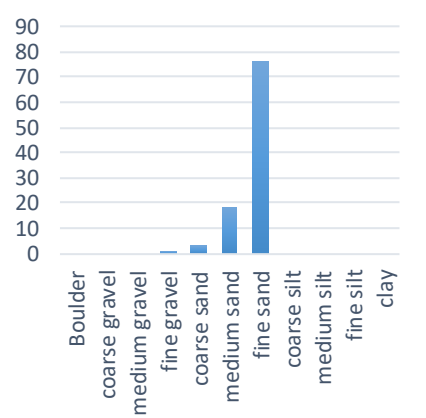
Well 050210/1-T4. Elevation 0.625 m AHD.

Grain Size Analysis Report

Mass Sample (g): 100 T (oC) 20

Uniform sand low in fines



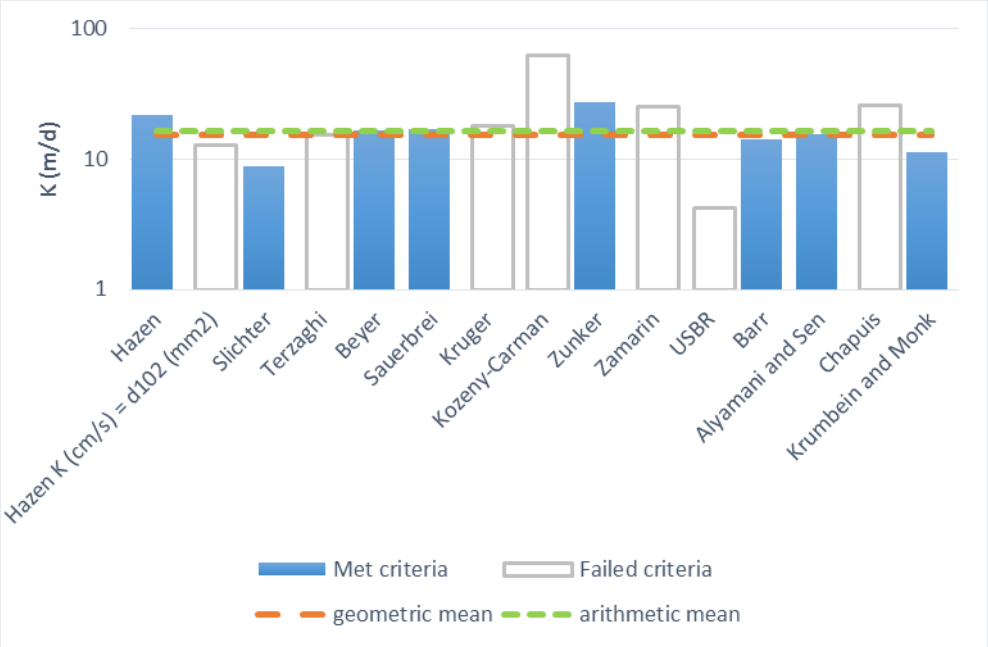


Sieve opening (ps) di (mm)	Mass of retained (mr) (g)	mass fraction (mf)	Percent Passing (pp)
2	0.70277	0.00703	99.2972
1	0.24363	0.00244	99.0536
0.5	3.06409	0.03064	95.9895
0.355	4.1979	0.04198	91.7916
0.25	14.0648	0.14065	77.7268
0.18	25.8996	0.259	51.8272
0.125	40.9202	0.4092	10.907
0.09	8.9955	0.08996	1.91154
0.063	0.84333	0.00843	1.06822

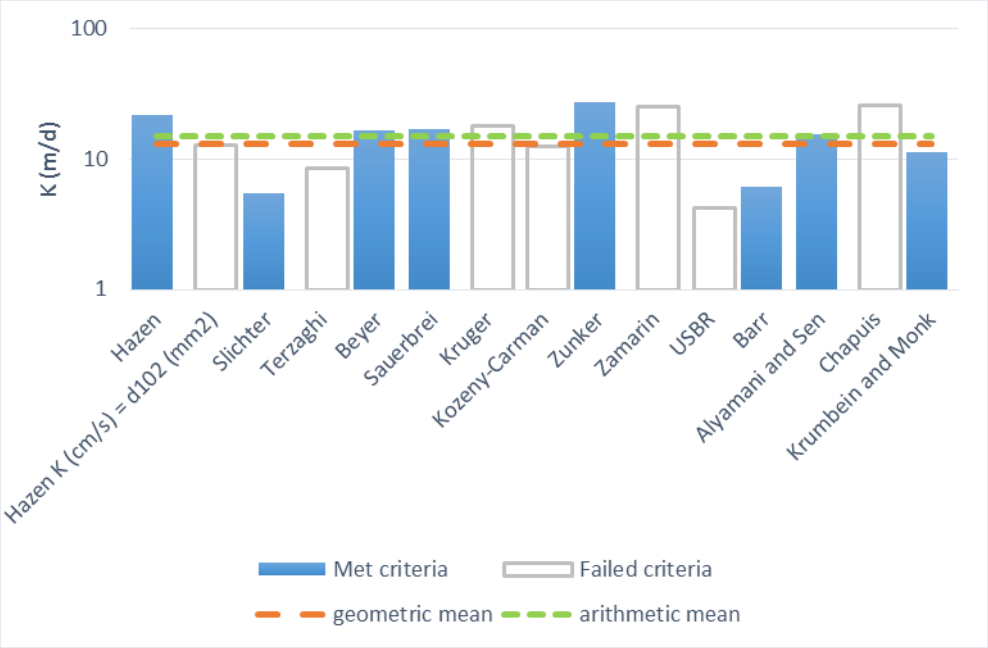
Effective Grain Diameters (mm)		Other Useful Parameters	
d10	0.121	Uniformity Coef.	1.66
d17	0.133	n computed	0.44
d20	0.137	g (cm/s^2)	980.00
d50	0.178	ρ (g/cm^3)	0.9981
d60	0.202	μ (g/cm s)	0.0098
de (Kruger)	0.184	ρg/μ (1/cm s)	9.9327E+04
de (Kozeny)	0.178	tau (Sauerbrei)	1.053
de (Zunker)	0.180	$d_{geometric\ mean}$	0.198
de (Zamarin)	0.182	σ_ϕ	0.625
Io (Alyameni	0.107		

mm	0	% in sample
>64	Boulder	
16 - 64	coarse gravel	
8 - 16	medium gravel	
2 - 8	fine gravel	0.702773613
0.5 - 2	coarse sand	3.307721139
0.25 - 0.5	medium sand	18.26274363
0.063 - 0.25	fine sand	76.65854573
0.016 - 0.063	coarse silt	
0.008 - 0.016	medium silt	
0.002 - 0.008	fine silt	
<0.002	clay	

Slichter, Terzaghi, Kozeny-Carman and Barr with d_{VS}:



Slichter, Terzaghi, Kozeny-Carman and Barr with d_{UU}:

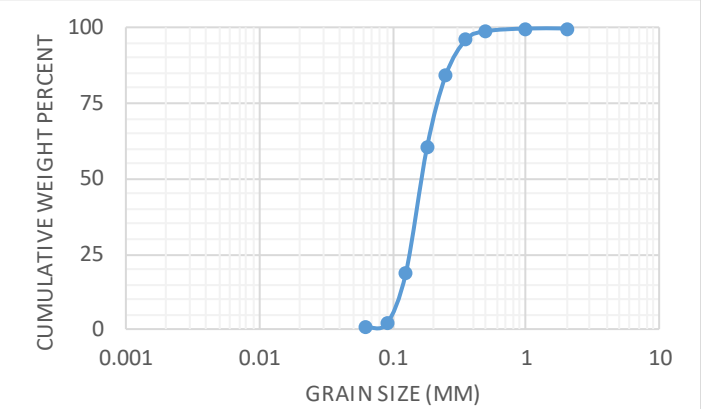


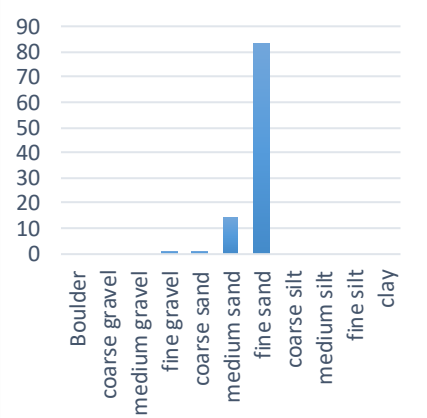
Well 050210/1-T4. Elevation 0.575 m AHD.

Grain Size Analysis Report

Mass Sample (g): 100 T (oC) 20

Uniform sand low in fines



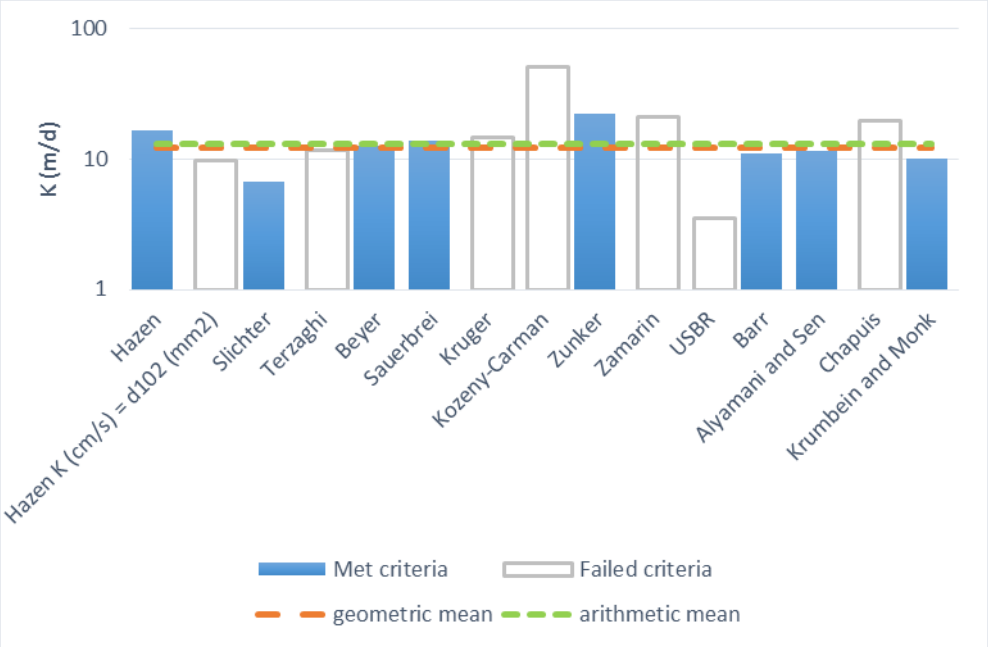


Sieve opening (ps) di (mm)	Mass of retained (mr) (g)	mass fraction (mf)	Percent Passing (pp)
2	0.26667	0.00267	99.7333
1	0.0127	0.00013	99.7206
0.5	0.88889	0.00889	98.8317
0.355	2.71746	0.02717	96.1143
0.25	11.746	0.11746	84.3683
0.18	24.1397	0.2414	60.2286
0.125	41.5619	0.41562	18.6667
0.09	16.8	0.168	1.86667
0.063	0.85079	0.00851	1.01587

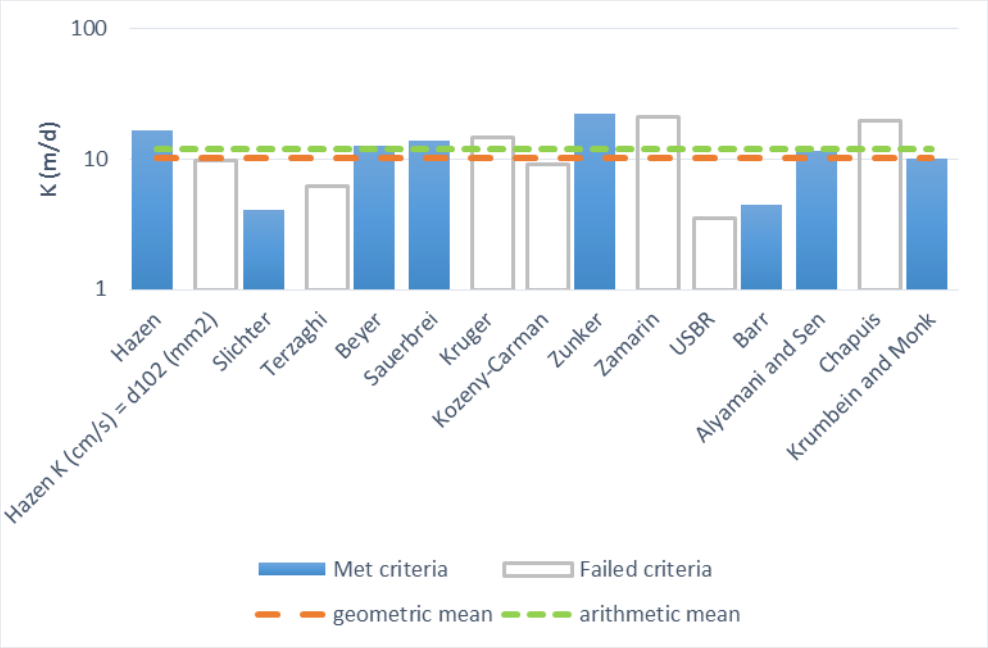
Effective Grain Diameters (mm)		Other Useful Parameters	
d10	0.107	Uniformity Coef.	1.68
d17	0.122	n computed	0.44
d20	0.127	g (cm/s^2)	980.00
d50	0.166	ρ (g/cm^3)	0.9981
d60	0.180	μ (g/cm s)	0.0098
de (Kruger)	0.167	ρg/μ (1/cm s)	9.9327E+04
de (Kozeny)	0.162	tau (Sauerbrei)	1.053
de (Zunker)	0.164	$d_{geometric\ mean}$	0.177
de (Zamarin)	0.165	σ_ϕ	0.543
Io (Alyameni	0.092		

mm	0	% in sample
>64	Boulder	
16 - 64	coarse gravel	
8 - 16	medium gravel	
2 - 8	fine gravel	0.266666667
0.5 - 2	coarse sand	0.901587302
0.25 - 0.5	medium sand	14.46349206
0.063 - 0.25	fine sand	83.35238095
0.016 - 0.063	coarse silt	
0.008 - 0.016	medium silt	
0.002 - 0.008	fine silt	
<0.002	clay	

Slichter, Terzaghi, Kozeny-Carman and Barr with d_{VS}:



Slichter, Terzaghi, Kozeny-Carman and Barr with d_{UU}:

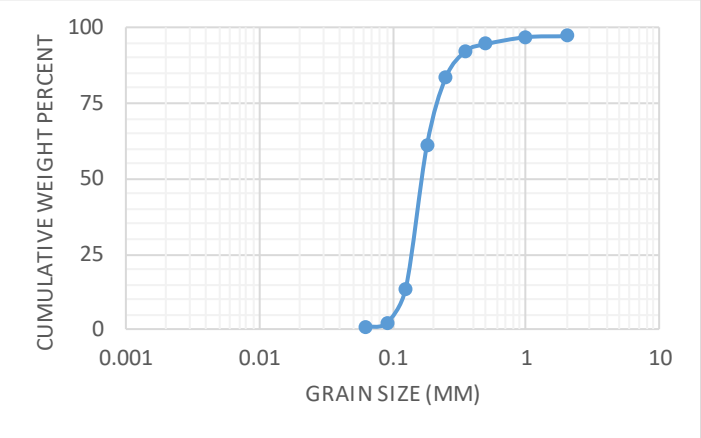


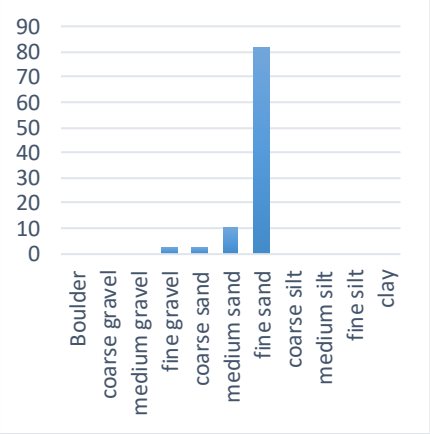
Well 050210/1-T4. Elevation 0.525 m AHD.

Grain Size Analysis Report

Mass Sample (g): 100 T (oC) 20

Uniform sand low in fines



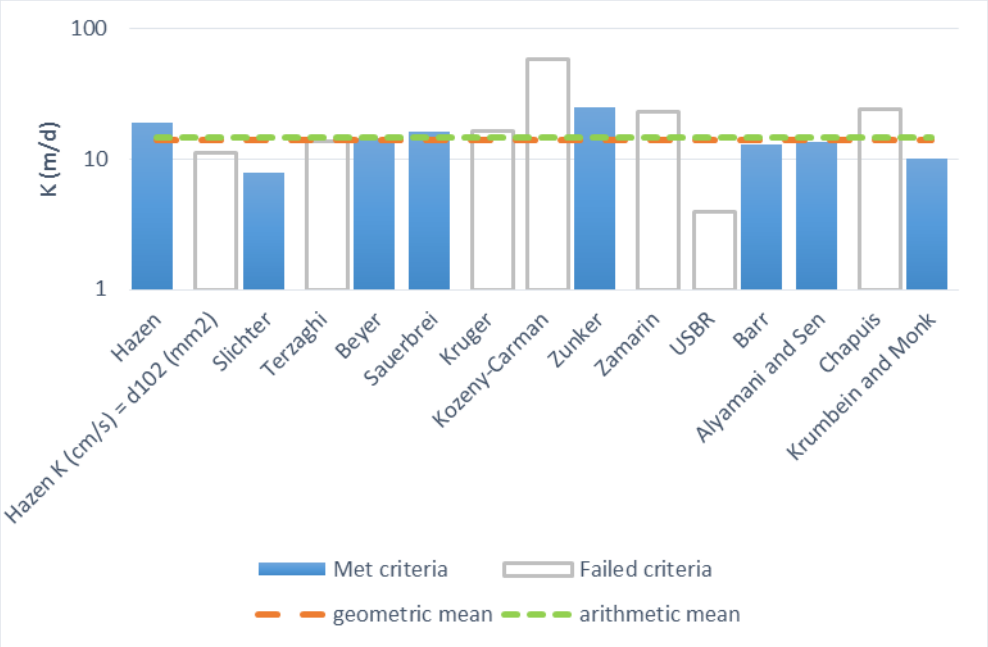


Sieve opening (ps) di (mm)	Mass of retained (mr) (g)	mass fraction (mf)	Percent Passing (pp)
2	2.83856	0.02839	97.1614
1	0.31998	0.0032	96.8415
0.5	2.28117	0.02281	94.5603
0.355	2.25021	0.0225	92.3101
0.25	8.72213	0.08722	83.5879
0.18	22.5743	0.22574	61.0136
0.125	47.2956	0.47296	13.718
0.09	11.5297	0.1153	2.18827
0.063	1.06317	0.01063	1.1251

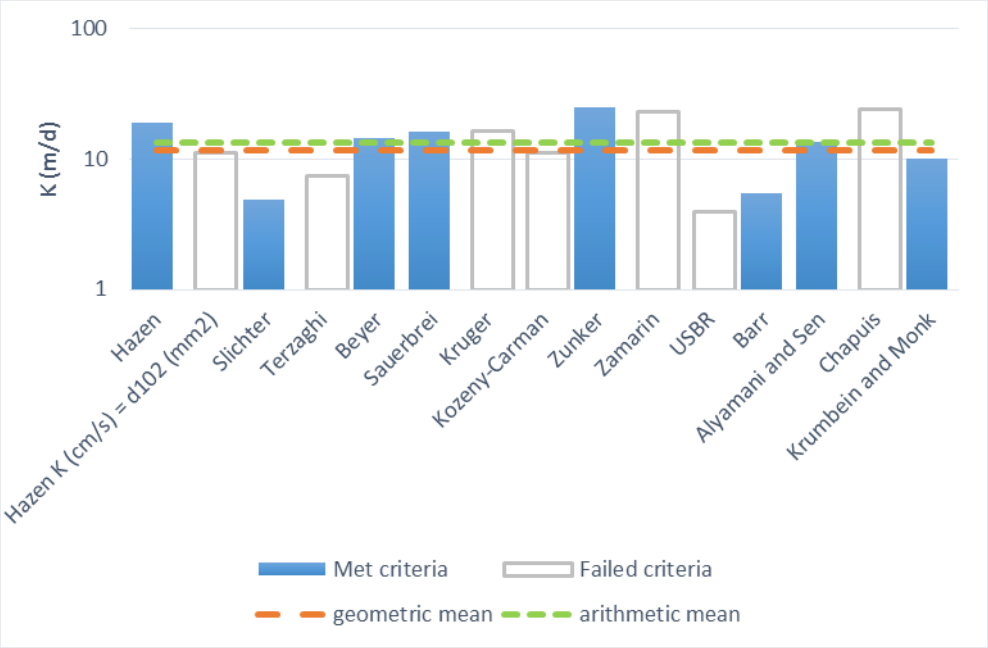
Effective Grain Diameters (mm)		Other Useful Parameters	
d10	0.114	Uniformity Coef.	1.57
d17	0.129	n computed	0.45
d20	0.132	g (cm/s^2)	980.00
d50	0.167	ρ (g/cm^3)	0.9981
d60	0.179	μ (g/cm s)	0.0098
de (Kruger)	0.174	ρg/μ (1/cm s)	9.9327E+04
de (Kozeny)	0.169	tau (Sauerbrei)	1.053
de (Zunker)	0.171	$d_{geometric\ mean}$	0.189
de (Zamarin)	0.173	σ_ϕ	0.643
Io (Alyameni	0.100		

mm	0	% in sample
>64	Boulder	
16 - 64	coarse gravel	
8 - 16	medium gravel	
2 - 8	fine gravel	2.838563171
0.5 - 2	coarse sand	2.601156069
0.25 - 0.5	medium sand	10.97233691
0.063 - 0.25	fine sand	82.46284063
0.016 - 0.063	coarse silt	
0.008 - 0.016	medium silt	
0.002 - 0.008	fine silt	
<0.002	clay	

Slichter, Terzaghi, Kozeny-Carman and Barr with d_{VS}:



Slichter, Terzaghi, Kozeny-Carman and Barr with d_{UU}:

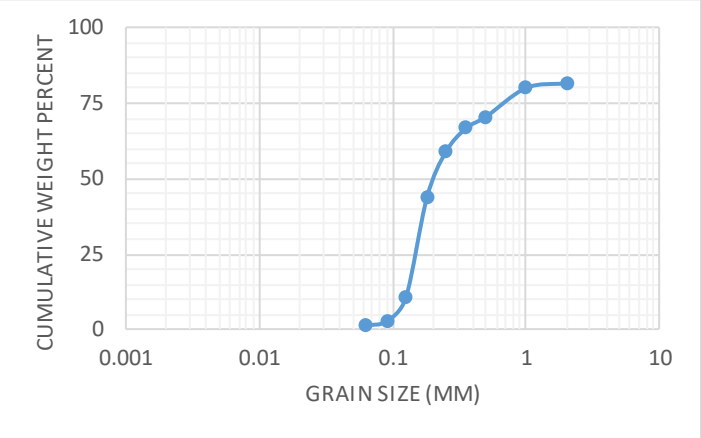


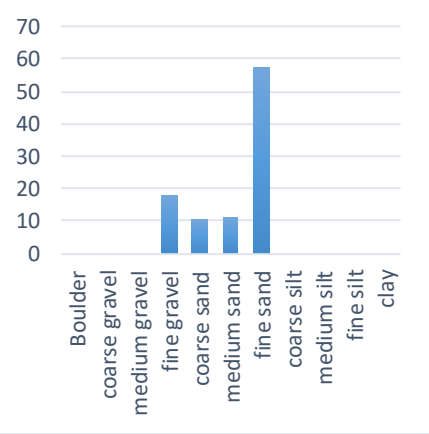
Well 050210/1-T4. Elevation 0.475 m AHD.

Grain Size Analysis Report

Mass Sample (g): 100 T (oC) 20

Moderately well sorted gravelly sand low in fines



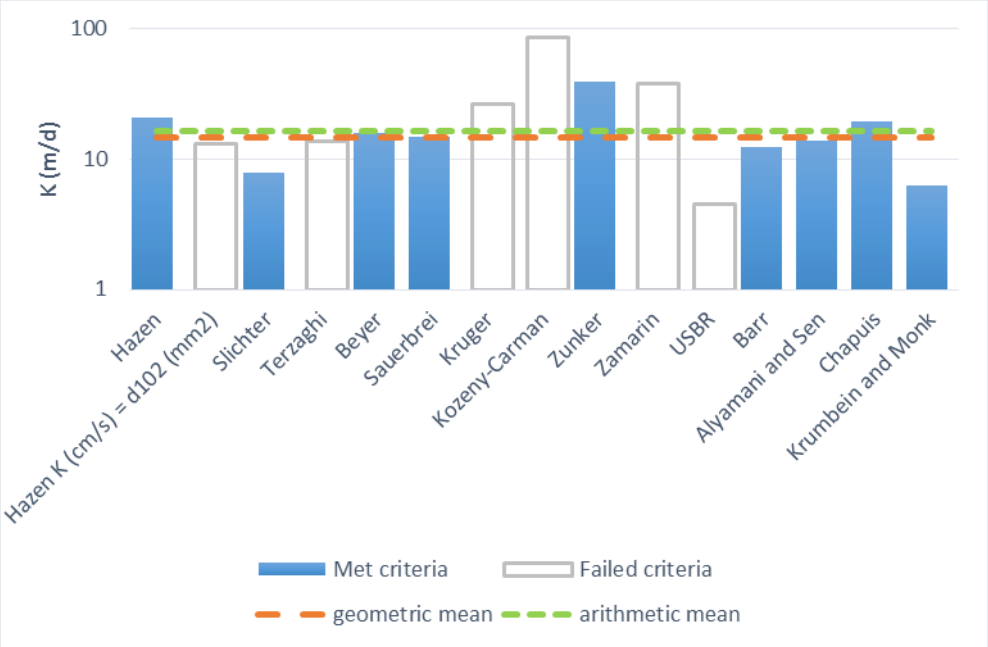


Sieve opening (ps) di (mm)	Mass of retained (mr) (g)	mass fraction (mf)	Percent Passing (pp)
2	18.4266	0.18427	81.5734
1	1.53995	0.0154	80.0334
0.5	9.53889	0.09539	70.4945
0.355	3.76628	0.03766	66.7283
0.25	7.83175	0.07832	58.8965
0.18	15.1883	0.15188	43.7082
0.125	33.2101	0.3321	10.4981
0.09	7.77015	0.0777	2.72791
0.063	1.25836	0.01258	1.46955

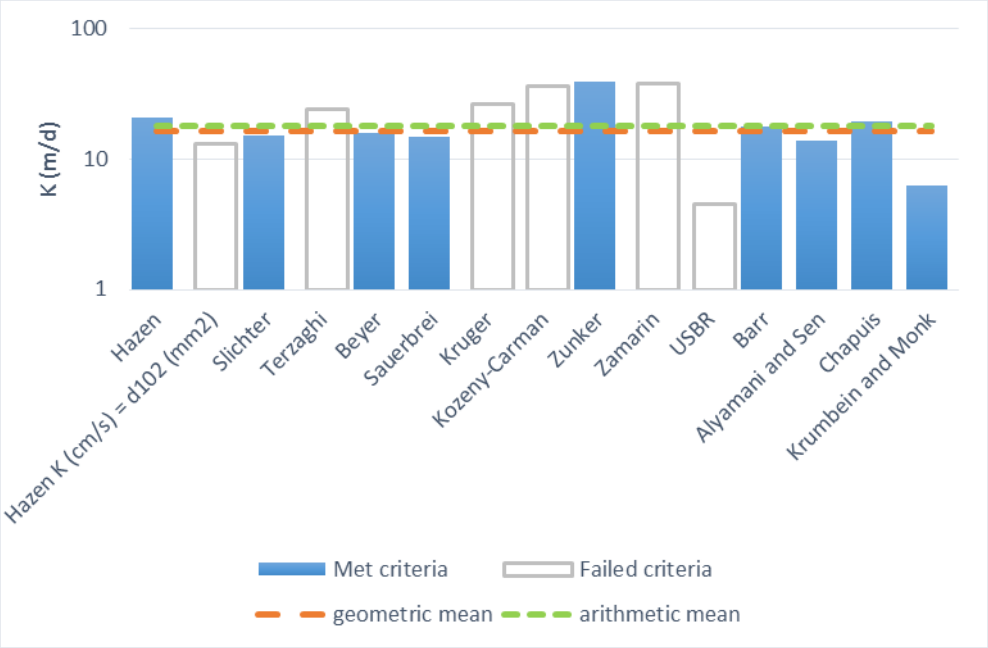
Effective Grain Diameters (mm)		Other Useful Parameters	
d10	0.123	Uniformity Coef.	2.16
d17	0.136	n computed	0.43
d20	0.141	g (cm/s^2)	980.00
d50	0.209	ρ (g/cm^3)	0.9981
d60	0.265	μ (g/cm s)	0.0098
de (Kruger)	0.235	ρg/μ (1/cm s)	9.9327E+04
de (Kozeny)	0.227	tau (Sauerbrei)	1.053
de (Zunker)	0.230	$d_{geometric\ mean}$	0.293
de (Zamarin)	0.232	σ_ϕ	1.673
Io (Alyameni	0.101		

mm	0	% in sample
>64	Boulder	
16 - 64	coarse gravel	
8 - 16	medium gravel	
2 - 8	fine gravel	18.42661035
0.5 - 2	coarse sand	11.07884548
0.25 - 0.5	medium sand	11.59802886
0.063 - 0.25	fine sand	57.42696234
0.016 - 0.063	coarse silt	
0.008 - 0.016	medium silt	
0.002 - 0.008	fine silt	
<0.002	clay	

Slichter, Terzaghi, Kozeny-Carman and Barr with d_{VS}:



Slichter, Terzaghi, Kozeny-Carman and Barr with d_{UU}:

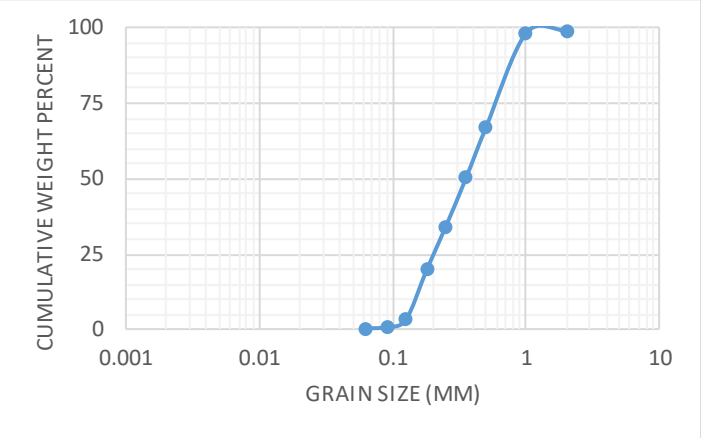


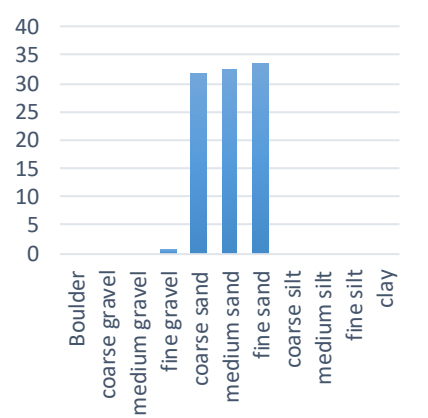
Well 040610/6-T4. Elevation 1.385 m AHD.

Grain Size Analysis Report

Mass Sample (g): 100 T (oC) 20

Moderately well sorted sand low in fines



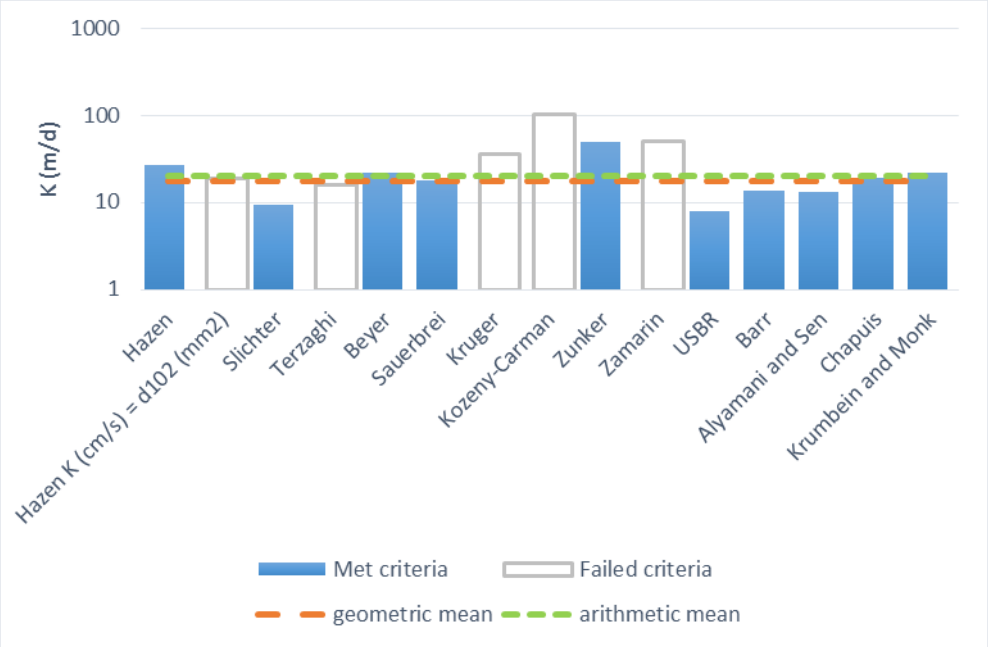


Sieve opening (ps) di (mm)	Mass of retained (mr) (g)	mass fraction (mf)	Percent Passing (pp)
2	0.90439	0.00904	99.0956
1	0.90439	0.00904	98.1912
0.5	31.18	0.3118	67.0112
0.355	16.6236	0.16624	50.3876
0.25	16.1585	0.16158	34.2291
0.18	14.255	0.14255	19.9742
0.125	16.7528	0.16753	3.22136
0.09	2.42033	0.0242	0.80103
0.063	0.34453	0.00345	0.4565

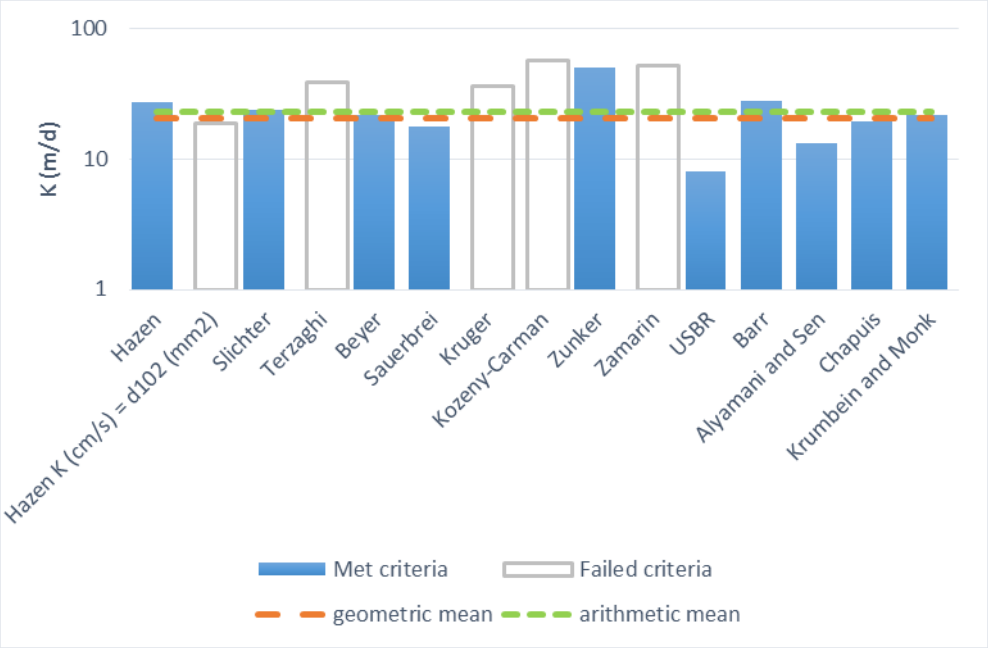
Effective Grain Diameters (mm)		Other Useful Parameters	
d10	0.147	Uniformity Coef.	2.98
d17	0.170	n computed	0.40
d20	0.180	g (cm/s^2)	980.00
d50	0.352	ρ (g/cm^3)	0.9981
d60	0.439	μ (g/cm s)	0.0098
de (Kruger)	0.296	ρg/μ (1/cm s)	9.9327E+04
de (Kozeny)	0.284	tau (Sauerbrei)	1.053
de (Zunker)	0.288	$d_{geometric\ mean}$	0.351
de (Zamarin)	0.292	σ_ϕ	0.986
Io (Alyameni	0.096		

mm	0	% in sample
>64	Boulder	
16 - 64	coarse gravel	
8 - 16	medium gravel	
2 - 8	fine gravel	0.904392765
0.5 - 2	coarse sand	32.08440999
0.25 - 0.5	medium sand	32.78208441
0.063 - 0.25	fine sand	33.77260982
0.016 - 0.063	coarse silt	
0.008 - 0.016	medium silt	
0.002 - 0.008	fine silt	
<0.002	clay	

Slichter, Terzaghi, Kozeny-Carman and Barr with d_{VS}:



Slichter, Terzaghi, Kozeny-Carman and Barr with d_{UU}:

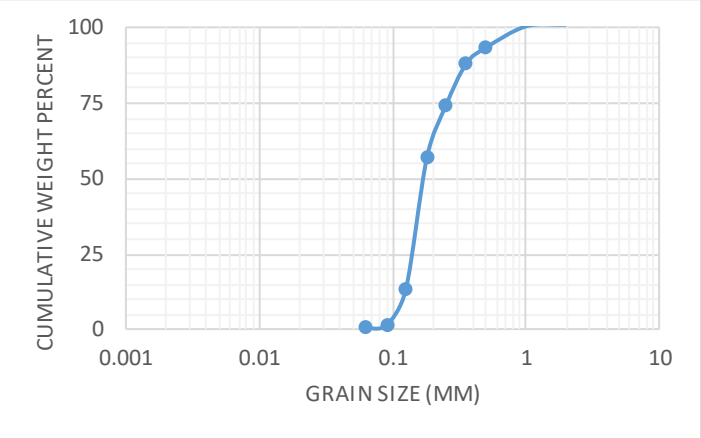


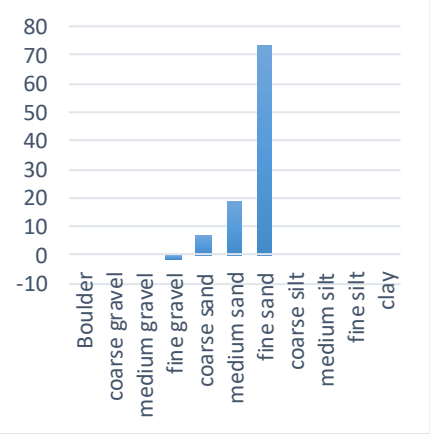
Well 040610/6-T4. Elevation 1.335 m AHD.

Grain Size Analysis Report

Mass Sample (g): 100 T (oC) 20

Uniform sand low in fines



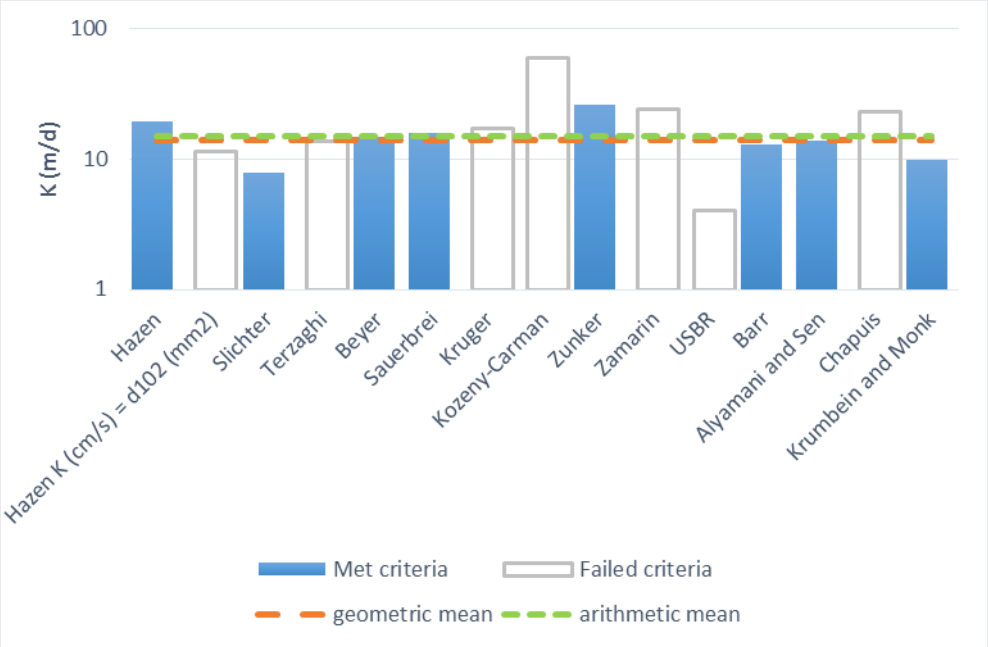


Sieve opening (ps) di (mm)	Mass of retained (mr) (g)	mass fraction (mf)	Percent Passing (pp)
2	-0.9814	-0.0098	100.981
1	0.53074	0.00531	100.451
0.5	7.04987	0.0705	93.4008
0.355	5.31744	0.05317	88.0833
0.25	13.8694	0.13869	74.2139
0.18	17.2241	0.17224	56.9898
0.125	43.7412	0.43741	13.2485
0.09	11.7364	0.11736	1.51212
0.063	0.90126	0.00901	0.61086

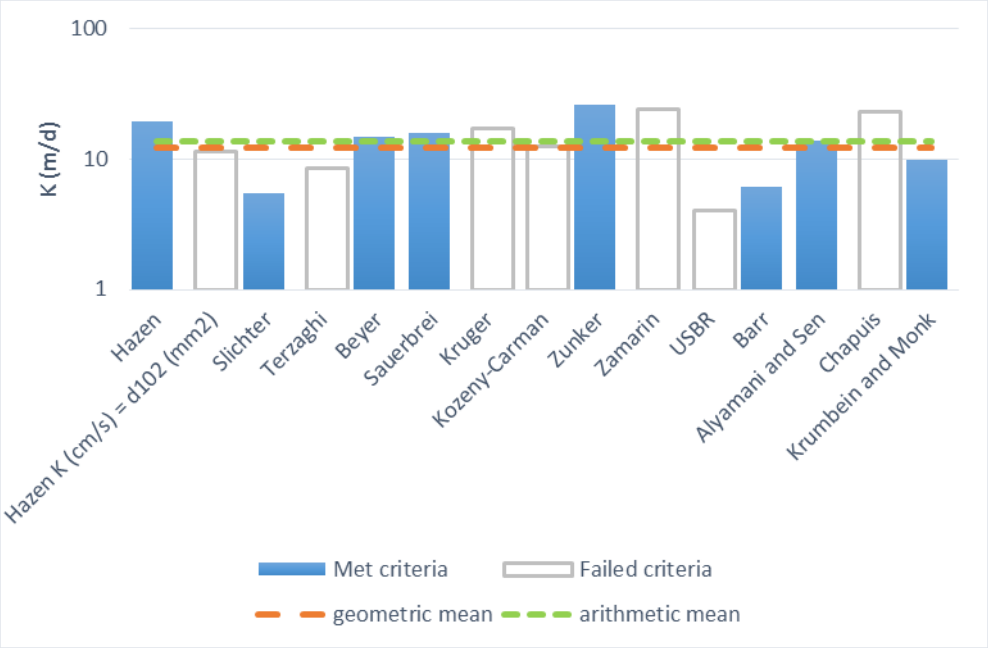
Effective Grain Diameters (mm)		Other Useful Parameters	
d10	0.115	Uniformity Coef.	1.67
d17	0.130	n computed	0.44
d20	0.133	g (cm/s^2)	980.00
d50	0.171	ρ (g/cm^3)	0.9981
d60	0.192	μ (g/cm s)	0.0098
de (Kruger)	0.180	ρg/μ (1/cm s)	9.9327E+04
de (Kozeny)	0.174	tau (Sauerbrei)	1.053
de (Zunker)	0.176	$d_{geometric\ mean}$	0.198
de (Zamarin)	0.178	σ_ϕ	0.729
Io (Alyameni	0.101		

mm	0	% in sample
>64	Boulder	
16 - 64	coarse gravel	
8 - 16	medium gravel	
2 - 8	fine gravel	-0.981373923
0.5 - 2	coarse sand	7.580612858
0.25 - 0.5	medium sand	19.18686161
0.063 - 0.25	fine sand	73.60304426
0.016 - 0.063	coarse silt	
0.008 - 0.016	medium silt	
0.002 - 0.008	fine silt	
<0.002	clay	

Slichter, Terzaghi, Kozeny-Carman and Barr with d_{VS}:



Slichter, Terzaghi, Kozeny-Carman and Barr with d_{UU}:

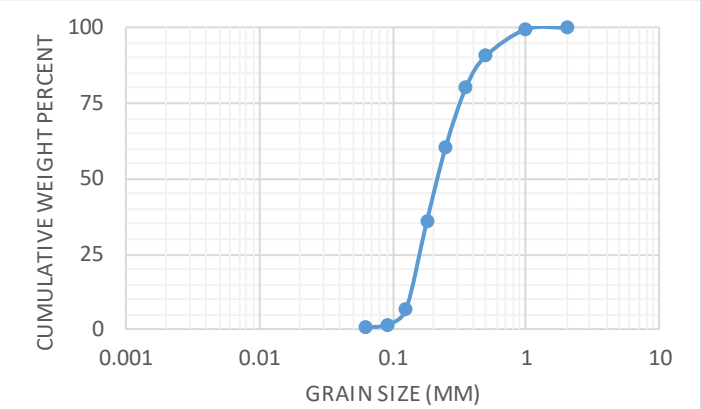


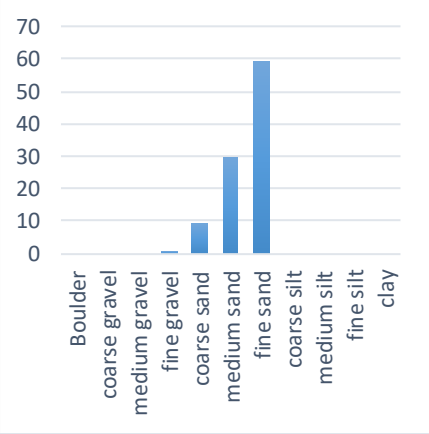
Well 040610/6-T4. Elevation 1.285 m AHD.

Grain Size Analysis Report

Mass Sample (g): 100 T (oC) 20

Uniform sand low in fines



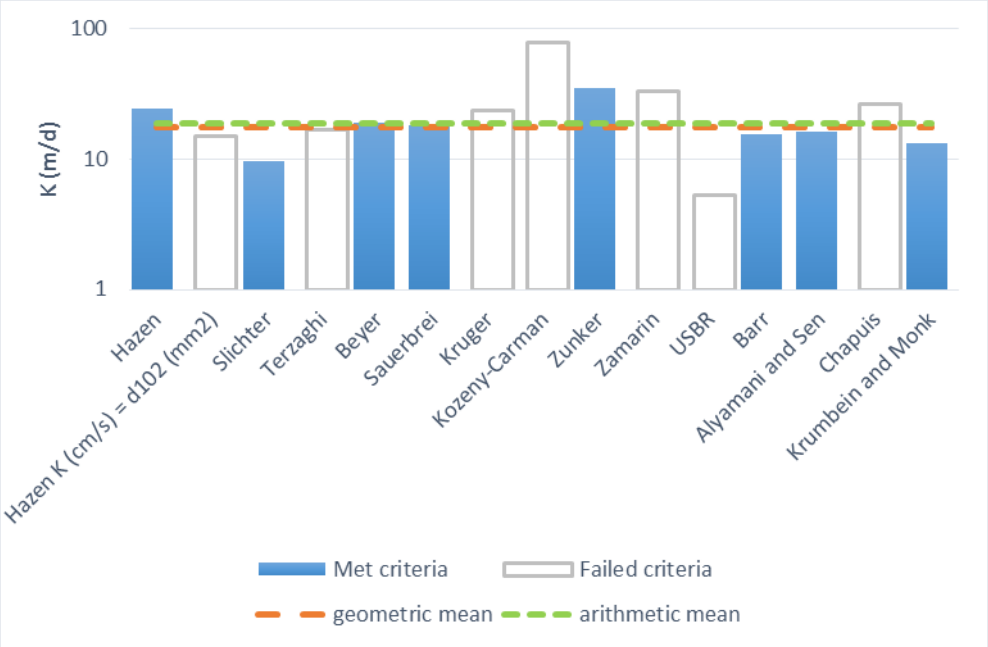


Sieve opening (ps) di (mm)	Mass of retained (mr) (g)	mass fraction (mf)	Percent Passing (pp)
2	0.00983	9.8E-05	99.9902
1	0.51116	0.00511	99.479
0.5	8.78797	0.08788	90.691
0.355	10.3116	0.10312	80.3794
0.25	19.6599	0.1966	60.7196
0.18	24.7223	0.24722	35.9972
0.125	29.48	0.2948	6.51725
0.09	4.97395	0.04974	1.5433
0.063	0.6881	0.00688	0.8552

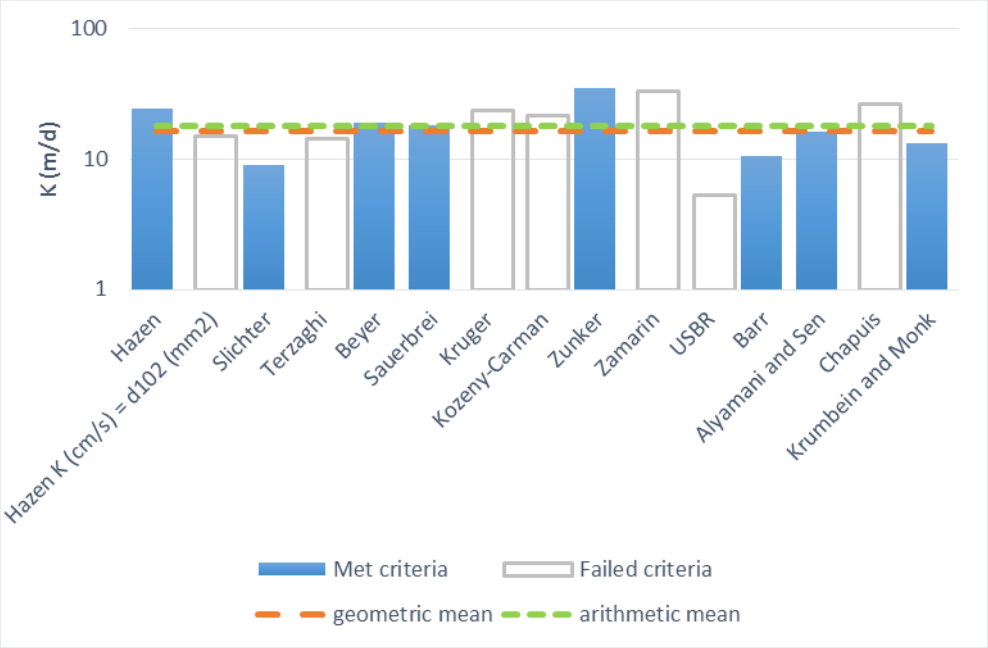
Effective Grain Diameters (mm)		Other Useful Parameters	
d10	0.131	Uniformity Coef.	1.89
d17	0.145	n computed	0.43
d20	0.150	g (cm/s^2)	980.00
d50	0.220	ρ (g/cm^3)	0.9981
d60	0.248	μ (g/cm s)	0.0098
de (Kruger)	0.215	ρg/μ (1/cm s)	9.9327E+04
de (Kozeny)	0.208	tau (Sauerbrei)	1.053
de (Zunker)	0.211	$d_{geometric\ mean}$	0.240
de (Zamarin)	0.213	σ_ϕ	0.787
Io (Alyameni	0.109		

mm	0	% in sample
>64	Boulder	
16 - 64	coarse gravel	
8 - 16	medium gravel	
2 - 8	fine gravel	0.009829942
0.5 - 2	coarse sand	9.299125135
0.25 - 0.5	medium sand	29.97149317
0.063 - 0.25	fine sand	59.8643468
0.016 - 0.063	coarse silt	
0.008 - 0.016	medium silt	
0.002 - 0.008	fine silt	
<0.002	clay	

Slichter, Terzaghi, Kozeny-Carman and Barr with d_{VS}:



Slichter, Terzaghi, Kozeny-Carman and Barr with d_{UU}:

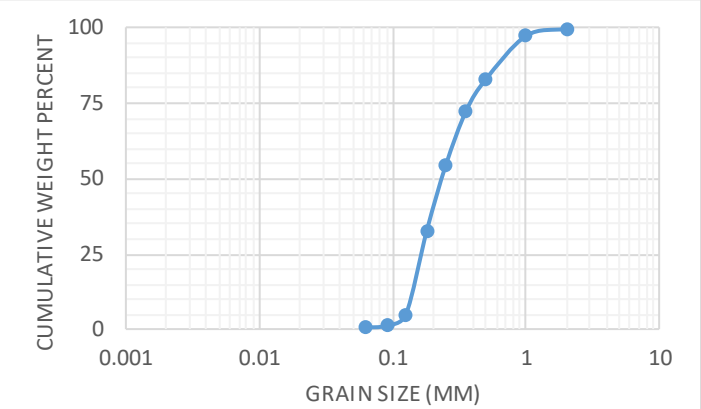


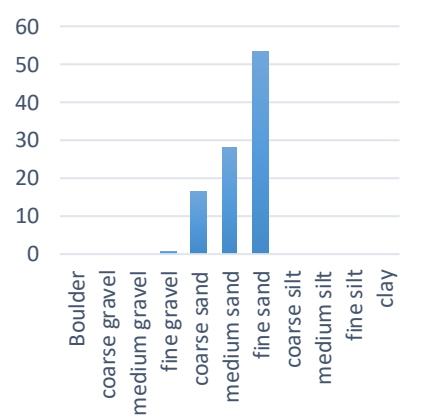
Well 040610/6-T4. Elevation 1.235 m AHD.

Grain Size Analysis Report

Mass Sample (g): 100 T (oC) 20

Moderately well sorted sand low in fines



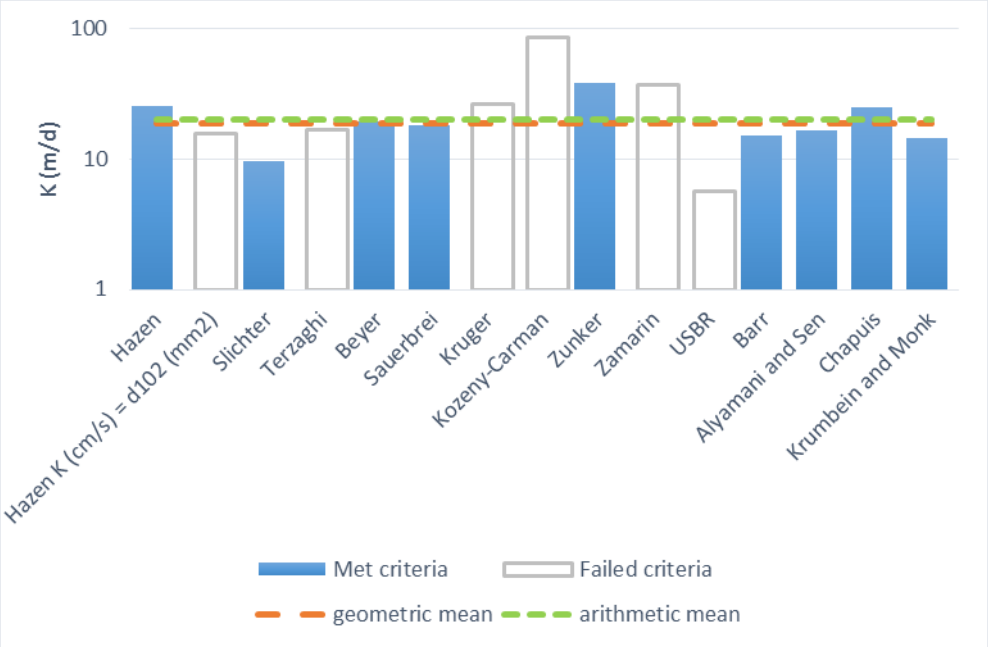


Sieve opening (ps) di (mm)	Mass of retained (mr) (g)	mass fraction (mf)	Percent Passing (pp)
2	0.3634	0.00363	99.6366
1	2.32948	0.02329	97.3071
0.5	14.331	0.14331	82.9761
0.355	10.464	0.10464	72.5121
0.25	17.9184	0.17918	54.5937
0.18	21.6549	0.21655	32.9389
0.125	27.9724	0.27972	4.96646
0.09	3.67126	0.03671	1.29519
0.063	0.57771	0.00578	0.71748

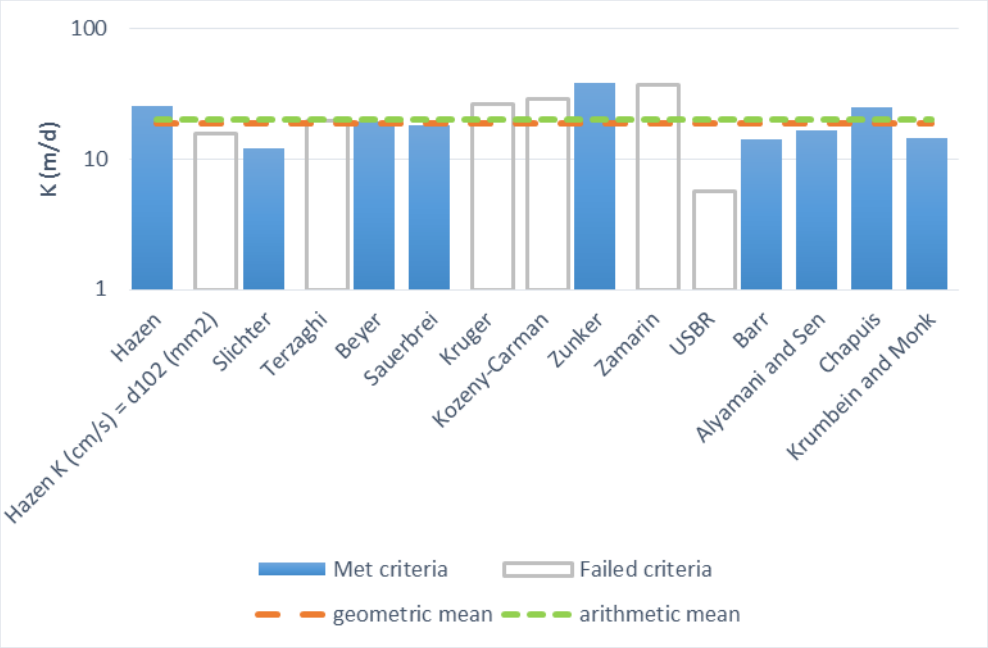
Effective Grain Diameters (mm)		Other Useful Parameters	
d10	0.135	Uniformity Coef.	2.09
d17	0.149	n computed	0.43
d20	0.155	g (cm/s^2)	980.00
d50	0.235	ρ (g/cm^3)	0.9981
d60	0.282	μ (g/cm s)	0.0098
de (Kruger)	0.232	ρg/μ (1/cm s)	9.9327E+04
de (Kozeny)	0.224	tau (Sauerbrei)	1.053
de (Zunker)	0.227	$d_{geometric\ mean}$	0.269
de (Zamarin)	0.230	σ_ϕ	0.903
Io (Alyameni	0.110		

mm	0	% in sample
>64	Boulder	
16 - 64	coarse gravel	
8 - 16	medium gravel	
2 - 8	fine gravel	0.36339918
0.5 - 2	coarse sand	16.66045471
0.25 - 0.5	medium sand	28.38240775
0.063 - 0.25	fine sand	53.87625792
0.016 - 0.063	coarse silt	
0.008 - 0.016	medium silt	
0.002 - 0.008	fine silt	
<0.002	clay	

Slichter, Terzaghi, Kozeny-Carman and Barr with d_{VS}:



Slichter, Terzaghi, Kozeny-Carman and Barr with d_{UU}:

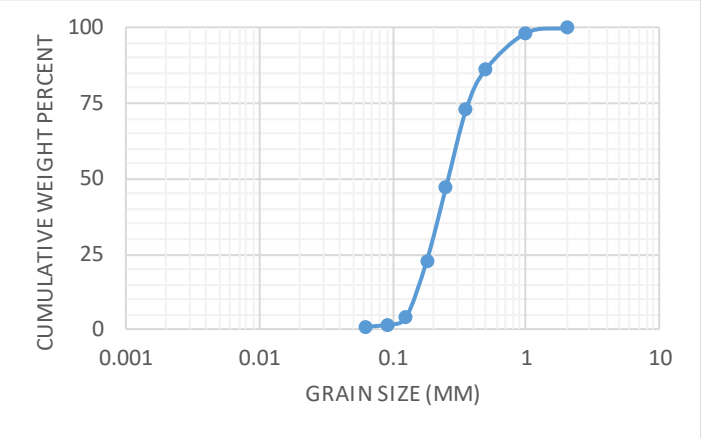


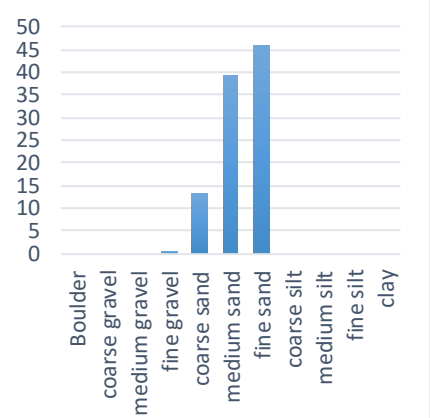
Well 040610/6-T4. Elevation 1.185 m AHD.

Grain Size Analysis Report

Mass Sample (g): 100 T (oC) 20

Moderately well sorted sand low in fines



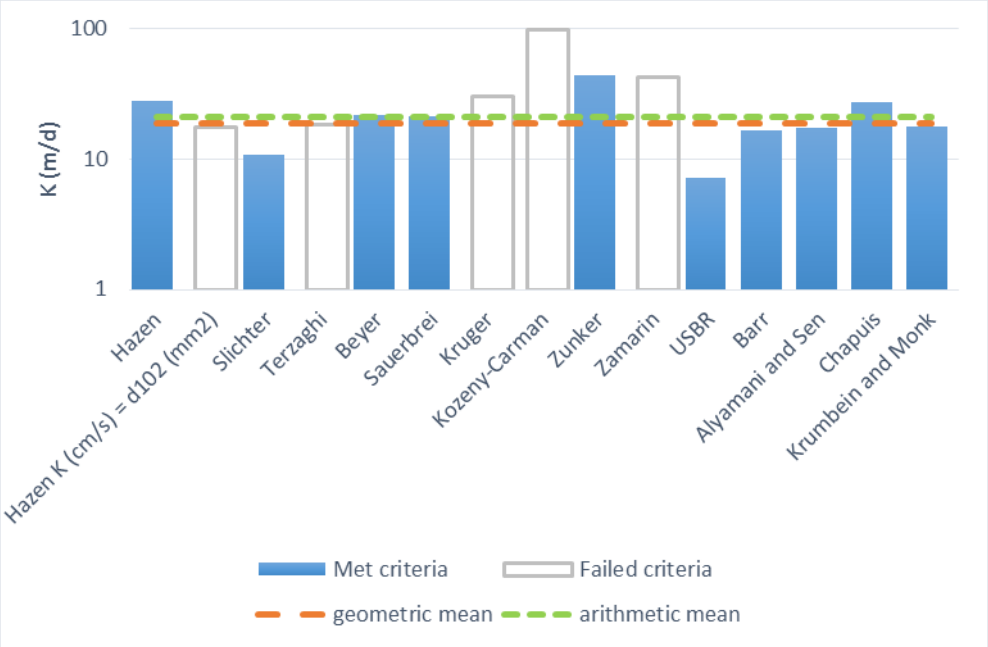


Sieve opening (ps) di (mm)	Mass of retained (mr) (g)	mass fraction (mf)	Percent Passing (pp)
2	0.15307	0.00153	99.8469
1	1.58806	0.01588	98.2589
0.5	11.9392	0.11939	86.3197
0.355	13.3359	0.13336	72.9838
0.25	25.9734	0.25973	47.0104
0.18	24.0122	0.24012	22.9982
0.125	19.0376	0.19038	3.96059
0.09	2.32469	0.02325	1.63589
0.063	0.65053	0.00651	0.98536

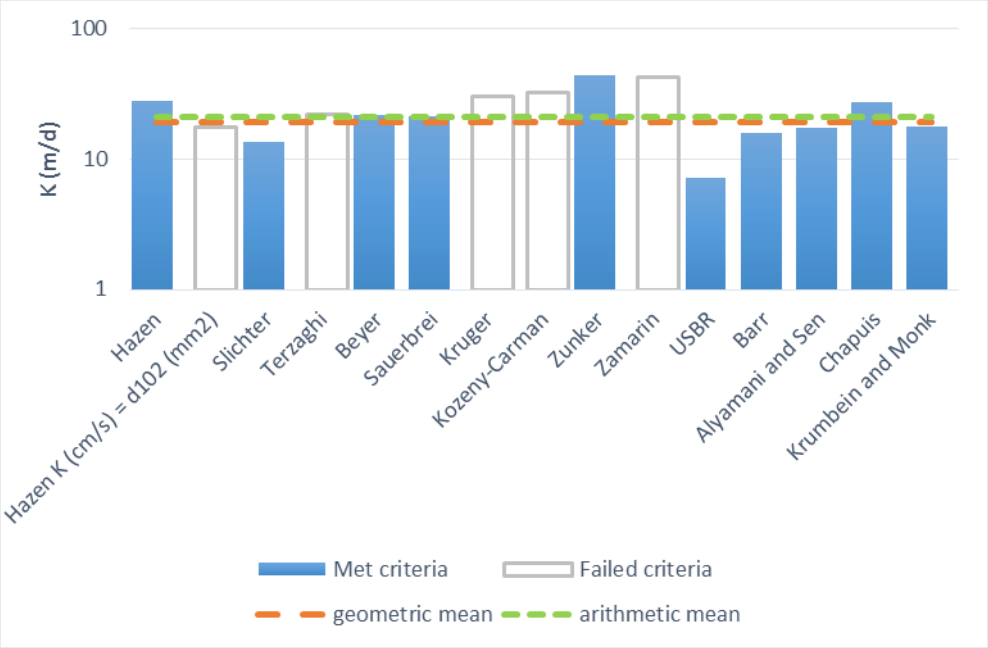
Effective Grain Diameters (mm)		Other Useful Parameters	
d10	0.142	Uniformity Coef.	2.12
d17	0.163	n computed	0.43
d20	0.171	g (cm/s^2)	980.00
d50	0.262	ρ (g/cm^3)	0.9981
d60	0.303	μ (g/cm s)	0.0098
de (Kruger)	0.250	ρg/μ (1/cm s)	9.9327E+04
de (Kozeny)	0.241	tau (Sauerbrei)	1.053
de (Zunker)	0.244	$d_{geometric\ mean}$	0.281
de (Zamarin)	0.247	σ_ϕ	0.810
Io (Alyameni	0.113		

mm	0	% in sample
>64	Boulder	
16 - 64	coarse gravel	
8 - 16	medium gravel	
2 - 8	fine gravel	0.153066105
0.5 - 2	coarse sand	13.52721707
0.25 - 0.5	medium sand	39.3092892
0.063 - 0.25	fine sand	46.02506457
0.016 - 0.063	coarse silt	
0.008 - 0.016	medium silt	
0.002 - 0.008	fine silt	
<0.002	clay	

Slichter, Terzaghi, Kozeny-Carman and Barr with d_{VS}:



Slichter, Terzaghi, Kozeny-Carman and Barr with d_{UU}:

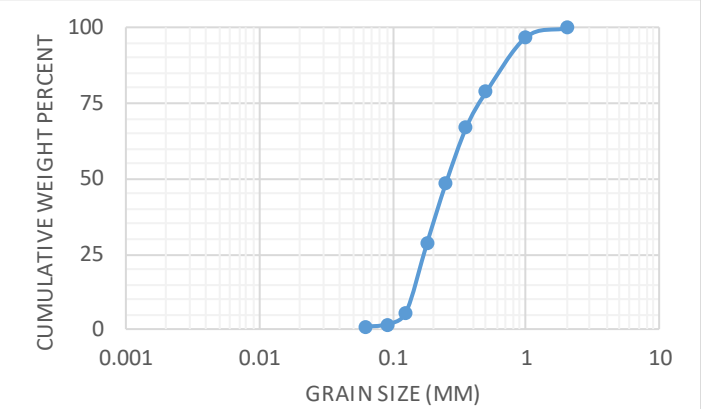


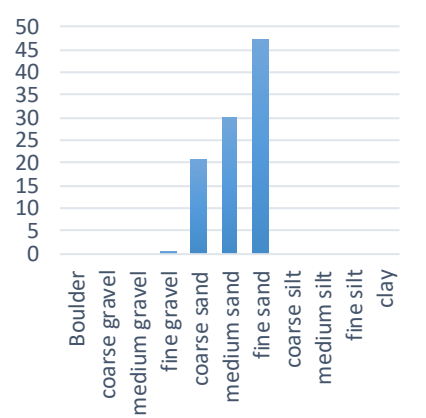
Well 040610/6-T4. Elevation 1.135 m AHD.

Grain Size Analysis Report

Mass Sample (g): 100 T (oC) 20

Moderately well sorted sand low in fines



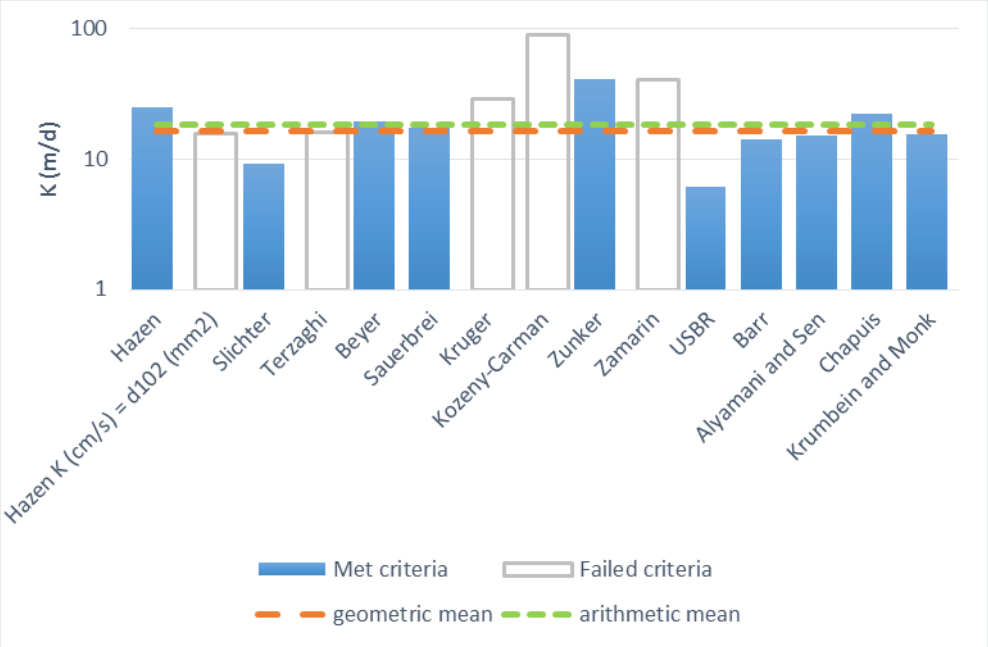


Sieve opening (ps) di (mm)	Mass of retained (mr) (g)	mass fraction (mf)	Percent Passing (pp)
2	0.21684	0.00217	99.7832
1	2.90374	0.02904	96.8794
0.5	18.2615	0.18262	78.6179
0.355	11.7092	0.11709	66.9086
0.25	18.4312	0.18431	48.4774
0.18	19.9397	0.1994	28.5378
0.125	22.9565	0.22957	5.58122
0.09	3.80881	0.03809	1.77241
0.063	0.72594	0.00726	1.04648

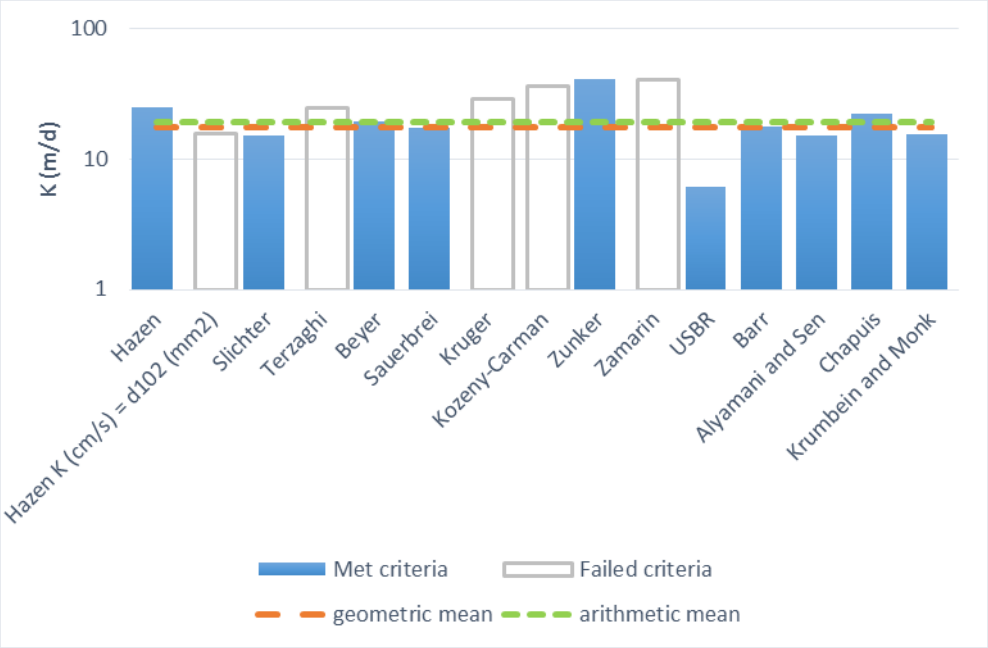
Effective Grain Diameters (mm)		Other Useful Parameters	
d10	0.136	Uniformity Coef.	2.33
d17	0.152	n computed	0.42
d20	0.160	g (cm/s^2)	980.00
d50	0.259	ρ (g/cm^3)	0.9981
d60	0.316	μ (g/cm s)	0.0098
de (Kruger)	0.248	ρg/μ (1/cm s)	9.9327E+04
de (Kozeny)	0.239	tau (Sauerbrei)	1.053
de (Zunker)	0.242	$d_{geometric\ mean}$	0.293
de (Zamarin)	0.245	σ_ϕ	0.980
Io (Alyameni	0.105		

mm	0	% in sample
>64	Boulder	
16 - 64	coarse gravel	
8 - 16	medium gravel	
2 - 8	fine gravel	0.216837937
0.5 - 2	coarse sand	21.16526822
0.25 - 0.5	medium sand	30.14047327
0.063 - 0.25	fine sand	47.43094183
0.016 - 0.063	coarse silt	
0.008 - 0.016	medium silt	
0.002 - 0.008	fine silt	
<0.002	clay	

Slichter, Terzaghi, Kozeny-Carman and Barr with d_{VS}:



Slichter, Terzaghi, Kozeny-Carman and Barr with d_{UU}:

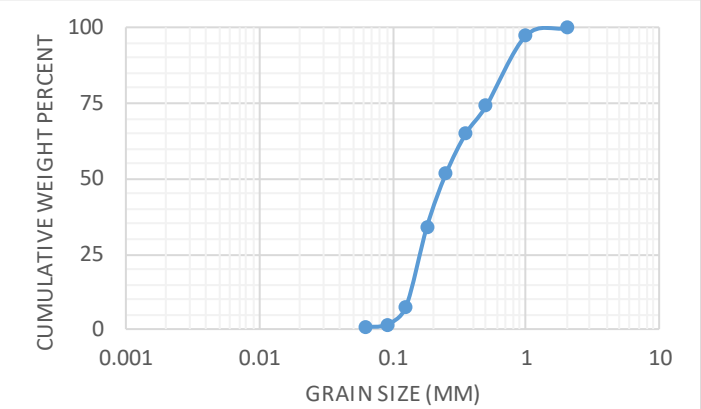


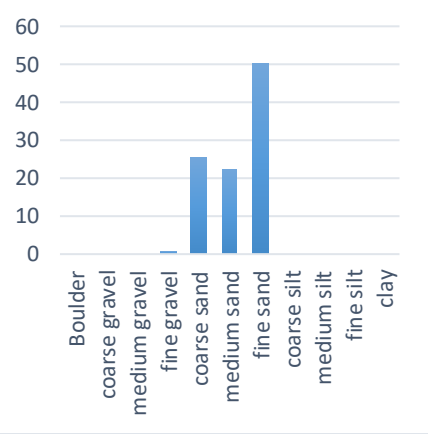
Well 040610/6-T4. Elevation 1.085 m AHD.

Grain Size Analysis Report

Mass Sample (g): 100 T (oC) 20

Moderately well sorted sand low in fines



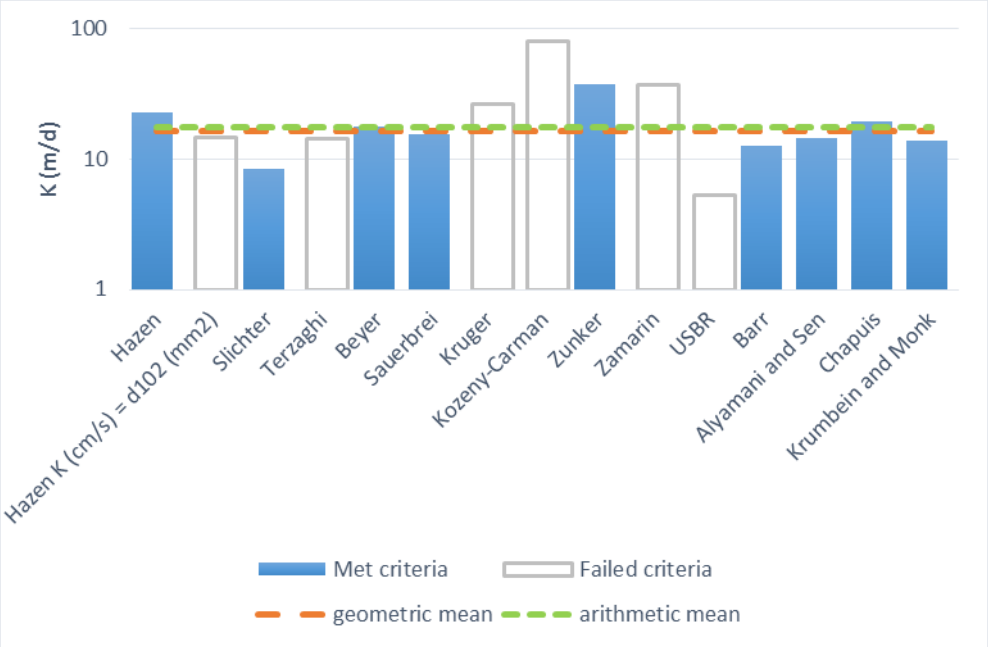


Sieve opening (ps) di (mm)	Mass of retained (mr) (g)	mass fraction (mf)	Percent Passing (pp)
2	0.21136	0.00211	99.7886
1	2.35373	0.02354	97.4349
0.5	23.4413	0.23441	73.9937
0.355	8.83851	0.08839	65.1552
0.25	13.546	0.13546	51.6092
0.18	17.5521	0.17552	34.0571
0.125	26.6308	0.26631	7.42627
0.09	5.75464	0.05755	1.67163
0.063	0.74935	0.00749	0.92228

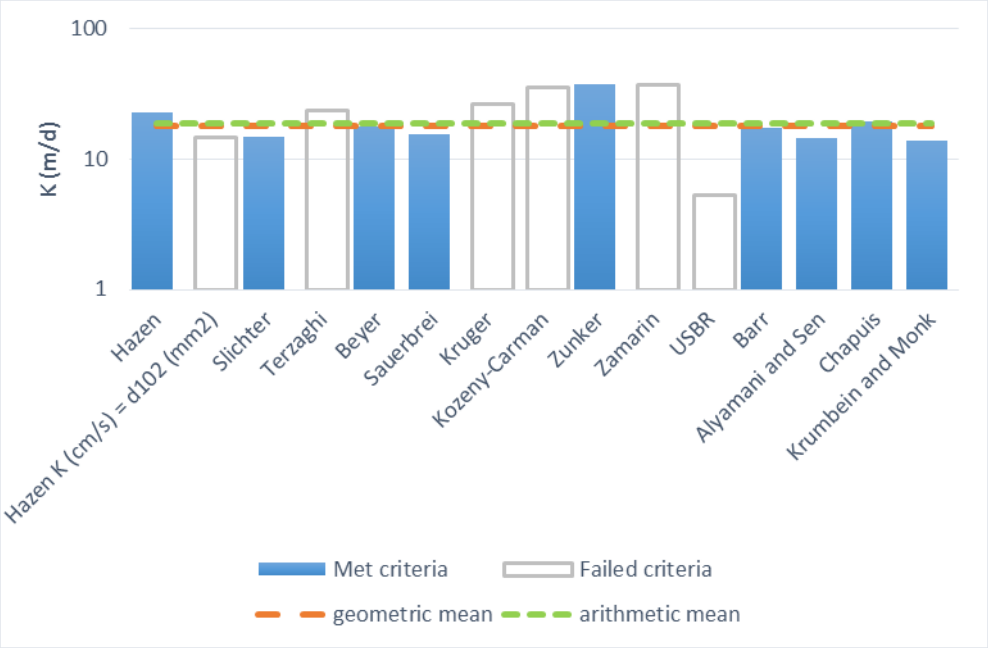
Effective Grain Diameters (mm)		Other Useful Parameters	
d10	0.130	Uniformity Coef.	2.42
d17	0.145	n computed	0.42
d20	0.151	g (cm/s^2)	980.00
d50	0.244	ρ (g/cm^3)	0.9981
d60	0.315	μ (g/cm s)	0.0098
de (Kruger)	0.239	ρg/μ (1/cm s)	9.9327E+04
de (Kozeny)	0.230	tau (Sauerbrei)	1.053
de (Zunker)	0.233	$d_{geometric\ mean}$	0.290
de (Zamarin)	0.236	σ_ϕ	1.051
Io (Alyameni	0.102		

mm	0	% in sample
>64	Boulder	
16 - 64	coarse gravel	
8 - 16	medium gravel	
2 - 8	fine gravel	0.211355558
0.5 - 2	coarse sand	25.79498511
0.25 - 0.5	medium sand	22.38447497
0.063 - 0.25	fine sand	50.68690556
0.016 - 0.063	coarse silt	
0.008 - 0.016	medium silt	
0.002 - 0.008	fine silt	
<0.002	clay	

Slichter, Terzaghi, Kozeny-Carman and Barr with d_{VS}:



Slichter, Terzaghi, Kozeny-Carman and Barr with d_{UU}:

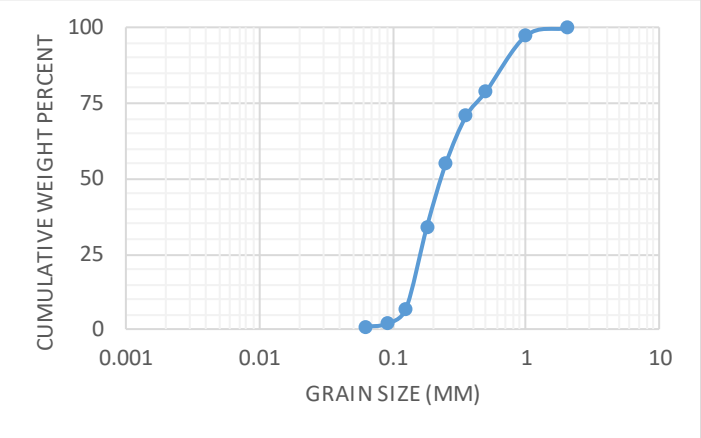


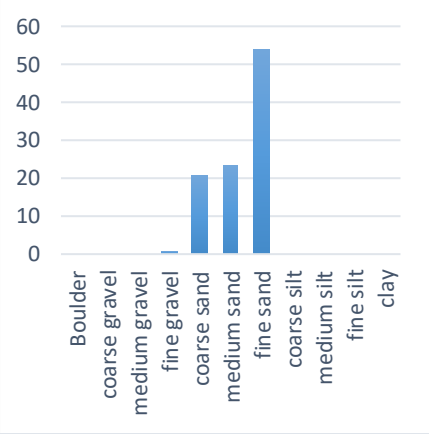
Well 040610/6-T4. Elevation 1.035 m AHD.

Grain Size Analysis Report

Mass Sample (g): 100 T (oC) 20

Moderately well sorted sand low in fines



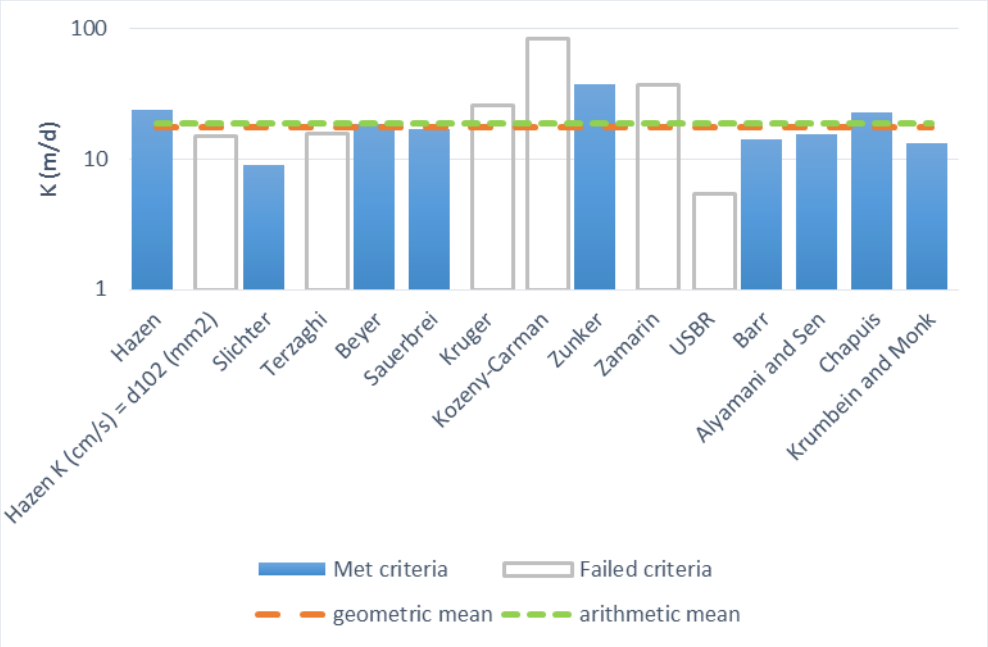


Sieve opening (ps) di (mm)	Mass of retained (mr) (g)	mass fraction (mf)	Percent Passing (pp)
2	0.19236	0.00192	99.8076
1	2.43945	0.02439	97.3682
0.5	18.4839	0.18484	78.8843
0.355	8.09653	0.08097	70.7878
0.25	15.7034	0.15703	55.0844
0.18	21.002	0.21002	34.0824
0.125	27.3149	0.27315	6.76751
0.09	4.8789	0.04879	1.88861
0.063	0.83938	0.00839	1.04923

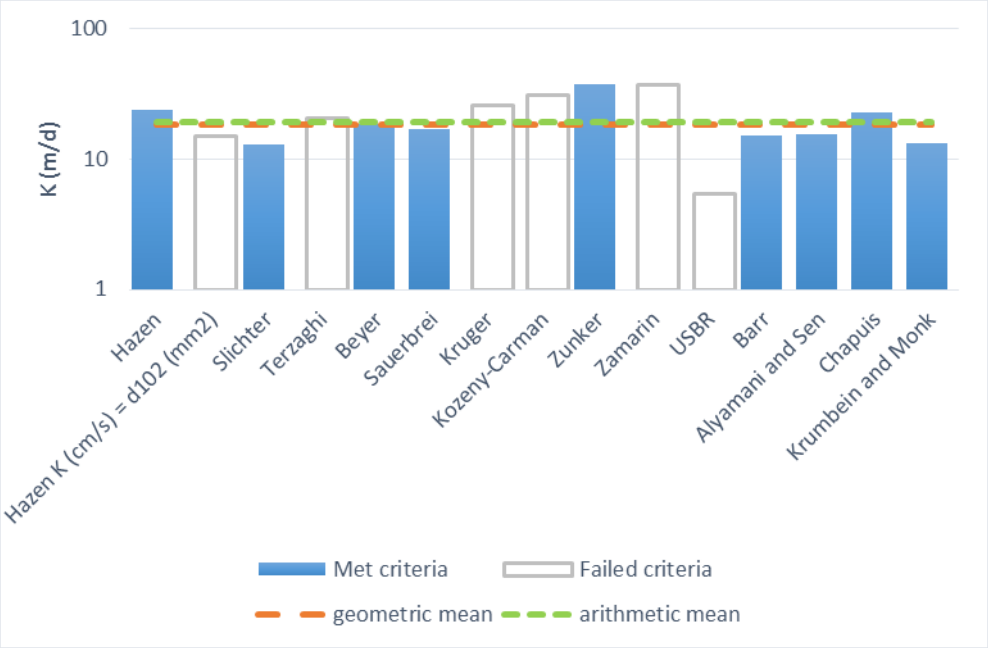
Effective Grain Diameters (mm)		Other Useful Parameters	
d10	0.132	Uniformity Coef.	2.15
d17	0.146	n computed	0.43
d20	0.152	g (cm/s^2)	980.00
d50	0.233	ρ (g/cm^3)	0.9981
d60	0.283	μ (g/cm s)	0.0098
de (Kruger)	0.232	ρg/μ (1/cm s)	9.9327E+04
de (Kozeny)	0.224	tau (Sauerbrei)	1.053
de (Zunker)	0.227	$d_{geometric\ mean}$	0.275
de (Zamarin)	0.230	σ_ϕ	1.002
Io (Alyameni	0.106		

mm	0	% in sample
>64	Boulder	
16 - 64	coarse gravel	
8 - 16	medium gravel	
2 - 8	fine gravel	0.192358136
0.5 - 2	coarse sand	20.92331905
0.25 - 0.5	medium sand	23.79994754
0.063 - 0.25	fine sand	54.03514908
0.016 - 0.063	coarse silt	
0.008 - 0.016	medium silt	
0.002 - 0.008	fine silt	
<0.002	clay	

Slichter, Terzaghi, Kozeny-Carman and Barr with d_{VS}:



Slichter, Terzaghi, Kozeny-Carman and Barr with d_{UU}:

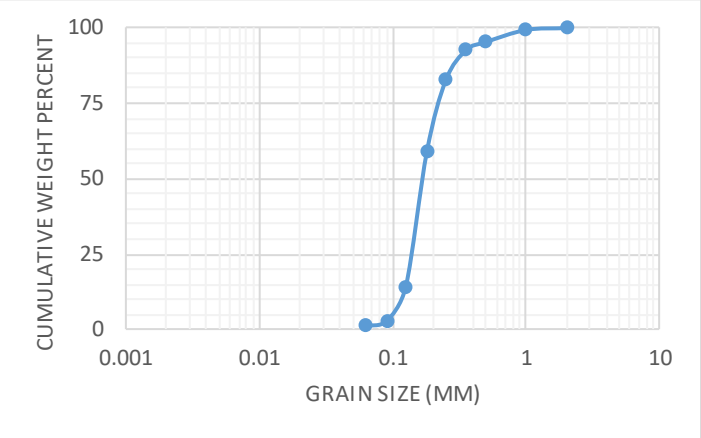


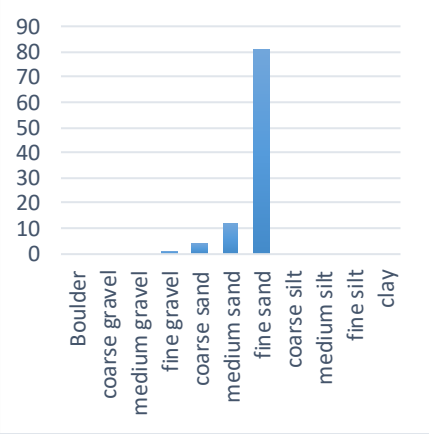
Well 040610/6-T4. Elevation 0.985 m AHD.

Grain Size Analysis Report

Mass Sample (g): 100 T (oC) 20

Uniform sand low in fines



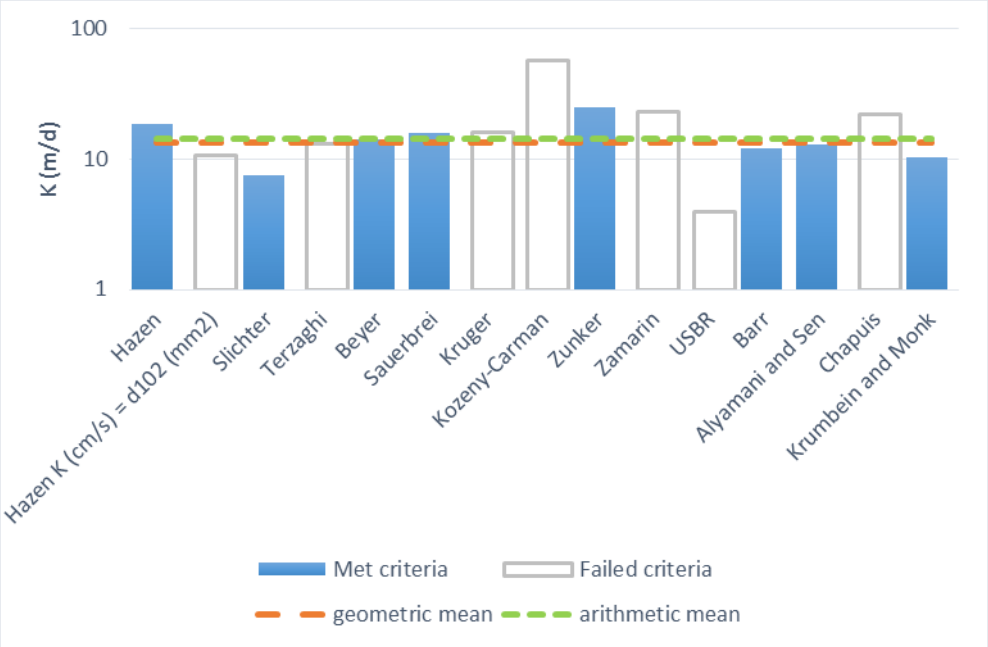


Sieve opening (ps) di (mm)	Mass of retained (mr) (g)	mass fraction (mf)	Percent Passing (pp)
2	0.15663	0.00157	99.8434
1	0.58473	0.00585	99.2586
0.5	3.99916	0.03999	95.2595
0.355	2.67307	0.02673	92.5864
0.25	9.90916	0.09909	82.6772
0.18	23.6295	0.2363	59.0477
0.125	44.8157	0.44816	14.232
0.09	11.3501	0.1135	2.8819
0.063	1.49316	0.01493	1.38874

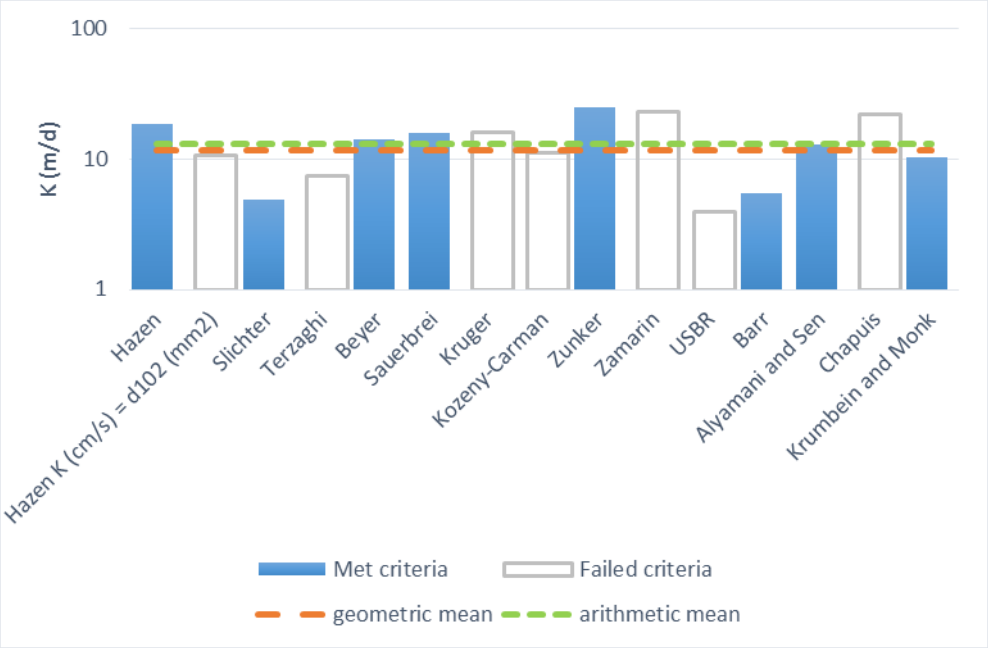
Effective Grain Diameters (mm)		Other Useful Parameters	
d10	0.112	Uniformity Coef.	1.63
d17	0.128	n computed	0.44
d20	0.132	g (cm/s^2)	980.00
d50	0.169	ρ (g/cm^3)	0.9981
d60	0.183	μ (g/cm s)	0.0098
de (Kruger)	0.174	ρg/μ (1/cm s)	9.9327E+04
de (Kozeny)	0.169	tau (Sauerbrei)	1.053
de (Zunker)	0.171	$d_{geometric\ mean}$	0.189
de (Zamarin)	0.173	σ_ϕ	0.617
Io (Alyameni	0.098		

mm	0	% in sample
>64	Boulder	
16 - 64	coarse gravel	
8 - 16	medium gravel	
2 - 8	fine gravel	0.156625248
0.5 - 2	coarse sand	4.583898925
0.25 - 0.5	medium sand	12.58222826
0.063 - 0.25	fine sand	81.28850371
0.016 - 0.063	coarse silt	
0.008 - 0.016	medium silt	
0.002 - 0.008	fine silt	
<0.002	clay	

Slichter, Terzaghi, Kozeny-Carman and Barr with d_{VS}:



Slichter, Terzaghi, Kozeny-Carman and Barr with d_{UU}:

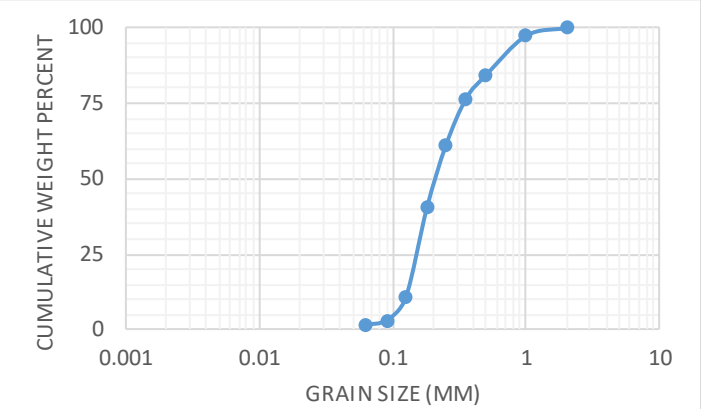


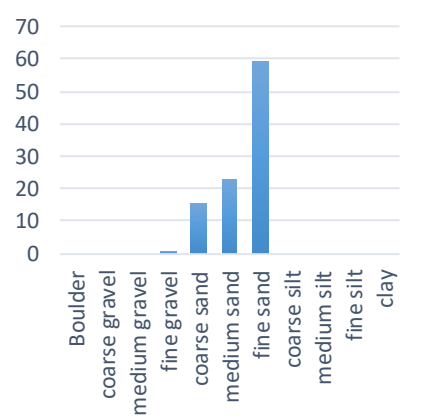
Well 040610/6-T4. Elevation 0.935 m AHD.

Grain Size Analysis Report

Mass Sample (g): 100 T (oC) 20

Moderately well sorted sand low in fines



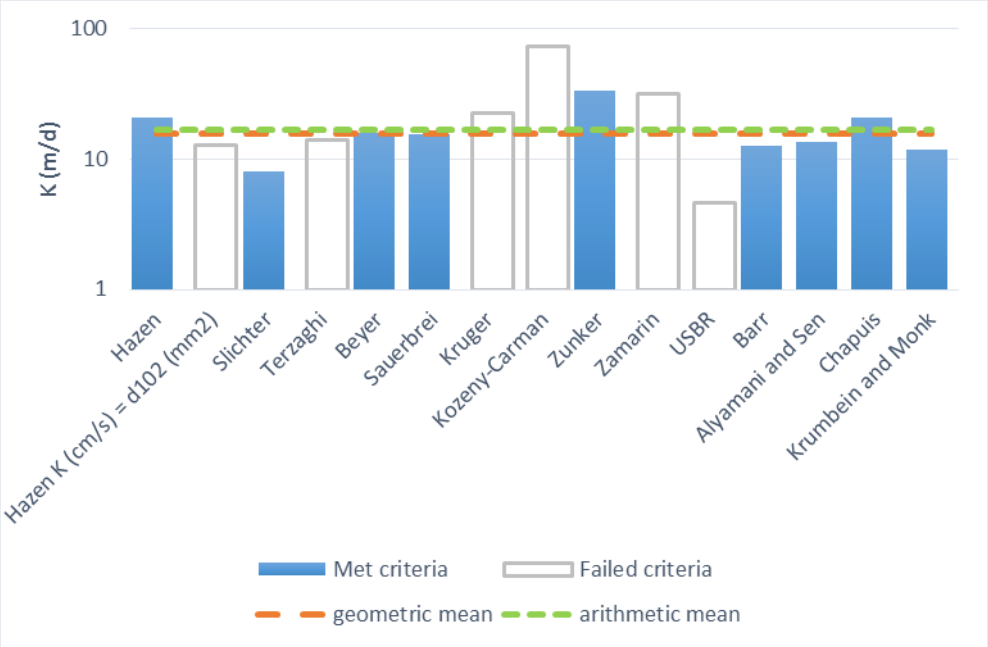


Sieve opening (ps) di (mm)	Mass of retained (mr) (g)	mass fraction (mf)	Percent Passing (pp)
2	0.12329	0.00123	99.8767
1	2.5607	0.02561	97.316
0.5	13.0406	0.13041	84.2754
0.355	7.67261	0.07673	76.6028
0.25	15.5444	0.15544	61.0584
0.18	20.7132	0.20713	40.3452
0.125	29.6851	0.29685	10.6601
0.09	7.53983	0.0754	3.12026
0.063	1.44158	0.01442	1.67868

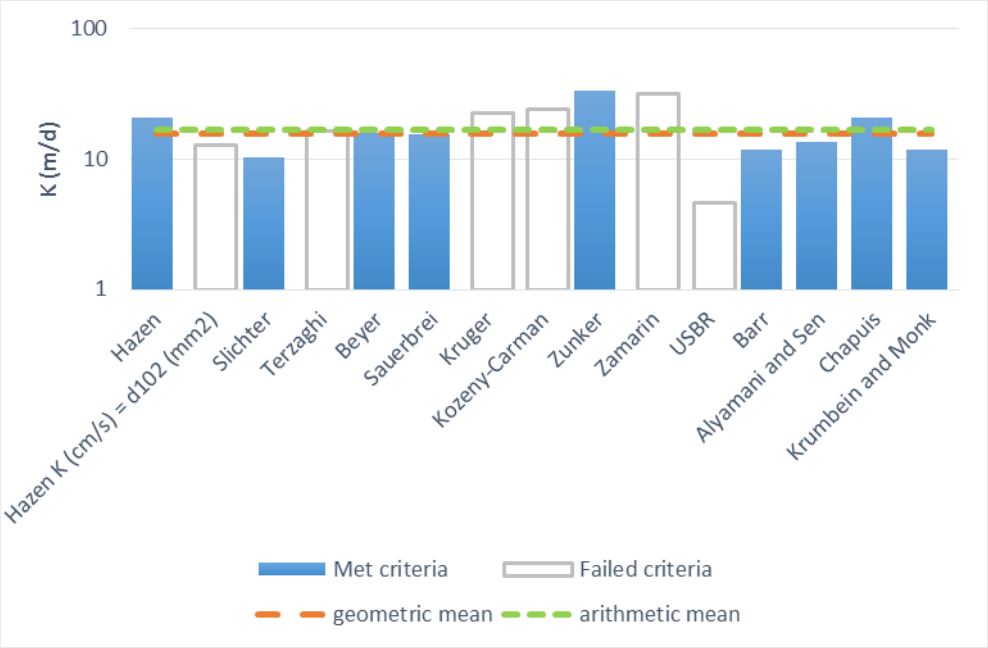
Effective Grain Diameters (mm)		Other Useful Parameters	
d10	0.122	Uniformity Coef.	2.02
d17	0.137	n computed	0.43
d20	0.142	g (cm/s^2)	980.00
d50	0.213	ρ (g/cm^3)	0.9981
d60	0.246	μ (g/cm s)	0.0098
de (Kruger)	0.213	ρg/μ (1/cm s)	9.9327E+04
de (Kozeny)	0.206	tau (Sauerbrei)	1.053
de (Zunker)	0.209	$d_{geometric\ mean}$	0.251
de (Zamarin)	0.211	σ_ϕ	0.955
Io (Alyameni	0.099		

mm	0	% in sample
>64	Boulder	
16 - 64	coarse gravel	
8 - 16	medium gravel	
2 - 8	fine gravel	0.123292868
0.5 - 2	coarse sand	15.60128983
0.25 - 0.5	medium sand	23.21699545
0.063 - 0.25	fine sand	59.37974203
0.016 - 0.063	coarse silt	
0.008 - 0.016	medium silt	
0.002 - 0.008	fine silt	
<0.002	clay	

Slichter, Terzaghi, Kozeny-Carman and Barr with d_{VS}:



Slichter, Terzaghi, Kozeny-Carman and Barr with d_{UU}:

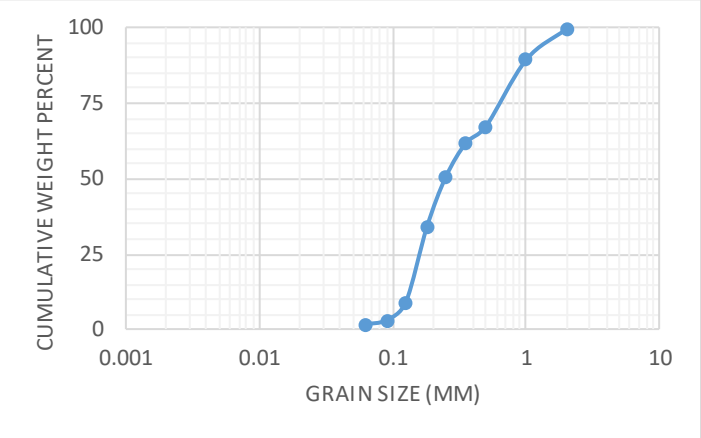


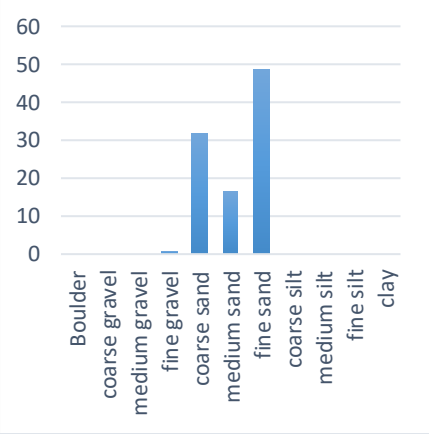
Well 040610/6-T4. Elevation 0.885 m AHD.

Grain Size Analysis Report

Mass Sample (g): 100 T (oC) 20

Moderately well sorted sand low in fines



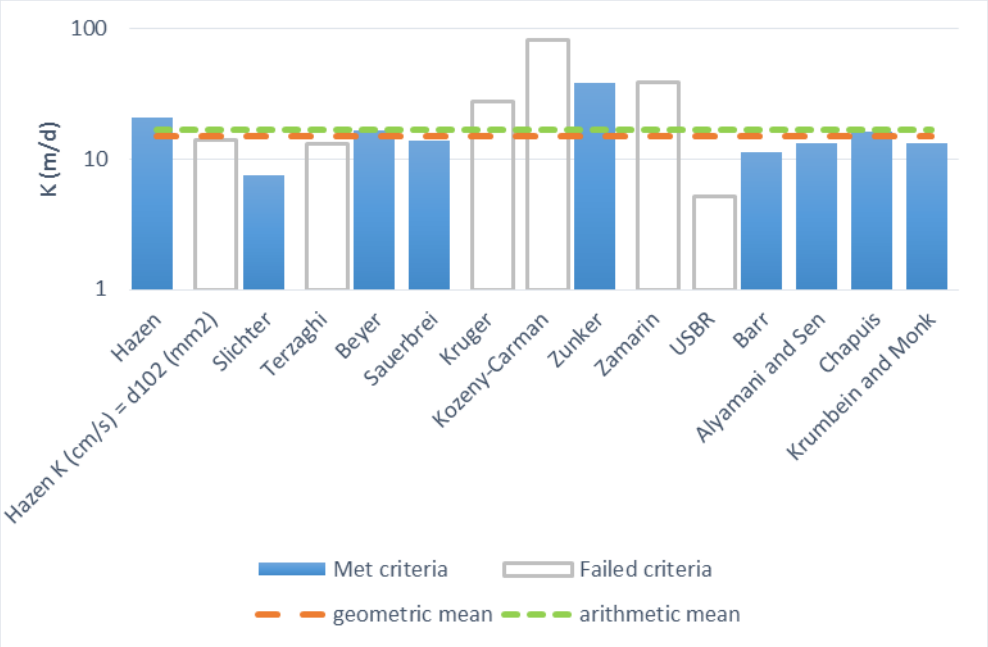


Sieve opening (ps) di (mm)	Mass of retained (mr) (g)	mass fraction (mf)	Percent Passing (pp)
2	0.46588	0.00466	99.5341
1	10.1672	0.10167	89.3669
0.5	22.0152	0.22015	67.3518
0.355	5.41701	0.05417	61.9348
0.25	11.2816	0.11282	50.6531
0.18	16.6438	0.16644	34.0093
0.125	24.9292	0.24929	9.08011
0.09	5.92856	0.05929	3.15155
0.063	1.31543	0.01315	1.83612

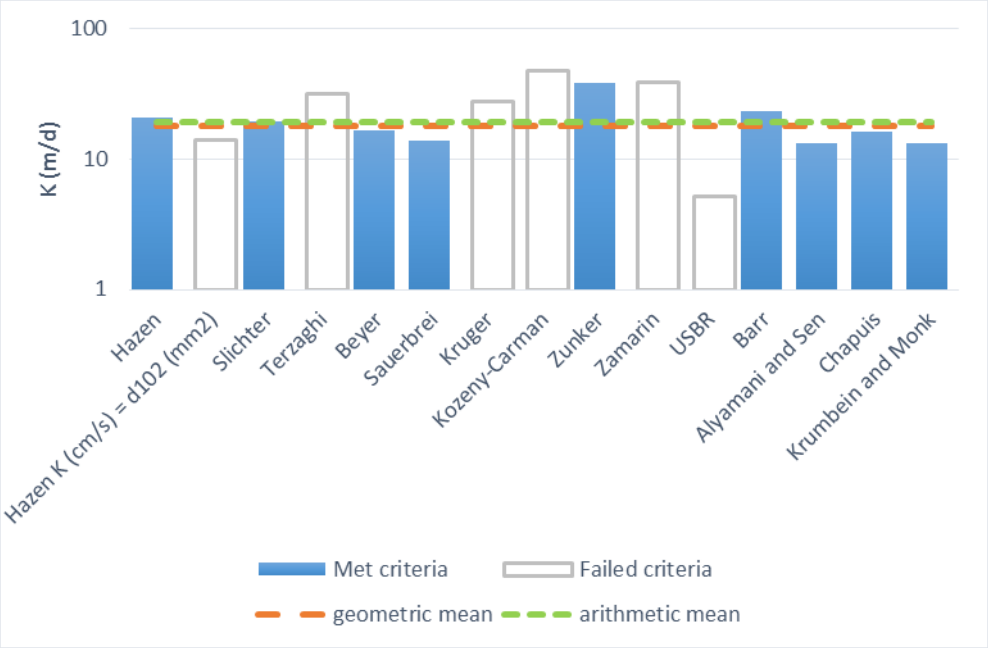
Effective Grain Diameters (mm)		Other Useful Parameters	
d10	0.127	Uniformity Coef.	2.65
d17	0.142	n computed	0.41
d20	0.149	g (cm/s^2)	980.00
d50	0.247	ρ (g/cm^3)	0.9981
d60	0.337	μ (g/cm s)	0.0098
de (Kruger)	0.250	ρg/μ (1/cm s)	9.9327E+04
de (Kozeny)	0.241	tau (Sauerbrei)	1.053
de (Zunker)	0.244	$d_{geometric\ mean}$	0.325
de (Zamarin)	0.247	σ_ϕ	1.259
Io (Alyameni	0.097		

mm	0	% in sample
>64	Boulder	
16 - 64	coarse gravel	
8 - 16	medium gravel	
2 - 8	fine gravel	0.465881063
0.5 - 2	coarse sand	32.18233306
0.25 - 0.5	medium sand	16.6986389
0.063 - 0.25	fine sand	48.8170275
0.016 - 0.063	coarse silt	
0.008 - 0.016	medium silt	
0.002 - 0.008	fine silt	
<0.002	clay	

Slichter, Terzaghi, Kozeny-Carman and Barr with d_{VS}:



Slichter, Terzaghi, Kozeny-Carman and Barr with d_{UU}:

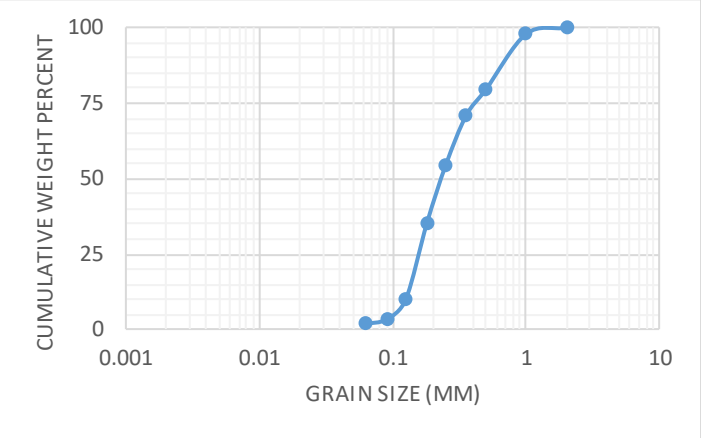


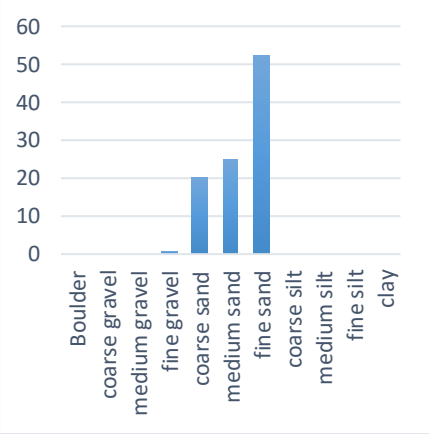
Well 040610/6-T4. Elevation 0.785 m AHD.

Grain Size Analysis Report

Mass Sample (g): 100 T (oC) 20

Moderately well sorted sand low in fines



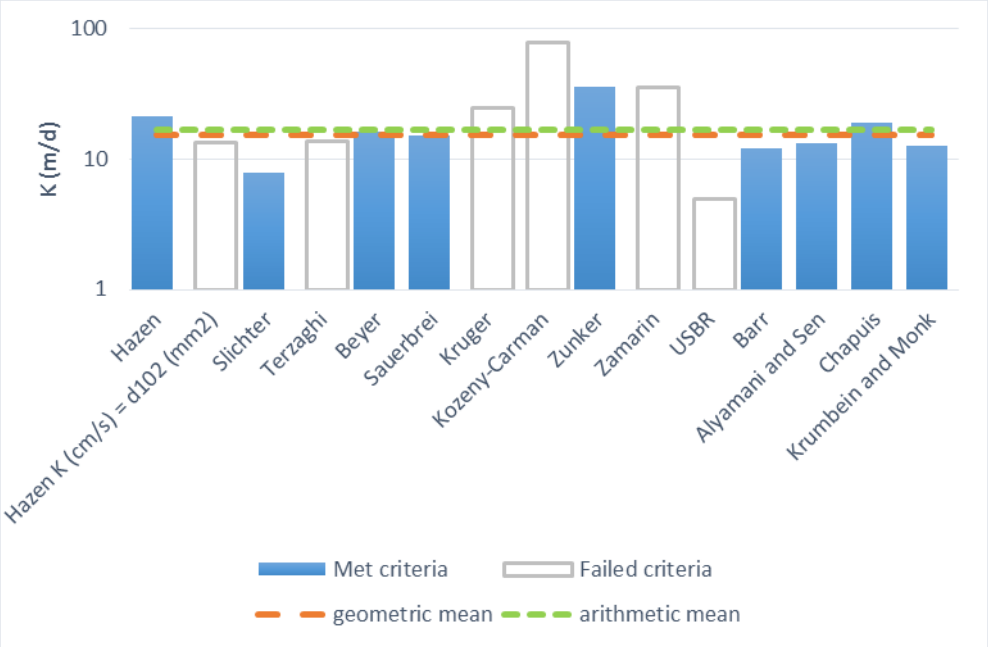


Sieve opening (ps) di (mm)	Mass of retained (mr) (g)	mass fraction (mf)	Percent Passing (pp)
2	0.07675	0.00077	99.9232
1	1.99559	0.01996	97.9277
0.5	18.3249	0.18325	79.6028
0.355	8.64434	0.08644	70.9585
0.25	16.3101	0.1631	54.6484
0.18	19.361	0.19361	35.2873
0.125	25.2614	0.25261	10.0259
0.09	6.61998	0.0662	3.40593
0.063	1.41994	0.0142	1.98599

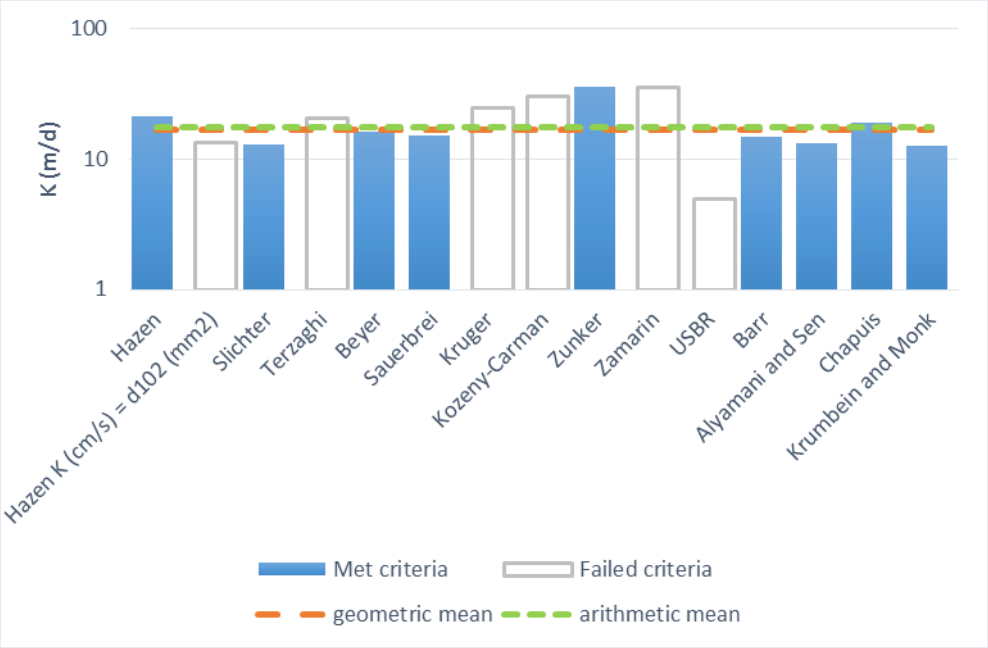
Effective Grain Diameters (mm)		Other Useful Parameters	
d10	0.125	Uniformity Coef.	2.28
d17	0.140	n computed	0.42
d20	0.147	g (cm/s^2)	980.00
d50	0.233	ρ (g/cm^3)	0.9981
d60	0.284	μ (g/cm s)	0.0098
de (Kruger)	0.229	ρg/μ (1/cm s)	9.9327E+04
de (Kozeny)	0.221	tau (Sauerbrei)	1.053
de (Zunker)	0.224	$d_{geometric\ mean}$	0.274
de (Zamarin)	0.227	σ_ϕ	1.030
Io (Alyameni	0.098		

mm	0	% in sample
>64	Boulder	
16 - 64	coarse gravel	
8 - 16	medium gravel	
2 - 8	fine gravel	0.076753334
0.5 - 2	coarse sand	20.32044517
0.25 - 0.5	medium sand	24.95442771
0.063 - 0.25	fine sand	52.66238127
0.016 - 0.063	coarse silt	
0.008 - 0.016	medium silt	
0.002 - 0.008	fine silt	
<0.002	clay	

Slichter, Terzaghi, Kozeny-Carman and Barr with d_{VS}:



Slichter, Terzaghi, Kozeny-Carman and Barr with d_{UU}:

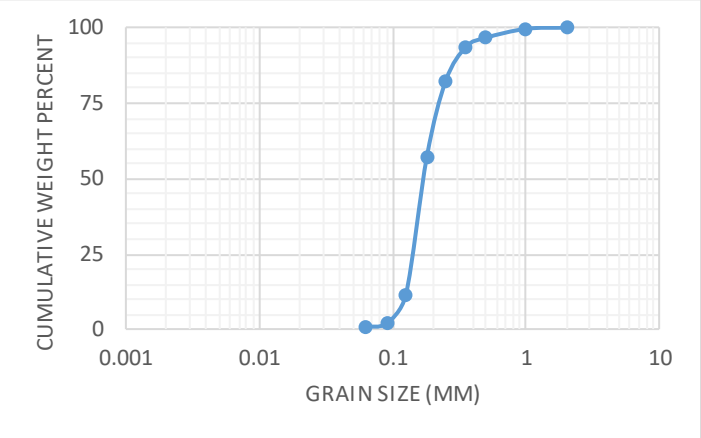


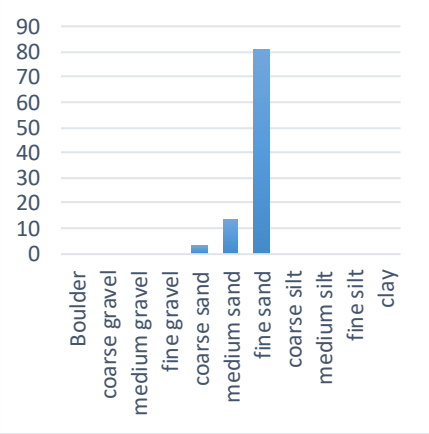
Well 040610/6-T4. Elevation 0.735 m AHD.

Grain Size Analysis Report

Mass Sample (g): 100 T (oC) 20

Uniform sand low in fines



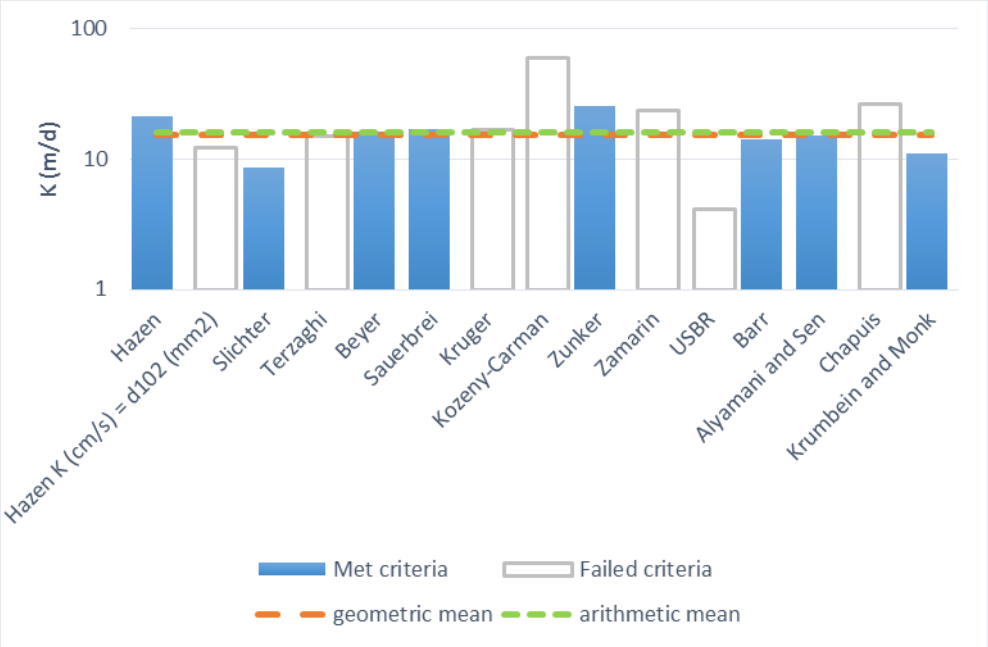


Sieve opening (ps) di (mm)	Mass of retained (mr) (g)	mass fraction (mf)	Percent Passing (pp)
2	0	0	100
1	0.37518	0.00375	99.6248
0.5	2.95571	0.02956	96.6691
0.355	2.97401	0.02974	93.6951
0.25	11.1365	0.11137	82.5586
0.18	25.1556	0.25156	57.403
0.125	45.9279	0.45928	11.4751
0.09	9.39788	0.09398	2.07723
0.063	1.06149	0.01061	1.01574

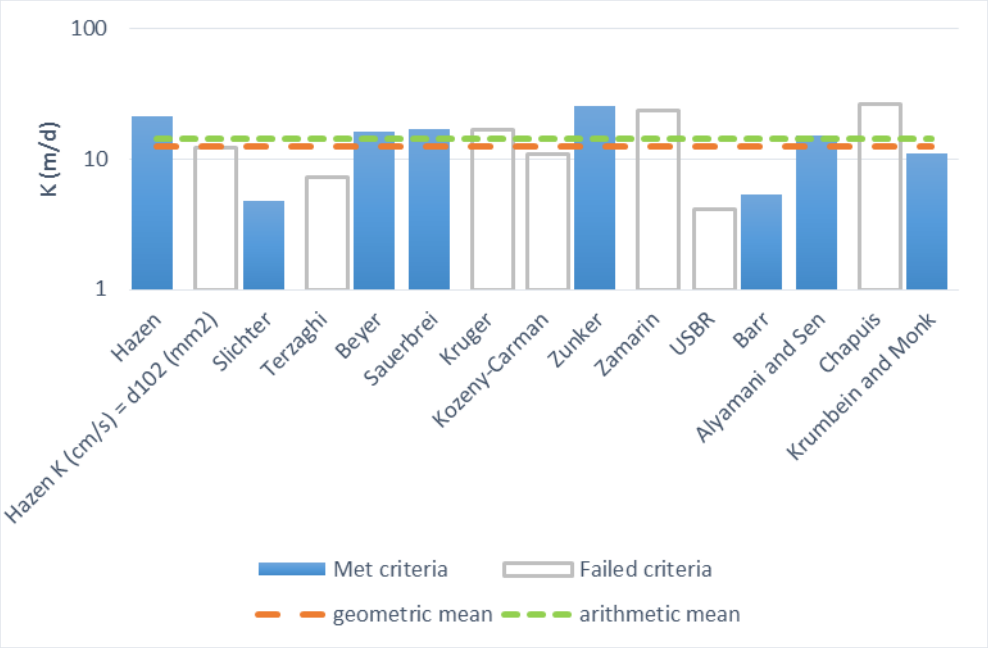
Effective Grain Diameters (mm)		Other Useful Parameters	
d10	0.120	Uniformity Coef.	1.57
d17	0.132	n computed	0.45
d20	0.135	g (cm/s^2)	980.00
d50	0.171	ρ (g/cm^3)	0.9981
d60	0.187	μ (g/cm s)	0.0098
de (Kruger)	0.176	ρg/μ (1/cm s)	9.9327E+04
de (Kozeny)	0.171	tau (Sauerbrei)	1.053
de (Zunker)	0.173	$d_{geometric\ mean}$	0.188
de (Zamarin)	0.174	σ_ϕ	0.565
Io (Alyameni	0.107		

mm	0	% in sample
>64	Boulder	
16 - 64	coarse gravel	
8 - 16	medium gravel	
2 - 8	fine gravel	0
0.5 - 2	coarse sand	3.330893119
0.25 - 0.5	medium sand	14.11054173
0.063 - 0.25	fine sand	81.54282577
0.016 - 0.063	coarse silt	
0.008 - 0.016	medium silt	
0.002 - 0.008	fine silt	
<0.002	clay	

Slichter, Terzaghi, Kozeny-Carman and Barr with d_{VS}:



Slichter, Terzaghi, Kozeny-Carman and Barr with d_{UU}:

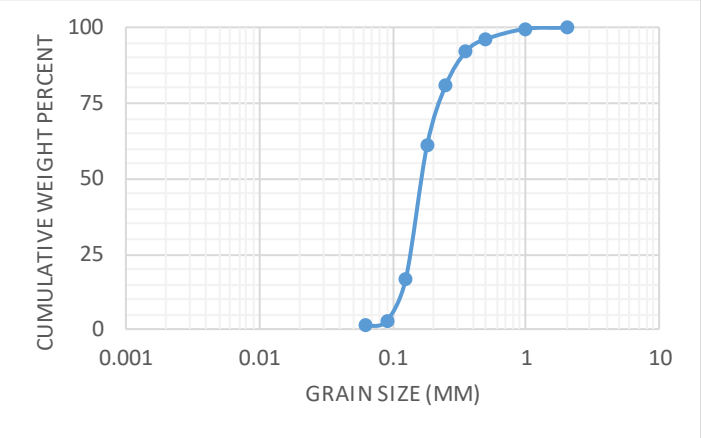


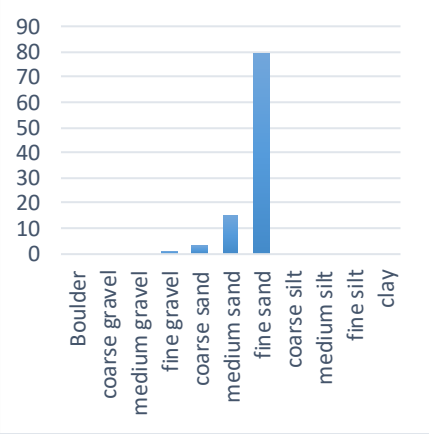
Well 040610/6-T4. Elevation 0.685 m AHD.

Grain Size Analysis Report

Mass Sample (g): 100 T (oC) 20

Uniform sand low in fines



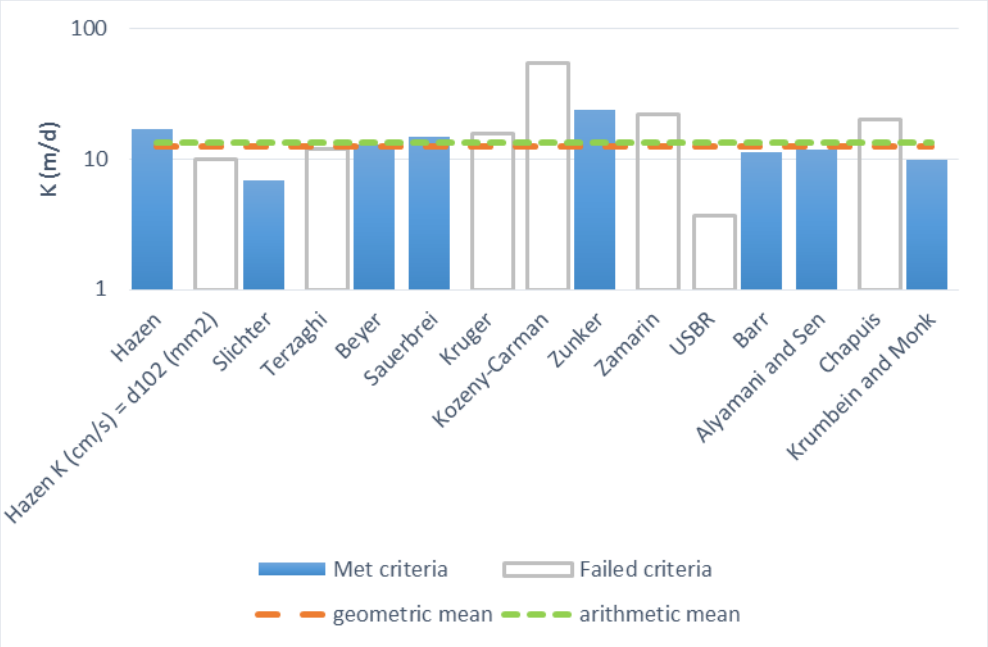


Sieve opening (ps) di (mm)	Mass of retained (mr) (g)	mass fraction (mf)	Percent Passing (pp)
2	0.06368	0.00064	99.9363
1	0.28658	0.00287	99.6497
0.5	3.42302	0.03423	96.2267
0.355	4.04394	0.04044	92.1828
0.25	11.1447	0.11145	81.0381
0.18	20.2675	0.20267	60.7706
0.125	43.9739	0.43974	16.7967
0.09	13.9468	0.13947	2.84986
0.063	1.5125	0.01512	1.33737

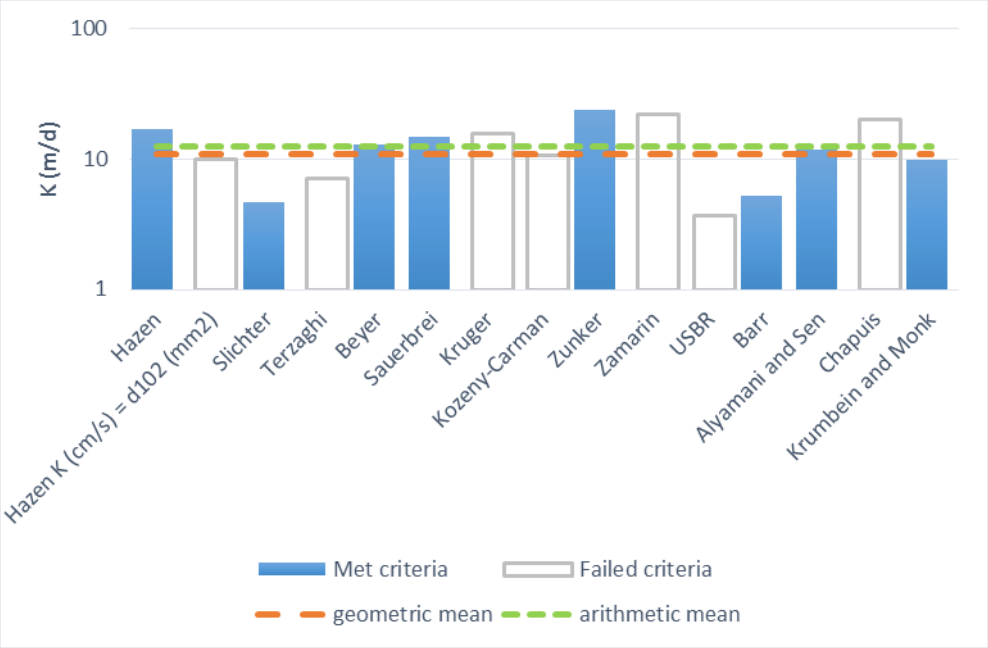
Effective Grain Diameters (mm)		Other Useful Parameters	
d10	0.108	Uniformity Coef.	1.66
d17	0.125	n computed	0.44
d20	0.129	g (cm/s^2)	980.00
d50	0.167	ρ (g/cm^3)	0.9981
d60	0.179	μ (g/cm s)	0.0098
de (Kruger)	0.171	ρg/μ (1/cm s)	9.9327E+04
de (Kozeny)	0.166	tau (Sauerbrei)	1.053
de (Zunker)	0.168	$d_{geometric\ mean}$	0.186
de (Zamarin)	0.170	σ_ϕ	0.636
Io (Alyameni	0.093		

mm	0	% in sample
>64	Boulder	
16 - 64	coarse gravel	
8 - 16	medium gravel	
2 - 8	fine gravel	0.063684127
0.5 - 2	coarse sand	3.709600382
0.25 - 0.5	medium sand	15.18866423
0.063 - 0.25	fine sand	79.7006846
0.016 - 0.063	coarse silt	
0.008 - 0.016	medium silt	
0.002 - 0.008	fine silt	
<0.002	clay	

Slichter, Terzaghi, Kozeny-Carman and Barr with d_{VS}:



Slichter, Terzaghi, Kozeny-Carman and Barr with d_{UU}:

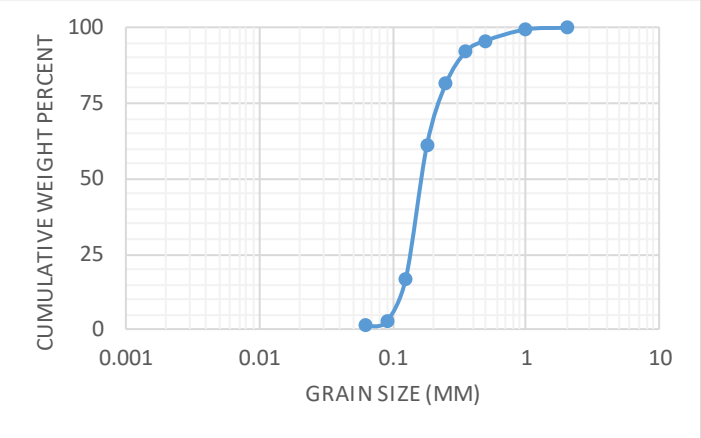


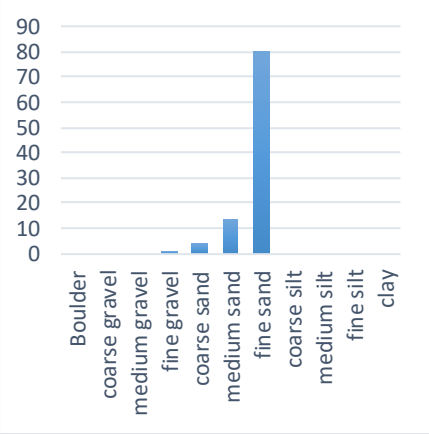
Well 040610/6-T4. Elevation 0.635 m AHD.

Grain Size Analysis Report

Mass Sample (g): 100 T (oC) 20

Uniform sand low in fines



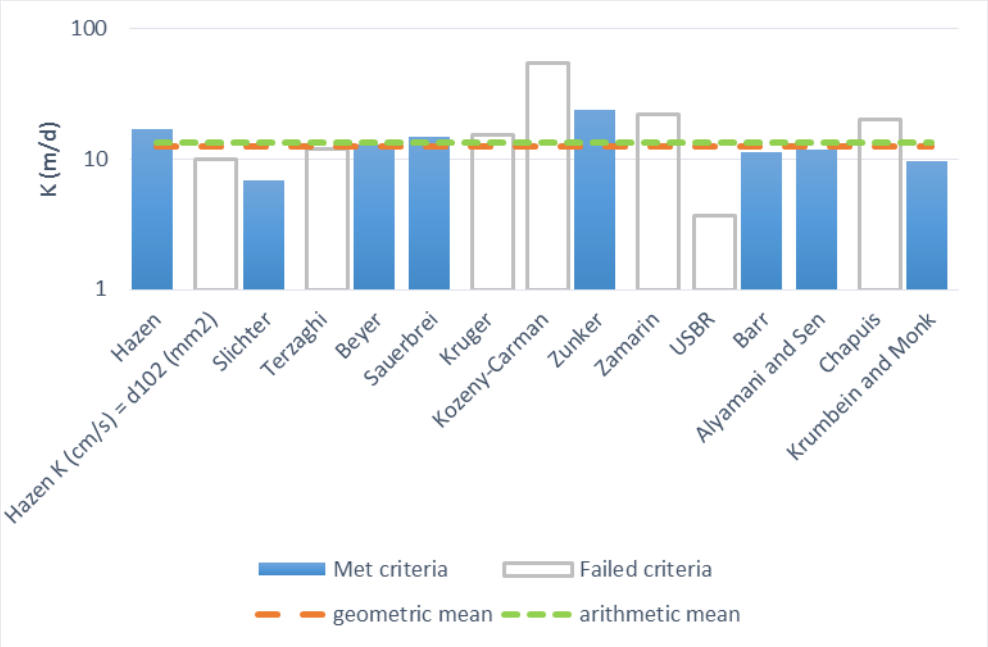


Sieve opening (ps) di (mm)	Mass of retained (mr) (g)	mass fraction (mf)	Percent Passing (pp)
2	0.04311	0.00043	99.9569
1	0.51732	0.00517	99.4396
0.5	3.70743	0.03707	95.7321
0.355	3.53499	0.03535	92.1972
0.25	10.7343	0.10734	81.4629
0.18	20.4052	0.20405	61.0576
0.125	44.2018	0.44202	16.8559
0.09	14.1543	0.14154	2.70154
0.063	1.43699	0.01437	1.26455

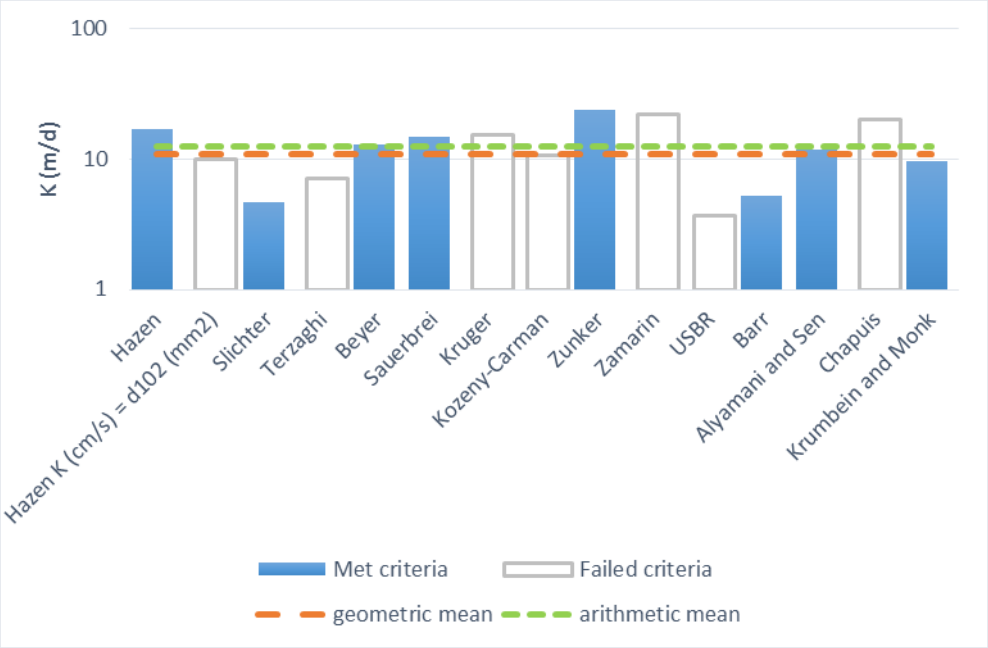
Effective Grain Diameters (mm)		Other Useful Parameters	
d10	0.108	Uniformity Coef.	1.65
d17	0.125	n computed	0.44
d20	0.129	g (cm/s^2)	980.00
d50	0.166	ρ (g/cm^3)	0.9981
d60	0.179	μ (g/cm s)	0.0098
de (Kruger)	0.171	ρg/μ (1/cm s)	9.9327E+04
de (Kozeny)	0.166	tau (Sauerbrei)	1.053
de (Zunker)	0.168	$d_{geometric\ mean}$	0.186
de (Zamarin)	0.169	σ_ϕ	0.638
Io (Alyameni	0.093		

mm	0	% in sample
>64	Boulder	
16 - 64	coarse gravel	
8 - 16	medium gravel	
2 - 8	fine gravel	0.043109642
0.5 - 2	coarse sand	4.224744935
0.25 - 0.5	medium sand	14.26929156
0.063 - 0.25	fine sand	80.19830435
0.016 - 0.063	coarse silt	
0.008 - 0.016	medium silt	
0.002 - 0.008	fine silt	
<0.002	clay	

Slichter, Terzaghi, Kozeny-Carman and Barr with d_{VS}:



Slichter, Terzaghi, Kozeny-Carman and Barr with d_{UU}:

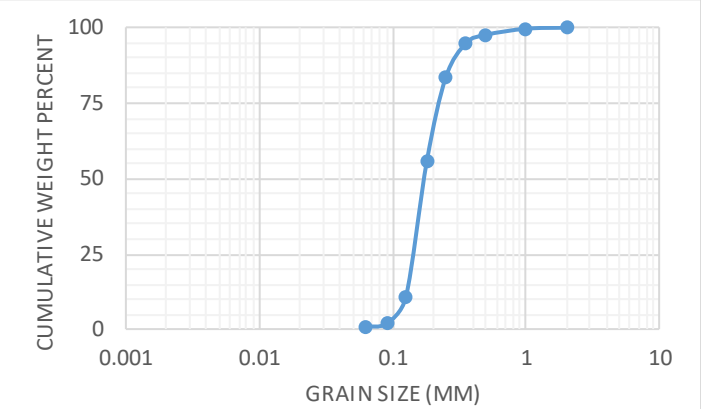


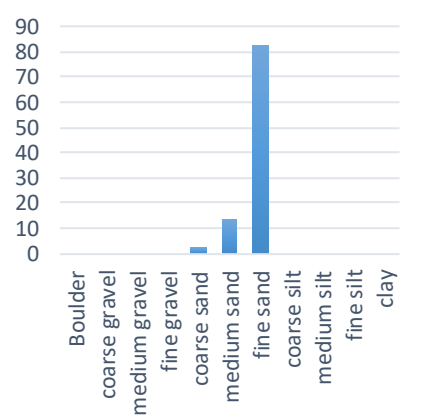
Well 040610/6-T4. Elevation 0.585 m AHD.

Grain Size Analysis Report

Mass Sample (g): 100 T (oC) 20

Uniform sand low in fines



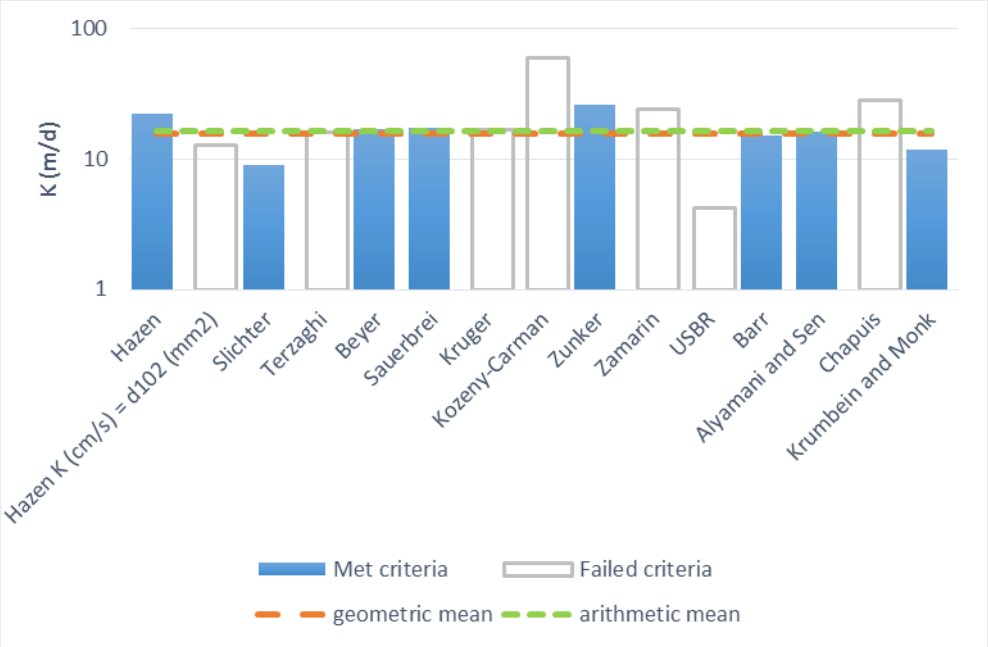


Sieve opening (ps) di (mm)	Mass of retained (mr) (g)	mass fraction (mf)	Percent Passing (pp)
2	0	0	100
1	0.34416	0.00344	99.6558
0.5	2.03462	0.02035	97.6212
0.355	2.71283	0.02713	94.9084
0.25	11.2157	0.11216	83.6927
0.18	27.7154	0.27715	55.9773
0.125	45.2981	0.45298	10.6792
0.09	8.67497	0.08675	2.00425
0.063	0.94139	0.00941	1.06286

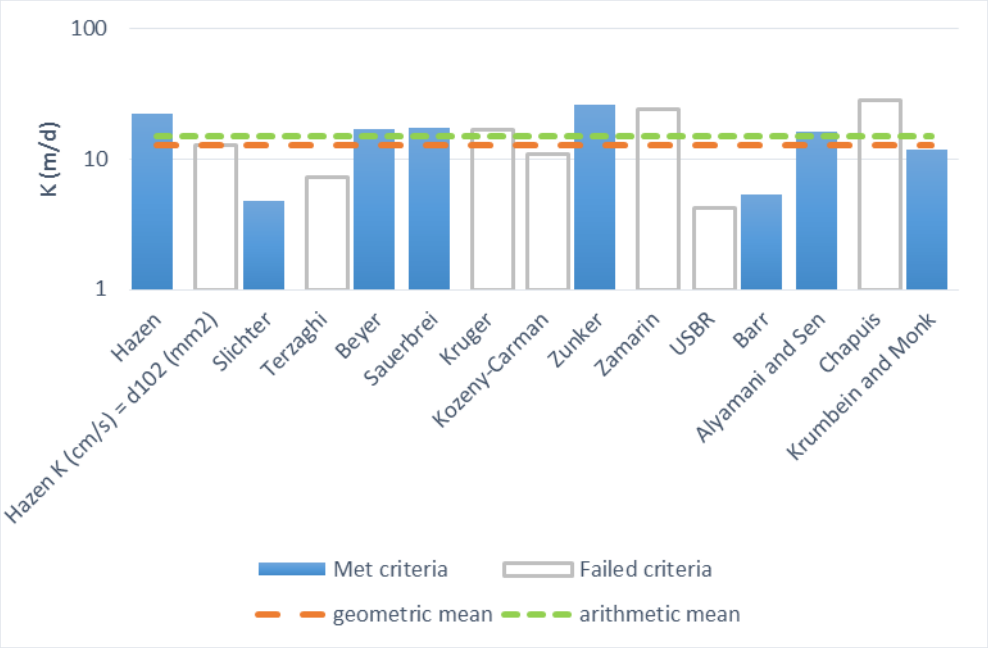
Effective Grain Diameters (mm)		Other Useful Parameters	
d10	0.122	Uniformity Coef.	1.56
d17	0.133	n computed	0.45
d20	0.136	g (cm/s^2)	980.00
d50	0.173	ρ (g/cm^3)	0.9981
d60	0.190	μ (g/cm s)	0.0098
de (Kruger)	0.177	ρg/μ (1/cm s)	9.9327E+04
de (Kozeny)	0.171	tau (Sauerbrei)	1.053
de (Zunker)	0.173	$d_{geometric\ mean}$	0.188
de (Zamarin)	0.175	σ_ϕ	0.511
Io (Alyameni	0.110		

mm	0	% in sample
>64	Boulder	
16 - 64	coarse gravel	
8 - 16	medium gravel	
2 - 8	fine gravel	0
0.5 - 2	coarse sand	2.378783278
0.25 - 0.5	medium sand	13.92853528
0.063 - 0.25	fine sand	82.62982083
0.016 - 0.063	coarse silt	
0.008 - 0.016	medium silt	
0.002 - 0.008	fine silt	
<0.002	clay	

Slichter, Terzaghi, Kozeny-Carman and Barr with d_{VS}:



Slichter, Terzaghi, Kozeny-Carman and Barr with d_{UU}:

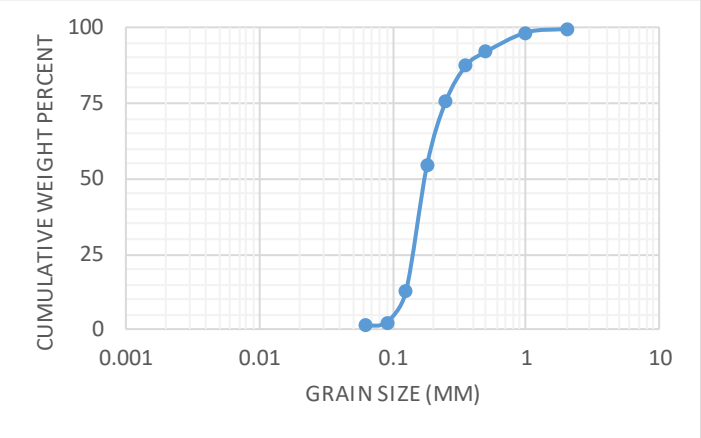


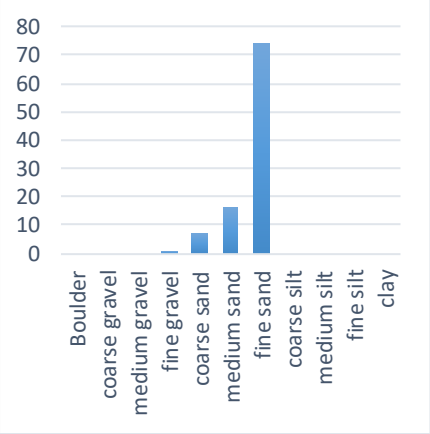
Well 040610/6-T4. Elevation 0.535 m AHD.

Grain Size Analysis Report

Mass Sample (g): 100 T (oC) 20

Uniform sand low in fines



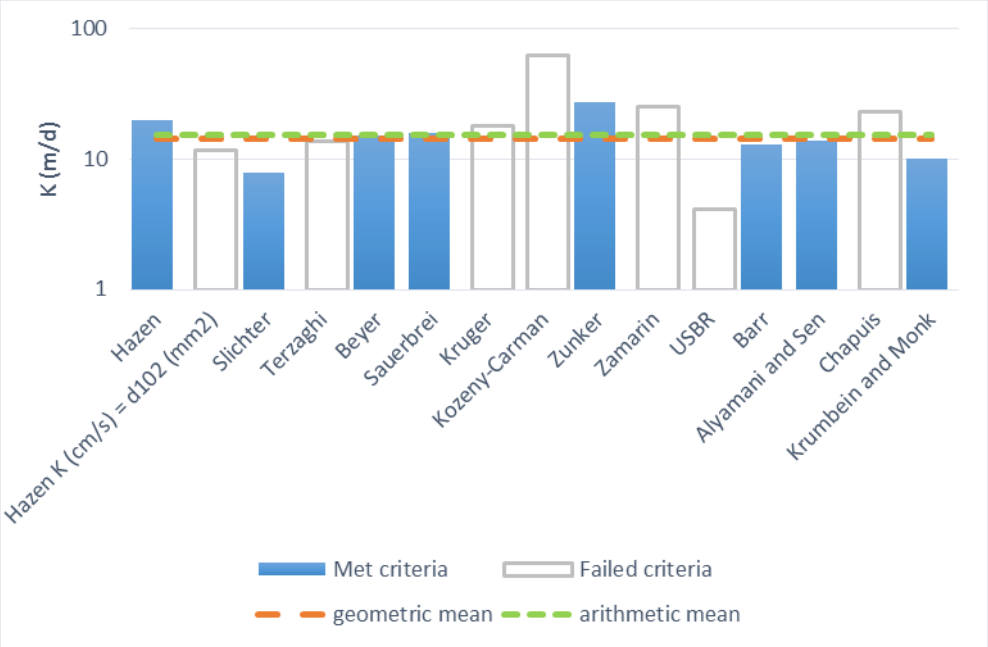


Sieve opening (ps) di (mm)	Mass of retained (mr) (g)	mass fraction (mf)	Percent Passing (pp)
2	0.43174	0.00432	99.5683
1	1.14104	0.01141	98.4272
0.5	6.38363	0.06384	92.0436
0.355	4.55387	0.04554	87.4897
0.25	11.7907	0.11791	75.699
0.18	21.4021	0.21402	54.2969
0.125	41.8586	0.41859	12.4383
0.09	9.97122	0.09971	2.46711
0.063	1.14104	0.01141	1.32607

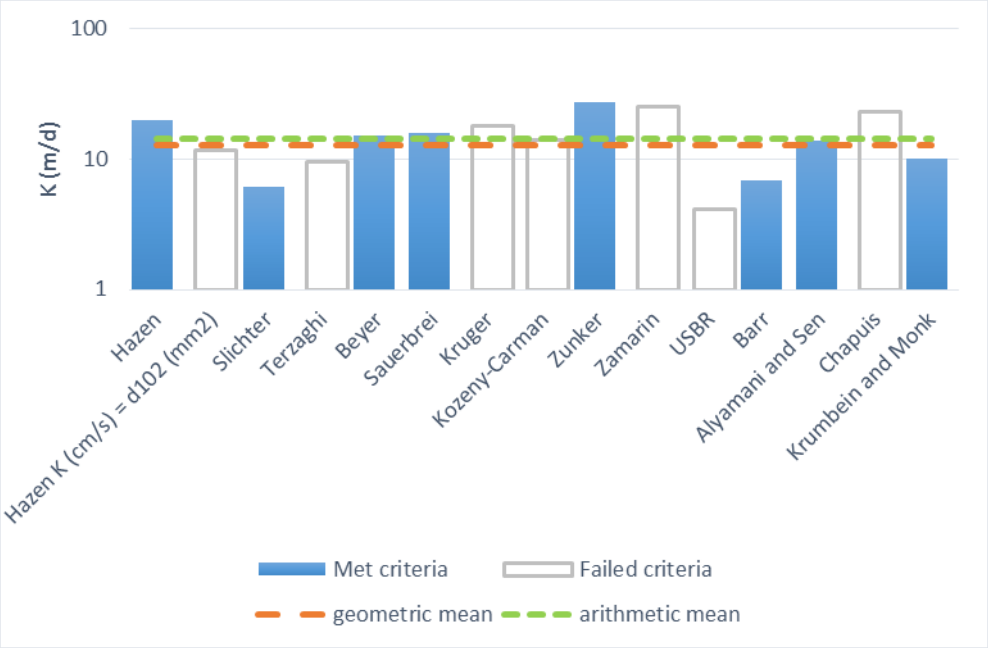
Effective Grain Diameters (mm)		Other Useful Parameters	
d10	0.116	Uniformity Coef.	1.71
d17	0.131	n computed	0.44
d20	0.135	g (cm/s^2)	980.00
d50	0.174	ρ (g/cm^3)	0.9981
d60	0.199	μ (g/cm s)	0.0098
de (Kruger)	0.185	ρg/μ (1/cm s)	9.9327E+04
de (Kozeny)	0.179	tau (Sauerbrei)	1.053
de (Zunker)	0.181	$d_{geometric\ mean}$	0.206
de (Zamarin)	0.183	σ_ϕ	0.768
Io (Alyameni	0.102		

mm	0	% in sample
>64	Boulder	
16 - 64	coarse gravel	
8 - 16	medium gravel	
2 - 8	fine gravel	0.431743421
0.5 - 2	coarse sand	7.524671053
0.25 - 0.5	medium sand	16.34457237
0.063 - 0.25	fine sand	74.37294408
0.016 - 0.063	coarse silt	
0.008 - 0.016	medium silt	
0.002 - 0.008	fine silt	
<0.002	clay	

Slichter, Terzaghi, Kozeny-Carman and Barr with d_{VS}:



Slichter, Terzaghi, Kozeny-Carman and Barr with d_{UU}:

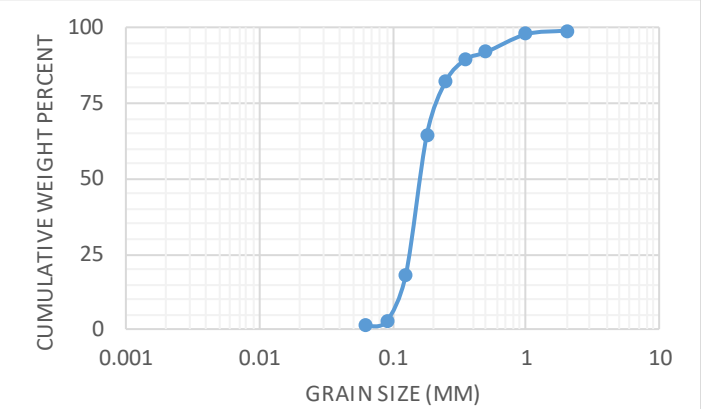


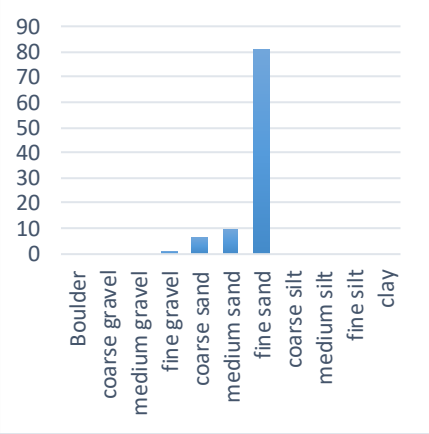
Well 040610/6-T4. Elevation 0.485 m AHD.

Grain Size Analysis Report

Mass Sample (g): 100 T (oC) 20

Uniform sand low in fines



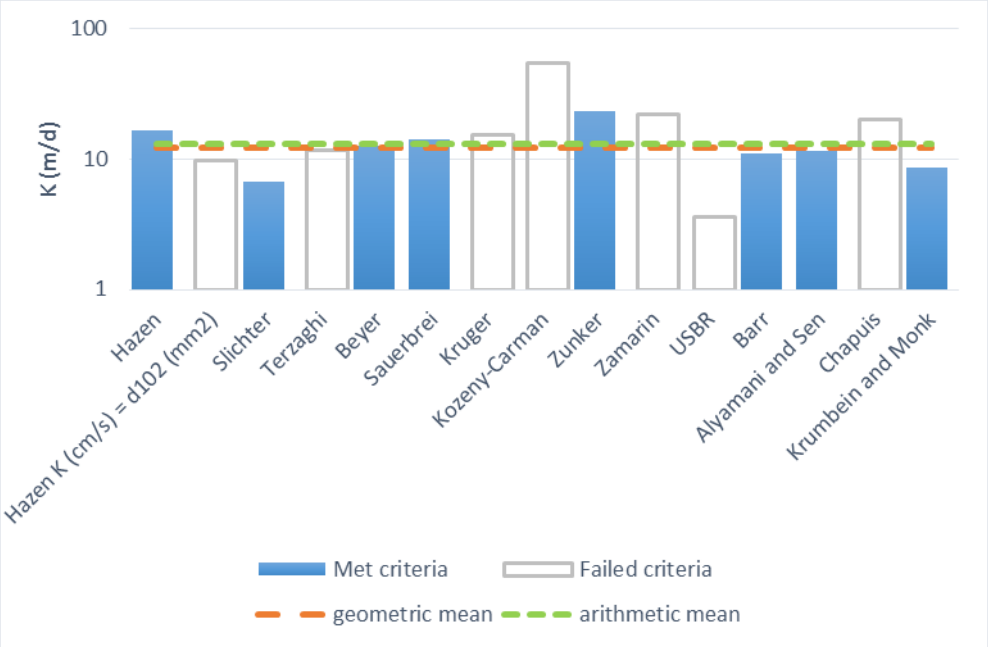


Sieve opening (ps) di (mm)	Mass of retained (mr) (g)	mass fraction (mf)	Percent Passing (pp)
2	0.97436	0.00974	99.0256
1	1.2014	0.01201	97.8242
0.5	5.93132	0.05931	91.8929
0.355	2.31766	0.02318	89.5753
0.25	7.24624	0.07246	82.329
0.18	17.6615	0.17662	64.6675
0.125	46.5424	0.46542	18.1251
0.09	15.3439	0.15344	2.78119
0.063	1.50412	0.01504	1.27708

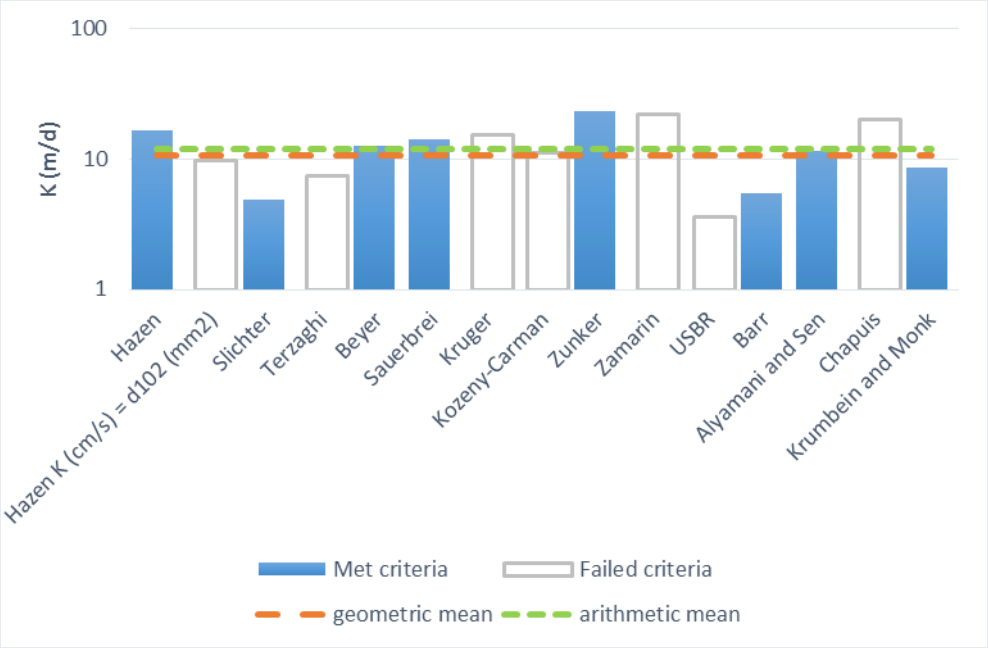
Effective Grain Diameters (mm)		Other Useful Parameters	
d10	0.106	Uniformity Coef.	1.64
d17	0.122	n computed	0.44
d20	0.127	g (cm/s^2)	980.00
d50	0.163	ρ (g/cm^3)	0.9981
d60	0.174	μ (g/cm s)	0.0098
de (Kruger)	0.170	ρg/μ (1/cm s)	9.9327E+04
de (Kozeny)	0.165	tau (Sauerbrei)	1.053
de (Zunker)	0.167	$d_{geometric\ mean}$	0.189
de (Zamarin)	0.168	σ_ϕ	0.753
Io (Alyameni	0.092		

mm	0	% in sample
>64	Boulder	
16 - 64	coarse gravel	
8 - 16	medium gravel	
2 - 8	fine gravel	0.974363826
0.5 - 2	coarse sand	7.132721597
0.25 - 0.5	medium sand	9.563901239
0.063 - 0.25	fine sand	81.05193454
0.016 - 0.063	coarse silt	
0.008 - 0.016	medium silt	
0.002 - 0.008	fine silt	
<0.002	clay	

Slichter, Terzaghi, Kozeny-Carman and Barr with d_{VS}:



Slichter, Terzaghi, Kozeny-Carman and Barr with d_{UU}:

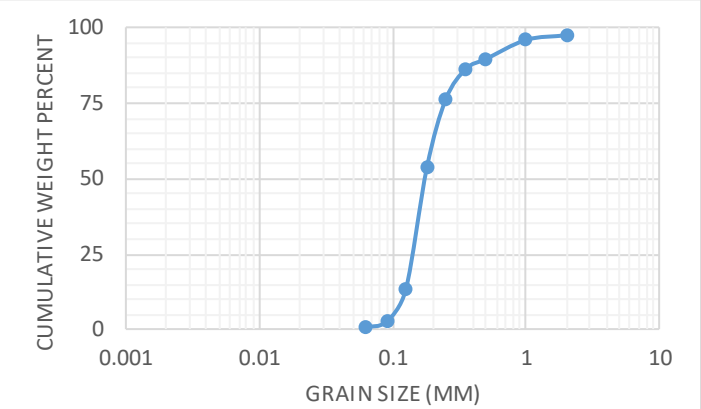


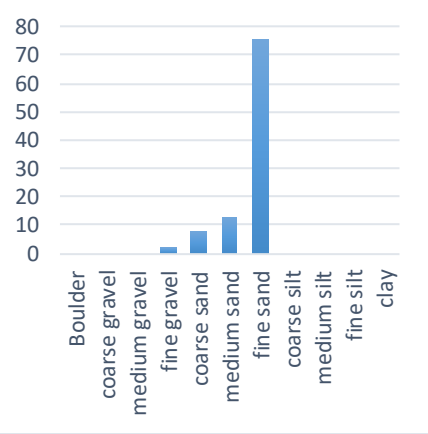
Well 040610/6-T4. Elevation 0.435 m AHD.

Grain Size Analysis Report

Mass Sample (g): 100 T (oC) 20

Uniform sand low in fines



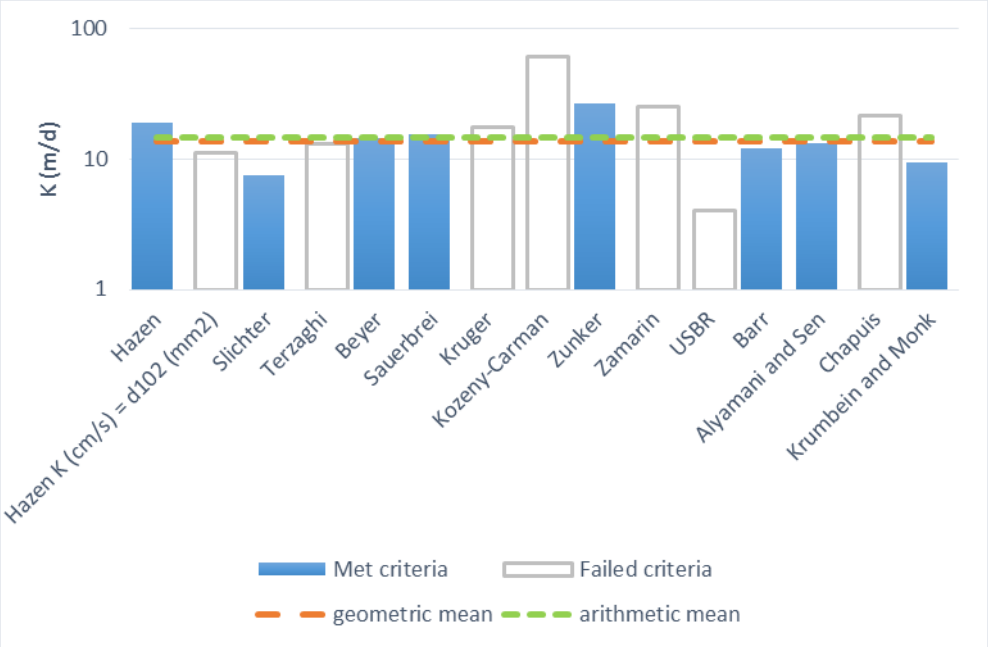


Sieve opening (ps) di (mm)	Mass of retained (mr) (g)	mass fraction (mf)	Percent Passing (pp)
2	2.53063	0.02531	97.4694
1	1.51637	0.01516	95.953
0.5	6.32657	0.06327	89.6264
0.355	3.2135	0.03213	86.4129
0.25	10.0221	0.10022	76.3908
0.18	22.625	0.22625	53.7658
0.125	40.5101	0.4051	13.2557
0.09	10.5945	0.10594	2.66118
0.063	1.79755	0.01798	0.86363

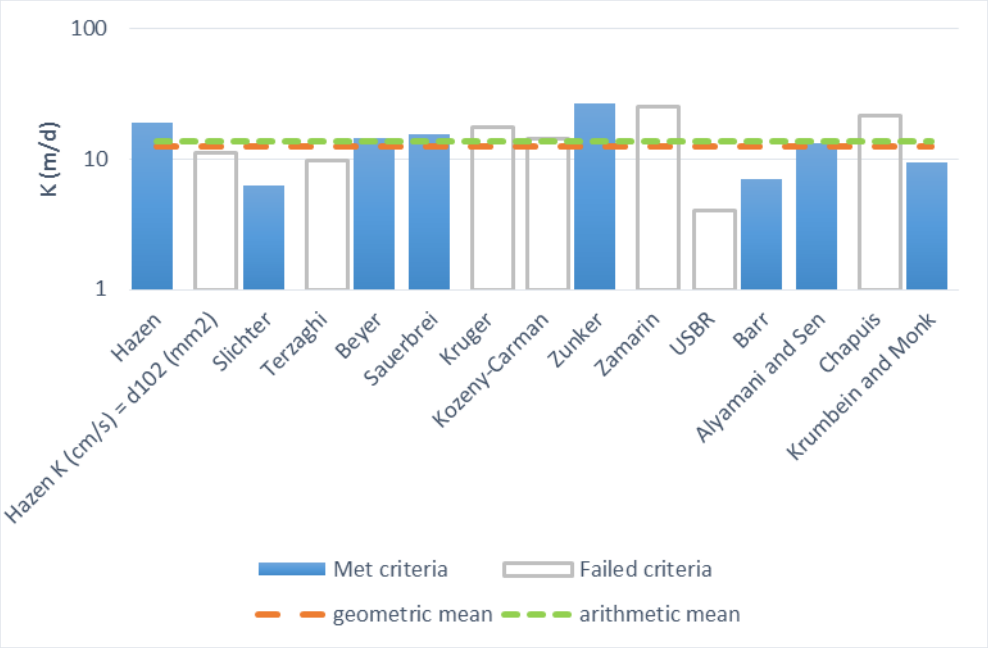
Effective Grain Diameters (mm)		Other Useful Parameters	
d10	0.114	Uniformity Coef.	1.74
d17	0.130	n computed	0.44
d20	0.134	g (cm/s^2)	980.00
d50	0.175	ρ (g/cm^3)	0.9981
d60	0.199	μ (g/cm s)	0.0098
de (Kruger)	0.184	ρg/μ (1/cm s)	9.9327E+04
de (Kozeny)	0.178	tau (Sauerbrei)	1.053
de (Zunker)	0.180	$d_{geometric\ mean}$	0.208
de (Zamarin)	0.182	σ_ϕ	0.830
Io (Alyameni	0.099		

mm	0	% in sample
>64	Boulder	
16 - 64	coarse gravel	
8 - 16	medium gravel	
2 - 8	fine gravel	2.53062864
0.5 - 2	coarse sand	7.842940349
0.25 - 0.5	medium sand	13.23558948
0.063 - 0.25	fine sand	75.5272143
0.016 - 0.063	coarse silt	
0.008 - 0.016	medium silt	
0.002 - 0.008	fine silt	
<0.002	clay	

Slichter, Terzaghi, Kozeny-Carman and Barr with d_{VS}:



Slichter, Terzaghi, Kozeny-Carman and Barr with d_{UU}:

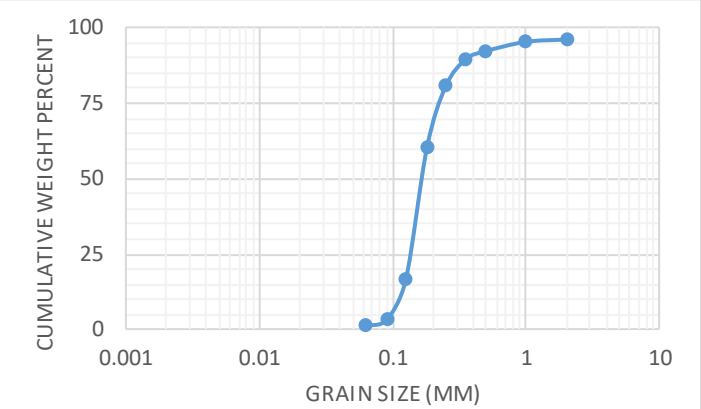


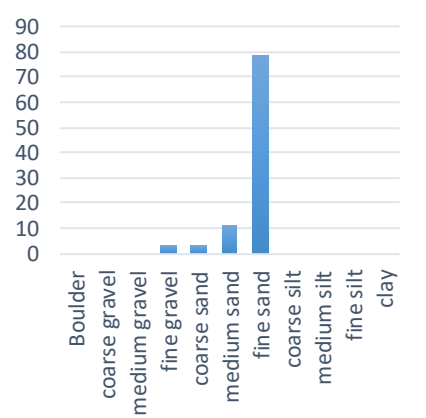
Well 040610/6-T4. Elevation 0.385 m AHD.

Grain Size Analysis Report

Mass Sample (g): 100 T (oC) 20

Uniform sand low in fines



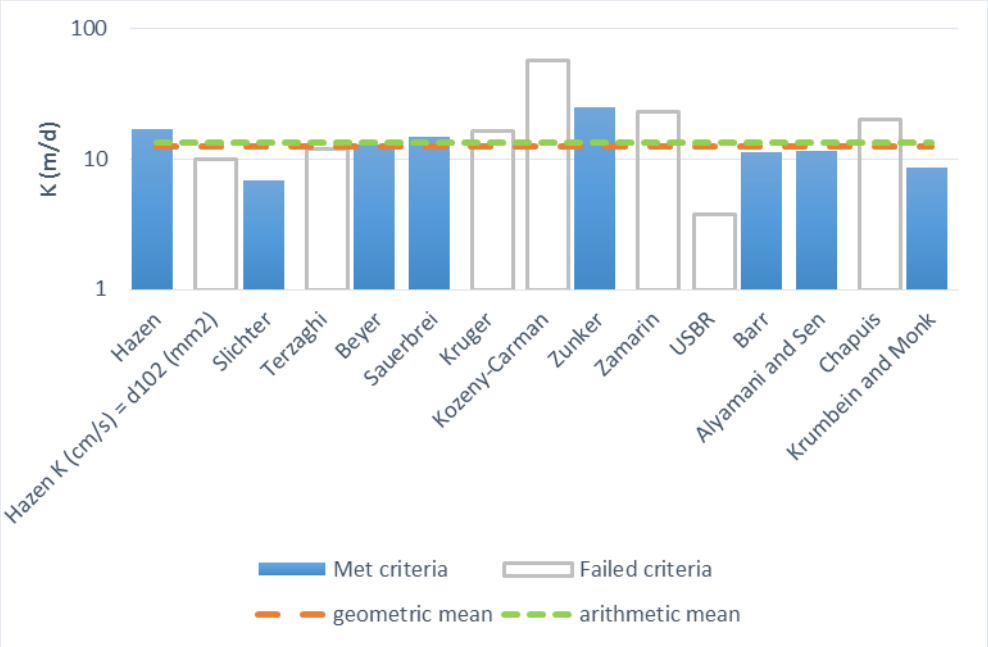


Sieve opening (ps) di (mm)	Mass of retained (mr) (g)	mass fraction (mf)	Percent Passing (pp)
2	3.93258	0.03933	96.0674
1	0.74906	0.00749	95.3184
0.5	3.08052	0.03081	92.2378
0.355	2.63109	0.02631	89.6067
0.25	8.84831	0.08848	80.7584
0.18	20.5243	0.20524	60.2341
0.125	43.7172	0.43717	16.5169
0.09	13.2303	0.1323	3.28652
0.063	1.82584	0.01826	1.46067

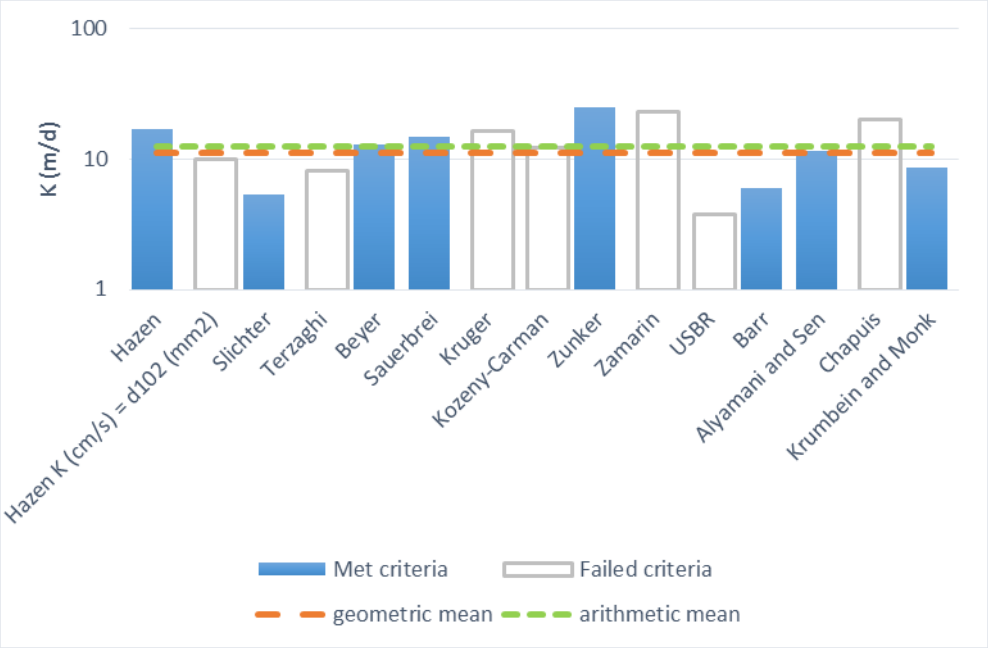
Effective Grain Diameters (mm)		Other Useful Parameters	
d10	0.108	Uniformity Coef.	1.67
d17	0.126	n computed	0.44
d20	0.129	g (cm/s^2)	980.00
d50	0.167	ρ (g/cm^3)	0.9981
d60	0.180	μ (g/cm s)	0.0098
de (Kruger)	0.176	ρg/μ (1/cm s)	9.9327E+04
de (Kozeny)	0.170	tau (Sauerbrei)	1.053
de (Zunker)	0.172	$d_{geometric\ mean}$	0.196
de (Zamarin)	0.174	σ_ϕ	0.810
Io (Alyameni	0.093		

mm	0	% in sample
>64	Boulder	
16 - 64	coarse gravel	
8 - 16	medium gravel	
2 - 8	fine gravel	3.93258427
0.5 - 2	coarse sand	3.829588015
0.25 - 0.5	medium sand	11.47940075
0.063 - 0.25	fine sand	79.29775281
0.016 - 0.063	coarse silt	
0.008 - 0.016	medium silt	
0.002 - 0.008	fine silt	
<0.002	clay	

Slichter, Terzaghi, Kozeny-Carman and Barr with d_{VS}:



Slichter, Terzaghi, Kozeny-Carman and Barr with d_{UU}:

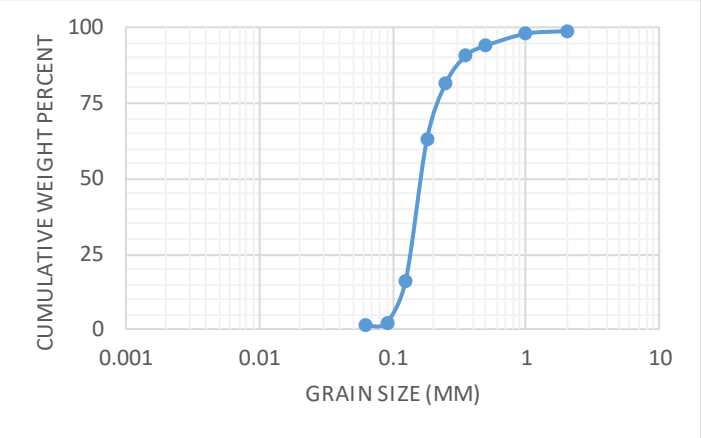


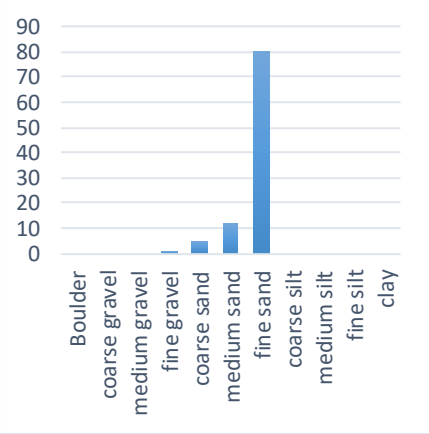
Well 040610/6-T4. Elevation 0.285 m AHD.

Grain Size Analysis Report

Mass Sample (g): 100 T (oC) 20

Uniform sand low in fines



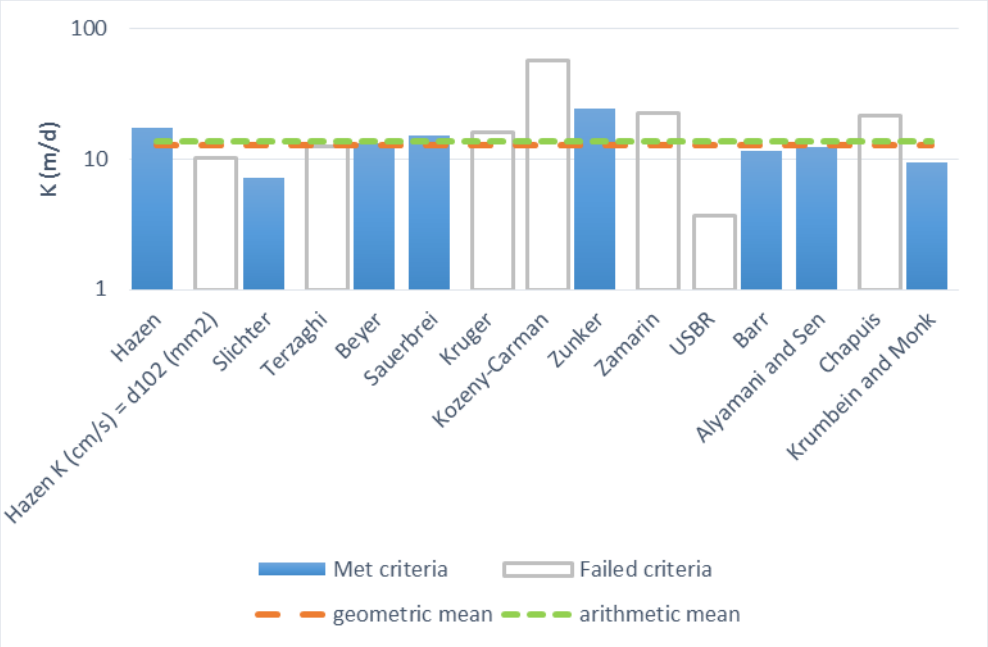


Sieve opening (ps) di (mm)	Mass of retained (mr) (g)	mass fraction (mf)	Percent Passing (pp)
2	1.14286	0.01143	98.8571
1	0.84262	0.00843	98.0145
0.5	3.97094	0.03971	94.0436
0.355	3.27361	0.03274	90.77
0.25	9.05569	0.09056	81.7143
0.18	18.7215	0.18722	62.9927
0.125	46.615	0.46615	16.3777
0.09	14.0726	0.14073	2.30508
0.063	0.76513	0.00765	1.53995

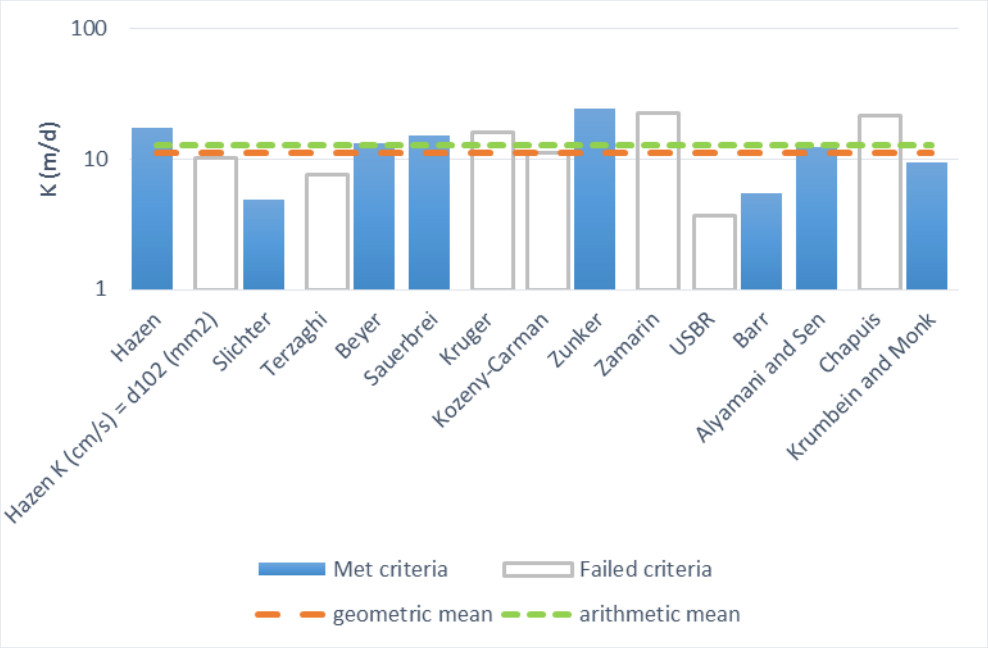
Effective Grain Diameters (mm)		Other Useful Parameters	
d10	0.109	Uniformity Coef.	1.62
d17	0.126	n computed	0.44
d20	0.129	g (cm/s^2)	980.00
d50	0.165	ρ (g/cm^3)	0.9981
d60	0.176	μ (g/cm s)	0.0098
de (Kruger)	0.173	ρg/μ (1/cm s)	9.9327E+04
de (Kozeny)	0.168	tau (Sauerbrei)	1.053
de (Zunker)	0.170	$d_{geometric\ mean}$	0.190
de (Zamarin)	0.171	σ_ϕ	0.695
Io (Alyameni	0.095		

mm	0	% in sample
>64	Boulder	
16 - 64	coarse gravel	
8 - 16	medium gravel	
2 - 8	fine gravel	1.142857143
0.5 - 2	coarse sand	4.813559322
0.25 - 0.5	medium sand	12.32929782
0.063 - 0.25	fine sand	80.17433414
0.016 - 0.063	coarse silt	
0.008 - 0.016	medium silt	
0.002 - 0.008	fine silt	
<0.002	clay	

Slichter, Terzaghi, Kozeny-Carman and Barr with d_{VS}:



Slichter, Terzaghi, Kozeny-Carman and Barr with d_{UU}:

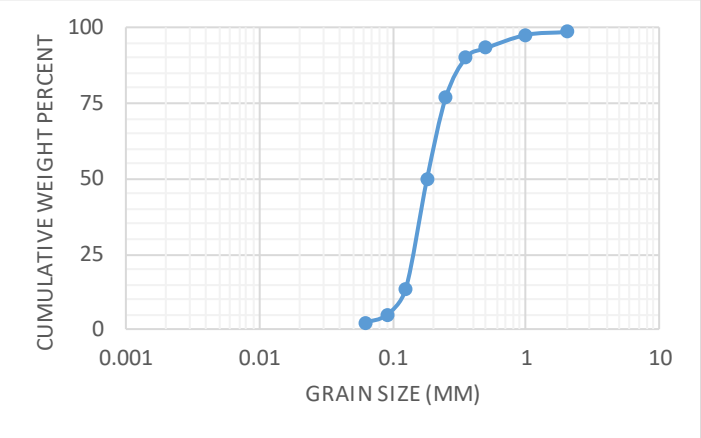


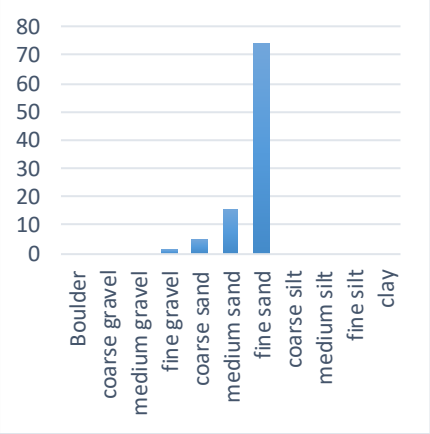
Well 040610/6-T4. Elevation 0.235 m AHD.

Grain Size Analysis Report

Mass Sample (g): 100 T (oC) 20

Uniform sand low in fines



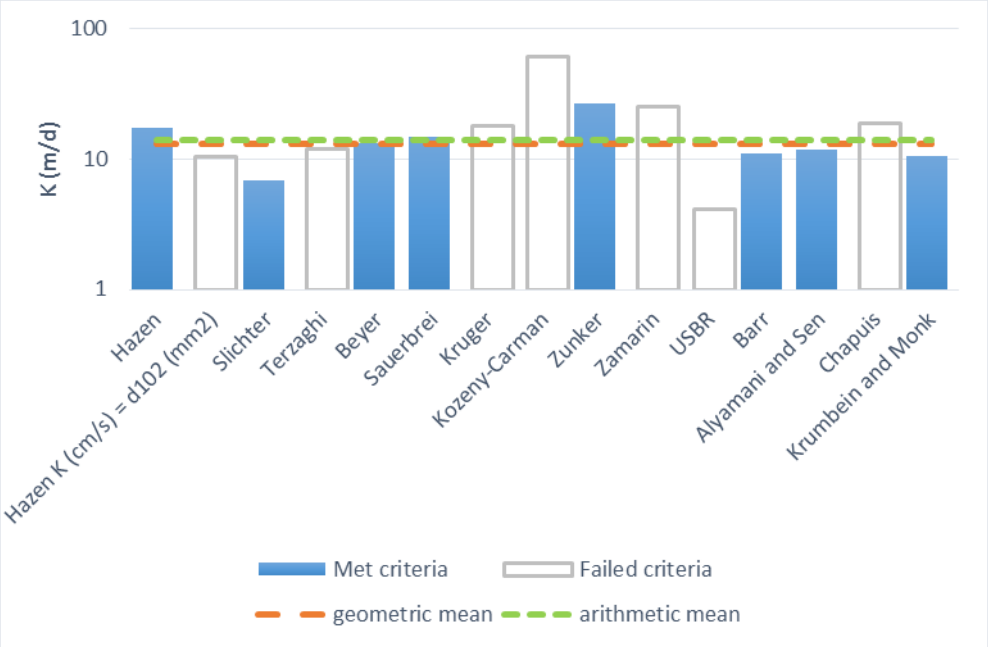


Sieve opening (ps) di (mm)	Mass of retained (mr) (g)	mass fraction (mf)	Percent Passing (pp)
2	1.47045	0.0147	98.5295
1	0.91786	0.00918	97.6117
0.5	4.40199	0.04402	93.2097
0.355	3.10012	0.031	90.1096
0.25	13.1029	0.13103	77.0066
0.18	27.2455	0.27245	49.7612
0.125	36.1993	0.36199	13.5619
0.09	8.69158	0.08692	4.87028
0.063	2.39768	0.02398	2.4726

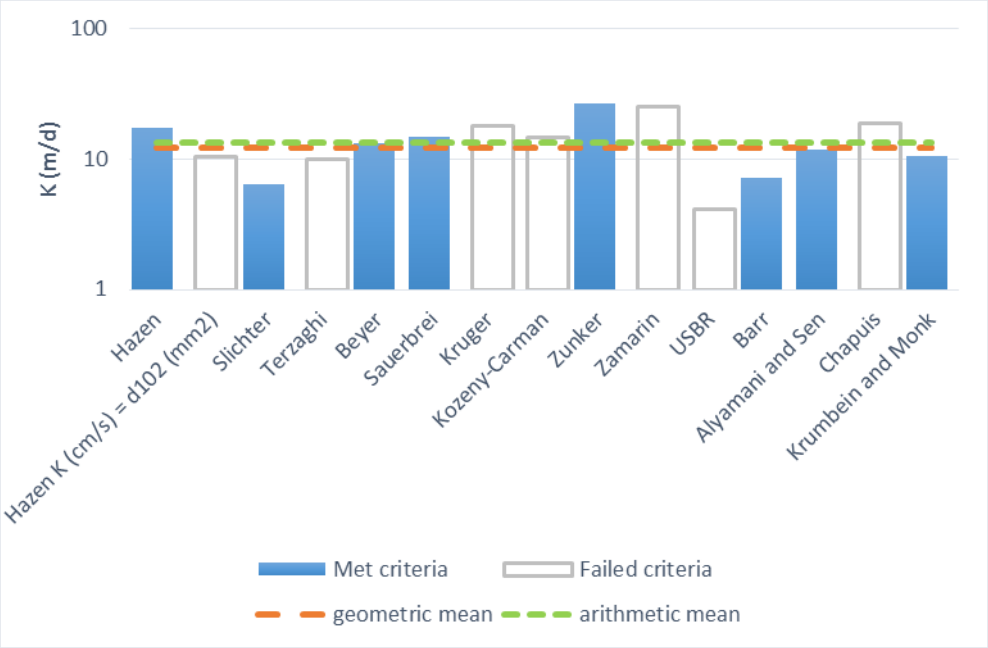
Effective Grain Diameters (mm)		Other Useful Parameters	
d10	0.111	Uniformity Coef.	1.86
d17	0.130	n computed	0.44
d20	0.135	g (cm/s^2)	980.00
d50	0.181	ρ (g/cm^3)	0.9981
d60	0.206	μ (g/cm s)	0.0098
de (Kruger)	0.187	ρg/μ (1/cm s)	9.9327E+04
de (Kozeny)	0.182	tau (Sauerbrei)	1.053
de (Zunker)	0.184	$d_{geometric\ mean}$	0.209
de (Zamarin)	0.186	σ_ϕ	0.761
Io (Alyameni	0.093		

mm	0	% in sample
>64	Boulder	
16 - 64	coarse gravel	
8 - 16	medium gravel	
2 - 8	fine gravel	1.470450501
0.5 - 2	coarse sand	5.319846399
0.25 - 0.5	medium sand	16.20305329
0.063 - 0.25	fine sand	74.53404514
0.016 - 0.063	coarse silt	
0.008 - 0.016	medium silt	
0.002 - 0.008	fine silt	
<0.002	clay	

Slichter, Terzaghi, Kozeny-Carman and Barr with d_{VS}:



Slichter, Terzaghi, Kozeny-Carman and Barr with d_{UU}:

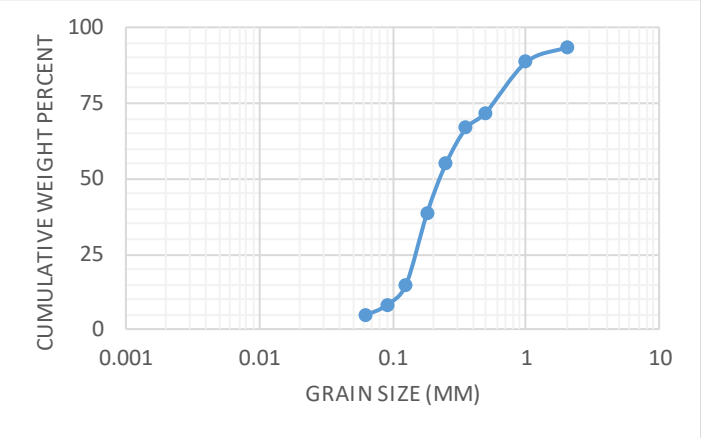


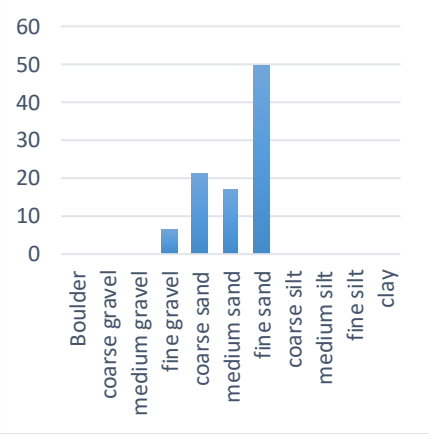
Well 040610/6-T4. Elevation 0.185 m AHD.

Grain Size Analysis Report

Mass Sample (g): 100 T (oC) 20

Moderately well sorted sand low in fines



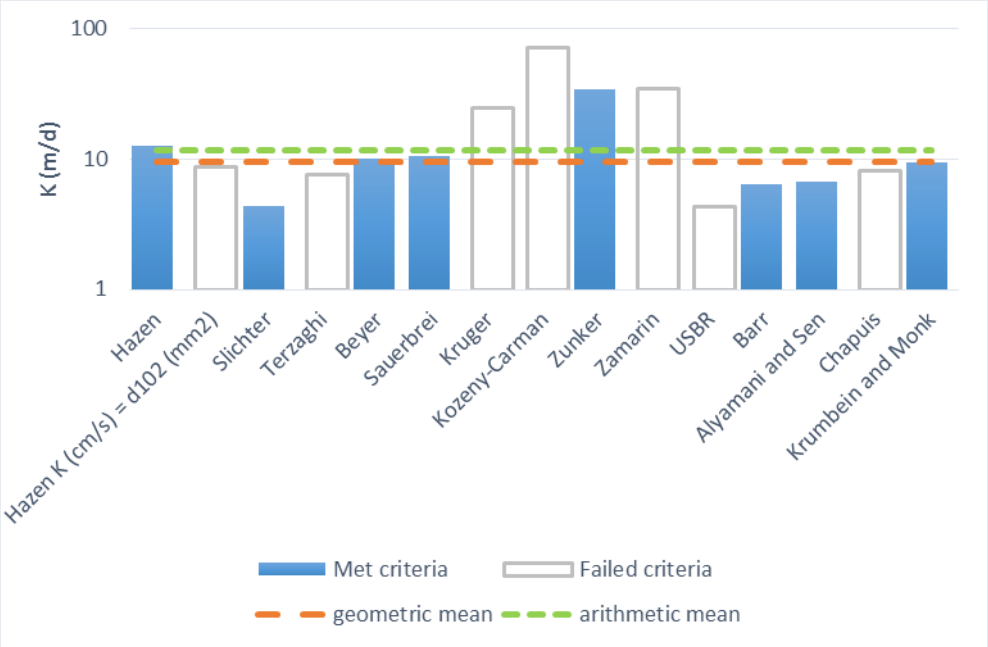


Sieve opening (ps) di (mm)	Mass of retained (mr) (g)	mass fraction (mf)	Percent Passing (pp)
2	6.57298	0.06573	93.427
1	4.83857	0.04839	88.5885
0.5	16.6059	0.16606	71.9826
0.355	5.21213	0.05212	66.7704
0.25	11.8474	0.11847	54.9231
0.18	16.5347	0.16535	38.3883
0.125	23.6947	0.23695	14.6936
0.09	6.63524	0.06635	8.05835
0.063	3.1931	0.03193	4.86525

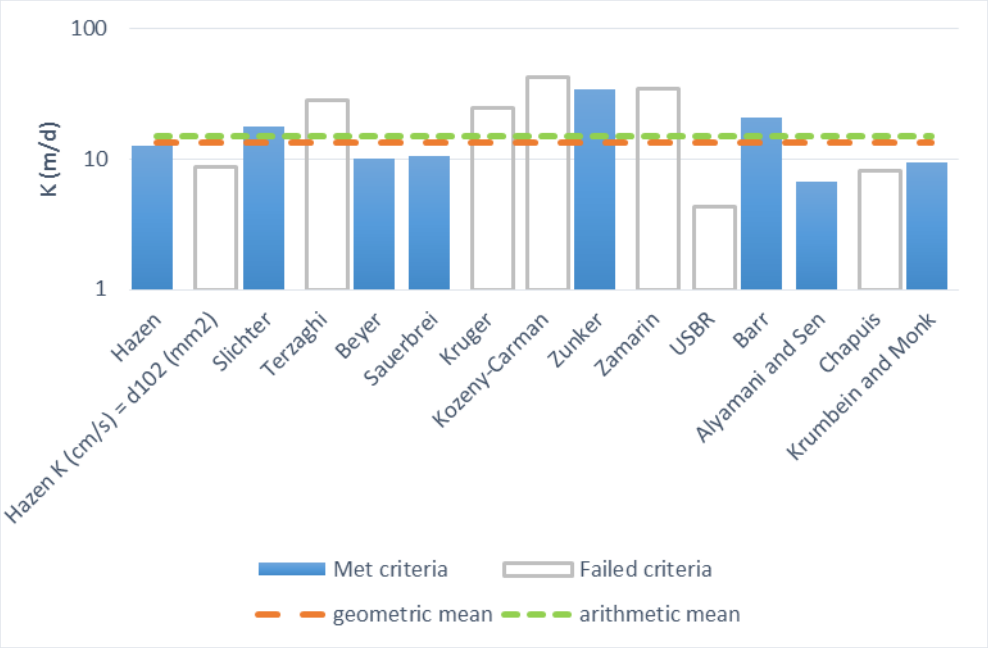
Effective Grain Diameters (mm)		Other Useful Parameters	
d10	0.100	Uniformity Coef.	2.94
d17	0.130	n computed	0.40
d20	0.137	g (cm/s^2)	980.00
d50	0.229	ρ (g/cm^3)	0.9981
d60	0.295	μ (g/cm s)	0.0098
de (Kruger)	0.242	ρg/μ (1/cm s)	9.9327E+04
de (Kozeny)	0.234	tau (Sauerbrei)	1.053
de (Zunker)	0.237	$d_{geometric\ mean}$	0.311
de (Zamarin)	0.240	σ_ϕ	1.443
Io (Alyameni	0.068		

mm	0	% in sample
>64	Boulder	
16 - 64	coarse gravel	
8 - 16	medium gravel	
2 - 8	fine gravel	6.572978742
0.5 - 2	coarse sand	21.44445433
0.25 - 0.5	medium sand	17.05950369
0.063 - 0.25	fine sand	50.05781375
0.016 - 0.063	coarse silt	
0.008 - 0.016	medium silt	
0.002 - 0.008	fine silt	
<0.002	clay	

Slichter, Terzaghi, Kozeny-Carman and Barr with d_{VS}:



Slichter, Terzaghi, Kozeny-Carman and Barr with d_{UU}:

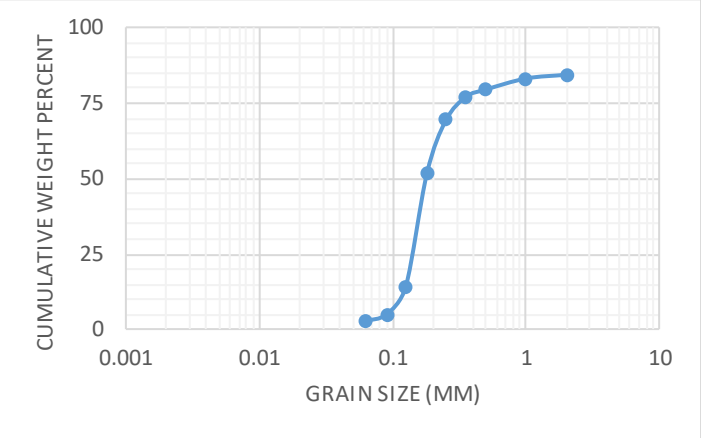


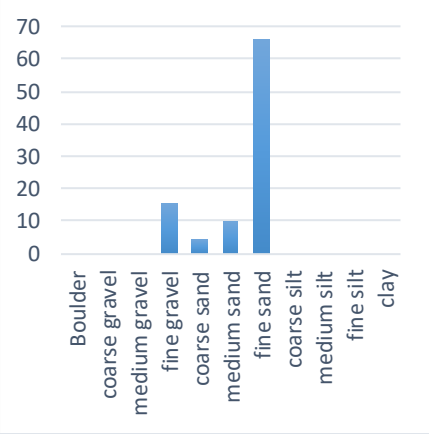
Well 040610/6-T4. Elevation -0.095 m AHD.

Grain Size Analysis Report

Mass Sample (g): 100 T (oC) 20

Uniform gravelly sand low in fines



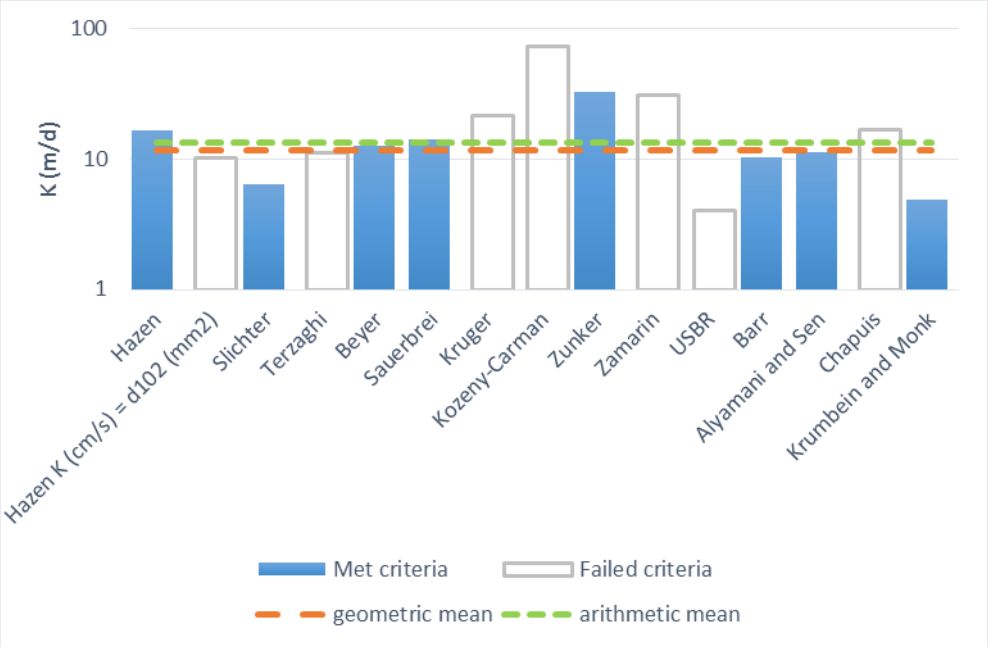


Sieve opening (ps) di (mm)	Mass of retained (mr) (g)	mass fraction (mf)	Percent Passing (pp)
2	15.593	0.15593	84.407
1	1.23241	0.01232	83.1745
0.5	3.64479	0.03645	79.5298
0.355	2.40364	0.02404	77.1261
0.25	7.7703	0.0777	69.3558
0.18	17.6034	0.17603	51.7525
0.125	37.4618	0.37462	14.2907
0.09	9.195	0.09195	5.09571
0.063	2.16764	0.02168	2.92807

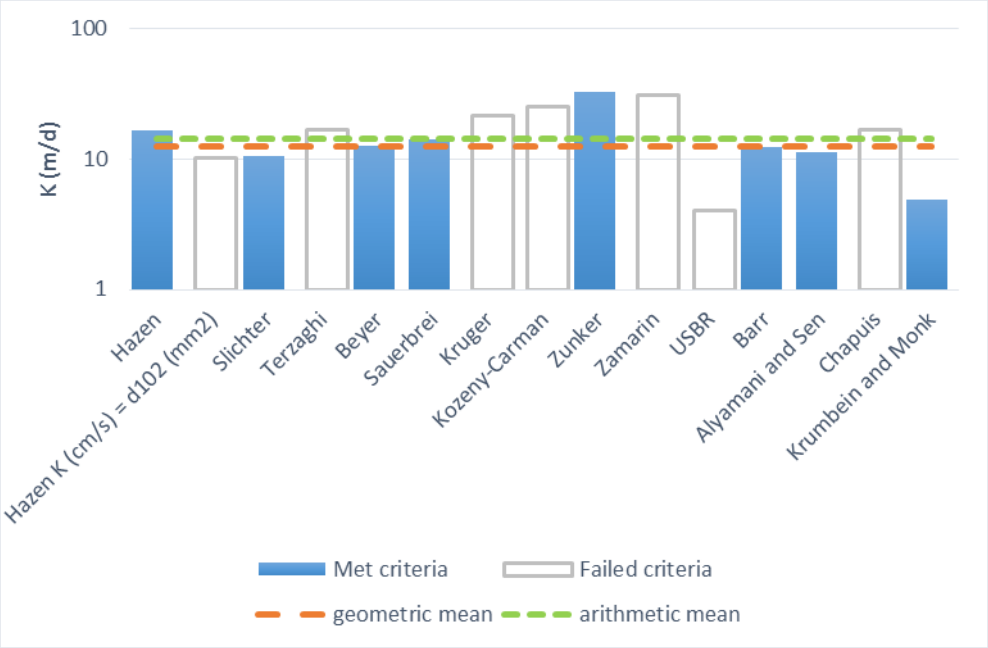
Effective Grain Diameters (mm)		Other Useful Parameters	
d10	0.109	Uniformity Coef.	1.96
d17	0.129	n computed	0.43
d20	0.133	g (cm/s^2)	980.00
d50	0.177	ρ (g/cm^3)	0.9981
d60	0.213	μ (g/cm s)	0.0098
de (Kruger)	0.209	ρg/μ (1/cm s)	9.9327E+04
de (Kozeny)	0.203	tau (Sauerbrei)	1.053
de (Zunker)	0.205	$d_{geometric\ mean}$	0.254
de (Zamarin)	0.207	σ_ϕ	1.634
Io (Alyameni	0.091		

mm	0	% in sample
>64	Boulder	
16 - 64	coarse gravel	
8 - 16	medium gravel	
2 - 8	fine gravel	15.59304257
0.5 - 2	coarse sand	4.877196049
0.25 - 0.5	medium sand	10.17393584
0.063 - 0.25	fine sand	66.42775981
0.016 - 0.063	coarse silt	
0.008 - 0.016	medium silt	
0.002 - 0.008	fine silt	
<0.002	clay	

Slichter, Terzaghi, Kozeny-Carman and Barr with d_{VS}:



Slichter, Terzaghi, Kozeny-Carman and Barr with d_{UU}:



Appendix F: Retention curves

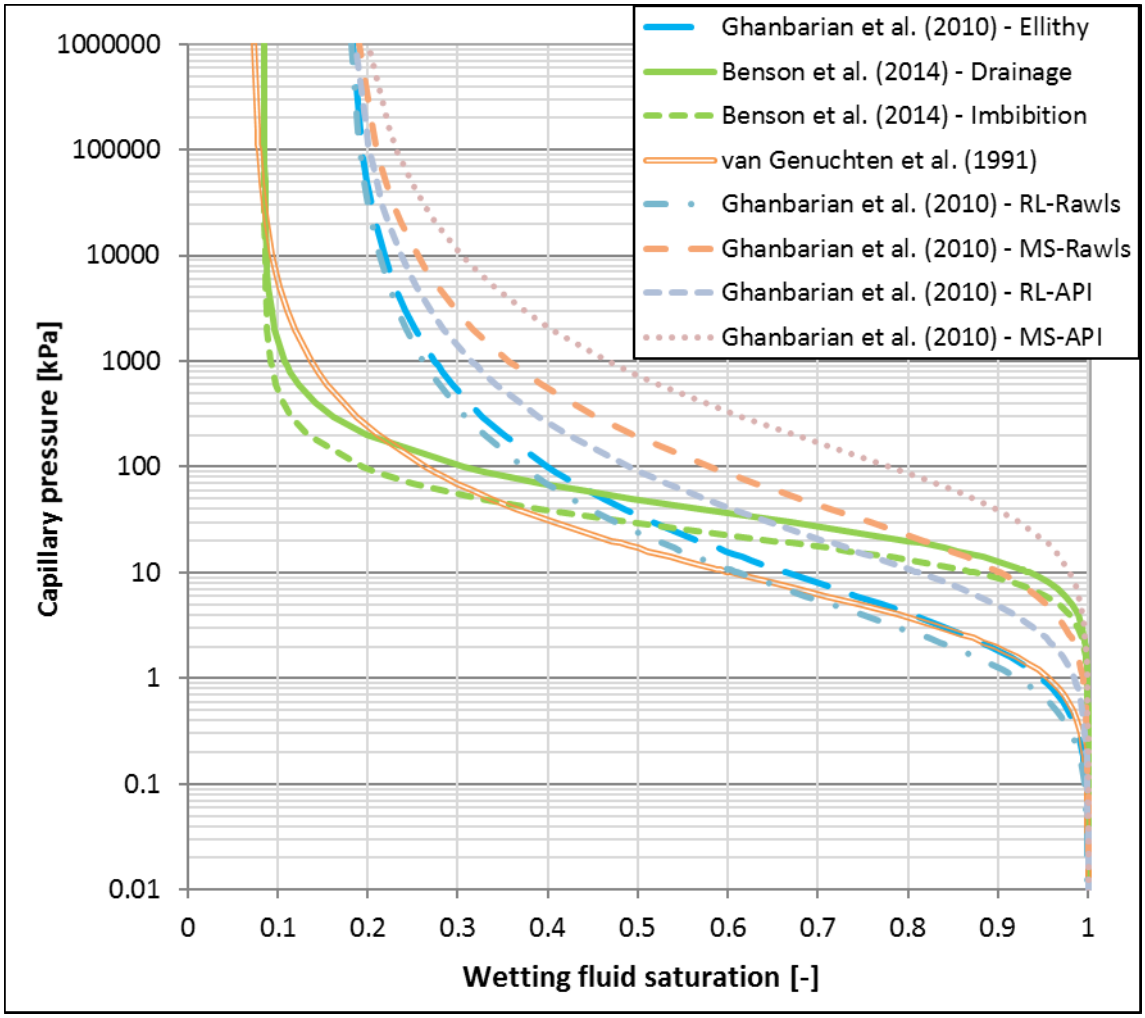
Contents

Well PB13-C. Elevation 58.980 m AHD. F-5
Well PB12-C. Elevation 58.906 m AHD. F-6
Well PB13-C. Elevation 58.530 m AHD. F-7
Well MP44-C. Elevation 57.16 m AHD. F-8
Well PB39-C. Elevation 57.051 m AHD. F-9
Well MP44-C. Elevation 56.76 m AHD. F-10
Well PB39-C. Elevation 56.401 m AHD. F-11
Well PB27-B. Elevation 56.12 m AHD. F-12
Well ML32. Elevation 55.917 m AHD. F-13
Well MP44-C. Elevation 55.76 m AHD. F-14
Well MP50-A. Elevation 55.681 m AHD. F-15
Well PB39-C. Elevation 55.501 m AHD. F-16
Well PB28. Elevation 55.436 m AHD. F-17
Well MP50-A. Elevation 55.186 m AHD. F-18
Well PB13-C. Elevation 55.18 m AHD. F-19
Well MP44-C. Elevation 55.16 m AHD. F-20
Well ML15. Elevation 55.147 m AHD. F-21
Well PB13-C. Elevation 55.03 m AHD. F-22
Well PB27-B. Elevation 54.71 m AHD. F-23
Well PB39-C. Elevation 54.601 m AHD. F-24
Well ML15. Elevation 54.207 m AHD. F-25
Well PB27-B. Elevation 54.16 m AHD. F-26
Well MP44-C. Elevation 53.96 m AHD. F-27
Well MP50-A. Elevation 53.886 m AHD. F-28
Well PB27-B. Elevation 53.16 m AHD. F-29
Well 040610/1-T4. Elevation 1.025 m AHD. F-30
Well 040610/1-T4. Elevation 0.975 m AHD. F-31
Well 040610/1-T4. Elevation 0.925 m AHD. F-31
Well 040610/1-T4. Elevation 0.875 m AHD. F-31
Well 040610/1-T4. Elevation 0.825 m AHD. F-32
Well 040610/1-T4. Elevation 0.775 m AHD. F-33
Well 040610/1-T4. Elevation 0.725 m AHD. F-33

Well 040610/1-T4. Elevation 0.675 m AHD. F-33
Well 040610/1-T4. Elevation 0.625 m AHD. F-34
Well 040610/1-T4. Elevation 0.575 m AHD. F-35
Well 040610/1-T4. Elevation 0.525 m AHD. F-35
Well 040610/1-T4. Elevation 0.475 m AHD. F-35
Well 040610/1-T4. Elevation 0.425 m AHD. F-36
Well 040610/1-T4. Elevation 0.375 m AHD. F-37
Well 040610/1-T4. Elevation 0.325 m AHD. F-37
Well 040610/1-T4. Elevation 0.275 m AHD. F-37
Well 040610/1-T4. Elevation 0.225 m AHD. F-38
Well 040610/1-T4. Elevation 0.175 m AHD. F-39
Well 040610/1-T4. Elevation 0.125 m AHD. F-39
Well 040610/1-T4. Elevation 0.075 m AHD. F-39
Well 040610/3-T4. Elevation 0.975 m AHD. F-40
Well 040610/3-T4. Elevation 0.925 m AHD. F-41
Well 040610/3-T4. Elevation 0.875 m AHD. F-41
Well 040610/3-T4. Elevation 0.825 m AHD. F-41
Well 040610/3-T4. Elevation 0.775 m AHD. F-42
Well 040610/3-T4. Elevation 0.725 m AHD. F-43
Well 040610/3-T4. Elevation 0.675 m AHD. F-43
Well 040610/3-T4. Elevation 0.625 m AHD. F-43
Well 040610/3-T4. Elevation 0.575 m AHD. F-44
Well 040610/3-T4. Elevation 0.525 m AHD. F-45
Well 040610/3-T4. Elevation 0.475 m AHD. F-45
Well 040610/3-T4. Elevation 0.425 m AHD. F-45
Well 040610/3-T4. Elevation 0.375 m AHD. F-46
Well 050210/1-T4. Elevation 0.875 m AHD. F-47
Well 050210/1-T4. Elevation 0.825 m AHD. F-47
Well 050210/1-T4. Elevation 0.775 m AHD. F-47
Well 050210/1-T4. Elevation 0.725 m AHD. F-48
Well 050210/1-T4. Elevation 0.675 m AHD. F-49
Well 050210/1-T4. Elevation 0.625 m AHD. F-49
Well 050210/1-T4. Elevation 0.575 m AHD. F-49
Well 050210/1-T4. Elevation 0.525 m AHD. F-50

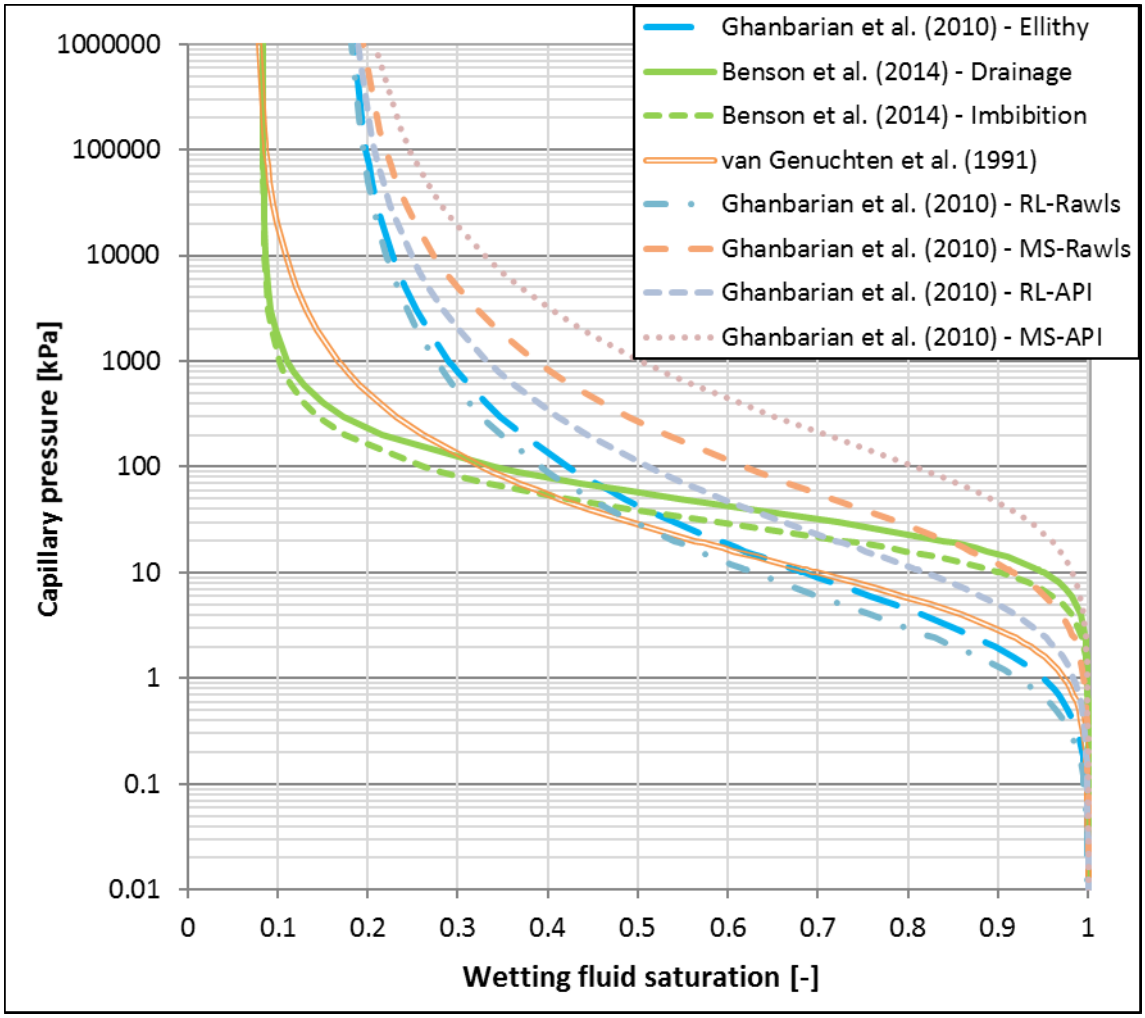
Well 050210/1-T4. Elevation 0.475 m AHD. F-51
Well 040610/6-T4. Elevation 1.385 m AHD. F-51
Well 040610/6-T4. Elevation 1.335 m AHD. F-51
Well 040610/6-T4. Elevation 1.285 m AHD. F-52
Well 040610/6-T4. Elevation 1.235 m AHD. F-53
Well 040610/6-T4. Elevation 1.185 m AHD. F-53
Well 040610/6-T4. Elevation 1.135 m AHD. F-53
Well 040610/6-T4. Elevation 1.085 m AHD. F-54
Well 040610/6-T4. Elevation 1.035 m AHD. F-55
Well 040610/6-T4. Elevation 0.985 m AHD. F-55
Well 040610/6-T4. Elevation 0.935 m AHD. F-55
Well 040610/6-T4. Elevation 0.885 m AHD. F-56
Well 040610/6-T4. Elevation 0.785 m AHD. F-57
Well 040610/6-T4. Elevation 0.735 m AHD. F-57
Well 040610/6-T4. Elevation 0.685 m AHD. F-57
Well 040610/6-T4. Elevation 0.635 m AHD. F-58
Well 040610/6-T4. Elevation 0.585 m AHD. F-59
Well 040610/6-T4. Elevation 0.535 m AHD. F-59
Well 040610/6-T4. Elevation 0.485 m AHD. F-59
Well 040610/6-T4. Elevation 0.435 m AHD. F-60
Well 040610/6-T4. Elevation 0.385 m AHD. F-61
Well 040610/6-T4. Elevation 0.285 m AHD. F-61
Well 040610/6-T4. Elevation 0.235 m AHD. F-61
Well 040610/6-T4. Elevation 0.185 m AHD. F-62
Well 040610/6-T4. Elevation -0.095 m AHD. F-63
Well 040610/2-T4. Elevation 1.061-1.011 m AHD. Drainage curve. F-64
Well 040610/2-T4. Elevation 1.061-1.011 m AHD. Imbibition curve. F-66

Well PB13-C. Elevation 58.980 m AHD.



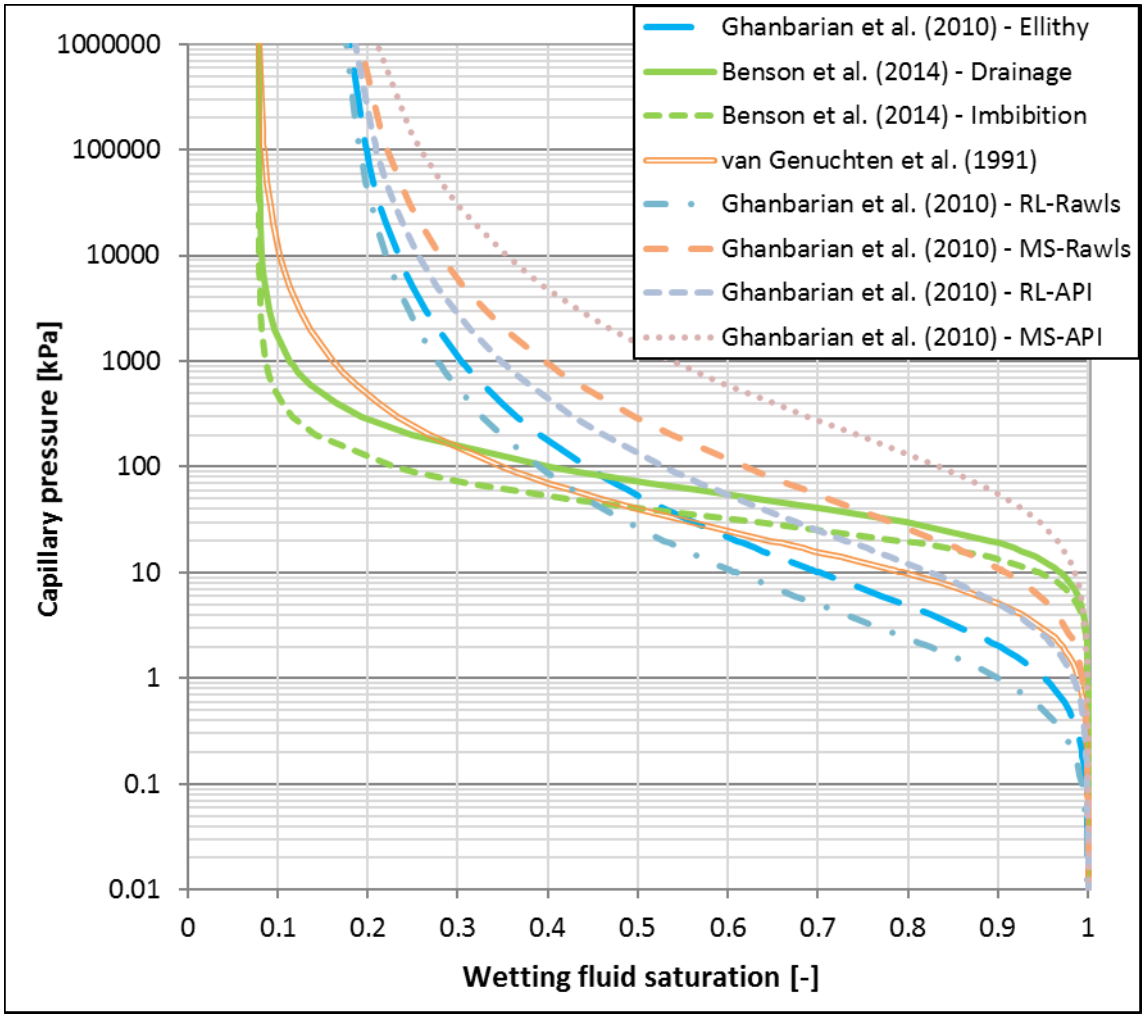
Well PB13-C. Elevation 58.98 m AHD.	Ghanbarian et al. (2010)					Benson et al. (2014)		van Genuchten et al. (1991)
	Ellithy (2017)	Lenhard et al. (1989)		Morel-Seytoux et al. (1996)		Drainage	Imbibition	
		Rawls	API	Rawls	API			
vG-α [m^{-1}]	3.8310	5.5575	1.4484	0.6927	0.1805	0.3922	0.5773	2.8600
vG-N [-]	1.3535					2.0000	2.1910	1.4639
S_{wr} [-]	0.1743					0.0854		0.0709

Well PB12-C. Elevation 58.906 m AHD.



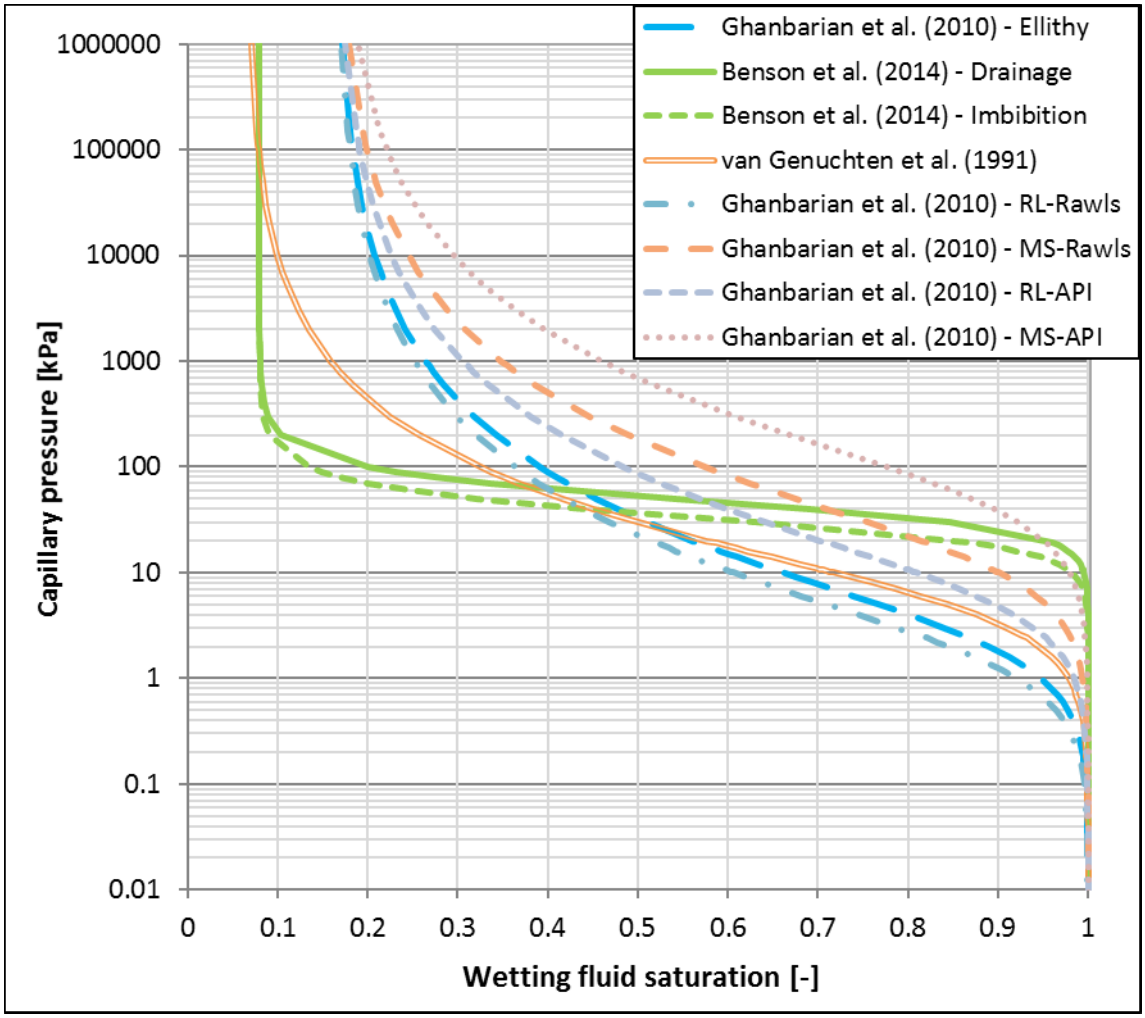
Well PB12-C. Elevation 58.906 m AHD.	Ghanbarian et al. (2010)					Benson et al. (2014)		van Genuchten et al. (1991)
	Ellithy (2017)	Lenhard et al. (1989)		Morel-Seytoux et al. (1996)		Drainage	Imbibition	
		Rawls	API	Rawls	API			
vG-α [m^{-1}]	3.8310	5.7192	1.4906	0.6153	0.1604	0.3355	0.4938	1.9600
vG-N [-]	1.3248					2.0000	2.0000	1.4320
S_{wr} [-]	0.1715					0.0840		0.0741

Well PB13-C. Elevation 58.530 m AHD.



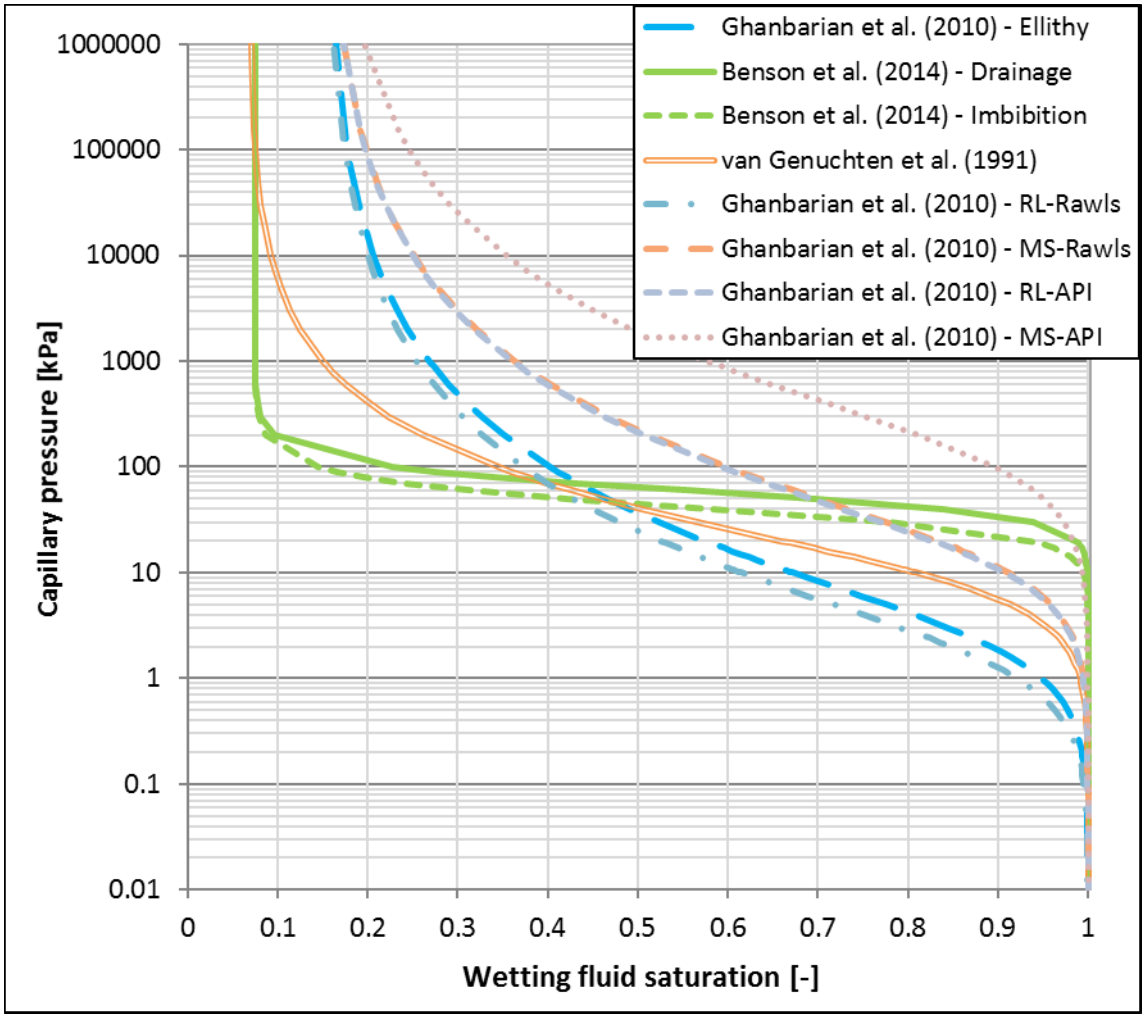
Well PB13-C. Elevation 58.53 m AHD.	Ghanbarian et al. (2010)					Benson et al. (2014)		van Genuchten et al. (1991)
	Ellithy (2017)	Lenhard et al. (1989)		Morel-Seytoux et al. (1996)		Drainage	Imbibition	
		Rawls	API	Rawls	API			
vG-α [m^{-1}]	3.8310	7.7517	1.5366	0.7102	0.1408	0.2609	0.3840	1.0500
vG-N [-]	1.2968					2.0000	2.3064	1.5102
S_{wr} [-]	0.1620					0.0793		0.0766

Well MP44-C. Elevation 57.16 m AHD.



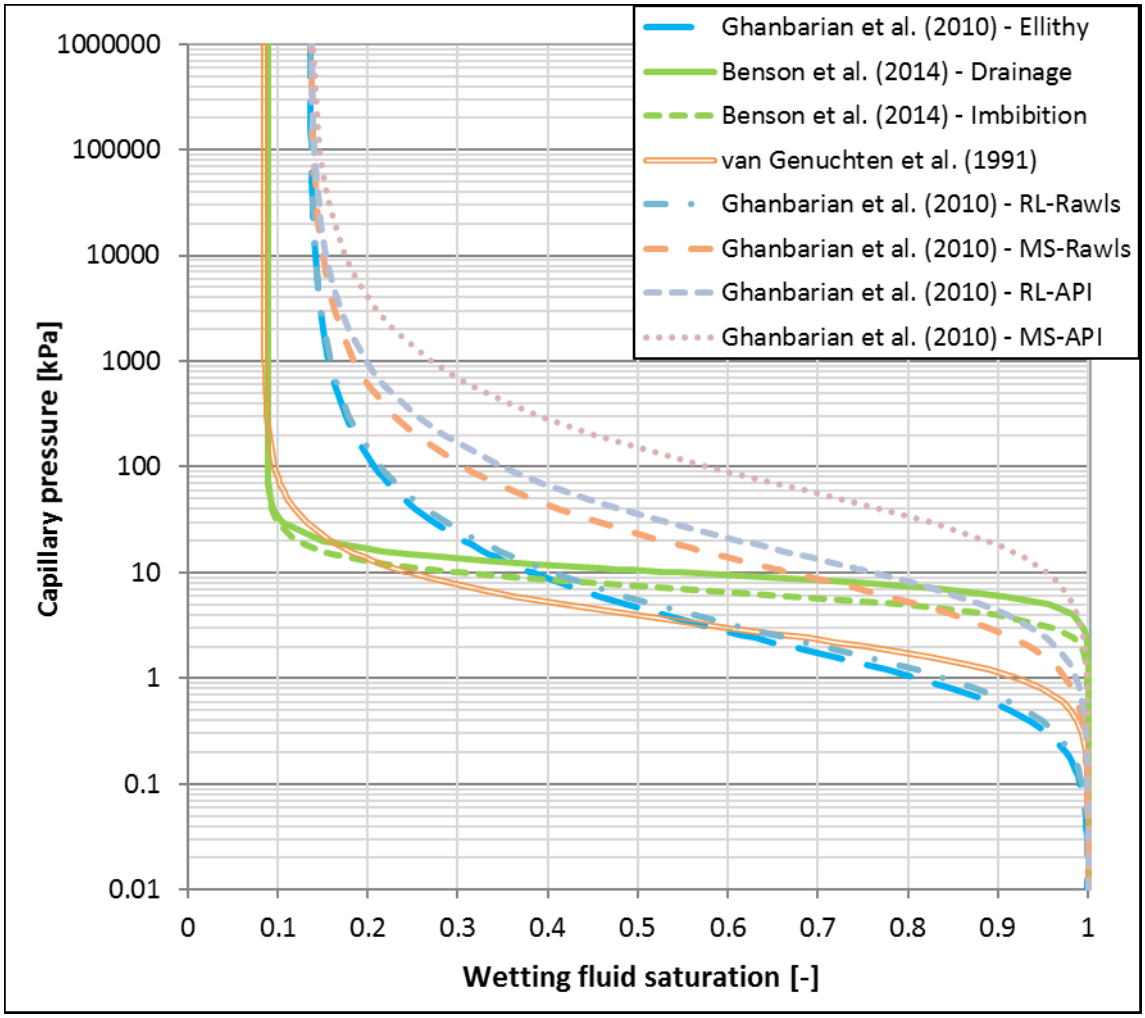
Well MP44-C. Elevation 57.16 m AHD.	Ghanbarian et al. (2010)					Benson et al. (2014)		van Genuchten et al. (1991)
	Ellithy (2017)	Lenhard et al. (1989)		Morel-Seytoux et al. (1996)		Drainage	Imbibition	
		Rawls	API	Rawls	API			
vG-α [m^{-1}]	3.8310	5.5570	1.4483	0.6930	0.1806	0.2277	0.3352	1.6900
vG-N [-]	1.3536					3.3621	3.2863	1.4498
S_{wr} [-]	0.1630					0.0798		0.0673

Well PB39-C. Elevation 57.051 m AHD.



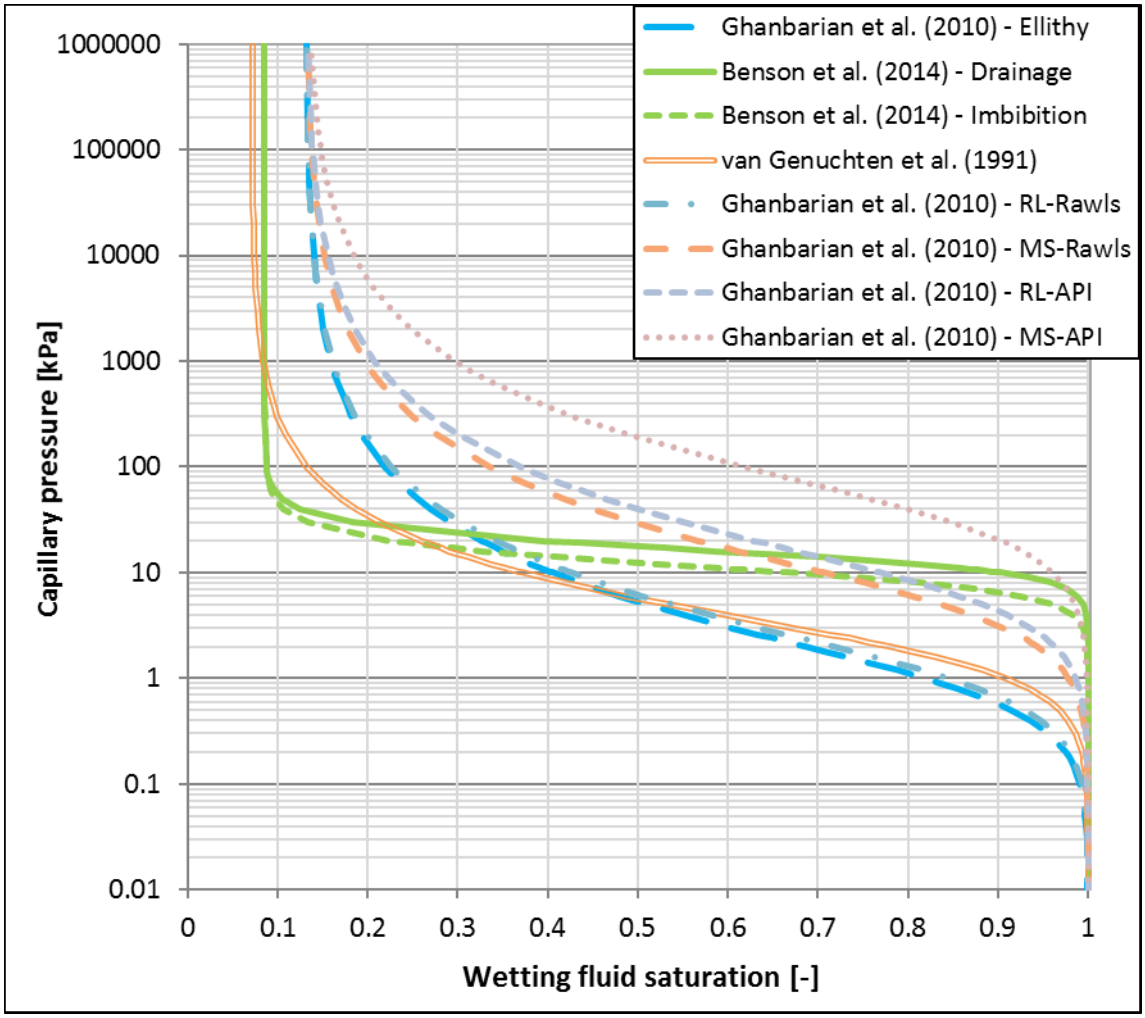
Well PB39-C. Elevation 57.051 m AHD.	Ghanbarian et al. (2010)					Benson et al. (2014)		van Genuchten et al. (1991)
	Ellithy (2017)	Lenhard et al. (1989)		Morel-Seytoux et al. (1996)		Drainage	Imbibition	
		Rawls	API	Rawls	API			
vG-α [m^{-1}]	3.8310	5.6771	0.6647	0.6346	0.0743	0.1787	0.2631	0.9400
vG-N [-]	1.3320					3.8808	3.5970	1.5321
S_{wr} [-]	0.1523					0.0746		0.0681

Well MP44-C. Elevation 56.76 m AHD.



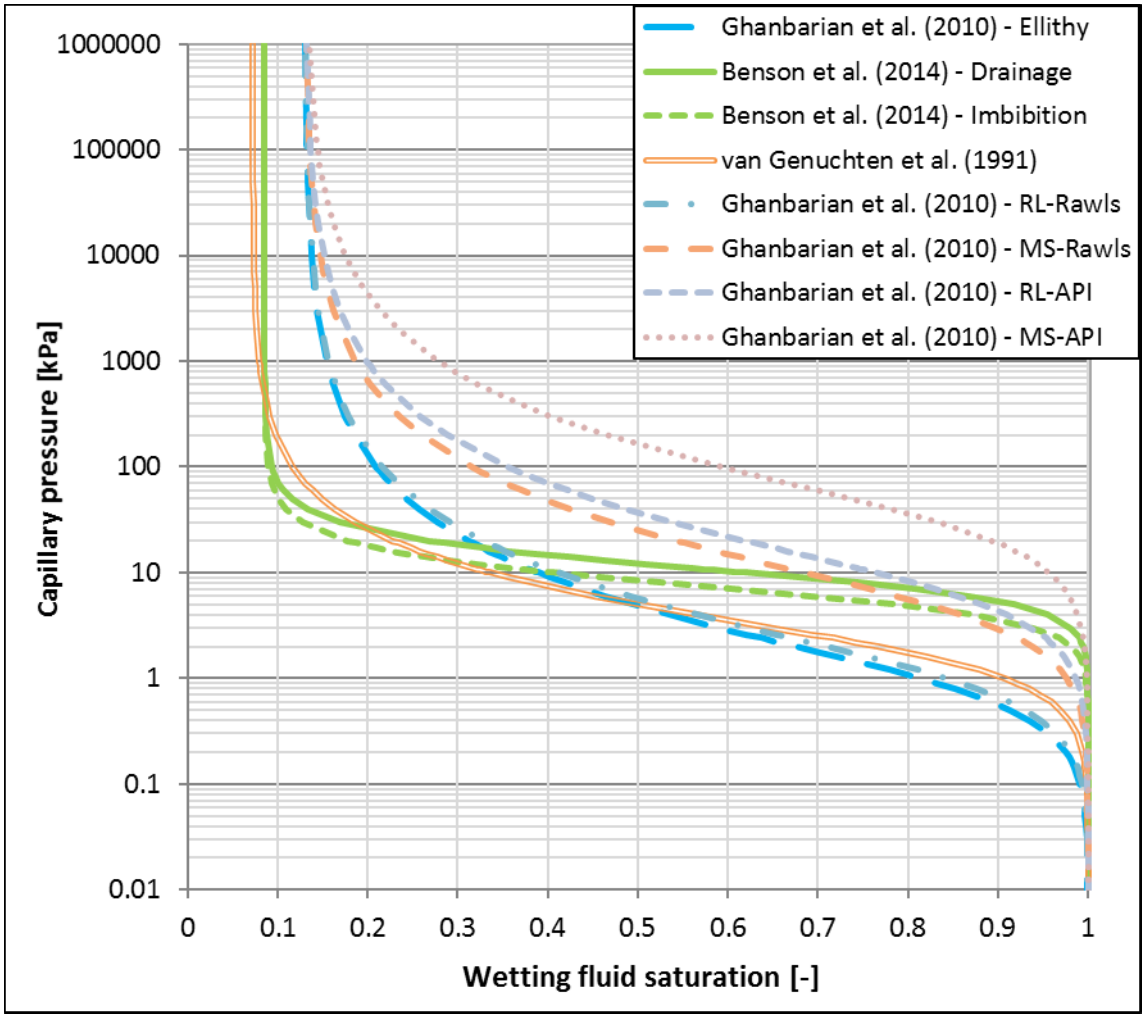
Well MP44-C. Elevation 56.76 m AHD.	Ghanbarian et al. (2010)					Benson et al. (2014)		van Genuchten et al. (1991)
	Ellithy (2017)	Lenhard et al. (1989)		Morel-Seytoux et al. (1996)		Drainage	Imbibition	
		Rawls	API	Rawls	API			
vG-α [m^{-1}]	9.9439	8.3771	1.2942	1.9929	0.3079	1.0637	1.5657	4.4200
vG-N [-]	1.5371					4.4392	3.8753	2.1413
S_{wr} [-]	0.1356					0.0889		0.0849

Well PB39-C. Elevation 56.401 m AHD.



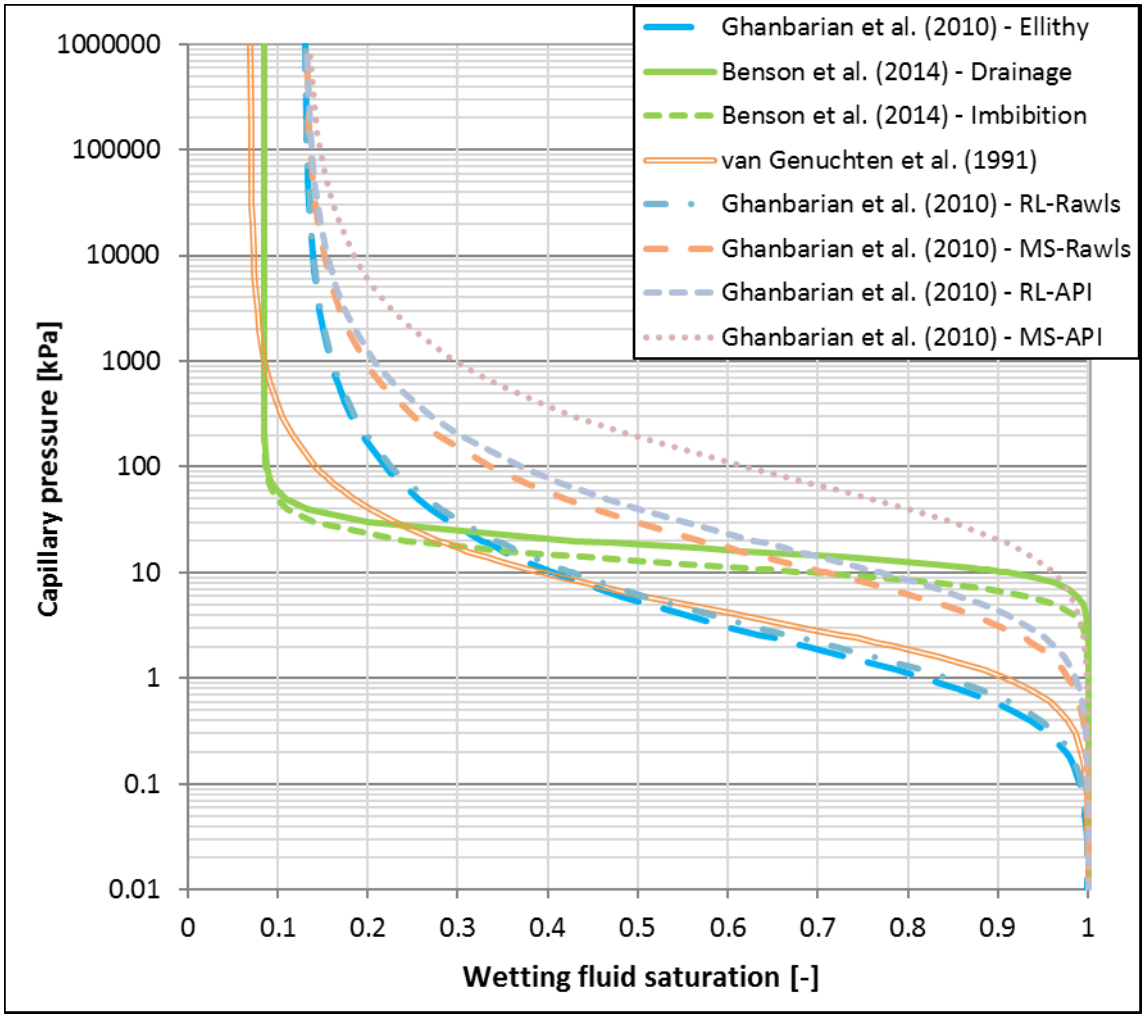
Well PB39-C. Elevation 56.401 m AHD.	Ghanbarian et al. (2010)					Benson et al. (2014)		van Genuchten et al. (1991)
	Ellithy (2017)	Lenhard et al. (1989)		Morel-Seytoux et al. (1996)		Drainage	Imbibition	
		Rawls	API	Rawls	API			
vG-α [m^{-1}]	9.9439	8.5190	1.3161	1.8028	0.2785	0.6386	0.9400	4.6800
vG-N [-]	1.4937					4.2808	3.7956	1.7046
S_{wr} [-]	0.1308					0.0857		0.0718

Well PB27-B. Elevation 56.12 m AHD.



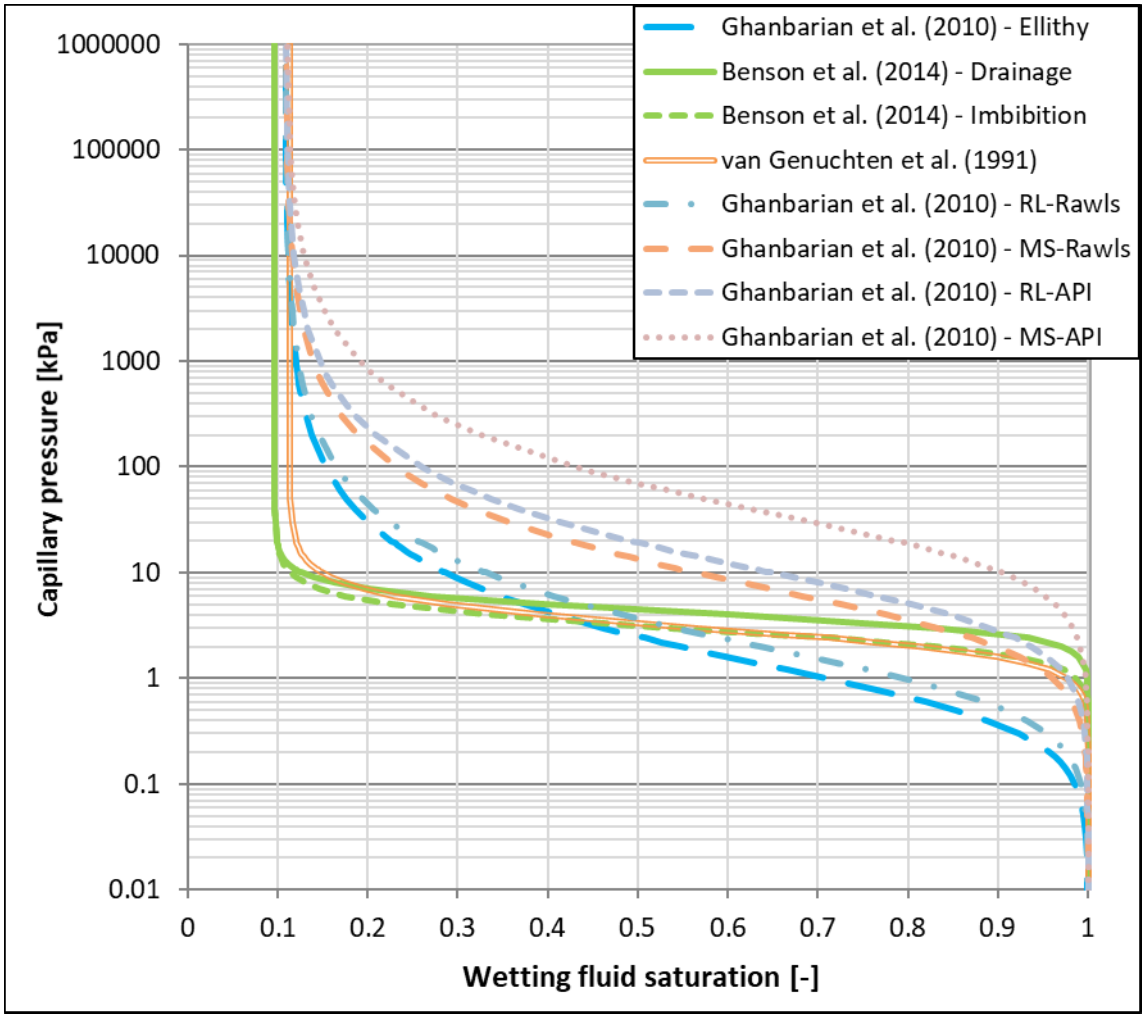
Well PB27-B. Elevation 56.12 m AHD.	Ghanbarian et al. (2010)					Benson et al. (2014)		van Genuchten et al. (1991)
	Ellithy (2017)	Lenhard et al. (1989)		Morel-Seytoux et al. (1996)		Drainage	Imbibition	
		Rawls	API	Rawls	API			
vG-α [m^{-1}]	9.9439	8.4306	1.3024	1.9152	0.2959	1.0517	1.5481	4.7100
vG-N [-]	1.5192					3.0267	2.9794	1.7860
S_{wr} [-]	0.1306					0.0857		0.0726

Well ML32. Elevation 55.917 m AHD.



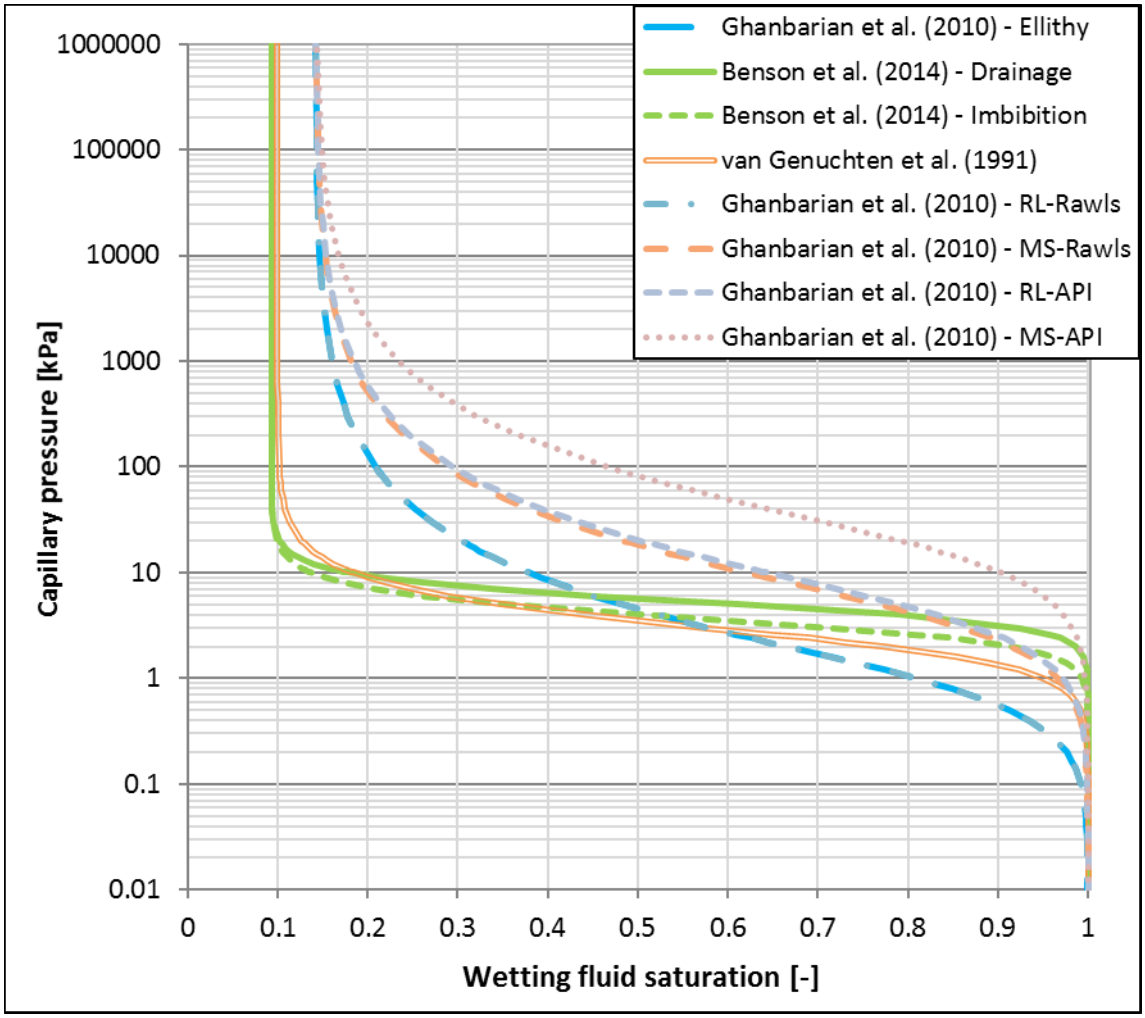
Well ML32. Elevation 55.917 m AHD.	Ghanbarian et al. (2010)					Benson et al. (2014)		van Genuchten et al. (1991)
	Ellithy (2017)	Lenhard et al. (1989)		Morel-Seytoux et al. (1996)		Drainage	Imbibition	
		Rawls	API	Rawls	API			
vG-α [m^{-1}]	9.9439	8.5279	1.3175	1.7925	0.2769	0.6175	0.9089	4.6900
vG-N [-]	1.4914					4.1666	3.7272	1.6575
S_{wr} [-]	0.1298					0.0851		0.0696

Well MP44-C. Elevation 55.76 m AHD.



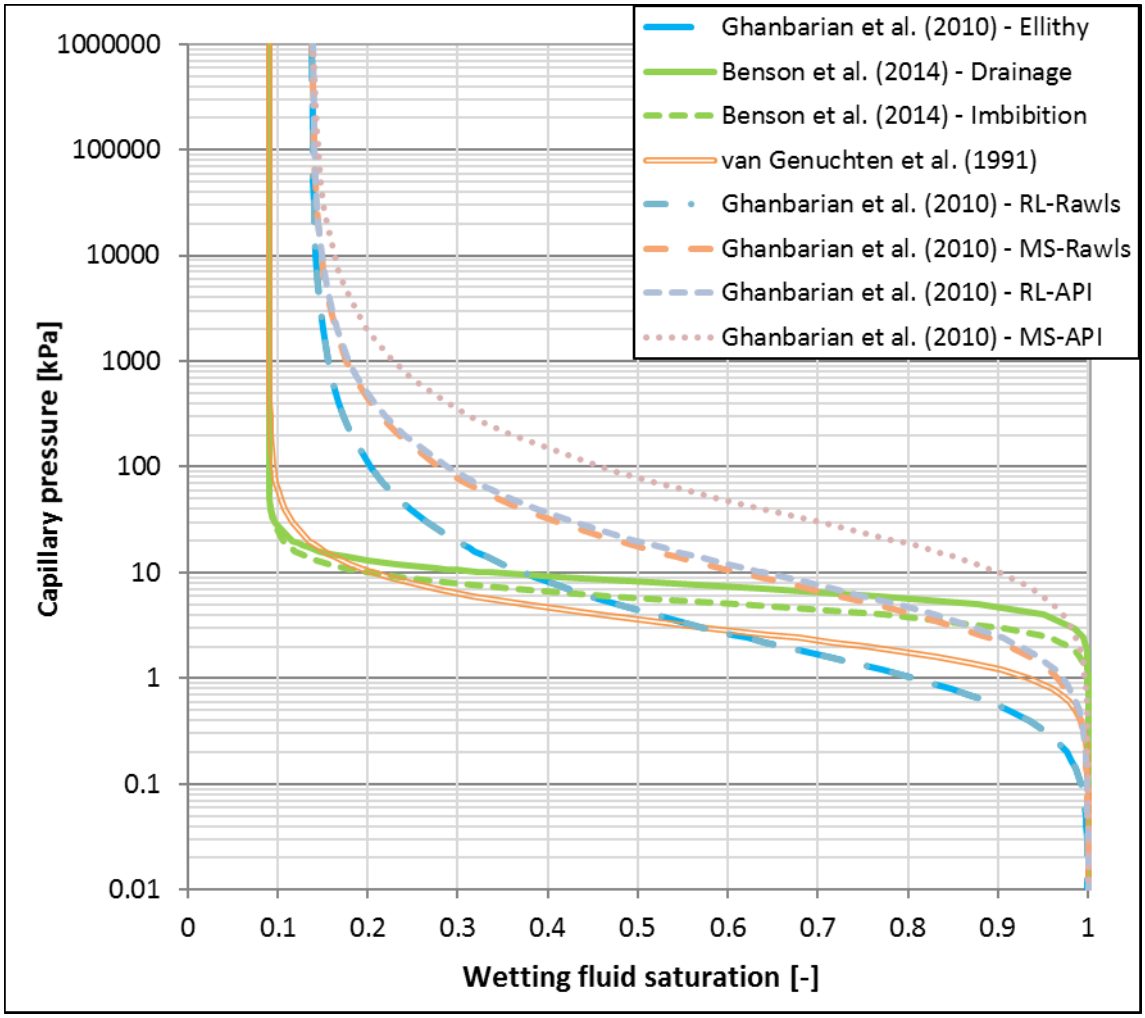
Well MP44-C. Elevation 55.76 m AHD.	Ghanbarian et al. (2010)					Benson et al. (2014)		van Genuchten et al. (1991)
	Ellithy (2017)	Lenhard et al. (1989)		Morel-Seytoux et al. (1996)		Drainage	Imbibition	
		Rawls	API	Rawls	API			
vG-α [m^{-1}]	14.4911	9.8576	1.8828	2.6982	0.5154	2.4980	3.6769	3.7400
vG-N [-]	1.5983					4.6323	3.9787	3.3901
S_{wr} [-]	0.1087					0.0967		0.1133

Well MP50-A. Elevation 55.681 m AHD.



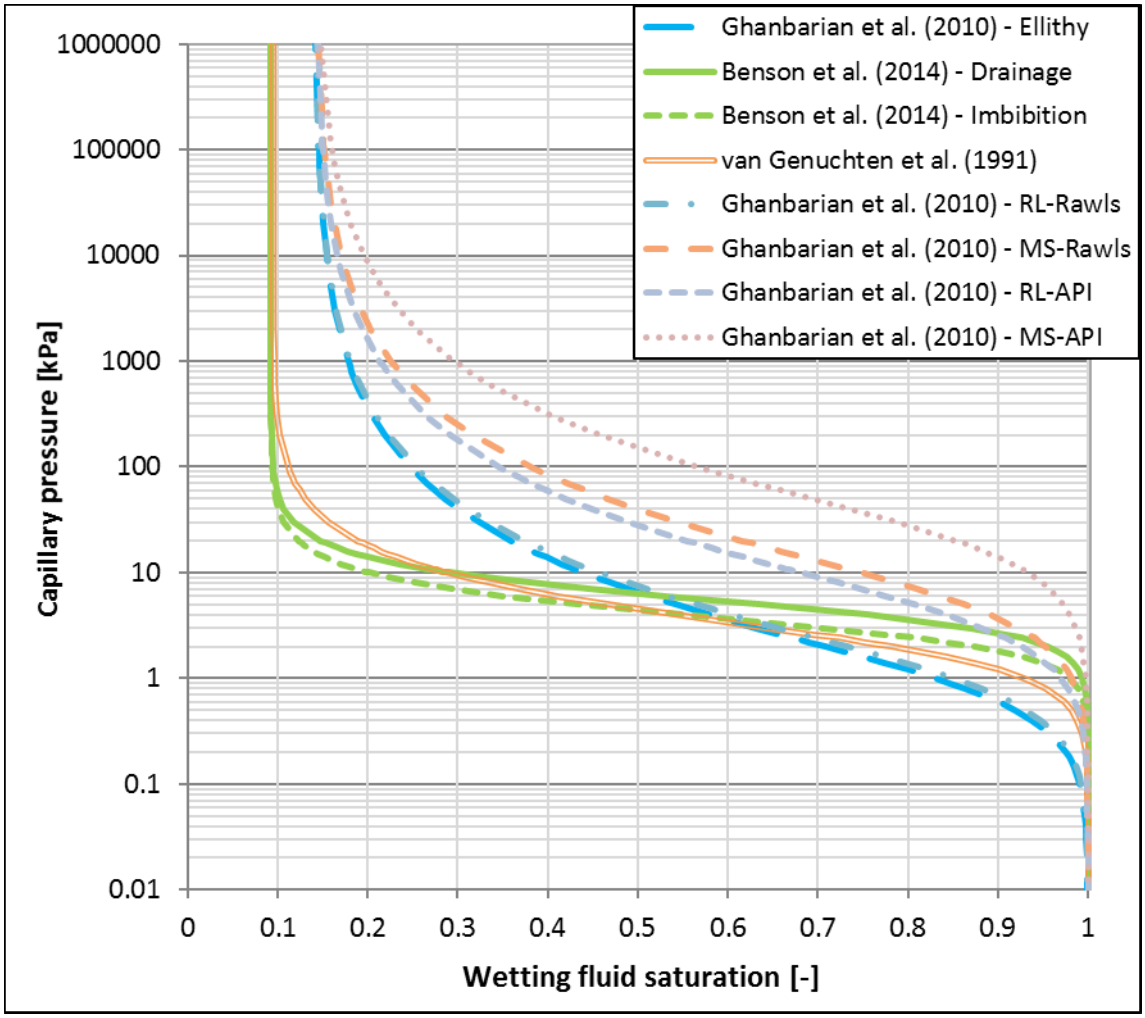
Well MP50-A. Elevation 55.681 m AHD.	Ghanbarian et al. (2010)					Benson et al. (2014)		van Genuchten et al. (1991)
	Ellithy (2017)	Lenhard et al. (1989)		Morel-Seytoux et al. (1996)		Drainage	Imbibition	
		Rawls	API	Rawls	API			
vG-α [m^{-1}]	9.9439	9.9775	2.2091	2.4657	0.5459	1.9886	2.9271	4.0300
vG-N [-]	1.5526					4.2876	3.7568	2.6635
S_{wr} [-]	0.1417					0.0929		0.0999

Well PB39-C. Elevation 55.501 m AHD.



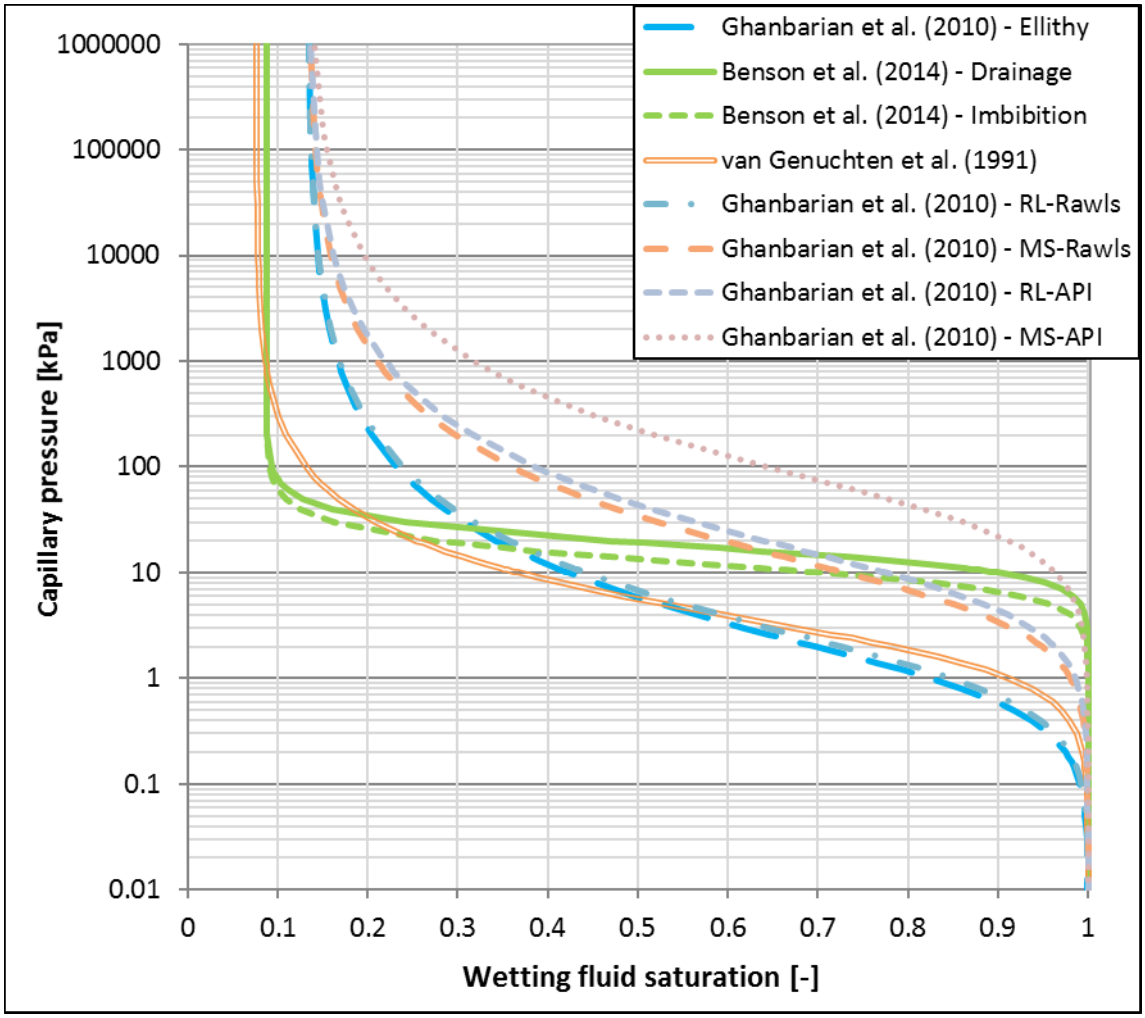
Well PB39-C. Elevation 55.501 m AHD.	Ghanbarian et al. (2010)					Benson et al. (2014)		van Genuchten et al. (1991)
	Ellithy (2017)	Lenhard et al. (1989)		Morel-Seytoux et al. (1996)		Drainage	Imbibition	
		Rawls	API	Rawls	API			
vG-α [m^{-1}]	9.9439	9.9616	2.2056	2.4931	0.5520	1.3698	2.0163	4.2700
vG-N [-]	1.5579					4.4392	3.8670	2.3904
S_{wr} [-]	0.1376					0.0902		0.0905

Well PB28. Elevation 55.436 m AHD.



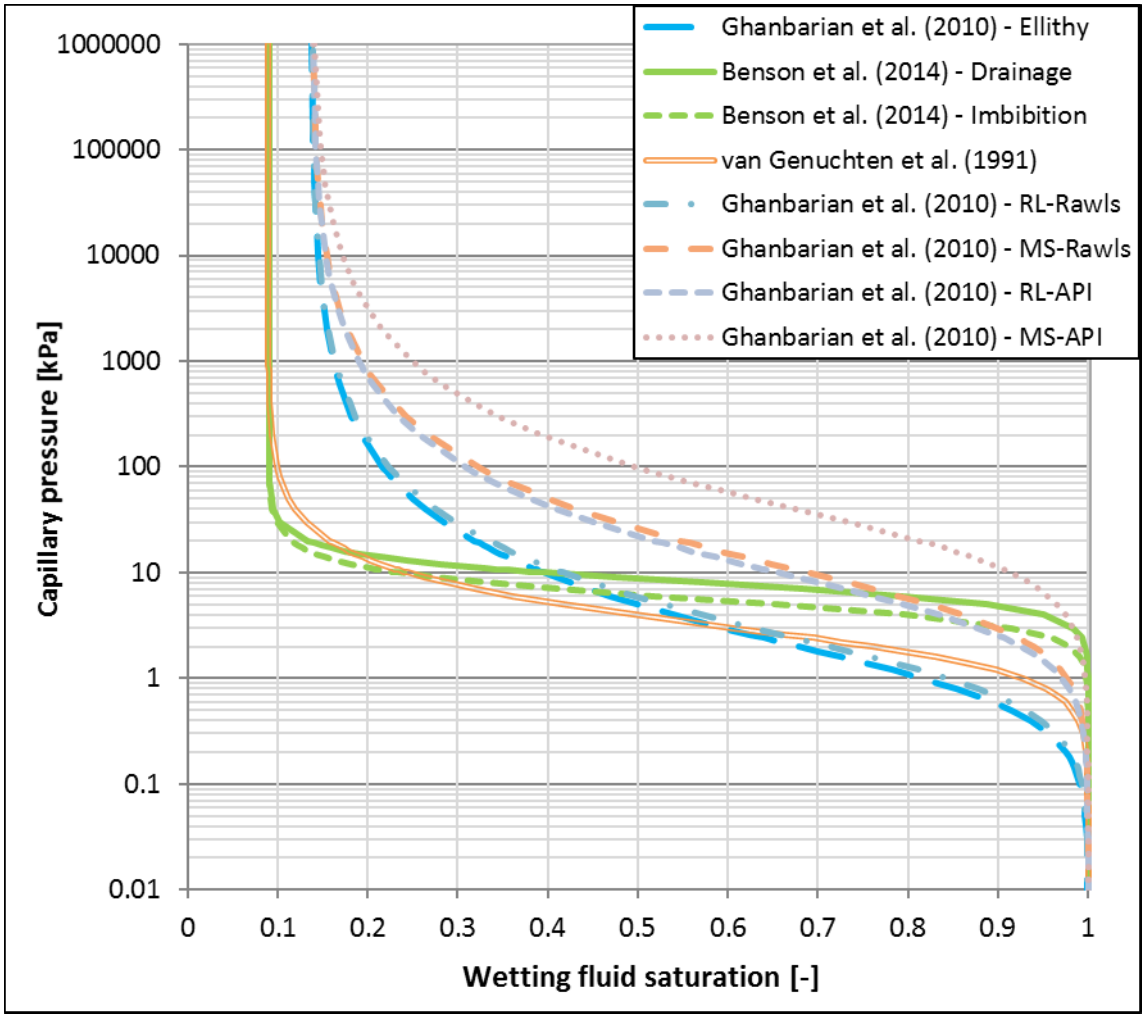
Well PB28. Elevation 55.436 m AHD.	Ghanbarian et al. (2010)					Benson et al. (2014)		van Genuchten et al. (1991)
	Ellithy (2017)	Lenhard et al. (1989)		Morel-Seytoux et al. (1996)		Drainage	Imbibition	
		Rawls	API	Rawls	API			
vG-α [m^{-1}]	9.9439	8.6982	2.3052	1.6188	0.4290	2.0731	3.0515	4.1500
vG-N [-]	1.4525					2.9329	2.8475	2.0525
S_{wr} [-]	0.1411					0.0925		0.0944

Well MP50-A. Elevation 55.186 m AHD.



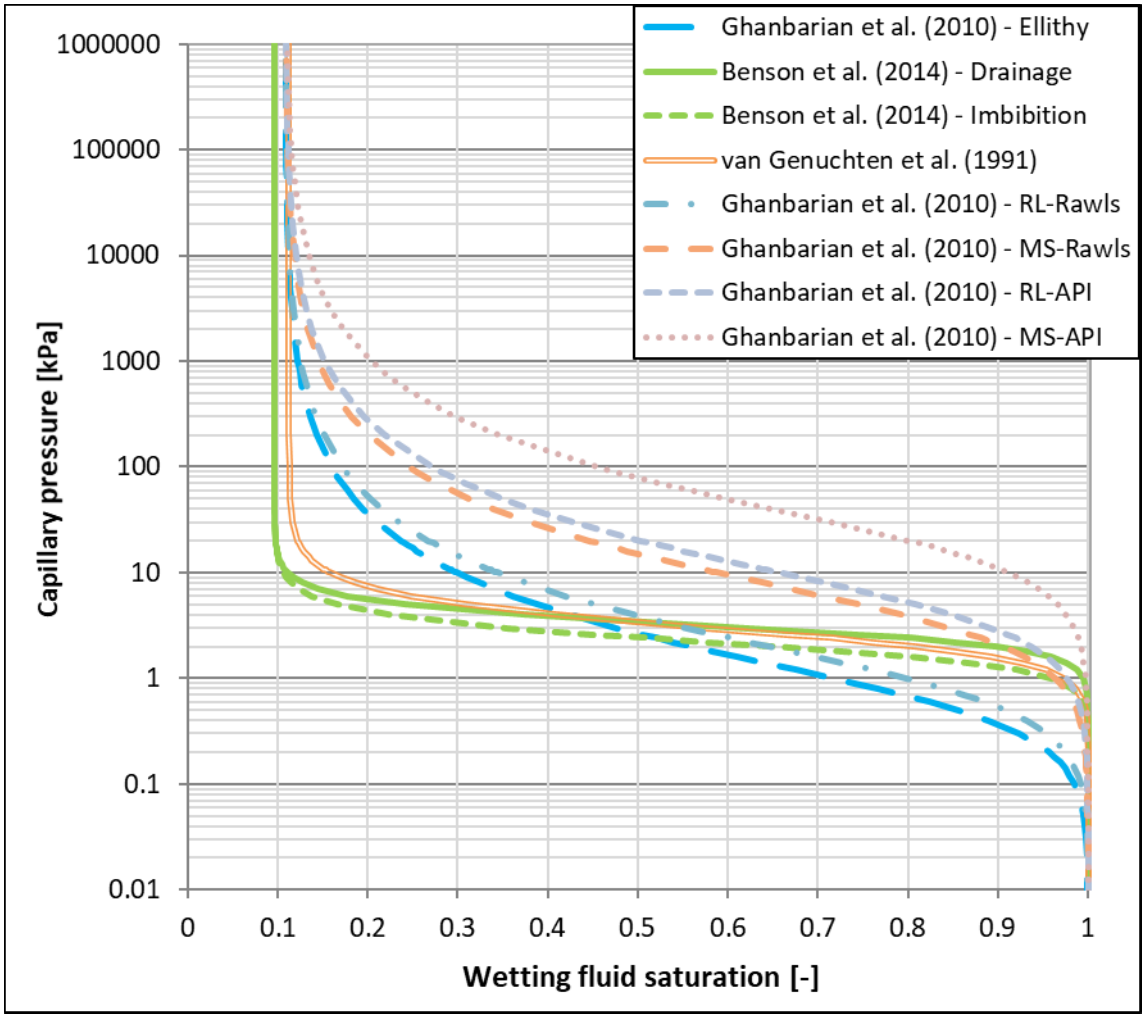
Well MP50-A. Elevation 55.186 m AHD.	Ghanbarian et al. (2010)					Benson et al. (2014)		van Genuchten et al. (1991)
	Ellithy (2017)	Lenhard et al. (1989)		Morel-Seytoux et al. (1996)		Drainage	Imbibition	
		Rawls	API	Rawls	API			
vG-α [m^{-1}]	9.9439	8.6174	1.3313	1.6960	0.2620	0.6122	0.9011	4.5600
vG-N [-]	1.4697					3.7229	3.4564	1.7343
S_{wr} [-]	0.1333					0.0874		0.0765

Well PB13-C. Elevation 55.18 m AHD.



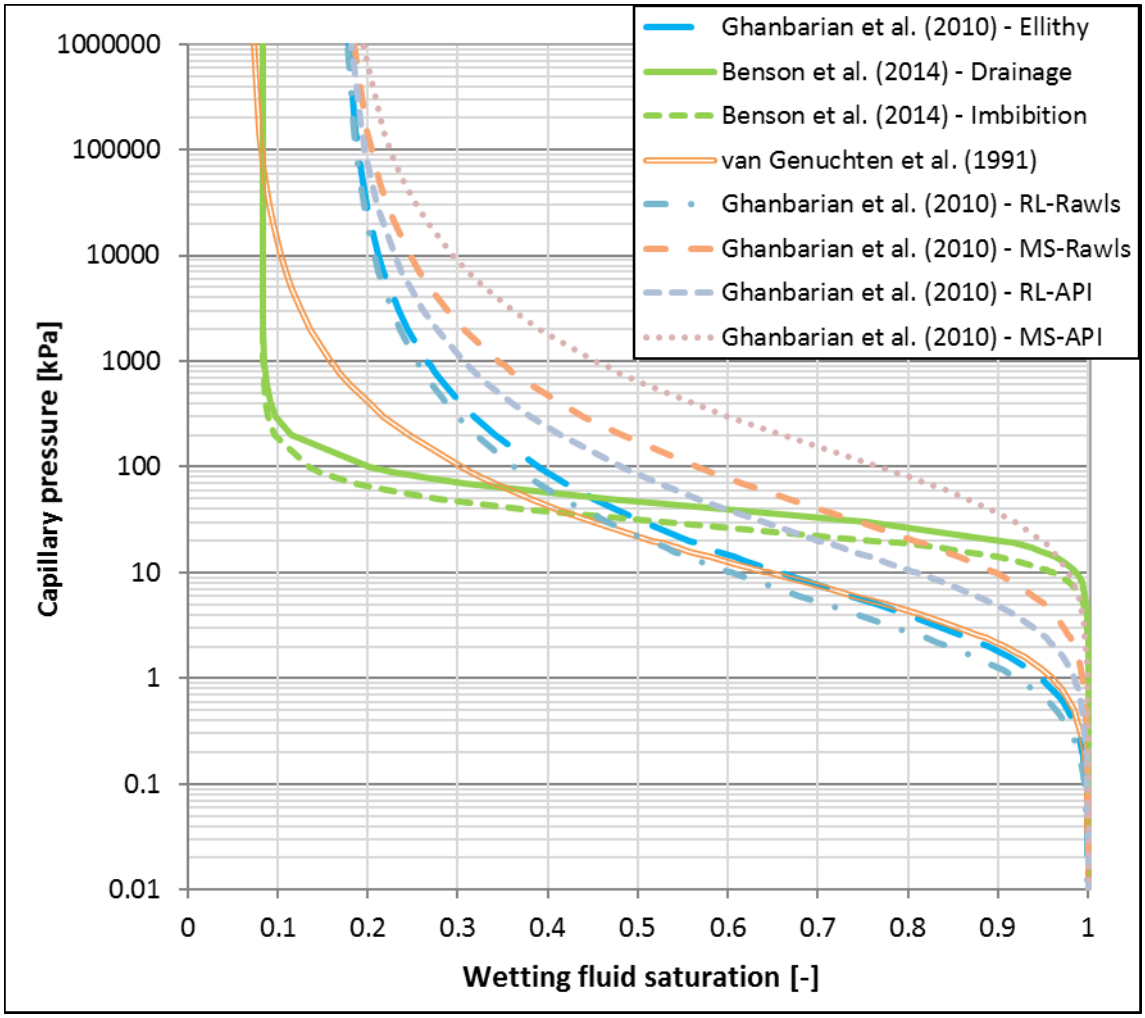
Well PB13-C. Elevation 55.18 m AHD.	Ghanbarian et al. (2010)					Benson et al. (2014)		van Genuchten et al. (1991)
	Ellithy (2017)	Lenhard et al. (1989)		Morel-Seytoux et al. (1996)		Drainage	Imbibition	
		Rawls	API	Rawls	API			
vG-α [m^{-1}]	9.9439	8.4365	2.2358	1.9071	0.5054	1.3078	1.9250	4.3000
vG-N [-]	1.5174					4.0895	3.6448	2.1853
S_{wr} [-]	0.1378					0.0903		0.0892

Well MP44-C. Elevation 55.16 m AHD.



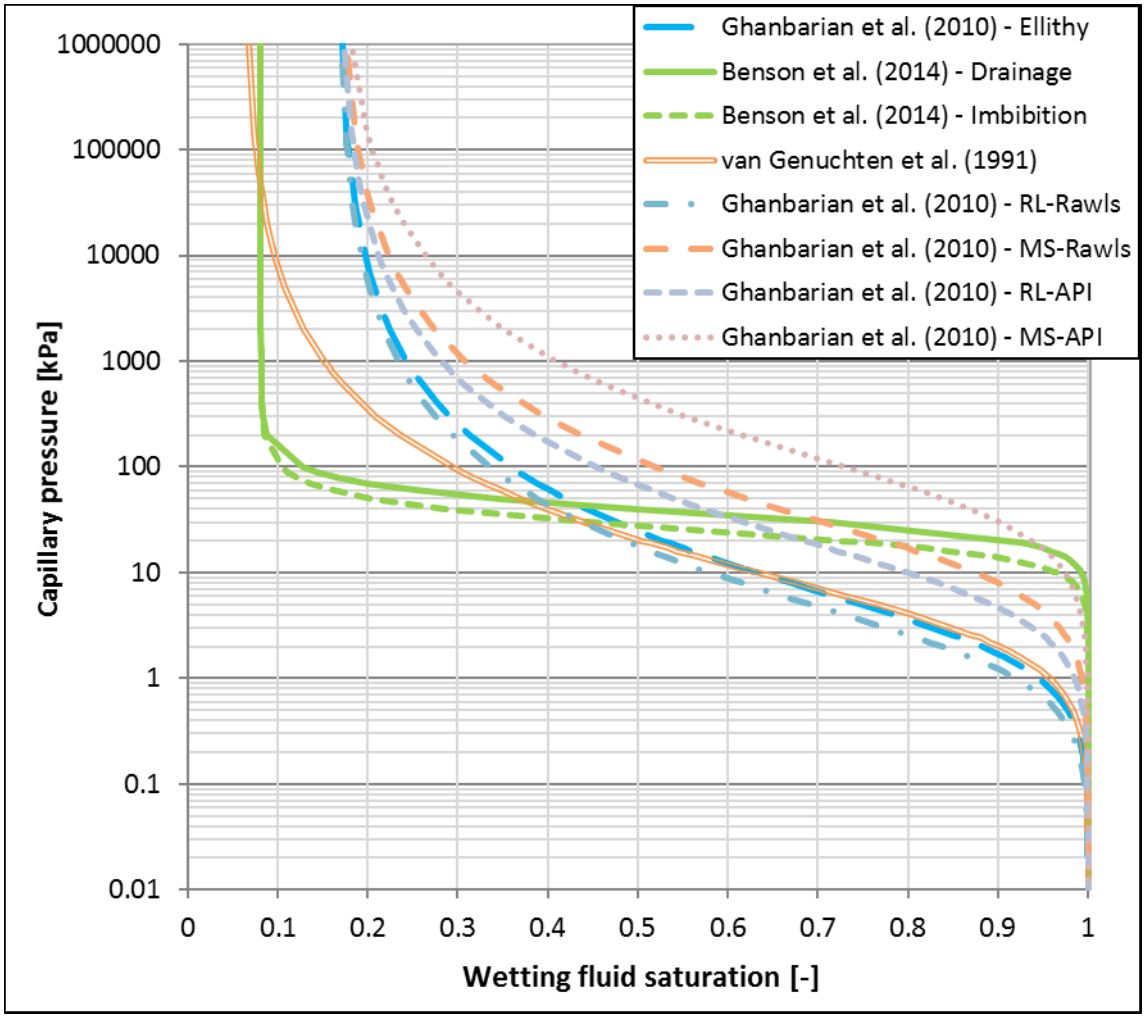
Well MP44-C. Elevation 55.16 m AHD.	Ghanbarian et al. (2010)					Benson et al. (2014)		van Genuchten et al. (1991)
	Ellithy (2017)	Lenhard et al. (1989)		Morel-Seytoux et al. (1996)		Drainage	Imbibition	
		Rawls	API	Rawls	API			
vG-α [m^{-1}]	14.4911	9.9240	1.8955	2.5616	0.4893	3.2708	4.8143	3.7500
vG-N [-]	1.5713					4.4218	3.8345	3.2059
S_{wr} [-]	0.1086					0.0965		0.1127

Well ML15. Elevation 55.147 m AHD.



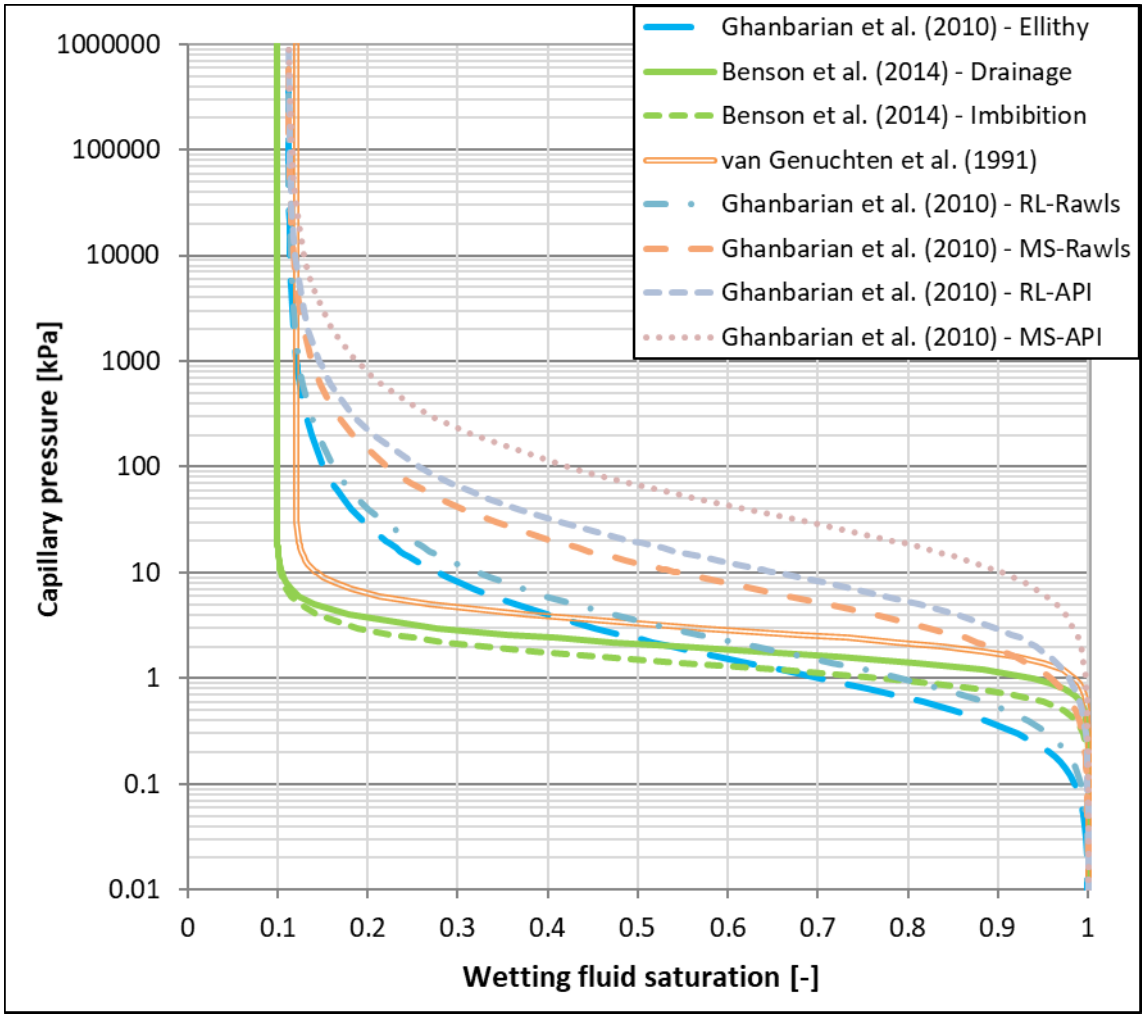
Well ML15. Elevation 55.147 m AHD.	Ghanbarian et al. (2010)					Benson et al. (2014)		van Genuchten et al. (1991)
	Ellithy (2017)	Lenhard et al. (1989)		Morel-Seytoux et al. (1996)		Drainage	Imbibition	
		Rawls	API	Rawls	API			
vG-α [m^{-1}]	3.8310	5.5075	1.4354	0.7190	0.1874	0.2746	0.4043	2.6900
vG-N [-]	1.3632					2.9579	3.0401	1.4145
S_{wr} [-]	0.1713					0.0839		0.0684

Well PB13-C. Elevation 55.03 m AHD.



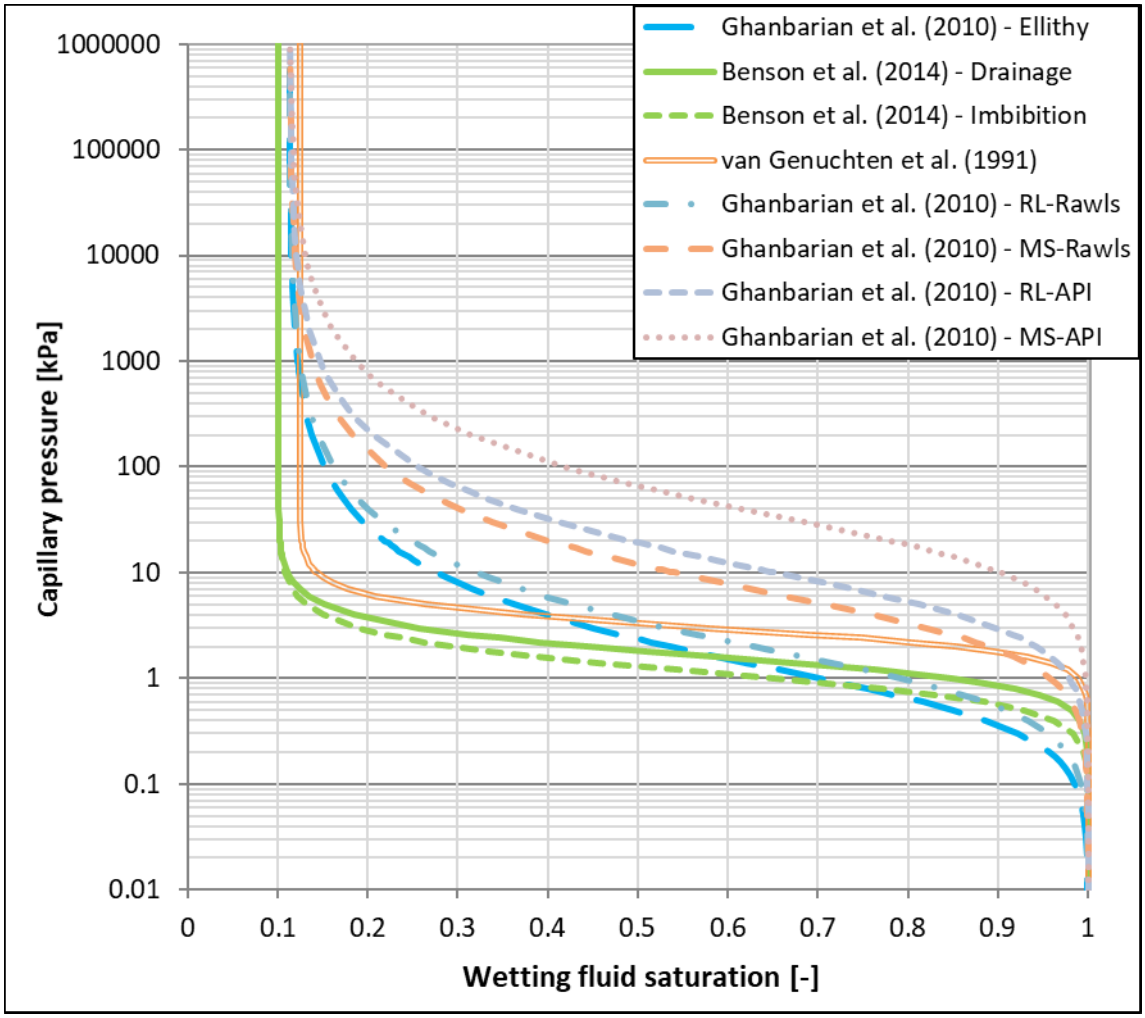
Well PB13-C. Elevation 55.03 m AHD.	Ghanbarian et al. (2010)					Benson et al. (2014)		van Genuchten et al. (1991)
	Ellithy (2017)	Lenhard et al. (1989)		Morel-Seytoux et al. (1996)		Drainage	Imbibition	
		Rawls	API	Rawls	API			
vG-α [m^{-1}]	3.8310	5.3444	1.3929	0.8155	0.2125	0.2928	0.4309	2.8200
vG-N [-]	1.3988					3.7204	3.4888	1.4157
S_{wr} [-]	0.1664					0.0815		0.0628

Well PB27-B. Elevation 54.71 m AHD.



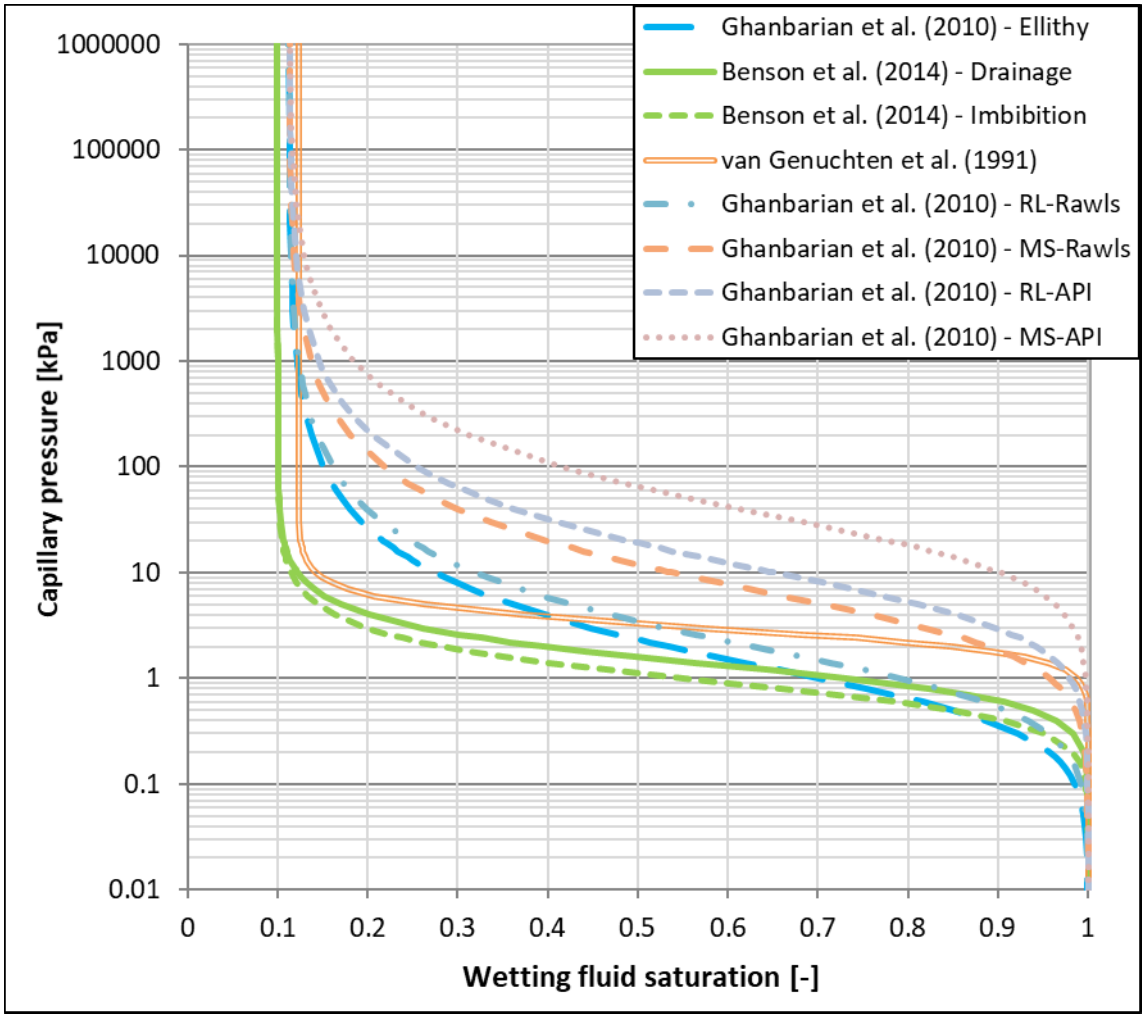
Well PB27-B. Elevation 54.71 m AHD.	Ghanbarian et al. (2010)					Benson et al. (2014)		van Genuchten et al. (1991)
	Ellithy (2017)	Lenhard et al. (1989)		Morel-Seytoux et al. (1996)		Drainage	Imbibition	
		Rawls	API	Rawls	API			
vG-α [m^{-1}]	14.4911	9.8096	1.7840	2.8123	0.5115	5.4662	8.0459	3.6200
vG-N [-]	1.6212					3.9716	3.5199	3.7889
S_{wr} [-]	0.1114					0.0990		0.1203

Well PB39-C. Elevation 54.601 m AHD.



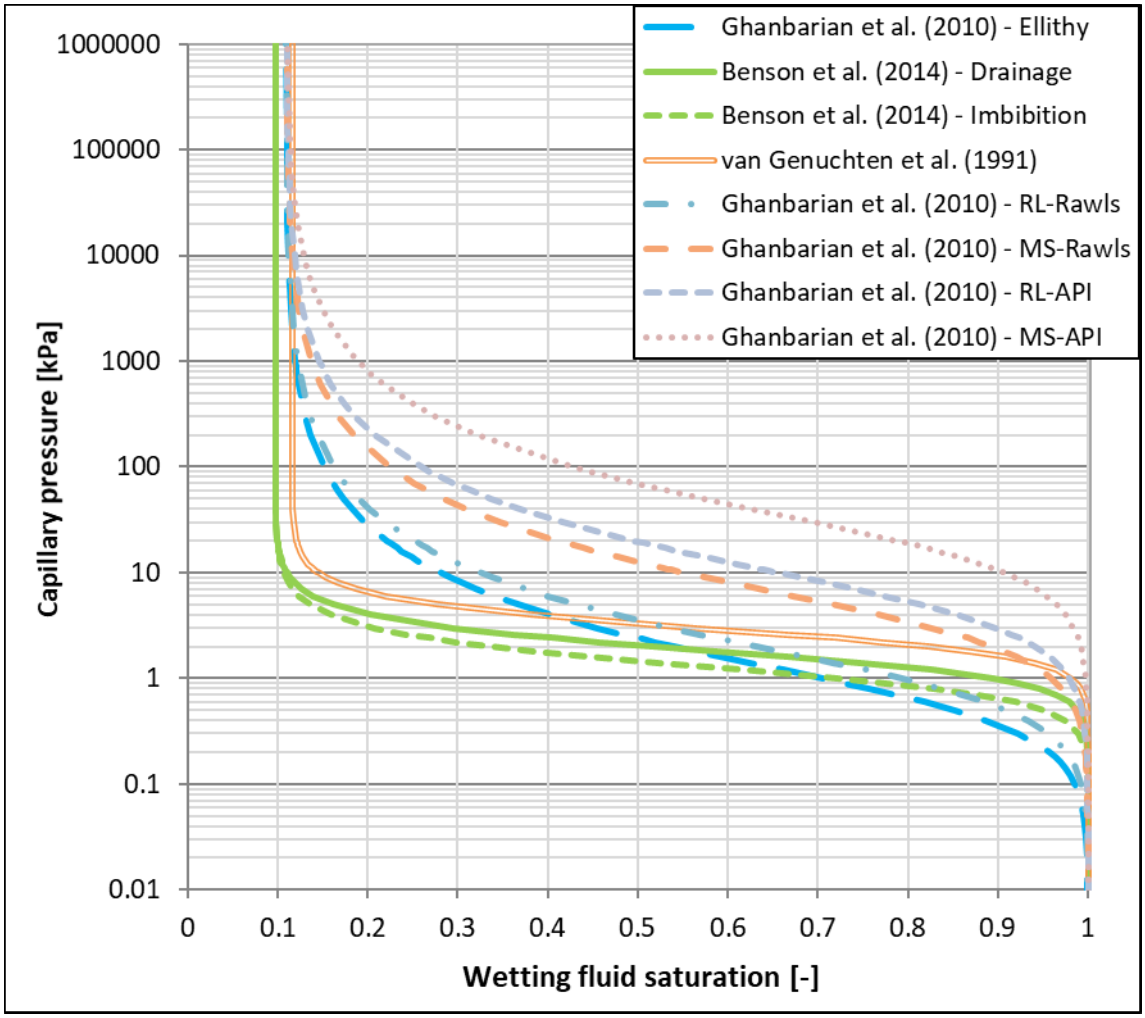
Well PB39-C. Elevation 54.601 m AHD.	Ghanbarian et al. (2010)					Benson et al. (2014)		van Genuchten et al. (1991)
	Ellithy (2017)	Lenhard et al. (1989)		Morel-Seytoux et al. (1996)		Drainage	Imbibition	
		Rawls	API	Rawls	API			
vG-α [m^{-1}]	14.4911	9.7981	1.7819	2.8422	0.5169	6.8102	10.0241	3.5500
vG-N [-]	1.6273					3.2981	3.0409	3.9820
S_{wr} [-]	0.1133					0.1007		0.1246

Well ML15. Elevation 54.207 m AHD.



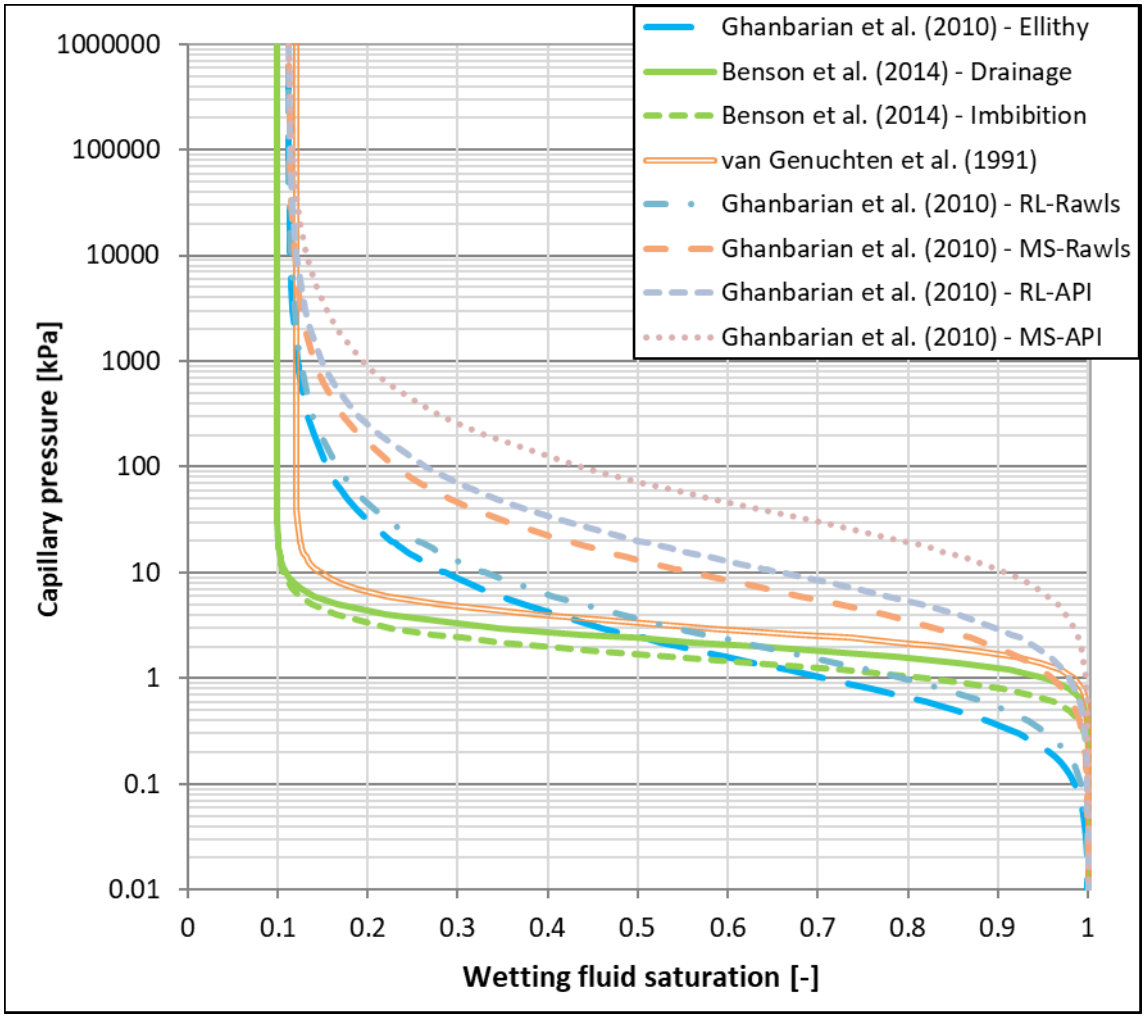
Well ML15. Elevation 54.207 m AHD.	Ghanbarian et al. (2010)					Benson et al. (2014)		van Genuchten et al. (1991)
	Ellithy (2017)	Lenhard et al. (1989)		Morel-Seytoux et al. (1996)		Drainage	Imbibition	
		Rawls	API	Rawls	API			
vG-α [m^{-1}]	14.4911	9.7936	1.7811	2.8541	0.5191	8.8248	12.9895	3.5800
vG-N [-]	1.6297					2.6875	2.5861	3.9401
S_{wr} [-]	0.1125					0.1000		0.1230

Well PB27-B. Elevation 54.16 m AHD.



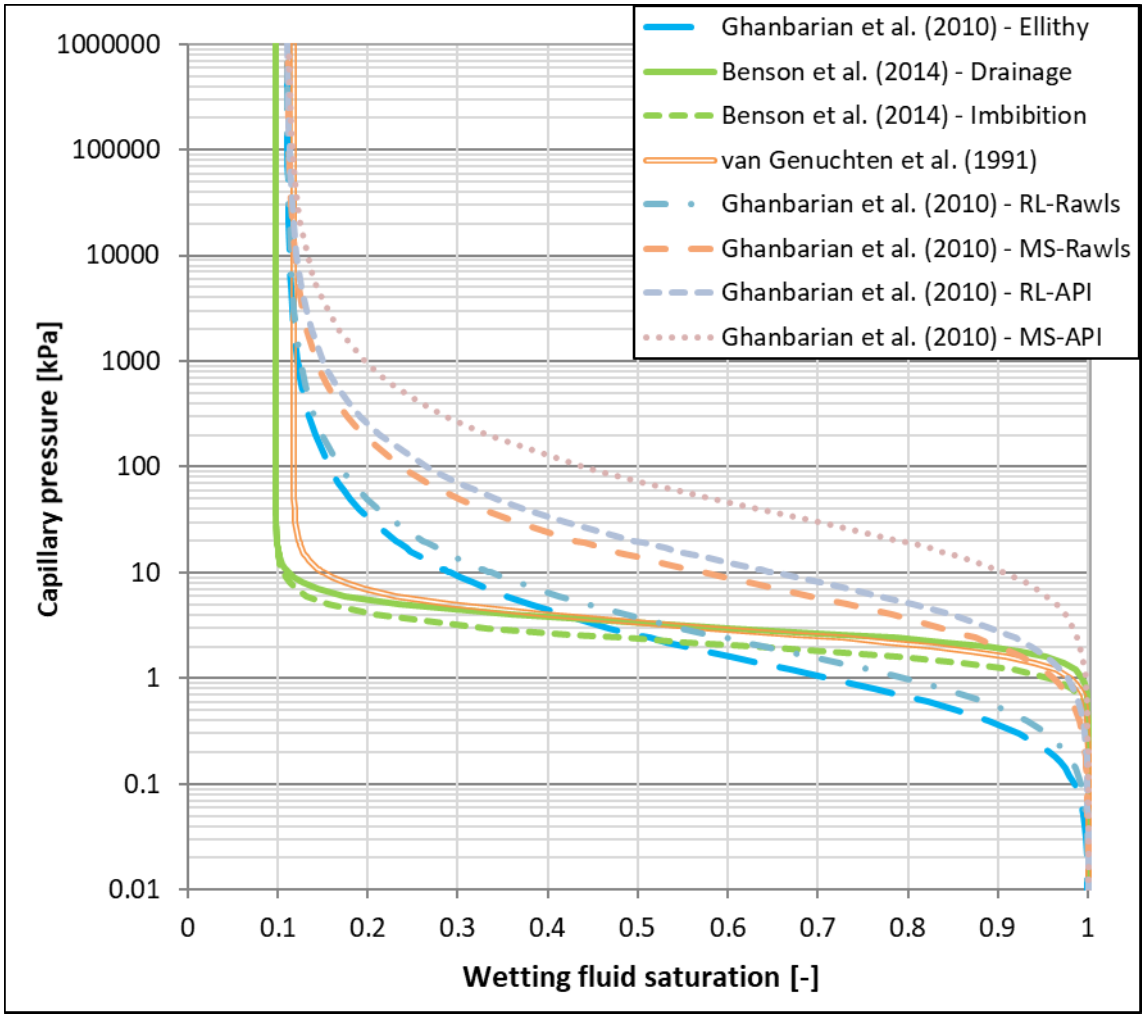
Well PB27-B. Elevation 54.16 m AHD.	Ghanbarian et al. (2010)					Benson et al. (2014)		van Genuchten et al. (1991)
	Ellithy (2017)	Lenhard et al. (1989)		Morel-Seytoux et al. (1996)		Drainage	Imbibition	
		Rawls	API	Rawls	API			
vG-α [m^{-1}]	14.4911	9.8265	1.7871	2.7704	0.5038	5.9916	8.8192	3.6900
vG-N [-]	1.6128					3.3579	3.0865	3.5810
S_{wr} [-]	0.1097					0.0975		0.1160

Well MP44-C. Elevation 53.96 m AHD.



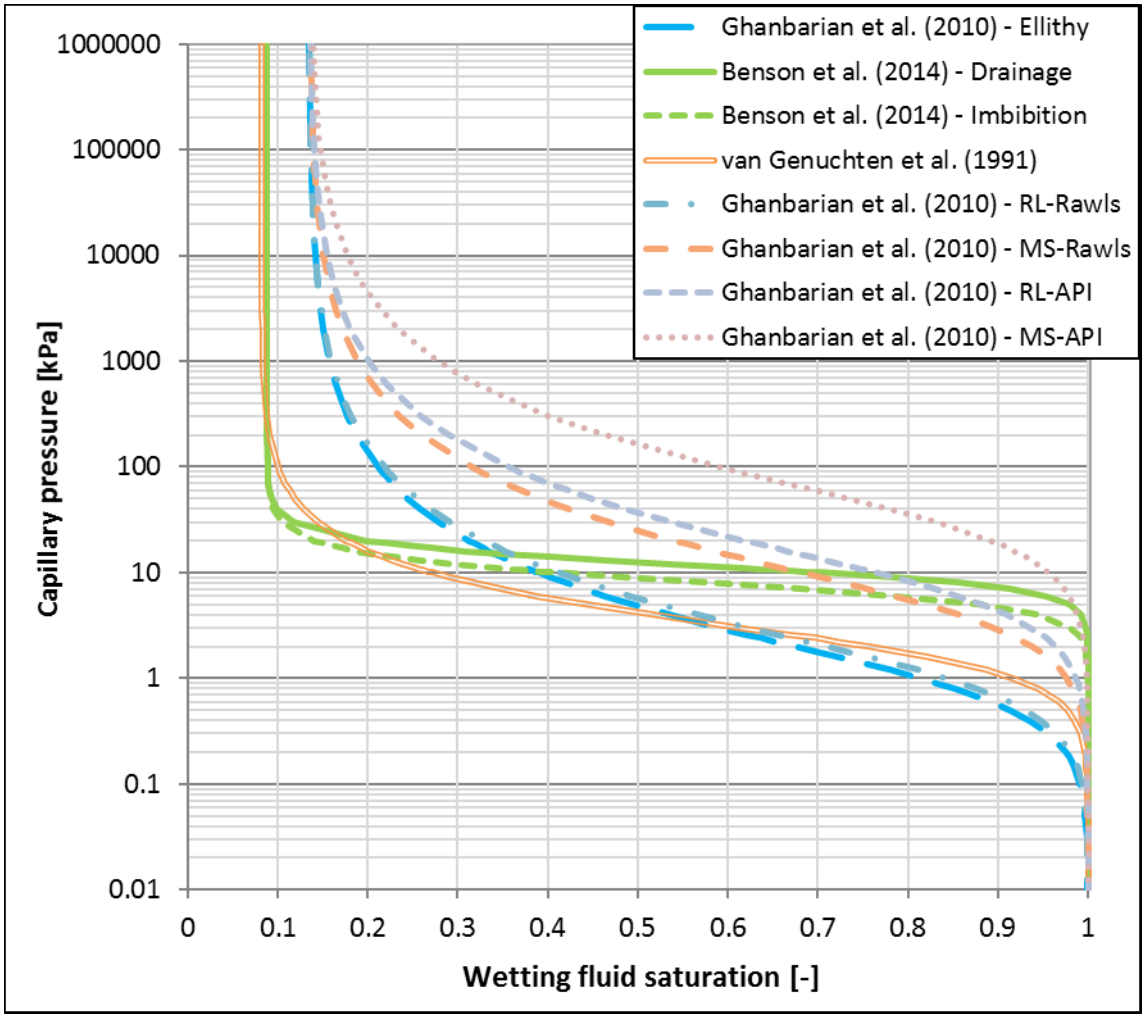
Well MP44-C. Elevation 53.96 m AHD.	Ghanbarian et al. (2010)					Benson et al. (2014)		van Genuchten et al. (1991)
	Ellithy (2017)	Lenhard et al. (1989)		Morel-Seytoux et al. (1996)		Drainage	Imbibition	
		Rawls	API	Rawls	API			
vG-α [m^{-1}]	14.4911	9.8455	1.7905	2.7256	0.4957	4.9376	7.2678	3.6100
vG-N [-]	1.6038					3.7842	3.3916	3.6866
S_{wr} [-]	0.1115					0.0991		0.1207

Well MP50-A. Elevation 53.886 m AHD.



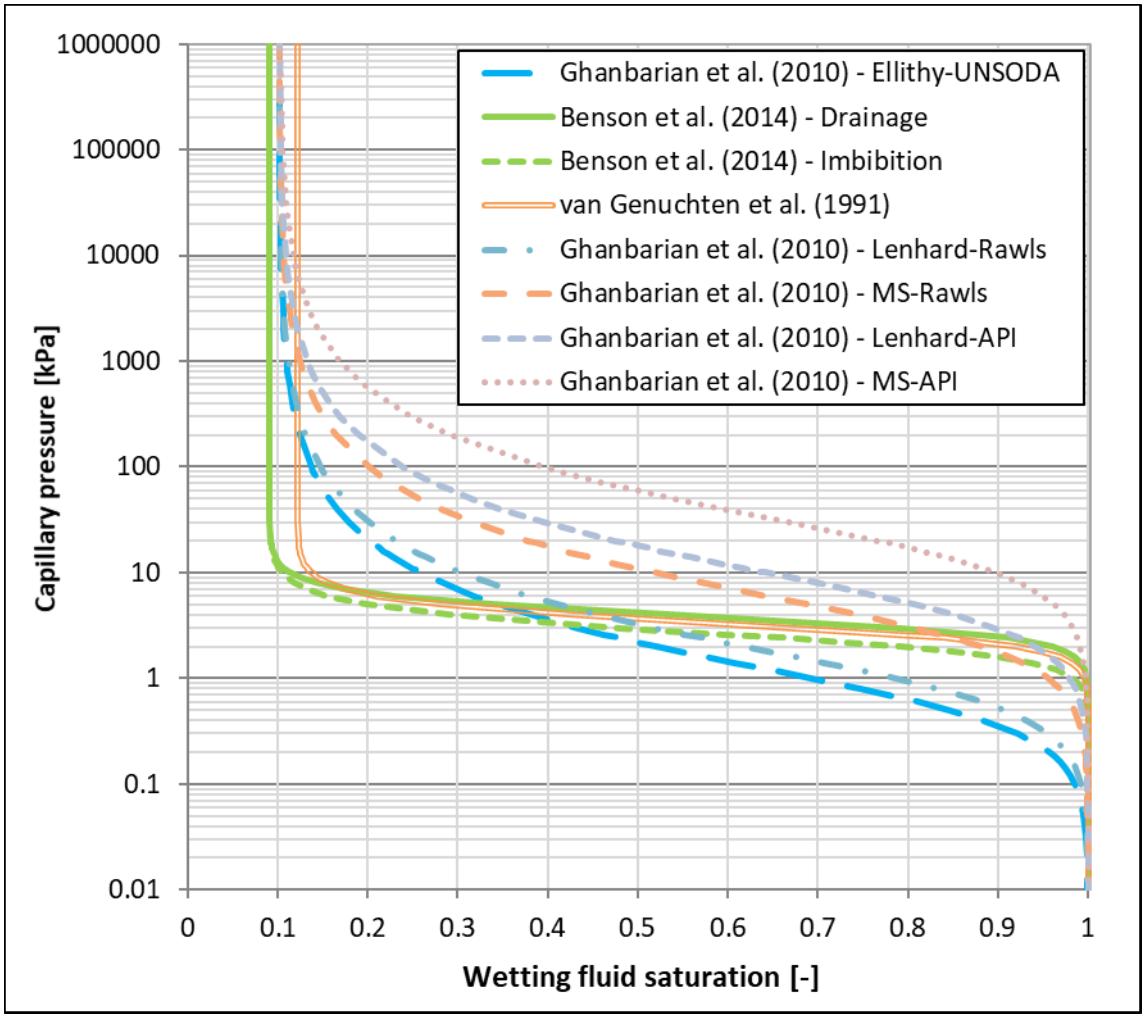
Well MP50-A. Elevation 53.886 m AHD.	Ghanbarian et al. (2010)					Benson et al. (2014)		van Genuchten et al. (1991)
	Ellithy (2017)	Lenhard et al. (1989)		Morel-Seytoux et al. (1996)		Drainage	Imbibition	
		Rawls	API	Rawls	API			
vG-α [m^{-1}]	14.4911	9.8789	1.8869	2.6518	0.5065	3.3509	4.9322	3.6500
vG-N [-]	1.5891					4.3908	3.9425	3.4968
S_{wr} [-]	0.1104					0.0981		0.1178

Well PB27-B. Elevation 53.16 m AHD.



Well PB27-B. Elevation 53.16 m AHD.	Ghanbarian et al. (2010)					Benson et al. (2014)		van Genuchten et al. (1991)
	Ellithy (2017)	Lenhard et al. (1989)		Morel-Seytoux et al. (1996)		Drainage	Imbibition	
		Rawls	API	Rawls	API			
vG-α [m^{-1}]	9.9439	8.4164	1.3002	1.9350	0.2989	0.8936	1.3153	4.4900
vG-N [-]	1.5237					4.4181	3.8681	2.0231
S_{wr} [-]	0.1346					0.0883		0.0821

Well 040610/1-T4. Elevation 1.025 m AHD.



Well 040610/1-T4. Elevation 1.025 m AHD.	Ghanbarian et al. (2010)					Benson et al. (2014)		van Genuchten et al. (1991)
	Ellithy (2017)	Lenhard et al. (1989)		Morel-Seytoux et al. (1996)		Drainage	Imbibition	
		Rawls	API	Rawls	API			
vG-α [m^{-1}]	14.4911	9.7638	1.7759	2.9380	0.5344	2.6660	3.9242	3.1100
vG-N [-]	1.6468					4.6567	3.9939	4.4873
S_{wr} [-]	0.1019					0.0906		0.1216

Well 040610/1-T4. Elevation 0.975 m AHD.

Well 040610/1-T4. Elevation 0.975 m AHD.	Ghanbarian et al. (2010)					Benson et al. (2014)		van Genuchten et al. (1991)
	Ellithy (2017)	Lenhard et al. (1989)		Morel-Seytoux et al. (1996)		Drainage	Imbibition	
		Rawls	API	Rawls	API			
vG-α [m^{-1}]	14.4911	9.7606	1.7753	2.9476	0.5361	5.2496	7.7270	3.2800
vG-N [-]	1.6488					3.8160	3.4125	4.3200
S_{wr} [-]	0.0932					0.0828		0.1137

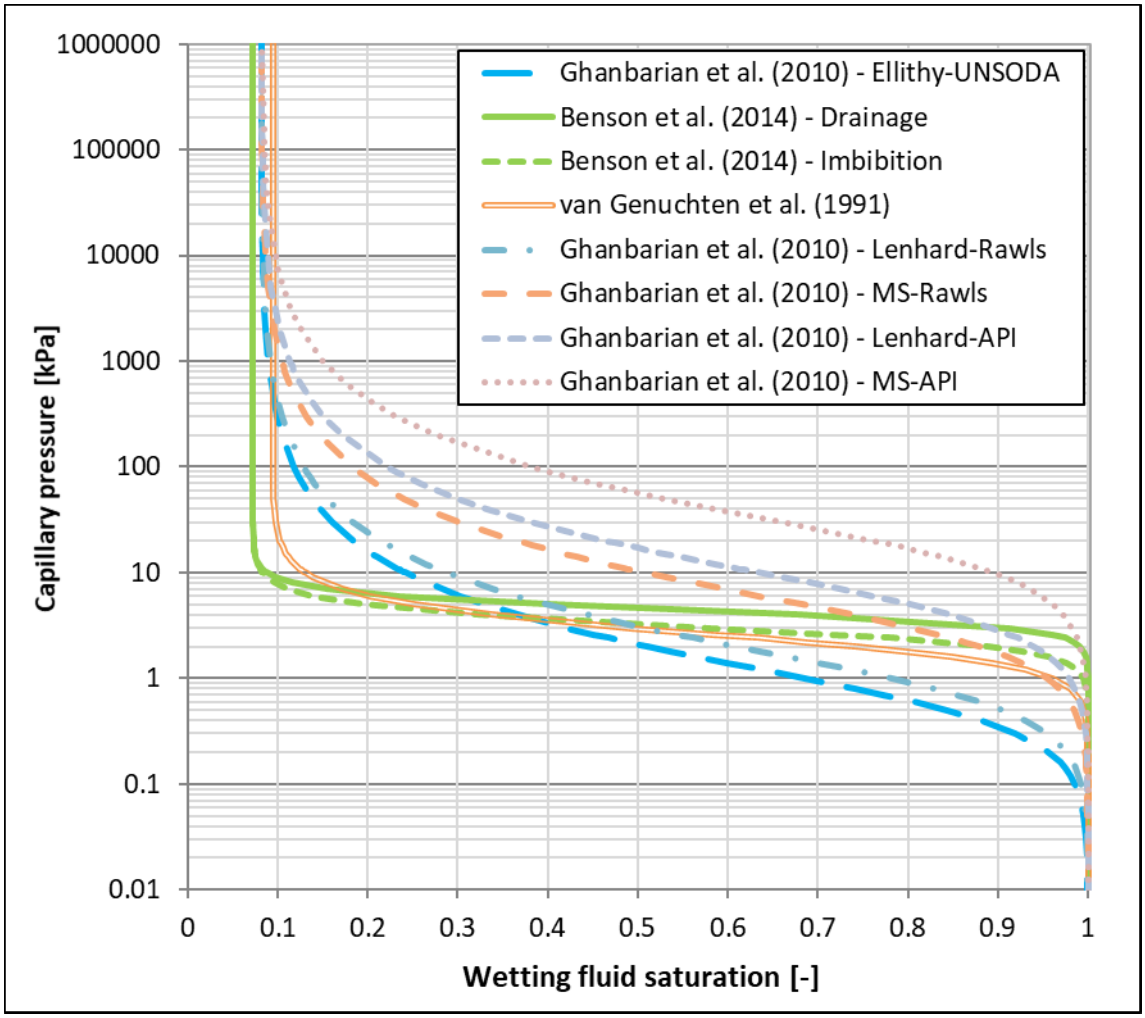
Well 040610/1-T4. Elevation 0.925 m AHD.

Well 040610/1-T4. Elevation 0.925 m AHD.	Ghanbarian et al. (2010)					Benson et al. (2014)		van Genuchten et al. (1991)
	Ellithy (2017)	Lenhard et al. (1989)		Morel-Seytoux et al. (1996)		Drainage	Imbibition	
		Rawls	API	Rawls	API			
vG-α [m^{-1}]	14.4911	9.7612	1.7754	2.9456	0.5358	3.9220	5.7729	3.8700
vG-N [-]	1.6484					4.0070	3.5502	3.5740
S_{wr} [-]	0.0846					0.0752		0.1005

Well 040610/1-T4. Elevation 0.875 m AHD.

Well 040610/1-T4. Elevation 0.875 m AHD.	Ghanbarian et al. (2010)					Benson et al. (2014)		van Genuchten et al. (1991)
	Ellithy (2017)	Lenhard et al. (1989)		Morel-Seytoux et al. (1996)		Drainage	Imbibition	
		Rawls	API	Rawls	API			
vG-α [m^{-1}]	14.4911	9.7621	1.7756	2.9431	0.5353	2.0685	3.0447	4.2600
vG-N [-]	1.6479					8.9425	5.9215	3.2017
S_{wr} [-]	0.0811					0.0721		0.0945

Well 040610/1-T4. Elevation 0.825 m AHD.



Well 040610/1-T4. Elevation 0.825 m AHD.	Ghanbarian et al. (2010)					Benson et al. (2014)		van Genuchten et al. (1991)
	Ellithy (2017)	Lenhard et al. (1989)		Morel-Seytoux et al. (1996)		Drainage	Imbibition	
		Rawls	API	Rawls	API			
vG-α [m^{-1}]	14.4911	9.7639	1.7759	2.9377	0.5343	2.2885	3.3685	4.2300
vG-N [-]	1.6468					5.8275	4.6135	3.2007
S_{wr} [-]	0.0817					0.0726		0.0946

Well 040610/1-T4. Elevation 0.775 m AHD.

Well 040610/1-T4. Elevation 0.775 m AHD.	Ghanbarian et al. (2010)					Benson et al. (2014)		van Genuchten et al. (1991)
	Ellithy (2017)	Lenhard et al. (1989)		Morel-Seytoux et al. (1996)		Drainage	Imbibition	
		Rawls	API	Rawls	API			
vG-α [m^{-1}]	14.4911	9.7655	1.7762	2.9330	0.5335	2.2947	3.3777	4.8300
vG-N [-]	1.6458					6.3669	4.8384	2.7700
S_{wr} [-]	0.0774					0.0688		0.0871

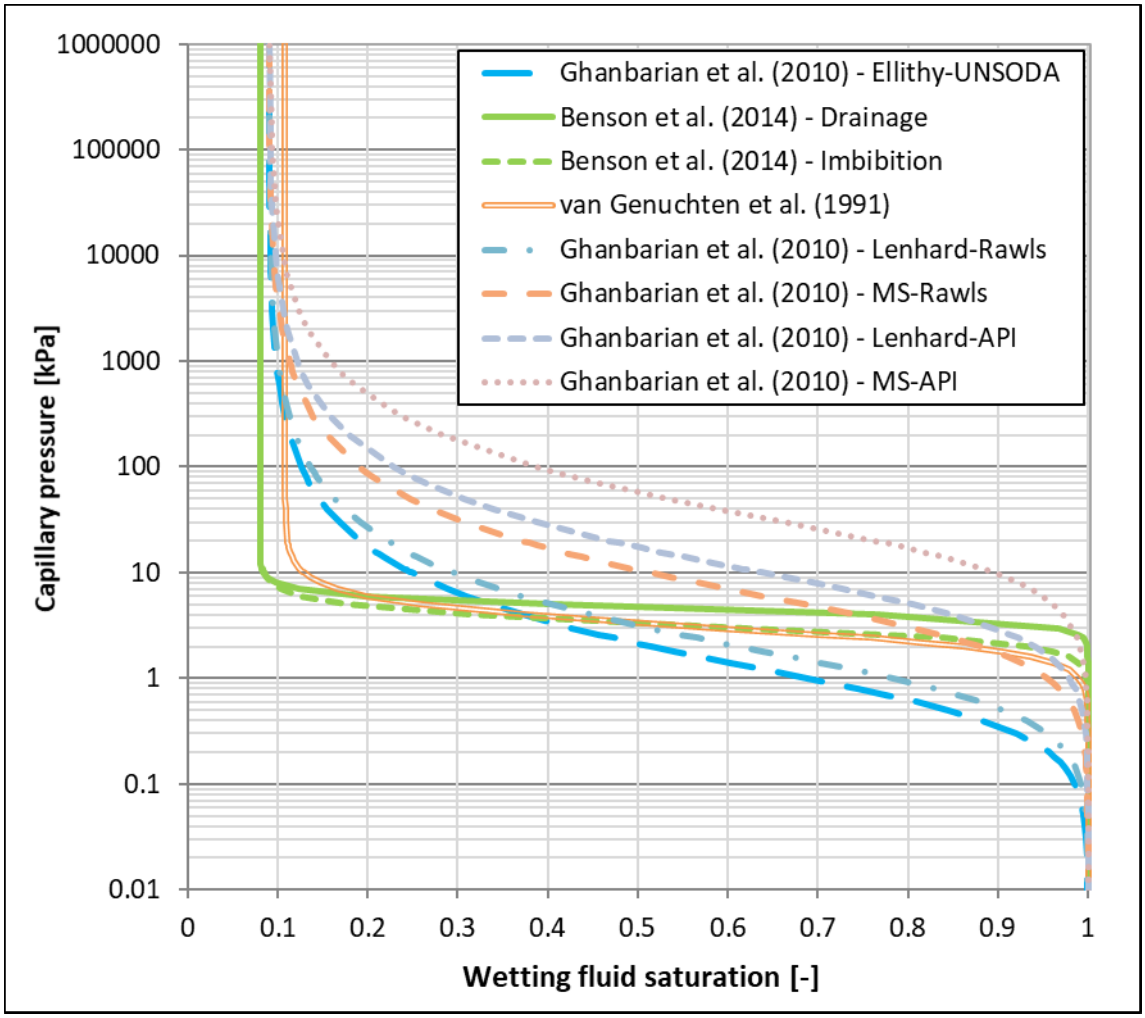
Well 040610/1-T4. Elevation 0.725 m AHD.

Well 040610/1-T4. Elevation 0.725 m AHD.	Ghanbarian et al. (2010)					Benson et al. (2014)		van Genuchten et al. (1991)
	Ellithy (2017)	Lenhard et al. (1989)		Morel-Seytoux et al. (1996)		Drainage	Imbibition	
		Rawls	API	Rawls	API			
vG-α [m^{-1}]	14.4911	9.7677	1.7766	2.9265	0.5323	2.1923	3.2269	3.5400
vG-N [-]	1.6445					6.7757	5.0146	3.8364
S_{wr} [-]	0.0903					0.0803		0.1066

Well 040610/1-T4. Elevation 0.675 m AHD.

Well 040610/1-T4. Elevation 0.675 m AHD.	Ghanbarian et al. (2010)					Benson et al. (2014)		van Genuchten et al. (1991)
	Ellithy (2017)	Lenhard et al. (1989)		Morel-Seytoux et al. (1996)		Drainage	Imbibition	
		Rawls	API	Rawls	API			
vG-α [m^{-1}]	14.4911	9.7657	1.7762	2.9324	0.5334	2.5735	3.7880	3.4700
vG-N [-]	1.6457					4.6384	3.9823	3.9675
S_{wr} [-]	0.0910					0.0809		0.1084

Well 040610/1-T4. Elevation 0.625 m AHD.



Well 040610/1-T4. Elevation 0.625 m AHD.	Ghanbarian et al. (2010)					Benson et al. (2014)		van Genuchten et al. (1991)
	Ellithy (2017)	Lenhard et al. (1989)		Morel-Seytoux et al. (1996)		Drainage	Imbibition	
		Rawls	API	Rawls	API			
vG-α [m^{-1}]	14.4911	9.7637	1.7759	2.9382	0.5344	2.1810	3.2102	3.4700
vG-N [-]	1.6469					7.8318	5.4550	3.9941
S_{wr} [-]	0.0903					0.0803		0.1084

Well 040610/1-T4. Elevation 0.575 m AHD.

Well 040610/1-T4. Elevation 0.575 m AHD.	Ghanbarian et al. (2010)					Benson et al. (2014)		van Genuchten et al. (1991)
	Ellithy (2017)	Lenhard et al. (1989)		Morel-Seytoux et al. (1996)		Drainage	Imbibition	
		Rawls	API	Rawls	API			
vG-α [m^{-1}]	14.4911	9.7632	1.7758	2.9398	0.5347	3.9890	5.8715	3.5500
vG-N [-]	1.6472					3.7725	3.3885	3.9081
S_{wr} [-]	0.0890					0.0791		0.1066

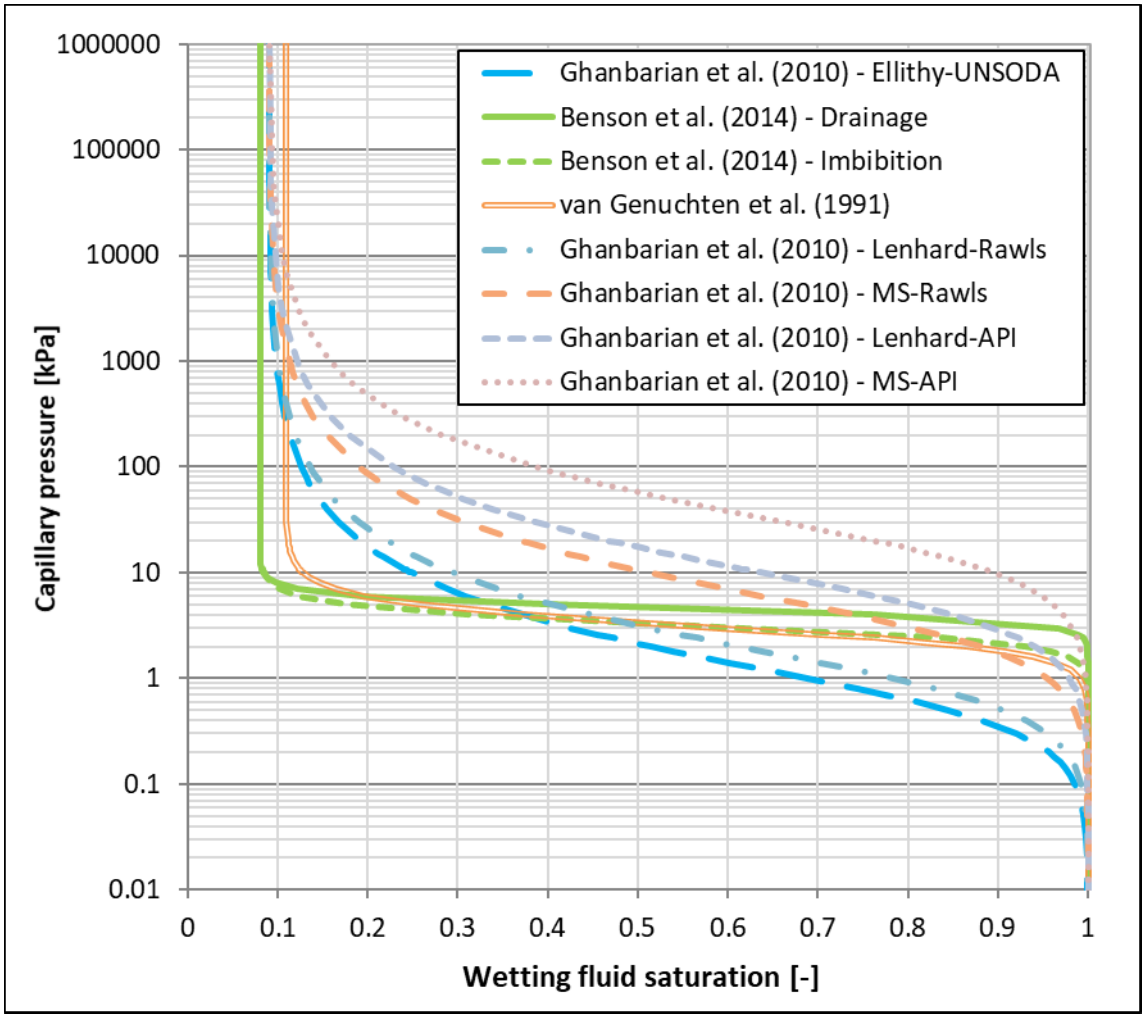
Well 040610/1-T4. Elevation 0.525 m AHD.

Well 040610/1-T4. Elevation 0.525 m AHD.	Ghanbarian et al. (2010)					Benson et al. (2014)		van Genuchten et al. (1991)
	Ellithy (2017)	Lenhard et al. (1989)		Morel-Seytoux et al. (1996)		Drainage	Imbibition	
		Rawls	API	Rawls	API			
vG-α [m^{-1}]	14.4911	9.7737	1.7777	2.9092	0.5291	1.9427	2.8596	3.9700
vG-N [-]	1.6409					6.0079	4.7093	3.2670
S_{wr} [-]	0.0858					0.0763		0.0972

Well 040610/1-T4. Elevation 0.475 m AHD.

Well 040610/1-T4. Elevation 0.475 m AHD.	Ghanbarian et al. (2010)					Benson et al. (2014)		van Genuchten et al. (1991)
	Ellithy (2017)	Lenhard et al. (1989)		Morel-Seytoux et al. (1996)		Drainage	Imbibition	
		Rawls	API	Rawls	API			
vG-α [m^{-1}]	14.4911	9.7624	1.7756	2.9420	0.5351	1.9842	2.9207	3.4900
vG-N [-]	1.6476					9.4560	6.1378	3.9928
S_{wr} [-]	0.0897					0.0797		0.1080

Well 040610/1-T4. Elevation 0.425 m AHD.



Well 040610/1-T4. Elevation 0.425 m AHD.	Ghanbarian et al. (2010)					Benson et al. (2014)		van Genuchten et al. (1991)
	Ellithy (2017)	Lenhard et al. (1989)		Morel-Seytoux et al. (1996)		Drainage	Imbibition	
		Rawls	API	Rawls	API			
vG-α [m^{-1}]	14.4911	9.7621	1.7756	2.9431	0.5353	2.1862	3.2179	3.4500
vG-N [-]	1.6479					7.8613	5.4670	4.0593
S_{wr} [-]	0.0903					0.0803		0.1092

Well 040610/1-T4. Elevation 0.375 m AHD.

Well 040610/1-T4. Elevation 0.375 m AHD.	Ghanbarian et al. (2010)					Benson et al. (2014)		van Genuchten et al. (1991)
	Ellithy (2017)	Lenhard et al. (1989)		Morel-Seytoux et al. (1996)		Drainage	Imbibition	
		Rawls	API	Rawls	API			
vG-α [m^{-1}]	14.4911	9.7638	1.7759	2.9379	0.5344	2.2889	3.3691	3.2700
vG-N [-]	1.6468					6.4921	4.8911	4.2672
S_{wr} [-]	0.0946					0.0841		0.1140

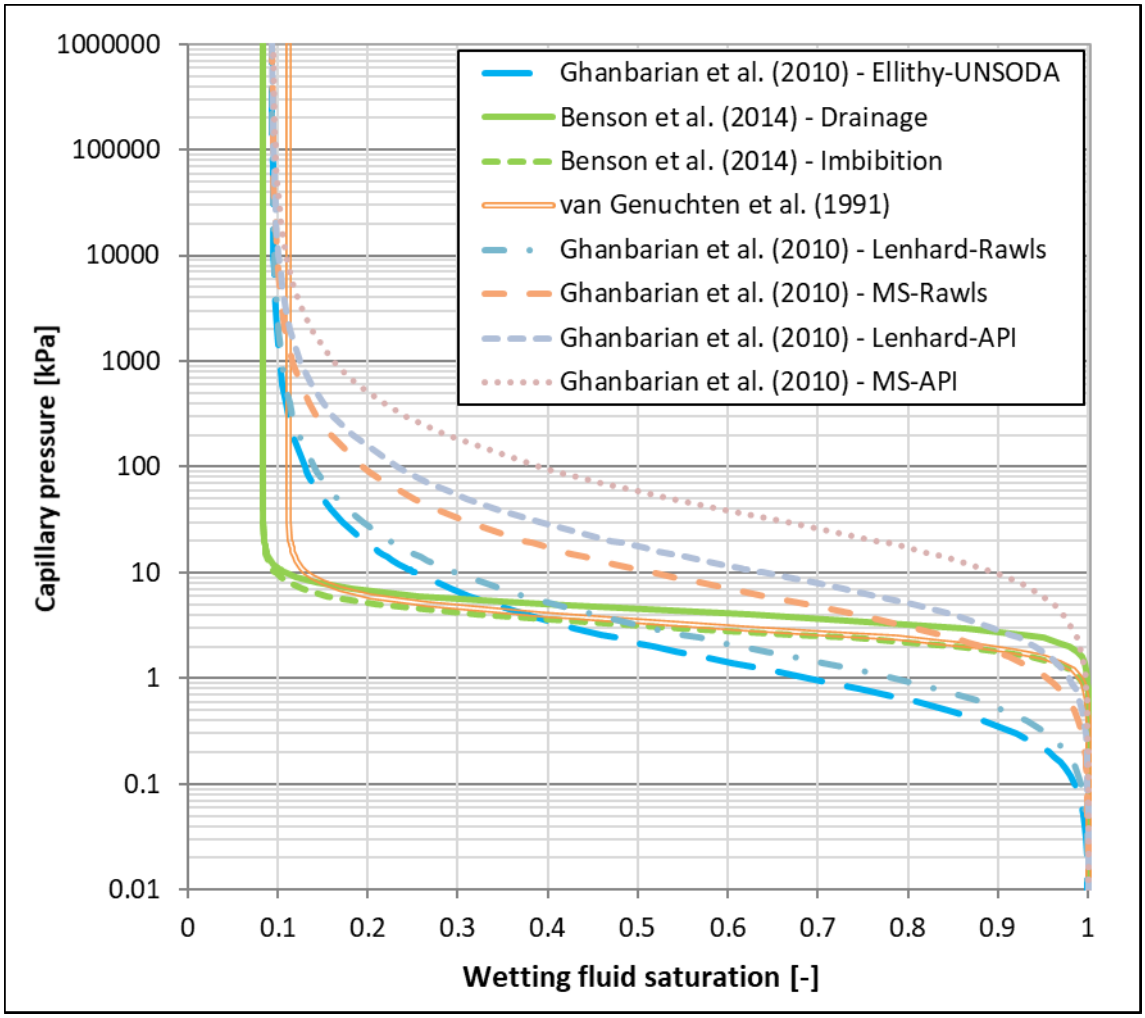
Well 040610/1-T4. Elevation 0.325 m AHD.

Well 040610/1-T4. Elevation 0.325 m AHD.	Ghanbarian et al. (2010)					Benson et al. (2014)		van Genuchten et al. (1991)
	Ellithy (2017)	Lenhard et al. (1989)		Morel-Seytoux et al. (1996)		Drainage	Imbibition	
		Rawls	API	Rawls	API			
vG-α [m^{-1}]	14.4911	9.7653	1.7762	2.9334	0.5335	2.3034	3.3904	3.7300
vG-N [-]	1.6459					5.8527	4.6232	3.6579
S_{wr} [-]	0.0870					0.0774		0.1027

Well 040610/1-T4. Elevation 0.275 m AHD.

Well 040610/1-T4. Elevation 0.275 m AHD.	Ghanbarian et al. (2010)					Benson et al. (2014)		van Genuchten et al. (1991)
	Ellithy (2017)	Lenhard et al. (1989)		Morel-Seytoux et al. (1996)		Drainage	Imbibition	
		Rawls	API	Rawls	API			
vG-α [m^{-1}]	14.4911	9.7671	1.7765	2.9283	0.5326	2.3533	3.4639	3.4500
vG-N [-]	1.6448					4.8445	4.1983	3.9580
S_{wr} [-]	0.0917					0.0815		0.1089

Well 040610/1-T4. Elevation 0.225 m AHD.



Well 040610/1-T4. Elevation 0.225 m AHD.	Ghanbarian et al. (2010)					Benson et al. (2014)		van Genuchten et al. (1991)
	Ellithy (2017)	Lenhard et al. (1989)		Morel-Seytoux et al. (1996)		Drainage	Imbibition	
		Rawls	API	Rawls	API			
vG-α [m^{-1}]	14.4911	9.7664	1.7764	2.9304	0.5330	2.4129	3.5517	3.3400
vG-N [-]	1.6453					4.9874	4.2543	4.1220
S_{wr} [-]	0.0939					0.0835		0.1121

Well 040610/1-T4. Elevation 0.175 m AHD.

Well 040610/1-T4. Elevation 0.175 m AHD.	Ghanbarian et al. (2010)					Benson et al. (2014)		van Genuchten et al. (1991)
	Ellithy (2017)	Lenhard et al. (1989)		Morel-Seytoux et al. (1996)		Drainage	Imbibition	
		Rawls	API	Rawls	API			
vG-α [m^{-1}]	14.4911	9.7666	1.7764	2.9297	0.5329	1.8851	2.7747	3.4800
vG-N [-]	1.6451					9.7145	6.2487	3.9288
S_{wr} [-]	0.0910					0.0809		0.1080

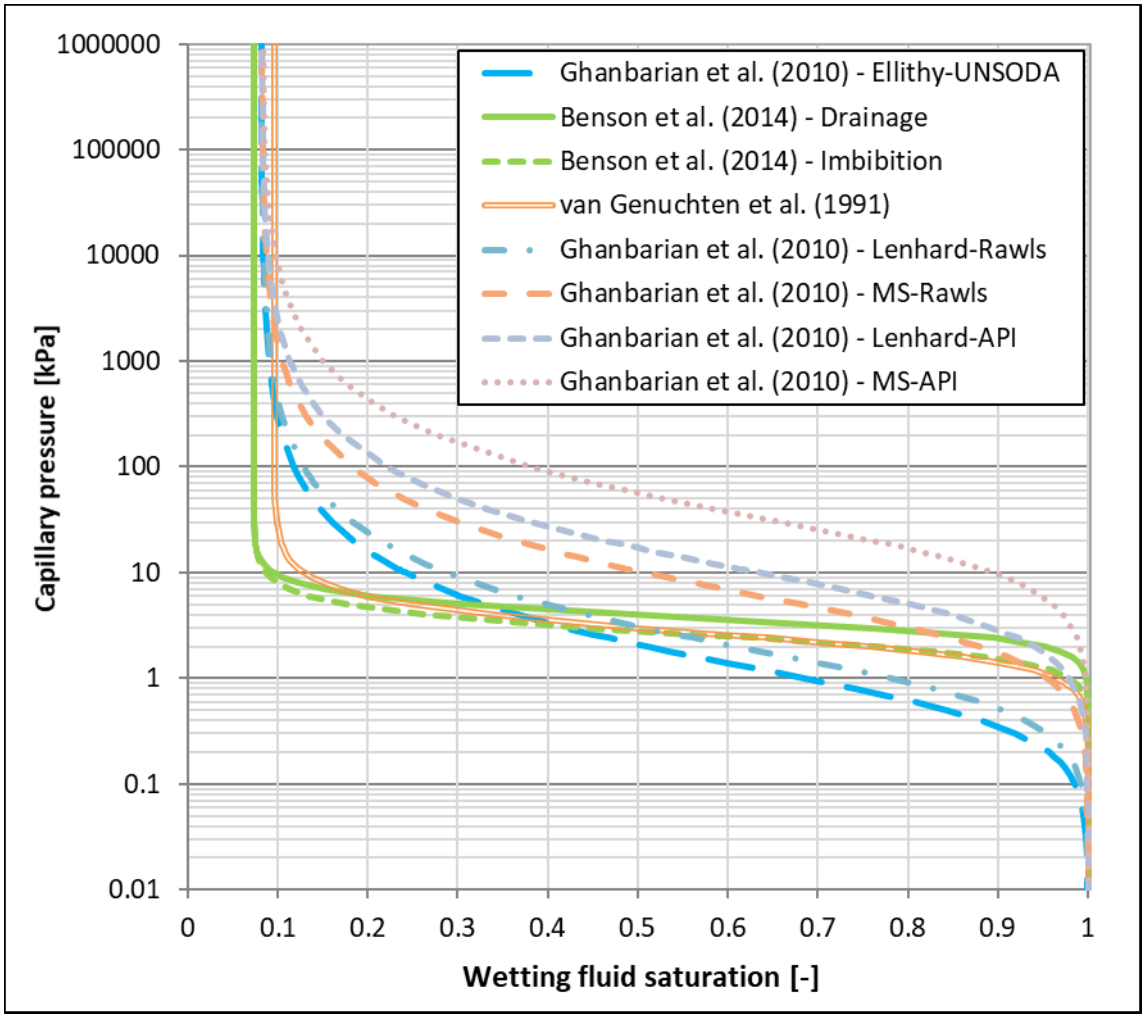
Well 040610/1-T4. Elevation 0.125 m AHD.

Well 040610/1-T4. Elevation 0.125 m AHD.	Ghanbarian et al. (2010)					Benson et al. (2014)		van Genuchten et al. (1991)
	Ellithy (2017)	Lenhard et al. (1989)		Morel-Seytoux et al. (1996)		Drainage	Imbibition	
		Rawls	API	Rawls	API			
vG-α [m^{-1}]	14.4911	9.7700	1.7770	2.9197	0.5311	1.7129	2.5212	3.3700
vG-N [-]	1.6431					8.7469	5.8560	4.0160
S_{wr} [-]	0.0946					0.0841		0.1113

Well 040610/1-T4. Elevation 0.075 m AHD.

Well 040610/1-T4. Elevation 0.075 m AHD.	Ghanbarian et al. (2010)					Benson et al. (2014)		van Genuchten et al. (1991)
	Ellithy (2017)	Lenhard et al. (1989)		Morel-Seytoux et al. (1996)		Drainage	Imbibition	
		Rawls	API	Rawls	API			
vG-α [m^{-1}]	14.4911	9.7703	1.7771	2.9190	0.5309	1.7124	2.5205	3.4000
vG-N [-]	1.6429					8.8289	5.8899	3.9654
S_{wr} [-]	0.0939					0.0835		0.1102

Well 040610/3-T4. Elevation 0.975 m AHD.



Well 040610/3-T4. Elevation 0.975 m AHD.	Ghanbarian et al. (2010)					Benson et al. (2014)		van Genuchten et al. (1991)
	Ellithy (2017)	Lenhard et al. (1989)		Morel-Seytoux et al. (1996)		Drainage	Imbibition	
		Rawls	API	Rawls	API			
vG-α [m^{-1}]	14.4911	9.7622	1.7756	2.9426	0.5352	2.7601	4.0627	4.1300
vG-N [-]	1.6478					4.5985	3.9549	3.3075
S_{wr} [-]	0.0822					0.0731		0.0963

Well 040610/3-T4. Elevation 0.925 m AHD.

Well 040610/3-T4. Elevation 0.925 m AHD.	Ghanbarian et al. (2010)					Benson et al. (2014)		van Genuchten et al. (1991)
	Ellithy (2017)	Lenhard et al. (1989)		Morel-Seytoux et al. (1996)		Drainage	Imbibition	
		Rawls	API	Rawls	API			
vG-α [m^{-1}]	14.4911	9.7630	1.7757	2.9403	0.5348	2.4604	3.6215	3.6900
vG-N [-]	1.6473					4.5793	4.0801	3.7443
S_{wr} [-]	0.0870					0.0774		0.1037

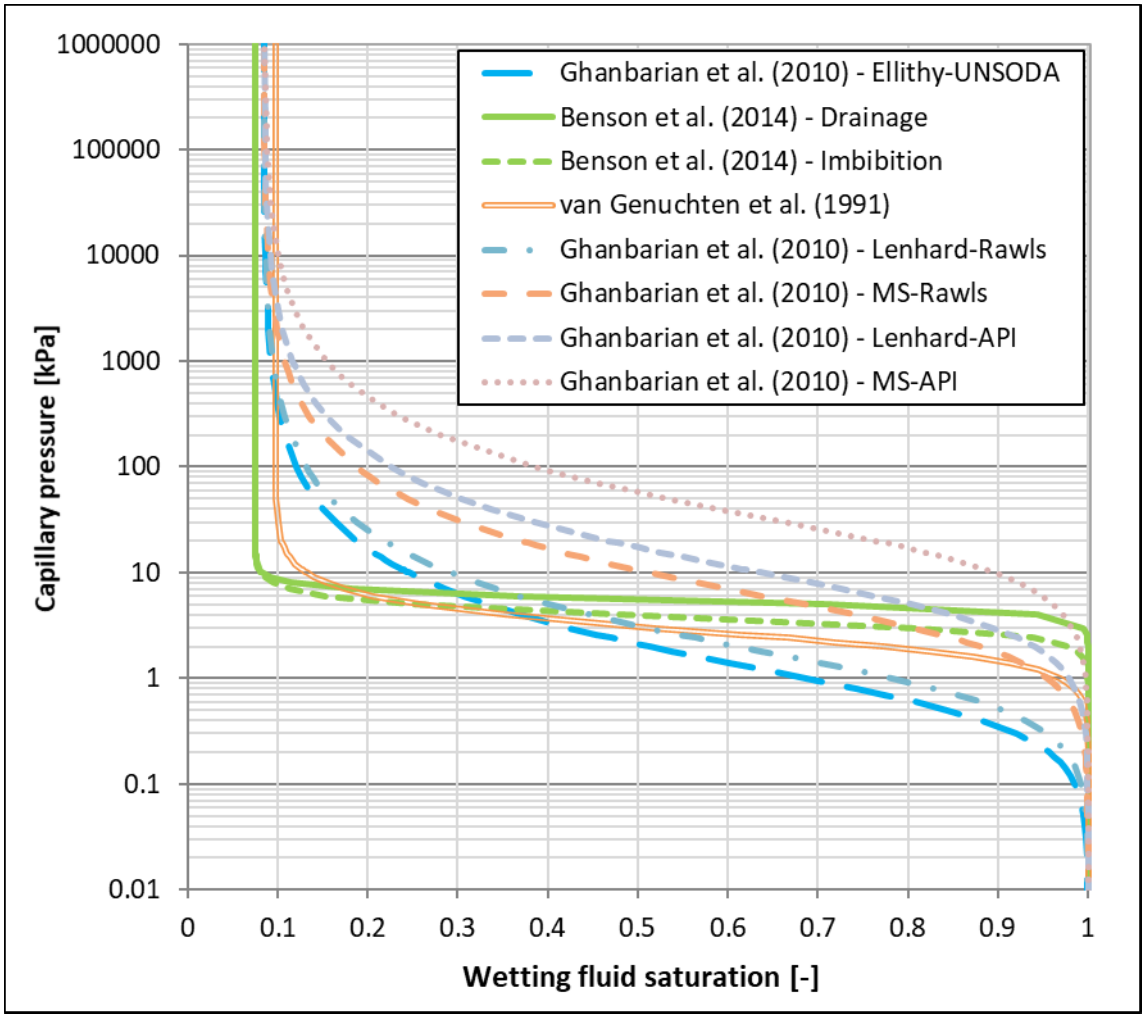
Well 040610/3-T4. Elevation 0.875 m AHD.

Well 040610/3-T4. Elevation 0.875 m AHD.	Ghanbarian et al. (2010)					Benson et al. (2014)		van Genuchten et al. (1991)
	Ellithy (2017)	Lenhard et al. (1989)		Morel-Seytoux et al. (1996)		Drainage	Imbibition	
		Rawls	API	Rawls	API			
vG-α [m^{-1}]	14.4911	9.7631	1.7758	2.9402	0.5348	2.1168	3.1158	4.0200
vG-N [-]	1.6473					6.8835	5.0636	3.3948
S_{wr} [-]	0.0834					0.0741		0.0978

Well 040610/3-T4. Elevation 0.825 m AHD.

Well 040610/3-T4. Elevation 0.825 m AHD.	Ghanbarian et al. (2010)					Benson et al. (2014)		van Genuchten et al. (1991)
	Ellithy (2017)	Lenhard et al. (1989)		Morel-Seytoux et al. (1996)		Drainage	Imbibition	
		Rawls	API	Rawls	API			
vG-α [m^{-1}]	14.4911	9.7681	1.7767	2.9254	0.5321	1.7885	2.6325	3.9300
vG-N [-]	1.6442					8.4624	5.7350	3.3968
S_{wr} [-]	0.0852					0.0757		0.0986

Well 040610/3-T4. Elevation 0.775 m AHD.



Well 040610/3-T4. Elevation 0.775 m AHD.	Ghanbarian et al. (2010)					Benson et al. (2014)		van Genuchten et al. (1991)
	Ellithy (2017)	Lenhard et al. (1989)		Morel-Seytoux et al. (1996)		Drainage	Imbibition	
		Rawls	API	Rawls	API			
vG-α [m^{-1}]	14.4911	9.7687	1.7768	2.9235	0.5317	1.8235	2.6841	4.0000
vG-N [-]	1.6439					8.8103	5.8773	3.3217
S_{wr} [-]	0.0846					0.0752		0.0974

Well 040610/3-T4. Elevation 0.725 m AHD.

Well 040610/3-T4. Elevation 0.725 m AHD.	Ghanbarian et al. (2010)					Benson et al. (2014)		van Genuchten et al. (1991)
	Ellithy (2017)	Lenhard et al. (1989)		Morel-Seytoux et al. (1996)		Drainage	Imbibition	
		Rawls	API	Rawls	API			
vG-α [m^{-1}]	14.4911	9.7682	1.7767	2.9252	0.5320	1.9958	2.9377	6.5100
vG-N [-]	1.6442					7.7474	5.4289	2.1099
S_{wr} [-]	0.0685					0.0609		0.0742

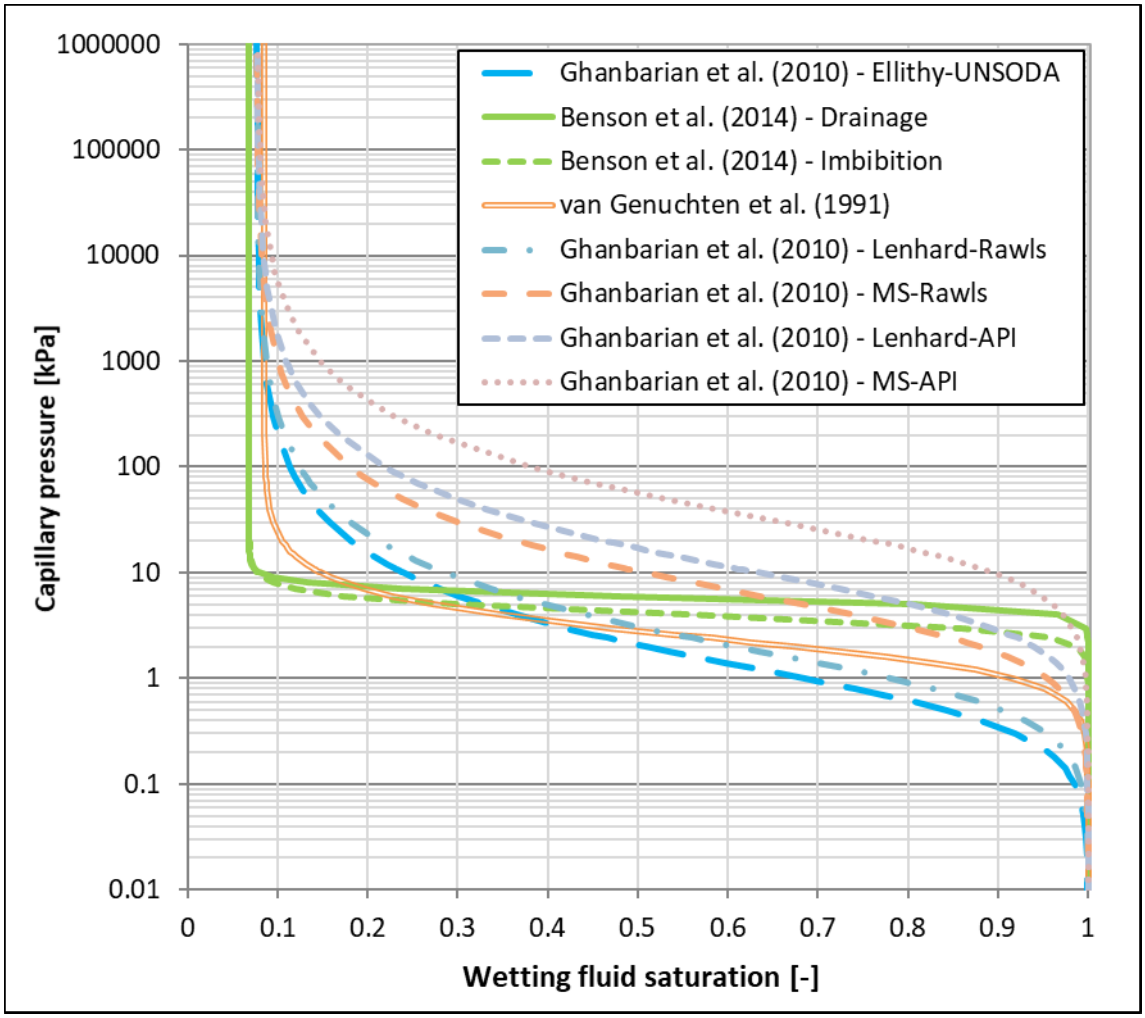
Well 040610/3-T4. Elevation 0.675 m AHD.

Well 040610/3-T4. Elevation 0.675 m AHD.	Ghanbarian et al. (2010)					Benson et al. (2014)		van Genuchten et al. (1991)
	Ellithy (2017)	Lenhard et al. (1989)		Morel-Seytoux et al. (1996)		Drainage	Imbibition	
		Rawls	API	Rawls	API			
vG-α [m^{-1}]	14.4911	9.7639	1.7759	2.9376	0.5343	2.1128	3.1099	5.2000
vG-N [-]	1.6467					7.3023	5.2381	2.6025
S_{wr} [-]	0.0750					0.0667		0.0838

Well 040610/3-T4. Elevation 0.625 m AHD.

Well 040610/3-T4. Elevation 0.625 m AHD.	Ghanbarian et al. (2010)					Benson et al. (2014)		van Genuchten et al. (1991)
	Ellithy (2017)	Lenhard et al. (1989)		Morel-Seytoux et al. (1996)		Drainage	Imbibition	
		Rawls	API	Rawls	API			
vG-α [m^{-1}]	14.4911	9.7679	1.7766	2.9259	0.5322	1.7459	2.5699	4.9400
vG-N [-]	1.6443					8.5849	5.7876	2.6751
S_{wr} [-]	0.0769					0.0684		0.0855

Well 040610/3-T4. Elevation 0.575 m AHD.



Well 040610/3-T4. Elevation 0.575 m AHD.	Ghanbarian et al. (2010)					Benson et al. (2014)		van Genuchten et al. (1991)
	Ellithy (2017)	Lenhard et al. (1989)		Morel-Seytoux et al. (1996)		Drainage	Imbibition	
		Rawls	API	Rawls	API			
vG-α [m^{-1}]	14.4911	9.7693	1.7769	2.9219	0.5315	1.7112	2.5187	4.9600
vG-N [-]	1.6435					8.8453	5.8967	2.6460
S_{wr} [-]	0.0769					0.0684		0.0850

Well 040610/3-T4. Elevation 0.525 m AHD.

Well 040610/3-T4. Elevation 0.525 m AHD.	Ghanbarian et al. (2010)					Benson et al. (2014)		van Genuchten et al. (1991)
	Ellithy (2017)	Lenhard et al. (1989)		Morel-Seytoux et al. (1996)		Drainage	Imbibition	
		Rawls	API	Rawls	API			
vG-α [m^{-1}]	14.4911	9.7752	1.7780	2.9048	0.5283	1.8107	2.6652	4.7500
vG-N [-]	1.6400					6.8029	5.0468	2.6742
S_{wr} [-]	0.0790					0.0702		0.0862

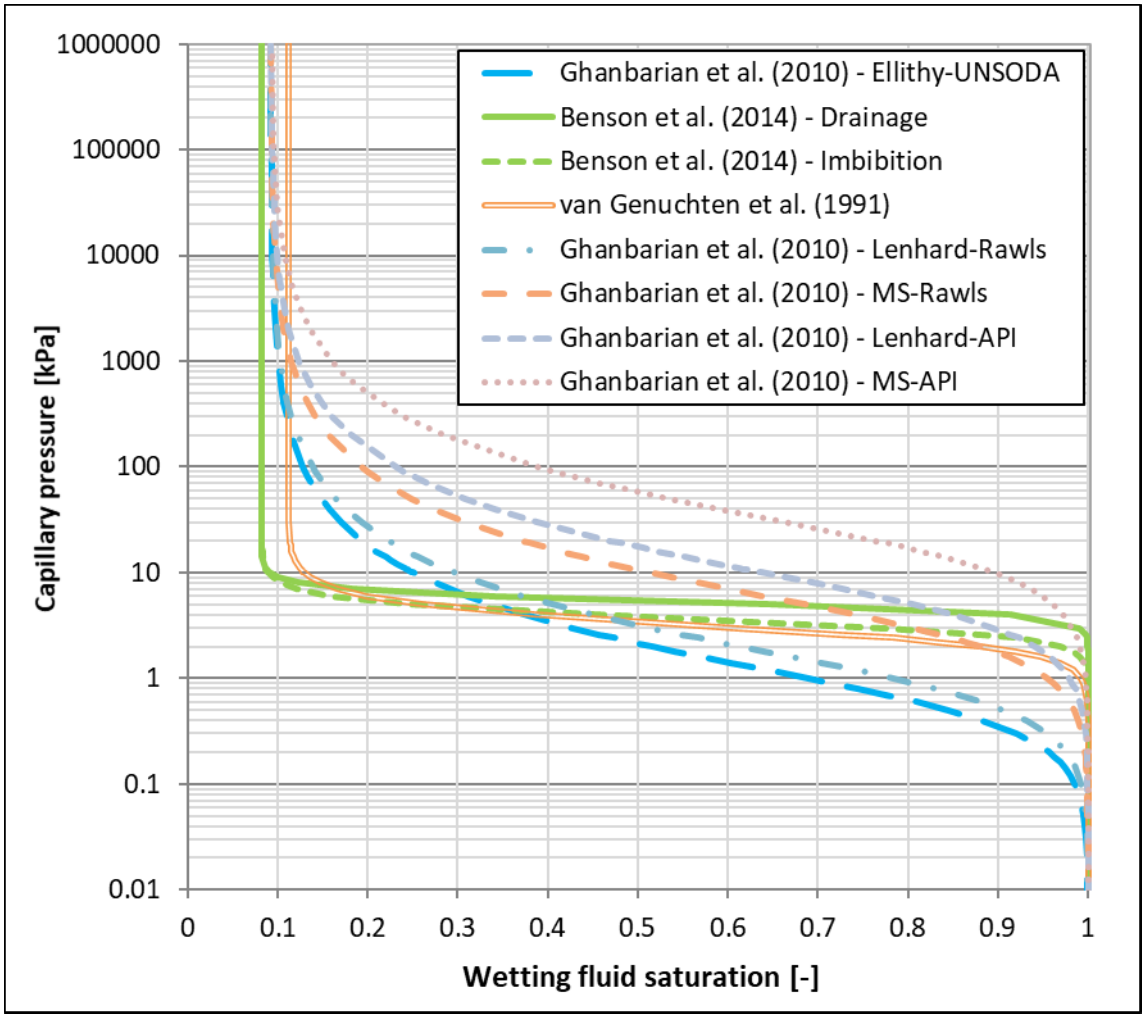
Well 040610/3-T4. Elevation 0.475 m AHD.

Well 040610/3-T4. Elevation 0.475 m AHD.	Ghanbarian et al. (2010)					Benson et al. (2014)		van Genuchten et al. (1991)
	Ellithy (2017)	Lenhard et al. (1989)		Morel-Seytoux et al. (1996)		Drainage	Imbibition	
		Rawls	API	Rawls	API			
vG-α [m^{-1}]	14.4911	9.7607	1.7753	2.9472	0.5360	2.1289	3.1336	4.2400
vG-N [-]	1.6487					7.6261	5.3719	3.2444
S_{wr} [-]	0.0811					0.0721		0.0950

Well 040610/3-T4. Elevation 0.425 m AHD.

Well 040610/3-T4. Elevation 0.425 m AHD.	Ghanbarian et al. (2010)					Benson et al. (2014)		van Genuchten et al. (1991)
	Ellithy (2017)	Lenhard et al. (1989)		Morel-Seytoux et al. (1996)		Drainage	Imbibition	
		Rawls	API	Rawls	API			
vG-α [m^{-1}]	14.4911	9.7612	1.7754	2.9457	0.5358	1.9742	2.9059	3.8700
vG-N [-]	1.6484					7.5762	5.3589	3.5759
S_{wr} [-]	0.0846					0.0752		0.1005

Well 040610/3-T4. Elevation 0.375 m AHD.



Well 040610/3-T4. Elevation 0.375 m AHD.	Ghanbarian et al. (2010)					Benson et al. (2014)		van Genuchten et al. (1991)
	Ellithy (2017)	Lenhard et al. (1989)		Morel-Seytoux et al. (1996)		Drainage	Imbibition	
		Rawls	API	Rawls	API			
vG-α [m^{-1}]	14.4911	9.7633	1.7758	2.9396	0.5347	1.8881	2.7791	3.3600
vG-N [-]	1.6471					8.1264	5.5913	4.1609
S_{wr} [-]	0.0924					0.0822		0.1115

Well 050210/1-T4. Elevation 0.875 m AHD.

Well 050210/1-T4. Elevation 0.875 m AHD.	Ghanbarian et al. (2010)					Benson et al. (2014)		van Genuchten et al. (1991)
	Ellithy (2017)	Lenhard et al. (1989)		Morel-Seytoux et al. (1996)		Drainage	Imbibition	
		Rawls	API	Rawls	API			
vG-α [m^{-1}]	14.4911	9.7607	1.7753	2.9471	0.5360	3.4781	5.1196	3.0400
vG-N [-]	1.6487					4.0969	3.6142	4.5511
S_{wr} [-]	0.1094					0.0972		0.1289

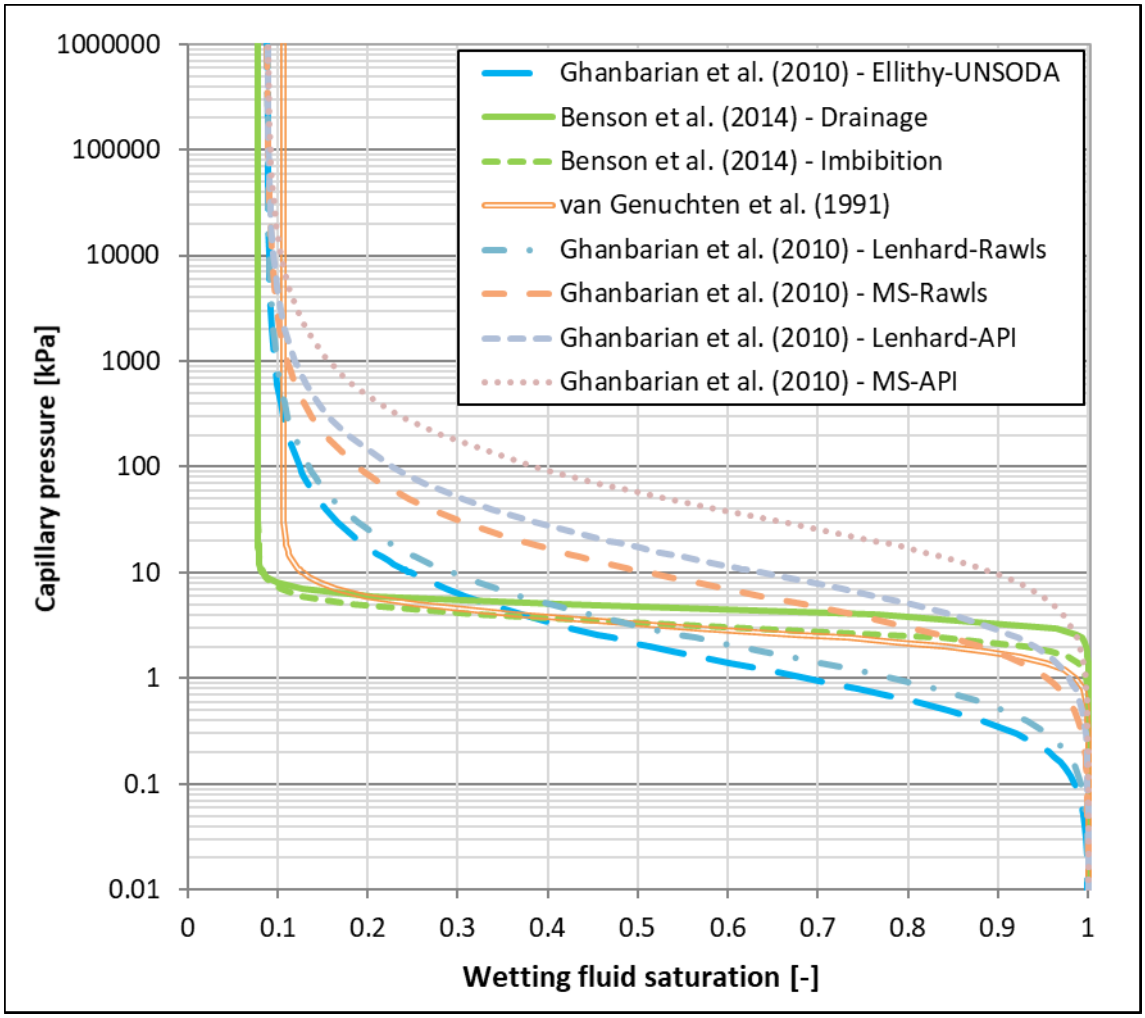
Well 050210/1-T4. Elevation 0.825 m AHD.

Well 050210/1-T4. Elevation 0.825 m AHD.	Ghanbarian et al. (2010)					Benson et al. (2014)		van Genuchten et al. (1991)
	Ellithy (2017)	Lenhard et al. (1989)		Morel-Seytoux et al. (1996)		Drainage	Imbibition	
		Rawls	API	Rawls	API			
vG-α [m^{-1}]	14.4911	9.7615	1.7755	2.9449	0.5356	4.5108	6.6397	4.6100
vG-N [-]	1.6482					3.7170	3.3467	2.9601
S_{wr} [-]	0.0785					0.0697		0.0901

Well 050210/1-T4. Elevation 0.775 m AHD.

Well 050210/1-T4. Elevation 0.775 m AHD.	Ghanbarian et al. (2010)					Benson et al. (2014)		van Genuchten et al. (1991)
	Ellithy (2017)	Lenhard et al. (1989)		Morel-Seytoux et al. (1996)		Drainage	Imbibition	
		Rawls	API	Rawls	API			
vG-α [m^{-1}]	14.4911	9.7647	1.7761	2.9352	0.5339	2.1825	3.2125	3.9300
vG-N [-]	1.6463					7.7768	5.4320	3.4522
S_{wr} [-]	0.0846					0.0752		0.0990

Well 050210/1-T4. Elevation 0.725 m AHD.



Well 050210/1-T4. Elevation 0.725 m AHD.	Ghanbarian et al. (2010)					Benson et al. (2014)		van Genuchten et al. (1991)
	Ellithy (2017)	Lenhard et al. (1989)		Morel-Seytoux et al. (1996)		Drainage	Imbibition	
		Rawls	API	Rawls	API			
vG-α [m^{-1}]	14.4911	9.7630	1.7757	2.9404	0.5348	2.1738	3.1997	3.5900
vG-N [-]	1.6473					7.5855	5.3528	3.8583
S_{wr} [-]	0.0883					0.0785		0.1058

Well 050210/1-T4. Elevation 0.675 m AHD.

Well 050210/1-T4. Elevation 0.675 m AHD.	Ghanbarian et al. (2010)					Benson et al. (2014)		van Genuchten et al. (1991)
	Ellithy (2017)	Lenhard et al. (1989)		Morel-Seytoux et al. (1996)		Drainage	Imbibition	
		Rawls	API	Rawls	API			
vG-α [m^{-1}]	14.4911	9.7631	1.7758	2.9400	0.5347	1.8671	2.7482	3.8500
vG-N [-]	1.6472					8.7628	5.8557	3.5661
S_{wr} [-]	0.0852					0.0757		0.1007

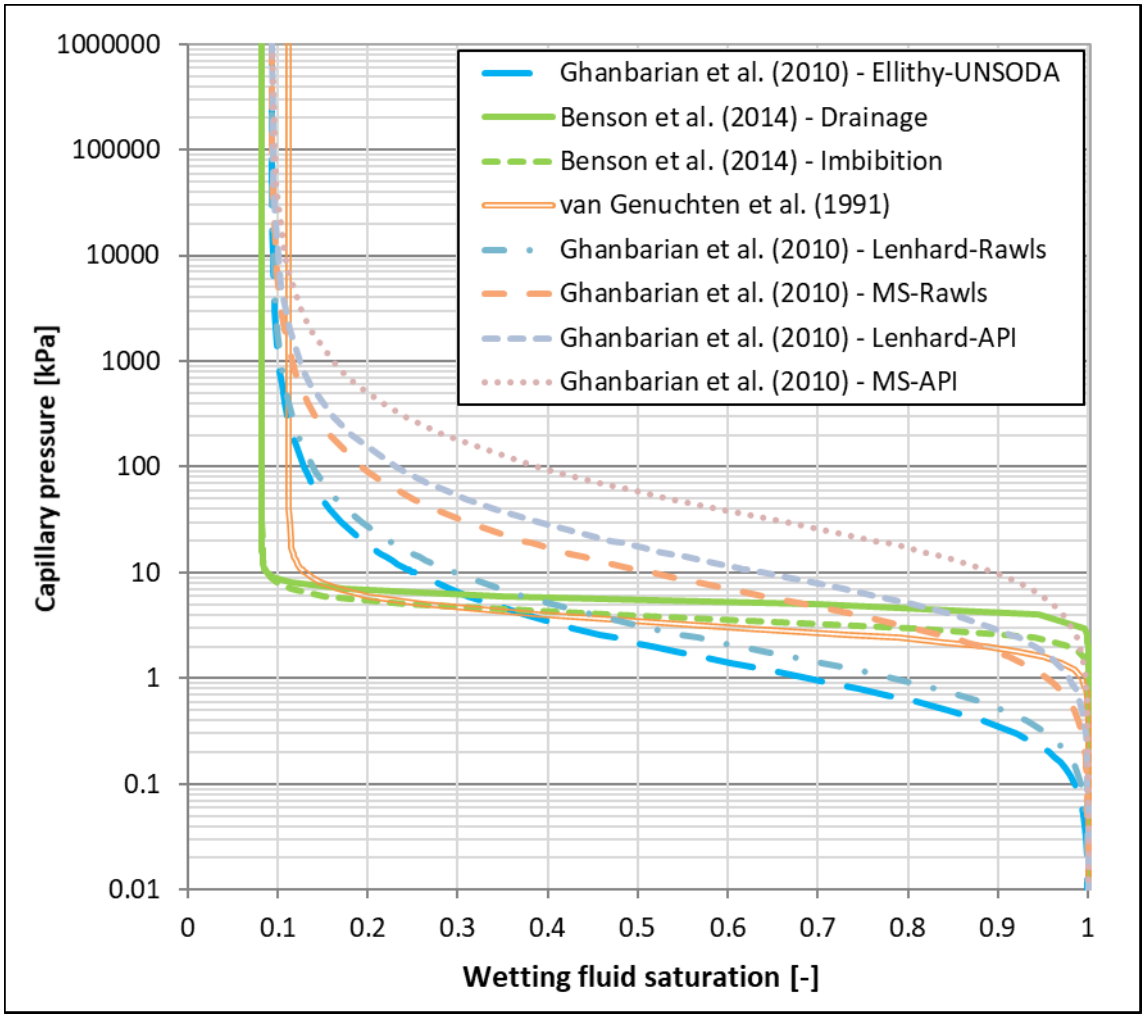
Well 050210/1-T4. Elevation 0.625 m AHD.

Well 050210/1-T4. Elevation 0.625 m AHD.	Ghanbarian et al. (2010)					Benson et al. (2014)		van Genuchten et al. (1991)
	Ellithy (2017)	Lenhard et al. (1989)		Morel-Seytoux et al. (1996)		Drainage	Imbibition	
		Rawls	API	Rawls	API			
vG-α [m^{-1}]	14.4911	9.7632	1.7758	2.9398	0.5347	2.0175	2.9697	3.8500
vG-N [-]	1.6472					8.4459	5.7177	3.5642
S_{wr} [-]	0.0852					0.0757		0.1007

Well 050210/1-T4. Elevation 0.575 m AHD.

Well 050210/1-T4. Elevation 0.575 m AHD.	Ghanbarian et al. (2010)					Benson et al. (2014)		van Genuchten et al. (1991)
	Ellithy (2017)	Lenhard et al. (1989)		Morel-Seytoux et al. (1996)		Drainage	Imbibition	
		Rawls	API	Rawls	API			
vG-α [m^{-1}]	14.4911	9.7629	1.7757	2.9405	0.5348	1.7844	2.6265	3.9000
vG-N [-]	1.6473					8.4085	5.7129	3.5136
S_{wr} [-]	0.0846					0.0752		0.0998

Well 050210/1-T4. Elevation 0.525 m AHD.



Well 050210/1-T4. Elevation 0.525 m AHD.	Ghanbarian et al. (2010)					Benson et al. (2014)		van Genuchten et al. (1991)
	Ellithy (2017)	Lenhard et al. (1989)		Morel-Seytoux et al. (1996)		Drainage	Imbibition	
		Rawls	API	Rawls	API			
vG-α [m^{-1}]	14.4911	9.7635	1.7758	2.9387	0.5345	1.8404	2.7089	3.3300
vG-N [-]	1.6470					9.1897	6.0335	4.1949
S_{wr} [-]	0.0932					0.0828		0.1124

Well 050210/1-T4. Elevation 0.475 m AHD.

Well 050210/1-T4. Elevation 0.475 m AHD.	Ghanbarian et al. (2010)					Benson et al. (2014)		van Genuchten et al. (1991)
	Ellithy (2017)	Lenhard et al. (1989)		Morel-Seytoux et al. (1996)		Drainage	Imbibition	
		Rawls	API	Rawls	API			
vG-α [m^{-1}]	14.4911	9.7663	1.7763	2.9306	0.5330	2.2976	3.3820	3.2000
vG-N [-]	1.6453					4.7864	4.1776	4.3202
S_{wr} [-]	0.0986					0.0876		0.1174

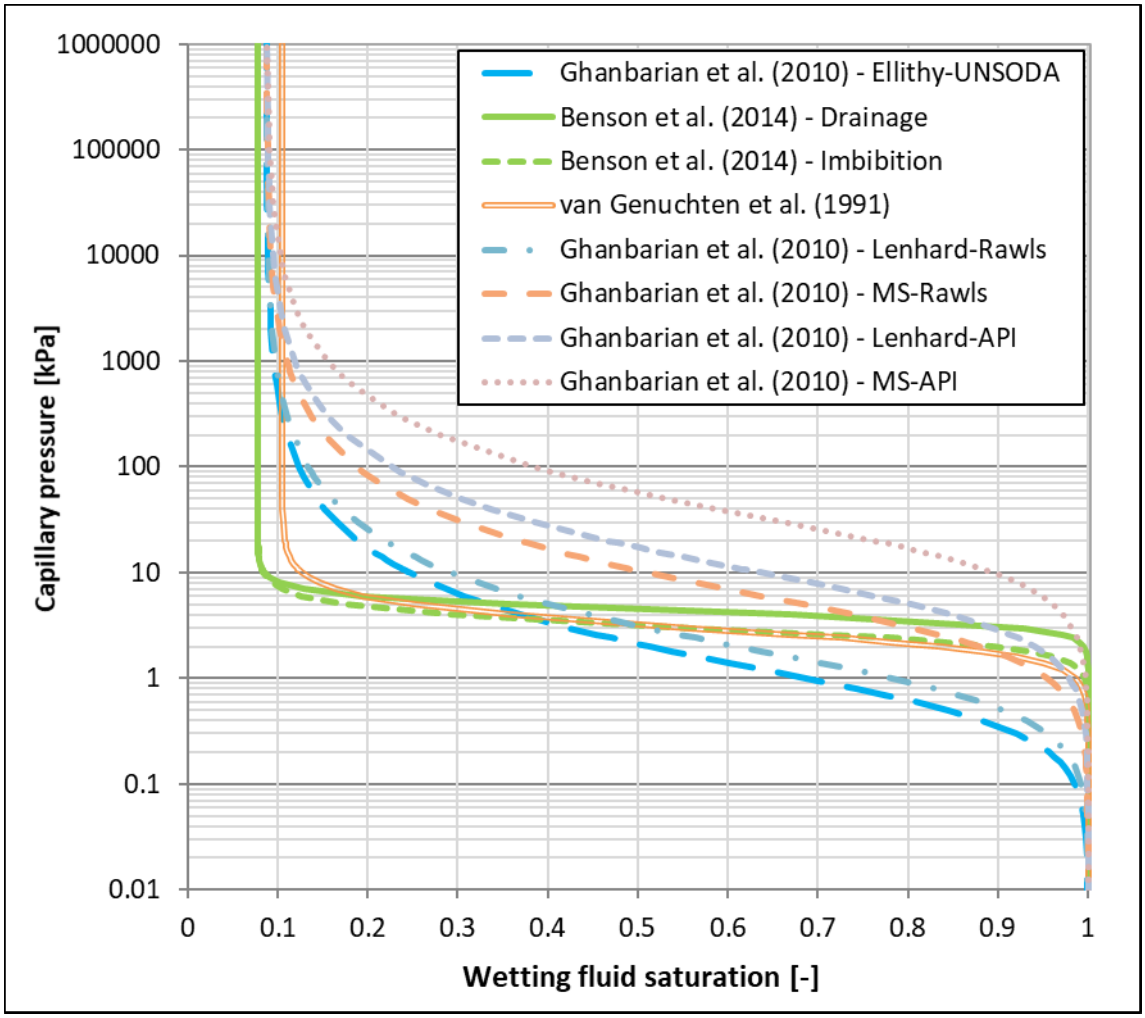
Well 040610/6-T4. Elevation 1.385 m AHD.

Well 040610/6-T4. Elevation 1.385 m AHD.	Ghanbarian et al. (2010)					Benson et al. (2014)		van Genuchten et al. (1991)
	Ellithy (2017)	Lenhard et al. (1989)		Morel-Seytoux et al. (1996)		Drainage	Imbibition	
		Rawls	API	Rawls	API			
vG-α [m^{-1}]	14.4911	9.7606	1.7753	2.9476	0.5361	3.1980	4.7072	3.5500
vG-N [-]	1.6488					4.3941	3.8163	3.9539
S_{wr} [-]	0.0883					0.0785		0.1068

Well 040610/6-T4. Elevation 1.335 m AHD.

Well 040610/6-T4. Elevation 1.335 m AHD.	Ghanbarian et al. (2010)					Benson et al. (2014)		van Genuchten et al. (1991)
	Ellithy (2017)	Lenhard et al. (1989)		Morel-Seytoux et al. (1996)		Drainage	Imbibition	
		Rawls	API	Rawls	API			
vG-α [m^{-1}]	14.4911	9.7612	1.7754	2.9458	0.5358	1.9170	2.8218	4.1200
vG-N [-]	1.6484					8.4578	5.7272	3.3420
S_{wr} [-]	0.0822					0.0731		0.0967

Well 040610/6-T4. Elevation 1.285 m AHD.



Well 040610/6-T4. Elevation 1.285 m AHD.	Ghanbarian et al. (2010)					Benson et al. (2014)		van Genuchten et al. (1991)
	Ellithy (2017)	Lenhard et al. (1989)		Morel-Seytoux et al. (1996)		Drainage	Imbibition	
		Rawls	API	Rawls	API			
vG-α [m^{-1}]	14.4911	9.7622	1.7756	2.9426	0.5352	2.3136	3.4055	3.6300
vG-N [-]	1.6478					6.7235	4.9863	3.8304
S_{wr} [-]	0.0877					0.0779		0.1050

Well 040610/6-T4. Elevation 1.235 m AHD.

Well 040610/6-T4. Elevation 1.235 m AHD.	Ghanbarian et al. (2010)					Benson et al. (2014)		van Genuchten et al. (1991)
	Ellithy (2017)	Lenhard et al. (1989)		Morel-Seytoux et al. (1996)		Drainage	Imbibition	
		Rawls	API	Rawls	API			
vG-α [m^{-1}]	14.4911	9.7617	1.7755	2.9443	0.5355	2.4874	3.6613	3.8200
vG-N [-]	1.6481					5.2277	4.3504	3.6181
S_{wr} [-]	0.0852					0.0757		0.1013

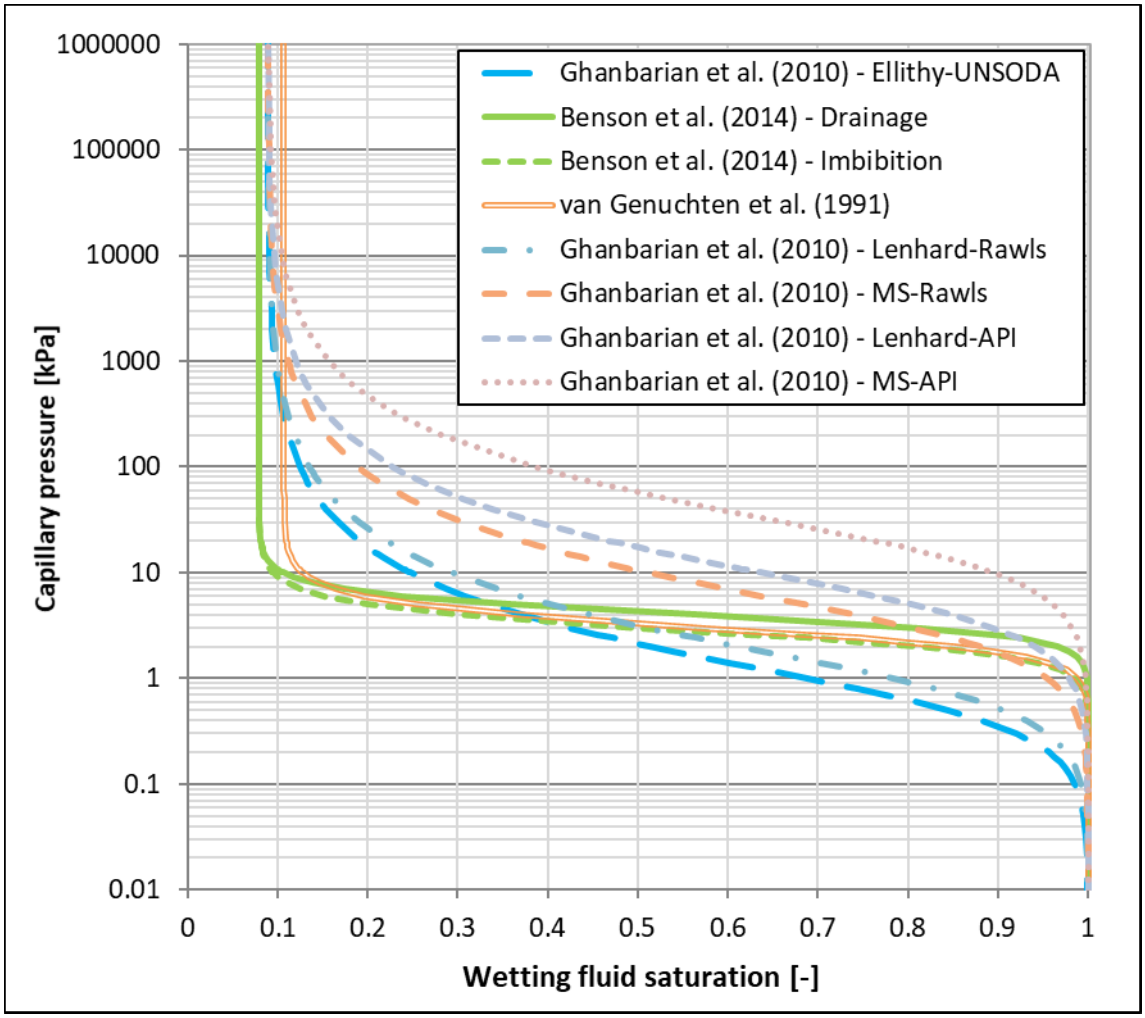
Well 040610/6-T4. Elevation 1.185 m AHD.

Well 040610/6-T4. Elevation 1.185 m AHD.	Ghanbarian et al. (2010)					Benson et al. (2014)		van Genuchten et al. (1991)
	Ellithy (2017)	Lenhard et al. (1989)		Morel-Seytoux et al. (1996)		Drainage	Imbibition	
		Rawls	API	Rawls	API			
vG-α [m^{-1}]	14.4911	9.7628	1.7757	2.9409	0.5349	2.6471	3.8964	3.6400
vG-N [-]	1.6474					4.9373	4.2184	3.8099
S_{wr} [-]	0.0877					0.0779		0.1048

Well 040610/6-T4. Elevation 1.135 m AHD.

Well 040610/6-T4. Elevation 1.135 m AHD.	Ghanbarian et al. (2010)					Benson et al. (2014)		van Genuchten et al. (1991)
	Ellithy (2017)	Lenhard et al. (1989)		Morel-Seytoux et al. (1996)		Drainage	Imbibition	
		Rawls	API	Rawls	API			
vG-α [m^{-1}]	14.4911	9.7631	1.7758	2.9401	0.5348	2.6284	3.8688	3.4600
vG-N [-]	1.6473					4.6625	3.9979	4.0203
S_{wr} [-]	0.0903					0.0803		0.1086

Well 040610/6-T4. Elevation 1.085 m AHD.



Well 040610/6-T4. Elevation 1.085 m AHD.	Ghanbarian et al. (2010)					Benson et al. (2014)		van Genuchten et al. (1991)
	Ellithy (2017)	Lenhard et al. (1989)		Morel-Seytoux et al. (1996)		Drainage	Imbibition	
		Rawls	API	Rawls	API			
vG-α [m^{-1}]	14.4911	9.7625	1.7757	2.9417	0.5351	2.5704	3.7835	3.5400
vG-N [-]	1.6476					4.6600	3.9966	3.9334
S_{wr} [-]	0.0890					0.0791		0.1070

Well 040610/6-T4. Elevation 1.035 m AHD.

Well 040610/6-T4. Elevation 1.035 m AHD.	Ghanbarian et al. (2010)					Benson et al. (2014)		van Genuchten et al. (1991)
	Ellithy (2017)	Lenhard et al. (1989)		Morel-Seytoux et al. (1996)		Drainage	Imbibition	
		Rawls	API	Rawls	API			
vG-α [m^{-1}]	14.4911	9.7631	1.7758	2.9401	0.5348	2.4582	3.6183	4.0800
vG-N [-]	1.6472					4.7913	4.1691	3.3381
S_{wr} [-]	0.0828					0.0736		0.0968

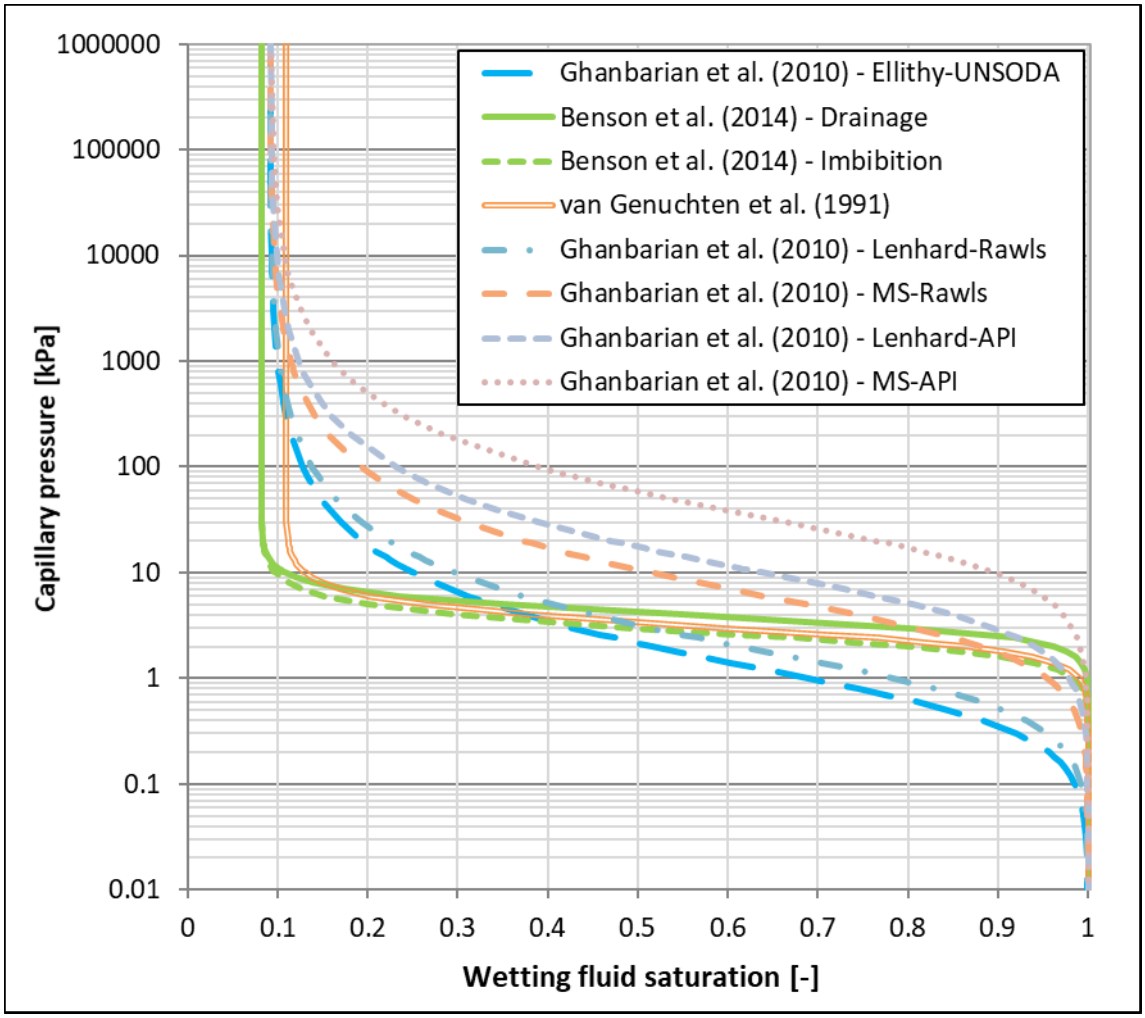
Well 040610/6-T4. Elevation 0.985 m AHD.

Well 040610/6-T4. Elevation 0.985 m AHD.	Ghanbarian et al. (2010)					Benson et al. (2014)		van Genuchten et al. (1991)
	Ellithy (2017)	Lenhard et al. (1989)		Morel-Seytoux et al. (1996)		Drainage	Imbibition	
		Rawls	API	Rawls	API			
vG-α [m^{-1}]	14.4911	9.7645	1.7760	2.9358	0.5340	1.8436	2.7136	3.9300
vG-N [-]	1.6464					8.7376	5.8463	3.4599
S_{wr} [-]	0.0846					0.0752		0.0990

Well 040610/6-T4. Elevation 0.935 m AHD.

Well 040610/6-T4. Elevation 0.935 m AHD.	Ghanbarian et al. (2010)					Benson et al. (2014)		van Genuchten et al. (1991)
	Ellithy (2017)	Lenhard et al. (1989)		Morel-Seytoux et al. (1996)		Drainage	Imbibition	
		Rawls	API	Rawls	API			
vG-α [m^{-1}]	14.4911	9.7658	1.7763	2.9321	0.5333	2.2148	3.2601	3.4700
vG-N [-]	1.6456					5.7795	4.5979	3.9633
S_{wr} [-]	0.0910					0.0809		0.1084

Well 040610/6-T4. Elevation 0.885 m AHD.



Well 040610/6-T4. Elevation 0.885 m AHD.	Ghanbarian et al. (2010)					Benson et al. (2014)		van Genuchten et al. (1991)
	Ellithy (2017)	Lenhard et al. (1989)		Morel-Seytoux et al. (1996)		Drainage	Imbibition	
		Rawls	API	Rawls	API			
vG-α [m^{-1}]	14.4911	9.7665	1.7764	2.9300	0.5329	2.6150	3.8491	3.4400
vG-N [-]	1.6452					4.6061	3.9607	3.9840
S_{wr} [-]	0.0917					0.0815		0.1091

Well 040610/6-T4. Elevation 0.785 m AHD.

Well 040610/6-T4. Elevation 0.785 m AHD.	Ghanbarian et al. (2010)					Benson et al. (2014)		van Genuchten et al. (1991)
	Ellithy (2017)	Lenhard et al. (1989)		Morel-Seytoux et al. (1996)		Drainage	Imbibition	
		Rawls	API	Rawls	API			
vG-α [m^{-1}]	14.4911	9.7671	1.7765	2.9282	0.5326	2.3965	3.5275	3.7600
vG-N [-]	1.6448					4.7281	4.0424	3.5932
S_{wr} [-]	0.0870					0.0774		0.1019

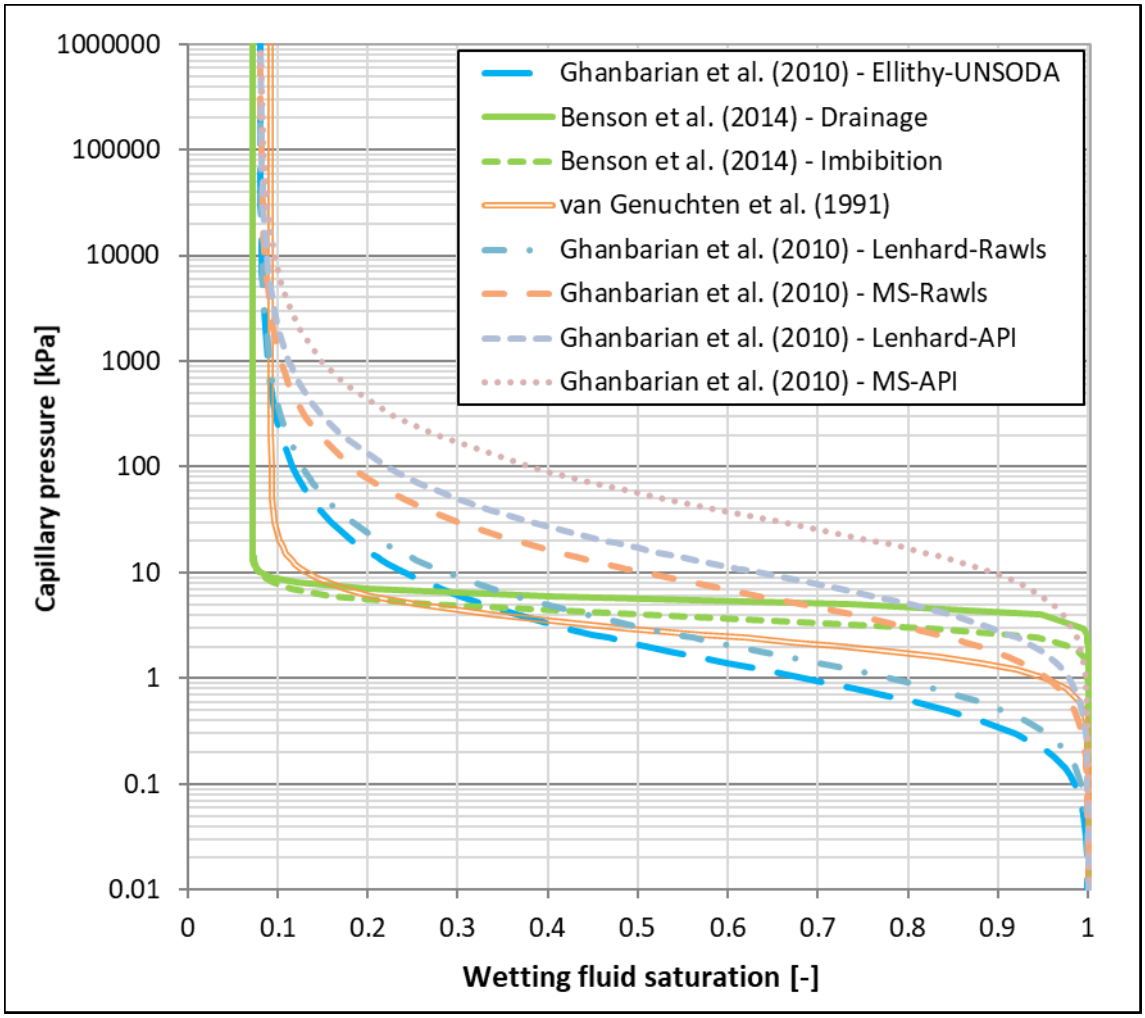
Well 040610/6-T4. Elevation 0.735 m AHD.

Well 040610/6-T4. Elevation 0.735 m AHD.	Ghanbarian et al. (2010)					Benson et al. (2014)		van Genuchten et al. (1991)
	Ellithy (2017)	Lenhard et al. (1989)		Morel-Seytoux et al. (1996)		Drainage	Imbibition	
		Rawls	API	Rawls	API			
vG-α [m^{-1}]	14.4911	9.7629	1.7757	2.9405	0.5348	1.9308	2.8420	3.9000
vG-N [-]	1.6473					9.1986	6.0334	3.5135
S_{wr} [-]	0.0846					0.0752		0.0998

Well 040610/6-T4. Elevation 0.685 m AHD.

Well 040610/6-T4. Elevation 0.685 m AHD.	Ghanbarian et al. (2010)					Benson et al. (2014)		van Genuchten et al. (1991)
	Ellithy (2017)	Lenhard et al. (1989)		Morel-Seytoux et al. (1996)		Drainage	Imbibition	
		Rawls	API	Rawls	API			
vG-α [m^{-1}]	14.4911	9.7643	1.7760	2.9365	0.5341	1.7903	2.6353	4.2300
vG-N [-]	1.6465					8.5674	5.7784	3.1895
S_{wr} [-]	0.0817					0.0726		0.0944

Well 040610/6-T4. Elevation 0.635 m AHD.



Well 040610/6-T4. Elevation 0.635 m AHD.	Ghanbarian et al. (2010)					Benson et al. (2014)		van Genuchten et al. (1991)
	Ellithy (2017)	Lenhard et al. (1989)		Morel-Seytoux et al. (1996)		Drainage	Imbibition	
		Rawls	API	Rawls	API			
vG-α [m^{-1}]	14.4911	9.7640	1.7759	2.9374	0.5343	1.7896	2.6342	4.3600
vG-N [-]	1.6467					8.6038	5.7934	3.0935
S_{wr} [-]	0.0806					0.0716		0.0928

Well 040610/6-T4. Elevation 0.585 m AHD.

Well 040610/6-T4. Elevation 0.585 m AHD.	Ghanbarian et al. (2010)					Benson et al. (2014)		van Genuchten et al. (1991)
	Ellithy (2017)	Lenhard et al. (1989)		Morel-Seytoux et al. (1996)		Drainage	Imbibition	
		Rawls	API	Rawls	API			
vG-α [m^{-1}]	14.4911	9.7631	1.7758	2.9399	0.5347	1.9687	2.8978	4.0900
vG-N [-]	1.6472					9.2680	6.0606	3.3364
S_{wr} [-]	0.0828					0.0736		0.0968

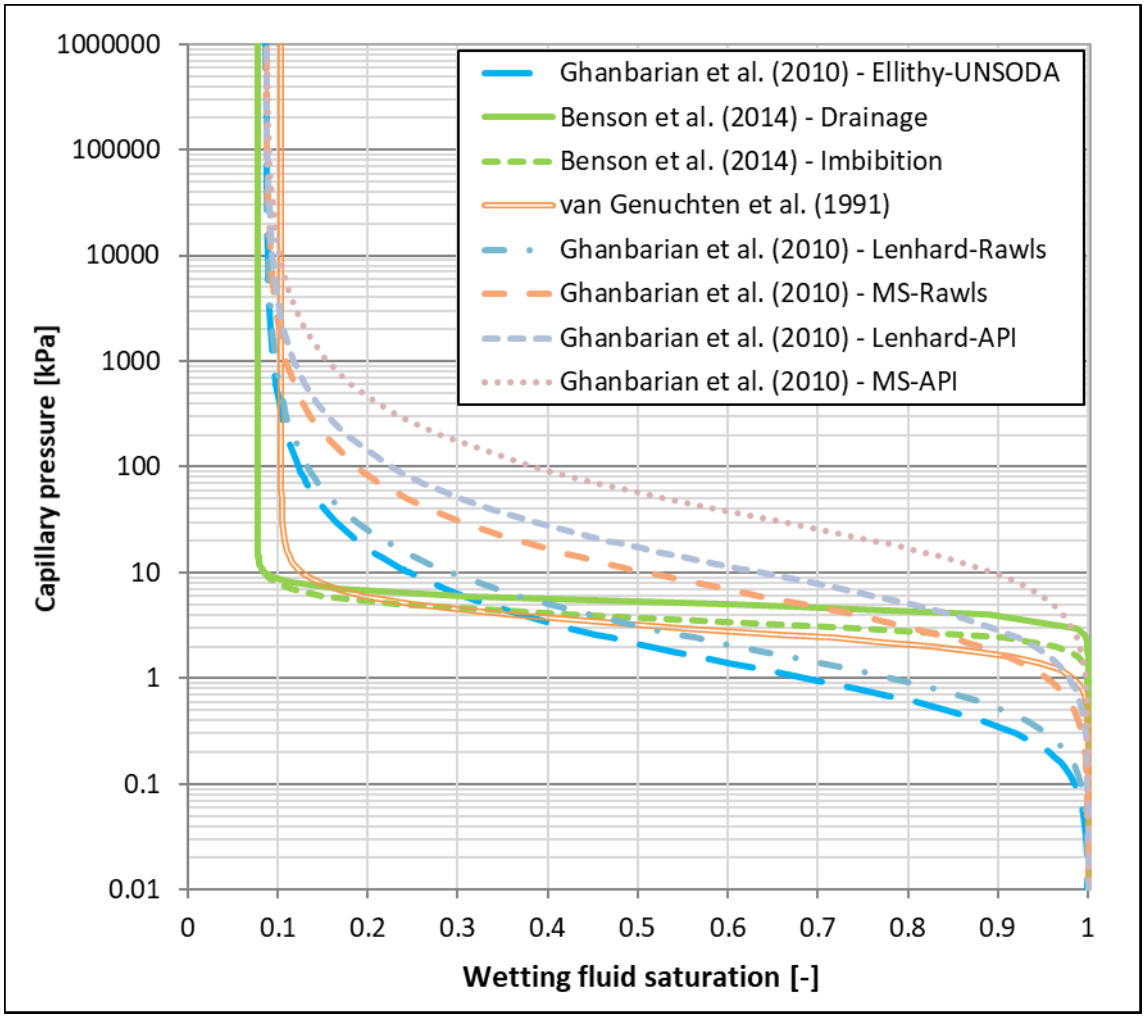
Well 040610/6-T4. Elevation 0.535 m AHD.

Well 040610/6-T4. Elevation 0.535 m AHD.	Ghanbarian et al. (2010)					Benson et al. (2014)		van Genuchten et al. (1991)
	Ellithy (2017)	Lenhard et al. (1989)		Morel-Seytoux et al. (1996)		Drainage	Imbibition	
		Rawls	API	Rawls	API			
vG-α [m^{-1}]	14.4911	9.7643	1.7760	2.9365	0.5341	1.9565	2.8798	3.7600
vG-N [-]	1.6465					8.1552	5.6000	3.6387
S_{wr} [-]	0.0864					0.0768		0.1022

Well 040610/6-T4. Elevation 0.485 m AHD.

Well 040610/6-T4. Elevation 0.485 m AHD.	Ghanbarian et al. (2010)					Benson et al. (2014)		van Genuchten et al. (1991)
	Ellithy (2017)	Lenhard et al. (1989)		Morel-Seytoux et al. (1996)		Drainage	Imbibition	
		Rawls	API	Rawls	API			
vG-α [m^{-1}]	14.4911	9.7641	1.7759	2.9371	0.5342	1.7561	2.5849	3.7600
vG-N [-]	1.6466					8.7272	5.8460	3.6466
S_{wr} [-]	0.0864					0.0768		0.1024

Well 040610/6-T4. Elevation 0.435 m AHD.



Well 040610/6-T4. Elevation 0.435 m AHD.	Ghanbarian et al. (2010)					Benson et al. (2014)		van Genuchten et al. (1991)
	Ellithy (2017)	Lenhard et al. (1989)		Morel-Seytoux et al. (1996)		Drainage	Imbibition	
		Rawls	API	Rawls	API			
vG-α [m^{-1}]	14.4911	9.7624	1.7756	2.9422	0.5351	1.9393	2.8546	3.6800
vG-N [-]	1.6477					7.8784	5.4860	3.7686
S_{wr} [-]	0.0870					0.0774		0.1041

Well 040610/6-T4. Elevation 0.385 m AHD.

Well 040610/6-T4. Elevation 0.385 m AHD.	Ghanbarian et al. (2010)					Benson et al. (2014)		van Genuchten et al. (1991)
	Ellithy (2017)	Lenhard et al. (1989)		Morel-Seytoux et al. (1996)		Drainage	Imbibition	
		Rawls	API	Rawls	API			
vG-α [m^{-1}]	14.4911	9.7651	1.7761	2.9341	0.5337	1.7918	2.6374	3.3500
vG-N [-]	1.6460					8.4997	5.7503	4.1304
S_{wr} [-]	0.0932					0.0828		0.1116

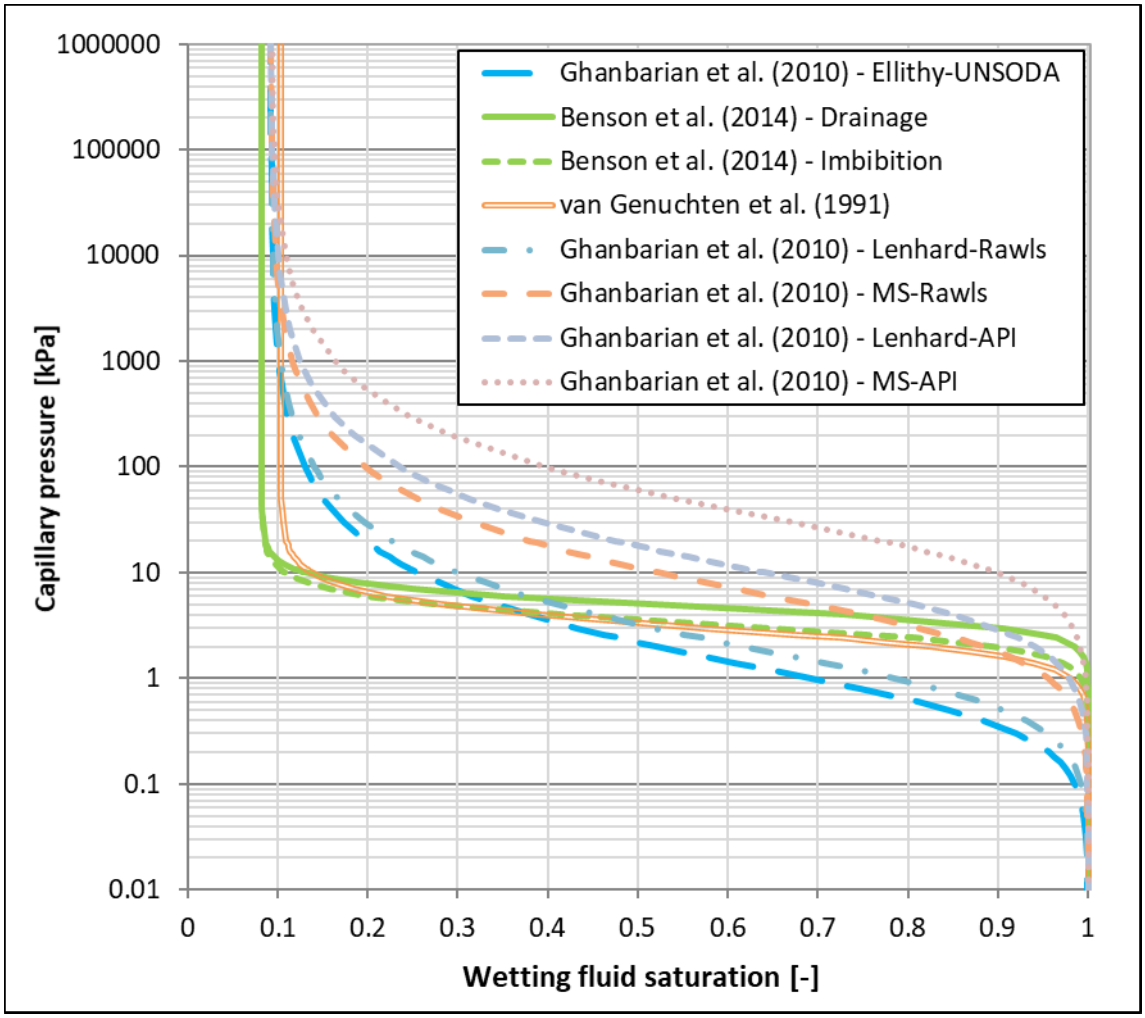
Well 040610/6-T4. Elevation 0.285 m AHD.

Well 040610/6-T4. Elevation 0.285 m AHD.	Ghanbarian et al. (2010)					Benson et al. (2014)		van Genuchten et al. (1991)
	Ellithy (2017)	Lenhard et al. (1989)		Morel-Seytoux et al. (1996)		Drainage	Imbibition	
		Rawls	API	Rawls	API			
vG-α [m^{-1}]	14.4911	9.7653	1.7762	2.9337	0.5336	1.7891	2.6334	3.7800
vG-N [-]	1.6459					8.8783	5.9069	3.6035
S_{wr} [-]	0.0864					0.0768		0.1018

Well 040610/6-T4. Elevation 0.235 m AHD.

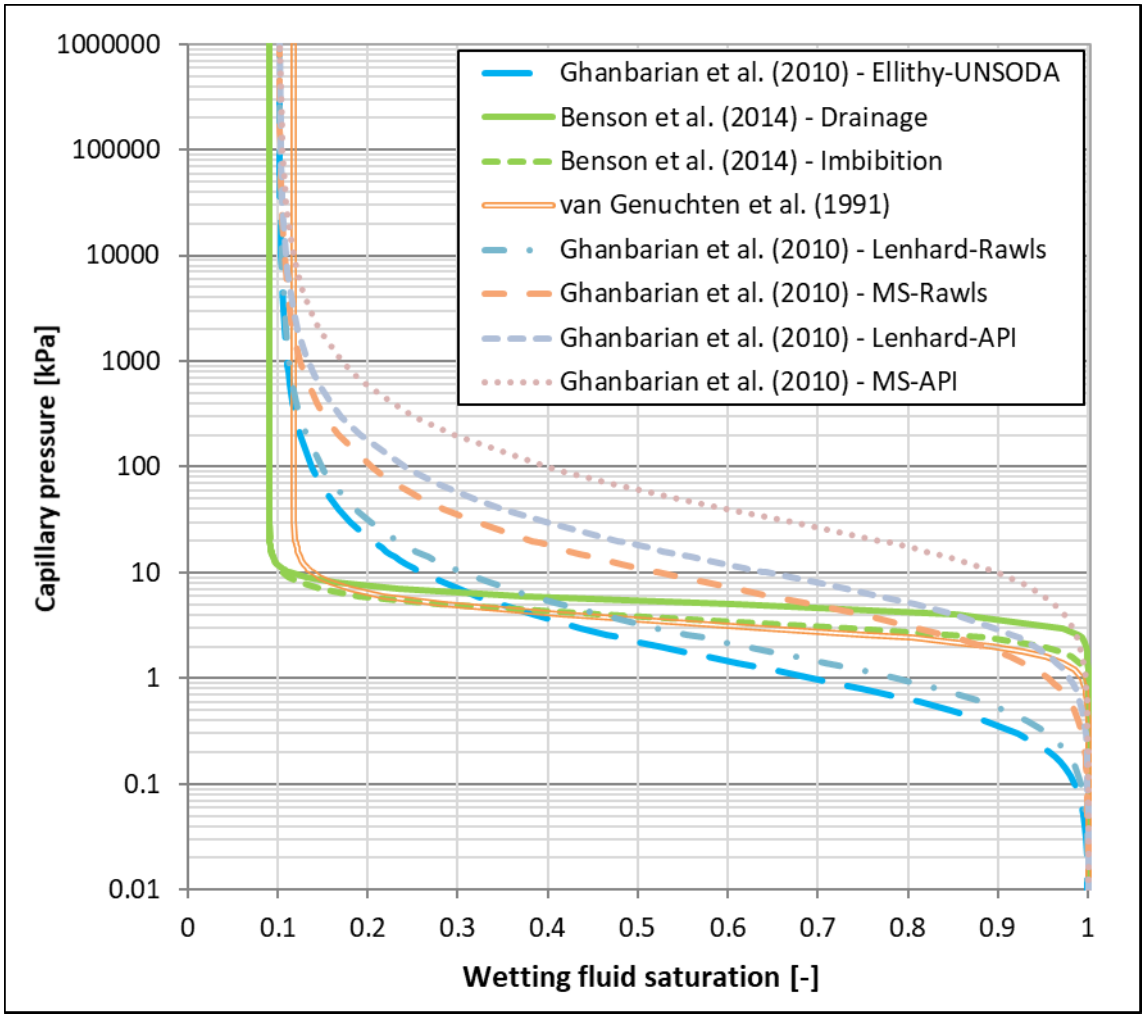
Well 040610/6-T4. Elevation 0.235 m AHD.	Ghanbarian et al. (2010)					Benson et al. (2014)		van Genuchten et al. (1991)
	Ellithy (2017)	Lenhard et al. (1989)		Morel-Seytoux et al. (1996)		Drainage	Imbibition	
		Rawls	API	Rawls	API			
vG-α [m^{-1}]	14.4911	9.7694	1.7769	2.9217	0.5314	1.9368	2.8508	3.3300
vG-N [-]	1.6435					6.9982	5.1209	4.0784
S_{wr} [-]	0.0954					0.0848		0.1124

Well 040610/6-T4. Elevation 0.185 m AHD.



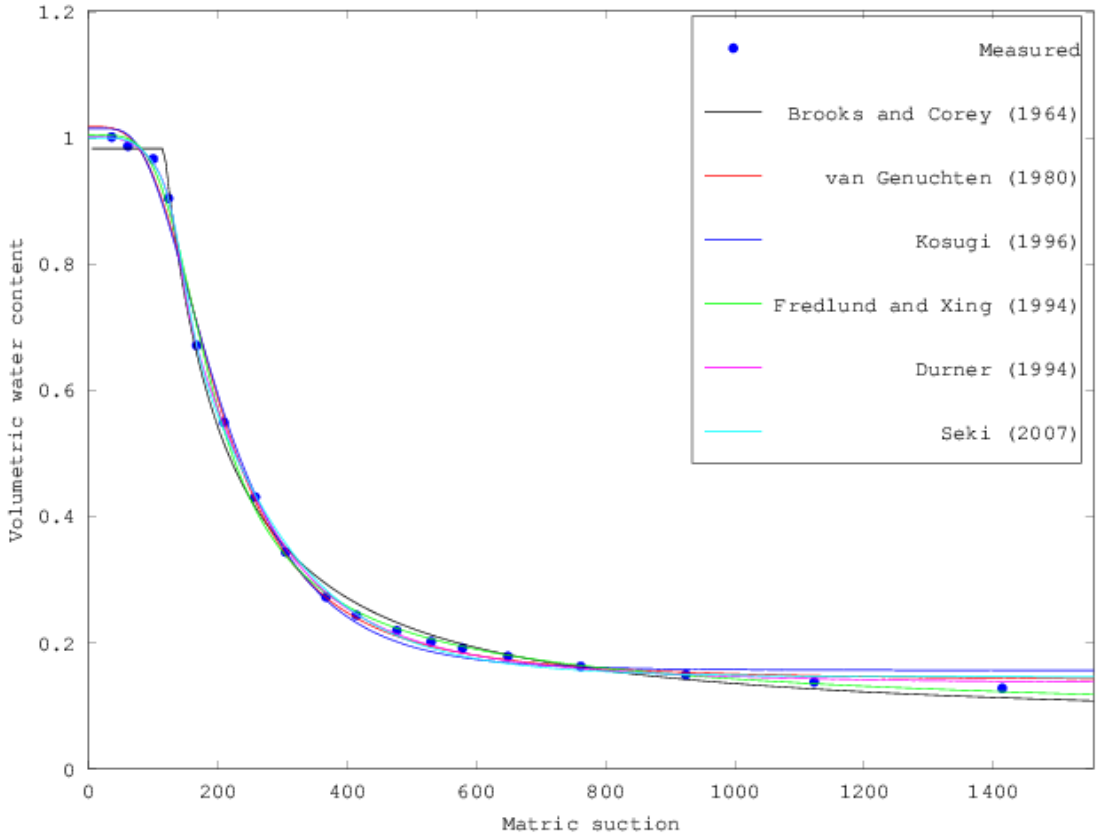
Well 040610/6-T4. Elevation 0.185 m AHD.	Ghanbarian et al. (2010)					Benson et al. (2014)		van Genuchten et al. (1991)
	Ellithy (2017)	Lenhard et al. (1989)		Morel-Seytoux et al. (1996)		Drainage	Imbibition	
		Rawls	API	Rawls	API			
vG-α [m^{-1}]	14.4911	9.7813	1.7791	2.8879	0.5253	2.1644	3.1859	3.6400
vG-N [-]	1.6366					4.6787	4.0114	3.4855
S_{wr} [-]	0.0924					0.0822		0.1035

Well 040610/6-T4. Elevation -0.095 m AHD.



Well 040610/6-T4. Elevation -0.095 m AHD.	Ghanbarian et al. (2010)					Benson et al. (2014)		van Genuchten et al. (1991)
	Ellithy (2017)	Lenhard et al. (1989)		Morel-Seytoux et al. (1996)		Drainage	Imbibition	
		Rawls	API	Rawls	API			
vG-α [m^{-1}]	14.4911	9.7736	1.7777	2.9096	0.5292	1.9454	2.8635	3.2500
vG-N [-]	1.6410					6.3106	4.8349	4.1034
S_{wr} [-]	0.1019					0.0906		0.1173

Well 040610/2-T4. Elevation 1.061-1.011 m AHD. Drainage curve.

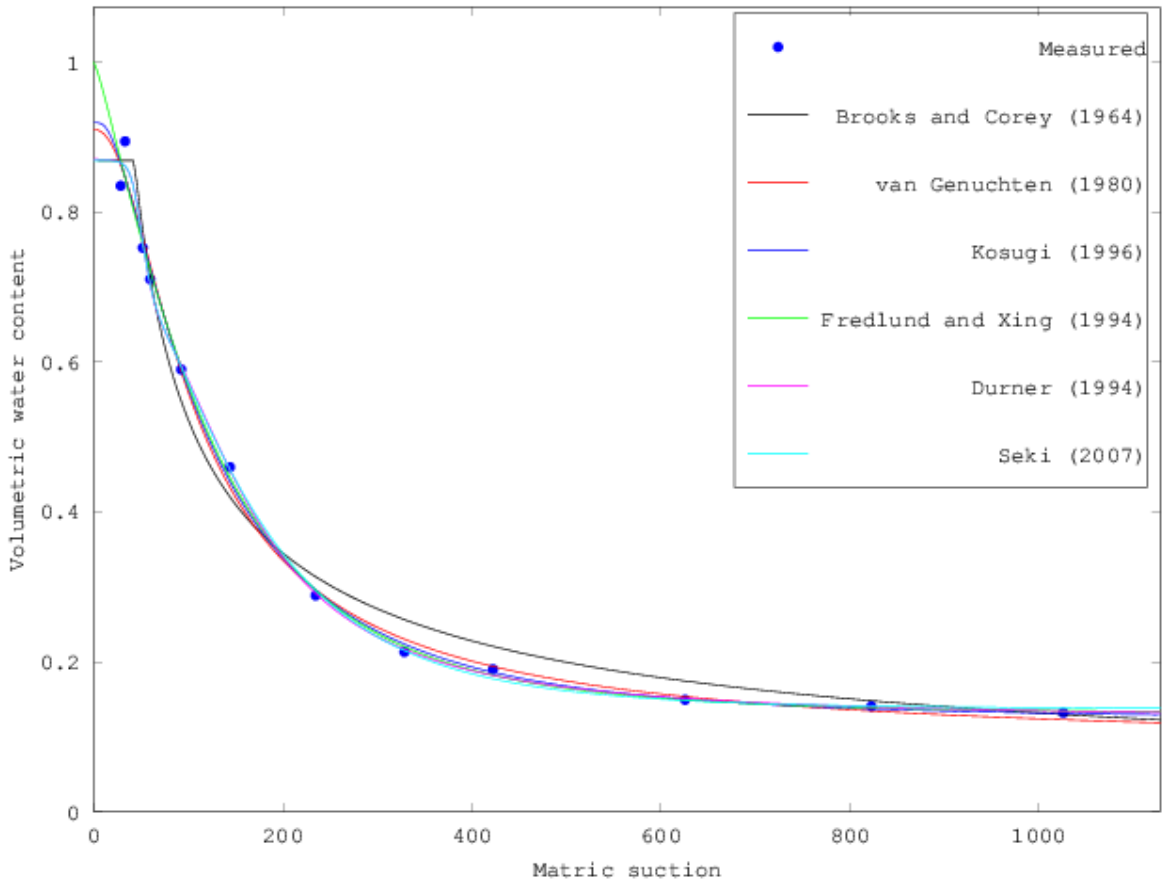


3.75-3.80 drainage

hc	Sw
35.973	1.0014
60.997	0.98696
100.1	0.96667
123.56	0.90435
167.35	0.67101
209.58	0.54928
258.06	0.43043
304.99	0.34348
367.55	0.27246
414.47	0.24348
477.03	0.21884
530.21	0.20145
578.69	0.1913
649.07	0.17826
761.68	0.16232
924.34	0.14928
1123	0.13768
1413.9	0.12754

Model	Equation	Parameters	R^2	AIC
Brooks and Corey	$S_e = \begin{cases} \left(\frac{h}{h_b}\right)^{-\lambda} & (h > h_b) \\ 1 & (h \le h_b) \end{cases}$	θ_s = 0.98318 θ_r = 0.070309 h_b = 117.23 λ = 1.2338	0.99774	-142.74
van Genuchten	$S_e = \left[\frac{1}{1+(\alpha h)^n}\right]^m \quad (m = 1 - 1/n)$	θ_s = 1.0179 θ_r = 0.13904 α = 0.0056838 n = 3.4969	0.99766	-142.13
Kosugi	$S_e = Q\left[\frac{\ln(h/h_m)}{\sigma}\right]$	θ_s = 1.0148 θ_r = 0.15624 h_m = 202.76 σ = 0.52807	0.99631	-133.97
Fredlund and Xing	$S_e = \left[\frac{1}{\ln\left[e+(h/a)^n\right]}\right]^m$	θ_s = 1.0047 θ_r = 2.1445e-08 a = 149.46 m = 0.91133 n = 4.4872	0.99871	-150.81
Durner	$S_e = w_1\left[\frac{1}{1+(\alpha_1 h)^{n_1}}\right]^{m_1} + (1-w_1)\left[\frac{1}{1+(\alpha_2 h)^{n_2}}\right]^{m_2}$	θ_s = 1.0015 θ_r = 0.13306 w_1 = 0.18863 α_1 = 0.0070768 n_1 = 14.857 α_2 = 0.0049447 n_2 = 3.4859	0.99970	-173.02
Seki	$S_e = w_1 Q\left[\frac{\ln(h/h_{m1})}{\sigma_1}\right] + (1-w_1) Q\left[\frac{\ln(h/h_{m2})}{\sigma_2}\right]$	θ_s = 1.0002 θ_r = 0.14566 w_1 = 0.21623 h_{m1} = 149.03 σ_1 = 0.13676 h_{m2} = 234.68 σ_2 = 0.54731	0.99916	-154.53

Well 040610/2-T4. Elevation 1.061-1.011 m AHD. Imbibition curve.



Appendix G: Computation of sensitivity indices

The values shown in Table G.1, Table G.2, Table G.3, and Table G.4 were used for the computation of SI values in section 8.4.2. D_i^{min} and D_i^{max} refer to the minimum and maximum value of total V_n or free T_n obtained after perturbing any input parameter within the most likely range (*i=1*), extended range (*i=2*), or conservative range (*i=3*).

Table G.1. LDRM predictions of V_n [m] employed in the computation of sensitivity indices.

	D_3^{min}	D_2^{min}	D_1^{min}	D_1^{max}	D_2^{max}	D_3^{max}
Φ [-]	0.025	0.050	0.069	0.078	0.104	0.119
k_{sw} [m/day]	0.074	0.074	0.074	0.074	0.074	0.074
vG-α [m^{-1}]	0.007	0.008	0.022	0.151	0.193	0.228
vG-N [-]	0.007	0.058	0.069	0.120	0.130	0.168
S_{wr} [%]	0.082	0.078	0.076	0.073	0.069	0.019
S_{nr}^{max} [%]	0.068	0.071	0.072	0.089	0.193	0.452
S_{ne}^{max} [%]	0.094	0.083	0.081	0.057	0.043	0.034
ρ_n [mg/cm^3]	0.074	0.074	0.074	0.074	0.074	0.074
η_n [cP]	0.067	0.070	0.073	0.077	0.077	0.078
σ_{an} [mN/m]	0.120	0.099	0.090	0.069	0.025	0.012
σ_{nw} [mN/m]	0.025	0.050	0.069	0.078	0.104	0.119
b_n [m]	0.017	0.046	0.070	0.079	0.107	0.153

Table G.2. LNAPLTRANS predictions of V_n [m] used for the computation of sensitivity indices.

	D_3^{min}	D_2^{min}	D_1^{min}	D_1^{max}	D_2^{max}	D_3^{max}
Φ [-]	0.034	0.068	0.034	0.106	0.141	0.162
k_{sw} [m/day]	0.101	0.101	0.101	0.101	0.101	0.101
vG-α [m^{-1}]	0.000	0.004	0.029	0.211	0.261	0.293
vG-N [-]	0.084	0.097	0.100	0.113	0.116	0.133
S_{wr} [%]	0.110	0.105	0.103	0.099	0.095	0.036
S_{nr}^{max} [%]	0.099	0.100	0.100	0.107	0.149	0.256
S_{ne}^{max} [%]	0.083	0.083	0.088	0.107	0.205	0.500
ρ_n [mg/cm^3]	0.128	0.112	0.110	0.077	0.058	0.047
η_n [cP]	0.101	0.101	0.101	0.101	0.101	0.101
σ_{an} [mN/m]	0.084	0.091	0.099	0.106	0.107	0.108
σ_{nw} [mN/m]	0.150	0.127	0.117	0.095	0.052	0.038
b_n [m]	0.032	0.066	0.095	0.107	0.142	0.202

Table G.3. LDRM predictions of T_n [m^2/day] employed in the computation of sensitivity indices.

	D_3^{min}	D_2^{min}	D_1^{min}	D_1^{max}	D_2^{max}	D_3^{max}
Φ [-]	0.095	0.095	0.095	0.095	0.095	0.095
k_{sw} [m/day]	0.000	0.001	0.024	0.826	3.151	315.109
vG-α [m^{-1}]	0.000	0.000	0.004	0.565	1.033	1.541
vG-N [-]	0.001	0.052	0.080	0.321	0.405	1.066
S_{wr} [%]	0.117	0.104	0.099	0.089	0.082	0.005
S_{nr}^{max} [%]	0.086	0.090	0.092	0.117	0.384	1.839
S_{ne}^{max} [%]	0.128	0.109	0.105	0.065	0.040	0.027
ρ_n [mg/cm^3]	0.108	0.105	0.097	0.070	0.060	0.059
η_n [cP]	0.089	0.091	0.094	0.096	0.097	0.097
σ_{an} [mN/m]	0.204	0.151	0.129	0.083	0.012	0.002
σ_{nw} [mN/m]	0.095	0.095	0.095	0.095	0.095	0.095
b_n [m]	0.006	0.040	0.085	0.105	0.178	0.329

Table G.4. LNAPLTRANS predictions of free T_n [m^2/day] for the computation of sensitivity indices.

	D_3^{min}	D_2^{min}	D_1^{min}	D_1^{max}	D_2^{max}	D_3^{max}
Φ [-]	0.053	0.053	0.053	0.053	0.053	0.053
k_{sw} [m/day]	0.000	0.000	0.013	0.464	1.770	177.000
vG-α [m^{-1}]	0.000	0.000	0.000	1.043	2.028	2.829
vG-N [-]	0.070	0.057	0.054	0.050	0.052	0.115
S_{wr} [%]	0.053	0.053	0.053	0.053	0.053	0.046
S_{nr}^{max} [%]	0.055	0.054	0.054	0.049	0.028	0.005
S_{ne}^{max} [%]	0.053	0.053	0.053	0.053	0.053	0.053
ρ_n [mg/cm^3]	0.124	0.079	0.073	0.017	0.003	0.001
η_n [cP]	0.060	0.059	0.054	0.040	0.034	0.033
σ_{an} [mN/m]	0.024	0.035	0.048	0.065	0.066	0.069
σ_{nw} [mN/m]	0.212	0.123	0.093	0.042	0.002	0.000
b_n [m]	0.000	0.010	0.044	0.064	0.155	0.397